Lecture Notes in Electrical Engineering 569

T. Hitendra Sarma
V. Sankar
Rafi Ahamed Shaik *Editors*

Emerging Trends in Electrical, Communications, and Information Technologies

Proceedings of ICECIT-2018

Springer

Lecture Notes in Electrical Engineering

Volume 569

Series Editors

Leopoldo Angrisani, Department of Electrical and Information Technologies Engineering, University of Napoli Federico II, Naples, Italy
Marco Arteaga, Departament de Control y Robótica, Universidad Nacional Autónoma de México, Coyoacán, Mexico
Bijaya Ketan Panigrahi, Electrical Engineering, Indian Institute of Technology Delhi, New Delhi, Delhi, India
Samarjit Chakraborty, Fakultät für Elektrotechnik und Informationstechnik, TU München, Munich, Germany
Jiming Chen, Zhejiang University, Hangzhou, Zhejiang, China
Shanben Chen, Materials Science and Engineering, Shanghai Jiao Tong University, Shanghai, China
Tan Kay Chen, Department of Electrical and Computer Engineering, National University of Singapore, Singapore, Singapore
Rüdiger Dillmann, Humanoids and Intelligent Systems Lab, Karlsruhe Institute for Technology, Karlsruhe, Baden-Württemberg, Germany
Haibin Duan, Beijing University of Aeronautics and Astronautics, Beijing, China
Gianluigi Ferrari, Università di Parma, Parma, Italy
Manuel Ferre, Centre for Automation and Robotics CAR (UPM-CSIC), Universidad Politécnica de Madrid, Madrid, Spain
Sandra Hirche, Department of Electrical Engineering and Information Science, Technische Universität München, Munich, Germany
Faryar Jabbari, Department of Mechanical and Aerospace Engineering, University of California, Irvine, CA, USA
Limin Jia, State Key Laboratory of Rail Traffic Control and Safety, Beijing Jiaotong University, Beijing, China
Janusz Kacprzyk, Systems Research Institute, Polish Academy of Sciences, Warsaw, Poland
Alaa Khamis, German University in Egypt El Tagamoa El Khames, New Cairo City, Egypt
Torsten Kroeger, Stanford University, Stanford, CA, USA
Qilian Liang, Department of Electrical Engineering, University of Texas at Arlington, Arlington, TX, USA
Ferran Martin, Departament d'Enginyeria Electrònica, Universitat Autònoma de Barcelona, Bellaterra, Barcelona, Spain
Tan Cher Ming, College of Engineering, Nanyang Technological University, Singapore, Singapore
Wolfgang Minker, Institute of Information Technology, University of Ulm, Ulm, Germany
Pradeep Misra, Department of Electrical Engineering, Wright State University, Dayton, OH, USA
Sebastian Möller, Quality and Usability Lab, TU Berlin, Berlin, Germany
Subhas Mukhopadhyay, School of Engineering & Advanced Technology, Massey University, Palmerston North, Manawatu-Wanganui, New Zealand
Cun-Zheng Ning, Electrical Engineering, Arizona State University, Tempe, AZ, USA
Toyoaki Nishida, Graduate School of Informatics, Kyoto University, Kyoto, Japan
Federica Pascucci, Dipartimento di Ingegneria, Università degli Studi "Roma Tre", Rome, Italy
Yong Qin, State Key Laboratory of Rail Traffic Control and Safety, Beijing Jiaotong University, Beijing, China
Gan Woon Seng, School of Electrical & Electronic Engineering, Nanyang Technological University, Singapore, Singapore
Joachim Speidel, Institute of Telecommunications, Universität Stuttgart, Stuttgart, Baden-Württemberg, Germany
Germano Veiga, Campus da FEUP, INESC Porto, Porto, Portugal
Haitao Wu, Academy of Opto-electronics, Chinese Academy of Sciences, Beijing, China
Junjie James Zhang, Charlotte, NC, USA

The book series *Lecture Notes in Electrical Engineering* (LNEE) publishes the latest developments in Electrical Engineering - quickly, informally and in high quality. While original research reported in proceedings and monographs has traditionally formed the core of LNEE, we also encourage authors to submit books devoted to supporting student education and professional training in the various fields and applications areas of electrical engineering. The series cover classical and emerging topics concerning:

- Communication Engineering, Information Theory and Networks
- Electronics Engineering and Microelectronics
- Signal, Image and Speech Processing
- Wireless and Mobile Communication
- Circuits and Systems
- Energy Systems, Power Electronics and Electrical Machines
- Electro-optical Engineering
- Instrumentation Engineering
- Avionics Engineering
- Control Systems
- Internet-of-Things and Cybersecurity
- Biomedical Devices, MEMS and NEMS

For general information about this book series, comments or suggestions, please contact leontina.dicecco@springer.com.

To submit a proposal or request further information, please contact the Publishing Editor in your country:

China

Jasmine Dou, Associate Editor (jasmine.dou@springer.com)

India

Swati Meherishi, Executive Editor (swati.meherishi@springer.com)
Aninda Bose, Senior Editor (aninda.bose@springer.com)

Japan

Takeyuki Yonezawa, Editorial Director (takeyuki.yonezawa@springer.com)

South Korea

Smith (Ahram) Chae, Editor (smith.chae@springer.com)

Southeast Asia

Ramesh Nath Premnath, Editor (ramesh.premnath@springer.com)

USA, Canada:

Michael Luby, Senior Editor (michael.luby@springer.com)

All other Countries:

Leontina Di Cecco, Senior Editor (leontina.dicecco@springer.com)
Christoph Baumann, Executive Editor (christoph.baumann@springer.com)

**** Indexing: The books of this series are submitted to ISI Proceedings, EI-Compendex, SCOPUS, MetaPress, Web of Science and Springerlink ****

More information about this series at http://www.springer.com/series/7818

T. Hitendra Sarma · V. Sankar ·
Rafi Ahamed Shaik
Editors

Emerging Trends in Electrical, Communications, and Information Technologies

Proceedings of ICECIT-2018

Springer

Editors
T. Hitendra Sarma
Department of Computer Science
and Engineering
Srinivasa Ramanujan Institute
of Technology
Anantapur, Andhra Pradesh, India

V. Sankar
Department of Electrical Engineering
JNTUA College of Engineering
Ananthapuramu, Andhra Pradesh, India

Rafi Ahamed Shaik
Department of Electronics
and Electrical Engineering
Indian Institute of Technology Guwahati
Guwahati, Assam, India

ISSN 1876-1100 ISSN 1876-1119 (electronic)
Lecture Notes in Electrical Engineering
ISBN 978-981-13-8941-2 ISBN 978-981-13-8942-9 (eBook)
https://doi.org/10.1007/978-981-13-8942-9

© Springer Nature Singapore Pte Ltd. 2020
This work is subject to copyright. All rights are reserved by the Publisher, whether the whole or part of the material is concerned, specifically the rights of translation, reprinting, reuse of illustrations, recitation, broadcasting, reproduction on microfilms or in any other physical way, and transmission or information storage and retrieval, electronic adaptation, computer software, or by similar or dissimilar methodology now known or hereafter developed.
The use of general descriptive names, registered names, trademarks, service marks, etc. in this publication does not imply, even in the absence of a specific statement, that such names are exempt from the relevant protective laws and regulations and therefore free for general use.
The publisher, the authors and the editors are safe to assume that the advice and information in this book are believed to be true and accurate at the date of publication. Neither the publisher nor the authors or the editors give a warranty, expressed or implied, with respect to the material contained herein or for any errors or omissions that may have been made. The publisher remains neutral with regard to jurisdictional claims in published maps and institutional affiliations.

This Springer imprint is published by the registered company Springer Nature Singapore Pte Ltd.
The registered company address is: 152 Beach Road, #21-01/04 Gateway East, Singapore 189721, Singapore

Organizing Committee

Chief Patron

Smt. J. Padmavathy, Chair Person, SRIT, Ananthapuramu

Patron

Sri. Aluru Sambasiva Reddy, Correspondent and Secretary, SRIT, Ananthapuramu

Co-patron

Mr. K. Jagan Mohan Reddy, Chief Executive Officer, SRIT, Ananthapuramu
Mr. M. Ranjit Reddy, Chief Administrative Officer, SRIT, Ananthapuramu

General Chair

Prof. L. M. Patnaik, Former Vice Chancellor, Defence Institute of Advanced Technology, Pune
Honorary Professor in National Institute of Advanced Studies, IISc, Bangalore

Organizing Chair

Dr. T. Hitendra Sarma, Principal, SRIT, Ananthapuramu

Program Chair

Prof. V. Sankar, JNTUA, Ananthapuramu
Prof. Rafi Ahamed Shaik, IIT, Guwahati
Dr. T. Hitendra Sarma, Principal, SRIT, Ananthapuramu

Program Co-Chair

Dr. G. Bala Krishna, HOD, EEE, SRIT, Ananthapuramu
Dr. M. L. Ravichandra, HOD, ECE, SRIT, Ananthapuramu
Dr. B. Lakshmi Narayana Reddy, HOD, CSE, SRIT, Ananthapuramu

International Program Committee

Dr. Susana Hernandez, Technical University, Madrid, Spain
Dr. Ulrik, Umea University, Sweden
Dr. Jack Singh, Director of Swinburne's Digital Innovation Lab, Australia
Dr. T. Gunashekaran, Muscat, Sultanate of Oman
Dr. Maheswara Rao Valluri, Fiji National University, Fiji
Dr. T. Sreenivas Sremath, Auckland University of Technology, New Zealand
Dr. N. Subba Reddy, Gyeongsang National University, South Korea
Dr. Christopher Shelley, USA
Dr. V. Suresh Babu, Arclabs Research and Innovation Center, Ireland

Technical Program Committee

Dr. Susana, Technical University of Madrid (UPM), Spain
Dr. V. Maheswara Rao, Fiji National University, Fiji
Dr. M. Thanveer, IIT, Indore
Dr. K. Sivakumar, IIT, Hyderabad
Dr. M. Veerachary, IIT, Delhi
Dr. B. S. Daya Sagar, ISI, Bangalore
Dr. P. Viswanath, IIIT, Sri City, Chittoor
Dr. E. Suresh Babu, NIT, Warangal
Dr. Altaf QH Badar, NIT, Warangal
Dr. A. Kirubakaran, NIT, Warangal
Dr. P. Suresh Babu, NIT, Warangal
Dr. D. Sreenivasa Rao, NIT, Warangal

Dr. Parthiban Perumal, NIT, Surathkal
Dr. Sachin Jain, NIT, Warangal
Dr. A. Mahesh, NIT, Kurukshetra
Dr. M. Pandu Ranga Prasad, NIT, Kurukshetra
Dr. G. L. Pahuja, NIT, Kurukshetra
Dr. K. Krishna Sharma, NIT, Kurukshetra
Dr. S. Kumarvel, NIT, Calicut
Dr. Aniruddha Bhattacharya, NIT, Agartala
Dr. P. Gopa Kumar, NIT, Calicut
Dr. Akhilesh Swarup, NIT, Kurukshetra
Dr. Biman Saharoy, NIT, Agartala
Dr. Nidul Sinha, NIT, Silchar
Dr. D. M. Vinod Kumar, NIT, Warangal
Dr. Manoranjan Sahoo, NIT, Trichy
Dr. T. Kishore Kumar, NIT, Warangal
Dr. N. V. S. Narasimha Sarma, NIT, Warangal
Dr. P. Srihari Rao, NIT, Warangal
Dr. M. V. Raghunadh, NIT, Warangal
Dr. P. Prithvi, NIT, Warangal
Dr. V. Rama, NIT, Warangal
Dr. Kalpana Naidu, NIT, Warangal
Dr. Rahul Jashvantbhai Pandya, NIT, Warangal
Dr. Mohammad Farukh Hashmi, NIT, Warangal
Dr. M. Surya Prakash, NIT, Calicut
Dr. K. Naga Srinivas Rao, NIT, Warangal
Dr. Gopiram, NIT, Warangal
Dr. Puli Kishore Kumar, NIT, Tadepalligudem
Dr. Saurabh Kumar, NIT, Tadepalligudem
Dr. Kiran Kumar Gurrala, NIT, Tadepalligudem
Dr. Naresh Kumar, ISRO, Bangalore
Mr. Abhishek Choudhary, IBM, Hyderabad
Mr. Abhisheik Kumar, IBM Research, Bangalore, India
Dr. C. Shoba Bindu, JNTUCEA, Ananthapuramu
Dr. K. Madhavi, JNTUCEA, Ananthapuramu
Dr. R. Kiranmayi, JNTUCEA, Ananthapuramu
Dr. P. Sujatha, JNTUCEA, Ananthapuramu
Dr. K. Jithendra Gowd, JNTUCEA, Ananthapuramu
Dr. G. Mamatha, JNTUCEA, Ananthapuramu
Dr. V. Ganesh, JNTUACEP, Pulivendula
Dr. S. Sivanagaraju, JNTUK, Kakinada
Dr. N. Visali, JNTUCEK, Kalikiri
Dr. S. Chandra Mohan Reddy, JNTUACEP, Pulivendula
Dr. A. Rama Mohan Reddy, Sri Venkateswara University, Tirupati
Dr. M. Humerakhanam, Sri Venkateswara University, Tirupati
Dr. T. Gowri Manohar, Sri Venkateswara University, Tirupati

Dr. R. Rama Krishna Reddy, Sri Krishna Devaraya University, Ananthapuramu
Dr. Arya Kumar Bhattacharya, MEC, Hyderabad
Dr. C. Naga Raju, Yogi Vemana University, Kadapa
Dr. V. Kiran Kumar, Dravidian University, Kuppam
Dr. K. G. Sreenivas, CBP Government Engineering College, Delhi
Dr. R. Bhaskaran, Anna University, Chennai
Dr. Pramod, Manipal Institute of Technology, Manipal
Dr. Kanthi, Manipal Institute of Technology, Manipal
Dr. Shailendar, Manipal Institute of Technology, Manipal
Dr. Vijay Kumar Banga, Amritsar College of Engineering and Technology, Amritsar
Dr. B. Vijay Babu, KLEF, Vijayawada
Dr. M. Akhil Jabbar, Vardhaman College of Engineering, Hyderabad
Dr. M. Babu Reddy, Krishna University, Machilipatnam
Dr. Mythili Thirugnanam, VIT University, Vellore
Dr. G. S. Sreedhar, KSRM College of Engineering, Kadapa
Dr. Y. K. Sundara Krishna, Krishna University, Machilipatnam
Dr. Ande Prasad, Vikrama Simhapuri University, Nellore
Dr. Kasi Viswanath, G. Pulla Reddy Engineering College, Kurnool
Dr. Suresh Babu Veluru, MITS, Madanapalle
Dr. Arif Sohel, Muffakham Jah College of Engineering and Technology, Hyderabad
Dr. B. G. Prasad, BMS, Bangalore
Dr. P. Chandra Sekher, CPRI, Bangalore
Mrs. K. Meera, Additional Director, CPRI, Bangalore
Dr. D. Ravikumar, VNRVJET, Hyderabad
Dr. M. S. Sujatha, Sree Vidyanikethan Engineering College, Tirupati
Dr. N. M. G. Kumar, Sree Vidyanikethan Engineering College, Tirupati
Dr. V. Arun, Sree Vidyanikethan Engineering College, Tirupati
Dr. P. Sreenivasa Varma, KLEF, Vijayawada
Dr. A. Pandian, KLEF, Vijayawada
Dr. Siva Reddy, GPCET, Kurnool
Dr. G. V. K. Murthy, SSN, Ongole
Dr. Ch. Venkata Suresh, VVIT, Nambur, Guntur
Dr. A. V. NareshBabu, VVIT, Nambur, Guntur
Dr. G. Venkateswarlu, NEC, Nellore
Dr. G. Pandu Ranga Reddy, GPEC, Kurnool
Dr. T. Jaya Chandraprasad, RGMCET, Nandyal
Dr. V. Adinarayana Reddy, Yogananda Institute of Technology, Tirupati
Dr. D. Srinivasulu Reddy, SV Engineering College for Women, Tirupati
Dr. G. V. Ramu, MJR College of Engineering and Technology, Pileru
Dr. S. A. K. Jilani, Madanapalle Institute of Technology and Science, Madanapalle
Dr. A. Subbi Rami Reddy, Gokula Krishna College of Engineering, Sullurupeta
Dr. G. Jagadeeswara Reddy, Vaagdevi Institute of Technology and Science, Proddatur

Dr. M. Siva Ganga Prasad, KKR & KSR Institute of Technology and Science, Guntur
Dr. Mahesh, Swami Vivekananda Institute of Technology, Secunderabad
Dr. P. V. Naganjaneyulu, Sri Mittapalli College of Engineering, Tummalapalem, Guntur
Dr. G. Chenchu Krishnaiah, Gokula Krishna College of Engineering, Sullurupet
Dr. K. Nagi Reddy, NBKR Institute of Science and Technology, Vidyanagar, Nellore
Dr. G. Harinath Reddy, NBKR Institute of Science and Technology, Vidyanagar, Nellore
Dr. B. Polaiah, KLEF, Vijayawada
Dr. N. Murali Krishna, Sreyas Institute of Engineering and Technology, Hyderabad
Dr. V. Vijaya Kishore, Ravindra College of Engineering for Women, Kurnool
Dr. A. Vani, CBIT, Hyderabad
Dr. R. Prabhkar, Gurunanak Institutions, Hyderabad
Dr. N. Rama Murthy, G. Pullaiah College of Engineering and Technology, Kurnool
Dr. K. C. T. Swamy, G. Pullaiah College of Engineering and Technology, Kurnool
Dr. M. V. Subramanyam, SREC, Nandyal
Dr. Ravilla Dilli, Manipal Institute of Technology, Manipal
Dr. Anantha Krishna, Manipal Institute of Technology, Manipal
Dr. Kumara Shama, Manipal Institute of Technology, Manipal
Dr. Ramya, Manipal Institute of Technology, Manipal
Dr. M. Sathishkumar, Manipal Institute of Technology, Manipal
Dr. M. Madhavi, Lakki Reddy Bali Reddy College of Engineering, Mylavaram
Dr. A. Narendra Babu, Lakki Reddy Bali Reddy College of Engineering, Mylavaram
Dr. S. V. Jagadessh Chandra, Lakki Reddy Bali Reddy College of Engineering, Mylavaram
Dr. Y. S. V. Raman, Lakki Reddy Bali Reddy College of Engineering, Mylavaram
Dr. M. Venkata Sudhakar, Lakki Reddy Bali Reddy College of Engineering, Mylavaram
Dr. P. Lachi Reddy, Lakki Reddy Bali Reddy College of Engineering, Mylavaram
Dr. G. Srinivasa Rao, Lakki Reddy Bali Reddy College of Engineering, Mylavaram
Dr. J. Babu, Lakki Reddy Bali Reddy College of Engineering, Mylavaram
Dr. M. Sandhya Rani, Mahaveer College of Engineering, Hyderabad
Dr. D. Ajitha, Vardhaman College of Engineering, Hyderabad
Dr. S. Pothalaiah, Vignayana Bharathi Institute of Technology, Hyderabad
Dr. M. Nagaraju Naik, CMR College of Engineering Technology, Hyderabad
Dr. Shaik Fahimuddin, Annamacharya Institute of Technology and Science, Rajampet
Dr. G. Hemalatha, KSRMCE, Kadapa
Dr. M. Venkata Narayana, KSRMCE, Kadapa
Dr. B. Abdul Rahim, Annamacharya Institute of Technology and Science, Rajampet

Dr. S. V. Jagadeesh Chandra, Lakki Reddy Bali Reddy College of Engineering, Mylavaram
Dr. Ch. Subramanyam, Vardhaman College of Engineering, Hyderabad
Dr. A. L. Srinivasulu, Gates Institute of Technology, Gooty

Advisory Committee

Dr. S. Srinivas Kumar, Vice-Chancellor, JNTUA Ananthapuramu
Dr. B. L. Deekshitulu, Fellow IEEE
Dr. Raghu Krishnapuramu, IISc, Bangalore, Fellow IEEE
Dr. P. N. Suganthan, Nanyang Technological University, Singapore. Fellow IEEE
Dr. Atul Negi, University of Hyderabad, Senior Member IEEE
Dr. Ramsubba Reddy, IIT, Madras
Dr. C. Rama Krishna, NITTTR, Chandigarh
Dr. K. Rajinikanth, Former Principal, MSRIT, Bangalore
Dr. M. L. Saikumar, Former Dean at Institute of Public Enterprise
Mr. E. S. Chakravarthy, Centre Head, TCS, Bangalore

Steering Committee

Dr. G. Sreenivasan, SRIT, Ananthapuramu
Dr. A. Siva Sankar, SRIT, Ananthapuramu
Dr. K. Nagaraju, SRIT, Ananthapuramu
Dr. P. Deepthi Jordhana, SRIT, Ananthapuramu
Mr. D. Nizam Basha, SRIT, Ananthapuramu
Mrs. G. Meerimatha, SRIT, Ananthapuramu
Mr. P. Veera Prakash, SRIT, Ananthapuramu
Mr. L. Suman, SRIT, Ananthapuramu
Mr. B. Suresh Babu, SRIT, Ananthapuramu
Mr. P. Raghavendra Sarma, SRIT, Ananthapuramu
Mr. T. Venkata Naga Jayudu, SRIT, Ananthapuramu

Contents

Computer Science and Engineering

Patient Nurse Communication with Vital Sign Monitoring and Alert

S. Darshan and Jyothi S. Nayak

Abstract With raising patient-to-nurse ratio in India, traditional patient monitoring system (drip systems) for intravenous infusion is a stressful challenge. The challenge arises due to the requirement of continuous monitoring of intravenous infusion with the aid of nurse or guardian. Any mistake or delays in tracking in this regard can cause diverse problems including reverse flow of blood upon entire draining of bottle, overdose of medicine or excess infusion of electrolytes and saline. To conquer this hassle, this work proposes a prototype to monitor drip infusion of patients where the status of the drip infusion is monitored using a sensor circuit and actuation as a voice alert to the nurse's android unit. Along with this functionality in the proposed prototype, a module to handle the status of Electrocardiogram (ECG) signal which is obtained from ECG sensors is incorporated. The ECG readings can be continuously monitored with the help of the waveforms observed on the android unit. These provisions incorporated makes ease for the nurse/guardian in monitoring the drip infusion and ECG readings of the patients. Key sets are also provided to the patients to help them in the time of emergency where a voice alert is sent to the nurse's android unit requesting for the service. Since all these functionalities have different levels of significance with respect to the nurse, this work provides a priority based service. Thus the work provides an effective way of monitoring the patients and utilizing man hours of the nurse efficiently.

Keywords Drip infusion · Key sets · ECG

S. Darshan · J. S. Nayak (✉)
Department of CSE, BMSCE, Bengaluru, India
e-mail: jyothinayak.cse@bmsce.ac.in

S. Darshan
e-mail: darshansatya@gmail.com

© Springer Nature Singapore Pte Ltd. 2020

T. Hitendra Sarma et al. (eds.), *Emerging Trends in Electrical, Communications, and Information Technologies*, Lecture Notes in Electrical Engineering 569,
https://doi.org/10.1007/978-981-13-8942-9_1

1 Introduction

The traditional/earlier health care systems are not able to satisfy everybody's requirements because of the enormous growth in population. Regardless of having an incredible framework and leading edge technologies, medical systems are not reachable to everybody. One of the objectives of smart healthcare services is to help people by teaching them about the medical importance and creating awareness of the health. Smart Healthcare services enable people/patients to take care of themselves independently in the case of emergency scenarios. From healthcare point of view, unique systems that provide various facilities differ from alerts on a health monitoring android applications to various protocols that involves cross connections which is needed for linked devices. Any alterations made to the present systems would make the task of integrating these features into smarter-healthcare easier.

Internet Of Things (IoT) in HealthCare domain is an integration of transmission of information, connections of various devices and data computations along with proper intelligence. This integration provides us the data in real time and keeps the related devices and wearables connected which aims in providing a unique and an efficient healthcare system. Along with a lots of advantages and qualities such as locating, sensing, identifying, and connecting the modules that is linked with the IoT, it has become the fundamental element of smart healthcare. In accomplishing a smarter healthcare system, the Internet of Things can be widely applied in all the areas such as calibrating the healthcare equipments to a customized system that monitors any individual.

Nurse calling system has been implemented in hospitals, nursing homes, and in other healthcare institutions from long time. As the size of the nursing homes increased and the earlier ward systems were converted to a unit which can accommodate multiple patients, the health care systems needed a unique method/module that would help in having a better and an efficient patient nurse communication. The present system and the earlier nurse calling system differ a lot in many ways. The current nurse calling systems have taken over the old system to a whole new level with the aid of modern and the progressive technologies. Day by day due to the continuous advancements in technologies, nurse calling system with wireless technology is gaining more importance. Also the medical institutions have started to enhance their IT systems with the aid of wireless technology. A basic nurse calling system comprises of a remote controller in the ward which is handled by the user/patient, a light indication and a main nurse panel unit where the notifications, calls or the alarms are handled/observed.

In this paper we propose a nurse calling system which is able to help the patient as well as utilize the service of the nurse effectively and efficiently.

2 Related Work

Communication between patient and nurse is crucial to the supply of compassionate, high-quality medical aid. Each individual hospital is lacking in providing the system of effective yet efficient way of communication between patient and nurse. Specially in case of monitoring the drip infusion patients lots of concentration and effective communication between the patient and nurse is highly required, which may turn to harm patients' body, if neglected. Many approaches have been proposed for monitoring the drip infusion patients where a sensor is used to detect the glucose level and based on the sensory data an alert is sent to a GUI placed near the vicinity of the Nurse, which notifies the nurse regarding the glucose level of that particular patient via ZigBee [1–3], and also measured the range of ZigBee in terms of vertical and horizontal distance to capture the efficient results within possible mentioned range. The ECG readings of the patients, which are also a high priority data must also be monitored very frequently and monitoring of this consumes lot of energy and time. This is avoided by monitoring the ECG reading of patient [4] using EPIC sensors which are connected to directly to fog device such as smart phone. The work proposed [5] monitors the ECG of the patient at his comfort and the anomalies found in the readings are the clinician is alerted. Nurse can immediately report to patient and resolve the issue [5]. The wireless body sensor networks used to monitor the vital signs of the patient [6] and emergency is detected at the local nodes for quick treatment of the patient. This approach mainly considers low power nodes of the network as well as quick response to the patient during an emergency. There are also multiple reasons for the errors or disasters that occur while monitoring the drip infusion patients by Nurse [7] and the study concentrated on collecting the key reasons for the same and tried to avoid the errors by implementing the approach that would reduce the cause. The unique methods of monitoring the patients were proposed which include RFID as the main technology where it is used to track the position of the patients along with other facilities like emergency push button on the RFID tag, monitoring health parameters via the readings captured through RFID wearables etc. [8]. A unique technology called Fiber Bragg grating was proposed for patient monitoring where optical fibers are used to build the integrated IoT sensors which helped in monitoring the vital signs like body temperature, respiration rate, pulse rate and it also concentrated on monitoring the unexpected bed exits of the patients [9]. Other than drip infusion there are many other vital signs of patients that must be monitored [10] and proposed a system to characterize the nurse–patient interactions arising throughout times of the day when vital signs monitoring typically occur and also to identify additional care resulting from nurse–patient interactions during vital signs monitoring.

The earlier survey shows that for the success of smart health care system patient nurse communication is very crucial and a system is required to incorporate this interaction effectively so that the clinicians and patients are benefitted.

3 Proposed System

The current Nurse calling systems are those which are capable of monitoring the patients by providing them a push button, which is helpful in the time of emergencies where an alert or alarm is triggered to the nurses/guardians panel which aims to provide a general nurse calling system. In majority of the works, to analyze and process the sensed data microcontrollers are used and the sensed data transmission from the patient to the nurse module is implemented using Zigbee technology.

The proposed system provides a module for sensing drip infusion with the use of sensor which senses the glucose level and then the sensed data is processed by Raspberry-Pi, where the sensing effects can be visible on the digital monitor/display. Similarly, statistics from the infusion and the effects of sensory facts can be transmitted through Bluetooth modules, in conjunction with the key sets that is provided to the patients which would be helpful in making a request to nurse/guardian for any sort of help. Along with this, the option of monitoring the ECG readings of the patients using the android app is also enabled where the patient can be continuously monitored by the nurse/guardian by observing ECG waveforms that will be displayed on Android application. The priority is set for each of the requests as well as sensed data so that the clinicians can decide on the emergency level of the requests and serve appropriately.

4 Methodology

Many embedded systems have substantially exclusive designs in line with their functions and utilities. In this design, the idea of structured modular layout is adopted and the whole structure is mainly composed of a Raspberry-Pi, ECG sensor, Bluetooth, Display monitor, CPU fan, glucose level detector (the sensor circuit inclusive of a moisture sensor and its circuit board) and an android device. Figure 1 depicts the schematic diagram of overall system. The Overall work flow is a continuous process of monitoring, where it begins from the patient's end, till the response from the nurse/guardian's end. Figure 2 is the sequence flow diagram of the overall system where the work flow and the procedure is described. Here the toggle switch is used to switch between the vital sign monitoring and non-vital sign monitoring.

4.1 Vital Sign Monitoring

The Vital signs are nothing but a set of four to six significant indications which describes the condition of the human body. These values provides us a clear picture in analyzing a patient's physical condition which acts as an indicator of diseases

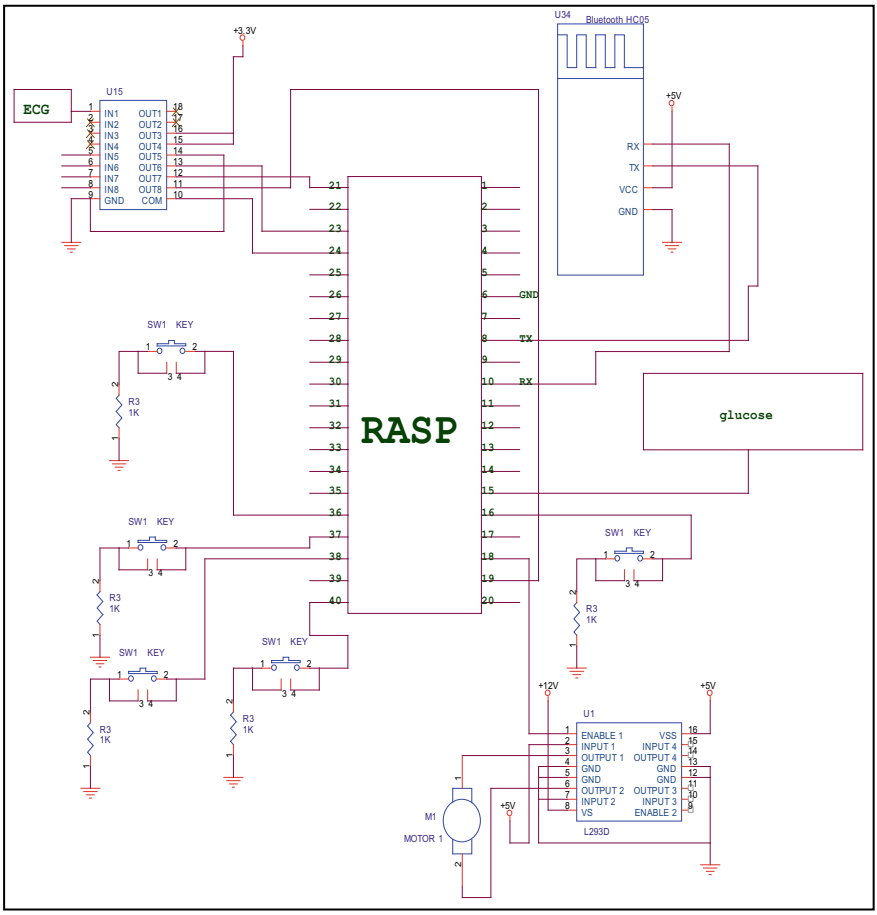

Fig. 1 Schematic diagram of the proposed system

that can possibly occur and also helps in process of recovery. Here in our proposed prototype, the vital sign that is being monitored is the heart rate by using ECG sensor. Electrocardiogram is a technique of observing/reading the heart rate using sensors/electrodes with some time intervals using the sensors/electrodes that will be in contact with the patient's skin. As shown in Fig. 2, when the toggle switch is switched to the upper side, the overall functionality of the module switches to ECG-monitoring. Here to fetch the ECG data, ECG-AD8232 sensor is used, which consists set of electrodes that is placed in contact with patient's skin. The sensor in turn is connected to Raspberry-Pi. Sensed data is processed using raspberry-pi and the corresponding varying electrical signal values are sent to android unit of nurse/guardian via Bluetooth. The application in the android unit is developed in such a way that, based on the received signal values it displays the corresponding

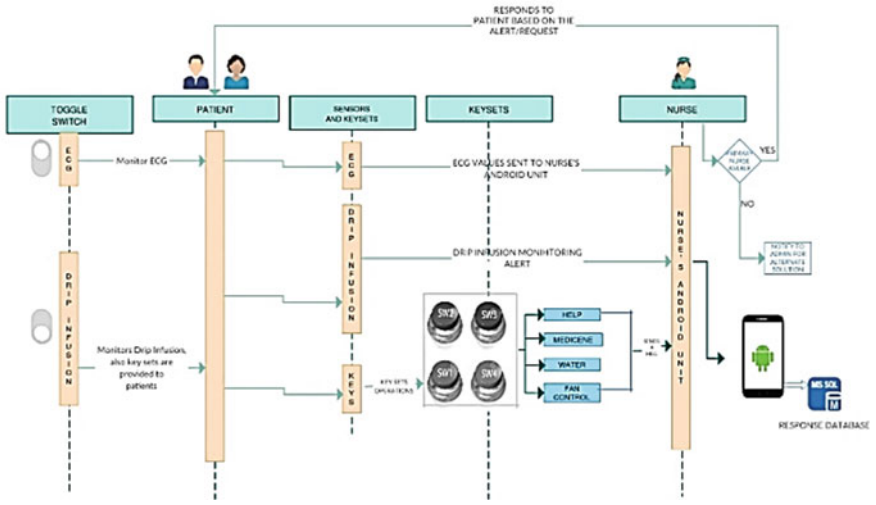

Fig. 2 Sequence flow diagram of the system

ECG waveforms. The display of the ECG using the android unit of the nurse/guardian can easily monitor the ECG readings without the necessity of coming frequently to the patient's place.

4.2 Drip Infusion Monitoring

Here the drip infusion in patients is monitored using the moisture sensors where the sensor is fixed inside the drip container to a position based on the alert requirement. Whenever the liquid goes below the sensor level or in other words when the liquid loses the contact with the sensor, variations in the sensed data in analyzed by raspberry-Pi and the same is transmitted to android unit via Bluetooth where a voice alert is popped out using the developed application. In case of drip infusion monitoring, a voice alert stating "GLUCOSE LEVEL LOW" is popped out. When the nurse/guardian receives this voice alert, he/she responds to the request based on their availability. If the nurse responds to the request, the nurse can press the push button, which is provided for the nurse in the developed android app where it is used to store the response database. As soon as the nurse presses that button the response data is stored along with the request value and the time of response which would be helpful in reviewing, analyzing and enhancing the service in future.

4.3 Key Sets Functionality

Along with drip infusion monitoring and ECG monitoring, the proposed prototype also provides a functionality where patients are provided with key sets (buttons) where they can use it in case of emergency, water-request or any other help. Based on the functionality, whenever the keys are pressed, the corresponding voice output is popped out in the android unit of the nurse/guardian. For example, when the patient presses a key whose functionality is to raise a request for providing water, a voice output is popped out stating "I NEED WATER" to the nurse's android unit. Other than "EMERGENCY" scenario, for other requests the nurse can respond even with some time delay if he/she is busy with higher priority task i.e. operations or meeting with doctor etc. In case of "EMERGENCY" or if the nurse is too busy such that the nurse cannot respond to the request, he/she can use the push button in the developed android application where a text message can be sent to nurse panel unit stating the same (busy/unavailability), so that the nurse panel unit can arrange a secondary nurse to respond to the request.

4.4 Priority Based Service

Many surveys and research has been done on nurse calling systems. Initially the nurse calling system was to just notify the nurse or to call the nurse using a LED buzzer or an alarm. Further the system was reviewed and feedbacks were obtained from the nurses or guardians regarding the problems they are facing, for example since it is a general nurse call system the nurse will not be aware of the purpose behind the call made. Consider a scenario where the call is made for a simple purpose like requesting for water or switching on the fan. If the nurse or the guardian is busy in some other higher priority work like operations, meetings etc. it would be a problem or hectic scenario to respond to those requests which is of lower priority which bothers a lot. Based on the above inputs, further the system was updated in such a way that, a patient can send a message stating the proper purpose of the request so that the nurse can read it and respond to it accordingly. Here in this case, the nurses/guardians faced the problem of reading the received text which requires little concentration. This scenario becomes a problem in the case of nurse being busy in some operation, or higher authority meeting where he/she will not have enough time to take out the device and take a look to the received request message which would consumes quite an amount of time. Further, based upon the feedbacks and inputs obtained from the previous system, the nurse calling system was again updated where an image or icon is sent to nurse device based on the request made, for example if at all the request is made for water, then an icon that includes a tumbler with water inside it, is sent to the nurse device. So based on the icon or image received, the nurse could respond accordingly.

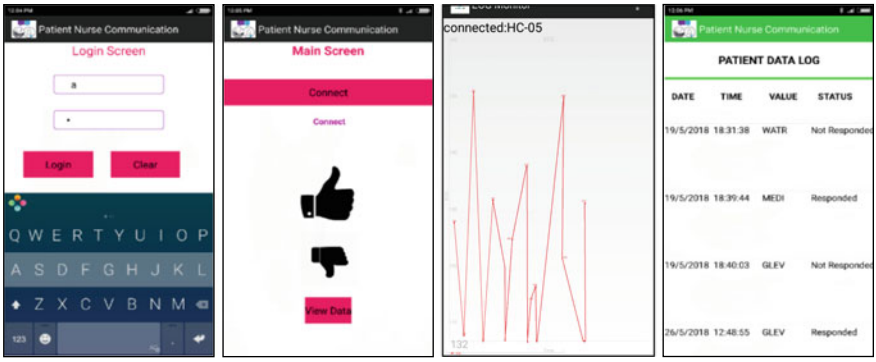

Fig. 3 Snapshots of login screen, main screen, ECG monitoring and response database of the developed app

In order to avoid the above scenarios and the problems, here in our proposed prototype, we have developed the module in such a way that, It only requires the audio attention, i.e., the alert or the request is sent to the nurse android unit where a voice alert is popped out in the android unit so that if they are busy in some higher priority work, they can react or respond accordingly without the need of taking the device out and checking it for a message in turn, which overall refers to priority based service.

5 Results

Based on the position of toggle switch, the functionality of the whole system is divided into vital sign monitoring and non-vital sign monitoring. Figure 3 lists the set of snapshots of the developed app which describes the login screen, main screen, and also the ECG monitoring interface. It also describes the response database that is being stored in the backend which includes the request value, response value and the time of response which further helps in reviewing, analyzing and enhancing the service in future.

6 Conclusion

This work mainly concentrated on Nurse calling systems using IoT, where Raspberry-Pi is used as the control unit, which processes and analyses the data received from the sensor circuits and switch keys, in turn a proper information is sent to the Nurse/guardian in time in the form of voice alert (waveforms in case of ECG readings) so that it avoids frequently visiting the patients which consumes large amount

of man hours. In future, even much more better and smart ways of monitoring the patients efficiently by reducing unnecessary man hours, can be developed where we need to mainly concentrate on monitoring each individual health condition like monitoring ECG, monitoring other vital signs like respiration rate, body temperature, blood pressure etc. along with the monitoring drip infusion monitoring, simultaneously, so that if any abnormalities found in the values, the system must be capable of analyzing it and send a proper alert to the nurse/guardian or the central nurse panel unit using efficient IoT technologies.

References

1. Rachman FZ (2015) Prototype development of monitoring system in patient infusion with wireless sensor network. In: IEEE International Seminar on Intelligent Technology and Its Applications (ISITIA). Surabaya, pp. 397–402
2. Trappey CV, Liu CS, Trappey AJC (2009) Develop patient monitoring and support system using mobile communication and intelligent reasoning. In: Proceedings of the IEEE International Conference on Systems, Man, and Cybernetics. San Antonio, TX, USA, pp. 1195–1200, October
3. Milenkovic A, Otto C, Jovanov E (2006) Wireless sensor networks for personal health monitoring: issues and an implementation. J Comput Commun 29(13–14):2521–2533 (2006)
4. Coulter S, Mostes M, Lightbody G, Popovici E, Fennell W (2017) Low power IoT platform for vital signs monitoring. In: 28th Irish Signals and Systems Conference (ISSC). Killarney, pp 1–5
5. Apostu O, Hagiu B, Paşca S (2011) Wireless ECG monitoring and alarm system using ZigBee. In: 7th International Symposium on Advanced Topics in Electrical Engineering (ATEE), Bucharest, pp. 1–4
6. Elghers, S, Makhoul A, Laiymani D (2014) Local emergency detection approach for saving energy in wireless body sensor networks. In: IEEE 10th International Conference on Wireless and Mobile Computing, Networking and Communications (WiMob). Larnaca, pp 585–591 (2014)
7. Han PY, Coombes ID, Green B (2005) Factors predictive of intravenous fluid administration errors in Australian surgical care wards. BMJ Qual Saf 14:179–184 (2005)
8. Shieh H-L, Huang C-C, Lyu F-S, Zhang Z-C, Zheng T-S (2016) An emergency care system using RFID and Zigbee techniques. In: Proceedings of IEEE International Symposium on Computer, Consumer and Control, pp. 65–68
9. Fook VFS, Jayachandran M, Jiliang EP, Yongwei Z, Jianzhong EH (2018) Fiber Bragg grating-based monitoring and alert system for care of residents in nursing homes. In: 2017 IEEE 28th Irish Signals and Systems Conference (ISSC). Fook VFS, Jayachandran M, Jiliang EP, Yongwei Z, Jianzhong EH (2018) Fiber Bragg grating-based monitoring and alert system for care of residents in nursing homes. In: IEEE 4th World Forum on Internet of Things (WF-IoT). Singapore, pp. 195–200
10. Cardona-Morrell M, Prgomet M, Lake R, Nicholson M, Harrison R, Long J, Westbrook J, Braithwaite J, Hillman K (2016) Vital signs monitoring and nurse–patient interaction: a qualitative observational study of hospital practice. Int J Nurs Stud 56:9–16

Proposed Method for Segmenting Skin Lesions Images

Enas Ibrahim, A. A. Ewees and Mohamed Eisa

Abstract This paper proposes a computer-based method to support medical science students in the detection of skin diseases accurately. It uses the Gaussian filter and applies the 2-D Wavelet Transformation and-2-D Inverse Wavelet Transformation techniques for the aim of image preprocessing in order to get rid of the noises, and segment skin cancer lesion by fusing edge-based and region-based segmentation approaches. The next step consists of applying Morphological filters to get rid of external noise and the interior one of the object, which remained in the segmented image as well as to soften the edges. Then, use the k-Nearest Neighbor (kNN) classifiers. The desired goal of this paper is to test the accuracy of the following proposed segmentation algorithm. The proposed method is tested on 133 images whereas 78 are malignant melanoma skin cancer type and 55 benign ones. This approach allowed detecting two different Pathological cases of skin lesions images which are malignant melanoma and benign nevi. The segmentation achieved 97.75% of accuracy for these two types of skin cancer lesions.

Keywords Skin lesion segmentation · Region based segmentation · Edge-based segmentation

1 Introduction

Nowadays there is a great interest in the analysis of skin lesions by applying the computer-based systems. These systems grant medical science students besides Specialists in skin diseases the early detection of skin cancer disease and prevent the development of the lesions. The increase of skin cancer cases resulted in the wide development of the computational systems. Skin cancer has distinctive and complex characteristics that must segment the images with accuracy [1, 2]. Image segmen-

E. Ibrahim · A. A. Ewees (✉)
Computer Department, Damietta University, Damietta, Egypt
e-mail: ewees@du.edu.eg

M. Eisa
Computer Department, Portsaid University, Portsaid, Egypt

© Springer Nature Singapore Pte Ltd. 2020

T. Hitendra Sarma et al. (eds.), *Emerging Trends in Electrical, Communications, and Information Technologies*, Lecture Notes in Electrical Engineering 569,
https://doi.org/10.1007/978-981-13-8942-9_2

tation has become one of the main applications that are participating in most of the operations of the image. It indicated in the process of partition or breaks an image [3]. Although image segmentation processes, like many image processing processes, also have some problems that make the segmentation process more complex [4]. A lot of work has done previously to overcome the complications during image segmentation. Several general-purpose techniques and algorithms have been produced for image segmentation [5, 6]. These techniques are typically fused with a domain's particular knowledge in order to solve the domain's segmentation problems effectively. In addition, image segmentation reduces the extracted features [7–9].

There are many different kinds of segmentation methods but there is no specific method which can be utilized for different image kinds which would generate the same result [10, 11]. The development of an algorithm for one set of images may not suitable to be reused for another set of images. So, several challenging problems such as developing unified image segmentation approach which can be utilized to whole kinds of images [12]. Even choosing a technique suitable for a particular set of images is a challenging matter.

Segmentation of the skin lesion is one of the important tasks to do. Segmentation divides an image into multiple segments which make the representation of an image simple and more meaningful to analyze. A segmentation algorithm must be used to locate and identify the skin defect before classifying the defect area as benign or malignant and extracting features from it. It is necessary that the skin defect segmentation algorithm be accurate as the result of the segmentation is used to be an input to the skin cancer classification algorithm.

2 Literature Review

Given the importance of early detection of skin lesions, there are many studies that suggest automatic methods to support medical science students and Specialists in skin diseases in their diagnosis. These studies provide different image processing techniques for segmenting different types of skin defect areas. An automated system proposed in [13]. It utilized an Ant colony based segmentation algorithm. It depended on three groups of features to define malignant lesion: texture properties, geometrical and relative colors from which related ones were selected. This system used two classifiers which were ANN and KNN. This automated system was tested on 172 dermoscopic images where 84 were benign lesions and 88 malignant melanomas. The results of the proposed segmentation algorithm were encouraging as they produced promising results. It used 12 features and it achieved that they were sufficient to detect malignant melanoma. Using automatic masks allows classifying 93.6% correctly against 86.6% for manual masks of images.

The authors of [14] presented an approach for segmenting and classifying the macroscopic pigmented skin lesions images. The approach depended on an anisotropic diffusion filter, Chan-Vese's model in the segmentation process and an SVM classifier to perform the process of extracting lesion features and the distin-

guishing comparatively among some skin lesions kinds. It used (ABCD) rule to calculate and extract properties which were considered for the classification process. The introduced approach achieved good segmentation results (94.36% Accuracy).

The authors in [15] presented a computer-assisted system to recognize Melanoma Skin Cancer employing Image processing tools. This system used images of skin lesion as an input and then applied the novel image processing techniques, to analyze the image to detect the existing of skin cancer. The Lesion Image analysis tools analyzed size, texture, and shape to be used in feature extraction and image segmentation phases. This system used the extracted feature to assort the image as Melanoma cancer lesion or Normal skin. Physicians and Patients could use this system effectively for the purpose of diagnoses skin cancer more accurately. For the provincial areas, the system could help in achieving automatic skin cancer diagnosis purpose.

A computer-assisted design for automatic cell segmentation and analysis of the cytoplasm ratio to detect skin cancer was proposed [16]. A watershed transformation method used to segment skin lesion cells. Images classified as normal and abnormal images using SVM classification method. The presented methodology provided objective segmentation results with high adequacy and accuracy proportionate with the cytoplasm ratio value.

The authors of [17] presented a way to detect the edge of the skin lesion. Use the Chan-Vese model to provide information about the edges of skin lesions, to help a dermatologist in diagnosing. The anisotropic diffusion non-linear filter was used to reduce the existence of noise on the images and smooth images without losing the rough edge. Active contour model without edges was applied In order to establish a better edge to the lesion. It could eliminate the noise partially excepting cases with the existence of shadows and reflections. The segmentation of images through the presented method located in most regions in images which have the same features of skin and also images with much noise, such as the human scalp. The presented method achieved 94.23% of accuracy in segmentation melanoma, 96.77% of accuracy for melanocytic nevi type and 93.03% accuracy for seborrheic keratosis skin cancer type.

The authors of [18] proposed a Mumford-Shah region growing method based application. It applied to realize the seeds which used by a seed-controlled watershed segmentation method automatically. To segment the original image besides obtaining a convergent contour of the existing skin lesion, the application applied a region growing method. The watershed method used points of the rough contour as seeds. A Dermatlas dataset was used to obtain color images with skin lesions to test the approach. The study used a set of 20 images for applying the proposed method as an experimental test. The method could satisfactory extracted and automatically detect contours for 90% approximately of the input images. Mumford-Shah method could identify the illness regions successfully and the applied watershed model used the resulting contours as the flood seeds effectively. The watershed approach preserved the lesions topology and irregularity. It allowed an excellent modification of the initial contours to the lesions' boundaries. An automated method in [19] was presented for the purpose of diagnosing melanoma. It applied on a collection of images examined by a dermatoscope. The study used a set of 102 dermoscopy images for different cases randomly sampled from the skin diseases Atlases and from doctor's dispensaries.

Images were split into two sets, three—quarters of the image collection for learning set and a quarter for the test set. This study utilized (GLCM) function to extract image properties and (MLP) multilayer perceptron classifier to distinguish the skin image to malignant melanoma or melanocytic Nevi. MLP classifier applied with two different proposed techniques which were Automatic MLP and Traditional MLP in the process of training and testing. Texture analysis achieved high accuracy and was a useful method for the differentiation between melanocytic skin lesions. The experimental result showed that the automatic MLP was fast but the traditional MLP, the second one gave a better performance with 100% of accuracy for the training set and 92% of accuracy for the test set.

3 Methodology

In this part, we present the development of the proposed approach for fusing region-based and edge-based approaches of skin cancer lesions segmentation. The method contains the following phases: (a) pre-processing of input images, (b) segmentation, (c) post-processing, (d) feature extraction and (e) the classification. The Flowchart of the proposed approach can be shown in Fig. 1.

3.1 Image Pre-processing

In this step, it was applied a smoothing technique in the database images, in order to soften the effects of noise, which may affect and impede the outcome of segmentation.

First, we implement a conversion to the color images to gray levels since it is not necessary to smooth the three RGB levels severally because the proposed method is applied to images is in gray levels. Then Gaussian filter is applied for noise elimination so the noise is smoothed out. The employment of a Gaussian filter for edge detection will be useful in edge position displacement, edges vanishing, and phantom edges.

Then morphological filter (opening filter) was applied to make the edge soft and eliminate exterior and interior noises of the spot of the lesion. A single-level discrete 2-D wavelet transform is used as a noise filtration technique, which in turn preserve edges and remove noise. Ostu's thresholding technique employed on each of the 4_wavelet outputs for obtaining a preliminary gross estimation of the lesion boundaries.

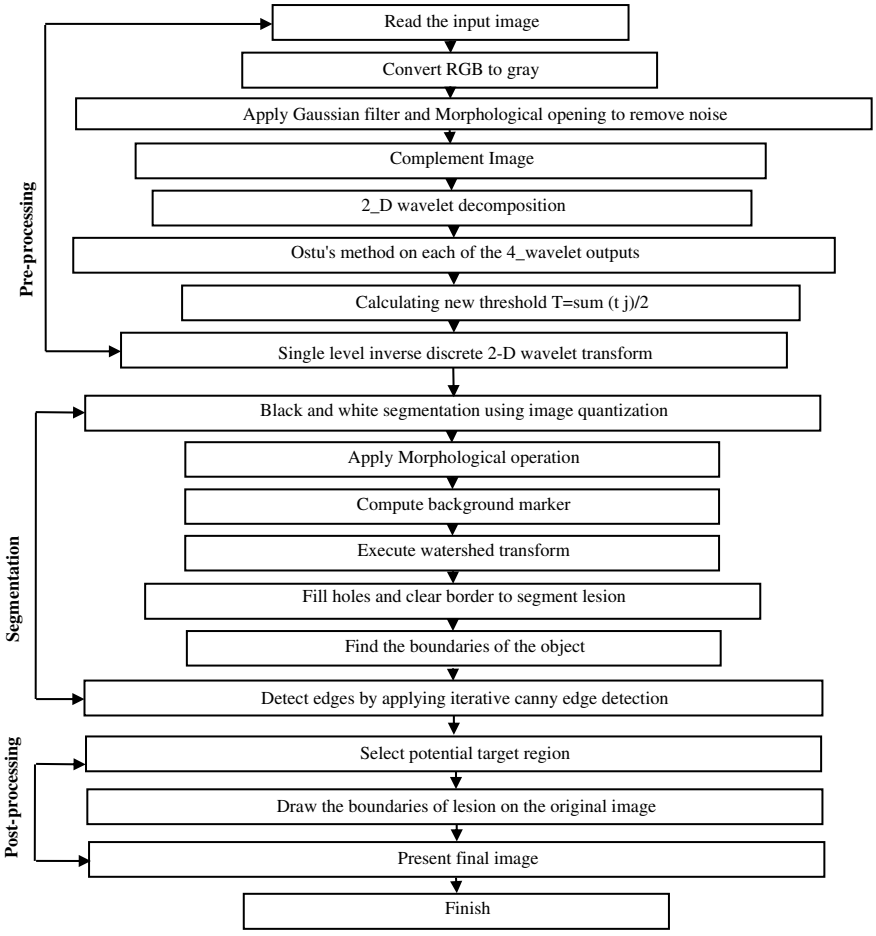

Fig. 1 Proposed segmentation algorithm

3.2 Image Segmentation

In region-based segmentation, regions are constructed by associating or dissociating neighbor pixels. It works on the basis of homogeneity, by taking into account the fact that neighboring pixels inside a region possess similar and dissimilar to the pixels in other regions. Each pixel in a region is compared with its neighboring pixel for similarity comparisons such as check grey level, color, and texture. If the similarity check result is positive, then that selective pixel added to the pixels to grow the region. This method has weaknesses represented in Sequential by nature and quite expensive in both computation time and memory, and to decide to stop criteria for segmentation is a challenging task and can have a considerable impact on minute regions. Finally, the selection of noisy seed by user leads to flawed segmentation

[20, 21]. While region-based approaches focus on grouping pixels using a measure of similarity, edge-based approaches attempt to add importance to the variation in the image. Many researchers have developed this approach under different theoretical frameworks as most of them have supported and improved image contrast in the area directly surrounding the edges. To compute the gradient image, traditional methods often rely on classical edge detectors, such as Canny, Roberts, and Prewitt. Although these methods can produce satisfactory results, they suffer from some weaknesses such as having trivial edges and the results will be noise-sensitive.

3.3 Proposed Segmentation Algorithm

According to the abovementioned analysis, using one of the edge-based or region-based techniques alone cannot provide good results in the segmentation process. So, the combination of these two methods is designed to overcome individual shortcomings that confront each method separately. In this paper, we propose to combine the previous methods to improve the accuracy of the segmentation practical use. The skin lesions segmentation process is applied to separate the spot of lesion of the healthy region. To extract skin cancer lesion with high accuracy first, we adopted the improved watershed segmentation as a type of region based method. The main problem with this technique is it produces excessive over-segmentation. We could overcome this snag by using Gaussian filter and 2_D wavelet transform before the segmentation process so we get better results than other pre-processing and noise reduction techniques. Then we apply Canny edge detector to trace the edges of the skin lesion. In the following, the proposed segmentation algorithm steps:

Algorithm 1

Input: preprocessed skin cancer image

- Step 1: Use the Gradient Magnitude as the Segmentation Function.
- Step 2: Make the objects in the foreground marked
- Step 3: computing the opening-by-reconstruction of the image
- Step 4: Apply the opening filter followed with a closing filter to remove the dark stains and stem signs.
- Step 5: obtain good foreground markers by calculating the regional maxima.
- Step 6: overlie the foreground marker image on the original image.
- Step 7: clear the edges of the marker points and then reducing them a bit
- Step 8: start to execute the thresholding method, and then apply the watershed transform of the distance transform and finally look for the watershed ridge lines of the result to compute background markers to compute Background Markers.
- Step 9: Browse the Result, one of the techniques is to overlie the foreground markers, background markers, and segmented object boundaries.
- Step 10: apply morphological opening and applies filling holes and clear border.
- Step 11: apply the improved canny edge detector to find edges to the image.

Output: skin lesion segmentation result

The novelty lies in the combination of two methods, which have different characteristics and thus show a different type of strengths.

3.4 Post Processing

Post-processing phase submitted by implementing the morphological filters to the binarized images. These morphological filters used to eliminate outside and inside noise from the segmented regions. Noises, such reflexes, can cause the misrepresentation of the border by the segmentation method.

This paper adopted "opening filters" and "closing filters". The structuring element has an elliptical shape. The application of the filters allowed smoothing the edge and eliminating interior or exterior noises of the spot of the lesion.

3.5 Features Extraction

Feature selection and extraction based on ABCD rule, including texture features and geometrical properties. The feature extraction purpose is a reduction of the original data set by calculating and evaluating certain features or properties, which differentiate one input pattern from another [20]. In this study texture features extracted are based on texture analysis using Gray Level co-occurrence Matrix. The effective GLCM is a tool for extracting the features from an image. It maps the grey level co-occurrence probabilities based on spatial relations of pixels in different angular directions. The extracted features based on GLCM are: Correlation, Cluster, Autocorrelation, entropy, Prominence, Entropy, Cluster, Contrast, Shade, probability, Dissimilarity, Variance, Energy, Homogeneity, Sum, Sum variance, Maximum, Difference, Sum of squares, Sum average, entropy, Difference variance, Inverse difference moment normalized, Inverse difference normalized (INN), Information measure of correlation 2, Information measure of correlation 1 and Inverse difference homogenous (INV).

The second features are the type based on ABCDE rules of skin cancer, represented in: A (Asymmetry): Skin cancers moles are usually asymmetric rather than regular moles, which are identical. B (Border): The melanocytic lesions are usually having misty and/or rough edges. C (Color): The melanocytic lesion has variant colors within the mole. D (Diameter): The lesions do not transcend a diameter of a (6 mm), otherwise it is suspicious.

3.6 Classification Phase

The selected features of images are utilized as input to the k-Nearest Neighbor (kNN) classifier. This study used kNN classifier which gathers closest objects measuring the Standard Euclidian distance of normalized features according to Eq. (1). K is the number of neighbor pixels and to distinguish benign lesion from a malignant melanoma. The different measurements based on features, representing the types of

malignant melanoma and benign nevi are given as input to the kNN classifier which consists of two phases (i.e. training and testing set).

$$d(x, y) = \sqrt{\sum_{j=1}^{n}(x_i - y_i)^2}. \quad (1)$$

where, n is the number of variables, x_i and y_i are two points in Euclidian n-space.

4 Experimental Results

The above-described methodology was applied on different skin lesion containing dermatology images which have been downloaded from Dermnet [22] skin disease Atlas consists of 133 images (78 images for benign nevi and 55 for malignant melanoma), a website with open access to dermatological images. After segmentation by the proposed method, we get the results as shown in Fig. 2.

4.1 Performance Measures

Accuracy, specificity, precision, recall, and F-measure are computed for kNN by the following Eqs. (2)–(6).

$$\text{Accuracy} = \frac{TP + TN}{TP + TN + FP} \times 100\%. \quad (2)$$

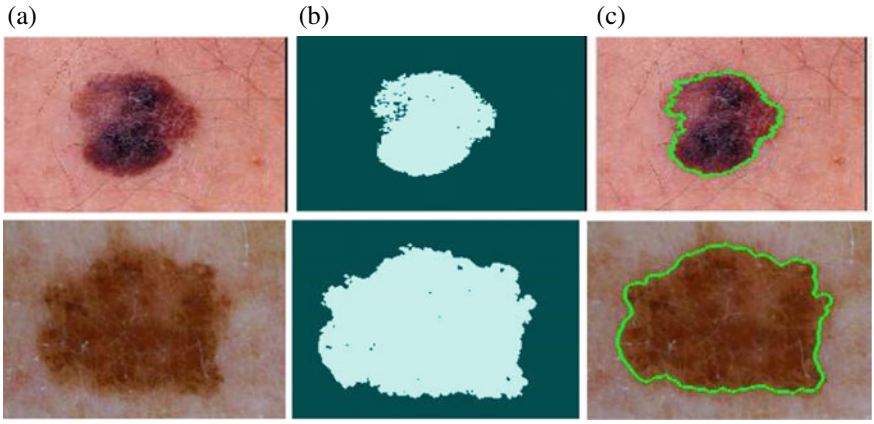

Fig. 2 **a** Original. **b** Pre-processed. **c** Segmented images using proposed algorithm

$$\text{Specificity} = \frac{\text{TN}}{\text{TP} + \text{FP}} \times 100\%. \tag{3}$$

$$\text{Precision} = \frac{\text{TP}}{\text{TN} + \text{FP}} \times 100\%. \tag{4}$$

$$\text{Recall} = \frac{\text{TP}}{\text{TP} + \text{FN}} \times 100\%. \tag{5}$$

$$\text{F-measure} = 2 \times \frac{\text{Precision} \times \text{Recall}}{\text{Precision} + \text{Recall}}. \tag{6}$$

where, TP is True positives, TN is True negatives, FP is false positives and FN is False negatives.

The proposed segmentation algorithm has approximately 14% segmentation Error. It obtained an average accuracy of 97.75% as in Table 1.

The second evaluation phase tries to compare the performance of the segmentation results that obtained through the proposed approach versus the results of the segmentation performance of other studies achieved by different segmentation approaches, using the same image dataset (i.e. Dermnet dataset) (Table 2).

The results obtained in our experiment show that, the proposed approach achieved promising results in segmenting skin lesions of benign nevi and malignant melanoma. Medical science students and the dermatologist can use information available by this method and benefit from this approach in order to assist them in the diagnosis and detection of skin lesions.

Table 1 Performance of the proposed segmentation algorithm on the dataset

Measure	Result (%)
RMSE	14.23
Accuracy	97.75
Specificity	96.75
Precision	97.47
Recall	98.56
F-measure	97.97

Table 2 Results of the proposed algorithm compared to the previous studies

Source	Year	Segmentation technique	Accuracy (%)
Proposed Algorithm	2018	Region-based and Edge-based segmentation combination	**97.75**
[13]	2017	Ant colony based segmentation algorithm	93.60
[16]	2013	Chan-Vese model	94.23
[18]	2013	Mumford-Shah region growing method	90

5 Conclusions

This paper presented a proposed approach for segmenting skin cancer images. It was used to different pigmented skin cancer lesion to perform segmentation with the high accuracy. After applying the proposed segmentation method, we found that the achieved results had a good and satisfactory accuracy. This segmentation method has the ability to isolate the lesion area from the image. The experimental results proved that the proposed approach achieved high accuracy of skin lesion segmentation; it successfully obtained 97.75% accuracy. For future work, this segmentation approach can be applied to other kinds of color images for target segmentation such as skin segmentation, etc. The proposed method can be reused depending on the usability and detecting the ability of target in different kind of images.

References

1. Eisa MM, Ewees AA, Refaat MM, Elgamal AF (2013) Effective medical image retrieval technique based on texture features. Int J Intell Comput Inf Sci 13(1)
2. Houssein EH, Ewees AA, ElAziz MA (2018) Improving twin support vector machine based on hybrid swarm optimizer for heartbeat classification. Pattern Recognit Image Anal 28(2):243–253
3. El Aziz MA, Ewees AA, Hassanien AE (2017) Whale optimization algorithm and moth-flame optimization for multilevel thresholding image segmentation. Expert Syst Appl 83:242–256
4. Roy P, Goswami S, Chakraborty S, Azar AT, Dey N (2014) Int J Rough Sets Data Anal (IJRSDA) 1(2)
5. El Aziz MA, Ewees AA, Hassanien AE (2016) Hybrid swarms optimization based image segmentation. In: Hybrid soft computing for image segmentation. Springer, Cham, pp 1–21. https://doi.org/10.1007/978-3-319-47223-2_1
6. Ewees AA, El Aziz MA, Hassanien AE (2017) Chaotic multi-verse optimizer-based feature selection. Neural Comput Appl 1–16. https://doi.org/10.1007/s00521-017-3131-4
7. Ibrahim RA, Elaziz MA, Ewees AA, Selim IM, Lua S (2018) Galaxy images classification using hybrid brain storm optimization with moth flame optimization. J Astron Telesc, Instrum, Syst 4(3)
8. Elaziz MEA, Ewees AA, Oliva D, Duan P, Xiong S (2017) A hybrid method of sine cosine algorithm and differential evolution for feature selection. In: International conference on neural information processing. Springer, Cham. https://doi.org/10.1007/978-3-319-70139-4_15
9. Ibrahim RA, Oliva D, Ewees AA, Lu S (2017) Feature selection based on improved runner-root algorithm using chaotic singer map and opposition-based learning. In: International conference on neural information processing. Springer, Cham. https://doi.org/10.1007/978-3-319-70139-4_16
10. El Aziz MA, Ewees AA, Hassanien AE, Mudhsh M, Xiong S (2018) Multi-objective whale optimization algorithm for multilevel thresholding segmentation. In: Advances in soft computing and machine learning in image processing. Springer, Cham, pp 23–39. https://doi.org/10.1007/978-3-319-63754-9_2
11. Ewees AA, Sahlol AT (2018) Bio-inspired optimization algorithms for improving artificial neural networks: a case study on handwritten letter recognition. Comput Linguist, Speech Image Process Arab Lang 4:249. https://doi.org/10.1142/9789813229396_0012
12. Gopinath J, Krishnan R (2015) A Survey on different types of segmentation techniques. Int J Mod Trends Eng Res 02(10)

13. Dalila F, Zohra A, Redab K, Hocine C (2017) Segmentation and classification of melanoma and benign skin lesions. Optik—Int J Light Electron Opt 140:749–761
14. Oliveira RB, Marranghellob N, Pereira AS, Tavares JMRS (2016) A computational approach for detecting pigmented skin lesions in macroscopic images. Expert Syst Appl: Int J Arch 61(C):53–63
15. Jain S, Jagtap V, Pise N (2015) Computer aided Melanoma skin cancer detection using image processing. Procedia Comput Sci 48:735–740
16. Lavanya S, Naveen Kumar B, Obuliraj R, Dhanalakshmi S (2014) Gradient watershed transform based automated cell segmentation for THG microscopy medical images to detect skin cancer. Int J Sci Technol 2
17. Oliveira RB, Tavares JMRS, Marranghello N, Pereira AS (2013) An approach to edge detection in images of skin lesions by Chan-Vese model. In: 8th Doctoral Symposium in Informatics Engineering Conference, Porto, vol 1
18. de Araujo AF, Tavares JMRS, Pereira AS, Marranghello N (2013) Segmentation of skin lesions by watershed using markers approximated by the Mumford-Shah region growing method, summer school and work shop on imaging science and medical applications. University of Coimbra, Portugal
19. Mabrouk MS, Sheha MA, Sharawy A (2012) Automatic detection of Melanoma skin cancer using texture analysis. Int J Comput Appl 42(20):22–26
20. El Aziz MA, Ewees AA, Hassanien AE (2018) Multi-objective whale optimization algorithm for content-based image retrieval. Multimed Tools Appl 77(19):26135–26172
21. Ewees AA, Elaziz MA, Oliva D (2018) Image segmentation via multilevel thresholding using hybrid optimization algorithms. J Electron Imaging 27(6):063008
22. Dermnet skin disease image atlas, http://www.dermnet.com. Accessed 11 Feb 2018

Extending a Flexible Searching Tool for Multiple Database Formats

Mohammad Halim Deedar and Susana Muñoz Hernández

Abstract Although all databases frameworks let us make conventional (crisp) searches, there are only a few of them that take into account some flexible, fuzzy, expressive criteria. The few of them that provide some of these searching characteristics are restricted to a particular database format, as FleSe that is devoted to search in a flexible way over Prolog databases. We have extended FleSe framework by an extraordinary feature that allows users to query various conventional and modern databases such as Prolog, CSV, XLS, XLSX, MySQL, and MongoDB or JSON in a fuzzy way. We have developed an adaptable and configurable platform for it so that any user can personalize at run-time. The fuzzy searching criteria can be created and added in a very user-friendly way, so that any user can upload his/her conventional (crisp) database, define the fuzzy search criteria that he/she is interested in and search at the database flexibly and expressively using concepts as similarity, fuzziness, qualification, and negation.

Keywords Fuzzy logic · Search engine · Databases · Database search framework

1 Introduction

Databases store crisp (non-fuzzy) information but the way a user wants to retrieve information most of the time is not crisp, because their thoughts are usually more expressive (fuzzy). For example, if a user is looking for a "cheap", "rather cheap", or "not very expensive" restaurant in a database, it is not functional to have the information already stored with those fuzzy concepts. Searching in a fuzzy way not only gives us the exact information we are looking for, but it lets us to retrieve all the possible and available information very close to the criteria we have set for

M. H. Deedar (✉) · S. M. Hernández
Universidad Politécnica de Madrid, Escuela Técnica Superior de Ingenieros Informáticos, Campus de Montegancedo s/n, Boadilla del Monte, 28660 Madrid, Spain
e-mail: halim.deedar@alumnos.upm.es

S. M. Hernández
e-mail: susana@fi.upm.es

© Springer Nature Singapore Pte Ltd. 2020

T. Hitendra Sarma et al. (eds.), *Emerging Trends in Electrical, Communications, and Information Technologies*, Lecture Notes in Electrical Engineering 569,
https://doi.org/10.1007/978-981-13-8942-9_3

our query. For example, if we are looking for food with a lower price than $10 in a restaurant database (having crisp information) and there is food whose price is $10.20, so our query will not retrieve, even if it might be a reasonable price for us. Although there are tools devoted on accessing databases (containing crisp information) in a fuzzy way, such as the approach presented by Bosc and Pivert in [1], with the syntax identical to SQL which is a bit difficult for the non-expert users to understand as it requires advanced users to understand the syntax. FleSe was presented by Pablos-Ceruelo and Muñoz Hernández in [2] which is a handy tool that mainly focused on providing flexible facilities for users in their fuzzy searching over Prolog databases. Its problem was that FleSe was constrained to search over Prolog databases. Considering those mentioned points, we present a framework that provides a simple syntax for any user to perform fuzzy or non-fuzzy query over any conventional and modern database formats (Prolog, CSV, XLS, XLSX, MySQL, and MongoDB or JSON) and we provide the users the facility of creating their fuzzy criteria effortlessly without having any knowledge about the mathematical syntax of fuzzy functions.

2 RFuzzy

RFuzzy [3] (see Fig. 1) is a library implemented for Ciao Prolog [4] to increase the expressiveness of Prolog with the possibility of creating fuzzy information. The purpose of developing RFuzzy is mainly focused on reducing the complex syntax of Fuzzy Prolog [5], and to provide an easy way for representing a problem using fuzzy reasoning with real numbers. RFuzzy represents the truth values using real numbers, and the answers provided by the RFuzzy are never constraints, and it can differentiate between the crisp and fuzzy predicates without the interferences of the user, it can manage the introduction of truth values.

The points that make RFuzzy so distinctive are that RFuzzy can define types, and default values (general and condition). RFuzzy is the first tool that implemented multi-adjoint logic and with the help of that RFuzzy was able to represent the concept of credibility of the rules.

In general, RFuzzy contains the following features that make it different from other approaches:

- It represents the truth values using real numbers instead of unions of intervals between real number.

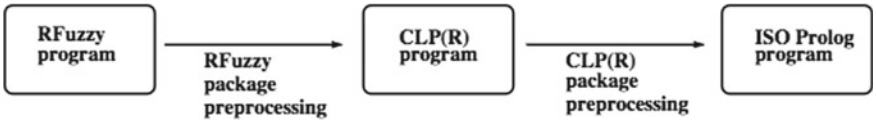

Fig. 1 RFuzzy architecture

- It provides a concrete syntax to define types so that the user does not need to code them in Prolog.
- It gives direct results to the queries instead of constraints.
- It can implement both the default and partial default values.
- RFuzzy uses multi-adjoint logic [6] to model its semantic.

3 FleSe

FleSe is a handy framework for performing fuzzy and non-fuzzy queries over Prolog databases containing crisp information. FleSe uses RFuzzy package which is a Prolog library developed for Ciao Prolog. FleSe uses fuzzy logic in a Prolog implementation. Fuzzy logic [7] assigns a membership degree to those elements which belong to a set. Therefore, FleSe has used this mechanism to perform the fuzzification of its searching criteria. Taking an example, a crisp database of restaurants (Table 1) and the fuzzy definition of function "cheap" related to the average menu price as shown in Fig. 2 with the query of "Is there any cheap restaurant?", with the help of Fuzzy logic we obtain that Ni Hao is "Very" cheap, Tapasbar is "almost" cheap, II_tempietto is "hardly" cheap, and Kenzo is "not" cheap, and the usual answers for each individuals (very, almost, hardly, and not) are the truth values "1", "0.9", "0.2" and "0", respectively.

Table 1 Restaurant database

Name	Price average	Food type
II_tempietto	90	Italian
Tapasbar	20	Spanish
Ni Hao	10	Chinese
Kenzo	100	Japanese

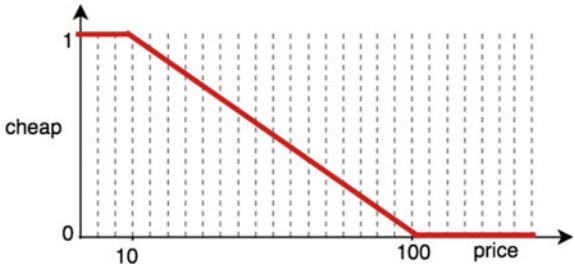

Fig. 2 Cheap fuzzification function

3.1 A Brief Review of Semantics Used by FleSe

FleSe semantics are structured using multi-adjoint algebra [8], which enabled FleSe to get the credibility for the rules that we obtain from real-world data. Besides, the multi-adjoint algebra helped FleSe to create priorities for its rules, that it leads FleSe to obtain more useful and accurate result by getting the answers as a truth value with the maximum priority not the maximum value.

The contribution of Pablos-Ceruelo and Muñoz Hernandez work in [9] based on multi-adjoint semantics provided a simple syntax and a complete semantics to the FleSe.

3.2 Query Syntax

FleSe gets the queries from users as input using the following syntax:

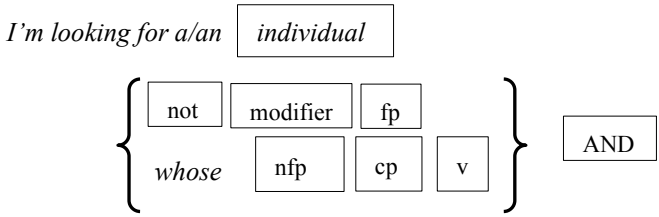

(1)

where:

- The *individual* represents the element we are looking for, such as (restaurant, film, car, …).
- *not* gives a negation mechanism to the queries.
- *modifier* gives (quite, rather, very, …) modifiers to the query.
- *fp* stands for fuzzy predicates such as (cheap, large, close, …).
- *nfp* contains non-fuzzy predicates like (price, size, and distance to the center).
- *cp* stands for comparison operand, and it consists of ("is equal to", "is different from", "is bigger than", "is lower than", "is bigger than or equal to", is lower than or equal to "and" "is similar to").
- *v* which stands for value, it asks for a crisp value when the users want to use the comp-op option such as ("is equal to", "is different from", or "is similar to"). The interface is more adaptable because the elements in the boxes can be modified and in case if we do not need any box we can leave it as blank.
- *AND* option will let the user add more options to the queries to make the query more efficient. Some examples to illustrate the syntax are: "*I am looking for a film not very comedy*" (Eq. 2), "*I am looking for a film whose genre is romantic, and the duration is not more than 1 hour and 50*" (Eq. 3).

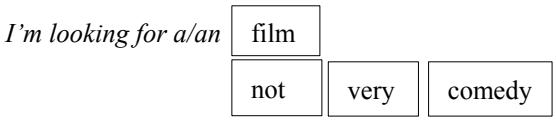

(2)

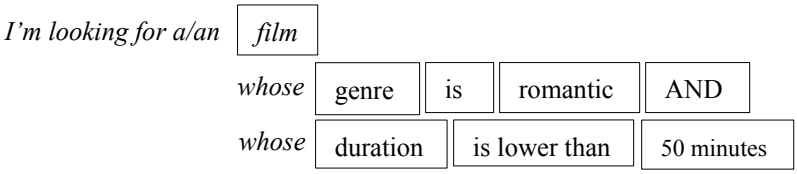

(3)

3.3 New Approaches Added to FleSe

The motivations of our work for introducing new approaches to FleSe includes the following points:

1. *Database used by FleSe*: FleSe allows the users to query only over Prolog databases, but the common databases that users are mostly dealing with are CSV, Excel and some modern databases such as MongoDB, MySQL, and so on.
2. *The User-friendly interface of FleSe*: The technical terms and some configuration options in the interface was not user-friendly enough for all types of users. Thus, our work devoted to the points as mentioned earlier includes:
   - Now FleSe allows users to work with various database formats such as MongoDB, MySQL, XLS, XLSX, and CSV, and to perform expressive (fuzzy) searches over these databases.
   - The interface is now more user-friendly having easy and non-technical terms for defining and searching any fuzzy or non-fuzzy criteria.

4 Implementation Details

4.1 Database Uploading Interface

We developed the uploading interface of FleSe, which is a web interface written in Java, JavaScript, and HTML. The interface will let the databases of formats MongoDB, MySQL, CSV, XLS, XLSX, and Prolog to be uploaded into the framework as shown in Fig. 3. We provided a better uploading mechanism for the framework that other database formats can easily contribute with FleSe. The uploading interface

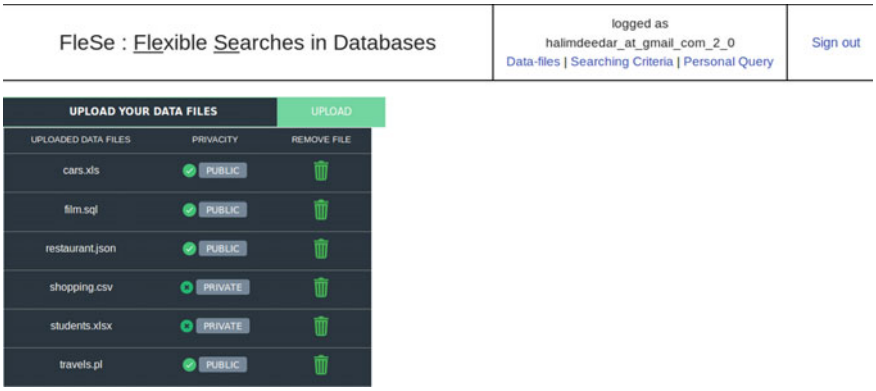

Fig. 3 Database uploading interface

includes a list of data-files, an option of sharing data-files with other users (Public or Private), and the option to remove uploaded data-files. The uploading process includes the following steps:

Step 1: Parsing and conversion of databases into CSV
The uploaded databases will get converted into Comma Separated Value (CSV) file after going through a parsing process of data-files. We made it so, that contents of the database files become more understandable and readable to the user, as there are some databases with a complex structure which are a bit difficult to be used by the user with less knowledge of databases such as syntax of MySQL, JSON, and so on.

Step 2: Defining column types
Once the data-file has been converted into CSV (automatically by the system) the user can define the data-types for each column of the database as shown in Fig. 4 we have uploaded a database of cars having ten columns (id, manufacturer, class, year_of_production, horsepower, max_speed_in_kph, number_of_cylinder, fuel_tank_capacity, _fuel_type, price_in_euros) and then we have manually assigned

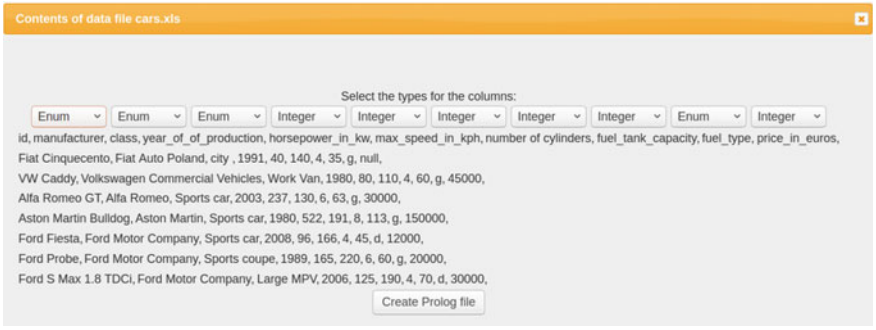

Fig. 4 Assigning data types for the column

the different data-types (enum_type, enum_type, enum_type, integer_type, integer_type, integer_type, integer_type, integer_type, enum_type, and integer_type.), respectively. After assigning the data-types, we need to click on "Create Prolog file" button to get the Prolog version of our database. The data-types offered by FleSe are boolean_type, enum_type, integer_type, float_type, and string_ type. We provided an example of a film database with four columns in (Eq. 4) to show the syntax of RFuzzy database definition in FleSe.

$$\begin{aligned} &\textit{define\_database(film/4,} \\ &\qquad \textit{[(film\_name, string\_type),} \\ &\qquad \textit{(genre, enum\_type),} \\ &\qquad \textit{(release\_year, integer\_type),} \\ &\qquad \textit{(durations\_in\_minutes, integer\_type)]).} \end{aligned} \tag{4}$$

Each data-types defines the characteristics of a column and they help us while performing fuzzy or non-fuzzy searching over a database. For example, there are a set of comparison operators defined in FleSe available for each column based on their data types. The available comparison operators for integer_type and boolean_type are "is_equal_to" and "is_different_from", for enum_type the available comparison operators are "is_equal_to", "is_different_from", and "is_similar_to", and for string_type & float_type the available comparison operators are "is_equal_to", "is_different_from", "is_bigger_than", "is_lower_than", "is_lower_than_or_equal_to", and "is_bigger_than_or_equal_to".

Step 3: Converting CSV into Prolog

Prolog is used for performing fuzzy searches in FleSe; Therefore, we have then converted our CSV intermediate data-file into a Prolog file; thus, our databases of any mentioned formats are ready for users in the system with the final format of Prolog database (containing crisp information) as shown in Fig. 5.

4.2 The Output Interface

The answering interface (shown in Fig. 6) presents different sets of results in different tabs, the tabs with results in the best 30%, the ones that satisfies the criteria more than the 50%, the ones that satisfy the criteria in a (even small) degree and finally, all the results (the results whose truth value is over 0.7, over 0.5, over 0 and all the results) so that user can choose the one which satisfies his/her requirements. We used Ajax to prevent the wastage of computing time for getting the result form each tab.

We have asked the system for providing the fast cars from the Cars database that by the way was in XLS format. In Fig. 6 the result of our query is shown. The criterion of being fast is defined over a crisp characteristic of the car that is the speed. From the different tags that are offered by the output interface, we have chosen the one that is showing the 70% best results.

```
:- module(cars ,_, [rfuzzy, clpr]).
define_database(cars/10,
[(id, rfuzzy_enum_type),
(manufacturer, rfuzzy_enum_type),
(class, rfuzzy_enum_type),
(year_of_of_production, rfuzzy_integer_type),
(horsepower_in_kw, rfuzzy_integer_type),
(max_speed_in_kph, rfuzzy_integer_type),
(number of cylinders, rfuzzy_integer_type),
(fuel_tank_capacity, rfuzzy_integer_type),
(fuel_type, rfuzzy_enum_type),
(price_in_euros, rfuzzy_integer_type)]).
cars('Fiat Cinquecento', 'Fiat Auto Poland', city , 1991, 40, 140, 4, 35, g, null).
cars('VW Caddy', 'Volkswagen Commercial Vehicles', 'Work Van', 1980, 80, 110, 4, 60, g, 45000).
cars('Alfa Romeo GT', 'Alfa Romeo', 'Sports car', 2003, 237, 130, 6, 63, g, 30000).
cars('Aston Martin Bulldog', 'Aston Martin', 'Sports car', 1980, 522, 191, 8, 113, g, 150000).
cars('Ford Fiesta', 'Ford Motor Company', 'Sports car', 2008, 96, 166, 4, 45, d, 12000).
cars('Ford Probe', 'Ford Motor Company', 'Sports coupe', 1989, 165, 220, 6, 60, g, 20000).
cars('Ford S Max 1.8 TDCi', 'Ford Motor Company', 'Large MPV', 2006, 125, 190, 4, 70, d, 30000).
```

Fig. 5 Contents of Prolog data-file

10 best results | Results over 70% | Results over 50% | Results over 0% | All results

car	id	manufacturer	class	horsepower in kw	max speed in kph	number of cylinders	fuel tank capacity in litres	fuel type	price in euros	Truth Value
nº.1	Mini Cooper	British Motor Corporation	Economy Car	120	198	4	40	g	24000	0.99
nº.2	Aston Martin Bulldog	Aston Martin	Sports Car	522	191	8	113	g	150000	0.95
nº.3	Ford S Max 1.8 TDCi	Ford Motor Company	Large MPV	125	190	4	70	d	30000	0.95
nº.4	Peugeot 306	Peugeot	Family Car	90	182	4	60	d	15000	0.91
nº.5	Ford Fiesta	Ford Motor Company	City Car	96	166	4	45	d	12000	0.82

Fig. 6 Output interface

5 Query Syntax

5.1 Combining Crisp and Fuzzy Queries

In FleSe we can execute a crisp and fuzzy query combined in a single query over a database of type SQL, JSON, XLS, XLSX, CSV, and Prolog. Taking an example of a film database with a query “Which drama films are not so long?” we can see that the first part of the query which is “looking for a drama film”, is a crisp query and the second part of the query which is “a film with a not very long duration”, is a

Fig. 7 Combining crisp and fuzzy queries

fuzzy query therefore, FleSe allows us to combine and execute both the queries. We show in Fig. 7 how we can combine fuzzy and crisp query and the result is shown in Fig. 8.

We can pose compound queries over various database formats such as SQL, JSON, CSV, XLS, XLSX, and Prolog. To clarify this, we take an example of a restaurant database with query "Which restaurants are costly, little traditional and rather close to the city center?". If we look to the query, in fact, it is three different fuzzy queries combined into a single query. Thus, FleSe allows us to create and execute such type of compound queries as shown in Fig. 9, we can see that the compound queries can be constructed using negation operator and quantifiers (little, rather, very) and the button ADD in the interface is helping us to add another condition or predicate in our query, and we have shown the result of our query in Fig. 10.

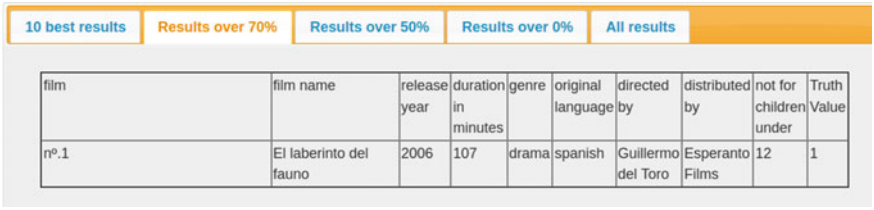

Fig. 8 Query result

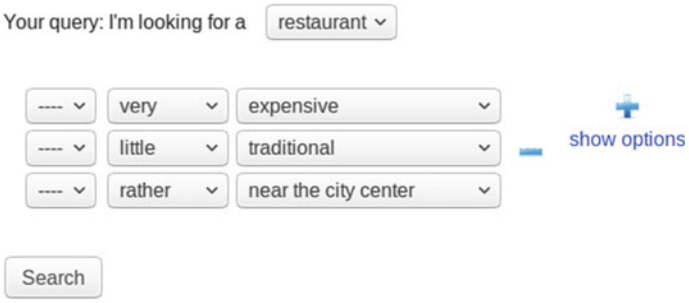

Fig. 9 Compound queries

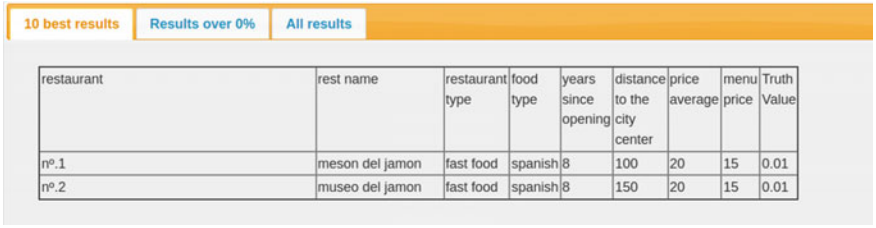

restaurant	rest name	restaurant type	food type	years since opening	distance to the city center	price average	menu price	Truth Value
nº.1	meson del jamon	fast food	spanish	8	100	20	15	0.01
nº.2	museo del jamon	fast food	spanish	8	150	20	15	0.01

Fig. 10 Query result

6 Conclusion

It is always a challenge creating bridges between different fields to achieve join advances. There are some advances from fuzzy logic to provide expressive searching queries that use fuzzy criteria. But the promising prototypes are devoted to minority data formats as Prolog where most data owners lose the possibility to experiment with their data in the prototype. With this work, we have tried to reduce the gap between the database users and the logic programming users to let the first ones be able to search their crisp data in conventional formats in a flexible and expressive way. We have presented an advanced framework that allows a regular user to perform fuzzy and non-fuzzy queries over multiple database formats such as MongoDB, MySQL, CSV, XLS, XLSX, and Prolog with a very user-friendly querying interface (understandable by any non-expert users), and our framework is very adaptable that means any other database formats can easily incorporate with it. Being able construct simple queries to search in a flexible way by using expressive concepts as fuzzy criteria and similarity is a clear advantage of our framework with respect to any other standard available tool, such as MySQL. The purpose of our research is to present an intelligent searching system for databases that understand the queries from users and provide the results that he/she expects to obtain from any conventional and modern databases. Our current research focuses on the development of the framework allowing users to pose their expressive queries based on defining similarity relations criteria.

References

1. Bosc P, Pivert O (1995) SQLf: a relational database language for fuzzy querying. IEEE Trans Fuzzy Syst 3(1):1–17. https://doi.org/10.1109/91.366566
2. Pablos-Ceruelo V, Muñoz-Hernández S (2014) FleSe: a tool for posing flexible and expressive (fuzzy) queries to a regular database. In: Proceedings of Distributed Computing and Artificial Intelligence, 11th International Conference, 2014, pp 157–164
3. Muñoz Hernández S, Pablos-Ceruelo V, Strass H (2011) RFuzzy: syntax, semantics and implementation details of a simple and expressive fuzzy tool over prolog. Inf Sci 181(10):1951–1970. https://doi.org/10.1016/j.ins.2010.07.033
4. The CLIP lab, The Ciao Prolog development system. http://www.clip.dia.fi.upm.es/Software/Ciao

5. Guadarrama S, Muñoz S, Vaucheret C (2004) Fuzzy Prolog: a new approach using soft constraints propagation. Fuzzy Sets Syst 144(1):127–150. https://doi.org/10.1016/j.fss.2003.10.017
6. Pablos-Ceruelo V, Strass H, Muñoz Hernández S (2009) RFuzzy-A framework for multi-adjoint fuzzy logic programming. In: Proceeding fuzzy information processing society, 2009, pp 1–6. https://doi.org/10.1109/nafips.2009.5156427.lncs
7. Zadeh LA (1988) Fuzzy logic. Computer 21(4):83–93. https://doi.org/10.1109/2.53
8. Medina J, Ojeda-Aciego M, Vojtas P, A procedural semantics for multi-adjoint logic programming. In: Proceeding Progress in Artificial Intelligence, pp 290–297
9. Pablos-Ceruelo, V, Muñoz Hernández S (2013) Getting answers to fuzzy and flexible searches by easy modelling of real-world knowledge. In: Proceeding of 5th International Joint Conference on Computational Intelligence, 2013, pp 265–275. https://doi.org/10.5220/0004555302650272

Surpassing Traditional Image-Colorization Problems with Conditional Generative Adversarial Networks

Vishnu Teja Yalakuntla, Rahul Kanojia, Kushagra Chauhan, Rohit Gurnani and Mukesh A. Zaveri

Abstract Color helps to understand the semantic information of the image more accurately and reveals a lot more details which grayscale images cannot. By looking at an image, humans can automatically segment different objects present in an image making it easier for us to color an image. We propose a completely automated system to colorize grayscale images which learns to segment and color images in a realistic manner. We leverage the recent advancements in deep learning, Generative Adversarial Networks and improved cost functions, to overcome the problems of traditional Convolutional Neural Networks with image colorization. Given the unconstrained nature of the problem, we propose this algorithm to make a colorization model that achieves realistic colorizations. We have experimented different deep network architectures with various training algorithms and cost functions to come up with this network where we can clearly see realistic colors for given gray scale image and differentiate the characteristics of generative adversarial network from a traditional convolutional neural network.

Keywords Conditional generative adversarial network · Skip connections · Localization · Image colorization

V. Teja Yalakuntla · R. Kanojia · K. Chauhan · R. Gurnani · M. A. Zaveri (✉)
Computer Engineering Department, Sardar Vallabhbhai National Institute of Technology, Surat 395007, Gujarat, India
e-mail: mazaveri@coed.svnit.ac.in

V. Teja Yalakuntla
e-mail: yvtheja@gmail.com

R. Kanojia
e-mail: kaanorahul8@gmail.com

K. Chauhan
e-mail: chauhankushagra1@gmail.com

R. Gurnani
e-mail: rkgi10@gmail.com

© Springer Nature Singapore Pte Ltd. 2020

T. Hitendra Sarma et al. (eds.), *Emerging Trends in Electrical, Communications, and Information Technologies*, Lecture Notes in Electrical Engineering 569,
https://doi.org/10.1007/978-981-13-8942-9_4

1 Introduction

Colorization is a task that is very simple for humans; with impressive imagination skills built on a composite platform of experiences and the brains power to abstract, the complexity of the problem is not even realized. With a machine, without these human skills, coloring an image without any manual input is a increasingly challenging task. Image colorization can make an image lively, but current techniques demand major user-interaction and involvement. Moreover, users can find it difficult to provide consistent and coherent color models/scribbles.

Generally classifying, there have been two directions in which colorization methods have been developed. The first approach focus more to reduce the effort and speed up the process of using tools with a need for human interaction, thus lowering the cost of colorization process. The later focus mainly to eliminate the user inputs completely from the system. Our objective is to eliminate user involvement completely, while improving the end result to be consistent, coherent and as natural looking as possible, doing it in a way thats computationally feasible.

Features are rich piece of information extracted from images in terms of numerical values that are difficult to understand and correlate by human. Several features can be extracted from a single image, such as corners, edges and blobs. The extraction of these features are the major overheads in processing an image.

To color an image accurately, different types of features on different scales are needed. Local features like, segmentation information and global features like, weather on the image are necessary to color an image. Global image features describes an image as whole whereas local feature represents more of pixel level information. Global features are generally used in image retrieval, object detection and classification, while the local descriptors used for object recognition/identification. A combination of both has served as a good input for a number of applications in computer vision.

In recent times, Convolutional Neural Networks (CNN) have served as an excellent tool to extract both global and local features, with various applications like object class recognition [2] and image retrieval [3]. Recent systems have used different approaches to embed and merge these features into the pipelines. Maintaining completely different networks to extract global and local features [4], constructing a new 3D layer called hypercolumns [1] by merging higher layers for semantic details and lower layers for localization details are significant examples. In both ways, the results have been improved and merging of global and local features played a crucial role in achieving them.

Some of the approaches like [5–11], are more of semi-automatic way, in which some or the other form of user input is required such as sparse inputs in the form of colors, or regionality of colors and color histograms. These systems require human intervention, but usually have more accurate results. For example, the approach followed in [5] requires a huge amount of color details from the user, which enables the system to generate variety of vibrant color images. However, designing a system which is completely independent and which wouldn't require any user inputs is a promising problem.

2 Approach

2.1 LAB Colorspace

In 1976, CIE defined a new colorspace named LAB. It expresses color as three numerical values L* represents the lightness channel while a* and b* represents the color channels. The three channels can represented in a three dimensional space where each channel is located at one of the axis. The vertical L* axis ranges from 0–100 depicting lightness. The other (horizontal) axes are represented by a* and b*. The a* is a green-red component being green at one extremity of axis (represented by −a) and red at other (+a). Similarly, b* is blue-yellow component. In practice, the values of horizontal axis ranges from −128 to +127 (256 values).

In colorizing grayscale images, the LAB colorspace is preferred over RGB as LAB encoded image has one layer of grayscale (lightness channel L*) and have packed three color layers namely RGB, into two (a* and b*). This means we can utilize raw grayscale images in colorization and only need to predict only two channels. Additionally, LAB colorspace encompasses the entire spectrum, resulting in more realistic color predictions.

2.2 Generative Adversarial Networks

Firstly proposed by Ian J. Goodfellow [12], Generative Adversarial Networks is an example of adversarial learning from generative models. A GAN [13] comprises of two competing neural network models, G a generative model that learns to generates new data and a discriminative model D that computes the probability that whatever sample data G produces to feed it, whether it is from training data or from G itself.

The two models play a minimax game against each other—minimizing a maximum possible loss that one of two players can make. G is fed with noise and it generates new data based on the discriminations of discriminator; every time G generates a new sample, D will try to determine if the sample is from the model or the training set. Ultimately G will learn to create data which is nearly impossible for the discriminator D to distinguish.

To reproduce images that looks similar to images in the sample, generator G is fed with noise z. The mapping can be represented as G(z) where G is a differential function. The output is then fed to discriminator D along with the ground truth image x represented as D(G(z)) and D(x) respectively. D is trained to maximize the probability of assigning correct labels while simultaneously G is trained to minimize the same. This can be expressed mathematically using a value function V(G, D) [12] as shown in Eq. 1.

$$\min_{\mathbf{G}} \max_{\mathbf{D}} V(G, D) = E_{x \approx p_{data}(x)}[log\, D(x)] + E_{z \approx p_z(z)}[log(1 - D(G(z)))] \quad (1)$$

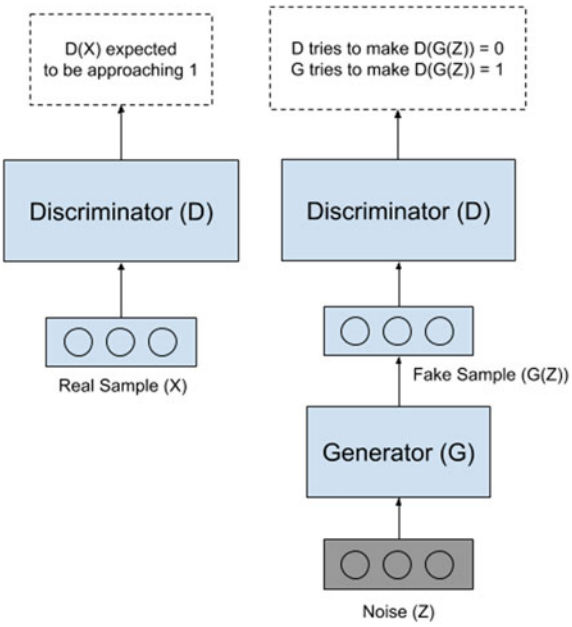

Fig. 1 Basic working of GAN [1]

In value function V(G, D), the first term is entropy that the data x is from real distribution (pdata(x)) and is fed to discriminator. Discriminator tries to maximize D(x) to 1. The second term is entropy that the data from random noise p(z) is input to generator, which generates a sample using z and feed it to discriminator. Discriminator tries to maximize D(G(z)) to 0 (i.e. the log probability that the data from generator is fake and therefore is equal to 0). Overall discriminator tries to maximize function V. On the other hand, generator tries to minimize this function so that both real and fake images become indistinguishable. Figure 1 depicts the basic algorithm for a GAN.

2.3 Conditional GAN

In ordinary GANs, the input to generator is only the randomly generated noise z, and for that reason we have no control in directing the data generation process. Mirza et al. [14] extended idea of GAN and proposed a conditional model called Conditional Generative Adversarial Networks (CGAN). Using the conditional version of GAN, one can direct the data generation process of generator and restrict it to a desired subset.

Basically, in CGAN both generator and discriminator are conditioned on additional information y, which could be any auxiliary information such as class labels or data from other modalities [14]. The conditioning is performed by feeding y into both discriminator and generator as an additional input layer. We can think of this

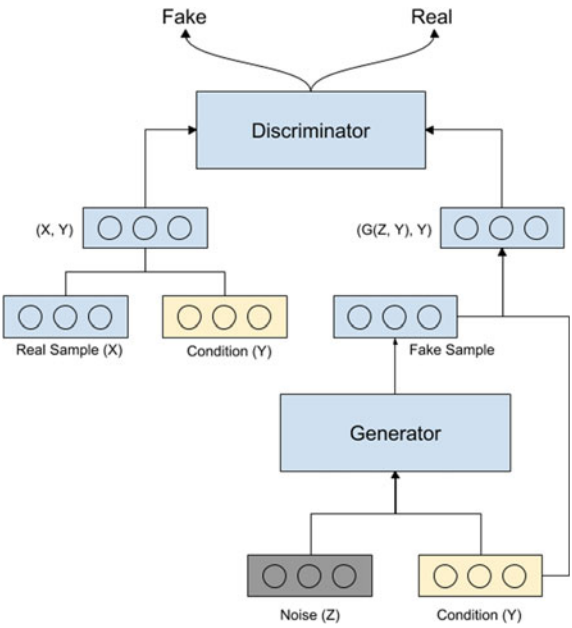

Fig. 2 Simple structure of conditional GAN

information y as a particular setting or *mode* in which the model will be working. The consequence of making model work in a particular *mode* is that we can directly control the output of generator. Altogether it's like restricting generator in it's output and discriminator in it's input.

As a result of conditioning input y, the generator function G(z) now becomes G(z, y) and similarly discriminator function D(x) becomes D(x, y) where z is random noise and x is an input from dataset. The objective function will be transformed to:

$$\min_{\mathbf{G}} \max_{\mathbf{D}} V(G, D) = E_{x \approx p_{data}(x)}[log D(x, y)] + E_{z \approx p_z(z)}[log(1 - D(G(z, y)))] \tag{2}$$

Figure 2 illustrates basic structure of conditional GAN. In contrast with the conventional GANs, we now has an additional input layer in both generator and discriminator network.

2.4 Network Architecture

Colorization with CGANs have shown success in overcoming the problem of picking average colors from the training dataset which is a major problem faced by a CNN network. We propose training a CGAN with condition as a gray scale along with the noise making generator produce LAB colorspace images. Discriminator is trained to classify between fake and real images with LAB image along with the condition, a grayscale image, as input. Figure 3 represents the overview of the network.

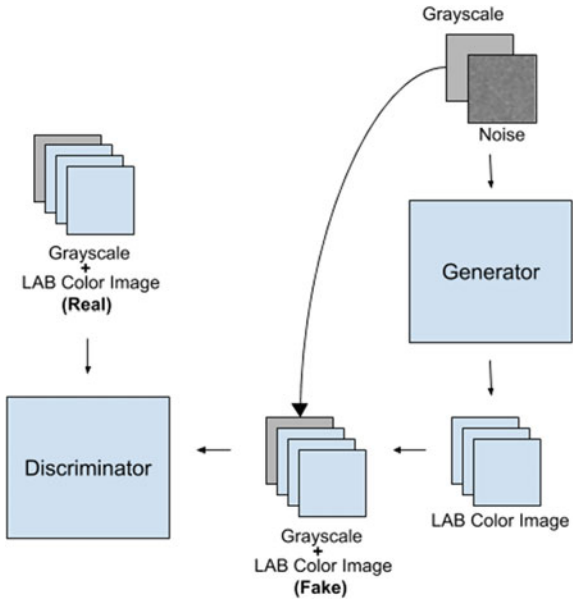

Fig. 3 Overview of GAN for image colorization

Initially, generator network produces fake color images which can be easily differentiated from real color images making the job too easy for the discriminator. Receiving strong gradients at this phase, generator starts to get better at producing fake color images making the job gradually difficult for discriminator. As the generator gets fully trained, it produces fake color images which are almost indistinguishable from the real color images making it impossible for discriminator to differentiate between fake and real color images. As a result, discriminator makes random guesses for predictions and its loss keeps oscillating around 0.5 making the GAN fully trained.

Generator is a convolutional neural network with 17 convolutional layers and zero pooling layers. Strides of length more than one is used instead of pooling layers to make network to learn the effective downsampling. As the number of layers increases, the localization, or pixel information is lost and upper layers are more likely to learn global features [15]. To effectively color the images pixel level information is very much need in the upper layers of the CNN. As the Generator predict colors on pixel level, the localization information present in the lower level layers of the network is crucial to segment different objects in the image and draw accurate boundaries for the colors. To assist the network to pass this localization information to higher level layers, skip connections are added in the generator network (Fig. 4).

Initially filter maps are downsampled gradually with stride length of two and Batch normalization with Leaky ReLu as an activation function is used for all convolutional layers except for the last layer of the generator which uses hyperbolic tangent function as the activation. At the skip connections, the filter maps are upscaled by resizing them with bilinear interpolation technique and added to the corresponding upper

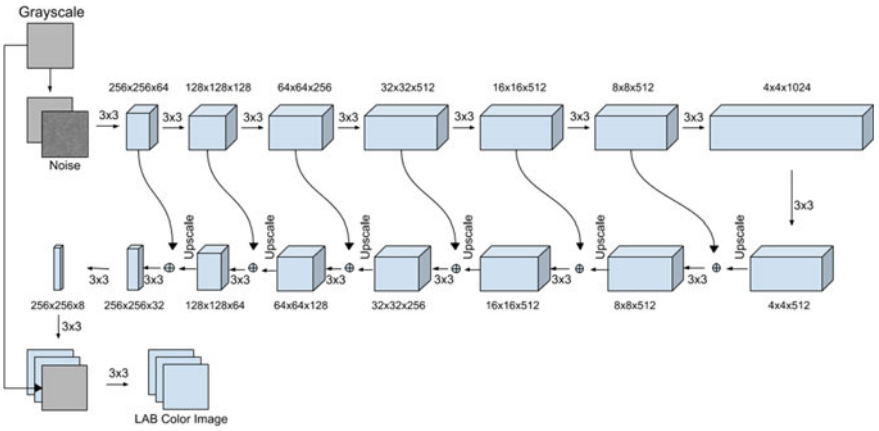

Fig. 4 Generator network

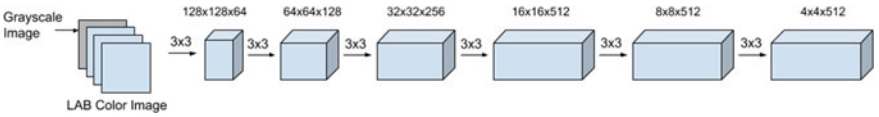

Fig. 5 Discriminator network

layers of the network. Figure 5 shows the architecture of the generator network. Skip connections play a very important role in passing the localization information to upper layers of the network and it is found that the generator is incapable in producing color samples without them. Even concatenating the grayscale image to filter maps of last few layers couldnt help overcome the problem. Hypercolumns [5] can also be used to preserve the localization information till the output layer [12]. Concatenating all the filter maps and adding convolutional layers on top of this huge number of filter maps require a lot of memory and computational power. By downsampling the image for only four times, a hypercolumn containing 932 filter maps has to be generated which couldnt be trained on 4GB Nvidia Quadro M1000M GPU. However, skip connections are known to perform better compared to hypercolumns.

Discriminator is a simple classification network which tries to classify based on the condition and color image fed to it. Figure 5 shows the architecture of the discriminator network. Discriminator network can be very easily trained and once it becomes very confident about its predictions, the gradients for the generator network vanishes. To avoid this, discriminator is trained once for every three times the generator is trained.

$$\min_{\theta_G} J^{(G)^*}(\theta_D, \theta_G) = \min_{\theta_G} -E_z[log D(G(z))] + \lambda \, ||G(z) - y|| \tag{3}$$

The above cost function explained in [14] has been used with λ as 100. From the loss plots of both generator and discriminator networks, the characteristics of a

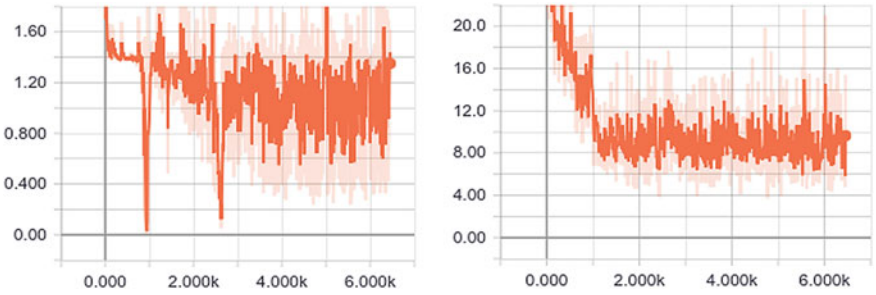

(a) Discriminator Loss Plot (b) Generator Loss Plot

Fig. 6 GAN loss plots

GAN can be clearly observed. Figure 6a shows the generator loss and Fig. 6b shows the combined loss for fake and real images of discriminator during the training. As the generator network gets better at producing fake color images, as the loss of the generator decreases, the discriminator gets more confused about its predictions.

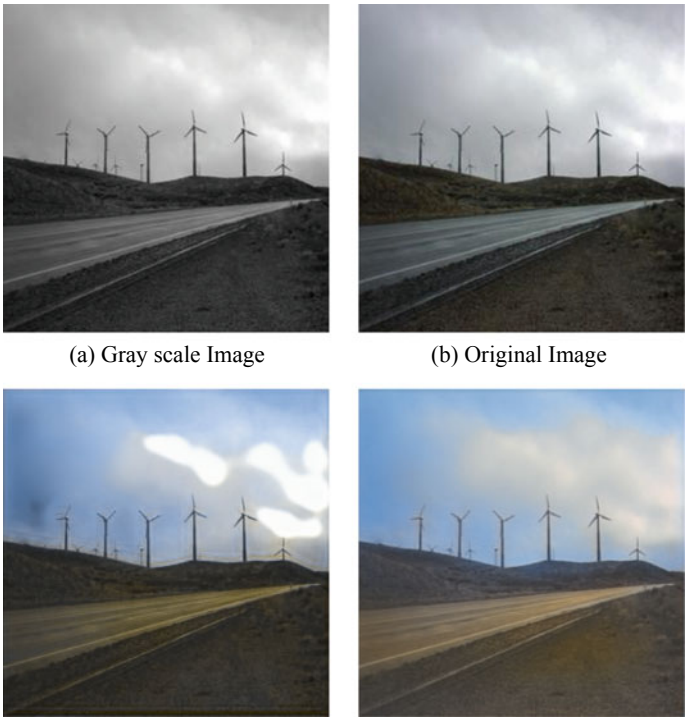

(a) Gray scale Image (b) Original Image

(c) CNN Output (d) GAN Output

Fig. 7 Color comparison between GAN and CNN

3 Results

To compare results between a normal CNN and a GAN, only the generator network is trained with Least Absolute Deviations (l^1) cost function. After training with around 4000 images of wind farm from place 365 [16] dataset the characteristics of GAN is clearly observed and could be differentiated from the results of normal CNN. For instance, from Fig. 7d it can be observed that GAN network colored the sky with more of sky blue color but the normal CNN colored with a shade of blue which appears to be an average from dataset. The same can be observed with the color of grass in Fig. 9d.

The CNN network also didn't learn to pass on the localization information to the high level layers. From Fig. 8 it can be observed that some part of the image is lost and covered with a uniform color trying to reduce the loss. This effect is not seen in the GAN as the discriminator is trained to discriminate these type of images as fake.

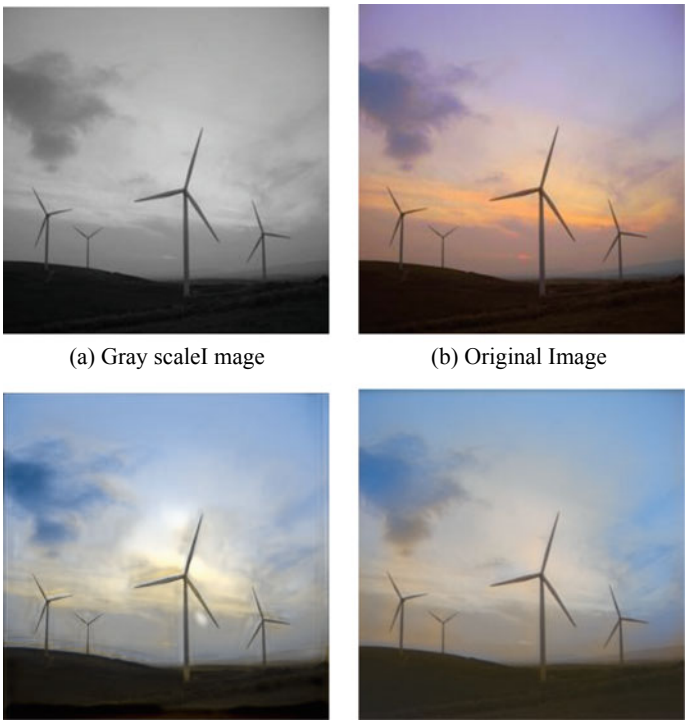

(a) Gray scaleI mage (b) Original Image

(c) CNN Output (d) GAN Output

Fig. 8 Localization problem with CNN network

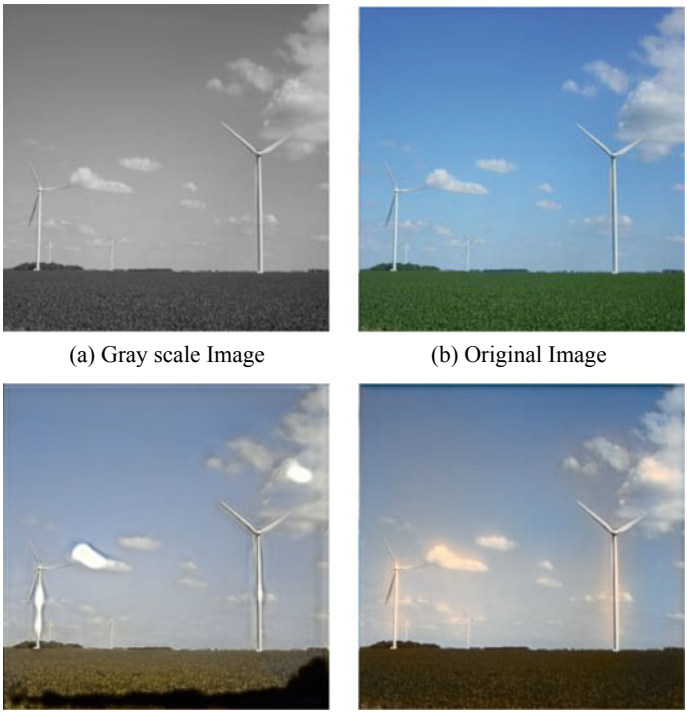

(a) Gray scale Image (b) Original Image

(c) CNN Output (d) GAN Output

Fig. 9 Localization problem with CNN network

4 Conclusion

Auto colorization of gray scale images has seen rapid research in recent years with new papers being published each month; although the limited realism and accuracy of these implementations leaves further scope of more novel and complex iterations of improving results. Our implementation offer a novel addition to the techniques that can be used for colorization by incorporating skip connections and modified cost functions, features at different scales and GANs which have significantly overcome the problem of picking average colors and color localization in general.

GANs are capable of producing high quality images at higher resolution [13]. When it comes to problems like images colorization, where there a conditional input, localization information becomes crucial. As seen in the Figs. 8c and 9c, the objects are not accurately localized because of which the colors are incorrectly spread across different objects. Building a RNN network on top of the CNN would be one of the solutions to address this problem.

The loss function for generator network includes L1-norm as one of the components which makes the network to produce average colors to a small extent. Removing

this component made the generator network more sensible and as the discriminator became more confident of its predictions the generator network couldn't receive any gradients. To rectify this, l1 weight can be decayed over iterations which helps generator network to initially train properly and regain its GAN characteristics as the l1 weight decreases.

Coloring a gray scale image with desired qualities is also more important. Global features of the image such as whether it is cloudy, landscape, portrait will affect the colorization to a large extent. To achieve this, more than one condition can be fed to generator network. Additional conditions such as color histograms, hue, saturation, weather and camera mode will help to achieve desired colors for a gray scale image. Video colorization would be the next appendage to image colorization. Instead of colorizing a video frame by frame using a CNN model, LSTM networks can be used to store the color histograms and semantics of a buffer of frames and use them to color the adjacent or similar frames.

References

1. Yu F, Koltun V (2016) Multi-scale context aggregation by dilated convolutions. In: Proceedings of international conference on learning representations
2. Lisin DA, Mattar MA, Blaschko MB, Benfield MC, Learned-Mille EG (2005) Combining local and global image features for object class recognition. In: IEEE computer society conference on computer vision and pattern recognition (CVPR), p 47. https://doi.org/10.1109/CVPR.2005.433
3. Ng JY-H, Yang F, Davis LS (2015) Exploiting local features from deep networks for image retrieval. In: IEEE conference on computer vision and pattern recognition workshops (CVPRW), pp 53–61
4. Iizuka S, Simo-Serra E, Ishikawa H (2016) Let there be Color!: joint end-to-end learning of global and local image priors for automatic image colorization with simultaneous classification. ACM Trans Graph (Proc SIGGRAPH 2016) 35(4)
5. Zhang R, Zhu J-Y, Isola P, Geng X, Lin AS, Yu T, Efros AA (2017) Real-time user-guided image colorization with learned deep priors. In: SIGGRAPH
6. Charpiat G, Hofmann M, Schlkopf B (2008) Automatic image colorization via multimodal predictions. In: Forsyth D, Torr P, Zisserman A (eds) ECCV 2008, Part III. LNCS, vol 5304. Springer, Heidelberg, p 126139
7. Chia AYS, Zhuo S, Gupta RK, Tai YW, Cho SY, Tan P, Lin S (2011) Semantic colorization with internet images. ACM Trans Graph (TOG) 30:6. ACM
8. Gupta RK, Chia AYS, Rajan D, Ng ES, Zhiyong H (2012) Image colorization using similar images. In: Proceedings of the 20th ACM international conference on multimedia. ACM
9. Irony R, Cohen-Or D, Lischinski D (2005) Colorization by example. In: Eurographics symposium on rendering
10. Levin A, Lischinski D, Weiss Y (2004) Colorization using optimization. In: SIG-GRAPH
11. Sapiro G (2005) Inpainting the colors. In: IEEE international conference on image processing (ICIP). Genova
12. Goodfellow I, Pouget-Abadie J, Mirza M, Xu B, Warde-Farley D, Ozair S, Courville A, Bengio Y (2014) Generative adversarial nets. In: Advances in neural information processing systems, pp 2672–2680
13. Wang X, Gupta A (2016) Generative image modeling using style and structure adversarial networks. In: Leibe B, Matas J, Sebe N, Welling M (eds) Computer vision ECCV 2016. Lecture notes in computer science, vol 9908. Springer, Cham

14. Mirza M, Osindero S (2014) Conditional generative adversarial nets. arXiv:1411.1784
15. Hariharan B, Arbelaez P, Girshick R (2015) Hypercolumns for object segmentation and fine-grained localization. In: Proceedings of conference on computer vision and pattern recognition (CVPR)
16. Goodfellow I (2016) NIPS 2016 tutorial: generative adversarial networks. arXiv:1701.00160
17. Dahl R (2016) Automatic colorization. http://tinyclouds.org/colorize. Accessed 30 Aug 20108
18. Nazeri K, Ng E, Ebrahimi M (2018) Image colorization with generative adversarial networks. In: Perales F, Kittler J (eds) Articulated motion and deformable objects. AMDO 2018. Lecture notes in computer science, vol 10945. Springer, Cham. arXiv:1803.05400
19. Karras T, Aila T, Laine S, Lehtinen J (2018) Progressive growing of GANs for improved quality, stability, and variation. In: Proceeedings of international conference on learning representations (ICLR). Vancouver
20. Zhou B, Lapedriza A, Khosla A, Oliva A, Torralba A (2017) Places: a 10 million image database for scene recognition. IEEE Trans Pattern Anal Mach Intell (ICLR) 40:1452–1464. https://doi.org/10.1109/TPAMI.2017.2723009

Memristor—The New Computing Element for Data-Centric Real-Time Image Processing

Bindu Madhavi Tummala and Soubhagya Sankar Barpanda

Abstract CMOS technology and its sustainable scaling have been the facilitators for the design and modeling of computers that have been inciting a wider range of applications. A broad dependence on technology, voluminous data, and rising processing needs have imposed the technology-computer architecture duos to suffer from serious hardships that hinder transistor utilization and advertise the need for new devices. This stimulates novel architectures equidistant to novel technologies. With zillion advantages like tiny size, high power tolerance, remembering capacity, huge retention, high persistence, low reads and writes, 3D design ability, tight fit with portable devices, made memristor a breakthrough technology for all ongoing data-centric applications. This paper review about memristor In-Memory computing capabilities, and its potency in Combinational logic and propose an architecture that suits for real-time Image processing applications.

Keywords Memristors · In-memory computing · Combinational logic · Real-time image processing

1 Introduction

Nowadays, technology is demanding the computation speed of a supercomputer with constraints on size, power consumption with guaranteed response time. But ongoing computer architectures are facing problems to cope up with the trending technologies. The main trio walls are: (1) the memory wall due to the speed gap between processor and memory. This leads to bandwidth limitation which is a performance killer in data storage-hungry applications; e.g. big data; (2) the Instruction Level Parallelism(ILP)

B. M. Tummala (✉) · S. S. Barpanda
Department of Computer Science and Engineering, VIT-AP University, Inavolu(v), Amaravati, AP, India
e-mail: bindumadhavibobba@gmail.com

S. S. Barpanda
e-mail: soubhagya.barpanda@vitap.ac.in

© Springer Nature Singapore Pte Ltd. 2020

T. Hitendra Sarma et al. (eds.), *Emerging Trends in Electrical, Communications, and Information Technologies*, Lecture Notes in Electrical Engineering 569,
https://doi.org/10.1007/978-981-13-8942-9_5

wall due to difficulty in finding enough parallelism in software w.r.t to the hardware; (3) the power wall due to the utmost utilization of CPU clock speed [1]. For unceasing benefits to the future society, alternative *computer architectures with new device technologies* should be evolved. Memristor is an ingenious candidate to complement and/or replace CMOS technology(at least in few applications) due to its unique capabilities like zero standby power, CMOS processing abilities and super dense and scalable. Memristor device is the promising favorite in the future neuromorphic architectures, analog memory computations, and other nanosize applications.

This paper survey about the sturdiness of memristor device in designing diversified logic frameworks which boost In-Memory Computing that is beneficial for Image processing applications. First, the paper provides a brief introduction of a memristor device along with its fingerprint properties. Second, it discusses the different logic styles designed by the researchers. Finally, the paper proposes a memristive architecture that suits for real-time Image processing using the MAGIC logic family and VTEAM model, which are best in their categories.

2 Memristor—What's that All About?

The electronic world is familiar with the trinity of fundamental circuit elements, which are passive in nature, named resistors, capacitors, and inductors. These are built on four basic variables- current i, voltage v, charge q and magnetic flux φ. As stated in Table 1, the two of them (Eqs. 1, 2) represent the definitions of current and voltage respectively. The other three (Eqs. 3, 4, and 5) represents the orthodox two-terminal passive elements. For the sake of integrity, Leon Chua gauge a fourth device that joins the charge and flux and hypothesized (Eq. 6). He named it as a memristor(memory + resistor) because it has the properties of a resistor along with non-volatile memory [2].

Table 1 Fundamental circuit elements

Sr. No	Definition	Equation
1.	Current	$dq = idt$
2.	Voltage	$d\varphi = vdt$
3.	Resistor	$dv = Rdi$
4.	Capacitor	$dq = Cdv$
5.	Inductor	$d\varphi = Ldi$
6.	Memristor	$d\varphi = Mdq$

2.1 Memristor Definition

Leon Chua defines that *A two-terminal device marking a pinched hysteresis loop, always passing through the origin in the voltage-current plane when driven by any periodic current or voltage source with zero DC component is called as an* ***ideal memristor*** [3]. This annotation clearly states that the memristor device making is irrelevant to the internal material composition. Thus, memristors can be made from different materials (Fig. 1). Memristor can be defined in two ways based on its input. If the input source is current, it is called *flux- controlled* memristor with characteristic called as memristance. It is defined as:

$$i(t) = M(\varphi(t))v(t) \tag{1}$$

where

$$M(\varphi) = \frac{dq(\varphi)}{d\varphi} \tag{2}$$

If the input source is voltage, it is called as *charge-controlled* memristor with a characteristic called as memductance. It is defined as:

$$v(t) = M(q(t))i(t) \tag{3}$$

where

$$M(q) = \frac{d\varphi(q)}{dq} \tag{4}$$

$M(\varphi)$, M(q) are memristance and memductance. Chua stated three features that a device has to exhibit to be called as memristor [3]. They are listed as follows:

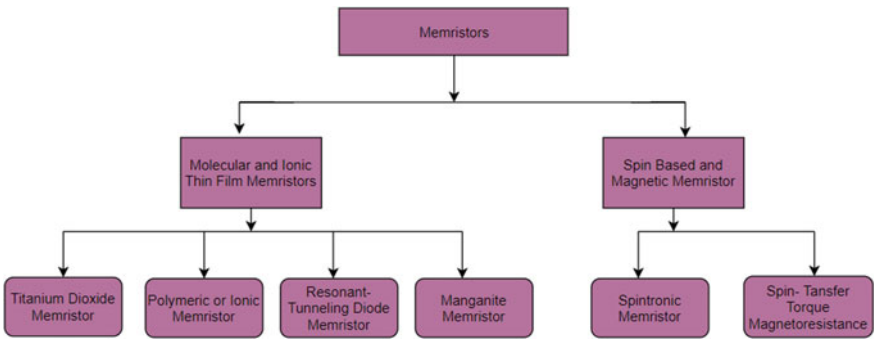

Fig. 1 Memristor taxonomy

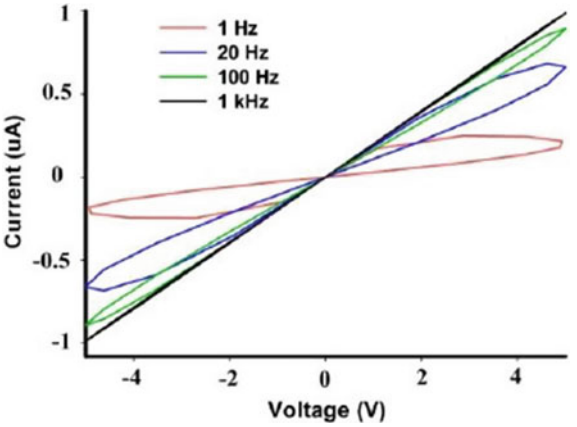

Fig. 2 Memristor fingerprint: pinched hysteresis loop

- It is a passive, non-linear two-terminal device. When voltage is applied the resistance decreases (i.e. the device shrinks) and after sometime the resistance increases due to reverse direction of current. This varying behaviour is known as memristive property.
- When i-v plot is taken with respect to time, the slope represents the multivalued resistance and drops to zero at $v(t) = i(t) = 0$. Henceforth *Pinched hysteresis loop* (Fig. 2).
- When the frequency is increased continously, the loop shrinks to a straight line resembling a linear resistor.

2.2 HP Memristor

A breakthrough in the electronic world is done by HP labs by unfolding the mystery behind the fourth circuit element. Finding the missing element remained evasive for long 3 decades because, its nature of varying resistance is best noticeable at the nanoscale. In 2008, while HP lab team are working on a nanoscale crossbar switch, they found the unique properties, which are of a memristor [4]. They designed the primal mathematical and physical model of a memristor (Fig. 3) and open the doors for new research field and IC technology.

The memristor is fabricated as metal-insulator-metal electrodes. Titanium dioxide is selected as the insulator and partitioned into doped (oxygen vacancies are introduced, Tio_{2-x}) and undoped (Tio_2) regions. The doped region acts as a conductor, having low resistance value R_{on}. The undoped region act as a pure insulator, having high resistance value R_{off}. Platinum is selected as the metal electrode. When the voltage is applied, the oxygen vacancies travel towards the direction of the current, because the oxygen atoms are electron donors. This effect causes the doped region to increase its width, making the total resistance within the device as R_{on}. When

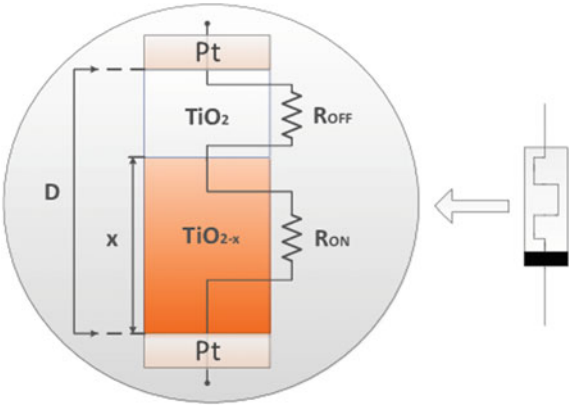

Fig. 3 First physical memristor

negative polarity is introduced, the oxygen vacancies attract to the metal electrode, causing the undoped region width to increase, making the total resistance as R_{off}.

The mathematical model of HP memristor with total device length D and doped region width x, and the ion mobility μ_v is given in terms of memristance:

$$V(t) = \left[R_{on} \frac{x(t)}{D} + R_{off} \left(1 - \frac{x(t)}{D} \right) \right] I(t) \tag{5}$$

where

$$\frac{dx}{dt} = \frac{\mu_v . R_{on}}{D} . I(t) \tag{6}$$

3 Memristor for a True in—Memory Computing

3.1 Memristor for Non-volatile RAM's

Consider the charge-controlled memristor stated by Leon Chua (Eqs. 3, 4) and apply Faraday's Law $\varphi = \int V(t)dt$ and current formula $i = \frac{dq}{dt}$ to it. Thus, the memristor can be rewritten in terms of magnetic flux as

$$\varphi(q) = \int M(q(t))i(t)dt = \int M(q(t))dq \tag{7}$$

At $t = t_0$,

$$\varphi(q) = \int_{t=-\infty}^{t=t_0} M(q(t))dq \tag{8}$$

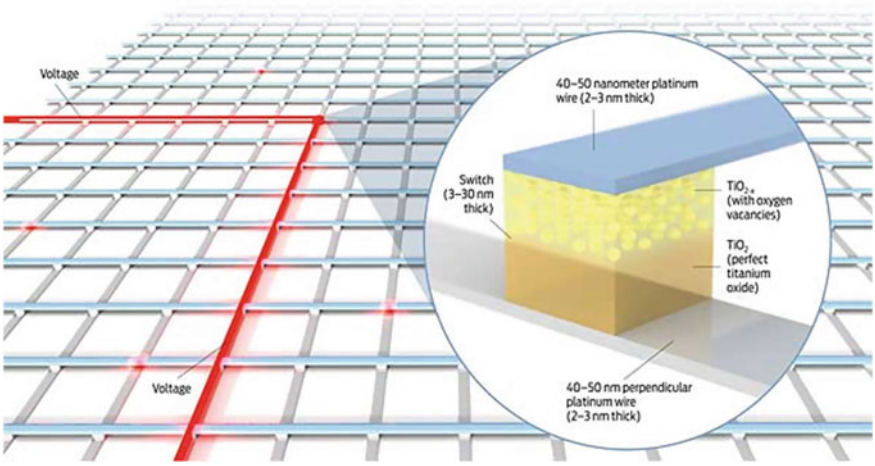

Fig. 4 Memristor crossbar

The magnetic flux depends on the history of charge i.e. the present current value is dependent on the past charge flown within the device. At zero current stage, the memristor holds the past charge until the current supply is given. This *'memory effect'* makes the memristor to store data permanently in all sort of conditions. Memristive memory devices make the best combination with future NVM devices, due to its fast switching time, large resistance ratio, low power reads and writes. Memristive memories have dense storage capacity when configured as a crossbar (Fig. 4). A memristor crossbar is a collection of perpendicular wires, with a memristor at every crosspoint. To make large data to store, 3D design style is preferable and it has the capacity to store even 1 TB of data. It is constructed as follows: Memristor crossbar array has two different pins called- Blues and Reds, with its own decoding scheme for each array. This decoding scheme is called as Double decoding scheme. An array of blue and red pins are accessed by their corresponding control signals. Memristor is connected to the two pins within the cell. The maximum layers within the 3D stacking are depicted as follows:

Theorem 1 *We can have a maximum of* $\frac{C^2}{(r^2-1)}$ *crossbar layers within a 3D design style of memristive crossbar resistive switching memories.*

Proof Each crossbar is like a C X C matrix. Each cell has two pins; one blue and one red. Therefore, C^2 blue pins with $2C$ control signals and C^2 red pins with $2C$ control signals respectively. There are $r^2 - 1$ crosspoints per cell. So, the total crosspoints per layer are $C^2(r^2 - 1)$. Double encoding scheme can access upto C^4 locations. So, the maximum crossbar memristive layers can be:

$$\frac{C^4}{C^2(r^2-1)} = \frac{C^2}{(r^2-1)} \tag{9}$$

Table 2 NVM comparison table

Parameters	Memristors	PCM	STTRAM	DRAM	Flash	HDD
Density (F^2)	**<4**	8–16	37–64	6–8	4–6	2–3
Energy per bit (pJ)	**0.1–3**	2–27	0.1	2	10,000	$1–10\times10^9$
Read time (ns)	**10–100**	20–70	10–30	10–50	25,000	$5–8\times10^6$
Write time (ns)	**10**	50–500	13–95	10–50	200,000	$5–8\times10^6$
Retention	**years**	years	weeks	<<seconds	years	years
Endurance (cycles)	$>10^{12}$	10^7	10^{15}	10^{15}	10^6	10^4

The number of memristors are increased by increasing the number of layers. Layers are limited to have an effective working within the crossbar. The 3D multi-cell configuration of a memristive device is another design style that can fit within a mobile, by occupying less space and it has the capability to replace NAND flash memory, a monopoly of mobile industry.

Memristor has the potential to replace all type of memories in the known memory heirarchy. The parameter comparison between memristor and other resistive switching devices like Phase Changing Memory (PCM), DRAM, flash memory (Table 2). Memristor clearly shows the uniqueness w.r.t. other Non-volatile memories.

3.2 Memristor Logic Styles

The 'memory wall' bottleneck, that slow down the CPU performance due to elapsed swing between memory and processor can be removed by memristor logic styles. The resistance of memristor is considered as logic. High resistance state (HRS) as logic 0 and Low resistance state (LRS) as logic 1. Memristive memories offer the logic operations to be done within the memory, that reduce fetching data time. This combo of storage and computation near the data leads to true *'In- Memory Computing architectures'*. The different logic styles are reviewed in detail because they are the building blocks where the images are stored as well as processed.

The memristive logic styles can be designed by using bipolar memristors or unipolar memristors. In bipolar memristors, the resistance state depends upon the intensity and direction of the given voltage. If a positive voltage grater than V_{RESET} is given, the device reaches to HRS. If a negative voltage greater than V_{SET} is applied, the device reaches to LRS. Whereas in unipolar memristors, the given voltage intensity decides the state of the device. If a voltage in any direction greater than$|V_{RESET}|$ is applied, the resistance increases. Similarly, if a voltage greater than $|V_{SET}|$ is applied, the resistance drops. At LRS state, a compliance current is given to safeguard the device from failure. The v-i curves of the both memristor types (Fig. 5).

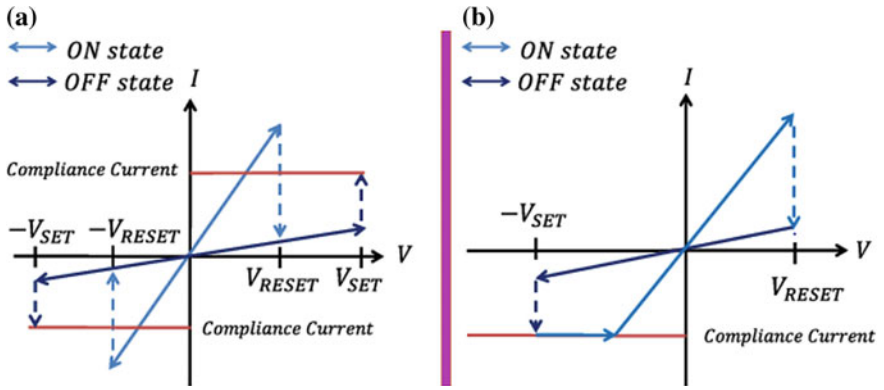

Fig. 5 **a** Unipolar and **b** bipolar memristors v-i curves

3.3 Different Memristor Based Logic Styles

Researchers developed many logic frameworks using both types of memristors. The proposed implementations are:

- CMOS-Like Memristor based logic design (CML) [5], implements the complete logic family by substituting the pull-up and pull-down networks.
- Memristor Ratioed Logic design (MRL) [6], integrates CMOS circuitary and memristors and obtain a CMOS integrated memristive logic family. OR and AND logic gates are computed memristive devices, and CMOS inverters are added to provide a complete logic structure and signal restoration.
- Memristor Aided Logic (MAGIC) [1], is built only with memristors. Firstly the MAGIC-NOR is consructed, from which remaining all other logic gates can be obtained. In every MAGIC logic, memristors serve as inputs with previous values, and an extra memristor for an output. It is best suited logic within memristor crossbar, with MAGIC-NOR gates but requires a resistor for every row in case of other logics.
- Crossbar memristor based logic [5], uses various control signals and procedures like inverting and noninverting gates, and even latches and sum-of-product logic functions to acheive any logic function within seven steps. This framework is useful for complex computing systems.
- Implication logic (IMPLY) [7], is built using only memristors. The universal gate in this type is implication logic. During execution, state drift occur because the voltages try to change the internal state of Q memristor. It may require refreshing the state; otherwise, incorrect logic switch happens. Along with imply gate and a flase gate aii other logics can be constructed. The only overhead is it store values in the form of esistances which needs CMOS converters for crossbar implementations.

- Programmable CMOS/Memristor Logic (PCML) [5], implements ratioed diode-resistor logic along with CMOS circuitry for signal amplification and inversion; this logic is very compact, thus in-field configurable and has the potential to use in neuromorphic computing due to its integration with CMOS.
- In Hybrid Current Mirror Logic [1], the weights of a threshold function are represented with memristance such that Ohms Law is used to convert voltage signal inputs into weighted inputs represented by currents. It is the best threshold logic useful neural networks.

4 Proposed Memristive Framework for Image Processing

Digital image processing is the study of analyzing and manipulating digitized images to obtain enhanced images or some extract useful information. Altering images require data intensive processing, often in realtime. As the image resolution becomes higher, the data movement between the memory and processor increases. Therefore, real time image processing applications suffer from high power consumption and processing time. Memristor as stated, has the capabiltities to store huge data within less space and its memory has computing abilities. So, we proposed an efficient memristive architecture for real-time data-centric image processing applications. Our proposed architecture performs both storage and computing operations and can be called as Memory Processing Unit (MPU). This architecture comprises of:

- Memristor Aided Logic style (**MAGIC**) as the memory element within the crossbar memory that can store as well as compute [8].
- Voltage Threshold Adaptive Memristor Model (**VTEAM**) as a memristive mathematical model [9].

The benefits of each component is discussed below:

4.1 Memristor Aided LoGIC

To integrate the logic style to the crossbar, two requirements has to be satisfied: (1) Logic gate structure should exactly match the crossbar structure. (2) The state of the logic must be in terms of resistance.

MAGIC satisfies the two properties. It is a method for stateful memristor only logic. It does not require any complex structure for stable evaluation. It is evaluated using a single voltage pulse. MAGIC benefits image processing because computations are done in parallel [8]. For large images, we can increase the parallelism with increase in memristors within the crossbar. So, computation with less data movement and immense parallelism boost the performance of image processing applications. In MAGIC stateful logic, NOR gate is the basic building block, which can be set with a single voltage named V_G to the input memristors and V_{GND} to the output

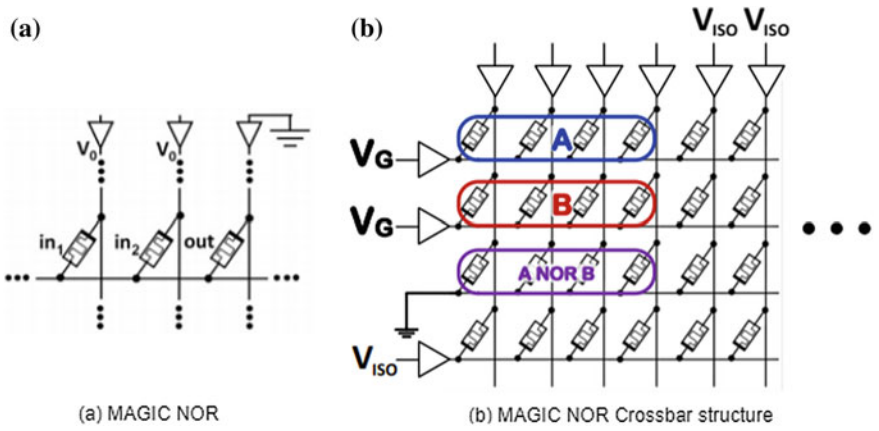

Fig. 6 MAGIC NOR and its schematic crossbar structure

memristor. The MAGIC NOR and its schematic crossbar structure (Fig. 6). MAGIC is better when compared to other stateful logics because it does not need any additional circuitary to integrate with crossbar and also only one voltage supply control for all the logic gates.

4.2 Voltage-Controlled ThrEshold Adaptive Memristor Model

To design memristor circuits, the memristor behaviour has to be modelled by using a mathematical model. VTEAM is also a mathematical model [9]. This mathematical model of memristor is called as memristive system. The designed model should be computationally efficient and has to exhibit the same physical device characteristics. The model must pose some additional advantages like simple, well-formed, intuitive, and general. This generalization behavior helps the model to tune according to the different type of applications like neuromorphic computing, image processing etc. A current controlled memristive system is defined as

$$\frac{dw}{dt} = f(w, i), \tag{10}$$

$$v(t) = R(w, i).i(t) \tag{11}$$

where w is an internal state variable, i(t) is the memristive device current, v(t)is the memristive device voltage, R(w,i) is the memristance, and t is time. TEAM memristive system is built on threshold current. A write operation on a particular cell is done by applying V_{RESET} or V_{SET} voltage to that cell alone. To write logic 0, the memristor current $I(t)$, must be greater than the generated current Ith. This

increase in resistance causes I(t) to reduce, which in turn slow down the writing process. To have an efficient write, high voltages are needed that may lead to high power consumption and unwanted OFF switching. So, a threshold voltage is needed to avoid reliability and performance issues. Since the initial and applied voltages are fixed there will be no disadvantages. VTEAM model is adapted from TEAM model by taking threshold voltage instead of threshold current. A voltage controlled memristive system is defined as

$$\frac{dw}{dt} = f(w, v), \tag{12}$$

$$i(t) = G(w, i).v(t) \tag{13}$$

where w is an internal state variable, v(t) is the voltage across the memristive device, i(t) is the current passing through the memristive device, G(w, v) is the device conductance, and t is time. The VTEAM model can fit into any type of memristor like ferroelectric, Pt-Hf-Ti.

5 Conclusion

Memristive devices have diversified properties like high reliability, dense memory capacity, high retention. Conventional systems can read 1 or 0, but the memristors can read all the values between 0 and 1 (0.4, 0.5 etc.). Many technologies can gain performance by adding memristors in their architectures. The work is extended by designing the algorithms for Image processing applications and simulate them on the proposed architecture that can be modeled by any one of the analog circuit simulators like Cadense VERILOG-A, SPICE. The performance has to be measured against the conventional structures.

References

1. Hamdioui S, Kvatinsky S, Cauwenberghs G, Xie L, Wald N, Joshi S, Elsayed HM, Corporaal H (2017) Bertel.: Memristor for computing: Myth or reality? In: Design, automation test in europe conference exhibition (DATE), pp 722–731
2. Chua L (1971) Memristor-the missing circuit element. IEEE Trans Circuit Theory 18:507–519
3. Chua LO, Kang SM (1976) Memristive devices and systems. Proc IEEE 64:209–223
4. Strukov DB, Snider GS, Stewart DR, Williams RS (2008) The missing memristor found. Nature 453:80
5. Gao L, Alibart F, Strukov DB (2013) Programmable CMOS/Memristor threshold logic. IEEE Trans Nanotechnol 12:115–119
6. Kvatinsky S, Wald N, Satat G, Kolodny A, Weiser UC, Friedman EG (2012) MRL memristor ratioed logic. In: International workshop on cellular nanoscale networks and their applications, pp 1–6

7. Kvatinsky S, Kolodny A, Weiser UC, Friedman EG (2011) Memristor-based IMPLY logic design procedure. In: IEEE 29th International Conference on Computer Design (ICCD), pp 142–147
8. Kvatinsky S, Belousov D, Liman S, Satat G, Wald N, Friedman EG, Kolodny A, Weiser UC (2014) MAGIC: Memristor-aided logic. IEEE Trans Circuits Syst II: Express Briefs 61:895–899
9. Kvatinsky S, Ramadan M, Friedman EG, Kolodny (2015) VTEAM: a general model for voltage-controlled memristors. IEEE Trans Circuits Syst II: Express Briefs 62:786–790

Data Analysis and Prediction of Survey on Effect of Smart Phones on Society

Ishaan Pradip Ballal and Kanika Prasad Nadkarni

Abstract With the advent of technology, the impact of smartphones on business, health, psychology, education and social relations has increased. This paper presents germinal results of a study conducted to not only analyse but also predict the negative impact of smartphone usage. A survey was conducted in two parts, one for identifying impact of smartphones on academics of student and other to identify the effect on lives of adults who have finished their education. We used Natural Language Processing to conduct sentiment analysis on answers to subjective questions. Supervised Machine learning algorithms were used to conduct the analyses of impact of smartphones on academics whereas Unsupervised Machine Learning Algorithms were used to analyse the survey on adults. Neural Networks model was trained and tested on both the survey data. The results of these algorithms were compared and analysed to find which algorithm is better in which situations.

Keywords Smartphones · Neural networks · Machine learning · Natural language processing · Sentiment analysis

1 Introduction

Since the dawn of technology, it has had a great influence on the academics, work and in general lives of human beings. One major addition to the communication devices has been the smartphone. Smartphones have not only benefited the students by allowing share of study material amongst them, but also has exposed them to a vast pool of information from various people in the world at the click of a button. Many educational oriented applications are being built and used. But, it is not surprising to notice that instead of using this internet facility at hand judiciously, students are getting engaged in it beyond limits and thus are wasting time, energy and emotions

I. P. Ballal · K. P. Nadkarni (✉)
Savitribai Phule Pune University, Pune, Maharashtra, India
e-mail: kanika.nadkarni9@gmail.com

I. P. Ballal
e-mail: ishaanballal21@gmail.com

© Springer Nature Singapore Pte Ltd. 2020

T. Hitendra Sarma et al. (eds.), *Emerging Trends in Electrical, Communications, and Information Technologies*, Lecture Notes in Electrical Engineering 569,
https://doi.org/10.1007/978-981-13-8942-9_6

on non-academic and unnecessary things instead. This negative effect of smartphone is not only being observed in students but also is seen amongst adults and in society in general. Smartphones are being used unnecessarily and dependency on them is increasing. It was against this background that this study was undertaken to analyse the usage of smartphones by students and people and to predicting the negative effect that it may have on them.

Different Machine Learning algorithms and Neural networks were used in our study. Machine Learning uses the theory of statistics in building mathematical models to teach machines to think. The model work is two-fold: Firstly, the mathematical model is trained by applying efficient algorithms on the training dataset. Secondly, once the model is trained, it can make predictions over unseen data. The efficiency of the learning algorithm is dependent on accuracy, precision and recall.

Artificial Neural Networks (ANN) is one of the method used in deep learning which can be used for classification and prediction. It consists of a pool of simple processing units called neurons which communicate by sending signals to each other over a large number of weighted connections. They have high parallel processing units and dynamic infrastructure. Activation functions like relu, sigmoid are used. MultiLayer Perceptron (MLP) Neural Network consists of perceptrons which are feed forward that is the output of the layer are given as the input to the next layer. All the arrows are going from one layer to the next in the direction of the output. There are no recurrent feedbacks from the output to the previous layers. This model consists of three types of layer:

(1) Input layer—It consists of the number of features/attributes for the network. A separate neuron is provided for each attribute.
(2) Hidden Layer—They are the intermediate layers that are used to process the input and forward it to further layers. Any neural network can have one or many number of hidden layers. More the number of layers, deeper is the network and more features are identified.
(3) Output Layer—It is the neuron where the desired output is found. It comes after processing from all the hidden layers.

In the study various Supervised Machine Learning algorithms like Naive Bayes Algorithm, Decision trees and Logistic Regression were applied on one part of the survey whereas Unsupervised Machine Learning algorithms like K-Means Clustering and Hierarchical Clustering were applied on other part of survey. Neural networks model was trained and tested on both parts of survey. The popular languages in Data Science: R and Python were both used considering its relevant and appropriate use wherever required. Natural Language Processing was used to carry out cleaning of the text and Sentiment analysis over subjective answers that had been taken through the survey.

2 Related Work

A related study was carried out by Abdulsalami et al. [1] Department of Computer Science, Ahmadu Bello University, Zaria Nigeria had used lexicon and machine learning based approach Sentiment Analysis of Students Perception on the use of Smart phones. It carried out the study of effect of smart phones on academics of students on the basis of three factors gender, level and phone usage. It presented the sentiment analysis of students comments on influence of smart phones on academic performance.

A study was made in the university of Dar es Salaam [2] to investigate the use of smart phones made by the students and its influence on academic life. This survey was conducted on 166 undergraduate students. The study showed that students use smart phones for many different purposes and it enhances their academic performance to a great extent. The survey showed that most of the students were using smartphones that was serving them positively in academics. The university decided to maximize academic usage of smartphone watching at these results.

King and Dong [3] of Fayetteville State University, NC, USA conducted a study to investigate the impact of smart phone addiction on college students academic performance. The effect of life stressor on smartphone addiction was also examined. The study provided a link between smartphone addiction and retention, academic performance etc. They also found out that life became stressor with the addiction of smartphones.

Kibona and Mgaya [4] carried out a survey in Ruaha Catholic University Iringa, Tanzania on whether addiction of smartphones is more in higher learning students or lower learning students. Data was analysed using SPSS and excel tools, and then analysis was done on it to find its contribution to academic performance. They found that the impact was more on higher learning students. The study showed that more females were addicted to smartphones than males.

Qasim et al. [5] carried out a study to investigate the excessive use of smartphones. They conducted the study in Jordan to determine how smartphones have an impact on health and human behaviour which has now become a crucial issue. Using this data, they concluded that there is a strong connection between the amount of time a person spends using a smartphone and type of pains that may occur in the human body.

3 Methodology

A questionnaire was prepared which contained a variety of questions like the amount of data used by the person, amount of talk-time used, age, gender, time given for gaming, watching videos, camera, data usage, internet browsing, primary purpose of using smart phone etc. In the first part of the survey, this questionnaire was distributed to students between the age of 16–23 years of age. The students varied from different

streams and branches. The questionnaire was in the form of a google form. Around 232 responses were received for this survey. In the second part of the survey, a similar questionnaire was prepared for people ranging from age of 20–70. Around 177 responses were recorded in this survey.

Prior to filling the questionnaire, the respondents were assured that their data won't be shared with anyone and the data won't be used for any other purpose apart from the survey. They were also assured that their identity wont be revealed out. The questionnaire contained some multiple choice questions and some textual questions.

3.1 Survey I

In survey I, Supervised Machine Learning algorithms were used to predict negative effect of smartphone. The Natural Language Tool Kit (NLTK) was used to process the textual data. By identifying the number of positive and negative words in the subjective answer with reference to the lexicon dictionary of positive and negative words, the overall sentiment of the answer was calculated. Weights were given to all the multiple choice questions in the survey and the total sum of the weights was calculated according to the option the person choose. The label of negative effect was determined by the overall score of each sentiment. The data was split where in 70% of it was used to train the model where as remaining 30% test the model. Over this data, classifier algorithms like Naive Bayes algorithm, Decision trees and Logistic Regression were applied. Logistic regression was applied on the data using sklearn library in python where l2 regularisation was used and C (inverse of regularisation) was set to 1. As the dataset is small, we used liblinear solver for optimisation and dual was set to False as number of samples were greater the number of features. For Naive Bayes, the prior probabilities were set to None and var-smoothing to 1e-9. Each algorithm provided results with different accuracy. Also neural networks model was used over the same normalized data where we used 8000 epoches and 2 hidden layers. ReLu activation function was used and the learning rate for the algorithm was 0.001.

3.2 Survey II

In survey II, Unsupervised Machine Learning Algorithms were used to determine the positive and negative impact of smartphones. For answers to subjective questions, the text was cleaned using R by removing the stopwords, punctuations, numbers, special characters, extra spaces etc. in the answer and converting it to lower case. The sentiment value of this cleaned text was found using syuzet package in R. The categorical features were mapped into their numerical equivalents. Missing values were dealt with in the process. Thus the dataset was ready for Machine Learning algorithm application.

In K-Means, the total sum of squares of distances (SST) is equal to sum of squares of distances between clusters (BCSS), that is between the centroids of clusters and the sum of squares of distances between points (WCSS) within the clusters. To keep separated clusters, we have to increase BCSS and thus WCSS. By the elbow method the optimal number of clusters is determined. The elbow plot for our dataset was visualized to find optimal number of clusters. We clustered the people into two clusters using K-Means and Hierarchical clustering, one cluster representing probability of a negative impact of smartphone on people and the other representing no significant impact on them. For each column in dataset, two pie charts, one for each cluster, with fractions according to the categorical answer selected were plotted. For example Fig. 3. It was observed that 109 people were classified into the first cluster and 68 in the second using K-means, while 116 people were clustered into the first cluster and 61 into the second using Agglomerative Hierarchical Clustering. Data analytics was done from the visualizations obtained using R to analyse the impact of each feature on the clustering. Only the data entries where both K-means and agglomerative have predicted the same class, that is 0 or 1, were taken into consideration for this visualization. Training dataset was created for Neural Networks by appending the K-Means predictions to the cleaned and prepared survey data. Neural Networks model with 8000 epoches and 2 hidden layers was used over this training data. ReLu activation function was used and the learning rate for the algorithm was 0.001.

4 Results

4.1 Survey I

For survey I, three Supervised Machine Learning algorithms were used over survey data of 232 responses. After hard coding it was observed that 154 students while remaining 78 students remained unaffected. An efficiency of 85.71% was achieved using the Naive Bayes Algorithm. Decision trees gave an accuracy of 75.71% whereas Logistic Regression gave an accuracy of 77.14%. Neural networks gave an accuracy of 90%. Thus it has been observed that Neural Networks gave the maximum accurate answer. Among the Supervised Machine Learning algorithms, Naive Bayes algorithm gave the best results as the attributes considered were mostly independent of each other and the dataset was small in size (Fig. 1).

4.2 Survey II

Figure 2 gives the elbow plot for our dataset which shows that 2 clusters should be formed.

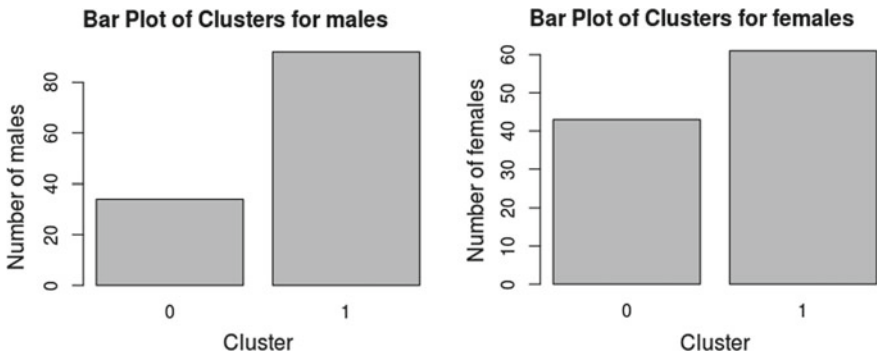

Fig. 1 Bar plot of clusters by gender where cluster 1 denotes people who are negatively affected by smart phone whereas cluster 0 denotes people who are not affected by it

Fig. 2 Elbow plot

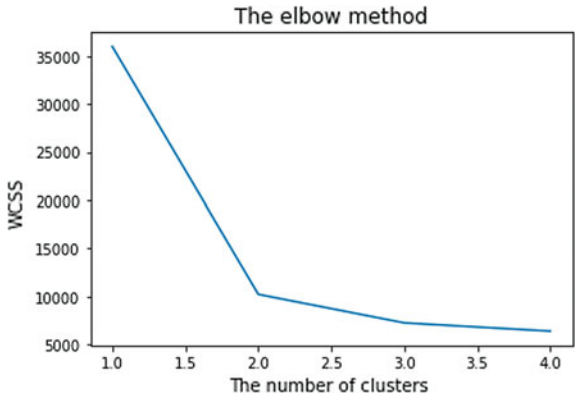

For survey II, after classification of adults into two clusters depending on negative impact of smartphones, the data entries where both K-Means and Agglomerative clustering have predicted the same class were used for analysis of impact of particular attribute on prediction (the number of entries classified into Cluster 1 by both K-Means and Agglomorative clustering is 61 while that classified into Cluster 0 by both is 109).

It was observed that, people who were affected negatively by smart phones:

(1) Used high data: 39.7% people who were classified as negatively affected use 501 MB–1 GB data daily and 23.5% of them use 101–500 MB data daily. Whereas, 45.87% of people not affected use 101–500 MB and 22.9% use 0–100 MB data daily.
(2) Used the smart phone a lot for browsing internet, email and texting: 16% of people classified as affected browse internet for 1–3 h and 17.6% for more than 3 h daily. 50.5% of people not affected browse the internet for less than 15 min

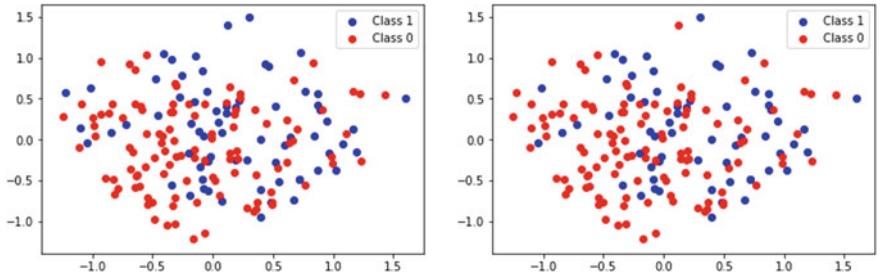

Fig. 3 K-Means and Agglomorative clustering scatter plots after dimensionality reduction using PCA respectively

daily and 22% used 15–30 min. 52.9% of the people affected use email on smart phone for less than 15 min and 16% use it for 15–30 min.

(3) There primary purpose to use the smart phone was to watch youtube videos while those who were not affected used it primarily for emails: As shown in Fig. 3, for 25% of the people affected, the primary purpose to use the smartphone is watching youtube videos for entertainment. While amongst those not affected 35.7% primarily for email.

(4) They considered smart phone as vital part for their work whereas those not affected considered it as just an useful aid. Amongst the people affected 27.9% think of smart phone as a vital part amongst those not affected 67.8% think of it as just an useful aid.

(5) Maximum of the people affected have given smartphone checking as their free time activity: 35% of the people affected use smartphone in their free time, while 59% of the people not affected spend time with family in their free time. Features such as gender, age, talk-time, amount of time used over camera, PDF reading and business applications did not affect the people negatively.

(6) Majority of the people who are not affected have no psychological, physical health effects and effects on eyes, whereas majority of those affected had one of these: 66% of the people affected by smartphone were experiencing psychological, physical health effects and effects on eyes, while 55.96% of those not affected had none of these.

(7) Maximum of the people affected check there smart phones before and after sleep: 60% of the people affected check their smartphones before and after sleep, while 35% of the people not affected check their smart phones just before and after sleep.

(8) Most of the people affected by smart phones use smart phones while having meal: 37% of the people affected check their smartphones while having meal, while only 15% of those not affected do this. Whereas features such as gender, age, talk-time, amount of time used over camera, PDF reading and business applications did not affect the people negatively. Majority of the people from both the clusters thought that it was better before the smart phones were invented.

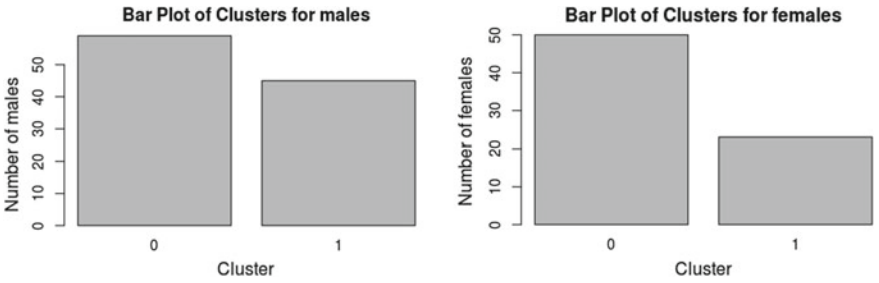

Fig. 4 Bar plot of clusters by gender where cluster 1 denotes people who are negatively affected by smart phone whereas cluster 0 denotes people who are not affected by it

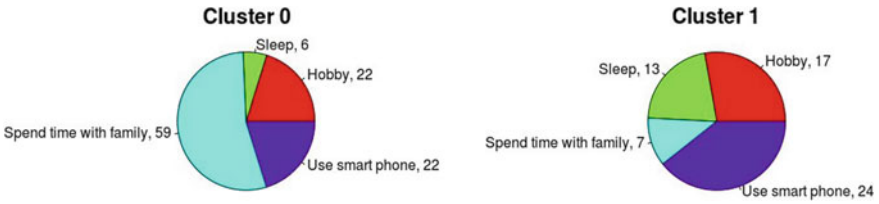

Fig. 5 Pie chart of what people do in their free time where cluster 1 denotes people who are negatively affected by smart phone whereas cluster 0 denotes people who are not affected by it

Secondly, people in both the clusters believed that it will not be better to have cell phones with basic facilities than smart phones. Also, majority of the people preferred to call and talk rather than text or meet in both clusters. The accuracy of Multi Layer Perceptron Neural Network on the survey 2 data is 88%. K-Means classified 68 into Cluster 1 and 109 into Cluster 0. Agglomorative classified 61 into Cluster 1 and 116 into Cluster 0.

Following are the Figs. 4, 5 and 6 from visualizations of the features that impact the clustering the most.

5 Conclusion

This paper presented data analysis and prediction of negative impact of smartphones on academical performance of students and life of adults. 16 survey questions were formulated for part one of the survey and 26 questions for the second one including multiple choice questions as well as subjective questions. This study found that relationship existed between emotion polarity of textual answer, the categorical factors namely the amount of data used by the person, amount of talk-time used, age, gender, time given for gaming, watching videos, camera, data usage, internet browsing,

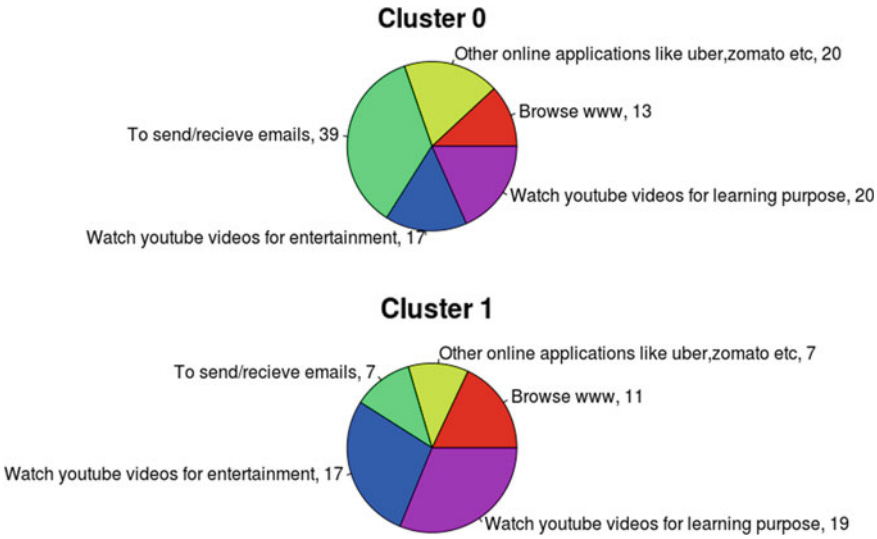

Fig. 6 Pie chart of primary purpose of people for using smart phones where cluster 1 denotes people who are negatively affected by smart phone whereas cluster 0 denotes people who are not affected by it

primary purpose of using smart phone etc. and the negative impact of smartphone. This relationship was throughly investigated. Thus prediction of negative impact of smartphone can be made from the response to the research questions in the survey. The paper presented a preliminary finding of use of Machine Learning algorithms and Neural Networks for this prediction. If further a survey is conducted on a large scale, Neural Networks will work best for the huge dataset of responses thus collected unlike our study where Naive Bayes worked the best for small dataset. Therefore in future a more detail analysis may be conducted in order to have an in-depth understanding of subject matter of the present study.

References

1. Abdulsalami AO, Ahmad BI, Umar MA, Abubakar AH, Jauro F, Kufena AM, Ekoja EA (2017) Sentiment analysis of students perception on the use of smartphones: a cross sectional study. In: 2017 Second International Conference on Informatics and Computing (ICIC), 2017. https://doi.org/10.1109/iac.2017.8280625
2. Mwabungulu E, Mungwabi H (2015) The impact of smart-phones usage on third-year undergraduates in Tanzania: a case of the University of Dar es Salaam. Univ Dar es Salaam Libr J
3. King RC, Dong S (2017) The impact of smart phone on young adults. Bus Manag Rev 8(4)
4. Kibona L, Mgaya G (2015) Smartphones effects on academic performance of higher learning students. A case of Ruaha Catholic University Iringa. Tanzan J Multidiscip Eng Sci Technol

(JMEST) 2(4). ISSN: 3159-0040
5. Qasim T, Obeidat M, Al-Sharairi S (2017) The effect of smartphones on human health relative to users addiction: a study on a wide range of audiences in Jordan, World Academy of Science, Engineering and Technology. Int J Med Health Sci 11(5)
6. Abu-Shanab E, Haddad E (2015) The influence of smart phones on human health and behavior: Jordanians' Perception. Int J Comput Netw Appl 2(2)

An Efficient Constraint-Based Local Search for Maximizing Water Retention on Magic Squares

Mahadi Hasan and Md. Masbaul Alam Polash

Abstract Water retention on magic square is a very recently introduced variation of magic square problem which has attracted a lot of attention from the research community over the years. Different approaches have been used to tackle this highly combinatorial optimization problem. In this paper, we have proposed an improved constraint-based local search approach that remedies all the identified shortcomings of the state-of-the-art technique. Several new methods such as greediness reduction technique, incremental calculation of the objective function and solving cycling problem through similarity checking have been incorporated within the proposed local search approach. Experimental results show that our proposed algorithm performs better than the existing technique with regards to solution quality and execution time.

Keywords Magic square · Local search · Tabu meta-heuristics

1 Introduction

Magic square of size n is defined as a mathematical problem where each square contains a different value from $1 \ldots n^2$. The sum of the rows, columns and main diagonals are equal to a constant value known as the magic sum. Water retention on magic squares is defined as the amount of water retained by the magic square when viewed as a height map. The water retention can be calculated by pouring water from above and then the amount of water retained after dropping out over the edges. To tackle this challenging combinatorial problem, we have proposed a constraint-based local search (CBLS) approach because of its efficiency and Scalability. A brief overview of the CBLS approach is follows: Recently, constraint-based local search [2, 7, 10, 11] has become an emerging approach for solving hard optimization prob-

M. Hasan (✉) · Md. Masbaul Alam Polash
Department of Computer Science and Engineering, Jagannath University, Dhaka, Bangladesh
e-mail: mahadi129727@gmail.com

Md. Masbaul Alam Polash
e-mail: mdmasbaul@gmail.com

© Springer Nature Singapore Pte Ltd. 2020

T. Hitendra Sarma et al. (eds.), *Emerging Trends in Electrical, Communications, and Information Technologies*, Lecture Notes in Electrical Engineering 569,
https://doi.org/10.1007/978-981-13-8942-9_7

lems. It is among the most successful techniques for solving computationally complex problems from computer science, operations research and various application areas (e.g traveling salesman problem, routing and scheduling problems) [1]. The key idea is that the CBLS starts at a randomized initial solution and iterative-ly improves the current candidate solution with small modifications until the termination criteria are met. In general, CBLS is able to find a good solution but cannot guarantee, but it has the advantage of using less memory and being able to find acceptable solutions in a reasonable time for large and complex problems. In this paper, we have proposed an efficient CBLS method to maximize water retention in magic square. Our methodology handles all the limitations of the existing techniques and incorporates several new methods such as greediness reduction technique, incremental calculation of the objective function and solving cycling problem through similarity checking. Empirical analysis reveals that our algorithm outperforms the state-of-the-art techniques in every aspect. Rest of the paper is organized as follows: Sect. 2 defines the basic terminologies related to water retention, Sect. 3 presents an overview of the existing approaches to handle this problem, Sect. 4 outlines our proposed methodology, Sect. 5 shows the experimental analysis and comparison of the proposed technique with existing techniques and finally Sect. 6 concludes this paper.

2 Basic Terminologies Related to Water Retention

Magic square is a very well known constraint satisfaction problem that has been used as a benchmark problem for many approaches [3, 5, 8]. Recently this satisfaction problem is updated as an optimization problem by introducing an objective function to maximize the amount of water a magic square can contain. This modified version is called water retention on magic square problem which was first introduced by Knecht [5] in 2007. After that an international contest was arranged in 2010 to attract researchers in solving this problem. At that time, a lot of researchers submitted their best found magic square of size n which have maximum water retention value. Later this results were used as benchmarks in [4]. In the following section, we will provide more detailed discussion on magic square and its new variation.

2.1 Magic Squares

Magic squares is an interesting and very popular problem which can be found in many research work. Formally, a magic square is defined as follows:

Definition 1 Given a size n, find out a square matrix of size $n \times n$ containing the numbers 1 to n^2 such that each row, column and main diagonal equal to the same sum, S.

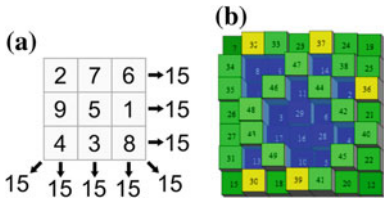

Fig. 1 **a** A magic square of size 3 and **b** Height map of a magic square of size 7 [4]

Let $n \in N$, $S \in N$ and M be a square matrix of size $n \times n$ such that $M[i, j] \in \{1 \ldots n^2\}$ where $i, j \in \{1 \ldots n\}$. M is a magic square if it satisfies the following constraints

– Row constraints:

$$\sum_{j=1}^{n} M[i, j] = S : \forall(i) \in \{1 \ldots n\}$$

– Column constraints:

$$\sum_{i=1}^{n} M[i, j] = S : \forall(j) \in \{1 \ldots n\}$$

– Diagonal constraints:

$$\forall(i = j), \sum_{i=1}^{n} M[i, j] = S$$

$$\forall(j = n + 1 - i), \sum_{i=1}^{n} M[i, j] = S$$

where $S = n(n^2 + 1)/2$. Figure 1a shows a magic square of size $n = 3$ where the magic sum is $S = 15$.

2.2 *Water Retention on Magic Squares*

A given magic square, M can be viewed as a height map where elements $M_{ij} \geq 0$. Retaining water means if water is poured above the surface of M, how much water it can reserve after spilling out at the edges and flooding between non-diagonally adjacent cells. One cell will retain some water if all of its surrounding cells height is greater than its own height. Thus to maximize the water retention, we have to place large walls, the taller the better, along in edges and smaller values in the middle. Figure 1b shows a 3-dimensional perspective view of size 7 magic square with retaining water. Here the color blue represents that water has been retained on the top of that cell and green means dry land. Color yellow shows the soft cells which if lowered then the water will be level of the whole adjacent lake. Maximizing water retention on magic squares is a challenging constraint optimization problem. The state-of-the-art approaches to handle this problem is discussed in the subsequent section.

3 Related Work

Water retention on magic square problem has attracted a lot of researcher due to its simple to understand but yet complex to find optimal solution nature. The basic algorithm to calculate the water retention of a given magic square is introduced in [6] which is shown in Fig. 2. Although its complexity is determined as $O(n^4)$, this algorithm works as a building block for all the existing algorithms. Different approaches [4, 9] have been presented to tackle this interesting problem. However, the state-of-the-art method outlined in [4] uses a constraint-based local search for this problem. To overcome the cycling problem of local search, the authors have used tabu search technique and as a neighborhood generation function, the pair swapping method is used in this work. A few interesting approximations is introduced as well in [4] to build an upper bound on water retention problem. Although, this algorithm [4] performs better for small size problem but for larger-size problem, it fails to find high-quality solution efficiently (Fig. 3).

```
1: WATER-RETENTION(M, W, n, M_max)
2: // Pre: M[*,*] ∈ {0,M_max},n > 0,M_max > 0 and W contains the water levels
3: Let Q be a minimum priority queue of elements W[i, j]
4: for i from 1 to n do // Initialization
5:     for j from 1 to n do
6:         if i = 1 or i = n or j = 1 or j = n//Edge elements
7:             W[i, j] := M[i, j]
8:             ENQUEUE(Q, i, j) // Add edges to queue
9:         else
10:            W[i, j] :=M_max
11:    end for
12: end for
13: while Q ≠ ∅ do // Calculate water levels
14:    (i, j) := DEQUEUE(Q)
15:    DRAIN(M, W, n, Q, i − 1, j, W[i, j]) //Drain adjacent elements
16:    DRAIN(M, W, n, Q, i + 1, j, W[i, j])
17:    DRAIN(M, W, n, Q, i, j − 1, W[i, j])
18:    DRAIN(M, W, n, Q, i, j + 1, W[i, j])
19: end while
20: r := 0 // r be an integer
21: for i from 1 to n do // Calculate retention from water levels matrix
22:    for j from 1 to n do
23:        r := r + W[i, j] − M[i, j] // r contains the retention value
24:    end for
25: end for
```

Fig. 2 Water retention algorithm

Fig. 3 Water retention algorithm-DRAIN sub procedure

```
1: DRAIN(M, W, n, Q, i, j, p)
2: if i > 1 and i < n and j > 1 and j < n
3:       x := MAX(M[i, j], p) // x be an integer
4:       if x < W[i, j] //If there is water to drain..
5:             W[i, j] := x
6:             ENQUEUE(Q, i, j)
```

4 Our Proposed Approach

Our proposed methodology is based on the state-of-the-art approach mentioned in [4]. We have improved the existing algorithm by first identifying its limitations that hinder its success and then handling those shortcomings. Our proposed Constraint-Based Local Search approach (CBLS) approach starts with a random initialization of a square matrix, M and then calculating its violation. Here violation means the number of constraints that are unsatisfied by the current configuration. When the violation becomes 0, then M is termed as a magic square. Also, the value of the objective function is determined to identify the quality of the current configuration. The objective function simply returns the amount the water retained by M. Here the goal is to maximize the objective function while the violation have to be 0. To better understand CBLS Algorithm, let's have a look at Fig. 7. After initialization, to find a better solution, search moves from one neighborhood to another. In the existing method, the pair-wise swapping technique is used to generate the neighbors. It always chooses a pair that gives the best objective function value. To determine this so called best pair, this algorithm simulates all possible pairs and picks the best. But the limitation of this approach is that for each pair, the objective function value is calculated from scratch which is very time consuming. To better understand this problem, let's have a look at Fig. 4b. Here to find out the effect of swapping 8 and 7, all the row, column, and diagonal constraints are calculated once again which is very costly. But after through analysis, we realize that only all but a few rows and columns gets affected by swapping two elements i and j. So, in our proposed algorithm, we only calculate the violation of the affected rows, columns or diagonals and use the previous violations for the non-affected rows/columns. This is shown in Fig. 4c where we only calculate the violations only 1 diagonal, 2 row and 2 column positions. By doing this, we got rid of a lot of calculations and in the process our algorithm becomes more efficient in terms of time. For convenience, in this paper, we will call this approach as *incremental calculation*. After performing all-pair swapping, the existing algorithm chooses a neighbor greedily i.e. the best pair. Due to this greedy nature, the search get stuck very quickly in a local optima and thus wastes a lot of time without any improvement. To reduce this greediness, in our approach, we have maintained both best and second best pair and pick either of them as a neighbor. In our proposed method, we keep selecting the best pair until it gets stuck in a local minima.

When search gets stuck, we try to select the second best pair from the current configuration. To implement this, we maintain a parameter called noise, β as shown in Fig. 5. Initially, β is set 0 and when search gets stuck, we increase β by one. When β is greater than 0, we select the second best pair with a random probability. When search gets out of a local minima, we reset β to 0 once again to select the best pairs. This technique is termed in this paper as *greediness reduction technique*. By applying this technique, we can quickly get out of the local minima and thus reduce the wastage of time. Another classic problem of local search approach is that it comes back to the previously visited solutions again and again, known as the cycling problem. Although tabu meta-heuristics is used in the existing work to remedy this problem, but for long term, tabu search is not enough. Thus, in this paper, we have proposed a *similarity checking technique* to mitigate this long-term cycling problem. To implement this technique, shown in Fig. 6, we store the previously visited solutions and whenever a new solution is found, it is checked against the stored solutions before exploring further. Since, storing all the visited solutions will require huge memory, we only store solutions after a fixed number of iterations. Before storing a solution, we determine the similarity measure of this solution with the stored solutions. Then if the similarity measure is greater than a predefined threshold value, we discard this new solution and look for another solution. Otherwise, we store the new solution and keep exploring it. By applying this methodology, we were being able to overcome the cycling problem of local search and thus made our algorithm more efficient (Fig. 7).

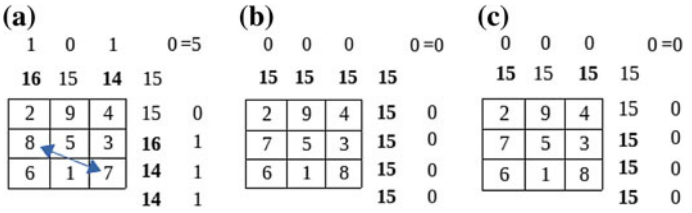

Fig. 4 **a** Previous violation and sum value, **b** Violation calculation from scratch and **c** Incremental violation calculation in a magic square of size 3

1: **SecondBestSelector**(f) ▷ where f is a objective function
2: **if**(f is not improve)
3: $\beta := \beta + 1$
4: **if**($p < \beta$) // p a random probability
5: Select second best
6: **if**(f is improve)
7: $\beta := 0$

Fig. 5 Algorithm for second best selector

1: **Sim-Checking**(s') ▷ where s' is a solution
2: **for** storeItr from 1 to $solCount$ **do** // solCount saves the no. of solution
3: **if** ($s'similarity \geq proximity$)
4: discard this solution
5: **Break**
6: **end for**
7: **if** ($storeItr = solCount$) // not similar
8: storeSol[++storeItr]:=s // $storeSol[]$ saves the solution

Fig. 6 Algorithm for similarity checking

1: **CBLS-TABU**($s, iteraions, tabulength$)
2: // **Signature:** Initial state s →new state s'
3: // **Post:** s' is a state satisfying the objective function f ($f := StateViolation(n) + \alpha(t).Cost(n,t)$, same as state-of-the-art approach) or shows a time error message
4: $t := 0$ and $\beta := 0$ // β for choosing second best and t is a integert
5: Let $TABU[1..|s|][1..|s|]$ be an 2-D array
6: Initialize $TABU[*][*] := 0$
7: **while** ($StateViolation(s) > 0$ and $t < iterations$) **do**
8: **Sim-Checking**(s') // Call the Sub-Procedure Method
9: Select x_1 and x_2 variable which are not Tabu
10: **SecondBestSelector**(f) // Call the Sub-Procedure Method
11: $s := n$ // Make the selected n the new current state
12: $t := t + 1$
13: $TABU[x_1][x_2] := t + tabulength$ // Make it tabu for feature
14: $TABU[x_2][x_1] := t + tabulength$
15: $s' := s$ // Assign s to s'
16: **end while**
17: **if** ($StateViolation(s) > 0$)
18: TIMEOUT // runs failure

Fig. 7 Constraint-based local search algorithm with tabu search

5 Experimental Results

All the mentioned algorithms are implemented using C++. We ran our experiments on High Performance Computing Cluster Gowonda provided by Griffith University, Australia. Each node of the cluster is equipped with Intel Xeon CPU E5-2650 processors @2.60 GHz. Each algorithm runs on a single threaded process. Our search algorithm is run 100 times with maximum iteration count set to 1000 for each given size n of the magic square. The tabu tenure is fixed at $2n/3$. Table 1 shows the comparison between our algorithm and state-of-the-art algorithm [4] with regards to the maximum retention found with corresponding minimum time.

Here we can see that in all cases except for 9, our algorithm produces better results i.e. our results are much closer to the best known solution within minimum time. We have also compared average and minimum retention found using both these algorithms which is shown in Fig. 8a, b respectively. These bar charts show

Table 1 Performance of our algorithm when compared to the algorithm of [4]

Size of order	Retention			Minimum time	
	OurBest	Prev.Best	Best known	Our time	Prev time
7	**417**	416	418	**0.22**	0.23
8	**792**	788	797	**0.41**	0.46
9	1380	**1382**	1408	0.77	0.83
10	**2236**	2227	2267	**1.43**	1.69
11	**3426**	3373	3492	**2.26**	2.88
12	**5064**	5028	5185	**3.98**	4.88
13	**7243**	7171	7442	**6.4**	8.04

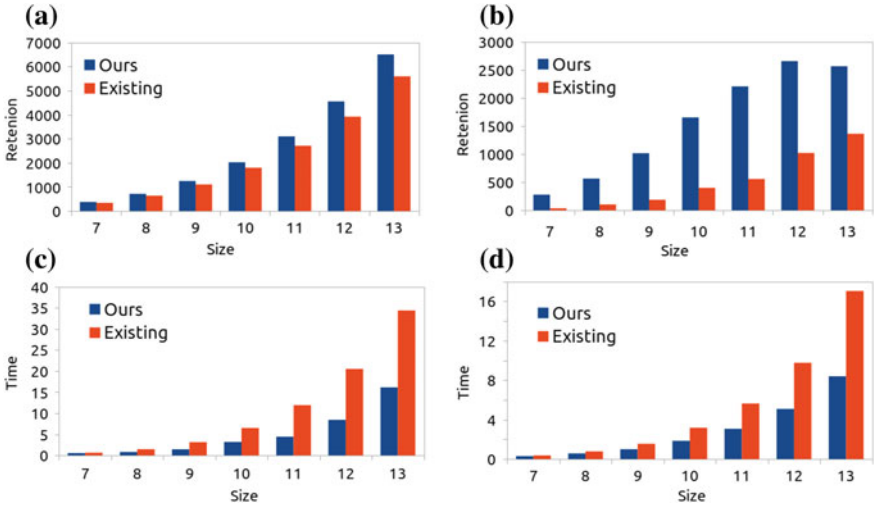

Fig. 8 Comaprison of our algorithm with [4] based on **a** average retention, **b** minimum retention, **c** maximum time and **b** average time taken to find the best retention

the efficiency of our algorithm in maximizing the retention value for each size. Figure 8b also reveals that our algorithm produces high quality solution very quickly with compared to the existing algorithm. We have also compared the time required to find the maximum retention found by both these algorithms. The comparison of the time is shown in Fig. 8c, d. It shows that for all sizes, our algorithm requires less amount of time than the existing technique.

6 Conclusion

In this paper, we have proposed a constraint-based local search approach to solve the highly combinatorial optimization problem called Water Retention on Magic Squares. The violation function of our proposed method guides the search to move

from one neighbor to another by minimizing it's degree of dissatisfaction. To calculate the objective function during variable selection phase, we have used incremental violation calculation which saves a lot of time. Also to reduce greediness of the existing technique, we picked the second best pair based on some random probability. To handle the cycling problem, we have proposed a similarity checking procedure that discards similar solutions. Experimental results show that our proposed algorithm outperforms the existing technique with regards to solution quality and execution time.

Acknowledgements The authors would like to acknowledge the support of Information and Communications Ministry of the people's republic of Bangladesh for conducting this research work.

References

1. Gonzalez T (2007) Handbook of approximation algorithms and metaheuristics. Computer and information science series, Chapman and Hall/CRC
2. Hentenryck PV, Michel L (2009) Constraint-based local search. The MIT press
3. HS W (2002) Magic squares. http://users.eastlink.ca/sharrywhite
4. Johan O (2012) Water retention on magic squares with constraint-based local search
5. Knecht C (2007) Magic squares. www.knechtmagicsquare.paulscomputing.com
6. McCaughan G. Water retention algorithom. http://www.knechtmagicsquare.paulscomputing.com/Water
7. Newton MH, Pham DN, Sattar A, Maher M (2011) Kangaroo: an efficient constraint-based local search system using lazy propagation. In: International conference on principles and practice of constraint programming. Springer, Berlin, pp 645–659
8. Sloane NJA. Number of different magic squares of order n that can be formed from the numbers 1.. n*n. http://oeis.org/A006052
9. van der Plancke F (2010). http://www.tech.groups.yahoo.com/group/AlZimmermannsProgrammingContests/message/4706
10. Polash MA, Newton MH, Sattar A (2015) Constraint-based local search for golomb rulers. In: International conference on AI and OR techniques in constriant programming for combinatorial optimization problems. Springer, Berlin, pp 322–331
11. Polash M, Newton MH, Sattar A (2017) Constraint-based search for optimal golomb rulers. J Heuristics 23(6):501–532

Predicting the Degree of Emotional Support in an Online Health Forum for HIV Using Data Mining Techniques

Ponnam Naveen, Priyanka C. Nair and Deepa Gupta

Abstract Online Health Community (OHC) services are mostly employed for resolving problems of people with chronic diseases. OHCS also provide social support in addition with solutions to the problems. Social Support is of two forms: Emotional Support, Informational Support. The objective of this work is to analyze online healthcare forum and find the degree of support provided by the forum. In this work, 1200 discussions have been extracted from POZ, an Online HIV Forum. Initially the type of support groups has been identified by application different semi supervised approach. As a result, it has been identified that emotional support is more in the messages of the forum. Further regression has been applied to quantify the amount of emotional support in the discussion of the POZ forum. Various kinds of regression algorithms have been applied to model the degree of support in the messages.

Keywords Natural language processing · Web scraping · Online health community services · Social support · Semi-supervised learning · Regression

1 Introduction

Due to the advancements in communication technology, internet is becoming popular, various social-media sites are creating a new avenue to the people and providing information explicitly. Internet provides numerous services as per the requirement of the user. Interpersonal organizations are a capable web-based social networking for sharing essential data about different issues and can be utilized to bring issues

P. Naveen (✉) · P. C. Nair · D. Gupta
Department of Computer Science and Engineering, Amrita School of Engineering, Amrita Vishwa Vidyapeetham, Bengaluru, India
e-mail: ponnamnaveen1207@gmail.com

P. C. Nair
e-mail: v_priyanka@blr.amrita.edu

D. Gupta
e-mail: g_deepa@blr.amrita.edu

© Springer Nature Singapore Pte Ltd. 2020

T. Hitendra Sarma et al. (eds.), *Emerging Trends in Electrical, Communications, and Information Technologies*, Lecture Notes in Electrical Engineering 569,
https://doi.org/10.1007/978-981-13-8942-9_8

to light and gather pointers about related hazard elements and preventive measures in various fields. A Social network is a collection of performers connected by some kind of relationship. For example, performers might be the entities in an organization and relationship can be of any kind. Study is done on social media sites of different domain like travel, health care, product review to get insights on various factors including customer sentiments, customer choice etc.

Now-a-days many Machine Learning (ML) techniques are explored on data from various areas such as robotics [1], health care, social web sites [2–5] etc. Health care is one major area where various ML approaches like classification, clustering, association rule mining etc. are applied to obtain various insights [6–8]. OHCS (Online Health Community Services) is one of the major social media where the patients and their family attempt to understand more about chronic disease. There is large amount of information in the internet. But when the information is shared by the people who undergo similar health condition, then it becomes more convincing and give more satisfaction to the patients who have related queries about their illness. Doctors are also involved in the discussions in various health forums. Various online health communities are helpful for providing moral support for the people who are affected with chronic diseases. A chronic disease persists for a long time and it may cause various symptoms and conditions which may lead to death. Various types of Chronic Diseases HIV/AIDS, Heart Diseases, Cancer, Diabetes etc. Each disease has their own OHCS (Online Health Community Services) which provides different types of services like forums, dashboards etc. Each forum can provide different types of social support which may vary on the people interacting in a forum.

Many Online Health Forums provide Social Support in the form of discussions. In online forum different threads would be available where each thread contains multiple discussions. Generally, the social support from the health forums can be broadly categorized into emotional and informational support. Informational support can be defined as medical terms, experiential information, etc., which it has been provided in the online health forums. A patient can receive Emotional support can be defined as care, cheer, comfort, which it has been provided in the forum. In OHCS, a tremendous volume of client created content exists today on different issues identified with particular disease. This may include vital data, for example, individuals encounter with diseases, proposals and inputs about specific meds or medicinal methodology, and enthusiastic help as support, sensitivity, and examples of overcoming adversity. Mining and analyzing the data from these kind of forums can give insight on what kind of support the social media is able to provide to the patients.

It is important to analyze the degree of support in the messages of the health forums. To obtain this, as an initial phase work has been done to identify the type of support in the forum. Various research has been done on classification of the OHCS support into emotional and informational support using like Naïve Bayes, Support Vector Machine, Regression [9], etc. The supervised approach requires large amount of label data to attain good accuracy and hence needs manual labelling of large amount of data. This is often a difficult task. One of the approach like semi supervised learning which is a part of supervised learning are applied on the data for

prediction. Hence in the proposed approach, semi supervised algorithms are applied on the data for classifying the discussions into emotional and informational support. Semi supervised approach requires only a seed labelled dataset which is feasible. The next phase involves the task of building a regression model to predict the degree of emotional support in the discussions of the forum. Various robust features are identified for evaluating the degree of emotional support in messages of POZ forum using multiple regression algorithms.

The paper content is organized into various sections as follows. The related works in this research area is discussed in Sect. 2. Section 3 describes the proposed methodology. The results and its analysis are described in Sect. 4. Section 5 discusses the conclusion and future work.

2 Literature Survey

Online Health forums has large amount of data in the form of continuous text. In [9], data collected from the POZ forum for analyzing the self-care behaviour. Tobit regression has been applied on the data. Explanatory variables like emotional tone, self-disclosure, crowd consensus, experiential information, objective information, thread duration, are recommended for building a hypothesis model to analyze the self-care behaviour. Mining the data from the forums and constructing a model for predicting the patient's satisfaction. Text mining is an effective technique to discover the knowledge from an unstructured data as mentioned in [10]. Various research works that has been carried out on online health forums for analyzing the medical data. The work in [11] classify the comments about drugs on different discussion forums into positive and negative reviews. Manual annotation has been done on the sentences to obtain 150 positive and 150 negative reviews The Naïve Bayes classifier has been applied and compared with rule based classification. In [12], messages have been collected from an online forum on diabetes and text classification has been performed to 4 domain specific models—Emotions, Sentiment, Personality Traits and Patient Journey. 3309 texts have been manually labeled as one of these models and has been given as input for different classifiers (Multinomial Naive Bayes, Linear Support Vector Classifier, Logistic Regression, Passive-Aggressive classifier and Support Vector Machines). The results of the different classification algorithms have been analyzed and Linear SVC and Passive Aggressive has been identified as best performing classifier. In a work, discussed in [13] messages were retrieved from Cancer Survivor Networks (CSN) forum and has been classified into informational support and emotional support. High weighted words for the two classes has been ranked using Term Frequency-Inverse Document Frequency (TF-IDF) scheme. Top ten words for the two classes are Good, Know, Glad, News, Hope, Keep, Prayers, Luck, Hugs, Better (Emotional support) and Chemo, After, Radiation, First, Herceptin, Treatment, Tamoxifen, Cancer, Because, Pain (Informational Support). 1066 messages have been manually annotated and different classification algorithms (Naive Bayes, Support Vector Machines, Logistic Regression, Bagging, Boosting, etc.) has been

applied. Another work mentioned in [14] focuses on understanding the types of social support exchanges in online HIV/AIDS self-help groups. This work attempts to classify social support into information support, emotional support, network support, esteem support, and tangible support. Two types of analysis are conducted to identify the type of support from the HIV/AIDS forum. Content analysis is performed to assess the social support and Thematic analysis was conducted for further patterns related to the group interactions. Clustering of breast cancer symptoms has been performed on data obtained from medhelp.com based on symptom similarity which is ASW (Average Silhouette Width) as discussed in the work in [15]. The enhanced K-Medoid grouping enhances the clustering execution by reassigning a portion of the negative-ASW symptoms to different clusters without giving up the general ASW. Performance comparison was done between k-means and k-Medoid clustering [15]. Oncological drugs reviews are taken from online forums and compared with Food and Drug Administration (FDA) drug labels for specifying efficiency of a drug and drug rating is generated with the help of FDA drug labels for further improvements in a work in [16]. A research in [17] discusses about application of text mining techniques on data of diabetes patients obtained from various social media and MEDLINE database. Intuitive and descriptive prediction are the two approaches that have been used for prediction. Descriptive task identifies explicit references and the predictive task focuses on treatment/diagnosis of the disease which is not explicitly stated. Kahina text analytic tool is used for computing the pair of the similarity of the sentences. In [18] work has been done to examine how unique types and measures of social support in an online cancer support group are related with member's length of participation. Machine learning models were worked to naturally recognize the degree to which messages contained social support. For this, 1000 messages from the discussion forum for breast cancer has been manually rated, using a 7-point Likert scale, in terms of the amount of support contained in the message. Then regression has been applied on the data with the help of Weka. In [19], sentiment change patterns and factors affecting it has been discovered in CSN members using Machine Learning and text mining techniques. Ada Boost, Logistic Regression, Bayes Net, SVM are applied for classifying the positive or negative emotions in CSN forum. Various threads which are collected from the Quit Stop forum for analyzing the user intention and the social support classification. Feature set for building the classification model are text and health which achieves good accuracy. Naïve Bayes classifier and genetic algorithms are developed for optimizing the classification results in [20].

The proposed work attempts to identify the degree of support provided in the health forum. The type of support need to be categorized into various categories. The existing works use different supervised approaches for classification of type of online support into emotional and informational support. The supervised algorithms need class labels for prediction. This requires manual labelling of large amount of data which is tedious task. But the proposed work attempts to classify the type of support in the messages as informational/emotional support using semi supervised approach where a seed labelled data is used for prediction. Then the degree of support in the health forum is analyzed using different regression models.

3 Methodology

The proposed work attempts to predict the degree of support in POZ forum, an online HIV (Human Immune Deficiency Virus) forum in mainly two phases. The initial phase includes the identification of type of support group in the forum, the second phase focusses on studying the degree of support provided in various discussion in the forum using difficult regression models. The approaches used in both phases are discussed in the subsections. The proposed system for analyzing the online forum is shown in Fig. 1.

3.1 Data Acquisition

Data has been extracted from an online HIV Forum (POZ) since Jan 2016–Aug 2017. A multiple thread which has around 1200 discussions has been extracted for analyzing the type and degree of support provided in the forum. Data extraction has been performed with the help of Beautiful soup, Urllib2 packages in python.

3.2 Data Preprocessing

The scraped data has been preprocessed with several Natural Language Processing (NLP) techniques. Stanford POS tagger has been used for tagging. Tokenization and removal of Punctuations, Stop Words, Special Characters, Url's, Digits and Lemmatization have been done for removal of noise in the scraped data. Python Natural Language Tool Kit (NLTK) package is used to perform the data preprocessing techniques.

3.3 Behavioral Support Group Identification

In this approach, inferences are drawn from the dataset for which the class labels are not known. In the proposed model, all the data preprocessing techniques and word to vector model has been constructed with 1200 samples. Dataset (1200 * 735) which is input to the PCA been reduced to 1200 * 391. The type of support in POZ forum is identified using semi supervised approach where only a seed labelled data is provided for training the model and a large amount of unlabeled data is given for prediction. Collective EM and Chopper are the semi supervised algorithms applied in this work.

Data Representation. The count of each unique word in all 1200 files is calculated. If this total count is above the set minimum threshold 13, those words are selected

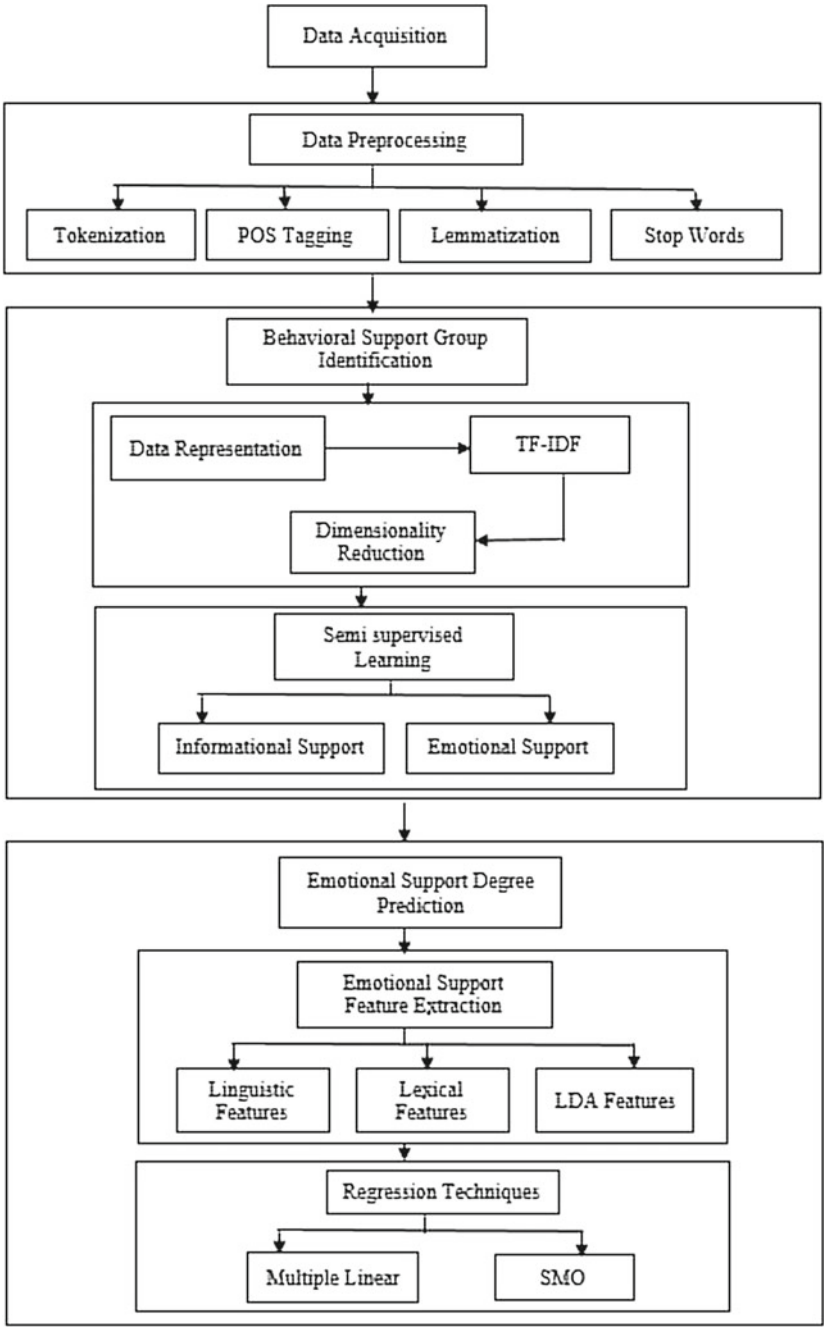

Fig. 1 Proposed system model

as the features. TF-IDF for those words are only considered. Identification of the textual features using TF-IDF weighting scores from each in the forum is helpful for building a dataset. Python Text Blob package is helpful for implementation of a TF-IDF scheme. TF-IDF is a useful technique to identify crucial information from the data.

Term Frequency-Inverse Document Frequency (TF-IDF). It gives unique words in a document related to incorporate with whole documents operation of Term Frequency (TF) and is calculated as (1). Inverse Document Frequency (IDF), given by (2) is invoked to reduce the weights of most frequent words. TF-IDF weighting scores is calculated as (3).

$$TF_{mn} = \frac{f_{mn}}{\max_k f_{kn}} \tag{1}$$

$$IDF_m = \log \frac{N}{n_m} \tag{2}$$

$$TF{-}IDF\ score{:}\ w_{mn} = TF_{mn} \times IDF_m \tag{3}$$

where f_{mn} = frequency of term (feature) m in samples (item) n, n_m = Number of samples that mention term m, N = Total number of samples.

Dimensionality Reduction. The main objective of Principal Component Analysis (PCA) is dimensionality reduction [21]. The TF-IDF word to vector model has been constructed from the data. TF-IDF model fed as input to the PCA for reducing the dimensionality of the feature set. It generally performs covariance analysis among different attributes calculated as (4), (5).

$$S^2 = \frac{1}{n} \sum_{i=1}^{n} (M_i - \bar{M})^2 \tag{4}$$

$$Cov(M, N) = \frac{1}{n} \sum_{i=1}^{n} (M_i - \bar{M})(N_i - \bar{N}) \tag{5}$$

where M, N is feature, n is number of samples and $\bar{M}, \bar{N}$ are the mean values. Variance measure is used to map the data into a new coordinate system. It acquaints a numerical technique with transmute related features into directly uncorrelated features called principal components. PCA analysis was performed using WEKA tool.

Collective EM (Expectation Maximization). Collective classification techniques which is used in different areas such as malware detection [22], text classification [23] etc. The given base classifier trains on the training set and then label the instances of the test set. i.e., the original test set is duplicated and each part is assigned one class, the distribution of the classifier is used to set the weight of the instances in each part. The weights from then on are calculated with the formula (6).

$$mean(n+1) = q * mean(n) + (1-q) * dist(n) \tag{6}$$

where n is the number of samples and q is the value used for averaging the distributions of the classifier. Due to keeping track of the mean and using that in the calculation of the new weight, one avoids oscillating behavior.

Chopper. In a work [23] discusses about collective classification for spam filtering with a partially labelled data. Collective Classifier that uses one classifier for labelling the test data after training on the train set. The trained classifier determines the distributions for all the instances in the test set and uses the difference between the two confidences to rank the instances. The fold with the highest ranking (biggest difference between the two confidences) is then added to the training set—after the labels have been determined. This new training set is once again input for a classifier (if there are more than two classifiers given, then the classifiers 2 to n are used in turns for training on the newly generated data and classifying the rest of the test data for the next one) which determines once again the distributions for the remaining instances of the test set.

3.4 Emotional Support Degree Prediction

To identify the degree of support, the types of support in POZ forum has been identified using semi supervised algorithms as mentioned in Sect. 3.3. The application of semi supervised algorithms on the forum data has revealed the fact that the discussions contain more emotional support compared to informational support. Hence it has been proposed to analyze the amount of emotional support in each discussion using different regression techniques. For this all messages of the discussion from POZ forum has been manually rated on a scale of 1–7 (Likert Scale Rating) where 1-denotes the message has low Emotional support and 7-denotes the message has high emotional support [18]. Data preprocessing techniques are applied on the discussions as mentioned in Sect. 3.2. 13 Significant features that can contribute in prediction of degree of emotional support in the messages of the forum has been identified which falls into three main categories, namely LDA Features, Linguistic Features, and Lexical features.

Feature Set. Few explanatory variables have been identified as suggested by the existing work [18] and few other variables are also tried for analyzing the amount of emotional support provided in the online health forums. Predicting the length of support in each discussion under each of these type of features namely (Linguistic, Lexical, LDA) [18]. 13 robust features have been identified for quantifying the extent of the emotional support provided in an online health forum.

Linguistic Features. Four features namely word count, sentence count, positive words, negative words, are examined as a linguistic feature. Count of words, sen-

tences in each discussion are implemented with NLTK package. Number of sentences containing positive, negative words are implemented with SentiWordNet package.

Lexical Features. Six features namely compound, negative, neutral, positive, strong subjectivity, weak subjectivity. Compound, negative, neutral, positive sentiment scores are generated from the social media text using a Vader toolkit. Vader Sentiment Analysis toolkit in python has been used to identify the four types of emotional scores in each discussion. Sentiment evaluation metrics are calculated with subjectivity words in discussions. Weak, strong subjectivity word dictionaries are implemented through Lexicon Opinion Finder [24].

LDA Features. Latent Dirichlet Allocation (LDA) is used to discover hidden topics in documents as well as the words associated with each topic [25]. LDA model has been trained using 1200 discussions with varied N value where N is the number of topics. In proposed model, it is set to derive 3 topics after various experiments. 500 words which are relevant to a particular topic has been identified and a topic dictionary has been built. For each topic average value is calculated in discussions. Few sample words under each topic has been listed in Table 1. In [18] assigning a class label for the topics based on the words that are relevant to the topics are discussed in topic vocabulary. Similar words obtained in the proposed work has been given similar topic names as mentioned in [18]. Genism package in python has been used for implementing the LDA Model.

A total of 13 features are identified for predicting the degree of emotional support. Various standard Regression techniques like Multiple linear, SMO regression have been applied on the data. Multiple Linear Regression is a statistical Measure model relationship among several explanatory variables and response variables [26]. (Ordinary Least Squares) model has been applied in multiple linear regression for identifying unknown parameters from the technique. Stat models package in python is helpful for implementing the technique. SMO Regression implements the support vector machine for regression. The parameters can be learned using various algorithms. The algorithm is selected by setting the RegOptimizer [27]. Weka data mining toolkit is used for implementation. The performance of the two different algorithms are measured using R^2 metric. R-Squared which is sustainable for measuring the performance of the model. Different regression techniques that are compared with

Table 1 LDA topic vocabulary

Labelled topic	Topic vocabulary
Emotional reaction	Good, help, hugs, sorry, find, life, time, people, one, like, would, going, want, go, really, take, still, someone, friend, find, etc.
Thoughts or feelings	Concern, start, week, depressed, people forum, support, tested, told, much, need, well, may, taking, sure, say, want, body, you're, better, keep, etc.
Adjusting to diagnosis	Feeling, positive, diagnosed, cd4, Viral load, atripla, thought, health, blood, medication, experience, information, problem, healthy, ill, drug, virus, probably, viral, etc.

a r-squared measure (7). Residual sum of squares (RSS) is used to evaluate performance of the model. (Residual Sum of Squares) which is calculated as shown in (7).

$$R^2 = 1 - \Sigma \frac{(Actual - Predicted)^2}{(Actual - Mean)^2} \tag{7}$$

where Actual is the actual response value predicted is the predicted response value from the model and Mean is the mean of the actual class labels (7).

P-Value is a statistical measure used in regression model. *P*-Value which it has been used as a feature importance measure for building a model. If the *P*-Value (Positive rate Value) is < 0.05 alpha value, the explanatory variable which it rejects null hypothesis else the variable is insignificant for prediction.

4 Experimental Results

The work aims at identifying the degree of support in POZ forum. This is carried out as two phases as behavioral support group identification and emotional support degree prediction. The results of the two phases are discussed in the subsections and the results obtained are discussed in this section.

4.1 Behavioral Support Group Identification

The proposed work attempts to identify the support group in POZ forum. The data scrapped from the POZ forum is pre-processed. Out of 1200 messages obtained by scraping the forum, 200 messages are manually labelled and given as seed data for the semi supervised algorithm to group the type of support in the forum. Semi-supervised Learning Algorithms Collective EM and Chopper are implemented in Weka with the help of collective package. Out of the predicted labels, 200 samples have been verified by labelling them manually and the accuracy for Chopper and Collective EM are found to be 87% and 73% respectively. Chopper exhibits a better performance when compared to Collective EM. Predicted labelling for two instances in each support group by Chopper has been shown in Table 2.

The Chopper performs well in identification of the type of behavioral support. The results obtained from both the algorithm shows that more discussions in POZ belong to emotional support group compared to informational support group. Now the next phase helps in predicting the degree of emotional support in the messages. Regression techniques were applied on the discussions for performing this.

Table 2 Predicted labelling of instances by chopper

Support Group type prediction	Messages belonging to the respective group
Emotional support	Great job!!!!! Lol … I hope you are doing well … I think about you often
	Very sorry to hear of your diagnosis … I was working in Korea when I got my diagnosis … test in Thailand
Informational support	As for treatment well its recommended to … of CD4 or VL counts
	Infectious disease … medications for surgeons … meds and … I stop antiretroviral for any reason

4.2 Emotional Support Degree Prediction

To predict the degree of support in the discussions in the forum, different regression techniques are applied on the data where 80% of the data is used as training and 20% used as testing. Multiple linear regression is implemented in python and SMO with Weka toolkit.

Each R^2 measure in different algorithms are shown in Fig. 2. Multiple linear, SMO regression techniques are performed on the data and the R^2 measures obtained are 0.78, 0.91 respectively. SMO regression which is a machine learning based regression technique is found to perform better compared to Multiple linear regression which is statistical approach. Regression techniques are compared using R^2 measure shown in Fig. 2. Multiple Linear regression line equation shown in (8) and SMO regression line equation shown in (9). Each coefficient explains about dependency of explanatory variables with its response variable.

$$Rating = 0.1382 + 0.3953 * Compound + 2.1722 * Negative$$

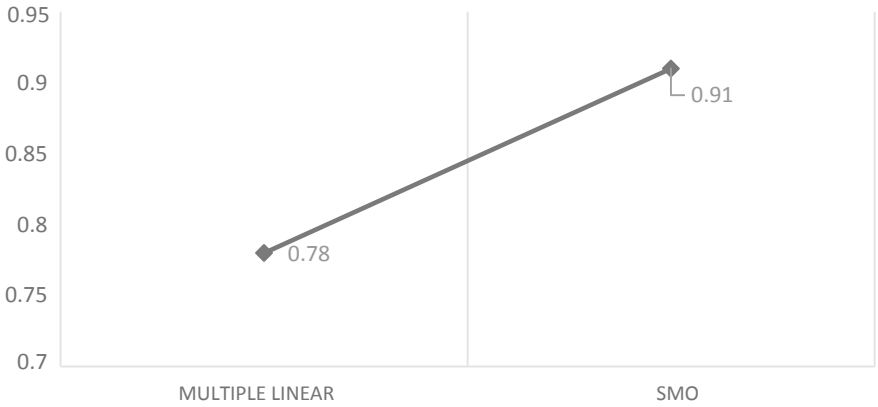

Fig. 2 Results comparison in term of R^2 regression metric

Table 3 *P*-value regression measures

Explanatory variables	Multiple linear	SMO
Compound	0.017	0.002
Negative	0.002	0.000
Neutral	0.000	0.000
Positive	0.000	0.000
Word count	0.017	0.046
Sentence count	0.023	0.038
Positive words	0.165	0.031
Negative words	0.011	0.051
Strong subjectivity	0.017	0.026
Weak subjectivity	0.026	0.041
Emotional reaction	0.903	0.037
Thoughts or feelings	0.028	0.907
Adjusting to diagnosis	0.077	0.614

$$+\ 3.0255 * Neutral + 5.2404 * Positive + 0.7998 * Word\ Count - 1.7545 * Sentence\ Count - 1.5779 * Positive\ Words + 3.0670 * Negative\ Words - 0.4723 * Strong\ Subjectivity - 3.9308 * Weak\ Subjectivity + Emotional\ \text{Reaction} + 3.6981 * Thoughts\ or\ Feelings\ - 3.0587 * Adjusting\ to\ Diagnosis \quad (8)$$

$$Rating = 0.1102 + 0.3361 * Compound\ - 0.1438 * Negative + 0.0224 * Neutral\ + 0.1761 * Positive + 0.0513 * Word\ Count - 0.0671 * Sentence\ Count\ - 0.2774 * Positive\ Words + 0.3 Negative\ Words - 0.1237 * Strong\ Subjectivity - 0.20. Weak\ Subjectivity + 0.1592 * Emotional\ \text{Reaction} + 0.2793 * Thoughts\ or\ Feelings - 0.0853 * Adjusting\ to\ Diagnosis. \quad (9)$$

Emotional Reaction, Positive Words, Adjusting to Diagnosis variables which are insignificant identified in the Multiple Linear Regression model. In SMO variables like Adjusting to Diagnosis, Thoughts or Feelings are less significant for model prediction shown in Table 3.

5 Conclusion and Future Work

Information from the (POZ) forums has been taken and data mining techniques are applied on raw data to identify the degree of support in the discussions. To

identify the type of support, Semi-supervised approach which requires only seed labelled dataset has been applied on the data. Chopper and Collective EM are the two semi-supervised algorithms used in the proposed work. It has been identified that the messages from POZ forum contain more emotional support compared with the non-emotional support. This could be because people tend to rely on online social media for health to get more emotional support. Next phase of the work focuses on identifying the degree of the emotional support from the forum using different regression mechanisms. Quantifying the degree of the emotional support from the forum is helpful for resolving the various real world situations such as self-care, Medical diagnosis, etc.

In this proposed system model only one thread and its discussions are scraped for analyzing the forum and some of the Preprocessing techniques has been applied on the data. In future work, huge amount of data from the forum can be extracted for further analysis of the data Various other features can be extracted and the satisfaction of users for each discussion can be predicted. The proposed work aims only at identifying the degree of emotional support in discussions of POZ forum. Various other relevant features can be extracted and used to find the customer satisfaction of different discussions in the forum. Discussions from multiple forum of the same disease can be scraped and analyzed to identify which forum is more active for a particular disease

References

1. Nair PC, Radhakrishnan G, Gupta D, Sudarshan TSB (2015) Clustering of robotic environment using image data stream. In: Communication, control and intelligent systems (CCIS), 2015. IEEE, pp 208–213
2. Qasem M, Thulasiram R, Thulasiram P (2015) Twitter sentiment classification using machine learning techniques for stock markets. In: 2015 international conference on advances in computing, communications and informatics (ICACCI). IEEE, pp 834–840
3. Venugopalan M, Gupta D (2015) Exploring sentiment analysis on twitter data. In: 2015 eighth international conference on contemporary computing (IC3). IEEE, pp 241–247
4. Priyanka C, Gupta D (2013) Identifying the best feature combination for sentiment analysis of customer reviews. In: 2013 international conference on advances in computing, communications and informatics (ICACCI). IEEE, pp 102–108
5. Spielhofer T, Greenlaw R, Markham D, Hahne A (2016) Data mining Twitter during the UK floods: investigating the potential use of social media in emergency management. In: 2016 3rd international conference on information and communication technologies for disaster management (ICT-DM). IEEE, pp 1–6
6. Dominic V, Gupta D, Khare S, Aggarwal A (2015) Investigation of chronic disease correlation using data mining techniques. In: 2015 2nd international conference on recent advances in engineering and computational sciences (RAECS). IEEE, pp 1–6
7. Shastri SS, Nair PC, Gupta D, Nayar RC, Rao R, Ram A (2017) Breast cancer diagnosis and prognosis using machine learning techniques. In: The international symposium on intelligent systems technologies and applications. Springer, Cham, pp 327–344
8. Khare S, Kavyashree S, Gupta D, Jyotishi A (2017) Investigation of nutritional status of children based on machine learning techniques using Indian demographic and health survey data. Procedia Comput Sci 115:338–349

9. Wang X, Parameswaran S, Bagul D, Kishore R (2017) Does online social support work in stigmatized chronic diseases? A study of the impacts of different facets of informational and emotional support on self-care behavior in an HIV online forum
10. Otsuka N, Matsushita M (2014) Constructing knowledge using exploratory text mining. In: 2014 joint 7th international conference on and advanced intelligent systems (ISIS); 15th international symposium on soft computing and intelligent systems (SCIS). IEEE, pp 1392–1397
11. Asghar MZ, Qasim M, Ahmad B, Ahmad S, Khan A, Ali Khan I (2013) Health miner: opinion extraction from user generated health reviews. Int J Acad Res 5(6)
12. Reichert J-R, Kristensen KL, Mukkamala RR, Vatrapu R (2017) A supervised machine learning study of online discussion forums about type-2 diabetes. In: IEEE healthcom 17th international conference on e-health networking, application and services. IEEE, pp 1–7
13. Biyani P, Caragea C, Mitra P, Yen J (2014) Identifying emotional and informational support in online health communities. In: Proceedings of COLING 2014, the 25th international conference on computational linguistics. Technical papers, pp 827–836
14. Coursaris Constantinos K, Liu Ming (2009) An analysis of social support exchanges in online HIV/AIDS self-help groups. Comput Hum Behav 25(4):911–918
15. Ping Qing, Yang Christopher C, Marshall Sarah A, Avis Nancy E, Ip Edward H (2016) Breast cancer symptom clusters derived from social media and research study data using improved K-Medoid clustering. IEEE Trans Comput Soc Syst 3(2):63–74
16. Mishra A, Malviya A, Aggarwal S (2015) Towards automatic pharmacovigilance: analysing patient reviews and sentiment on oncological drugs. In: 2015 IEEE international conference on data mining workshop (ICDMW). IEEE, pp 1402–1409
17. Marir Farhi, Said Huwida, Al-Obeidat Feras (2016) Mining the web and literature to discover new knowledge about diabetes. Procedia Comput Sci 83:1256–1261
18. Wang Y-C, Kraut R, Levine JM (2012) To stay or leave? The relationship of emotional and informational support to commitment in online health support groups. In: Proceedings of the ACM 2012 conference on computer supported cooperative work. ACM, pp 833–842
19. Qiu B, Zhao K, Mitra P, Wu D, Caragea C, Yen J, Greer GE, Portier K (2011) Get online support, feel better–sentiment analysis and dynamics in an online cancer survivor community. In: 2011 IEEE third international conference on social computing (SocialCom); 2011 IEEE third international conference on privacy, security, risk and trust (PASSAT). IEEE, pp 274–281
20. Zhang M, Yang CC (2014) Classifying user intention and social support types in online healthcare discussions. In: 2014 IEEE international conference on healthcare informatics (ICHI). IEEE, pp 51–60
21. Hadsell R, Chopra S, LeCun Y (2006) Dimensionality reduction by learning an invariant mapping. In: 2006 IEEE computer society conference on computer vision and pattern recognition, vol 2. IEEE, pp 1735–1742
22. Santos I, Laorden C, Bringas PG (2011) Collective classification for unknown malware detection. In: 2011 proceedings of the international conference on security and cryptography (SECRYPT). IEEE, pp 251–256
23. Laorden C, Sanz B, Santos I, Galán-García P, Bringas PG (2011) Collective classification for spam filtering. In: Computational intelligence in security for information systems. Springer, Berlin, pp 1–8
24. Wilson T, Wiebe J, Hoffmann P (2005) Recognizing contextual polarity in phrase-level sentiment analysis. In: Proceedings of the conference on human language technology and empirical methods in natural language processing. Association for computational linguistics, pp 347–354
25. Yang F-C, Lee AJT, Kuo S-C (2016) Mining health social media with sentiment analysis. J Med Syst 40(11):236
26. Baker C, Blackwood J, Hartless C, Pirro J, Flower AA (2017) Healthcare analytics and visualization using SEMantic open source software (SEMOSS). In: Systems and information engineering design symposium (SIEDS). IEEE, pp 144–149
27. Shevade SK, Keerthi SS, Bhattacharyya C, Murthy KRK (2000) Improvements to the SMO algorithm for SVM regression. IEEE Trans Neural Netw 11(5):1188–1193

PLEACH-U: An Energy Efficient Uniformly Distributed Cluster Heads Routing Protocol

K. Chandana Rani and Ravi Sankar Sangam

Abstract In Wireless Sensor Network (WSN), the lifetime of sensor nodes strongly depends on battery power. Clustering provides an effective way for extending the life time of WSN by efficiently transferring data packets from source to sink. LEACH and PEGASIS are two popular hierarchical based routing protocols in WSN. LEACH goes through some limitations due to its cluster-based architecture, while PEGASIS lacks with dynamic nature. In this paper, we introduce an energy efficient routing protocol, named it as Pegasis-LEACH using Uniform distribution of cluster heads (PLEACH-U). The proposed method, PLEACH-U, addresses the hotspot issue and also the aforesaid issues of LEACH and PEGASIS. We show the efficacy our proposed routing protocol using simulations.

Keywords Cluster head · Wireless sensor networks · LEACH · Energy efficient routing

1 Introduction

Wireless Sensor Network (WSN) is a self-organized network containing large number of sensor nodes deployed randomly in the physical phenomenon which are limited in energy source, computational capability, and storage capacity. WSNs are broadly applied in several fields due to its characteristics like high-density, large-scale, self-organization of sensor nodes, reliability and etc. Applications of WSNs are environmental monitoring, military monitoring, health monitoring, temperature detection like pressure, humidity, sound. We can also deploy sensor nodes randomly in the forest for monitoring temperature in case of forest fire disaster.

K. Chandana Rani (✉) · R. S. Sangam
Department of Computer Science and Engineering, VIT AP University, Amaravathi, India
e-mail: jchandanarani@gmail.com

R. S. Sangam
e-mail: srskar@gmail.com

© Springer Nature Singapore Pte Ltd. 2020

T. Hitendra Sarma et al. (eds.), *Emerging Trends in Electrical, Communications, and Information Technologies*, Lecture Notes in Electrical Engineering 569,
https://doi.org/10.1007/978-981-13-8942-9_9

In WSN, routing plays a significant role in extending the life time of network, as all the nodes are equipped with limited powered batteries and replacing batteries of such sensors is not cost effective, by efficiently transferring data packets from source nodes to Base Station (BS). In [1, 2], two hierarchical based protocols namely, LEACH and PEGASIS are discussed, respectively, to improve the life time of WSN. LEACH is a self-adaptive and self-organized protocol which is working based on cluster formation. Sensor nodes in the network organize themselves in a local cluster and select a Cluster Head (CH) which collects information from cluster member and transmits it to the BS. LEACH protocol increases the network lifetime, but reduces the total energy consumption because they consume more energy in the formation of CH node. If CH dies all the nodes that are associated with that cluster becomes inaccessible. On other-hand in PEGASIS, each node maintains global information about all other nodes in the network which consumes more energy of the nodes.

As a result in this paper, we propose a routing algorithm, named it as Pegasis-LEACH using Uniform distribution of cluster heads (PLEACH-U) to efficiently send data packets from source nodes to BS by minimizing the energy consumption. We show the efficiency of our proposed scheme using simulations.

The rest of the paper is organized as follows: Sect. 2 briefly describes the latest improvements in the field of WSNs routing. Section 3 describes the PLEACH-U, Sect. 4 demonstrates the efficacy using simulation results occurred, and finally Sect. 5 concludes the discussion.

2 Related Work

LEACH and PEGASIS are two different energy efficient hierarchical routing protocols, which follows their individual aim to transmit data from source to destination. As LEACH is one of the cluster based protocols, many protocols have been derived from LEACH with few modifications and applying few advanced routing techniques [3]. Here, we focus on reviewing some of the important LEACH and PEGASIS based routing protocols.

In LEACH-B (Balanced LEACH) protocol [4], the CH selection in the first round is similar that of LEACH, but from the second round onwards the CHs are selected based on nodes residual energy. As a result the CHs count is constant, compared to LEACH, and hence obtains optimal energy consumption in each round. In [5], centralized routing protocol called LEACH-C is discussed. It uses central control algorithm to form the clusters and also creates a superior clusters by distributing CH nodes in the system. LEACH-C produces superior results through scattering CH nodes in the network. LEACH-C can transmit the large amount of data per unit area

as compared to LEACH. In [6], enhancement of LEACH protocol called LEACH-F (Fixed number of Cluster LEACH) is introduced. The cluster formation in this routing is similar to LEACH-C. But it has the disadvantage of having fixed clusters which results in poor energy management. In [7], the algorithm Energy-Efficient Distributed Unequal Clustering (EEDUC) is introduced. In EEDUC algorithm, every node sets the waiting time, which is used for distributing CHs.

A routing protocol called PEGASIS-for energy reduction has been proposed in [8], in which the sensor nodes are systematized in a way where the data packets reaches a destination via shortest path by reducing total energy consumption. The structure of chain is improved such that distance between the nodes will always be minimized. Further, the data aggregation also reduces the entire energy consumption in the network. In all the afore discussed routing protocols greedy approach has been used for chain formation. But, in [9], ANT colony based routing algorithm, PEGASIS-ANT, has been proposed for constructing a chain, to transfer the data. This helps in achieving the global optimization. Besides, the concept of Double Cluster Head is also introduced, which balances the load of every node and increases the network lifetime.

Although LEACH holds dynamic nature, it is cluster-based protocol that employs random rotation of Cluster-Heads (CHs). So, there is an option that elected CHs will be focused in certain part of the network. For this reason, few nodes may not have access to any CHs in their environment. The nodes form into group of clusters which organizes themselves into local clusters, with one node performing as the local BS or CH. Every node concludes to which cluster group it belongs to, by selecting the CH that needs the low communication energy. Although LEACH and PEGASIS have good features of energy efficiency, they contain few limitations that must overcome.

i. At present there are no techniques for uniform distribution to predetermine [2].
ii. To become a CH it follows probability function which is based on the assumption that all the nodes will contain same initial energy.
iii. Breakdown of CH causes the failure for entire cluster, as other nodes within this cluster have no access to other CHs.
iv. Maintaining all the global information of every node will consume more energy in PEGASIS.

The combination of both protocols LEACH and PEGASIS is to design an ideal routing protocol for wireless transmission of data in the network. So, we introduce a new approach called PLEACH-U which integrates both the chain formation technique inside the clusters for forwarding data. It may be noted that in our approach, we are constructing unequal sized clusters.

3 Proposed Work

In this section, we introduce our scheme, PLEACH-U, describes the Uniform Distribution Technique for selecting CH's. We divide entire WSN into uniform partitions, in each partition a node with maximum residual energy is elected as CH and the nodes are structured in a systematic way into clusters of various size. We keep track of clusters size in a tabular form, so that information of every node is maintained to which cluster it belongs to, due to that the consumption of energy globally reduces. All the nodes are formed into clusters where no node should remain outside the transmission range. Our aim is to construct a WSN in which CHs are equally selected based on the remaining energy of the sensor nodes, so that every node remains inside the transmission range of CHs. So that the network has higher lifetime, less energy consumption.

In Fig. 1, the nodes that are represented within the diameter are said to be one cluster and the CHs are represented with green color dots. This figure illustrates the data transmission from nodes to BS within a WSN.

Figure 2, the blue color line that is passing through the nodes represents optimized path from CHs to BS. Every CH makes a communication with other CH nodes in the network and hence forms a chain to the BS. The CH that contains closer distance to the BS is chosen as a leader node of the chains, where the leader node is responsible for forwarding the data directly to the BS.

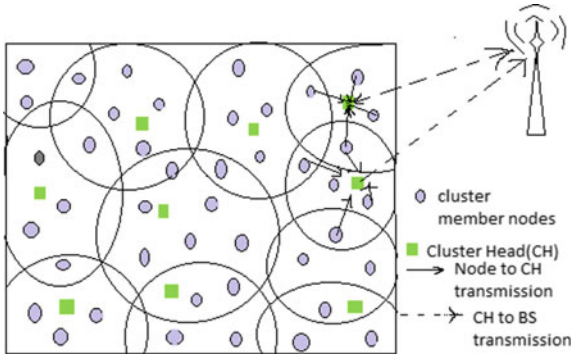

Fig. 1 Architecture of PLEACH-U

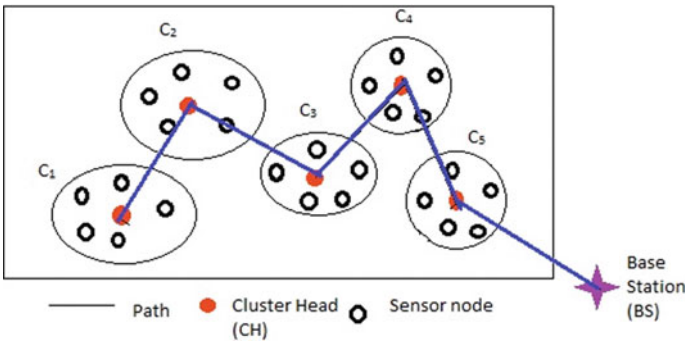

Fig. 2 Chain-based architecture of PLEACH-U

Primarily, all the sensor nodes are homogeneous. First, a node with the highest value of remaining energy, announce itself as a first CH. At that time the first CH selects a coverage area, where no other node in that particular area can announce itself as a CH. After that one, newer CH is chosen from remaining network. This is the way where entire network is separated into few predefined partitions. Every CH consists of some coverage area and all other cluster member nodes form a cluster with that CH, where no node should be remained outside of those areas. So, that the CH's are equally distributed entirely throughout the network. Choosing coverage area for particular CH, can be decided by selecting an Energy-Balancing Unequal Clustering Mechanism (EB-UCP) [10].

In our protocol, the coverage area of each node is a known priori, this will in-turn improve the distribution of CH's. Hotspot [10] is one of the problems that occur in typical cluster based protocols. Clusters that are placed near to the BS have high probability, which means more CH occupies less number of cluster member nodes and small cluster coverage area. This influence in less energy dissolution for intra-cluster traffic and can save the energy for inter-cluster routing. The tentative CH's are selected based on the residual energy of a node to equalize the energy consumption. When two nodes contain same residual energy, CH selects the relay node randomly from these nodes. The main motive of this metric is benefiting in saving of energy efficiently as it is always necessary for a CH to stay at correct location. The Cluster Head competition is shown in Algorithm 1.

Algorithm :1 Cluster Head formation in PLEACH-U

1. *Node ch is Cluster Head (CH) in partition P:*
2. *Form Mesg_Competition (ID,PID,R_c)*
3. *Announcement Mesg (Mesg_Competition)*
4. *Sensor Node n:*
5. *Receive Mesg_Competition $C_1, C_2, \ldots, C_i$*
6. *Start*
7. *To Mesg_Competition C_m ($m \in [1,1]$)*
8. $if(Cm, PID = n.PID)$
9. $n.Competition\_data\_Table \leftarrow Cm$
10. *Else if*
11. *Abandon C_m*
12. *For each Mesg j in n. Competiotion_data_ Table*
13. $Ck.Rc == min(j.Rc)$
14. *End for*
15. *CM $n \in$ CH k*
16. *CM n sends Mesg_followed (ID, CHID(i))*
17. *CH k accepts Mesg_followed (ID,CHID(i))*
18. *k.Memeber_data _Table ←n.ID*
19. *End*
20. *End Procedure*

After completion of electing CHs, the CHs announce Mesg_Competition within maximum radio range Rc to present their willingness (See Lines 1 and 2 in Algorithm 1). Every Cluster Member (CM) node receives few parts of Mesg_Competition $C1, C2, \ldots Ci$, and checks if the Partition ID (PID) of Mesg_Competition is equal to its PID as shown in lines 3–10 of Algorithm 1. Assume that there is CM node n, n always finds the minimum of R_c and it will join in that cluster (See Lines 11–16 in Algorithm 1).

In Fig. 3 both S1 and S2 can become CHs, but in case of S3 and S4 both cannot become CHs as they belong to same partition. Hence, the CHs distribution can be managed over the network. For example R^0_{comp} is the max competition radius that is predefined. By assigning R^0_{comp} of S_j as function of distance to the BS [1]

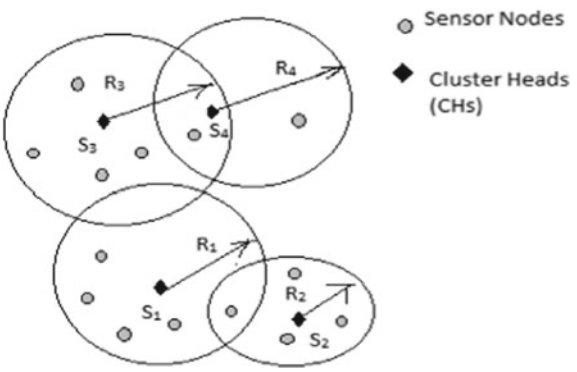

Fig. 3 Competition between tentative cluster heads

$$S_i \cdot R_{comp} = \left[1 - c\frac{d\max - d(s_i, BS)}{d\max - d\min}\right] R^0_{comp} \quad (1)$$

Here, $d_{\max}$, $d_{\max}$ describes the minimum and maximum distance between all sensor nodes and BS, $d(S_j, BS)$ is the distance between jth node, S_j, and the BS, c is a constant coefficient which lies between 0 and 1. The competitive radius changes from $(1 - c)\ R^0_{comp}$ to R^0_{comp}. Every tentative CH maintains a set S_{CH} of its adjacent CHs. The tentative cluster head S_a is an adjacent node S_j, if S_a is in S_j's area of competition diameter or S_j is in S_a's area of competition diameter. It depends on which tentative CH S_j will finally become a CH it depends on the number of nodes in the S_{CH}. The CH nodes having the nearest distance to the BS are chosen as a leader for all the chains, it is the responsibility of the leader to send the data to the BS directly. The algorithm for selecting a leader node is explained in algorithm.

Algorithm :2 Chain construction in PLEACH-U

1. *Initially, the network consists of (Nodes (M), Base Station (BS), Location I(a , b), Energy (E))*
2. *Selection of CH , if Energy(E) of any node is equal to maximum energy(Emax) then that node is selected as CH.*
3. *The node receives acknowledgement for transmitting and receiving messages from BS.*
4. *Construction of chain and selecting the leader.*
5. *Data transmission starts from source to destination via chain.*
6. *If CH energy is less than Maximum energy it goes to step 2*

The Algorithm 2 describes that all the nodes M, send their location data I (a, b) and energy (E) information to BS. BS receives location (I) and energy (E) from nodes $M_{1,i}$, $M_{2,i}$, $M_{3,i}$, …, $M_{ni,i}$ in ith cluster. If CH is unsuccessful in maintaining the similar maximum energy, then the node that contains the CH with second highest

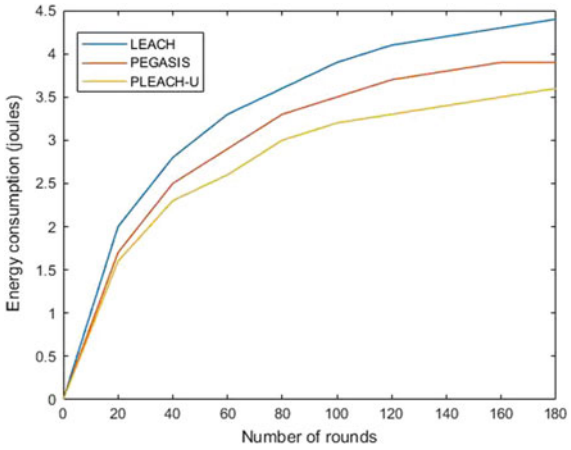

Fig. 4 Average energy of nodes

maximum energy is chosen and announced as the CH. This guarantees successful working of the CH in cluster-chain-based design of the PLEACH-U routing protocol.

4 Simulations Results

In this section, we evaluate the efficiency of our proposed routing protocol (PLEACH-U) through simulations. We have implemented our algorithm in MATLAB and executed on i3 processor running on Windows 10 Operating system with 4 GB. We compared our routing algorithm with LEACH [3] and PEGASIS [2]. We have deployed randomly 300 nodes in the area of 1000 sqft. First, we have considered the number of rounds and the consumption of energy. Each node in every network has an initial energy consisting of five joules and there is unlimited data to be sent or transmitted to the BS. Every node has reserved energy which is limited, when the energy is utilized more it leads to energy depletion. A node which is depleted of its limited energy is said to be dead node. As shown in the Fig. 4, our approach outperforms LEACH and PEGASIS in terms of energy management. This can be explained by the reason that our approach uniformly distributes the cluster heads.

We have also compared number of dead nodes after each round. As evident from Fig. 5, our approach has significantly reduced number of dead nodes in each round. Therefore, PLEACH-U is more feasible and it preserves energy.

5 Conclusion

The routing protocols in WSNs plays significant role in prolonging the life time of the network. It is a well-known fact that the algorithms LEACH and PEGASIS are

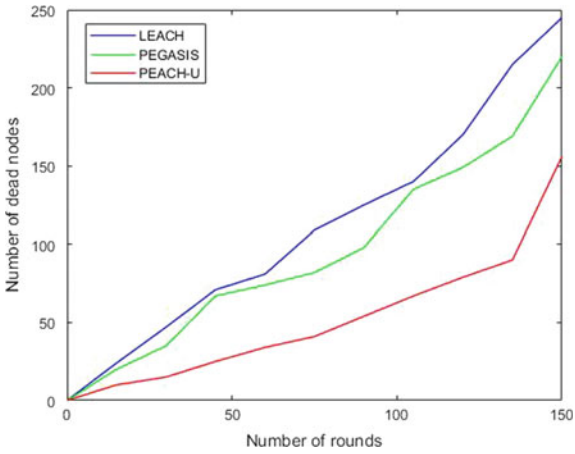

Fig. 5 Average number of dead nodes

two states of art energy efficient routing protocols. In this paper, we have discussed some of the issues of these two protocols. We have proposed the approach called PLEACH-U routing protocol for increasing the energy efficiency in WSNs. The performance of PLEACH-U is compared with both LEACH and PEGASIS using simulations. The simulations have shown that our routing approach prolonged the network life time as compared to the LEACH and PEGASIS. Since the proposed algorithm works on homogeneous sensor nodes, in future as an enhancement to PLEACH-U will be employed in a WSN with heterogeneous type of nodes which are ubiquitous in nature.

References

1. Majadi N (2012) U-LEACH: a routing protocol for prolonging lifetime of wireless sensor networks. Int J Eng Res Appl 2(4):1649–1652
2. Lindsey S, Raghavendra CS (2002) PEGASIS: power-efficient gathering in sensor information systems. In: IEEE aerospace conference proceedings, vol 3, pp 3–3
3. Tripathi M, Battula RB, Gaur MS, Laxmi V (2013) Energy efficient clustered routing for wireless sensor network. In: IEEE ninth international conference on mobile ad-hoc and sensor networks (MSN), pp 330–335
4. Tong M, Tang M (2010) LEACH-B: an improved LEACH protocol for wireless sensor network. In: 6th international conference on wireless communications networking and mobile computing (WiCOM). IEEE, pp 1–4
5. Heinzelman WB, Chandrakasan AP, Balakrishnan H (2002) An application-specific protocol architecture for wireless microsensor networks. IEEE Trans Wirel Commun 1(4):660–670
6. Manimala P, Selvi RS (2013) A survey on leach-energy based routing protocol. Int J Emerge Technol Adv Eng 657–660
7. Lee S, Lee J, Sin H, Yoo, S, Lee S, Lee J, Lee Y, Kim S (2008) An energy-efficient distributed unequal clustering protocol for wireless sensor networks. World Acad Sci Eng Technol 48:443–447

8. Khamforoosh K, Khamforoush H (2009) A new routing algorithm for energy reduction in wireless sensor networks. In: 2nd IEEE international conference, ICCSIT. IEEE, pp 505–509
9. Rana H, Vhatkar S, Atique M (2014) Comparative study of PEGASIS protocols in wireless sensor network. IOSR J Comput Eng (IOSR-JCE) e-ISSN: 2278-0661
10. Arjunan S, Pothula Sujatha (2017) A survey on unequal clustering protocols in wireless sensor networks. J King Saud Univ Comput Inf Sci (Elsevier)

IOT Based Smart Home and Prediction of Energy Consumption

Vishakha Vaidya and Pinki Vishwakarma

Abstract In early days the concept of Internet of Things (IOT) was focused on industrial automation only. But as the technology evolves people use IOT in different areas like commercial, health, residential and transportation. It helps to bring all individual devices on a common platform so that controlling and monitoring of individual device from centralized system is possible. Smart home system proves the IOT concept very finely. A home can be called as smart if it is remotely controlled and monitored, automated, secure and where home appliances are smart enough to change their status. This paper presents an Android mobile application implementation of smart home and prediction of electricity energy consumption which uses Wi-Fi and GSM as a communication media to communicate with Beagle Bone Black, the central processing system and for data analysis simple linear regression analysis is used. Smart home system is mainly concerned with the Automation and Security followed further with energy management and prediction of electricity energy consumption.

Keywords Smart home automation · Energy consumption prediction · Linear regression analysis

1 Introduction

Now a days there are four basic needs of human's food, cloths, house and electricity. Electricity demands increases in residential as well as industrial areas. Without electricity it is not possible to complete household or office work. The concept of internet of things (IOT) is defined as connectivity of physical devices, home appliances and other electronics devices which are working with software and some set of sensors using internet in a network for communication purpose. Automation of

V. Vaidya (✉) · P. Vishwakarma
Department of Computer Engineering, Shah and Anchor Kutchhi Engineering College, Mumbai, India
e-mail: vishakha.vaidya@sakec.ac.in

P. Vishwakarma
e-mail: pinki.vishwakarma@sakec.ac.in

© Springer Nature Singapore Pte Ltd. 2020

T. Hitendra Sarma et al. (eds.), *Emerging Trends in Electrical, Communications, and Information Technologies*, Lecture Notes in Electrical Engineering 569,
https://doi.org/10.1007/978-981-13-8942-9_10

home appliances and energy monitoring & prediction helps to use electricity efficiently [1]. Security of house is another as important as major issue [2]. This system mainly consist of two parts smart home [3] and prediction of energy consumption [4], mainly based on IOT. There are two modes in system IN and OUT.

If person is inside home then he can turn on the IN mode of system. In IN mode, system will use Wi-Fi as a communication media for the communication between central processing system and server and server to android mobile app. If system is working in IN mode then user can change the status of light, fan by sending the commands through Wi-Fi using android mobile app. If any nasty situation arises then buzzer will start ringing and system user will get notification on his mobile. To reduce or to manage the usage of electricity, along with home automation, there is on more facility is provided i.e. sunlight sensor which detects the sun light and notify user that sufficient sun light is available, no need of artificial light so that user can take decision to turn OFF the light.

If user is going outside, then he/she must have to on OUT mode. The system will communicate with the user via GSM [5]. The user can change the status from outside also by sending the command in form of SMS. Also user will get notified in form of SMS, in case of any theft or fire detected so that user can take required action as soon as possible.

In case of energy consumption and prediction user will set a limit of energy consumption for a time period [4]. If limit exceeded, user will get notified to control the usage of electrical appliances. For prediction of electricity, based on the historical monitored data user will get a predicted amount of electricity bill and usage. All data analyzed using linear regression analysis [6].

A new era with so-called 'homes of the future' is started. As of now not all people are used to or aware of this smart homes. So it is quite possible people will take time to understand the system. The people who are going to use this system, at least should have awareness to use of smart phone. In case of system failure, an alternate plan should be always be ready for emergency purposes. Security is also provided, so users have to make sure that no third parties will be able to hack/collapse system. Keeping the IOT home systems updated with new features and technologies is also a big responsibility. Big challenge is to make isolated devices run properly with multiple controlling commands on one platform. As per the view as a consumer, everyone wants a device which reduces efforts, easy to use and durable devices which does not require rapidly changing operate methods. To solve these issues developers are putting the serious efforts and making the new strategies to have a fully satisfied, solved and easily controllable smart home systems.

2 Related Work

Prediction of electricity consumption is make work using IOT and disaggregated database. The all data will be gathered at some central meter system which can be used to monitor current and future energy consumption [4]. Historical data from

disaggregated database can be very helpful for the energy consumption prediction. They have used number of techniques for prediction like Linear Regression, Sequential Minimal Optimization, Gaussian Process, Multilayer Perceptron, and Regression Decision Trees [4]. The motto behind the smart home automation is to reduce energy electricity consumption and hence electricity bill too [7]. Smart home automation system can be controlled through the personal computers using internet [1].

Smart home which runs on a single board computer using IOT technique can also have the same feature of automation. Single board computer i.e. Raspberry pi is used to communicate with web server and provides status ON/OFF [8]. Same single board computer used to control and monitor home appliances through relay switch. Smart [8]. Raspberry pi is working on Advanced Reduced Instruction Set machine (ARM) technology [9]. Smart home system can be accomplished using different technologies like IOT, GSM, Bluetooth and PIC Microcontroller with ZigBee [10]. All these technologies are worked as communication media to secure and automate the home [10].

IOT is remotely controlling and monitoring devices through the internet [11]. Implemented system uses smart phone keys to control and manage home automation and security instead of using any application or GUI. The TICC3200 Launchpad is used as central system [12]. A smart home which uses Raspberry pi with motion sensor and cameras can give the surety about smart security using IOT [9].

3 Proposed System

3.1 System Architecture

As shown in Fig. 1, system architecture consist of 1 energy meter, 1 PIR motion sensor, 1 daylight sensor and 1 gas leakage sensor i.e. MQ2 sensor [13]. Energy meter and all sensors are act as input to the system which gives output as automation of home appliances, security alarm, security alert message, electricity energy consumption status by home appliances and prediction. Energy meter is connected to Beagle bone black via router. All other sensors are connected directly to central system which is beagle bone black. We are using beagle bone black as a small computer. Beagle bone black is palm size embedded Linux development board. Whole system working on command of central processing unit. Database server is also located in central system to save data and perform useful operations.

An alert alarm is connected to system directly which will ring in dangerous situation. Android mobile is also an important part of system. When system want to send alert then in OUT mode system and user will communicate with each other via GSM module in form of SMS [5]. To automate the home appliances when user is outside, android application send SMS to system. For IN mode also it works actively to get alerts and to automate home appliances. GSM module is also connected to the system vie Wi-Fi.

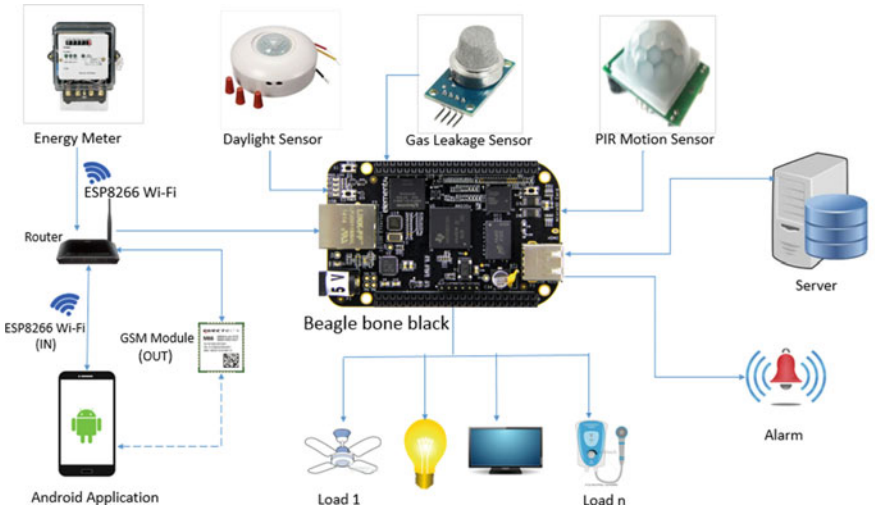

Fig. 1 System architecture

In system, data from energy meter are send to database server using ESP8266 Wi-Fi. Sensors are directly connected to the system and data gathered from sensor also store in database. Based on gathered data in database, central system take action. Energy meter is used to provide the data about electricity energy consumption in KW. If user is about to exceed limit of electricity usage, he/she will receive a notification on mobile. Daylight sensor, senses the sun light and ask user to change the status of hall light, if there is sufficient sunlight outside.

Gas leakage sensor (MQ2) is used to provide security from gas leakage and fire breakouts even if user is not present at home. In case of gas leakage or fire breakouts, system alarm start ringing and send alert message on user's mobile. In case of trespass detection, the system work the same way as working in gas leakage solution.

Android mobile application plays major role in this whole system. There are the two modes in system IN and OUT mode. Mode IN working when user inside home by using Wi-Fi as communication media to automate home appliances and to know the energy consumption and prediction. Mode OUT working when user is outside home by using GSM as a communication media to automate home appliances and to get security alert.

The proposed system will be used to provide the facility to predict the electricity consumption of home, to control home appliances and secure home from intruder and fire.

3.2 Working of System

The system is divided in two parts: Client Side and Server Side.

Figure 2 shows working sequence of system, at CLIENT end, should initialize the sensor port. After initializing the sensor port, client should send request to server to make connection. If server accepts the connection from client, read and send the energy meter and sensor data to server. At SERVER end, server first create the socket, then bind the IP address and listen for new connection request. If connection is accepted by server, then it reads data from energy meter and sensors and store it in created database.

Proposed System have two modes IN and OUT. User of system can manually change the mode OUT to IN or vice versa.

IN Mode

- When user is at home switch on IN mode.
- Using this IN functionality, user can directly communicate with the system through the WIFI module ESP2866.

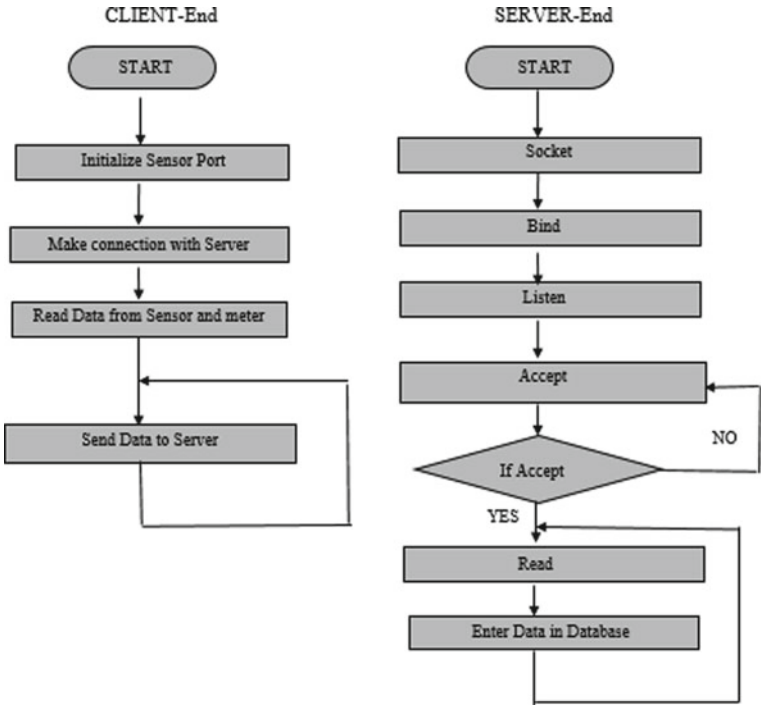

Fig. 2 Flow chart of system

- If User wants to control the home appliances he/she can send the command through android mobile application to central processing system.
- After receiving command from android application, system will change status of the device ON/OFF.
- One more functionality provided in IN mode is along with home appliance automation is user will get notified if there is sufficient sun light outside day light sensor senses that light and send a notification to user to turn off the light.
- Due to this feature user can save and mange electricity usage.

Prediction and management of electricity energy consumption: Prediction and management of electricity consumption is worked in IN mode only. To achieve this, user can set the limit of electricity usage for per day basis. If user is about to cross the limit, he will get notified to manage the electricity usage by turning OFF the unwanted electricity sources. This used electricity historical data is stored in database server which is created using sqlite3. This data is very useful to predict monthly electricity usage and bill accordingly [4]. The algorithm working behind this operation is simple linear regression analysis [6].

OUT Mode

- When there is no one available at home user can switch on OUT mode.
- In OUT mode user can get the facilities of home automation and home security.
- In this mode communication can be by using GSM module and in form of SMS from both side either from system side or from user side [5].
- If user wants to change the status of electrical devises, he have to select OUT mode in Android application and after that he can see the list of electric devices.
- From that list he can press the switch button in front of device to turn ON/OFF devices.
- When SEND button is pressed, SMS will gone in form of predefined ASCII code.
- To accomplish the home security we have provided facilities to get alert in two situation: trespass and gas leakage.
- PIR motion sensor is used to detect motion of any unwanted activity. As soon as, sensor sense the motion user will get message via GSM on his android mobile and alert on android application.
- At the same time one alert alarm start ringing at home so that neighbors will alert.
- In same way system work in case of gas leakage also.
- When user get alert and SMS about any nasty situation, he/she can take the required and useful action as soon as possible.

3.3 System Modules

Database Server
A server is a computer, a device or a program that is dedicated to managing network resources. In this system server is created using C socket programming on Linux operating system. Our system server is used to save the live data about energy consumption and to store data gathered from sensors. According to this data, server can send alert to user if needed and also predict the electricity energy consumption [4].

We have implemented database using SQLite C. Database is a collection of different types of database. Database is a part of server only.

IOT Device-Beagle Bone Black
Beagle bone black is used as central processing system. It is based on Cortex A8 microprocessor. Beagle bone black is come with a capacity of 4 GB ROM and 256 MB RAM. After collecting all data from energy meter and sensors, it will store data in database server. All data will be send through ESP2866 Wi-Fi from central system to server.

Simple Linear Regression Analysis Algorithm
For prediction of energy electricity consumption implemented simple linear regression analysis algorithm is implemented [6]. It working on historical data and predict about electricity energy consumption.

Android Application
An android application is developed to control home appliances, get alert in nasty situations and get alert in case user crosses the electricity consumption limit set by his own.

An android application provide GUI to work in both IN or OUT mode.

4 Result and Analysis

We have basically implemented a simulation of system. To have the clear idea about the functionality, we made 1 bedroom hall kitchen (1 BHK) house model.

In order to show all system functionality, 3 LEDs for 3 light, 1 LED for TV, 1 LED for geyser and 2 fans are shown Table 1. The beagle bone black is connected to 7 pin.

Figure 3 shows 1 BHK model to show the result of smart home system simulation with beagle bone black. It also has 153 general purpose input output port pin for user interface.

Figure 3 shows simulation of working system in 1BHK model with beagle bone black. This simulated 1 BHK module is connected with sensors and alarm through beagle black bone. In this house module, hall having 2 LEDs which indicate bulb and

Table 1 PINOUT Table for hardware

PIN	Button
PIN 0	Light 1 ON Light 1 OFF
PIN 1	Light 2 ON Light 2 OFF
PIN 2	Light 3 ON Light 3 OFF
PIN 3	Fan ON Fan 1 OFF
PIN 4	Fan 2 ON Fan 2 OFF
PIN 5	TV ON TV OFF
PIN 6	Geyser ON Geyser OFF

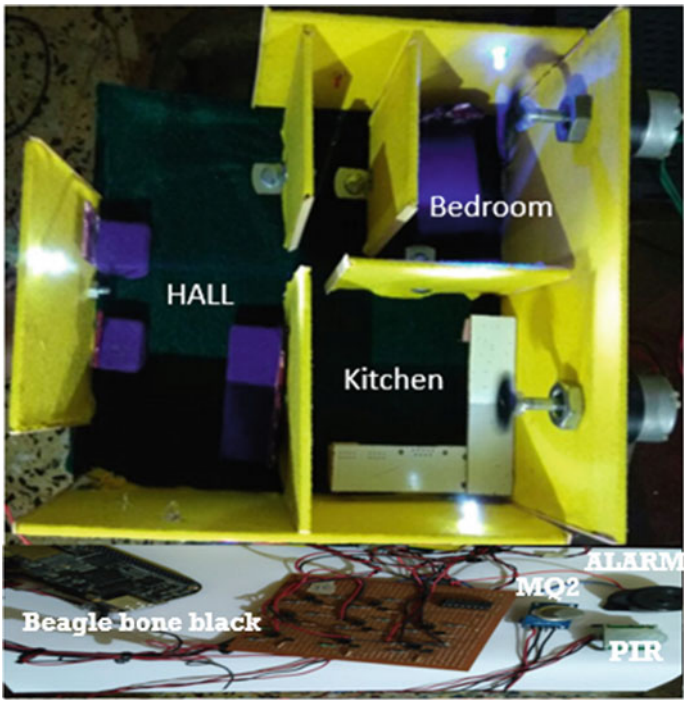

Fig. 3 Simulation of working system in 1BHK model with beagle bone black

Table 2 Database fields with description

Column name	Description
Time period	Time period of unit consumption
Month	Month of the year
Year	Used to store historical data for that month/year
Unit consumption	Monthly unit consumption in KW

second as TV. Kitchen and bedroom having 1 LED and 1 fan for each room. System responds finely for each and every command. For electricity energy consumption and prediction, we have developed on database which have one table and four fields (Table 2).

This data can be used in algorithm for prediction of electricity consumption. Time period is used as time period of unit consumption such as 1 for January month unit consumption, 2 for February month unit consumption and so on. Month and year indicates the month and year for which we provide the historical energy consumption data. Unit consumption is monthly unit consumed by home appliances.

The simple regression analysis is a method to find out the relationship between two variables i.e. one is on y axis for energy consumption and second on x axis for time period. To achieve prediction algorithm, we have followed the steps of simple linear regression analysis [6].

The first step in simple regression analysis is to calculate intercept between dependent y values and independent x values. Equations 1 and 2 show the formula to calculate intercept [6].

$$a = \frac{(\sum y)(\sum x^2) - (\sum x)(\sum xy)}{n(\sum x^2) - (\sum x)^2} \tag{1}$$

$$b = \frac{n(\sum xy) - (\sum x)(\sum y)}{n(\sum x^2) - (\sum x)^2} \tag{2}$$

Here x is taken as time period and y is taken as electricity unit consumption per month. Second step is to calculate the slope [6].

$$y = mx + b \tag{3}$$

where m is slope of line and b is intercept of y. After calculating the intercept and slope the main step is to calculate prediction of electricity consumption [6].

$$\text{Prediction} = m + bx \tag{4}$$

By using Eq. 4, we can calculate prediction the electricity energy consumption [4]. Algorithm for prediction is implemented in C using simple linear regression analysis.

Period	Month-year	Consumption	Prediction	Error	ABS Error	Sq. Error
1	Jan-17	133	127.5897436	5.41025641	5.41025641	29.27087442
2	Feb-17	133	128.3310023	4.668997669	4.668997669	21.79953923
3	Mar-17	86	129.0722611	-43.07226107	43.07226107	1855.219674
4	Apr-17	122	129.8135198	-7.813519814	7.813519814	61.05109188
5	May-17	155	130.5547786	24.44522145	24.44522145	597.5688515
6	Jun-17	154	131.2960373	22.7039627	22.7039627	515.4699225
7	Jul-17	138	132.037296	5.962703963	5.962703963	35.55383855
8	Aug-17	123	132.7785548	-9.778554779	9.778554779	95.62013356
9	Sep-17	165	133.5198135	31.48018648	31.48018648	991.0021408
10	Oct-17	117	134.2610723	-17.26107226	17.26107226	297.9446156
11	Nov-17	121	135.002331	-14.002331	14.002331	196.0652735
12	Dec-17	133	135.7435897	-2.743589744	2.743589744	7.527284681
	INTERCEPT=	126.8484848		2.36848E-15	15.77855478	392.00777
	SLOPE=	0.741258741		ME	MAE	MSE

Sheet1 Sheet2 Sheet3

Fig. 4 Prediction of energy consumption

Figure 4 shows the table for historical data saved and Prediction of next month/year. It shows the linear regression analysis algorithm implementation in excel. First column is period, second is month/year for which we have stored electricity unit consumption in third column. Forth column used to calculate prediction. Error is calculated to check the difference between consumption and prediction. ABS Error is absolute error, calculate the absolute value for error. Last column shows the square of error value. The terms ME, MAE and MSE are the mean average values for Error, ABS Error and Square Error respectively.

Figure 5 shows the graphical analysis for electricity energy consumption and prediction. In which blue line indicates the electricity energy consumption, stored as historical data for further calculation and orange lines indicate the predicted values for next month/year.

5 Conclusion and Future Work

The proposed system focuses on developing a secured and automated smart home system with energy consumption prediction facility for users. Smart home with prediction system will limit the electricity usage by providing the feature of home automation and daylight sensor. User can set monthly limit of electricity consumption according to their need and save that data in SQLite database which is very useful in prediction. By seeing the pattern of usage, user can predict monthly tentative electricity bill using simple linear regression analysis. Smart home system facilitates the

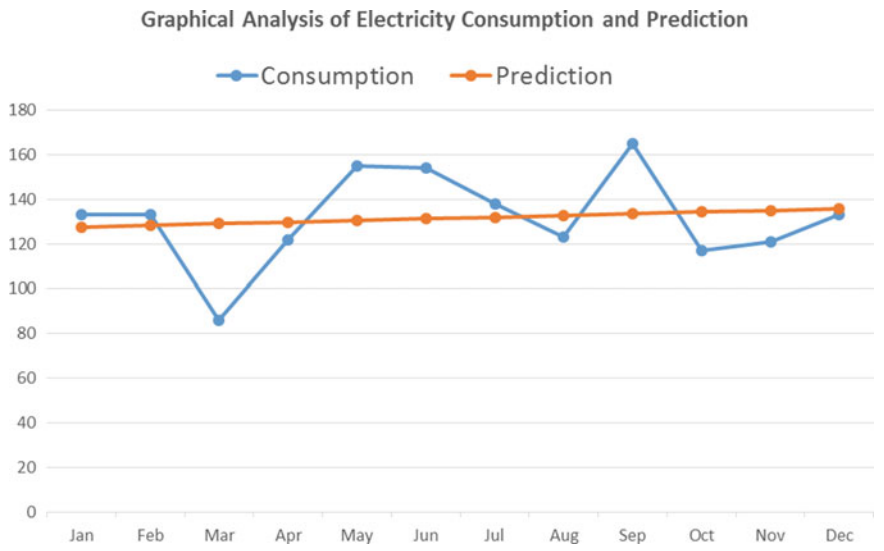

Fig. 5 Graphical analysis for prediction of energy consumption

user to automate home appliances and secure home from gas leakage and intruder. Android application GUI helps to manage home automation and get alert from sensor as well as in nasty situation. IOT based system payback us with benefits like reduces electricity usage, save money and time.

In future, the extension of this system is possible with accepting the voice commands for automation and security. For security purpose we can upgrade system to live video streaming.

References

1. Selve PB, Geethamani R (2015) A survey on various home automation system and security. Int J Eng Modern Trends Eng Res (IJMTER) 02(12), ISSN 2349-9745 (Online)
2. Naresh D, Chakradhar B, Krishnveni S (2013) Bluetooth based home automation and security system using ARM9. Int J Eng Trends Technol (IJETT) 4(09)
3. Vaishnavi SG, Pratibha SY (2016) Smart home automation: a literature review. Int J Comput Appl (0975-8887)
4. Wesllen S, Eduardo S, Thiago R, Namedin Peeter K, Peter R (2016) Prediction of electrical energy consumption for internet of things in disaggregated databases. In: 2016 IEEE symposium on computers and communication (ISCC), ISBN: 978-1-5090-0679-3, Messina, Italy
5. Akanksha S, Arijit P, Bijay R (2015) GSM based home automation, safety and security system using android mobile phone. Int J Eng Res Technol (IJERT) 4(05), ISSN: 22278
6. Jiawei H, Micheline K (2006) Data mining concepts and techniques, 2nd edn. Morgan Kaufmann, San Francisco, CA
7. Mihaly S, Dejan M, Dejan M, Bojon B (2012) Smart home automation. In: 20th telecommunications forum TELEFOR 2012, 1512–1515(2012)

8. Patil SA, Pinki V (2017) Home automation using single board computing as an internet of things application. In: Modi N, Verma P, Trivedi B (eds) Proceedings of international conference on communication and networks. Advances in intelligent systems and computing, vol 508. Springer, Singapore
9. Vamsikrishna P, Hari BK (2015) A smart home automation technique with Raspberry Pi using IOT. In: 2015 international conference on smart sensors and systems (IC-SSS), ISBN: 978-1-4673-9328-7/15/$31.00 © 2015. IEEE
10. Vishakha DV, Pinki V (2018) A comparative analysis on smart home system to control, monitor and secure home based on technologies like GSM, IOT, bluetooth and PIC microcontroller with ZigBee modulation. In: International conference on smart city and emerging technologies (ICSCET 2018), Mumbai, India
11. Himanshu V, Madhu J, Khushhali G, Aditya V, Gaurav V (2016) Smart home system based on internet of things. In: 3rd international conference on computing for sustainable global development (INDIAcom), ISBN: 978-9-3805-4421-2/16/$31.00 © 2016. IEEE, India
12. Ravi KK, Vishal J, Suvadeep B, Lakshmi B (2016) IOT based smart security and home automation system. In: International conference on computing, communication and automation (ICCCA2016), ISBN: 978-1-5090-1666-2/16/$31.00 © 2016. IEEE, Busan, Korea
13. Hina R, Chandana R, Nandini R, Surekha TP (2014) Internet of things (IoT) based real time gas leakage monitoring and controlling. Int J Electron Commun Eng Technol (IJECET) 5(08), ISSN: 0976-6472

Need for Hybrid Lexicon Based Context Aware Sentiment Analysis for Handling Uncertainty—An Experimental Study

K. E. Naresh Kumar and V. Uma

Abstract In this modern era, the rapid improvement of internet technologies makes the user comfortable in generating the data in an easier way. To analyse the user-generated data for classifying sentiment polarity into one of the three categories namely positive, negative and neutral, sentiment analysis is required. Sentiment analysis is the computational study of user opinions, moods, sentiments and other subjective elements of the text. Sentiment analysis can be implemented using lexicon based approaches and machine learning approaches (Bnadhane et al. in Procedia Comput Sci 45: 808-814 (2015), [1]). Sentiment lexicon can be used to maintain terms and their respective sentiment values. But, the existing sentiment lexicons cannot handle improved internet slang data and missing data. Hybrid lexicon can be generated by combining sentiment lexicon with domain-specific sentiment-bearing terms. In this work, we analyse and find the need for improving sentiment classification with derived knowledge from domain-specific contextual analysis and domain adopted lexicons. Finally, the analysis shows the need for the proposed sentiment classification to handle missing data.

Keywords Sentiment analysis · Sentiment classification · Lexicon based approach · Context aware system · Context aware sentiment analysis · Hybrid lexicon

1 Introduction

The rapid improvement of internet technologies increases human activities with huge amount of data generation through social media platforms like facebook, twitter, LinkedIn etc. Social websites can perform thousands of user actions within a second. Opinions or comments are to be considered to determine the sentiment polarity of

K. E. Naresh Kumar (✉) · V. Uma
Department of Computer Science, Pondicherry University, Kalapet, India
e-mail: nareshforgovt@gmail.com

© Springer Nature Singapore Pte Ltd. 2020

T. Hitendra Sarma et al. (eds.), *Emerging Trends in Electrical, Communications, and Information Technologies*, Lecture Notes in Electrical Engineering 569,
https://doi.org/10.1007/978-981-13-8942-9_11

given text. Sentiment polarity plays a significant role in social media platforms, marketing and opinion sites [2].

Sentiment analysis (SA) is also referred as opinion mining. SA is the computational study of user opinions and emotions. Sentiment analysis can be implemented on two types of information namely Facts about an entity and Opinions of an object [3]. SA is similar to OM but slightly differentiated in terms of notions [4]. SA identifies the sentiment in the given text. But, OM extracts and analyses the user opinions. The key implementation of Sentiment Analysis is to determine the sentiment polarity of user generated text. Sentiment analysis can be implemented at various levels of sentiment classification. The main task of sentiment analysis is to perform the analysis of user data into five components namely: Sentiment Polarity, Entity, Opinion holder, Time and Context [5].

Sentiment Analysis is part of Natural Language Processing tasks. Sentiment Analysis is also called subjectivity analysis [6]. Subjectivity analysis mainly focuses on the subjectivity part of text that decides the sentiment polarity of given text. Sentiment analysis can be implemented at different granularities viz. document, sentence, clause, phrase and words depending on the context in which sentiment classification is required [7].

Document Level SA can be performed to classify whether a document is expressing a positive or negative sentiment [8]. Sentence Level SA can be implemented to identify the sentiment expressed in each sentence [9]. Sentence Level SA is not suitable when the structure of sentence is complex [10]. Aspect Level SA [4] can be performed in two steps. First, identifying the aspects of an entity. Later, the sentiment is identified with respect to aspects. Clause Level SA can be performed by sentence delimitation, proposition detection and polarity assignment [11].

A context-aware system [12] can be defined as one that autonomously adapts operations by providing more functionalities to users based on contextual information. Context aware SA can be used to determine the positivity or negativity of the document or sentence with respect to the context. In [13], domain specific sentiment analysis is performed by context feature generation and sentiment classifier. Along with the context of a document, feature or aspects can also be considered to perform sentiment classification. Consider an example sentence:

I don’t like the idea of copying data

The above statement can classified as positive because it is dominated by positive terms. The negation word ‘don’t’ gives a negative impact to the sentence [14]. The decision can be addressed by performing contextual analysis using valence shifters.

Context Aware SA mainly handles the ambiguity problem by the specification of super ordinate concept of sentiment term in a given opinionated text. Basic common sense and domain specific knowledge are used to solve the problem successfully. Based on [15], Exploitation of user context information can be determined effectively

by using social relation graph structure. Context aware SA can be performed by creating and applying context aware sentiment lexicons. Context Aware Sentiment analysis can be performed by following the 3 steps [16]:

1. Identification of Ambiguous terms.
2. Collecting context terms for each ambiguous term.
3. Augment the context terms to refine sentiment analysis process.

An instance of context aware SA can be performed by creating a new dictionary containing domain specific contextual words of financial domain [17] and comparison shows that domain specific lexicon performs better than static lexicon. Hybrid lexicon can be generated by combining static lexicon and context terms that replaces the ambiguity terms [18]. Hybrid Lexicon can also be determined from multiple domains and multiple sources to increase its efficiency for handling missing data.

Missing data and noisy data can cause uncertainty in user generated text in absence of sentiment bearing terms. The handling of uncertainty can be a challenging task in context aware sentiment analysis and the creation of hybrid lexicon can overcome the issue to some extent.

This paper analysis the issues related to context aware SA and tries to propose a solution consisting of the following 3 steps. Firstly, the construction of hybrid lexicon based on identified context related ambiguous terms present in existing sentiment lexicons. Secondly, hybrid lexicon is used to perform context aware sentiment analysis. Thirdly, results produced by hybrid lexicon based context aware sentiment analysis can be effective for handling missing data also. Based on the experimental analysis performed, it is found that the proposed work can improve the performance of Lexicon based context aware sentiment analysis.

The structure of the paper is as follows: in Sect. 2 literature work is present; related terms and concepts of lexicon based context aware sentiment analysis are presented in Sect. 3, and the experimental study is described in Sect. 4. Finally, in Sect. 5 the directions for future research are described.

2 Literature Review

This section explains the works related to lexicon based context aware sentiment analysis. Context aware sentiment analysis can be performed by Lexicon based unsupervised methods and supervised machine learning algorithms.

Lucas et al. proposed a method of building lexicon based classifier by considering prior polarity words based on sentiment lexicon and also used other linguistic features regarding contextual valence shifters to determine the sentiment polarity of each sentence or given text. Polarity value can be calculated by the aggregation of prior polarities of sentiment words and context valence shifters. If the sum value is positive then opinion can be classified as positive otherwise opinion is considered to be negative [19].

Sattem et al. [20] proposed a strategy to search for extreme opinions by constructing corpus based polarity lexicon with very positive, very negative, not very positive and not very negative values. Later, sentiment classification was carried out on the lexical resource. Sentiment classification is performed with basic word matching procedure and based on that unsupervised sentiment analysis is performed. Lexicons are built automatically and compared with hand crafted lexicons by partitioning the lexicon. This method determines extreme opinions and performs better than SO-CALL and SentiWords.

Zubair et al. proposed a work based on rule based approach for opinion classification of user reviews on various products. This work mainly focuses on classification of user reviews from social websites as subjective and objective. It determines polarity value of subjective reviews considering each word. Content classification methods do not perform in an effective manner when a feasible solution is required [21]. The work can be extended by using lexical rules of natural language and opinionated text can be incorporated into an intelligent framework to determine effectiveness of the method.

Cataldo et al. proposed a lexicon based approach for implementing sentiment classification of Twitter posts based on lexical resources of SentiWordNet, Word-Net effect, MPQA and Sentic- Net. MPQA can perform better than a general purpose lexicon SentiWordNet. Word-Net cannot exhibit good performance. SenticNet is found to be better on SPS datasets and performance is poor on SemiEval datasets [22].

Rahul Rajput et al. performed a comparative study [22] of various lexicon based sentiment analysis methods. It was found that lexicon based approaches with semantic knowledge can exhibit better performance than lexicon based approach with SVM machine learning algorithm. From the survey done, some challenges in Sentiment Analysis are identified. They are finding spam and fake reviews, identifying domain dependent nature of sentiment words, specifying opinions that are changing with time, handling uncertain and missing data, identifying sarcastic or ironic sentences which leads to perform erroneous sentiment analysis and specifying relevant knowledge about facts, events and people to perform an effective sentiment analysis.

In this work, we are trying to show the importance of handling missing data and the literature review works [19–22] is summarized with respect to the above mentioned issue (Table 1).

Based on the analysis of literature review work, lexicon based context-aware sentiment analysis approaches is found to exhibit good performance on various lexicons like MPQA, SentiWordNet and SenticNet. For instance, considering that any one of these lexicons have missing data then lexicon based context-aware sentiment analysis cannot provide better results. So, the existing work can be extended to handle missing data by constructing hybrid lexicon (sentiment lexicon) with updated internet slang. By using the hybrid lexicon, context aware sentiment analysis can provide better results.

Table 1 Summarized work of literature review

S. no.	Paper	Technique used	Pros	Cons	Handling missing data
1.	[19]	Sum of prior polarities	Build union lexicon	Cannot neutralize when positive and negative impressions are in the same review	No
2.	[20]	Build polarity lexicon	Automatic construction of lexicon	Handles extreme opinions only	No
3.	[21]	Subjective reviews	Rule based approach	Complex to categorize opinions due to variation and inflections in language	No
4.	[22]	Study of lexicons	MPQA works well	WordNet lexicon can't give better results	No

3 Related Terms and Concepts

In this section the terms and concepts related to sentiment analysis are defined.

1. **Context**: Context is a framework that provides relevant resources for implementation of an operation corresponding to events or concepts. A domain can be defined as genre attribute which describes broad environment of a particular subject.
2. **Context Aware System**: **C**ontext-aware system is defined as that dynamically and individually adapt its operations to provide most relevant functionalities to users based on the contextual information.
3. **Lexicon Based Approach**: It is an approach that can be implemented by the collection of opinionated words used in sentiment classification tasks. The collection of opinionated words can be performed with automated approach. These words can be verified final check to perform sentiment classification.
4. **Static Lexicon**: It is a sentiment lexicon which mainly consists of sentiment bearing terms and their associated sentiment values.
5. **Hybrid Lexicon**: It is a lexicon that can be generated by combining static lexicon with context terms and associated ambiguous terms and sentiment values.
6. **Transfer Learning**: It can also be referred as cross domain classification, that can be implemented by analysing the data with one domain and then make use of results in any other target domain.

4 Dataset and Analysis

Sentiment analysis can be implemented by various distant supervision algorithms called machine learning algorithms to perform sentiment classification. Popular machine learning algorithms are Support Vector Machines Classifiers (SVM), Decision Tree Algorithm (J48) and Maximum Entropy Classifier. Based on the study of machine learning algorithms the SVM outperforms when dataset does not have missing values. Maximum Entropy outperforms when dataset has missing values.

The experimental study of sentiment analysis is performed by using the SMS spam collection dataset. The dataset consists of 5574 messages having positive and negative sentiments. The format of dataset consists of message id and message. To make a simple analysis the subset of dataset consisting of 59 entries are considered. The dataset is divided into training set and Test set having 50 positives and 9 negatives. The analysis is performed with five cross-fold validation. The experiment was conducted by using WEKA.

In WEKA, Filtered classifier StringToWordVector feature is used to perform pre-processing. Pre-processing of the data is done with Inverse Document Frequency Transform, Term Frequency transform and Output Word Counts assigned with True Values. IteratedLovinsStemmer is used. Decision Tree Algorithm, a machine learning approach is chosen as Filtered Classifier. Support Vector Machine and Maximum Entropy Algorithm are used to perform sentiment classification. Decision Tree Algorithm resulted in finding 43 True Positives, 5 True Negatives and 7 Neutral Sentiments with an accuracy of 81%. Support Vector Machine Algorithm resulted in finding 47 True Positives, 1 True Negatives and 11 Neutral Sentiments with an accuracy of 81.3%. Maximum Entropy based Algorithm resulted in finding 44 True Positives, 11 True Negatives and 4 Neutral Sentiments with an accuracy of 93.2% (Fig. 1).

Similar dataset of SMS spam collection was considered with missing data. Decision Tree Algorithm resulted in finding 17 True Positives, 2 True Negatives and 8 Neutral Sentiments with an accuracy of 60.3%. Support Vector Machine Algorithm resulted in finding 18 True Positives, 2 True Negatives and 7 Neutral Sentiments are determined with an accuracy of 74%. Maximum Entropy based Algorithm resulted in

Fig. 1 SMS spam collection dataset without missing values

Fig. 2 SMS spam collection dataset with missing values

finding 14 True Positives, 6 True Negatives and 7 Neutral Sentiments are determined with an accuracy of 74% (Fig. 2).

The above two experimental studies shows the effect of missing data on the performance of sentiment classification. It is found that Maximum Entropy performs better with an accuracy of 74% even dataset can also have missing values. Hence, to maintain the stable performance dataset with missing values are to be handled by constructing context aware sentiment analysis which is our future work.

5 Conclusion and Future Work

Analysing the data to determine sentiment polarity can be performed by using sentiment analysis. In the experimental study, Maximum entropy algorithm achieves an accuracy of 93.2% when the dataset does not have missing data. Similar, Maximum Entropy algorithm achieves an accuracy of 74% when the dataset has missing data. The existing classifiers when executed on SMS spam collection dataset yielded lesser accuracy in the presence of missing data. So, the hybrid lexicon when constructed by sentiment lexicon and context terms and their respective sentiment values can improve the sentiment classification performance.

The future work is to improve sentiment classification with derived knowledge from domain-specific contextual analysis and domain adopted lexicons. The work can also be extended to handle missing data and implemented on multiple domains using transfer learning.

References

1. Bnadhane C, Dalal H, Doshi H (2015) Sentiment analysis: measuring opinions. Procedia Comput Sci 45:808–814
2. Vindohini G, Chandrasekharan RM (2012) Sentiment analysis and opinion mining: a survey. Int J Adv Res Comput Sci Softw Eng 2(6), ISSN: 2277 128X

3. Singh V, Dubey SK (2014) Opinion mining and analysis: a literature review. In: Proceedings of 5th IEEE international conference-confluence-2014, pp 232–239
4. Medhat W, Hassan A, Korashy H (2014) Sentiment analysis algorithms and applications: a survey. Ain Shams Eng J 5:1093–1113
5. Liu B (2012) Sentiment analysis and opinion mining. In: Synthesis lectures on human language technologies series, 1st edn. Morgan and Claypool Publishers
6. Montoyo A, Matrinez P, Balahur A (2012) Subjectivity and sentiment analysis: an overview of the current state of the area and envisaged developments. Elsevier Decis Support Syst 53(4):675–679
7. Wang J Sun, Jian Ma KXu, Gu J (2014) Sentiment classification: the contribution of ensemble learning. Elsevier Decis Support Syst 57:77–93
8. Devika MD, Sunitha C, Ganesh Amal (2016) Sentiment analysis: a comparative study on different approaches. Procedia Comput Sci 87:44–49
9. Zia S, Fatima S, Mala I, Khan MSA, Naseem M, Das B (2018) A survey on sentiment analysis, classification and applications. Int J Pure Appl Math 119:1203–1211
10. Avanco LV, Nunes MGV (2014) Lexicon-based sentiment analysis for reviews of products in Brazilian portuguese. Braz Conf Intell Syst, Electronic ISBN: 978-1-4799-5618-0
11. Muhammad AB (2016) Ph.D thesis on contextual lexicon based sentiment analysis for social media
12. Liu B (2017) Many facets of sentiment analysis. In: A practical guide to sentiment analysis. Springer International Publishing, pp 11–39
13. Lee Sangkeun, Chang Juno, Lee Sang-goo (2011) Survey and trend analysis of context-aware systems. Inf-An Int Interdiscip J 14(2):527–548
14. Liu B (2015) Sentiment analysis: mining opinions, sentiments and emotions. Cambridge University Press
15. Kanayama H, Nasukawa T (2006) Fully automatic lexical expansion for domain oriented sentiment analysis. In: Proceedings of the 2006 conference on empirical methods in natural language processing, pp 355–363
16. Albert W, Gindl S, Scharl Arno (2013) Extracting and grounding context aware sentiment lexicons. IEEE Intell Syst 28(2):39–46
17. Tabari N, Hadzikadic M (2018) Context sensitive sentiment analysis of financial tweets: a new dictionary. J Intell Methods Big Data Ind Appl, pp 367–374
18. Choi Y, Kim Y, Myaeng S-H (2009) Domain-specific sentiment analysis using contextual feature generation. In: Proceedings of the 1st international CIKM workshop on topic-sentiment analysis for mass opinion, pp 37–44
19. Almatarneh S, Gamallo P (2018) A lexicon based method to search for extreme opinions, PLoS ONE 13(5):e0197816
20. Asghar MZ, Ullah R, Ahmad S, Kundi FM, Nawaz IU (2014) Lexicon based approach for sentiment classification of user reviews. Artic Life Sci J
21. Musto C, Semeraro G, Polignano M (2014) A comparison of Lexicon-based approaches for Sentiment Analysis of microblog posts. In: Proceedings of the 8th international workshop on information filtering and retrieval. pp 59–68
22. Rajput Rahul, Solanki Arun Kumar (2016) Review of sentimental analysis methods using lexicon based approach. Int J Comput Sci Mob Comput 5(2):159–166
23. Nguyen M (2016) Context aware text representation for social relation aided sentiment analysis. In: Proceedings of WWW'16 companion

Intelligent Computing for Air Pollution Monitoring Using GIS, Remote Sensing and Machine Learning

Tilottama Goswami and Hitendra Sarma

Abstract With an alarming increase in pollution level in various parts of the world, the study of air pollution monitoring has become one of the most demanding areas in national and international arena. The paper makes an attempt to serve as a concise guide in providing basic understanding of types of remote sensing, sources of satellite data, geospatial data analysis, aerosol optical depth for air pollution monitoring. The paper gives important references on the datasets and available formats, prerequisite tools required for processing and analysis of the data. The futuristic insights finally discuss the role of machine learning in correcting AOD values as well as filling gaps for missing aerosol values when compared to ground based sensors.

Keywords Air pollution · Aerosol optical depth (AOD) · Remote sensing · Machine learning

1 Introduction

Air is basic necessity for all living beings. In today's world of air pollution due to innumerable reasons, air monitoring proves to be of great importance. The victims of this pollution are in vast number. According to a report published by the World Health Organization, air pollution now kills approximately seven million people annually, worldwide. Critical issues are addressed in the world forum at various international conferences on air pollution and health [1]. This accounts by far one of the single biggest environmental health risk. As a precautionary measure, In order to counteract this alarming statistic and take action to clean up air it's important to first understand

T. Goswami (✉)
Anurag Group of Institutions, Hyderabad 500088, Telangana, India
e-mail: tilottama.goswami@ieee.org
URL: https://anurag.edu.in/

H. Sarma
Department of Computer Science and Engineering, Srinivasa Ramanujan Institute of Technology, Anantapur 515002, India
URL: http://srit.ac.in/

© Springer Nature Singapore Pte Ltd. 2020

T. Hitendra Sarma et al. (eds.), *Emerging Trends in Electrical, Communications, and Information Technologies*, Lecture Notes in Electrical Engineering 569,
https://doi.org/10.1007/978-981-13-8942-9_12

where the pollution is most concentrated, how it occurs, what elements are involved and how we can neutralize them. In order to do this, comprehensive air monitoring must be undertaken on a national and international scale.

Air quality can be monitored based on various parameters such as CO,SO_2, NO_x, etc.; one of them is the aerosol content in the atmosphere measured by satellite measurements of aerosols called as Aerosol Optical Thickness (AOD) [2]. AOD is a quantitative measure of the amount of light aerosols that are prevented from travelling through the atmosphere. The study and analysis of air pollution monitoring requires lots of intelligent computing in interdisciplinary fields. The domain knowledge involves broadly three areas remote sensing, geospatial data analysis, environmental science, physics and artificial intelligence (AI). Machine learning is a subset of AI which has the ability to learn how to classify, cluster the data points, do regression analysis for missing data.

The paper is a concise guide which in Sect. 2 briefs about the aerosol (natural source and composition), its detrimental effect in environmental science based on Aerosol Optical Depth (AOD—satellite derived and land derived). Section 3 next briefs about the domains related to the means of capturing the data geographically for air pollution monitoring such as remote sensing (satellites for aerosol data capture) and geospatial data analysis (data sources and formats of such data). Section 4 focuses on the role of artificial intelligence in implementing various machine learning tasks (classification, clustering, regression) applicable to air pollution monitoring (aerosol types classification; SOM unsupervised classification, multivariate, non-linear and non-parametric ML approach to understand the relationship between aerosol PM2.5 (ground based AOD) and AOD (satellite data), automate aerosol source identification and diagnosis of time evolution, predictive analytics and tackling huge data for knowledge extraction and interpretation tools, regression analysis for missing AOD values. Section 5 concludes with future work.

2 Aerosol

Atmosphere consists of aerosols. An aerosol is a suspension or mixture of fine solid particles or liquid droplets whose diameter is smaller than 1 μm or so, suspended in air or another gas. Aerosols can be natural or human produced. Examples of natural aerosols are fog, dust, sea salt, forest exudates and geyser steam, volcanic eruptions. Examples of anthropogenic aerosols are haze, particulate air pollutants and smoke, industry smoke and vehicular emissions in the atmosphere. Natural aerosols are usually larger than human produced. Aerosols can be considered as pollutants and have a detrimental effect in human health. Hence aerosol size distribution study is an interesting way to monitor the quality of air over the study region. Geospatial statistics on this distribution will help in understanding the most populated area and the reasons of occurrence can be investigated further. The paper will subsequently in the next section discuss the process as how to measure the size and distribution of aerosols. Natural composite coloring is used to make the maps more understandable

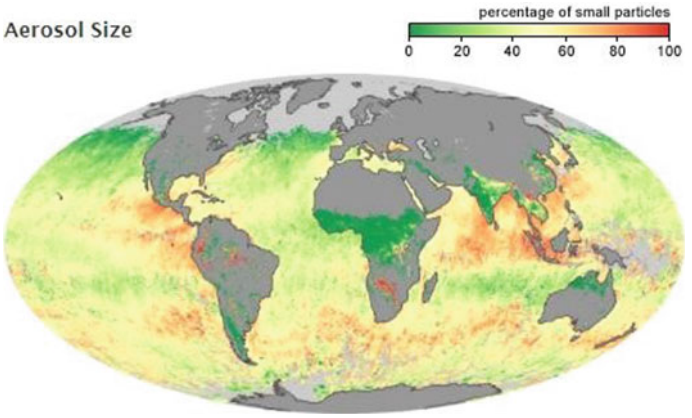

Fig. 1 Aerosol distribution for world map in terms aerosol size [https://www.ecmwf.int/]

to the users. Different color code used for large sized particles, mix of small and large, small sized particles and a separate code where sensor did not collect any data (Fig. 1).

Aerosol Optical Depth (AOD) Aerosol has effect on the physical environment around its vicinity, as they can absorb and scatter incident solar radiation. The capability of aerosols to deplete solar radiation is measured in terms of aerosol optical depth. AOD can be retrieved from an instrument present in the satellite. The sensors and algorithms used for retrieval for the AOD which will be discussed in subsequent section of remote sensing. The quality of the AOD varies, because of climate and environment, uncertainty arises especially when its cloudy. It may happen that AOD values have not been recorded at all for regions which had cloudy weather. AOD can be retrieved in two ways—(1) satellite sensors, (2) network of ground based sensors called AERONET (AErosol RObotic NETwork) [3]. AERONET is a federation of ground-based remote sensing aerosol networks established by NASA and PHOTONS. Discrepancy is found between these two readings. The shortcomings of missing AOD data, validation of AOD data can be solved using intelligent computing based on machine learning which will be discussed in Sect. 4.

3 Aerosol Data Acquisition and Geospatial Analysis Using Remote Sensing and GIS

Remote Sensing techniques collect data about the earth using various earth observing satellites without taking any sample of the earth's surface. Sensors are mounted on a satellite orbiting the earth or in general any airborne structure. These sensors capture the data during day time. Various types of sensors are used depending upon applications. A sensor is used to measure the energy reflected from the earth, which

is captured as digital image. The major applications of remote sensing are related to ecosystem management such as air pollution, water management, vegetation study, land cover management. Multispectral and Hyperspectral are two types of remote sensing. In multispectral remote sensing, earth data image acquisition is done simultaneously in multiple wavelengths—bands used are visible, near infrared, short-wave infrared, etc. This helps to gather information for monitoring temporal changes of various types of surfaces which reflect different intensity for different wavelengths.

Hyperspectral data is more informative than multispectral data, because it consists of hundreds of contiguous spectral bands with narrow spectrum. Each pixel has its characteristic spectrum which allows direct identification of individual materials such as particular mineral, rock.. The aerosol size maps are based on data from Moderate Resolution Spectro-radiometer (MODIS) instrument on NASA's Tera satellite (Fig.2a, b).

Aerosol Monitoring—Remote sensing plays a very important role indirectly in addressing the governing process for aerosol monitoring system based on existing networks worldwide. Air quality, health and environment study are global problems to be tackled. Many policy driven programme across the countries work under the International bodies such as Convention on Long-range Transboundary Air Pollution (CLRTAP), global bodies such as Global Atmosphere Watch (GAW) [4, 5] Interagency Monitoring of Protected Visual Environments (IMPROVE). A strong coordination is necessary, which involves inter-collaboration of the networks, which integrates existing and future satellite data

MODerate-Resolution Imaging Spectro Radiometer (MODIS) Aerosol features and characteristics can be explained with high spatial and temporal resolution. MODIS is one of the five sensors or instruments, launched into Earth orbit by NASA in 1999 on the board of Terra and Aqua satellites [6]. MODIS has 36 spectral channels. Channels are used for data acquisition for different spatial resolutions such as Channels 1 and 2 for 250 m, 3 to 7 for 500 m, and 8 to 36th channel for 1 km,

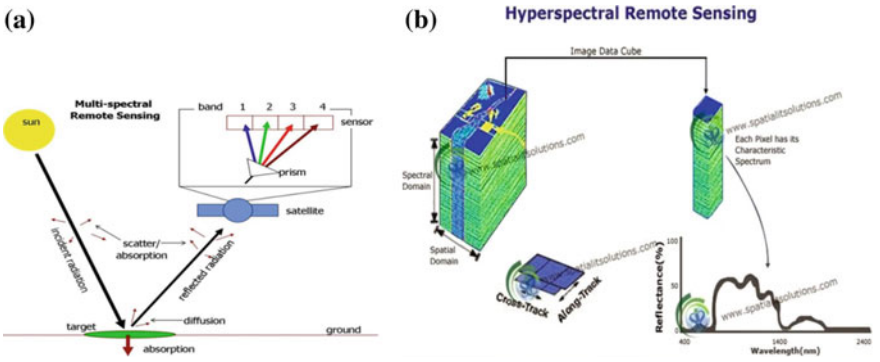

Fig. 2 **a** Multi-spectral remote sensing. **b** Hyperspectral remote sensing. *Courtesy* www.spatialsolutions.com

covering the visible, near-infrared, shortwave infrared, and thermal-infrared bands. MODIS is one of the most popularly used aerosol sensing instrument to study spatio-temporal variations over larger areas. Monthly mean data operationally is available from MODIS AOD at a 1^0 x 1^0 spatial resolution, useful for analyzing regional statistics based on spatial-temporal modeling and analysis. A study area is chosen for data selection. For example, MODIS AOD data are extracted to Indian region, i.e. 0–400 N latitude and 60–1000 E longitude with grid of 1^0* 1^0.

Sources for Remotely Sensed Data: The U.S. Geological Survey (**USGS**) is both a user and a provider of remotely sensed data, which archives aerial photography, hyperspectral imagery from various sources such as government, foreign and commercial satellites. The data can be downloaded for a particular study region from the web-enabled archive, for various applications such as global ecosystem, natural calamities, health monitoring, natural resource utilization over the years, etc.

Bhuvan, is Indian Space Research Organisation ISRO's geo-portal which mainly focuses on 1) providing Earth observation data to users in public domain for remote sensing needs and 2) image and map visualization services.

WorldView Tool is a part of Earth Observing System Data and Information System (EOSDIS) which allows the users to both browse the satellite imagery interactively and download the underlying data. The data is updated within three hours of observation, hence it supports time critical applications such as natural calamities, air quality monitoring. Figure 3 a shows the portal and b depicts the study region.

Data File Formats—The imagery downloaded from the above mentioned portals are of various types and suitable for various purposes. It can originate directly from satellite imagery instruments, elevation models or can be results of geospatial operations. National Center for Supercomputing Applications (NCSA) designed a platform independent Hierarchical Data Format (**HDF**) files of two versions (HDF4, HDF5), and also utility software for creating and manipulating the files. The file contains data and also its metadata in hierarchical format. Another file format popularly used is Tagged Image File Format (**TIFF**). For example, in [7], Aerosol optical depth have been obtained using Level-3 MODIS gridded atmosphere monthly global product'MOD08_M3' (ESDT Long Name: MODIS/Terra Aerosol Cloud Water Vapor

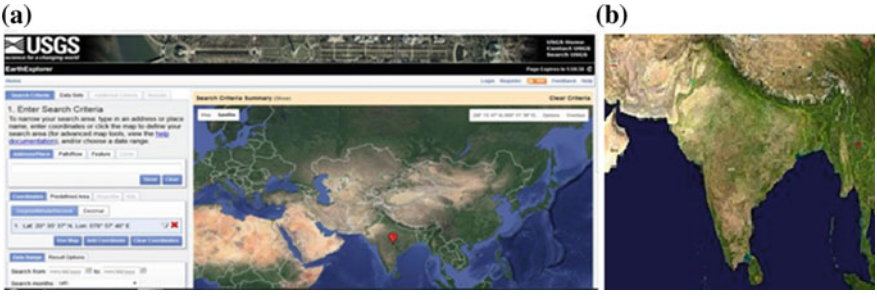

Fig. 3 **a** USGS portal. **b** Study area

Ozone Monthly L3 Global 1Deg CMG). Monthly average MOD08_M3 product files are available in Hierarchical Data Format (HDF-EOS) at spatial resolution of 1^0 by 1^0. Seasonal analysis can be done collectively for respective months by taking mean data in time-series analysis to study the air pollution trend analysis.

Geospatial Data and Geographical Information System—Processing and rendering of data obtained from satellite with a geographic element component makes analysis more understandable when it is based on visualization of maps. The processed data from image is interpreted to extract the information and assist in providing solutions. Geospatial data has geographic positioning information in a geo-referenced satellite image. Spatial Data in GIS can be satellite imagery, maps, surfaces, networks, point cloud (LiDAR), which can be represented using two models—raster and vector. Vector data uses geometric objects such as points, lines and polygons to represent the spatial features with spatial reference frame (latitude, longitude). Raster data is based on grid view consisting of cells to represent its geographic information. Satellite data uses raster data format. It is used for storing continuous data, e.g. humidity, temperature, elevation. Both the formats are interchangeable, but can be approximately transformed (Fig. 4).

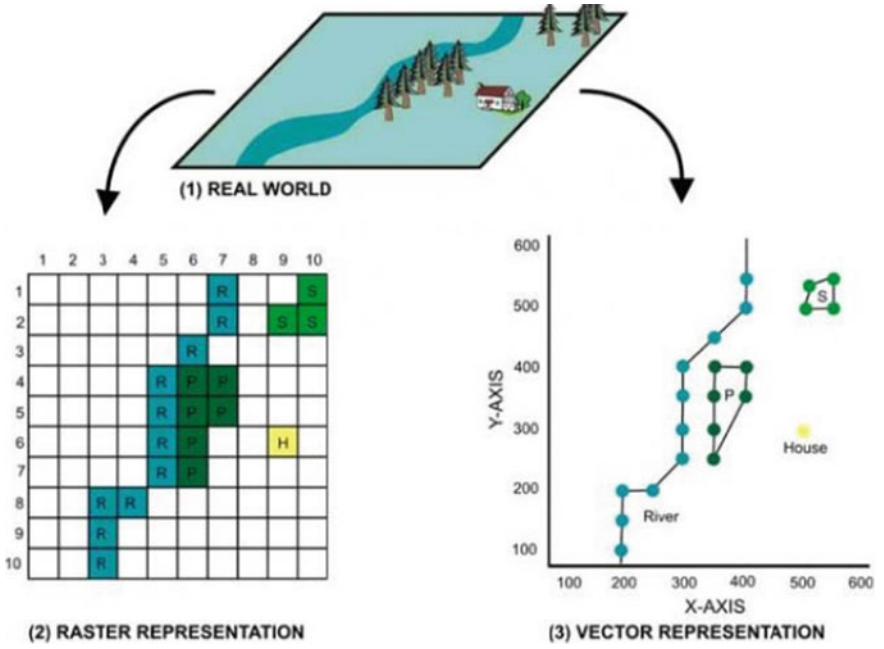

Fig. 4 Representation of (1) Real world image to (2) Raster format and (3) Vector format. *Courtesy* http://www.bowdoin.edu/~ltoma/

4 Intelligent Computing for Air Pollution Monitoring

Machine Learning The ML based techniques are increasingly growing in the areas of remote sensing images. Data is collected in large scale with the advancement in satellite industry. The need of the day is to analyze this data from various sources. The so called 'Big Data Analytics and ML' play a pivotal role in remote sensing for knowledge extraction and predictive analytics. Machine learning algorithms are universal approximators, i.e. approximately learn the underlying pattern of the training set data points. Care must be taken to sample the training data spanning the globe for more than a decade. Multivariate, nonlinear, nonparametric ML approach is used, which handles continuous real and categorical variables. Aerosol particles have distinct physical characteristics and distinct reflectance signature, which helps in aerosol types classification and recognition [8]. Typical machine learning tasks are estimation or prediction of missing AOD data, monitoring the quality of air by predicting $PM_{2.5}$ [9] using multivariate linear regression model [10], used random forests, gradient boosting; mapping of aerosol size distribution, low level image processing such as segmentation to detect abnormalities in the images, air pollution distribution analysis, validation of the atmospheric aerosols with the ground based sensors using Artificial Neural Networks and Support Vector Machine [11]. Spatial evolution of aerosols, their change in distribution with time across the globe, helps in study of the aerosol sources and automates the dust source identification.

Image Processing High-resolution satellite data plays an important role in atmospheric monitoring, when an aerosol optical thickness inversion algorithm is developed and validated with ground data. Dark pixel and dark blue algorithm are used to identify dark target and bright target respectively. Aerosol retrieval algorithm is mentioned in [12]. Correlation coefficient between satellite inversion and AERONET is depicted in [13]. Case study of few research works done on comparison of MODIS AOD retrievals with ground based measurements in tropical environment of Thailand [14]. The authors procured sunphotometers and installed at 4 solar radiation monitoring stations in four main regions of Thailand. The satellite data has been obtained from MODIS Terra in HDF format. The difference in the AOD values on daily basis measured at 4 ground stations and AOD values retrieved from MODIS over these 4 areas is measured in Root Mean Squared Difference (RMSD), the monthly AOD values when compared came out to be in the range of 33.8–53.7%. It has been found that AOD retrieved from MODIS data is overestimated for clean air and underestimated for turbid/biomass burning aerosols from ground based measurements. The correlation between the measurements vary from place to place [15]. The authors in [15] studied and compared over tropical urban location of Hyderabad. The ground measurements have been taken from India Meteorological Department situated near state highway where source of aerosols are mainly due to vehicular emission, biomass burning and industrial emissions. For ground based observation, Aethalometer measures the absorbing component of aerosol and Nephelometer is used for measuring scattering component of aerosol. The author uses Cloud–Aerosol Lidar Pathfinder Satellite Observations (CALIPSO) data to study the vertical extent of aerosol parti-

cles. A study on AOD over India Subcontinent using MODIS data shows its variability based on monthly average [16].

Software and Tools

Python libraries for Geospatial Data Processing are available [17], for dealing with map projections, analyzing and manipulating the data. GDAL (Geospatial Data Abstraction Library) is a translator library for raster and vector geospatial data formats. QGIS is geographic information system for analyzing and editing spatial information.

5 Conclusions

Remote sensing & GIS provides complete view of large areas in one image to be analyzed further and extract knowledge. With an increase in voluminous data captured by remote sensing, more and more application areas are growing for the ecosystem management such as pollution monitoring, vegetation study, land cover use. Air pollution monitoring can be done using satellite data and ground observation data. The paper give a summary of how the remote sensing and GIS together with intelligent computing and machine learning can overcome the various issues faced such as reducing the health hazardous environment, predicting the missing aerosol values, obtain the relationship between AOD(satellite) and PM2.5 (ground based AOD), validation of satellite data with ground stations, classification of the aerosol types.

References

1. How air pollution is destroying our health, World Health Organization. https://www.who.int/air-pollution/news-and-events/how-air-pollution-is-destroying-our-health
2. El Askary H, Kafatos M (2008) Dust storm and black cloud influence on aerosol optical properties over Cairo and the Greater Delta region, Egypt. Int J Remote Sens 29(24):7199–7211. https://doi.org/10.1080/01431160802144179
3. Aerosol Robotic Network, Goddard Space Flight Center. https://aeronet.gsfc.nasa.gov/
4. Global Atmosphere Watch (GAW), World Meteorological Organization. https://www.wmo.int/pages/prog/arep/gaw/monitoring.html
5. IMPROVE - Interagency Monitoring of Protected Visual Environments. http://vista.cira.colostate.edu/Improve/improve-program/
6. NASA MODIS WEB. http://modis.gsfc.nasa.gov/
7. Prasad AK, Singh RP, Singh A (2004) J Indian Soc Remote Sens 32:313. https://doi.org/10.1007/BF03030855
8. Kumar KR, Sivakumar V, Reddy RR, Gopal KR, Adesina AJ (2014) Identification and classification of different aerosol types over a subtropical rural site in Mpumalanga, South Africa: seasonal variations as retrieved from the AERONET Sunphotometer. Aerosol Air Qual Res 14:108–123
9. Zhao R, Gu X, Xue B, Zhang J, Ren W (2018) Short period PM2.5 prediction based on multivariate linear regression model. PLoS ONE 13(7):e0201011

10. Just A, De Carli M, Shtein A, Dorman M, Lyapustin A, Kloog I (2018) Correcting measurement error in satellite aerosol optical depth with machine learning for modeling PM2.5 in the Northeastern USA. Remote Sens 10:803. https://doi.org/10.3390/rs10050803
11. Lanzaco Bethania L, Olcese Luis E, Palancar Gustavo G, Toselli Beatriz M (2017) An improved aerosol optical depth map based on machine-learning and MODIS data: development and application in South America. Aerosol Air Qual Res 17:1523–1536
12. Wahab AM, Sarker ML (2014). In: IOP conference series: earth and environmental science vol 18, p 012098
13. Zhang L et al (2017). In: IOP conference series: earth and environmental science vol 68, p 012001
14. Jantarach T, Masiri I, Janjai S (2012) Comparison of MODIS aerosol optical depth retrievals with ground-based measurements in the tropics. Procedia Eng 32:392–398
15. Jose S, Niranjan K, Gharai B, Rao PVN, Nair VS (2016) Characterisation of absorbing aerosols using ground and satellite data at an urban location, Hyderabad. Aerosol Air Qual Res 16:1427–1440
16. Prasad AK, Singh RP, Singh A (2004) Variability of aerosol optical depth over Indian subcontinent using MODIS data. J Indian Soc Remote Sens 32(4)
17. Westra E (ed) Python geospatial development—second edition, 2nd revised ed, ISBN-13: 978-1782161523

Electrical and Electronics Engineering

Distribution Power Quality Improvement Using Impedance Source Inverter (ZSI)

G. Mounika Sharon, T. KrantiKiran and Ravilla Madhusudan

Abstract Power quality plays an important role while transferring power to maintain uninterrupted and continuous supply to the consumer. Voltage sags, voltage swells, flickers, etc., are the common problems which degrade the power quality. So, this paper presents one of the means to overcome this, by including FACTS devices like ZSI (Impedance source inverter) based STATCOM in the network. The device is controlled using proposed unipolar and bipolar PWM techniques. The proposed methods can be used to overcome the disadvantages of the existing devices. Simulations of the proposed circuitsare shown and it is done using MATLAB/SIMULINK software.

Keywords Impedance source inverter (ZSI) · Unipolar and bipolar inverters · Proposed control techniques and STATCOM

1 Introduction

Many applications in power systems use converters for conversion of ac to dc or dc to dc or dc to ac or ac to ac power. These converters are used in power system, where conversion of power is needed, for example, (i) in HVDC transmission, (ii) uninterrupted power supplies and (iii) in FACTS devices like STATCOM, DVR, etc.

Conventional Voltage source inverter (VSI) and Current source inverter (CSI) have already been in existence and usage for power conversion. However, there are limitations to these existing devices.

G. Mounika Sharon (✉) · T. KrantiKiran · R. Madhusudan
Department of Electrical and Electronics Engineering, Sir C R Reddy College of Engineering, Eluru, Andhra Pradesh, India
e-mail: gsharon553@gmail.com

T. KrantiKiran
e-mail: krantikiran.mtech@gmail.com

R. Madhusudan
e-mail: sudhankumar266@gmail.com

© Springer Nature Singapore Pte Ltd. 2020

T. Hitendra Sarma et al. (eds.), *Emerging Trends in Electrical, Communications, and Information Technologies*, Lecture Notes in Electrical Engineering 569,
https://doi.org/10.1007/978-981-13-8942-9_13

- VSI behaves as a buck converter alone as it cannot produce an output greater than the given input. Insertion of shoot through state in a conventional VSI is strictly forbidden as the shorting of devices in the same leg causes shorting of the input source.
- CSI behaves as a boost converter alone as it cannot produce an output lower than the given input. (This cannot tolerate an open circuit.)

So, to overcome these disadvantages, we go for the Impedance source inverter, which can work both as buck and boost converter. Here, we discuss about z source inverter (ZSI). ZSI was first proposed by Peng [1]. The buck-boost feature of ZSI can be achieved by insertion of shoot through states (shorting of one leg or two legs or all the three legs of the inverter) and controlling of their duty cycle.

2 Impedance Source Inverter (ZSI)

The Impedance source inverter (ZSI) circuit is shown Fig. 1.

In ZSI [2], the DC source of the inverter is connected to the inverter bridge using an impedance (consisting of inductors and capacitors) network.

The working of ZSI is in two modes:

(i) Non-shoot through mode, (ii) Shoot through mode

We assume that the [3] inductors L1 and L2 and capacitors C1 and C2 are having equal values, i.e., L1 = L2 = L and C1 = C2 = C. So, from this, we can say,

$$V_{L1} = V_{L2} = V_L, V_{C1} = V_{C2} = V_C \tag{1}$$

And, V_{dc}—DC source voltage, V_d—The Voltage across diode and V_{PN}—DC link voltage of inverter bridge.

During shoot through mode (ST, T_0 time interval)

$$V_d = 2V_C \tag{2}$$

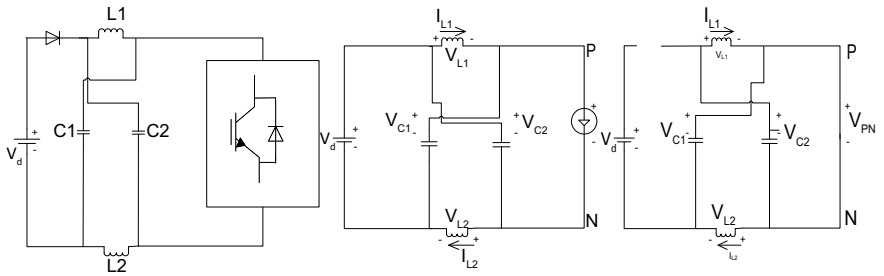

Fig. 1 ZSI, non-shoot through mode and shoot through modes respectively

$$V_d = 2V_C \tag{3}$$

$$V_{PN} = 0 \tag{4}$$

During non-shoot through mode (non ST, T_1 time interval)

$$V_L \neq V_C, V_d = V_{dc} = V_L + V_C \tag{5}$$

$$V_L = V_{dc} - V_C = V_C - V_{PN} \tag{6}$$

$$V_{PN} = V_C - V_L = 2V_C - V_{dc} \tag{7}$$

We know that, $T = T_0 + T_1$, where T is the time period of switching frequency. During steady state, average voltage value across L1 is zero over the switching period, T.

$$\overline{V_L} = V_C * T_0 + (V_{dc} - V_C) * T_1 = 0 \Rightarrow \frac{V_C}{V_{dc}} = \frac{T_1}{T_1 - T_0} \tag{8}$$

where T_1 is the non shoot through time period and T_0 is the shoot through time period.

Average DC link voltage of the inverter bridge

$$\overline{V}_{PN} = \frac{T_0 * 0 + T_1 * (2V_C - V_{dc})}{T} \Rightarrow \overline{V}_{PN} = \frac{T_1}{T_1 - T_0} V_{dc} = V_C \tag{9}$$

Peak DC link voltage during non ST,

$$\widehat{V}_{PN} = V_C - V_L = 2V_C - V_{dc} \tag{10}$$

Substitute V_C from (8) in (10),

$$\widehat{V_{PN}} = \frac{T}{T_1 - T_0} V_{dc} \Rightarrow \hat{V}_{PN} = B * V_{dc} \tag{11}$$

where B is the boosting factor

$$B = \frac{T}{T_1 - T_0} = \frac{1}{1 - \left(2\left(\frac{T_0}{T_1}\right)\right)} \Rightarrow B \geq 1 \tag{12}$$

The output peak phase voltage from the inverter can be expressed as,

$$\widehat{V}_{AC} = M \frac{\widehat{V_{PN}}}{2} = \frac{MBV_{dc}}{2}, \tag{13}$$

where M is the modulation index ($M \leq 1$)

Let $B^{|} = MB$, which is the buck-boost factor. By choosing the appropriate value for $B^{|}$, output voltage can be stepped up or down.

From (8), $V_C = \frac{T_1}{T_1 - T_0} V_{dc}$. By using (12), the above equation is simplified by writing in terms of B as,

$$V_C = \frac{B+1}{2} \tag{14}$$

2.1 Inductor Design

Inductor value can be calculated using,

$$L = \frac{V * T_0}{\Delta I} \tag{15}$$

where V can be calculated using (14) since during ST, $V_L = V_C = V$,

T_0 is the shoot through timeperiod, and $\Delta I = \widehat{I_L} - \check{I_L}$,

$\widehat{I_L}$—Maximum current through the inductor, $\widehat{I_L} = \overline{I_L} + 30\%$

$\check{I_L}$—Minimum current through the inductor, $\check{I_L} = \overline{I_L} - 30\%$

(The general rule for most of the cases which involve ZSI is that about 30% current ripple is chosen for the design.)

$\overline{I_L} = \frac{P}{\text{Vdc}}$, P is the total power, $\overline{I_L}$ is the average current through the inductor.

2.2 Capacitor Design

Capacitor voltage is calculated as,

$$C = \frac{\overline{I_L} * \text{T0}}{\Delta \text{VC}} \tag{16}$$

where T_0 and $\overline{I_L}$ are as explained before and $\Delta V_C = \text{V} * 3\%$

3 Proposed Control Methods

For applying the proposed techniques, the single-phase inverter is modified by adding an impedance network (Figs. 2 and 3).

The architecture of proposed control techniques is shown below.

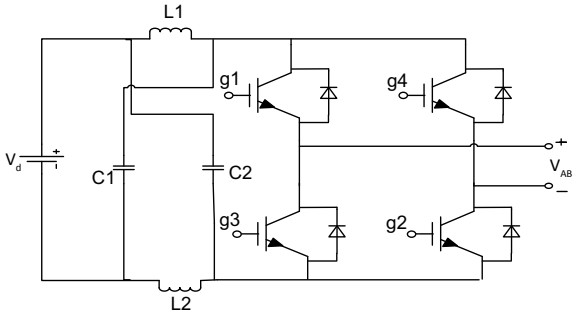

Fig. 2 ZSI based single phase inverter

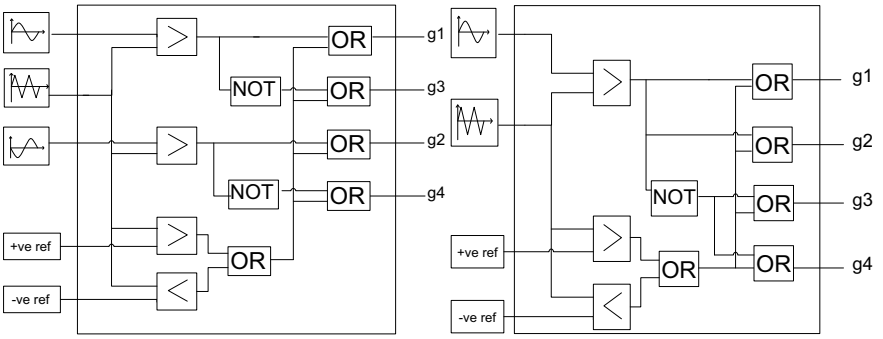

Fig. 3 Architecture of modified Unipolar and Bipolar techniques respectively

3.1 Modified Unipolar Pulse Width Modulation (PWM) Technique

In normal unipolar PWM method [4, 5], we take two sinusoidal signals with the same magnitude but 180° out of phase. Each of the signals is compared with a triangular carrier wave. Let V_m and V_{m-} be the two sinusoidal signals, which are also called as modulating waves. Each is compared with a carrier wave V_{Cr}. Here, $Vm = -V_{m-}$. By passing V_m and V_{Cr} through a comparator we get triggering signal for the upper switch (g^1) of one leg of the inverter and by inverting the above signal, we get triggering pulses for the corresponding lower switch (g^3) of the same leg. Similarly, by passing V_{m-} and V_{Cr} through a comparator, we get triggering pulses for the other leg (g^2 and g^4) of the inverter.

In any half cycle of the output, we find that the output of the inverter switches between either 0 and $+V_{DC}$ (during the positive half cycle) or 0 and $-V_{DC}$ during (negative half cycle) and hence the name unipolar technique.

In the existed method, we have only one device on each leg turned ON at any given instant of time. This implies that we cannot short any leg/legs (which is called shoot through state) of the inverter using this technique. So, we move to a modified technique.

This proposed technique is differentiated from the existing technique, by adding two additional reference lines. One reference line is taken above or equal to the upper envelope of reference wave and this is called as upper reference line/positive reference line. The other line is taken below or equal to the lower envelope of the reference waves and this is called as lower reference line/negative reference line.

Whenever the triangular wave is greater than the upper reference line or lower than the lower reference line, i.e., when either of these conditions is satisfied, then regardless of their present state, all devices are turned ON causing shoot through condition (This can be implemented using OR gates). Otherwise, it works in the normal manner.

The waveforms for the modified unipolar PWM technique are as shown in Figs. 4 and 5.

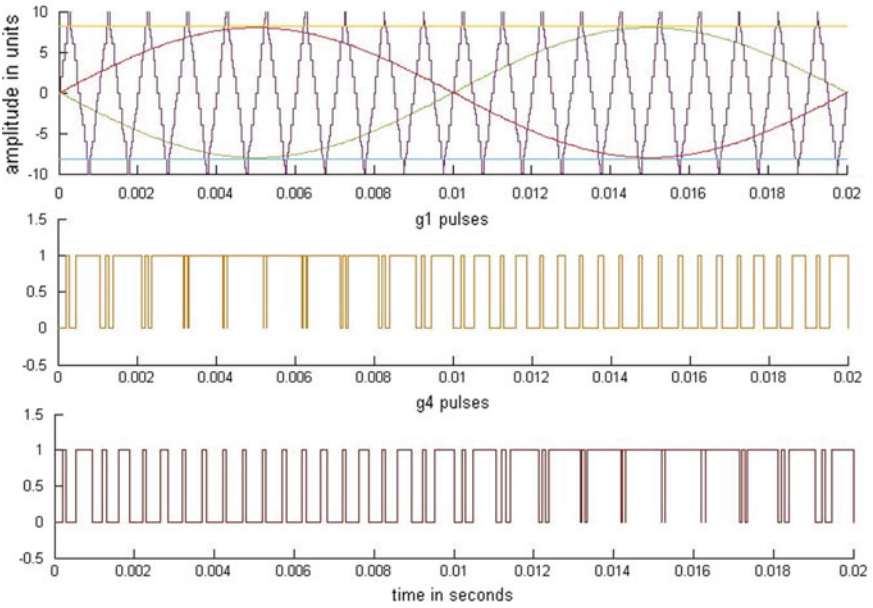

Fig. 4 Unipolar waveforms (i) carrier wave, sine wave, positive reference line and negative reference line, gate pulses (ii) g^1, (iii) g^4

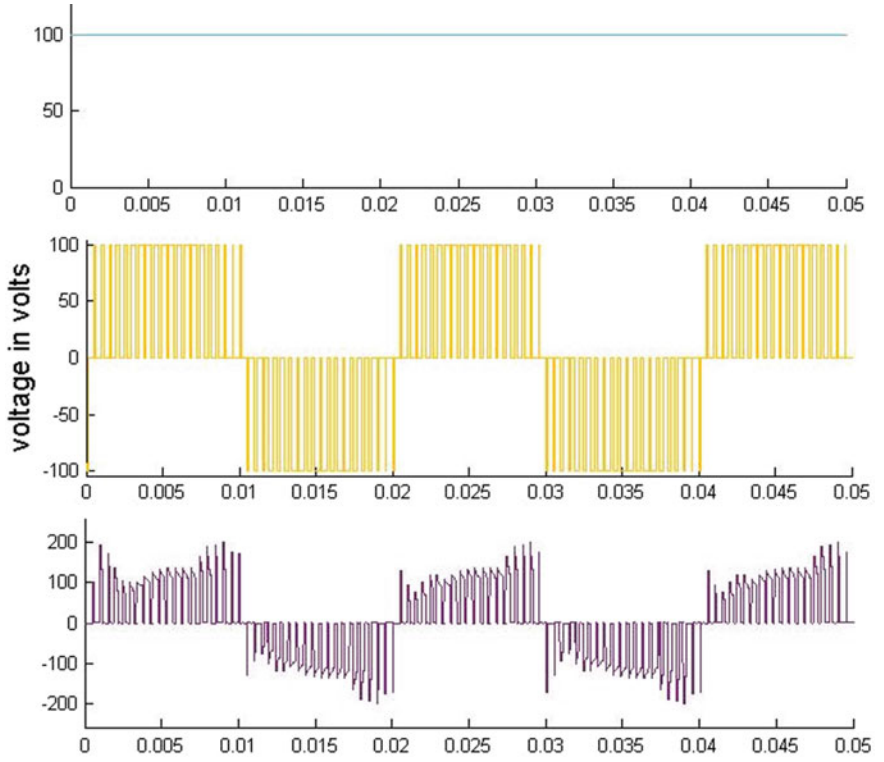

Fig. 5 (i) Input DC voltage, (ii) output of the normal inverter, (iii) output of inverter controlled by the proposed technique

3.2 Modified Bipolar Pulse Width Modulation (PWM) Technique

In this technique, we require only one sinusoidal modulating signal Vm, instead of two signals as in unipolar method. The working of the two switches, i.e., upper and lower switches, of any inverter leg, complement each other. That is, if one upper switch is switched ON then the lower one is switched OFF and vice versa.

The proposed technique is applied in the same way as it is explained in the unipolar method. We take two reference lines, one lower and one upper and the working is the same as explained before.

The waveforms for modified bipolar PWM technique is shown below in Figs. 6 and 7.

As we can see from the waveforms, the output of the inverter switches between positive V_{DC} and negative V_{DC} and hence the name bipolar technique.

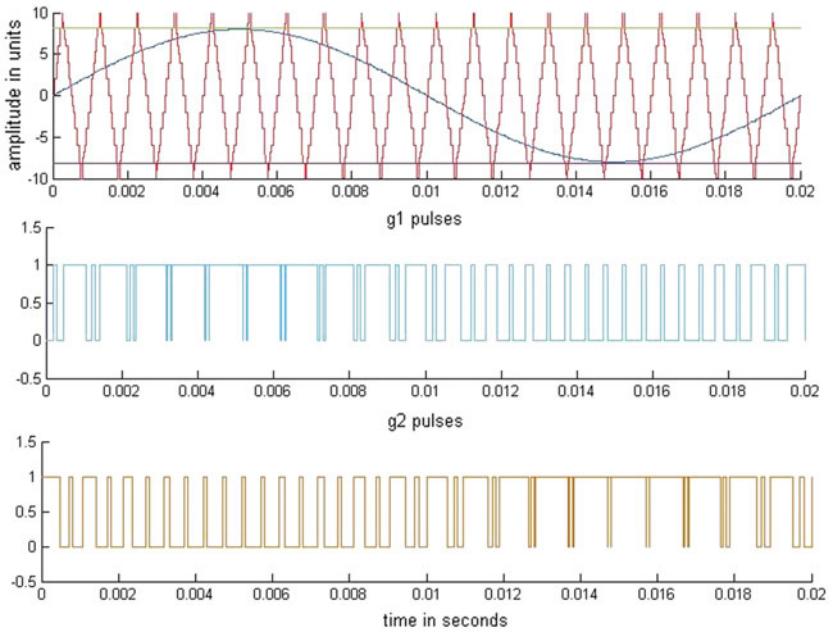

Fig. 6 Bipolar waveforms (i) carrier wave, sine wave, positive reference line and negative reference line, (ii) gate pulses g^1, (iii) gate pulses g^4

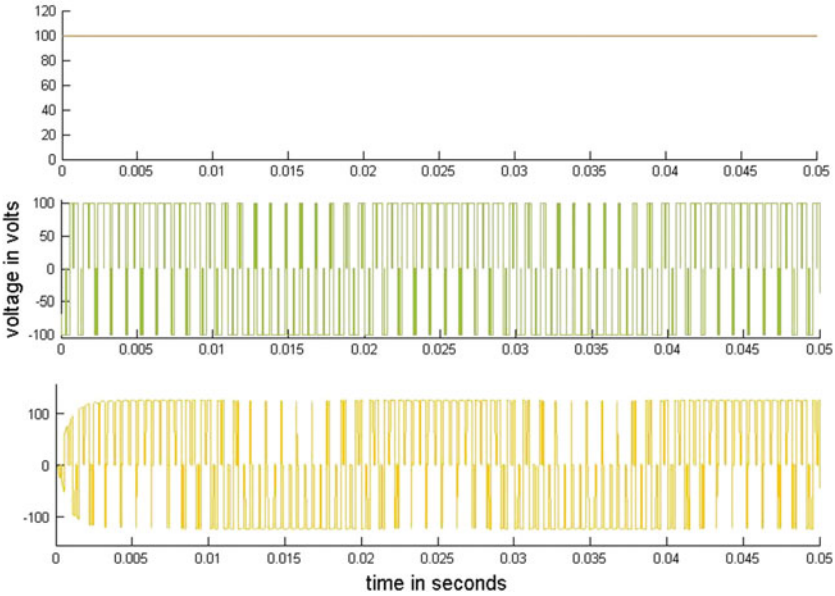

Fig. 7 (i) Input DC voltage, (ii) output of the normal inverter, (iii) output of inverter controlled by the proposed technique

4 Distribution STATCOM in Power System

A system with three phase source is connected [6] to a load via transformer of 11 kV/415 V is taken. A three-phase to ground fault is applied to this test system during 0.2–0.4 s with a fault resistance of 1.2 Ω (Fig. 8).

For the same system, Impedance source converter based STATCOM [7, 8] is connected via a coupling transformer. The device is controlled using the proposed control method to insert shoot through states (Table 1).

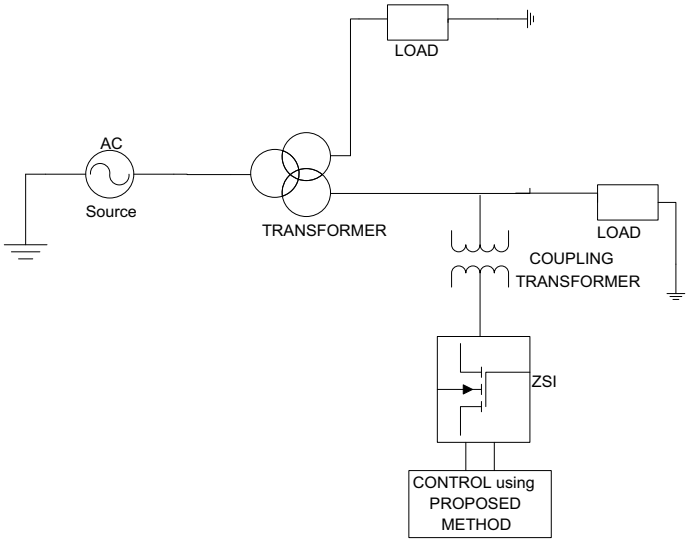

Fig. 8 Single line diagram of test system, which is a three phase network with STATCOM

Table 1 Distribution STATCOM parameter values

Parameters	Values
DC source voltage	415 V
Inductance (L)	19.055 mH
Capacitance (C)	3.88 μF
Carrier wave frequency	1000 Hz
Modulation index	0.8
Load resistance	24 Ω
Load inductance	0.01 H
Filter inductance	40 mH
Filter capacitance	87 μF

5 Results and Findings

The results are plotted with and without STATCOM included in the network using MATLAB. Both unipolar and bipolar methods gave good results for the parameters considered in this paper. However, Unipolar technique gave slightly better output, in the view of THD analysis.

5.1 Proposed Unipolar PWM Technique Applied for Distribution STATCOM

The test system is subjected to a three phase fault with a fault resistance of 1.2 Ω. The output voltage is taken at RL load. The output voltage is 410 V. Three phase fault is applied from 0.2 to 0.4 s, which creates a voltage sag as shown in Fig. 9. ZSI based STATCOM, which is controlled by the proposed unipolar method, is connected to the same network and when fault is applied during 0.2 to 0.4 s, the results are as shown in Fig. 10. The output voltage of each phase is separately shown. The voltage sag is compensated with the help of the reactive power supplied by the STATCOM.

The three phase injected voltage of STATCOM is shown in Fig. 11.

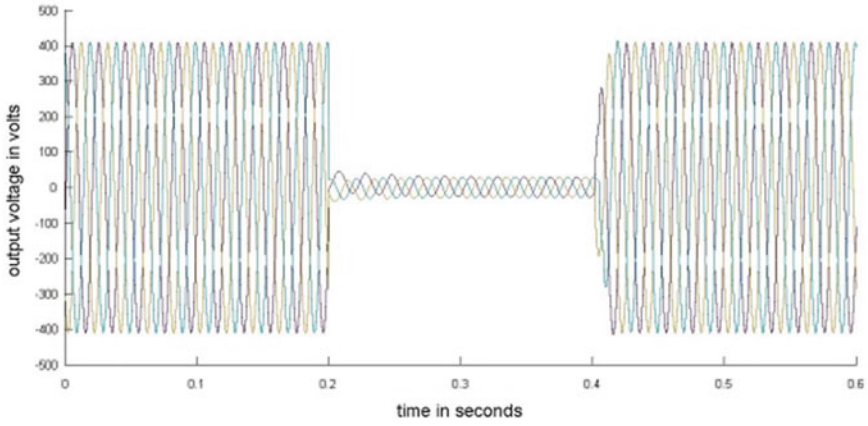

Fig. 9 Three phase output voltage during the fault condition without STATCOM

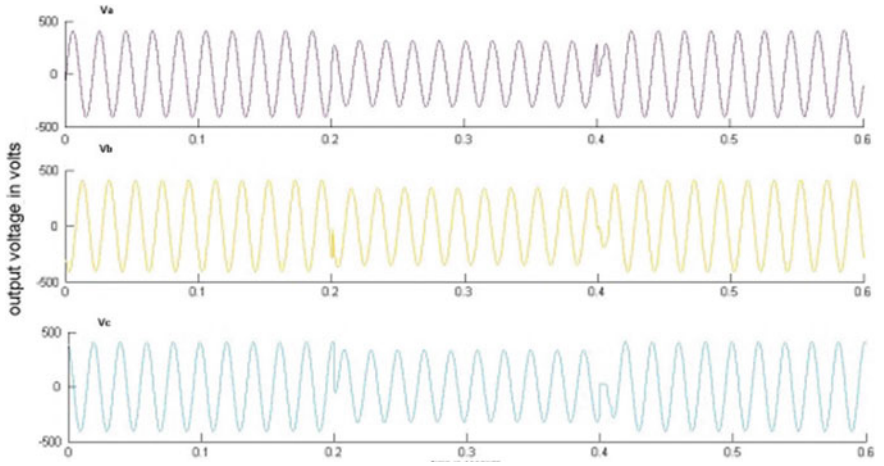

Fig. 10 Output voltage of each phase during fault with STATCOM

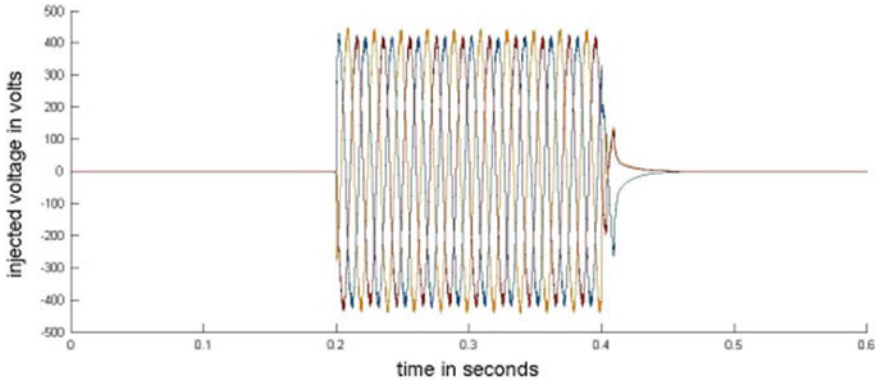

Fig. 11 Three phase injected voltage by STATCOM during the fault

5.2 Proposed Bipolar PWM Technique Applied for Distribution STATCOM

The earlier system with same conditions is used, but here, STATCOM is controlled using the proposed bipolar method. A three phase fault is applied during 0.2–0.4 s to create voltage sag and the waveform is same as shown in Fig. 9. For the same system, ZSI based STATCOM is connected and when fault is applied during 0.2–0.4 s, the compensated voltage waveform is as shown in Fig. 12. The injected voltage of STATCOM is shown in Fig. 13.

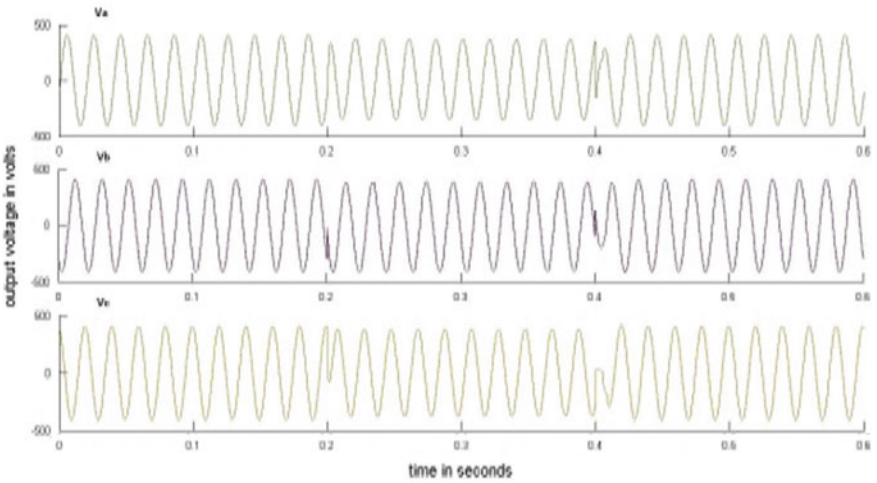

Fig. 12 Output voltage of each phase during the fault with STATCOM

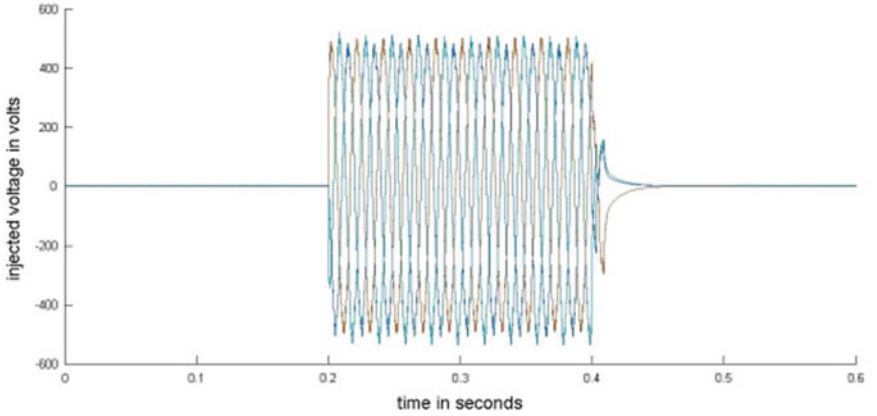

Fig. 13 Three phase injected voltage by STATCOM during the fault

6 Conclusion

A three-phase fault is simulated and the output voltage waveforms with and without STATCOM are shown in this paper. STATCOM, used in this paper consists of the converter which is an impedance source inverter (ZSI) controlled by the proposed control techniques. The unipolar PWM facilities the choice of the filter and has a better output waveform. The bipolar PWM is widely used in the full-bridge inverter to its straightforward implementation. In this paper, both methods gave good results for the system considered. An impedance network comprising of inductors and capacitors, is used to couple the main converter circuit to the load or power source. So,

ZSI is neither a VSI nor a CSI and hence it does not comprise the disadvantages of a voltage source or a current source network. ZSI provides a new single stage power conversion. The output voltage of the impedance source inverter is boosted using these proposed methods. The voltage sag in the distribution system is mitigated. The THD values, of the output obtained using modified unipolar and bipolar PWM techniques are, 6.95% and 8.26% respectively. Comparing these with standard IEEE value [9] which is 8%, we can say that unipolar technique gave good results comparatively and hence power quality is improved.

References

1. Peng FZ (2003) Z-source inverter. IEEE Trans Ind Appl 39(2):504–510
2. Suresh L, Kumar GN, Sudarsan MV (2012) Modelling and simulation of Z source inverter
3. Hanif M, Basu M, Gaughan K (2011) Understanding the operation of a Z-source inverter for photovoltaic application with a design example. IET Power Electron J 4(3):4088–4097
4. Namboodiri A, Wani HS (2014) Unipolar and Bipolar PWM inverter. Int J Innov Res Sci Technol 1(7)
5. Algaddafi A, Elnaddab K, Al Ma'mari A, Esgiar AN (2016) Comparing the performance of bipolar and unipolar switching frequency to drive DC-AC inverter. IEEE
6. Madhusudan R, Rao GR (2012) Modeling and simulation of a Dynamic Voltage Restorer (DVR) for power quality problems-voltage sags and swells In: IEEE-international conference on advances in engineering, science and management (ICAESM-2012)
7. Trivedi S, Chattopadhyay D (2013) Voltage sag mitigation in the distributed generation system with STATCOM. Int J Emerg Technol Adv Eng 3(10)
8. Borse PA, Thosar AG, Shaha SS (2014) Modeling and Simulation of STATCOM. Int J Eng Res Technol (IJERT) 3(12)
9. Langella R, Testa A, Alii E (2014) IEEE recommended practice and requirements for harmonic control in electric power systems. IEEE Std 519™

Techno Economic Analysis of Hybrid Renewable Electrification System in Different Climatic Zones

Murugaperumal Krishnamoorthy, P. Ajay D. Vimal Raj, S. Suresh and Karuppiah Natarajan

Abstract This paper deals with the investigation on renewable energy potential areas in the union of Puducherry for the development of the standalone Hybrid (PV/Wind) electrification system. Optimization cum sensitivity results and ranking process are the basic evaluation parameters for this investigation. The various climatic zones identified (Puducherry, Karaikal, Mahe and Yanam) are located in the union territory of Puducherry region, India. A typical consumer demand profile was created for the selected zones on the basis of the database relating to the local distribution agency. The renewable resource availability ranges were obtained from NASA's surface mythology database. HOMER Pro software has been used for estimation of the different feasible hybrid configurations. Region-wise winning configurations were treated into sensitivity analysis through different rates of diesel price variables. The investigations indicate Yanam Zone as a highly potential area for implementing the standalone hybrid electrification system among the other climatic zones of Puducherry union. The sensitivity analysis proves renewable energy rich area system holding the top rank, in terms of the best Techno-Economic Eco friendly electrification system. The system maintains the renewable fraction as 0.99 with a high quantity of power production and least Cost of Energy with reduced Net Present Cost (reduced into half value over normal system) and low green gas emission.

Keywords Standalone hybrid renewable electrification system (HRES) · Techno-economic analysis · Sensitivity analysis · RE potential area analysis · Ranking process

M. Krishnamoorthy (✉) · P. A. D. V. Raj
Department of EEE, Pondicherry Engineering College, Puducherry, India
e-mail: murugaee@gmail.com

S. Suresh
Department of EEE, Bharath Institute of Engineering and Technology, Hyderabad, India

K. Natarajan
Department of EEE, Vardhaman College of Engineering, Hyderabad, India

© Springer Nature Singapore Pte Ltd. 2020

T. Hitendra Sarma et al. (eds.), *Emerging Trends in Electrical, Communications, and Information Technologies*, Lecture Notes in Electrical Engineering 569,
https://doi.org/10.1007/978-981-13-8942-9_14

1 Introduction

As on March 2018, the major share (65%) of the utility energy of India is from burning of fossil fuels such as coal, oil etc. Only 19.2% of energy was obtained from Renewable energy sources. The Government of India has initiated many renewable energy promoting schemes for increasing the contribution from the renewable energy sources. These include RVEP-Remote Village Electrification Program, RGGVY-Rajiv Gandhi Gramean Vidyutikaran Yojana, JNNSM-Jawaharlal Nehru National Solar Mission etc. The primary objective of these schemes is to meet the increasing energy demand in a sustainable manner [1]. The Union Territory of Puducherry consists of four past French reimbursements namely Puducherry, Karaikal, Mahe and Yanam which are unconnected regions with continuous increasing energy demand from all sectors. These four regions of the UT of Puducherry have an average solar irradiation in the range between 5.5 Kwh/m^2/day and 6 Kwh/m^2/day, nearly 300 sunny days in a year as registered. These regions have a reasonable wind potential in the range between 3 m/s and 6 m/s. Now the Puducherry government is considering the abundant values of RE resource potentials and has started its drive towards development of a new energy strategy including demand side management cum distributed renewable energy generation. Also the government motivates the investors to invest in eco-friendly environment projects, inviting private investors into energy generation opportunity, thus transforming from electricity consumers to prosumers (producer-consumers). Basaran et al. [2] have reported about the importance of energy management and the importance of hybrid energy system. This article clearly explains the effective usage of village resources along with the conventional grid power. Khalid et al. [3] and Parida et al. [4] have explained about the design of Hybrid Renewable System that matches the supply-demand of the village. They have designed the HRS model using an objective function with user friendly constraints and optimized it to fulfil the rural power demand. Rajbongshi et al. [5] have developed a hybrid electrification system using PV/Biomass/diesel for rural environment and optimized its performance for different load demand patterns using HOMER package.

The need for resolving the electrification issues is a primary concern in most of the developed and developing countries. The focus of most of the developed countries is on the implementation of advanced technologies like the hydrogen fuel system. Khan and Iqbal [6] have examined the feasibility of some advanced technologies and found that hydrogen fuel system was suitable in Newfoundland, Canada. Barsoum and Vacent [7] and Karakoulidis et al. [8] have recommended the usage of hybrid renewable solutions for developing countries with advanced technologies such as hydrogen fuel generators, fuel cell storage system and alternative fuel system. In case of developing countries, researchers have find an optimal configuration with an economically dominated hybrid system as suitable. Givler and Lilienthal [9] have made a case study in Sri Lanka where they recognized a PV/diesel hybrid as cost effective over a stand-alone home system. Munuswamy et al. [10] have attempted a simulation of a rural health centre load fulfilment with grid connected hybrid system

and found 44 km as the breakeven grid extension distance. Hafez and Bhattacharya [11] have designed a micro-grid system for a hypothetical rural community with an electrical demand of 5000 kwh/day through solar, wind, hydro and diesel resources with the least net present cost of project.

The arrangement of this paper is as follows: Sect. 2 explains the methodology selected for this investigation. Section 3 presents a description of the hybrid model. Section 4 presents an optimum and sensitivity analysis to search for a suitable HRES implementation based on a case study. Section 5 deals with evidence evaluation for the best and the worst zones identification through results and discussion. Concluding remarks are presented in Sect. 6.

2 Methodology

The Physical behaviour of a sample micro grid system was evaluated through a hybrid optimization model for Electrical Renewable structure using HOMER. While designing the system model, the challenges in the basic micro grid were taken into consideration. These were: (i) A suitable hybrid combination among the identified renewable energy generators (solar, wind with Battery and DG backups) (ii) optimum size of hybrid configuration to meet developed consumer demand on a continuous basis irrespective of the uncertain nature of RE source availability. (iii) Sustainable energy generation through the best Techno-Economic Eco friendly electrification system. The consumer demand of four regions of Puducherry was collected from the local power distribution agency and a profile of seasonal variations in typical load profile was created [12]. The climatic nature and availability of renewable resources in the four regions were analysed by the parameters used in the measurement of geographical characteristics. Solar irradiation and wind speed data were collected from NASA's surface methodology data base. The collected data set were synchronized with HOMER simulator through 8760 h based time set series. This step was used to dissect the system into hourly based annual performance of RE component's simulation. Figure 1 explains the different steps involved in finding the Renewable Energy potential for implementation of the hybrid system. Figure 2 shows the graphical representation of solar radiation availability, average wind speed and clearness index of the four regions considered for case study in UT of Puducherry.

3 Hybrid Model Description

3.1 Consumer Demand Assessment

A typical daily load profile for the coastal area of Puducherry region is estimated using the local distribution agency data. The minimum power consumption (1.1 Kw)

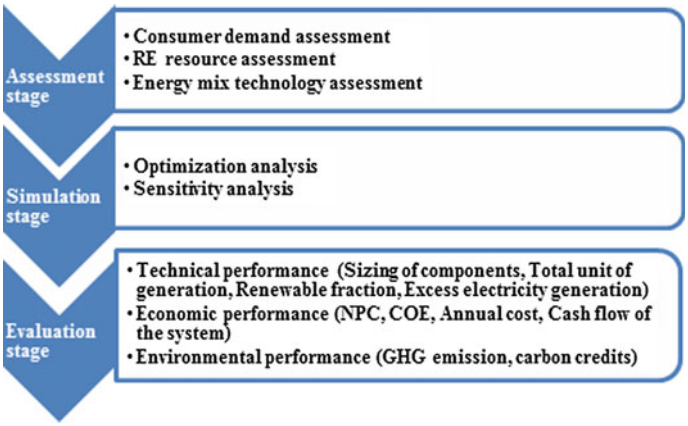

Fig. 1 Methodology to find potential area for hybrid system implementation

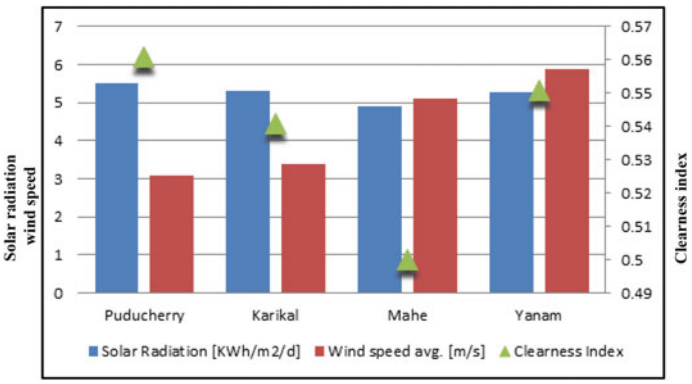

Fig. 2 Solar and wind potential in UT of Puducherry Regions

is seen between 3 AM and 6 AM and the maximum power consumption is (8.8 Kw) from 11 AM to 12 Noon. Annual seasonal variations are also observed in the load profile as summer (from December to May) and winter (June to November). The Average day demand is 51 Kwh/day. Peak demand of day is 9.4 Kw and load factor is 0.217.

3.2 RE Resource Assessment

Unfortunately, the four regions of UT of Puducherry come under different climatic zone conditions (as per Koppen classification). Three of the regions have a coastline (Table 1). All the four regions have solar irradiation in abundance. Maximum irradi-

Table 1 Climatic Zone of UT–Puducherry Regions (as per Koppen classification)

Sl. No	Zone description	District centre	Latitude (N)	Longitude (E)	Coast length (Kms)
1	Arid interior	Puducherry	11.52	79.1	23.25
2	Hot interior	Karaikal	10.15	79.5	17.4
3	Tropical wet and dry	Yanam	16.43	82.1	10 (river)
4	Tropical wet	Mahe	11.42	75.32	2.47

ation registered is 6.585 Kwh/m^2/day in the region of Puducherry during March and minimum irradiation registered is 3.907 Kwh/m^2/day in the region of Mahe during July. Due to the coastal area environment, the maximum wind potential observed is 7.59 m/s in the region of Mahe and the minimum wind potential observed is 2.27 m/s in the region of Puducherry (Fig. 2). These statistics relating to the location have the influence from the upcoming climatic change. This issue can be overcome by finding a suitable energy alternative mix irrespective of the uncertain behaviour of resources [13]. Generally, in India, a combination of solar and wind is the best alternative for energy production. The main objective of this study is promoting the promising regions among UT of Puducherry, which is highly suitable for implementing the standalone renewable Hybrid electrification system.

3.3 Hybrid System Components and Specifications

The proposed hybrid system consists of solar PV array (PV), Wind turbine (WP), Diesel generator (DG), Inverter, Controller, Battery bank and other accessory components with distribution cables (Table 2). The system operating constraints have been identified as: (i) At every instant of system operation, solar DC power and Wind AC power generated, find the top priority to meet the developed consumer demand. The excess power remaining is used for charging the battery bank and supply to other damped loads. (ii) If the renewable power is unable to meet the developed demand,

Table 2 Cost and specification table

Components	Rating (KW)	Model and specifications	Price in Rs.
Battery	1	Generic 12 V, 24 Ah, η_{RT}-86%, LT-4 years	16,200
Solar panel	1	Sun power XFP 1KW, η-21%, LT-20 years	60,000
Regulator	1	Generic R1000, LT-20 years	3,500
Generator	5.5	Generic DG 5.5, fuel curve slope-0.222 L/hr/kw	71,000
Converter	75	Generic C75, η_I /η_R-90/85%, THD $_{FP}$-4%	35,000
Wind turbine	6	Prover 6 vertical axis, cut in speed-2.5 m/s	2,50,000

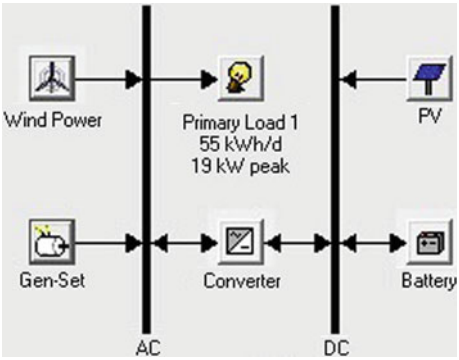

Fig. 3 Block diagram of proposed HRES

the battery stored energy tries to fulfil the demand at that instant. (iii) The DG set used for peak load management purpose provides the power supply contribution when both renewable energy and battery energy are insufficient to meet the developed demand [14]. Figure 3 depicts the various components present in the proposed Hybrid Renewable Electrification System.

Table 1 gives a detailed view of the climate condition and coast length of the different regions considered in the UT of Puducherry.

The solar PV array and Battery bank are connected to the DC Bus of the system. The wind turbine generator and DG set are connected with the AC Bus of the system. The Inverter and the controller are connected in between the AC and DC Bus of the system. The AC bus takes care of the entire connected load supply (assuming all loads are AC Nature of power utility).

3.4 Power Dispatch Strategy

The usage of DG and enabling of battery bank is governed by two dispatch strategies namely the load following strategy and cycle charging strategy. This helps in deciding the system performance in terms of optimization, sizing of components and economic cost of hybrid power generation.

Load following strategy: DG set is ON only to meet the developed primary load demand, when the renewable source is inadequate for fulfilling the net load. DG power is never used for Battery charging and any other deferrable load supply in this mode [15, 16]. Cycle charging strategy: DG power is used for charging the battery till it reaches its maximum SOC level and then it is used for fulfilling the net load supply. Table 2 portrays the rating and specifications of different components used in this hybrid model and their price in rupees.

4 Homer Analysis

4.1 Optimization Analysis

The entire data relating to the assessment was fed into the Hybrid optimum model for evaluation of the optimum performance of the proposed system. Based on the consumer demand, the meteorological data and operating constraints, thousands of feasible combinations were created to achieve a regional wise optimal system (Fig. 4). The different regions of Puducherry were satisfied with different fitness of sizing and production range of RE Components as the basis of the resource potential. Region wise optimum configuration of Hybrid system was evaluated based on measuring parameters such as Net Present Cost (NPC) of the system, Cost of Energy (COE), Capacity shortage and Renewable fraction.

NPC is defined as the present value of all components over their lifetime minus the present value of revenue achieved over its lifetime. CoE is defined as the average cost of producing one unit of electricity from all the components [12]. The capacity shortage fraction expresses the relationship between load shortage quantities to the total production quantity. This parameter is advisable in lesser values. Renewable fraction, provides the idea about renewable energy penetration over the total production quantity of electricity.

The modelling equation for NPC and cost recovery factors are given as Eqs. 1 and 2

$$M_{npc} = \frac{M_{ann,Tot}}{CRF\left(i, R_{proj}\right)} \tag{1}$$

M_{npc} is the net present cost in Rs. M_{ann}, Tot is annual total cost in Rs/yr. CRF is the Capital recovery factor with I % interest rate and Rth year as project life time in year.

PV (kW)	Wind	DG (kW)	Battery	Conv. (kW)	Disp. Strgy	Initial Capital	Operating Cost ($/yr)	Total NPC	COE ($/kWh)	Ren. Frac.	Diesel (L)	DG (hrs)	Batt. Lf. (yr)
20	1	10	150	75	LF	$ 1,607,500	96,825	$ 2,845,250	11.944	0.99	131	71	4.4
20	1	10	150	75	CC	$ 1,607,500	98,526	$ 2,866,999	12.035	0.99	160	59	4.4
20	1	20	150	75	LF	$ 1,615,000	100,753	$ 2,902,964	12.186	1.00	116	37	4.2
20	1	20	150	75	CC	$ 1,615,000	100,816	$ 2,903,762	12.189	0.99	114	20	4.2
20	1	50	150	75	LF	$ 1,637,500	104,426	$ 2,972,421	12.478	0.99	163	21	4.2
20	1	50	150	75	CC	$ 1,637,500	105,107	$ 2,981,114	12.514	0.99	170	19	4.1
1	1	10	100	1	LF	$ 553,500	353,749	$ 5,075,605	21.306	0.70	4,862	2,863	5.0
5	1	10	100	1	LF	$ 733,500	342,159	$ 5,107,435	21.440	0.76	4,657	2,793	5.0
	1	10	100	1	LF	$ 508,500	367,388	$ 5,204,947	21.849	0.67	5,086	2,947	5.0
10	1	10	100	1	LF	$ 958,500	342,261	$ 5,333,746	22.390	0.80	4,637	2,785	5.0
1	1	10	150	1	LF	$ 678,500	373,399	$ 5,451,797	22.886	0.70	4,819	2,835	5.0
20	1	10	50	1	LF	$ 1,283,500	329,580	$ 5,496,634	23.074	0.85	4,648	2,794	4.0
5	1	10	150	1	LF	$ 858,500	364,069	$ 5,512,524	23.141	0.76	4,649	2,788	5.0
1	1	10	150	1	CC	$ 678,500	378,667	$ 5,519,138	23.169	0.69	4,910	2,791	5.0
5	1	10	150	1	CC	$ 858,500	367,591	$ 5,557,548	23.330	0.75	4,708	2,785	5.0
	1	10	150	1	LF	$ 633,500	387,145	$ 5,582,516	23.435	0.68	5,045	2,920	5.0
	1	10	150	1	CC	$ 633,500	390,699	$ 5,627,950	23.625	0.67	5,111	2,837	5.0

Fig. 4 Feasible combinations of Hybrid system for Yanam regions

$$CRF(i,n) = \frac{i(1+i)^n}{(1+i)^n - 1} \tag{2}$$

Hear I is the real interest rate, n is the number of years. The mathematical model equation for COE in Eq. 3

$$COE = \frac{M_{ann,tot} - M_{boiler}E_{thermal}}{E_{prim\,AC} + E_{prime\,DC} + E_{def} + E_{grid\ sales}} \tag{3}$$

$M_{ann,tot}$—Annualized total cost in Rs/yr, M_{boiler} is the marginal cost of the boiler in Rs/KWh, $E_{thermal}$—thermal load served in KWh/yr, $E_{prim\ AC}$—AC primary load served in KWh/yr, $E_{prime\ DC}$—DC primary load served in KWh/yr, E_{def}—DC primary load served in KWh/yr, $E_{grid\ sales}$—total grid sales in KWh/yr. Equation 4 is for the mathematical model for hybrid renewable energy system.

$$F_{ren} = \frac{P_{ren} + T_{ren}}{P_{Tot} + T_{Tot}} \tag{4}$$

P_{ren}, T_{ren} are the renewable electrical production and thermal production in KWh respectively. P_{Tot}, T_{Tot} are the total power and thermal production in KWh from the entire system [17–20].

4.2 Sensitivity Analysis

System sensitivity analysis was performed considering the multiple values for a particular simulating parameter [21]. Optimization process was carried out for each individual value and the influence level on the overall performance values of the system was checked. Here, the diesel price (two slaps of subsidized price and price without subsidy) of the DG set was taken as a sensitivity variable. The main reason behind the selection of this parameter was (i) It is one of the peak load management parameter that plays a vital role in system control dispatch strategy). (ii) Also it directly affects the system economics and GHG emissions (more usage of fuel results in high CoE and high GHG emissions).

5 Results and Discussion

From HOMER optimization analysis, the finest configuration of HRE system is created. The system requires acceptance from all the regions. This system consists of solar, wind, battery bank and diesel generators. The abundant range of solar and wind resources forces the solar and wind based generator into the winning configuration. The observed values of the load factor and the range of minimum and

maximum demand of load profiles were included in the backup components into HRE solutions such as battery, Diesel generator especially DG set needed as peak load management of the system. Here the battery bank was used for maintaining power dispatch constraints within the system.

Then system performance stability was evaluated through the sensitivity analysis. Diesel price value was selected as sensitivity variable, considering the behaviour of the fuel price as a dynamic rate of change and also the utility of fuel which claims over the subsidy benefits as per RE development harmony. Therefore the diesel prices at three levels have been considered in this analysis. These are: (i) cost of DG fuel with 50% of subsidy (Rs. 30), (ii) cost of DG fuel with 25% of subsidy (Rs. 45), (iii) cost of DG fuel without subsidy (Rs. 60). These values were passed with the region wise fitted optimum configuration. The influence on the results were used for further searching investigation on the potential rich area identification. The results of system analysis are shown in the Tables 3 and 4.

The different zone sensitivity cases are denoted as follow, P1, P2, P3 belonging to the Puducherry region with three sensitivity variables. K1, K2, K3 belong to the Karaikal region. M1, M2, M3 are for the Mahe region. Y1, Y2, Y3 are for the Yanam region. The system payback periods have been calculated from [20] appraisal over selected case of merit with base case of the system.

Table 3 HRE Plant structure for different climatic zone with diesel prize sensitivity

City	Puducherry			Karaikal		
	50% subsidy	75% subsidy	Without Subsidy	50% subsidy	75% subsidy	Without subsidy
Solar panel	10	10	10	10	10	20
Wind turbine	1	1	1	1	1	1
Gen-set	20	20	20	20	10	20
Battery	400	400	400	400	400	400
City	Yanam			Mahe		
Solar panel	5	5	10	20	20	10
Wind turbine	1	1	1	1	1	1
Gen-Set	20	20	20	20	20	20
Battery	200	200	200	200	200	400

Table 4 HRE Plant performance for different climatic zones with diesel prize sensitivity

Region cases	Total NPC	COE	DG power	Total units produced	Renewable fraction	Excess electricity	CO_2 emission	BE grid ext. dist	Battery throughput
	Rs	Rs/KWh	KWh/Yr	KWh/Yr		KWh/Yr	Kg/Yr	Km	KWh/Yr
P1	42,07,461	15.233	3,009	29,943	0.9	5,240	3,877	158.93	6,447
P2	43,69,503	15.821	2,607	29,541	0.91	4,490	3,330	168.04	7,234
P3	44,46,285	16.098	145	42,904	1	18,056	184	172.36	6,421
K1	42,50,847	15.39	3,011	29,421	0.9	4,694	3,878	161.37	6,540
K2	44,00,610	15.932	2,568	28,978	0.91	3,898	3,275	169.79	7,347
K3	45,09,444	16.326	205	41,754	1	16,923	253	175.91	6,526
M1	33,07,798	11.975	591	65,275	0.99	41,686	760	108.34	3,710
M2	32,93,131	11.922	357	65,041	0.99	41,359	442	107.52	3,934
M3	39,06,749	14.144	623	50,879	0.99	26,579	773	142.02	5,632
Y1	24,58,993	8.902	2,438	63,238	0.96	40,105	2,692	60.61	3,242
Y2	23,68,201	8.574	1,138	61,937	0.98	38,427	1,385	55.51	3,939
Y3	25,33,310	9.171	254	68,992	1	45,570	315	64.79	3,684
Base case	111,20,530	40.266	27,819	27,819	0	0	24,563	547.67	12,227

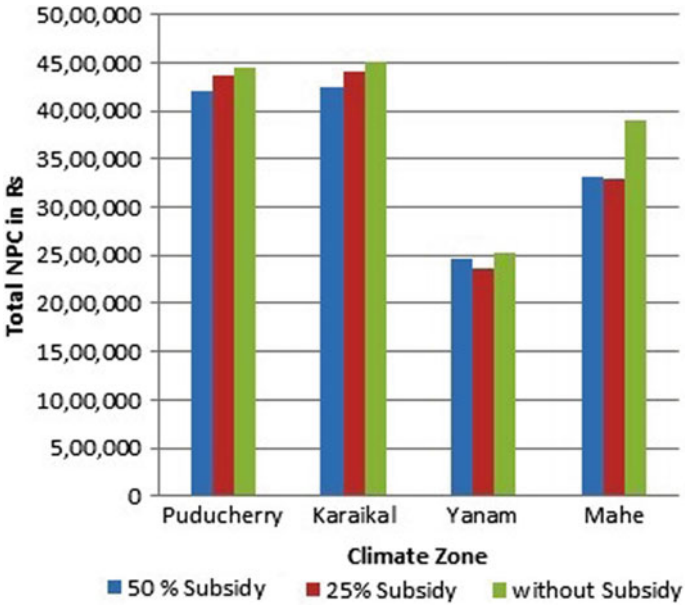

Fig. 5 NPC summary for different case of HRE solutions

5.1 Evidence on NPC

Figure 5 shows the NPC values of HRES solutions for all the regions of UT of Puducherry with three cases relating to sensitivity. From the Investor point of view, a lower value of NPC system was the optimal solution. The Karaikal region based system carries high NPC value due to hot nature of climate in the interior. Generally these climates have more temperature differences and a smaller clearness index. It affects the renewable based energy generation and support to the usage of DG in maintaining energy balance. The Yanam (Tropical wet and dry climate) region HRES solutions takes a smaller NPC value of Rs. 25,33,310, due to the impact of a larger renewable energy resource on that area. Out of the total energy needed, nearly 96% units were generated from renewable source base and the remaining 4% of energy only depends on DG set operation.

5.2 Evidence on COE

Based on the sensitivity variables, the COE for the four regions have the range between from Rs. 8 and Rs. 16. A minimized COE of Rs 8.902 was observed in Yanam base and a maximum COE of Rs. 16.32 was observed for Karaikal region based system. When the system produced more units for use, it has a smaller value of

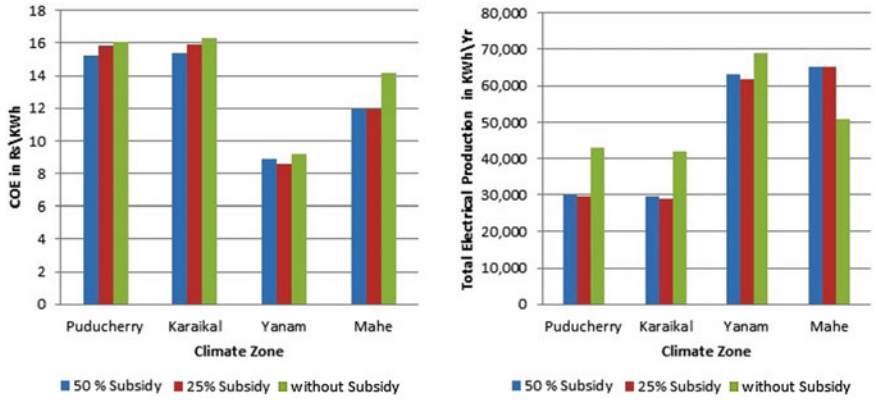

Fig. 6 COE and Total electrical production summary

COE. Accordingly the total production of Yanam region was seen as high as 68,992 Kwh/yr over that of the other regions. On the other hand, a smaller production value was only observed in Karaikal region due to its renewable potential lags as shown in Fig. 6.

5.3 Renewable Fraction Impacts

High renewable fraction is a good solution for the implementation of the HRE system. All the four regions of Puducherry have reasonable renewable fraction (between 0.9 and 1). But the highest renewable fraction with lowest COE is really the required solution. It is achieved in Yanam based HRES system.

5.4 Diesel Consumption and Carbon Emission

Greenhouse gas emissions are directly related to the fuel consumption of the DG set in every situation for meeting the developed demand. The system requires balancing the power generation through its components. When the region has a good potential for generating renewable power there is economy as seen in the reduction in the fuel required. Mahe (Tropical wet zone) has a high wind potential between June and August, enabling the maximum power contribution by wind turbine. Considering all the three cases of sensitivity, the system belonging to this region consumes fuel in the range from 300 litres to 600 litres only (Fig. 7). Hence, from the carbon credit point of view, Mahe region has the best HRES solution.

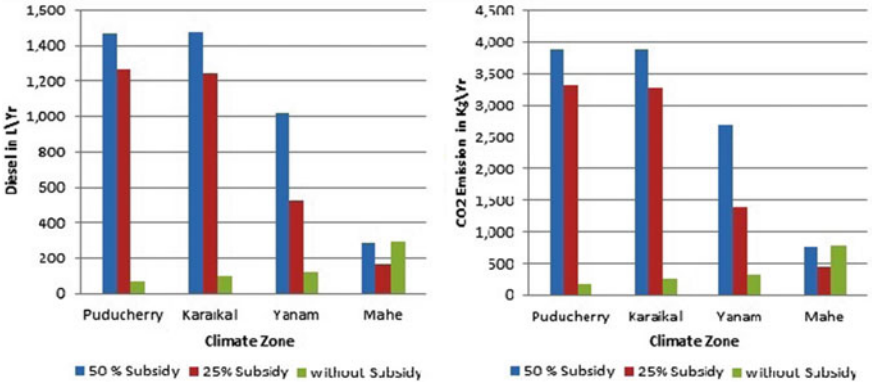

Fig. 7 Diesel consumption and CO_2 emission for different cases of HRES

5.5 Ranking Process

In this evaluation process, cases relating to the four regions of the UT of Puducherry were assigned 1–4 ranks position based on the technical, economic and environmental performance. The region with the maximum number of 1's was considered as a highly potential area for standalone hybrid renewable electrification system implementation among the different climatic zones of UT of Puducherry. Based upon this ranking process (Table 5) Yanam region was found to be a highly potential area and Karaikal region the hardest area for HRES implementation.

6 Conclusion

This paper has proposed the investigation reports on the techno economic feasibility HRE system in different climatic zones among the UT of Puducherry. Out of four different climatic zones are in Puducherry regions, India, the Topical Wet and Dry climate zone (Yanam) is the finest climatic zone to install a PV/Wind/DG/Battery based hybrid electrification system based on the NPC, COE, Renewable fraction, Diesel consumption and Carbon emission in the year. The optimum HRES solution for this Yanam region with different subsidy slabs of diesel price as sensitivity includes 5 Kw of solar panel array, 6 Kw of vertical axis wind turbine, 20 Kw capacity of diesel generator, 20 numbers of strings of Battery bank and 75 Kw of converter setup. The sensitivity treatment of the optimal configuration results on this region produced Rs. 2 lakhs variation in NPC, 7000 units of annual power production and reduced carbon emission from 1385 tonnes/yr into 315 tonnes/yr. This significance change in the CO_2 emission helps to energise the society with Eco-friendly hybrid electrification systems.

Table 5 Ranking process for potential area identification

Regions	Wind speed(m/s)	Solar irradiation (Kwh/m^2/day)	Total NPC	COE	Total units production	Renewable fraction	Excess electricity	CO_2 emission	Break even distance for grid extension
Puducherry	3.067	5.495	3	3	3	1	2	1	3
Karikal	3.401	5.324	4	4	4	1	1	2	4
Mahe	5.119	4.902	2	2	2	2	3	4	2
Yanam	5.878	5.291	1	1	1	1	4	3	1

References

1. 'Ministry of Power, Government of India'. http://powermin.nic.in Accessed April 2018
2. Basaran K, Cetin NS, Borekci S (2017) Energy management for on-grid and off-grid wind/PV and battery hybrid systems. IET Renew Power Gener 11(5):642–649. https://doi.org/10.1049/iet-rpg.2016.0545
3. Khalid M, Al Muhaini M, Aguilera RP Savkin AV (2018) Method for planning a wind–solar–battery hybrid power plant with optimal generation-demand matching. IET Renew Power Gener. https://doi.org/10.1049/iet-rpg.2018.5216
4. Parida A, Choudhury S, Chatterjee D (2017) Microgrid based hybrid energy co-operative for grid-isolated remote rural village power supply for east coast zone of India. IEEE Trans Sustain Energy 9(3):1375–1383. https://doi.org/10.1109/tste.2017.2782007
5. Rajbongshi R, Borgohain D, Mahapatra S (2017) Optimization of PV-biomass-diesel and grid base hybrid energy systems for rural electrification by using HOMER. Energy 126:461–474. https://doi.org/10.1016/j.energy.2017.03.056
6. Khan M, Iqbal M (2005) Pre-feasibility study of stand-alone hybrid energy systems for applications in Newfoundland. Renew Energy 30(6):835–854
7. Barsoum NN, Vacent P (2007) Balancing cost, operation and performance in integrated hydrogen hybrid energy system. In: Proceedings of the first Asia international conference on modelling and simulation (AMS'07). IEEE
8. Karakoulidis K, Mavridis K, Bandekas DV, Adoniadis P, Potolias C, Vordos N (2011) Techno-economic analysis of a stand-alone hybrid photovoltaic/diesel/battery/ fuel cell power system. Renew Energy 36:2238–2244
9. Givler T, Lilienthal P (2005) Using HOMER- software, NREL's micro power optimization model, to explore the role of gen-sets in small solar power systems case study: Sri Lanka. Technical Report NREL/TP-710-36774. http://www.osti.gov/bridge
10. Munuswamy S, Nakamura K, Katta A (2011) Comparing the cost of electricity sourced from a fuel cell-based renewable energy system and the national grid to electrify a rural health centre in India: a case study. Renew Energy 36:2978–2983
11. Hafez O, Bhattacharya K (2012) Optimal planning and design of a renewable energy based supply system for microgrids. Renew Energy 45:7–15
12. 'HOMER' NREL, available at http://www.nrel.gov/international/tools/HOMER/ homer.html, accessed April 2017
13. Islam MS A techno-economic feasibility analysis of hybrid renewable energy supply options for a grid-connected large office building in south eastern part of France. Sustain Cities Soc https://doi.org/10.1016/j.scs.2018.01.0225253.31
14. Dekker J, Chowdhury S, Chowdhury SP (2010) Economic viability of PV/diesel hybrid power systems in different climatic zones in South Africa. IEEE PES General Meeting. https://doi.org/10.1109/pes.2010.5588197
15. Wang R, Li G, Ming M, Wu G, Wang L (2017) An efficient multi-objective model and algorithm for sizing a stand-alone hybrid renewable energy system. Energy. https://doi.org/10.1016/j.energy.2017.11.085
16. Tezera Tuba, Yamanb Ramazan, Yamanc Gülşen (2017) Evaluation of approaches used for optimization of stand-alone hybrid renewable energy systems. Renew Sustain Energy Rev 73:840–853
17. Hartvigsson E, Stadler M, Cardoso G (2018) Rural electrification and capacity expansion with an integrated modeling approach: Renew Energy 115:509–520
18. Singh S, Kaushik SC (2016) Optimal sizing of grid integrated hybrid PV-biomass energy system using artificial bee colony algorithm. IET Renew Power Gener 10(5):642–650

19. Bhattacharyya SC (2012) Energy access programmes and sustainable development: a critical review and analysis. Energy Sustain Dev 16(3):260–271
20. Deshmukh MK Modeling of hybrid renewable energy systems. Renew Sustain Energy Rev 12:235–249
21. Nandi S, Ghosh HR (2010) Prospect of wind-PV-battery hybrid system as an alternative to grid extension in Bangladesh. Energy 35(7):3040–3057

Mathematical Modelling of STATCOM for Reactive Power Compensation in Power System and Approach to the Renewable Energy

Sandeep Ushkewar

Abstract To maintain the voltage stability in the power system it is necessary to balance the flow of real and reactive power which can be achieved by the compensation techniques in the power system. Reactive power plays an important role to maintain the voltage stability in the power system because the flow of reactive power is depends upon the voltage magnitude, in case of voltage magnitude dips the unbalance of reactive power flow will occurs which results in overall instability of the power system So, there is need to design an model which can compensate the reactive power in the system to maintain the system voltage. STATCOM is one of the FACTs device used to maintain the flow of reactive power and hence, voltage stability in power system (Hingorani and Gyugyi, Understanding FACTS: concepts and technology of flexible AC transmission systems, [1]). This paper describes the mathematical modeling with inherent controlling capability of STATCOM helps to compensate the reactive power flow in the system which maintain the voltage stability. This will approach to the DFIG based wind farms using STATCOM also had been applied for offshore wind power plants to satisfy the grid codes (Tanaka et al., Reactive power compensation capability of a STATCOM based on two types of modular multilevel cascade converters for offshore wind application, 2017, [2], Ushkewar and Bodke, Compensation of reactive power in DFIG based wind farm using STATCOM, 2018, [3], Pereira et al., STATCOM to improve the voltage stability of an electric power system with high penetration of wind generation, 2016, [4]).

Keywords STATCOM · Reactive power compensation · Voltage stability · DFIG

S. Ushkewar (✉)
SVKM'S Institute of Technology, Dhule, Maharashtra 424001, India
e-mail: Sandeep.Ushkewar@svkm.ac.in

© Springer Nature Singapore Pte Ltd. 2020

T. Hitendra Sarma et al. (eds.), *Emerging Trends in Electrical, Communications, and Information Technologies*, Lecture Notes in Electrical Engineering 569,
https://doi.org/10.1007/978-981-13-8942-9_15

1 Introduction

The Static Synchronous Compensator (STATCOM) is shunt connected reactive power compensation equipment that can generate and/or absorb the reactive power as per the condition in power system [5]. The STATCOM can be worked as static device which will gives the same operating characteristics as of rotating synchronous compensator without the mechanical inertia, for this purpose the it requires the solid state power switching devices like SCR, GTO or IGBT, they gives the rapid controllability of the voltages in terms of magnitude and phase angle both. A STATCOM can be used to enhancing power system oscillation stability for voltage regulation in a power system, to the increase in transmittable power and improvements of steady-state transmission characteristics and of the overall stability in the system [6]. Under light load conditions, to minimize the Ferranti effect in the power system, the STATCOM can be used. To prevent the massive cascade blackout or voltage instability condition it is necessary to use dynamic compensation in system [7]. The Table 1 shows nomenclature of mathematical modelling used for the derivation.

$$I = \frac{E - V}{X} \tag{1}$$

The reactive power flow through the system is,

Table 1 Nomenclature

Nomenclature of mathematical modelling
1. I_{stat} = STATCOM current
2. V_{stat} = STATCOM Voltage
3. X_s = STATCOM reactance
4. δ_{stat} = Angle of STATCOM
5. S_{stat} = Complex power of STATCOM
6. P_r = Real power of line
7. Q_r = Reactive power of line
8. P_{stat} = Real power of STATCOM
9. Q_{stat} = Reactive power of STATCOM
10. V_{ref} = Reference Voltage
11. V_m = Bus Voltage Magnitude
12. V_r = STATCOM Target Voltage
13. T_r = Control Time Constant
14. K_r = Gain of control of STATCOM
Where V = Bus voltage X = Total reactance E = Voltage of the voltage source converter So, I is current flowing through it

$$Q = \frac{1 - \frac{E}{V}}{X} \tag{2}$$

By controlling the excitation of the machine, the reactive power can be controlled so the amplitude E of its internal voltage which can be compared to the amplitude V of the system voltage and below giving two cases can be considered [1].

Figure 1 Shows the origin of the basic principal of the STATCOM .

Case I—Over excitation

As we increase the amplitude E of its internal voltage above the amplitude V of the system voltage that results in a leading current causes machine to be acts as a capacitor.

Case II—Under excitation

As decrease in the amplitude E of its internal voltage below the amplitude V of the system voltage which produces a lagging current as a result machine acts as an inductor.

Under operating condition, to supply the system mechanical losses as well as electrical losses a small amount of real power flows from the ac system to the machine.

Now considering the STATCOM representation with converter shown in Fig. 2 consists of inverter as a converter [1].

In steady state operation V_{stat}, is generated by VSC (Voltage Source Converter) through a DC capacitor is in phase with the system voltage V_k.

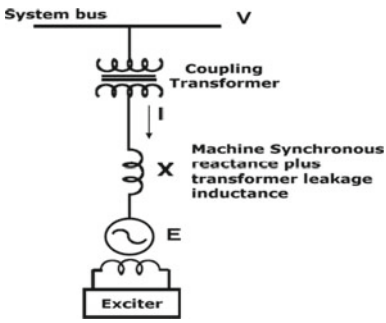

Fig. 1 Basic STATCOM [1]

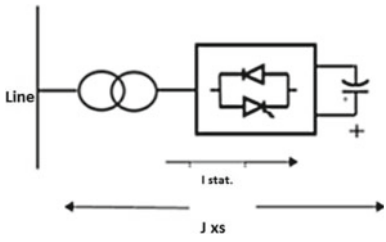

Fig. 2 STATCOM representation with converter [1]

As the reactive power is flowing, we have the value Xs = reactance of transformer, line and converter.

Now by Kirchhoff's Law,

$$I_{stat} = \frac{V_k - V_{stat}}{jX_s} \tag{3}$$

$$S_{stat} = V_{stat} * I_{stat} \tag{4}$$

For V_{stat}, we are considering control parameters.

As shown in Fig. 3 control block of STATCOM controls the given set value. Initially by setting the minimum and maximum value of voltage we can control the magnitude voltage of the system. Following equation shows the transfer function of the control block of STATCOM, from which we can measure the reference value which we have to set at the starting.

$$\frac{V_m}{V_{ref}} = \frac{K_r}{(1 + sT_r)} \tag{5}$$

By putting the values of individual in above Eq. 5 we have,

$$\frac{V_m}{V_{ref}} = \frac{\frac{K_r}{T_r}}{\frac{1}{T_r} + s} \tag{6}$$

Now get the value of V_{ref},

$$V_{ref} = \frac{\mathrm{T_r}}{\mathrm{K_r}} * \frac{1}{\frac{-1}{\mathrm{e}^{\mathrm{Tr}}}\mathrm{t}} V_m \tag{7}$$

There is need of finding the voltage across STATCOM i.e. V_{stat},

$$V_{stat} = V_k \angle\delta + I_{stat} * jX_s \tag{8}$$

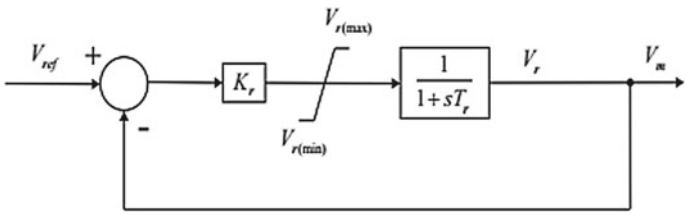

Fig. 3 Control block of STATCOM

Bus connected STATCOM is PV bus. This may change to PQ which the event of unit being violated.

As STATCOM is voltage source converter we can write it as,

$$E_{statcom} = V_{stat} * (\text{Cos}\delta_{\text{stat}} + \text{jSin}\delta_{\text{stat}}) \tag{9}$$

As we are connecting in shunt, considering as shunt compensation,

$$S_{stat} = V_{stat}[(V_{stat} - V_k)Y_{stat}] \tag{10}$$

Putting value and solving the Eq. 10 we have,

$$S_{stat} = V_{stat} * \left[\frac{((Vk\angle\delta) - V_{stat})}{jXs}\right] \tag{11}$$

$$S_{stat} = V_{stat} * \left[j\left[\frac{(Cos\angle\delta st + jSin\angle\delta st)(ek - jfk) - V_{stat}}{Xs}\right]\right] \tag{12}$$

By solving Eq. 12 we get,

Now separating the real and reactive part in the equation,

$$S_{stat} = P_{stat} + jQ_{stat} \tag{13}$$

From above equations we get the real and reactive power of STATCOM flowing through or into the system,

$$P_{stat} = \frac{Vstat(fkCos\delta_{stat} - ekSin\delta_{stat})}{Xs} \tag{14}$$

$$Q_{stat} = \frac{Vstat(ek\cos\delta_{stat} + fkSin\delta_{stat})}{Xs} \tag{15}$$

This P_{stat} and Q_{stat} represent as real and reactive power flow through a STATCOM. Now considering the transmission line model as shown in Fig. 4.

From above model of transmission line current flowing through line is

$$I_a = \frac{Vs - Vr}{Zs} \tag{16}$$

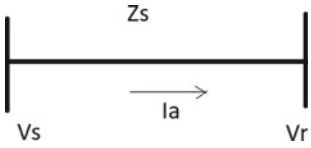

Fig. 4 Transmission line model

$$I_a = \frac{Vs\angle\delta - Vr\angle 0}{Zs} \tag{17}$$

From the transmission parameter we have,

$$I_a = \frac{Vs}{Zs}\angle(\delta - \beta) - \frac{Vr}{Zs}\angle -\beta \tag{18}$$

$$S_{out} = Vr \times I_a* \tag{19}$$

By solving equation we get the complex power flow in the transmission system.

$$S_{out} = \frac{|Vr||Vs|}{Zs}\angle(\beta - \delta) - \frac{|Vr|^2}{Zs}\angle(\beta - \alpha) \tag{20}$$

Here we are considering the A, B, C, D parameter of transmission line, generalize equation of sending end voltage and sending end current i.e. V_{sph} and I_{sph} respectively.

$$V_{sph} = AV_{rph} + BI_{rph} \tag{21}$$

$$I_{sph} = CV_{rph} + DI_{rph} \tag{22}$$

We insert these parameters in above equation,
A = $|A|\angle\alpha \leq 1$, $|A| \leq 1$ and α = 0–10°
B = $|B|\angle\beta$, β = 60–90°
C = $|C|\angle\gamma$, $\gamma = 90°$
D = $|D|\angle\Delta$, Δ = 0–10°
So, complex power is

$$S_r = \frac{|Vr||Vs|}{|B|}\angle(\beta - \delta) - \frac{|A|}{|B|}|Vr|^2\angle(\beta - \alpha) \tag{23}$$

Whereas,

$$S_r = P_r + jQ_r \tag{24}$$

From the above equation we have P_r & Q_r,

$$P_r = \frac{V_r V_s}{B}\angle Cos(\beta - \delta) - \frac{A}{B}V_r^2\angle Cos(\beta - \alpha) \tag{25}$$

$$Q_r = \frac{V_r V_s}{B}\angle Sin(\beta - \delta) - \frac{A}{B}V_r^2\angle Sin(\beta - \alpha) \tag{26}$$

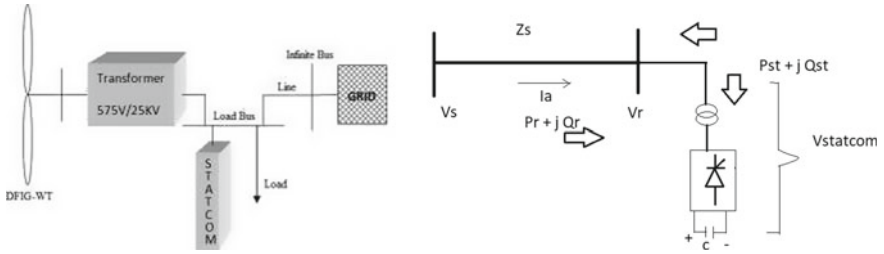

Fig. 5 Power flow model of STATCOM [3] and test system using DFIG [3]

The Fig. 5 shows the power flow model of STATCOM, which is connected to the one of the end of the line or receiving station to maintain the reactive power balance in the system [8, 9]. When system voltage is high it acts as inductor and it will absorb reactive power. When system voltage is low it acts as a capacitor and it will generate or inject the reactive power into the system [1].

2 Conclusion

This paper investigates the inherent capabilities of the STATCOM in terms of mathematical modeling which can be used to improve the dynamic performance of the power system in terms of voltage characteristics like sag and swell [10] and hence can be approach to the renewable energy in DFIG based wind farms also had been applied for offshore wind power plants to satisfy the grid codes under both normal operation and grid fault conditions.

References

1. Hingorani NG, Gyugyi L Understanding FACTS: concepts and technology of flexible AC transmission systems. Wiley–IEEE press, December. ISBN: 0-7803-3464-7
2. Tanaka T, Wang H, Ma K, Blaabjerg F (2017) Reactive power compensation capability of a STATCOM based on two types of modular multilevel cascade converters for offshore wind application. In: 2017 IEEE 3rd international future energy electronics conference and ECCE Asia (IFEEC 2017 - ECCE Asia), Kaohsiung, 2017, pp 326–331
3. Ushkewar S, Bodke M (2018) Compensation of reactive power in DFIG based wind farm using STATCOM. In: 2018 fourth international conference on advances in electrical, electronics, information, communication and bio-informatics (AEEICB), Chennai, 2018, pp 1–5
4. Pereira RMM, Pereira AJC, Ferreira CMM, Barbosa FPM (2016) STATCOM to improve the voltage stability of an electric power system with high penetration of wind generation. In: 2016 51st international universities power engineering conference (UPEC), Coimbra, 2016, pp 1–5
5. Tien DV, Hawliczek P, Gono R (2017) Analysis and modeling of STATCOM for regulate the voltage in power systems. 978-1-5090-6406-9/17/31.00 c 2017 European Union
6. Wang HF (1999) Modelling STATCOM into power systems. PowerTech Budapest 99. Abstract records. (Cat. No.99EX376), Budapest, Hungary, 1999

7. Ushkewar S, Chaube S, Komawar N, Tirpude N, Ansari MS (2017) Controlled islanding scheme for power system protection: guidelines and approach: Case study: Bhopal. In: 2017 Third (AEEICB) Chennai, 2017, pp 117121. https://doi.org/10.1109/aeeicb.2017.7972394
8. Guo WM, Wei Q, Liu GJ, Yang M, Zang XK (2013) Transmission switching to relieve voltage violation in low load period. In: 2013 IEEE PES ISGT Europe
9. Slootweg JG, de Haan SWH, Polinder H, Kling WL (2003) General. model for representing variable speed wind turbines in power system dynamics simulations. IEEE Trans Power Syst 18(1)
10. Madhusudan R, Rao GR (2012) Modeling and simulation of a distribution STATCOM (D-STATCOM) for power quality problems-voltage sag and swell based on Sinusoidal Pulse Width Modulation (SPWM). In: IEEE-international conference on advances in engineering, science and management (ICAESM-2012), Nagapattinam, Tamil Nadu, 2012, pp 436–441

Constant Current Analysis of Shell Type Transformer at Different Temperatures of Core by Using Quickfield Software

S. Krishnarjuna Rao, D. Lenine and P. Sujatha

Abstract This paper presents a FEM analysis on impact of temperature variation on electrical parameters in a single phase shell type transformer. The designed transformer model is supplied by a constant current source. The open circuit voltage and core losses have been measured at two different temperatures of 300 K and 600 K respectively. From the analysis it is observed that the secondary voltage losses are increased with respect to temperature at a constant frequency of 50 Hz. The FEM studies are carried out by using QuickField software with more than 2.8 K nodes to improve the accuracy of measurements.

Keywords Finite element analysis · Core temperature · Transformer · Core losses

1 Introduction

Transformer is a most important part of the electrical transmission system as well as distribution system. The essential parts of the transformer are core and windings. The core serves as path for magnetic flux. The time varying flux produced from an excited coil will flow through it, from the past decades ferromagnetic materials of high permeability are used as core material. The performance of the transformer will also depend on the properties of the core.

One of the parameter that changes the properties of the core material is temperature. Takahashi et al. [1] measured the magnetic properties of Fe and Ni materials and observed that the permeability is increasing with temperature just below the Curie point. Chiba et al. [2] measured the temperature dependence of losses in ferrites noticed that the losses are decreasing. While studying the properties of ferromag-

S. Krishnarjuna Rao (✉)
Research Scholar, Department of EE, JNTUA, Ananthapuramu, AP, India
e-mail: s.krishnarjuna@gmail.com

D. Lenine
Department of EEE, RGMECT, Nandyal, AP, India

P. Sujatha
Department of EE, JNTUCEA, Ananthapuramu, AP, India

© Springer Nature Singapore Pte Ltd. 2020

T. Hitendra Sarma et al. (eds.), *Emerging Trends in Electrical, Communications, and Information Technologies*, Lecture Notes in Electrical Engineering 569,
https://doi.org/10.1007/978-981-13-8942-9_16

netic induction heater [3] by FEM the value of induced voltage is increasing due to change in permeability. On extension of this work is done to evaluate the percentage increase of voltage by temperature [4, 5], gives 25% increment. The losses for different temperatures in different electrical machines like synchronous and induction machines are calculated [6]. Winding loss separation in Electromagnetic devices from thermal analysis derived by Wrobel and Simpson [7]. The eddy current loss and equivalent circuit of transformer considering all types of losses including harmonic components are calculated [8–10]. The characteristics of steel laminations and soft magnetic materials [11–13] are and their dependency on temperature is measured.

In this paper a constant current source is fed to the model to calculate the amount of voltage induced in the secondary winding for variation in the core temperature. The shell transformer model consider in this model is of 1:1 turns ratio and also the transition temperature from the core to windings is zero. That is the primary and secondary voltages are same.

2 Temperature Dependence of Core Parameters

2.1 Core Loss

As the temperature of the core increases the energy required for transition of charges is very low which will reduce the hysteresis loop area as shown in Fig. 1. This decrease in loop will partially affect the maximum flux density of the core. This phenomenon is observed only in low density.

The Bertotti expression for core loss for a maximum flux density of B_m Tesla and frequency of f Hz is the sum of hysteresis, eddy current and excess loss. The expression for core loss is given by Eq. (1).

$$P_{Core} = K_h f B_m^2 + K_c f^2 B_m^2 + K_e (f B_m)^{3/2} \tag{1}$$

where K_h, K_c and K_e are coefficients of the respective losses.

2.2 Core Loss

The permeability of core will reaches maximum just before the Curie temperature by Hopkinson effect in ferromagnetic materials. That increase in permeability is due to sudden decrement in the magnetic anisotropy K.

$$\mu = 1 + \chi \tag{2}$$

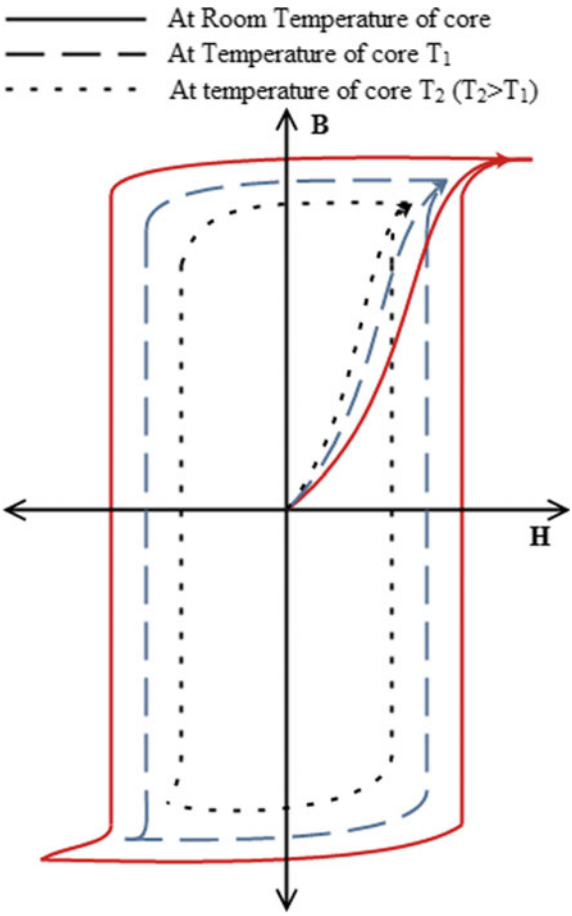

Fig. 1 Hysteresis loop at various temperatures

$$\chi \alpha \frac{M}{\sqrt{K}} \tag{3}$$

After the Curie temperature the core material will enters into paramagnetic state and in this state the loss is more.

3 Design of 2D Transformer Model

The 2D transformer model is designed for AC Magnetic analysis in Quickfield software. Quickfield is a power full and simple tool for field analysis. The 3D model of shell type transformer and it's equivalent 2D cut section view is shown in Fig. 2.

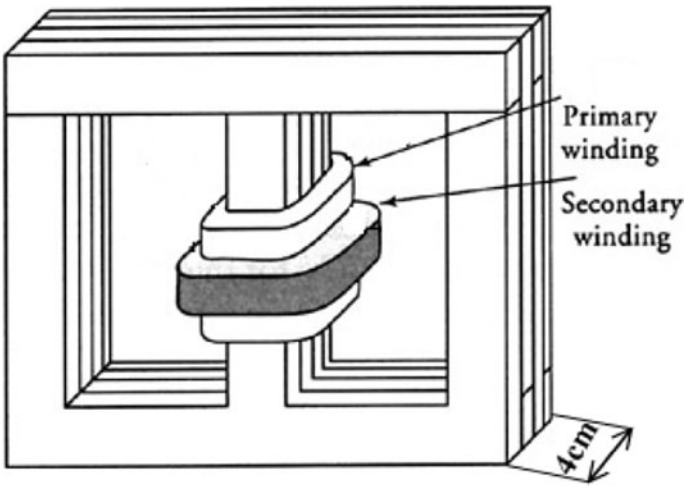

(a) 3D-Model

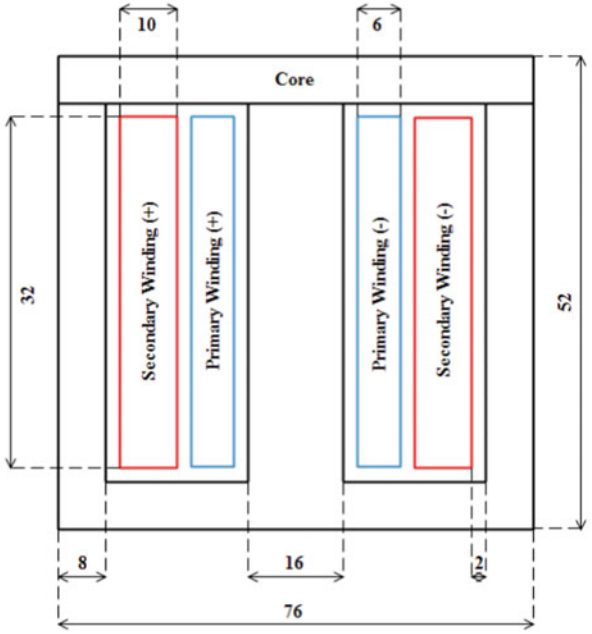

(b) 2d-Model in Cut View

Fig. 2 3D & 2D models of shell transformer

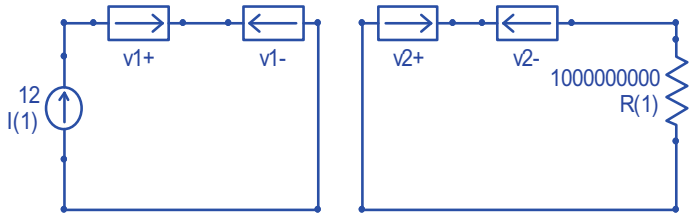

Fig. 3 Electrical connections of windings

The shell type transformer contains the windings in the shell. The central limb of the core is wound by the primary and secondary coils as shown in Fig. 2a. Each winding and the core is separated by insulation as shown in Fig. 2b.

The designed model has a core thickness of 4 cm, height of 52 cm and width of 76 cm. To form shell type model E and I shaped core stampings are joined together with two windows each having a window area of 22 cm × 36 cm. The width of the outer core limbs is 8 cm and the width of the middle limb is 16 cm. The total area of the core including E and I stampings is 560 cm^2. The primary winding is wound around the central limb with an insulation of 2 cm width. The primary winding is designed to have of an area occupation of 32 cm × 10 cm in each of the windows. The winding portion in the left side and right side of the windows are labeled as v1+ and v1−. The secondary winding placed on the former winding and core with insulation gap of 2 cm. Similar to primary winding the two parts of secondary winding around the core in 2D view are labeled as v2+ and v2−.

The electrical connections of the windings are shown in Fig. 3. The windings are connected in series on both the primary and secondary sides. The direction of v1+ and v1− are altered to indicate the polarity of induced EMF depending on dot connection.

The primary winding is connected to a current source of 12 A peak value. The secondary coil is connected to a resistance of 1000 MΩ. Since connection of higher value of resistance the current flowing through the secondary winding is very small and can be considered as an open circuit connection.

The conductors of primary and secondary are of copper with area of 20 cm^2, conductivity of 56 × 10^6 S/m and permeability is equal to one. The boundaries of the transformer are designed to have low leakage flux that is magnetic potential at the boundaries is zero.

The complete designed model including mesh is shown in Fig. 4 with winding labels.

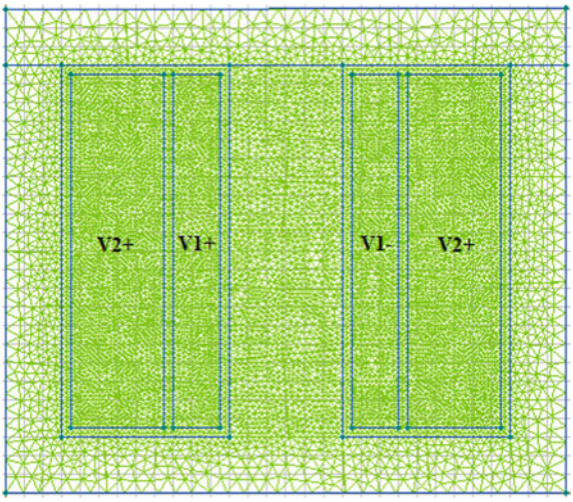

Fig. 4 Meshed diagram of 2D transformer model

4 Results and Discussion

The designed model is tested at two temperatures of core. Depending on the core temperature the solution is divided into two cases. In both the cases to measure the impact of the temperature the liner portion of the B-H curve is opted for the analysis. For the total core loss estimation a closed contour of length 256 cm is considered for total volume of 0.016 m^3.

4.1 Case-I

In this case the core temperature is set to 300 K. The primary coil is supplied by 12 A current source with a voltage of 1.5058 at angle of 89.678°. The current in the coil is the cause to produce a peak magnetic flux of 3.75 wb in the core. The magnetic flux in the core at 0° is high as shown in Fig. 5a because the supplied current has a phase angle of 0°. Always the phase angle between the current and flux is 90°. As the time approaches to 900 the flux in the core is reduced to zero value as shown in Fig. 5b. The maximum current density is 5200 A/m^2.

4.2 Case-II

The temperature of the core is set to 600 K. The primary coil is supplied by 12 A of current. To drive this current into the winding the voltage of the source is raised to 1.7214 V with a phase angle of 89.632°. The magnetic flux the core is 3.8 wb.

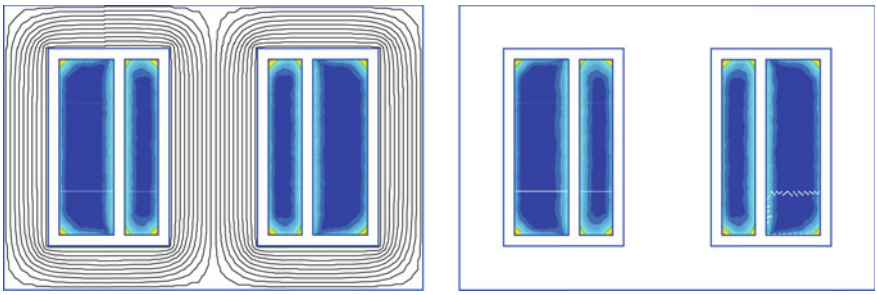

(a) Current Density at 0^0 (b) Current Density at 90^0

Fig. 5 Magnetic flux and current density at different phase angles

In this case also the distribution of flux is same as previous as shown in Fig. 5 but the current density of the transformer is 5270 A/m^2. The core loss distribution in the transformer is shown in the Fig. 6a, in this the loss at in the inner corner of the core is greater than the outer corners. The voltage distribution in the windings is shown in Fig. 6b, the positive group of conductors will have higher than the negative group as indicated by different colors.

The variation of magnetic flux density in the central limb and side limb at two different temperatures are shown in Fig. 7. For a constant current the flux density is increasing. The central limb has low flux density at center of the core than the sides. As the temperature of the core is increasing for low density the permeability of the core is high as shown in Fig. 7a. In the side limb the flux at outer edge is lower than the inner edges as shown in Fig. 7b. The power loss in the side limb at lower temperature is low as the temperature is increasing the power loss will increases.

The B-H curve values considered for the analysis is shown in Fig. 8. The slope of the curve at low flux density is greater than compared to normal temperature. As

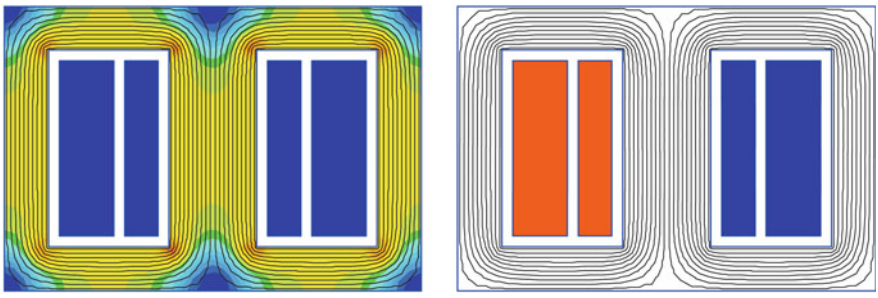

(a) Power Loss (b) Voltage

Fig. 6 Power loss and voltage distribution in the transformer

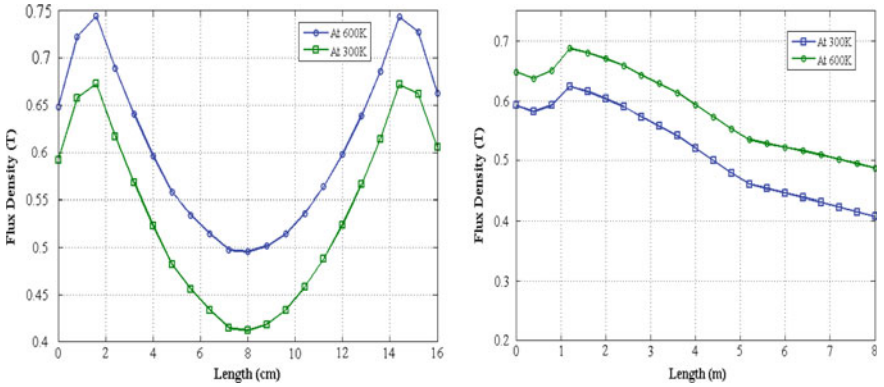

(a) Flux density in the central limb (b) Flux density in the side limb

Fig. 7 Flux density at various positions of core

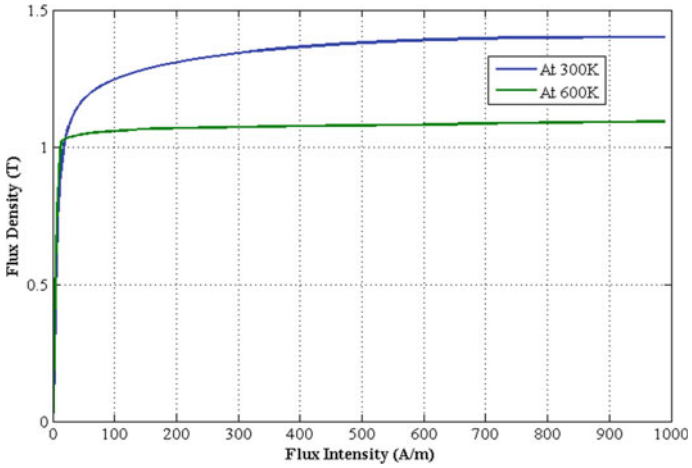

Fig. 8 B-H curve of the core at different temperatures

the temperature of the core increasing the maximum flux density will falls below the normal temperature. The variation of different parameters of core and the windings under different temperatures for a constant current excitation is presented in the Table 1. The power loss increased due to increase in voltage to maintain same current.

Table 1 Variation of parameters at room temperature

Temperature of the core (K)	300	600
Current density (A/m^2)	5200	5270
Potential A (Wb/m)	0.0424	0.0484
Flux density (T)	0.744	0.813
Strength H (A/m)	40.6	41.5
Power loss Q (W/m^3)	13,600	16,300
Energy density (J/m^3)	4.65	5
Core loss (W)	59.254	77.432
Magnetic flux (Wb)	3.75	3.8767
Flux linkage per one turn	6.7006×10^{-7}	8.6242×10^{-7}
Voltage of source (V)	1.5058	1.7214
Secondary voltage (V)	1.5058	1.7214

5 Conclusion

A FEM analysis on single phase shell type transformer with a constant current source at different temperatures has presented to measure the electrical quantities such as secondary voltage and core losses. For a constant current source with increase in core temperature causes an increment in both secondary voltage and core losses. In addition, the current density in the core and maximum flux are also in the same manner. The increased temperature of the core affects the area of B-H curve which will cause an increment in the flux and fluxdensity of the core.

Acknowledgements We thank Quickfield Software Company for providing free license for this work. We also thank RGM college of Engineering and Technology for supporting research work in the laboratory.

References

1. Takahashi N, Morishita M, Miyagi D, Nakano M (2010) Examination of magnetic properties of magnetic materials at high temperature using a ring specimen. IEEE Trans Magn 46(2):548–551
2. Chiba T, Yamada S, Otsuki E (1998) Temperature dependence of eddy current loss and residual loss in Mn–Zn Ferrites. J Magn Soc Jpn 22(S1):301–304
3. Kagimoto H, Miyagi D, Takahashi N, Uchida N, Kawanaka K (2010) Effect of temperature dependence of magnetic properties on heating characteristics of induction heater. IEEE Trans Magn 46(8):3018–3021
4. Subrahmanyam R (2009) Temperature coefficients of permeability and induced EMF in ferromagnetic material. J Pure Appl Phys 21(2):273–280
5. Mandava S, Ramachandrula S, Yarramareddy A (2014) Effect of thermal treatment of a ferro magnetic core on induced EMF. Procedia Mater Sci (Elsevier) 6

6. Schützhold J, Hofmann W (2013) Analysis of the temperature dependence of losses in electrical machines. IEEE Power Eng J
7. Wrobel R, Simpson N (2016) Winding loss separation in thermal analysis of electromagnetic devices. IEEE Ind Appl J
8. Gyselinck J, lde L, Melkebeek J (1999) Calculation of eddy currents and associated losses in electrical steel laminations. IEEE Trans Magn 35(3)
9. Lu HY, Zhu JG, Hui SYR, Ramsden VS (1998) A generalized dynamic transformer circuit model including ai1 types of core losses. IEEE J Electr Mach
10. Schützhold J, Hofmann W, Blümel R (2011) Measurement and analysis of the temperature dependent losses of the synchronous motor in the drive trains of a horizontal high speed packaging machine. ETGFachtagung: Fachbericht 130, in German language, Würzburg
11. Cheng Z, Takahashi N, Forghani B, Gilbert G, Zhang J, Liu L, Fan Y, Zhang X, Du Y, Wang J, Jiao C (2009) Analysis and measurements of iron loss and flux inside silicon steel laminations. IEEE Trans Magn 45(3)
12. Moses AJ (2004) Characterisation of the loss behavior in electrical steels and other soft magnetic materials. In: Metallurgy and magnetism: workshop proceedings, Freiberg
13. Rao SK, Lenine D, Sujatha P (2017) Enhancement of induced EMF through heat treatment of ferromagnetic core. In: 2017 IEEE international conference on power, control, signals and instrumentation engineering (ICPCSI), IEEE, pp 875–879

Effect of Load Model and Load Level on DG Placement by Crow Search Algorithm

Mareddy Padma Lalitha and Oruganti Hemakesavulu

Abstract Distributed generation is the promising solution for most of the problems faced by Indian radial distribution system like high losses, low end voltages and peak demand. Determining the optimal location and optimal size is one of significant issues in the placement of distributed generation in the distribution system. This paper presents two methods, an Analytical method and CSA (Crow Search Algorithm) for the implementation of distributed generators (DG) on the radial feeders of the distribution systems. The analytical method is so simple and requires load flow solution only twice for determination of site and capacity of DG simultaneously. These methods determine the locations of DG to achieve minimum losses in the system. The main aim of this paper is to know the effect of load modeling and time varying loads on Distributed Generators placement. Distribution system loads are highly voltage sensitive and they are varying continuously. The methods are tested on IEEE standard 69-Bus system and the consequences are discussed and presented. The proposed methods have been implemented using "MATLAB" program and are capable of performing on a radial distribution system of any number of buses and laterals.

Keywords DG Placement · Crow Search Algorithm · Load level · Time varying loads · Soft computing techniques

1 Introduction

Small-scale power generation that is usually embedded to or connected in the distribution system is defined as Dispersed or Distributed generation (DG) or Embedded generation (EG). The usage of any modular technology which is sited in the entire utilities service area is the predominant issue of DG to lower the cost of service [1, 2]. DG can act as an expensive alternate to the general source of electrical power

M. Padma Lalitha (✉) · O. Hemakesavulu
Department of Electrical & Electronics, Annamacharya Institute of Technology & Sciences, Rajampet, Andhra Pradesh, India
e-mail: padmalalitha_mareddy@yahoo.co.in

© Springer Nature Singapore Pte Ltd. 2020

T. Hitendra Sarma et al. (eds.), *Emerging Trends in Electrical, Communications, and Information Technologies*, Lecture Notes in Electrical Engineering 569,
https://doi.org/10.1007/978-981-13-8942-9_17

for residential, commercial and industrial applications. The intention of these DG's is to deal with need for growing electricity demand in some specific areas and turn certain activities self sufficient in terms of power production which leads to achieve energy savings. Due to changes in the infrastructure for electric utility fashioned the opportunities for several technological innovations which includes the application of distributed generation to achieve various benefits. To achieve the benefits, many factors have to be considered such as usage of the most excellent technology, the figure and the competence of the units, the best site and the network connection. Therefore, the factors of the best location and sizing are the one of important issues in the implementation of distributed generation in the distribution system. Hence the placement of DG in a distribution system with well planning may lead to best performance of the network in terms of reduction in line losses, voltage profile improvement and power quality improvement [3–5]. Finally the reduction in demand required from the grid takes place which results in strengthening the feeders connecting the network and the grid.

The cautious approach is to be taken into consideration in view of problem of DG site and size i.e., placement of DG units at non-optimal site with undetermined capacity may lead to have increased system losses, thus resulting in increased costs [3]. Abundant papers have been published on this subject, referring to either "DG placement", "optimal capacity allocation" or even "capacity evaluation" [6]. Although the literature suggests a wide variety of objectives and constraints, two main approaches emerge: finding optimal locations for a defined DG capacity and finding optimal capacity at defined locations [7]. Inspite of several advantages and objectives of DG implementation, special attention is taken for implementation of DG for loss reduction.

DG placement is done basically on two variables namely site and size which are not independent i.e., optimal site of a DG with a different size leads to have increased system losses and also with the optimal size of DG connected to a bus different from the optimal one, leads to have increased system losses. This is the reason where the solution methodology for DG allocation plays a key role and it has to provide *simultaneously* both values of the variables [8]. This paper proposes two methods for single DG placement problem viz.

- Single DG Placement Method which is an analytical method
- CSA Algorithm.

The detailed description of the two methods is presented in following sections. Here both site and size of DG unit are determined simultaneously. The objective is to curtail the entire real power loss of the system. A model distribution system is required for this work which is able to represent the real distribution system so that once the approach for loss reduction is successfully applied onto the test model; it can be applied to a practical system. The IEEE 69-bus Test System is used as the test model in this work (Fig. 1). Both methods are tested on standard IEEE 69-Bus system and comparison of the results is also presented in this paper. At the same time, this method was compared with an existing method [9]. Percentage saving in total

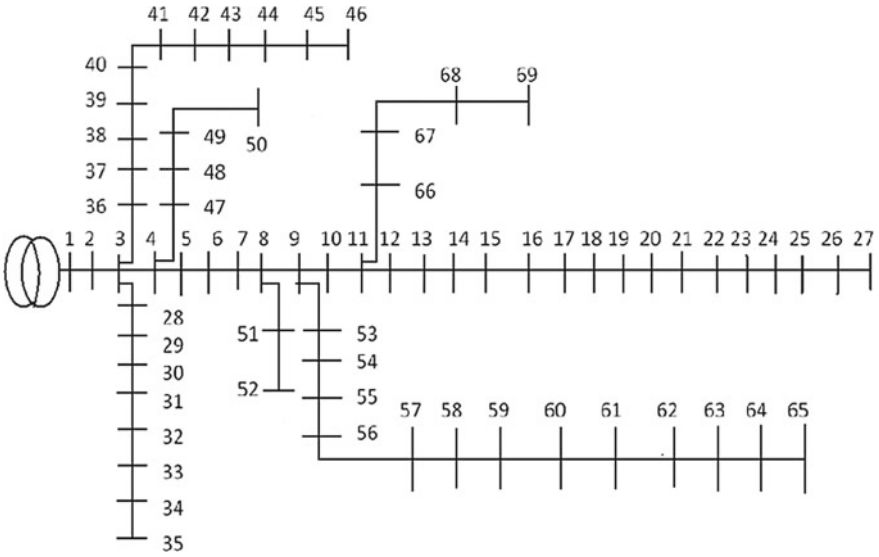

Fig. 1 Structure of IEEE 69-bus test system

loss is used to see the efficiency of the method. The greater the percentage, greater is the efficiency of the method.

The inter relationship between the optimal site and size is to be studied carefully by allocating the optimal size of DG's at almost all the buses in the network and by allocating different DG capacities at the optimal bus resulted from the proposed methods [5].

The loads in the distribution system are not constant, they are varying with time. Similarly the loads in distribution system are highly voltage sensitive and voltages are uncontrolled [10], hence constant power model of the loads leads to wrong results. The effect of time varying loads and voltage dependent load modeling on DG placement is not investigated in available literature. This work takes up this job and the effects are studied on single DG placement [1]. In the conclusion, the results prove that the proposed method has the upper hand as compared to the existing approach as it is computationally more efficient than the existing method. This proposed method can be applied and implemented in any radial distribution system.

2 Analytical Method

The proposed method determines the optimal site and size of DG units for minimum loss. Initially the optimum sizes of DG units for each and every node in the test system are determined for base case and top one among all is chosen based on the utmost loss saving [7]. The process is terminated here only if single DG placement

is required or else the process is continued and repeated if multiple DG sites are required by modifying the base system or by inserting a DG unit into the system one-by-one [3]. In this paper the DG unit is implicit to be able of producing only real power.

2.1 Methodology

The total power loss (P_{Lt}) in the distribution system [11] which has n number of branches is given by:

$$P_{Lt} = \sum_{i=1}^{n} I_i^2 Ri \tag{1}$$

And the loss related with the active and reactive components of branch currents can be written as

$$P_{La} = \sum_{i=1}^{n} I_{ai}^2 Ri \tag{2}$$

$$P_{Lr} = \sum_{i=1}^{n} I_{ri}^2 Ri \tag{3}$$

Here I_{ai} is active and I_{ri} is reactive component of branch currents which are obtained from the load flow solution. For the selected arrangement of a single-source radial network in the test system, the active power loss cannot be reduced since all the active power required by the system must be supplied by the source itself. However the P_{La} loss of the system can be reduced by the preface of distributed generators in the radial system [12].

Consider the radial distribution system having single-source with n branches and a DG is to be located at bus m, α be a set of branches connected between the source and bus m. The DG placed in the test system gives active current I_{DG}, which changes only the active component of current of branch set α for a given radial network. Due to the DG placement, the currents of remaining branches are unaffected. Thus the new active current I_{ai}^{new} of the i^{th} branch is given by [12]

$$I_{ai}^{new} = I_{ai} + D_i I_{DG} \tag{4}$$

where

$$\begin{aligned} D_i &= 1; \text{ if branch i} \in \alpha \\ &= 0; \text{ otherwise} \end{aligned}$$

The loss P_{La}^{new} the loss related with the active component of branch currents when the DG is connected can be written as

$$P_{La}^{new} = \sum_{i=1}^{n} (I_{ai} + D_i I_{DG})^2 \; R_i \tag{5}$$

The saving in Loss S is the difference between Eqs. 2 and 5 and is given by

$$\begin{aligned} S &= P_{La} - P_{La}^{new} \\ &= -\sum_{i=1}^{n} \left(2 D_i I_{ai} I_{DG} + D_i I_{DG}^2\right) R_i \end{aligned} \tag{6}$$

The DG current I_{DG} which gives the minimum loss can be obtained from

$$\frac{\partial S}{\partial I_{DG}} = -2 \sum_{i=1}^{n} (D_i I_{ai} + D_i I_{DG}) R_i = 0 \tag{7}$$

Thus the DG current for the maximum loss saving is

$$I_{DG} = -\frac{\sum_{i=1}^{n} D_i I_{ai} R_i}{\sum_{i=1}^{n} D_i R_i} = -\frac{\sum_{i \in \alpha} I_{ai} R_i}{\sum_{i \in \alpha} R_i} \tag{8}$$

The corresponding DG size is

$$P_{DG} = V_m I_{DG} \tag{9}$$

where V_m is the magnitude of voltage at bus *m*. The optimum size of DG for each bus and then possible loss saving for each DG are determined using Eqs. (9) and (6). The DG unit which has maximum loss saving is identified as candidate location for DG placement. After identification of the candidate bus and placement of DG, the technique expelled above can also be used to recognize the next location for DG for further loss reduction.

2.2 Algorithm for DG Placement

1. Initially perform the load flow analysis for the given original power system network.
2. Find out the DG currents (I_{DG}) by using Eq. 8 and also determine the size of DG by using Eq. 9 at all buses in the network except for source bus.
3. By using Eq. 6, find out the loss saving (S) all buses in the network except for source bus.

4. Select the bus which has greatest saving and the corresponding size of DG and treat that bus as candidate bus to locate the DG.
5. Change the active load on the network and perform the load flow again.

In this algorithm, the consequence of DG placement only on real power loss is measured. However, the consequences of DG placement on Reactive power loss, improvement of voltage profile and rise in the system capacity are ignored.

2.3 Crow Search Algorithm

There is a behavior which has many similarities with an optimization process in crow flock. According to this crows veil their excess food in certain thrashing places of the environment and the stored food is retrieved when food is needed. As the crows are greedy birds, they follow one another to achieve superior food condition. Finding out the food source hidden by a crow is a difficult task since once it notices that another crow is tracing out the food source of it then automatically the crow moves to a new position of environment to hoodwink the crow which is following it. From optimization perspective, the searchers are assigned as crows, environment itself be the search space, environment position corresponds to a feasible solution, the objective function is quality of food source and global solution to the problem is best food source. Crow Search Algorithm (CSA) try to simulate the performance of crows to obtain the solution for optimization problems [13].

The principles of CSA are given as follows:

Crows always try to live in group
Crows do not forget the position of their own hiding places
Crows follow each other to do thievery
Crows protect their catches by a prospect from being pilfered.

It is implicit that there is a d-dimensional environment which includes number of crows. N is the number of crows (group size) and the position of *crow i* at iteration *iter* in the search space is specified by a vector.

$x^{i,iter}$ ($i = 1, 2, \ldots, N$, $iter = 1, 2, \ldots, iter_{max}$) where $x^{i,iter} = [x_1^{i,iter}, x_2^{i,iter}, x_3^{i,iter}, \ldots, x_d^{i,iter}]$ and $iter_{max}$ is the maximum number of iterations. All the crows do not forget the food hiding place position in its own memory. $m^{i,iter}$ at iteration *iter* gives the hiding place position of *crow i*. This is the finest position so for *crow i* has obtained. Crows try to move in the environment to search for their better food resources that are hiding places. Suppose that *crow j* wishes to visit its hiding place $m^{i,iter}$ at iteration *iter* and *crow i* decides to go after *crow j* to arrive at the hiding place of *crow j* at this iteration, this may leads to have two different situations illustrated below.

Situation 1: *Crow j* fails to notice that *crow i* is tracing out its path of hidden food source and *crow i* approaches the hiding place of *crow j*. The latest position of *crow i* is determined as follows.

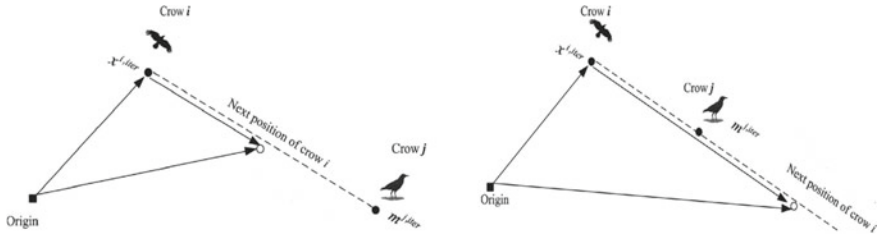

Fig. 2 Effect of flight length on search capability

$$x^{i,iter+1} = x^{i,iter} + r_i \times FL^{i,iter} \times \left(m^{j,iter} - x^{i,iter}\right) \tag{10}$$

where r_i is the random number between 0 and 1 and $FL^{i,iter}$ is the flight length of *crow i* at iteration *iter*.

The effect of FL on search capability and this situation and are illustrated in Fig. 2. Large values of flight length results in global search where as small values of FL leads to local search.

Situation 2: Crow *j* notices that *crow i* is tracing out its path of hidden food source as a consequence *crow j* to another search space position in order to protect its food being pilfered.

Entirely situation i and 2 are expressed as follows

$$\begin{aligned} x^{i,iter} &= x^{i,iter} + r_i \times FL^{i,iter} \times \left(m^{j,iter} - x^{i,iter}\right) \quad \text{if } r_j \geq AP^{j,iter} \\ &= \text{a random position} \quad \text{otherwise} \end{aligned} \tag{11}$$

where, $AP^{j,iter}$ is the awareness probability of the crow *j* at iteration *iter*. Awareness probability controls the intensification and diversification. Using small values of AP increases intensification where as using large values of AP increases diversification.

3 Time Varying Loads in Distribution Systems

Though the loads in distribution systems are continuously varying with time, the loads can be divided into three loading levels [5]. The load levels are shown in Table 1. The manner in which DG sites and sizes vary as a function of time-varying load levels is investigated.

Table 1 Load levels and their percentages in terms of peak load

Load level	% of peak load
Peak	100
Medium	70
Low	50

4 Load Modeling in Distribution Systems

Previous works assumed constant real and reactive loads at buses. But the loads in distribution system are highly sensitive to bus voltages. The load modeling is necessary in distribution systems as most of the buses in distribution system are load buses and hence voltages are not controlled. The loads in a distribution system consist of three types namely house hold (residential), commercial and industrial. The real and reactive power characteristics of theses loads differ from each other. Correct modeling of composite loads is an essential pre requisite [14, 15].

In perspective of optimization, Placement of DG might be similar to that of placement of capacitor in nature as discussed earlier. In almost all the planning methods power flow programs which normally utilize constant real and reactive power load model representation are used invariably. From the literature survey it is noticed that the load models were not at all considered in planning the site and size.

The loads are modeled depending on their relation with voltage. They can be mathematically expressed as

$$P_i = P_{0i}\, V_i^{K1} \tag{16}$$

$$Q_i = Q_{0i}\, V_i^{K2} \tag{17}$$

where P_i represents real power at bus i and Q_i represents reactive power at bus i,

P_{0i} represents nominal active power at bus i and Q_{0i} represents nominal reactive power at bus i,

V_i represents the magnitude of voltage at bus i,

K1 represents real power exponents and K2 represents reactive power exponents.

In a constant power model which is conventionally used in power flow studies $K1 = K2 = 0$ is assumed. The values of the real and reactive exponents used in the present work for industrial, residential and commercial loads are given in Table 2.

Table 2 Load types and exponent values

Load type K1	K1	K2
Constant power	0	0
Industrial load	0.18	6
Residential load	0.92	4.04
Commercial load	1.51	3.4

5 Results and Discussions

Load flow is conducted to determine the losses of the system. Then, algorithms are applied to sort for the bus locations and optimal DG sizes that results the maximum loss saving. The results are compared with an existing approach.

The two proposed methods for solving single DG placement problem are applied to IEEE 69-Bus standard test system. First the effect of time varying load level on DG placement is investigated and the load is considered to be constant load. Then effect of load modeling on DG placement is examined. All the results and discussion are presented in this section. First the results of Peak load level with constant power load modeling are presented and discussed.

5.1 Effect of Load Level

The real and reactive loss for the 69-bus system is 317.696 kW and 143.799 KVAR respectively. The real loss can be further decomposed into loss due to active and reactive component of branch current. The loss associated with the active and reactive components of branch current are determined as 218.1041 kW and 99.592 kW respectively.

The losses of the system before and after placement of DG by analytical method and CSA method are shown in Table 3. The loss due to active component of current is reduced to 21.94 kW and 21.78 kW from 218.1 kW by AM and CSA method respectively for peak load level. The saving in loss due to active component of current by the placement of DG at bus 61 is around 90% for all load levels.

The losses of the system before and after placement of DG by analytical method and CSA are shown in Table 3. The loss due to active component of current is reduced to 21.94 kW and 21.78 kW from 218.1 kW by AM and CSA method respectively for peak load level. The saving in loss due to active component of current by the placement of DG at bus 61 is around 90% for all load levels.

Though the aim is to reduce loss due to active component of current, the loss due to reactive component is also reduced to 90.25 and 90.28 kW from 99.59 kW by AM and CSA method respectively for peak load level. The total loss of the system is reduced to 112 kW from 317.69 kW by both the methods for peak load. The saving in total loss by DG placement is 205.69 kW for peak load. The saving in total system loss is 64–69% for all load levels.

Another advantage of placing DGs is that the improvement in voltage profile of the system. This is because the current flowing in the line is reduced due to flow of less active component of branch current, the voltage drop (IR) will decrease and hence improvement in voltage profile. From Table 3 it is evident that there is no change in location of DG with load level but the size varies with load level considerably.

Table 3 Analytical method results for all load levels of 69 bus system

Load	DG location		DG Size		Loss before DG placement			Loss after DG placement					
	AM	CSA	AM	CSA	PLa	PLr	PLt	PLa		PLr		PLt	
								AM	CSA	AM	CSA	AM	CSA
Peak	61	61	1.84	1.87	218.1	99.59	317.69	21.94	21.75	90.25	90.26	112.2	112.03
Medium	61	61	1.28	1.30	97.88	46.19	144.08	10.44	10.42	43.40	43.40	53.84	53.80
Low	61	61	1.02	1.03	60.35	28.89	89.250	6.59	6.55	27.54	27.51	34.14	34.10

5.2 *Effect of Load Modeling*

During investigation, the comparison of constant power load model assumption with the practical load models is emphasized. While investigating the effect of residential load model it was assumed that the system is supplying power to residential consumers only (all loads are residential type). Similarly, for industrial and commercial load it was assumed that all the loads are industrial and commercial type respectively.

The real (PD*)* and reactive (*QD)* loads at buses corresponds to peak load. The synopsis of outcome obtained for optimal size of DG (P_{DG}) and site for least amount of power loss configuration is depicted in Table 4. For different load models, Real power loss, Reactive power loss, Real power intake, Reactive power intake and MVA intake from the main substation, and System MVA and percentage reduction in these values are indicated in the Table 5. The expressions to calculate Real power intake, Reactive power intake, MVA intake and Total System MVA are given below.

$$\text{Real Power Intake } (\text{P}_{\text{intake}}) = \text{PD} + \text{PL}$$

$$\text{Reactive Power Intake } (\text{Q}_{\text{intake}}) = \text{QD} + \text{QL}$$

$$\text{MVA intake} = \sqrt{P_{\text{int}ake}^2 + Q_{\text{int}ake}^2} \tag{18}$$

$$\text{System MVA} = \sqrt{(P_{\text{int}ake} + P_{DG})^2 + Q_{\text{int}ake}^2} \tag{19}$$

where PD and PL are real power demand and real power loss of the system and QD and QL are reactive power demand and reactive power loss of the system.

From Table 4 for constant power load model the optimal size of DG that can be placed without need for upgrading the actual system for minimum loss is 1.8371 MW at bus 61. When DG is placed optimally, the loss is reduced to 112.0678 kW as

Table 4 Minimum loss configuration for different load models

Load type	DG location		DG size (MW)		Loss before DG placement (MW)	Loss after DG placement (MW)	
	AM	CSA	AM	CSA	PLt	PLt	
						AM	CSA
Constant Power	61	61	1.8371	1.8910	317.6958	112.2054	112.0678
Residential	61	61	1.6761	1.8614	219.8940	95.4731	95.3772
industrial	61	61	1.7651	1.8855	231.1090	90.5217	90.3064
Commercial	61	61	1.603	1.8530	209.331	97.2924	97.1012

Table 5 Effect of load modeling on system variables

		Load type					
		Real loss	Reactive loss	P_{intake}	Q_{intake}	Sys_{intake}	Sys MVA
Constant Power	Without DG	317.6962	143.7919	4.120	2.838	5.003	5.268
	With DG	112.0678	54.5340	2.020	2.747	3.226	3.478
% reduction		64.72	62.07	3.145	3.145	35.472	33.921
Residential	Without DG	219.8943	101.7729	3.826	2.263	4.445	4.636
	With DG	95.3775	47.1584	1.973	2.555	3.178	3.288
% reduction		56.63	53.66	48.43	−12.91	28.51	29.08
Industrial	Without DG	231.1091	106.5009	3.993	2.055	4.491	4.697
	With DG	90.3067	44.9258	1.995	2.474	3.235	3.235
% reduction		60.92	57.82	50.04	−20.35	27.95	31.12
Commercial	Without DG	209.333	97.2487	3.707	2.342	4.385	4.563
	With DG	97.1016	47.8854	1.945	2.585	3.242	3.295
% reduction		53.61	50.76	47.53	−10.39	26.06	27.8

against the case without DG (317.6958 kW). The reduction in loss is 64.72% due to DG placement for constant power load model. From Table 4 it is observed that Pintake, Qintake, MVAintake, and System MVA are also decreased in consistent with constant power load model assumption. The real power intake from substation is reduced by more than 50% and the reduction in system intake from substation is 35.47%.

The optimal loss configuration for residential model is obtained by placing 1.8618 MW at bus 61. There is no change in the optimal location but the optimal DG size is decreased to 1.8618 from 1.8913 MW of constant load model. A similar trend of reduction is observed for real power loss, reactive power loss, real power intake, MVA intake and System MVA except for reactive power intake with DG placement. For residential load model with DG placement there is an increase in reactive power intake from the main substation. It is noted that reduction in all the variables like real power intake, system MVA, real, and reactive losses are significantly smaller than those of constant load model. As far as reactive power demand at the main substation is concerned, it is seen that in case of residential load model placement of DG raises reactive demand (by 12.91%) whereas in case of constant load model the reactive demand (by 3.1%) is decreased. The real power intake and System MVA intake from substation are reduced by more than 48% and 28.5% respectively as against to 50.9% and 35.47% respectively in case of constant load model.

The optimal size of DG for minimum loss configuration is 1.8857 MW at bus 61 for industrial load model. It is observed that the location is same but DG size is

Table 6 Comparison between proposed method and existing method

Test system	Location			Size (MW)		
	AM	CSA	Other method	AM	CSA	Other method
69 bus	61	61	61	1.8371	1.8910	1.8761

significantly different from that of constant power and residential load models. When DG is placed reduction in real power loss is 60.92% as against to 64.72% in constant power load model. After DG placement all the variable values are reduced except reactive power intake like in residential load model. Optimal size of DG in industrial load model is close to that of constant load model and is significantly different than that of residential load model.

The optimal size of DG for minimum loss configuration is 1.8531 MW at bus 61 for commercial load model. It is remarkable to note that the DG size is significantly different from the load models considered so far and it is the lowest of all the cases. The location is same as that of constant power, residential and industrial load models. After DG placement the reduction in real power loss and System MVA intake are 53.61% and 27.4% respectively which are significantly low compared to constant load model. Similar results are obtained for other standard test systems also.

5.3 Comparison with Existing Method

To prove the validity of the method the results of proposed analytical method are compared with an existing method. The results of 69 bus system for peak load of the method developed by Adivesh et al. [13] and the proposed method are given in Table 6.

6 Conclusions

Optimal DG unit sizes and locations are determined for maximum loss reduction by successful implementation of algorithm. The programs for calculating the DG sizes and identifying the bus locations for maximum loss are written in MATLAB. The proposed algorithm is tested on IEEE 69-bus test system. The result shows that the loss due to active branch currents is reduced by proposed method. The total loss is reduced by around 50%. The effect of load level on DG placement is that there is no change in location of DG but the size of it varies with load level. Similar result obtained in case of load modeling also. Assumption of Constant load model leads to non optimum size of DG. The validity of the results of proposed method has been verified by comparing them with other existing method. This method can be applied to any radial distribution system with any number of busses and laterals.

References

1. Haque MH (1999) Capacitor placement in radial distribution systems for loss reduction. In: IEE proceedings—generation, transmission and distribution, vol 146, pp 501–505, Sept 1999
2. Veera Reddy VC, Padma Lalitha M. Loss reduction in distribution network by capacitor placement. M.Tech Thesis, S.V.U, India
3. Acharya N et al (2006) An analytical approach for DG allocation in primary distribution network. Electr Power Energy Syst 28:669–678
4. Das D, Ghosh S (1999) Method for load flow solution of radial distribution networks. IEE Proc
5. Bindumol EK, Babu CA (2017) A novel analytical approach for sizing and placement of DG in radial distribution system. Int J Energy Technol Policy 13(1–2)
6. Celli G, Pilo F (2001) Optimal Distributed generation in MV distribution networks. IEEE Trans
7. Wang C (2004) Analytical approaches for optimal placement of distributed generation sources in power system. IEEE Trans PWRS 19(4):2068–2076
8. Row NS, Wan YH (1994) Optimum location of resources in distributed planning. IEEE Trans PWRS 9(4):2014–2020
9. Wang C, Nehrir MH (2004) Analytical approaches for optimal placement of distributed generation sources in power systems. IEEE Trans PWRS 19(4):2068–2076
10. Dorahak S (2016) Optimal DG placement with the aim of profits maximization. Indones J Electr Eng Comput Sci 1(2):249–254. https://doi.org/10.11591/ijeecs.v1.i2
11. Cheng M-Y, Prayogo D (2014) Symbiotic organisms search: a new metaheuristic optimization algorithm. Comput Struct 139:98–112
12. Kanth DSK, Lalita MP, Babu PS (2013) Siting & sizing of DG for power loss & THD reduction, voltage improvement using PSO & sensitivity analysis. Int J Eng Res Dev 9(6):1–6
13. Padma Lalitha M, Suresh Babu P, Adivesh B (2016) CSA algorithm for DG placement for loss minimization considering reverse power flow in the distribution systems. In: International conference on advanced communication control and computing technologies (ICACCCT). IEEE Explore. https://doi.org/10.1109/icaccct.2016.7831678
14. Lalitha MP, Reddy VCV, Usha V (2010) Optimal DG placement for minimum real power loss in radial distribution systems using PSO. J Theor Appl Inf Technol 13:107–116
15. Kaur P, Kaur S, Khanna R (2016) Optimal placement and sizing of DG comparison of different techniques of DG placement. In: IEEE 1st international conference on power electronics, intelligent control and energy systems (ICPEICES). https://doi.org/10.1109/icpeices.2016.7853653

A Control Strategy for Optimal Coordination of Interconnected Distribution System Using Dual Setting Directional over Current Relays (DSDOR)

K. Srikumar

Abstract With the development of distributed generation (DG), the radial distribution systems are now being transformed to interconnected systems. So, it is essential to provide faster protection system to assure reliability. In this paper, a proposed strategy involving dual setting directional over current relays (DOCR) is used to design protection system. These relays are provided with standard inverse characteristics for over current elements and are designed to operate differently in forward and reverse directions based on the direction of fault current. So, the coordination problem with in the elements is designed with objective of minimizing overall operating time of relays. The optimization problem is taken as constrained non-linear programming problem. The proposed scheme is tested and compared with conventional approach, where relays are equipped with unidirectional settings. Both schemes are tested using the IEEE-14 bus test system and is designed to use synchronous generation for DG. The proposed scheme is found to be better and act faster than the conventional scheme, thus providing a quicker and reliable protection.

Keywords Dual setting DOCRs · Optimization · Protection coordination · Relay settings (TDS and pickup currents)

1 Introduction

Protection plays a crucial role in operation of any interconnected power system. The Relay coordination is most important aspect to be considered to design the protection system. These schemes should guarantee fast, reliable and selective operation of relays to isolate faulted sections of the power system. Generally, Over current relays are mostly preferred for the protection of distribution system. But due to the increasing penetration of DG, the distribution systems are transforming towards

K. Srikumar (✉)
Department of Electrical and Electronics Engineering, JNTU Kakinada, Kakinada, Andhra Pradesh, India
e-mail: kotni.77@gmail.com

© Springer Nature Singapore Pte Ltd. 2020

T. Hitendra Sarma et al. (eds.), *Emerging Trends in Electrical, Communications, and Information Technologies*, Lecture Notes in Electrical Engineering 569,
https://doi.org/10.1007/978-981-13-8942-9_18

meshed nature from conventional radial systems. So directional over current relays have become primary choice of these systems.

Generally integration of DG imposes several challenges on the protection of distribution system [1, 2]. The impacts are transformation to meshed nature for distribution system and increase in fault current levels for the protection system. From [3], it has been evident that contribution to fault current levels is far higher from synchronous based DG compared to inverter based DG and thus has more impact on the protection system.

In meshed distribution system, after the isolation of faulted section, power supply can be continued with help of interconnections. So to assure reliability, fast acting devices which can provide quicker fault isolation are required to ensure that low voltage condition is of short duration and thus increasing DG fault ride through [4]. For the protection of meshed systems, the most suitable relays are DOCRs due to their ability to sense fault currents in both directions. The relay settings are coordinated optimally, in order to minimize the total operating time of all relays [5]. Due to the presence of DG fault current level increases, so to overcome this effect, new set of optimal settings are to be determined considering the DG connection. Different methods and techniques are being used to determine the relay settings optimally by ensuring coordination and minimization of overall operating time [6–9]. Also the protection coordination strategies make use of digital or microprocessor based relays to improve the system performance involving DG, by using different groups of relay characteristics and settings [10–12]. In a power system where fault currents flow in both directions, it is desirable to have protective devices which can act accordingly to each direction [13]. Such relays with dual settings have been proposed by manufacturers [14, 15]. These Relays are equipped with two different settings for each direction. These two different settings are programmed to over current element in DOCRs, with one to operate in forward direction and other to operate in reverse direction.

In this paper, under the proposed scheme dual setting relays are used for protection coordination of the system. Here two pairs of settings are considered one pair for each direction, i.e. for Time multiplier setting and pickup current setting in each direction will be found out. Here, both conventional and proposed schemes are tested for the IEEE-14 bus test system involving DG of synchronous type. The problem is developed as non-linear optimization model and the results of both schemes are compared to test the supremacy.

2 Protection Coordination Schemes

The relay settings Time dial settings (TDS) and Pickup current settings (Ip) defines the characteristics of relay operation. These settings are derived in optimal way by minimizing the overall relay operating time under the constraints of protection coordination. Here in this paper two schemes are tested on the meshed test bus system. Firstly, in the conventional scheme, only unidirectional relays are employed

for coordination. In this scheme, if a fault occurs in a line, the connected relays at both ends act as primary relays. For selection of backup relay to each primary relay, the farther relays connected to the bus on which primary relay is connected act as backup. But in proposed scheme, the backup relays are the adjacent relays to primary relays on the same bus. For example in the figure, for relay R5, relays R1, R7, R13 act as backup in conventional scheme. For the same relay in proposed scheme, relays R3, R4, R6 act as backup relays.

So, in conventional scheme, only TDS and Ip settings are to be optimized, where as in the proposed scheme, ($TDS_{fw,}$ Ip_{fw}) and ($TDS_{rv,}$ Ip_{rv}) are to be optimized.

3 Problem Formulation

The operational or operating time of directional over current relay with inverse characteristics is given by

$$t_{jk} = TDS_j \times \frac{A}{\left[\frac{I_{sc_{jk}}}{I_{p_{jk}}}\right]} \tag{1}$$

A, B are relay constants and for standard inverse characteristics, they are taken as 0.14, 0.02 respectively. 'j' denotes relay number and 'k' denotes fault location. 'Isc' represents fault current. As shown in the above equation each relay has one pair of settings (TDS, Ip). So in proposed scheme, with two pairs of settings each for forward (primary) and reverse (backup) are to be optimized. Here the objective function is to lessen the total operating time considering primary and Secondary or backup relays satisfying the constraints of protection coordination. Now to define the objective function mathematically

$$T = \sum_{i=1}^{N} \left(\sum_{j=1}^{M} t_{fwij} + \sum_{k=1}^{M} t_{rvi} \right) \tag{2}$$

'N' represents fault locations and 'M' represents number of relays. The variables t_f and t_r represents time of operation of relays ' j', 'k' at fault location 'i' for forward and reverse operation respectively, we need to consider operating time for forward direction and reverse directions separately and thus making use of these times, we can write objective function 'T' as shown in (2), where the final objective is to minimize "T".

These operating times can be written similar to first equation, from which variables (TDS_{fw}, Ip_{fw}) and (TDS_{rv}, Ip_{rv}) are the required relay settings under proposed scheme to be optimized.

When solving the coordination problem, the constraints need to be satisfied, which are

$$t_{rvik} - t_{fwij} \geq CTD$$

CTD is coordination time delay, which is usually 0.2–0.5, here set to 0.3 s.

$$I_{p,min} \leq I_p \leq I_{p,max}$$
$$TDS_{min} \leq TDS \leq TDS_{max}$$

The limits on pickup currents depend on system rated current, such that relay doesn't operate for overload condition. Maximum setting should be fault current.

TDS could be anywhere between 0.1 and 3 s.

So for each study in this paper, firstly fault analysis at different locations is done and then optimization is carried out. Since the relation between pickup current and operating time is nonlinear, the optimization problem is set as a non-linear programming problem.

4 System and Simulation Setup

The protection coordination schemes are tested on IEEE-14 bus test system [16] as given in the figure. The system is connected to two DGs at buses 1 and 2. The system operates at nominal voltage of 138 kV and has 40 DOCRs for which settings are to be optimized. Faults are located at the midpoint of the line at which short circuit fault analysis is carried out. In this paper an unsymmetrical (LG) fault is considered for analysis.

As earlier stated, optimization is done for 40 relays in conventional scheme and also different backup relays are considered compared to those for proposed scheme, where as in proposed scheme, optimization is done for 40 relays, but two different settings for each relay,.

The optimization model is developed and solved using MATLAB. Before optimization, fault analysis is carried out on different branches involving mid-line fault locations, and the rated operating currents and short circuit (fault) currents are noted. Two models are developed separately for each scheme and are solved using MATLAB simulation with minimum constrained for a nonlinear multivariable function. Here we used function 'fmincon' to solve the problem There are different methods (algorithms) for solving constrained nonlinear programming problems and the algorithm used under 'fmincon' is sequential quadratic programming (SQP) (Fig. 1).

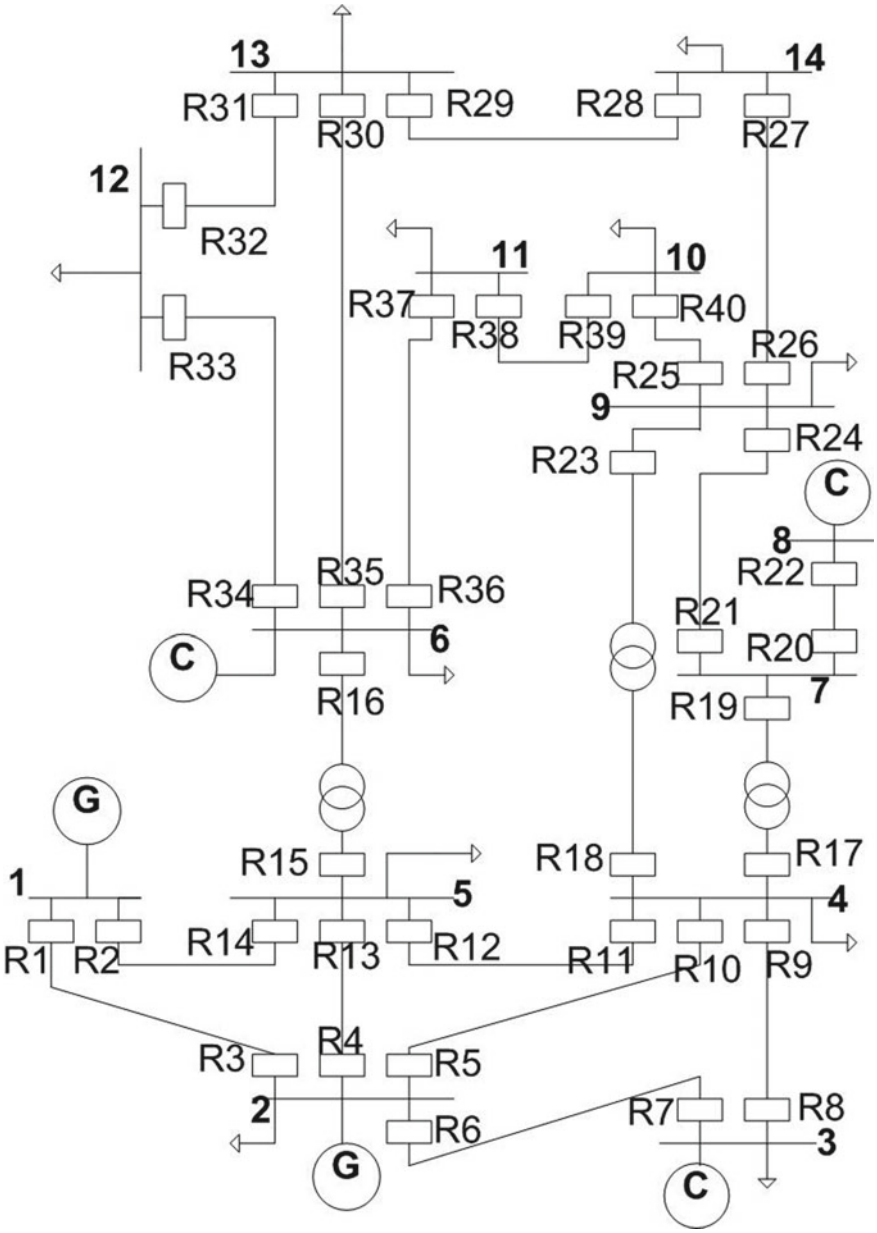

Fig. 1 Test bus system used for study

5 Results and Analysis

Here, optimal relay settings for each conventional and proposed coordination schemes are given along with their relay operating times. Table 1 represents optimal relay settings for conventional protection coordination scheme. Here we obtain the time -dial and pickup current settings for relays. Table 2 represents relay operating times at each fault location for both primary and backup relays, which are obtained from the optimal settings from Table 1. The total or overall operating time of relays considering conventional protection coordination scheme is found to be 94.11 s. Also, each primary, backup relay satisfies coordination time delay of 0.3 s. in this analysis fault F10 between buses 7–8 is not shown as they didn't have significant fault currents.

Also proposed scheme is employed on the same system and results are tabulated. Table 3 represents optimal relay settings for proposed protection coordination scheme. Here optimal settings for relays in both forward and reverse direction are obtained. Table 4 represents relay operating times at each fault location for both (primary and backup) relays considering dual settings. The total operating time of relays considering for proposed protection coordination scheme is found to be 62.57 s.

Table 1 Optimal relay settings for conventional protection coordination scheme

TDS in (s) and Ip in (p.u.)					
Relay	TDS	Ip	Relay	TDS	Ip
R1	0.1	0.8846	R21	0.1	0.236
R2	0.1007	0.4537	R23	0.1685	0.0325
R3	0.1	0.3977	R24	0.1	0.1697
R4	0.2363	0.0939	R25	0.1	0.2225
R5	0.2163	0.1078	R26	0.1	0.1366
R6	0.1	0.4341	R27	0.1	0.0855
R7	0.1	0.2518	R28	0.1	0.091
R8	0.2771	0.0471	R29	0.1	0.1061
R9	0.1	0.2582	R30	0.1899	0.0332
R10	0.1607	0.1078	R31	0.1	0.0725
R11	0.1	0.3164	R32	0.225	0.0124
R12	0.1	0.4113	R33	0.1	0.03
R13	0.1657	0.0907	R34	0.1	0.1203
R14	0.1	0.174	R35	0.1	0.1413
R15	0.1	0.221	R36	0.1	0.1877
R16	0.1	0.1202	R37	0.1185	0.0813
R17	0.1	0.212	R38	0.1	0.1388
R18	0.1	0.0942	R39	0.1	0.1485
R19	0.1	0.0957	R40	0.2102	0.0483

Table 2 Optimal operation of time of primary and backup relays for the conventional protection coordination scheme

Relay operating time in seconds (p = primary relay, b = backup relay)					
Fault	P	b1	b2	b3	b4
F1	R1	R14			
	0.4207	0.7207			
	R3	R13	R10	R7	
	0.4048	0.7048	0.7048	0.7048	
F2	R6	R1	R13	R10	
	0.3855	0.8083	0.7979	0.8331	
	R7	R9			
	0.3988	0.6988			
F3	R5	R1	R13	R10	
	0.4711	0.7711	0.8806	0.8884	
	R10	R8	R12	R19	R23
	0.3923	0.8042	0.7565	0.7617	0.8717
F4	R2	R3			
	0.3857	0.6857			
	R14	R11	R4	R16	
	0.2987	0.8749	0.5987	0.6763	
F5	R4	R1	R10	R17	
	0.4921	0.7921	0.8535	0.8071	
	R13	R11	R2	R16	
	0.3777	0.9848	0.7093	0.6777	
F6	R8	R6			
	0.537	0.837			
	R9	R5	R12	R19	R23
	0.3268	0.771	0.6268	0.719	0.8309
F7	R11	R8	R5	R19	R23
	0.3619	0.6619	0.6619	0.7708	0.8997
	R12	R4	R2	R16	
	0.3937	0.6937	0.6937	0.6937	
F8	R15	R11	R4	R2	
	0.29	1.1943	0.8323	0.5984	
	R16	R33	R30	R37	
	0.3858	0.6858	0.7819	0.6858	
F9	R17	R8	R5	R12	R23
	0.2786	0.7611	0.6858	0.6974	

(continued)

Table 2 (continued)

Relay operating time in seconds (p = primary relay, b = backup relay)					
Fault	P	b1	b2	b3	b4
	R19	R22	R24		
	0.3408	1.1141	0.6408		
F11	R18	R8	R5	R12	R19
	0.2523	0.923	0.8169	1.2633	0.5523
	R23	R21	R40	R27	
	0.3653	1.0702	0.9422	0.925	
F12	R21	R17	R22		
	0.7376	1.0376	1.0376		
	R24	R18	R40	R27	
	0.616	0.9762	0.916	0.916	
F13	R25	R18	R21	R27	
	5973	0.8973	0.8973	1.0081	
	R40	R38			
	0.7887	1.0887			
F14	R36	R15	R33	R30	
	0.5682	0.8682	0.8682	0.7921	
	R37	R39			
	0.5572	0.8572			
F15	R34	R15	R30	R37	
	0.3985	0.8453	0.9086	0.9001	
	R33	R31			
	0.3311	0.6311			
F16	R35	R15	R33	R37	
	0.4415	0.8392	0.8617	0.8985	
	R30	R28	R32		
	0.5604	0.8604	1.0284		
F17	R26	R18	R21	R40	
	0.4487	0.954	0.9936	1.2103	
	R27	R29			
	0.545	0.845			
F18	R39	R25			
	0.5271	0.8271			
	R38	R36			

(continued)

Table 2 (continued)

Relay operating time in seconds (p = primary relay, b = backup relay)					
Fault	P	b1	b2	b3	b4
	0.6454	0.9454			
F19	R32	R34			
	0.4708	0.7708			
	R31	R28	R35		
	0.3317	0.8587	0.7913		
F20	R29	R35	R32		
	0.441	0.7441	0.7441		
	R28	R26			
	0.4775	0.7775			

Table 3 Optimal relay settings for proposed protection coordination scheme

TDS in (s) and Ip in (p.u.)				
Relay	TDS fw	Ip fw	TDS rv	Ip rv
R1	0.1	0.2886	0.1016	0.289
R2	0.1	0.1388	0.1	0.1388
R3	0.1	0.2885	0.1186	0.4526
R4	0.1	0.0798	0.1634	0.0798
R5	0.1	0.1078	0.1467	0.1078
R6	0.1	0.1367	0.1491	0.1367
R7	0.1	0.1367	0.136	0.1517
R8	0.1	0.0471	0.1672	0.1009
R9	0.1	0.0472	0.2256	0.0471
R10	0.1	0.1078	0.1764	0.1078
R11	0.1	0.1216	0.1695	0.1216
R12	0.1	0.1216	0.176	0.1216
R13	0.1	0.0798	0.1937	0.0798
R14	0.1	0.1388	0.1701	0.1388
R15	0.1	0.0821	0.1163	0.0821
R16	0.1	0.0821	0.139	0.0821
R17	0.1	0.0566	0.1238	0.0566
R18	0.1	0.0325	0.1176	0.0325
R19	0.1	0.0566	0.1	0.1279
R21	0.1	0.0566	0.181	0.0566
R23	0.1	0.0325	0.1	0.0615
R24	0.1	0.0566	0.1	0.1187

(continued)

Table 3 (continued)

TDS in (s) and Ip in (p.u.)				
Relay	TDS fw	Ip fw	TDS rv	Ip rv
R25	0.1	0.0121	0.2656	0.0121
R26	0.1	0.0194	0.1993	0.0194
R27	0.1	0.0194	0.124	0.0571
R28	0.1	0.0097	0.1202	0.0531
R29	0.1	0.0097	0.1	0.0637
R30	0.1	0.0332	0.1638	0.0332
R31	0.1	0.0028	0.1907	0.0062
R32	0.1	0.0028	0.1173	0.0492
R33	0.1	0.0147	0.1177	0.0474
R34	0.1	0.0147	0.1431	0.0147
R35	0.1	0.0332	0.1707	0.0332
R36	0.1	0.0123	0.2802	0.0123
R37	0.1	0.0123	0.1275	0.0573
R38	0.1	0.0055	0.1271	0.0585
R39	0.1	0.0055	0.1206	0.0517
R40	0.1	0.0121	0.1356	0.0639

Table 4 Optimal operational time of primary and backup relays for the protection backup relays for the protection coordination using proposed scheme

Relay operating times in seconds (p = primary relay, b = backup relay)					
Fault	P	b1	b2	b3	b4
F1	R1	R2			
	0.247	0.5793			
	R3	R4	R5	R6	
	0.3395	0.6395	0.6395	0.6396	
F2	R6	R3	R4	R5	
	0.2312	0.5312	0.7393	0.7233	
	R7	R8			
	0.2928	0.5928			
F3	R5	R3	R4	R6	
	0.2178	0.5178	0.798	0.7288	
	R10	R9	R11	R17	R18
	0.2441	0.6526	0.5441	0.5948	0.6084

(continued)

Table 4 (continued)

Relay operating times in seconds (p = primary relay, b = backup relay)					
Fault	P	b1	b2	b3	b4
F4	R2	R1			
	0.2281	0.5281			
	R14	R12	R13	R15	
	0.2713	0.5713	0.654	0.5713	
F5	R4	R3	R5	R6	
	0.1981	0.5258	0.7368	0.714	
	R13	R12	R14	R15	
	0.2184	0.6251	0.6117	0.5722	
F6	R8	R7			
	0.1939	0.4939			
	R9	R10	R11	R17	R18
	0.1774	0.6248	0.4992	0.573	0.5799
F7	R11	R9	R10	R17	R18
	0.2384	0.5384	0.5384	0.5992	0.6279
	R12	R13	R14	R15	
	0.2292	0.5292	0.5292	0.582	
F8	R15	R12	R13	R14	
	0.2023	0.5711	0.6211	0.6493	
	R16	R34	R35	R36	
	0.3166	0.6167	0.6166	0.6167	
F9	R17	R9	R10	R11	R18
	0.1786	0.5852	0.6145	0.5248	0.4786
	R19	R20	R21		
	0.2688	0.5925	0.5688		
F11	R18	R9	R10	R11	R17
	0.179	0.6605	0.7391	0.659	0.479
	R23	R24	R25	R26	
	0.2168	0.5168	0.6114	0.6138	
F12	R21	R19	R20		
	0.2886	0.5886	0.5886		
	R24	R23	R25	R26	
	0.308	0.608	0.6082	0.608	
F13	R25	R23	R24	R26	
	0.1651	0.5762	0.4722	0.6276	
	R40	R39			
	0.2107	0.5107			

(continued)

Table 4 (continued)

Relay operating times in seconds (p = primary relay, b = backup relay)					
Fault	P	b1	b2	b3	b4
F14	R36	R16	R34	R35	
	0.1707	0.534	0.653	0.7122	
	R37	R38			
	0.2017	0.5019			
F15	R34	R16	R35	R36	
	0.176	0.5275	0.817	0.6807	
	R33	R32			
	0.2447	0.5447			
F16	R35	R16	R34	R36	
	0.2258	0.5258	0.6503	0.6803	
	R30	R29	R31		
	0.2951	0.5951	0.5951		
F17	R26	R23	R24	R25	
	0.1937	0.5992	0.498	0.7002	
	R27	R28			
	0.2473	0.5473			
F18	R39	R40			
	0.1449	0.4453			
	R38	R37			
	0.1557	0.4559			
F19	R32	R33			
	0.1415	0.4418			
	R31	R29	R30		
	0.1249	0.5943	0.4821		
F20	R29	R30	R31		
	0.1706	0.4706	0.4707		
	R28	R27			
	0.1833	0.4833			

From Tables 1 and 3, we can notice that the values of pickup currents are lesser in proposed scheme than the conventional scheme for the primary (forward) relay settings. The reason is that in proposed scheme each relay need not satisfy both primary and backup conditions. So, it is allowed to be better tuned for each function. From Table 5, we observe that in the proposed scheme the operating or operational time of relays is improved (fastened) in both primary and backup operation, thus providing faster protection compared to the conventional approach.

Table 5 Comparison of operating times of both schemes

Operating time	Conventional scheme (s)	Proposed scheme
Primary relays	17.9573	8.3374
Backup relays	76.1544	54.2347
Total	94.1117	62.5721

6 Conclusion

In this paper, proposed scheme uses bidirectional settings for relays, which are capable of operating with different settings in both directions, there by achieving a faster and reliable protection system design. As it can be seen and proved from Table 5 a reduction of 35% in overall operating time w.r.t Primary relays, Backup Relays with the proposed scheme is observed to have better sensitivity as compared to the conventional scheme. Hence, this scheme can be mentioned as superior to other existing protection schemes. This proposed scheme has been tuned for all the functions within the stipulated conditions as considered.

Although this scheme provides economical and technical benefits, it is important to consider additional costs incurring due to these relays compared to unidirectional over current relays. These costs are not high enough as compared to the fault eventualities.

References

1. Zeineldin HH, Sharaf HM, Ibrahim DK, El-Zahab EEA (2015) Optimal protection coordination for meshed distribution systems with DG using dual setting directional over-current relays. IEEE Trans Smart Grid 6(1):115–123
2. Mozina CJ (2013) Impact of smart grids and green power generation on distribution systems. IEEE Trans Ind Appl 49(3):1079–1090
3. Nimpitiwan N, Heydt GT, Ayyanar R, Suryanarayanan S (2007) Fault current contribution from synchronous machine and inverter based distributed generators. IEEE Trans Power Deliv 22(1):634–641
4. Erlich I, Winter W, Dittrich A (2006) Advanced grid requirements for the integration of wind turbines into the German transmission system. In: Proceedings of the IEEE PES general meeting, Montreal, QC, Canada, pp 1–6
5. Zeineldin HH, El-Saadany EF, Salama MA (2005) Optimal coordination of directional overcurrent relays. In: Proceedings of the power engineering society general meeting, pp 1101–1106
6. Zeineldin HH (2008) Optimal coordination of microprocessor based directional overcurrent relays. In: Proceedings of the Canadian conference of electrical and computer engineering (CCECE), pp 289–294
7. Ojaghi M, Sudi Z, Faiz J (2013) Implementation of full adaptive technique to optimal coordination of overcurrent relays. IEEE Trans Power Deliv 28(1):235–243
8. Amraee T (2012) Coordination of directional overcurrent relays using seeker algorithm. IEEE Trans Power Deliv 27(3):1415–1422
9. Noghabi S, Sadeh J, Mashhadi HR (2009) Considering different network Topologies in optimal overcurrent relay coordination using hybrid GA. IEEE Trans Power Deliv 24(4):1857–1863

10. Chabanloo RM, Abyaneh HA, Kamangar SSH, Razavi F (2011) Optimal combined over current distance relay coordination incorporating intelligent over current relay characteristic selection. IEEE Trans Power Deliv 26(3):1381–1391
11. Kei T, Jager J (2008) Advanced coordination method for overcurrent protection relays using nonstandard tripping characteristics. IEEE Trans Power Deliv 23(1):52–57
12. Khederzadeh M (2012) Adaptive setting of protective relays in microgrids in grid connected and autonomous operation. In: Proceedings of the 11th international conference on development in power system protection (DPSP), Birmingham, U.K., pp 1–4
13. Horak J (2006) Directional overcurrent relaying (67) concepts. In: Proceedings of the 59th annual conference on protective relay engineering, College Station, TX, USA, pp 13–18
14. http://www.easunreyrolle.com/product.php?id=67. Accessed 15 Jan 2014
15. http://www.toshibatds.com/tandd/products/pcsystems/en/grd100.html. Accessed 15 Jan 2014
16. University of Washington (2006) Power systems test case archive. http://www.ee.washington.edu/research/, Mar 2006
17. Sulaiman M, Waseem, Muhammad S (2018) Improved solutions for the optimal coordination of DOCRs using Fire fly Algorithm. Wiley-Hindawi

An Investigation of Li-Ion Battery Performance for AC Drives Used in Electric Vehicular Technology

Mondru Chiranjeevi, D. V. Ashok Kumar and R. Kiranmayi

Abstract This paper demonstrates charging and discharging analysis of Li-Ion battery by the simulation model. It is present most commonly used rechargeable battery for Electric Vehicular Technology (EVT) in the year of 2016–17 by various companies at various power ratings. The desired parameters of the Li-Ion battery is used as a storage device for EVT and adopting parameters of the Li-Ion battery to the AC drives are tabulated and demonstrates. The Li-Ion battery results to the IM and PMSM drives of the different operating modes are discussing. Performance analysis of the battery parameters such as voltage, current, State Of Charge (SOC), and power is observed with the help of the MATLAB/Simulink platform for variable speed operation. The combination of Li-Ion battery and PMSM drive is suitable to the EVT, due to regenerative operation, less power consumption, high efficiency and high performance.

Keywords Li-Ion battery · EVT · Motor drives · Parameters · Voltage · Current · SOC · Power · IM and PMSM

1 Introduction

The first Electric Vehicle (EV) adopts chargeable battery prior to the lead acid battery for some part of a century. Latterly, numerous combinations have been advanced as mercantile rechargeable electric batteries acceptable for the vehicle's better performance [1, 2]. Now a days most frequently using rechargeable battery is Li-Ion because of its features [3]. The prime characteristic of vehicular Energy Storage Sys-

M. Chiranjeevi (✉) · R. Kiranmayi
JNTUA, Ananthapuramu, India
e-mail: chiru.carey@gmail.com

R. Kiranmayi
e-mail: kiranmayi0109@gmail.com

D. V. Ashok Kumar
RGMCET, Nandyal, India
e-mail: rgmdad09@gmail.com

© Springer Nature Singapore Pte Ltd. 2020

T. Hitendra Sarma et al. (eds.), *Emerging Trends in Electrical, Communications, and Information Technologies*, Lecture Notes in Electrical Engineering 569,
https://doi.org/10.1007/978-981-13-8942-9_19

tem (ESS) comprises specific energy, energy density, specific power, power density, working temperature, self-discharging rates, recycle times, SOC, commercial availability, cost, maintenance and life time. Recent trends, Ultra-Capacitors (UCs) and batteries are the almost general features for vehicular ESS. Batteries are accumulating the majority of the electrical energy and mostly have higher energy densities [2, 4–10].

An investigation is going for EVT, researchers are written papers on various motors advantages and limitations [11–15, 19]. To use the existing motor drives for the EVT, the parameters such as high power density, a fast torque response, high instantaneous power, low cost, robust, constant-torque regions, constant-power regions, high efficiency, high torque at low speed of initial acceleration, and reliability [17, 21, 22].

This paper demonstrates and investigates on the present usage of rechargeable battery for vehicular applications. Section 2 demonstrates the mathematical modelling of Li-Ion battery; in Sect. 3 various EVT manufacturers are used Li-Ion Battery in 2016–17 is tabulated. Li-Ion nominal cell and adopted Li-Ion battery pack parameters for EVT is tabulated in Sect. 4. Section 5 concentrates on results and discussions; and the conclusion is disclosed in Sect. 5.

2 Mathematical Modelling of Li-Ion Battery

This section, demonstrates the charging and discharging modelling of Li-Ion battery in terms of mathematical expressions and simulation model.

From Fig. 1 the following equations can be written as

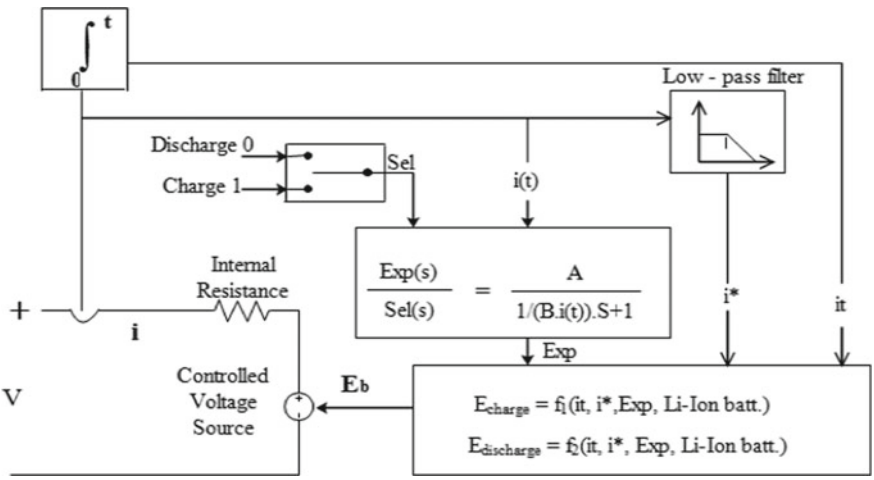

Fig. 1 Li-Ion battery charging and discharging modelling

Modelling equation of the Li-Ion Battery for charging is:

$$E_{charge} = V = E_b - R * i - k\frac{Q}{it - 0.1Q} * i^* - k\frac{Q}{Q - it} * it + A\exp(-B * it) \tag{1}$$

Modelling equation of the Li-Ion Battery for discharging is:

$$E_{dischaege} = V = E_b - R * i - k\frac{Q}{Q - it}\left(it + i^*\right) + A\exp(-B * it) \tag{2}$$

where

V Nonlinear Voltage (V)
Eb Constant Voltage (V)
R Internal Resistance (Ω)
K Polarization Constant (Ah − 1) or Polarization Resistance (Ω)
i Battery Current (A)
it Extracted Capacity (Ah)
i* Low Frequency Current Dynamics (A)
Q Maximum Battery Capacity (Ah)
A Exponential Voltage (V)
B Exponential Capacity (Ah)

The SOC is one of the most important parameter for batteries, but its definition presents many issues. In general, the SOC of a battery is defined as the ratio of its maximum usable capacity (Q(t)) to the nominal capacity (Qn). The nominal capacity is given by the manufacturer and represents the maximum amount of charge that can be stored in the battery. The SOC can be defined as [3]

$$SOC = 100\left(1 - \frac{1}{Q}\int_0^t i(t)\,dt\right) \tag{3}$$

where

SOC State of Charge (%)
Q Capacity of battery (Ah)
t Time (sec)
i(t) Battery current with time variant function

SOC = 0%, (Battery is empty)
SOC = 100%, (Battery is fully charged)

SOC is depending on charging and discharging rates of the battery, while SOC is low it means that a battery is discharging or low charge and SOC is high it means the battery is charged or low discharging. It is required the battery should maintain always high SOC and low discharge rate.

Table 1 Various EVT manufacturers used Li-Ion battery in 2016–17

Battery	Power (KW)	Manufacturer	Model	Motor	Type of vehicle
Li-Ion (33.5 KWh)	107	Ford	Focus electric	PMSM	HEV
Li-Ion (6.6 KWh)	83	Fiat	500e	PMSM	EV
Li-Ion (15.1 KWh)	30	Mahindra	Reva e2o plus rear	IM	EV
Li-Ion (60 KWh)	156.6	Chevrolet	Bolt	PMSM	EV
Li-Ion (50/75 KWh)	192	Tesla	S Y	PMSM	EV
Li-Ion (25.5 KWh)	120	Honda	–	PMSM	EV
Li-Ion (8.8 KWh)	90	Toyota	–	PMSM	HEV

3 Comparative Analysis of Various EVTmanufacturers

The usage of Li-Ion battery by various companies for EVT in the year 2016–17 is listed in Table 1.

The main purpose of Table 1 is to bring out in recent year all manufacturers are spreading world-wide, designing of an EV with Li-Ion battery as an energy storage device for various power ratings and different vehicle models. One of the problems associated with EVT is battery power density, SOC and charge cycles by comparing all existing batteries Li-Ion battery has shown greater performance [3]. The IM and PMSM drives have simulation modelling for EVT [16, 18, 20]. In this paper, the purposed Li-Ion battery (60 KWh) is modelled for EVT in MATLAB/Simulink.

4 Li-Ion Battery Performance Results

In the evaluation of performance analysis of Li-Ion battery for IM and PMSM drives of EVT applications, mainly three modes of operations are considered. Those operating modes are acceleration, deceleration, and variable speed operation. These modes are applied for the IM and PMSM having same operated voltage and rated speed. The reference speeds of those operating modes for time duration of 12 s are shown in Table 2.

From Table 2, in this paper only one operating mode was considered that is variable speed operation because the driving cycle of the vehicle is always different speed variations are present. During this operation the results of the Li-Ion battery are voltage, current, and SOC for IM and PMSM drives as shown in Figs. 2 and 3.

Table 2 Drive cycles of the various drives for EVT

Time (Sec)/Speed (RPM)		0	4	6	8	10	12
Operating modes	Acceleration	1500	1600	1650	1700	1750	1800
	Deceleration	1500	1450	1450	1200	1100	900
	Variable	1500	1300	1100	1500	1700	1500

From the Fig. 2 and, the Li-Ion battery results are observed that the SOC (%) of the battery is varied from 100 to 99.9975. The SOC of the battery for IM is compared with the using of PMSM drive is slowly varied with respect to time; values are as shown in Table 3. The Li-Ion battery current is discharged for IM is higher than PMSM drive and the resultant values are shown in Table 3 and the voltage of the battery is constant for both IM and PMSM drives.

From Figs. 4 and 5 observed that the battery power was delivered to the IM and PMSM drive is for variable speed operation, at the initial condition of the drives is needs high power option to reach the base speed than the running speed. It is varied with respect to the speed, speed is suddenly varied from lower to higher at

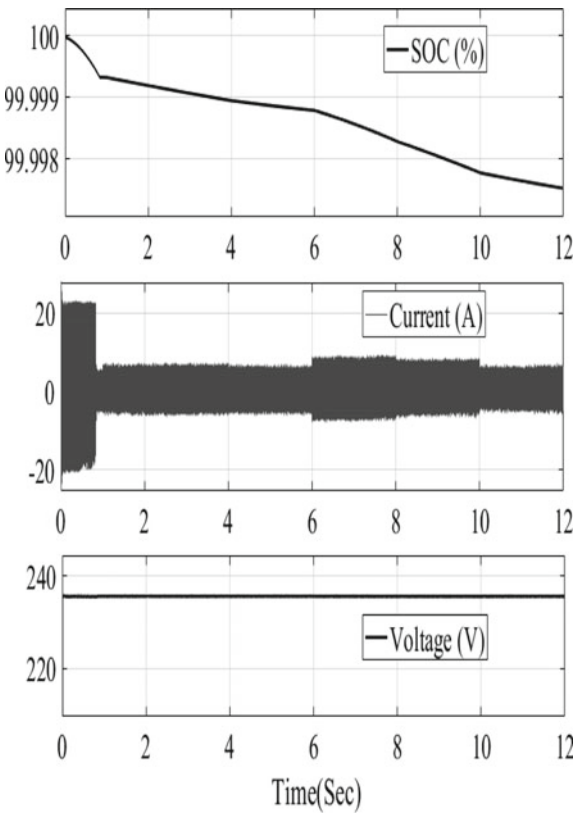

Fig. 2 Battery SOC, current, and voltage for IM

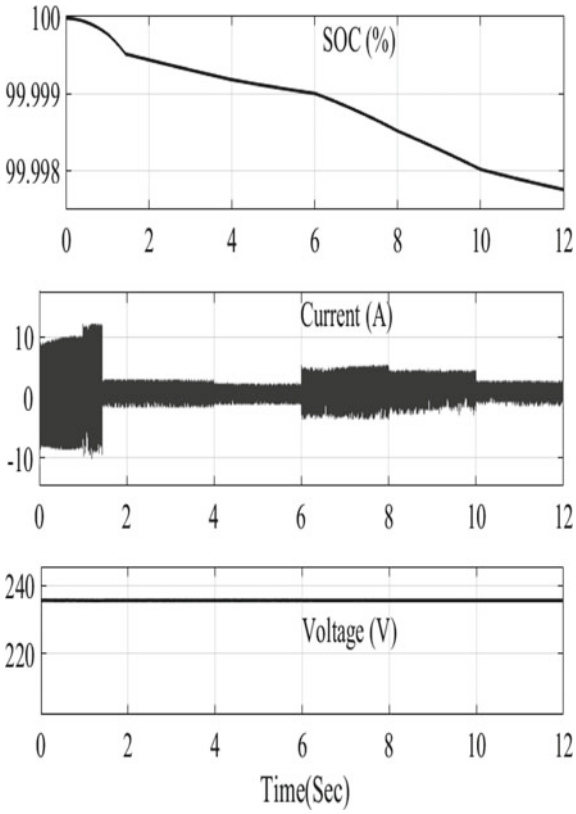

Fig. 3 Battery SOC, current, and voltage for PMSM

this condition it requires high power. The Li-Ion battery power is discharged for IM drive is higher than the PMSM drive and the resultant values are shown in Table 3.

In Table 3, battery voltage is constant for variable speed operation of the both IM and PMSM drives. In case of the battery current, the IM drive has higher value than

Table 3 Li-Ion battery simulation result values for IM and PMSM drives

S. No.	Parameters	IM	PMSM
1	Voltage (V)	235	235
2	Current (A)	Peak = 23 Low = 5.8 Constant = 7	Peak = 17 Low = 2.5 Constant = 4
3	SOC (%)	99.999 at 4 s Below 99.999 at 6 s Below 99.998 at 10 s	Above 99.999 at 4 s 99.999 at 6 s 99.998 at 10 s
4	Power (W)	Peak = 5400 Low = 1300 Constant = 1700	Peak = 2880 Low = 520 Constant = 750

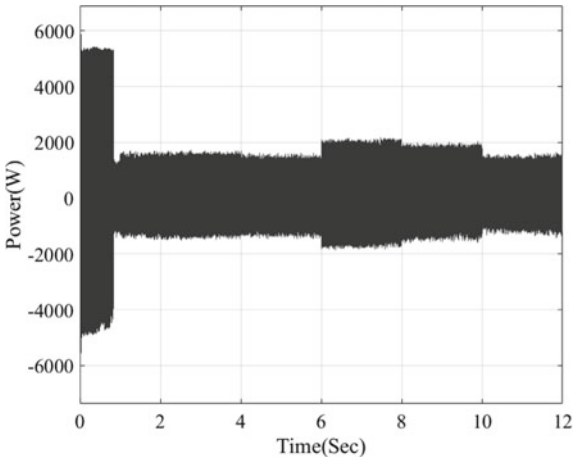

Fig. 4 Battery power for IM

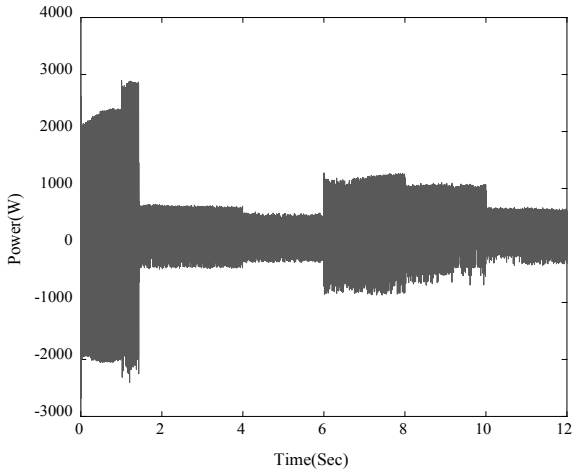

Fig. 5 Battery power for PMSM

the PMSM drive due to this battery is quickly discharged. When observed Figs. 2, 3 and Table 3, the battery SOC (%) for PMSM drive is slowly decreased than the IM drive due to huge amount of current was discharged. The power consumption of the battery is low for a PMSM drive as compared to IM drive due to this, the performance of the battery is high, and it increases the operating time of the PMSM drive.

The power characteristics of the IM and PMSM are shown in Fig. 6a, b. In Fig. 6a the power was increased from zero to maximum (3250 W) as the speed attaining it's rated value, and then after reaching the base speed of the motor the power is suddenly decreased to a minimum (450 W) due to change in current. For variable speed operation, it was varied in between 1000 and 450 W. But in case of PMSM drive the motor power is 5000 W at the base speed which is greater than IM drive

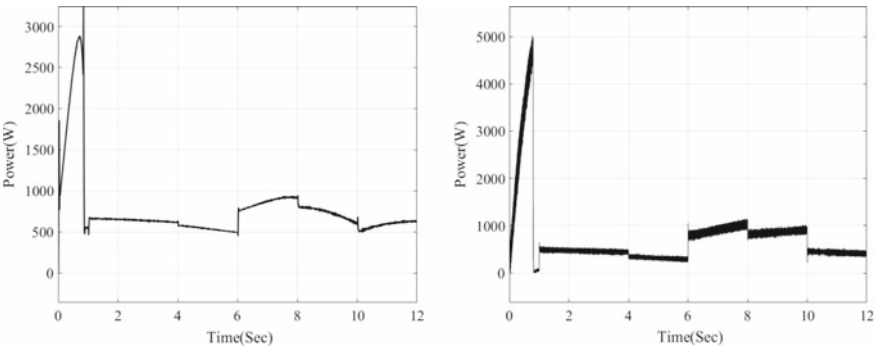

(a) Power of IM (b) Power of PMSM

Fig. 6 Motor power for variable speed operations

and it is linearly increased up to reaching base speed. It maintains the constant power region and linearly increasing/decreasing power for different speed operations.

5 Conclusion

The simulation results of the Li-Ion battery for AC drives, such as IM and PMSM to the different operating modes are discussed. And the battery performance of the result analysis for variable speed operation was explained. And also Investigated adopted Li-Ion battery parameters such as voltage, current, SOC, and power to the PMSM drive was suitable to the EVT. Because of less power consumption of PMSM drive and Li-Ion battery, and also it has regenerative operation while battery was charged, then battery performance will be increased. But Li-Ion battery has low power density; it is the most challenging area for future researchers to improve the power density of the energy storage device for EVT.

References

1. Khaligh A, Li Z (2010) Battery, ultra-capacitor, fuel cell, and hybrid energy storage systems for electric, hybrid electric, fuel cell, and plug-in hybrid electric vehicles: state of the art. IEEE Trans Veh Technol 59(6)
2. Larminie J, Lowry J (authorized reprint) Electric vehicle technology explained. Second edn. Wiley, India Pvt. Ltd., pp 4435–36/7
3. Dr. Mondru Chiranjeevi D,. Ashok Kumar V, Dr. Kiranmayi R (2017) Batteries comparative analysis and their dynamic model for electric vehicular technology. Int J Pure Appl Math 114(07):629–637. ISSN: 1311-8080 (printed version); ISSN: 1314-3395 (on-line version)
4. Burke AF (2007) Batteries and ultracapacitors in electric, hybrid, and fuel cell vehicles. IEEE 95(4):806–820

5. Wijewardana1 S (2014) New Dynamic battery model for hybrid vehicles. ISO 9001:2008 Certif J. 4. www.ijetae.com, ISSN 2250-2459
6. Zhou Y, Li X (2015) Overview of lithium-ion battery SOC estimation. In: Proceeding of the 2015 IEEE international conference on information and automation, Lijiang, China
7. Trembla O, Dessaint L-A (2009) Experimental validation of a battery dynamic model for EV applications. World Electric Veh J 3:13–16
8. Zhu C, Li X, Song L, Xiang L, Development of a theoretically based thermal model for lithium ion battery pack. J Power Sources 223:155–164
9. Kumar Lalit, Jain Shailendra (2014) Electric propulsion system for electric vehicular technology: a review. Renew Sustain Energy Rev 29:924–940
10. Hoelscher D, Scores A, Gao Y, Ehsani M (2006) Hybridized electric energy storage systems for hybrid electric vehicles. IEEE vehicle power propulsion conference, pp 1–6
11. De Santiago Juan et al (2012) Electrical motor drivelines in commercial all-electric vehicles: a review. IEEE Trans Veh Technol 61(2):475–484
12. Nanda G, Kar NC (2006) A survey and comparison of characteristics of motor drives used in electric vehicles. CCECE'06. Canadian conference on electrical and computer engineering 2006. IEEE
13. Zhu ZQ, Howe David (2007) Electrical machines and drives for electric, hybrid, and fuel cell vehicles. Proc IEEE 95(4):746–765
14. Zeraoulia Mounir, Benbouzid Mohamed El Hachemi, Diallo Demba (2006) Electric motor drive selection issues for HEV propulsion systems: a comparative study. IEEE Trans Veh Technol 55(6):1756–1764
15. Zhu ZQ, Chan CC (2008) Electrical machine topologies and technologies for electric, hybrid, and fuel cell vehicles. In: VPPC'08. IEEE. Vehicle power and propulsion conference 2008. IEEE
16. West JGW (1993) DC, induction, reluctance and PM motors for electric vehicles. In: IEE colloquium on motors and drives for battery powered propulsion, pp 1/1–111
17. Prasetyo HF et al (2016) Controls of BLDC motors in electric vehicle testing simulator. 2016 6th international conference on system engineering and technology (ICSET). IEEE
18. El-Sharkawi MA (2000) fundamental of electric drives. Brooks/Cole, Pacific Grove
19. Dr. Mondru Chiranjeevi D, Ashok Kumar V, Dr. Kiranmayi R (2017) Mathematical analysis & modeling of Li-Ion battery with PMSM based plug-in electric vehicles. In: IEEE international conference, pp 217–221
20. Krause P et al (2013) Analysis of electric machinery and drive systems. vol. 75. Wiley
21. Yildirim M, Polat M, Kürüm H (2014) A survey on comparison of electric motor types and drives used for electric vehicles. In: 2014 16th international power electronics and motion control conference and exposition (PEMC). IEEE
22. Mounir Z, Benbouzid EH, Diallo D (2006) Electric motor drive selection issues for HEV propulsion systems: a comparative study, IEEE 55(6):1756–1764

Fuzzy Based Fractional Order Integer Controller for LFC of Multi Area Deregulated Power System

Kurakula Vimala Kumar and V. Ganesh

Abstract Fractional order PI Controller studies has been highlighted recently and it accepted as a best fit to conventional IOPI Controller. Still, FOPI Controller brings more tuning parameters into the restructured power system network. To analyze the potential of proposed system, FOFPI (Fuzzy + FOPI) Controller is placed to resolve the Load Frequency Control problem in a power system. The fuzzy logic control is non-linear and adaptive nature and this technique relies based on qualitative control rules and membership functions. Dynamic performance of the system is examined by area control error and error criteria. The FOFPI Controller designed in MATLAB or Simulink for the LFC problem shows better responses.

Keywords FOFPI controller · FOPI controller · Fuzzy logic controller · IOPI controller

1 Introduction

Electrical form of energy is a medium between same of energy sources or different energy sources. Due to even tariff schemes and unethical system direction leads to many vertical integrated utility services moved to restructure their power sector units under disappointment from irrational blocking sectors [1]. A DISCO in a power system network under deregulated condition has a freedom to have contracts with any GENCO (it may be present in other area). All the communication contracts and power transactions are done through an entity called Independent System Operator (ISO). This non-discriminatory entity ISO will be responsible to all auxiliary equipments under bilateral contracts.

K. Vimala Kumar (✉) · V. Ganesh
Research Scholar, JNT University Anantapur, Anantapur, India
e-mail: princevimal81@gmail.com

V. Ganesh
e-mail: ganivg@gmail.com

Department of Electrical and Electronics Engineering, JNTUA College of Engineering Pulivendula, Pulivendula, Andhra Pradesh 516390, India

© Springer Nature Singapore Pte Ltd. 2020

T. Hitendra Sarma et al. (eds.), *Emerging Trends in Electrical, Communications, and Information Technologies*, Lecture Notes in Electrical Engineering 569,
https://doi.org/10.1007/978-981-13-8942-9_20

All the appliances which utilize electric power one must operate at constant frequency. Standard frequency is analyzed as the nature of the provided power to consumers and primary indication of healthy action of system. To enact frequency as constant major factors were scheduled and actual tie-line power and load-generation values. A large change in frequency causes power system network operate in unstable region, it is necessary to make frequency constant load frequency at constant value is maintained by placing AGC devices [2], if there is no AGC in power system network [3]. It will face many problems even though it is properly designed. Integer order controllers are placed to get good response decrease the steady state error and perturbations [4].

Classical IO Controllers were not efficient to get good dynamic performance characteristics for different load cases and they cause changes in the interconnected power system [5–8]. FOPI Controller has one extra tuning slot than IOPI Controller to improve stability and output response of system. However, after the new inventions in fuzzy theory provided to control and modeling of the non-linearity and intricacy of the system to enhance system performance.

1.1 Deregulated Power System

Under deregulated environment condition power system network important objectives are network communications with appropriate values for all controlling areas and frequency retrieval. In deregulated power system, VIU models emerged as various branches namely GENCOs, TRANSCOs, and DISCOs. A DISCO in a power system network under deregulated condition has a freedom to have contracts with any GENCO (it may be present in other area) [1, 9, 10]. All of the contracts involved between GENCOs and DISCOs are anticipated by DPM [1] (DISCO Participation Matrix) (Fig. 1).

$$DPM = \begin{bmatrix} cpf_{11} & cpf_{12} & cpf_{13} & cpf_{14} \\ cpf_{21} & cpf_{22} & cpf_{23} & cpf_{24} \\ cpf_{31} & cpf_{32} & cpf_{33} & cpf_{34} \\ cpf_{41} & cpf_{42} & cpf_{43} & cpf_{44} \end{bmatrix}$$

In DPM number of columns and rows are equivalent to the total number of discoms and gencos in whole power system network. Elements present in a DPM resembles power contracts between discom and respective genco i.e., from where it must be supplied. The cpf_{xy} is the contract participation factor among xth Genco and yth Discom. The cpf_{xy} coincide with the total load power contracted by the discom-m from a genco-y. All elements sum in a column of DPM is unity.

$$\sum_{m} cpf_{xy} = 1 \tag{1}$$

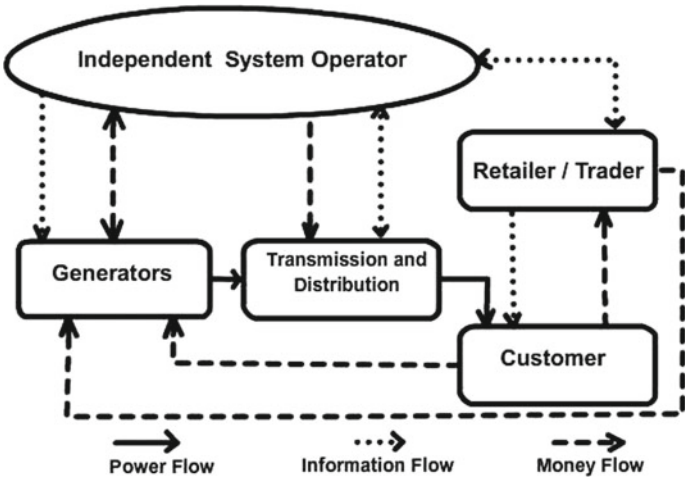

Fig. 1 Deregulated power system

where cpf_{xy} = xth genco Contract Participation Matrix in order to supply the load of yth dicom.

This work is for a sample two-area system in a competitive environment. Each area is operating with two Discoms and two Gencos. Consider genco1 and genco2 are generation companies, discom1 and discom2 are distribution companies in control area1. Genco3 and genco4 are generation companies, discom3 and discom4 are distribution companies in control area2. At any instant change in load presented in this restructured power system, only the specific genco assigned for that variation in load has to supply it to discom.

In this process, information signals are useful in order to supply the load demanded from the GENCOs to the DISCOs. These signals were acquired by 'transaction tags', in case of OASIS system in the US and they have the information regarding "which DISCO has to act in order to fulfill the load supplied by which GENCO".

The planned steady state power over the tie line is as follows [11].

$$\begin{aligned}\Delta P_{tie1-2:Schedule} = {} & (\text{DISCOMs Load Demand of in CA-II from GENCOs in Area-I}) \\ & - (\text{DISCOMs Load Demand of in CA-I from GENCOs in CA-II})\end{aligned}$$

Actual power flow on line is given by

$$\Delta P_{tie1-2actual} = \Delta(2\Pi T_{12}/S)(\Delta f_1 - \Delta f_2) \tag{2}$$

Deviated tie-line power on line is as below

$$\Delta P_{tie1-2error} = \Delta P_{tie1-2actual} - \Delta P_{tie1-2schedula}$$

$\Delta P_{tie1\text{-}2,\,error}$ is nullified in the steady-state condition when actual line power flow attains the scheduled line power flow.

The ACE for two area system is as follows [2]

$$\begin{aligned} ACE_1 &= B_1 \Delta f_1 + \Delta P_{tie1-2error} \\ ACE_2 &= B_2 \Delta f_2 + \Delta P_{tyie2-1error} \end{aligned} \tag{3}$$

generally dynamic behavior of the system control model is assessed by IAE, ISE, ITSE, and ITAE error criteria.

2 Fractional Calculus

Fractional order calculus method explains real things more promptly than the integer order [12]. The usual differential-integrator defines non-integer order operator $aD_t^{-\alpha}$ as follows [13]

$${}_aD^{\alpha} = \begin{cases} \frac{d^{\alpha}}{dt^{\alpha}} & \alpha > 0 \\ 1 & \alpha = 0 \\ \int_a^t (dt)^{-\alpha} & \alpha < 0 \end{cases} \tag{4}$$

Riemann-Liouville definition to Fraction Order differentiation is generally explained as

$$a\partial_t^{\beta} f(t) = \frac{d^n}{dt^n}\left[{}_a\partial_t^{-(n-\beta)} f(t)\right] = \frac{1}{\Gamma(n-\beta)}\frac{d^n}{dt^n}\left[\int_{\alpha}^{t} \frac{f(t)}{(t-\tau)^{\beta-n+1}} d\tau\right] \tag{5}$$

Fractional-order integration is defined by Caputo's

$${}_0D^{\gamma} = \frac{1}{\Gamma(-\gamma)}\int_0^t \frac{y(\tau)}{(t-\tau)^{1+\gamma}} d\tau, \gamma < 0 \tag{6}$$

Transfer functions of Fractional order and integer order systems have nearly similar performance. This work presents fractional order elements justified with Oustaloup's recursive filter. It could be stated that filter approximation is viable in the frequency range (ω_b, ω_h) [14].

$$K(s) = \lim_{N\to\infty} K_N(s) = \lim_{N\to\infty} \prod_{K=-N}^{N} \frac{1 + s/\omega_k'}{1 + s/\omega_k} \tag{7}$$

The recursive distribution to the pole and zero having rank k can be given by

$$\omega_k' = \left(\frac{d\omega b}{b}\right)^{\frac{\alpha-2k}{2N+1}}, \quad \omega_k = \left(\frac{d\omega h}{d}\right)^{\frac{\alpha-2k}{2N+1}} \tag{8}$$

2.1 Fractional-Order Fuzzy PI Controller

The Fractional Order PID controller action is defined by integro-differential equation as [13]

$$G_{FFPID}(s) = K_p + K_i s^{-\lambda} + K_d s^{\mu} \tag{9}$$

If $\lambda = 0$–1 and $\mu = 0$ in controller transfer function FOPI controller is obtained [15].

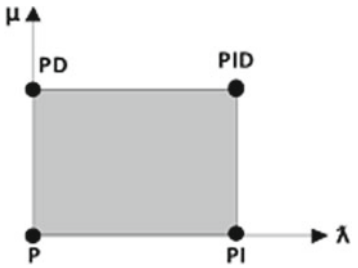

By fetching $\mu = 0$, λ value is in between 0 and 1 and added fuzzy gives FOFPI Controller. FOFPI can be configured with more degree of state in the control area and thus, upgraded the performance of classical PI.

3 Fuzzy Logic Controller

The fuzzy logic idea was modernized at the California University by the Prof. Dr. Lotfi Zadeh, in Berkeley as a control approach [16]. The simple rule of Fuzzy Logic is on the basis of "If and Then" and this logic constitute in between 0 and 1. The Fuzzy Logic Controller works same way as human by adjusting the system input signal based on changes in output approach consists of four elements i.e., Fuzzification, Interference system, Rule Base, Defuzzification [17]. Fuzzification is an conversion process of crisp values to fuzzy values. This fuzzy value carries unpredictable in it. This value is denoted by membership functions ($\mu_{\tilde{A}}(x)$). Fuzzy control loop consists of fuzzy reasoning and rule base to give decision. Knowledge base defines the parameters and variables of the fuzzy set. Defuzzification is the process of converting fuzzy

values to crisp value. It is clarifying fuzzy set membership degree into decisions or real values [18–20].

The Fuzzy Logic based LFC is designed with two inputs one is area control error (ACE), and second one is differential of area control error (ACE). Membership functions ($\mu_{\tilde{A}}(x)$) [21] are used to narrate the linguistic variables. If-Then statement is used for designing the control rules. The system is developed in the actual system to enhance the nature of the system [22]. For LFC issue the inputs of the Fuzzy logic control are e and Δ_e and the outputs of the Fuzzy logic are K_P and K_i are figured out by the rule base in Fuzzy Logic controller [23]. The fuzzy membership Functions are (Figs. 2, 3, 4, 5 and 6).

Rule base based on the IF-THEN rule. If e is NB and Delta_e is NB then K_P is PB and K_i is NB. The present system has 25 rules.

The two parameters of Fractional Order PI arithmetic will influence stability, response speed, overshoot and steady precision of the system [22]. In the process operation system, the auto modification rules for e, and Δ_e. We make some control-rule figures in the following tables according to the setting principle and the simulation test. It needs you to transform the output energy of fuzzy controller into accurate quantity after the design of control rules.. The Tables 1 and 2 are showing the fuzzy control rules. If the e and Δ_e is negative big, then the Kp is positive big and Ki is negative big. It avoids the larger overshoots. The rules are made by using the IF and Then rule. And Method = 'prod' OrMethod = 'probor', ImpMethod = 'prod', AggMethod = 'sum', DefuzzMethod = 'centroid'. The file is saved and loaded into workspace when you want to simulate the module.

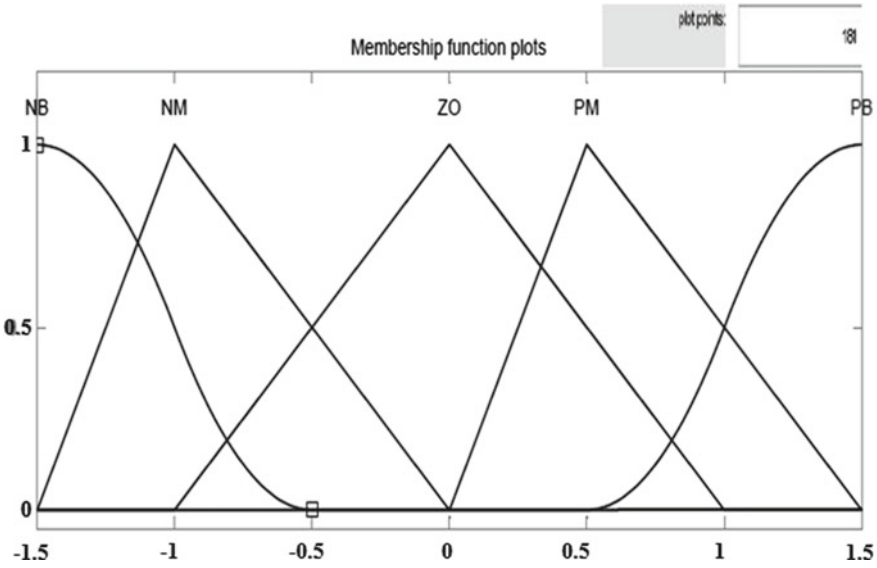

Fig. 2 MSF for input1 (e)

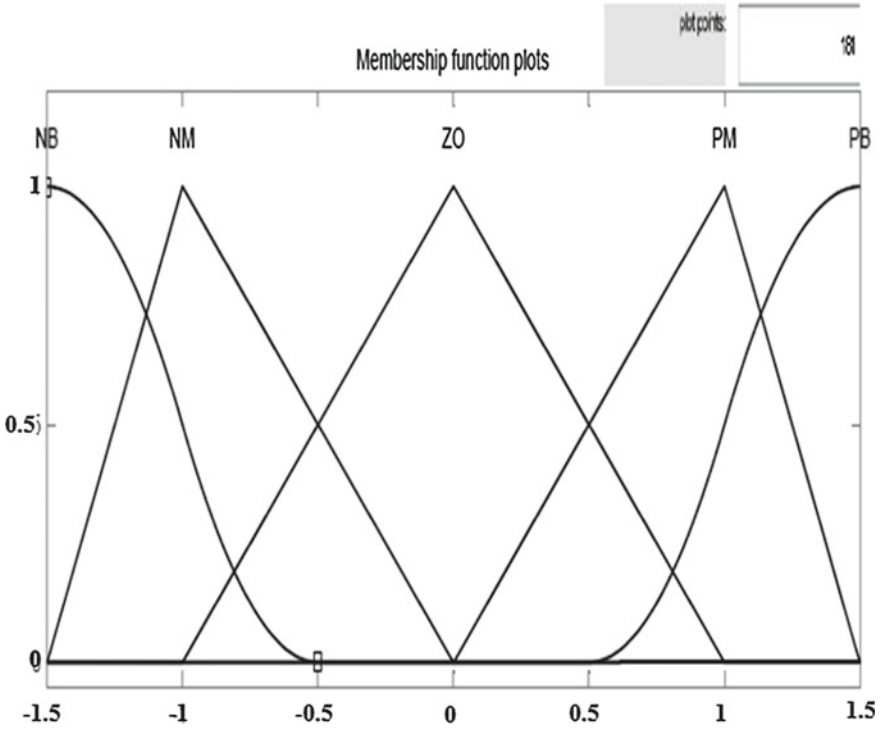

Fig. 3 MSF for input2 (Δ_e)

4 Simulation Results

The simulation results were carried out for thermal-thermal system and hydro-thermal system. In the absence of controller the system causes perturbations and they are sustained for long time duration and error was present in the output. By introducing IOPI and FOPI controllers oscillations can be reduced to some extent. but in the event when FOFPI controller is present the oscillations can be reduced to larger extent than IOPI and FOPI controller cases. The Fluctuations in each area frequency, tie-line power variations, real power generation and turbine power generation are shown in figures.

4.1 Thermal-Thermal Power System

The simulations are performed under possible bilateral transaction scenario. DISCOs in one CA can transact with GENCOs in other CA and vice versa. In each case DISCOMs drawing a power of 0.1 Pu MW.

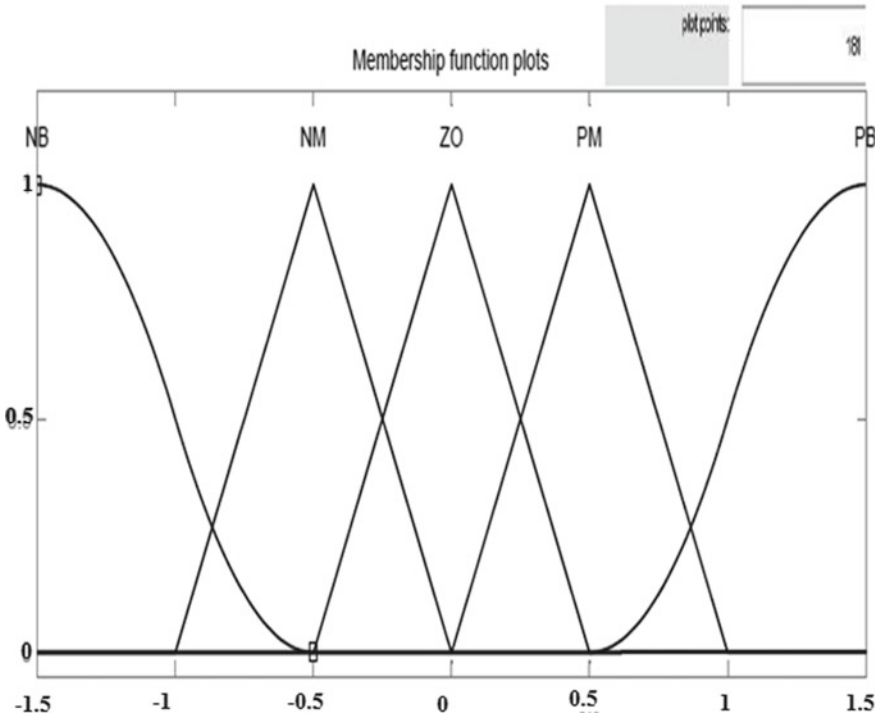

Fig. 4 MSF for output1 (K_P)

in AGC the GENCOs participation based on the following *a p f's*

$$\mathrm{apf}_1 = 0.6, \quad \mathrm{apf}_2 = 1 - \mathrm{apf}_1 = 0.4$$
$$\mathrm{apf}_3 = 0.6, \quad \mathrm{apf}_4 = 1 - \mathrm{apf}_3 = 0.4$$

In two area thermal-thermal power system

$$DPM = \begin{bmatrix} 0.5 & 0.3 & 0.1 & 0.3 \\ 0.1 & 0.2 & 0.6 & 0.2 \\ 0.4 & 0.0 & 0.2 & 0.1 \\ 0.0 & 0.5 & 0.1 & 0.4 \end{bmatrix}$$

$$\Delta P_{mx} = \sum_{x}^{y} cpf_{xy} \Delta P_{Ly}$$

$$\Delta P_{m1} = 0.5(0.1) + 0.3(0.1) + 0.1(0.1) + 0.3(0.1) = 0.12 \,\mathrm{pu\,MW}$$
$$\Delta \mathrm{P_{m2}} = 0.11 \,\mathrm{pu\,MW};\ \Delta P_{m3} = 0.07 \,\mathrm{pu\,MW};\ \Delta P_{m4} = 0.1 \,\mathrm{pu\,MW};$$

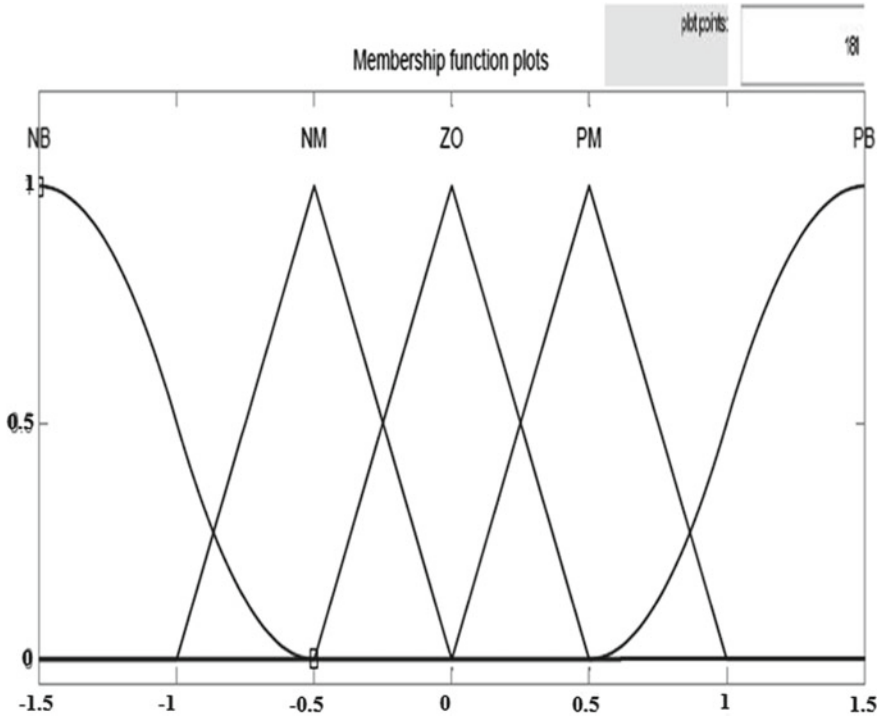

Fig. 5 MSF for output2 (K_i)

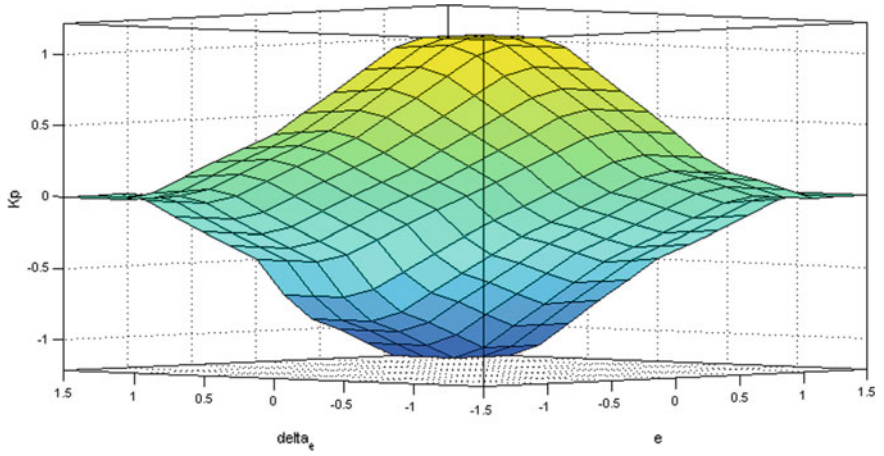

Fig. 6 Fuzzy surface view

Table 1 Rule base for output1 K_P

e	Δ_e				
	NB	NM	ZO	PM	PB
NB	PB	PB	PM	ZO	ZO
NM	PB	PB	PM	ZO	ZO
ZO	PM	PM	ZO	NM	NM
PM	ZO	ZO	NM	NB	NB
PB	ZO	ZO	NM	NB	NB

Table 2 Rule base for output2 K_i

e	Δ_e				
	NB	NM	ZO	PM	PB
NB	NB	NB	NM	ZO	ZO
NM	NB	NM	NM	ZO	ZO
ZO	NM	NM	ZO	PM	PM
PM	ZO	ZO	PM	PB	PB
PB	ZO	ZO	PM	PB	PB

From the Figs. 7 and 8, In Thermal-Thermal Power System in case of without controller large overshoots and no settling time in both control areas, with PI Controller overshoots and settling time are 0.1652 and 6.8 s in control area 1 and 0.3084 and 10.8 s in area 2. This transient behaviour is further reduced by Fractional Order PI control methodology, overshoots and settling time are 0.1202 and 10.2 s in Control area 1, and 0.1862 and 10.8 s in Control area 2. This transient behaviour is reduced by proposed Fuzzy based Fractional Order PI control methodology, overshoots and

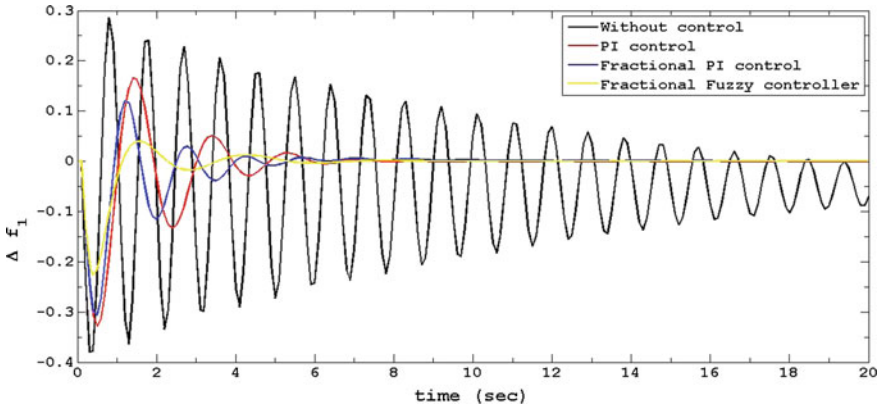

Fig. 7 Δf of CA-I

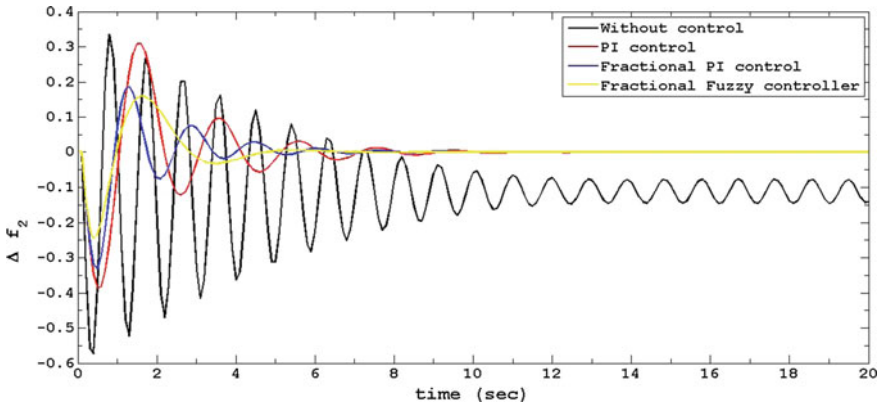

Fig. 8 Δf of CA-II

settling time are 0.0398 and 8.2 s in Control area 1, and 0.1591 and 6.4 s in Control area 2.

From the Figs. 9, 10, 11 and 12, in Thermal-Thermal Power System that change in power generation at governor in case of without controller large overshoots and no settling time in both control areas, with PI Controller overshoots and settling time are 0.2872 and 7 s for governor 1, 0.2574 and 7 s for governor 2 in control area 1 and 0.3059 and 11 s for governor 3, 0.2936 and 9 s for governor 4 in control area 2. This transient behaviour is further reduced Fractional Order PI control methodology, overshoots and settling time are 0.3160 and 6 s for governor 1, 0.2746 and 6.8 s for governor 2 in control area 1 and 0.3307 and 10.2 s for governor 3, 0.3053 and 8.8 s for governor 4 in control area 2. This transient behaviour is further reduced by proposed Fuzzy based Fractional Order PI control methodology, overshoots and settling time are 0.2820 and 3 s for governor 1, 0.2271 and 2.8 s for governor 2 in

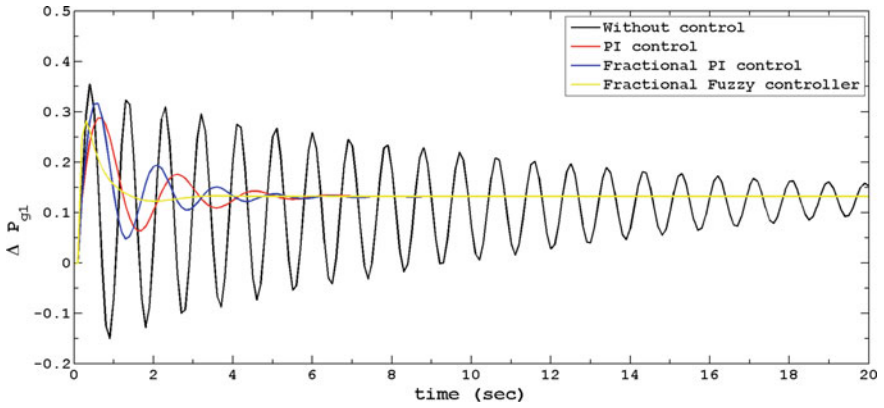

Fig. 9 ΔP_{g1}

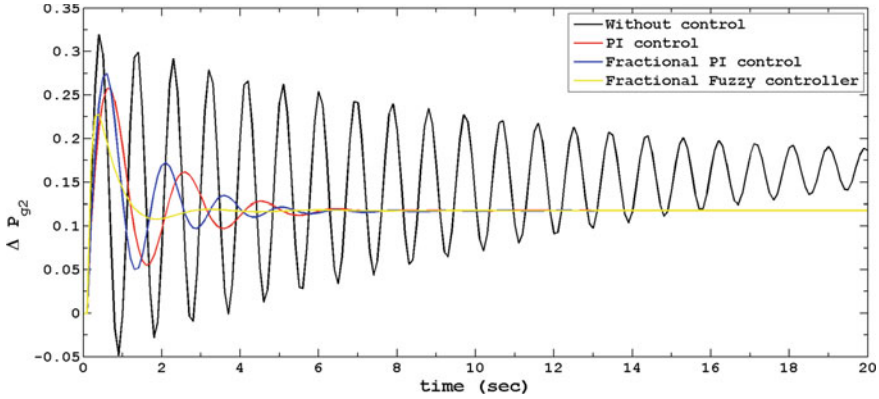

Fig. 10 ΔP_{g2}

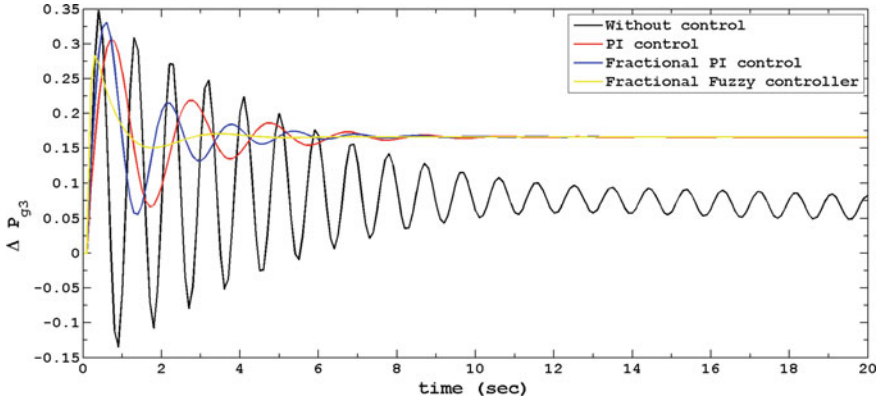

Fig. 11 ΔP_{g3}

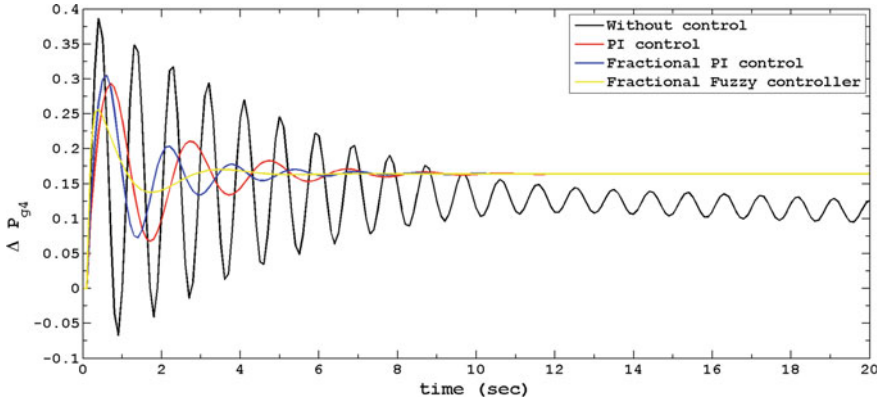

Fig. 12 ΔP_{g4}

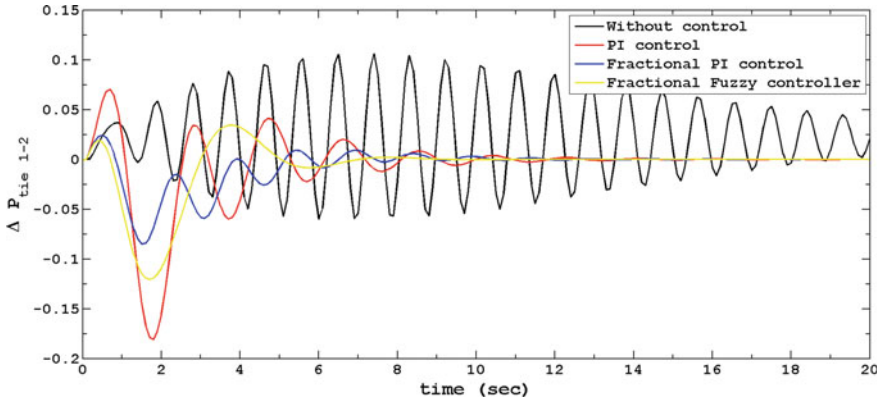

Fig. 13 $\Delta P_{tie\ 1\text{-}2}$

control area 1 and 0.2834 and 6 s for governor 3, 0.2563 and 6.2 s for governor 4 in control area 2.

From the Fig. 13, in Thermal-Thermal Power System that change in power at tie-line in case of without controller large overshoots and no settling time in both control areas, with PI Controller overshoots and settling time are 0.0703 and 14.4 s. This transient behaviour is further reduced by Fractional Order PI control methodology, overshoots and settling time are 0.0243 and 15.2 s. This transient behaviour is further reduced by proposed Fuzzy based Fractional Order PI control methodology, overshoots and settling time are 0.0344 and 11 s.

From the Figs. 14, 15, 16 and 17, in Thermal-Thermal Power System that change in power generation at turbine in case of without controller large overshoots and no settling time in both control areas, with PI Controller overshoots and settling time are 0.2374 and 6.4 s for turbine 1, 0.2149 and 6.4 s for turbine 2 in control area 1 and 0.2590 and 10.4 s for turbine 3, 0.2443 and 10.4 s for turbine 4 in control area 2. This

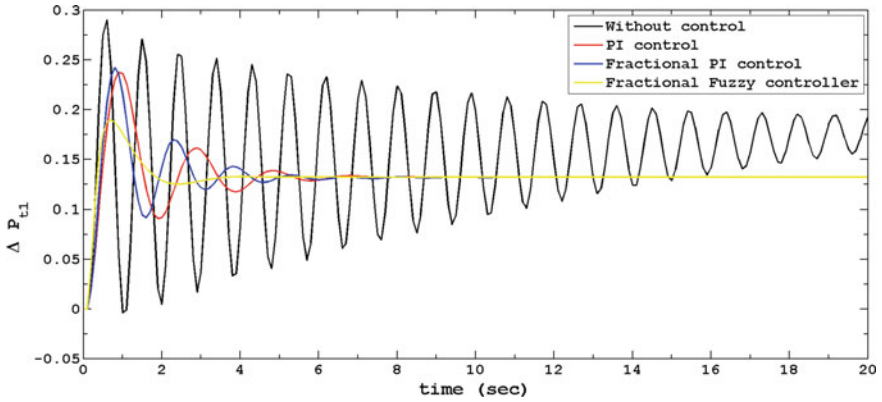

Fig. 14 ΔP_{t1}

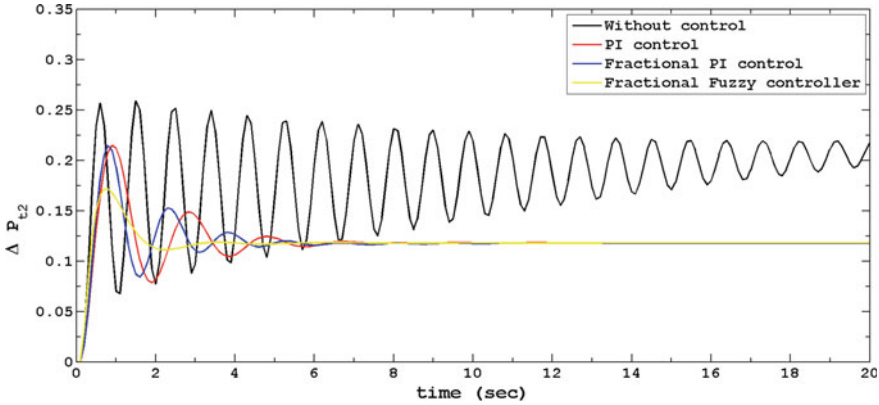

Fig. 15 ΔP_{t2}

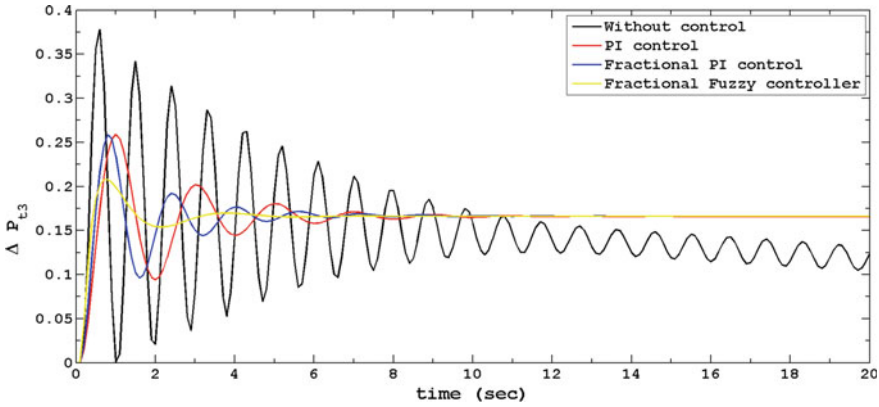

Fig. 16 ΔP_{t3}

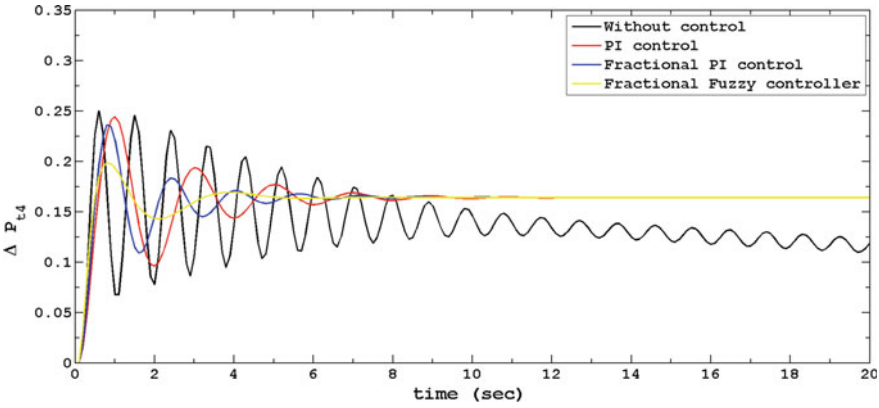

Fig. 17 ΔP_{t4}

transient behaviour is further reduced by Fractional Order PI control methodology, overshoots and settling time are 0.2419 and 7.6 s for turbine 1, 0.2146 and 9 s for turbine 2 in control area 1 and 0.2585 and 7.2 s for turbine 3, 0.2360 and 7.4 s for turbine 4 in control area 2. This transient behaviour is further reduced by proposed Fuzzy based Fractional Order PI control methodology, overshoots and settling time are 0.1895 and 3.2 s for turbine 1, 0.1715 and 3.2 s for turbine 2 in control area 1 and 0.2078 and 6.2 s for turbine 3, 0.1955 and 6 s for turbine 4 in control area 2.

4.2 Hydro-thermal Power System

The simulations are performed under one possible bilateral transaction scenario. In bilateral transaction scenario DISCOs in one CA can transact with GENCOs in other CA and vice versa. In each case DISCOMs drawing a power of 0.1 Pu MW.

$$DPM = \begin{bmatrix} 0.5 & 0.3 & 0.1 & 0.3 \\ 0.1 & 0.2 & 0.6 & 0.2 \\ 0.4 & 0.0 & 0.2 & 0.1 \\ 0.0 & 0.5 & 0.1 & 0.4 \end{bmatrix}$$

$$\Delta P_{mx} = \sum_{x}^{y} cpf_{xy} \Delta P_{Ly}$$

$$\Delta P_{m1} = 0.5(0.1) + 0.3(0.1) + 0.1(0.1) + 0.3(0.1) = 0.12 \text{ pu MW}$$

$$\Delta \text{P}_{\text{m2}} = 0.11 \text{ pu MW}; \ \Delta P_{m3} = 0.07 \text{ pu MW}; \ \Delta P_{m4} = 0.1 \text{ pu MW};$$

From the Figs. 18 and 19, In Hydro-Thermal Power System in case of without

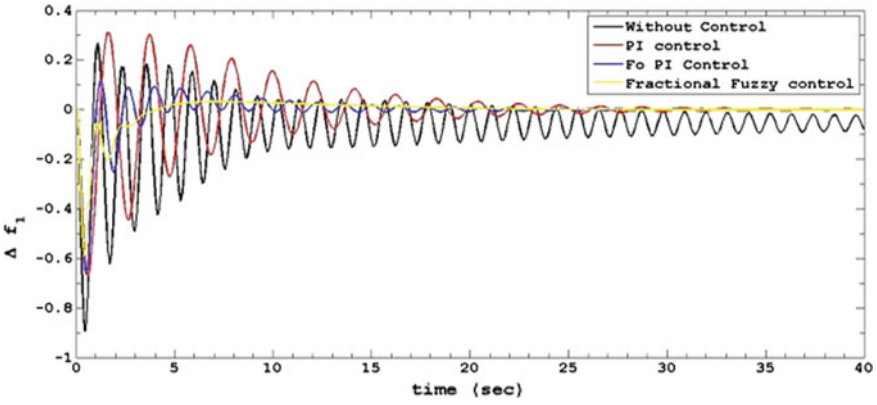

Fig. 18 Δf of CA-I

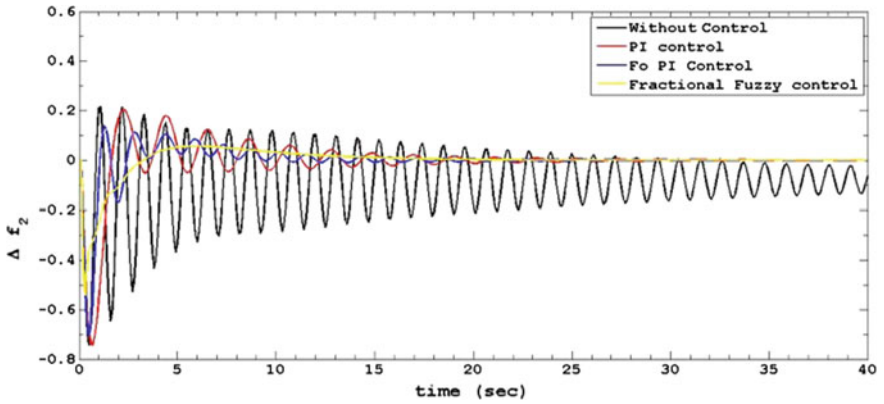

Fig. 19 Δf of CA-II

controller large overshoots and no settling time in both control areas, with PI Controller overshoots and settling time are 0.3121 and 37 s in control area 1 and 0.2046 and 35 s in area 2. This transient behaviour is further reduced by Fractional Order PI control methodology, overshoots and settling time are 0.1148 and 35 s in Control area 1, and 0.1385 and 35 s in Control area 2. This transient behaviour is further reduced by proposed Fuzzy based Fractional Order PI control methodology, overshoots and settling time are 0.0319 and 19 s in Control area 1, and 0.0569 and 18.6 s in Control area 2.

From the Figs. 20, 21, 22 and 23, in Hydro-Thermal Power System that change in power generation at governor in case of without controller large overshoots and no settling time in both control areas, with PI Controller overshoots and settling time are 0.5500 and 32 s for governor 1, 0.1425 and 36 s for governor 2 in control area 1 and 0.4275 and 24 s for governor 3, 0.1671 and 20 s for governor 4 in control area 2. This

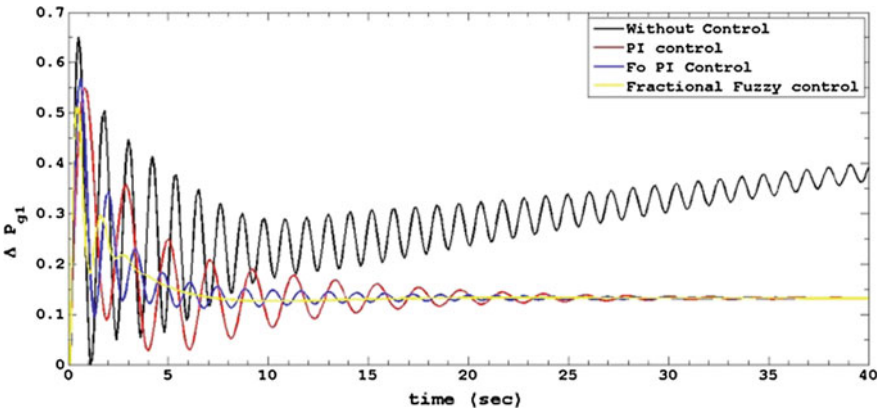

Fig. 20 ΔP_{g1}

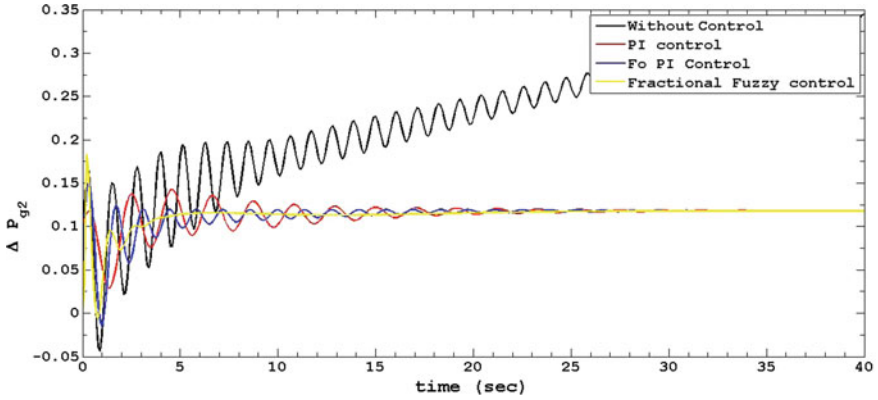

Fig. 21 ΔP_{g2}

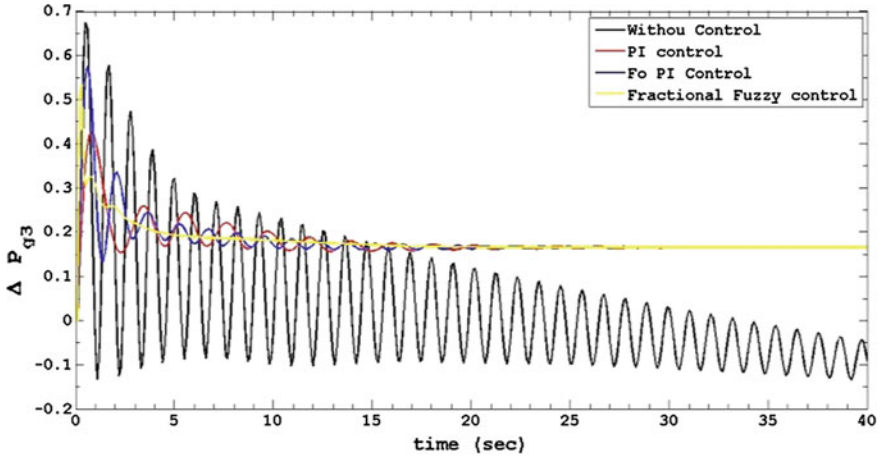

Fig. 22 ΔP_{g3}

transient behaviour is further reduced by Fractional Order PI control methodology, overshoots and settling time are 0.5678 and 25 s for governor 1, 0.1534 and 23 s for governor 2 in control area 1 and 0.5765 and 21 s for governor 3, 0.1659 and 40 s for governor 4 in control area 2. This transient behaviour is further reduced by proposed Fuzzy based Fractional Order PI control methodology, overshoots and settling time are 0.5099 and 18.2 s for governor 1, 0.1830 and 18.2 s for governor 2 in control area 1 and 0.5352 and 18.6 s for governor 3, 0.3209 and 18.4 s for governor 4 in control area 2.

From the Fig. 24, in Hydro-Thermal Power System that change in power at tie-line in case of without controller large overshoots and no settling time in both control areas, with PI Controller overshoots and settling time are 0.3998 and 37 s. This transient behaviour is further reduced by Fractional Order PI control methodology,

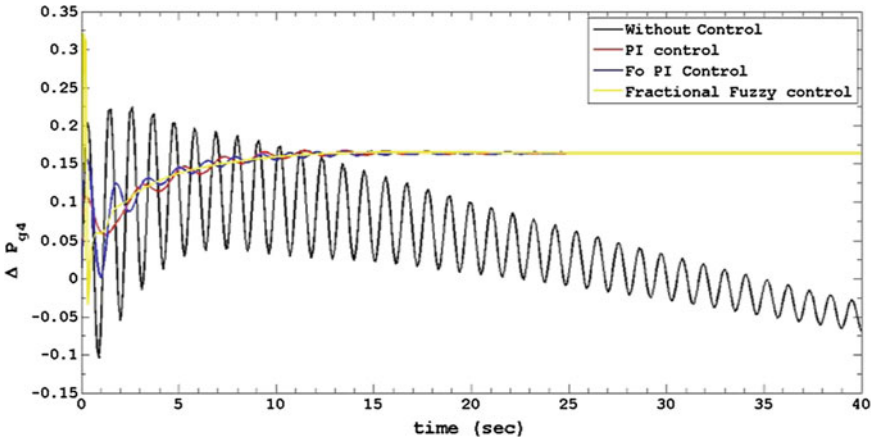

Fig. 23 ΔP_{g4}

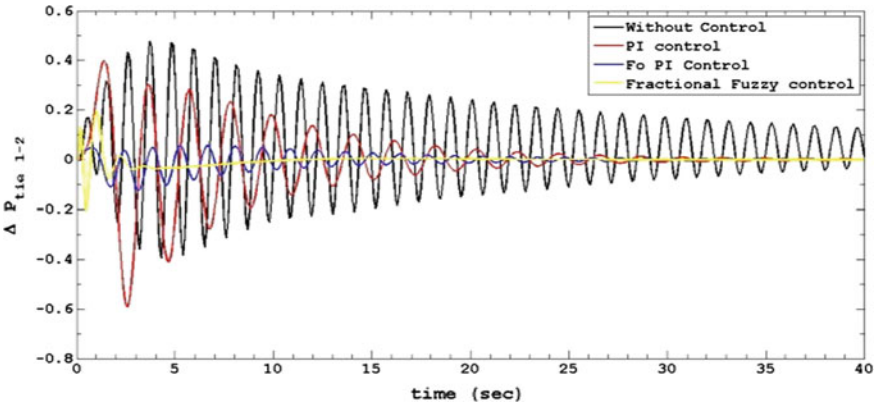

Fig. 24 $\Delta P_{tie\ 1\text{-}2}$

overshoots and settling time are 0.0555 and 40 s. This transient behaviour is further reduced by proposed fuzzy based Fractional Order PI control methodology, overshoots and settling time are 0.1967 and 18.4 s.

From the Figs. 25, 26, 27 and 28, in Hydro-Thermal Power System that change in power generation at turbine in case of without controller large overshoots and no settling time in both control areas, with PI Controller overshoots and settling time are 0.4708 and 34 s for turbine 1, 0.1595 and 34 s for turbine 2 in control area 1 and 0.3769 and 27 s for turbine 3, 0.1689 and 24 s for turbine 4 in control area 2. This transient behaviour is further reduced by Fractional Order PI control methodology,

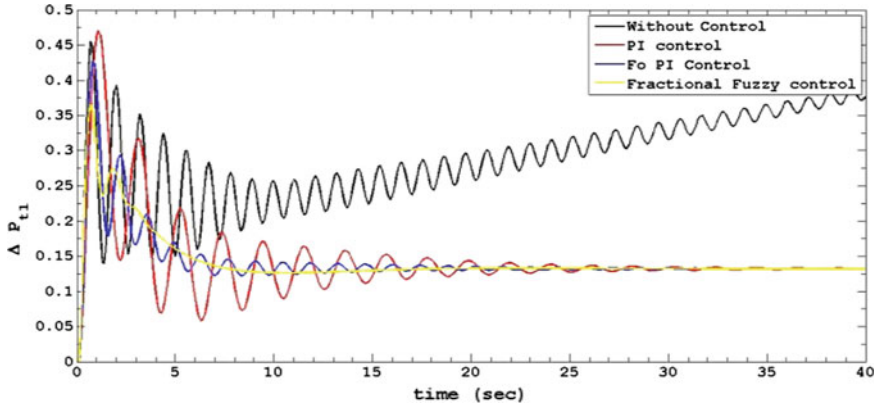

Fig. 25 ΔP_{t1}

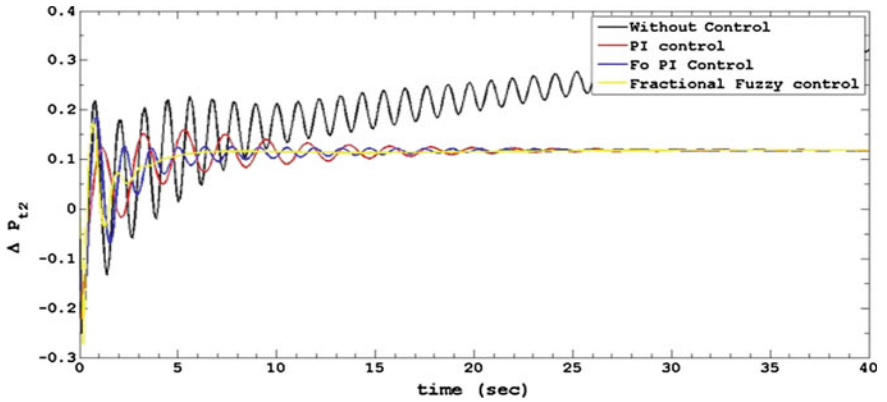

Fig. 26 ΔP_{t2}

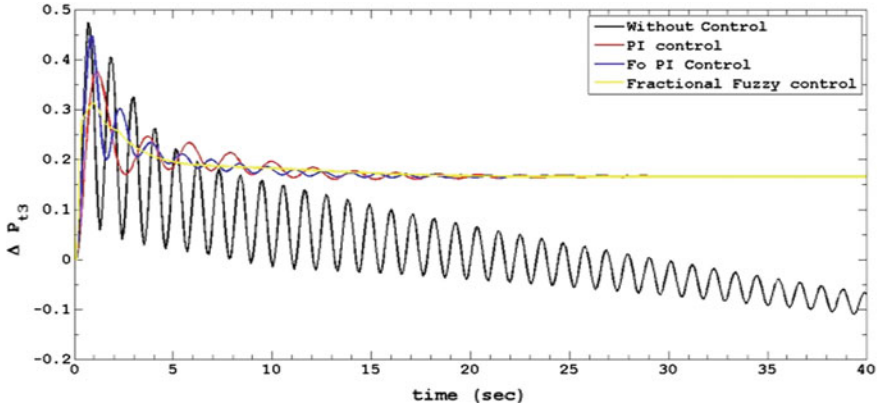

Fig. 27 ΔP_{t3}

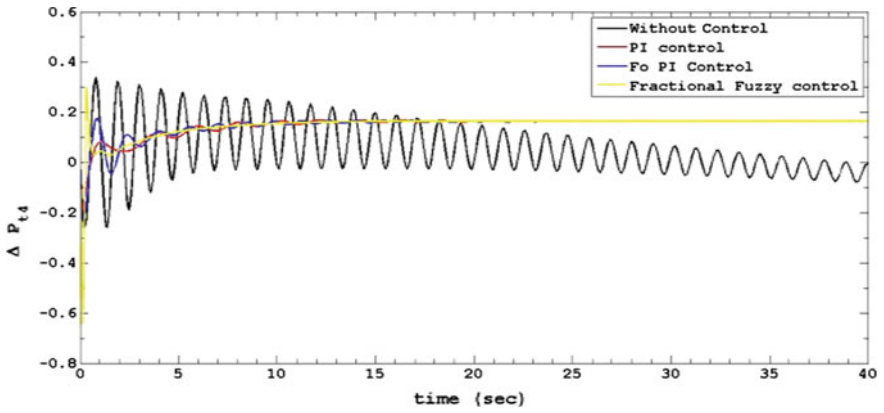

Fig. 28 ΔP_{t4}

overshoots and settling time are 0.4166 and 27 s for turbine 1, 0.1843 and 33 s for turbine 2 in control area 1 and 0.4473 and 21 s for turbine 3, 0.1749 and 32 s for turbine 4 in control area 2. This transient behaviour is further reduced by proposed Fuzzy based Fractional Order PI control methodology, overshoots and settling time are 0.3659 and 18.6 s for turbine 1, 0.1745 and 18.2 s for turbine 2 in control area 1 and 0.3126 and 19.2 s for turbine 3, 0.2985 and 18.4 s for turbine 4 in control area 2. In the event when FOPI is put into the action overshoots, rise times and setting times are lower than IOPI controllers (Tables 3, 4, 5, 6, 7, 8 and 9).

Table 3 Performance values of settling time and overshoot for thermal Pi controller

Thermal PI controller	Settling time (s)	Overshoot
f1	6.8	0.1652
f2	10.8	0.3084
g1	7	0.2872
g2	7	0.2574
g3	11	0.3059
g4	9	0.2936
Ptie	14.4	0.0703
t1	6.4	0.2374
t2	6.4	0.2149
t3	10.4	0.2590
t4	10.4	0.2443

Table 4 Performance values of settling time and overshoot for thermal FOPI controller

Thermal FOPI controller	Settling time (s)	Overshoot
f1	10.2	0.1202
f2	10.8	0.1862
g1	6	0.3160
g2	6.8	0.2746
g3	10.2	0.3307
g4	8.8	0.3053
Ptie	15.2	0.0243
t1	7.6	0.2419
t2	9	0.2146
t3	7.2	0.2585
t4	7.4	0.2360

Table 5 Performance values of settling time and overshoot for thermal FOFPI controller

Thermal FOFPI controller	Settling time (s)	Overshoot
f1	8.2	0.0398
f2	6.4	0.1591
g1	3	0.2820
g2	2.8	0.2271
g3	6	0.2834
g4	6.2	0.2563
Ptie	11	0.0344
t1	3.2	0.1895
t2	3.2	0.1715
t3	6.2	0.2078
t4	6	0.1955

Table 6 Performance values of settling time and overshoot for hydro-thermal PI controller

Hydro-thermal PI controller	Settling time (s)	Overshoot
f1	37	0.3121
f2	35	0.2046
g1	32	0.5500
g2	36	0.1425
g3	24	0.4275
g4	20	0.1671
Ptie	37	0.3998
t1	34	0.4708
t2	34	0.1595
t3	27	0.3769
t4	24	0.1689

Table 7 Performance values of settling time and overshoot for hydro-thermal FOPI controller

Hydro-thermal FOPI controller	Settling time (s)	Overshoot
f1	35	0.1148
f2	35	0.1385
g1	25	0.5678
g2	23	0.1534
g3	21	0.5765
g4	40	0.1659
Ptie	40	0.0555
t1	27	0.4166
t2	33	0.1843
t3	21	0.4473
t4	32	0.1749

Table 8 Performance values of settling time and overshoot for hydro-thermal FOFPI controller

Hydro-thermal FOFPI controller	Settling time (s)	Overshoot
f1	19	0.0319
f2	18.6	0.0569
g1	18.2	0.5099
g2	18.2	0.1830
g3	18.6	0.5352
g4	18.4	0.3209
Ptie	18.4	0.1967
t1	18.6	0.3659
t2	18.2	0.1745
t3	19.2	0.3126
t4	18.4	0.2985

Table 9 Error calculation for hydro-thermal system

Errors	PI controller		FOPI controller		FOFPI controller	
	Hydro-thermal	Thermal-thermal	Hydro-thermal	Thermal-thermal	Hydro-thermal	Thermal-thermal
IAE	2.8907	0.3402	0.7107	0.1852	0.0667	0.2564
ISE	0.6756	0.0290	0.0342	0.0081	0.0069	0.0187
ITAE	23.5888	1.0685	6.7358	0.5766	0.0302	0.6939
ITSE	3.2487	0.0606	0.1953	0.0183	0.0017	0.0400
Sum	30.4038	1.4983	7.676	0.7882	0.1005	1.009

5 Conclusions

This work presents Fractional order fuzzy PI Controller under deregulated environment. The Performance FOPI controller is compared with Integer Order Controller (PI) and Fractional Order PI Controller in multi area Hydro-Thermal system and Thermal-Thermal system. From the results of FOFPI Controller it is effective and superior to FOPI Controller in improving system dynamic behavior in settling time and peak over shoot with reduced perturbations in the tie-line power deviation and frequency.

References

1. Donde V, Pai MA, Hiskens IA (2001) Simulation and optimization in AGC system after deregulation. IEEE Trans Power Syst 16(3):481–489
2. Bevarni H, Hiyama T (2011) Intelligent automatic generation control. CRC Press, New York
3. Parmar KPS, Majhi S, Kothari DP (2014) LFC of an interconnected power system with multi source power generation in Deregulated power environment. Int J Electr Power 57:277–286
4. Pandey SK, mohanty SR, Kishore N (2013) A literature survey on load frequency control for conventional and distribution generation power systems. Renew Sustain Energy Rev 25:318–344
5. Nanda J, Mangla A, SanjaySuri, "Some new findings on automatic generation control of an Interconnected hydrothermal system with conventional controllers. IEEE Trans Energy Convers 21(1):187–194
6. Nanda J, Kaul BL (1978) Automatic generation control of an interconnected power system. IEE Proc 125(5):385–390
7. Kothari ML, Satsangi PS, Nanda J (1981) Sampled data automatic generation control of interconnected reheat thermal systems considering generation rate constraints. IEEE Trans Power Appar Syst PAS-100(5):2334–2342
8. Ibraheem, Kumar P, Kothari DP (2005) Recent philosophies of automatic generation control strategies in power system. IEEE Trans Power Syst 20(1):346–357
9. Chidambaram paramasivam B (2013) Optimized load frequency simulation in restructured power system with redox flow batteries and interline power flow controller. Int J Electr Power 50:9–24
10. Bhatt P, Roy R, Ghoshal SP (2010) Optimized multi-area AGC simulation in restructured power systems. Int J Electr Power Energy Syst 32(4):311–322
11. Tyagi B, Srinivastava SC (2006) A decentralized automatic generation control scheme for competitive electricity markets. IEEE Trans Power Syst 21(1):312–320
12. Podlubny I (1999) Fractional Order systems and $PI^{\lambda}D^{\mu}$-controller. IEEE Trans Autom Control 44(1):208–214
13. Pan I, Das S (2012) Intelligent fractional order systems and control: an introduction, vol 438. Springer
14. Oustaloup A, Mathieu B, Lanusse P (1995) The CRONE control of resonant plants: application to a flexible transmission. Eur J Control 1(2)
15. Oustaloup A, Moreau X, Nouillant M (1996) The CRONE suspension. Control Eng Pract 4(8):1101–1108
16. Singh B, Mishra AK (2015) Fuzzy logic control system and its applications. Mechanical Engineering Section, Shalala College of Technology, Shalala, Sultanate of Oman. Mechanical Engineering Department, B.A. College of Engineering & Technology, Jamshedpur, India

17. Pandey KS, Mohanty SR, Kishor N (2013) A literature survey on load–frequency control for conventional and distribution generation power systems. Renew Sustain Energy Rev 25:318–334
18. Shankar R, Pradhan SR, Chatterjee K, Mandal R (2017) A comprehensive state of the art literature survey on LFC mechanism for power system. Renew Sustain Energy Rev 76:1185–1207
19. Vijaya Chandrakala KRM, Balamurugan S, Sankaranarayanan K (2013) Variable structure fuzzy gain scheduling based load frequency controller for multi source multi area hydro thermal system. Electr Power Energy Syst 53:375–381
20. Hajiloo A, Xie W-F (2013) Fuzzy fractional-order PID controller design using multi-objective optimization, 978-1-4799-0348-1/13/$31.00 ©2013 IEEE
21. Pancholi N, Parmar Y, Patel P, Mali U, Thakor C (2017) LFC in hydro thermal system using conventional and fuzzy logic controller 6(3)
22. Sondhi S, Hote YV (2014) Fractional order PID controller for load frequency control. Energy Convers Manag 85:343–353 (Elsevier)
23. Jin J, Huang H, Sun J, Pang Y (2013) Study on fuzzy self-adaptive PID control system of biomass boiler drum water. J Sustain Bioenergy Syst 3:93–98. https://doi.org/10.4236/jsbs.2013.31013

Design of a 22 W (0.7 A) Current Controlled DC-DC Flyback Converter Operating in DCM Mode

Ananya Bhattacharya and Shubhankar Majumdar

Abstract In this paper, the fabrication and characterization of a current mode, primary side controlled Flyback converter is carried out. Furthermore, the converter design specifications for Discontinuous Mode Conduction (DCM) of the converter are derived and used for simulation and designing purpose. The simulated results are then verified with the characterization results using a 30 W street light.

Keywords Flyback converter · DCM · Current-mode control · SMPS

1 Introduction

Flyback converter is an isolated SMPS circuit used widely for low power applications owing to its simple topology, wide input voltage variation and low cost [1]. For low power applications, flyback converters are the most commonly used LED drivers due to their electrical isolation and simple structure [2], however the major drawback is the decrease in the efficiency of the converter due to switching losses.

In a Flyback converter, the output voltage is isolated from the input main supply. The input is an unregulated DC voltage which is obtained by rectification of a wide range AC input. The isolation in the circuit is provided by a Flyback transformer. The primary winding of the transformer is driven by a switch. The switch used here is a MOSFET. The transformer, apart from providing isolation, also behaves like an output inductor, providing multiple output voltages.

When the switch is closed (ON state), the magnetizing inductance causes the current to build up in a ramp as the primary is directly connected to the input voltage source. As the primary current and magnetic flux across the primary increases, magnetic energy starts getting stored in the transformer. Since the secondary winding has a negative flux, the diode in the secondary is now reverse biased and the energy to the

A. Bhattacharya (✉) · S. Majumdar
Electronics and Communication Engineering, National Institute of Technology Meghalaya, Shillong, Meghalaya, India
e-mail: ananyabh17@gmail.com

© Springer Nature Singapore Pte Ltd. 2020

T. Hitendra Sarma et al. (eds.), *Emerging Trends in Electrical, Communications, and Information Technologies*, Lecture Notes in Electrical Engineering 569,
https://doi.org/10.1007/978-981-13-8942-9_21

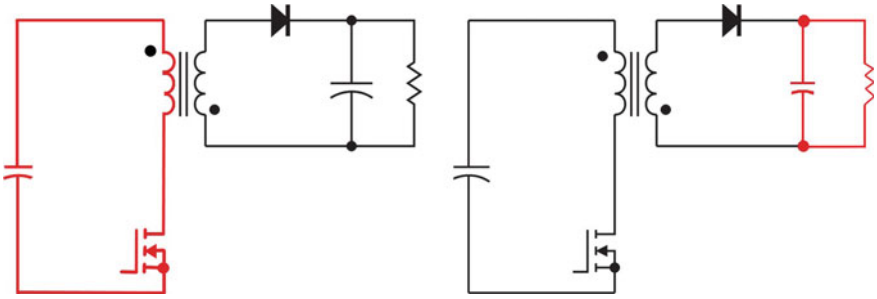

Fig. 1 Operating waveform of flyback converter in DCM mode [5]

output load is supplied by the output capacitor [3]. When the switch is open (OFF state) the primary current falls to zero as the magnetic field in the core is released to the secondary. The voltage across the output winding rises very quickly. As the diode is now in forward bias, secondary current will flow in the form of descending ramp. The energy from the core recharges the output capacitor and supplies the load [3]. This has been shown in Fig. 1.

The Flyback converter can be operated under voltage mode control and current mode control. Current mode control is generally preferred for stability during operations [1]. This is obtained in this project by a primary side sensing technique [1, 2]. This technology is accurate, more economical than the other available methods and requires a minimum load to keep the discharge-events occurring providing the opportunities to sample the 1: N secondary voltage at the primary winding. PSR controls the output current precisely, removes the current sensing loss and eliminates the requirement for a secondary circuitry. Thus, the driver circuit becomes smaller and more compact and can be fit in small-form lamps that meet international regulations [4–6]. Various PSR control algorithms are currently being studied. However, some of the proposed algorithms have persisting control inaccuracy in various input voltage applications [5, 6]. Various control ICs can be used to maintain the DCM operation of the converter. It can greatly enhance the voltage conversion ratio [7].

In this paper, a controller IC is used which regulates the output voltage and current by monitoring the waveforms in the auxiliary winding which is used to power the control IC itself, thereby improving the accuracy of current and voltage regulation [2].

2 Mode of Operation

Secondary side controlled flyback transformers along with improved drain-source voltage sensing for more precise gate signals and reduced losses can be used to make LED drivers that give an efficiency of about 89.90% [8] but a PSR technique is used for more accurate output current control [5, 6]. PSR can also be used along

with a digitally variable on-time control to realize a power factor correction flyback converter to give a power factor above 0.95 and a THD less than 10% [9].

The output of a Flyback converter can be negative or positive (depending upon the dot convention). It has two basic energy transfer modes of operation. In continuous conduction mode (CCM), the energy stored in the primary of the transformer does not collapse to zero completely. A part of the energy is retained in the winding before the next ON period. In discontinuous conduction mode (DCM), the entire energy stored in the primary of the transformer during the ON period is transferred to the load during the OFF period. However, the inductance value will remain zero until the switch is gated again i.e. it touches the zero value before the end of the switching period. A third mode of operation that exists between CCM and DCM is called critical conduction mode or transition mode or boundary mode. In this mode, the stored energy touches the zero value at the end of the switching period.

Constant current control in DCM mode is realized by keeping the ratio of the demagnetization time to the switching period constant [10]. In this paper, the design parameters are calculated considering that the Flyback converter is operating in DCM. This has been shown in Fig. 1.

The flyback transformer has three windings, the primary winding, secondary winding and auxiliary winding. i_p is the current through primary of transformer, I_{pmax} and I_{pmin} is the maximum and minimum current through primary, i_s is the current through the secondary of the transformer, i_{smax} and i_{smin} is the maximum and minimum secondary current. I_{sav} is the average secondary current and $I_{pav}$is the average primary current. The auxiliary circuit functions as a sensor to feedback the primary demagnetization time to the IC [5, 7]. In our designed primary side regulated flyback converter, the auxiliary winding is used for estimating the output current [1, 5, 11]. The secondary diode has a forward bias voltage of V_{FB}.

The magnetizing inductance value for a Flyback converter operating in DCM should be less than the critical inductance (the value of inductance for which the converter will operate in critical conduction mode) [5, 10]. An inductance value higher than the critical inductance will make the converter operate in CCM. If L_{DCM} and L_{CCM} are the magnetizing inductance for DCM and CCM operation respectively, then

$$L_{DCM} < L_{CCM}$$

or,

$$L_{DCM} = \xi L_{CCM}, \text{ where } 0 < \xi < 1$$

In the Flyback topology, constant turn on time and frequency in the discontinuous conduction mode (DCM) can achieve a high-power factor and low THD (total harmonic distortion) [4, 11, 12].

3 Circuit Analysis and Design

The design procedure for a single stage Flyback LED driver is presented here. The reference circuit is given. in Fig. 2.

The design example is presented for a 22 W–0.7 A LED driver. The specifications are given below:

- Input voltage range: 180–240 VAC and 50–60 Hz
- Nominal output voltage and current: 31 V/0.7 A
- Minimum efficiency: 88%
- Operating switching frequency: 60 kHz.

The output current can be estimated using the peak drain current of MOSFET ($I_{DS.PK}$) and inductor current discharge time (t_{DIS}) because output current is the same as the average of the diode current in steady state. The peak value of the drain current is determined by the CS peak voltage detector and the inductor current discharge time is sensed by the t_{DIS} detector. By the end of inductor current discharge time (t_{DIS}), all energy stored in the transformer has been delivered to the output. The diode current (I_D) is given by [4]:

$$I_D = I_{DS.PK} \cdot \frac{N_p}{N_s} \tag{1.a}$$

And the output current I_0 is given as [4]:

$$\mathrm{I_o} = \frac{1}{2}\left(\frac{t_{DIS}}{ts}\right) \cdot V_{CS} \cdot \frac{N_p}{N_s} \cdot \frac{1}{R_s} \tag{1.b}$$

As,

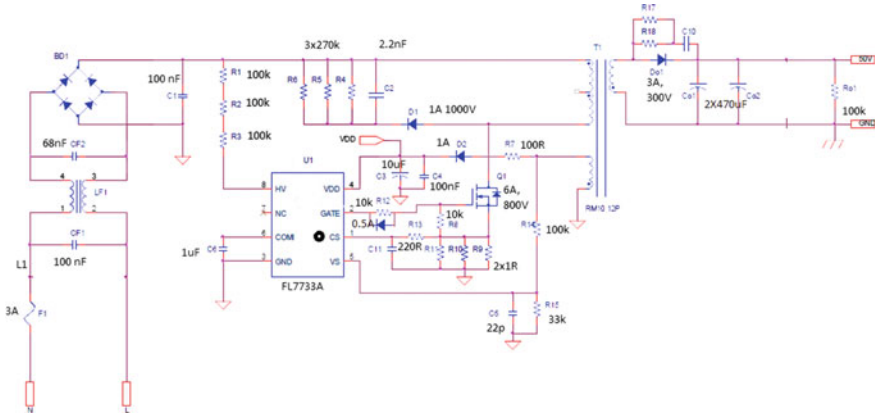

Fig. 2 Flyback converter circuit schematic [4]

$$\left(\frac{t_{DIS}}{ts}\right) \cdot V_{CS} = 0.25$$

So,

$$\mathrm{I_o} = 0.125\frac{N_p}{N_s} \cdot \frac{1}{R_s} \tag{1.c}$$

where N_p/N_s is the primary to secondary turns ratio and R_s is the sensing resistor value.

During the MOSFET ON time (t_{ON}), the input voltage is applied across the magnetizing inductance (L_m), charging the magnetizing energy in L_m. The maximum peak switch current (IDS.PK) of the MOSFET occurs at peak point of line voltage. Since our switching frequency (fs) is 60 kHz, the switching time (ts) will be [4]:

$$\mathrm{t_s} = \frac{1}{fs} = \frac{1}{60 \times 10^3} = 16.6\,\mu\mathrm{s}$$

So, we decide the MOSFET ON time (t_{ON}) to be around 5 µs. Once the maximum t_{ON} is decided, $I_{DS.PK}$ of MOSFET is obtained at the minimum line input voltage and full-load condition as [4]:

$$\mathrm{I_{DS.PK}} = \frac{(\mathrm{t}_{ON} \cdot \mathrm{V}_{IN.PK})}{L_m} \tag{2}$$

Using Eq. (2), the peak input current is obtained by [4]:

$$\mathrm{I_{IN.PK}} = \frac{\left(t_{ON}^2 \cdot \mathrm{V}_{IN \cdot PK}\right).\mathrm{fs}}{2L_m} \tag{3}$$

then, $V_{IN.PK}$ and $I_{IN.PK}$ can be expressed as [4]:

$$\mathrm{I_{IN.PK}} = \sqrt{2}\,\mathrm{I_{IN.rms}} \tag{4}$$

$$\mathrm{V_{IN.PK}} = \sqrt{2}\,\mathrm{V_{IN.rms}} \tag{5}$$

where, $I_{IN.rms}$ and $V_{IN.rms}$ are rms line input current and voltage, respectively.

Hence, from Eqs. (3)–(5), t_{ON} is obtained as [4]:

$$\mathrm{t_{ON}^2} = \frac{(2 \cdot L_m \cdot \mathrm{I}_{IN.rms})}{(\mathrm{V}_{IN.rms} \cdot \mathrm{fs})} \tag{6}$$

Input power is given as [4]:

$$\mathrm{P_{IN}} = \mathrm{V_{IN.rms}} \cdot \mathrm{I_{IN.rms}} = \frac{Po}{\eta} \tag{7}$$

Using Eqs. (6) and (7), we get L_m as [4]:

$$L_m = \frac{\left(\eta \cdot V_{IN.rms}^2 \cdot fs \cdot t_{ON}^2\right)}{2Po} \tag{8}$$

Considering the minimum input voltage to be 180 VAC, MOSFET ON time (t_{ON}) to be 5 μs, switching frequency (fs) of 60 kHz and a minimum efficiency of 88%, the magnetizing inductance value will be:

$$L_m = \frac{\left(0.88 \times 180^2 \times 60 \times 10^3 \times \left(5 \times 10^{-6}\right)^2\right)}{2 \times 25}$$

$$L_m = 855\,\mu H$$

Using Eq. (2),

$$I_{DS.PK} = \frac{\left(5 \times 10^{-6} \times \sqrt{2} \times 180\right)}{855} = 1.488\,A$$

From Eq. (1.c) the output current is directly proportional to the primary to secondary turns ratio of the flyback transformer and inversely proportional to the sensing resistor value. The IC controller implements cycle by cycle current limit by detecting the V_{CS} to protect the LED from overload or short [4, 13]. So, V_{CS} should be able the handle the rated power without triggering the the current-limit protection. So, typically, $V_{CS.PK}$ is set at 0.85 V for the IC controller in use. The MOSFET peak current $I_{DS.PK}$ is related to the $V_{CS.PK}$ as [4]:

$$V_{CS.PK} = I_{DS.PK} \cdot R_S \tag{9}$$

$$R_S = \frac{V_{CS.PK}}{I_{DS.PK}} = \frac{0.85}{1.488} = 0.571\,\text{ohm}.$$

According to Eq. (1.c), primary to secondary turns ratio is [4]:

$$N_{ps} = \frac{N_p}{N_s} = \frac{I_{o \times R_S}}{0.125} = \frac{0.7 \times 0.571}{0.125} = 3.1976$$

The turns ratio of the flyback converter is so selected so as to get a proper duty cycle.

The IC controller, FL7733A, has an overvoltage protection which is triggered at a V_{DD} voltage of 23 V. So, the auxiliary to secondary turns ratio N_{AS} is given as [4]:

$$N_{AS} = \frac{V_{DD.OVP}}{V_{O.OVP}} = \frac{23}{V_{O.OVP}}$$

Considering the output overvoltage at 50 V,

$$N_{AS} = \frac{23}{50} = 0.46$$

$$\mathrm{N_{AP}} = \frac{N_{AS}}{N_{PS}} = \frac{0.46}{3.1976} = 0.14$$

4 Design Considerations and Selection of Switching Devices

The maximum drain voltage of the MOSFET is calculated by assuming an approximate value for the drain voltage overshoot ($\mathrm{V_{OV}}$). Assuming that the maximum drain voltage overshoot is 100 V, the value of MOSFET drain voltage is [4, 13]:

$$\mathrm{V_{DS.max}} = \mathrm{V_{IN.max.pk}} + \mathrm{V_{OV}} + \mathrm{N_{PS}}(\mathrm{V_{O.OVP}}\mathrm{V_F}) \tag{10}$$

where, $\mathrm{V_F}$ is the diode forward bias voltage and it is assumed to be 1 V.

$$\mathrm{V_{DS.max}} = \left(\sqrt{2} \times 240\right) + 100 + 3.1976\,(50 + 1) = 602.4376\ \mathrm{V}$$

where, $\mathrm{V_{IN.max.pk}}$ is the maximum value of the peak input line voltage.

The selected MOSFET should have a voltage rating above 602.4 V.

For this particular design, we choose a MOSFET with voltage and current rating 800 V/6 A respectively.

Secondary side diode is selected after calculating the maximum reverse voltage and rms current of the diode.

$$\mathrm{V_D} = \mathrm{V_O} + \frac{N_s}{N_p}\mathrm{V_{in.max.pk}} \tag{12}$$

$$\mathrm{V_D} = 35 + (0.312 \times \sqrt{2} \times 240) = 141\ \mathrm{V}$$

So, we select a diode with voltage and current rating 300 V and 3 A respectively for the secondary side of the converter.

5 Other Design Specifications

The fuse used in the input side has voltage and current rating 250 V/3A.

EMI filter: We use an EMI filter in the input side of the converter, made up of two inductances L1 and LF1 having values 3 mH and 130 mH respectively and two capacitors of 150 nF each. LF1 is the EMI coil.

Rectifier: A bridge rectifier is used for AC to DC conversion of the input signal followed by a filter capacitor of 2.2 μF.

Snubber circuit: The snubber circuit used in the design consists of a bleeder resistor of 90 kilo-ohm, a capacitor of 2.2 nF and a 1000 V/1 A diode. The snubber circuit resistor with proper rated wattage is chosen based on power loss [4].

IC controller: The IC controller used for the design is FL3377A. [4]

6 Results and Verification

The pictures of the designed hardware of a Flyback converter are given in Fig. 3. The input and output parameters as measured in the oscilloscope are shown in the Table 1.

The secondary side parametric values are enumerated in Table 2. The input or primary current and voltage is found by taking the current and voltage reading across the MOSFET. The primary side current and voltage waveforms are shown in Fig. 4.

The MOSFET current and voltage depicted by the waveform (Fig. 4a, b) is about 1.4 A and 560 V, respectively. The result is close to the computed MOSFET peak current of 1.488 A and 602 V.

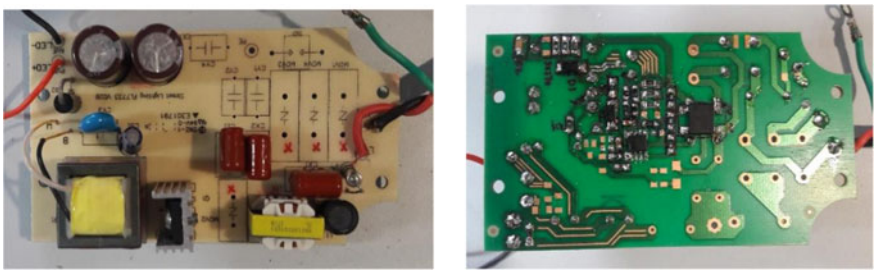

(b) Front side (a) Back side

Fig. 3 Pictorial view of the designed flyback converter hardware

Table 1 Measured input and output parameters

	Input	Output
Voltage	240 VAC	29.53 V
Current	0.1080 A	0.728 A
Power	24.04 W	21.67 W

Table 2 Other parametric values at secondary side

THD	5.725%
Power loss	2.3741 W
Secondary peak current	1.023 A
Output RMS current	0.7603
I-ripple	46.013%
Efficiency	90.126%

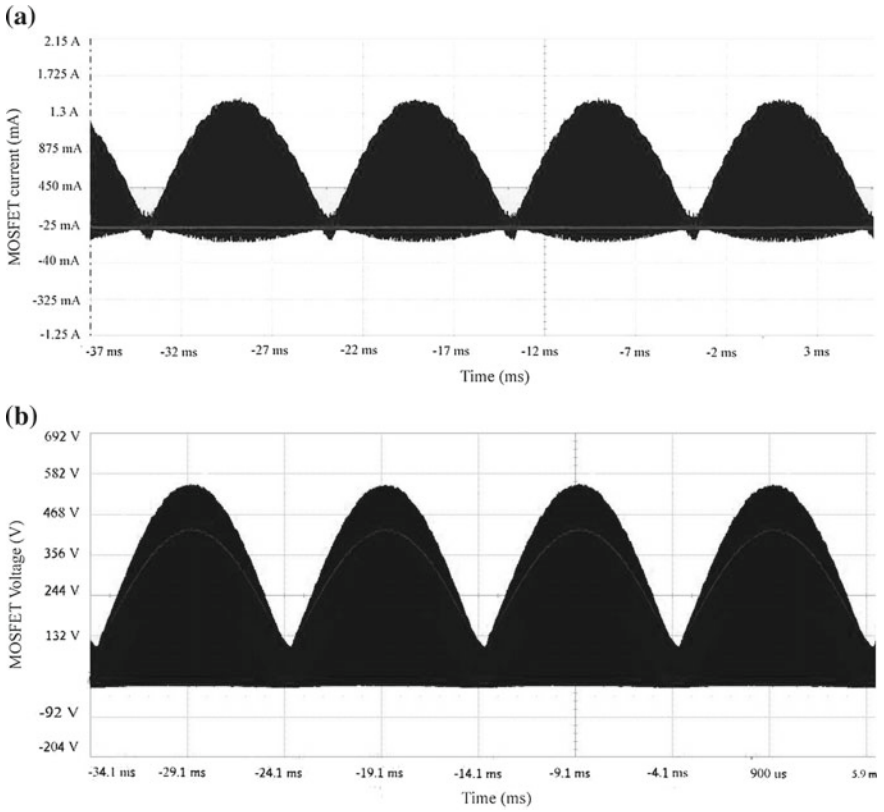

Fig. 4 **a** MOSFET current waveform in the primary side. **b** MOSFET voltage waveform in the primary side

Whereas, the voltage overshoot is around 112 V as against the assumed value of 100 V. The operating frequency of the designed Flyback converter is found from the current waveform across the primary side. The waveform obtained is given in Fig. 5.

The waveform of the primary side current when zoomed gives us the above pattern which confirms that the designed flyback convert is operating under DCM mode with an operating frequency of 46.2 kHz. The zoomed pattern is shown in Fig. 5.

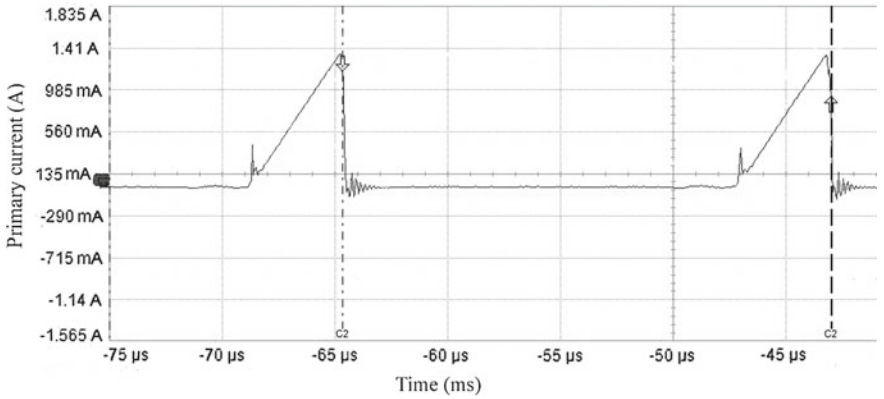

Fig. 5 Primary current of MOSFET showing DCM mode of operation of the designed converter

The secondary side current and voltage are obtained by taking the voltage and current reading across the diode in the secondary circuit. The current waveform and the voltage waveform taken across the diode are shown in Fig. 6.

The diode peak current from the waveform in Fig. 6 is found to be around 6 A. The diode voltage or the secondary voltage shown in Fig. 7 is found to be around 150 V. The computed value of the diode voltage is 141 V.

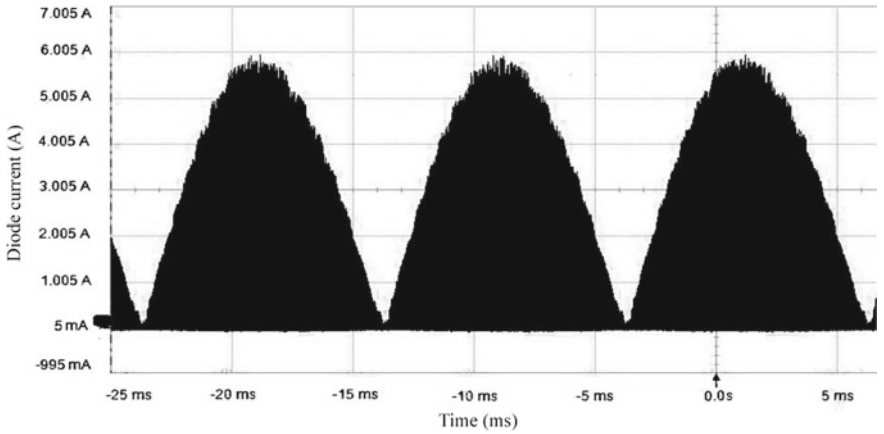

Fig. 6 The diode current waveform in the secondary side

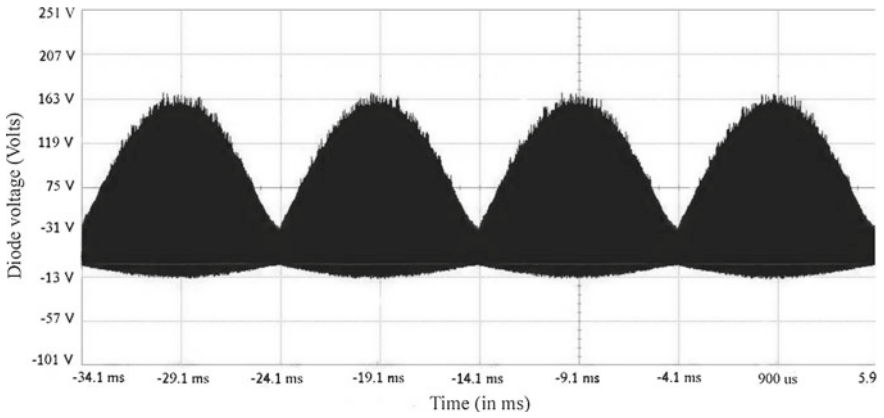

Fig. 7 The diode voltage waveform at the secondary side

7 Conclusion

Thus, from the characterization of primary side current controlled flyback converter operating in DCM mode, the output is found as 21.67 W with an output voltage of 29.13 V and a current of 0.7281 A. The efficiency at output is 90.126%. In this paper, the main design calculations have been considered and subsequently simulated in LTSpice. After that the optimized design has been successfully fabricated on PCB which gives us output values within the bounds of permissible range.

References

1. Liang TJ, Chen KH, Chen JF (2018) Primary side control for flyback converter operating in DCM and CCM. IEEE Trans Power Electron 33(4):3604–3612
2. Li JS, Liang TJ, Chen KH, Lu YJ, Li JS (2015) Primary-side controller IC design for quasi-resonant flyback LED driver. In: 2015 IEEE energy conversion congress and exposition (ECCE)
3. The flyback converter—lecture notes—ECEN4517—Department of Electrical and Computer Engineering, University of Colorado, Boulder
4. Design a high-power factor flyback converter using FL7733A for an LED driver with ultra-wide output Voltage, Fairchild
5. Panov Y, Jovanovic MM (2002) Adaptive off-time control for variable-frequency, soft-switched flyback converter at light loads. IEEE Trans Power Electron 17(4):596–603
6. Adragna C (2018) Design-oriented small-signal modelling of primary-side regulated flyback converters. In: IEEE 19th workshop on control and modeling for power electronics (COMPEL). Padova, Italy
7. Li JS, Chen KH, Lai JH, Huang JX (2018) Control IC for boost-flyback converter for energy harvesting applications. In: International power electronics conference (IPEC-Niigata 2018 -ECCE Asia)
8. Wang C, Xu S, Lu S, Sun W (2018) A low-cost constant current control method for DCM and CCM in digitally controlled primary-side regulation flyback converter. IEEE J Emerg Selected Topics Power Electron 6(3)

9. Lin HC, Chu WM, Tsai CH, Su WC (2018) A digitally variable on-time controlled PFC flyback converter with primary-side regulation. In: 7th international symposium on next generation electronics (ISNE)
10. Connaughton A, Talei AP, Leong KK, Krischan K, Muetze A (2018) Variable ON-Time control scheme for the secondary side controlled flyback converter. IEEE Trans Power Electron
11. Erickson RW, Maksimovic D (2001) Fundamentals of power electronics. Kluwer Academic Publishers
12. Das S, Sudhakar P Power factor correction & harmonic distortion control for AC-DC fault tolerant power distribution system & power quality qualification test results as per IEC 61000-3-2, BARC Newsletter, April–March 2017
13. Primary side control for flyback converter operating in DCM and CCM, FL3377A, Fairchild

Two Loop PI Controlled Cascaded Re-Boost Seven Level Inverter Fed Induction Motor System with Superior Dynamic Response

P. Bhaskara Prasad, M. Padma Lalitha and B. Sarvesh

Abstract In recent times boost converter with seven-level inverter is a best choice of PV system with ac load. For elevating the DC level a reboost technology was used. DC can be converted into the AC with employment of seven level inverter. The very purpose of reboost is to enhance voltage gain. The purpose of the recommended closed loop Reboost Seven Level Inverter fed Induction Motor (RBSLIIM) system is to enhance the dynamic response of RBSLIFIM using two PI controllers. Simulink models are developed for PI and PI-PI controlled RBSLIIM systems. The results of PI and PI-PI RBSLIIM scheme point out that the dynamic behavior of Two loop PI is superior to PI controlled RBSLIIM system.

Keywords PV cell · Multi-level inverter · Boost converter · PI controller

1 Introduction

The widespread utilization of fossil fuels effects the environment and also increases the universal Problem of greenhouse gas emissions. Furthermore availability of fossil fuels will worn-out in future and definitely becomes more and pricier. As a result, solar power is more attractive and also significant since it generates a lesser amount of pollution as well as the rate of fossil fuel power will be rising, whereas the expenditure for manufacturing the solar arrays is diminishing. Meticulous, distributed power generation systems with solar energy will be common and increasingly used in housing applications in the vicinity of future [1, 2].

The interface between grid and with PV systems is significant since it has to convert the DC power produced by the PV system into AC power, and it has to

P. B. Prasad (✉)
Department of Electrical & Electronics Engineering, JNTUA, Ananthapuramu, AP, India
e-mail: bhaskara.papugari@gmail.com

M. Padma Lalitha
Department of Electrical & Electronics Engineering, AITS, Rajampet, India

B. Sarvesh
Department of Electrical & Electronics Engineering, JNTUK, Kakinada, Andhra Pradesh, India

© Springer Nature Singapore Pte Ltd. 2020

T. Hitendra Sarma et al. (eds.), *Emerging Trends in Electrical, Communications, and Information Technologies*, Lecture Notes in Electrical Engineering 569,
https://doi.org/10.1007/978-981-13-8942-9_22

nourish AC power into the utility grid. Inverter is essential for the power alteration that is to translate the power (DC) to power (AC) [3, 4]. The output voltages of a PV array may be small so there is a need of using a DC-DC power converter (Boost) for low and medium capacity solar power generation systems to boost up the output voltage from small voltages, just to match the system DC bus voltage. The power alteration efficiency of a power converter interface is important to make sure that no energy generated from the solar cell array can be wasted. The active elements as well as passive elements in inverter generate a power loss. The power losses owing to active devices contains mutually the conduction losses and also the switching losses [5]. Conduction loss consequence from the utilization of active devices, where as the switching losses are relatively proportional to voltage-current values for each switching as well as switching frequency. A filter reactor has to be used to eliminate or suppress switching harmonics of the inverter, and also the power loss as it is Proportional to the amount of switching harmonics.

The change in voltage for every switching function of a multilevel inverter must be condensed in order to look up its power conversion efficiency [6] and also the switching stresses on the active devices. The content of the switching harmonics have to be soothed, so one can easily reduce the power loss caused by means of the filter inductor. For this reason, a large amount of investigation on multilevel inverter technology is going on from years. In theory, multilevel inverters must be supposed to design with higher voltage levels just to improve the conversion efficiency and also to lessen harmonic content and electromagnetic interference (EMI).

Conventional multilevel inverter topologies take account of the diode clamped the flying-capacitor linked to the grid [7–10], and J. Pereda and J. Dixon, also discussed the cascade H-bridge types in [11] diode-clamped as well as the flying capacitor multilevel inverters employs capacitors to build up a number of voltage levels. Other than it is more complicate to normalize the voltages of the clamped capacitors. in view of the fact that it is difficult to produce an asymmetric voltage technology in both of the diode-clamped and also the flying- capacitor topologies, the power circuit is difficult with the increment in the voltage levels which is obligatory in multilevel inverter concept. For single phase seven level multi level inverter, 12 power electronic switches have to be used in the diode-clamped and also in the flying capacitor topologies. An Asymmetric voltage concept has been in usage in cascade H-bridge type multilevel inverter to generate increased number of levels of voltage. Hence the cascade H-bridge type multilevel inverter is an opt for applications where there is a need of increased output voltage levels.

To generate seven levels at output two cascaded H bridges consisting of eight power electronic switches with cascaded connection should be connected for a two different DC bus voltages. A number of novel topologies for seven- level inverters were proposed in past year one such concept with a single phase system of seven level grid associated inverter was developed for photovoltaic system by N. A. Rahim in [12].

A grid connected Seven level inverter includes 6 semi conductor switches and a single DC capacitor leads to building up the single voltage level, which produces a balanced voltage for a seven-level inverter topology, and configured by a level cre-

ation part and a polarity creation part, is proposed by Y. Ounejjar in [13] Only power electronic switches for level generation part switch in high frequency, but ten power electronic switches and single DC capacitors are used. In [14] by J. Mei, a modular multilevel inverter for new modulation method photovoltaic grid coupled generator was highlighted. The modular multilevel inverter is analogous to cascade H-bridge type. A new modulation system is planned to accomplish dynamic balancing capacitor voltage. In [15] by I. Abdalla, a multilevel DC-link inverter is offered to conquer the trouble of partial shadow of individual photovoltaic system that are connected in series.

A full bridge inverter compiled with solar cells, semi conductor switches and diodes. Minimization of THD in output voltage of system, power semiconductor switches can be controlled and by doing the same dc can be controlled and converted into AC based on Bus voltages.

2 Lay Out of Planned System

Figure 1 shows the block diagram of PV system connected to the Load. The solar energy is boosted with boost converter and its response is inverted using a multi-level inverter.

The projected RBSLIIM with single loop PI controller is pictorially given in Fig. 2. The output voltage of Photo Voltaic panel can be boosted utilizing a re-boost converter and its output acts as one of the input sources of a multilevel inverter. The other input source is a wind generator. The output of wind generator is rectified using a rectifier. The output of the rectifier is enhanced by means of a re-boost converter. The amount produced of Reboost Converter acts as the second input of the seven level inverter.

The Closed loop RBSLIIM system with two loop PI controller is shown in Fig. 3. The speed will be measured and compared with reference speed and the error is applied to the single PI' controller.

The output with single PI is compared with Torque (current) and the result is given to control output voltage of re-boost converters with PV and wind systems.

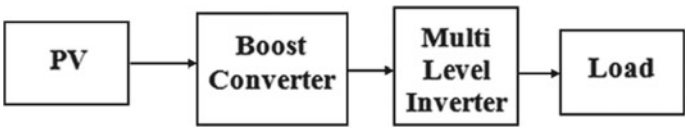

Fig. 1 Block diagram of the existing system

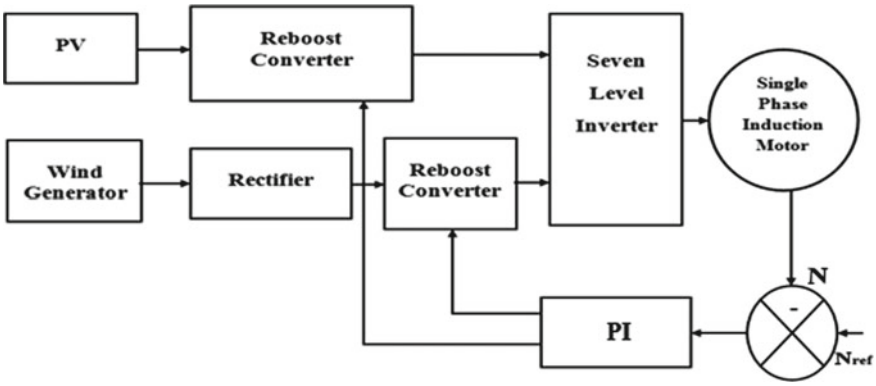

Fig. 2 Block diagram of the single loop RBSLIIM system

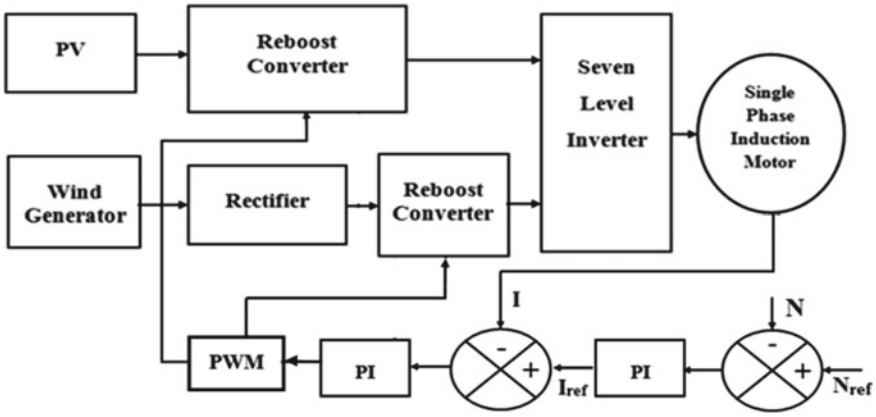

Fig. 3 Block diagram of the two loop RBSLIIM system with two PI Controllers

3 Simulation Diagram and Results

3.1 Closed Loop RBSLIIM System with Single PI Controller

The Simulation diagram of Closed loop RBSLIIM system with single PI controller has shown in Fig. 4. The voltage input to the reboost converter of Closed-loop RBSLIIM system with single PI-controller in Fig. 5 and its value augments from 48 to 60 V. The amount of voltage produced in inverter of Closed loop RBSLIIM system with PI-controller is given in Fig. 6 and its value is 210 V. Motor speed of Closed loop RBSLIIM system with PI-controller is publicized in Fig. 7 and its value is 1500 RPM. The speed oscillates and reaches the set value. The torque response of

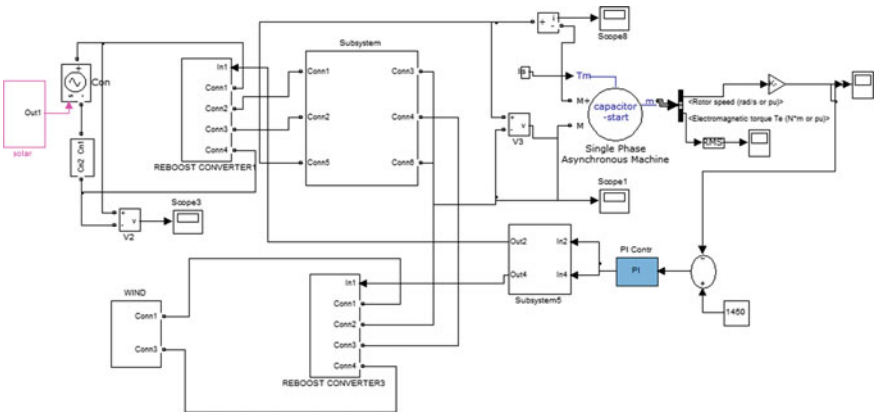

Fig. 4 Simulink diagram of RBSLIIM with two PI-controllers

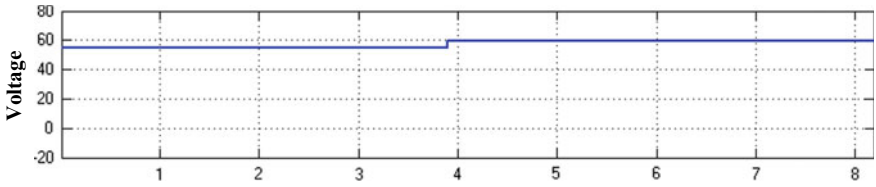

Fig. 5 Input Voltage to MLI of RBSLIIM system with two PI-controllers

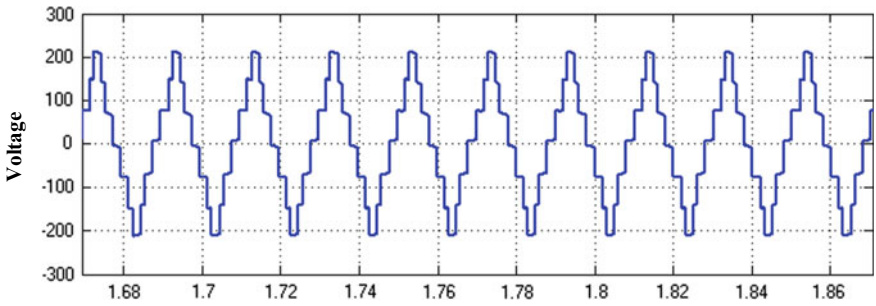

Fig. 6 Output voltage of MLI in closed loop RBSLIIM with two PI-controllers

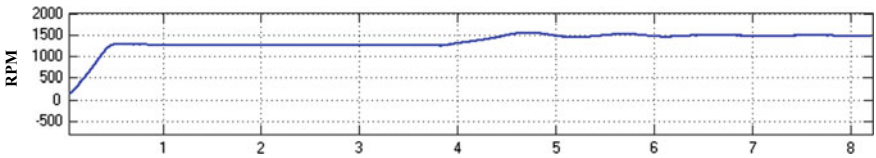

Fig. 7 Motor speed of RBSLIIM

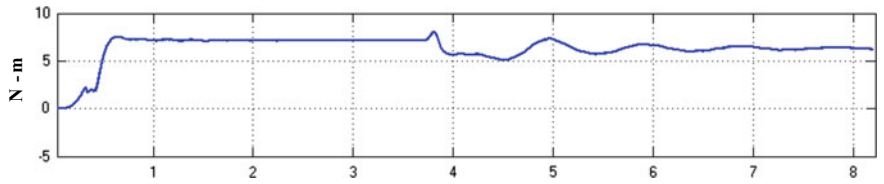

Fig. 8 Torque of RBSLIIM

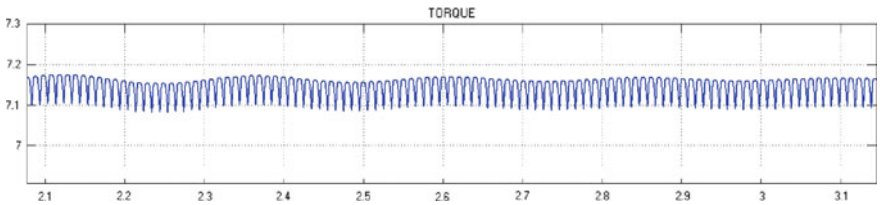

Fig. 9 Torque ripple of RBSLIIM

Closed loop RBSLIIM system with single PI-controller is appeared in Fig. 8 and its value is 7 Nm. It is known from the Fig. 9 torque ripple is 0.07 Nm.

3.2 Closed Loop RBSLIIM System with PI-PI Controller

The disadvantages of PI controller are increased settling time, high torque ripple content and higher steady state error. In order to pick up dynamic response and to reduce the ripple of torque, PI controller may be replaced with two loop PI controller. The circuit diagram of the closed loop-RBSLIIM system using PI-PI-controller has shown in Fig. 10. Input voltage of closed loop RBSLIIM system with two PI-controller has been shown in Fig. 11 whose value is 60 V. And the Output side voltage of the system with PI-PI-controller is disclosed in Fig. 12 whose value is 210 V. The motor speed of the CLRBSLIIM system with two PI controller is disclosed in Fig. 13 and its value can be seen as 1450 RPM. The speed oscillates and reaches the set value. The amplitude of oscillations is less than that of PI controlled RBSLIIM system. The Torque response of the CLRBSLIIM system with two PI controllers is appeared in Fig. 14 its value is 5 Nm. Ripple content in the torque was given in Fig. 15 and the value is 0.06 Nm and it is reduced when compared with two PI controllers.

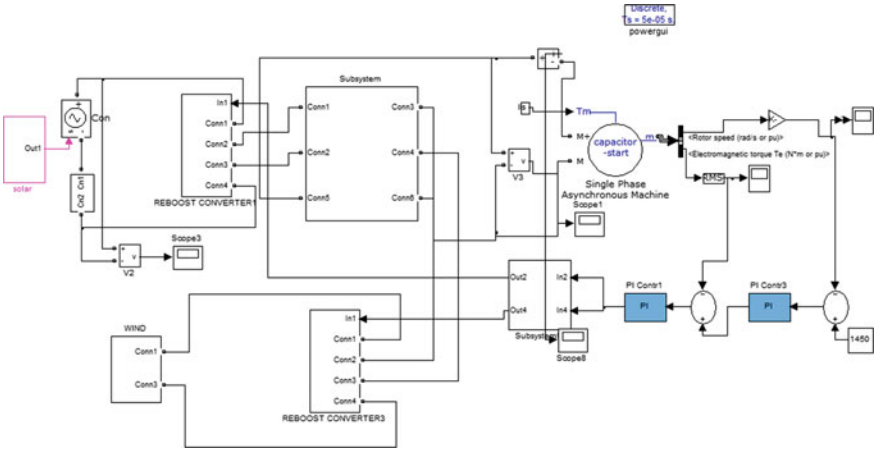

Fig. 10 Simulink diagram of the two loop RBSLIIM using two PI controller

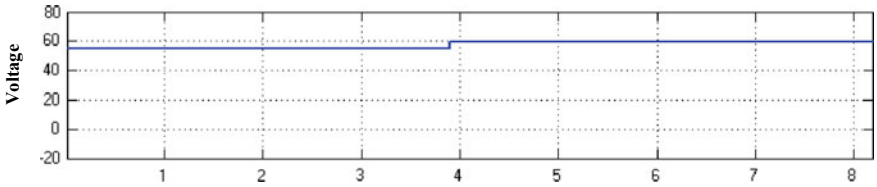

Fig. 11 Input voltage the closed loop RBSLIIM system using two PI controller

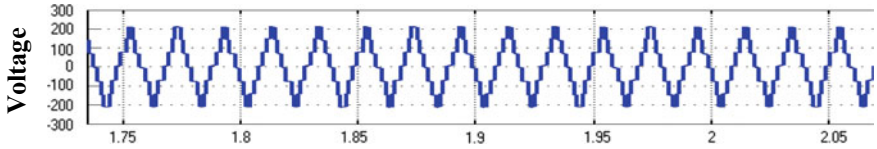

Fig. 12 Voltage of the inverter of closed loop RBSLIIM system with PI-PI controller

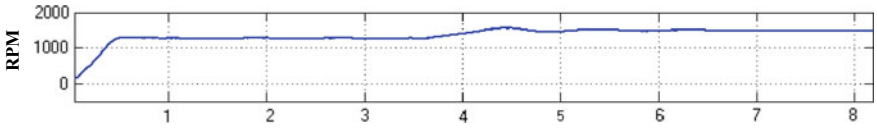

Fig. 13 Motor speed of the CL RBSLIIM scheme with PI-PI controller

4 Results and Discussion

The assessment of Time domain specifications is given in Table 1 and also torque ripple in Table 2. It can be noticed that settling time is condensed from 6.0 to 4.5 s

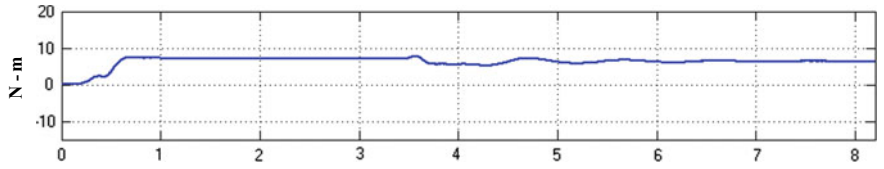

Fig. 14 Torque of the CLRBSLIIM scheme with PI-PI controller

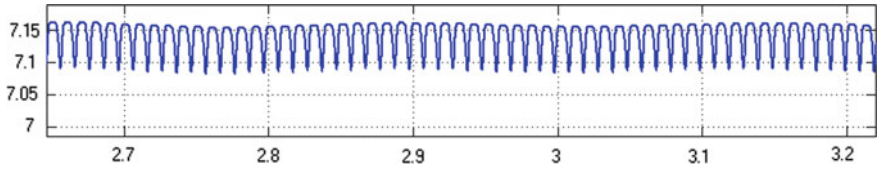

Fig. 15 Torque ripple of two loop PI PI controller

and also steady state error is condensed from 5.3 to 5.2 RPM using a PI-PI controller. The torque ripple was reduced from 0.07 to 0.06 Nm using two loop PI controllers.

5 Conclusion

The PV fed RBSLIIM system is efficaciously demonstrated and simulated. The case studies with P-I and PI-PI controllers are exhibited in detail. It can be noticed that the settling time is abridged to 4.5 s from 6 s and the steady state error in the output power is abridged from 5.3 to 5.2 RPM by replacing P-I controller with an PI-PI controller. The torque ripple was reduced from 0.07 to 0.06 Nm using two loop PI controller. The outcome from waveforms indicate that two loop PI supported RBSLIIM system gives the best dynamic response and also reduced ripple content in the torque. The studies indicated that RBSLIIM system is a viable alternative to the existing converters. The benefits of the suggested system are high voltage gain, diminished ripple in torque

Table 1 Comparison between single and two loop PI controllers

Controller	Rise time (s)	Peak time (s)	Setting time (s)	Steady state error
PI	4.3	4.6	6.0	5.3
PI-PI	4.2	4.5	5.2	5.2

Table 2 Comparison of torque ripple

Controller	Torque ripple (Nm)
PI	0.07
PI-PI	0.06

and reduced steady state error. The weakness of recommended system is appropriate for low-power loads.

The opportunity of the current work is to compare PI-and two loop PI based RBSLIIM systems.

References

1. Sayed MA, Elsheikh MG, Orabi M, Ahmed EM, Takeshita T (2014) Grid connected single phase Multi level inverter. IEEE Trans
2. Zhao Z, Xu M, Chen Q, Lai JS, Cho Y (2012) Derivation analysis and implementation of a boost converter based high efficiency PV inverter. IEEE Trans
3. Hu W, Wu H, Xing Y, Sun K (2014) A full bridge three port converter for renewable energy application. IEEE
4. Shen JM, Jou HL, Wu JC (2012) Novel Transformer-less-grid-connected power converter with negative grounding for Photo voltaic generation system. IEEE Trans Ind Electron
5. Mohan N, Undeland TM, Robbins WP (2010) Power electronics converter applications and design. Media Enhanced 3rd Ed. New York, Wiley
6. Srikanthan S, Mishra MK (2010) DC capacitor voltage equalization in neutral clamped inverters for DSTATCOM application. IEEE Trans Ind Electron 57(8):2768–2775
7. Kim Y, Cha H, Song B-M, Lee KY (2012) Design and control of a grid-connected three-phase 3-level NPC inverter for building integrated photovoltaic systems. IEEE PES Innovative Smart Grid Technologies (ISGT) 2012:1–7
8. Sadigh AK, Hosseini SH, Sabahi M, Gharehpetian GB (2010) Double flying capacitor multicell converter based on modified phase shifted pulse width modulation. IEEE Trans Power Electron 25(6):1517–1526
9. Thielemans S, Ruderman A, Reznikov B, Melkebeek J (2012) Improved natural balancing with modified phase-shifted PWM for single-leg five- level flying- capacitor converters. IEEE Trans Power Electron 27(4):1658–1667
10. Choi S, Saeedifard M (2012) Capacitor voltage balancing off lying capacitor multilevel converters by space vector PWM. IEEE Trans Power Delivery 27(3):1154–1161
11. Pereda J, Dixon J (2011) High-frequency link: a solution for using only one DC source in a symmetric cascaded multilevel inverters. IEEE Trans Ind Electron 58(9):3884–3892
12. Rahim NA, Chaniago K, Selvaraj J (2011) Single-phase seven-level grid-connected inverter for photovoltaic system. IEEE Trans Ind Electron 58(6):2435–2443
13. Ounejjar Y, AlHadded K, Dessaint LA (2012) A novel six-band hysteresis control for the packed U cells seven-level converter: experimental validation. IEEE Trans Ind Electron 59(10):3808–3816
14. Mei J, Xiao B, Shen K, Tolbert LM, Zheng JY (2013) Modular multilevel inverter with new modulation method and its application to photovoltaic grid connected generator. IEEE Trans Power Electron 28(11):5063–5073
15. Abdalla I, Corda J, Zhang L (2013) Multilevel DC-link inverter and control algorithm to overcome the PV partial shading. IEEE Trans Power Electron 28(1):11–18

Load Sharing in Parallel Converters Using Adaptive Voltage Control for DC Micro-grid Application

Lokendra Singh, Kartik Sharma, Aswant Kumar Sharma and D. K. Palwalia

Abstract DC devices are gaining popularity in the present era, because of its reliability, efficiency, and ease of connection ReS because of its inexhaustible nature and abundant apply, are gaining. To harness DC supply from these sources DC/DC Converters (DC Conv) are required. But the DC supply is intermittent in nature from renewable energy sources (ReS), because of many dependencies like solar radiation for solar PV, wind velocity for wind mill, manure for bio-gas plant and gravitational pull of moon for tidal wave plant thus, we need multiple sources connected in proper series and parallel combinations to get required sustainable supply. Beside this DC micro-grid itself involves these disadvantages like it needs private DC distribution lines, protection of DC system is more difficult, load in DC systems needs power supply of higher efficiency. The paralleling of these DC Conv provides a pass way when load current exceeds a single module's rating and helps when greater fault tolerance is required but it involves problems like power losses, circulating current, to system reset or shutdown or to even system damage. The problem here can be resolved by application of adaptive method as presented in the following paper.

Keywords Adaptive voltage control · Parallel operation · DC/DC converters · DC Micro-grid · Load sharing

1 Introduction

Traditionally, Power Grids have large capacity power plants consuming fossils and power is transmitted and then distributed to different areas by long-distance transmission lines. By the time, new concepts like microgrid and local small or medium capacity renewable energy power plants gained attention, new topologies evolved that can be used for integration of different scattered energy sources like wind, Photo Voltic (PV) etc. as distributed generators in a microgrid.

L. Singh (✉) · K. Sharma · A. K. Sharma · D. K. Palwalia
Department of Electrical Engineering, Rajasthan Technical University, Kota, India
e-mail: singhlokendra0909@gmail.com

© Springer Nature Singapore Pte Ltd. 2020

T. Hitendra Sarma et al. (eds.), *Emerging Trends in Electrical, Communications, and Information Technologies*, Lecture Notes in Electrical Engineering 569,
https://doi.org/10.1007/978-981-13-8942-9_23

The increasing popularity of the renewable energy sources like solar, biomass, wind energy, efforts are made to integrate them with grids/microgrids. For more reliable, easy distribution and cost-effective operation which leads to the need of the intervention of power electronic devices such as DC Conv. Designing of aspects of some of these DC Conv is shown in [1]. These converters are used in parallel to control the output voltage and frequency to address the issues like installation cost, voltage regulation, load sharing, system flexibility and better safety. Some of the control schemes and controller design aspects are discussed in [2, 3].

Paralleling of converters or using distributed unit of smaller capacity rather than single large capacity unit, reduces electrical and thermal stress on a converter unit, although number of components increases. But it rather reduces the complexity of the circuit. Some basic schemes of parallel operation of DC Conv is as shown in [4]. Although there are some problems associated with paralleling of converters like unequal load sharing [5], the stress imbalanced, resulting in some units operating with higher temperature—a recognized contributor to reduced reliability. In this manner, paralleling guarantees predictability, uniform current sharing, paying little heed to load current and the quantity of modules required. Most common methods for paralleling of converters are Master Slave control and Droop Based control.

1.1 Master Slave Control

In this type of control scheme one converter operate in voltage-controlled mode while other converters in current controlled mode. Master is responsible for generating reference current for slaves based on total current [6, 7].

1.2 Droop Based Control

In this method all converters in parallel, must be in voltage-controlled mode, by measuring local parameters and V_{ref} is calculated as:

$$V_{ref_k} = V_{o_k} - d_k i_k \tag{1}$$

where, V_{ref_k}, d_k and V_{o_k} are the reference voltage, droop gain and nominal voltage of kth converter. It is one of the most famous method utilized for parallel operation of converters as it consequently enhances current sharing without hampering individual voltage sources, making the system more robust [8]. It is a decentralized voltage control strategy in which every converter yield voltage reference is controlled in view of its yield current. The significant constraint of this scheme is poor voltage

control [9]. The proposed adaptive droop resistance (ADR) procedure [10] can shift the droop resistance to the point where variety of the load current can be traced. This method is advantageous over master slave method as reference value to slaves from master side need to be communicated quickly and simultaneously to each slave as: (a) It increase constructional cost because optical fiber cables are required for fast communication. (b) It is highly sensitive to noise interference so it can't be used for high power systems [9]. Figures 1 and 2 explains droop strategy for a system where mismatch in the converter currents I_{01}, I_{02}, converter voltage V_{01}, V_{02}, V_o is the voltage at I_o ($I_{01} = I_{02} = 0$ or minimum).

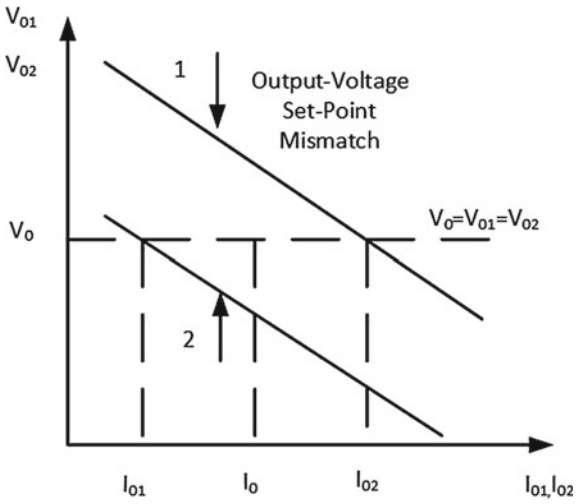

Fig. 1 Effect of output-voltage set-point mismatching on current-sharing accuracy small mismatch

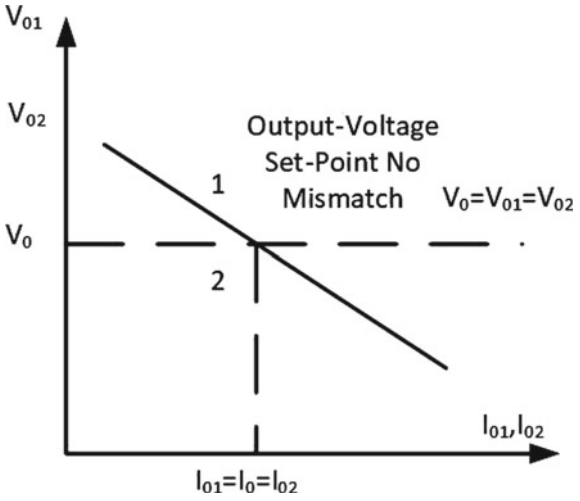

Fig. 2 Effect of output-voltage set-point mismatching on current-sharing accuracy no mismatch

But in droop control scheme besides all these advantages it suffers a serious drawback of voltage regulation, when small error in nominal voltage takes place source current deviate significantly. To deal with such problems and to get better results following scheme is proposed. Utilization of master–slave controller for paralleling is restricted on account of its surprising expense, low dependability and multifaceted nature. Although conventional droop controllers defeat these constraints, they can't all the while guarantee equal current sharing (in per unit) and voltage regulation. This is due to the error in measurement of voltage feedback signal can hamper current drastically. To address this constraint, modified droop controller is proposed in the paper [11]. Circulating current between converters is utilized to adjust nominal voltages with the goal that error between them is decreased. This enhances current sharing among converters. The advantage of the proposed technique is that, equivalent current sharing is accomplished alongside low-voltage control.

In this paper adoptive droop algorithm is implemented on a parallel boost converter system with reference to load current and converter voltage employing adjustments by monitoring output converter power, voltage and droop resistances.

2 Methodology for Equal Current Sharing

The following scheme introduces a new approach by take droop index (DI) and droop resistance Rd into account. DI is a nominalized function of current sharing between the converters and output power loss, it can be expressed as:

$$DI = \min\left[\frac{1}{2}\left[\left|I_{diff}\right|N_i + (P_{loss})N_p\right]\right] \tag{2}$$

And R_d can be evaluated as:

$$R_{dknew} = R_{dk} + (KS * IL) \tag{3}$$

Proposed scheme (PS) can be expressed by following pseudocode:

- Declare variables: voltages, load and reference currents, power, droop resistances and droop constant
- Initialize droop resistance for converter 1 and converter 2 as Rd1old, Rd2old
- Calculate power loss, reference current for both converters and droop index to generate new reference voltages
- IF DInew is less than DIold
  THEN decrease old droop resistances by load current multiplied by droop correction factor
  IF difference of Vdc1 and Vdc2 equals to 0
  THEN Assign Rd1old to Rd1new and Rd2old to Rd2new
  ELSE
  IF vdc1 is less than Vdc2
  THEN Increase Rd1old by ΔRd1
  assign it as Rd1new and Decrease Rd2old by ΔRd, assign it as Rd2new
  ELSE
  Decrease Rd1old by ΔRd1, assign it as Rd1new and, Increase Rd2old by ΔRd2, assign it as Rd2new
  END IF-ELSE
  IF Iref1 is less than I1 or Iref2 is less than I2 THEN
  Increase Rd1old by ΔRd1, assign it as Rd1new and Decrease Rd2old by ΔRd2, assign it as Rd2new
  ELSE
  Decrease Rd1old by ΔRd1, assign it as Rd1new and Increase Rd2old by ΔRd2 assign it as Rd2new
  END IF-ELSE
- Update new reference voltage Vdc with new updated Rd1new and Rd2new
- Stop

3 Modelling of the System

The system comprises of two parallel DC Conv, here boost converters is used in parallel as generation is generally preferred at low voltage and then boosted or stepped up to required voltage levels. The asynchronous boost converter can be converted into synchronous boost converter by replacing the diode with another similar MOSFET as switch and the gate pulse of the second switch will be 180 out of phase with the first switch gate pulse. For the system to be in continuous conduction mode (CCM), specific value of capacitor and inductor are required. To determine the value of inductor (L) and capacitor (C) applied input voltage (V_{in}) and nominal output voltage (V_0) is required. The general configuration of parallel boost converter is shown in Fig. 1. Due to very high switching frequency (105 kHz) of the switch in the Boost converter the switch produces discontinuous current but capacitor keeps output current continuous. The capacitor voltage varies between $V_{\max}$ and $V_{\min}$, and the difference between the $V_{\max}$ and $V_{\min}$ is peak-to-peak capacitor voltage ripple Δv_c. The key factor for choosing the inductor value is peak to peak inductor current Δi_l [11]. The peak to peak inductor current should be 30–40% of average output current i_{avg}. The equation for finding inductor value L in CCM is given below.

$$C = \frac{V_0(D)T}{\Delta v_c} \tag{4}$$

The equation for finding the value of inductance L in CCM is giver below:

$$L = \frac{V_0 D(1-D)T}{\Delta i_l} \tag{5}$$

where, V_0 Average output voltage (Volt), Δv_c Maximum inductor ripple current (Amp.), T Switching time period (Sec.), D Duty ratio and Δi_l Inductor current ripple. When these type DC Conv are connected in parallel (as shown in Fig. 3), the challenge in paralleling modules is to ensure predictable, uniform current sharing-regardless of load levels and the number of modules, control scheme is shown in Fig. 4.

Mathematical expression for load current sharing and circulating current for n parallel connected converters [4, 12] can be given as:

$$I_{ok} = \frac{\left[V_{rk} - \frac{1}{n}\sum_{j=1}^{n} V_{rj}\right] + \left[I_{av,k}K_{pk} - \frac{1}{n}\sum_{j=1}^{n}(I_{av,j}K_{pj})\right]}{K_{pk} + Z_{ok}} + \frac{1}{n}\sum_{j=1}^{n}\left(I_{oj}\frac{K_{pj} + Z_{oj}}{K_{pk} + Z_{ok}}\right) \tag{6}$$

$$I_{ck} = \sum_{j}^{n} \frac{I_k - I_j}{n} \tag{7}$$

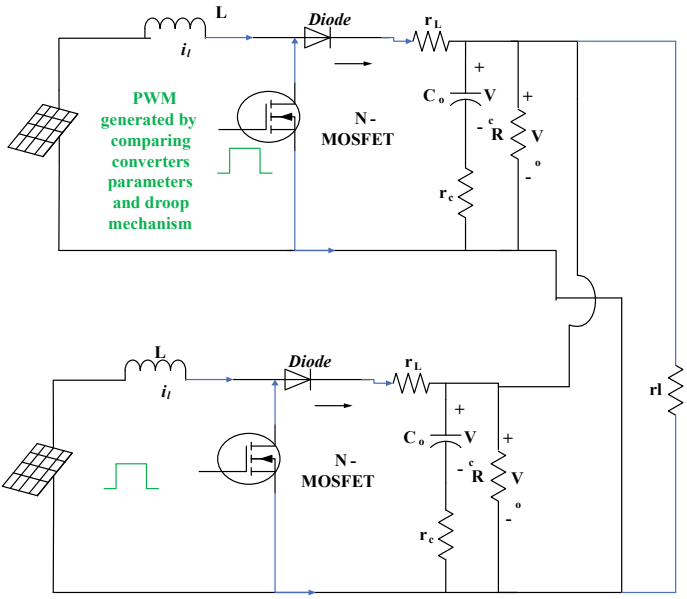

Fig. 3 Circuit diagram of parallel boost converter

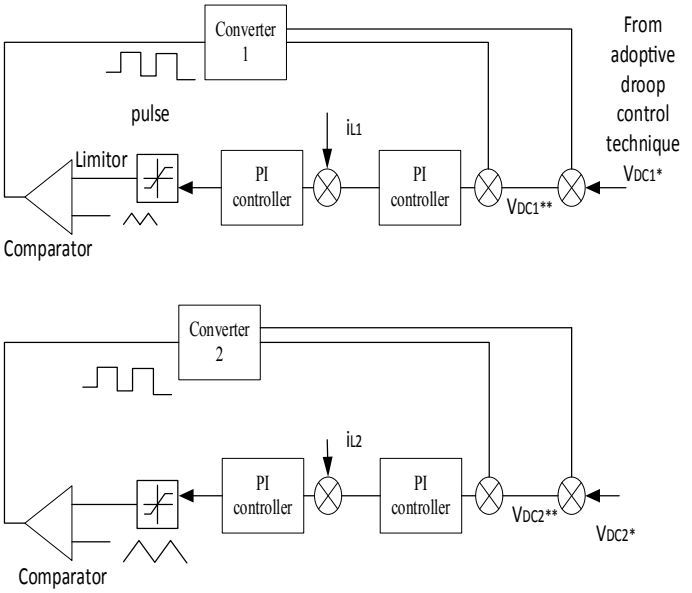

Fig. 4 Control scheme for adoptive droop control of parallel operation of boost converter

where K_{pk} is current feedback gain, I_{ok} is load current, I_{av} is average output current of all converters, V_{rj} is reference voltage obtained and Z_{ok} is output resistance of k^{th} converter in parallel and circulating current I_{ck} for kth converter in n parallel converter combination. For the converters to be parallel. There are two basic conditions i.e. each converter must share equal load and voltage regulation must be within acceptable limit to load.

4 Simulation Results

To understand the simulation scheme of two parallel converters like boost converter in Simulink/MATLAB consider the following block diagram Fig. 5:

The specification of Boost Convertors are described with parameter and their values as Input voltage (V_{in}) is 24 V, Output voltage (V_o) is 48V, Switching frequency (f) is 100 kHz, Filter capacitance (C) is 220 μF, Inductance (L) is 100 μH, Load resistance (R) is 11.5 and Nominal current (I) is 2 Amp (Fig. 5).

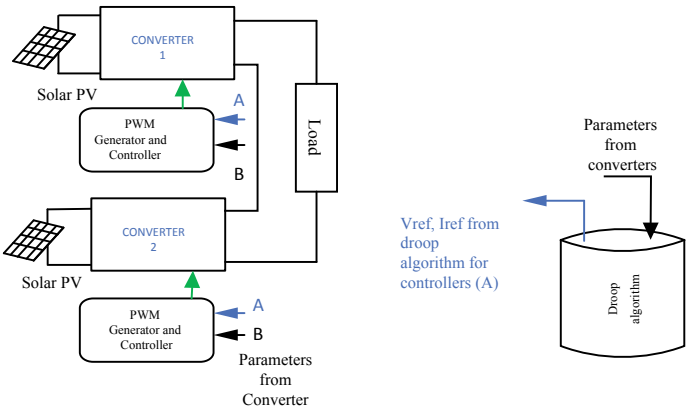

Fig. 5 System block diagram

4.1 By Varying Cable Resistance R1, R2

Here, reference voltage and source voltage are kept constant, but cable resistance is slowly varied. Initial value of R1 and R2 is kept 0.02 Ω, the converter current comes out to be 1.898 and 1.98 Amp while with Proposed droop scheme (PD) droop resistance comes out to be 0.118 and 0.204 after simulating it to 1 s. If R2 is increased from 0.02 to 0.07 Ω, circulating current also increases from 0 to 0.387 but with PD scheme it comes out be 0.0668 Amp. On keeping R2 as 0.07 Ω and increasing R1 to 0.04 circulating current in normal case without droop control is 0.2208 while with PD it is 0.0084 Amp as shown in Table 1 and Fig. 6.

Table 1 System response by varying cable resistance R1, R2

	Variables	R1	R2	I1	I2	Ic	Rd1	Rd2
R1 = R2	Without droop control	0.02	0.02	2.00	2.001	0	–	–
	With droop control	0.02	0.02	2.033	2.033	0	0.007	0.204
By varying R2	Without droop control	0.02	0.07	2.066	1.944	0.0980	–	–
	With droop control	0.02	0.07	2.075	1.989	0.086	0.0071	0.0204
By varying R1	Without droop control	0.04	0.07	2.013	2.001	0.00994	–	–
	With droop control	0.1	0.02	1.731	2.3	−0.569	0.007	0.204

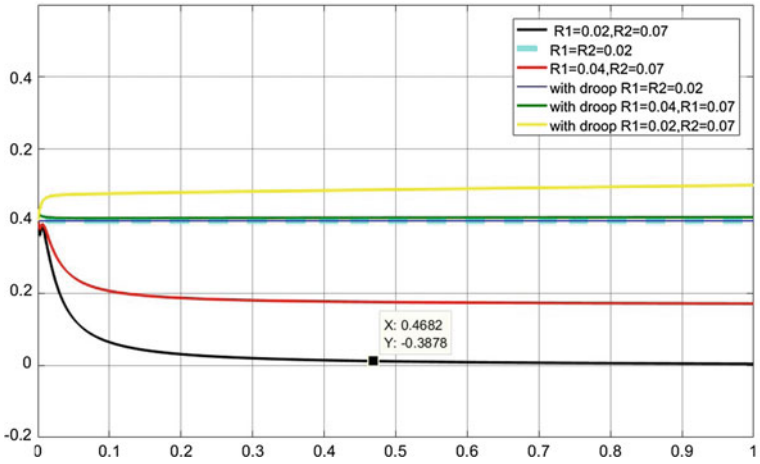

Fig. 6 Circulating current with proposed droop control technique and without droop control technique for Case 1

The above statics can be represented in graphical form as in Fig. 4, when I_C is plotted with respect to simulation time as 1 s at different values of R1 and R2 with PD and PD scheme.

4.2 By Varying Cable Resistance Along with Output Reference Voltage

Here, source voltage is kept constant but cable resistance R1 and R2 is varied slowly with reference voltages Vdc1, Vdc2 with 48 V. Initially R1 and R2 is kept 0.02 Ω, then converter current comes out to be 2.00 and 2.001 Amp with droop resistances 0.12 and 0.24 after simulating it to 1 s. If R2 is varied to 0.03 and R1 to 0.02 circulating current Ic increases from 0 to 0.083 with 10% variation in reference voltage Vdc1 as 43.2 and keeping Vdc2 constant as 48 V. If R1 is increased to 0.1 keeping other parameters same, then Ic further increase to 0.58 Amp. If R2 is varied to 0.02 again and R1 to 0.02 Ic becomes 0 with 15% variation in reference voltage Vdc1 as 40.8 and keeping Vdc2 constant as 48 V as shown in the Table 2 and Fig. 7.

Circulating current with proposed droop control technique by varying cable resistance & reference voltage depicted in Fig. 5.

Table 2 System response by varying cable resistance R1, R2 and reference voltage Vdc1, Vdc2

Vdc1	Vdc2	R1	R2	I1	I2	Ic	Di	Rd1	Rd2
48 43.2	48	0.02	0.02	1.995	1.995	0	–	0.24	0.12
	48	0.02	0.03	2.076	1.99	0.083	0.09913	0.01	0.019
43.2 40.8\40.8	48	0.1	0.02	1.736	2.325	0.6	–	0.007	0.02
	48	0.02	0.02	2.033	2.033	0	0.0881	0.0071	0.0204
	48	0.02	0.03	2.075	1.989	0.09607	0.0999	0.0071	0.024

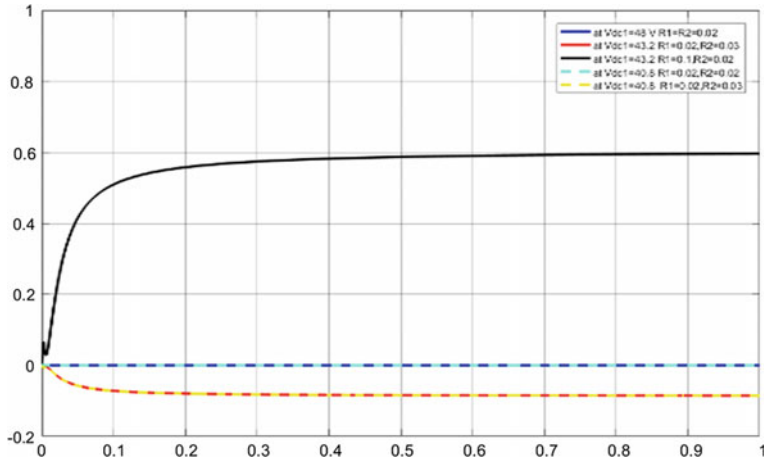

Fig. 7 Circulating current with proposed droop control technique by varying cable resistance and reference voltage

5 Conclusion

The paper presents a modified control scheme using DC/DC Boost parallel converters which offers better voltage regulation with considering cable resistances. For this type of voltage control topologies, no communication system and heavy installations are required. This method can also be used for other DC/DC converters like buck, cuk and sepic converter. The method employs voltage control technique further voltage and frequency control techniques, and stability analysis can also be done in this area.

References

1. Jayaswal K, Palwalia DK, Jain G, Kumar P (2015) Design-orinented analysis of non-isolated DC-DC buck converter. Cienc. e Tec. Vitivinic. 30:177–213
2. Sharma K, Palwalia DK (2017) Design of digital PID controller for voltage mode control of DC-DC converters. ICMDCS, Vellore, 2017, pp 1–6
3. Palwalia DK, Singh SP (2009) New load controller for single-phase self-excited induction generator. Electr Power Components Syst 37(6):658–671
4. Wu R-HH, Kohama T, Kodera Y et al (1993) Load-current-sharing control for parallel operation of DC-to-DC converters. In Proceedings of IEEE power electronics specialist conference-PESC'93. IEEE, pp 101–107
5. Singh L (2018) Adaptive control of parallel power converters for load sharing in DC micro-grid. ICRIEECE, KIIT, Bhubaneshwar
6. Majumder R, Chaudhuri B et al (2010) Improvement of stability and load sharing in an autonomous microgrid using supplementary droop control loop. IEEE Trans Power Syst 25(2):796–808
7. Lin BR, Huang CL (2011) Analysis and implementation of zero voltage switching integrated buck-flyback converter. Int Rev Electr Eng 6(7):2846–2852

8. Efimov D, Schiffer J, Ortega R (2015) Application to droop-controlled inverter-based Robustness of delayed multistable systems with application to droop-controlled inverter-based microgrids. vol 7179, no. December, pp 0–14
9. Kim JW, Choi HS, Cho BH, Member S (2002) A novel droop method for converter parallel operation, vol 17, no 1, pp 25–32
10. Augustine S, Lakshminarasamma N, Mishra MK (2016) Control of photovoltaic-based low-voltage dc microgrid system for power sharing with modified droop algorithm, vol 9, pp 1132–1143
11. Fernandes BGG, Anand S (2012) Modified droop controller for paralleling of dc–dc converters in standalone dc system. IET Power Electron 5(6):782–789
12. Augustine S (2014) Proportional droop index algorithm for load sharing in DC microgrid, pp 1–6

PSO Based Reactive Power Coordination of PV System and Voltage Controlled Devices

Sankaraiah Mogaligunta, S. Suresh Reddy and M. Vijaya Kumar

Abstract Solar type distributed generation (DGs) becomes popular and extensively used by consumers as well as power producers on radial distribution systems. The presence of solar type DGs on radial lines affecting the switching operations of under load tap changers (ULTC) and shunt capacitors (SCs) in addition to power loss. This paper proposes a novel method in which reactive power of solar type DG and voltage controlled devices coordinated with particle swarm optimization (PSO) algorithm with the help of forecast load. Problem formulated as multi objective function with switching operational cost and power loss cost. Proposed method tested on 10 kV, 16 buses practical system in Matlab environment and results compared with conventional method to demonstrate the effectiveness without failing the grid conditions.

Keywords Particle swarm optimization (PSO) · Voltage controlled devices (VCDs) · Distributed generation (DG)

1 Introduction

Nowadays the involvement of distributed generation (DGs) on radial lines increases to maintain voltage within the limits and also to reduce the radial system losses. DGs are classified into Dispatchable and non-dispatchable DGs. Solar and wind power type DGs are well-known non-dispatchable DGs (NDDG) because of input available with free of cost [1]. DGs penetrating on radial lines affect the life of voltage controlled devices (VCDs) by increasing the switching operations [2]. ULTC and CSs as VCDs connected to DG with automatic voltage regulator causes great impact on VCDs [3]. In [4], DG connected to VCDs and this system controlled by SCADA, which increasing the SOs of VCDs by more than two times. Dynamic programming

S. Mogaligunta (✉) · M. Vijaya Kumar
EEE Department, JNTUA, Anantapur 515002, Andhra Pradesh, India
e-mail: sankar.neeru@gmail.com

S. Suresh Reddy
EEE Department, NBKRIST, Nellore 524413, Andhra Pradesh, India

© Springer Nature Singapore Pte Ltd. 2020

T. Hitendra Sarma et al. (eds.), *Emerging Trends in Electrical, Communications, and Information Technologies*, Lecture Notes in Electrical Engineering 569,
https://doi.org/10.1007/978-981-13-8942-9_24

method proposed to control and coordinated DG and VCDs [5] and combined voltage control method proposed for coordinating DG and VCDs [6]. These papers reported that, while scheduling the reactive power impact of DGs not accounted.

ULTC and SCs reactive power coordinated with synchronous machine [7]. Power loss minimization done by using optimal power flow method in the presence of DG and VCDs [8]. TRSQP method was applied to control the reactive power of DG in the presence of VCDs [9]. Two types of DGs like synchronous generator and asynchronous generator connected with VCDs and reactive power coordinated using voltage control method [10]. Adaptive control method proposed to coordinate the reactive power among DG and VCDs [11]. Dynamic programming method proposed for coordination of reactive power between DG and VCDs [12]. Particle swarm optimization method proposed for coordination purpose among DG and VCDs [13]. The importance given for dispatchable type DGs are more and relatively very less importance given for non-dispatchable DGs.

This paper focused on solar system reactive power coordination together with ULTC and SCs with objectives of switching operations and power loss reductions. Particle swarm optimization (PSO) algorithm is used for solving the objective function.

2 Modeling of PV System

Power generated by solar system depends on too many factors like material properties and geographical conditions (temperature and radiation) at solar plant locations etc. [14]. Simple mathematical equations proposed by sarkar for power generation of solar unit as follows [15]:

$$\eta_m = \eta_C(1 - \alpha_C(T_C - T_S) + IC \times \log SI) \tag{1}$$

$$T_S = T_{at} + (T_{SC} - 20^{\circ}C) \times \frac{SI}{800\frac{w}{m^2}} \tag{2}$$

where η_m is efficiency of the module, η_C is solar cell module, α_C is power temperature coefficient of solar cell, T_C is cell temperature, T_S represents temperature at standard conditions, IC and SI indicates irradiation coefficient and solar irradiation respectively, ambient temperature represented by T_{at}. ω Indicates watts and m stands for meters.

$$P_m = \frac{SI}{1000\frac{w}{m^2}} \times P_{np} \times (1 - \alpha_C(T_C - T_S)) \tag{3}$$

where P_m and P_{np} are power generated by module and nominal power of solar cell respectively.

3 Problem Formulation

Solar system connected to grid through transmission line and transformer is shown in Fig. 1.

where,

E_1, E_2 and E_3 are Grid voltage, sending end and receiving end voltages respectively.

P and Q are real and reactive powers respectively, suffix 1, 2, 3, L and C indicates grid, sending end, receiving end, load and capacitors respectively. P_{PV} & Q_{PV} are the real and reactive power supplied by solar system.

r is the tap position of ULTC, R and X indicates transmission line or feeder resistance and reactance respectively.

Mathematical model of multi objective function can be expressed as follow:

$$J = \min\left(\sum_{h=1}^{24}\left(\begin{array}{l}\left(C_1 \times P_L^h\right) + \left(C_2 \times \left|r^h - r^{h-1}\right|\right) \\ +\left(C_3 \times \left|k_1^h - k_1^{h-1}\right|\right) \\ +\left(C_4 \times \left|k_2^h - k_2^{h-1}\right|\right)\end{array}\right)\right) \tag{4}$$

where C, P_L, h, k_1 and k_2 stands for cost weighting factor, active power loss, hours and number of shunt capacitors at sending end and feeders respectively.

Power loss mathematical expression is as follows:

$$P_L^h = I_L^2 \times R_L \tag{5}$$

where I_L is the current in the transmission line, which can be expressed in terms of sending end and receiving end voltages.

The solution of multi objective function includes equality and inequality constraints to obtain proper reactive power coordination. Equations 6 and 7 represents mathematical representation of equality constraints. Equations 8–12 represents mathematical representation of inequality constraints, which includes DG reactive power limits, voltage limits and maximum and minimum number of capacitors.

$$P_{PV} - P_L = P_{loss} \tag{6}$$

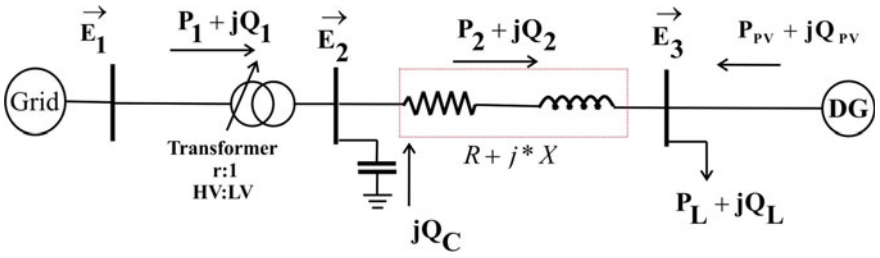

Fig. 1 Solar system grid connected single line diagram

$$Q_{PV} - Q_L = Q_{loss} \tag{7}$$

$$Q_{PV}^{\min} \leq Q_{PV} \leq Q_{PV}^{\max} \tag{8}$$

$$\left|E^{\min}\right| \leq |E| \leq \left|E^{\max}\right| \tag{9}$$

$$\left|r^{\min}\right| \leq |r| \leq \left|r^{\max}\right| \tag{10}$$

$$k_1^{\min} \leq k_1 \leq k_1^{\max} \tag{11}$$

$$k_2^{\min} \leq k_2 \leq k_2^{\max} \tag{12}$$

4 Particle Swarm Optimization (PSO) Algorithm

Particle swarm optimization (PSO) algorithm is very popular for optimizing the objective function. This algorithm has favourable performance as compared with other heuristic algorithms [16, 17]. In this paper, we preferred PSO for minimizing the multi objective function.

Particle swarm optimization method works on particle movements. Initially all the particles are starting from a random position and moves randomly with relative velocities, then updating their positions based best particle position decided in the previous iteration. The description of PSO can be mathematically modelled as.

$$Y_i^{k+1} = \begin{pmatrix} round\left(w \cdot Y_i^k\right) + round\begin{pmatrix} c_1 \cdot rn(0,1) \\ \left(P_i^k - X_i^k\right) \end{pmatrix} \\ +round\left(c_2 \cdot rn(0,1) \cdot \left(G^k - X_i^k\right)\right) \end{pmatrix} \tag{13}$$

$$w = w_{\max} - \left(w_{\max} - w_{\min}\right) \times \frac{k}{k_{\max}} \tag{14}$$

$$X_i^{k+1} = X_i^k + Y_i^k \tag{15}$$

Equation 13 is velocity update equation in which first term indicates the inertial behaviour of ith particle and the remaining terms represents cognitive and social behaviours of a particle that changes particle velocity by its self-experience and knowledge of swarm collection respectively. $rn(a, b)$ is a random value which varies uniformly within the range of $[a, b]$ and round accounts for ULTC and SCs discretized operation. P_i^k and G^k responsible for movement of particles towards optimal value. ULTC, SCs and PV inertia weights were taken as 3, 2 and 0.040. The round functions just for the operation of ULTC and SCs not for the PV voltage variations. In this

work there are four optimizing parameters, first one is power loss reduction and the remaining three are switching operations of ULTC and SCs. The proposed algorithm is written in the following steps.

Step 1 Assume all node voltages 1 p.u.
Step 2 Read distribution system data and initialize PSO parameters.
Initialize PSO parameters, system line and bus data, controllable parameters (power loss, ULTC tap position and capacitor positions at substation and feeders) minimum and maximum values.
Step 3 Calculate power loss using Backward/Forward algorithms.
Power loss of radial distribution system calculated using backward/forward algorithm with initial voltages at all nodes and minimum position of controllable parameters.
Step 4 PV is located at specified bus.
Select the proper location of solar system.
Step 5 Multi objective Fitness function (MOF) calculation.
Calculate multi objective fitness function using backward/forward algorithm with initial positions of controllable parameters.
Step 6 Initialize iteration count.
Step 7 Minimization of MOF.
Apply PSO to minimize the MOF by optimizing power loss and controllable parameters.
Step 8 Constraints verification.
If all the constraints are satisfied then display power loss, tap position and positions of substation and feeder capacitors. else increase iteration count and go to step 6.

5 Test System

10 kV practical Test system shown in Fig. 2, it consists of 16 buses and three feeders of lengths 1.2 km, 1 km and 1.1 km respectively. At bus 1 three capacitors of 2.5 MVAR connected, at bus 4 and 9 five capacitors of 1.5 MVAR connected, at bus 13 four capacitors of 1.5 MVAR connected [12]. Solar system (PV) connected at different locations like at 5, 8 and 14 to demonstrate the effectiveness of proposed method.

Forecasted load at all the buses shown in Figs. 3, 4 and 5. All the loads are lagging type with a power of 0.8 and solar system operating power factor is 0.8 lag or lead.

6 Results and Discussion

Results consolidated into three cases depending upon location of solar type DG.

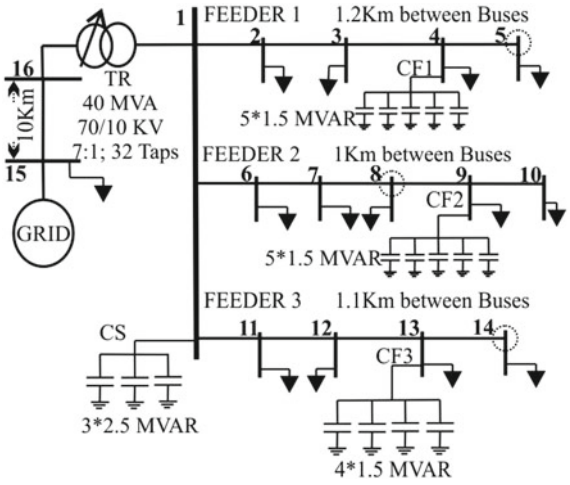

Fig. 2 Single line diagram of 10 kV practical system

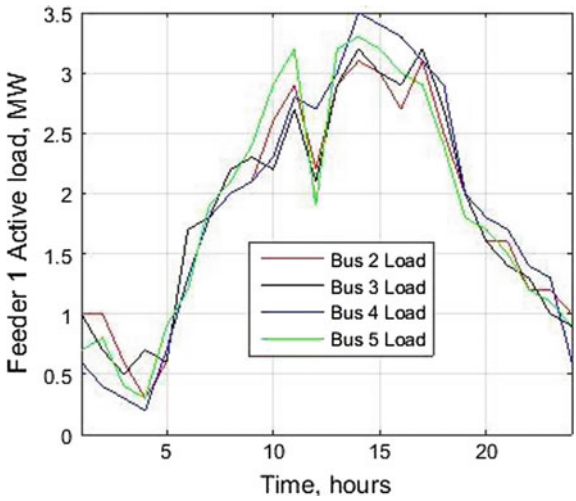

Fig. 3 Feeder 1 forecasted load of 10 kV practical system

Case 1 PV type DG located at bus 5 on feeder 1, results shown in Table 1.
Case 2 PV type DG located at bus 8 on feeder 2, results shown in Table 2.
Case 3 PV type DG located at bus 14 on feeder 3, results shown in Table 3.

Figures 6 and 7 clearly indicates how reduction of switching operations of ULTC and source capacitor. Tables 1, 2 and 3 shows the results for all the cases, cost of power loss is obtained by multiplying power loss with cost weighting factor of 80. Cost of switching loss is sum of ULTC switching cost and shunt capacitors switching cost. ULTC switching cost obtained multiplying ULTC variations with cost weighting factor 80, switching cost of source capacitors obtained by multiplying capacitor variations with 60 and other capacitors with 40.

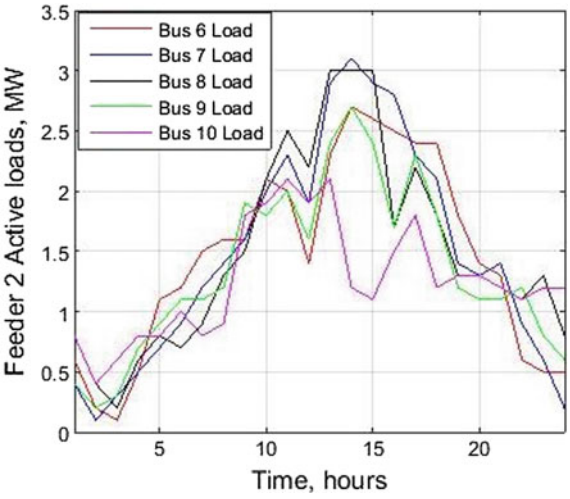

Fig. 4 Feeder 2 forecasted load of 10 kV practical system

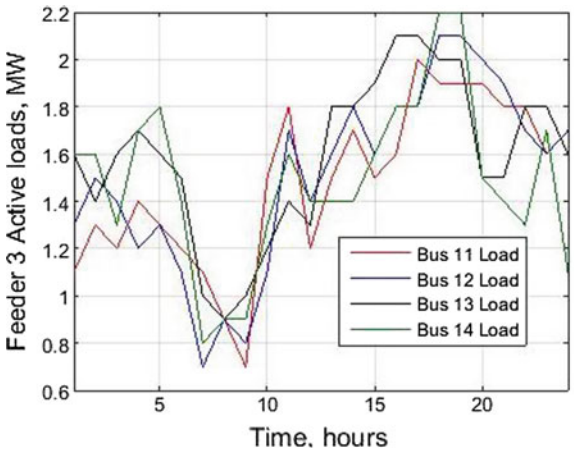

Fig. 5 Feeder 3 forecasted load of 10 kV practical system

7 Conclusion

In this paper a novel method for reactive power coordination between solar type DG, ULTC and SCs proposed and tested on 10 kV practical system. The proposed method clearly indicated that power loss and total number of switching operations of VCDs decreased effectively as compared with conventional method. This method ensures maximum power loss reduction of 7.57%, switching loss reduction of maximum 51.51% and total loss reduction of maximum 31.48% in comparison with conventional method.

Table 1 Solar type DG located at bus 5 (Case 1)

PV location		At bus 5	
Control methods		Conventional method	PSO method
Power loss (MWh)		12.8981	12.1433
Switching operations of VCDs	ULTC	4	2
	CS	10	0
	CF1	5	7
	CF2	3	4
	CF3	2	1
Power loss ($)		1031.848	971.464
Switching loss ($)		1320	640
Total loss ($)		2351.848	1611.464

Table 2 Solar type DG located at bus 8 (Case 2)

PV location		At bus 8	
Control methods		Conventional method	PSO method
Power loss (MWh)		12.92	12.173
Switching operations of VCDs	ULTC	6	0
	CS	10	10
	CF1	5	8
	CF2	3	4
	CF3	2	3
Power loss ($)		1033.6	973.84
Switching loss ($)		1480	1200
Total loss ($)		2513.6	2173.84

Table 3 Solar type DG located at bus 14 (Case 3)

PV location		At bus 14	
Control methods		Conventional method	PSO method
Power loss (MWh)		13.021	12.0346
Switching operations of VCDs	ULTC	4	2
	CS	10	1
	CF1	6	11
	CF2	3	4
	CF3	2	1
Power loss ($)		1041.68	962.768
Switching loss ($)		1360	860
Total loss ($)		2401.68	1822.768

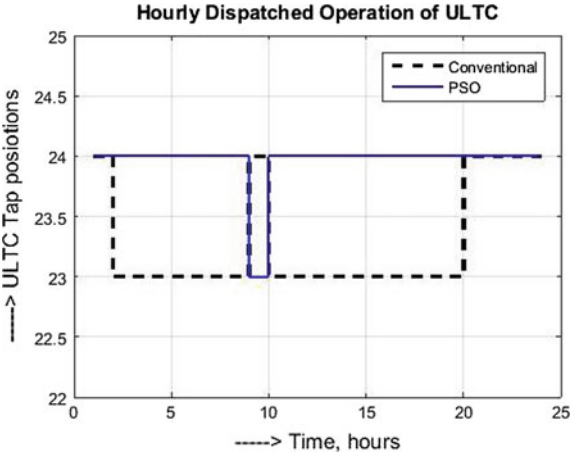

Fig. 6 ULTC scheduled operation for 24 h with conventional and PSO methods

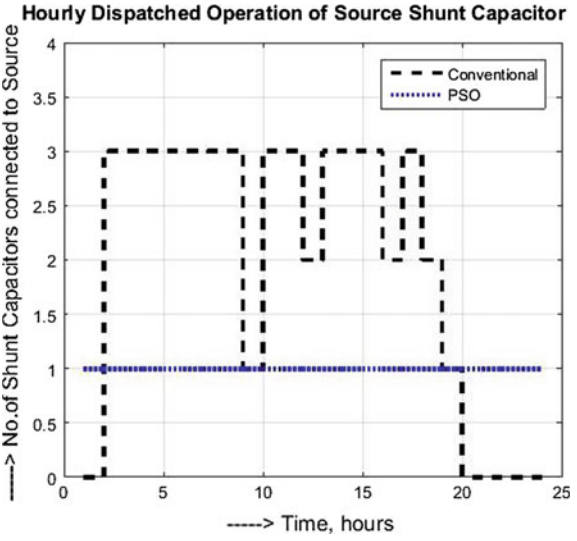

Fig. 7 Source capacitor scheduled operation for 24 h with conventional and PSO methods

References

1. Jiayi H, Chuanwen J, Rong X (2008) A review on distributed energy resources and micro grid. Renew Sustain Energy Rev 12(1):2472–2483
2. Hsun R, Chen Kuo L (2001) Dispatch of main transformer ULTC and capacitors in a distribution system. IEEE Trans Power Delivery 16(4):625–630
3. Donnel JO (2007) Voltage Management of Networks with Distributed Generation. PhD thesis. Edinburgh, UK
4. Vivan FA (2008) Voltage control and voltage stability of power distribution systems in the presence of distributed generation. PhD thesis. Sweden, U.T.
5. Lu FC, Hsu YY (1995) Reactive power/voltage control in a distribution substation using dynamic programming. Proc. Inst. Elect. Eng., Gen., Trans., Dist 142(6):639–645

6. Vivan FA, Karlsson D (2007) Combined local and remote voltage and reactive power control in the presence of induction machine distributed generation. IEEE Trans Power Syst 22(4):2003–2012
7. Vivan FA, Karlsson D (2008) Voltage and reactive power control in systems with synchronous machine based distributed generation. IEEE Trans Power Delivery 23(2):1079–1087
8. Dent CJ, Ochoa LF, Harrison GP (2010) Network distributed generation capacity analysis using OPF with voltage step constraints. IEEE Trans Power Syst 25(1):296–304
9. Ahmadi AR, Green TC (2009) Optimal power flow for autonomous regional active network management systems. In: IEEE power & energy society general meeting, pp 1–7
10. Sheng W, Liu KY, Cheng YS (2015) A trust region SQP method for coordinated voltage control in smart distribution system. IEEE Trans Smart Grid 7(1):381–391
11. Li H, Li F, Xu Y, Riyaz DT, Kueck JD (2010) Adaptive voltage control with distributed energy sources: Algorithm, theoretical analysis, simulation, and field test verification. IEEE Trans Power Syst 25(3):1638–1647
12. Kim YJ, Ahn SJ, Hwang PI, Chan PG, Moon SI (2013) Coordinated control of a DG and voltage controlled devices using a dynamic programming algorithm. IEEE Trans Power Syst 28(1):42–51
13. Sankaraiah M, Suresh Reddy S, Vijaya Kumar M (2017) Particle swarm optimization based reactive power coordinated control of distributed generation and voltage controlled devices. The Journal of CPRI. 13(3):447–454
14. Kumar Manish, Kumar Ashwani, Sandhu KS (2016) PV-WT based distribution generator location minimizing transmission loss in pool/Bilateral electricity market model. Procedia Technology 25(1):692–701
15. Sarkar S (2013) Minding the P's and Q's: Real and reactive power assessment of hybrid energy conversion systems with wind and solar resources. PhD thesis. Iowa State University, Ames
16. Niknam T, Narimani MR, Aghaei J, Azizipanah RA (2012) Improved particle swarm optimisation for multi-objective optimal power flow considering the cost, loss, emission and voltage stability index. IET Gener Transm Distrib 6(6):515–527
17. Gaing ZL (2003) Particle swarm optimization to solving the economic dispatch considering the generator constraints. IEEE Trans Power Syst 18(3):1187–1195

An Overview of Gasifier and Its Application in Indian Context

Rakesh Kumar Dabkeya, Dheeraj Kumar Dhaked and Mahendra Lalwani

Abstract The one of most compelling challenges in the recent time is finding a way to encounter global and national energy demand with reducing harm to the environment. Those challenges can be encountered by the application of biomass gasifiers. The utilisation of biomass gasifiers are the vital source outcome of energy in various areas of the world, especially for remote areas, where electricity transmission is not possible by the supply of high-quality fossil fuels. Gasifier application plays key role in biomass utilization same as a renewable power resource by the gasification process; gasification is the thermo-chemical method by which carbonaceous (hydrocarbon) ingredients (like coal, petroleum coke, and biomass) can be transformed into synthesis gas or producer gas. Design of biomass gasifier is determined by the category of source fuel utilized and the portability of gassifier. Various categories of gasification arrangements have been established out of which some are commercialised. In Indian market, commonly downdraft type of gasifier is utilized because of the application of mechanical mode. The biomass gasifier application is also appropriate for the thermal type of energy mode. It will replace the abundant use of fossils fuels like petrol, diesel, naphtha oil, etc. This manuscript discusses about type of gasifiers used, their application, drawbacks associated with biomass and statistics of renewable in India.

Keywords Gasifier · Biomass · Gasification · Downdraft · Applications

R. K. Dabkeya
Department of Renewable Energy, Kota, India
e-mail: rakeshkumar0707@gmail.com

D. K. Dhaked (✉) · M. Lalwani
Department of Electrical Engineering, Kota, India
e-mail: ddhakar9@gmail.com

M. Lalwani
e-mail: mlalwani@gmail.com

© Springer Nature Singapore Pte Ltd. 2020

T. Hitendra Sarma et al. (eds.), *Emerging Trends in Electrical, Communications, and Information Technologies*, Lecture Notes in Electrical Engineering 569,
https://doi.org/10.1007/978-981-13-8942-9_25

1 Introduction

There are various renewable power sources in which, biomass is the important energy source. It will stand on third most usable major energy resource next to the coal and petroleum in the upcoming nearby future [1] because it is available in huge wide spread amount, enormous potential, non-conventional in nature with the reduction in the global warming emission advantages [2]. The potential of biomass energy to fulfill the global energy/power demand is already been broadly accepted. It will reduce the demand of the trade in methods of power/energy with the management of inadequate quantity of conventional type of fuels like petroleum, coal, oil, gas etc., based on the application of all additional indigenous fuel energy sources. Other than to fossil fuel like coal, the biomass commonly has more oxygen, smaller amount of carbon, large amount of potassium (K) and silica, a lesser amount of aluminum (Al) with iron (Fe), lesser heating significance, greater moistness, and inferior density with friability [3]. This has resulted in the utilization of biomass is to be used as alternate energy basis intended for developing nations since the economies of these countries are mainly based on agricultural and forestry. These countries generate the energy by two routes viz: Bio-chemical and thermo-chemical processes [4]. In thermo-chemical route mostly Klin and Gasifiers are used.

2 Classification of Gasifiers

The biomass gasifier converts the hydrocarbon material into high eminence producer gases. The gasifiers are categorized into three major groups by the base of its applicability as shown in Figs. 1 and 2. The technique by which the biomass components and gasifying agents originate into interaction with the biomass gasifier is significant and forms the root for categorization of gasifier (Table 1) [5].

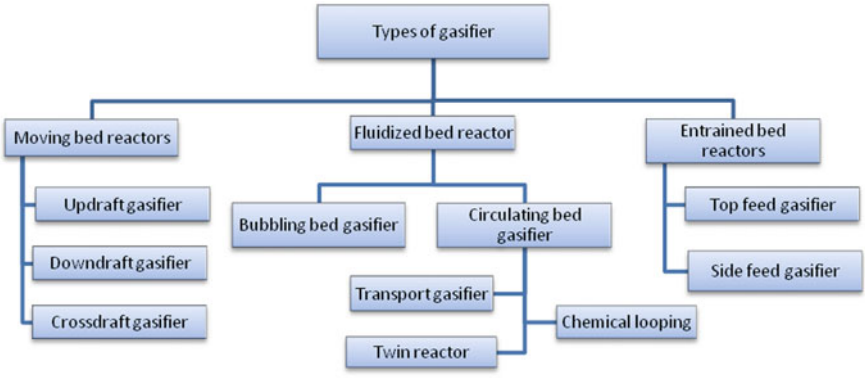

Fig. 1 Categorization of biomass gasifier

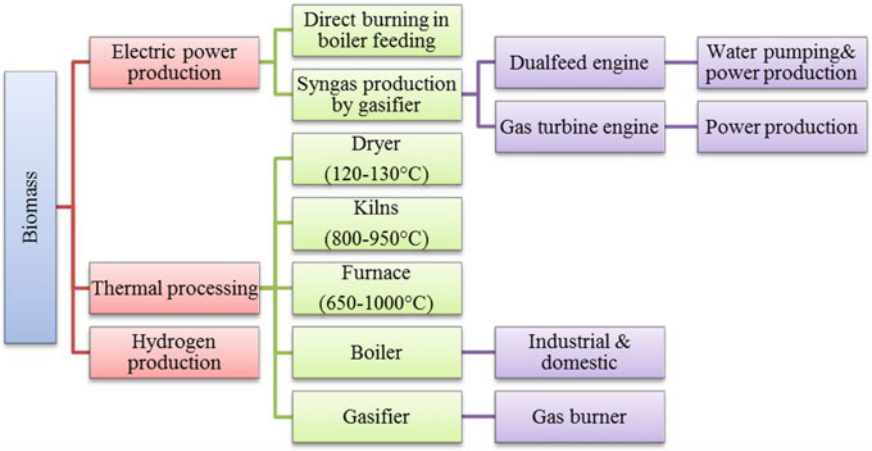

Fig. 2 Classification of gasifier on the basis of application of gasifiers

Table 1 Types of biomass applications

S. no.	Types of applications	Mode of energy	Applications
1	Utilization	Production of fuel gas	Industrial uses
		Production of electrical and mechanical power for stationary set ups	Domestic and industrial uses
		Hydrogen gas production	Uses in advanced vehicle
2	Load	Large scale applications (above 500 kW)	Industrial uses
		Medium scale applications (30–500 kW)	Domestic and industrial uses
		Small-scale applications (7–30 kW)	Heating purpose
		Micro scale applications (1–7 kW)	Cook stoves
3	Mobility	Standalone power production for movable objects	Mobile tower, vehicle propulsion

There are various gasification methodologies presently under improvement, such as:

- Plasma gasification
- Supercritical water gasification.

2.1 Conversion Route of Biomass

Biomass to energy conversion is followed by below mentioned two conversion routes.

Biochemical conversion. Biochemical conversion involves in breaking down the biomass to make carbohydrates available for processing into sugars, which can be converted into bio-fuels and bio products by the use of micro-organisms and catalysts. Biochemical conversion includes the considerable cost and difficulty involved in breaking down the bio-fuels and during the purification of them [6]. Biochemical conversion steps:

- Feedstock supply
- Pre-treatments
- Hydrolysis
- Biological conversion and Chemical conversion
- Product recovery
- Product distribution
- Heat and Power

Thermo chemical conversion. Thermo chemical processing offers opportunities for rapid processing of diverse feed stocks, including recalcitrant materials and unique intermediate feed stocks for the production of fuels, chemicals, and power. The classification of thermo chemical process is shown in Fig. 3.

Leading modern biomass advancements for utilization of biomass. These are some basic technologies of biomass utilization in domestic and industrial purpose [7, 8]:

- Disparaging carbonization of woodland biomass tocharcoal.
- Supercritical fluid abstractions form biomass into liquid products.
- Liquefaction of the biomass into liquid products.
- Gaseous products after gasification process of biomass.
- Pyrolysis of the biomass with solid wastes to gaseous, solid and liquid products.
- Hydrolysis of biomass to sugars and ethanol.

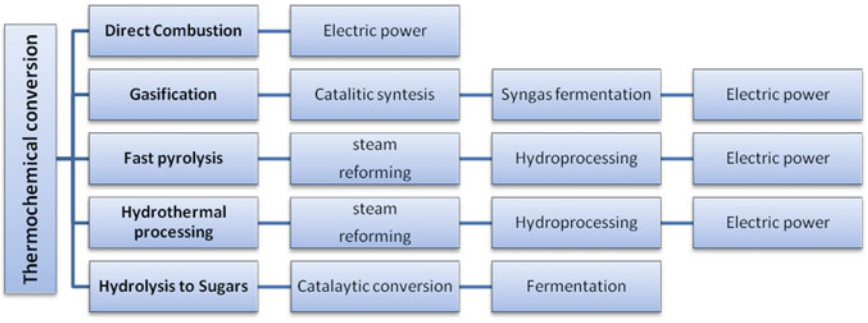

Fig. 3 Classification of thermochemical conversion

- Anaerobic digestion of biomass to gaseous products.
- Biomass power for producing electrical energy by gasification process or direct combustion.
- Pyrolysis.
- Co-firing of biomass with coal.
- Biological conversion of biomass and waste (biogas production, wastewater treatment).
- Biomass densification (briquetting, pelleting).
- Domestic cook-stoves and heating appliances of fuel wood.
- Biomass energy conservation in households and industry.
- Solar photovoltaic and biomass based rural electrification.
- Transformation of biomass into pyrolytic oil (biofuel) for the use of automobile fuel.

3 Application of Gasifiers

Biomass gasifier is called a device in which transformation of the biochemical fuels in gaseous forms takes place. After that, those products are used for different application. Gasifiers have three categories of applications viz. biomass to electrical energy, heating mode of gasifier and hydrogen production.

3.1 Biomass to Electrical Energy

Electricity production by gasifier has been in real after the IGCC (Integrated Gasification Combined Cycle) plant was started for industrial uses. There are numerous techniques for transforming biomass to electrical energy. In the rural regions the operation and setting up of steam engines were deliberated to be robust.

However, this technique underwent most important hindrance because of the unavailability of the engines and employment of the guidelines concerning qualified workers for boilers. BIGCC (Biomass Integrated Gasification Combined Cycle) with steam-injected gas turbine was anticipated to have much higher conversion efficiency though improvement of this procedure was not noticeable.

For the commercial development of bagasse gasification didn't showed that much prospective but the electricity production power generation (Coupled with an IC engine operating on producer gas) by exhausting biomass and boiler steam turbine route or cogeneration are the commercially feasible expertise. Biomass gasification is appropriate for decentralized and distributed power production in isolated localities of villages.

Bagasse-based cogeneration has previously been implemented by numerous sugar mills. Typically, the charge of electrical energy produced through this way is some-

what cheaper than biomass gasification method; in the range of INR 3–4 crore/MW. Revenues earned from electricity cogeneration have improved economy of sugar mills. However, cogeneration units are preferred only for capacities >5 MW and these units could be installed and implemented in an industrial area. Thus, they are not appropriate designed for applications in isolated remote zones of country where grid connectivity is not possible. Here, the IC engine with gasification combination will be a better option for power demand meeting [9].

3.2 Power Generation by Gasifier

Power generation unit which comprises of biomass gasifier arrangement has a gas refrigeration and vacuuming division, a biomass gasifier and a dual-fuel-engine-electrical.

Design of gasifier be determined by category of fuel used and its portability. In Indian market, commonly downdraft gasifiers are available because of the operation of mechanical approach [10].

Gasification process. It consists following four stage of process as shown in Fig. 4.

Working process of down-draft gasifier. The bio fuel is presented at the uppermost and the air is ordinarily brought together at specific intermediary level and the pro-

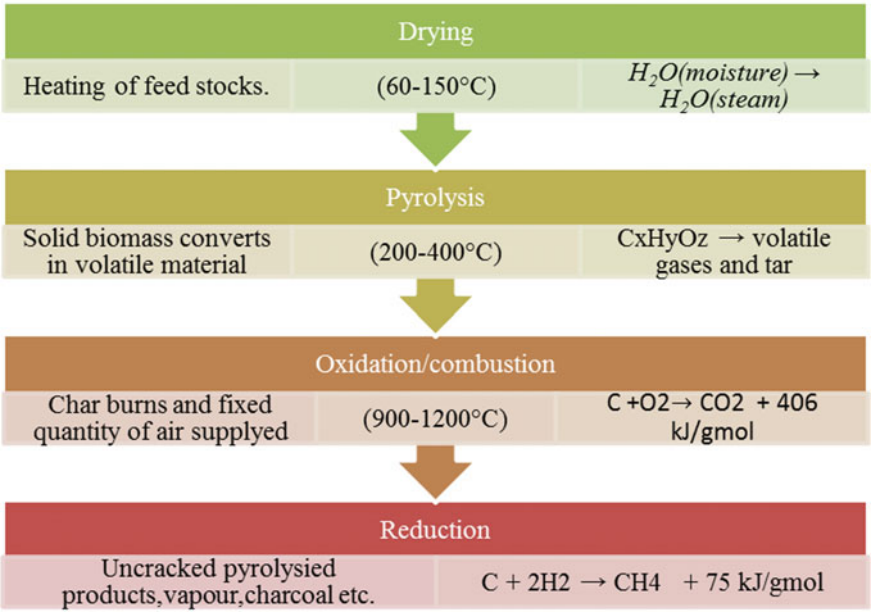

Fig. 4 Gasification stages of biomass

ducer gas is yield out at the lowermost part [10]. This is conceivable to differentiate four distinct parts of gasifier, every single of them is categorized by one significant phase in the development of transforming the bio fuel to a flammable producer gas. The procedures in these four regions are inspected below and the four parts of the gasifier are given below [11, 12]:

- Bunker division (Dehydrating zone)
- Pyrolysis zone
- Oxidation zone
- Reduction zone
- Cooling with cleaning zone
- Generator zone
- Dual-fuel mode operation.

3.3 Thermal Mode of Gasifier

Gasifiers can be a good option for the Applications which necessitate thermal form of energy. Thermal energy of the range of 5 MJ is obtained, by burning 1 m^3 amount of the producer gas in the burning chamber. Flame temperature of 1550 K can be attained by optimum pre-mixing of air with the gas. Few of the devices which gasifier could be retrofitted [13]. The thermal form of energy will be recycled in the industries at different stages which are given in the subsequent sections:

- Used as dryers
- Used as klins
- Used as furnaces
- Used as boilers

Heating mode of gasifier. Thermal mode application of gasifier characterized in two categories of following modes [14].

Scrubbed gas mode. In this type of thermal application of gasifier, the coarse filter is placed among the producer gas burner and the productivity of the producer gas from gasifier. So the gas was cleaned in the coarser filter zone by precipitating the tar particle and removes the moisture. Now the hot gas is delivered to gas burner by gas blower as shown in Fig. 5.

Hot gas mode. In this type of thermal application of gasifier, the rigid metal pipeline is placed between the producer gas burner and the output of the producer gas from gasifier, for the gas was supplied directly to gas burner. Now the warm gas is transported to gas burner by gas blower as displayed in Fig. 6.

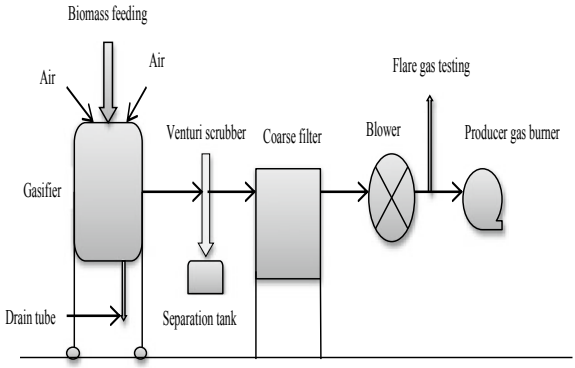

Fig. 5 Scrubbed gas mode of gasifier

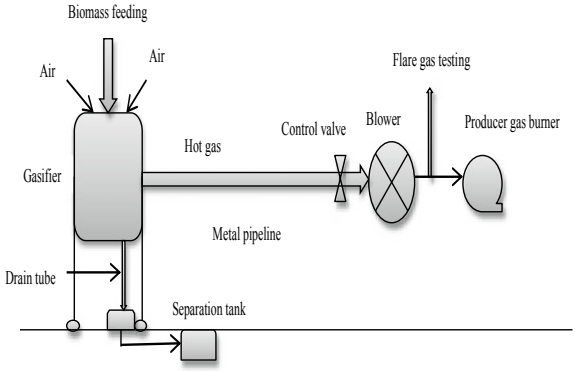

Fig. 6 Hot gas mode of gasifier

3.4 Biomass Gasifier Centered Other Application

Major share of the domestic cooking requirement is met with biomass fuels. Biomass fuels have the best place for boiler applications for the rice mills, sugar manufacturing work and numerous additional agriculture based productions. However, in many of these applications, the proficiency of utilization is rather low and it is authoritative to improve energy efficient technologies for biofuel utilizations. In acquaintance of the gigantic potential of biomass gasification engineering for meeting electrical energy demand, mechanical energy and thermal energy necessities in numerous subdivisions of our Indian economy, Administration of Indian government propelled an motivated investigation proposal for biomass cooking and biomass water pumping.

Institutional food preparation in India. In case of institutional cooking, cooling plus cleaning entity is not compulsory and gas is openly nourished into burning chamber from a dust filter. A minor blower is prerequisite for preliminary start-up of the arrangement. A representation of the biomass gasifier centered food preparation arrangement is prearranged in Fig. 7. Producer gas is generated through a biomass

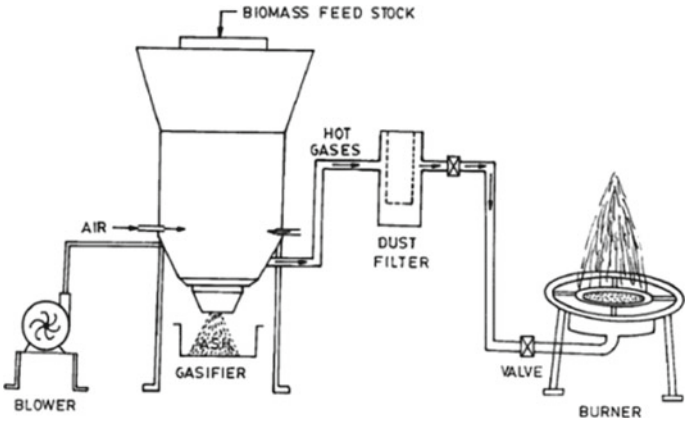

Fig. 7 Representation of a gasifier centered institutional food preparation arrangement

gasifier, which can be utilized for diverse thermal applications like, institutional food preparation in hostels, drying purposes and temperature maintaining of homes etc.

It is obvious that the utilization of a biomass gasifier-based system for institutional cooking may provide a general productivity of about 40% as compared to 8–20% from traditional oven/furnace [15].

Biomass gasifier constructed water propelling. Small size gasifiers coupled to diesel engine pump sets are moreover being deliberated for irrigation pumping [16] as displayed in Fig. 8.

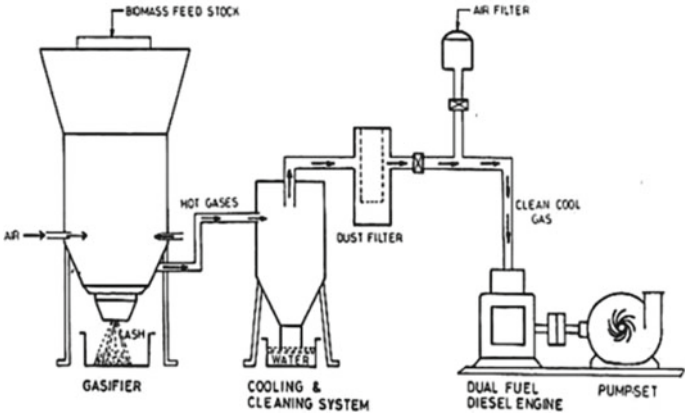

Fig. 8 Representation/schematic of a biomass gasifier founded water propelling arrangement

3.5 *Recent Status of Hydrogen (a Rich Gas) Manufacturing from Bio Fuel Gasification in a Downdraft Gasifier*

The paramount technique for production of the renewable hydrogen is the biomass gasification. Conversely, this expertise stagnant in the laboratory measures for the reason of its very large amount of energy consumption. Paralleled to biomass gasification, biomass O_2 or vapor gasification develops hydrogen harvest contingent on the measurements of downdraft gasifier. This also approximately increases up, double in amount of the heating system value the fuel gas [17].

4 Drawbacks/Problems in Biomass Gasification with Probable Solutions

During the gasification progression, with the concession of engendering advantageous merchandises, numerous wastes like the tar, NO_x, SO_x and fly ash are also produced. Another most important problem related to the applications of gasification expertise is the elimination and dumping of ash. Therefore, before using producer gas for other applications, the main impurities should be removed. The treatment methods and feasible solutions to the tar and ash removal issues are deliberated below in detail.

The parameters with the greatest impact on the gasification process are the temperature of gasification reaction and the equivalent ratio, both are interrelated. To control of these parameters ensures that (i) a syngas with a tolerable content of tars and particles is formed and (ii) there are no redundant ash sintering effects caused by high temperatures in the reactor [18].

More energy is using in drying process if moisture contented biomass is higher; it will decrease the gasification efficiency. Additionally, moisture substances higher than 15% will enhance to discrepancies in the attentiveness of the syngas engendered, and consequently in its calorific value, in this manner the process turns unstable. Prior biomass preparation procedures, like pyrolysis or torrefaction, may help to provide the fuel with energy regularity and stabilizes gasification [19]. Estimation will have to be made of the energy costs of the earlier processes, with an evaluation of their feasibility.

The supreme common problem in the improvement of gasification technique is the existence of the tars in syngas [20]. Current research in work on the gasifier, like (i) its design characteristics and shape, (ii) the optimal setting of the working parametric characteristics that have a direct impact upon the volume of tars engendered, and (iii) the addition of catalytic agents and other additives, (iv) the stream of syngas engendered by different gasification, (v) Improvement in technologies for vacuuming or converting the tar [21–25].

The application and uses of gasifier survey of some authors is mentioned in Table 2.

Table 2 The applications of gasifier survey of some authors

Application	Types of gasifier	Feed stocks	Capacity of gasifier	Modification
Power of 30 kW and 60 kW of heat [26]	Modified a throated downdraft gasifier		30 kW	Reduces the grate spacing and increase the height of grate, bringing it near to the hearth
Power generation [27]	Modular type, down-draft gasifier		125–375 kg h^{-1}	Works on modular design of throat type
Power generation [28]		Rice husk		Calculate per unit cost of electricity generation using rice husk
Power generation [29]	Down-draft gasifier		1 MW	Comparisons made between gasifier/engine and steam-cycle
Thermal draying for rural applications [30]		Wood and agro waste		Improving product quality and processing rates, due to controlled burning of gaseous fuel
Boiler power systems [31]		Wood and briquettes		Give a direct combustion systems design for boiler
Power generation [32]	Fixed bed gasifier			The composition of the gasification gas depends upon gasification route and temperature
Hydrogen rich gas production [33]	Circulating fluidized bed gasifier	Wood chips, annual crops, perennial energy crops	500 kW	Used FICFB (Fast internally circulating fluidized bed configuration) with Ni-catalysts

(continued)

Table 2 (continued)

Application	Types of gasifier	Feed stocks	Capacity of gasifier	Modification
Hydrogen rich gas production [17]	Fluidized-bed gasifier	Pine sawdust (0.3–0.45 mm)		Used calcined dolomite catalysts
Low temperature for drying [34]	Biomass gasifier dryer by Agro Biochem (India) Pvt. Ltd.	Briquettes	2 MW thermal power equivalent hot gases at 373 ± 5 K	Drying about 800–900 kg of marigold flower. Drier efficiency is about 62%
High temperature drying (600–920 °C) [35]	Biomass gasifier dryer	Briquettes and agricultural residue	1.2 MW thermal power	One gasifier run eight furnaces with different temperature arrangements
Generate electricity [34]	Fixed bed gasifier	Wood	500 kW	The engine run on duel fuel mode wood and diesel
Generate electricity [36]	Downdraft fixed-bed gasifier	Rice husk and rice husk pellet	10 kW	Shows the opportunity of constant energy generation with atmospheric air

5 Overview of Non-conventional Energy Information in India

Biomass will be the principal source of energy in the unindustrialized nations like India. Biomass energies are principally utilized in rural families for food preparation and water heating system, as well as by old-fashioned and craftsperson manufacturing etc. The Department of India like Ministry of Non-conventional and Renewable Energy (MNRE) has been assisting the investigation and improvement of bio fuel gasification expertise in the nation by the support of administration of India to encourage the uses of non-conventional energy in industrial and domestic purpose. The cumulative achievements of India are 71526.30 MW in renewable energy for grid-interactive power and 1097.07 MWEQ off grid/captive power as on 31.07.2018. The Ministry for Non-conventional and Renewable Energy (MNRE) gives the uncertain State based opportunity data of non-conventional energy generation objective to be accomplished with the 2022 which is shown in Figs. 9, 10, 11, 12, 13 and 14. So that cumulative achievement of our nation is 175,000 MW by all renewable sources [25].

Under the Rajiv Gandhi Grameen Vidhyutikaran Yojana in the XI Plan—Scheme of Rural electricity infrastructure and household electrification, the village electrifi-

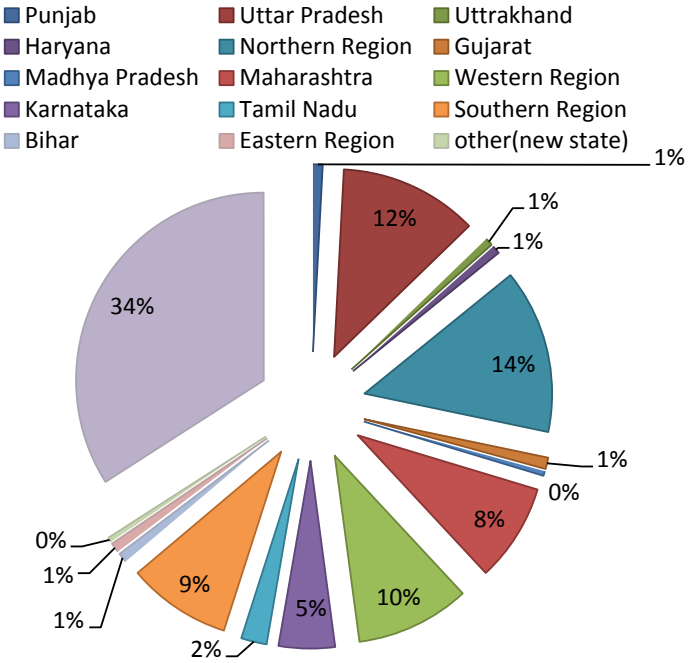

Fig. 9 Tentative state-wise biomass power (MW) break up of non-conventional energy goal to be accomplished by 2022 [37]

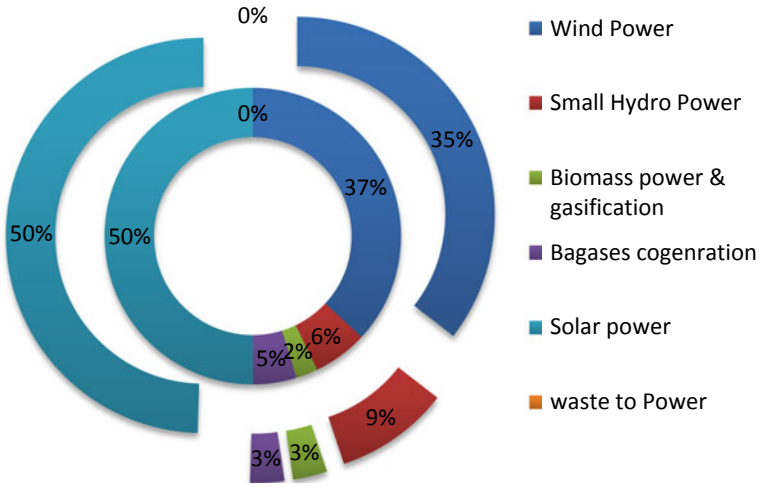

Fig. 10 Grid cumulative power (capacities in MW) 2007 and 2015 [37]

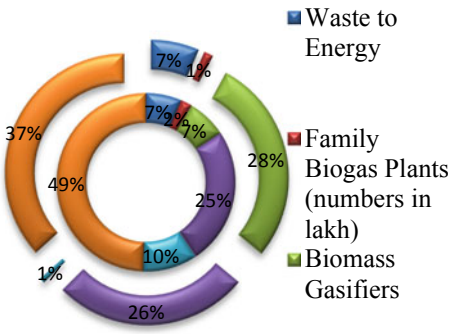

Fig. 11 Off-grid/captive in mw) 2007 and 2015 [37] power (capacities)

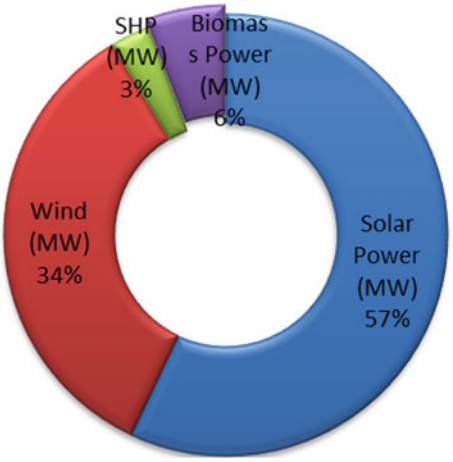

Fig. 12 Grid-interactive power (capacities in MW) 2007 and 2015 [37]

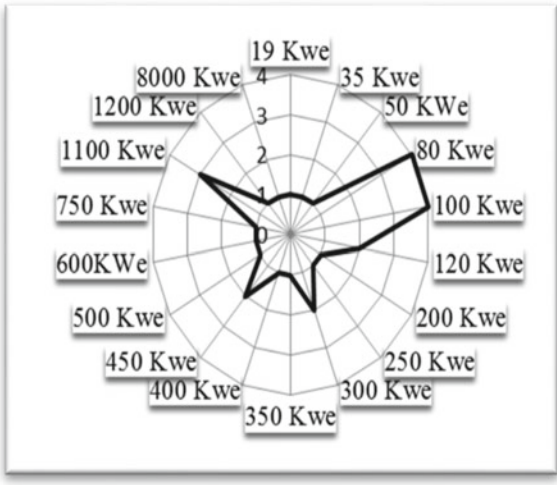

Fig. 13 Total gasifier installed capacity (thermal) of India [38]

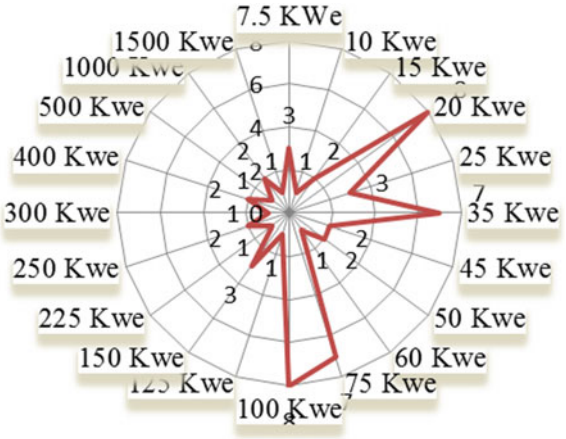

Fig. 14 Total gasifier installed capacity (electrical) of India [38]

cation through Decentralized Distributed Generation (DDG). Gasifier based systems are mostly used as they are fairly established as a DDG technology, and at the present point of time, is a preferred option compared to biogas based engines. The various sources of renewable include solar, small hydro, wind, biomass and other type are also included and their power is fed into grid by using power electronics converters and the power quality can be improved by compensators and FACTS controller utilization in the power system [39–43].

6 Conclusion

The employment of biomass is much easier for reorganized power production and heating mode by gasifier comparative to biogas production. Gasifier centered Power Producing arrangements are technically feasible and financially more viable during 100% producer gas mode not during dual fuel mode.

In this manuscript the reviews of status and prospective of biomass gasifier technology is discussed for thermal applications, heating solicitations and power production solicitation in India to meet the growing power burdens. The Ministry of New and Renewable Energy (MNRE) also promoting the biomass energy production and gasification program through subsidies for enhancement of bio wastes use. The problems of the biomass gasification process are also discussed here in this manuscript and the possible solutions are also suggested for the same.

It is very much suitable for thermal mode as heating application in domestic and industrial process. For good operational of power production, properties of feed stoke and the operational parameters of gasifier should be maintained. Some other application of gasifier like cooking, water pumping, are also beneficial, but since hydrogen production is under laboratory levels.

References

1. Werther M, Saenger E, Hartge U (2000) Combustion of agricultural residues. Prog Energy Combust Sci 26
2. Abbas T, Costen PG (1996) Solid fuel utilization: from coal to biomass. In: 26th symposium (international) on combustion, the combustion institute, Pittsburgh, pp 3041–3058
3. Demirbas A (2005) Potential applications of renewable energy sources, biomass combustion problems. Prog Energy Combust Sci 31(2):171–192
4. Grassi G, Delmon B, Molle JF, Zibetta H (1990) Biomass for energy and industry. Elsevier Applied Science, London
5. Bhavanam A, Sastry RC (2011) Biomass gasification processes in downdraft fixed bed reactors: a review. Int J Chem Eng Appl 2(6):425–433
6. Brown RC (2011) Thermochemical processing of biomass: conversion into fuels, chemicals and power, 1st ed. Wiley. ISBN 978-0-470-72111-7
7. Demirbas A (2004) Combustion characteristics of different biomass fuels. Prog Energy Combust Sci 30(2):219–230
8. Mondal PG, Dang S, Garg MO (2011) Syngas production through gasification and clean-up for downstream applications-recent developments. Fuel Process Technol 92(1):1395–1410
9. Buragohain B, Mahanta P, Moholkar VS (2010) Biomass gasification for decentralized power generation: the Indian perspective. Renew Sustain Energy Rev 14(1):73–92
10. Wood gas as engine fuel. FAO Forestry Department. ISBN 92-5-102436-7
11. Dogru M, Howarth CR, Akay G, Keskinler B, Malik AA (2002) Gasification of hazelnut shells in a downdraft gasifier. Energy 27(5):415–427
12. Tripathi AK, Iyer PVR, Kandpal TC (1997) A financial evaluation of biomass gasifier-based power generation in India. Bio Resour Technol 61(1):53–59
13. Biomass gasification heat power. http://www.ankurscientific.com/. Accessed 10 Sept 2018
14. Tripathi AK, Iyer PVR (1999) Biomass gasifier based institutional cooking in India: a preliminary financial evaluation. Biomass Bioenergy 17(1):165–173
15. Tripathi AK, Iyer PVR (1999) Financial analysis of biomass gasifier based water pumping in India. Energy 24(1):511–517
16. Lv P, Yuan Z, Ma L, Wu C, Chen Y, Zhu J (2007) Hydrogen-rich gas production from biomass air and oxygen/steam gasification in a downdraft gasifier. Renew Energy 32(1):2173–2185
17. Salam PA, Kumar S (2010) The status of biomass gasification. Energy Environment Partnership
18. Zhao M, Fennell PS (2016) An overview of advances in biomass gasification. Energy Environ Sci 9(1):2939–2977
19. Ruiz JA, Morales MP, Munoz P (2013) Biomass gasification for electricity generation: review of current technology barriers. Renew Sustain Energy Rev 18(1)
20. Warren JB, Poulter R, Parfitt RI (1995) Converting biomass to electricity on a farm-sized scale using downdraft gasification and a spark-ignition engine. Bioresour Technol 52(1):95–98
21. Verma R, Kumar M (2018) Symmetrical analysis of bio mass gasification techniques. MR Int J Eng Technol 5(1):17–24. http://mrijet.manavrachna.edu.in/index.php/journal/article/view/193. Accessed 12 Sept 2018
22. Kaushal P, Tyagi R (2017) Advanced simulation of biomass gasification in fluidized bed reactor using ASPEN plus. Renew Energy 101(1):629–635
23. Rupesh S, Murleedharan C, Arun P (2016) Aspen plus modelling of air-steam gasification of biomass with sorbent enabled CO_2 capture. Resour Effic Technol 2(2):94–103
24. Lopez MF, Pedroche J, Valverde JL, Sanchez-Silva L (2017) Simulation of the gasification of animal wastes in a dual gasifier using Aspen Plus®. Energy Convers Manag 140(1):211–217
25. Lalwani M, Singh M (2010) Conventional and renewable energy scenario in India: present and future. Can J Elect Electron Eng 1(6):122–140
26. Pathak BS, Patel SR, Bhave AG, Bhoi PR (2008) Performance evaluation of an agricultural residue-based modular throat-type down-draft gasifier for thermal application. Biomass Bioenergy 32(1):72–77

27. Kapur T, Kandpal TC, Garg HP (1996) Electricity generation from rice husk in Indian rice mills: potential and financial viability. Biomass Bioenergy 10(1):340–393
28. Quaak P, Knoef H, Stassen HE (2016) A review of combustion and gasification technologies, energy from biomass. World Bank technical paper no. 422. ISSN: 0253-7494
29. Palit D, Mande S (2007) Biomass gasifier systems for thermal applications in rural areas. Boil Point (The Energy and Resources Institute) 53(1):17–19
30. Demirbas A (2005) Potential applications of renewable energy sources, biomass combustion problems in boiler power systems and combustion related environmental issues. Prog Energy Combust Sci 31(2):171–192
31. Boerrigter H, Rauch R (2005) Review of applications of gases from biomass gasification. In: Handbook biomass gasification
32. Boerrigter H, Rauch R, Foscolo P, Matera D (2000) Hydrogen rich gas from biomass steam gasification. In: Proceedings of the 1st world conference and exhibition on biomass for energy and industry, Sevilla, Spain, pp 212–221
33. Dasappa S, Sridhar HV, Sridhar G, Paul PJ (2003) Biomass gasification—a substitute to fossil fuel for heat application. Biomass Bioenergy 25(1):637–649
34. Ghosh D, Sagar AD, Kishore VVN (2006) Scaling up biomass gasifier use: an application-specific approach. Energy Policy 34(1):1566–1582
35. Yoon SJ, Son YI, Kim YK, Lee JG (2012) Gasification and power generation characteristics of rice husk and rice husk pellet using a downdraft fixed-bed gasifier. Renew Energy 42(1):163–167
36. Biomass gasification heat power, Electricity generation by gasifier in India. http://www.eai.in/ref/reports/biomass_gasification_based_power_production.pdf. Accessed 10 Sept 2018
37. Biomass gasification, Thermal power production in India. https://mnre.gov.in/biomass-gasification. Accessed 10 Sept 2018
38. Loha C, Karmakar K, Santanu D, Pradip K (2017) Gasifiers: types, operational principles, and commercial forms. Coal and biomass gasification. Energy Environ Sustain (Springer) 63–91
39. Dhaked DK, Lalwani M (2017) A comprehensive review on a D-facts controller: enhanced power flow controller (EPFC). Int J Adv Eng Technol (IJAET) 10(1):84–92
40. Dhaked DK, Lalwani M (2017) Modeling and analysis of a D-facts device: enhanced power flow controller. Imanager's J Electr Eng (JEE) 11(1):41–49
41. Dhaked DK, Saini S, Sharma P (2018) Analysis of different converters for reduced total harmonic distortion and improved power factor. In: Fifth international conference on signal processing and integrated networks (SPIN), IEEE Conference. Amity University, UP
42. Khusalani G, Patel S, Dhaked DK, Sharma O (2018) FACTS controllers for power flow control: a brief review, ICCITD'18, Udaipur, Rajasthan, India. Int J Adv Eng Res Dev (IJAERD) 5(5):1–5
43. Gopal Y, Kumar K, Birla D, Lalwani M (2017) Banes and boons of perturb & observe, incremental conductance and modified regula falsi methods for sustainable PV energy generation. J Power Technol 97(1):35–43

Comparative Analysis of Flying Capacitor and H-Bridge Multilevel Matrix Converters for DFIG Based Wind Energy Conversion System

G. Pandu Ranga Reddy, J. N. Chandra Sekhar, B. Naresh and M. Vijaya Kumar

Abstract This paper discuss the comparative analysis of the Flying Capacitor Multi Level Matrix Converter and the H-Bridge Multi Level Matrix Converter topologies (replacing the conventional two stage converter and simple matrix converter) connected to a DFIG machine feeding the rotor from the grid to increase the efficiency of the machine. The THDs are compared with the interconnection of the DFIG machine to the grid with flying capacitor and H-Bridge multi level matrix converter. The complete analysis and graphical representations of the voltage and currents of the DFIG machine stator are shown with FFT analysis of current waveform in MATLAB Simulink software.

Keywords Double fed induction generator · Flying capacitor multilevel matrix converter · FFT-Fast Fourier transformation · H-bridge multilevel matrix converter · THD-Total harmonic distortion

1 Introduction

Over the past few years demand of electrical power is increasing day by day, leading to increase in power production using fossil fuels. To replace the fossil fuel energy generation, renewable sources are penetrated into the grid system. These renewable sources support the conventional sources with small capacities denoted as distribution generation [1]. In distribution generation the solar energy generation is vastly

G. Pandu Ranga Reddy (✉)
G.P.C.E.T., Kurnool, Andhra Pradesh, India
e-mail: gprreee@gmail.com

J. N. Chandra Sekhar
S.V.U., Tirupathi, Andhra Pradesh, India

B. Naresh
JNTUK, Kakinada, Andhra Pradesh, India

M. Vijaya Kumar
JNTUA, Anantapuramu, Andhra Pradesh, India

© Springer Nature Singapore Pte Ltd. 2020

T. Hitendra Sarma et al. (eds.), *Emerging Trends in Electrical, Communications, and Information Technologies*, Lecture Notes in Electrical Engineering 569,
https://doi.org/10.1007/978-981-13-8942-9_26

used to support the conventional source output, however the wind energy system is considered as the most efficient and higher capacity generation of renewable energy systems. With the use of dynamic elements (synchronous machines or induction machines) sinusoidal waveforms are generated rather than PWM output as that of the solar power (static elements) generation systems. In wind generation topologies the DFIG [1] machine is considered to be the most efficient generator with constant speed operations even with the change in the wind speeds. As the feeding of the rotor winding can be controlled with respect to the change in the mechanical torque of the turbine by controlling the power electronic converters connected to the rotor of the DFIG machine as shown in Fig. 1.

The converters used to feed the rotor can be cyclo converters or two stage VSIs (Voltage Source Inverters) with a DC link capacitor in between two VSIs [2]. All these conventional converters use sinusoidal PWM (Pulse width Modulation) scheme to control the power electronic devices connected. The usage of the two level or three level PWM techniques may lead to increase in THD in the rotor which induces the THD in the stator in turn feeding the THD to the grid, increasing the THD of the supply source affecting the loads connected to the grid and DFIG [3, 4]. To overcome the above problems, that is to reduce the THD even with the usage of power electronic equipments, a hybrid model (combination of matrix and multilevel converters) such as multi level matrix converters are introduced to replace the conventional two level and three level VSI converters. This multilevel matrix converter is an innovative technology, which incorporates the multilevel concept into the matrix converter. Among several multi level matrix converters, we consider the top priority converters with lesser THD generations and compare the results with implementation in DFIG design. As per [5, 6] the Flying Capacitor Multi Level Matrix Converter (FCMMC) topology and the H-Bridge Multi Level Matrix Converter (HBMMC) topology are considered to be the top priority converters to generate less THD compared to other multi level matrix converters.

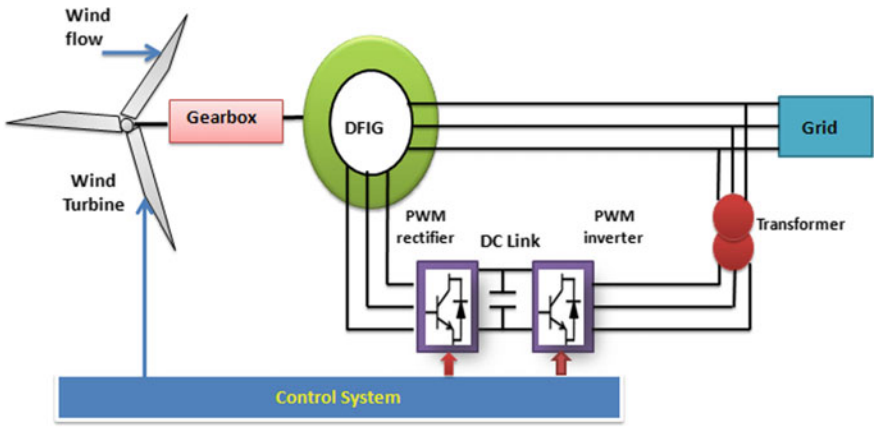

Fig. 1 DFIG based WECS integrated to grid

2 Modeling and Control of Flying Capacitor Multilevel Matrix Converter Topology

The Flying Capacitor Multilevel Matrix Converter topology [7] is advancement to the conventional nine switch matrix converter topology. The circuit topology can be seen in Fig. 2. As it can be observed that the number of bidirectional switches used in the above circuit are doubled as compared to the conventional converter. Each switch has two MOSFETs [6] (Metal Oxide semi-conductor field effect transistor) connected in anti parallel with two anti parallel diodes for bidirectional freewheeling operation. Six capacitors [7] with same values are used to create voltage dividing generating multilevel voltage output from the output of the topology. Each bidirectional switch is fed with the same PWM signal, so that 18 PWM signals are generated to run the proposed flying capacitor model with multilevel inverting operation.

2.1 Control Strategy of Flying Capacitor Multilevel Matrix Converter

Space vector modulation control technique is employed to generate PWM signals for the 18 bidirectional switches of the FCMMC topology. Considering a sinusoidal waveform [8] as the reference fundamental signal to generate space vector control signal with sector selection from the alpha and beta waveforms, by applying Clarke's

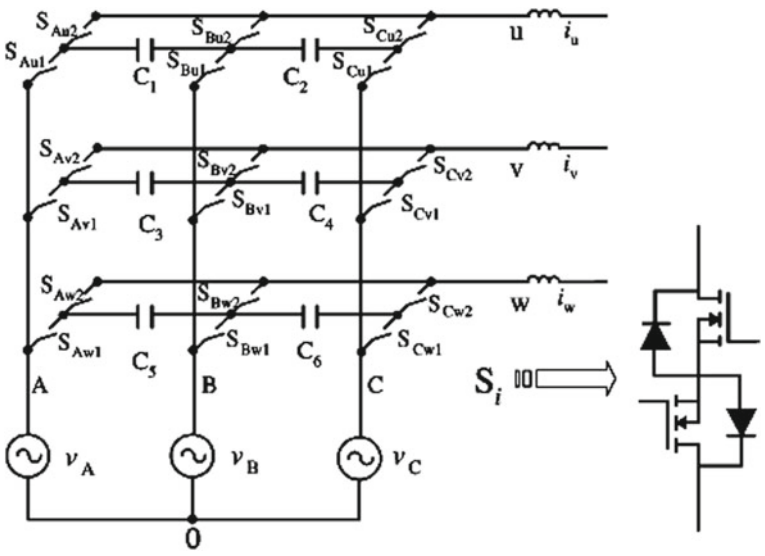

Fig. 2 Flying capacitor multilevel matrix converter topology

transformation to the sinusoidal signal.

$$i_{\alpha\beta}(t) = \frac{2}{3}\begin{bmatrix} 1 & -\frac{1}{2} & -\frac{1}{2} \\ 0 & \frac{\sqrt{3}}{2} & -\frac{\sqrt{3}}{2} \end{bmatrix}\begin{bmatrix} i_a(t) \\ i_b(t) \\ i_c(t) \end{bmatrix} \tag{1}$$

The alpha beta waveform denotes the sector consideration of the space vector trajectory and based on the vector of the trajectory the sector selection takes place. The sector selection with the alpha and beta components can be seen below in Fig. 3. The space vector switching diagram consists of six active vectors and the two zero vectors. With the six active vectors and two zero vector is considered for generation of pulses, accumulating all the switching states [9] depending on the sector selection the output gate signals are generated. The switches are energized with the equal distribution of voltages supplied by the capacitors. The input and output voltage of the FCMMC are expressed as

$$V_s = \begin{bmatrix} v_A(t) \\ v_B(t) \\ v_C(t) \\ \frac{v_A(t)+v_B(t)}{2} \\ \frac{v_B(t)+v_C(t)}{2} \\ \frac{v_A(t)+v_C(t)}{2} \end{bmatrix} \quad V_o = \begin{bmatrix} v_u(t) \\ v_v(t) \\ v_w(t) \end{bmatrix} \tag{2}$$

Table 1 is the switching states of the proposed topology. This table represents the one of the phase U, with nine switching states generating multilevel inverting operation.

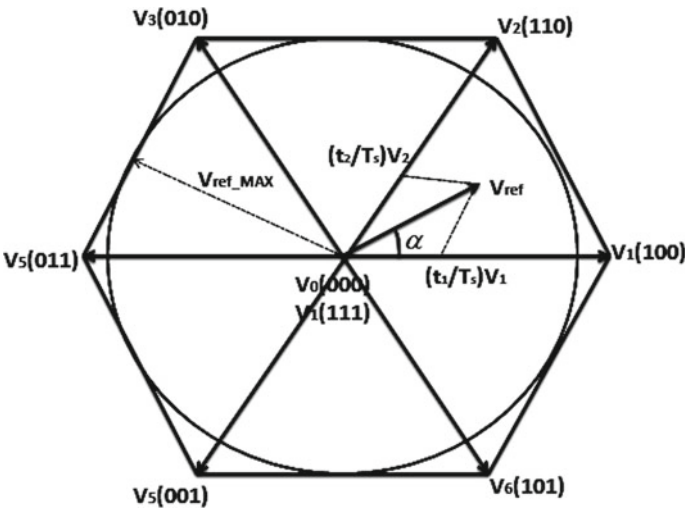

Fig. 3 Sector selection based on alpha beta components

Table 1 Switching states of flying capacitor multilevel matrix converter

Switching mode (on: 1, off: 0)						Voltage level of phase a
SAa1	SAa2	SBa1	SBa2	SCa1	SCa2	
1	1	0	0	0	0	V_A
1	0	0	1	0	0	$(V_A + V_B)/2$
1	0	0	0	0	1	$(V_A + V_C)/2$
0	1	1	0	0	0	$(V_A + V_B)/2$
0	0	1	1	0	1	V_B
0	0	1	0	0	1	$(V_B + V_C)/2$
0	1	0	0	1	0	$(V_A + V_C)/2$
0	0	0	1	1	0	$(V_B + V_C)/2$
0	0	0	0	1	1	V_C

3 Modeling and Control of Cascaded H-Bridge Multilevel Matrix Converter Topology

With further advancements in the conventional matrix converter topology and to reduce the THD, all the nine bidirectional switches of the traditional matrix converter are replaced with H-bridges. The H-bridge multi level converter topology [10] can be seen below in Fig. 4 with nine H-bridges. As compared to several multi level PWM inverters (diode clamped, flying capacitor) the cascaded H-Bridge Multilevel inverter is considered to be more efficient, and generates PWM voltages [8] with

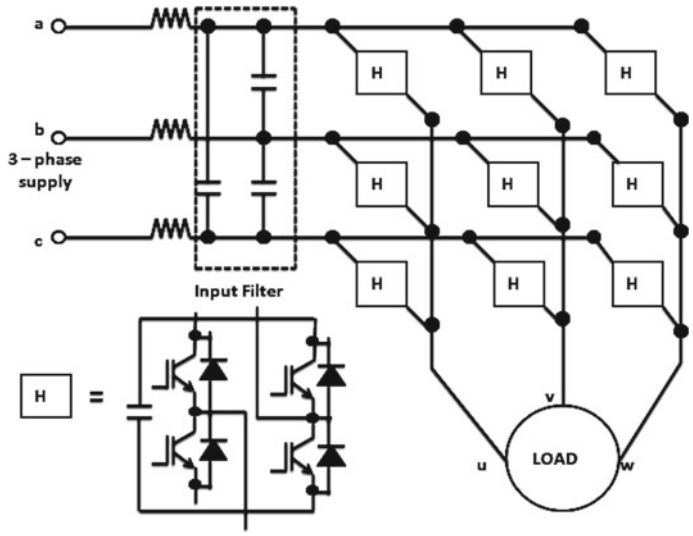

Fig. 4 Multilevel cascaded H-bridge multilevel matrix converter

lesser THD even with equal levels of the inverter. As a result the implementation of the multi level cascaded H-Bridge in the matrix converters may reduce the THDs to an extreme level as compared to any other Multilevel Matrix Converters. Figure 4 has n-modules of H-bridges which are cascaded in series to create levels in the voltage and all the modules represent one switch of the matrix converter. Each module has four switches operating diagonally at every change in the switching state. A capacitor is added at the DC side of the module to stabilize the output voltage of the H-bridge.

3.1 Control of Cascaded H-Bridge Multilevel Matrix Converter

As similar in the previous Sect. 2, the sector selection takes place with respect to the alpha and beta components. Whereas, the sector generation takes place for each H-bridge creating multiple space vector trajectories [11], can be seen below in Fig. 5. Each space vector trajectory generates it own switching signals to control its respective H-bridge in the cascaded module [12]. The total 19 space vectors can be divided into 1 Zero vector, 6 Small vectors, 6 Medium vectors and 6 Large vectors. With help of these space vectors and switching trajectory the controlled pulses are calculated for the H-Bridge Converter with the help of following equations [10, 13].

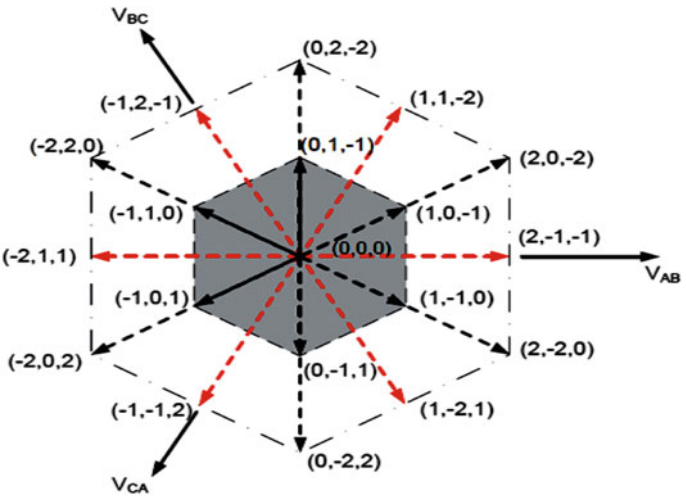

Fig. 5 Space vector trajectory of cascaded H-bridge multilevel matrix converter

4 Simulation Results and Discussion

4.1 Result Analysis of SVPWM Based Flying Capacitor MMC for DFIG System

The following figures show the simulation results of DFIG system in wind energy conversion system employing SVPWM based Flying Capacitor Multilevel Matrix Converter. Figure 6 and Fig. 7 shows the simulation results of source voltages and currents of DFIG based WECS with FCMMC and their corresponding voltage and

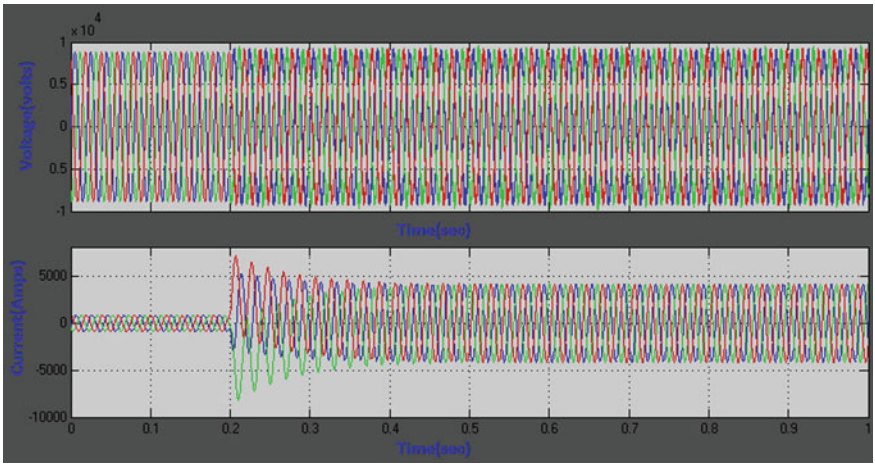

Fig. 6 Three phase source voltages and currents with respect to time of DFIG system

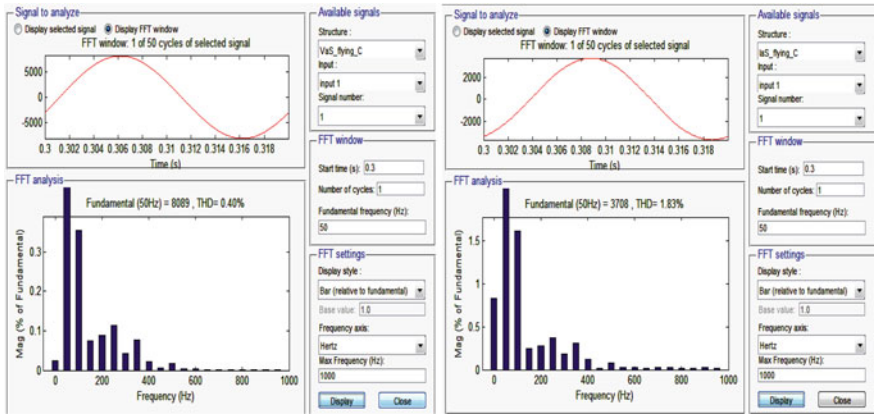

Fig. 7 FFT analysis of source voltage and current harmonic spectrum

current THD values respectively. From Fig. 7 the THD values of source voltage and current are 0.40% and 1.83% respectively. Figure 8 and Fig. 9 shows the simulation results of load voltages and currents of DFIG based WECS with FCMMC and their corresponding voltage and current THD values respectively. From Fig. 9 the THD values of load voltage and current are 0.39% and 0.41% respectively.

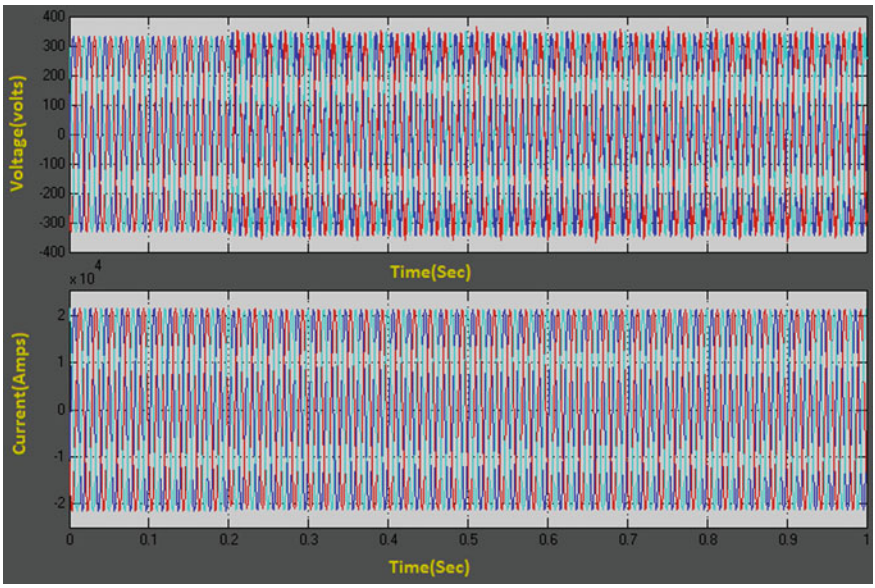

Fig. 8 Three phase load voltages and currents with respect to time of DFIG system

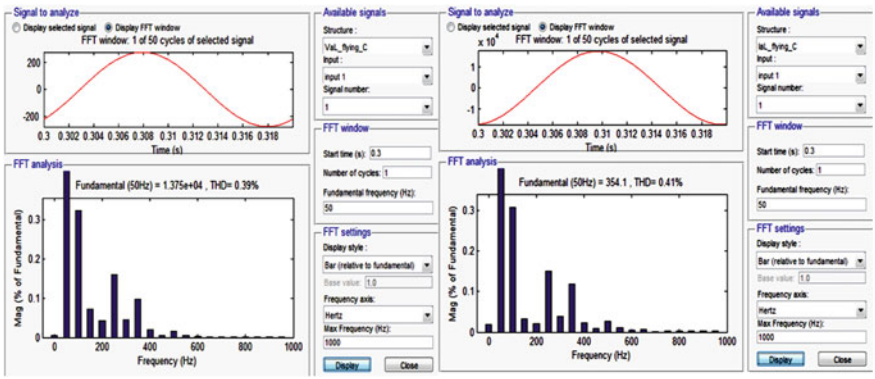

Fig. 9 Three phase load voltages and currents with respect to time of DFIG system

4.2 Result Analysis of SVPWM Based H-Bridge MMC for DFIG System

Figure 10 and Fig. 11 shows the simulation results of source voltages and currents of DFIG based WECS with HBMMC and their corresponding voltage and current THD values respectively. From Fig. 11 the THD values of source voltage and current are 0.29% and 0.96% respectively. Figure 12 and Fig. 13 shows the simulation

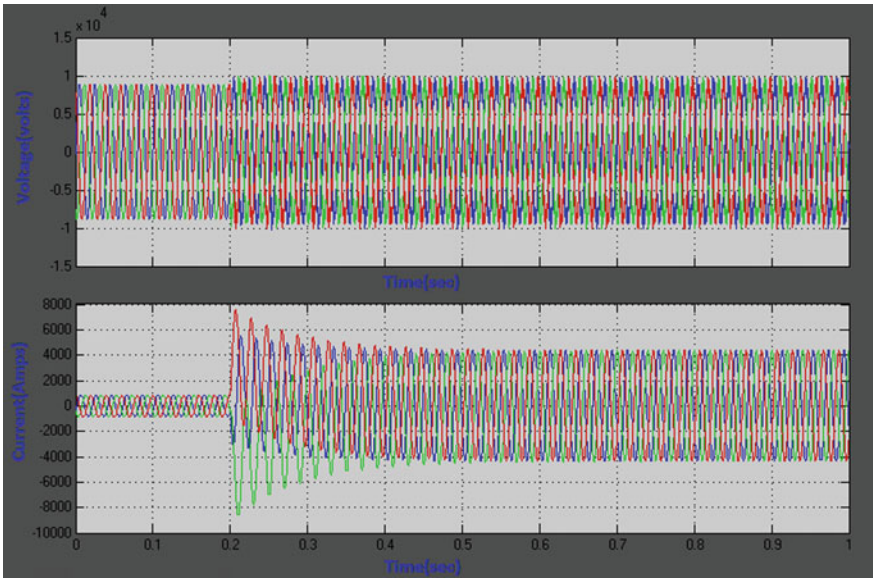

Fig. 10 Three phase source voltages and currents with respect to time of DFIG system

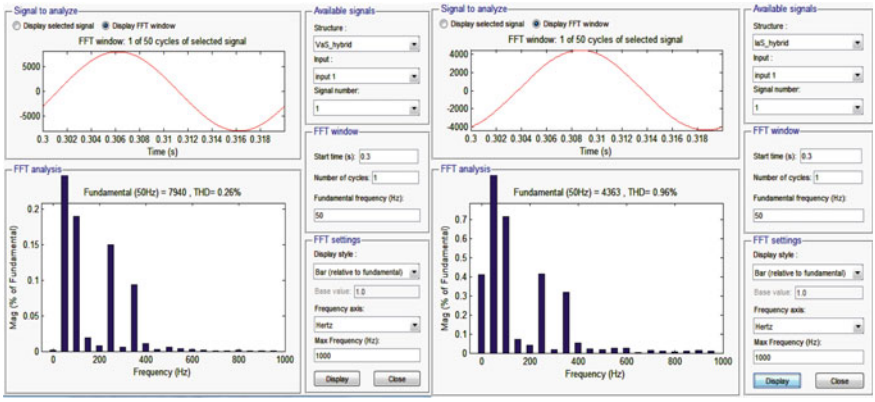

Fig. 11 FFT analysis of source voltage and current harmonic spectrum

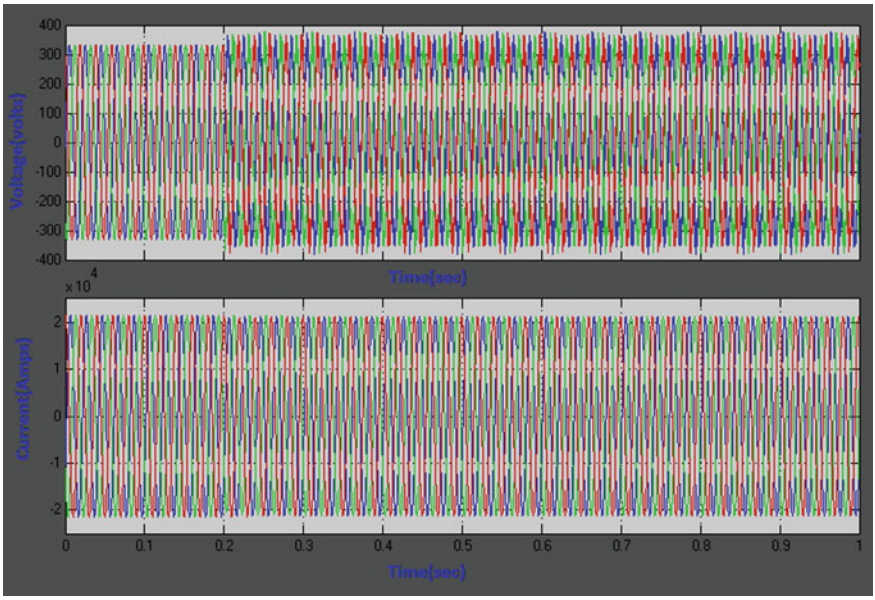

Fig. 12 Three phase load voltages and currents with respect to time of DFIG system

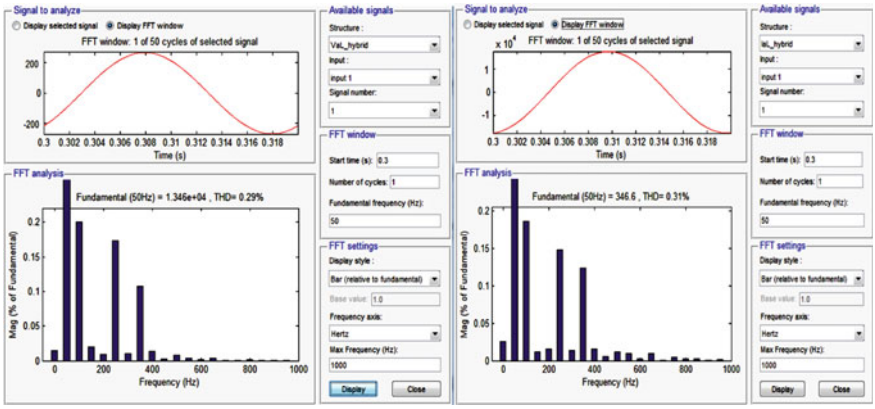

Fig. 13 FFT analysis of load voltage and current harmonic spectrum

results of load voltages and currents of DFIG based WECS with HBMMC and their corresponding voltage and current THD values respectively. From Fig. 13 the THD values of load voltage and current are 0.26% and 0.96% respectively. The THD values of generator voltages and currents at various points of both the converters are shown in Table 2.

Table 2 THD comparisons between flying capacitor MMC and H-bridge MMC

Parameter	FCMMC with SVPWM (%)	H-Bridge MMC with SVPWM (%)
Source voltage at point B1	0.40	0.26
Source current at point B1	1.83	0.96
Integrated voltage at point B2	5.66	4.21
Integrated current at point B2	1.76	1.04
Load voltage at point B3	0.39	0.29
Load current at point B3	0.41	0.31

5 Conclusion

With the above modeling and analysis of the Flying Capacitor and Cascaded H-Bridge Multi Level Matrix Converter topologies in DFIG wind generation systems, the comparisons of the converters are made. With interconnection of DFIG to the grid system with replacement of the rotor fed converter, the FFT analysis on the various points of the generators voltages, currents are carried out to get the THD values. As per the FFT analysis tool consideration the Cascaded H-Bridge topology is considered to be more efficient than the Flying Capacitor Multi Level Matrix Converter.

References

1. Abo-Khalil AG, Lee D-C, Lee S-H (2006) Grid connection of doubly-fed induction generators in wind energy conversion system. IEEE Digital Explore, pp 1–5
2. Pandu Ranga Reddy G, Vijaya Kumar M (2015) Analysis of wind energy conversion system employing DFIG with SPWM and SVPWM type converters. J Electr Eng 5(Edition-4):95–106
3. Reis A, Moura LP, de Oliveira JC (2016) Mitigation of harmonic current produced by wind turbine throughout converter switching control. Published in IEEE Digital Explore, pp 255–260
4. Purushothaman SK (2014) Design and analysis of elimination of harmonics using wind energy conversion systems. J Theor Appl Inf Technol 515–522. e-ISSN: 1817-3195
5. Erickson RW, Al-Naseem OA (2001) A new family of matrix converters. In: Proceedings of the IEEE IECON'01, Denver, CO, pp 1515–1520
6. Wheeler P, Lie X, Lee MY, Empringham L, KIumpner C, Clare J (2013) A review of multi-level matrix converter topologies. Power Electronics, Machines and Control Group, University of Nottingham, Published in IEEE Digital Explore, pp 286–290
7. Shi Y, Yang X, He Q, Wang Z. Research on a novel capacitor clamped multilevel matrix converter. IEEE Trans Power Electron 20(5)

8. Angkititrakul S, Erickson RW (2004) Control and implementation of a new modular matrix converter. In: Applied power electronics conference and exposition, 2004, APEC '04. Nineteenth annual IEEE
9. Lee MY, Wheeler P, Klumpner C (2010) Space-vector modulated multilevel matrix converter. IEEE Trans Industr Electron 57(10):3385–3394
10. Nguyen TD, Lee H-H (2014) Multilevel indirect matrix converter with carrier-based pulse width modulation. Published in IEEE Digital Explore, pp 3318–3323
11. Lie X, Clare JC, Wheeler PW, Empringham L, Yongdong L (2012) Capacitor clamped multilevel matrix converter space vector modulation. IEEE Trans Industr Electron 59(1):105–115
12. Veeranna SB, Beig AR, Yaragatti UR (2011) Performance analysis of PWM strategies for cascaded H-bridge three-level inverter. In: IEEE GCC conference and exhibition, Dubai, United Arab Emirates. Published in IEEE Digital Explore, pp 81–84
13. Yao LI, Lie XU, Yongdong LI (2014) Control of the cascaded H-bridge multilevel matrix converter. PCIM Europe, Nuremberg, pp 20–22

A Modified EHO Algorithm Utilized DPFC for Power Quality Enhancement in Smart Grid

P. Malleswara Reddy, A. Srinvasula Reddy and P. Sujatha

Abstract In the study the modified Elephant Herd Optimization (EHO) algorithm is developed and designed by utilizing the distributed power flow controller (DPFC) for improving power quality (PQ) in smart grid (SG). The modification of the EHO algorithm is performed based on the Recurrent Neural Network (RNN) algorithm. The novelty in this proposed study is the enhancement of the PQ in SG from the disturbances occurred power system controller utilized the DPFC. Initially, the proposed system power flow is evaluated and the Multi Wavelet Transform (MWT) is employed to feature extraction process of the power parameters for PQ disturbances. If the output signal has any disturbances then the output signal is controlled by the proposed controller based DPFC. The proposed algorithm is employed to retain the sustained DC-link voltage of DPFC by controlling the output voltage to improve the PQ. Then the implementation process is made by the Matlab/Simulink simulation platform. The capability of the proposed system is based an evaluation of the output response and the comparative analysis with some different techniques like PSO, BAT and CFA-PSO algorithm.

Keywords Smart grid · Power quality · MWT · DPFC · EHO algorithm · RNN algorithm

P. Malleswara Reddy (✉)
Research Scholar, JNTUA University, Ananthapuramu, India
e-mail: mallesh.palla@gmail.com

A. Srinvasula Reddy
CMR College of Engineering, Hyderabad, India
e-mail: svas_a@yahoo.com

P. Sujatha
EEE Department, JNTUCEA, Ananthapuramu, India
e-mail: psujatha1993@gmail.com

© Springer Nature Singapore Pte Ltd. 2020

T. Hitendra Sarma et al. (eds.), *Emerging Trends in Electrical, Communications, and Information Technologies*, Lecture Notes in Electrical Engineering 569,
https://doi.org/10.1007/978-981-13-8942-9_27

1 Introduction

The effect of PQ disturbances in SG and some different controlling techniques are discussed in this section. In recent years, the incorporation of distributed generation (DG) systems established with renewable energy resources like the photovoltaic (PV) system, wind energy conversion system (WECS), biomass and geothermal resources [1]. One of the concerns of PQ issue is unbalanced voltages and currents in a network. The Integrated grid with PV and WECS generates some harmonics, heat, and other complicated PQ issues. There are many controlling processes was utilized for the desired PQ level for a smart grid [2]. Recently, the power flow controller is a fast and consistent control to increase demand for energy, the deteriorating of flow and DGs. In transmission systems, the flexible AC transmission system (FACTS) is utilized in power electronics and the purpose is to regulate and order the power constraints in the power systems [3]. There are various FACTS devices such as Unified Power Quality Conditioner (UPQC), TCSC, IPFC and UPFC are utilized to improve the capability of the power flow in the transmission lines. The UPFC is the best controller that can concurrently control the parameters such as bus voltage, the line impedance and transmission angle in the system [4]. The UPFC is composite of a static synchronous compensator (STATCOM) and a static synchronous series compensator (SSSC) that joined with a DC storage capacitor becomes as common DC-link, to permit bi-directional dynamic power flow among the SSSC in series ends and the STATCOM in shunt ends. The DC storage capacitor between the series and shunt converters is excluded in DPFC. The distributed FACTS operational principle is implemented by the series converter in the DPFC [5]. In this study, the PQ issues are detected and mitigated by utilizing the DPFC with the help of the proposed modified EHO algorithm. The voltage of the DC-link is retained by the proposed modified EHO algorithm based DPFC. The literature of the FACT devices based on controlling the PQ issues in SG is reviewed in the Sect. 2. The proposed system and the modified EHO algorithm are explained in the Sect. 3. Then in Sect. 4, the simulated results and discussions of the proposed system responses are illustrated. Finally, Sect. 5 establishes the proposed system of good performance in unbalanced conditions. The following section presents the recent research works.

2 Recent Research Works: A Brief Review

In this section, the recent research works based on the PQ issues in the FACTS integrated smart grid are reviewed. The literary works are cited below.

Agalar et al. [6] has offered the utilization of quality wind energy increased by suggesting the static transfer switch (STS) and Dynamic voltage restorer (DVR). Maximizing the monitoring redundancy of the VS the PQ monitors were allocated in Distribution Systems (DS) by a multi-objective optimization approach which has been proposed by Branco et al. [7]. In radial distribution networks, Lakshmi et al.

[8] have presented the modeling and allocation strategy for the PV integrated UPQC power generation system for improving efficiency and PQ. The optimal placement of open UPQC with PV array was determined by the PSO algorithm. An active power compensation of a microgrid using fuzzy control has investigated by Bhattacharjee et al. [9]. A Fuel Cell (FC) based renewable energy sources grid integrated at PCC have introduced by Mosaad et al. [10]. The PI controller was used to improve the PQ of the FC combined into the power network over a chopper and an inverter. In general, the anxiety of services, end users, manufacturers, and further consumers were considered as electric PQ. Likewise, in the form of voltage waveforms, the harmonics and notch are obtained with the help of solid condition devices and nonlinear loads. The voltage or current sag and swell are provoked by the non-linear loads. And the UPQC regulator diminishes these PQ concerns. Hence the modified EHO algorithm is proposed by utilizing the DPFC with EHO and RNN algorithm for detection and mitigation of the PQ issues in SG. The dc-link voltage is maintained by utilizing the proposed technique. In the following section, the proposed methodology and the proposed technique offered in the current study is discussed.

3 Modified EHO Algorithm Based DPFC for Mitigation of PQ Issues

Here, the quick and clear explanation about the proposed DPFC integrated smart grid system for detection and mitigation of the PQ issues by utilizing the modified EHO algorithm. The PQ issues are related to the unbalance power constraints of the proposed system. The control structure of the proposed DPFC integrated smart grid system is presented in Fig. 1 shows to control the PQ issues by using the DPFC to compensate the power parameters and improve the PQ. Initially, the power parameters

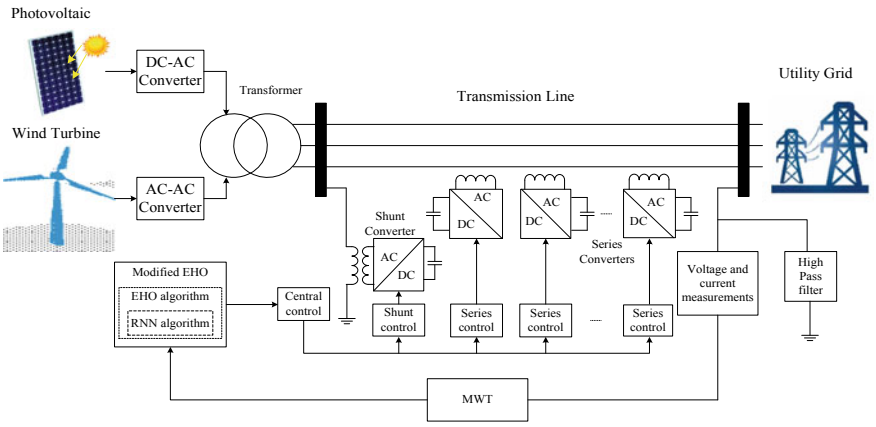

Fig. 1 The proposed structure of the grid-connected power system

are measured from the proposed system without any disturbances. Then, the PQ issue occurs in the transmission line which may affect the quality of power and also affect the smart grid. After detecting the disturbance of the power parameters the mitigation process starts. The mitigation process has to classify the PQ issues and then improve the PQ with the help of the proposed modified EHO algorithm utilized DPFC.

Initially, the affected signal is measured and illustrated in the feature extraction process, which plays a vital role in PQ analysis. The feature extraction process is made by the MWT, which is capable of efficient signal representation. Then the signal is classified based on the features of the affected signal and the normal signal. After the classification process, the modified EHO algorithm control the switching pulse of the series and shunt converter that utilized to maintain the dc-link voltage of the DPFC. The modified EHO algorithm is the modification of the EHO algorithm with RNN algorithm. In this proposed system power generation is made from PV and WES. Based on the variation of PV irradiance and wind speed of the WES the output of the power may vary. By controlling the DPFC, we can inject or absorb the voltage for maintaining the PQ. Finally, the proposed DPFC integrated smart grid system is simulated by utilizing the Matlab/Simulink platform. Then the output response is assessed and associated with different techniques such as PSO [11], BAT [12] and CFA-PSO respectively. Based on the generation of the PV and WCS is connected to the smart grid by coupling the transformer and converters. Then the PQ disturbance signal is measured and proceed for the classification process. The classification of the signal is based on the MWT, which extracts the features of the disturbance signal and this process is presented in the following section.

3.1 MWT Based Feature Extraction

The MWT is an expanded form of the scalar wavelet; however, there have some main differences. The scalar wavelets have a single scaling and wavelet function but the MWT have more than one scaling and wavelet functions. The MWT produces the property of having an extra degree of freedom for producing multi-wavelets. The Multiwavelets are an expansion to the wavelet theory and have been acknowledged as matrix-valued filter banks. Multiwavelets contrast from scalar wavelets as they require at least two information streams to the filter banks. Daubechies said that no single scaling function can have properties like orthogonality, second-order accuracy, short support and symmetry [13]. With a specific goal to achieve these properties together with the two wavelets must be utilized in the matrix frame. Multiwavelets give orthogonality to all expansions and the utilization of the matrix rather than scalar coefficients gives higher degrees of freedom. The theory of real MWT is associated with the theory of real vector-valued functions. This family is symmetrical reason for square integral function, precisely as in the standard instance of a single wavelet.

3.2 Controlling Process of DPFC

The DPFC comprises one shunt and a few series associated converters. The shunt converter resembles SATCOM, while the series converters utilize the D-FACTS idea. Each converter inside the DPFC is independent and has a different DC interface capacitor to give the required DC voltage. The structure of DPFC is utilized in a change framework with two parallel lines. The DPFC has a typical association between the AC terminals of the shunt and the series converters, which is the transmission line. Along these lines, it is permitted to exchange the dynamic power through the AC terminals of the converters. At that point, the dynamic power theory for non-sinusoidal parts from various frequencies is being converted (or) transformed from voltage or current. Mathematically the active power is given in the following Eq. (1),

$$P = \sum_{i=1}^{\infty} V_i I_i cos\varnothing_i \tag{1}$$

Here, $\varnothing_i$ is the angle among the same frequency for the voltage and current. Similarly V_i is the voltage and I_i is the current is at the ith harmonic. The high pass filter in the DPFC blocks and the major frequency segments are taken into account and the consonant parts to pass in the ground and along with these lines a return way for the harmonic components are taken into consideration. The series and shunt converter, the ground, and the high-pass filter from the closed loop for the harmonic current because of the unique characteristics of third consonant frequency components. It is taken to trade the dynamic power among series and shunt converters in the DPFC. To control different converters, a DPFC comprises three kinds of controllers, for example, central control, shunt control and series control. The parameters of series and parallel control are kept up without anyone else's input they are additionally called as local controllers. At the system level, the central controller controls the DPFC functions. The Central control gives the relating reference voltage signals for the series converters and a responsive current signal for the shunt converter as indicated by the system utility. All the reference signals created by the central control concern the major frequency components. Its control work relies upon the specifics of the DPFC application at the power system level, for example, power flow control, low-frequency power oscillation damping and adjusting of asymmetrical components. The Series control is utilized to keep up the capacitor DC voltage of its own converter, by utilizing third consonant frequency components, notwithstanding producing a series voltage at the fundamental frequency as required by the central control. Each series converter has its own series control. The Shunt control is utilized to infuse a consistent third consonant current into the line to supply dynamic power for the series converters [14]. In the meantime, it keeps up the capacitor DC voltage of the shunt converter at a steady as an incentive by retaining dynamic power from the grid at the fundamental frequency and infusing the required reactive current at the fundamental frequency into the grid. Then the power flow is utilized with the DPFC

and control dc-link voltage. The controlling parameter of the DPFC is optimized by using the improved EHO algorithm, which is explained as the followed section.

3.3 The Power Flow Control Using Proposed Modified EHO Algorithm

This section describes the optimization parameters and the procedure of the proposed modified EHO algorithms. The EHO algorithm elitism strategy is modified by the RNN algorithm. The proposed algorithm is utilized for controlling the DPFC series and shunt converter controlling pulse and the RNN to enhance the elitism search strategy of the EHO. These algorithms are utilized to select the optimal solution in numerical optimization problems. The flow diagram of the proposed modified EHO algorithm is illustrated in Fig. 2.

This concept is a straightforward and effective in usage to calculate both memory requirements and speed. Of course in the toolbox of MATLAB, the estimations of the considerable number of parameters, for example, the size of a swarm, inertia coefficient and factors of attraction have been characterized. It will update the EHO parameters after getting the optimal solution.

3.3.1 Elephant Herding Optimization Based Control Pulse Generation

The EHO is a swarm based heuristic algorithm for finding the optimal solution in the search space. When all is said in done, a matriarch in every clan is the oldest one, and this can be envisioned as the fittest elephant individual in this family for the improvement issue. Herding behavior of elephants is considered as two operators; the first one is clan updating operator and second is separating operator. Every one of the elephants lives together under the leadership of a matriarch in each clan. In this manner, for every elephant in the clan *ci*, its next position is impacted by a matriarch. In the wake of isolating the most exceedingly worst qualities from the population, the fittest values are updated utilizing clan updating operator and worst values are discarded. For the elephant *j* in the clan, it may be updated as in Eq. (2),

$$x_{ci,j}^{new} = x_{ci,j} + \alpha \times \left(x_{ci}^{best} - x_{ci,j}\right) \times r \tag{2}$$

Here, $x_{ci,j}^{new}$ and $x_{ci,j}$ are recently updated and old position for the elephant in the clan, separately. The scale factor is $\alpha \in [0, 1]$ which decides the impact of the matriarch on $x_{ci,j}$. The best matriarch is signified as x_{ci}^{best}, which is the fittest elephant individual in the clan. It is a sort of stochastic distribution that can altogether enhance the diversity of population in the later search phase. For the present work, uniform distribution is utilized [15]. It should be noticed that the fittest elephant in every clan can't be updated. With a specific goal to stay away from this circumstance, for the

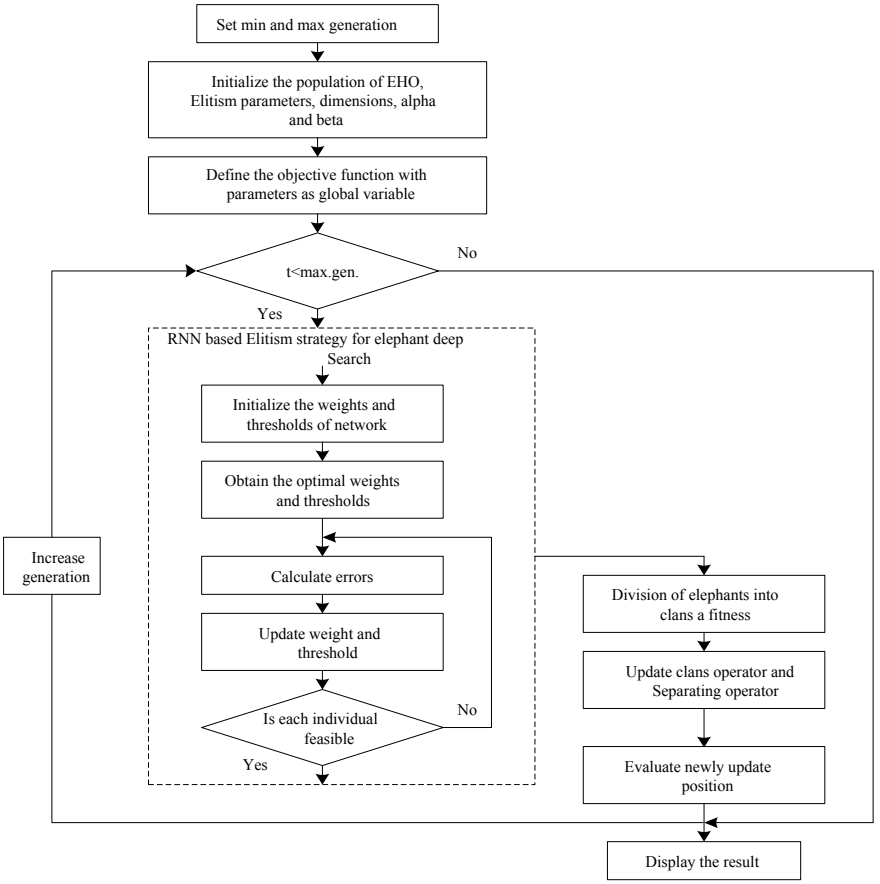

Fig. 2 The flow diagram of the proposed modified EHO algorithm

fittest elephant, it may be updated as shown in Eq. (3),

$$x_{ci,j}^{new} = \beta \times x_{ci}^{center} \tag{3}$$

where β is a factor that decides the impact of the x_{ci}^{center} on $x_{ci,j}^{new}$. The new individual $x_{ci,j}^{new}$ is created by the data obtained by all the elephant individuals in the clan. The focal point of the clan ci is depicted as x_{ci}^{center} and for the dth dimension, it may be calculated as shown in Eq. (4),

$$x_{ci,d}^{center} = \frac{1}{n_{ci}} \times \sum_{j=1}^{n_{ci}} x_{ci,j,d} \tag{4}$$

Here $x_{ci,d}^{center}$ shows the dth dimension and D is its total dimension. The quantity of elephants in the clan is n_{ci}. The dth elephant individual $x_{ci,j}$ is $x_{ci,j,d}$. This separating procedure can be displayed as separating operator when taking care of enhancement issues. In order to additionally enhance the accessibility of the EHO technique, let us accept that the elephant people with the most exceedingly awful wellness will execute the separating operator at each generation as appeared in Eq. (5),

$$x_{ci}^{worst} = x^{\min} + \left(x^{\max} - x^{\min} + 1\right) \times rand \tag{5}$$

Here $x^{\max}$ and $x^{\min}$ are separately upper and lower bound of the situation of elephant individual. The most exceedingly awful elephant individual in the clan is portrayed as x_{ci}^{worst}. The stochastic distribution is $rand \in [0,\ 1]$ and uniform distribution in the range [0, 1] is used in the current study. Like other metaheuristic algorithms, a kind of elitism strategy is used with the aim of protecting the best elephant individuals from being ruined by clan updating and separating operator. In the beginning, the best elephant individuals are saved, and the worst ones are replaced by the saved best elephant individuals at the end of the search process. This elitism strategy ensures that the later elephant population is not always worse than the former one. Then, this searching behavior process can be enhanced by the RNN algorithm, which is explained in the following section.

3.3.2 Improving the Searching Behavior of EHO Using RNN

The RNN contains two stages and three layers, for example, the training stage and testing stage and input layer, hidden layer and output layer. Here hidden layer comprise of hidden and context layer, which is 'n' neurons are utilized in the hidden and context layer. There is a one-step time delay in the feedback path so that previous outputs of the hidden layer, additionally called the states of the network, are utilized to compute new output values. The topology is like that of a feed-forward system, with the exception of that the outputs of the hidden layer are utilized as the feedback signals. The RNN has two inputs namely, error voltage (e) and change of error voltage (Δe). The output of RNN is a control signal (I_{out}), which is created for controlling the load reference current. The RNN output is given to the inverter current controller. Here, the input layers to hidden layer weights are determined as ($w_{11}, w_{12}, \ldots, w_{1n}$) and ($w_{21}, w_{22}, \ldots, w_{2n}$). The self-assertive weights of the recurrent layer and the output layer neuron are produced in the predefined interval [$w_{\min}, w_{\max}$]. For every neuron of the input layer weight is allotted with the unity value. The RNN is prepared by utilizing backpropagation through time delay (BPTT) algorithm with Bayesian regulation [16]. Generally, until the point the BP error gets diminished to the least value the procedure is rehashed. The very much prepared networks are obtained from the output of the neural network process. The current control law is created from this network. Finally, with the assistance of RNN, the EHO exhibitions are enhanced and the adequacy of the proposed strategy is assessed by Matlab/Simulink platform and the results are displayed in the following segment.

4 Results and Discussion

In this segment, the simulated results of the proposed system and controlled the PQ events by utilized the proposed modified EHO algorithm are discussed. The proposed system is implemented in MATLAB/Simulink 7.10.0 (R2015a) platform, Intel(R) Core(TM) i5 processor and 4 GB RAM. The combination of PQ events illustrated in this system are voltage unbalance-interrupt, voltage unbalance-sag, voltage unbalance-swell, voltage sag-interrupt, voltage swell-interrupt and voltage sag-swell. Primarily, the source voltage is given to the input of the system, as the performances are examined. Then the output response is analyzed with MWT and checked whether the PQ events occurred or not. The output response of the proposed DPFC integrated SG is described as follows. The performance analyses are based on the PQ events, which shows the effectiveness and also compared with some existing techniques. Here, combined PQ events are presented for analyzing the improved EHO algorithm optimized DPFC connected to SG. The EHO optimization algorithm parameters are tabulated in Table 1.

In this output response is formed as the combination of Voltage sag, swell, interrupt and unbalance PQ issues are illustrated in Fig. 3. Normally the one disturbance occurs in 0.1–0.2 s and the next disturbance is happened in 0.3–0.4 s. The performance of the proposed system is based on the THD evaluation of output voltage with some different techniques.

The output compensated voltage signal and the THD comparison analysis of the disturbed voltage signal is presented in Fig. 4, which evaluates the response of the PQ events with some existing techniques. The proposed DPFC integrated system compensates the output voltage by put some balanced voltages to control the PQ. Finally, the THD of the proposed system with presented PQ events are analyzed in this simulated result clearly. Based on the above evaluation the DPFC device is more effective for PQ issues reduction. To enhance the performance of DPFC, the improved EHO algorithm is utilized for controlling the injected voltages to compensate the output voltage of the proposed system. Based on the output response the proposed DPFC integrated system is giving good performance and compactable for all PQ events. Finally, the DPFC connected proposed system is concluded for better performance in all PQ events.

Table 1 EHO algorithm implementation parameters

Parameters	Values
Keep	2
Alpha	0.5
Beta	0.1
Population index	1
Display flag	1
Random seed	5

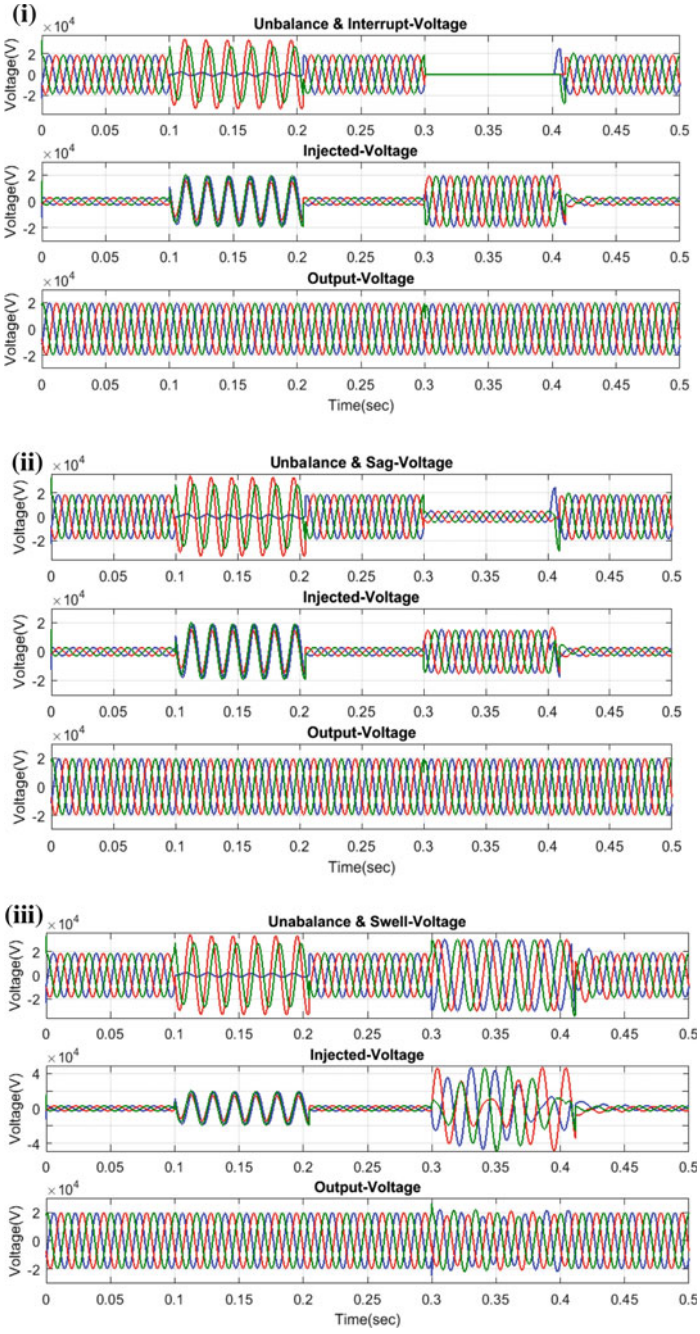

Fig. 3 The output response of (i) voltage unbalance-interrupt (ii) voltage unbalance-sag (iii) voltage unbalance-swell affected voltage, injected voltage and output voltage

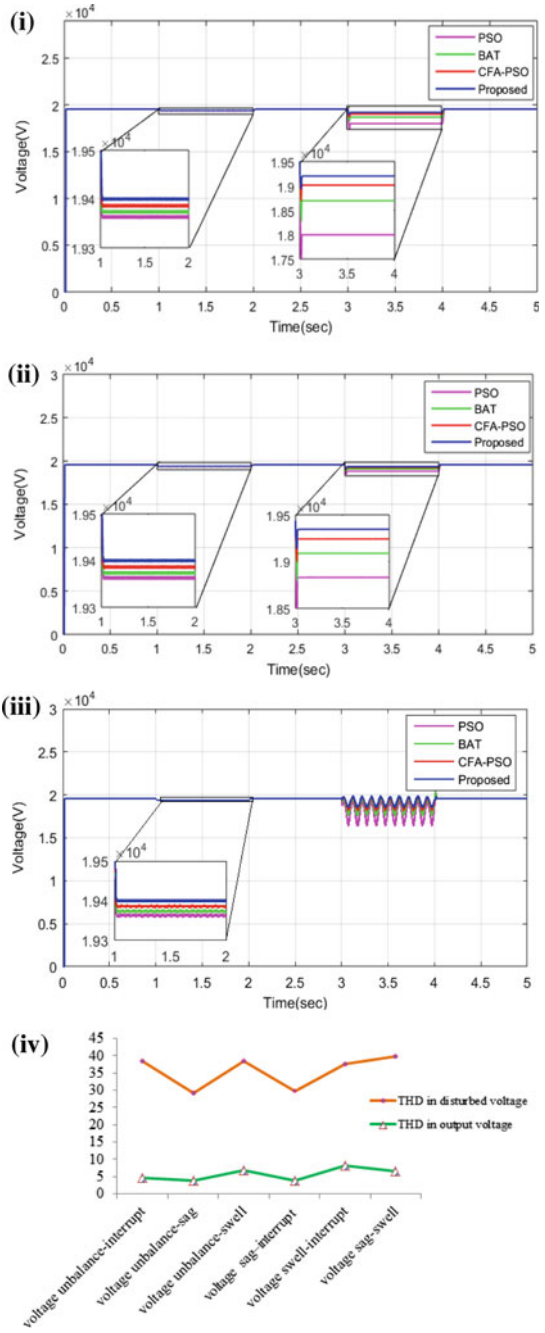

Fig. 4 The comparison analysis (i) voltage unbalance-interrupt, (ii) voltage unbalance-sag, (iii) voltage unbalance-swell and (iv) THD response of the proposed system

5 Conclusion

The present paper proposed the improved EHO algorithm based DPFC device for developing the PQ in power distribution system by eliminating the PQ events. The proposed algorithm is utilized for improving the DPFC performance and the RNN algorithm is utilized for enhancing the searching behavior of the EHO algorithm also to regulate the DC-link voltage of the DPFC. Before controlling the PQ events the MWT was used to extract the features of the simulated signals for classification purpose. The DPFC was controlled by the compensated output voltage by injecting some voltage based on their requirements. The injected voltage of the DPFC device was controlled by utilizing the improved EHO algorithm. The effectiveness of the proposed algorithm was proven by evaluating the combination of voltage sags, voltage swell, voltage short interruptions and voltage unbalance PQ events. The DPFC was capable of reducing the level of THD in all PQ events. The controls of the PQ events were compensated and the THD of the PQ events were evaluated and the output voltage response was compared with some existing techniques.

References

1. Vadivel S, Baskaran B (2016) Distributed power flow controller (DPFC) to improve the power quality of thirty three bus radial system. Int J Eng Inven 5(10):31–44
2. Shaik AG, Mahela OP (2018) Power quality assessment and event detection in hybrid power system. Int J Electr Power Syst Res 161:26–44
3. Santhosh Kumari B (2016) Improved performance and power quality with application of DPFC in transmission system connected to non-linear load. Int J Innov Technol Res 4(5):3668–3673
4. Narasimha Rao D, Surnedra T, Tara Kalyani S (2016) Improved performance of DPFC using sliding mode controller method. Int J Electr Comput Eng (IJECE) 6(5):2073–2079
5. Narasimha Rao D, Surnedra T, Tara Kalyani S (2016) DPFC performance with the comparison of PI and ANN controller. Int J Electr Comput Eng (IJECE) 6(5):2080–2087
6. Agalar S, Kaplan YA (2018) Power quality improvement using STS and DVR in wind energy system. Int J Renew Energy 118:1031–1040
7. Branco HMGC, Oleskovicz M, Coury DV, Delbem ACB (2018) Multiobjective optimization for power quality monitoring allocation considering voltage sags in distribution systems. Int J Electr Power Energy Syst 97:1–10
8. Lakshmi S, Ganguly S (2018) Modelling and allocation of open-UPQC-integrated PV generation system to improve the energy efficiency and power quality of radial distribution networks. IET Trans Renew Power Gener 12(5):605–613
9. Bhattacharjee C, Roy BK (2018) Fuzzy-supervisory control of a hybrid system to improve contractual grid support with fuzzy proportional–derivative and integral control for power quality improvement. IET Trans Gener Transm Distrib 12(7):1455–1465
10. Mosaad MI, Ramadan HS (2018) Power quality enhancement of grid connected fuel cell using evolutionary computing techniques. Int J Hydrog Energy 43(25):11568–11582
11. Mahesh Babu B, Ravi Srinivas L, Tulasi Ram SS (2018) Power quality improvement based on PSO algorithm incorporating UPQC. J Eng Technol 9(1):1–16
12. Balasubramaniyan S, Sivakumaran TS (2014) Optimal location of facts devices for power quality issues using PSO and BAT algorithm. J Theor Appl Inf Technol 64(1):148–157
13. Kapoor R, Saini MK (2012) Multiwavelet transform based classification of PQ events. Eur Trans Electr Power 22:518–532

14. Martins IM, Silva FA, Pinto SF, Martins IE (2014) Sliding mode active and reactive power decoupled control for distributed power flow controllers. Int J Electr Power Syst Res 112:65–73
15. Wang G-G, Deb S, Gao X-Z, dos Santos Coelho L (2016) A new metaheuristic optimisation algorithm motivated by elephant herding behaviour. Int J Bio-Inspired Comput 8(6):394–409
16. Fairbank M, Li S, Xingang F, Alonso E, Wunsch D (2014) An adaptive recurrent neural-network controller using a stabilization matrix and predictive inputs to solve a tracking problem under disturbances. Int J Neural Netw 49:74–86

Day and Night Analysis of PV-STATCOM for Power Compensation Using Hybrid Technique

K. Sudarsan and G. Sreenivasan

Abstract Now a days the Energy change and environmental troubles like air pollution and global warming are increases. To mitigate these troubles the renewable energy sources such as photo voltaic energy, Wind energy and etc. are introduced. This paper presents the analysis of day and night utilization of PV Solar farm as STATCOM to meet the load demand without Power Quality disturbances. The PV Solar farm produce power during day time and made completely idle during night time. During day time the inverter is used for real power generation and during night time it is used to meet the load demand with enhanced efficiency by controlling Voltage, Current, Real, Reactive powers and with Damping controls. For the analysis of PV-STATCOM performance it is proposed a hybrid algorithm which includes the principles of CSO and PSO algorithms. The CSO algorithm is used to achieve the control of above parameters and PSO algorithm is used to enhance the position of roosters of CSO algorithm. The Control Strategies of Voltage, Current, Real and Reactive powers were validated through MATLAB/Simulink Platform.

Keywords PV-STATCOM · PSO (particle swarm optimization) · CSO (chicken swarm optimization)

1 Introduction

Reduction of emissions and minimize reliance on fossil fuels is the main cause behind the generation of electrical energy in bulk from renewable sources. Solar PV has emerged as one of the most promising renewable sources. Shah [1] carried out modeling of large scale solar PV for stability studies. The Sub Synchronous Resonance (SSR) problems may lead to Turbine-Generator shaft failure and electrical

K. Sudarsan (✉)
Research Scholar, JNTUA University, Ananthapuramu, India
e-mail: suda.abhi@gmail.com

G. Sreenivasan
Srinivasa Ramanujan Institute of Technology, Ananthapuramu, India
e-mail: gsn.anusree@gmail.com

© Springer Nature Singapore Pte Ltd. 2020

T. Hitendra Sarma et al. (eds.), *Emerging Trends in Electrical, Communications, and Information Technologies*, Lecture Notes in Electrical Engineering 569,
https://doi.org/10.1007/978-981-13-8942-9_28

instability at oscillation frequencies lower than the normal system frequency. To avoid the SSR in power systems, the use of FACTS Devices has been proposed. Widyan [2] studied the effect of Static Synchronous Series Compensation (SSSC) on the bifurcation of heavily loaded SMIB system experiencing SSR. The robustness of the SSSC compensation scheme and its controller is verified in this paper by subjecting a single line to ground fault at the end of transmission line.

The assessment of the effects of SSSC based controller for damping SSR has been carried out by designing IEEE SBM model when it is subjected to a three phase fault [3]. A fractional order proportional integrator (FOPI) controller based UPFC is analyzed to damp out sub synchronous oscillations in turbine-generator shaft due to SSR [4].

Varma et al. [5] proposes a novel voltage control together with auxiliary damping control for a grid connected PV Solar farm inverter. The studies are performed for two varieties of SMIB systems. A simple proportional SSR damping controller is designed in order to damp the SSR phenomena. For this purpose the rotor side converter (RSC) and grid side converter (GSC) controllers of DFIG were utilized [6]. The gate controlled Series Capacitor (GCSC) is applied for SSR damping in fixed speed wind forms and compared its performance with TCSC. For the evaluating the performance of both GCSC and TCSC in damping SSR, a time frequency analysis is used [7]. A wide Area Measurement System (WAMS) based conventional damping controller is designed and added to the main control loop of PV plant in order to damp the SSR [8]. In this paper a hybrid CSO-PSO algorithm is utilized for the analysis of PV Solar farm as STATCOM during day and night.

The paper is organized as follows. A design of the PV-STATCOM system and proposed control structure is given in Sect. 2. To demonstrate the effectiveness of the proposed strategy, the simulation results are presented in Sect. 3. Finally, the conclusions are given in Sect. 4.

2 Design of the PV-STATCOM with Control Structure

During day time and night time the optimal utilization of wind system, PV solar system inverter as a STATCOM. The STATCOM is utilized for the voltage control and damping control. The day time the PV solar system and wind system is generating power for meeting the load from the load side which time inverter act as a conventional inverter. The night time, the wind energy generation and STATCOM meets the load demand because of the sunlight is not present in the night time so the PV solar system is absent [9]. That times the inverter act as a PV-STATCOM with voltage and power factor control. The proposed structure is illustrated in the Fig. 1. The PV-STATCOM model with controller is presented in this figure. The PV and Wind is connected for generation power for meet the load demand. After Wind, the converter is used to change the current AC-DC for consumer's purpose. The capacitors are used for soft switching and reduce the passive snubber (voltage spike) as well.

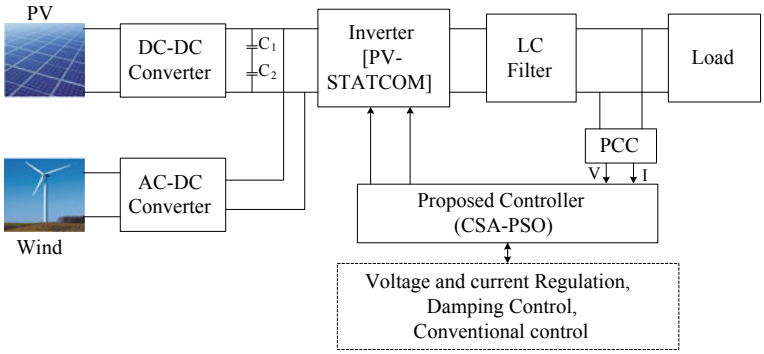

Fig. 1 Block diagram for proposed method

In proposed method a PVSTATCOM which can operate as a STATCOM throughout the day is presented. The PV inverter as STATCOM operation is 24 h control the voltage and reactive power compensation with the load connected system. The STATCOM has an advantage, it is compensating device of the connected system. PV array and the inverter setup are analogous to the design of conventional STATCOM. The proposed method analyzed with day and night time. The day time, PV and wind energy generation is compensating the load demand and the inverter act as a conventional inverter. The night time, PV is absent condition and wind energy generation is does not compensated the load demand, that is inverter act as STATCOM for compensation and control the voltage by the utilization of the proposed controller. The PV-STATCOM based mode of operation is explained below.

Day time mode: In this mode, the PV output voltage is equal to the requirement of the boost converter. Same time, it is meet the load demand. But in the mode the capacitor is not connect.

Night time mode: The night time mode of operation, the PV output is absent because the light energy not presented. The STATCOM is providing the power through the boost converter for power compensation in the night time.

2.1 Control Structure of the Proposed Method

Generally, the paper is proposed voltage control, current control, damping control and conventional Reactive power control for PV solar farm with load. In the PV connected with load system, inverter to acts as a STATCOM both during night and day for increase the stability and meet the load demand. In this design structure utilize a PV solar farm to a STATCOM so it is called PV-STATCOM. The aggregate solar farm inverter power is used at the night time and the extra inverter limit after real power generation amid the daytime, the two of which stay idle in conventional solar farm activity [10]. The night time the PV-STATCOM, the PV is disjointed

from the inverter which time small amount of real power is drained from the load side for the purpose of charge the dc capacitor. In the day time and night time, the PV-STATCOM system need to be optimized with the control strategies. Here, in this proposed model control structure is divided into four groups for optimization. The control structure types are defined as the current, voltage, reactive power and damping control respectively. The various control structure of the proposed method is explained in the below section briefly. Based on the control structure, the PV-STATCOM is optimized with help of the proposed algorithm. The control structures are utilized to compensating the error voltage, current, real and reactive power.

Conventional Reactive power control:
The reactive power is controlled for regulate the output reactive power of the PV-STATCOM system. The control method is achieved with the utilization of the proposed controller. The actual and reference reactive power is calculated for error calculation. The error value is minimized with the help of controller. Initially, the three phase currents are calculated and transformed to direct and quadrature axis. Using controller, the error values are minimized. The controller diagram is presented in the Fig. 2.

Current control:
The load currents from the abc frame are first converted to d-q frame. The Phase Locked Loop (PLL) is used to synchronize the three phase signals with a PCC voltage. Using the low pass filter, the dc component of i_d and i_q are obtained by passing a d-q current component [11].

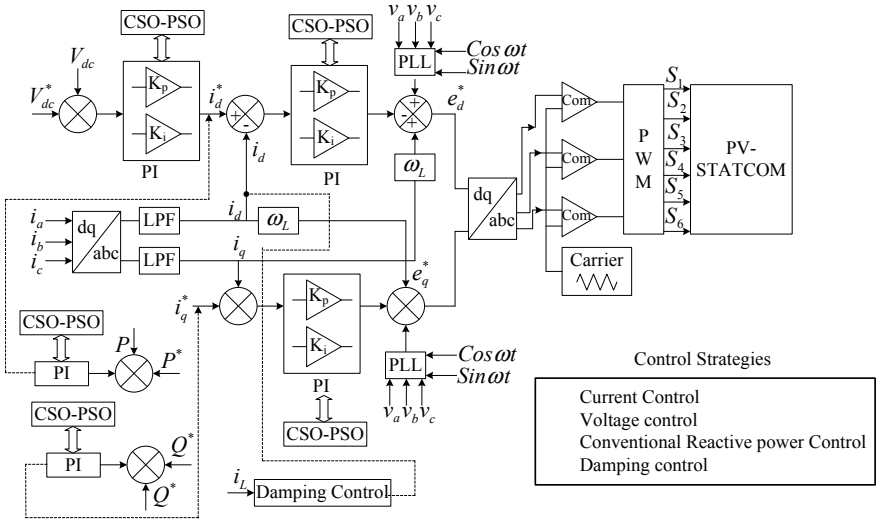

Fig. 2 Control structure of the proposed method

The control methods are achieved through the utilization of the hybrid CSO-PSO algorithm. The error values are minimized by the way of controllers and proposed algorithms. The PV-STATCOM system with control techniques are illustrated in the Fig. 2. With the purpose of achieve the optimal results of the control loops of the proposed method the PI controllers need be properly tuned. The normal objectives of the PI controller tunings are the rapid response of the system in the way of increase the cutoff frequency as high and small overshoot value and excellent damping of oscillations. Here, the proper tuning process is achieved with the help of the proposed algorithm CSO-PSO. The CSO algorithm is utilized to tuning with error minimization of voltage, current, real and reactive power. The PSO algorithm is utilized to enhance the updation operation in the CSO algorithm. The detailed process of the proposed algorithm is explained as below section.

2.2 *Enhanced CSO Algorithm with Aid of PSO for Control Analysis*

The CSO algorithm is utilized to minimize the error values of the current, voltage, real and reactive power. For the most part, which recreates chickens swarm progressive system and their food seek actions. The entire chicken swarm is separated into cockerel swarm, hen swarm, and chick swarm [12]. The CSO algorithm, the best fitness value is assigned to rooster swarm and the worst fitness value is assigned to chick swarm. The rest of the values are assigned to hen swarm. The working process of the CSO algorithm is follows,

Steps of CSO algorithm

Step1: Initialize the population of N chicken x, and the value of current, voltage, real and reactive power errors and change in errors.

$$x_{i,j}^{t+1} = lb + Rand\,(ub - lb) \tag{1}$$

with lb and ub are lower bound and upper bound of the search space. It is given so that obtained candidate solutions located in the search space.

Step2: Evaluate the fitness and initialize the personal best position N_{best} t = 1

$$F = Min(EV, EI, EP, EQ) \tag{2}$$

The error value minimization is fixed as a fitness for optimize the PV-STATCOM system.

Step3: Rank the fitness of the chicken swarm, and establish hierarchal order in the swarm; divide the chicken swarm into several subgroups and determine the relation.

$$x_{i,j}^{t+1} = x_{i,j}^{t} + S1 * Rand * \left(x_{r1,j}^{t} - x_{i,j}^{t}\right) + S2 * Rand * \left(x_{r2,j}^{t} - x_{i,j}^{t}\right) \tag{3}$$

Step4: Update the position of the roosters, the hens and the chicks. The updations of the roosters are achieved in the utilization of the PSO algorithm.

$$x_{i,j}^{t+1} = x_{i,j}^{t} * (1 + Rand(0, \sigma^2) \tag{4}$$

$$\sigma^2 = \left\{ \begin{array}{ll} 1, & if\ f_i \leqslant f_k \\ \exp\left(\frac{f_k - f_i}{|f_i| + \varepsilon}\right) & otherwise\ k \in [1, N], k \neq 1 \end{array} \right\} \tag{5}$$

The PSO algorithm is utilized to update the position of the roosters in CSO algorithm. The measures used to perform the forecast mechanism in PSO technique is detailed below.

The positions of the roosters are updated using the PSO algorithm. Here, the position of roosters' updation is fixed as a fitness function.

$$F = Update\ (P(Roosters)) \tag{6}$$

The rooster position is updated using the PSO algorithm. The expression with highest fitness value is selected as the global best.

Step5: Update the personal best position N_{best}.

Step6: $t = t+1$, if the iteration stops condition is met, output the optimum; otherwise, go to step3. The process of CSO algorithm is used to achieve the optimization in the PV-STATCOM system. The proposed method performance is analyzed with the simulation results. The results of the proposed method is explained in the below section clearly.

3 Results and Discussions

In this paper, analysis the PV-STATCOM based proposed controller, which is utilized to achieve the control the voltage, current, real power, reactive power and damping controller. Here the operating performance of the proposed controller with PV-STATCOM is implemented in the MATLAB/Simulink platform and to verify the control techniques with two cases. The two cases are during day time and nighttime. In this result analysis, compensate the load with voltage, current, real and reactive power and damping controller is analyzed in these cases. From the compensation of the load with PV-STATCOM at daytime and nighttime are achieved through the utilization of the CSO with PSO algorithm. Here, proposed algorithm is utilized to compensate the load with the help of inverter during absent of the PV. Figure 3 illustrates the MATLAB/Simulink implementation model of the proposed CSO with PSO controller in PV-STATCOM and addition of the voltage and damping controller. The performance of the proposed method is analyzed with the simulation results.

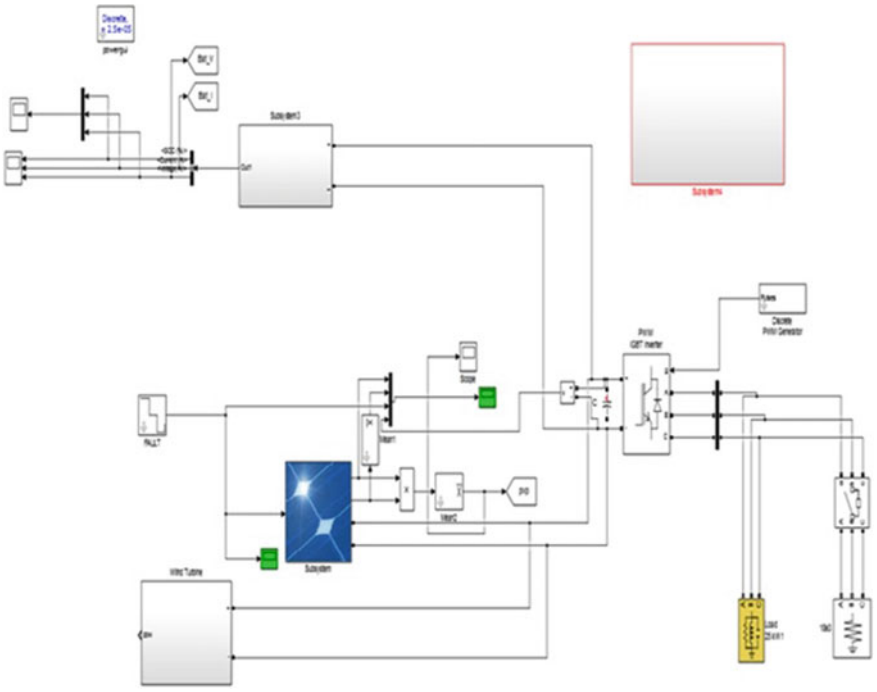

Fig. 3 MATLAB/Simulink model of **a** proposed method

The control strategy has a voltage, reactive power, damping control and current control. The proposed controller of CSO-PSO algorithm is used to enhance the power sharing in the PV-STATCOM structure. The investigation of the executions results are depicted in the beneath segment.

3.1 Performance Analysis

In this section, the performance of the proposed controller is investigated. The proposed system is used to control the voltage, current and damping and enhance the power management during PV-STATCOM. The simulated result of the proposed controller is examined in two distinct cases and mentioned as beneath. The investigated outputs of the proposed strategy are contrasted and CSO and PSO strategies. The cases are,

Case 1: PV-STATCOM day time mode

Case 2: PV-STATCOM night time mode

The detailed analysis of the proposed method is described in the following section.

Case 1: PV-STATCOM daytime mode

The performance PV-STATCOM using CSO with PSO algorithms are analyzed separately based on the simulation results of both compensated and uncompensated system during day time and night time. In this case analysis, the day time the PV power is active because of the irradiance level is high. The day time the PV and wind is compensated the demand power related to the load side with controller. In this analysis, the load demand is variation at different time seconds. In this case, the load is varied and the load demand is assumed to be 8000 W. For the day time analysis with controller, the condition to be checked, it must meet the load demand by the utilization of the generation of wind and PV power. The renewable energy resources are varied that represents the irradiance of PV and wind speed. The demand power is illustrated in the Fig. 4. The PV generated power is 8000 W at 0–1.2 s, 5000–4200 W at 1.2–2.5 s, 2000 W at 2.5–3.3 s and 3000 W at 3.4–4 s. Initially, the irradiance value is 300, 200, 100, and 150 W/m^2 at 0–1.2, 1.2–2.2, 2.2–6 s for analysis the performance of the proposed method. The approximate generated power of wind and PV are 8000 and 9000 W. During day time, the wind and PV power is compensated the load demand of the consumer side. The PV and wind power is illustrated in Figs. 5 and 6.

Figure 7a illustrates the variation of the demand with generated power. The reference power is 8000 W, it is described the load demand and it is mentioned with the black colour. Using the proposed algorithm, the load demand is met by the PV and wind generation power. Similarly, the load is varied after the particular time instant, and then assumed the powers. To meet the load demand, again the generated power is evaluated. For the optimal process of meet load demand the various controllers are developed.

Case 2: PV-STATCOM night time mode

In this night mode of operation, the PV array output power is equal to zero and it is inactive. Without PV generation the load demand is need to meet. The night time the damping control and conventional control is achieved with the utilization of the

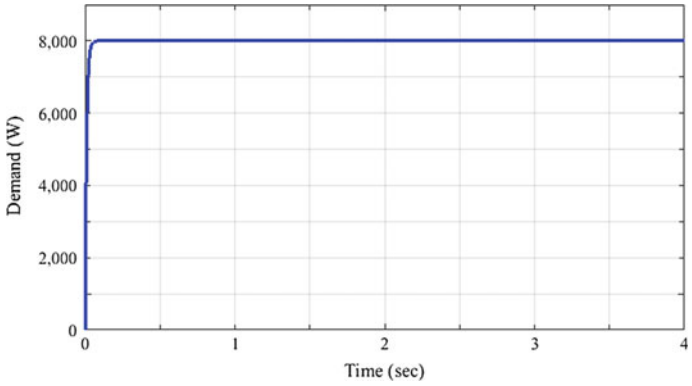

Fig. 4 Analysis of demand power

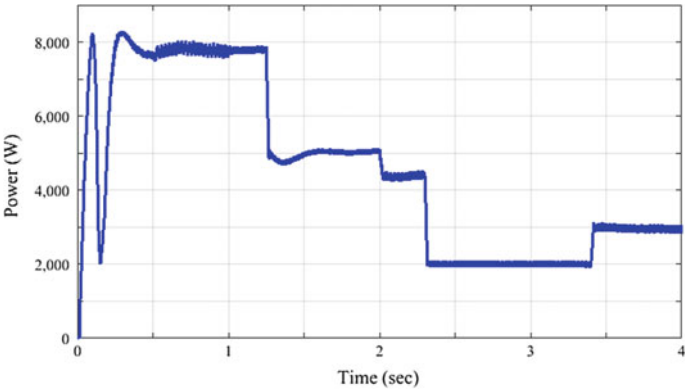

Fig. 5 Analysis of PV output power

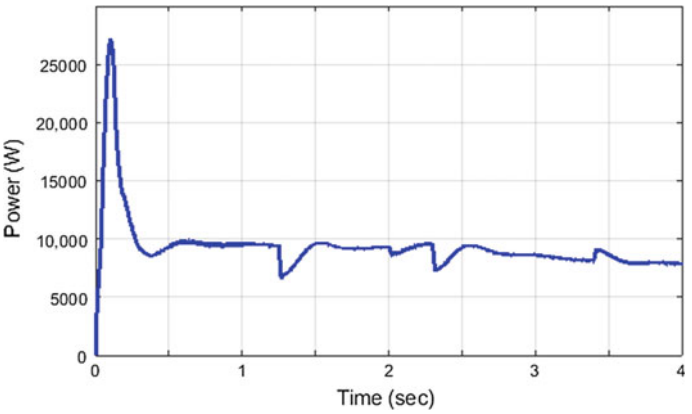

Fig. 6 Analysis of wind output power

CSO with PSO algorithm. Damping controller utilizes full rating of inverter at night to provide controlled reactive power and effectively damps the oscillations. The PV power is not generated in the power; the STATCOM is injecting the power to meet the load at the night time. In this case analysis, the demand is various at different time instant.

In this case analysis, the load demand is fixed to 9000 W at 0–1 s, 11,000 W at 1–2 s, 9000 W at 2–3 s and 10,000 W at 3–4 s. The load demand of the system is compensated by the utilization of the PV, wind generation system. Here, the PV is not generating power compare to the daytime analysis. The STATCOM is injecting the power to be lagging amount power. The figure illustrates the Load demand analysis of the night time. The total generated power is 10,000–11,000 W using the wind and STATCOM. Using the proposed method, the load demand is met in the night time. The STATCOM is injected the Power to compensate the variation power. Comparing

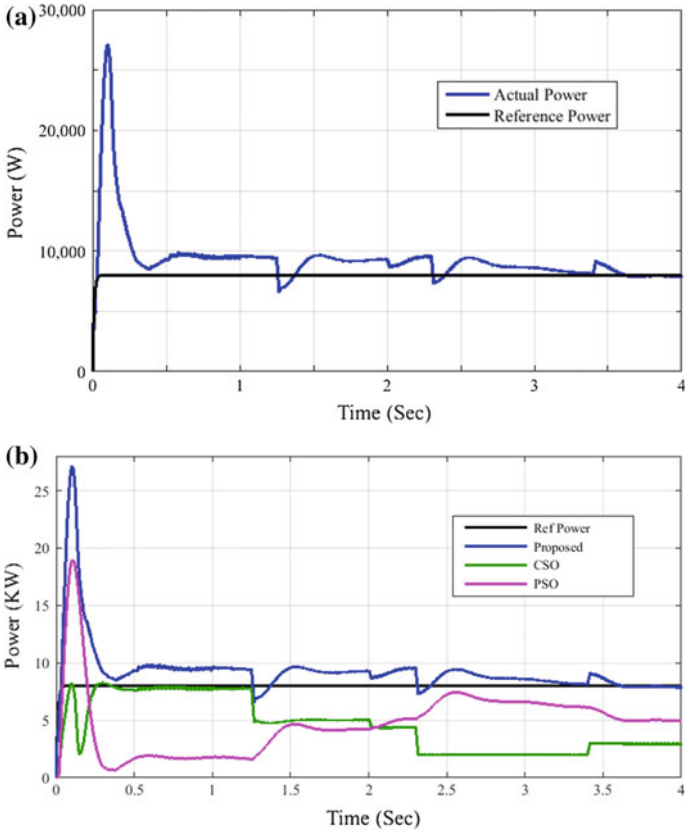

Fig. 7 Analysis of **a** output power with demand power and **b** comparison

to the other methods, the efficiency of the proposed method is high it proves via the Fig. 8.

4 Conclusion

The control of the PV-STATCOM at day and night time analysis is presented in this paper. The PV-STATCOM operation is analyzed via load variation cases in the day and nighttime. The PV-STATCOM simulation results show the various output of PV irradiance, power, wind speed, power during both cases. In same, the proposed method simulation of the Wind and PV with voltage, current, real power, reactive power and damping controller have been done and respective outputs have been presented. The efficacy of the proposed method was demonstrated through a comparative analysis with different conventional techniques such as CSO and PSO. From

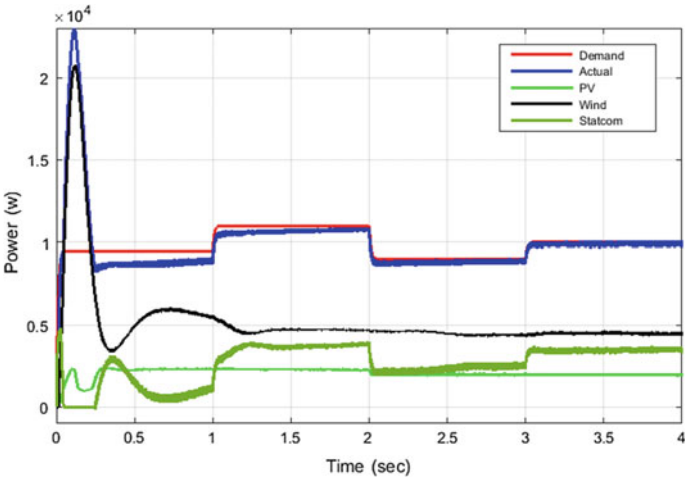

Fig. 8 Analysis of the output power with demand power

the comparison analysis, it has been found that the proposed control technique was very much effective in enhancing the operation of the PV-STATCOM of the system than the other techniques.

References

1. Shah R, Mithulananthan N, Bansal RC, Ramachandaramurthy VK (2015) A review of key power system stability challenges for large-scale PV integration. Int J Renew Sustain Energy Rev 41:1423–1436
2. Widyan MS (2013) Controlling chaos and bifurcations of SMIB power system experiencing SSR phenomenon using SSSC. Int J Electr Power Energy Syst 49:66–75
3. Panda S, Baliarsingh AK, Mahapatra S, Swain SC (2016) Supplementary damping controller design for SSSC to mitigate sub-synchronous resonance. Int J Mech Syst Signal Process 68:523–535
4. Varma RK, Auddy S, Semsedini Y (2008) Mitigation of subsynchronous resonance in a series-compensated wind farm using FACTS controllers. IEEE Trans Power Deliv 23(3):1645–1654
5. Varma RK, Rahman SA, Vanderheide T (2015) New control of PV solar farm as STATCOM (PV-STATCOM) for increasing grid power transmission limits during night and day. IEEE Trans Power Deliv 30(2):755–763
6. Mohammadpour HA, Santi E (2015) SSR damping controller design and optimal placement in rotor-side and grid-side converters of series-compensated DFIG-based wind farm. IEEE Trans Sustain Energy 6(2):388–399
7. Mohammadpour HA, Islam MM, Santi E, Shin Y-J (2016) SSR damping in fixed-speed wind farms using series FACTS controllers. IEEE Trans Power Deliv 31(1):76–86
8. Khayyatzadeh M, Kazemzadeh R (2017) Sub-synchronous resonance damping using high penetration PV plant. Int J Mech Syst Signal Process 84:431–444
9. Varma RK, Siavashi EM (2018) Enhancement of solar farm connectivity with smart PV inverter PV-STATCOM. IEEE Trans Sustain Energy

10. Kishor MK, Narasimhe Gowda TR, Sathyanarayana Rao RD, Nandini KK (2016) Control application of PV solar farm as PVSTATCOM for reactive power compensation during day and night in a transmission network. Int J Sci Dev Res 1(6)
11. Harish K, Vinod Kumar M, Azra F (2016) Control of solar PV-inverter fed to grid for active and reactive power control during day and night. Int J Adv Res Innov Ideas Educ 02(05):2395–4396
12. Irsalinda N, Thobirin A, Wijayanti DE (2017) Chicken swarm as a multi step algorithm for global optimization. Int J Eng Sci Inven 6(1):2319–6734

Optimal Tuning of Multi-machine Power System Stabilizer Parameters Using Grey Wolf Optimization (GWO) Algorithm

P. Dhanaselvi, S. Suresh Reddy and R. Kiranmayi

Abstract Optimal tuning of Power System Stabilizers (PSSs) parameters using Grey Wolf Optimization (GWO) algorithm is presented in this paper. Selection of the parameters of power system stabilizers which simultaneously stabilize system oscillations is converted to a simple optimization problem which is solved by a Grey Wolf Optimization (GWO) algorithm. The efficiency of the proposed method has been tested on two cases of multi-machine systems include 3-machine 9 buses system. The proposed method of tuning the PSS is an attractive alternative to conventional fixed gain stabilizer design as it retains the simplicity of the conventional PSS and at the same time guarantees a robust acceptable performance over a wide range of operating and system condition.

Keywords Grey wolf optimizer (GWO) · Conventional stabilizer (CS) · Power system stabilizer (PSS)

1 Introduction

A reliable operation of an interconnected power system requires a smooth delivery of real and reactive powers. Any change in real power affects mainly the system frequency and the reactive power is more sensitive to changes in the terminal voltage of the power system. Hence, Load Frequency Controller is employed to control the real power and Automatic Voltage Regulator is employed to control the terminal voltage and reactive power. However, both objectives can be achieved by Power System Stabilizer (PSS) which are added to individual generators to supply supplementary control signals for generator excitation system. The PSS compensates the local and inter-area mode of frequency oscillations that appears in power systems connected to long transmission lines.

P. Dhanaselvi (✉) · R. Kiranmayi
EEE Department, JNTUA, Anantapur 515002, Andhra Pradesh, India
e-mail: dhanaselvi.nbkrist@gmail.com

S. Suresh Reddy
EEE Department, NBKRIST, Nellore 524413, Andhra Pradesh, India

© Springer Nature Singapore Pte Ltd. 2020

T. Hitendra Sarma et al. (eds.), *Emerging Trends in Electrical, Communications, and Information Technologies*, Lecture Notes in Electrical Engineering 569,
https://doi.org/10.1007/978-981-13-8942-9_29

Much effort has been invested in recent years, in the development of power system stabilizers (PSSs) for improving the damping performance of power systems. To improve the system damping, stabilizing signals are introduced in the excitation systems through fixed parameters Lead/lag PSSs [1–4]. The parameters of the PSS are normally fixed at certain values which are determined under a particular operating condition. It is important to recognize that machine parameters change with loading, making the dynamic behavior of the machine quite different at different operating points [5–9]. So a set of PSS parameters that stabilizes the system under a certain operating condition may no longer yield good results when there is a change in the operating point.

In daily operation of a power system, the operating condition changes as a result of load changes. The power system under various loading conditions can be considered as a finite number of plants. The parameters of the PSS that can stabilize this set of plants can be determined by intelligent controllers which are designed with intelligent methods such as fuzzy logic controllers [10] and artificial neural network controllers [11]. Also, there are other novel methods to optimize the parameters of power system stabilizer such as Genetic Algorithm (GA), Anti Colony (AC) and particle swarm optimization (PSO). The earlier stabilizer designs were based on concepts derived from classical control theory [3–12]. Many such designs have been physically realized and widely used in actual systems. These controllers feedback suitably phase compensated signals derived from the power, speed and frequency of the operating.

The application of Grey Wolf Optimization (GWO) algorithm has recently attracted the attention of researchers in the control area [13–17]. Grey Wolf Optimization algorithms can provide powerful tools for optimization. The advantage of the Grey Wolf Optimization technique is that it is independent of the complexity of the performance index considered.

In this work the structure of PSS is imposed and search is done on the parameters of the PSS by GWO. The PSS designed in this manner will perform well under various loading conditions and stability of the system is guaranteed. However, the conventional PSS will only perform well at one operating point.

2 Overview of Grey Wolf Optimizer

The grey wolf optimization (GWO) algorithm is introduced by Mirjali et al. [18], which mimics the leadership hierarchy and hunting mechanism of grey wolves in nature. Grey wolves belongs to the Canidae family are considered as intruder at the top of the food chain and they have social dominant hierarchy as alpha (α) beta (β), delta (δ), and omega (ω) types of grey wolves. The grey wolves have different groups for different activities like make group for staying, hunting prey.

Grey wolves residing at the top of the hierarchy are called as alpha category wolves and they are considered as the leader of the group. They have decision-making power

about hunting, sleeping, time to wake, etc. Their decisions are communicated among the other members of the group.

The grey wolves present in the second level of the hierarchy are named as beta category wolves and they are subordinate of the alpha category wolves. They help the alpha category wolves' in their decision-making. The beta category wolves occupy the position of the alpha in case the alpha wolves pass away or become very old. It plays the role of subordinate to alphas in the group.

The wolves those occupy in the third stage of the hierarchy are called the omega type of wolves. They always follow the instruction given by other dominant wolves. Though, omega type's of wolves are not so much important in the pack, but the whole pack may face internal fighting in case it loses the omega. Omega category wolves always maintain the dominant structure of the hierarchy.

The wolves which don't belong to the alpha, beta and omega category wolves are called delta category wolves. Delta types of wolves always follow the alphas and betas but dominate omegas. Five basic type of wolves come under this hierarchy such as (i) scouts, (ii) sentinels, (iii) elders, (iv) hunters and (v) caretakers. Scouts are responsible for watching the boundaries and alert the pack for any danger. Sentinels ensure the safety of the pack. Elders are the experienced wolves and their experiences are used for attacking the prey or any target elements. Hunters help in hunting the prey and providing food for the pack. Finally, care takers are responsible for caring the feeble, sick and injured wolves.

Different phases of hunting behavior of grey wolves are described in this section.

2.1 Searching for Prey

The search process is started with random initialization of candidate solutions (wolves) from the search space. Grey wolves diverge from each other for searching the prey and converge after they find it.

2.2 Encircling Prey

After searching a prey, grey wolves encircle that prey. Encircling behavior can be mathematically represented [18] in (1) and (2) given below

$$\overrightarrow{E} = \left| \overrightarrow{O}\, cdot\, \overrightarrow{X}_p(i) - \overrightarrow{X}(i) \right| \tag{1}$$

$$\overrightarrow{X}(i+1) = \overrightarrow{X}_p(i) - \overrightarrow{B} \cdot \overrightarrow{E} \tag{2}$$

Here current iteration is represented by i. $\overrightarrow{B}$ and $\overrightarrow{O}$ is the coefficient vectors. $\overrightarrow{B}$ Is used for maintaining the distance between search agents grey wolves (GW) and prey.

$\overrightarrow{O}$ Represents obstacles in the hunting path of the grey wolves while approaches to the prey. $\overrightarrow{X}$ is the position vector of the grey wolf and $\overrightarrow{X}_p$ indicates the position vector of the prey.

The coefficient vectors Band are computed as respectively in (3) and (4):

$$\overrightarrow{B} = 2 \times \vec{a} \times \vec{r}_1 - \vec{a} \tag{3}$$

$$\overrightarrow{O} = 2 \times \vec{r}_2 \tag{4}$$

where, the component $\vec{a}$ decreases linearly from 2 to 0 at the time of iterations. $\vec{r}_1$ and $\vec{r}_2$ are random vectors in the interval [0, 1].

2.3 Hunting

After encircling the prey, grey wolves concentrate on hunting. The hunting is generally guided by α, β and δ types of wolves. Among these, α provides the best candidate solution. Mathematically, hunting behavior of grey wolves is formulated by (5)–(11) [18].

$$\overrightarrow{E_\alpha} = \left| \overrightarrow{O_1} \cdot \overrightarrow{X}_\alpha(i) - \overrightarrow{X}(i) \right| \tag{5}$$

$$\overrightarrow{E_\beta} = \left| \overrightarrow{O_2} \cdot \overrightarrow{X}_\beta(i) - \overrightarrow{X}(i) \right| \tag{6}$$

$$\overrightarrow{E_\delta} = \left| \overrightarrow{O_3} \cdot \overrightarrow{X}_\delta(i) - \overrightarrow{X}(i) \right| \tag{7}$$

$$\overrightarrow{X_1} = \overrightarrow{X_\alpha}(i) - \overrightarrow{B_1} \cdot \overrightarrow{E_\alpha} \tag{8}$$

$$\overrightarrow{X_2} = \overrightarrow{X_\beta}(i) - \overrightarrow{B_2} \cdot \overrightarrow{E_\beta} \tag{9}$$

$$\overrightarrow{X_3} = \overrightarrow{X_\delta}(i) - \overrightarrow{B_3} \cdot \overrightarrow{E_\delta} \tag{10}$$

$$\overrightarrow{X}(i+1) = \frac{(X_1 + X_2 + X_3)}{3} \tag{11}$$

2.4 Attacking Prey

After completion of hunting, grey wolves attack the prey. Based on the location of α, β and δ category grey wolves, the GWO algorithm allows the search agents, i.e., wolves to update their positions to attack the prey. It helps to make the solution reliable. In order to mathematically express the model for approaching to the prey, two parameters, $\vec{a}$ and $\overrightarrow{B}$ are considered. Here, $\vec{a}$ and $\overrightarrow{B}$ linearly decreases from 2 to 0 as the iteration increases and punctuations of $\overrightarrow{B}$ is also decreased with $\vec{a}$. In other words, $\overrightarrow{B}$ is a random value between [−a, a]. When random value of $\overrightarrow{B}$ is between [−1, 1], the next position of the agent may point between its current position and prey position.

2.5 Searching for Prey

Grey wolves mostly search according to the position of the alpha, beta, and delta. They diverge from each other to search for prey and converge to attack prey. In order to mathematically model divergence, we utilize B with random values greater than 1 or less than −1 to oblige the search agent to diverge from the prey. This emphasizes exploration and allows the GWO algorithm to search globally. If |B| > 1 then it forces the grey wolves to diverge from the prey to hopefully find a fitter prey. Another component of GWO that favors exploration is O.

3 Proposed Method Implementation

Implementation of GWO algorithm is as follows:

Step 1: Set all initial conditions.
Initialize number of searching agents, maximum iterations, number of parameters to be tuned and their minimum and maximum limits, initial values for alpha, beta and delta, forecasted load.

Step 2: Calculation of error and fitness function.
Run simulation file and calculate the integral time square error over a period with initial values of alpha, beta and delta. Calculate fitness function using ITAE error.

Step 3: Update alpha, beta and delta.
If fitness value is less than alpha score then update alpha with alpha score is equal to fitness, if fitness is greater than alpha score but less than beta score update beta with beta score is equal to fitness, if fitness is greater than alpha score and beta score but less than delta score then update delta with delta score is equal to fitness value.

Step 4: Update positions of search agents including omega.
Generate two random numbers r_{n1}, r_{n2} and then evaluate matrix B_1 and F_1 using the following Eqs. 12–13, update the distance of each search agent with the help of Eqs. 14–17.

$$B_1 = 2a_1 r_{n1} - a_1 \tag{12}$$

$$F_1 = 2r_{n2} \tag{13}$$

$$D_\alpha = F_1 P_\alpha - Best_\alpha \tag{14}$$

$$D_\beta = F_1 P_\beta - Best_\alpha \tag{15}$$

$$D_\delta = F_1 P_\delta - Best_\alpha \tag{16}$$

$$D_\omega = F_1 P_\omega - Best_\alpha \tag{17}$$

where P indicates present position, D indicates distance and Best indicates present best position.

Step 5: Update parameters to be tuned.
Based on the positions of search agents update the parameters which are to be determined.

Step 6: Calculation of error and fitness function.
Run simulation file and calculate the integral time square error over a period with initial values of alpha, beta and delta. Calculate fitness function using ITAE error.

Step 7: Stopping criteria.
If iterations are completed, then stop and display best results in every hour.

4 Test System and Results

The proposed method tested on three machine 9 bus standard system. Three phase fault created at 1 s; the deviations of speed and angle are shown in Figs. 1, 2, 3 and 4. Figure 1 represents delta deviations of machine2 with respect to machine1, from this figure it is concluded that conventional method shows 160° peak and more than 10 s settling time, GAPSS shows 148° peak and 5 s settling time, GWOPSS shows 145° peak and 4 s respectively.

Figure 2 represents delta deviations of machine3 with respect to machine1, from this figure it is concluded that conventional method shows 134° peak and 10 s settling time, GAPSS shows 119° peak and 6 s settling time, GWOPSS shows 131° peak

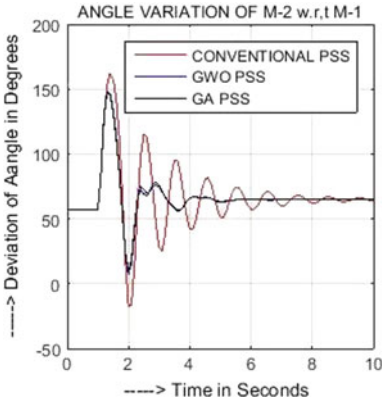

Fig. 1 Machine2 delta variations with respect to machine1

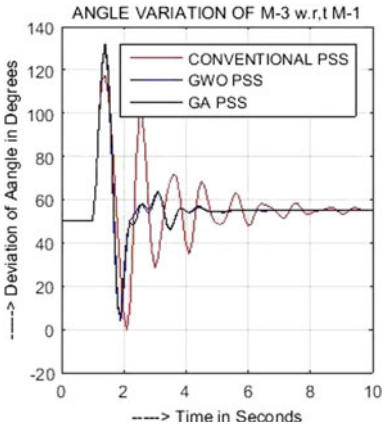

Fig. 2 Machine3 delta variations with respect to machine1

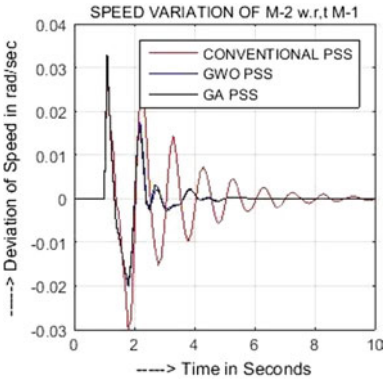

Fig. 3 Machine2 speed variations with respect to machine1

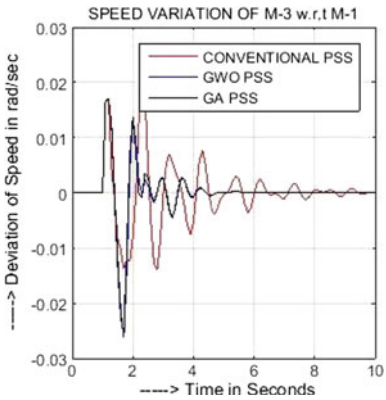

Fig. 4 Machine3 speed variations with respect to machine1

and 4.5 s respectively. Figure 3 represents speed deviations of machine2 with respect to machine1, from this figure it is concluded that conventional method shows 0.033 rad/s peak and more than 10 s settling time, GAPSS shows 0.032 rad/s peak and 5 s settling time, GWOPSS shows 0.032 rad/s peak and 4.5 s respectively. Figure 4 represents speed deviations of machine3 with respect to machine1, from this figure it is concluded that conventional method shows 0.022 rad/s peak and more than 10 s settling time, GAPSS shows 0.014 rad/s peak and 5.4 s settling time, GWOPSS shows 0.013 rad/s peak and 5 s respectively.

From the obtained results, The performance of proposed controller is better than conventional PSS and GA based PSS.

5 Conclusion

This paper proposes a new method, in which the parameters of PSS are tuned by GWO algorithm. The following conclusions derived based on the results:

1. Proposed method reduces peak overshoot by 9.375% (maximum) and 2.23% (minimum) compared with conventional method, 2.027% (maximum) and − 3.73% (minimum compared with GAPSS method.
2. Proposed method reduces settling time by more than 60% (maximum) and 55% (minimum) compared with conventional method, 25% (maximum) and 20% (minimum compared with GAPSS method.

The proposed method effectively reduced the objectives compared with conventional and GAPSS.

References

1. Demello FP, Concordia C (1969) Concept of synchronous machine stability as affected by excitation control. IEEE Trans PAS 88:316–329
2. Larsen EV, Swann DA (1981) Applying power system stabilizers, Part I–III. IEEE Trans PAS 100(6):3017–3046
3. Kundur P (1993) Power system stability and control. McGraw Hill Inc
4. Yu YN (1983) Electric power system dynamics. Academic Press
5. Kundur P, Klein M, Rogers GJ, Zywno MS (1989) Applications of power system stabilizers for enhancement of overall system stability. IEEE Trans PAS 4(2):614–626
6. Cheng S, Malik OP, Hope GS (1986) Design of self-tuning PID stabilizer for a multimachine power system. IEE Proc Part C 133(4):176–185
7. Hsu YY, Liou KL, Hsu YY, Cheng CV (1990) Design of fuzzy power system stabilizers for multimachine power systems. IEE Proc Part C 137(3)
8. Zhang Y, Chen GP, Malik OP, Hope GS (1993) An artificial neural based adaptive power system stabilizer. IEEE Trans Energy Convers 8(1):71–77
9. Zhang Y, Malik OP, Chen GP (1995) Artificial neural network power system stabilizers in multi-machine power system environment. IEEE Trans Energy Convers 10(1):147–154
10. Goldberge DE (1989) Genetic algorithms in search, optimization, and machine learning. Addison-Wesley Publishing Company Inc
11. Abdel-Magid YL, Bettayeb M, Dawoud MM (1997) Simultaneous stabilization of power systems using genetic algorithm. In: IEE proceedings-generation, transmission and distribution, vol 144, no 1
12. Abido MA, Abdel-Mazid YL (1998) A genetic-based power system stabilizer. Electr Mach Power Syst 26:559–571
13. Abido MA, Abdel-Magid YL (1999) Hybridizing rule-based power system stabilizers with genetic algorithms. IEEE Trans Power Syst 14:600–607
14. Afzalian, Linkens DA (2000) Training of neuro-fuzzy power system stabilizers using genetic algorithms. Electr Power Energy Syst 22:93–102
15. Lakshmi P, Abdullah Khan M (2000) Stability enhancement of a multimachine power system using fuzzy logic based power system stabilizer tuned through genetic algorithm. Electr Power Energy Syst 22:130–145
16. Wang YP, Watson NR, Chong HH (2002) Modified genetic algorithm to design of an optimal PID controller for AC-DC transmission systems. Int J Electr Power Energy Syst 24:59–69
17. Andreoiu A, Bhattacharya K (2002) Robust tuning of power system stabilizers using a Lyapunov method based genetic algorithm. In: IEE proceedings on generation, transmission and distribution, vol 149, no 5, September 2002, pp 585–592, Gainesville, Florida, 2007, pp 162–173
18. Mirjalili S, Mirjalili SM, Lewis A (2014) Grey wolf optimizer. Adv Eng Softw 69(1):46–61

A Novel Method for Dynamic Stability Enhancement of SMIB System

P. Amrutha, C. Srinivas Rao and M. Vijaya Kumar

Abstract This paper proposes a novel method (PSOMSF) to unified power flow controller (UPFC) for dynamic stability enhancement of single machine infinite bus system (SMIB). This method consists of multi stage fuzzy damping controller and particle swarm optimization (PSO) method used for fixing the fuzzy bounds. Two stages of fuzzy controllers are designed in such a way the first fuzzy controller exhibits PI behavior and second fuzzy controller exhibits PD behavior and the combination exhibits PID behavior. PSO adjusts the bounds of fuzzy sets to get minimum error in frequency deviations and hence to improve the dynamic stability. The proposed method designed in Matlab environment and tested SMIB system. Effectiveness of the proposed controller is compared with conventional power system stabilizer (PSS) and genetic algorithm based multi stage fuzzy damping controller (GAMSF).

Keywords Particle swarm optimization based multi stage fuzzy damping controller (PSOMSF) · Power system stabilizer (PSS) · Genetic algorithm based multi stage fuzzy damping controller (GAMSF)

1 Introduction

In general Power system stabilizers (PSS) were used for dynamic stability enhancement. These PSSs were unable to control low frequency oscillations under heavy loaded conditions. FACTs controllers are the preferable alternative solution for enhancement of dynamic stability due to their advantages [1, 2]. One of the most important FACTs devices is UPFC, it can control the power through the lines by controlling the bus voltages and line reactance simultaneously and individually [3, 4]. Low frequency oscillations damping with UPFC alone cannot be possible to

P. Amrutha (✉) · M. Vijaya Kumar
EEE Department, JNTUA, Anantapur 515002, Andhra Pradesh, India
e-mail: pnamrutha.reddy@gmail.com

C. Srinivas Rao
EEE Department, G. Pullaiah College of Engineering & Technology, Kurnool 518001, Andhra Pradesh, India

© Springer Nature Singapore Pte Ltd. 2020

T. Hitendra Sarma et al. (eds.), *Emerging Trends in Electrical, Communications, and Information Technologies*, Lecture Notes in Electrical Engineering 569,
https://doi.org/10.1007/978-981-13-8942-9_30

the required extent, therefore, additional controllers required for UPFC [5]. Initially UPFC additional controllers were conventional PSS and two PI controllers one for power and other for capacitor voltage. The parameters of these additional controllers were fixed values and cannot provide effective damping under different loading conditions, this leads to need of flexible parameter controllers for UPFC [6–12].

Wang et al. and Hawary et al. proposed a new controller based on fuzzy system for dynamic stability enhancement [13, 14]. Lo et al. and Lin et al. proposed a control strategy for control of multiple series compensators in interconnected power system [15] and Kazemi et al. proposed controllers for FACTs devices [16]. Dash et al. proposed hybrid fuzzy controller for series converters [17] and Annakage et al. proposed Fuzzy logic controller (FLC) for UPFC [18]. Hybrid micro genetic algorithm (HMGA) based FLC proposed by Khan et al. for TCSC and UPFC for transient stability enhancement in multi machine environment [19]. Mok et al. proposed a new method in which tuning mechanism for fuzzy controller based on genetic algorithm used for UPFC [20].

This paper proposes PSOMSF controller for dynamic stability enhancement of single machine infinite bus system (SMIB) and results compared with PSS and GAMSF controllers.

2 Modeling of Power System with UPFC

Figure 1 shows non linear model models of power system with UPFC respectively. Mathematical models of linear power system with UPFC are represented in Eqs. 1–15 [21].

$$\omega^{\bullet} = (P_m - P_e - D\Delta\omega)/M \tag{1}$$

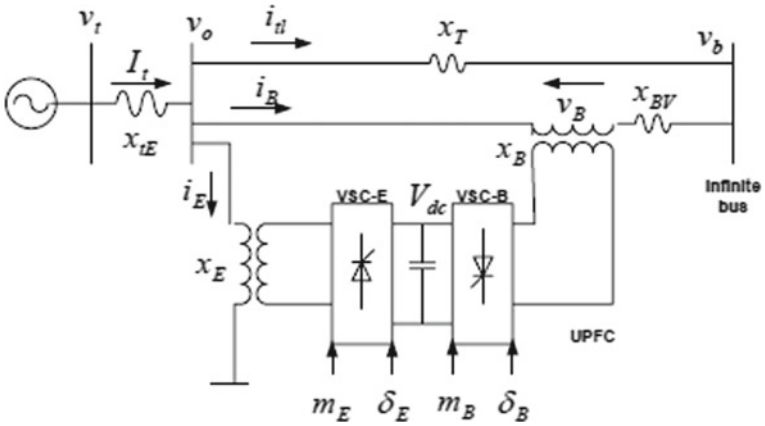

Fig. 1 SMIB power system with UPFC

$$\delta^{\bullet} = \omega_o(\omega - 1) \tag{2}$$

$$E_q^{\bullet\prime} = (-E_q + E_{fd})/T'_{do} \tag{3}$$

$$E_{fd}^{\bullet} = (-E_{fd} + K_a(V_{ref} - V_t))/T_a \tag{4}$$

$$\Delta\delta^{\bullet} = \omega_o \Delta\omega \tag{5}$$

$$\Delta\omega^{\bullet} = \frac{\Delta P_m - \Delta P_e - D\Delta\omega}{M} \tag{6}$$

$$\Delta E_{fd}^{\bullet} = -\frac{\Delta E_{fd}}{T_A} - \frac{K_A \Delta V}{T_A} \tag{7}$$

$$\Delta E_q = (X_d - X'_d 8)\Delta i_d - \Delta E'_q \tag{8}$$

$$\Delta V_{dc}^{\bullet} = K_7\Delta\delta + K_8\Delta E'_q - K_9\Delta V_{dc} + K_{ce}\Delta m_E + K_{c\delta e}\Delta\delta_E + K_{cb}\Delta m_B + K_{c\delta b}\Delta\delta_B \tag{9}$$

$$\Delta E_q^{\bullet\prime} = \frac{-\Delta E_q + \Delta E_{fd}}{T'_{do}} \tag{10}$$

$$E_q = (X_d - X'_d)i_d - E'_q \tag{11}$$

$$\Delta V = \Delta V_{ref} - \Delta V_t \tag{12}$$

$$\Delta P_e = K_1\Delta\delta + K_2\Delta E'_q + K_{pd}\Delta V_{dc} + K_{pe}\Delta m_E + K_{p\delta e}\Delta\delta_E + K_{pb}\Delta m_B + K_{p\delta b}\Delta\delta_B \tag{13}$$

$$\Delta E'_q = K_4\Delta\delta + K_3\Delta E'_q + K_{qd}\Delta V_{dc} + K_{qe}\Delta m_E + K_{q\delta e}\Delta\delta_E + K_{qb}\Delta m_B + K_{q\delta b}\Delta\delta_B \tag{14}$$

$$\Delta V_t = K_5\Delta\delta + K_6\Delta E'_q + K_{vd}\Delta V_{dc} + K_{ve}\Delta m_E + K_{v\delta e}\Delta\delta_E + K_{vb}\Delta m_B + K_{v\delta b}\Delta\delta_B \tag{15}$$

where $K_1, K_2 \ldots K_9, K_{pu}, K_{qu}$ and K_{vu} are the linearization constants. The 28 constants of the model depend on the system parameters and the operating condition.

P_1 is Transferred Power of Primary Line, P_2 is Transferred Power of secondary Line, P_e is generator output, P_m is mechanical input to generator, V_t is terminal voltage, X_d and X_q are Direct and quadrature axis steady state synchronous reactance of generator, δ and ω are rotor angle and speed respectively, D is damping factor, E_{fd} is Generator field voltage, E'_q is Generator internal voltage, K is Damping controller gain, KA is Exciter gain, TA is Exciter time constant, M is Inertia constant, T'_{do} is D-axis open circuit field time constant of generator, m_E and m_B are modulation control inputs for UPFC and δ_E and δ_B are phase angle control inputs of excitation transformer and boosting transformers for UPFC respectively.

3 Proposed Method

PSOMSF controller is shown in Figs. 2 and 3 shows fuzzy membership functions of PSOMSF controller. It consists of two fuzzy sets and one control switch. First fuzzy set is a PD fuzzy set which receives ΔV_{dc} as one input and differential error as second input. This fuzzy set generates output, which will become input for the second fuzzy set. The inputs for second fuzzy set are integral error and output of first fuzzy set. The combination of these two provides fuzzy PID type behavior. The second fuzzy set output connected to switch through gain blocks. The switching action is controlled by deviation of rotor angle. If rotor angle deviation is more than 70° it will prefer first path otherwise it will prefer second path. The first path provides high gain and second path provides low gain compared with first path in order to damp oscillations effectively.

Each fuzzy set (fuzzy controller) consists of seven membership functions equally distributed between −1 and +1. Each membership function consists of two boundaries, theses boundaries are adjusted by PSO algorithm by minimizing the objective function. The objective function is a integral time area error caused by deviations in capacitor voltage. The objective function and fitness function are shown Eqs. 16 and 17 respectively.

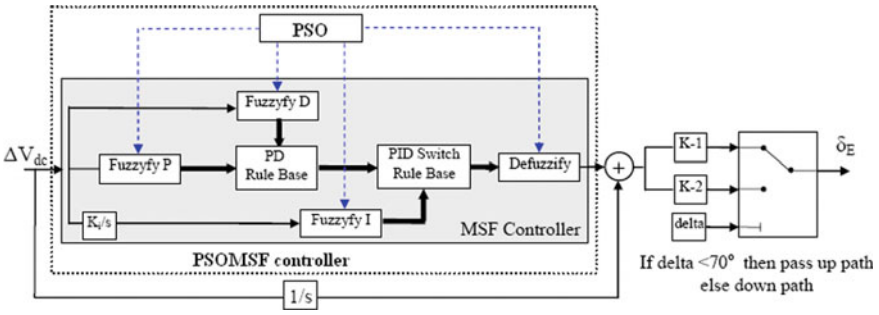

Fig. 2 Structure of proposed PSOMSF controller

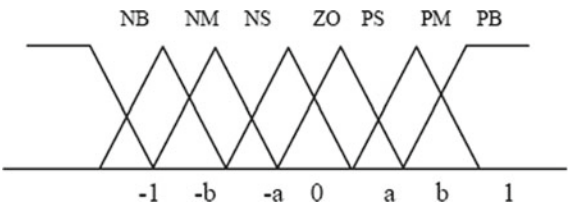

Fig. 3 Symmetric fuzzy partition

NB: Negative big PB: Positive big ZO: Zero
NM: Negative medium PM: Positive medium
NS: Negative small PS: Positive small

Table 1 PD rule base

$e = \Delta V_{DC}$	Δe						
	NB	NM	NS	ZO	PS	PM	PB
NB	NB	NB	NB	NB	NM	NS	ZO
NM	NB	NB	NB	NM	NS	ZO	PS
NS	NB	NB	NM	NS	ZO	PS	PM
ZO	NB	NM	NS	ZO	PS	PM	PB
PS	NM	NS	ZO	PS	PM	PB	PN
PM	NS	ZO	PS	PM	PB	PB	PB
PB	ZO	PS	PM	PB	PB	PB	PB

Table 2 PID switch rule base

$\int e$	PD values						
	NB	NM	NS	ZO	PS	PM	PB
NB	NM	NS	NB	PS	PM	PB	NM
NM	NM	NS	NM	PS	PM	PB	NM
NS	NM	NS	NS	PS	PM	PB	NM
ZO	NM	NS	ZO	PS	PM	PB	NM
PS	NM	NS	PS	PS	PM	PB	NM
PM	NM	NS	PM	PS	PM	PB	NM
PB	NM	NS	PB	PS	PM	PB	NM

$$ITAE = \int_0^t (t \times |\Delta V_{dc}|) \tag{16}$$

$$F = \frac{1}{10 \times ITAE} \tag{17}$$

Tables 1 and 2 represent rules for both fuzzy controllers (PD and PID). In this paper total number of generations taken as 50, 150 number of populations preferred.

4 Test System and Results

The disturbance is given as step input and the output response is taken from '$\Delta\delta$', '$\Delta\omega$', 'ΔP_e' and 'ΔV_{dc}'which gives rotor angle deviation, angular frequency deviation, deviation in 'P_e', deviation in capacitor voltage 'V_{dc}' respectively. The system shown in Fig. 4 is simulated with a step disturbance of 0.1pu at various operating

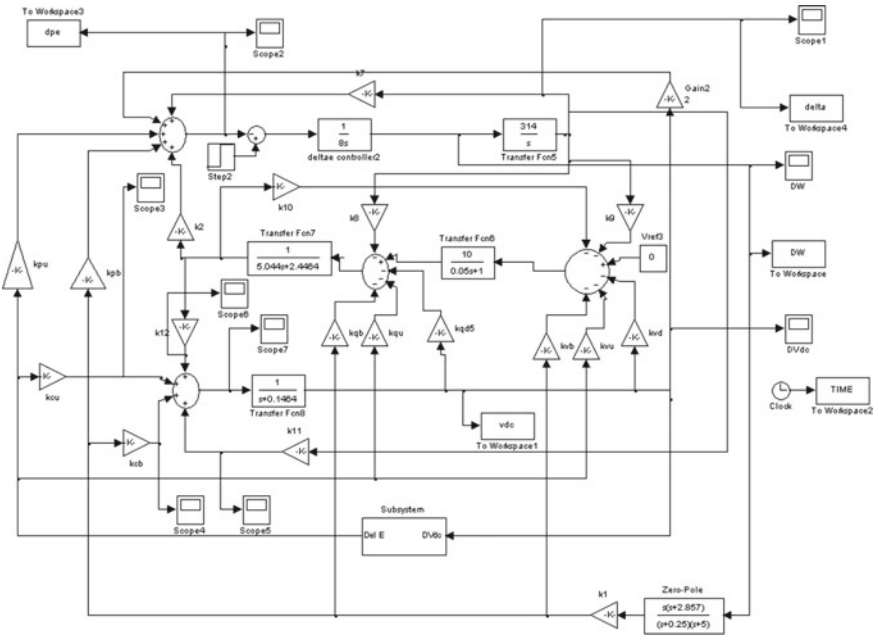

Fig. 4 Simulink model of a single-machine infinite-bus system with UPFC, damping controller and MSF DC-voltage regulator

conditions (operating point 1 (normal load): $P_e = 0.8$ $Q_e = 0.15$ $V_t = 1.032$; operating point 2 (heavy load): $P_e = 1.15$ $Q_e = 0.3$ $V_t = 1.032$) and the results are shown in figures from (5) to (12). Figures 5 and 9 represents the response of $\Delta\omega$ of SMIB system under normal and heavy loaded conditions with conventional PSS,

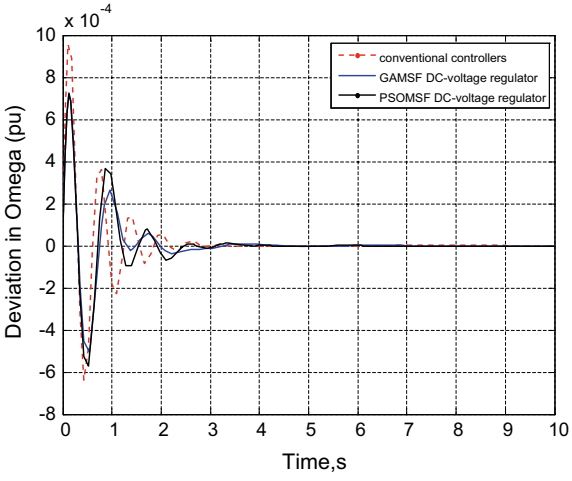

Fig. 5 Time response of $\Delta\omega$ with conventional controllers, GAMSF and PSOMSF at operating point 1

GAMSF and PSOMSF controllers with respect to time. Figures 6 and 10 represents the response of $\Delta\delta$ of SMIB system under normal and heavy loaded conditions with conventional PSS, GAMSF and PSOMSF controllers with respect to time. Figures 7 and 11 represents the response of ΔP_e of SMIB system under normal and heavy loaded conditions with conventional PSS, GAMSF and PSOMSF controllers with respect to time.

Figure 8 and 12 represents the response of ΔV_{dc} of SMIB system under normal and heavy loaded conditions with conventional PSS, GAMSF and PSOMSF controllers with respect to time. From Figs. 5, 6, 7, 8, 9, 10, 11 and 12, it is clear that PSOMSF controller damping oscillations effectively compared with conventional PSS and GAMSF. This controller reducing the peak overshoot, rise time, settling time and steady state errors effectively.

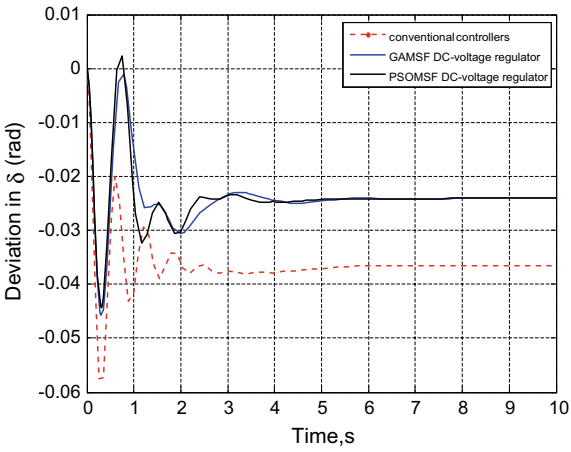

Fig. 6 Time response of $\Delta\delta$ with conventional controllers, GAMSF and PSOMSF at operating point 1

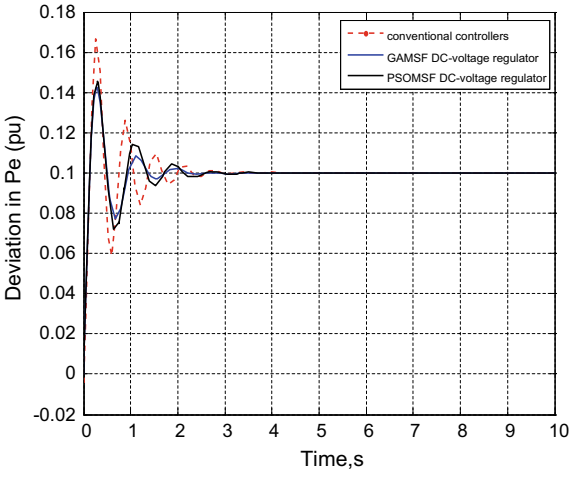

Fig. 7 Time response of ΔP_e with conventional controllers, GAMSF and PSOMSF at operating point 1

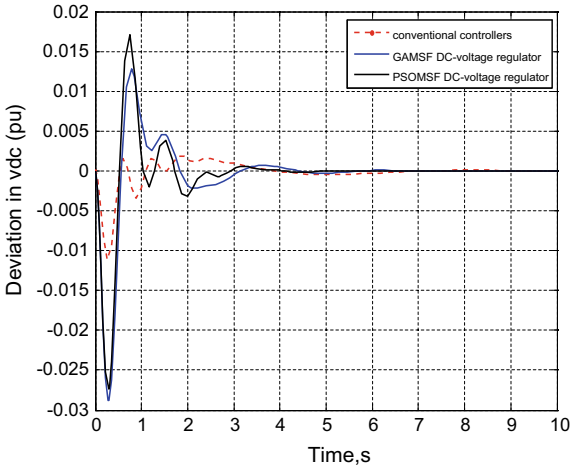

Fig. 8 Time response of ΔV_{dc} with conventional controllers, GAMSF and PSOMSF at operating point 1

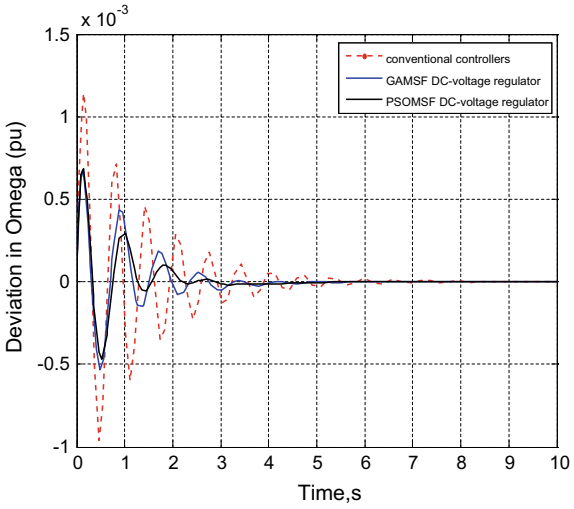

Fig. 9 Time response of $\Delta\omega$ with conventional controllers, GAMSF and PSOMSF at operating point 2

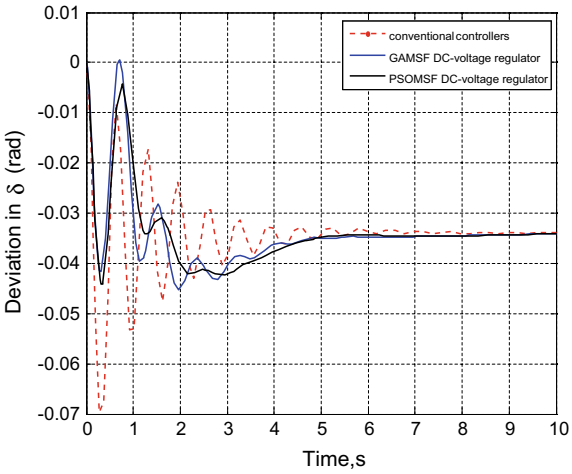

Fig. 10 Time response of $\Delta\delta$ with conventional controllers, GAMSF and PSOMSF at operating point 2

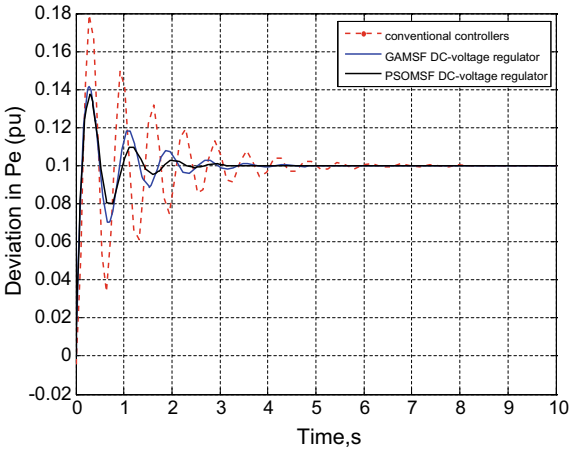

Fig. 11 Time response of ΔP_e with conventional controllers, GAMSF and PSOMSF at operating point 2

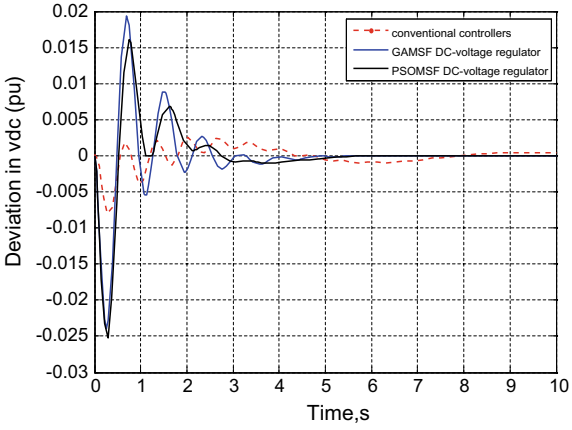

Fig. 12 Time response of ΔV_{dc} with conventional controllers, GAMSF and PSOMSF at operating point 2

5 Conclusion

This paper proposed particle swarm optimization based multi stage fuzzy damping controller for enhancement of dynamic stability of SMIB system. PSOMSF results compared with conventional PSS and GAMSF controllers, results demonstrated that PSOMSF controller reduced peak overshoot, settling time, rise time and steady state error effectively irrespective of loading condition of power system network.

References

1. Song YH, Johns AT (1999) Flexible AC transmission systems (FACTS). IEE Press, UK
2. Hingorani NG, Gyugyi L (1999) Understanding FACTS: concepts and technology of flexible AC transmission systems. Wiley-IEEE Press
3. Gyugyi L (1992) Unified power-flow control concept for flexible ac transmission systems. IEE Proc Gener Transm Distrib 139(4):323–331
4. IEEE Power Engineering Society and CIGRE, FACTS overview, IEEE Publication, No. 95 TP 108, 1995
5. Vilathgamuwa M, Zhu X, Choi SS (2000) A robust control method to improve the performance of a unified power flow controller. Electr Power Syst Res 55:103–111
6. Tambey N, Kothari ML (2003) Damping of power system oscillations with unified power flow controller (UPFC). IEE Proc Gene Transm Distrib 150(2):129–140
7. Farsangi MM, Song YH, Lee KY (2004) Choice of FACTS device control inputs for damping inter-area oscillations. IEEE Trans Power Syst 19(2):1135–1143
8. Padiyar KR, Saikumar HV (2005) Coordinated design and performance evaluation of UPFC supplementary modulation controllers. Electr Power Energy Syst 27:101–111
9. Stefanov PC, Stankovic AM (2002) Modeling of UPFC operation under unbalanced conditions with dynamic phasors. IEEE Trans Power Syst 17(2):395–403
10. Dash PK, Mishra S, Panda G (2000) A radial basis function neural network controller for UPFC. EEE Trans Power Syst 15(4):1293–1299
11. Pal BC (2002) Robust damping of interarea oscillations with unified power flow controller. IEE Proc Gene Transm Distrib 149(6):733–738
12. Seo J-C, Moon S-I, Park J-K, Choe J-W (2002) Design of a robust UPFC controller for enhancing the small signal stability in the multi-machine power systems. In Proceedings of the IEEE PES winter meeting, 28 January–1 February, vol 3, pp 1197–1202
13. Wang L-X (1997) A course in fuzzy systems and control. Prentice Hall, NJ
14. El-Hawary ME (1998) Electric power applications of fuzzy systems. IEEE Press, New York
15. Lo KL, Lin YJ (1999) Strategy for the control of multiple series compensators in the enhancement of interconnected power system stability. IEE Proc Gener Transm Distrib 146(2):149–158
16. Kazemi A, Vakili Sohrforouzani M (2006) Power system damping controlled facts devices. Electr Power Energy Syst 28:349–357
17. Dash PK, Mishra S, Panda G (2000) Damping multimodal power system oscillation using hybrid fuzzy controller for series connected FACTS devices. IEEE Trans Power Syst 15(4):1360–1366
18. Limyingcharone S, Annakkage UD, Pahalawaththa NC (1998) Fuzzy logic based unified power flow controllers for transient stability improvement. IEE Proc Gener Transm Distrib 145(3):225–232
19. Khon L, Lo KL (2006) Hybrid micro-GA based FLCs for TCSC and UPFC in a multi machine environment. Electr Power Syst Res 76:832–843

20. Mok TK, Liu H, Ni Y, Wu FF, Hui R (2005) Tuning the fuzzy damping controller for UPFC through genetic algorithm with comparison to the gradient descent training. Electr Power Energy Syst 27:275–283
21. Sankaraiah M, Sreerama Kumar R (2010) A new POD controller for UPFC for damping low frequency oscillations in power systems. In Proceedings of national symposium for post graduate students (NSPGS 2010), 24–25 April 2010, Electrical Sciences, vol 2, pp 301–306

Customer Loss Allocation Reduction Using Optimal Conductor Selection in Electrical Distribution System

T. Ramana, K. Nararaju, V. Ganesh and S. Sivanagaraju

Abstract Designing an electrical power distribution system requires many stages of planning and rigorous calculations. One of the vital, integral parts of the planning process is selection of the conductors for design and upgrade of the distribution system. An ideal conductor set should minimise the combined investment cost of conductors and the annual cost of distribution system energy losses while complying the thermal capacity of conductors, system voltage profiles limits and provide best voltage profile for farthest end customers. Proposed method aims to reach the best optimal conductor selection for existing distribution system by solving the optimisation technique using the teaching learning-based optimisation technique with less parameter control. Simulations are executed and discussed by calculating the customer loss allocation before and after the optimal conductor selection in the distribution system. The examined results show the efficacy of the proposed algorithm to satisfy the objective function and constraints.

Keywords Optimal conductor selection · Teaching-learning optimization · Electrical power distribution system

T. Ramana
EIT Services India Private Limited, DXC Technologies, Bangaluru 560100, India
e-mail: tramady@yahoo.co.in

K. Nararaju (✉)
SRIT, Anantapur 515701, India
e-mail: nagaraju.eee@srit.ac.in

V. Ganesh
JNTUA, Anantapur 515002, India
e-mail: ganivg@gmail.com

S. Sivanagaraju
JNTUK, Kakinada 533003, India
e-mail: sirigiri70@gmail.com

© Springer Nature Singapore Pte Ltd. 2020

T. Hitendra Sarma et al. (eds.), *Emerging Trends in Electrical, Communications, and Information Technologies*, Lecture Notes in Electrical Engineering 569,
https://doi.org/10.1007/978-981-13-8942-9_31

1 Introduction

Nowadays in developing countries, electrical energy demand is increasing more faster way and more power losses in the distribution systems in India because of stretching distribution feeders beyond the load centres causes an abnormal rise in demand due to the absence of studying distribution feeder maximum current carrying capacity. Therefore, best conductors selection of electrical distribution system is needed based on distribution feeder's current density and gradient of conductor selection. Based on the current carrying capacity, the conductor cross-section area is a change in distribution system feeders and not possible select uniform cross-section conductors for the entire system. Various mathematical methods have been suggested to derive the best location with right conductor cross-section and interconnection of substation and feeder to meet the current and forecasted future load demands [1]. The literature proposed methods can relegate as analytical [1–7] and meta-heuristic [7–22] methods.

In Sivanagaraju et al. [2] and Mandel and Pahwa [3] introduced an analytical approach to maximise savings in capital cost of conductor and cost of energy loss for a suitable conductor size selection based on consideration of several engineering and financial factors. Falaghi et al. [4] had presented an extension of the analytical method [2] to get the optimal conductor selection based on marginal benefits to check by minimising capital investment and power losses with voltage drop and current carrying capacity constraints by considering the time-varying load. Satyanarayana et al. [5] discussed the model of distribution system based optimal conductor selection improve the overloading capacity of the conductor.

Thenepalle [7] presented analytical and genetic algorithm (GA) heuristic approaches of optimal selection for conductors in a distribution network with the objective function of minimising the power losses and maximising the cost saving by maintaining the voltage limits. Legha et al. [8] presented an objective function to reduce the distribution system overall annual cost using GA. In [9] introduced optimal capacitors placement and optimal selection of conductors together via GA to minimise the distribution system losses and improve the voltage profile. Various optimization methods explained for the optimal conductor selection via Evolutionary Strategy (ES) [11], Evolutionary Programming (EP) [12], Modified Differential Evolution (MDE) [13], Imperialist Competitive Algorithm (ICA) [14], Particle Swarm Optimization (PSO) [15], Bacterial Foraging Algorithm (BFA) [16], Discrete Particle Swarm Optimization (DPSO) [17], Partial Enumeration Technique Optimization (PETO) [18], Harmony Search Algorithm (HSA) [19], HSA with a Differential operator (HSDE) [19], Cow Search Algorithm (CSA) [20] and SalpSwarm Optimization (SSO) [21] to minimize the annual cost of energy loss and investment cost of distribution system conductors subject to voltage limits and thermal capacities but most of the cases current density of the conductors in the same feeder not maintained in gradient.

In this paper, we have eliminated the missing factors in most of the optimisation techniques and explain the Teaching Learning Based Optimization (TLBO) for the optimal conductor selection by considering the voltage limits and thermal capacities by maintaining the better voltage profile to end customers.

2 Definition of Optimal Conductor Selection (OCS) Cost Function

In literature [2–21], the constrained objective function defined based on the minimisation of optimal conductor selection cost function with the combination of the investment cost of the conductors and the annual cost of energy losses. Constraints are the set of conductor electrical and mechanical properties and every conductor size. A mathematical function is the total cost function (C_T) describes as a combination of the investment cost of the conductors (C_{Inv}) and the annual cost of the system energy losses (C_{EL}) for the selected conductor type ct for feeder branch fb.

$$C_T(fb, ct) = C_{Inv}(fb, ct) + C_{EL}(fb, ct) \tag{1}$$

The investment cost of the conductors (C_{Inv}) is defined in terms of interest and depreciation factors of conductor (IDF_C) which will depends on the interest rate (ir) and life time of conductor (lt), length of feeder branch (L), and cost of conductor per unit area per unit length (C_C).

$$C_{Inv}(fb, ct) = IDF_C \times L(fb) \times C_C(ct) \tag{2}$$

where

$$IDF_C = \frac{ir(ir+1)^{lt}}{(ir+1)^{lt} - 1} \tag{3}$$

Accordingly the annual cost of the system energy losses (C_{EL}) is achieved from total system power losses (P_{loss}) under the peak load conditions, loss factor (LSF), cost of peak demand power loss (C_{pl}), cost of energy loss (C_{el}), and number of hours per year (h_y).

$$C_{EL}(fb, ct) = P_{loss}(fb, ct) \times \left[C_{pl} + \left(C_{el} \times LSF \times h_y\right)\right] \tag{4}$$

3 Optimization Problem for OCS

The optimal conductor selection objective function is the minimisation of the total cost of the distribution system (C_T) [2–21] defined as,

$$\boldsymbol{F} = \mathbf{min}(\boldsymbol{C_T}) \tag{5}$$

The following are the constraints considered in the optimisation problem.

(i) Bus voltage limits, $\left|\boldsymbol{V_{q_{min}}}\right| \leq \left|\boldsymbol{V_q}\right| \leq \left|\boldsymbol{V_{q_{max}}}\right|$
where

$\left|\boldsymbol{V_q}\right|$ is the absolute q node voltage
$\left|\boldsymbol{V_{q_{min}}}\right|$ is the absolute q node minimum voltage i.e. 0.90 pu
$\left|\boldsymbol{V_{q_{max}}}\right|$ is the absolute q node maximum voltage i.e. 1.05 pu

(ii) The thermal capacity of the branch, $|\boldsymbol{I}(\boldsymbol{fb}, \boldsymbol{ct})| \leq |\boldsymbol{I_{max}}(\boldsymbol{ct})|$
where
$|\boldsymbol{I}(\boldsymbol{fb}, \boldsymbol{ct})|$ is the absolute current for $\boldsymbol{fb}$ branch withe th $\boldsymbol{ct}$ type conductor
$|\boldsymbol{I_{max}}(\boldsymbol{fb})|$ is the absolute maximum current carrying capacity for ct type conductor.

4 Teaching-Learning Based Optimization Algorithm [23]

All meta-heuristic optimisation techniques required common control parameters and algorithm specific control parameters. The standard control parameters are like population size, number of generations, elite size. The algorithm-specific control parameters depend on evolutionary and swarm intelligence optimisation techniques, for example, GA uses selection probability, crossover probability and mutation probability; PSO uses social and cognitive parameters, and inertia weight etc. There is a need for the proper turning of these parameters required otherwise solution impacts or yields a locally optimal solution. Teaching-Learning Based Optimisation (TLBO) algorithm is needed only common control parameters and not necessary any algorithm-specific parameters where uses of algorithm simple and not expected to investigate any suitable value of algorithm-specific parameters. The TLBO describes two modes of phase: (i) Teacher phase and (ii) Learner phase.

(i) Teacher Phase

Teacher phase is the algorithm first part where the learner gets the knowledge from the teacher. Depending on the capability of the teacher, the teacher tries to improve the class mean result in the subject taught. In any iteration t, m number of subjects (i.e. variables $\boldsymbol{s} = 1, 2 \ldots$ m) with each subject score as $\boldsymbol{X_s}$, n number of learners (i.e. population size $\boldsymbol{p} = 1, 2 \ldots$ n), $\boldsymbol{M_{s,t}}$ mean of class in s subject and $\boldsymbol{X_{s,pbset,t}}$

be the best overall result of the learner for all subjects ($s = 1, 2 \ldots m$) in the entire population. The best learner is considered as a teacher who trains learners as a highly learned learner. The difference between best learner (i.e. teacher) of all subjects to the existing mean of each subject is calculating by

$$\boldsymbol{Diff\_Mean}_{s,p,t} = \boldsymbol{r}_t \times \left[\boldsymbol{X}_{s,pbest,t} - \boldsymbol{T}_F \times \boldsymbol{M}_{s,t}\right] \tag{6}$$

where

T_F decides the mean to be changed called as teaching factor which can be either 1 or 2. Teaching factor can decide randomly by the algorithm as

$$\boldsymbol{T}_F = \boldsymbol{round}[1 - \boldsymbol{rand}(0, 1) \times \{2 - 1\}] \tag{7}$$

r_t is random number and value in the rage [01].

The subject scores are improving by adding the $\boldsymbol{Diff\_Mean}_{s,p,t}$ to respective subject score of individual learner to get better subject score, mathematically,

$$\boldsymbol{X}'_{s,p,t} = \boldsymbol{X}_{s,p,t} + \boldsymbol{Diff\_Mean}_{s,p,t} \tag{8}$$

The new subject scores are accepted if the subject score improves otherwise it will consider the available subject scores and these subject scores become the learner phase input.

(ii) Learner Phase

Learner phase is the algorithm second part where learner enhance knowledge from the other learner if another learner has more experience than him or her. Consider n population size for learner phase explains below.

Select two learners x and y randomly after the end of the teacher phase such that $\boldsymbol{X}'_{total-x,t} \neq \boldsymbol{X}'_{total-y,t}$.

$$\boldsymbol{X}''_{s,x,t} = \boldsymbol{X}'_{s,x,t} + \boldsymbol{r}_t \times \left(\boldsymbol{X}'_{s,x,t} - \boldsymbol{X}'_{s,y,t}\right), \boldsymbol{If}\ \boldsymbol{X}'_{total-x,t} < \boldsymbol{X}'_{total-y,t} \tag{9}$$

$$\boldsymbol{X}''_{s,x,t} = \boldsymbol{X}'_{s,x,t} + \boldsymbol{r}_t \times \left(\boldsymbol{X}'_{s,y,t} - \boldsymbol{X}'_{s,x,t}\right), \boldsymbol{If}\boldsymbol{X}'_{total-y,t} < \boldsymbol{X}'_{total-x,t} \tag{10}$$

Equations (9) and (10) are related to minimisation problem as we need the minimisation expression in our challenge of interest.

Teaching learning-based optimisation (TLBO) is simulating the population based on a teaching-learning process in the classroom. The algorithm is not required any algorithm specific control parameters and only needed common control parameters such as generations number and population size.

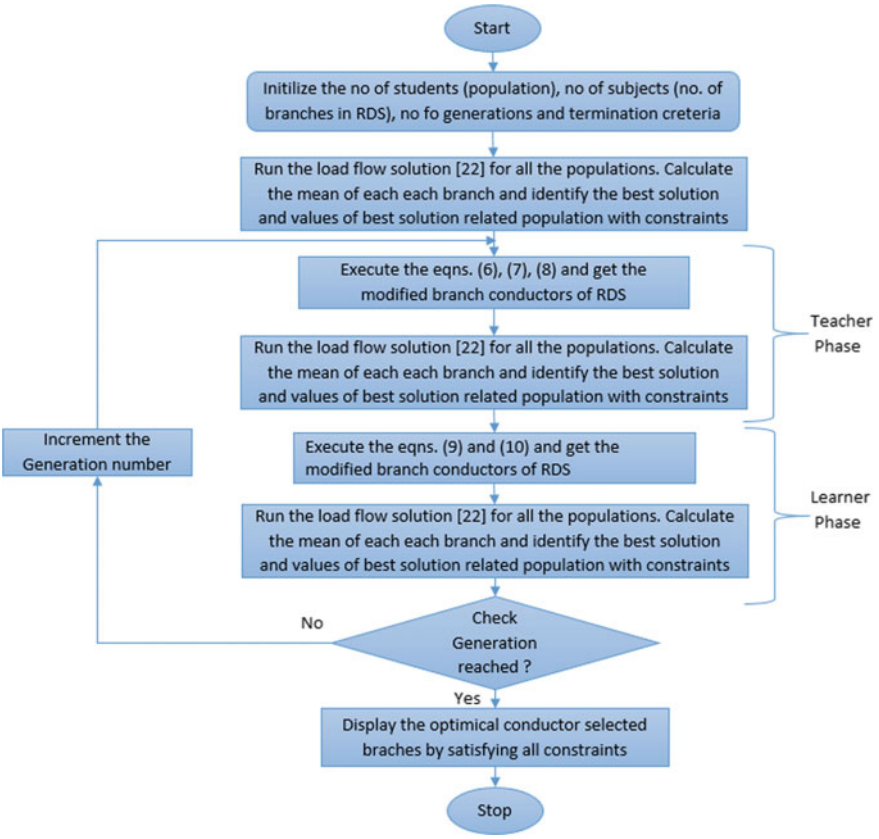

Fig. 1 Flowchart for the optimal conductor selection using TLBO technique

5 Flow Chart for OCS Using TLBO

Figure 1 is showing the flowchart for the optimal conductor selection using the TLBO.

6 Results and Discussion

The test case system is one feeder heavily loaded 16-bus electrical radial distribution system (RDS) during agriculture season in India and line and load data of the system [19]. The substation voltage is 11 kV and taken as one p.u. Total active power load and reactive power load of the 16-bus distribution system is 675.75 kW and 595.40 kVAr respectively.

The optimal conductor selection optimisation problem is solved using the TLBO, and there is no change in other infrastructure such as poles, towers etc. The common control parameters are considered in the TLBO as population size = 15 (which is equal to the number of branches in the distribution system) and number of generations = 100 for 16-bus distribution conductor optimal selection by considering the eight type of different conductors and their properties has given in [19]. There is no algorithm specific control parameter for TLBO. The other parameters considered in the solution process are $\boldsymbol{IDF_C} = 0.2$, $\boldsymbol{C_C}$ = Rs. 500/mm^2/km, $\boldsymbol{C_{el}}$ = Rs. 0.50/kWh, $\boldsymbol{C_{pl}}$ = Rs. 2500/kW, $\boldsymbol{LSF} = 0.2$ and $\boldsymbol{h_y} = 8760$.

The performance of TLBO to solve the optimal conductor selection for 16-bus distribution system is shown in Fig. 2. The convergence of the solution is obtained almost at 5th generation itself. Figure 3 shows the details before and after optimal conductor selection concerning the voltage at various nodes in p.u., active power losses in kW and reactive power losses in kVAr. It has observed that there is a lot of improvement in the individual details after optimal conductor selection.

Figure 4 is shown the customer allocation active power losses in kW and also observed the increase in % reduction of the active power losses allocation to the customer. Due to optimal conductor selection, the end customers are taking the breath from the significant loss allocation.

The summary of the result has presented in Table 1 for before and after the optimal conductor selection. The optimal conductor selection using TLBO has compared with other methods, and it has observed that the TLBO is considered the current gradient of conductors for an entire feeder with good voltage profit to end customers by reducing the loss allocation to end customers. Whereas in other most of the optimisation techniques [19] current gradient are not considering into account, due to this, some of the front conductors of the same feeder selecting less current density conductors compared with later conductors current density. Due to wrong selection of the conductors, during any critical loading on the following higher current density

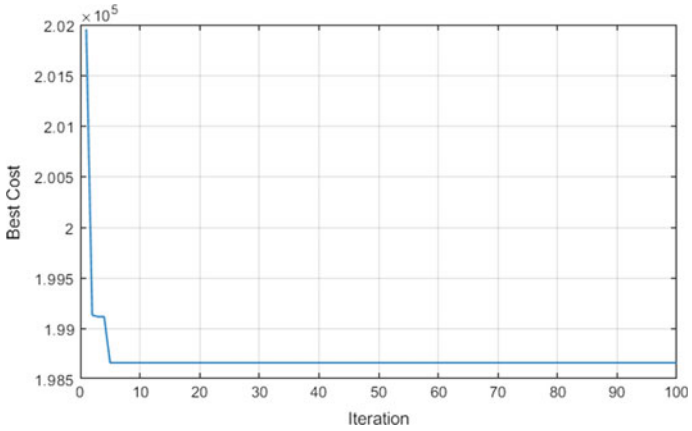

Fig. 2 Convergence of TLBO method for optimal conductor selection

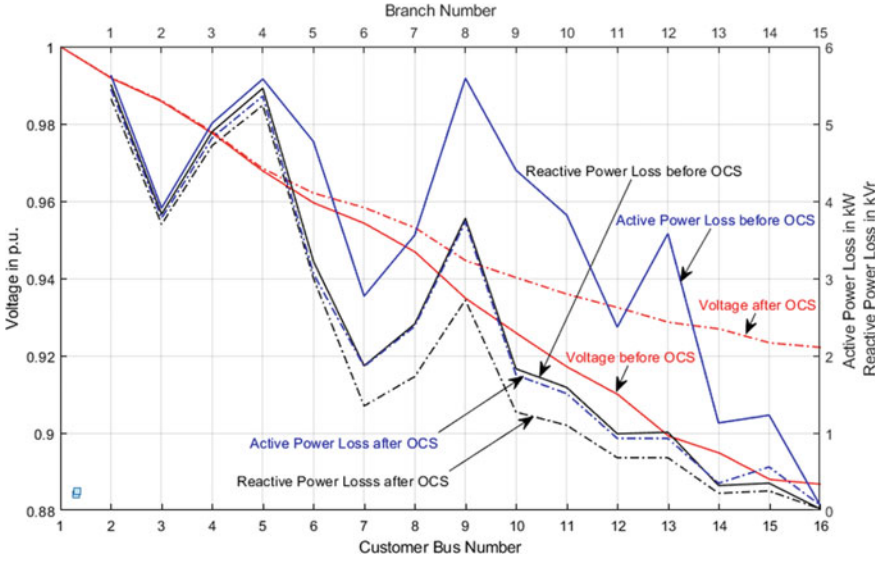

Fig. 3 Voltage, Total active and reactive power losses for optimal conductor placement

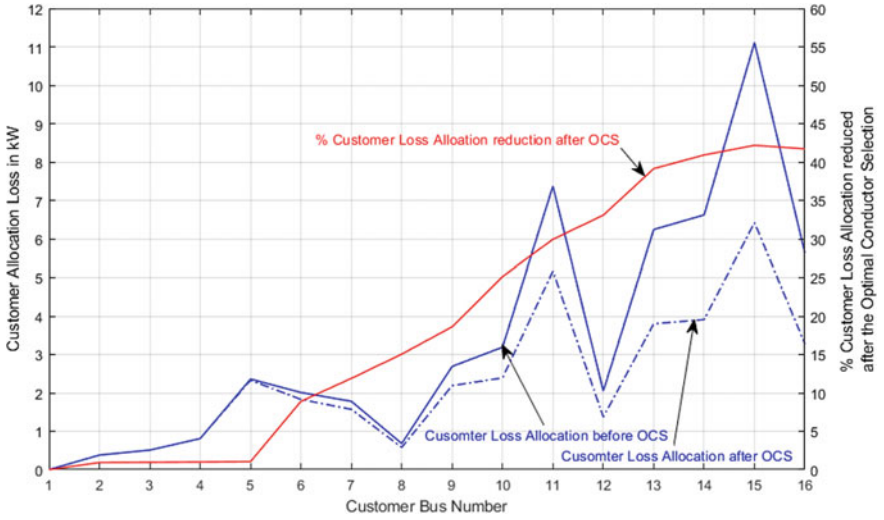

Fig. 4 Loss allocation of customers and % customer loss allocation reduction for OCS

Table 1 Summary of the results before and after optimal conductor selection for 16-bus RDS

Branch	Sending end bus	Receiving end bus	Original system	After optimal conductor selection			
				EP [12]	HSA [19]	HSDE [19]	TLBO
1	1	2	Raccoon	Raccoon	Raccoon	Raccoon	Raccoon
2	2	3	Raccoon	Raccoon	Raccoon	Raccoon	Raccoon
3	3	4	Raccoon	Raccoon	Raccoon	Raccoon	Raccoon
4	4	5	Raccoon	Raccoon	Raccoon	Raccoon	Raccoon
5	5	6	Rabbit	Raccoon	Beaver	Raccoon	Raccoon
6	6	7	Rabbit	Raccoon	Raccoon	Raccoon	Beaver
7	7	8	Rabbit	Raccoon	Raccoon	Raccoon	Beaver
8	8	9	Rabbit	Raccoon	Raccoon	Raccoon	Beaver
9	9	10	Weasel	Raccoon	Beaver	Beaver	Beaver
10	10	11	Weasel	Raccoon	Beaver	Beaver	Beaver
11	11	12	Weasel	Rabbit	Beaver	Raccoon	Beaver
12	12	13	Squirrel	Rabbit	Rabbit	Beaver	Beaver
13	13	14	Squirrel	Rabbit	Rabbit	Mink	Monk
14	14	15	Squirrel	Weasel	Beaver	Rabbit	Ferret
15	15	16	Squirrel	Squirrel	Squirrel	Mink	Squirrel
Minimum voltage (p.u.)			0.8868	0.9153	0.9269	0.9288	0.9222
Total active power losses (kW)			53.47	37.36	36.62	36.17	36.54
Loss reduction (%)			–	30.13	31.51	32.35	31.66
Optimal cost (Rs.)			2,31,990	2,08,796	2,02,156	2,00783	1,98,606
Saving cost (%)			–	10	12.86	13.45	14.39
Loss allocation to 16th bus customer			5.63	–	–	–	3.28
Loss allocation reduction % at 16th bus customer			–	–	–	–	41.71

conductors and front conductors might breakdown due to lower current density. Such issues have eliminated in the proposed TLBO of optimal conductor selection. All observations are well presented in Table 1.

7 Conclusion

In this paper, a method of optimal conductor selection presented using the TLBO. The proposed method has selected the optimal conductor by minimising the capital cost of the conductor and cost of the energy losses by properly maintain of the voltage limits, thermal capacities and feeder current density gradient using TLBO and

compared the results with other existing optimisation techniques. The customer loss allocation is also computed and observed the reduction of customer loss allocation compared with before and after conductor placement. It has been found that end customers benefited with good voltage profit and reduced loss allocation after the optimal conductor selection.

References

1. Chambiya AS, Kumar Sadana N, Mahajan S (2014) A method of selection of the optimal size of the conductor in radial distribution system—a review. Int J Adv Technol Eng Sci 2(6):190–298
2. Sivanagaraju S, Sreenivasulu N, Vijayakumar M, Ramana T (2002) Optimal conductor selection for radial distribution systems. Electr Power Syst Res 63(2):95–103
3. Mandal S, Pahwa A (2002) Optimal selection of conductors for distribution feeders. IEEE Trans Power Syst 17(1):192–197
4. Falaghi H, Ramezani M, Haghifam M-R, Roshan Milani K (2005) Optimal selection of conductors in radial distribution systems with time-varying load. In: 2005 CIRED 18th international conference and exhibition on electricity distribution in Turin, Italy, pp 6–9
5. Satyanarayana S, Ramana T, Rao GK, Sivanagaraju S (2006) Improving the maximum loading by optimal conductor selection of radial distribution systems. Electr Power Compon Syst 34(7):747–757
6. AbulWafa AR (2016) Multi-conductor feeder design for radial distribution networks. Electr Power Syst Res 140(11):184–192
7. Thenepalle MM (2011) A comparative study on optimal conductor selection for radial distribution network using conventional and genetic algorithm approach. Int J Comp Appl 17(2):6–13
8. Legha MM, Javaheri H, Legha MM (2013) Optimal conductor selection in radial distribution systems for productivity improvement using genetic algorithm. Iraq J Electr Electron Eng 9(1):29–35
9. Legha MM, Javaheri H (2013) Combination of optimal conductor selection and capacitor placement in radial distribution systems for productivity improvement using genetic algorithm. Int Res J Appl Basic Sci 6(10):1415–1422
10. Sharma D, Jha P, Vidyasagar S (2013) Optimal conductor selection using genetic algorithm. Int J Eng Res Technol 2(4):660–664
11. Mendoza F, Requena D, Bernal-Agustin JL, Dominguez-Navarro JA (2006) Optimal conductor size selection in radial power distribution systems using evolutionary strategies. In: 2006 IEEE PES transmission and distribution conference and exposition Venezuela, Latin America, pp 1–5
12. Ranjan R, Chaturvedi A, Solanki PS, Das D (2003) Optimal conductor selection of radial distribution feeders using evolutionary programming. In: 2003 TENCON conference on convergent technologies for the Asia-Pacific Region, Bangalore, India, pp 456–459
13. Kalesar BM (2014) Conductor selection optimization in radial distribution system considering load growth using MDE algorithm. World J Model Simul 10(3):175–184
14. Legha MM, Sangrood RA, Raeiszadeh AZ, Legha MM (2013) Conductor size selection in planning of radial distribution systems for productivity improvement using imperialist competitive algorithm. Int J Tech Phys Prob Eng 5(15):65–69
15. Legha MM, Ostovar F, Legha MM (2014) Combination of optimal conductor selection and capacitor placement in radial distribution systems using PSO method. Iraq J Electr Electron Eng 10(1):33–41
16. Legha MM, Noormohamadi H, Barkhori A (2015) Optimal conductor selection in radial distribution using bacterial foraging algorithm and comparison with ICA method. WALIA J 31(3):37–43

17. Sivanagaraju S, Viswanatha Rao J (2009) Optimal conductor selection in radial distribution system using discrete particle swarm optimization. World J Model Simul 5(2):96–104
18. Kaur D, Sharma J (2008) Optimal conductor sizing in radial distribution systems planning. Int J Electr Power Energy Syst 30(4):261–271
19. Rao RS, Satish K, Narasimham SVL (2012) Optimal conductor size selection in distribution systems using the harmony search algorithm with a differential operator. Electr Power Compon Syst 40(1):41–56
20. Abdelaziz AY, Fathy A (2017) A novel approach based on crow search algorithm for optimal selection of conductor size in radial distribution networks. Eng Sci Technol Int J 20(2):391–402
21. Ismael SM, Abdel Aleem SHE, Abdelaziz AY, Zobaa AF (2018) Practical considerations for optimal conductor reinforcement and hosting capacity enhancement in radial distribution systems. IEEE Access 6:27268–27277
22. Ramana T, Ganesh V, Sivanagaraju S (2013) Simple and fast load flow solution for electrical power distribution systems. Int J Electr Eng Inform 5(3):245–255
23. Rao RV, Savsani VJ, Vakharia DP (2011) Teaching-learning-based optimization: a novel method for constrained mechanical design optimization problems. Comput Aided Des 43(3):303–315

Analytical Approach Optimal Sizing and Time Scheduling of ESS Charging-Discharging Energy in Distribution Networks

Gadaram Meerimatha and B. Loveswararao

Abstract The paper illustrates analytical approach to integrate a hybrid PV-ESS unit for lowering energy losses and increasing voltage profile of distribution network and for optimal sizing and time scheduling of charging/discharging of Energy Storage System (ESS) which is integrated in distribution networks. The conceptual design and modeling of solar-PV unit, ESS unit and hybrid PV-ESS unit has been introduced to get individual unit sizes from hybrid PV-ESS unit. This approach makes non-dispatchable PV unit into a dispachable unit with a hybrid PV-ESS unit. Multi objective index, MOI based analytical terms have been developed to find the optimal size of hybrid unit (PV-ESS). This analytical approach was tested on IEEE-33 test system to obtain the performance characteristics: system losses, annual energy losses and voltage profile of distribution network with hybrid PV-ESS unit and to get optimal size of Energy storage system (ESS) and schedule of charging/discharging energy during a day cycle.

Keywords Annual energy loss · Charging/discharging schedule · Distribution networks · Hybrid PV-ESS unit · Solar-PV unit

1 Introduction

Power system networks evolving from conventional synchronized system, with centralized generation connected to the transmission networks, to a nonsynchronized

G. Meerimatha (✉) · B. Loveswararao
KLEF, Guntur, India
e-mail: gmeerimatha2k9@gmail.com

B. Loveswararao
e-mail: Loveswararao@kluniversity.in

G. Meerimatha
Department of EEE, SRIT, Anantapuramu, India

B. Loveswararao
Department of EEE, Vaddeswaram, Vijayawada, India

© Springer Nature Singapore Pte Ltd. 2020

T. Hitendra Sarma et al. (eds.), *Emerging Trends in Electrical, Communications, and Information Technologies*, Lecture Notes in Electrical Engineering 569,
https://doi.org/10.1007/978-981-13-8942-9_32

system that allows small generators to connect directly to the distribution networks. Thus such networks become active distribution networks, in which new technologies can make easy adaptation to such active environments and allow the use of smart-grid concepts. Energy storage systems (ESS) one of promising technology that can support the incorporation of smart-grids because of their capacity to permit successful islanding and to make possible the integration of high penetration levels of renewable energy sources (RES). ESSs can provide extra benefits for distribution utilities, such as efficient extension alternative, demand side management and methods of mitigating power quality issues [1]. With reference to [2], Distributed Energy Resources (DER) provides power to system loads during planned/unplanned network outages. As a result, there will be successful islanding operation which improves the reliability of system by reducing Energy loss supplied to non-affected consumers under network disturbances. Therefore, when a disturbance occurs in DN, the formation of island helps in improvement of system reliability when distributed energy resources are available and are able to operate in islanded mode. However, because of stochastic nature of the renewable power generated from renewable based client owned Distributed Generation (DG), like wind turbines and PV arrays, distribution utilities cannot rely only on such sources as a means of improving system reliability, they may use distributed storage (DS) units as a backup unit to address network disturbances. The main challenge in introduce of the concept in non-volatile DN is the high installation cost when associated with DS unit. To minimize installation costs and maximize the system reliability, distribution utilities should compute optimal size of the DS unit to be installed. Microgrid energy management strategy designed by control of out power of storage systems using fuzzy logic [3].

This paper reveals the integration of hybrid unit (PV-BES) in distribution networks (DN) with considering optimal power dispatch. Here, each non-dispatchable PV unit is converts into a dispatchable unit by adding ESS unit with suitable capacity rating and an analytical process is proposed to find out optimal size of PV-BES unit for lowering energy losses and enhancing voltage profile. This can be achieved by placing hybrid PV-ESS unit at the same location to avoid network energy losses for the period of charge of ESS unit. There by finding optimal size of individual units. The analysis has been done for summer daily load demand. During a day optimal scheduling of charging/discharging of ESS can be obtained for the proposed scenario with PV operation.

2 Conceptual Distribution Network Design and Modelling

2.1 System Load Modelling

Under distribution network study assumed to follow the normalized 24-h time varying constant real, P and reactive, Q power load model [2] as shown in Fig. 1.

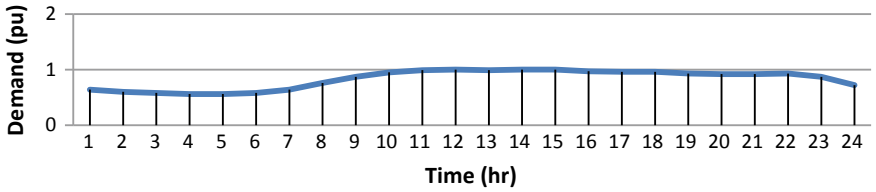

Fig. 1 Summer 24 h daily demand curve

2.2 PV Modelling (Solar)

Irradiance of solar for hour (h) of a day can be modelled by the Beta Probability Density Function (BPDF) [4]. To obtain Probability Density Function (PDF), a day can split into 24-h time segments, each of 1 h and have its own solar irradiance PDF. From the collected historical data, the mean standard deviation of hourly solar irradiance of a day can be planned. In this study, assumed each hour has 20-states for solar irradiance with a step of 0.05 kW/m^2. From the calculated mean standard deviation, the Probability Density Function (PDF) with 20-states for solar irradiance (SR) can generate for 1 h of a day and the probability of each solar irradiance state can be determined. Accordingly, the PV output power can be obtained for that hour. The mathematical equation can be written as follows.

During a specific h, the probability of the solar irradiance state s can be calculated as follows [4]:

$$\rho(s) = \int_{s1}^{s_2} f_b(s)ds \tag{1}$$

where s_1 and s_2 are limitations of solar irradiance state s; $f_b(s)$ is s state beta distribution function.

Over each h solar irradiance PDF for a state s can be expressed as [5–8]:

$$f_b(s) = \begin{cases} \dfrac{\Gamma(\alpha+\beta)}{\Gamma(\alpha)\Gamma(\beta)} s^{(\alpha-1)}(1-s)^{(\beta-1)} & 0 \le s \le 1 \; and \; \alpha, \beta \ge 0 \\ = 0 & \text{if not} \end{cases} \tag{2}$$

where s be the solar irradiance and is random variable of solar irradiance in kw/m^2, α and β are parameters of $f_b(s)$, which can be calculated as:

$$\beta = (1-\mu)\left(\frac{\mu(1+\mu)}{\sigma^2} - 1\right) \tag{3}$$

$$\alpha = \frac{\mu\,\beta}{1-\mu} \tag{4}$$

where μ and σ are mean—standard deviation of solar irradiance(s).

The total expected output power (TEOP) of a solar-PV unit during specific period t, be as follows:

$$P_{PV}(t) = \int_0^1 P_{PV_0}(s)\rho(s)ds \tag{5}$$

where $P_{PV_0}(s)$ is the output-power from PV unit at solar irradiance s, it can be given as [4, 5, 9]:

$$P_{PV_0}(s) = N * FF * V_y * I_y \tag{6}$$

where

$$FF = \frac{V_{MPP} * I_{MPP}}{V_{OC} * I_{SC}} \tag{7}$$

$$V_y = V_{OC} - (K_v * T_{cy}) \tag{8}$$

$$I_y = s\left[I_{SC} + K_i * \left(T_{cy} - 25\right)\right] \tag{9}$$

$$T_{cy} = T_A + s\left(\frac{N_{OT} - 20}{0.8}\right) \tag{10}$$

where, N is the number of units, T_{cy} is cell temperature and T_A is ambient temperature in °C; K_i is current temperature coefficient in A/°C and K_v is and voltage temperature coefficients in V/°C; N_{OT} is cell normal operating temperature in °C; FF is fill factor; V_{OC} is open circuit voltage in V and I_{SC} is short circuit current in A; V_{MPP} is maximum power point voltage and I_{MPP} maximum power point current.

2.3 Energy Storage System (ESS) Modeling

The Energy storage system (ESS) unit can be assumed to connect in AC distribution system through bidirectional converters (DC/AC) which can dispatch in all four quadrants. It can operate at any preferred lagging or leading pf to charge or discharge active power [10]. That is, ESS unit can operate as a load during charging periods and as a generator during discharging periods. ESS unit can inject or absorb reactive power as well. Energy storage system (ESS) unit can be modelled as a dispatchable source. The variation of energy at bus p during a period t can be expressed as [10]:

$$E_{ESS_P}(t) = E_{ESS_P}(t-1) - \frac{P_{ESS_P}^{disch}(t)}{\eta_d}\Delta t \quad \text{for } P_{ESS_P}(t) > 0 \tag{11}$$

$$E_{ESS_P}(t) = E_{ESS_P}(t-1) - \eta_c * P^{ch}_{ESS_P}(t)\Delta t \quad \text{for } P_{ESS_P}(t) \leq 0 \tag{12}$$

where E_{ESS_P} be the total energy stored (TES) in the ESS unit; $P^{disch}_{ESS_P}$ be discharge power and $P^{disch}_{ESS_P}$ be charge power of the ESS unit. η_c be charge efficiency and η_d be discharge efficiency of the ESS unit. Δt be time duration of period t.

The energy limitations of ESS unit at bus p can be as follows [11]

$$E^{\min}_{ESS_p} \leq E_{ESSp} \leq E^{\max}_{ESSp} \tag{13}$$

2.4 Conceptual Design of Distribution Network

Figure 2 shows the basic diagram of a grid-connected hybrid PV-ESS system (PV-ESS). Where Fig. 2a shows connection diagram of distribution network and Fig. 2b shows ESS unit charging and discharging characteristics and output power of PV unit. This system can plan to install on commercial building rooftops. Main intention of such a hybrid unit connection in DN is to convert each PV unit which is in non dispachable mode into dispachable mode and results lowering power losses. This unit combination can produce a daily dispachable energy, E_{PV-ESS}. In a 24-h day cycle, the PV unit generating energy E_{PV}. A part of E_{PV} energy delivered to the grid is E^{grid}_{PV}. The unneeded energy of the PV unit can use to charge ESS unit. The charge amount of ESS unit is E^{ch}_{ESS} and it happens during a day when PV unit output is high. The stored energy can then discharged to the grid with amount of energy, E^{disch}_{ESS}. It

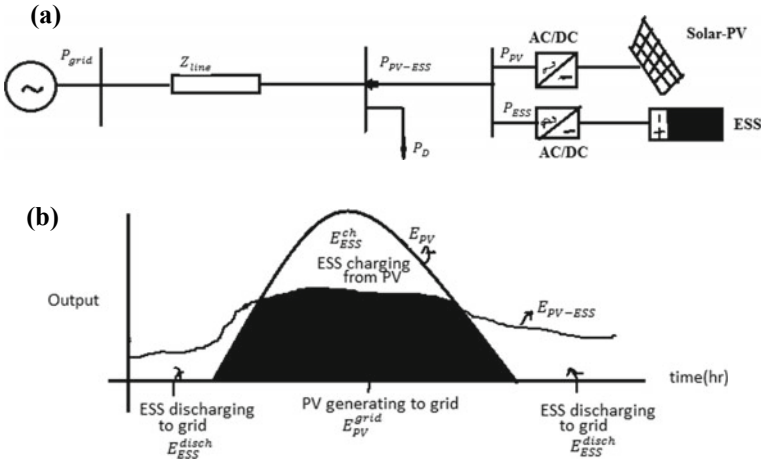

Fig. 2 **a** Connection diagram. **b** ESS unit charging and discharging characteristics and output power of PV unit, basic diagram of grid connected PV-ESS system

happens during a day when the PV unit output is small or approximately zero during night mode. The hybrid PV-ESS unit can be placed in the same location to avoid network energy losses during the charge of the ESS unit [12].

Total energy stored during a day in hybrid unit (PV-ESS unit) connected system at bus p can be written as:

$$E_{(PV-ESS)_p} = \int_0^T P_p(t)dt = \sum_{t=1}^{24} P_p(t)\Delta t \tag{14}$$

where $P_p(t)$ is hybrid PV-ESS unit active power at bus p at period t during a given day. Hybrid PV-ESS unit pf is optimally dispatched for each 1 h period. With utility perception, this unit model can reduce energy losses and enhance voltage profile, which are associated with active power loss index and reactive power loss index.

2.5 Impact Indices

2.5.1 Real Power Loss Index (RPLI)

Real power loss in b-branch system network without a PV-ESS unit be expressed as [13, 14]:

$$P_L = \sum_{k=1}^{b} \frac{P_{bk}^2 + Q_{bk}^2}{|V_k|^2} * R_k \tag{15}$$

where P_{bk} be real power flow through branch k and Q_{bk} be reactive power flow through branch k; R_k be branch k resistance; $|V_k|$ be voltage magnitude at bus k. Real power loss in b-branch system network with a PV-ESS unit be expressed as;

$$P_{L(PV-ESS)} = \sum_{k=1}^{p} \frac{(P_{bk} - P_p)^2}{|V_k|^2} * R_k + \sum_{k=p+1}^{b} \frac{P_{bk}^2}{|V_k|^2} * R_k + \sum_{k=1}^{p} \frac{(Q_{bk} - Q_p)^2}{|V_k|^2} * R_k + \sum_{k=p+1}^{b} \frac{Q_{bk}^2}{|V_k|^2} * R_k \tag{16}$$

where

$$Q_p = a_p P_p \tag{17}$$

Let

$$a_p = \pm \tan(\cos^{-1}(pf_p)) \tag{18}$$

where pf_p be PV-ESS unit operating pf at bus p. a_p is assumed positive value for the hybrid unit (PV-ESS)when unit injecting only reactive power and is assumed negative value for the hybrid unit (PV-ESS) when unit consuming only reactive power. The real power loss index (RPLI) can be written as the ratio of total real power loss (TPL) of system with hybrid unit to total real power loss (TPL) of system without hybrid unit:

$$RPLI = \frac{P_{L(PV-ESS)}}{P_L} \tag{19}$$

2.5.2 Reactive Power Loss Index (QPLI)

Reactive power loss in the b-branch system network without PV-ESS unit can be expresses as (et al.):

$$Q_L = \sum_{k=1}^{b} \frac{P_{bk}^2 + Q_{bk}^2}{|V_k|^2} * X_k \tag{20}$$

where P_{bk} be active power flow through branch k and Q_{bk} be reactive power flow through branch k; X_k be branch k reactance; $|V_k|$ be voltage magnitude at bus k.

Reactive power loss in the b-branch system network with PV-ESS unit can be expresses as;

$$\begin{aligned} Q_{L(PV-ESS)} = &\sum_{k=1}^{p} \frac{(P_{bk} - P_p)^2}{|V_k|^2} * X_k + \sum_{k=p+1}^{b} \frac{P_{bk}^2}{|V_k|^2} * X_k + \\ &\sum_{k=1}^{p} \frac{(Q_{bk} - Q_p)^2}{|V_k|^2} * X_k + \sum_{k=p+1}^{b} \frac{Q_{bk}^2}{|V_k|^2} * X_k \end{aligned} \tag{21}$$

The reactive power loss index (ILQ) can be written as the ratio of total reactive power loss (TQL) of system with hybrid unit to total reactive power loss (TQL) of system without hybrid unit:

$$QPLI = \frac{Q_{L(PV-ESS)}}{Q_L} \tag{22}$$

2.5.3 Multi-objective Index (MOI)

Combination of total active power loss index and total reactive power loss index gives Multi-objective (MOI). The MOI index can utilize to assess performance of a distribution system network with hybrid PV-ESS unit. Multi objective index, MOI can be expressed as;

$$MOI = \sigma_1 * RPLI + \sigma_2 * QPLI \tag{23}$$

where $\sum_{i=1}^{2} \sigma_i = 1 \Lambda \sigma_i \in [0, 1]$.

All impact indices were normalized values between zero and one (Ochoa LF, Padilha-Feltrin A, Harrison GP). In base system where hybrid unit not interconnected the multi objective index (MOI) will be 1. These weights are planned to each impact index for the connection of hybrid PV-ESS unit system and depends on required analysis e.g., planning and operation [14–17]. Based on experience and concerns of engineers suitable values for the weights will choose. Referring to previous research papers [14–17], this study assumes weights of 0.7 and 0.3. Currently, the energy loss is one of the major concerns at the DS networks due to its impact on the utilities' profit. The *MOI* at period t, $MOI(t)$ is obtained from Eq. (23). The average multi-objective index (AMOI) in a distribution system with an interval Δt of 1 h over a total period (T = 24 h) can be expressed as follows:

$$AMOI = \frac{1}{T} \int_0^T MOI(t)dt = \frac{1}{24} \sum_{t=1}^{24} MOI(t)\Delta t \tag{24}$$

The lower value of AMOI can implies the optimal location to integrate a hybrid PV-ESS unit for energy loss reduction and voltage profile enhancement.

2.6 Energy Loss (EL)

The Total Annual Energy Loss (TAEL) in distribution network with a time duration Δt of 1-h over a total period, T = 24 h can be expressed as:

$$E_{(PV-ESS)loss} = 365 \int_0^T P_{L(PV-ESS)}(t)dt = 365 \sum_{t=1}^{24} P_{L(PV-ESS)}(t)\Delta t \tag{25}$$

2.7 Proposed Mathematical Expressions for Sizing of Units

2.7.1 Sizing Hybrid PV-ESS Unit

The section illustrates an analytical expressions based on multi-objective index (MOI) to compute size and pf of a hybrid PV-ESS unit. From Eq. (23), the MOI variation is a function of the PV-ESS penetration level related to variables P_p and a_p (or pf_p: the power factor of the PV-ESS mix at bus p). To obtain minimum MOI, partial differentiate the Eq. (23) with respect to variables P_p and a_p at bus p and equate it to zero.

i.e.

$$\frac{\partial MOI}{\partial P_p} = 0 \tag{26}$$

$$\frac{\partial MOI}{\partial a_p} = 0 \tag{27}$$

By simplifying the above Eqs. (26) and (27) and solving it, we will get the optimal size and pf of hybrid PV-ESS unit at bus p. Optimal size of a hybrid PV-ESS unit (P_p) is

$$P_p = \frac{\sigma_1 A_p Q_L + \sigma_2 D_p P_L}{\sigma_1 B_p Q_L + \sigma_2 E_p P_L} \tag{28}$$

The optimal power factor (pf) of a hybrid PV-ESS unit is

$$pf_p = \cos\left(\tan -1\left(\frac{\sigma_1 C_p Q_L + \sigma_2 F_p P_L}{\sigma_1 A_p Q_L + \sigma_2 D_p P_L}\right)\right) \tag{29}$$

where

$$A_p = \sum_{k=1}^{b} \frac{R_k P_{bk}}{|V_k|^2};\ B_p = \sum_{k=1}^{b} \frac{R_k}{|V_k|^2}$$

$$C_p = \sum_{k=1}^{b} \frac{R_k Q_{bk}}{|V_k|^2};\ D_p = \sum_{k=1}^{b} \frac{X_k P_{bk}}{|V_k|^2}$$

$$E_p = \sum_{k=1}^{b} \frac{X_k}{|V_k|^2};\ F_p = \sum_{k=1}^{b} \frac{X_k Q_{bk}}{|V_k|^2}$$

2.7.2 Sizing of PV Unit

From Fig. 2a, b, the daily charging and discharging power energies at bus p can be obtained from the hourly input and output power of the ESS unit [6].

$$E^{ch}_{ESS_p} = \int_0^T P^{ch}_{ESS_p}(t)dt = \sum_{t=1}^{24} P^{ch}_{ESS_p}(t)\Delta t \tag{30}$$

$$E^{disch}_{ESS_p} = \int_0^T P^{disch}_{ESS_p}(t)dt = \sum_{t=1}^{24} P^{disch}_{ESS_p}(t)\Delta t \tag{31}$$

Total output power energies of a hybrid PV-ESS unit and PV unit at bus p can be calculated as;

$$E_{(PV-ESS)_p} = E^{grid}_{PV_p} + E^{disch}_{ESS_p} \tag{32}$$

$$E_{PV_p} = E^{grid}_{PV_p} + E^{ch}_{ESS_p} \tag{33}$$

where $E^{grid}_{PV_p}$ be the amount of energy of a Solar PV unit delivered to grid at bus p. The charging and discharging power energy of ESS unit at bus p with round trip efficiency can be expressed as [6]

$$E^{disch}_{ESS_p} = \eta_{ESS} E^{ch}_{ESS_p} \tag{34}$$

where round trip efficiency $\eta_{ESS} = \eta_c * \eta_d$.

Therefore total output power energy of a PV unit at bus p can be obtained from Eq. (33) as follows;

$$E_{PV_p} = \frac{E_{(PV-ESS)_p} - (1-\eta_{ESS})E^{grid}_{PV_p}}{\eta_{ESS}} \tag{35}$$

The maximum power generation of a PV unit during a specific duration i.e. over a 24-h day cycle, can be utilized to specify the rating/optimal size of the PV unit at bus p.

$$P_{PV_p} = k^{unit}_{PV} E_{PV_p} \tag{36}$$

where $k^{unit}_{PV} = \frac{P^{unit}_{PV}}{E^{unit}_{PV}}$.

P^{unit}_{PV} be the maximum power output of a PV unit and E^{unit}_{PV} be the amount of energy generated from a PV unit over a 24-h day. Assuming $\eta_{ESS} = 1$, $E_{PV_p} = E_{(PV-ESS)_p}$,

the initial PV size is calculated from the equation as $P'_{PV_p} = k_{PV}^{unit} E_{(PV-ESS)_p}$ and $E_{PV_p}^{grid'}$ is then obtained from the characteristics Fig. 2b.

When $\eta_{ESS} \langle 1, P_{PV_p}$ increases. $E_{PV_p}^{grid}$ rises insignificantly compared to $E_{PV_p}^{grid'}$. Hence the optimal PV size is obtained from the equations as follows;

$$P_{PV_p} = k_{PV}^{unit} \left(\frac{E_{(PV-ESS)_p} - (1 - \eta_{ESS}) E_{PV_p}^{grid'}}{\eta_{ESS}} \right) \tag{37}$$

2.7.3 Sizing ESS Unit

The best possible size of a ESS unit at bus p can be calculated with respect to the power rating (P_{ESS_p}) of a ESS unit and energy capacity (E_{ESS_p}) of a ESS unit. After that it can accommodate at a place where all redundant energy of the PV unit that needs to be curtailed to maintain the system loss for each period at the lowest level. The maximum charging and discharging power during a specified period over a 24-h day cycle can be used to specify the power rating of the ESS unit [6]. The maximum charging energy during this day cycle can be used to find out the energy capacity of the ESS unit.

3 Case Study

The proposed analytical methodology has applied to IEEE 33 bus distribution network (DN) which has total peak demand of 3715 KW and 2300 KVAR. The performance of the distribution network with integration of hybrid PV-ESS unit at bus which has minimum multi-objective index (MOI) was obtained for normalized daily (hourly) summer load demand as shown in Fig. 1. By the proposed analytical process identified the location (bus-18) to integrate the hybrid unit (PV-ESS) and found optimal size of the hybrid PV-ESS unit. The output of hybrid PV-ESS unit were dispatched optimally for each hour period across a 24-h day cycle as shown in Fig. 3. It was observed from Fig. 3 that maximum output dispatched at 12, 14 and 15 h. The maximum output dispatch at peak demand gives the optimal size of the hybrid PV-ESS unit. i.e. 0.7453 MW. Figures 4 and 5 shows the impact of hybrid unit which was integrated at bus 18 on network daily energy loss and magnitude of voltage profile. From Figs. 4 and 5 it was observed that distribution network with PV-ESS unit the energy losses had reduced and voltage profile has enhanced effectively. There by calculated annual energy losses using Eq. (25) and are tabulated in Table 1. For finding individual units PV and ESS size from hybrid unit PV-ESS unit, again observe Fig. 3 where the amount of energy that the PV unit can generate for each hour exhibits. PV unit generated maximum output for 13 h (i.e. 1.2295 MW). Sum of the hourly

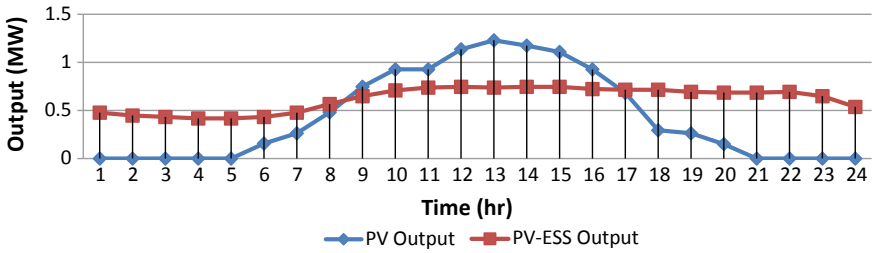

Fig. 3 Daily charging and discharging curves of ESS unit at bus 18

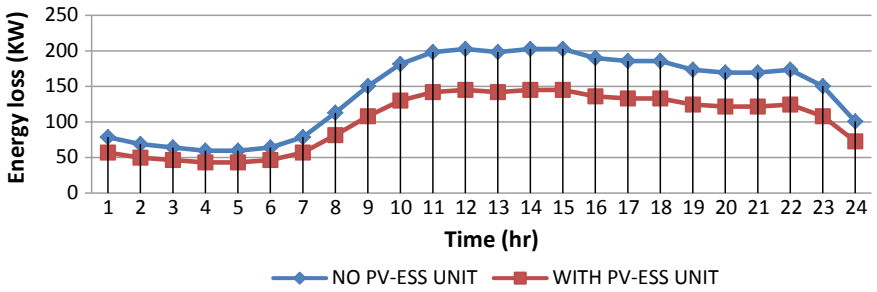

Fig. 4 PV-ESS unit impact on energy loss

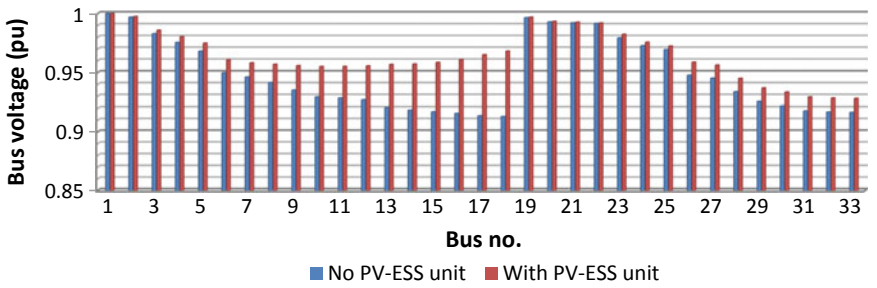

Fig. 5 Voltage profile of distribution network with PV-ESS unit

Table 1 Impact of PV-ESS integration at bus 18 on system performance

Case	System losses (KW)	Loss reduction (%)	Annual energy loss (MWh)	Annual energy loss reduction (%)
Base system (33 bus)	202.695	–	1248.55	
System with PV-ESS unit	145.040	28.44	896.3	28.21

Table 2 Optimal sizing of integrated renewable sources at bus 18

Unit	Size (MW)
PV-ESS	0.7453
Solar-PV	1.2295
ESS	0.4917
ESS charging capacity	2.3857
ESS discharging capacity	6.7522

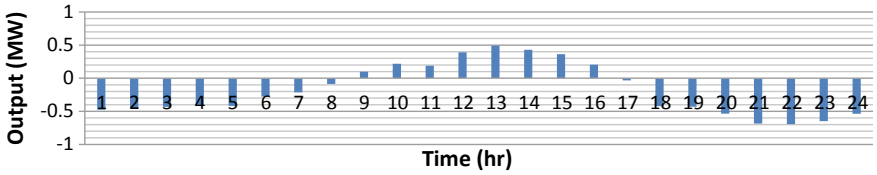

Fig. 6 Schedule of charging/discharging of ESS unit at bus 18

differences between the two performance curves of a PV unit and PV-ESS unit shown in Fig. 3 identified the total amount of energy charged and discharged by a ESS unit. The amount energy of a PV unit that needs to be curtailed to remain the minimum energy loss stored into ESS unit. The stored energy portion then discharged to the grid network following the PV-ESS unit output performance curve to keep the lowest energy loss as well. The maximum difference found at 13 h gives power rating of a ESS unit (P_{ESS_p}). The maximum charging energy over a 24 h day cycle used to get the energy capacity of ESS unit (E_{ESS_p}). Table 2 describes the optimal sizes of individual units PV and ESS. Figure 6 shows the optimal charging and discharging schedule of ESS unit for a day. During the period 1–8 h ESS unit can discharging to the grid network, during the period 8–16 h ESS unit can charging from PV unit and during the period 16–24 h ESS unit discharging to grid network. over all during a day ESS can charge for 8 h and remaining hours it can discharge the energy.

4 Conclusion

In this paper, an efficient analytical methodology introduced to integrate a hybrid PV-ESS unit for lowering energy losses and enhancing voltage profile of distribution network. In this analytical approach, each nondispatchable mode operated PV unit converted into a dispachable mode operated PV unit with an integration of a hybrid PV-ESS unit. Analytical expressions were presented to find the optimal size of hybrid unit (PV-ESS) based on MOI. Tables 3 and 4 shows the mean and standard deviation of solar irradiance and characteristics of PV Unit. Using these characteristics of Solar PV unit the expected power output of PV unit obtained as shown in Fig. 3. This proposed analytical process applied to IEEE 33 bus distribution network and found

Table 3 Mean and standard deviation of solar irradiance

Hour	μ (KW/m^2)	σ (KW/m^2)	Hour	μ (KW/m^2)	σ (KW/m^2)
6	0.019	0.035	13	0.648	0.282
7	0.096	0.110	14	0.590	0.265
8	0.222	0.182	15	0.477	0.237
9	0.381	0.217	16	0.338	0.204
10	0.511	0.253	17	0.190	0.163
11	0.610	0.273	18	0.080	0.098
12	0.657	0.284	19	0.017	0.032

Table 4 Characteristics of a solar-PV unit

Solar-PV unit characteristics	Value
N_{OT}	43 °C
I_{MPP}	7.76 A
V_{MPP}	28.36 V
I_{SC}	8.38 A
V_{OC}	36.96 V
K_i	0.00545 A/°C
K_v	0.1278 V/°C
T_A	30 °C

results as described in Tables 1 and 2. With integration of hybrid PV-ESS unit to the grid network annual energy losses effectively reduced by 28.44%, system peak load losses reduced by 28.21% and voltage profile improved as shown in Fig. 5. From this methodology also found the charging and discharging schedule of a ESS unit during a day and correspondingly got the charging and discharging capacity of ESS unit.

References

1. Khatod DK, Pant V, Sharma J (2013) Evolutionary programming based optimal placement of renewable distributed generators. IEEE Trans Power Syst 28(2):683–695. https://doi.org/10.1109/tpwrs.2012.2211044
2. Teng JH, Luan SW, Lee DJ, Huang YQ (2013) Optimal charging/discharging scheduling of battery storage systems for distribution systems interconnected with sizeable PV generation systems. IEEE Trans Power Syst 28(2):1425–1433. https://doi.org/10.1109/tpwrs.2012.2230276
3. Fossati JP, Galarza A, Martin A, Fontan L (2015, May) A method for optimal sizing energy storage system for micro grids. Renew Energy 77:539–549. Elsevier. https://doi.org/10.1016/j.renene2014.12.039
4. Soroudi A, Aien M, Ehsan M (2012) A probabilistic modeling of photo voltaic modules and wind power generation impact on distribution networks. IEEE Syst J 6(2):254–259. https://doi.org/10.1109/jsyst.2011.2162994

5. Gabash A, Pu L (2012) Active-reactive optimal power flow in distribution networks with embedded generation and battery storage. IEEE Trans Power Syst 27(4):2026–2035. https://doi.org/10.1109/tpwrs.2012.2187315
6. Chen SX, Gooi HB, Wang MQ (2012, March) Sizing of energy storage for microgrids. IEEE Trans Smart Grid 3(1)
7. IEEE guide for design, operation, and integration of distributed resource island systems with electric power systems, IEEE Std. 1547.4-2011, 2011
8. El-Zonkoly AM (2011) Optimal placement of multi-distributed generation units including different load models using particle swarm optimisation. IET Gener Trans Distrib 5(7):760–771. https://doi.org/10.1049/iet-gtd.2010.0676
9. Chen SX, Gooi HB, Wang MQ (2012) Sizing of energy storage for microgrids. IEEE Trans Smart Grid 3(1):142–151. https://doi.org/10.1109/tsg.2011.2160745
10. Atwa YM, El-Saadany EF, Salama MMA, Seethapathy R (2010) Optimal renewable resources mix for distribution system energy loss minimization. IEEE Trans Power Syst 25 (1):360–370. https://doi.org/10.1109/tpwrs.2009.2030276
11. Singh D, Verma KS (2009) Multiobjective optimization for DG planning with load models. IEEE Trans Power Syst 24(1):427–436. https://doi.org/10.1109/TPWRS.2008.2009483
12. Atwa YM, El-Saadany EF (2010, November) Optimal allocation of ESS in distribution systems with a high penetration of wind energy. IEEE Trans Powersyst 25(4)
13. Ochoa LF, Padilha-Feltrin A, Harrison GP (2008) Evaluating distributed time-varying generation through a multiobjective index. IEEE Trans Power Deliv 23(2):1132–1138. https://doi.org/10.1109/tpwrd.2008.915791
14. Ochoa LF, Padilha-Feltrin A, Harrison GP (2006) Evaluating distributed generation impacts with a multiobjective index. IEEE Trans Power Deliv 21(3):1452–1458. https://doi.org/10.1109/tpwrd.2005.860262
15. Casper SG, Nwankpa CO, Bradish RW, Chiang H-D, Concordia C, Staron JV, Taylor CW, Vaahedi E, Wu G (1995) Bibliography on load models for power flow and dynamic performance simulation. IEEE Trans Power Syst 10(1):523–538. https://doi.org/10.1109/59.373979
16. Enabling tomorrow's electricity system: report of the Ontario Smart Grid Forum. http://www.ieso.ca/MOIweb/pubs/smart_grid/Smart_Grid_Forum-Report.pdf
17. SolarAnywhere. https://solaranywhere.com/

Optimal Load Scheduling of Thermal Power Plants by Genetic Algorithm

K. Rajesh, N. Visali and N. Sreenivasulu

Abstract With the cumulative addition in power demand, interconnection of power system is crucial to route the power station operate in specific limitations to encounter the power burden optimally and also diminish the rate of active power generation. One of the objectives for the steam run power plants is to reduce fuel consumption by assigning source power to every component (economic dispatch) focus to equal and unequal limitations optimally. This importance is due to power savings. ELD is the utmost significant issues to be resolved in the process and forecasting of a electrical system. This work presents an approach of Genetic Algorithm (GA) for finest load scheduling of steam run power plants to catch the universal optimum dispatch clarification. The genetic set of rules centered best approach explains the ELD problem. The core indication behind genetic set of rules is, all units should allocate the essential power load at lowest coal cost, though sustaining the coordination limitations. Simulation is executed on assessment system with six generators using Mat-lab. The results are shown for 24 h loads with optimal generation of 6 generators including transmission losses and cost of real power generation.

Keywords Economic load (power) dispatch (ELD) · Genetic (set of rules) algorithm (GA) · Equality–inequality limitations · Transmission line losses (PL)

K. Rajesh (✉)
Research Scholar, Department of EEE, JNTUACE, Ananthapuramu, Andhra Pradesh, India
e-mail: 2016rajesh75@gmail.com

N. Visali
Department of EEE, JNTUACEK, Kalikiri, Andhra Pradesh, India
e-mail: nvisali@gmail.com

N. Sreenivasulu
Department of EEE, SRIT, Ananthapuramu, Andhra Pradesh, India
e-mail: nsratp@gmail.com

© Springer Nature Singapore Pte Ltd. 2020

T. Hitendra Sarma et al. (eds.), *Emerging Trends in Electrical, Communications, and Information Technologies*, Lecture Notes in Electrical Engineering 569,
https://doi.org/10.1007/978-981-13-8942-9_33

1 Introduction

The scope of active power coordination is cumulative quickly to encounter the energy necessities. Huge (many) power stations are connected together to source the system burden by coordination of active plants. Through the expansion of coordination of systems it is compulsory to activate the active unit maximum carefully. The commercial group forecast difficult includes two distinct stages specifically the active unit commitment and the connected profitable dispatch. The active commitment is the excellent of units that resolve source the predicted load of the scheme finished a mandatory duration of period at lowest price as well as scores a specified boundary of the functioning reserve. Meaning of operational financial dispatch is to dispense the power between the producing components truly paralleled by the structure in such a way as it diminish the complete price of the coal [1]. With the growth of combined power system, it develops essential to function the plant units cautiously. A significant independent in the process of active power coordination is toward produce and supply energy to encounter the coordination power demand at lowest coal cost by a finest synthesis of several categories of plants. Thus ELD inhabits an important place in the electric power system. For any stated burden condition, ELD defines the power output for each plant (and each generation inside the plant) that will reduce the whole cost of fuel required to assist the system load taking in attention all practical limitations [2]. The features of up-to-date components are typically extremely nonlinear (rate limits, valve-point effect, etc.) and consuming numerous native lowest points in the price purpose. Their appearances are approached to happen the supplies of traditional sharing set of rules foremost to best answers and ensures in high income loss in the meantime. Deliberation of extremely nonlinear features of the components necessitates extremely vigorous set of rules to avoid receiving impacted at native optima [3].

Genetic algorithm (GA) method is effectively applied to ELD. GA method is founded on the philosophy of usual genetics and normal selection. A good benefit of GA is by stochastic rules in its place of deterministic procedures to hunt the disconnection. Therefore universal finest of the problem can be advanced with prospect high [4]. There are dissimilar methods to resolve the ELD difficulties, many of those are measured programming approaches and remaining are finest techniques. The best shared recycled procedures in preceding investigation are Perturb and Observation, Lambda technique, Gradient approach, interior point approach, penalty function approach and Newton approach. These approaches are flawless in the illustration when the coal price curve of the steam power group components is lined and monotonically growing. However, the coal price plot is not linear in run-through. Consequently, empirical best approaches are measured well for solving composite ELD difficulties [5]. GA has remained cast-off to explain tough complications with unprejudiced purposes which do not own possessions such as stability, differentiability. These set of rules uphold and deploy a combination of answers and instrument an existence of the best plan in examine for a healthier answer. GA is recycled to solve the economic dispatch difficult under certain equal and unequal

limitations. The fairness limitation reproduces active power equilibrium, and the unequal limitation reproduces the limit of active source generation [6, 7].

These methods take countless computational periods because of indecorous collection of the switch limitations. GA is the stochastic universal exploration and finest process that imitates ordinary organic growth such as range, limit and alteration. GA is fashionable with a usual of applicant answers called inhabitants (signified by chromosomes). At every group, couples of chromosomes of current population are designated to friend with individually additional to harvest the offspring for the subsequent group. The genes that are designated to system the novel offspring are designated conferring to their capability. In common, the genes with established suitability values have advanced prospect to replicate and endure to the following generation. Although the genes with inferior best values incline designate rejected. The procedure is recurrent till a conclusion disorder is stretched for instance extreme number of groups [8].

2 Problem Formulation

The concept of the ELD approach is to reduce the entire coal cost of steam run power units exposed to the working limitations of an active system. The price purpose of popular of source elements is a non-linear purpose and cannot be cracked by methodical approaches, so an iterative procedure is suggested using GA approach. Here, the objective purpose of steam run-through active units is defined as [1]

$$C_i = a_i * P_{Gi}^2 + b_i * P_{Gi} + d_i \tag{1}$$

where a_i is a variable representing losses in the scheme, b_i is the variable representing coal cost and d_i is the variable for income and earnings, interest and decrease. The finest scheduling for steam run through active plants ought to be considered forecasting over-all electric active generation equal to the load requirement and line real power losses, which can be written as:

$$\sum_{i=1}^{n} P_{Si} + P_L + P_T = 0 \tag{2}$$

n = entire number of producing plants, P_{Si} = real power source of i-th plant, P_T = total real power transmission loss, P_L = coordination burden. The real power transmission line losses will increases with the real power, relocated from the source station to the load centers rises. Usually, the line losses are reflected to analyze from 5 to 15% of the entire burden. If the control factor of burden at all buses is presumed to continue same the system power loss P_T can be exposed to be a purpose of active power source at each plants i.e.

$$P_T = P_T(P_{S1}, P_{S2}, \ldots P_{Sn}) \tag{3}$$

Unique of the greatest important and humble method on behalf of transmission active line loss is an estimated way as a purpose of source powers through B-Coefficients is given by Kron's formula

$$P_L = \sum_{i=1}^{n} \sum_{j=1}^{n} P_{Si}\, B_{ij}\, P_{Sj} \tag{4}$$

where P_{Si}, and P_{Sj} are variables for active power source at ith and j-th power unit. B_{ij} is the variable for loss constants. The inequality limitation is given by

$$P_{Si}^{max} \geq P_{Si} \geq P_{Si}^{min} \tag{5}$$

Maximum real power source P_{Si}^{Max}, Minimum real power source P_{Si}^{Min}.

3 Methodology

Genetic set of rules are unique of the finest habits to resolve a difficult for which tiny information is identified. They remain actual set of rules and so resolve work efficient in some search universe. That is to be recognized is wanted in the resolution to be clever to do fit, and a hereditary procedure will be able to produce a high excellence solution. Genetic procedures usage the codes of range and development to crop several explanations to an assumed statement. Genetic procedures incline to flourish in setting a very huge set of applicant explanations and where the search universe is irregular and has numerous peaks and valleys. Genetic procedures will do well in any location. They are unique of the utmost influential approaches to rapidly make good excellence explanations to a declaration. GA's function on sequence organizations. The sequence is two numbers expressive a coding of control variables for a given statement.

The each variable of the given statement is coded with sequences of bits. The individual bit is termed 'gene' and the satisfied of the each gene is termed 'allele'. The complete sequence of such genes of all variables written in a sequence is called a 'chromosome' so there exist a chromosome for each theme in the search space. In this methodology, a GA candidate solution is signified as a linear sequence equivalent to a biological chromosome. The overall scheme of GAs starts from inhabitants of arbitrarily generated candidate clarifications (chromosomes). Respective chromosome is then estimated and given a rate which resembles to a fitness level in objective purpose space. In every generation, chromosomes are elected based on their fitness to replicate offspring. Chromosomes with a great level of capability are more expected to be reserved while the ones with little fitness tend to be rejected. This procedure is called selection. After selection, offspring chromosomes are made from parent chro-

mosomes consuming operators that look like crossover and mutation appliances in evolutionary concept. The crossover mechanism, occasionally called recombination, yields new offspring chromosomes that receive evidence from both edges of parents by uniting partial sets of fundamentals from them. The mutation operator arbitrarily changes basics of a chromosome with a little probability. Over numerous generations, chromosomes with advanced fitness values are left founded on the existence of the rightest.

Search space: The universe for all likely feasible resolution is called search space. A usual of search points designated and used for dispensation is named population i.e., population is a conventional of chromosomes. The amount of chromosome in a population is named population scope and the amount of gene's in each sequence is called string length. The population is treated and estimated through various operatives of GA to produce a new population and this procedure is conceded out till universal optimum points are touched. The objective occupation is used to deliver a amount of how individuals have achieved in the problematic domain. In the situation of a minimization difficult, the suitable individual will have the lowest arithmetical value of the allied objective function. This raw amount of fitness is typically only used as middle stage in defining the relative performance of entities in a GA. Another function, the ability function is generally used to transform the objective function value into a degree of relative aptness, thus

$$F(x) = g(f(x)) \tag{6}$$

where 'f' is the objective function, 'g' convert the value of the objective role to a non-negative value and 'F' is subsequent relative aptness. In many circumstances, the amount of offspring's that a distinct can but to harvest in the next generation. It includes nothing more than exchange of genes and sequence cloning. This lets GA to yield good outcomes in conditions which are rigid to attain through many conservative methods. The additional attraction to such a procedure is that it is enormously vigorous with respect to the difficulty of the problem [9].

3.1 Genetic Set of Rules Operator

At every generation, GA customs three operators to generate the new population from the preceding population.

Selection or Reproduction: Selection operator is typically the major operator realistic on the population. The chromosomes are designated founded on the Darwin's growth theory of existence of the appropriate. The chromosomes are nominated from the population to yield offspring founded on their values. The chromosomes with advanced suitability values are more probable to causal offspring and are simply derivative on into the following population. The usually used imitation operator is the proportionate replica operator. The ith sequence in the population is designated

with a probability relative to *Fi* where, *Fi* is the suitability value for that sequence. The probability of selecting the ith sequence is:

$$\mathrm{P_i} = \mathrm{F_i} / \sum_{j=1}^{n} Fj \tag{7}$$

where n is the variable for population size, the usually used choice operator is the roulette-wheel choice method. Meanwhile the circumference of the wheel is noticeable according to the sequence fitness, the roulette-wheel apparatus is expected to make *Fi/Favg* duplicates of the ith sequence in the mating pool. The average aptness of the population is:

$$\mathrm{F_{avg}} = \sum_{i=1}^{n} Fi/\mathrm{n} \tag{8}$$

Crossover or Recombination: The elementary operator for creating new chromosomes in the GA is that of crossover. The crossover yield new chromosomes have specific parts of both parent chromosomes. The humblest form of crossover is that of solo point crossover. In distinct point crossover, two chromosomes sequences are designated arbitrarily from the mating pool. Following, the crossover site is nominated arbitrarily along the sequence length and the binary digits are exchanged between the two sequences at crossover place.

Mutation: The mutation is the operator in GA. It stops the premature discontinuing of the set of rules in a native solution. This operator arbitrarily flip-flops or changes one or more bits at arbitrarily selected locations in a chromosome from 0 to 1 or vice versa.

3.2 Variables of GA

The presentation of GA depends on superior of GA parameters such as:

Population Size (N): The population magnitude affects the competence and presentation of the set of rules. Higher population scope increases its variety and decreases the probabilities of early unite to a local finest, but the time for the population to unite to the finest regions in the search space will also growth. On the additional hand, minor population scope may consequence in a poor presentation from the set of rules. This is due to the procedure not casing the whole problem space. A decent population size is about 20–30, nevertheless sometimes sizes 50–100 are reported as best.

Crossover Rate: The crossover rate is the variable that move the rate at which the procedure of cross over is applied. This rate usually should be high, about 80–95%.

Mutation Rate: It is a subordinate search operator which rises the variety of the population. Low mutation rate helps to stop any bit position from getting trapped at a single value, while high mutation rate can result in fundamentally random search. This rate should be very little.

Termination of the GA: The generational procedure is repetitive until a finish condition has been pleased. The common dismissing conditions are: fixed number of generations touched, a best solution is not different after a set number of repetitions, or a cost that is inferior to an acceptable minimum [8].

3.3 Proposed Algorithm

(1) Accept data, namely cost coefficients a_i, b_i, d_i, length of sequence, no. of iterations, population magnitude, chance of crossover and mutations, power demand and $P^{\min}$ and $P^{\max}$.
(2) Generate the initial population arbitrarily in the binary method.
(3) Interpret the sequence, or obtain the decimal integer from the binary sequence using equation

$$y^j = \sum_{i=1}^{l} 2^{i-1} b_i^j \quad (j = 1, 2, \ldots L) \tag{9}$$

where b_i^j variable ith binary value of the jth string, l is the length of the sequence; L is the number of sequences or population extent.
(4) Compute the real power in MW produced from the interpreted population by using equation

$$P_i^j = P_i^{min} + \frac{P_i^{max} - P_i^{min}}{2^l - 1} y_i^j \quad (i = 1, 2, \ldots NG, \ j = 1, 2, \ldots L) \tag{10}$$

where L is the variable number of sequences or population size, y_i^j is the binary coded assessment of the ith substring.
(5) Check $\mathrm{P_i^j}$

$$\begin{aligned} &\text{if } \mathrm{P_i^j} > \mathrm{P_i^{max}}, \text{ then set } \mathrm{P_i^j} = \mathrm{P_i^{max}} \\ &\text{if } \mathrm{P_i^j} < \mathrm{P_i^{min}}, \text{ then set } \mathrm{P_i^j} = \mathrm{P_i^{min}} \end{aligned} \tag{11}$$

(6) Discover fitness

$$\begin{aligned} &\text{if } \mathrm{f_j} > \mathrm{f_{max,}} \text{ then set } \mathrm{f_{max}} = \mathrm{f_j} \\ &\text{if } \mathrm{f_j} < \mathrm{f_{min,}} \text{ then set } \mathrm{f_{min}} = \mathrm{f_j} \end{aligned} \tag{12}$$

(7) Determine the population with maximum aptness and average aptness of the population.
(8) Select the parents for crossover by means of stochastic residue roulette wheel collection method.
(9) Achieve single point crossover for the designated parents.
(10) Execute mutation.
(11) If the number of iterations spreads the maximum, then go to step 12. Else, go to step 2.
(12) The aptness that generates the smallest total generation cost is the solution of the problem.

4 Results and Analysis

To authenticate the effectiveness of the planned algorithm, a six unit thermal power generating plant was verified. The proposed set of rules has been executed in MATLAB. The proposed set of rules is analyzed and applied to 6 generating units and 3 generating units with generator constraints and transmission real power losses.

4.1 Test Case I

The fuel cost figures of the six steam operating real power generating units were given in Table 1. The real power load demand for 24 h is given in Table 2. Transmission loss or B-loss coefficients of six units system is given in Table 3. Tables 4 and 5 gives the best forecast of all generating units, real power loss and total fuel cost for 24 h by using GA approach. Figures 1 and 2 show the relation between power generations of all units, power loss, fuel cost of each unit and 24 h load by the GA approach. Certain variables must be allocated for the use of GA to resolve the ELD difficulties as follows, Population scope = 50, number of generations = 500, Crossover probability = 0.8, Mutation probability = 0.05.

Table 1 Steam operating plant cost data of 6 units

Unit	a_i (Rs/MW^2)	b_i(Rs/MW)	d_i (Rs)	P_{Gi}^{min} (MW)	P_{Gi}^{max} (MW)
1	0.0070	7	240	100	500
2	0.0095	10	200	50	200
3	0.0090	8.5	220	80	300
4	0.0090	11	200	50	150
5	0.0080	10.5	220	50	200
6	0.0075	12	190	50	120

Table 2 Real power load for 24 h of 6 units

Time (h)	P_D (MW)	Time (h)	P_D (MW)	Time (h)	P_D (MW)	Time (h)	P_D (MW)
1	955	7	989	13	1190	19	1159
2	942	8	1023	14	1251	20	1092
3	935	9	1126	15	1263	21	1023
4	930	10	1150	16	1250	22	984
5	935	11	1201	17	1221	23	975
6	963	12	1235	18	1202	24	960

Table 3 B-coefficients

0.0017	0.0012	0.0007	−0.0001	−0.0005	−0.0002
0.0012	0.0014	0.0009	0.0001	−0.0006	−0.0001
0.0007	0.0009	0.0031	0	−0.0001	−0.0006
−0.0001	0.0001	0	0.0024	−0.0006	−0.0008
−0.0005	−0.0006	−0.0001	−0.0006	0.0129	−0.0002
−0.0002	−0.0001	−0.0006	−0.0008	−0.0002	0.0015

Table 4 Optimal load scheduling of 6 steam operating units

Time (h)	P_{G1} (MW)	P_{G2} (MW)	P_{G3} (MW)	P_{G4} (MW)	P_{G5} (MW)	P_{G6} (MW)
1	399.143	130.527	202.78	74.387	117.67	51.547
2	399.303	130.115	196.08	79.910	106.82	50.028
3	391.925	124.724	211.77	72.512	104.11	50.071
4	399.529	121.697	203.81	71.555	102.62	50.501
5	391.925	124.724	211.77	72.512	104.11	50.071
6	403.739	132.021	198.45	83.386	116.16	50.574
7	405.234	132.480	220.40	82.030	121.43	50.222
8	419.461	140.977	223.77	86.130	127.02	50.047
9	443.783	149.648	249.31	108.82	142.78	61.823
10	450.826	159.963	246.50	111.28	151.99	60.974
11	459.639	169.325	254.72	121.22	157.14	73.657
12	466.367	180.129	256.77	125.44	163.98	79.186
13	451.904	166.465	258.22	121.22	158.67	67.702
14	468.164	195.510	263.15	124.70	156.70	80.522
15	473.030	178.791	270.07	131.73	161.12	86.983
16	466.642	179.202	265.20	133.02	162.23	81.655
17	465.551	171.676	263.37	124.80	155.18	76.322

(continued)

Table 4 (continued)

Time (h)	P_{G1} (MW)	P_{G2} (MW)	P_{G3} (MW)	P_{G4} (MW)	P_{G5} (MW)	P_{G6} (MW)
18	468.446	167.737	257.40	121.97	152.58	68.395
19	448.653	162.078	245.19	110.49	154.93	69.847
20	434.927	152.313	232.37	105.44	140.18	54.907
21	421.756	135.992	227.75	82.271	126.61	53.043
22	410.560	134.740	210.84	80.725	118.86	50.643
23	398.277	135.136	217.50	83.410	110.95	51.771
24	398.672	126.857	207.66	88.734	108.89	50.433

Table 5 Power loss and fuel cost of 6 generating units

Time (h)	P_L (MW)	Fuel cost (Rs)	Time (h)	P_L (MW)	Fuel cost (Rs)
1	21.0647	11523	13	34.1951	14696
2	20.2641	11354	14	37.7624	15558
3	20.1175	11262	15	38.7380	15727
4	19.7206	11198	16	37.9422	15541
5	20.1175	11262	17	35.9231	15131
6	21.3429	11628	18	34.5417	14864
7	22.8117	11966	19	32.2034	14264
8	24.4093	12416	20	28.1603	13344
9	30.1812	13809	21	24.4307	12417
10	31.5489	14139	22	22.3769	11901
11	34.7154	14849	23	22.0556	11783
12	36.8903	15328	24	21.2574	11587
Total cost (Rs/day)					3,178,547

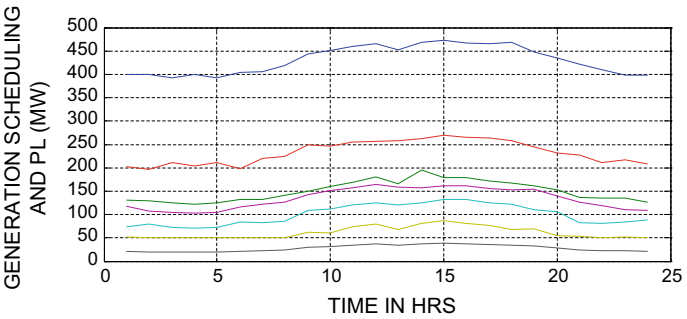

Fig. 1 Time in h versus generation scheduling and losses in MW

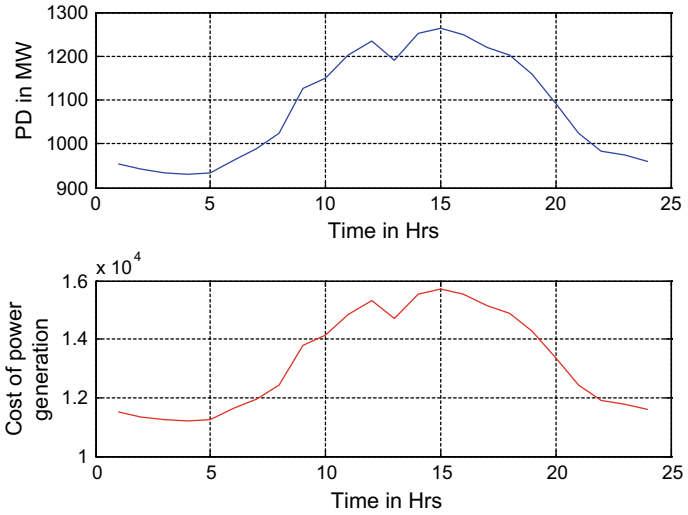

Fig. 2 Time (h) versus fuel cost (Rs/h) fitness value and load demand (MW)

4.2 Results for Test Case I

The values in Table 4 explains the optimal generation scheduling for different loads in 24 h. All generating units are within its constraints limits. The values in Table 5 shows power loss and cost of fuel for 24 h and the cost for generating real power for one day is shown.

The graphs is displayed for time in h in X axis and Real power generation of 6 thermal power plants, power loss, fuel cost in Y axis. Figure 1 shows time and real power generation along with real power loss. Figure 2 shows time and fuel cost along with load demand. Figure 3 shows graph of best fitness, Mean fitness with generation for load demand of 1201 MW. The number of variables and current best individual is shown in other graph.

4.3 Test Case II

The steam operating plant cost statistics of 3 producing units is shown in Table 6. The result for optimal load scheduling, power loss, cost of real power generation for load demand for 150 MW is shown in Table 7.

Figure 4 shows graph of best fitness, Mean fitness with generation for load demand of 150 MW. The number of variables and current best individual is shown in other graph.

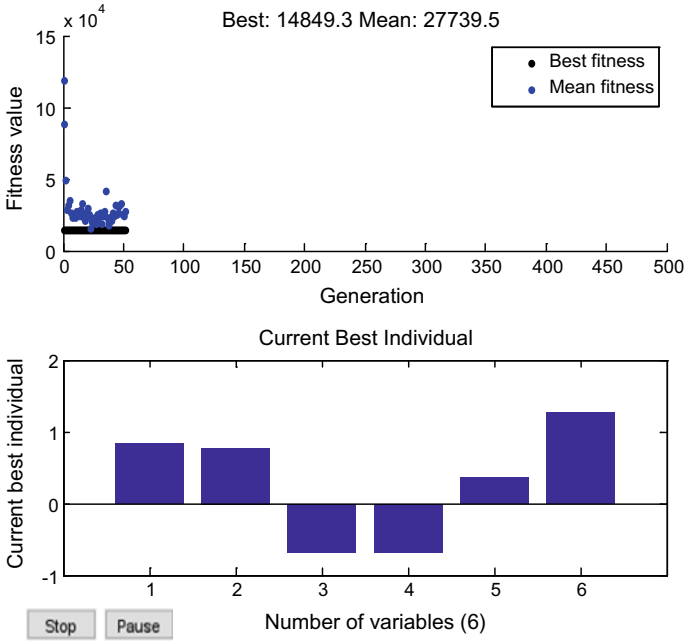

Fig. 3 Generation versus (Best and Mean)

Table 6 Data for cost coefficients

Unit	A_i (Rs/MW^2)	B_i (Rs/MW)	d_i (Rs)	P_{Gi}^{min} (MW)	P_{Gi}^{max} (MW)
1	0.008	7	200	10	85
2	0.009	6.3	180	10	80
3	0.007	6.8	140	10	70

Table 7 Optimal load scheduling for 150 (MW)

P_{G1} (MW)	P_{G2} (MW)	P_{G3} (MW)	P_L (MW)	Cost
33.2888	63.9447	55.432	2.665	1600

5 Conclusion

This approach gives Genetic set of rules (GA) used to explain the ELD statement. The planned set of rules has been executed for cracking the ELD statement of a power system contains of 6 units and 3 units. The total fuel cost obtained for optimal power scheduling of different loads by GA is shown. GA set of rules method offers high quality explanations with fast conjunction characteristic. The lambda repetition method is also appropriate, but it can unite to the least generation cost after so many

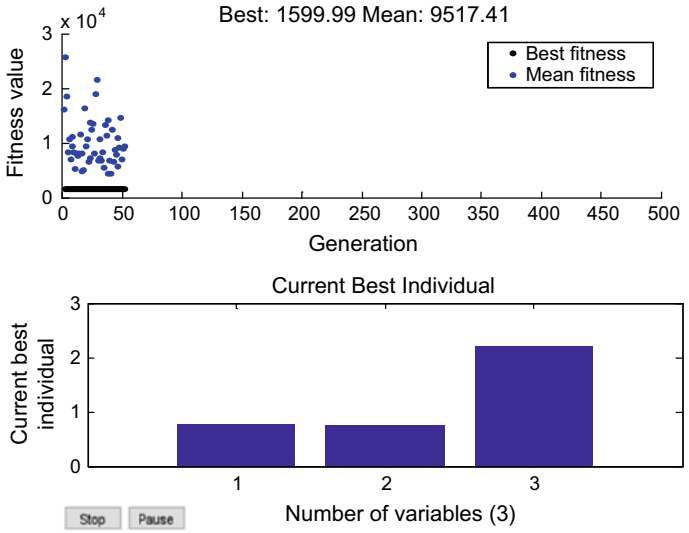

Fig. 4 Generation versus fitness value (Best and Mean)

repetitions. So, the computational time of the lambda repetition method is much better than the planned set of rules. It has been detected that genetic set of rules is capable of enhancing any kind of problems regardless of load demand. The results conferred above are attained after significant reduction in Fuel Cost of Generators and satisfies each and every limitation.

References

1. Visali N (2014) Real power scheduling of thermal power plants using evolution technique. J Electr Eng (JEE) 14:1–6
2. Singh SP, Tyagi R, Goel A (2014) Genetic algorithm for solving the economic load dispatch. IJEEE Publ **7**(5):523–528
3. Kaur A, Singh HP, Bhardwaj A (2014) Analysis of economic load dispatch using genetic algorithm. IJAIEM Publ 3(3):240–246
4. Sahu G, Swarnkar K (2014) Economic load dispatch by genetic algorithm in power system. IJSETR Publ 3(8):2167–2171
5. Khosa FK, Zia MF, Bhatti AA (2015) Genetic algorithm based optimization of economic load dispatch constrained by stochastic wind power, pp 36–40, Presented in ICOSST
6. Kumar V, Singh J, Singh Y, Sood S (2015) Optimal economic load dispatch using genetic algorithms. World Acad Sci Eng Technol 9(4):463–470
7. Ouiddir R, Rahli M, Abdelhakem-Korida L (2005) Economic dispatch using a genetic algorithm: application to Western Algeria electric power network. J Inf Sci Eng 21:659–668
8. Mansour W, Salama MM, Abdelmaksoud SM, Henry HA (2013) Dynamic economic load dispatch of thermal power system using genetic algorithm. Int J Eng Sci Technol 3(2):345–352
9. Garg J, Khatri P, Ahmad A (2011) Economic load dispatch using genetic algorithm. Int J Adv Res Comput Sci 2(3):451–454

A Novel Approach of Non-dominated Sorting TLBO for Multi Objective Short-Term Generation Scheduling of Hydrothermal-Wind Integrated System

Baburao Pasupulati, R. Ashok Kumar and K. Asokan

Abstract Generally, wind energy resources have characteristics of randomness and uncontrollability, which leads to uncertainty, intermittency and volatility of its outputs Therefore, great challenges in coordinating it with a large hydrothermal system. In this article, solves multi-objective short-term hydrothermal scheduling (MOSTHTS) problem integrated wind power generation using an effective and specific parameter less algorithm of Non-dominated Sorting Teaching Learning Based Optimization (NSTLBO) algorithm. The problem has been modelled in the form of multi-objective functions which includes fuel cost of thermal and wind generators, transmission loss and environmental emissions such as NO_x, SO_x and CO_x with various constraints of hydrothermal and wind systems. The interaction of the present NSTLBO algorithm is to decrease the operating cost of thermal and wind generators, transmission losses and different kinds of emissions. By applying this algorithm a set of non-dominated solutions are created. A fuzzy decision making approach has been involved on these solution in order to identify the best comprise solution among the group of solutions. The practicability of the proposed approach has been demonstrated on a sample test system which consists of four hydro, four thermal and two wind units. The experimental finding of this method has been compared with that of well established techniques in order to validate the performance of the test results.

Keywords Hydrothermal-wind system · Different emission · Fuel cost · Transmission loss · NSTLBO algorithm

1 Introduction

Wind power generation has effectively decreasing our dependence on fossil fuels. As one of the clean and renewable energy sources, wind power has gained wide attention due to its advantage with low operation cost and zero emission. The optimal

B. Pasupulati (✉) · R. A. Kumar · K. Asokan
Department of Electrical Engineering, Annamalai University, Annamalai Nagar 608002, Tamil Nadu, India
e-mail: pasupulatibaburao@gmail.com

© Springer Nature Singapore Pte Ltd. 2020

T. Hitendra Sarma et al. (eds.), *Emerging Trends in Electrical, Communications, and Information Technologies*, Lecture Notes in Electrical Engineering 569,
https://doi.org/10.1007/978-981-13-8942-9_34

generation scheduling of wind integrated hydrothermal plants are considered to be the interesting subject and perceives much observation in the arena of power engineering. Short-term wind integrated hydrothermal scheduling is a subject which effectively optimizes the generation scheduling of hydro, thermal and wind plants to meet the load demand. The optimization process has to be well modelled in such a way that it should minimize the total operational cost with the consideration of system operational costs of thermal and wind plants but hydro plants are not match with each other [1–3].

In a wind integrated hydrothermal system, the thermal units happened to be the sources for CO_x, SO_x, NO_x which causes environmental pollutions [4]. Hence emission must also be considered while deriving the solution for the optimal operation of hydrothermal-wind system. When the emission products are included in the objective function, STHTS problem will become as multi-objective short-term hydrothermal scheduling problem (MOSTHTS). The MOSTHTS problem are difficult to solve, because of varying production cost, transmission losses, load forecasting error, and in accuracies present in the information received from different sources [5]. Therefore it is inevitable to explore the possibility of newer technique for the solution of STHTS problem.

The significance of generation scheduling in hydrothermal with wind integrated system is rightly accepted. Hence variety of classical methods has been proposed to solve the STHTS problem. The methods are lambda-gamma iteration method (LGM) [6], an effective conventional method (ECM) based on multiplier theory [7], dynamic programming (DP) [8], Lagrange relaxation (LR) method [9], decomposition and coordination method [10], non-linear programming method (NLP) [11], progressive optimality algorithm [12], fuzzy decision making (FDM) approach [13, 14]. Among these methods Lagrangian multiplier theory based method does not give optimal solution and it has to be applied with optimization technique [15]. Even though, DP and LR methods are popular in solving these kind of problem, the computational and dimensionality of the DP method increases rapidly for large scale system, which is not preferable one. Normally, these classical methods may not work skilfully in evolving solution for STHTS problems [16].

Apart from above methods, hydrothermal problem have been assessed by intelligent computational algorithms which produces non-dominated solution [17–21]. It includes real coded genetic algorithm [17], integrated predator-prey optimization and Powell search method [18], particle swarm optimisation [19], artificial bee colony algorithm [20], differential evolution [21]. These approaches always uses the weighing parameter in this respective objective function and could not able to establish a true pareto optimal front.

In addition all, other techniques such as non-dominated sorting genetic algorithm-II [22, 23], strength Pareto evolutionary algorithm [24], Multi-objective particle swarm optimisation [25], multi-objective differential evolution [26], Non-Dominated Sorting Disruption Based Gravitational Search Algorithm [27], ant lion optimization technique [28], MO fuzzy optimization model [29] and Lexicographic optimization

technique [30] have been developed to overcome the hurdles of weighing parameter and to make a trade-off between the conflicting objectives. The methodological revolution in the energy market imposes the need for renewed formulation. From the literature reviews, it is understand that the applicability of NSTLBO has not yet been tested for the solution of MOSTHTS problem.

In this paper, a NSTLBO algorithm has been proposed to solve multi-objective STHTS problem considering wind generation. The algorithm does not depend upon any of the tuning parameters, which is common in other algorithms. The approach effectively allocates the expected total power generation among hydrothermal and wind plants so as to minimise the expected production cost, NO_x emission, SO_x emission, CO_x emission and losses of thermal plants Numerical example with four hydro and six thermal and two wind units are considered to illustrate the performance of the NSTLBO approach and the simulation results are compared with other available methods.

2 Problem Formulation

2.1 Multi-objective Functions

The emission constrained STHTS problem with wind power generation is modelled as a multi-objective optimization problem to perform the optimal power dispatch of hydrothermal and wind plants. It is planned to minimize the five of the components mentioned in the objective functions.

$$\min\{F_1, F_2, F_3, F_4, F_5\}$$

Subject to operating constraints of hydrothermal and wind system.

The objective functions, like are fuel cost with valve-point loading effect, different emissions such as NO_x, SO_x, CO_x, wind power and power losses. The optimization is done with equality and inequality constraints of hydrothermal plants. The valve-point loading effect is defined by assigning a sinusoidal term in the quadratic cost function and are mathematically presented as,

$$f_{it}(P_{sit}) = \left\{a_{si} + b_{si}P_{sit} + c_{si}P_{sit}^2 + \left|d_{si} \times \mathrm{Sin}\left[e_{si} \times \left(P_{si}^{min} - P_{sit}\right)\right]\right|\right\} \quad (1)$$

From Eq. (2), the fuel cost function of the thermal units and wind units is found to be non-smooth function of generated powers. The objective is minimising the total fuel cost of all thermal plants, wind generators and is given by

$$F_1 = \sum_{t=1}^{T}\left\{\sum_{i=1}^{N_s}[f_{it}(P_{sit})] + \sum_{k=1}^{N_w}[f_{wkt}(P_{wkt})]\right\} \tag{2}$$

Based on above, the WP cost of kth wind turbine at tth time can be computed as [30]:

$$f_{wkt}(P_{wkt}) = \left\{(K_k \times P_{wkt}) + C_{pkt}\left(W_{kt,av} - P_{wkt}\right) + C_{rkt}\left(P_{wkt} - W_{kt,av}\right)\right\} \tag{3}$$

The under estimation penalty will be proportional to the unutilized WP whereas the reserve cost will depend on the WP deficit. The penalty and reserve costs can be expressed as [30]:

$$\begin{aligned} C_{pkt}\left(W_{kt,av} - P_{wkt}\right) &= k_p \times \left(W_{kt,av} - P_{wkt}\right) \\ &= k_p \times \int_{P_{wkt}}^{W_T} (W - P_{wkt}) f_W(W) dw \end{aligned} \tag{4}$$

$$\begin{aligned} C_{rkt}\left(P_{wkt} - W_{kt,av}\right) &= k_r \times \left(P_{wkt} - W_{kt,av}\right) \\ &= k_r \times \int_{0}^{P_{wkt}} (P_{wkt} - W) f_W(W) dw \end{aligned} \tag{5}$$

$$f_w(W) = \frac{khv_{in}}{P_{wR^c}}\left[\frac{(1 + hw/P_{wR})v_{in}}{c}\right]^{k-1} \times \exp\left\{-\left[\frac{(1 + hw/P_{wR})v_{in}}{c}\right]^{k}\right\} \tag{6}$$

The WP characterization is done using Weibul pdf, $f_w(W)$. Here $h = (vr/v_{in}) - 1$. Further details can be found in Refs. [26, 30].

The NO_x,SO_x, and CO_x are declared as functions and are included in the following quadratic equation.

$$F_2 = \sum_{t=1}^{T}\left\{\sum_{i=1}^{N_s}\left[\propto_{ni} P_{sit}^2 + \beta_{ni} P_{sit} + \gamma_{ni}\right]\right\} (\text{Kg/h}) \tag{7}$$

$$F_3 = \sum_{t=1}^{T}\left\{\sum_{i=1}^{N_s}\left[\propto_{si} P_{sit}^2 + \beta_{si} P_{sit} + \gamma_{si}\right]\right\} (\text{Kg/h}) \tag{8}$$

$$F_4 = \sum_{t=1}^{T}\left\{\sum_{i=1}^{N_s}\left[\propto_{ci} P_{sit}^2 + \beta_{ci} P_{sit} + \gamma_{ci}\right]\right\} (\text{Kg/h}) \tag{9}$$

If the total number of units is $N_T = N_S + N_H + N_W$ and P_{it} represents the respective thermal, hydro and WP generation, and then the total transmission loss P_{Lt} at *t*th interval can be calculated using B-loss coefficient as [10].

$$F_5 = P_{Lt} = \sum_{i=1}^{T} \sum_{j=1}^{N_T} P_{it} B_{ij} P_{jt} + \sum_{i=1}^{N_T} B_{0i} P_{it} + B_{00} \tag{10}$$

2.2 System and Constraints of Hydrothermal-Wind System

Power balance constraint

$$\sum_{i=1}^{N_S} P_{sit} + \sum_{j=1}^{N_H} P_{Hit} + \sum_{k=1}^{N_w} P_{wkt} = P_{Dt} + P_{Lt} \tag{11}$$

The generation output *j*th hydro plant can be defined in terms of coefficients of hydro power as mentioned below. The storage volume of the jth reservoir is V_{Hjt} and water discharge rate is Q_{Hjt}.

$$P_{Hjt} = C_{1j} \times V_{Hjt}^2 + C_{2j} \times Q_{Hjt}^2 + C_{3j} \times V_{Hjt} \times Q_{Hjt} + C_{4j} \times V_{Hjt} + C_{5j} \times Q_{Hjt} + C_{6j} \tag{12}$$

Operating limits of hydro and thermal generating units

$$P_{si}^{min} \le P_{sit} \le P_{si}^{max} \tag{12}$$

$$P_{Hj}^{min} \le P_{Hjt} \le P_{Hj}^{max} \tag{13}$$

$$P_{wk}^{min} \le P_{wkt} \le P_{wk}^{max} \tag{14}$$

Time period coupling constraints of thermal units

$$P_{sit} - P_{si(t-1)} \le UR_i \tag{15}$$

$$P_{si(t-1)} - P_{sit} \le DR_i \tag{16}$$

Dynamic water balance equality constraints

$$V_{Hjt} = V_{Hj,t-1} + I_{Hjt} - Q_{Hjt} - S_{Hjt} + \sum_{m=1}^{R_{uj}} \left(Q_{Hm,t-\tau_{mj}} + S_{Hm,t-\tau_{mj}} \right) \tag{17}$$

In tth time, the usual inflow from river to storage reservoir is I_{Hjt} and spillage discharge outflow of the jth hydro plant is noted by S_{Hjt}.

Reservoir storage volume limit

$$V_{Hj}^{min} \leq V_{Hjt} \leq V_{Hj}^{max} \tag{18}$$

Water discharge rate limit

$$Q_{Hj}^{min} \leq Q_{Hjt} \leq Q_{Hj}^{max} \tag{19}$$

3 Solution Methodology

3.1 Overview of TLBO Algorithm

A unique optimization technique namely Teaching-Learning-Based Optimization algorithm (TLBO), which has been recently introduced in the references [15–25]. It works around the philosophy of the effect of a teacher on the result of learners in the school and consequently learning by interaction between class members, which helps to improve their grades. The method works on the principle of the process of teaching and learning.

The heuristic technique outplays the classical mathematical methods, but its quality of the observation is more sensitive to the algorithmic parameters like population size and iterations. The main drawbacks of these kind of algorithm are the existence of different parameter that has to be neatly tuned to attain the expected performance. Presently, Teaching Learning Based Optimization (TLBO) algorithm has been introduced. It is a process based algorithm that operates on the effect of guidance of a teacher on the result of learners in a class. It is a dominant evolutionary algorithm that involves a population of students, where each and every student has been recognised as a potential solution to an optimization problem. The searching process includes initialization of a class, teacher phase, learner phase and terminating point. The TLBO algorithm is simple and easy to implement in power system optimization problems. TLBO is a specific, parameter less algorithm and does not require the tuning of any algorithmic parameters. It has the capacity of finding the global optimal solution for non-convex, non-linear problems with less computational effort and high reliability.

3.2 Non-dominated Sorting TLBO Algorithm

This algorithm presents an exceptional methodology for producing the pareto optimal solutions for the multi-objective optimization problems namely (NSTLBO). The NSTLBO algorithm is a refurbished version of the TLBO algorithm [12]. The NSTLBO algorithm is an exclusive method for analysing multi-objective optimization problem and preserves the assorted set of solution. It is very similar to a TLBO algorithm with teacher phase and a learner phase. On the other way with a view to manage the multiple objective effectively and efficiently. The NSTLBO algorithm is equipped with non-dominated sorting approach and crowding distance computation mechanism [15]. The teacher phase and learner phase confirms a better exploitation of the search space while non-dominated sorting approach assures that the selection process in the search space is consistently moves on the way of best solution and the population is rushed towards the pareto front in each iteration process. The crowding distance assignment terminology ensures the choice of a teacher from the wide region of the search space. Hence the probability of premature convergence of the algorithm at local optima is averted.

In the NSTLBO algorithm, the updating of learners is done based on the teacher phase and learner phase of the TLBO algorithm. It is a simple matter in deciding the best solution in case of single objective optimization problem. But in multiple conflicting objectives, identifying the best solution from the set of solution is not easy job. In this algorithm, the process of finding the best solution is done by comparing the rank of which is assigned to the solution based on the non-dominated idea and the crowding distance value.

Initialization

The algorithm is initialized by a matrix of N rows and D columns with some arbitrarily generated values in the search space. In this case, the value of N indicates the population size of the 'class'. The value D gives the total number of subjects offered which is equal to the dimensionality of the problem considered. The algorithm is framed to run for 'g' number of iterations. The following equation is used to assign the values of *j*th parameter of the *i*th vector in the initial stage of iteration.

$$x^{1}_{(i,j)} = x^{\min}_{j} + \text{rand}_{(i,j)} \times \left(x^{\max}_{j} - x^{\min}_{j} \right) \tag{20}$$

where $\text{rand}_{(i,j)}$ denotes a uniformly distributed random variable within the limit (0,1). The components of the *i*th vector for the generation 'g' is shown by

$$X^{g}_{i} = x^{g}_{(i,1)}, x^{g}_{(i,2)}, \ldots, x^{g}_{(i,j)}, \ldots, x^{g}_{(i,D)} \tag{21}$$

The column vector is formed by the objective values at a particular generation. Two objective functions occupy the similar row vector in this kind of bi-objective problem. The bi-objective (a and b) can be formulated as

$$\begin{bmatrix} \frac{Y_{a_i^g}}{Y_{b_i^g}} \end{bmatrix} = \begin{bmatrix} fa\left(X_{(i)}^g\right) \\ fb\left(X_{(i)}^g\right) \end{bmatrix} \tag{22}$$

where i = 1,2,…,N; j = 1,2,…,D; g = 1,2,…,G.

Teacher phase

The mean vector which consists of the mean learners in the class for each subject is calculated. So the mean vector μ is shown as

$$M^g = \begin{bmatrix} \text{mean}([x_{(1,1)}^g, \ldots, x_{(i,1)}^g, \ldots, x_{(N,1)}^g \\ \text{mean}([x_{(1,j)}^g, \ldots, x_{(i,j)}^g, \ldots, x_{(N,j)}^g \\ \text{mean}([x_{(1,D)}^g, \ldots, x_{(i,D)}^g, \ldots, x_{(N,D)}^g \end{bmatrix}^T \tag{23}$$

Then

$$M^g = m_1^g, m_2^g, \ldots, m_j^g, \ldots, m_D^g \tag{24}$$

The best vector with less objective function value is considered as the teacher for this iteration.

The algorithm progress is well by moving the mean of the learners in the direction of the teacher. The current mean and competent mean vector are added to the present population of learners in order to form a advanced set of improved learners.

$$Xnew_{(i)}^g = X_{(i)}^g + rand^g \times \left(X_{Teacher}^g - T_F M^g\right) \tag{25}$$

Hence T_F is the teaching factor in the process of iteration which may be either 1 or 2.

The more skilful learners in the matrix X_{new} displace the sub standard learners in matrix S using the non-dominated sorting algorithm.

Learner phase

This phase is dedicated to interaction of learners among themselves. The practice of mutual interaction results in the improvement of the expertise of the learner. Each learner collaborates randomly with other learners and hence expedites the sharing of

knowledge. A particular learner ($X^{g}_{(i)}$), and the other learner ($X^{g}_{(r)}$) has been randomly chosen ($i \neq r$). Finally the ith vector of the matrix X_{new} in the learner phase seems

$$\text{Xnew}^{g}_{(i)} = \begin{Bmatrix} X^{g}_{(i)} + \text{rand}^{g}_{(i)} \times \left(X^{g}_{(i)} - X^{g}_{(r)}\right) \text{if}(Y^{g}_{i} < Y^{g}_{r}) \\ X^{g}_{(i)} + \text{rand}^{g}_{(i)} \times \left(X^{g}_{(r)} - X^{g}_{(i)}\right) \text{otherwise} \end{Bmatrix} \tag{26}$$

In multi-objective optimization problem, there is a possibility of multiple X_{new} matrices in the learner phase. So in case of a bi-objective problem the performance of learner phase may have formulation as

$$\text{Xnew}^{g}_{(i)} = \begin{Bmatrix} X^{g}_{(i)} + \text{rand}^{g}_{(i)} \times \left(X^{g}_{(i)} - X^{g}_{(r)}\right) \text{if}(Ya^{g}_{i} < Ya^{g}_{r}) \\ X^{g}_{(i)} + \text{rand}^{g}_{(i)} \times \left(X^{g}_{(r)} - X^{g}_{(i)}\right) \text{otherwise} \end{Bmatrix} \tag{27}$$

$$\text{Xnew}^{g}_{(i)} = \begin{Bmatrix} X^{g}_{(i)} + \text{rand}^{g}_{(i)} \times \left(X^{g}_{(i)} - X^{g}_{(r)}\right) \text{if}(Yb^{g}_{i} < Yb^{g}_{r}) \\ X^{g}_{(i)} + \text{rand}^{g}_{(i)} \times \left(X^{g}_{(r)} - X^{g}_{(i)}\right) \text{otherwise} \end{Bmatrix} \tag{28}$$

Finally, the X matrix and the X_{new} matrices are processed together in the NSTLBO, which gives the 'N' best learners for the ensuring iteration. The algorithm will be terminated after 'G' number of iteration is over Fig. 1.

3.3 *Fuzzy Membership Function*

The prime objective of the system engineer is to carry out the conflicting parameters by satisfying the constraints of the system. In most of the cases the results, constraints and outcomes of the suggested mechanism are not derived precisely. Much of this

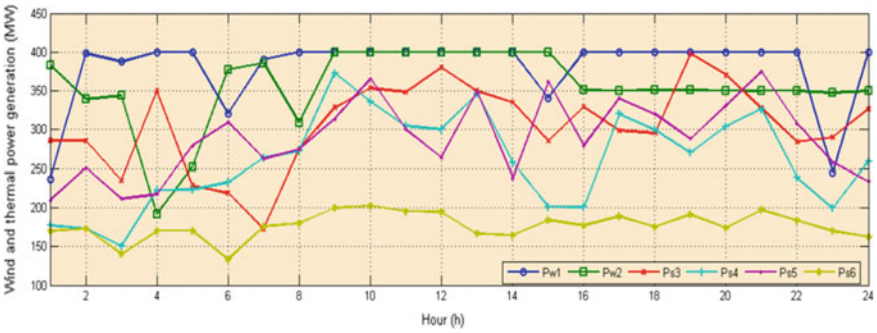

Fig. 1 Hourly power generation of wind and thermal units

error is not accessible. It may be due to vague, erroneous or fuzzy information. By looking on the imperfect manner of the decision maker's behaviour, it is understood that the decision maker may substitute fuzzy or erroneous goals for each objective function. The fuzzy sets are governed by equations called membership function. These functions are assigned by the values ranging from 0 to 1. By considering the minimum and maximum standards of objective function combined with rate of change of membership function, the decision maker must identify the membership function $\mu(j_i)$ in a constructive manner.

It is considered that $\mu(j_g)$ happened to be a linear decreasing and continuous function and is formulated as

$$\mu(j_g) = \begin{cases} 1 & j_g \le j_g^{\min} \\ \frac{j_g^{\max} - j_g}{j_g^{\max} - j_g^{\min}} & j_g^{\min} \le j_g \le j_g^{\max} \ (g = 1, 2, \ldots, Nob) \\ 0 & j_g \le j_g^{\max} \end{cases} \tag{29}$$

where $j_g^{\min}$ and $j_g^{\max}$ are the minimum and maximum values of objective function where in the solution is to be landed.
N_{ob} denotes the number of objective function in the problem.

Normalized membership values μ^k for each non-dominated solution is calculated by the following equation.

$$\mu^k = \frac{\sum_{i=1}^{Nobj} \mu_i^k}{\sum_{k=1}^{M_{nds}} \sum_{i=1}^{Nobj} \mu_i^k} \tag{30}$$

where, M_{nds} is the number of non-dominated solutions. Choose the best comprise solution that is having the greatest value of μ^k.

4 Numerical Results

The proposed NSTLBO algorithm is applied on a typical IEEE test system in order to estimate its performance in solving the Multi-objective short-term hydrothermal-wind scheduling problem with valve-point loading effect. The numerical results were used to assess the performance of the proposed methods with that of the similar algorithms. The prescribed algorithm has been experimented in MATLAB 14.0 platform on I3 processor, 2.40 GHz and 4 GB RAM system. The solution has been evolved in terms of individual plants of hydro, wind and thermal power generation by considering valve-point loading effect.

This section, explains the numerical test system and simulation results of various emission constrained STHTWS problem. A test system consists of a multi-chain cascade of four hydro units, two wind generators and four thermal units. The described scheduling period is chosen as one day with 24 intervals of 1 h each. The system data of load demand, hydro unit coefficients, reservoir inflows and reservoir limits considered from the reference [30]. The thermal cost coefficients, different emission coefficients of NOx, SOx and COx are also adopted from the same literature.

The resulting of integrated Hydrothermal-wind system is quite complex as a result of additional constraints appearing due to unpredictable nature of wind speed. The wind profile is modelled using Weibull probability density function as explained in Sect. 2.1. The Weibull shape and scale parameters are taken as 1.5 and 15 respectively, kp and kr both as 5, Pwr is 400 MW, the cut in, rated and cut out wind speeds are set at 5, 15 and 45 m per second respectively [30]. A simulation has been performed on the test system in order to demonstrate the performance of the proposed algorithm.

The optimal values of control parameters of proposed method were entertained by parameter setting through trial and error method for the present test system. The proposed algorithm has only two control parameter like population size and the maximum number of iteration. The best value of these two parameters is 50 and 250 respectively. These parameter settings are helpful in arriving the global optimal solutions.

The proposed NSTLBO efficiently optimises the system variables like water discharge, water storage volume, thermal power, wind power and transmission loss for the purpose of minimum fuel cost, limited emissions and less power loss. A fuzzy decision making approach has been involved on these solution in order to identify the best comprise solution among the group of solutions. The best optimized hydro water discharge rate and hydro power generation of the proposed test system are given in Table 1.

The simulation results of proposed test system is reported in Table 2, it includes tuned power despatches of two wind four thermal units, Total fuel cost, Total emission NO_x, Total emission SO_x, Total emission CO_x, and Total power loss The graphical representation of each wind and thermal power generation is displayed in Fig. 1 and total hydro, wind; thermal, power loss and system load demand are displayed in Fig. 2. Finally, the simulation results are compared with existing literature such as ALO, DE and ABC and displayed in Table 3. From the compression the proposed NSTLBO offer the best compromised solutions.

Table 1 Water discharge and hydro power generation of wind integrated hydrothermal system

Hour (h)	Hourly water discharge ($\times 10^4$ m^3)				Hourly hydro power generation (MW)				Total hydro power (MW)
	Q_1	Q_2	Q_3	Q_4	H_1	H_2	H_3	H_4	
1	6.9000	6.3000	10.8000	21.8000	66.2000	46.7000	53.1000	241.8000	407.8000
2	8.3000	5.0000	8.1000	7.1000	76.3000	38.5000	47.6000	107.0000	269.4000
3	12.5000	9.5000	7.5000	14.7000	94.3000	68.7000	47.4000	180.0000	391.1000
4	20.2000	5.0000	5.0000	5.0000	85.2000	40.1000	38.1000	74.4000	237.8000
5	5.6000	7.5000	5.7000	16.2000	52.2000	60.0000	42.7000	181.6000	336.4000
6	11.1000	9.4000	5.0000	9.9000	81.7000	71.0000	39.9000	124.8000	317.4000
7	9.0000	21.7000	11.2000	5.8000	72.7000	86.1000	61.9000	78.4000	299.1000
8	12.7000	6.1000	14.2000	7.5000	84.8000	39.0000	64.7000	99.4000	287.9000
9	6.4000	5.0000	5.6000	7.2000	57.2000	31.8000	41.7000	94.6000	225.4000
10	5.4000	9.9000	14.8000	6.2000	51.3000	63.6000	65.3000	82.1000	262.3000
11	8.5000	9.7000	5.0000	8.5000	74.1000	61.8000	36.6000	108.6000	281.2000
12	9.3000	5.5000	10.1000	20.2000	80.1000	36.7000	58.6000	194.6000	370.0000
13	5.0000	7.9000	6.8000	5.0000	50.9000	53.7000	46.2000	67.8000	218.7000
14	15.3000	7.3000	10.6000	29.4000	98.2000	50.3000	60.1000	196.4000	405.0000
15	9.3000	10.4000	13.7000	12.2000	81.3000	67.6000	64.9000	143.4000	357.2000
16	12.8000	14.1000	6.0000	9.3000	94.5000	78.5000	42.3000	117.5000	332.8000
17	10.1000	6.6000	5.0000	5.0000	84.7000	41.4000	36.7000	68.6000	231.4000
18	12.5000	16.3000	9.9000	5.0000	92.0000	76.8000	58.0000	70.7000	297.5000
19	10.1000	10.8000	12.2000	10.1000	82.0000	61.3000	63.2000	135.3000	341.8000
20	17.3000	18.9000	5.0000	114.0000	88.5000	73.4000	36.6000	151.8000	350.3000

(continued)

Table 1 (continued)

Hour (h)	Hourly water discharge ($\times 10^4$ m^3)				Hourly hydro power generation (MW)				Total hydro power (MW)
	Q_1	Q_2	Q_3	Q_4	H_1	H_2	H_3	H_4	
21	17.6000	5.0000	5.0000	8.4000	83.3000	28.5000	36.6000	115.3000	263.8000
22	9.7000	5.0000	7.2000	23.3000	75.8000	30.0000	48.0000	202.9000	356.7000
23	6.6000	6.4000	10.6000	17.5000	58.4000	41.7000	60.1000	179.0000	339.3000
24	16.1000	10.4000	5.0000	5.0000	87.6000	65.8000	36.6000	67.8000	257.8000

Table 2 Simulation results of wind integrated hydrothermal system

Hour (h)	W_1	W_2	T_3	T_4	T_5	T_6	Thermal power generation	Wind power generation (MW)	Power loss with wind
1	236.5429	383.1118	350.0000	177.0000	309.1000	170.0000	842.5453	619.6547	72.93
2	398.1619	339.1192	355.9000	252.9000	355.9000	173.3000	883.3189	737.2811	73.71
3	387.4089	344.1592	350.0000	180.4000	311.2000	170.0000	737.3319	731.5681	72.54
4	400.0000	191.9899	350.0000	222.8000	337.3000	170.0000	960.2101	591.9899	69.81
5	400.0000	251.9808	350.0000	223.5000	337.7000	170.0000	901.6192	651.9808	73.71
6	320.2691	377.5937	350.0000	242.8000	349.7000	171.0000	894.7372	697.8628	74.49
7	390.8514	385.7274	362.5000	263.7000	362.5000	175.7000	874.3212	776.5788	76.05
8	400.0000	309.2526	374.8000	283.6000	374.8000	180.2000	1002.847	709.2526	78
9	400.0000	400.0000	428.6000	370.9000	428.6000	199.9000	1214.6	800.0000	87.36
10	400.0000	400.0000	436.2000	383.3000	436.2000	202.7000	1257.7	800.0000	90.48
11	400.0000	400.0000	416.9000	351.9000	416.9000	195.6000	1148.8	800.0000	86.97
12	400.0000	400.0000	415.3000	349.4000	415.3000	195.0000	1140	800.0000	90.09
13	400.0000	400.0000	428.0000	369.9000	428.0000	199.7000	1211.3	800.0000	86.97
14	400.0000	400.0000	389.5000	307.6000	389.5000	185.6000	995	800.0000	85.8
15	340.5478	400.0000	385.6000	301.1000	385.6000	184.1000	1032.252	740.5478	83.07
16	400.0000	350.7226	379.3000	290.9000	379.3000	181.8000	986.4774	750.7226	80.73
17	400.0000	350.2691	407.9000	337.4000	407.9000	192.3000	1148.331	750.2691	83.07
18	400.0000	350.8514	398.0000	321.2000	398.0000	188.7000	1091.649	750.8514	83.46
19	400.0000	350.7664	407.9000	337.3000	407.9000	192.3000	1147.434	750.7664	87.36
20	400.0000	350.1586	413.5000	346.4000	413.5000	194.3000	1179.541	750.1586	88.92
21	400.0000	350.0000	421.8000	359.8000	421.8000	197.4000	1226.2	750.0000	87.36

(continued)

Table 2 (continued)

Hour (h)	W_1	W_2	T_3	T_4	T_5	T_6	Thermal power generation	Wind power generation (MW)	Power loss with wind
22	400.0000	350.0000	383.9000	298.4000	383.9000	183.5000	1013.3	750.0000	82.68
23	245.2096	347.6763	350.0000	201.7000	324.3000	170.0000	917.8141	592.8859	72.15
24	400.0000	350.0000	378.4000	289.4000	378.4000	181.5000	982.2	750.0000	77.61

Total fuel cost ($)—412,440.00
Total emission NO_x(Kg)—47,925.000
Total emission SO_x (Kg)—485,680.00
Total emission CO_x (Kg)—1204,500.0
Total power loss (MW)—2034.0876

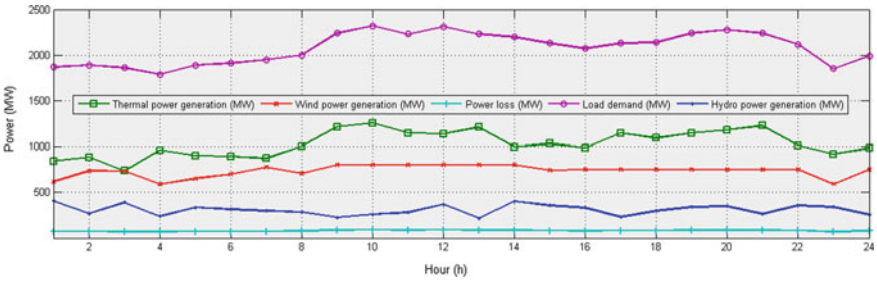

Fig. 2 Total power generation of thermal, wind, hydro units, power loss and load demand

Table 3 Comparison of fuel cost, various emissions and power loss by proposed with existing method

Methods	Fuel cost (S)	NO_X emission (kg)	SO_X emission (kg)	CO_X emission (kg)	Power loss emission (MW)
NSTLBO	**412,440.00**	**47,925.000**	**485,680.00**	**1204,500.000**	**2034.0876**
ALO	417899.4444	52661.5986	322093.5748	1352441.9211	2036.0672
DE	419566.1611	52753.8837	320631.0452	1349639.4655	2036.3876
ABC	419949.1163	52737.0713	320932.5688	1348715.9193	2036.3442

5 Conclusion

In this research work, proposes a intelligent computing tool using a NSTLBO algorithm to solve a multi-objective environmental emission constrained STHTS optimization problem considering wind power generation. An idea of multi-objective functions of fuel cost, power loss and different environmental emissions such as NOx, SOx and COx are considered in the wind integrated hydrothermal scheduling problem. The numerical results of the NSTLBO algorithm prove the satisfactory performance of the constrained optimization problem. A fuzzy decision making approach has been involved on these solution in order to identify the best comprise solution among the group of solutions. It deliberately handles the diverse set of solution. A comparison has also been made for proposed with existing benchmark methods. It indicates that the NSTLBO algorithm is better in terms of solution quality as well as computational time. From the contributions, the proposed NSTLBO has the ability to easily solve different types of Multi- objective power system optimization problems.

Acknowledgements The authors gratefully acknowledge the authorities of Annamalai University for the facilities offered to carry out this work.

References

1. Zahavi J, Eisenberg L (1975) Economic-enviromental power dispatch. IEEE Trans Syst, Man, Cybern 5:485–489
2. Nanda J, Kothari DP, Lingamurthy KS (1988) Economic-emission load dispatch through goal programming techniques. IEEE Trans Energy Convers 3(1):26–32
3. Dhillon JS, Kothari DP (2000) The surrogate worth trade-off approach for multiobjective thermal power dispatch problem. Electr Power Syst Res 56(2):103–110
4. Sasikala J, Ramaswamy M (2012) PSO based economic emission dispatch for fixed head hydrothermal systems. Electr Eng 94(4):233–239
5. Talaq JH, El-Hawary F, El-Hawary ME (1994) A summary of environmental/economic dispatch algorithms. IEEE Trans Power Syst 9(3):1508–1516
6. Wood AJ, Wollenberg BF (2012) Power generation, operation, and control. Wiley
7. Rashid AHA, Nor KM (1991) An efficient method for optimal scheduling of fixed head hydro and thermal plants. IEEE Trans Power Syst 6(2):632–636
8. Jin-Shyr Y, Nanming C (1989) Short term hydrothermal coordination using multi-pass dynamic programming. IEEE Trans Power Syst 4(3):1050–1056
9. Salam MS, Nor KM, Hamdam AR (1998) Hydrothermal scheduling based Lagrangian relaxation approach to hydrothermal coordination. IEEE Trans Power Syst 13(1):226–235
10. Li CA, Svoboda AJ, Tseng CL, Johnson RB, Hsu E (1997) Hydro unit commitment in hydrothermal optimization. IEEE Trans Power Syst 12(2):764–769
11. Agarwal SK (1973) Optimal stochastic scheduling of hydrothermal systems. In: Proceedings of the institution of electrical engineers, vol 120, no 6, pp 674–678. IET Digital Library
12. Nanda J, Bijwe PR, Kothari DP (1986) Application of progressive optimality algorithm to optimal hydrothermal scheduling considering deterministic and stochastic data. Int J Electr Power Energy Syst 8(1):61–64
13. Dhillon JS, Parti SC, Kothari DP (2002) Fuzzy decision-making in stochastic multiobjective short-term hydrothermal scheduling. IEE Proc-Gener, Transm Distrib 149(2):191–200
14. Dhillon JS, Parti SC, Kothari DP (2001) Fuzzy decision making in multiobjective long-term scheduling of hydrothermal system. Int J Electr Power Energy Syst 23(1):19–29
15. Benhamida F, Belhachem R (2013) Dynamic constrained economic/emission dispatch scheduling using neural network. Adv Electr Electron Eng 11(1):1–9
16. Dieu VN, Ongsakul W (2005) Hopfield Lagrange for short-term hydrothermal scheduling. In: Power Tech, 2005 IEEE Russia, pp 1–7. IEEE
17. Dhillon JS, Dhillon JS, Kothari DP (2011) Real coded genetic algorithm for stochastic hydrothermal generation scheduling. J Syst Sci Syst Eng 20(1):87–109
18. Narang N, Dhillon JS, Kothari DP (2012) Multiobjective fixed head hydrothermal scheduling using integrated predator-prey optimization and Powell search method. Energy 47(1):237–252
19. Umayal SP, Kamaraj N (2005) Stochastic multi objective short term hydrothermal scheduling using particle swarm optimization. In: INDICON, 2005 Annual IEEE, pp 497–501. IEEE
20. Zhou J, Liao X, Ouyang S, Zhang R, Zhang Y (2014) Multi-objective artificial bee colony algorithm for short-term scheduling of hydrothermal system. Int J Electr Power Energy Syst 55:542–553
21. Zhang H, Zhou J, Zhang Y, Fang N, Zhang R (2013) Short term hydrothermal scheduling using multi-objective differential evolution with three chaotic sequences. Int J Electr Power Energy Syst 47:85–99
22. Basu M (2011) Economic environmental dispatch of fixed head hydrothermal power systems using nondominated sorting genetic algorithm-II. Appl Soft Comput 11(3):3046–3055
23. Deb K, Pratap A, Agarwal S, Meyarivan TAMT (2002) A fast and elitist multiobjective genetic algorithm: NSGA-II. IEEE Trans Evol Comput 6(2):182–197
24. Zitzler E, Laumanns M, Thiele L (2001) SPEA2: improving the strength Pareto evolutionary algorithm. TIK-report, p 103
25. Cagnina L, Esquivel SC, Coello Coello C (2005) A particle swarm optimizer for multi-objective optimization. J Comput Sci & Technol 5

26. Xue F, Sanderson AC, Graves RJ (2003) Pareto-based multi-objective differential evolution. In: The 2003 congress on evolutionary computation, 2003. CEC'03, vol 2, pp 862–869. IEEE
27. Nadakuditi G, Sharma V, Naresh R (2016) Non-dominated sorting disruption-based gravitational search algorithm with mutation scheme for multi-objective short-term hydrothermal scheduling. Electr Power Compon Syst 44(9):990–1004
28. Dubey HM, Pandit M, Panigrahi BK (2016) Hydro-thermal-wind scheduling employing novel ant lion optimization technique with composite ranking index. Renew Energy 99:18–34
29. Wu XY, Cheng CT, Shen JJ, Luo B, Liao SL, Li G (2015) A multi-objective short term hydropower scheduling model for peak shaving. Int J Electr Power Energy Syst 68:278–293
30. Norouzi MR, Ahmadi A, Sharaf AM, Nezhad AE (2014) Short-term environmental/economic hydrothermal scheduling. Electr Power Syst Res 116:117–127

Reliability Improvement for the DC Link Capacitor with Integrated Active Filter Capabilities in Wind Power Converter

S. Rajeswari and J. Sreenivasulu

Abstract Now a day's, population and their requirements are increasing rapidly. Hence, enhancement of reliability of electrical components in power system also increases. In wind power conversion dc capacitor plays an important role to minimize harmonics, ripple currents and voltage spikes. Hence, improving the life span and reliability of a capacitor is more important. In literature, back to back converter has been used for improving life time of a capacitor. Apart from this PI controller is also used to improving the voltage profile. In a case study 1.2 MW Permanent Magnetism Synchronous Generator (PMSG) wind turbine is considered and real field mission profiles are transformed (i.e. wind speed and ambient temperature) into thermal and current stresses to estimate the reliability of dc-link capacitor. In this paper, Maximum Power Point Tracking (MPPT) controller for DC-DC Booster converter having the Power Signal Feedback is proposed to get better reliability or life time of a dc-capacitor. In addition to this, reduction of ripple current and losses is also proposed. The proposed method is implemented in MATLAB simulation software.

Keywords dc-link capacitor · Evaluation of dc-link lifetime · Mission profiles · Power converter of the wind turbine · Boost converter · Power signal feedback controller

1 Introduction

Wind capacity reached closed to 539 GW due to uninterrupted development of power machinery [1], and wind turbines reliability constraints are also rising. However, power electronic converter and its capacitor experience from unfavourability of the power loading which are associated with operation environment, high fault rate [2, 3] regarding statistical results.

S. Rajeswari (✉) · J. Sreenivasulu
JNTUA CEA (Autonomous), Ananthapuramu 515 002, India
e-mail: rajeswarisake16@gmail.com

J. Sreenivasulu
e-mail: jsreenivasulu.eee@jntua.ac.in

© Springer Nature Singapore Pte Ltd. 2020

T. Hitendra Sarma et al. (eds.), *Emerging Trends in Electrical, Communications, and Information Technologies*, Lecture Notes in Electrical Engineering 569,
https://doi.org/10.1007/978-981-13-8942-9_35

Due to the property of dc-link, place the dc-link capacitor in between wind turbine rotor side and grid side converter for balancing the instant power difference, to mitigate the dc-link voltage fluctuation. The capacitor physical failure analysis has been observed in [4, 5]. DC-link capacitor instant thermal modeling approach in photovoltaic inverter is based on Fast Fourier Transformed [6]. Considered the capacitor's power loss observed by voltage-managing and life-cycle monitoring method existing in [7].

Considerable approach for reliability estimation of the capacitor is introduced in part II. Transforming the real field mission profiles into the electrical and thermal behaviors taking into consideration of dc-link with high frequency ripple current is discussed in part III. To end with, conclusions are mentioned in part IV.

2 System Configuration

In Aluminum electrolytic capacitor, foremost failure mechanisms are Electrolyte vaporization and electrochemical reaction in [8, 9], which affect capacitor Equivalent Series Resistance (ESR) and increase of leakage current. Thermal stress and electrical stress are analyzed by considering the thermal model of dc-link capacitor.

2.1 Structure of Wind Turbine

In this paper, Fig. 1 shown the voltage source converter with two-level back-to-back topology, and listed some important specifications of wind turbine in Table 1. It can

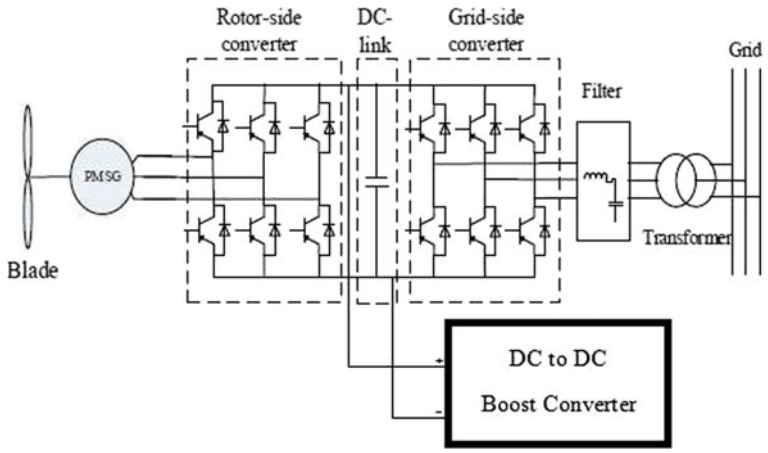

Fig. 1 Topology for the wind turbine

Table 1 A 1.2 MW PMSG system specifications for simulation

Parameter	Value
Estimate active power output	1.2 MW
break in wind speed	2.5 m/s
Estimate wind speed	10.5 m/s
Cut-out wind speed	20 m/s
Estimate wind turbine frequency	16 Hz
Grid link rated voltage	690 V
Switching frequency	3 kHz
Voltage of the DC bus	1100 V
Turbine assess voltage at highest speed	690 V

generate the wind turbine power from the cut-off wind speed at 20 m/s until the cut-in or break in wind speed of 2.5 m/s, estimation of wind speed is 10.5 m/s [10].

2.2 DC-Link Capacitor Thermal Model

The correlation among thermal and electric stress can be developed when ESR in string with an Equivalent Series Inductor (ESL) and an ideal capacitor, which is a simple thermal model representation of dc-link capacitor [11]. The electric stress of dc-link capacitor can be modeled as:

$$dv \approx \frac{P_0}{2\pi f_g C_{dc} V_{dc}} \tag{1}$$

$$i_{c,RMS} \approx \frac{P_0}{\sqrt{2} V_{dc}} \tag{2}$$

where,

d_v = DC-link Peak-to-Peak ripple voltage
P_0 = Grid converter input power
f_g = Grid Frequency of
C_{dc} = DC-link Capacitance
V_{dc} = Voltage of the dc-link
$i_{c,RMS}$= Capacitor ripple current in Root-Mean-Square (RMS).

2.3 Bidirectional DC–DC Converter and MPPT Controller

The dc-link capacitor voltage profiles vary while it discharges energy. To integrate the dc-link structure through a bidirectional dc-dc converter, to retain a rigid dc-link voltage. When dc-link voltage decreases while discharging and increases while charging.

The bidirectional dc–dc converter is developed to operate in boost mode when it's reached to minimum boost converter voltage. To control the output voltage of the bidirectional dc–dc converter in boost modes an Average current mode control is used while charging and discharging the dc-link.

When compared to other methods such as peak current and voltage mode control this method tends to be more stable. Where compared and actual output and dc-link voltage (V_{out}) with the reference voltage $\left(V_{ref}\right)$ and the error is given to the voltage compensator, which provides the average reference current $\left(I_{avref}\right)$ and reference voltage error is negative. When the error is positive dc-dc converter operates in boost mode [12] and if it is negative it will feed back to the compensator.

Equation (3) is a turbine power used for obtaining reference power for PSF based on MPPT control of PMSG wind turbine. In Fig. 2, shown the PSF control signal generation block diagram.

$$P_{max} = 0.3 + 1.08V_w - 0.125V_w^2 + 0.842V_w^3 \tag{3}$$

where,

V_w= Velocity of the wind.

With the maximum power of turbine, the rectifier reference power at output is computed given by

$$P_{ref} = n_G n_R P_{max} \tag{4}$$

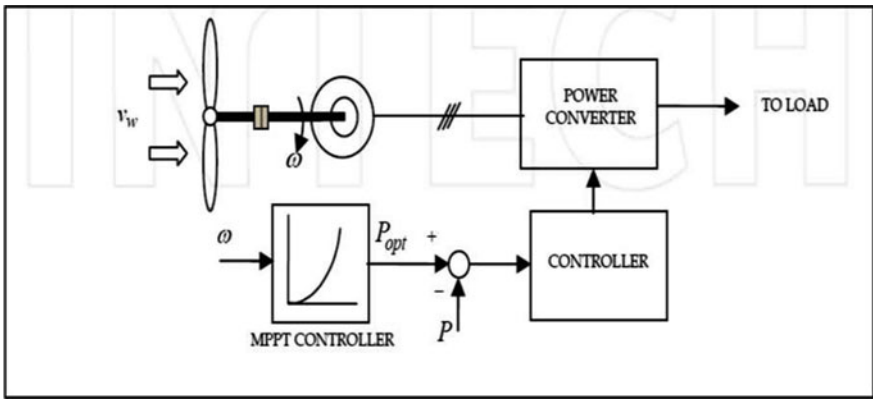

Fig. 2 Power signal feedback control

where,

n_G = Generator efficiency
n_R = Rotor efficiency
P_{max} = Maximum power of the wind turbine.

Maximum power is extracted by comparing rectifier output with reference power. Calculates the dc-link capacitor power loss using the Eq. (5) and reliability indices like hot-pot temperature and life time estimation of a dc-link capacitor are to be evaluated by using the Eqs. (6) and (7).

$$P_{C,loss} = \sum_{h=1}^{N} I_{ch}^2 . R_{ESR}(f_h) \tag{5}$$

where,

I_{ch} = Harmonic currents of dc-link capacitor in RMS
N = Total number harmonics
$R_{ESR}(f_h)$ = Harmonic frequency f_h with corresponding ESR.

$$T_c = P_{C,loss} \cdot (R_{thhc} + R_{thca}) + T_a. \tag{6}$$

where,

$P_{C,loss}$ = Power loss of the capacitor
T_C = DC-link capacitor hot-pot temperature
R_{thhc} = Hot-pot to casing thermal resistance
R_{thca} = Casing to air-cooling system thermal resistance
T_a= Ambient temperature.

The lifetime can be estimated with the study of thermal and electrical stress.

2.4 Evaluation of dc-Link Lifetime

Analyze the relationship between lifetime of the capacitor and hot-pot temperature by various models. One of the models [13] for capacitors is explained as follows:

$$L = L_0 \cdot \left(\frac{V}{V_0}\right)^{-n} \cdot \text{Exp}\left[\left(\frac{E_a}{K_b}\right) \cdot \left(\frac{1}{T} - \frac{1}{T_0}\right)\right] \tag{7}$$

where,

L = Under the real operating condition lifetime of the dc-link
L_0 = The lifetime under rated condition

V = Under the real operating condition of dc-link voltage
V_0 = Under the rated operating condition dc-link voltage
E_a = Activation energy
K_b = Boltzmann constant
T = Real operating condition temperature of the dc-link
T_0 = Rated operating condition temperature of the dc-link.

3 MATLAB Simulation Results Analysis

Based on the simulation model for wind power conversion with booster converter is represented in Fig. 3. For this system, one day wind speed profile shown in Fig. 4. And ambient temperature is as shown in Fig. 5. Taken as inputs for analyzing or estimating the life time of capacitor by considering electrical and thermal stress.

3.1 Electrical Stress of dc-Link

The dc-link capacitor electrical stresses can be formed by the real filed mission profiles like ripple current and voltage of the dc-link Figs. 6 and 7. It is observed that

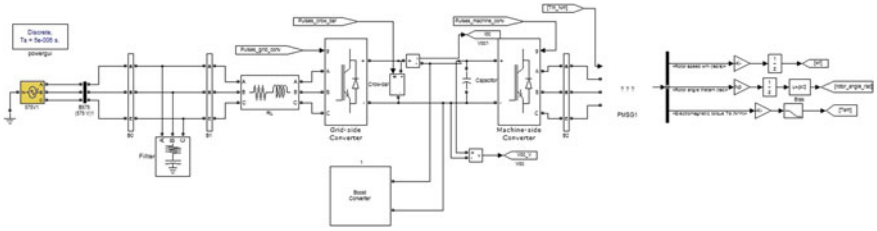

Fig. 3 Simulink model for wind power conversion with booster converter

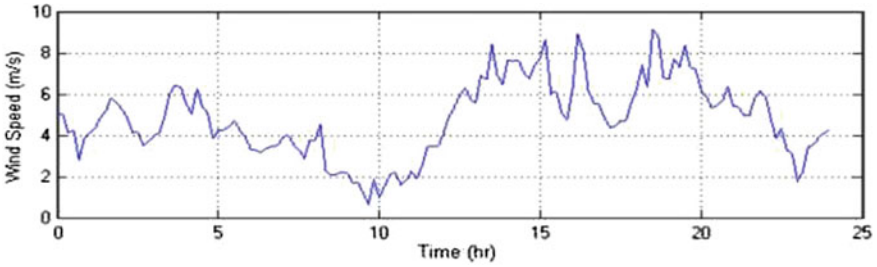

Fig. 4 A 1-day profile for wind speed

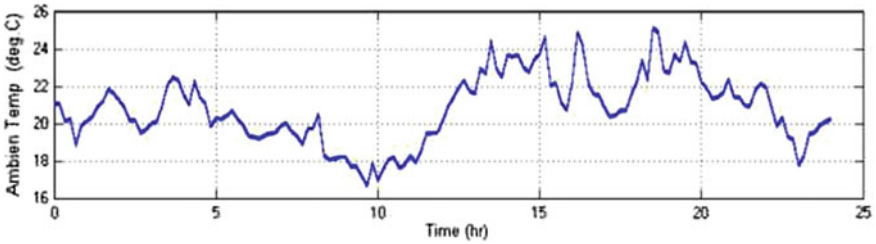

Fig. 5 Ambient temperature profile of the wind turbine

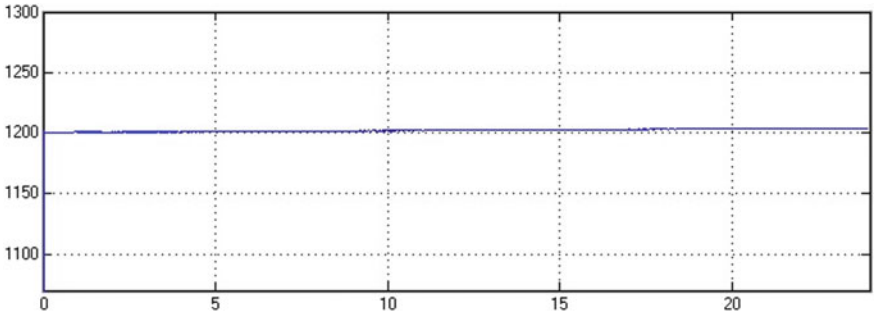

Fig. 6 A 1-day dc-link capacitor voltage mission profile

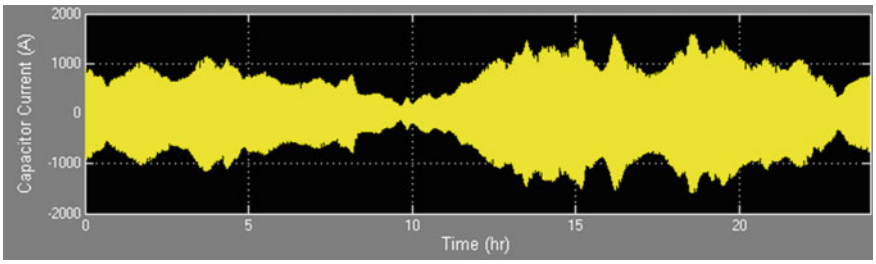

Fig. 7 A 1-day dc-link capacitor current mission profile

huge change of one day wind speed profile due to these dc-links current and voltage have large variation. Hence, it is observed that with booster converter voltage spikes and ripple currents are reduced when the wind speed fluctuation is small.

Booster converter helps in reduction the total harmonic distraction of the dc-link capacitor currents and here loss also reduced due to the function of rectification and dc-ripples avoided. As shown in Fig. 8.

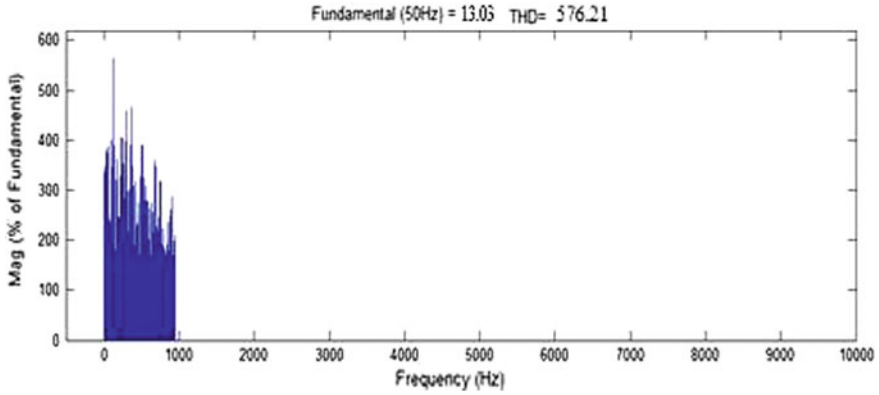

Fig. 8 The dc-link capacitor ripple currents harmonic spectrum

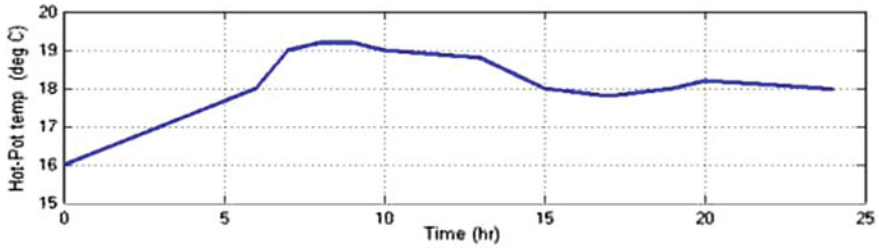

Fig. 9 DC-link capacitor hot-pot temperature

3.2 Thermal Stress

DC-link capacitor electrical stress is translated to the thermal stress, due to the ripple current and high voltage capacitor is experience high temperature as shown in Fig. 9. And manage stability of the capacitor temperature when the ripple current and voltage stay balanced.

Number of harmonic currents of dc-link capacitor is considered for a limit (e.g. 3000 and 5000 Hz).

3.3 Reliability Evaluation

With elevate of the ambient temperature cause incremented the hot-pot temperature, there by resultant in the lifetime decrementation of the dc-link capacitor. Accordingly, it is necessary to control cooling behavior of power converter.

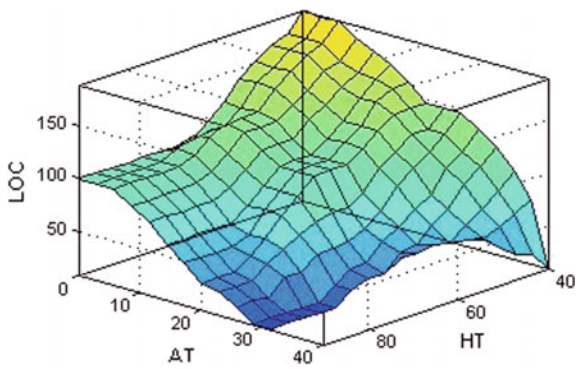

Fig. 10 Reliability analysis of dc-link

In this paper considered one day real field mission profile, and immediate change of dc-link capacitor voltage and current leads to presence the sudden change of mission profile, which will influence the capacitor hot-pot temperature.

The Aluminum electrolytic capacitor EPCOS B43310A9228M with DC to DC Boost Converter is considered for reliability improvement in this paper. From datasheet of manufacturers can be obtained its rated voltage input, values at ESR, rated lifetime and ripples current. The DC-link capacitor reliability is evaluated, under a mixture of considerable temperatures analyzes the hot-pot temperature, life-time and power loss of the capacitor.

From Fig. 10 it is observed that life time of a capacitor increased when booster converter with MPPT is considering.

4 Conclusion

In this paper presented a dc-link capacitor lifetime estimation method in the PMSG with Active filter (DC to DC Boost Converter). Considered the long-term ambient temperature for complete mission profile and it's considered at the same time of wind speed. Due to fundamental frequency analyzed consumed lifetimes of dc-link Capacitor by individual characteristics.

Unluckily, the wind power appliance stimulating reliability estimation methods of power electronic converter are not yet appropriate. DC-link capacitor lifetime is affected by ambient temperature and various electrical stress it is observed from the MATLAB simulation results.

Proved that with DC to DC Boost Converter is cooperative for improving the reliability by reducing the thermal stress caused by the electrical stress and its also help to reduce the total harmonic distractions.

References

1. Wind capacity in India 2017. [Online]. Available: http://newenergy.in-en.com/html/newenergy-2260360.shtml
2. Bertling L, Ribrant J (2007) Survey of failures in wind power systems with focus on Swedish wind power plants during. IEEE Trans Energy Convers 22:137–167
3. Qian Z, Zhang J, Sheng K (2014) Status and development of power semiconductor devices and its applications. Proceeding CSEE 34:5149–5161
4. Wang H, Liserre M, Blaabjerg F, Landkilldehus J (2014) Transitioning to physics-of-failure as a reliability driver in power electronics. IEEE J Emerg Sel Top Power Electron 2:97–114
5. Wang H, Blaabjerg F (2014) Reliability of capacitors for DC-link applications in power electronic converters—an overview. IEEE Trans Ind Appl 50:3569–3578
6. Yang Y, Ma K (2015) Instantaneous thermal modeling of the DC-link capacitor in PhotoVoltaic systems. IEEE Appl Power Electron Conf Expo 2733–2739
7. Vogelsberger MA, Wiesinger T, Ertl H (2011) Life-cycle monitoring and voltage-managing unit for DC-link electrolytic capacitors in PWM converters. IEEE Trans Power Electron 26:493–503
8. Alwitt RS, Hills RG (1965) The chemistry of failure of aluminum electrolytic capacitors. IEEE Trans Parts, Mater, Packag, PMP-I:28–34
9. Aluminum Electrolytic Capacitor, and its types. [Online]. Inhttp://www.cde.com/catalogs/AEappGUIDE.pdf
10. Wang H, Blaabjerg F (2014) Reliability of capacitors for DC-link applications in power electronic converters—an overview. IEEE transactions on industry applications by the department of energy technology, Aalborg University, Denmark
11. Xue S, Zhou Q, Li J, Xiang C, Chen (2016) Reliability evaluation for the DC-link capacitor considering mission profiles in wind power converter. In: 2016 IEEE international conference on high voltage engineering and application (ICHVE)
12. Thongam JS, Ouhrouche M (2011) MPPT control methods in wind energy conversion systems. Department of Renewable Energy Systems, STAS Inc. Electric Machines Identification and Control Laboratory, Department of Applied Sciences, University of Quebec at Canada
13. Minford WJ (1982) Accelerated life testing and reliability of high K multi-layer ceramic capacitors. IEEE Trans Compon, Hybrids, Manuf Technol CHMT-5(3):297–300

Electronics and Communications Engineering

Design and Full Wave Green's Function Analysis of Two Layer Hemispherical DRA

Gitimayee Sahu and Sanjay S. Pawar

Abstract A Two layer hemispherical dielectric resonator antenna (HDRA) fed by a coaxial probe is rigorously analyzed here. The method of moment technique and Green's function is used to obtain the probe current from which the input impedance of the DRA is calculated. The magnetic frill source model is considered. The piecewise sinusoidal (PWS) expansion mode is used and the results are compared. The Dielectric layers Permittivites and layer thickness between the outer and inner hemisphere are optimized for broadband operation of the coaxial probe fed DRA. Frequency tuning of the antenna structure is demonstrated, which maintains the broadband characteristics. Probe location (centered and offset) and length of the coaxial probe are optimized to obtain better impedance bandwidth and stable radiation pattern. The radiation characteristic of the antenna is also investigated in this research work. Simulations were carried out using HFSS v12.0 and it is observed that better impedance bandwidth and stable radiation pattern are obtained across the frequency range between 4–11 GHz.

Keywords Two layer DRA · Coaxial-probe-coupled · Green's function · Impedance bandwidth · Radiation pattern

1 Introduction

At millimetre and microwave frequencies, the conductor loss is very high and it makes conventional antennas unrealizable at those frequencies. But the Dielectric Resonator Antennas (DRA), due to absence of conductor loss is an efficient candidate for low-loss applications. The wavelength in dielectric is $\frac{\lambda_0}{\epsilon_r}$ where, λ_0 is the free space wavelength and ϵ_r is the relative dielectric permittivity. So the size of the antenna can be reduced to a very large extent with materials of high permittivity. DRA offers

G. Sahu (✉) · S. S. Pawar
Department of Electronics and Telecommunication, UMIT, Juhu, Mumbai, India
e-mail: giti.sahoo@gmail.com

S. S. Pawar
e-mail: drsanjayspawar@gmail.com

© Springer Nature Singapore Pte Ltd. 2020

T. Hitendra Sarma et al. (eds.), *Emerging Trends in Electrical, Communications, and Information Technologies*, Lecture Notes in Electrical Engineering 569,
https://doi.org/10.1007/978-981-13-8942-9_36

wide impedance bandwidth compared to Microstrip antenna (~10% for dielectric constant $\in_r \sim 10$) [1, 2]. This is because the Microstrip antenna radiates only through two narrow radiation slots, whereas the DRA radiates through the whole DR surface except the grounded part. Avoidance of surface waves is another attractive advantage of the DRA over the Microstrip antenna. The DRA, owing to its negligible conductor loss and dielectric properties, behaves as low profile, highly efficient antenna that could be used even in millimeter wave frequencies. Its small size makes it useful to be integrated in miniature circuits [3].

With advantages of high radiation efficiency (virtually no metallic loss), shape flexibility (rectangular, cylindrical, hemispherical etc.), different available feeding mechanisms (probes, slots, Microstrip lines, dielectric image guides, coplanar lines), a wide range of available materials (dielectric constant ranges from about 4 to 100), easily controlled characteristics (input impedance, bandwidth and radiation patterns) and small size, DRAs have a number of features that make them attractive as antenna element for array applications [4].

The DRA was originally proposed by Leung et al. as radiating element in [1] is characterized by low loss due to the absence of conductor losses. One of the technique to extend the bandwidth of DRA element is the two layer DRA configuration. A broadband hemispherical DRA topology consisting of an inner resonator surrounded by a dielectric cell, slot-coupled to the Microstrip line has been reported in [2, 5]. A two-layer hemispherical broadband DRA excited by a coaxial probe is discussed here.

In the following work, the Green's function approach is presented for the analysis of two layer HDRA. The analysis is accomplished by separation of source terms from the field-matching equations at the dielectric interfaces and incorporating them in the potential Green's function. The resultant matrix can be easily solved. This analysis, to the best of our knowledge, has not been reported elsewhere. The Green's function technique used in this paper is distinctly different from the Green's function approach used in [6, 7] to analyze two layer hemispheres.

In addition, the Green's function approach in this work is developed from the fundamentals taking into account i.e. the configuration of the antenna and coaxial probe fed. As such, all the components of Dyadic Green's function need not to be computed and is beyond the scope of this research work.

The Green's function analysis contributes enhanced efficiency of our proposed technique compared to the approach in [6] and it is seen that this method need significantly less computational time and memory compared to finite-element based electromagnetic software e.g. High Frequency Structure Simulator (HFSS) [8], particularly when the number of dielectric layer increases.

The simulation time and memory requirement are almost independent of the number of layers, which is one of the main advantage of this approach over other simulation software.

In addition, the double-summation representation of the homogeneous Green's function has also been extended for the two layer case, with large reduction in computation time.

Also, further decrease in time is achieved for the centred probe by suitable dissociation of the Green's function and expressing the impedance matrix element as product of two single integrations.

This technique is used to design broadband coaxial-fed two layer HDRA. It is shown that the layer permittivity should be appropriately chosen to minimize the quality factor of the antenna and to achieve optimum broadband behaviour of the two layer structure. A bandwidth of 67.21% is obtained with the centrally located probe, which is contributed by the probe resonance. Frequency tuning and the effect of probe offset are also investigated for this antenna structure.

2 System Model

The two layer hemispherical Dielectric resonator antenna configuration is shown in Fig. 1, where the two layers DRA is excited by a $\hat{Z}$ directed probe of length 'l' and radius 'a' located at a displacement 'c' along the x-axis from the centre of the DRA. The DRA rests on an infinite ground plane. The inner hemispherical DRA of the two layer configuration with radius r_1, permittivity $\in_{r_1}$ and permeability μ_1 and is surrounded by outer hemispherical cell of radius r_2, permittivity $\in_{r_2}$ and permeability μ_2.

In this formulation, the electromagnetic fields are assumed to vary harmonically. Furthermore $\vec{r}\,(r, \theta, \phi)$ refers to the field point and $\overrightarrow{r'}\,(r, \theta, \phi)$ refers to the source point. To find the Green's function $G_{J_z}^{E_z}$ ($\hat{Z}$-directed electric field due to $\hat{Z}$-directed point current), first resolve the $\hat{Z}$-directed current into a $\hat{Z}$-directed and an $\hat{r}$ directed components. It should be mentioned that $\hat{\theta}$-directed current will excite both TE to r and TM to r modes [9].

Therefore two potential functions $G_{J_\theta}^{A_r}$ and $G_{J_\theta}^{F_r}$ are required to represent all the possible fields excited by a $\hat{\theta}$-directed current, but $\hat{r}$-directed current will excite

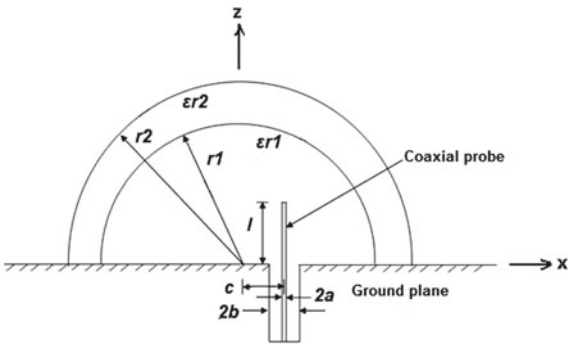

Fig. 1 Configuration of the two layer hemispherical DRA excited by a coaxial probe

only *TM to r* mode, so only one potential function $G_{J_r}^{A_r}$ alone is sufficient for an $\hat{r}$-directed one [1]. The Green's function $G_{J_r}^{F_r}$ and $G_{J_r}^{A_r}$ denote, the electric potential green's function and magnetic potential green's function due to $\hat{r}$-directed current respectively. Once the potential Green's function are derived the various field components and hence the input impedance and the radiation pattern can be evaluated. To begin with we represent the various Green's function as a sum of particular G_p and homogeneous G_h solutions which would enhance the efficiency of the numerical computation. The particular solution alone represents a source radiating in an unbounded dielectric medium whereas the homogeneous solution accounts for the spherical discontinuity. The merit of this procedure will be observed soon.

Expressions for $G_{J_\theta}^{F_r}$ *and* $G_{J_\theta}^{A_r}$:

Particular Solution:

$$G_{J\theta}^{F_{rp}} = \frac{1}{r' \sin\theta'} \sum_{n=1}^{\infty} \sum_{m=1}^{n} A_{nm} P_n^m(\cos\theta) P_n^m(\cos\theta')$$
$$\sin m(\phi - \phi') \begin{cases} \widehat{H_n^{(2)}}(K_1 r') \overset{\wedge}{\underset{n}{J}}(K_1 r) \, for (r < r') \\ \hat{J}_n(K_1 r') \widehat{H_n^{(2)}}(K_1 r) \, for (r > r') \end{cases} \tag{1}$$

$$G_{J\theta}^{A_{rp}} = \frac{1}{r'} \sum_{n=1}^{\infty} \sum_{m=0}^{n} D_{nm} \frac{d P_n^m(\cos\theta')}{d\theta'} P_n^m(\cos\theta)$$
$$\cos m(\phi - \phi') \begin{cases} \widehat{H_n^{(2)}}(K_1 r') \overset{\wedge}{\underset{n}{J}}(K_1 r) \, for \, (r < r') \\ \widehat{J_n'}(K_1 r') \widehat{H_n^{(2)}}(K_1 r) \, for \, (r > r') \end{cases} \tag{2}$$

Homogenous Solution:

$$G_{J\theta}^{A_{rh}} = \sum_{n=1}^{\infty} \sum_{m=-n}^{n} P_n^m(\cos\theta) e^{jm\phi} \begin{cases} B_{nm1} \overset{\wedge}{\underset{n}{J}}(K_1 r) for (r \le r_1) \\ B_{nm2} \overset{\wedge}{\underset{n}{J}}(K_1 r) + B_{nm3} \overset{\wedge}{\underset{n}{N}}(K_1 r) for (r_1 \le r \le r_2) \\ B_{nm4} \widehat{H_n^2}(K_1 r) for (r \ge r_2) \end{cases} \tag{3}$$

$$G_{J\theta}^{F_{rh}} = \sum_{n=1}^{\infty}\sum_{m=-n}^{n} P_n^m(\cos\theta)e^{jm\phi}\begin{cases} C_{nm1}\overset{\wedge}{\underset{n}{J}}(K_1 r)\, for (r \le r_1) \\ C_{nm2}\overset{\wedge}{\underset{n}{J}}(K_1 r) + C_{nm3}\overset{\wedge}{\underset{n}{N}}(K_1 r)\, for (r_1 \le r \le r_2) \\ C_{nm4}\widehat{H_n^2}(K_1 r)\, for (r \ge r_2) \end{cases} \tag{4}$$

$$G_{Jr}^{A_{rh}} = \sum_{n=1}^{\infty}\sum_{m=-n}^{n} P_n^m(\cos\theta)e^{jm\phi}\begin{cases} E_{nm1}\overset{\wedge}{\underset{n}{J}}(K_1 r)\, for (r \le r_1) \\ E_{nm2}\overset{\wedge}{\underset{n}{J}}(K_1 r') + E_{nm3}\overset{\wedge}{\underset{n}{N}}(K_1 r)\, for (r_1 \le r \le r_2) \\ E_{nm4}\widehat{H_n^2}(K_1 r)\, for (r \ge r_2) \end{cases} \tag{5}$$

$\widehat{J_n(x)}$ is the spherical Bessel function of first kind. $\widehat{H_n^{(2)}}$ is spherical Henkel function of the second kind. P_n^m is the associated Legendre function of first kind with order 'm' and degree 'n'.

3 Numerical Results and Discussion

To verify with the theoretical value, measurements of two layer hemispherical DRA are carried out using the specified parameters as, $\in_{r_1}= 8$, $r_1 = 12.5$ mm $\in_{r_2}= 3, r_2 = 19.5$ mm. The ground plane was 20 * 20 cm in size. Figure 2 shows the simulated impedance bandwidth, which is found to be 67.21%. Three reso-

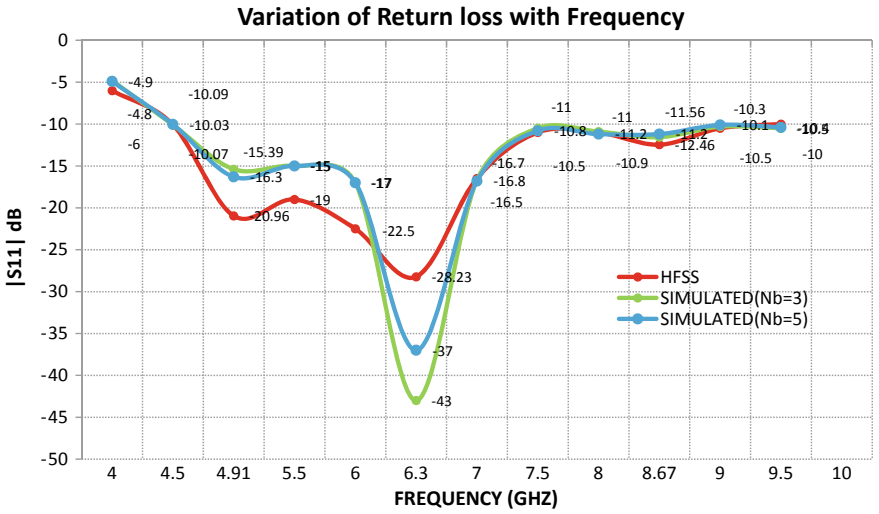

Fig. 2 Computed and simulated return loss versus frequency

nant modes are observed. The first dip is obtained at resonance frequency $f_{r_1} = 4.91\,\text{GHz}(-20.96\,\text{dB})$, the second dip is obtained at $f_{r_2} = 6.31\,\text{GHz}(-28.23\,\text{dB})$ and the third dip is obtained at $f_{r_3} = 8.67\,\text{GHz}(-12.46\,\text{dB})$.

Figure 2 shows the comparison between theoretical and HFSS simulation results for the Return loss of the DRA. In this figure computed results using MATLAB 14b for number of basis functions $N_b = 3$ and $N_b = 5$ are shown and as observed the values are very close to each other. Moreover they agree reasonably well with the HFSS simulated result.

Figure 3 shows the comparison between mathematical computed and HFSS simulated results using MATLAB 14b the input resistance of the HDRA. In this figure computation for $N_b = 3$ and $N_b = 5$ is shown and the values are close to each other as well with the simulated result.

Figure 4 shows the comparison between theoretical and HFSS simulated results for the input reactance of the HDRA. In this figure MATLAB computation for $N_b = 3$ and $N_b = 5$ is shown and the values are close to each other as well with the simulated result.

As shown in Fig. 5 the impedance bandwidth for $\in_{r_1} = 8$ and $\in_{r_2} = 3$ is 58.75% and for $\in_{r_1} = 8$ and $\in_{r_2} = 5$ is 57.35% and the bandwidth is nearly remain constant for variation of $\in_{r_2}$ between 3–5 and $\in_{r_1}$ is 8.

The maximum impedance bandwidth of 67.21% is obtained at the centred probe location i.e. $c = 0$ mm for probe length 'l' of 6 mm for $\in_{r_1} = 8$, $\in_{r_2} = 3$ and radius of inner probe i.e. $a = 0.65$ mm.

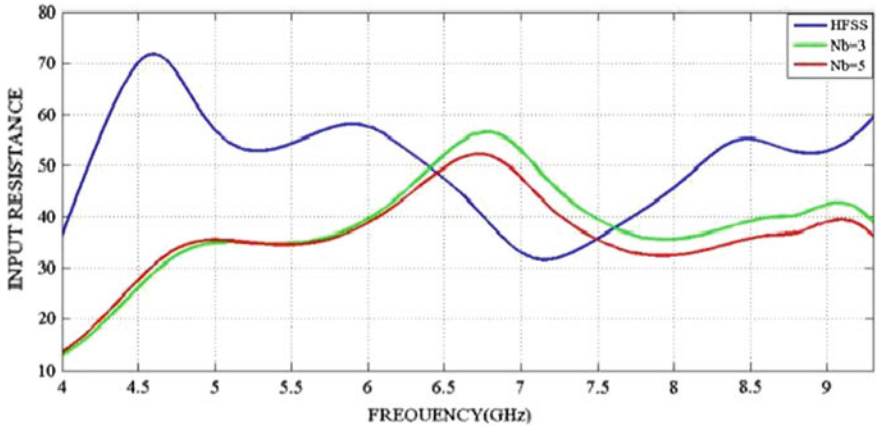

Fig. 3 Computed and simulated input resistance versus frequency

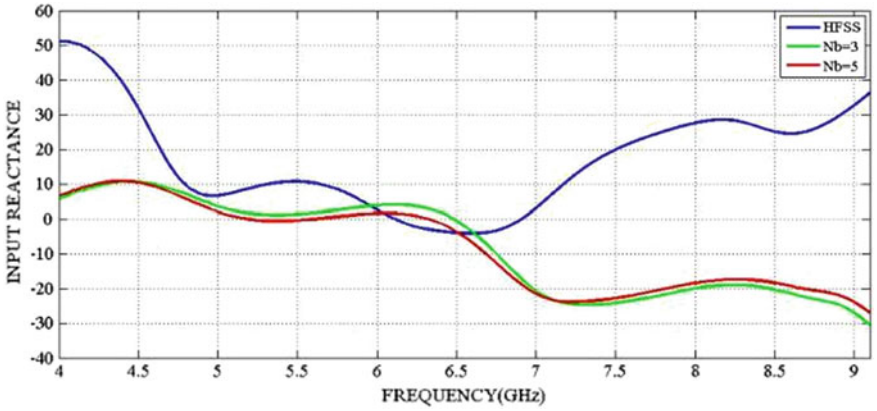

Fig. 4 Computed and simulated input reactance versus frequency

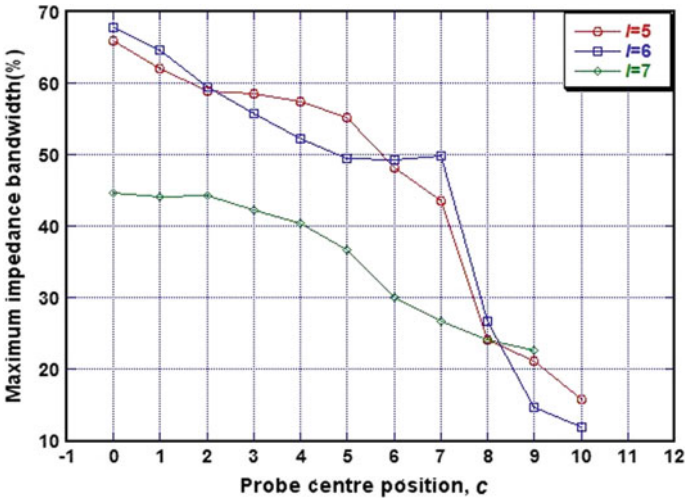

Fig. 5 Maximum impedance bandwidth as a function of probe centre position c for probe lengths $l = 5, 6, 7$ mm

3.1 Maximum Impedance Bandwidth

As shown in Fig. 6 the lower cut off frequency $f_l = 4.49$ GHz and upper cut off frequency $f_h = 9.06$ GHz.

Maximum Impedance bandwidth of 67.21% is obtained with the configuration i.e. $c = 0$ mm, $\in_{r_1} = 8$, $\in_{r_2} = 3$, $r_1 = 12.5$ mm, $r_2 = 19.5$ mm, $l = 6$ mm, $a =$

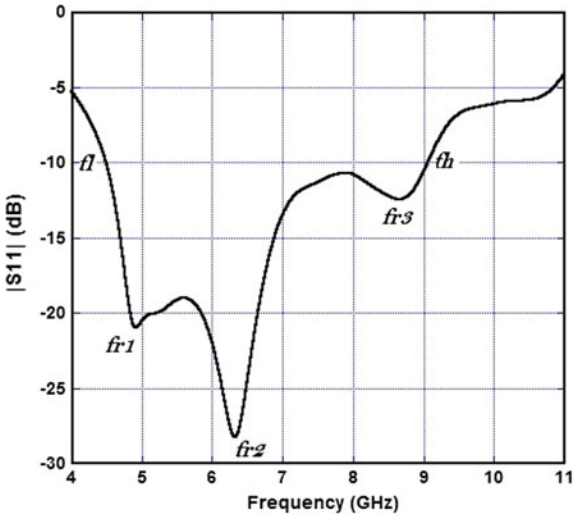

Fig. 6 HFSS Simulated return loss of the probe coupled two layer HDRA with centered probe

0.65 mm, $b = 2$ mm. Where, 'a' is the inner radius of the coaxial probe and 'b' is the outer radius of the coaxial probe.

Three Resonances are obtained and the frequencies and return losses are,

i. $f_{r_1} = 4.91\,\text{GHz}(-20.96\,\text{dB})$
ii. $f_{r_2} = 6.31\,\text{GHz}(-28.23\,\text{dB})$
iii. $f_{r_3} = 8.67\,\text{GHz}(-12.46\,\text{dB})$

3.2 Radiation Pattern

The radiation pattern for the centred probe is like monopole with low cross-pole levels as shown in Fig. 7. The simulated cross-pole levels are below -20 dB and are not visible. It is observed that for the centred probe-fed HDRA the radiation pattern is stable with low cross-pole levels around the impedance bandwidth (Fig. 7).

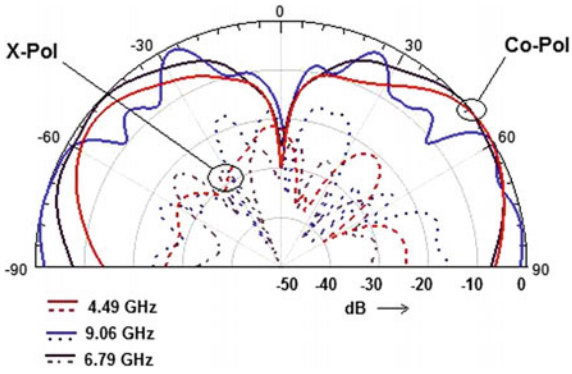

Fig. 7 Simulated Radiation pattern in the X-Z plane for the centered probe-fed two layer DRA at 4.49, 6.78 and 9.06 GHz

4 Conclusion

In this paper HFSS simulation and full wave Green's function analysis of coaxial probe fed two layer HDRA is presented. From the mathematical analysis and simulation it is concluded that this antenna gives wider impedance bandwidth of 67.21% and higher gain of 9.8 dBi at 4.5 GHz. Thus a broadband HDRA can be obtained. This work can further extended for more number of layers and for different structures e.g. cylindrical and rectangular in future. This antenna radiates in broadside direction with high gain. This type of antennae can be used in wireless and 5G mobile communication applications where high gain and low loss characteristic are required. This work can be further extended for MIMO DRA [10] multi layer structure operating at multi band spectrum for next generation 5G network. MIMO DRA can also be designed using millimeter wave beam forming technique for 28 GHz spectrum which is the operating frequency range of 5G network. Whether lower frequency or higher frequency the advantages of using DRA to improve the performance of the network are appreciable. High efficiency, good bandwidth and increased antenna isolation implying to improved coverage, definite beam steering and reliable next generation network.

Acknowledgements This work was supported in part by Visvesvaraya PHD scheme/DIC/MeitY/ of govt. of India under ESDM/5G communications research scheme with reference number VISPHD-MEITY-779.

References

1. Luk KM, Leung KW (eds) (2003) Dielectric resonator antennas. Research Studies Press, Baldock
2. Long SA, McAllister MW, Shen LC (1983) The resonant cylindrical dielectric cavity antenna. IEEE Trans. Antennas Propagat. 31(5):406412

3. Kishk AA (2005) Experimental study of broadband embedded dielectric resonator antennas excited by a narrow slot. IEEE Antennas Propag Lett 4:79–81
4. Kishk AA, Zhou G, Glisson AW (1994) Analysis of dielectric-resonator antennas with emphasis on hemispherical structures. IEEE Antennas Propag Mag 36(2)
5. Leung KW (2000) Analysis of aperture-coupled hemispherical dielectric resonator antenna with a perpendicular feed. IEEE Trans, Antenna Propagat 48(6)
6. Wong KL, Chen NC, Chen HT (1993) Analysis of a hemispherical dielectric resonator antenna with an air gap. IEEE Microwave Guided Wave Lett 3(10):355–357
7. Kishk AA, Ahn B, Kajfez D (1989) Broadband stacked dielectric resonator antennas. Electron Lett 25:1232–1233
8. Ansoft HFSS 12.0. Ansoft Corporation, Pittsburgh
9. Leung KW, So KK (2000) Analysis of two layer spherical dielectric resonator. IEEE Microw Guided Wave Lett 10(4):139141
10. Zhang, Y., Deng, J. Y., Li, M. J., Sun, D., & Guo, L. X. (2019, April). A MIMO dielectric resonator antenna with improved isolation for 5G mm-wave applications. *IEEE Antennas and Wireless Propagation Letters, 18*(4), 747–751

Gitimayee Sahu is doing her Ph.D. from Usha mittal institute of technology under SNDT Women's University, Mumbai. She has pursued her M.Tech. from IIT kharagpur in RF and Microwave Engg. She has total 14 years of experience in teaching, industry and research. She has many publications in national and international conferences. She is student member of IEEE and life member of ISTE. Her research interest includes 5G, Heterogeneous cellular Network, cognitive radio and co-operative communications, RF, Microwave and Dielectric resonator antenna.

Sanjay S. Pawar is currently serving the Dept. of Electronics and Telecommunication in Usha Mittal institute of technology under SNDT Women's University, Mumbai. He has pursued his Ph.D. and M.Tech. from IIT, Bombay. He has total 24 years of teaching, research and industry experience. He has published many papers in international conferences and journals including IEEE. He has given various talks at National and International Conferences, Short term Training Programs, Workshops etc. in the area of Optical Networks, 5G Wireless Communications, Software Defined Networks, Mobile Cloud computing. He is senior member of IEEE, IEEE Communication Society and life member of ISTE. His research interest includes Optical Communication Network, Access and backbone Network, Software Defined Network and Storage and 5G Wireless Network.

Design and Implementation of Argo NI-NoC Micro-architecture for MPSoC Using GALS Architecture

H. R. Shashidhara, S. Nagendra Prasad, B. L. Prabhudeva and Subhash S. Kulkarni

Abstract As the networks on chips is used for designing the multi-processor system on chips, this platform have been typically guaranteed for hard real time property, and for the use of shared resources in a network. The service guarantees has to be provided by the network with respect to bandwidth and latency for a different communications flow. Thus message passing communications between the processor cores are implemented for the network on chip. The TDM is used for controlling the communications over the structures of router, links and network interface. The two main contribution of area efficient are (i) The TDM schedule with combined asynchronous router and (ii) The micro-architecture of NIs. In concert with the design resulted with the transforming the data in a pipelined manner which means transmitting the data from the local memory of send core to the local memory of the receive core, without using any dynamic attributions, buffering and local synchronization. The router also uses the two phase bundled data hand shake latches based on the mousetrap latch controller and it is extended with the gated mechanism for reducing the energy consumption. Network interface is used for integrating the DMA and the TDM functionalities. The dual ported local memory is used for avoiding buffering, flow controls and synchronization. Thus obtained result is verified with respect to area, power and gates.

Keywords Direct memory access (DMA) · Multi-processor system-on-chip · Open core protocol (OCP) · Time division multiplexing (TDM)

H. R. Shashidhara (✉)
National Institute of Engineering, Mysuru 570008, India
e-mail: shashidharahr@nie.ac.in

S. Nagendra Prasad · S. S. Kulkarni
PES University, Bangalore, India
e-mail: nagendraprasads@pes.edu

S. S. Kulkarni
e-mail: sskul@pes.edu

B. L. Prabhudeva
JSS Academy of Technical Education, Bengaluru 560060, India
e-mail: blprabhu14@gmail.com

© Springer Nature Singapore Pte Ltd. 2020

T. Hitendra Sarma et al. (eds.), *Emerging Trends in Electrical, Communications, and Information Technologies*, Lecture Notes in Electrical Engineering 569,
https://doi.org/10.1007/978-981-13-8942-9_37

1 Introduction

Network on Chip (NoC) is come forth as a very hopeful paradigm for scheming scalable communication architecture for System on chip. NoC is well designed to accomplish the bandwidth requirements between the cores of System on chips for the certain set of running application may be optimal for another sets of applications. In the other circumstances, the method for the designing of the initial NoC to change the working condition at each moment in time for variable set of real time applications, and also they are important for scheming competitor NoC in the industrial system on chips. However, the new NoC models are dynamically produce/cancel the lines between SOCs components and execute the run time topology for NoC and also the interconnection congestion to handle routing table reconfiguration, with the overhead of the limited operation. [1–6] However, in our experiment result, the addition of dynamic reconfigurations capacities into an introductory network on chips are used in our models implies an area limited overhead with respect to initial NoC pattern. Thus, the great benefits are provided when it is compared with tradition non-reconfigurable NoC pattern for worst case bandwidth requirement in SOC with potential set of running application.

Latest application in an embedded system such as communication protocol and a scalable video rendering uses a large power for computation, while some of the embedded design constraints as to be meat such as reduce implementation size, less energy consumption and short time to market. Hence, System on chip used in an embedded system are complex because embedded system are composed of large numbers of a factors such as reconfigurable devices, processing elements and a storage elements, to increase the tractability of the system on chip which can be used in a different environment condition. Never the less, the multi-processor system on chip (MPSOC) is designed by interconnecting the sub-system of the system on chip components, referable to the architecture and physical scalability vexation. The MPSOC is a system on chip which uses a multiprocessor or a multi-core for a communication inside a chip which are mainly used in embedded system applications. In order to match the large communication requirements of SOC, the scalable and the modular network on chips are used [10]. While designing a custom tailored network on chip interconnects, in order to satisfy the performance and the design constraint of the system on chip for many combinations of applications are the key goals in order to achieve optimal commercial products.

Since the processor cores are used to run the software tasks for the different applications in a system on chip, thus the communicating between the processor cores cannot be completely optimized and pre-characterized because the processes application can be mapped differently to the processors with the help of compiler. Hence, for providing the predictable performances of the network on chips, the capacity of the bandwidth for a different link is sufficient to provide the peak rate of traffic on the links in which the different possible mapping task are provided for a final system on chip design. Other than, the network might undergo traffic over-crowding and the traffic streams for the latency. Thus, the interlink performance become unaccepted

which as to be nullify to render the reserve consumer device. As a result, network on chips intently guarantees bandwidth worst case condition for system on chip operations with multiple co-occurring applications frequently leads to the outsized topologies and the regular operation links of the SOC. In other circumstances, the evolution of new method and framework will increases the run time wide variety of initial NOC design for a different working condition, developed by the variety of application at each moments, it is one of the important research area in field of the network on chip domain. However, the run time reconfigurable NOC frame-work have been introduced which can exploit the partial reconfigurable capability for field programmable gated arrays to adapt the implementation of network on chip interconnection for the specific functional requirement of the system on chips at each time consequence. Thence, the dynamically configured SOC can be used in the circuit switching communications. While add-on to this framework enables the fast dynamic re-configuration of the routing table with few cycles and the overall network topologies with few milliseconds delay, which in turn leads to the new promising think to get over the excessive crowding and providing large reliable and high performance network on chip models. [16–18] In the above cases suggested approaches enable the communication infrastructure which are dynamically reconfigured consequently to the need, which are spring up at the run time, in order to meet the latency and the throughput requirements. In turn this is possible by reducing the number of hops between switches which in turn reduces the latency between the two switches and their by introduces the new expression lines in the topologies which in turn increases the overall throughput of the network on chip directly.

The 2D mesh topologies of a multiprocessor platform are shown in Fig. 1. The processor consists of some amount of local memories such as caches memory and scratch pad memories (SPMs). The scratch pad memories are used as the source and object for the message passing between the processor cores.

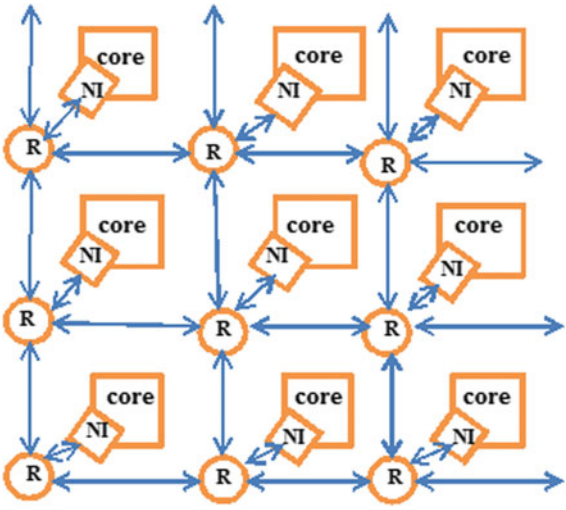

Fig. 1 2D mesh topology of NoC-based multiprocessor

The GALS architecture for the general purpose platforms are betrothed specifically used for the hard real time systems. And the message passing between the Network on chips is the main of this project, the two main requirement of the architecture and implementation are, (1) substantiates for a hard real time environment and (2) the GALS implementation. The detailed architecture of a processor core and Network interfaces are shown in Fig. 1. The processor and the router are connected through the network interface. The direct memory access (DMA) controller in the network interface lead up the message transmits from the scratch pad memory of one core to another core, by generating a specific NoC packet stream towards the network of router. Open Core Protocol (OCP) transmits a standard read and write transactions interface towards the processor cores are used to set up the DMA controller.

However in the hard real time system, the worst case execution time is necessary for executing the task on the processor and also for the execution of the set of communication tasks on the set of processor that are executed. The component included in the network on chip must be analyzed and time predictable to make the circuit enable. Most of the network on chip supports for the best traffic efforts and where some of the network on chip offers the multiple priority level in order to provide the quality of service, but none of this are tolerable for hard real time system. In order to keep away from the traffic interference and also for obtaining time predictability, the end to end virtual circuits must be provided for the network on chips with a given throughput and latency guarantees.

The statically scheduled time division multiplexing are used in the message passing network on chips for implementing the end to end circuit and for predicting the time. And the primary reason for choosing time division multiplexing as the alternative approach for predicting the time is ease: (1) ease of calculating the communication latency and (2) ease of implementing the hardware for the routers by using pipelined crossbar and without using any circuit for arbitration. This ease may results in disadvantages such as; (1) increasing the complexities of the network interfaces and (2) communications latencies are increased as a result time division multiplexing is not work conserving, which is the first main drawback for designing the architecture of network interfaces.

Time division multiplexing require the mutual opinion of the time across the platform to assure that the router and network interface in the network on chip mesh in synchronize with the global time division scheduling which in turn lead to the mesochronous executions used in the clocked router. Operating with the same frequency with delimited skew is known as mesochronous. The distinctive way of load bearing mesochronous synchronized by using mesochronous synchronizers. In demarcation with the designs using a pipelined asynchronies router. And the pipelined asynchronous offers some underlying first-in first-out capability. By exploiting the behavior of joined pipeline and first-in first-out, and also nullify the per-link synchroniser required for the mesochronous clocked network on chips. In this model, the router asynchronous of network is embedded in case of mesochronous Network interface which will derive the asynchronous router under the maximum speed. In the each clock cycle, the network interfaces transmit and receive a data token which can neither be valid nor void from the routers of network. Data will be sending from

the local memory of the processor core to the local memory of receiver processing core without overtaking any arbitrament buffering or clock domain synchronization circuits [26–32].

Transfer of data takes place through buses, as it is traditional method of transferring data. According to Moore's law the integration of the circuit is increasing exponentially to reduce the size and area occupied by the circuit on the chip, by making complexity in circuit connection. The design of traditional bus architecture is difficult for such complex circuit, which contain different processors in the same SOC. Hence, to transfer of the data a layered approach is used, so that they can be separately optimized. The two main layers used in the layered architecture are physical layer and transaction layer. Transaction layer work based on the application requirement on the other hand the physical layer work based on the characteristic of a silicon processes. Therefore the independent optimizations are possible for the layered architecture. The physical optimizations are used inside the network on chips for a several types of cell and thereby minimize the numbers of gate and wires. Some of the major benefits are;

Scalability: As the fabric size is reducing and it only deals with the packets transformation, many numbers of transaction such as request and waiting for channel can be handled. Contrarily, the transactions are controlled by Network Interface Unit's (NIU). Anyhow, in each NIU's the local performances can be adjusted which as the no determine over setups and the performances of the switching fabrics.

Effective throughput: is defined as the maximum amount of message delivered per unit time. Throughput of a particular path can be increased by selecting the appropriate physical transports and also the allocated several physical link for logical paths. As transition state is not stored in the switch fabric, effective throughputs only scales the operating frequencies and switches for width and link between them.

Quality of service: The service qualification that allowed by the network for demanding the processor core is known as quality of service. Higher priority packets interrupt long packets transparency to the transaction layer.

Timing convergence: The clock doesn't have any control over transaction and transport layers the physical layer is implemented based on the clocking scheme. GALS approach is the first implementation which is used by Aeteris. The traditional synchronous design style based for implementing the network on chip unit, it can be illustrated using the switches/NUI, and set of unit it can either uses a common clocks and/or independent clocks.

Easier verification: Main benefits of layering fits of designing and verification of the fabric can be done by divide and conquer method. This can be illustrated by the major portions of the verification of the fabric is required for functionality of the IP and transport level rules, as most of the behavior of the switching fabrics can independently verifies the transactions state.

The rest of this paper is organized as follows. The Background and related work is explained in Sect. 1. Overall architecture is explained in Sect. 2. And in Sect. 3, we present simulation results showing the efficiency of architecture. Finally, the conclusion is drawn in Sect. 4.

2 Overall Architecture

The overall architecture illustrating the end to end message transfer between the two processor cores is explained with the help of Fig. 2; a processor consists of some memories such as a cache memory and/or scratch-pad memories and a Direct-memory access controller. The scratch-pad memory and a DMA controller is used in embedded system in a many number of multiprocessor. In this architecture the SPM are used for the message passing seeable for the application programmers and for the avoiding the inexplicit cost with respect to the area, power, and latency which of using the cache memories.

The DMA controllers are designated for implementing the background direct memory access for driving the block transferring from the local memory of a processor cores into the local memory of another processor cores. Hence, the executing of programs inside the processor cores and transferring of data across the network on chip is entirely detached from each other, processor off loadings and analyzing

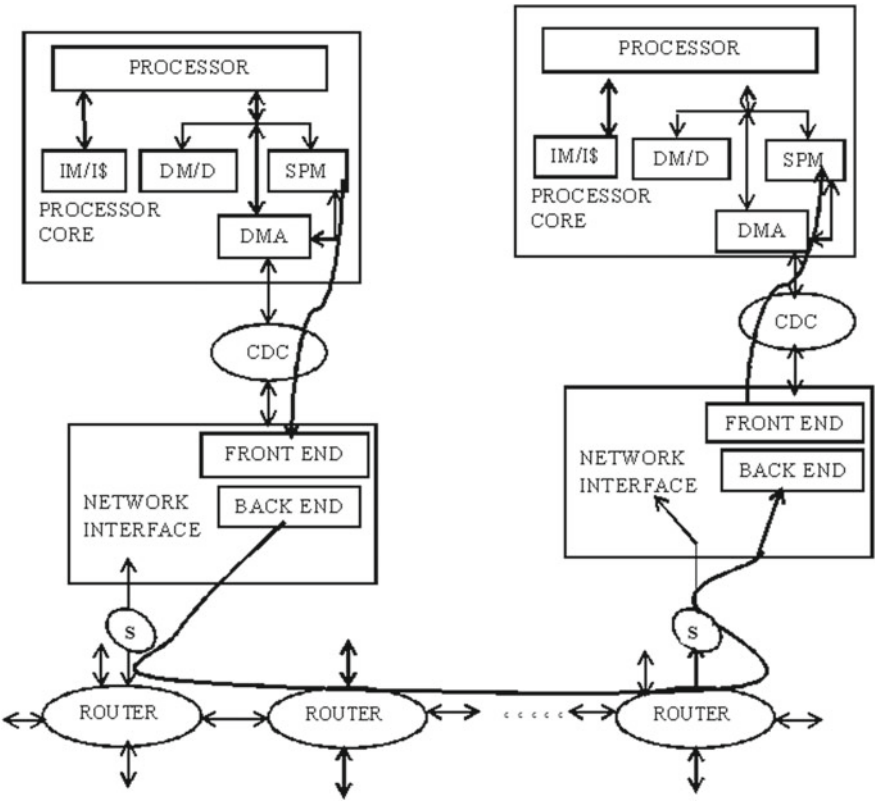

Fig. 2 Implementation of GALS multiprocessors architecture illustrating message passing between cores

the worst case execution time. The network interfaces are broadly classified as front end and a back end. The front end allows the one or more port is implemented in a standard bus style for interfacing the read and writes transitions towards the attached core. The network interface front end deals with the transformation data into another form of connections oriented cyclosis of packet. The network interface back end deals with the issues of lower level are specified for the specifics network on chips are used for packetization, routing, buffering and for the flow control, frequently used for implementing the credit based schemes. Large amount of data involves the data transaction for read and write operation and needed for transmitting a sequence of data packet. And also the back end handles the reassembling and splitting. The autonomous processes performs the three forms of message transfer is,

- Direct memory access controllers in the source nodes transfer the message/data into a buffer inside the network interface.
- The network interface inside the source nodes are used for packetizing the data and send the data. The packet denies the network on chips and is received at the destinations of network interface.
- From the destination node the direct memory access controllers for transferring the data from network interface into the scratch pad memories.

For implementing the GALS architecture, the processor core and the network interfaces operates at different and independent clock rate. Therefore the above three process are completely asynchronous in nature and the flow control is needed for this reason. The network interface must be in signal buffering status whether it is full/empty toward the direct memory access controller and there is some form of credit based flow controls are typically used between the network interfaces. In add on to this flow control, the end to end path requires two clock domains crossing between the processor cores and their NI, and also the FIFO synchronizers between the mesochronous network interface and the router.

The network interface in the network on chip plays a major role in implementation of end to end message passing between communication processor cores. Figures 3 and 4 indicates the design of the NI, consists of the slot counter, slot table, direct memory access table and scratch pad memories. The slot table stores time division multiplexing schedules, meanwhile the information of route of each channel is stored in the direct memory access table. The slot counter is reset and the network interface is incremented using the mesochronous clock. The current slots in the time division multiplexing period defines the slot counter. The slot table indicates the slot counter, where every entry contains the valid bit and is indicated in the direct-memory access table. The valid bit indexes the time slots is assigning for the leaving channel. If the valid bit is true, the entries accommodate the pointer for the relevant entries in the direct memory access table. An entry in the direct memory access table receives all the registers that are found in a normal DMA controller. In add-on to the required source routing with route for the remote transacting, this has been included in the direct memory address entries. The data will read from the scratch-pad memories address at the beginning of the read pointer address when direct memory access is activated. Since the data received will written to scratch pad memories at the terminus, thus

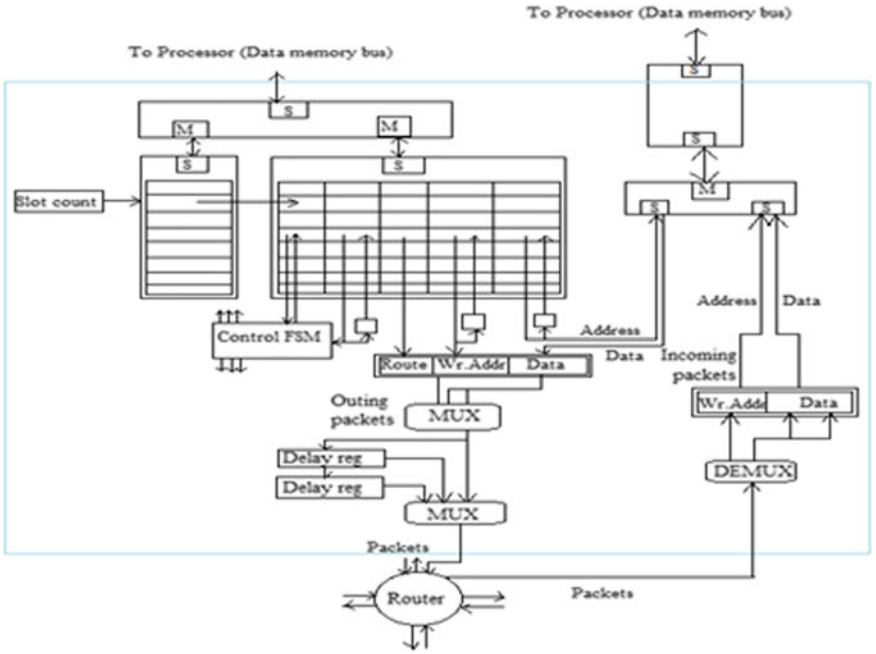

Fig. 3 Network interface architecture

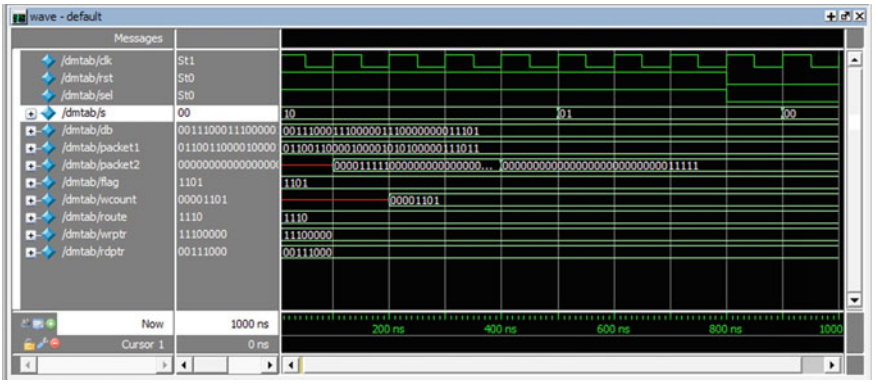

Fig. 4 Simulation results on Argo NI-NoC

the write pointer addresses the read and write of the SPM are done through network interface, since the scratch pad memory is dual ported. The network interface as two interfaces towards the processor. The OCP specifications are followed by this two processor and support the unique words are used for reading and writing transaction. Unique interfaces are used for configuring network interface and for writing the command and also reading the status from the direct memory access controller. Since the processor cores and network interface is at separate domain of clock, interface requires a clock domain for crossing. And also the interfacing uses for the data payloads and also across SPMs. Open core protocol is used for interfacing the processor with the NIs for providing dissociating form the processor designs and integration is simplified.

3 Simulation Results

Figure 5 shows the synthesis report of the top module of Argo NIs which includes memory bus, Multiplexer, De-Multiplexer, D-Flip Flop and an FSM control as sub modules. To evaluate and characterize the Argo NIs we have implemented its individual components. The designs were described in Verilog, simulated using ModelSim and the synthesis is done using CADENCE Tool. The design is verified with respect to power, area and timing. The simulation results shown in Fig. 4 verifies the functionality of the data flits. The wave form in the figure shows the packet formation with data.

In the above simulation results, to evaluate and characterize Argo, have implemented its individual components i.e., the asynchronous router and NI, as well as a complete 4 × 4 instance of the Argo NoC, including NIs, an input of 2048 bits of

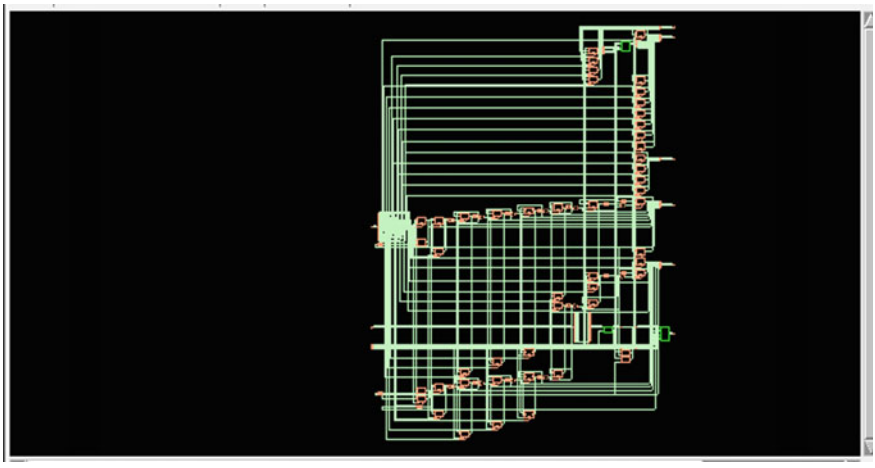

Fig. 5 RTL Schematic of Argo NI

Table 1 Cel number, Cell and Total Area of AGRO NI

Instance	Cells	Cell area	Total area
dmtab	304	3416	3416
×3	163	1878	1878
l3	32	654	654
l2	32	654	654
l4	67	352	352
l1	32	218	218
×2	62	420	420
×4	2	29	29

data bits are considered and reference of 8 bits of the data bits is considered. Then check for the repetition of the data bits with respect to the reference bits and store the repetition information in a position register in the proposed technique.

Table 1 shows the total area of the design after synthesis in cadence. The total cells areas used for particular instance are tabulated in Table 1. The cell area of the DMA table used is 3416. The fourth column shows the total area of the particular instance.

The total power of the design after synthesis in cadence are tabulated as shown in Table 2, the leakage power and dynamic power for each instance are shown in third and fourth column of Table 2. The fifth column show the total power consumed by the instance after synthesis.

Table 3 shows the number of gates used in the NI design after synthesis. It also the different types of gates such as Sequential, Inverter and Logic statistical report. It gives the number of gates in the different part of the circuit schematics.

Table 2 Power utilization report of Agro NI

Instance	Cells	Leakage power (nW)	Dynamic power (nW)	Total power (nW)
dmtab	304	19,814.873	52,427.164	72,242.037
×3	163	10,201.592	11,153.771	21,355.362
l2	32	3856.576	4476.851	8333.427
l3	32	3856.576	4382.676	8239.252
l1	32	1733.840	229.796	1963.636
l4	67	754.600	2064.448	2819.047
×2	62	2092.894	6456.976	8549.870
×4	2	217.706	573.125	790.831

Table 3 Different gates with area occupied

Gate	Instances	Area	Area%
Sequential	127	2519.720	73.8
Inverter	54	122.618	3.6
Logic	123	773.552	22.6
Total	304	3415.890	100.0

4 Conclusion

This work studies the Argo NI-network on chip which as planned statically and the time division multiplex of NoC supports the passing of messages between the processors among the multi-processor platforms and optimize for the use of hard real time system. And also the GALS timing organization uses the individually clocking processors core and mesochronous Network interfaces which are supported by the Argo. Network on chip processor are modeled with an outlook of enclosing and the layering of resource for the use of buffering and for flow control. In the clocked domains synchronized for the significant amount of the implemented costs with respect to area. As the work presents the architecture, model, Argo implementations, and also presents the extended result for the speed, area, and power characterization. The passing of message is completely predicted by the time and the end to end message passing latencies are analyzed statically. The Argo based network on chip is 3.5 times leastwise smaller than the existent model with standardized functionality. Thus by making the Argo suitable for the communications and for developing future multiprocessor system for hard real time applications.

References

1. Dally WJ, Towles B (2001) Route packets, not wires: on-chip interconnection networks. In: Proceedings of the Design Automation Conference, pp 684–689
2. Benini L, De Micheli G (2002) Networks on chips: a new SoC paradigm. Computer 35(1):70–78
3. Clermidy F et al (2010) A 477 mW NoC-based digital baseband for MIMO 4G SDR. In: IEEE international solid-state circuits conference on digital technical papers, pp 278–279
4. Howard J et al (2011) A 48-core IA-32 processor in 45 nm CMOS using on-die message-passing and DVFS for performance and power scaling. IEEE J Solid-State Circuits 46(1):173–183
5. Plana LA et al (2011) SpiNNaker: design and implementation of a GALS multicore system-on-chip. ACM J Emerg Technol Comput Syst 7(4), Art. ID 17
6. Benini L, Flamand E, Fuin D, Melpignano D (2012) P2012: building an ecosystem for a scalable, modular and high-efficiency embedded computing accelerator. In: Proceedings design, automation test in Europe (DATE), pp 983–987
7. Schoeberl M, Chong DV, Puffitsch W, Sparsø J (2014) A time predictable memory network-on-chip. In: Proceedings of the 14th international workshop worst-case execution time analysis (WCET), p 53
8. Accellera Systems Initiative (2013) Open core protocol specification, Release 3.0. [Online]. Available: http://www.accellera.org/ downloads/standards/ocp/ocp_3.0/

9. Moraes FG, Mello A, Möller L, Ost L, Calazans NLV (2003) A low area overhead packet-switched network on chip: architecture and prototyping. In: IFIP/IEEE International Conference on Very Large Scale Integration (VLSI-SOC), pp 318–323
10. Beigne E, Clermidy F, Vivet P, Clouard A, Renaudin M (2005) An asynchronous NOC architecture providing low latency service and its multi-level design framework. In: Proceedings of the 11th IEEE International symposium asynchronous circuits system (ASYNC), pp 54–63
11. Dall'Osso M, Biccari G, Giovannini L, Bertozzi D, Benini L (2012) Xpipes: a latency insensitive parameterized network-on-chip architecture for multi-processor SoCs. In: Proc. IEEE 30th international conference on computer design (ICCD), pp 45–48
12. Dobkin R, Vishnyakov V, Friedman E, Ginosar R (2005) An asynchronous router for multiple service levels networks on chip. In: Proceedings of the 11th IEEE international symposium of the asynchronous circuits system (ASYNC), pp 44–53
13. Felicijan T, Furber SB (2004) An asynchronous on-chip network router with quality-of-service (QoS) support. In: Proceedings of the IEEE international system-chip conference (SOCC), pp 274–277
14. Goossens K, Hansson A (2010) The Æthereal network on chip after ten years: goals, evolution, lessons, and future. In: Proceedings of the ACM/IEEE design automation conference (DAC), pp 306–311
15. Bjerregaard T, Sparsø J (2005) Scheduling discipline for latency and bandwidth guarantees in asynchronous network-on-chip. In: Proceedings of the 11th IEEE International symposium asynchronous circuits system (ASYNC), pp 34–43
16. Sutherland IE (1989) Micropipelines. Commun ACM 32(6):720–738
17. Sparsø J, Kasapaki E, Schoeberl M (2013) An area-efficient network interface for a TDM-based network-on-chip. In: Proceedings of the design, automation test in Europe (DATE), Mar. 2013, pp. 1044–1047
18. Kasapaki E, Sparsø J, Sørensen RB, Goossens K (2013) Router designs for an asynchronous time-division-multiplexed network-onchip. In: Proceedings of the Euromicro conference digital system design (DSD), pp 319–326
19. Kasapaki E, Sparsø J (2014) Argo: a time-elastic time-division multiplexed NOC using asynchronous routers. In: Proceedings of the 20th IEEE international symposium asynchronous circuits system (ASYNC), pp 45–52
20. Sørensen RB, Sparsø J, Pedersen MR, Højgaard J (2014) A metaheuristic scheduler for time division multiplexed networks-on-chip. In: Proceedings of the IEEE/IFIP workshop software technology future embedded ubiquitous system (SEUS), pp 309–316
21. Singh M, Nowick S (2007) MOUSETRAP: high-speed transition signaling asynchronous pipelines. IEEE Trans Very Large Scale Integr (VLSI) Syst 15(6):684–698
22. Wolkotte PT, Smit GJM, Rauwerda GK, Smit LT (2005) An energy-efficient reconfigurable circuit-switched network-on-chip. In: Proceedings of the 19th IEEE international parallel distributed processing symposium (IPDPS), p 155a
23. Wiklund D, Liu D (2003) SoCBUS: switched network on chip for hard real time embedded systems. In: International parallel & distributed processing symposium (IPDPS), p 78a
24. Goossens K, Dielissen J, R˘adulescu A (2005) Æthereal network on chip: concepts, architectures, and implementations. IEEE Des Test Comput 22(5):414–421
25. Hansson A, Goossens K (2011) On-chip interconnect with aelite/composable and predictable systems. Springer, New York
26. Millberg M, Nilsson E, Thid R, Jantsch A (2004) Guaranteed bandwidth using looped containers in temporally disjoint networks within the nostrum network on chip. In: Proceedings of the design, automation test in Europe (DATE), pp 890–895
27. Schoeberl M (2007) A time-triggered network-on-chip. In: Proceedings of the international conference field-programming logic and application (FPL), pp 377–382
28. Paukovits C, Kopetz H (2008) Concepts of switching in the time triggered network-on-chip. In: Proceedings of the 14th IEEE international conference embedded real-time computing systems and applications (RTCSA), pp 120–129

29. Zhang H (1995) Service disciplines for guaranteed performance service in packet-switching networks. Proc IEEE 83(10):1374–1396
30. Harrand M, Durand Y (2013) Network on chip with quality of service. U.S. Patent 8 619 622, Dec 31. [Online]. Available: http://www.google.com/patents/US8619622
31. Sparsø J (2012) Networks-on-chip for real-time multi-processor systems-onchip. In: Proceedings of the international conference application of concurrency to system design (ACSD), pp 1–5
32. Le Boudec J-Y (1998) Application of network calculus to guaranteed service networks. IEEE Trans Inf Theory 44(3):1087–1096
33. Bakhouya M, Suboh S, Gaber J, El-Ghazawi T (2009) Analytical modeling and evaluation of on-chip interconnects using network calculus. In: Proceedings of the 3rd ACM/IEEE international symposium network-chip (NOCS), pp 74–79
34. Zheng S, Burns A, Indrusiak LS (2010) Schedulability analysis for real time on-chip communication with wormhole switching. Int J Embedded Real-Time Commun Syst 1(2):1–22
35. Indrusiak LS (2014) End-to-end schedulability tests for multiprocessor embedded systems based on networks-on-chip with priority-preemptive arbitration. J Syst Archit 60(7):553–561
36. Qian Y, Lu Z, Dou Q (2010) QoS scheduling for NoCs: strict priority queueing versus weighted round robin. In: Proceedings of the IEEE international conference computer design (ICCD), pp 52–59
37. Modarressi M, Sarbazi-Azad H, Arjomand M (2009) A hybrid packetcircuit switched on-chip network based on SDM. In: Proceedings of the conference design, Automation and test in Europe (DATE), pp 566–569
38. Chen G et al (2014) 16.1 A 340 mV-to-0.9 V 20.2 Tb/s source-synchronous hybrid packet/circuit-switched 16 × 16 network-on-chip in 22 nm trigate CMOS. In: IEEE international solid-state circuits conference on digest of technical papers (ISSCC), pp 276–277
39. Ou P et al (2013) A 65 nm 39 GOPS/W 24-core processor with 11 Tb/s/W packet-controlled circuit-switched double-layer network-on-chip and heterogeneous execution array. In: IEEE international solid-state circuits conference on digest of technical papers (ISSCC), pp 56–57
40. Goossens K, Dielissen J, Radulescu A, Rijpkema E, Wielage P (2006) Electronic device and a method for arbitrating shared resources. WO Patent 2 006 092 768, 8 Sept 2006
41. The International Technology Roadmap for Semiconductors (2011) ITRS 2011 Edition—Design. [Online]. Available: http://www.itrs.net/
42. Panades IM, Greiner A, Sheibanyrad A (2006) A low cost network on-chip with guaranteed service well suited to the GALS approach. In: Proceedings of the 1st international conference on nano-network (Nano-Net), pp 1–5
43. Dally WJ, Poulton JW (1998) Digital systems engineering. Cambridge University Press, Cambridge
44. Panades IM, Greiner A (2007) Bi-synchronous FIFO for synchronous circuit communication well suited for network-on-chip in GALS architectures. In: Proceedings of the IEEE/ACM International Symposium Network-Chip (NOCS), pp 83–92
45. Wielage P, Marinissen EJ, Altheimer M, Wouters C (2007) Design and DfT of a high-speed area-efficient embedded asynchronous FIFO. In: Proceedings of the design, automation test in Europe (DATE), pp 1–6
46. Bainbridge J, Furber S (2002) Chain: a delay-insensitive chip area interconnect. IEEE Micro 22(5):16–23
47. Flachs B et al (2006) The microarchitecture of the synergistic processor for a cell processor. IEEE J Solid-State Circuits 41(1):63–70
48. Berozzi D (2006) Network interface architecture and design issues. In: DeMicheli G, Benini L (eds) Networks on chips, Ch 6, pp 203–284. Morgan Kaufmann, San Mateo
49. Sparsø J (2001) Asynchronous circuit design—A tutorial. In: Sparsø J, Furber S (eds) Principles of asynchronous circuit design—a systems perspective, Chs 1–8, pp 1–152. Kluwer, Norwell

High Speed, Low Matchline Voltage Swing and Search Line Activity TCAM Cell Array Design in 14 nm FinFET Technology

K. Prasanth, M. Ramireddy, T. Keerthi priya and S. Ravindrakumar

Abstract To design cost and energy efficient memory cell various designs are introduced in recent days. The power consumed by the memory cell array is reduced at nanometer scale but increases if frequency of operation increases. The search operation consumes more power and to reduce it TCAMs were introduced which compares entire data with search bit in single clock cycle. In past TCAMs were designed using MOSFET devices. These devices suffer from second order effects below 45 nm. This paper presents a FinFET based TCAM cell array designed in 14 nm technology. The memory device proposed works faster, has Low Matchline Voltage Swing and Search Line Activity. The proposed FinFET design is efficient when compared to CMOS methods where a 93.3 and 96% less power is obtained. An energy reduction of 10.97 and 60.08% is observed when compared to existing method 1 and 2 respectively.

Keywords FinFET · CMOS · Energy efficient · Power saving · TCAM · Matchline · Search line activity · Low area

1 Introduction

The advantages of TCAM (ternary content-addressable memory) have spread its utilization in several application. Unlike RAM, the TCAM access the memory using query rather than the direct mapped addressing in RAM devices. TCAM cell shows excellent tolerance to the variations of device characteristics under the same oper-

K. Prasanth · M. Ramireddy · T. Keerthi priya
ECE Department, Srinivasa Ramanujan Institute of Technology, Anantapur, Andhra Pradesh, India
e-mail: prashanthk.ece@srit.ac.in

M. Ramireddy
e-mail: ramireddy.ece@srit.ac.in

T. Keerthi priya
e-mail: keerthipriya.ece@srit.ac.in

S. Ravindrakumar (✉)
Sri Shakthi Institute of Engineering and Technology, Coimbatore, Tamil Nadu, India
e-mail: gsravindrakumar7@gmail.com

© Springer Nature Singapore Pte Ltd. 2020

T. Hitendra Sarma et al. (eds.), *Emerging Trends in Electrical, Communications, and Information Technologies*, Lecture Notes in Electrical Engineering 569,
https://doi.org/10.1007/978-981-13-8942-9_38

ating condition and device variations. It shows smaller failure rate. But this type of TCAM suffers from complexity design and high power consumption. To improve the disadvantages this paper presents the FInFET—Fin Field Effect Transistor based TCAM cell array design. Reduction of power consumption is one of the biggest challenges in TCAM design with decrease the speed or memory density. During the analyses of match detection, switching of highly capacitive Match lines (ML) and Search lines (SL) cause huge power consumption. Several further modified schemes are discussed and compared in literature [1]. A 16 × 16 bit TCAM powered by 1.8 V is presented with dedicated comparison circuitry of ML sensing schemes reduces power consumption by minimizing and limiting voltage swing of MLs. TCAM can only report the first matching entry because updating TCAM entries would be slow down entry reordering [2]. Trie-based algorithm, longest suffix split, to reduce the number of TCAM entries for IP address lookup.

A new ternary content addressable memory (TCAM) was presented by Sho Hayakawa et al. [3]. A novel 13T-4R NV-TCAM cell has a symmetric structure and a current limiter in order to improve the DC and leakage current problems for previous NV-TCAM cells [4]. Fonseca et al. [5] presented the functionality of NML, and shown that the memories work as expected. This work shows a potential tool for NML components design. By employing the gated ML pull down path and ML boosting scheme, the redundant ML discharging and SL switching are eliminated while improving the search speed in TCAM [6]. The present number of mismatch and ML discharging speed, the ML discharging is adaptively controlled in TCAM. A magnetic tunneling junction (MTJ)-based ternary content-addressable memory (TCAM) cell which consists of 12 transistors and two MTJs [7] consumes low static power during search operation and therefore ensures highly energy efficient operation. For processing Open Flow compliant a low-power dynamic is reconfigurable in TCAM design [8]. Pipelined-TCAM can achieve lower energy-delay products than traditional TCAM. It is very suitable for the emerging high performance packet processing. But the design complexity increases. Meng-Chou Chang presented [9] FinFET based TCAM in 32 nm. A MTCAM with 2-Transistors-2 Memristors bit-cell has storing and fetching capabilities which builds on a bipolar memristor model based on the actual current-voltage behavior [10]. The emulation suffers from reduced memory efficiency while mapping the TCAM table this is due to the limited capacity of the physical addresses in the SRAM unit [11]. This approach virtually increases the overall address space in SRAM unit for mapping a greater portion of the TCAM table to increase the TCAM bits/SRAM at the cost of reduced throughput. The other works include a 3T-2R nonvolatile ternary CAM and Gate-Based Area-Efficient Ternary Content-Addressable Memory. Different Match line sensing schemes in high speed Ternary content addressable memory is available.

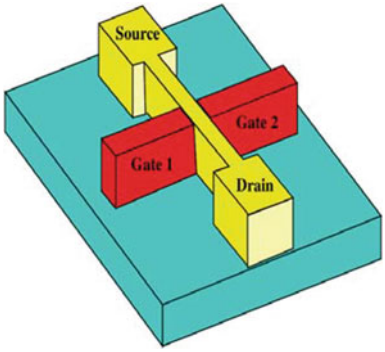

Fig. 1 Triple-gate version of FinFET architecture

1.1 FinFET Fundamentals

FinFETs have been an alternate technology for CMOS [12]. The continued scaling has created new challenges in design [13]. But the compatibility of FinFET's fabrication with the CMOS helped the designers to ease the complexity. Figure 1 Shows the triple gate version of FinFET. Using FinFET several circuits are designed in literature [14] width quantization and electrical confinement (quantum-mechanical effect) even in subthreshold regime [15].

2 Existing Method

The charge sharing based match line sensing scheme [16] is shown in Fig. 2. To achieve lower energy consumption during match line sensing, this method was implemented. Here the charge sharing circuits, sensing circuits, TCAM Cell and other circuits are designed and implemented in 130 nm CMOS technology. Less energy consumed circuits are attained by reducing the number of control signals, which need to be generated off-chip. The circuit consists of two segments—Match

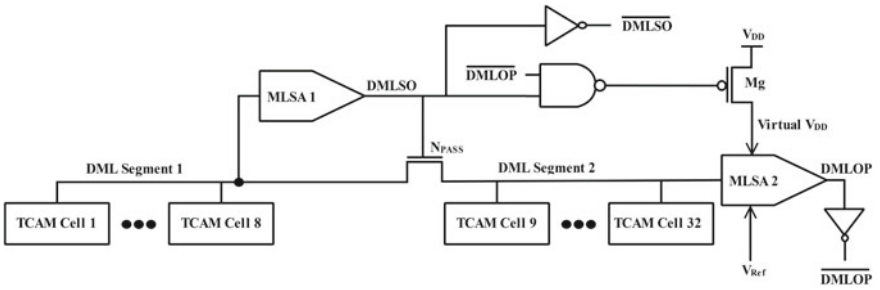

Fig. 2 Block diagram representation of the charge sharing based match line sensing scheme

Line Sensing Amplifier MLSA 1 and 2. The first segment consists of charging and sensing unit. The second segment consists of sensing unit followed by differential amplifier. The entire system will get reset once the match line reset signal (MLRST) signal is enabled. The system became active when the MLEN (Match Line Enable) signal becomes high. To reduce the energy consumption the circuit sensing operation is carried out using match and mismatch condition. The entire search word is sensed with each word and to reduce energy consumption 8 MSB (Most Significant Bit) are compared with TCAM memory. During the search operation charging current is transferred through N_{PASS} transistor. In case of matched condition, segment 1 is get charged through transferred charge up to its threshold value (N1). Then the sensing outputs MLSO and DMLSO go high. Once these signals are high, the M1 stops its charging process. And its reverse procedure is followed by segment 2 in the mismatch condition.

The another existing method [17] implemented in 65 nm and having low voltage match line sensing scheme is shown in Fig. 3. The sub circuits are used to reduce power consumption during match line sensing process. The circuits contributing major role to reduce power consumption are voltage down converter, differential sense amplifier with match line isolation and reference voltage generation scheme. The authors presented the energy consumption alone which is 1651 fJ. Power consumption was not presented. But the proposed method energy consumption is less as per Table 2.

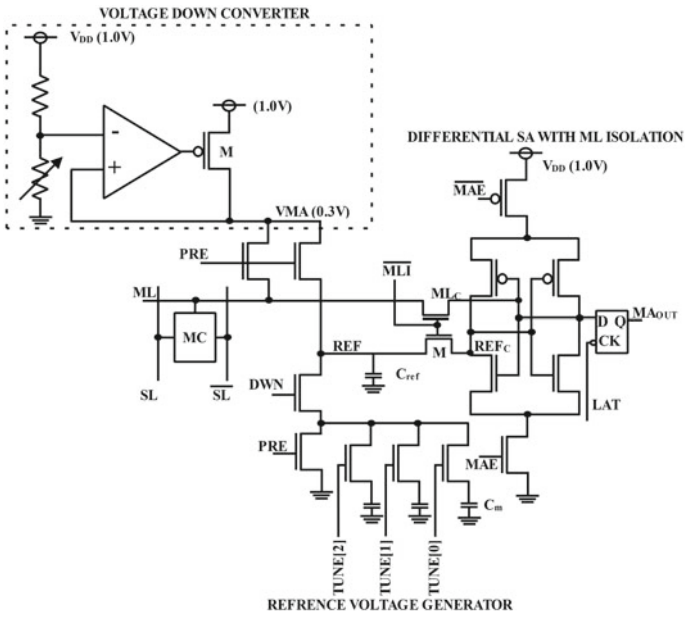

Fig. 3 An existing full ternary CAM with low-voltage matchline sensing scheme

Other novel methodologies and features were included and done in literature for the design of TCAM with non volatile feature [19], decoupled dynamic type [20], low power matchlines [21] and high reliability [21, 22]. The memory becomes a part of larger signal processing architectures which can be designed using FinFET devices [23].

3 Proposed Method

To design cost and energy efficient memory cell, various designs are introduced in recent days. While accounting power consumption, there are various parameters which causes power consumption in memory. Among all those search operation is most important parameter which consumes more power. It can be observed that as the feature size of CMOS reduces below 45 nm and smaller, short channel effects will rise. Due to that power dissipation is also increases. The structure of TCAM cell is shown in Fig. 4. It is a combination of both Data SRAM and MASK SRAM. The structure of TCAM cell consists of four NFinFET transistors rather than two RAM cells. From those transistors N5 and N6 transistors are used to compare stored data with search data. It compares data stored in RAM (Q/Q_{Bar}) with search data (SL/SL_{Bar}). On the other hand N7 and N8 are used to create discharge path to Match Line (ML). These two transistors plays important role in reducing the power consumption. Once the original data is matched with search data, after that both the transistor can create the discharge path. The circuit operation of proposed low voltage swing Match Line Accelerating Sense Amplifier (MLA-SA) consists of three operating cases such as Reset Phase, Match and Mismatch case which is shown in Fig. 5. During the reset phase MLRST signal is logic 1 and the entire system get reset, then the node $B = 0$ and node SN and A become charged to V_{DD}.

After the reset phase, the search operation is initiated by P3 transistor. It is provided with short I_{PULSE} current instead of constant current source. This idea also results in low power consuming design. Since ML get discharge, instead it boost up the node X, once the node X is high it will turn ON the transistor N6. It adds some additional current to charge the ML. Obviously the node SN starts to discharge. Then the match line (ML) becomes high and shows match case. In mismatch condition the I_{PULSE} cannot turn on the transistor N6. Then the node SN becomes high because it is associated with N6. If SN is high then MLSO becomes low and shows that Mismatch condition.

4 Results and Discussion

The proposed method is executed with three different frequencies like 1, 2 and 3 GHz. In the existing method 1 GHz frequency is used. Table 1 shows the performance comparison of the proposed FinFET based TCAM cell with the existing method.

Table 2 shows the performance of proposed TCAM cell for different frequencies. The average power, average current and average energy are observed and tabulated. On analysis the proposed method consumes 93.3% less power than the existing method 1 and consumes 96.32% less power than the existing method 2. When energy is considered, the proposed method consumes 10.97% less energy than the existing method 1 and consumes 60.08% less energy than the existing method 2. For the simulation of the circuits, Synopsis HSpice and PTM models were utilized.

5 Conclusion and Future Work

In this paper a FinFET based TCAM Cell array is designed and implemented in 14 nm technology. The problem with the CMOS TCAM Cell array was addressed and experimented. From the analysis it's been found that the FinFET based device performance is superior than the CMOS technology below 45 nm. To overcome

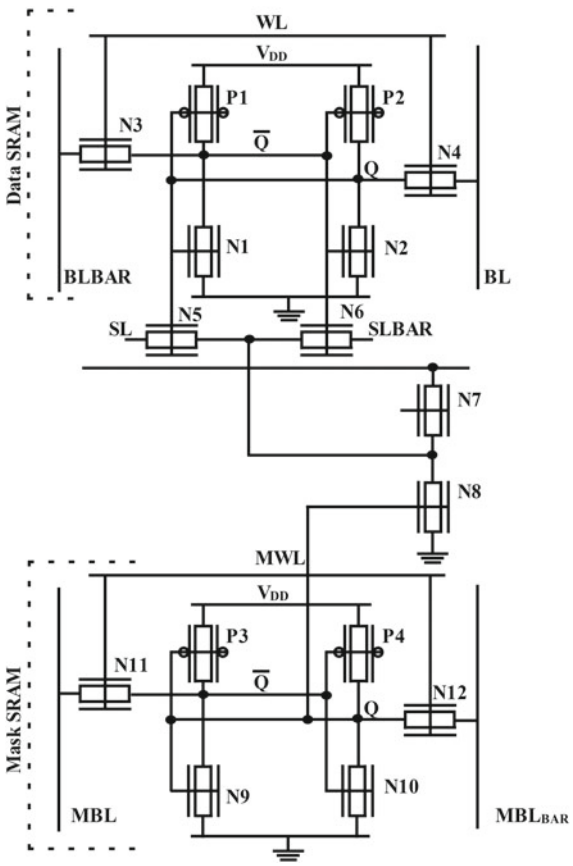

Fig. 4 TCAM cell

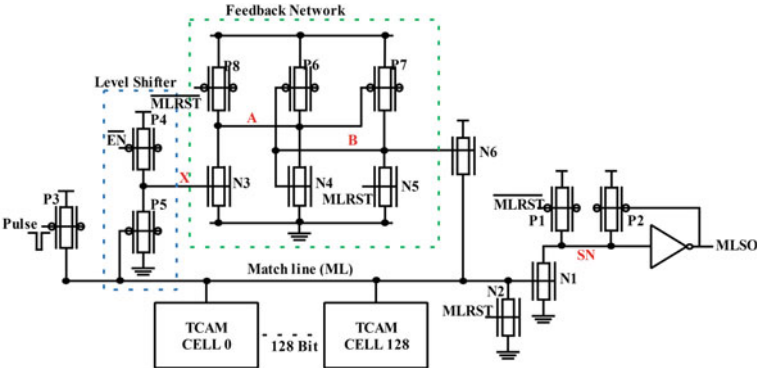

Fig. 5 Proposed FinFET based TCAM cell with match line accelerating sense amplifier

Table 1 Performance of 32 bit TCAM cell array for existing and proposed method (frequency = 1 GHz)

Methods	Average current (A)	Average power (W)	Average energy (J)
Existing method [16]	–	8.32×10^{-6}	310.22×10^{-15}
Existing method [18]	184×10^{-6}	470×10^{-6}	696.36×10^{-15}
Proposed method	265.33×10^{-9}	506.83×10^{-9}	276.18×10^{-15}

Table 2 Performance of the proposed FinFET based 32-bit TCAM cell array for different frequencies

Frequency (GHz)	Average current (A)	Average power (W)	Average energy (J)
1	265.33×10^{-9}	506.83×10^{-9}	276.18×10^{-15}
2	46.331×10^{-9}	486.17×10^{-9}	305.46×10^{-15}
3	1.5343×10^{-6}	1.606×10^{-6}	849.28×10^{-15}

this small area, low power design is proposed using FinFET in shorted gated mode. Performance was reported. From the analysis it's been found that the FinFET design seems efficient when compared to CMOS. The proposed method consumes 93.3% less power than the existing method 1 and 96.32% less power than the existing method 2. An energy reduction of 10.97 and 60.08% is observed when compared to existing method 1 and 2 respectively.

References

1. Foysal MA, Anam MZ, Islam MS, Tahmid I, Mondal K (2015) Performance analysis of ternary content addressable memory (TCAM). In: International conference on advances in electrical engineering (ICAEE), pp 105–108

2. Huang JY, Wang PC (2018) TCAM-based IP address lookup using longest suffix split. IEEE/ACM Trans Netw 26(2):976–989
3. Hayakawa S, Yoshida M (2016) Interrogation properties of ternary content addressable memory using a CMOS-SRAM cell. In: SAI computing conference (SAI), pp 1361–1364
4. Park HK, Song B, Jung SO (2018) Low search power and high reliability 13T-4R MTJ based nonvolatile ternary content-addressable memory. In: International conference on electronics, information, and communication (ICEIC), pp 1–4
5. Fonseca AF, Willian DL, Soares TRBS, Melo LGC, Neto OPV (2017) CAM/TCAM—NML: (ternary) content addressable memory implemented with nano magnetic logic. In: 30th symposium on integrated circuits and systems design (SBCCI), pp 174–179
6. Choi W, Lee K, Park J (2018) Low cost ternary content addressable memory using adaptive match line discharging scheme. In: IEEE international symposium on circuits and systems (ISCAS), pp 1–4
7. Cho D, Kim K, Yoo C (2018) A non-volatile ternary content-addressable memory cell for low-power and variation-toleration operation. IEEE Trans Magn 54(2):1–3
8. Chen TS, Lee DY, Liu TT, Wu AY (2016) Dynamic reconfigurable ternary content addressable memory for open flow-compliant low-power packet processing. IEEE Trans Circuits Syst I Regul Pap 63(10):1661–1672
9. Chang MC, Liu SS (2016) FinFET-based TCAMs with match line-accelerating sense amplifiers. In: IEEE 5th global conference on consumer electronics, pp 1–2
10. Bahloul MA, Naous R, Masmoudi M (2017) Hardware emulation of memristor based ternary content addressable memory. In: 14th international multi-conference on systems, signals & devices (SSD), pp 446–449
11. Ahmed A, Park K, Baeg S (2017) Resource-efficient SRAM-based ternary content addressable memory. IEEE Trans Very Large Scale Integr (VLSI) Syst 4(25):1063–8210
12. Hadia SK, Patel RR, Kosta YP (2011) FinFET architecture analysis and fabrication mechanism. IJCSI Int J Comput Sci Issues 8:235–240
13. Rudenko T, Kilchytska V, Collaert N, Nazarov A, Jurczak M, Flandre D (2007) Electrical characterization and special properties of FinFET structures. In: Proceedings of conference on nano scaled semi conductor on insulator structures and devices, pp 199–220
14. Duarte JP, Khandelwal S, Medury A, Hu C, Kushwaha P, Agarwal H, Dasgupta A, Chauhan YS (2015) BSIM-CMG: standard FinFET compact model for advanced circuit design. In: 41st European solid-state circuits conference (ESSCIRC), pp 196–201
15. Rasouli SH, Endo K, Banerjee, K (2009) Variability analysis of FinFET based devices and circuits considering electrical confinement and width quantization. In: Proceedings of IEEE/ACM international conference on computer aided design, pp 505–512
16. Ali IS, Islam MS (2011) A novel low-energy match line sensing scheme for ternary content addressable memory using charge sharing. In: Proceedings of NORCHIP, pp 1–4
17. Hayashi I, Amano T (2013) A 250-MHz 18-Mb full ternary CAM with low-voltage matchline sensing scheme in 65-nm CMOS. In: Proceedings of IEEE journal of solid-state circuits, pp 2671–2680
18. Chang MC, Liu SS (2016) FinFET-based TCAMs with matchline-accelerating sense amplifiers. In: Proceedings of IEEE 5th global conference on consumer electronics, pp 1–2
19. Cho D, Kim K, Yoo Y (2018) A non-volatile ternary content-addressable memory cell for low-power and variation-toleration operation. In: IEEE transactions on magnetics, pp 1–3
20. Delgado-Frias JG, Nyathi J, Tatapudi SB (2005) Decoupled dynamic ternary content addressable memories. In: IEEE transactions on circuits and systems, pp 2139–2147
21. Yang S, Huang Y, Li J (2012) A low-power ternary content addressable memory With Pai-Sigma matchlines. In: IEEE transactions on very large scale integration (VLSI) systems, pp 1909–1913
22. Park H, Song B, Jung S (2018) Low search power and high reliability 13T-4R MTJ based nonvolatile ternary content-addressable memory. In: International conference on electronics, information, and communication, pp 1–4

23. Senthilkumar VM, Ravindrakumar S (2018) A low power and area efficient FinFET based approximate multiplier in 32nm technology. In: springer—book on soft computing and signal processing

Low-Power and Area-Efficient Design of Higher-Order Floating-Point Multipliers Using Vedic Mathematics

Haripriya Loganathan, Patnaikuni Rohit, Polamarasetty Sai Suneel and Karthi Balasubramanian

Abstract Floating-point arithmetic units form the backbone of the state-of-the-art digital signal processing algorithms. Low power and area efficient design is always a key requirement for applications that use these algorithms. This requirement is more relevant for computationally intensive jobs that use higher-order multipliers. This paper attempts to study the possibility of addressing this issue using vedic arithmetic based floating-point unit. Vedic mathematics is an ancient Indian mathematics system that has come back to prominence in the last century. In this paper, we design a IEEE 754 single precision floating-point multiplier with the integer multiplication being carried out in a vedic mathematics style using different sutras. Nikhilam and Urdhva Tiryagbhyam sutras and their combination are used to design the same. This implementation is compared with conventional implementations using Booth and array multipliers. The designs are simulated using Verilog and synthesized using gpdk 90 nm technology. The results show that vedic multiplier based design gives competing results for multipliers of larger sizes. Low power and area efficient design is achieved for higher order multipliers when the design is based on the combination of Nikhilam and Urdhva Tiryagbhyam sutras. Thus for DSP applications using large multipliers, it is envisaged this approach of vedic multiplier design would lead to more efficient system implementations.

Keywords Floating-point unit · IEEE 754 standard · Vedic multiplier · Urdhva Tiryagbhyam sutra · Nikhilam sutra

1 Introduction

Demand for high speed and low power computations has been steadily increasing for various digital signal processing (DSP) systems [1]. Floating-point multipliers (FPM) are widely used in DSP systems and the efficiency of these DSP systems rely heavily on the constituent FPM. Due to the complexity of the arithmetic involved

H. Loganathan · P. Rohit · P. S. Suneel · K. Balasubramanian (✉)
Department of Electronics and Communication Engineering, Amrita School of Engineering, Amrita Vishwa Vidyapeetham, Coimbatore, India
e-mail: b_karthi@cb.amrita.edu

© Springer Nature Singapore Pte Ltd. 2020

T. Hitendra Sarma et al. (eds.), *Emerging Trends in Electrical, Communications, and Information Technologies*, Lecture Notes in Electrical Engineering 569,
https://doi.org/10.1007/978-981-13-8942-9_39

in analyzing floating-point numbers, FPMs are generally area and power hungry devices. Hence, it becomes imperative to look at design solutions for FPMs that have low power and area especially for multipliers of larger sizes.

Floating-point multiplier uses adders, shifters and integer multipliers to perform floating-point multiplication [2–4]. The design of the integer multiplier block is one of the key components in the FPM design. Traditionally, array multipliers and Booth multipliers [5, 6] have been used by researchers for designing the integer multiplier in FPMs [7, 8]. Array and Booth multipliers are fast but they consume large area and power respectively.

One alternative that is less explored is the use of Vedic multipliers to do the same. Vedic multipliers are generally designed using two sutras (aphorisms) namely Urdhva Tiryagbhyam and Nikhilam. Tiwari et al. in [9], Kanhe et al. in [10] and Havaldar et al. in [11] have used Urdhva Tiryagbhyam sutra for the multiplier implementation while Patel et al. in [12] and Budhiraja in [13] have designed both Urdhva Tiryagbhyam and Nikhilam based multipliers. An example of a vedic mathematics based multiplier-accumulator block is given in [14]. Works like these have analyzed and shown the implementation results for different multiplier sizes using the above two sutras independently but they have not explored the possibility of using both the sutras in one design itself.

The hardware structure of the Urdhva Tiryagbhyam based design is very similar to an array multiplier that requires multiple adders at the final stage of calculation. Thus it becomes less efficient while dealing with large numbers. Nikhilam sutra based design is more effective for large numbers but its efficiency is fully harnessed only when the numbers being multiplied are close to a reference value. This paper is aimed at designing an integer multiplier by using the combination of both the sutras and analyzing the area and power of the resultant floating-point multiplier.

It has been also noticed that a relative analysis of the effect of multiplier size among the different implementations is missing in most of the published work. This paper analyzes the area and power overhead for different multiplier sizes for both the vedic and the conventional methods and shows how the vedic multiplier out-performs the conventional methods, especially for large multiplier sizes.

This paper is organized as follows. Section 2 introduces the IEEE 754 floating point representation that is followed by the description of the floating-point multiplication algorithm in the subsequent section. Vedic multiplication is introduced in Sect. 4 where the various sutras and the multiplier design based on those are discussed. Section 5 details the reader with the results and discussions and the paper concludes in Sect. 5.

2 IEEE 754 Standard for Floating-Point Representation

Floating-point number representation is a method to represent a wide range of real numbers using limited number of bits. The decimal point is not fixed and is made to float i.e., the decimal point can be located anywhere with respect to the significant numeral of the specified number. Floating-point numbers are represented using IEEE

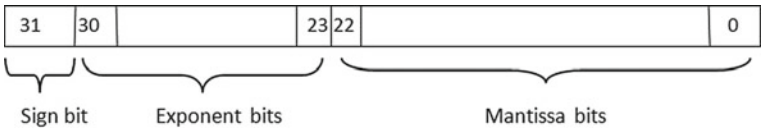

Fig. 1 IEEE 754 standard of a single precision floating-point number

754 standard and can be either based on single or double precision methodology. Floating-point numbers are represented using significant (mantissa), the base and an exponent. Single precision involves the use of 32 bits with 8 bits for the exponent and 23 bits for the mantissa with one bit as the sign bit [15]. Figure 1 shows the single precision floating- point representation.

Apart from this, the standard also describes double and quadruple precision formats that use 62 and 128 bits for representation respectively [16].

3 Floating-Point Multiplication

Figure 2 shows the flowchart used for the design of the floating-point multiplication unit for multiplying 2 numbers *M* and *N*.

The main component is the integer multiplier that is designed using multiple techniques including Booth recording, array multiplication with carry look-ahead

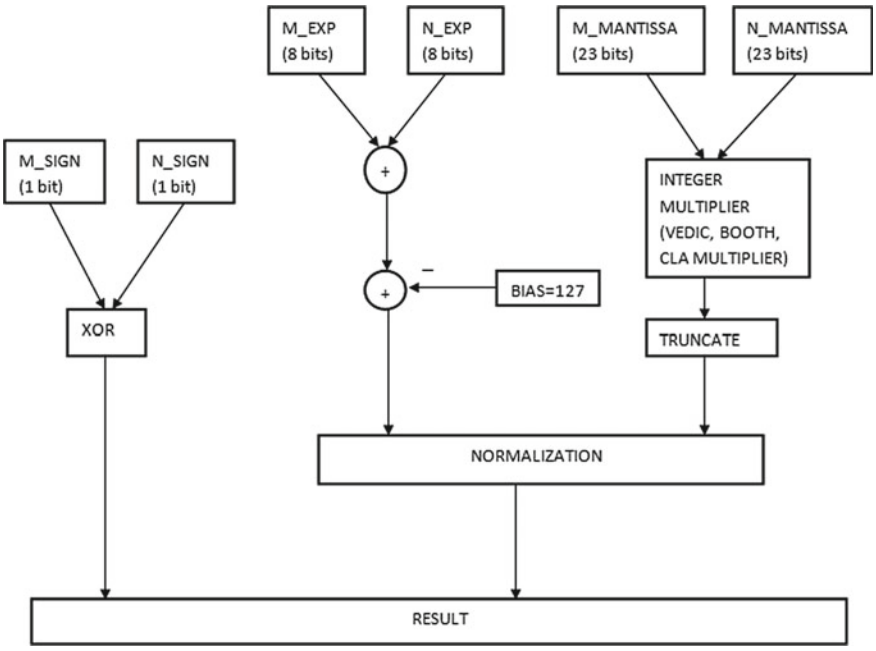

Fig. 2 Single precision floating-point multiplier structure

adder and vedic sutras. Booth multiplier and carry-look ahead adder based array multiplications are designed using conventional methods [5, 6]. The reader is now guided through the design of the vedic sutras based technique in the following section.

4 Vedic Multiplier

Vedic sutras (aphorisms)

In vedic mathematics, all the mathematical principles are presented in the form of aphorisms known as sutras. There are sixteen fundamental sutras that cover all the branches of mathematics [17]. The list of these sutras along with their meanings are elucidated in [9] and is being reproduced here. The sutras are as follows:

- (Anurupye) Shunyamanyat
- Chalana-Kalanabyham
- Ekadhikena Purvena
- Ekanyunena Purvena
- Gunakasamuchyah
- Gunitasamuchyah
- Nikhilam Navatashcaramam Dashatah
- Paravartya Yojayet
- Puranapuranabhyam
- Sankalana-vyavakalanabhyam
- Shesanyankena Charamena
- Shunyam Saamyasamuccaye
- Sopaantyadvayamantyam
- Urdhva-Tiryagbhyam
- Vyashtisamanstih
- Yaavadunam

In this work, we use the Urdhva Tiryagbhyam and the Nikhilam Sutras for the design of our integer multiplier.

4.1 Urdhva Tiryagbhyam Sutra

Urdhva Tiryagbhyam, that translates to 'Vertically and Crosswise', is a multiplication formula that can be used for numbers in any base. Figure 3 shows an example for multiplying two 3-bit numbers using this sutra. The same methodology can be extended for multiplication of larger numbers also.

Figure 4 shows the gate level implementation of a Urdhva Tiryagbhyam sutra based 2 * 2 multiplier and Fig. 5 shows the hierarchical design of a 4 * 4 multiplier

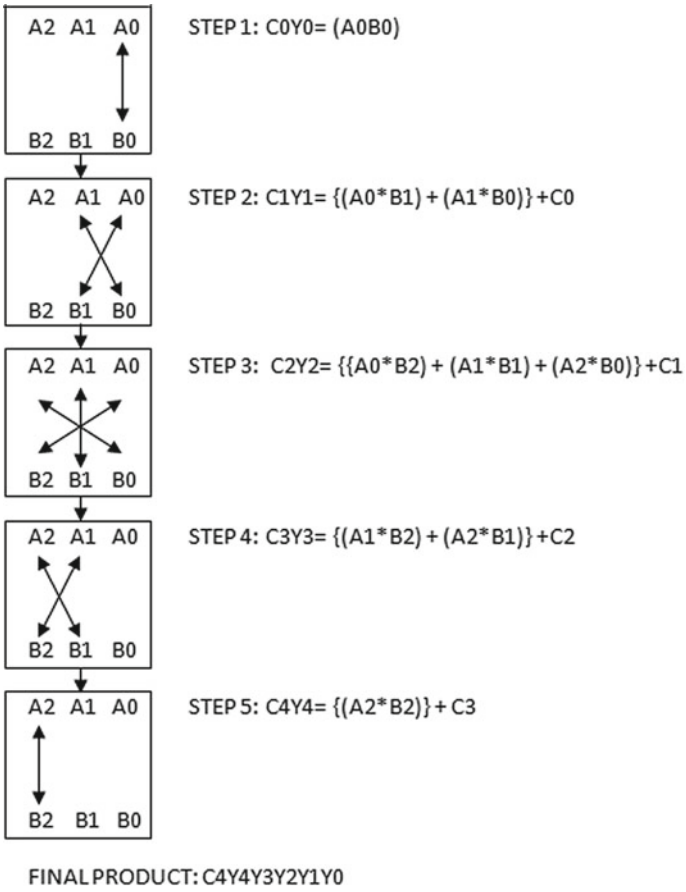

Fig. 3 An example for Urdhva Tiryagbhyam sutra

using 2 * 2 component multipliers. In the same manner, higher order multipliers can be built using the corresponding lower level component multipliers.

Similar to array multipliers, it can be seen that the partial products are generated in parallel and not in a sequential manner which makes it relatively fast since the delay associated is mainly the carry propagation delay through the adders in the array. However, this design is not very efficient while dealing with large numbers since the size of the adder array increases and carry propagation logic suffers from large delay [9]. To overcome this, carry look ahead adder may be used in the final stage but that will come with higher area penalty.

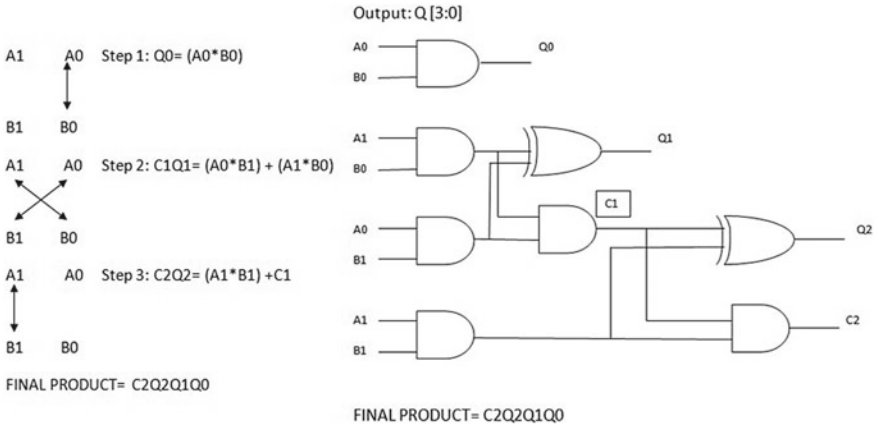

Fig. 4 Design of 2 * 2 vedic multiplier using Urdhva Tiryagbhyam sutra

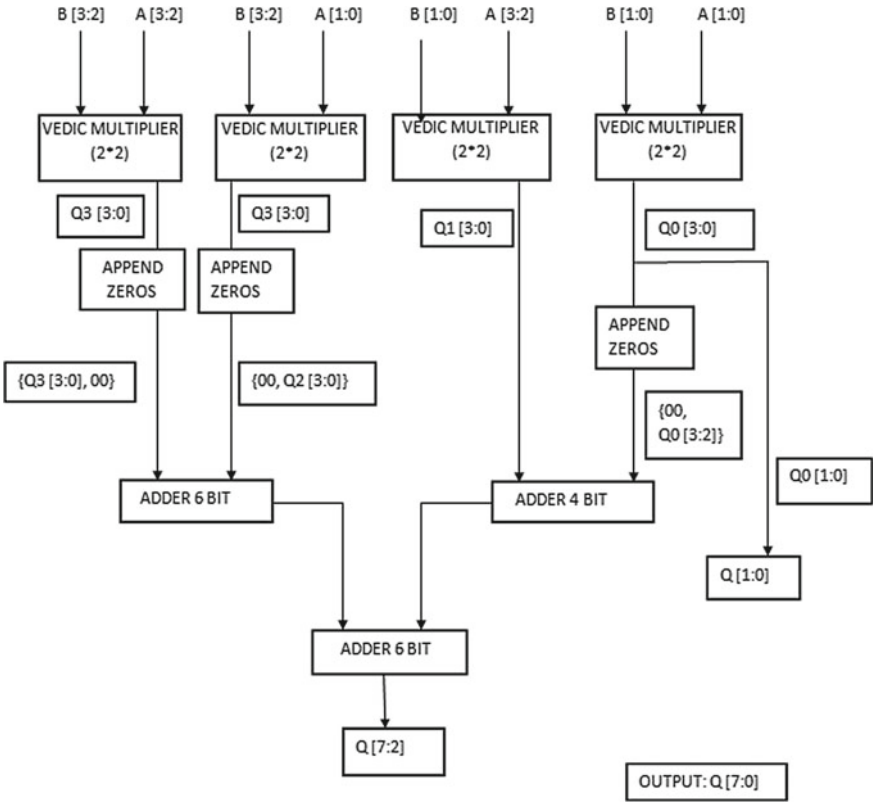

Fig. 5 Design of hierarchical 4 * 4 vedic multiplier using Urdhva Tiryagbhyam sutra based 2 * 2 component multipliers

4.2 Nikhilam Sutra

Nikhilam sutra is an alternative sutra that is commonly used for multiplying large numbers. This sutra can be used for multiplying all numbers, however its effectiveness is more while dealing with large numbers. Figure 6 runs through an example using two numbers G and H. In this example, the numbers are in base 10 (decimal) and the common reference is taken as some power of the base such that both the numbers are either lesser or greater than the common reference. Here, both numbers are less than 10^2 and so we take the reference as 100.

Figure 7 shows the generalized algorithm for a 16 * 16 multiplier. In this case, since we deal with 16 bit binary numbers we take the reference as 2^{16}.

Effectiveness of Nikhilam sutra: Nikhilam sutra analysis involves calculating the complements of numbers from the common reference. A detailed hardware implementation of a multiplier using Nikhilam sutra has been performed by Patel et al. in [12] and they show how Nikhilam sutra implementation is more effective than the

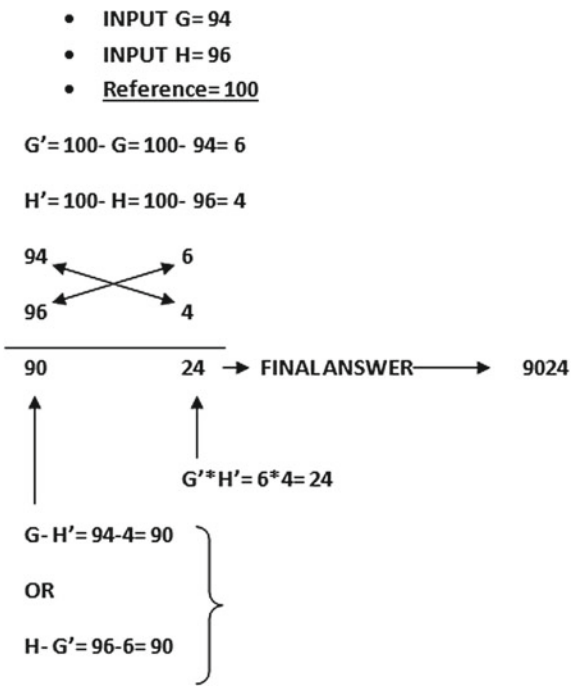

Fig. 6 An example for Nikhilam sutra

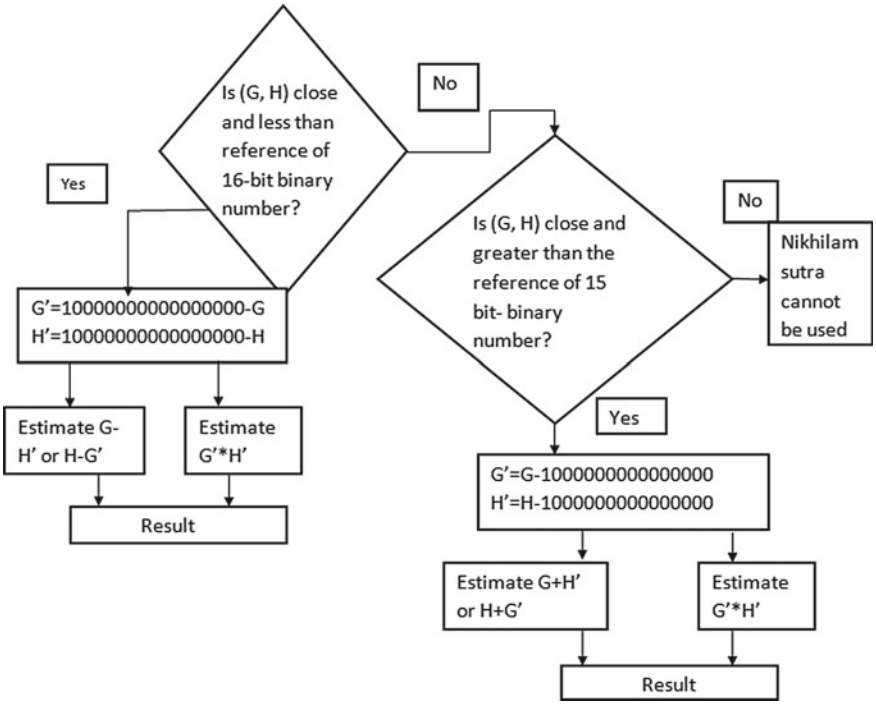

Fig. 7 Algorithm for 16 bit multiplication using Nikhilam sutra

Urdhva Tiryagbhyam sutra. However, they also point out that this is valid only when the numbers are close to the reference value.

4.3 Fusion of Nikhilam and Urdhva Tiryagbhyam Sutras

To overcome the limitations of Urdhva Tiryagbhyam and Nikhilam sutras based multiplier designs, an implementation that combines both the sutras at different levels of hierarchy is being proposed in this paper. This combined design is produced by modifying the Urdhva Tiryagbhyam based design by using Nikhilam based multipliers as the sub-modules for lower level multiplications. For e.g., a combined implementation of the 4 * 4 design is got by replacing the 2 * 2 multipliers in Fig. 5 with the Nikhilam equivalent multiplier. Similarly, for 8 * 8, 16 * 16 and 32 * 32 multipliers, the underlying sub-multipliers are designed using 4 * 4, 8 * 8 and 16 * 16 Nikhilam based designs respectively. Figure 8 shows the block level design of a 32 * 32 multiplier designed by this methodology.

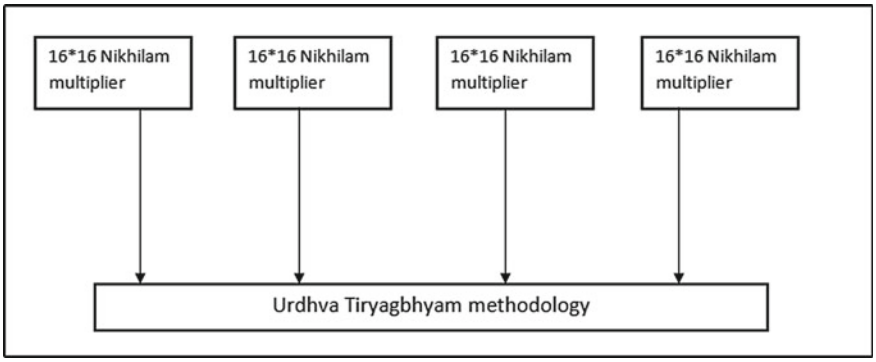

Fig. 8 Hierarchical structure of a 32 bit vedic multiplier using Nikhilam-Urdhva Tiryagbhyam combination

5 Results and Discussions

The following multipliers were designed and performance was analyzed.

- Conventional Multipliers
  - Array multiplier with carry look ahead adder
  - Booth multiplier
- Vedic Multipliers using
  - Urdhva Tiryagbhyam sutra
  - Nikhilam sutra
  - Nikhilam-Urdhva Tiryagbhyam combination

Multipliers of sizes 2 * 2, 4 * 4, 8 * 8, 16 * 16 and 32 * 32 were designed using Verilog and synthesized using gpdk 90 nm technology in Synopsys. Total power consumed and the area utilized were calculated and Tables 1 and 2 show the results for all the cases.

Table 1 Power (μW) dissipated for multipliers of different orders

Multiplier order	Multiplier type				
	Array	Booth	Urdhva Tiryagbhyam	Nikhilam	Urdhva Tiryagbhyam + Nikhilam
4 * 4	01.12	1.75	00.48	02.73	02.02
8 * 8	08.07	08.59	02.80	07.89	02.46
16 * 16	49.83	48.05	14.11	40.835	08.87
32 * 32	275.49	263.60	62.96	197.75	39.77

Table 2 Area (μm^2) utilized for multipliers of different sizes

Multiplier order	Multiplier type				
	Array	Booth	Urdhva Tiryagbhyam	Nikhilam	Urdhva Tiryagbhyam + Nikhilam
4 * 4	17.27	21.77	10.75	42.61	33.19
8 * 8	79.29	80.01	52.53	103.86	48.41
16 * 16	353.00	328.48	247.92	438.73	139.40
32 * 32	1577.41	1335.19	1167.35	1756.44	456.00

The same results are plotted graphically and given in Figs. 9 and 10 showing the power and area for the different order multipliers for each of the five different implementations.

It can be seen that as the multiplier size increases, there is a rapid increase in the power and area of the conventional multipliers while the increase is gradual for the vedic multipliers (one exception being the area of the Nikhilam based design). Among the vedic multipliers, Nikhilam and Urdhva Tiryagbhyam based designs by

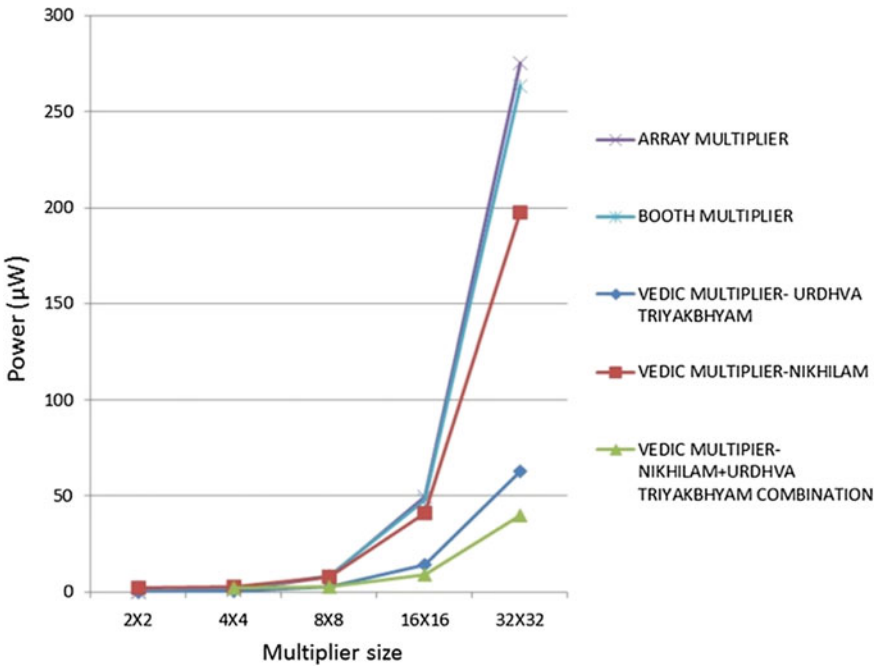

Fig. 9 Power plot of different multipliers of different orders. It can be seen that the combined use of Nikhilam and Urdhva Tiryagbhyam sutras results in the least power dissipation and the difference is prominently seen for higher order multipliers

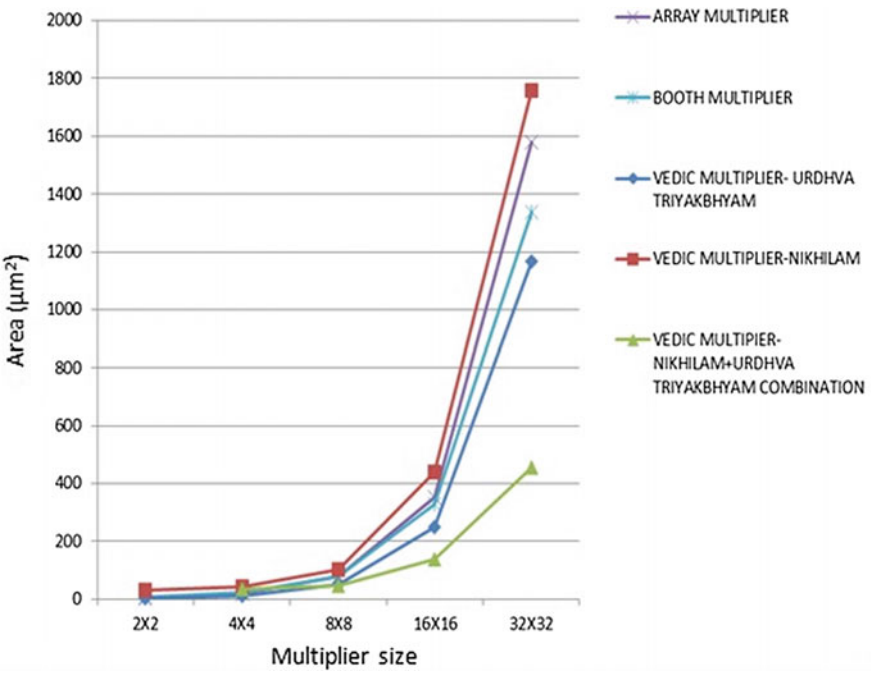

Fig. 10 Area plot of different multipliers of different orders. It can be seen that the combined use of Nikhilam and Urdhva Tiryagbhyam sutras results in the least area utilization and the difference is prominently seen for higher order multipliers

themselves are not very much area-power efficient while considering multipliers of large sizes. On the other hand, multiplier design using Nikhilam-Urdhva Tiryagbhyam combination gives the least area and power and the difference is significant for higher order multipliers.

6 Conclusions

A comparative analysis of floating-point multipliers using conventional multipliers (array and Booth) and vedic multipliers as the component integer multiplier unit has been done. Urdhva Tiryagbhyam sutra and Nikhilam sutra based designs were explored and a new design utilizing the two sutras together is proposed. Calculation of area and power of the different designs showed that the combined use of Nikhilam and Urdhva Tiryagbhyam based design is very efficient in terms of power and area for higher order multipliers and can be used for designing large multipliers for DSP applications.

References

1. Andraka R (1998) A survey of CORDIC algorithms for FPGA based computers. In: Proceedings of the 1998 ACM/SIGDA sixth international symposium on field programmable gate arrays. ACM, pp 191–200
2. Hamid LSA, Shehata K, El-Ghitani H, El- Said M (2010) Design of generic floating point multiplier and adder/subtractor units. In: 2010 12th international conference on computer modelling and simulation (UKSim). IEEE, pp 615–618
3. Marcus G, Hinojosa P, Avila A, Nolazco-FIores J (2004) A fully synthesizable single-precision, floating-point adder/substractor and multiplier in VHDL for general and educational use. In: Proceedings of the fifth ieee international caracas conference on devices, circuits and systems, 2004, vol 1. IEEE, pp 319–323
4. Prabhu E, Mangalam H, Karthick S (2016) Design of area and power efficient Radix-4 DIT FFT butterfly unit using floating point fused arithmetic. J Cent South Univ 23(7):1669–1681
5. M. M. Mano *et al.*, "Computer system architecture," 1982
6. Booth AD (1951) A signed binary multiplication technique. Q J Mech Appl Math 4(2):236–240
7. Al-Ashrafy M, Salem A, Anis W (2011) An efficient implementation of floating point multiplier. In: 2011 Saudi international electronics, communications and photonics conference (SIECPC). IEEE, pp 1–5
8. Ramteke P, Mhala N, Lakhe P (2014) An efficient implementation of double precision floating point multiplier using booth algorithm. Int J Adv Res Electr Electron Instrum Eng 3(7)
9. Tiwari HD, Gankhuyag G, Kim CM, Cho YB (2008) Multiplier design based on ancient indian vedic mathematics. In: ISOCC'08. international SoC design conference, 2008, vol 2. IEEE, pp II–65
10. Kanhe A, Das SK, Singh AK (2012) Design and implementation of floating point multiplier based on vedic multiplication technique. In: 2012 international conference on communication, information & computing technology (ICCICT), 2012, pp 19–20
11. Havaldar S, Gurumurthy K (2016) Design of vedic IEEE 754 floating point multiplier. In: IEEE international conference on recent trends in electronics, information & communication technology (RTEICT). IEEE, pp 1131–1135
12. Patel P, Shandilya A, Brahmbhatt N, Raval K, Deb D (2015) Vedic and conventional methods of n n binary multiplication with hardware implementation. In: International conference on smart sensors and systems (IC-SSS). IEEE, pp 1–6
13. Budhiraja H, Syed M, Ramya MA (2016) Verilog implementation of vedic multiplier. Int J Adv Eng Tech, Manag Appl Sci 3(5)
14. Jithin S, Prabhu E (2015) Parallel multiplier-accumulator unit based on vedic mathematics. ARPN J Eng Appl Sci 9(22):3608–3613
15. Zuras D, Cowlishaw M, Aiken A, Applegate M, Bailey D, Bass S, Bhandarkar D, Bhat M, Bindel D, Boldo S et al (2008) IEEE standard for floating-point arithmetic. IEEE Std 754-2008, pp 1–70
16. Rao YS, Kamaraju M, Ramanjaneyulu D (2015) An FPGA implementation of high speed and area efficient double-precision floating point multiplier using Urdhva Tiryagbhyam technique. In: 2015 conference on power, control, communication and computational technologies for sustainable growth (PCCCTSG). IEEE, pp 271–276
17. Bharath JSS, Tirathji K (1986) Vedic mathematics or sixteen simple sutras from the vedas. Motilal Banarsidas, Varanasi (India)

Design and Development of IoT Based Intravenous Infusion System

Kanchi Raghavendra Rao and Koluthuri Evangili Supriya

Abstract Health care organizations are adopting IoT Cloud with wireless sensor networks that is beneficial, especially when administering the condition of a greater number of patients and their resulting data storage are taken into account. Considering the case of patients fed with Intravenous [IV] fluids in Intensive Care Unit [ICU], it is essential to administer the flow rate and fluid level of gravity fed bottles in real-time, either by an attendant or duty nurse allotted to that bed. Manual negligence in such a scenario may lead to the death of patient, in the worst case. In this paper, a new design for IV bottle is suggested and a wireless sensor network [WSN]-based liquid level and drop count measuring system is developed. The system is built around the Texas Instruments CC3200, Ultrasonic sensor HC-SR04, LM35 temperature sensor, and GSM SIM900A. The proposed system can also be used to track the status anywhere wirelessly by Wi-Fi and Cellular systems. Thus, possible danger to the patient such as blood loss, back flow of blood due to negligence of nursing can be overcome by monitoring to fluid level and flow-rate. Whole day, 24 h. It is possible to extend the work for private cloud of a nursing home or hospital to maintain secrecy.

Keywords Intravenous system · IoT · Ultrasonic sensor HC-SR04 · GSM SIM900A

1 Introduction

Development in the fields: Information and Communication Technology [ICT], Nano sensors fab [NEMS] and Internet of Things [IoT] have brought in tremendous development in the fields of health care and bio-medical engineering. It is this which paved way to the development of wearable health care parameters such as blood pressure, heart rate, sugar levels etc. Besides this, such parameters can be displayed

K. R. Rao (✉) · K. E. Supriya (✉)
Department of Physics, Sri Krishnadevaraya University, Anantapuram 515003, India
e-mail: kanchiraghavendrarao@gmail.com

K. E. Supriya
e-mail: evangilisupriya.k@gmail.com

© Springer Nature Singapore Pte Ltd. 2020

T. Hitendra Sarma et al. (eds.), *Emerging Trends in Electrical, Communications, and Information Technologies*, Lecture Notes in Electrical Engineering 569,
https://doi.org/10.1007/978-981-13-8942-9_40

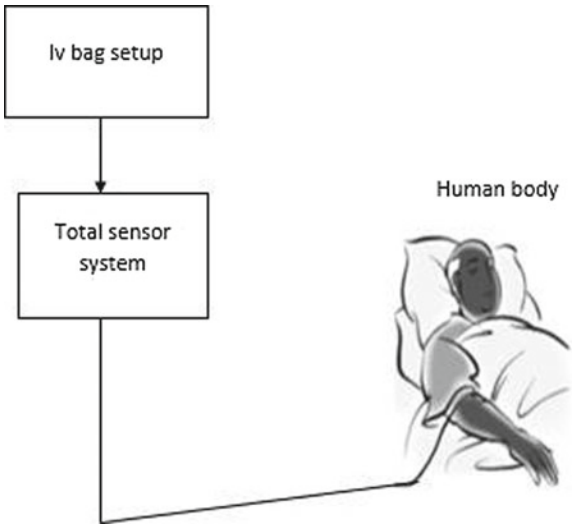

Fig. 1 Intravenous setup

and transmitted using Wi-Fi and cellular technologies. Considering the health industry, nothing is more precious than the patient's life. In such a scenario, it is not the number of patients or money turn over that counts but it is the quality of treatment that is important. Thus, the instruments used in administering any ailment should be self-sufficient and should be in a position to communicate to the hospital's dashboard in general and nursing staff in particular, so there is a need to develop the E-fluid monitoring in the present situation. Keeping view in this point, the total sensor setup is developed as shown in Fig. 1, where the setup detects the drop count, measures the fluid level and sends an alert signal to the attendant when the fluid reaches the threshold level. Pharmacology activities that are involved in the treatment of diseases include the medical administration by oral, intramuscular, subcutaneous, intra-arterial and intravenous [IV].

2 Literature Review

Huang and Lin [1] developed a warning system based on radio frequency identification [RFID]. This RFID technology acts like a triggering device for the developed system. The specially fabricated RF tag can be attached to any kind of IV liquid package available on the market. Zhang et al. [2] developed a novel RFID-Based intravenous infusion monitoring based on fork type light barrier as a sensor with Zigbee protocol, which helps in monitoring the velocity of IV system with high accuracy and reliability. Bhavasaar et al. [3] developed intravenous fluid monitoring system where load cell checks the level of the fluid by weighing the IV bag. Amanu et al. [4] suggested a drip infusion monitoring system using Bluetooth technology

where it consists of various infusion monitoring devices that helps in detecting the infusion rate and the collected data is send to the central monitor placed at the nurse station so that required action can be taken. Yanan et al. [5] developed a health information alarm system using Bluetooth and GPRS technologies in which the system monitors, collects data and sends information to analysing counter using artificial intelligence [AI]. Ogawa et al. [6] developed a drip monitoring system based on electrical impedance. The electrodes used are in non-contact with the system which determines parameters of each fluid drop. Ahouandjinou et al. [7] developed a Smart and Pervasive ICU system using Automatic Detection of risk situation and alert [ADSA] method consists of multi camera system and collaborative sensor Network which helps in real-time monitoring to the patients especially facing danger and chronic conditions. Rachman [8] developed a monitoring system regarding patient infusion where laser photodiode is used. This sensor kit collects, process and further sends data to Zigbee transmission device to display them in the form of GUI. Yadav and Jain [9] developed real-time E-saline monitoring system where IR sensor used to detect drop rate, infusion capacity and servo meter used to control drip rate mechanism.

From the above literature survey, it is clear that various workers have used technologies like RFID, Zigbee, GPRS etc. for IV infusion monitoring. Further, IoT-based IV infusion monitoring and alerting system is very rarely seen in the literature. Keeping this in view point, IoT-based IV infusion monitoring and alerting system is designed.

3 Salient Features of the Developed System Include

- The liquid [drug] level and drop rate are constantly monitored and its level is sent to the dashboard of the monitoring system and also to the mobile of the nursery staff.
- When the drug level reaches a threshold value or the set drop rate changes then an alert signal goes to both dash board and nursing staff.

4 General Description of the Hardware Components

The present developed system consists of Texas Instrument CC3200 microcontroller, HC-SR04 Ultrasonic sensor, LM35 temperature sensor, IR senor consists of IR transmitter-receive pair, GSM SIM 900A module.

4.1 CC3200-XL Launchpad

The CC3200 launchpad is the industry's first single chip microcontroller with built in Wi-Fi connectivity. It has an arm cortex core at 80 MHz and contains two on-chip sensors, Thermopile sensor and Accelerometer [BMA222]. It has an embedded memory up to 256 KB. It has an integrated DC-DC converter which operates with wide-voltage mode of 2.1–3.6 V. The board has built in USB-to-JTAG for debugging, flash memory of 8 MB for programming. It has input peripherals like 4-ADC channels and 20 pin headers that provides general purpose input and output pins, three LED's. It has multiple protocols like SPI, I^2C, UART, TCP/IP and TLS/SSL status and HTTP server [10]. The hardware overview of the CC3200 launchpad is shown in Fig. 2.

HC-SR04 Ultrasonic Sensor:

Ultrasonic sensor is now a days recognized as being as simple and cheap answer to many typical demands [11]. The human ear can hear sound frequency around 20 Hz–20 kHz and ultrasonic is the sound wave beyond 20 kHz. Ultrasonic sensors are often used in applications like distance measurement, level measuring etc. It provides excellent non-contact measurement with high accuracy. It has a resolution of 0.3 cm and the ranging distance is from 2 to 400 cm. It has measuring angle of 15° and works with 5 V. It has features like stable performance and accurate distance

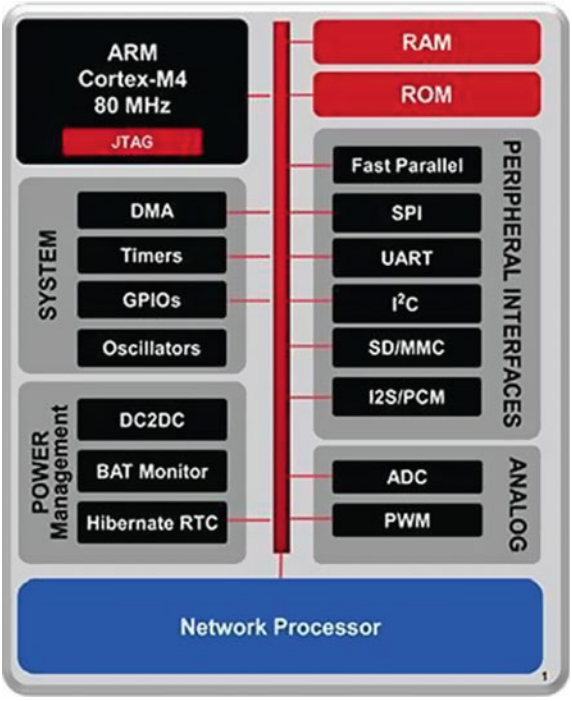

Fig. 2 Hardware overview of CC3200 launchpad (*source* CC3200 datasheet from Texas instruments)

measurement. In the developed system ultrasonic senor is used as a level sensor. The block diagram of HC-SR04 is shown in Fig. 3.

Working Principle:

Ultrasonic transmitter emits an ultrasonic wave in one direction and started timing when it launched. Ultrasonic spread in the air and would return immediately when it encountered obstacles on the way. At last, the ultrasonic receiver would stop timing when it received the reflected wave. The working principle of ultrasonic sensor is shown in Fig. 4.

Timing Diagram:

By applying a short 10 µs pulse to the trigger input will start ranging, then the module raises its echo by sending out an 8-cycle burst of ultrasound at 40 kHz. The range can be calculated through the time interval between trigger signal and echo signal. The timing diagram of ultrasonic sensor is shown in Fig. 5. The two basic blocks of ultrasonic sensor are transmitter and receiver [12].

Fig. 3 Block diagram of HC-SR04 ultrasonic sensor (*source* HC-SR04 datasheet)

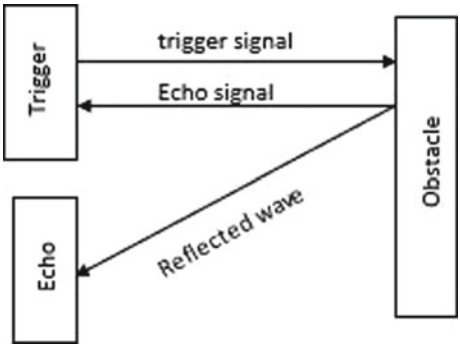

Fig. 4 Ultrasonic sensor working principle

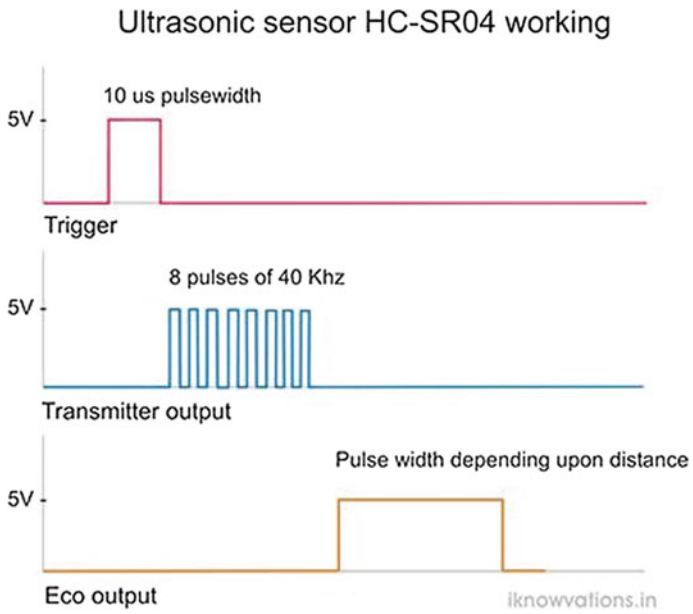

Fig. 5 Timing diagram of ultrasonic sensor (*source* ultrasonic sensor HC-SR04 datasheet)

4.2 LM35 Temperature Sensor

LM35 sensor is used for measuring temperature. These are specially designed sensors whose output voltage is linearly proportional to the Celsius. It has a 0.5 °C accuracy. It has three terminals namely Vs, Vout and Ground as shown in Fig. 6.

It is a low-cost sensor used for many typical applications due to water level trimming and it can operate at 5 V. The low output impedance, linear output and

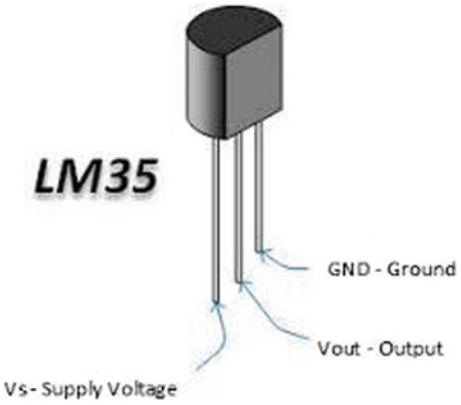

Fig. 6 Pin diagram of the LM35 Temperature sensor (*source* LM35 datasheet)

Fig. 7 Photograph of the IR sensor [IR transmitter-receiver pair]

precise inherent calibration of the LM35 sensor makes interfacing to read out or control circuitry especially easy. LM35 temperature sensor has an advantage over linear temperature sensor which can calibrate in kelvin as the user is not required to subtract a large constant voltage from the output [13].

4.3 Infrared Sensor

Infrared sensor is used to detect the drop count. This sensor is low-cost, small in size and having good precision. Infrared [IR] Sensor consists of an IR emitting diode which acts as an emitter and IR phototransistor which acts as a detector. It works in low-voltage mode [3–5 V]. The photograph of the IR transmitter receiver pair which is used in the present work is shown in Fig. 7.

It has the advantage of fast response time and high sensitivity. IR sensor is having a feature of non-contact measurement [14]. Thus, IR sensor is used in various applications like embedded fields, distance measurement, medical and engineering field for obstacle detection.

4.4 GSM SIM900A Module

GSM SIM 900A [global system for mobile communication subscriber identity module] built with SIMCOM makes SIM900 works on frequencies 900/1800 MHz. It is very compact in size and easy to use as plug in GSM modem. The baud rate is between 9600 and 115,200 through AT command. The built in low-drop linear voltage regulator allows you to connect wide range of unregulated power supply [4.2–13 V]. It has features like sending and receiving SMS, making audio calls and receiving calls. It has built in SIM card holder and network status LED [15]. The AT commands of GSM module used in the system are shown in Table 1.

Table 1 AT commands of GSM module used in the present study

Instructions	Meaning
AT	Attention
AT + CMGF	Set module in message mode
AT + CMGS	Set module in call mode

5 System Architecture

The block diagram of the system (Fig. 8) developed in the present work consists of:

- US senor: Ultrasonic sensor HC-SR04
- V: +5 V
- G: ground
- E: Echo Output US senor: Ultrasonic sensor HC-SR04
- T: Trigger Input
- LM35 TS: LM35 Temperature sensor

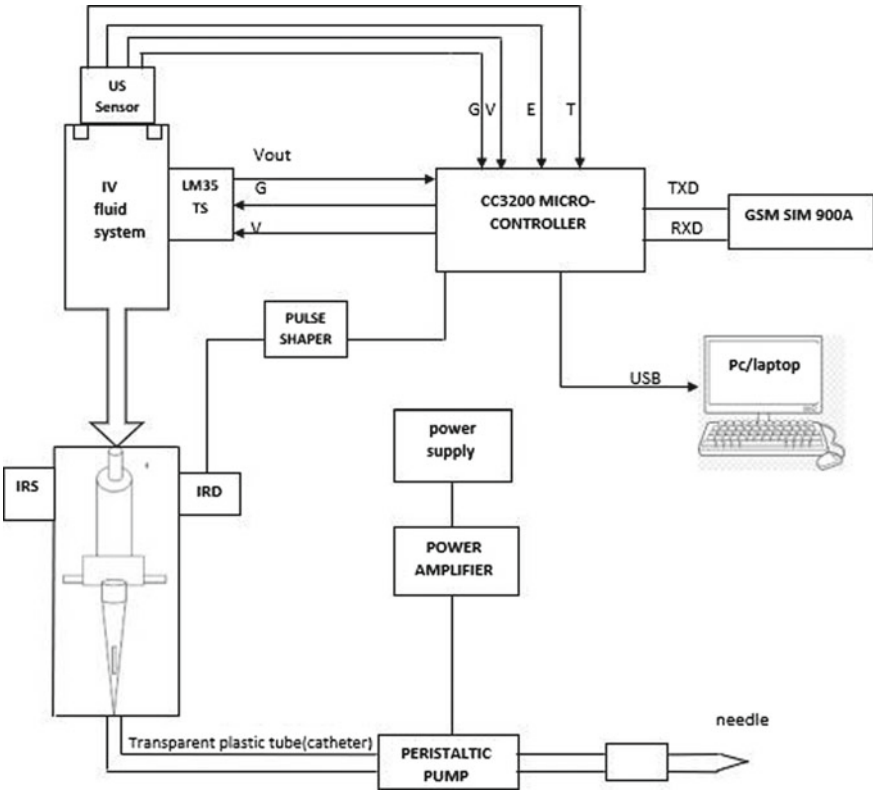

Fig. 8 Block diagram of the developed system

- GSM SIM900A: Global System for Mobile Communication Subscriber Identity module
- IRS: Infrared source, IRD: Infrared detector
- TXD: Transmit data, RXD: Receive data.

6 Working Principle

In the developed system as shown in Fig. 8. ultrasonic sensor is used as a level sensor to the check the fluid level of the system. The sensed level of the fluid is converted into electrical signal and is send to the CC3200 microcontroller. The level of the fluid is sensed by the ultrasonic sensor, by applying a short pulse 10 μs pulse to the trigger input, then the echo is a distance object that is pulse width and range in proportion. And also, temperature sensor LM35 is used to measure the temperature, which can operate with low voltage that is 5 V.

In the above intravenous setup where the Infrared [IR] sensor is kept in the drip chamber. The main blocks of the IR sensor are IR Emitter and IR emitter which is used to emit the light and the IR photodiode which acts as a detector used to detect the light of same wavelength. Normally, in IR senor, the phototransistor does not receive any radiation from IR LED but when it detects an object and the object becomes closer then the photo transistor which is acting as a detector reflects and receiver radiation [16]. The IR detector and IR source/emitter are placed side by side in the drip chamber. Suppose, if the droplet blocks in the drip chamber then the light emitted by the LED of IR and the detector automatically receives the radiation from the object. Thus, each drop can be counted by IR sensor.

7 Power Amplifier LM393

Lower power dual voltage comparator consists of two independent low voltage comparators designed especially over a wide range of voltages [17]. In the developed system, LM393 is used to amplify the generated signal. Suppose when there is a droplet going through infrared emitting diode, the phototransistor receives radiation and the receiver of the IR sensor will generate a signal, then that signal will be sent to the microcontroller. Also, there is an LED connected to signal output interface, indicating that infrared emitting diode is working properly.

8 Software Description

In the present work, the software is developed using Energia IDE. It works with windows, Linux and Mac operating systems. The program is developed in embedded C. It's very easy for the user to program in this IDE. The flowchart of the related firmware is shown in Fig. 9.

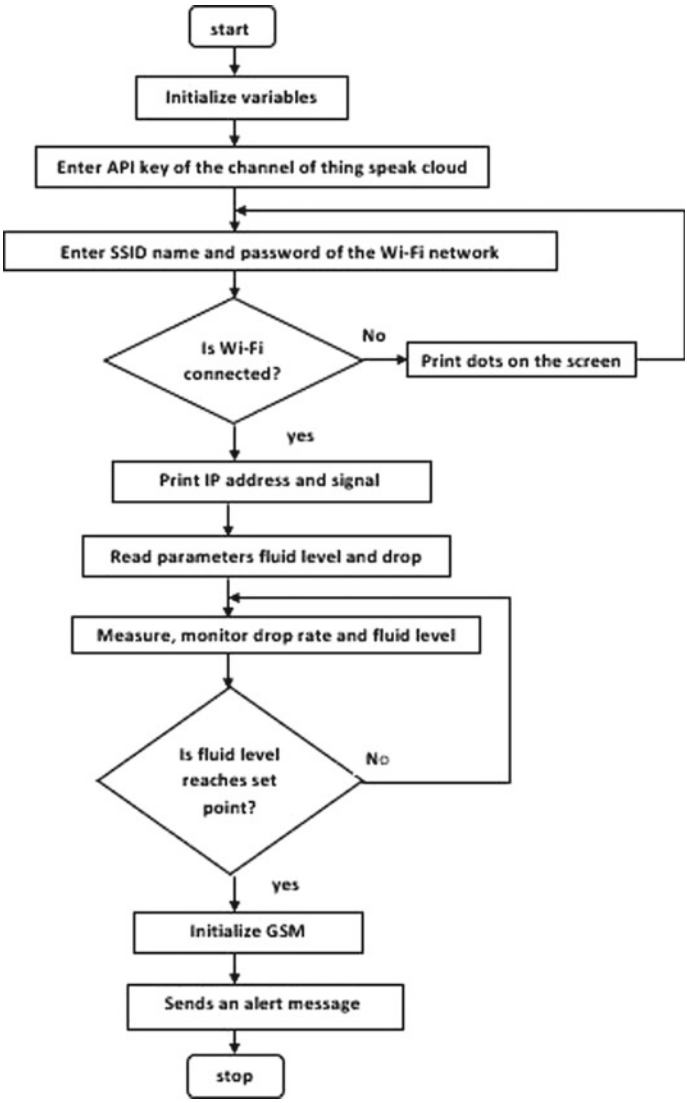

Fig. 9 Flowchart of the program developed in the work

9 Message Transmission

After the liquid level and drop rate are monitored, collected, if the value reaches the set point then an alert signal sends to the concerned nurse through GSM. The block diagram of the message transmission is shown in Figs. 10 and 11 and the screen shot of getting alert message is shown in Fig. 12.

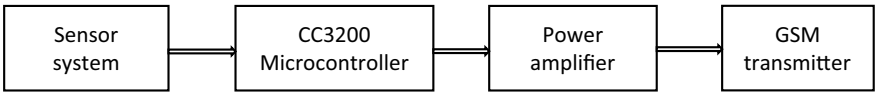

Fig. 10 Signal generation from sensor system to GSM module

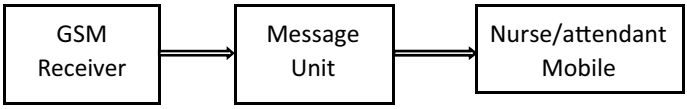

Fig. 11 Signal generation from GSM to nurse mobile

Result:

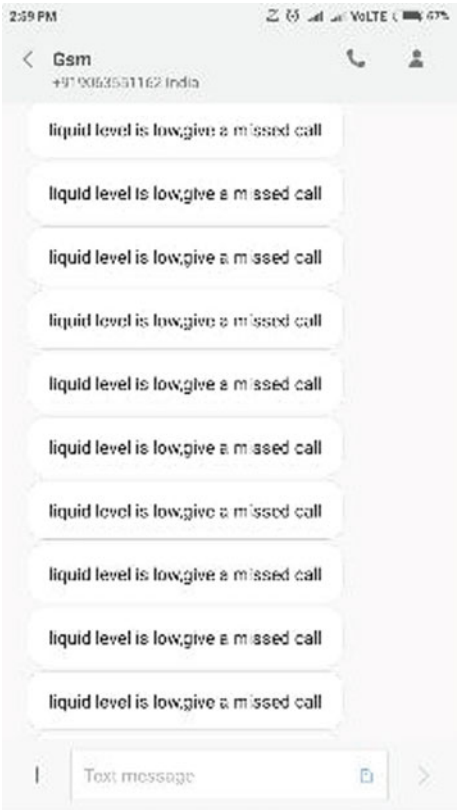

Fig. 12 Screenshot of getting message to the registered mobile number

10 Conclusion

The developed Intravenous Infusion system determines the fluid level and drop rate which are continuously monitored and display to the dashboard and to the mobile of the nurse/attendant. And also, if the drug level reaches the set point and the drop rate changes then the alert signal goes to monitoring system and to the nurse/attendant. The performance of the developed system was found to be much superior and better performance when compared to the other types of similar developed systems in the market. The system has been composed of with minimum hardware components and in minimum power consumption.

Acknowledgements K. Evangili supriya is thankful to the Department of Science and Technology (DST), New Delhi, for sanctioning the INSPIRE fellowship and the authors are thankful to DST for sanctioning FIST program in establishing VLSI and Embedded Laboratory in the Department of Physics.

References

1. Huang C-F, Lin J-H (2011) A warning system based on the RFID technology for running-out of injection fluid. In: 33rd annual international conference of the IEEE. IEEE, Boston, pp 2212–2215. https://doi.org/10.1109/iembs.2011.6090418
2. Zhang Y, Zhang SF, Wu GX, Ji Y (2011) Wireless sensor network-enabled intravenous Infusion monitoring system. In: IET wireless sensor systems, China, pp 241–247. https://doi.org/10.1049/iet.wss.2011.003
3. Bhavasaar MK, Nithya M, Praveena R, Bhuvaneswari N, Kalaiselvi T (2016) Automatic intravenous fluid monitoring and alerting system. In: IEEE international conference on technological Innovations in ICT for agriculture and rural development TIAR. IEEE, India, pp 77–80. https://doi.org/10.1109/tiar.2016.7801217
4. Amanu H, Ogawa H, Maki H, Tsukamotu S, Yonezawa Y, Caldwell WM (2012) A remote drip infusion monitoring system employing Bluetooth. In: 34th annual international conference of the IEEE engineering in medicine and biology society [EMBS]. IEEE, USA, pp 2029–2032. https://doi.org/10.1109/embc.2012.6346356
5. Yanan F, Xinghua L, Huaizu L (2006) Real-time health information acquisition and alarm system based on Bluetooth and GPRS communication technologies. In: IEEE international conference on systems, man and cybernetics. IEEE, Taiwan, pp 4717–4721. https://doi.org/10.1109/icsmc.2006.385049
6. Ogawa H, Maki H, Tsukamoto S, Yonezawa Y, Amano H, Caldwell WM (2010) A new drip infusion solution monitoring with a free-flow detection function. In: 32nd annual international conference of the IEEE engineering and medicine biology society. IEEE, Argentina, pp 1214–1217. https://doi.org/10.1109/iembs.2010.5626449
7. Ahouandjinou ASRM, Assogba K, Motamed C (2017) Smart and pervasive ICU based-IoT for improving intensive health care. In: International conference on bio-engineering and smart technologies [BIOSMART]. IEEE Xplore, Dubai. https://doi.org/10.1109/biosmart.2016.7835599
8. Rachman FZ (2015) Prototype development of monitoring system in patient infusion with wireless sensor network. In: International seminar on intelligent technology and its applications [ISITIA]. IEEE Xplore, Indonesia, pp 397–402. https://doi.org/10.1109/isitia.2015.7220013

9. Yadav S, Jain P (2016) Real-time cost-effective e-saline monitoring and control system. In: International conference on control, communication and materials [ICCCCM], IEEE Xplore, Indore. https://doi.org/10.1109/iccccm.2016.7918254
10. CC3200 Launchpad Specifications. http://www.ti.com/general/docs/lit/getliterature.tsp?genericPartNumber=cc3200&fileType=pdf
11. Koval L, Vanus J, Bilik P (2016) Distance measuring by ultrasonic sensor. In: International federation of automatic control. Elsevier, pp 153–158. https://doi.org/10.1016/j.ifacol.2016.12.026
12. HC-SR04 Ultrasonic Sensor Datasheet. https://cdn.sparkfun.com/datasheets/sensors/Proximity/HCSR04.pdf
13. LM 35 Temperature Sensor Datasheet. http://www.ti.com/lit/ds/symlink/lm35.pdf
14. IR Sensor Datasheet. http://www.everlight.com/file/ProductFile/ITR8102.pdf
15. SIM900A GSM Module Datasheet. https://elementzonline.com/sim900a-gsm-modem-module-with-sma-antenna-ttl-output
16. delas Alas GR Jr, Padilla JN, Tanguilig BT III (2016) Intravenous piggyback infusion control and monitoring system using wireless technology. Int J Adv Technol Eng Explor. Philippines, pp 50–57. https://doi.org/10.19101/ijatee.2016.317002
17. LM393 Datasheet. www.ti.com/lit/dis/symlink/lm393-n-pdf

ROI Segmentation and Detection of Neoplasm Based on Morphology Using Segmentation Operators

V. Vijaya Kishore and V. Kalpana

Abstract Modern medical imaging studies have a defiance problem to detect the abnormalities that lead to early diagnosis of the disease. Medical image processing deals with the detailed study of human organs and extracting the discernible information called ROI. In medical images even a minute portion of the image has a great concern in diagnosis and also has chances for wrong prophesy. Image segmentation is highly referred technique for exact separation of image for the accurate diagnosis. In this paper segmentation of brain image is implemented using morphology and segmentation operators to simplify image description, distinguishing the quality, perceptibility and cognizability of the image. The image segmentation operators like Sobel, Prewitt, Gaussian, Average, Laplacian, LoG and Unsharp are applied on DICOM brain image having tumor. The results are evaluated considering the ROI pertaining to tumor. This paper submits a comprehensive report of the techniques to perceive brain image segmentation and find out the abnormality. These results exemplify the segmented image and the best suitable operator for brain tumor segmentation and the ROI. Exact identification and separation of tumor helps for quality of appearance and classification of malignancy for the possible treatment.

Keywords Neoplasm · DICOM · Segmentation · Operators · ROI and morphology

1 Introduction

Neoplasm is contemplated to unusual thickening of tissue and further creating mass that is frequently termed as tumor. Brain tumors are regarded to be the second often occurring cancers with 15–25% of leukaemia. Death rates can be controlled by deploying features, recognition and the degree of malignancy growth in the region [1].

V. Vijaya Kishore
Department of ECE, G. Pullaiah College of Engineering and Technology, Kurnool, India
e-mail: kishiee@rediffmail.com

V. Kalpana (✉)
Department of ECE, Sree Vidyanikethan Engineering College, Tirupathi, India
e-mail: ksh.v1227@gmail.com

© Springer Nature Singapore Pte Ltd. 2020

T. Hitendra Sarma et al. (eds.), *Emerging Trends in Electrical, Communications, and Information Technologies*, Lecture Notes in Electrical Engineering 569,
https://doi.org/10.1007/978-981-13-8942-9_41

Medical imaging is basically one of the means to achieve patient data and to bring a detailed knowledge about the disease [2]. In medical imaging, pictures are seized and are converted into digital form for further operation [3]. Medical imaging also has dominant features like maintaining the sequence of records and occurrences of the identified diseases of the patients assess the procedures that relate to surgery [2]. Greater degree of biomedical data with exorbitant features is fetched daily from imaging scans. To variate the brain regions with variation in the other regions is a complicated assignment [4]. Majority of medical images accommodate deliberations and areas that have a smallest degree of significance than the other regions of the image. DICOM has extensive scope in the science of medicine and vastly used modality with vigorous quality. To extract the image and to identify the disease segmentation is performed [5]. Segmentation is a procedure to recognise and describe the purposeful regions to absolutely separate the brain tissues [2, 3]. The foremost demands of brain tumor are to validate the existence, determine and identify the position of malignancy for the choice of treatment. Unambiguous identification of the tissue patterns helps the specialists to promote exact treatment. Segregation of shapes with malformation of brain is a crucial problem [6]. This paper proposes segmentation techniques to ascertain brain tumor from DICOM images. DICOM allude to Digital Imaging and Communications in Medicine and typify ubiquitous and rudimentary archetype for generating, storing and processing of image [7]. This standard is not precisely considered as a picture or a dossier. It furnishes incumbent contrivance for meticulous determination, delineation and handling of medical information. It is an extensive medical facet that consigns and keeps the documents with extortionate identification features and interpretation [5, 8]. DICOM bestows reliable representation of physical compositions negligible effect of electromagnetic emissions [9].

2 Literature Review

The initial information regarding brain tumor was widely presented by Rudolf Virchow in 1863. In the year 1926, Harvey Cushing and Percival Bailey have formally presented linguistic articles in association with the performance of brain and its tumor existence. In 1949 James Watson Kernohan submitted the concept of brain functioning that relates to the categorization of brain abnormalities into grades rather representing them as individual functions. Later WHO has printed massive molecular outcomes as four editions from 1993 to 2007. David Louis preferred histology with molecular pathology to designate brain tumors and used the concept for practical examination and then applied to the revised fourth edition of the WHO brain [10]. J. Zhou performed brain tumor segmentation using vector machine method which is widely applicable for obtaining intensity features to gather the diffused tumor regions. Segregation of the affected regions are recognized relying on region based thresholding techniques. Hassan Khotanlou initiated their work for tumor segmentation by incorporating the methods by numerically examining and representing the

results graphically (histogram), morphological behavior of images and perusal of reflected regions [6]. Current methods focus on separating the areas with growth of tissues in the brain which may be also containing benign tumors and also taking the account of distribution characteristics of the image [11]. Correlation between the contiguous pixel distributions plays a vital role of segregation of the image [12]. Nobuyuki Otsu has submitted the ramifications on the disconnection of gray levels based on the most favorable intensity phenomenon. Michael R. Kaus et al. entitled an algorithm for rapid determination of the cell growth [13]. The potentiality of neonatal brain figures has advanced in the recent years. Distributed features of the images can be noticeably extracted depending on the segmentation implemented [14].

3 Brain Tumor

Brain has an exceptional composite formation with white matter and grey matter and cerebrospinal fluid as shown in Fig. 1a, b, c. Taking out helpful details from brain is a arduous problem [6].

Brain tumor is an anomalous thickening or ballooning of brain tissue that can emanate from the brain itself called primary brain tumors or they can emerge as breast (mammary glands) or lung cancer or from variant organs and proliferate to brain called as secondary brain tumors. Various classifications of primary tumors are glioblastoma, astrocytoma, meningioma, ependymoma and oligodendroglioma [3, 6, 15]. The primary and secondary tumors are shown in Fig. 2.

Two predominant categorizations of brain tumor are benign and malignant. Benign tumors cells are not cancerous, non invasive and sedate development. These tumors retaliate for therapies and can be operated and eliminated in majority of the occurrences and are not commonly peril to existence. Malignant tumors are cancerous, have rapid extension and are unmanageable, intrusive and pervade and metastasize. These tumors can be likely primary tumors or secondary tumors [13, 16]. These cells are unevenly formed and grouped in the tissues. These cells destruct the brain

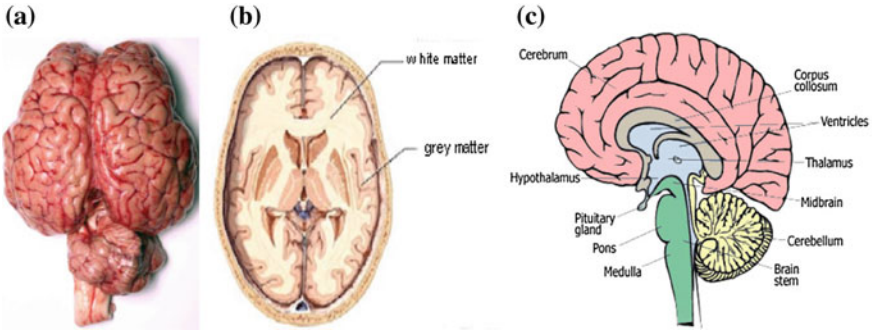

Fig. 1 **a** Live brain image. **b** White and grey matter of brain. **c** Regions of brain

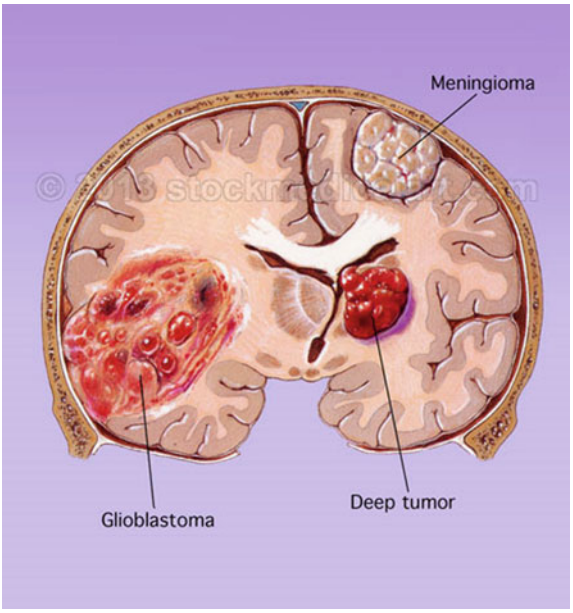

Fig. 2 Primary and secondary tumors

matter and fail the vital functioning of parts near to it and ultimately consequences to death. Apart from benign tumors these tumors are allied with torment and affliction and further more do not have understandable partitions [13, 16]. Benign and malignant tumors are shown in Fig. 3a, b, c, d. Tumor compositions diverge greatly between sufferers with conditions like dimensions, growth and confinement that can be conceptualised from assorted of imaging modalities [11] as shown in Fig. 4. The features of brain tumor are ceaseless headache, vomiting, problem to perceive sounds, visibility, behavioural changes and difficulty to talk, loss of consciousness, perception problems and loss of remembrance [1, 13]. By August 8, 2017 year-long prevalence frequency of all brain abnormalities is 7 per one lakh recording 2% of malignant brain tumors and 86% of gliomas including astrocytomas, glioblastomas and oligodendroblastomas [1].

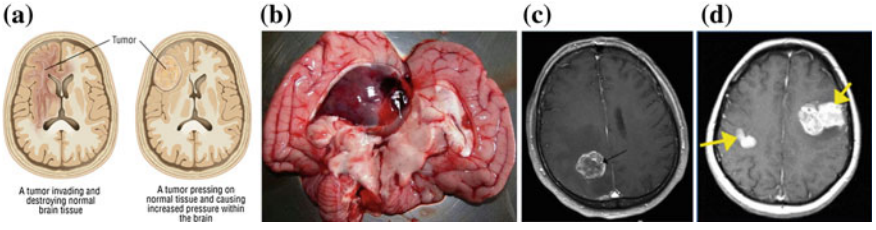

Fig. 3 **a** Tumors. **b** Tumor in live brain. **c** Benign tumor. **d** Malignant tumor

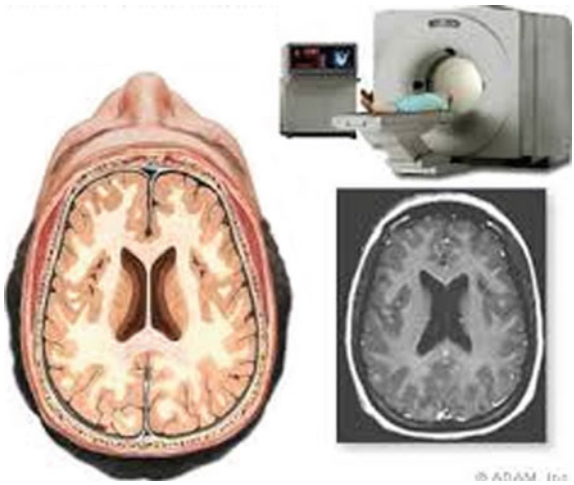

Fig. 4 Medical image modality

Brain tumor is a serious problem that has ravaged many lives that has perishable rates. To transcend demanding and dreadful cases researchers are combining professional specialisations that necessitate greater degree of theoretical and practical understanding of the disease [6, 17]. Forethought of treatment from investigations perpetrates an indispensable part in ameliorating the deceasing figure of victims due to cancer progression [17].

4 Medical Image Segmentation Operators

Medical image segmentation is one of the key parameter for recognizing the condition of the disease and its treatment. The earliest pace to examine the image is to section the image [5, 18]. Segmentation severs the picture into its component proportions or fractions. Segmentation can be elucidated as stratifying the object representation into a distinct collection of common structures or forms [5, 9]. The process of segregating the brain abnormalities can also be done physically but it wastes time and also gives raise to misconception that eventually results in fallacious prognosis. Choosing a suitable approach for image sectoring depending on its characteristics is a strenuous concern. Ultimate outcome of segmenting an image notifies the localised positions that include the whole resemblance of medical information [16, 19]. This paper concisely demonstrates the segmentation operators used in the extraction of neoplasm. Sobel operator is a kernel that accomplishes 2D slope distribution considering the edges in vertical and horizontal illumination points of the image. Gaussian edge detector is a logical operator which incorporates Gaussian smoothing filter and gradient estimation having high degree of responsiveness to noise [20]. Laplacian Edge detector measures of 2nd spatial derivatives in different directions and emphasizes the expeditious adaptions in the object magnitude levels. Average or Mean detector

quantifies the configuration and magnitude of the image to minimize the amount of intensity discrepancies. Prewitt operator is congruent to Sobel operator other than the constant c = 1 and focuses edges. Laplacian of Gaussian (LOG) is association of Gaussian filter and Laplacian. Unsharp operator is used to improve the features of the image [8, 9]. First and second derivative detectors have complicated calculations and determinations and are also imbibes time. To manually separate brain image it takes eight weeks of period as the forming of brain very complicated [21, 22]. So morphological techniques are used to diminish the difficulties of derivative operators and for specific realizations. Morphology is a broad purview of approaches for managing the image based on the appearance and features of the image. Morphological operations situates structuring element on a concentrated object and constructs images of identical magnitude to remove deflections. Watershed segmentation, a notion of mathematical morphology is strategy for identifying the outlines and also regions in the image deploying markers [5, 19].

5 Algorithm

Step1: Collect the CT lung images in DICOM format.
Step2: Pre-processing by filtering.
Step3: Apply Sobel, Prewitt, Gaussian, Average, Laplacian, LoG and Unsharp edge operators to extract the ROI.
Step4: Compare the edge images of different operators by Ground truth image.
Step5: Compute the similarity index between the images and tabulate.

6 Results and Discussions

There has been the imperative role of many leading institution and corporations to bring a frame work for ROI segmentation of different organs of human body for early detection for the abnormality. Emphasis of such frame work for brain tumor pattern is performed based on ROI segmentation. The potential of this algorithm is highlighted by the extraction of tumor edges using seven edge detection operators as shown in Fig. 5c, d, e, f, g, h, i. The resultant edge patterns obtained from various operators is compared with ground truth image (Fig. 5b) of the brain tumor. It can be observed that a clear edge pattern of brain tumor exhibit a high quality visual screening of extracted patterns. The study of the edge images will give an idea about which operator can be used for extracting the gradient image in different views of the tumor present. The quality of segmentation should be evaluated using certain performance measures. These parameters serve as a pointer in identifying and presenting the quality of segmentation. These parameters are usually evaluated by comparing the segmented image with that of the ground truth.

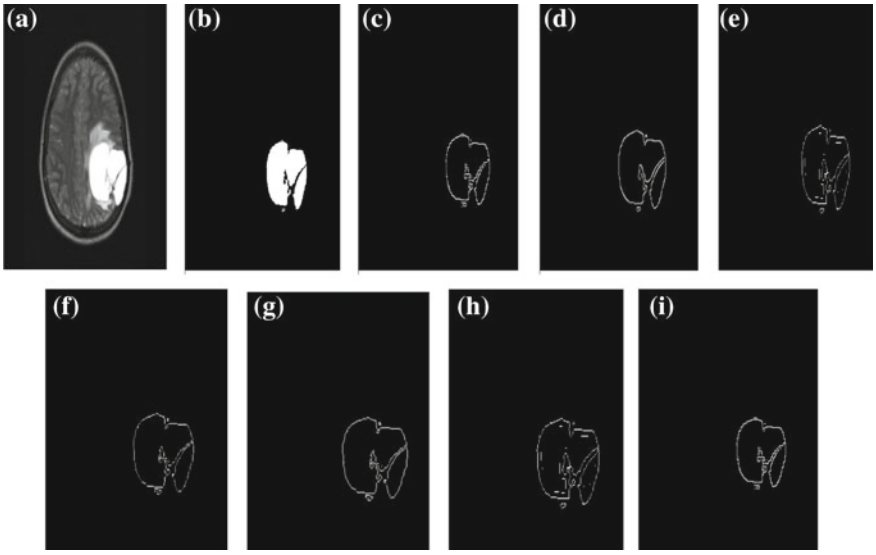

Fig. 5 **a** DICOM brain image. **b** Ground truth ROI image. **c** ROI of average operator. **d** ROI of Gaussian operator. **e** ROI of Laplacian operator. **f** ROI of Prewitt operator. **g** ROI of Sobel operator. **h** ROI of LOG operator. **i** ROI of Unsharp operator

7 Conclusions

The extraction of neoplasm using different segmentation operators like Sobel, Prewitt, Gaussian, Average, Laplacian, LoG and Unsharp is evaluated with the Ground truth image measuring the correlatedness is shown in Table 1. From the results obtained it can be observed that the Sobel operator has the highest matching parameter with the ground truth ROI edge. This quantification helps in abstracting clinical opinion to provide a better diagnosis and prognosis. The performance measures of the operator suitability and reliability of ROI segmentation helps for providing an authenticated secondary opinion.

Table 1 Measure of relatedness of different segmentation operators with ground truth ROI image

Segmentation operators	Correlatedness
Sobel	0.9200
Prewitt	0.9113
Gaussian	0.8287
Average	0.9163
Laplacian	0.8262
LoG	0.8972
Unsharp	0.8289

8 Future Scope

The algorithm can be extended to extract the tumor region by region growing segmentation process. Further the comparison can be extended to other parameters such as Global consistency error. The evaluation can also be extended to estimate the parameters in the presence of image noise.

References

1. Sirin T, Saglam MI et al, A comparative evaluation of competitive learning algorithms for edge detection enhancement
2. Vijaya Kishore V, Satyanarayana RVS (2012) Computer-aided diagnosis tool for honeycomb detection by using morphology and wavelet transform in lung CT images. IFRSA's Int J Comput 2(2)
3. Yu-Qian Z, Wei-Hua G (2005) Medical images edge detection based on mathematical morphology. In: Proceedings of 2005 IEEE engineering in medicine and biology 27th Annual Conference
4. Janaki R, Tamilarasi A (2012) Enhanced ROI (Region of Interest Algorithms) for medical image compression. Int J Comput Appl 38(2):0975–8887
5. Vijaya Kishore V, Satyanarayana RVS (2012) A modified mathematical morphology-based approach for medical image edge detection and restoration. IUP J Electr Electron Eng 5(2)
6. Ritter F, Boskamp T, Homeyer A, Laue H, Schwier M, Link F, Peitgen H-O (2011) Medical image analysis. In: Proceedings of CVPR'96 IEEE PULSE, pp 2154–2287
7. Chang, P-L, Teng W-G Exploiting the self-organizing map for medical image segmentation. In: IEEE international symposium on computer-based medical systems (CBMS'07)0-7695-2905-4/07
8. Soliman A, Khalifia F, Shaffie A, Liu N, Dunlap N, Wang B (2016) Image based CAD system for accurate identification of lung injury. IEEE
9. Kalpana V, Varadarajan S, Milinda Purna T (2015) Performance evaluation of DICOM Lung ROI with different sizes of morphological structuring elements and noise. Int J Appl Eng Res 10(6):4991–4996
10. Vijaya Kishore V, Satyanarayana RVS (2009) Comparative study of performance of edge detecting methods on medical image in the presence of Gaussian and poison noise. Int J Electron Electr Eng 5(7)
11. Vijaya Kishore V, Satyanarayana RVS (2013) A multi-functional interactive image processing tool for lung CT images. Int J Biomed Clin Eng 2(1):1–11
12. Roushdy M (2006) Comparative study of edge detection algorithms applying on the gray scale noisy image using morphological filter. GVIP J 6(4)
13. Garcia P, Pla F, Garcia I (1999) Detecting edges in colour images using dichromatic differences. In: Seventh international IEEE conference on image processing and ITS applications, vol 1, pp 363–367
14. Chang SG, Bin Y, Vetterli M (2006) Adaptive wavelet thresholding for image denoising and compression. IEEE Trans. Image Process 9(9):1532–1546
15. Vijaya Kishore V, Satyanarayana RVS (2013) A matlab based GUI for detection and classification of lung nodules in CT images. Int J Biomed Res Anal 4(1)
16. Shen T, Li H, Huang X (2011) Active volume model for medical image segmentation. IEEE Trans Med Imaging 30(3)
17. Roy KK, Phadikar A (2011) Automated medical image segmentation: a survey. In: Proceedings of the international conference on computing, communication & manufacturing

18. Bovik A (2000) Handbook of image and video processing. Academic Press
19. Adegoke BO, Olawale BO, Olabisi NI (2013) Overview of medical image segmentation. Int J Eng Res Dev 8(9):13–17
20. Kalpana V, Rajini GK, Segmentation of lung lesion nodules using DICOM with structuring elements and noise-a comparative study. IEEE digital xplore library. https://doi.org/10.1109/upcon.2016.7894661
21. Cronin P et al (2008) Solitary pulmonary nodules: meta-analytic comparison of cross-sectional imaging modalities for diagnosis of malignancy. Radiology 246:772–782
22. Durdick HE (1977) Digital imaging: theory and applications. McGraw-Hill

A Common Framework for the Extraction of ILD Patterns from CT Image

V. Kalpana, V. Vijaya Kishore and K. Praveena

Abstract Majority of the pulmonary diseases and their identification rely on geometric progression of lung spaces. Most common types of lung diseases include abnormalities categorised as Interstitial lung diseases (ILD) like sarcoidosis, idiopathic pulmonary fibrosis (IPF), malignant nodules, extrinsic allergic alveolitis (EAA) and honey comb structures from the infectious disorders is a very difficult task for diagnosis. For clinical practices, images are accumulated and stored in digital representation like MRI and CT to facilitate corresponding diagnosis. Some of the physicians can't provide inadequacy in image parts which are known as (ROI) region of interest. Researchers converse at focusing on ROI coding to guarantee the use of multiple and randomly shaped ROI's in image depicting the importance of ROI confining the background regions that can be exhibited by varying the levels of quality. This paper highlights the medical image ROI segmentation that delineates the diseased part using morphological algorithm. This paper addresses working on reliable methods for diagnosis and prognosis of the pulmonary diseases. Segmentation of ROI for the detection of CT lung pattern abnormalities likely nodules, sarcoidosis, IPF and honeycomb are done based on morphology in this research work. The techniques used to decoct medical information helps the radiologists for early diagnosis of ILD to figure out appropriate treatment.

Keywords ILD · IPF · Nodules · Sarcoidosis · Honeycomb · CT · ROI · Segmentation · Morphology

V. Kalpana · K. Praveena
Department of ECE, Sree Vidyanikethan Engineering College, Tirupathi, India
e-mail: ksh.v1227@gmail.com

K. Praveena
e-mail: kakarlapraveenasvec@gmail.com

V. Vijaya Kishore (✉)
Department of ECE, G. Pullaiah College of Engineering and Technology, Kurnool, India
e-mail: kishiee@rediffmail.com

© Springer Nature Singapore Pte Ltd. 2020

T. Hitendra Sarma et al. (eds.), *Emerging Trends in Electrical, Communications, and Information Technologies*, Lecture Notes in Electrical Engineering 569,
https://doi.org/10.1007/978-981-13-8942-9_42

1 Introduction

The area of medical imaging has developed into a significant scientific discipline. The examination of patient data is gained by image modalities such as CT, MRT, PET and US. Those imaging methods propose unachieved advancements for diagnosis and therapy evaluation. Medical image processing is necessary to influence increasing aggregation of scientific information and to examine information for specific medical objective [1]. Medical image analysis need image processing techniques and pre-processing functions like noise removal, image enhancement and edge detection. Feature extraction is executed to acknowledge the ROI which may be tumour, lesion or abnormality [2]. For suspicious connected parts in the image, abnormal colours and appearance are to be physically differentiated by radiologists for advanced observations. For further processing of medical imaging, particular methods to fulfil image segmentation are sorted with separate assortative biomedical applications [3]. The main intention of medical image processing is to provide valued representation of the contents [1]. Computed Tomography is more likely known as computed axial tomography or CAT scan is a principle that assists X-rays (radiographs) and computers (for computations) to generate three-dimensional likeliness of the human body. Other than methods using photographic films that signify opaque physical organs like bones, CT stipulates thorough range of the contrast tissues, such as lymph's, muscle tissue for fluid pumping and body parts like lungs. CT images render a physical representation which assists in identifying distinct pneumonic diseases like ILD and also tumours. Several pulmonic diseases can be determined by studying the lung tissue patterns of pulmonary CT images. So segmentation of lung is a primitive operation to acquire texture extraction and analysis [4]. ILDs are more than 200 different types which are heterogeneous group of parenchymal lung disorders due to alveolar septal thickening, fibroblast proliferation, collagen decomposition and pulmonary fibrosis. Majority of ILDs are due to unknown causes. Known causes may be inhaling organic or inorganic dusts, gases, fumes, drugs, radiation and smoking infections. ILDs are classified into acute, chronic and episodic. Acute ILDs are because of infection, allergy or toxins. Episodic ILDs are due to pulmonary eosinophilia or Extrinsic Allergic Alveolitis. Chronic ILDs are caused by drug side effects and most common are cancer, IPF sarcoidosis and honey combing [1]. A pulmonary lung nodule is any space occupying lesion either solitary or multiple on the lung that is 3 cm in diameter or less and if larger considered as Lung mass, are cancerous [5]. Malignancy of lung nodules in elder people seems to be more cancerous and serious issue for mortality [6]. Recognition of nodules from regular structures is focused as they are extremely identical with additional sections of lung parenchyma.

Nodules have dissimilar aspects: round, flat or speculate appearing on the edge regions [7]. Classification of ILDs is shown in Fig. 1. Different types of ILDs for lung nodules are shown in Fig. 2a, b, c.

Honey combing refers to the CT manifestation of diffuse pulmonary fibrosis. The clustered cystic air spaces are between 3–10 mm in diameter but occasionally as large as 2.5 cm which are usually sub pleural and basal in distribution. Honey combing patterns and affected lung images are shown in Fig. 3a, b, c. Sarcoidosis

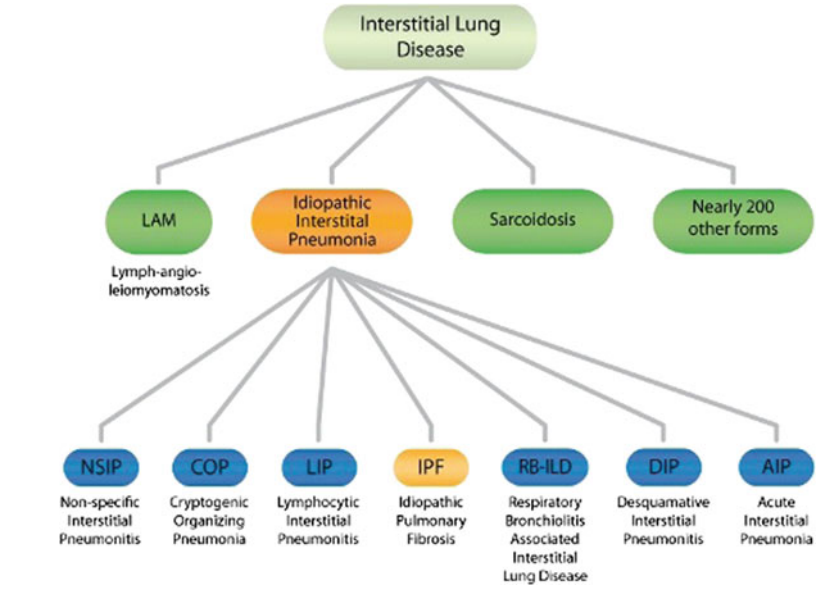

Fig. 1 Classification of ILD

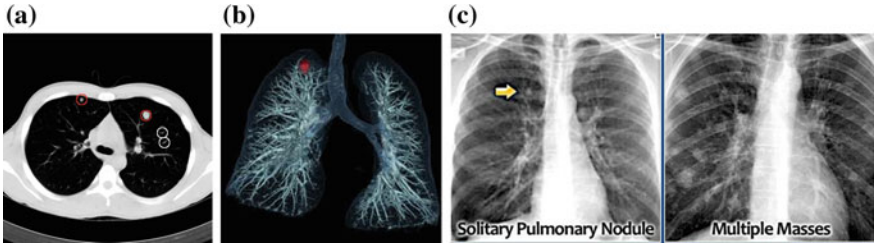

Fig. 2 **a** Pulmonary lung nodules causing lung cancer. **b** Lung nodules in 3D display, **c** mass

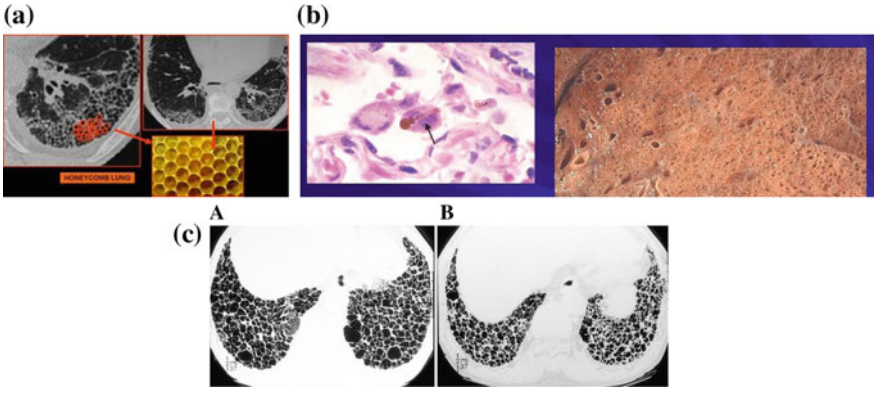

Fig. 3 **a** Honey comb lung. **b** End stage honey comb model. **c** End stage honey comb

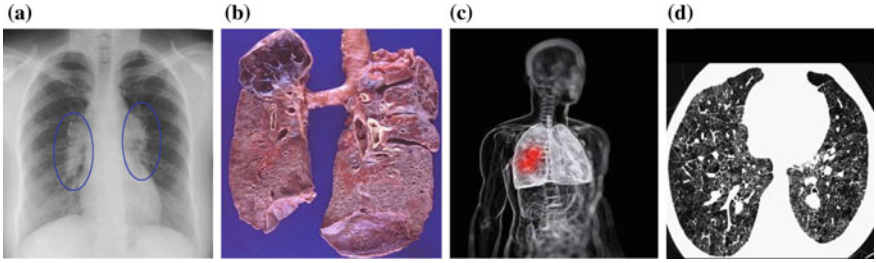

Fig. 4 **a** Sarcoidosis. **b** Sarcoidosis lung. **c** Sarcoidosis lung in 3D. **d** Severe sarcoidosis

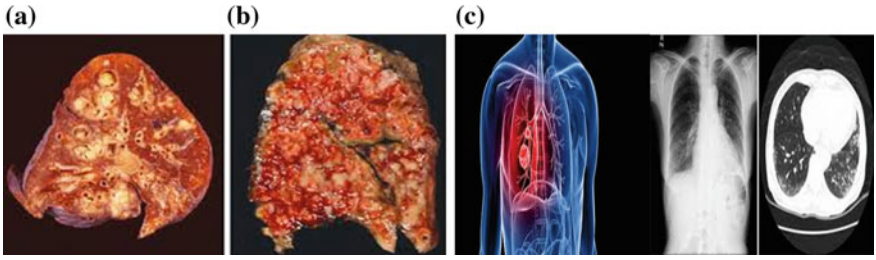

Fig. 5 **a** IPF lung. **b** IPF 3D lung and IPF lung slice

is a disease involving abnormal collection of inflammatory cells that form lumps known as granulomas. The abnormalities of sarcoidosis are shown in the Fig. 4a, b, c. Idiopathic pulmonary fibrosis mean scarring of lung tissue and is the cause of worsening dyspnoea, shortness of breath. The idiopathic lung severity and 3D structuring is shown in Fig. 5a, b, c.

2 Literature Review

Summarized method of medical image segmentation is split into three successions. The primary categorisation is one of the easiest ways of analysing medical image by using the techniques to measure luminance and connected points. The preceded method is depicted by the applying of interpretation, design and processing techniques, while the third group obtains segmentation using ingredient information. An effective and essential stage in the medical image analysis (MIA) is Segmentation [8]. In recent years, hierarchical clustering methods were commonly used as they are capable of extracting images from their backgrounds. These techniques are based on collection of images considering image colour, appearance and spatial coordinates. In spite, a significant difficulty existing with these techniques is to predefine the cluster count needed for image segmentation. There by, the possible benefits and use of these techniques has gradually decreased. The traditional approaches for medical image

segmentation are setting boundary limitations, connecting of the located image parts and creating exact pixel values. To overcome the identified drawbacks of these conventional principles this paper was devised with morphological algorithm to segment the ROI of various types of diseases. To support the progress of image segmentation, mathematical analysis and interpretation methods are accustomed from the image patterns based on the aspect and condition of their physical existence. When applied to object segmentation there is a basic operation of identifying ROI of the image appearance statistics [8]. Density based techniques are thresholding, region growing, opening and closing. Model based techniques determine the design to abstract irregular shapes of the lung [5]. Morphological and anatomy based techniques classify insignificant three dimensional mass in the lung [9] using size, brightness, region of interests. Xiaolei and Gavrii consigned their theories to establish and accomplish to decoct significant features comprising of image dimensions, appearance and irregularities in medical images. Rastgarpour and Shanbehzadeh ascertained peculiar methods for segmenting the truthful image features. These techniques used to divide the image rely on many constraints like class of the disease and distinguishing the structure of image. These results provoke a difficult task for the researchers to project on literatures dealing with image segmentation [8].

3 Medical Image Segmentation

Segmentation is a pertinent stratagem in medical image processing and it has been used in several cases to obtain information for better opinion about the type, location and detection of the various diseases. The illustrations of medical imaging comprehends revelation of the veins and blood vessels in X-ray image, determining pulmonary artery injuries, incision behaviour, surgical contingencies, quantifying neoplasm abnormalities and the process of treatment, controlled blood cells count, mechanism of directed growth in brain, identifying contrast levels of calcareous causing breast cancer from mammograms, alignment of images based on their colour, bounding collection of images and their pattern recognition, extracting heart images from cardiac images of fluoroscopy and identification of lesion. For therapeutic improvements segmentation technique is highly relevant to distinguish structural characteristics, calculating image information and pictorial representation [10]. The accuracy and judging certainty in classifying any lung abnormality lies on relevant segmentation technique. Image segmentation is used to describe boundaries or objects in pictures. The consequence of dividing an image from its background defines attached areas which record the entire image region, or determines the outline or boundaries obtained from the image. The representation of image in a particular region is characterised with the aspect of certain features such as hue, degree of radiance, or shape of the image. Common boundaries in an image are considerably variant when the area of the object is analysed [4]. Medical image segmentation applications for determined regions have diagnostic importance in an image. Owing to the remarks that only some part of image actually is of interest, ROI based tech-

niques are becoming popular [8]. The functions of detecting edges also recognise the contours of homogenous areas of an image based on their shape and appearance [11]. Proper identifications of edges in image processing play a continuous part in medical image analysis. Medical decision supports system commonly depends on the sustainability to classify an image and describe its rapid gaps which helps in obtaining structural characteristics and to construction content of the picture for ROI [12]. Medical image segmentation accomplishes visual characteristics of image with same objects belonging to those intensities as a group [7, 13]. Image segmentation is mainly schemed to infuse region of interest (ROIs) presenting aggregations and particularly spot the distrustful regions from the ROI causing the disease growth. The segmented outcome of extracted results of the image helps the radiologists for decision making and for further prognosis [14]. Some of applications of image segmentation are locating tumors and other pathologies, determining tissue volumes, studying of anatomical structures, finding, simplification, classification, recognition of Region of Interest (ROI) [2].

4 Concept of Morphology in Medical Image Processing

Morphological image processing is a set of nonlinear operations related to the shape and features of the image [15]. Morphology is a wide scope of image processing applications based on the shapes of the image [16]. Morphological operations places structuring element to an processed image and produces same size of images eliminating irrelevancies. To acquire the calculations accurately than common opening by reconstruction and abstains inconvenience. For this task mathematical morphology uses set of operators. Binary morphological operations can be widely used in gray-scale morphology [13, 17]. Usually structuring element is 3×3 sized and has its origin at the centre pixel. For fundamental morphological operators the structuring element has only elements close to the picture plane i.e. ones. Morphological edge detection algorithm privileges structuring element for basic theory of morphology which comprehends the operations like erosion, dilation, opening and closing. Dilation grows image points, erosion shrinks image areas, opening makes organised dismissal of object contour exhibition and closing fills the image region boundary pixels [7]. The identification of ROI using CT scans is done by extraction of useful and texture features. Depending upon the pattern and dimensions of the structuring element, the extraction of the image and its further diagnosis will focus [18]. Morphological image processing is systemised to gray level images via level sets [6, 19]. A difficult circumstance is to separate the connected surfaces that show boundary inadequacies i.e., preoccupied edges and deficient texture contrast between ROI and background. Sobel operator is used as filter for measuring 2D spatial gradient and emphasizes regions of high spatial frequencies. This filter gives the point of horizontal and vertical edges [18]. Watershed algorithm is used taking the account of the concept of mathematical morphology [16, 20]. Its classification depends on region-

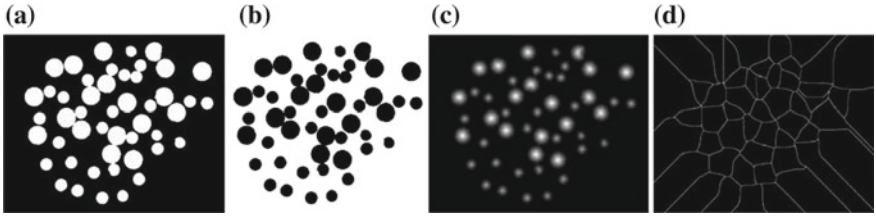

Fig. 6 **a** Original image. **b** Negative of a, **c** transform of b, **d** watershed of c

based segmentation approach where filling of water is made into the sinister regions. The event stops when the maximum reference limit is reached.

The entire picture is divided into portions appearing as dams called 'watershed lines' and are obtained by multiscale morphological reconstruction. It seems like "water ridge lines" when the outlines of the image are considered [13, 21]. It works essentially if near observed objects and darker positions are characterised. Watershed segmentation veracity lies on ridges to carry out a particular segmentation which is exhibited by edge detection where the outlines of the region of interest are indicated as ridges and the Fig. 6a, b, c, d illustrates the explanation [7].

5 Algorithm

Step1: Collecting the DICOM images.
Step2: Pre-processing by applying thresholding to images.
Step3: Discontinuity based image segmentation to detect edge using Sobel derivative operator.
Step4: Computing the gradient magnitude image.
Step5: Closing and Opening morphological operations on input image and reconstructing the image based on Morphology.
Step6: Watershed algorithm based extraction of lung region.
Step7: Applying Markers and boundaries to the foreground & back ground image.
Step8: Compute a segmentation function for the image whose objects are dark regions.
Step9: Compute foreground markers by connecting blobs of pixels within each of the objects.
Step10: Compute background markers which are pixels that are not part of any object.
Step11: Modify the segmentation function so that it only has minima at the foreground and background marker locations.

6 Results and Discussions

This paper emphasises a common frame work, performing ROI segmentation of four types of ILD patterns. The algorithm implemented in this research work has the potential of extracting various ILD patterns. The results provide a high quality visual screening of extracted patterns of different ILD patterns such as malignant nodules, sarcoidosis, IPF and honey combing. The resulting images provide valuable information about the structures and their growth over duration of examination which helps the clinicians for early diagnosis and prognosis. In this paper, the ROI segmentation approach focuses on four set of images with different ILD patterns as shown in the Figs. 7, 8, 9 and 10 for different ILDs. Figure 7 demonstrates the extraction of ROI i.e. nodules. Figure 8 shows the ROI of the image affected with sarcoidosis.

Figure 9 displays the ROI of pulmonary lung affected with Idiopathic pulmonary fibrosis. Figure 10 presents the final stage of ILDs mentioned to as honey combing lung.

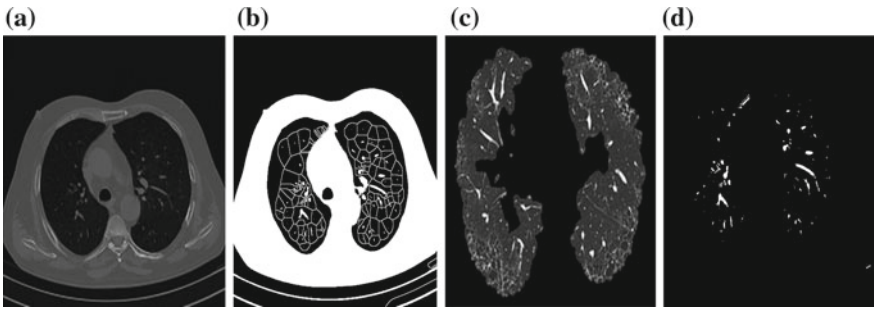

Fig. 7 **a** Original lung nodule image. **b** Markers and boundaries. **c** Segmented image. **d** ROI

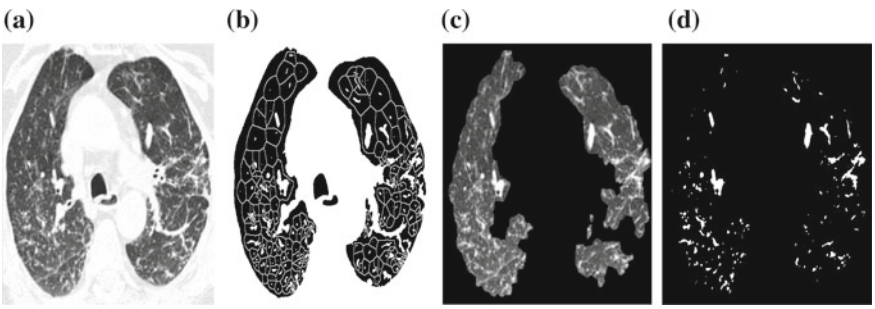

Fig. 8 **a** Original sarcoidosis lung image. **b** Markers and boundaries. **c** Segmented image. **d** ROI

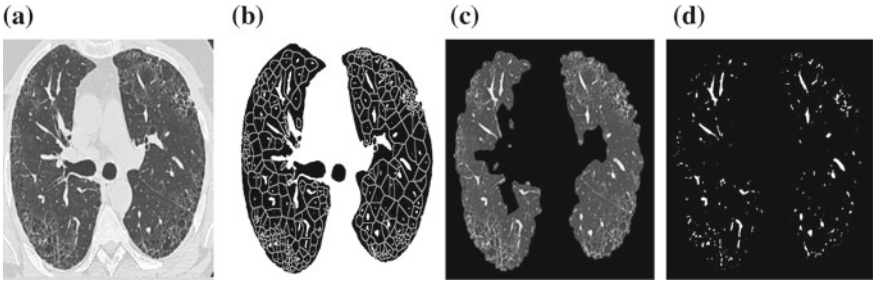

Fig. 9 **a** Original IPF lung image. **b** Markers and boundaries. **c** Segmented image. **d** ROI

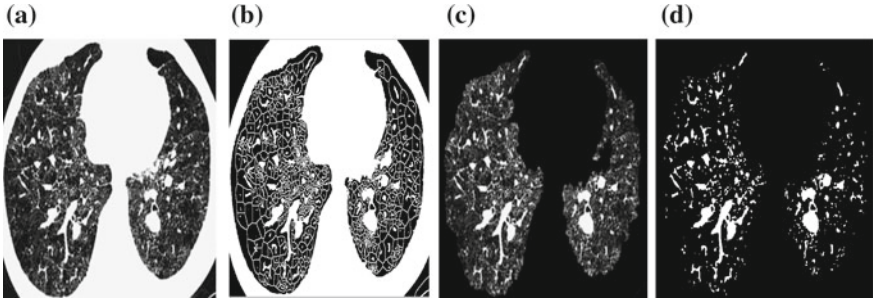

Fig. 10 **a** Original honey comb lung. **b** Markers and boundaries. **c** Segmented image. **d** ROI

7 Conclusions

Detecting abnormality at the earliest stage and screening effectiveness depends on reliable improved image modalities and ROI segmentation techniques. In this paper a common platform is implemented for extracting four different patterns in ILD. The use of morphology with ROI segmentation techniques of lung patterns enhances the visual appearance of extracted ILD patterns. These results will have a impact on evaluation of indeterminate lesions. In addition the analysis can be made about the advancement of disease about the content of lung region affected by the disease. The results allow effective screening of ILD patterns avoiding poor diagnosis and for early detection, diagnosis and treatment.

8 Future Scope

Further the procedure can be enhanced to assess the extracted patterns by changing the structuring elements for morphology based ROI segmentation. Further the susceptibility of the approach can be examined in noisy environment also.

References

1. Ritter F, Boskamp T, Homeyer A, Laue H, Schwier M, Link F, Peitgen H-O (2011) Medical image analysis. In: Proceedings of CVPR'96 IEEE PULSE, pp 2154–2287
2. Roy KK, Phadikar A (2014) Automated medical image segmentation: a survey. In: Proceedings of the international conference on computing, communication & manufacturing
3. Chang P-L, Teng W-G, Exploiting the self-organizing map for medical image segmentation. In: IEEE international symposium on computer-based medical systems (CBMS'07) 0-7695-2905-4/07
4. Vijaya Kishore V, Satyanarayana RVS (2012) Computer-aided diagnosis tool for honeycomb detection by using morphology and wavelet transform in lung CT images. IFRSA's Int J Comput 2(2)
5. Kalpana V, Rajini GK, Segmentation of lung lesion nodules using DICOM with structuring elements and noise-a comparative study. IEEE digital xplore library. https://doi.org/10.1109/upcon.2016.7894661
6. Cronin P et al (2008) Solitary pulmonary nodules: meta-analytic comparison of cross-sectional imaging modalities for diagnosis of malignancy. Radiology 246:772–782
7. Kalpana V, Varadarajan S, Milinda purna T (2015) Performance evaluation of DICOM lung ROI with different sizes of morphological structuring elements and noise. Int J Appl Eng Res 10(6):4991–4996
8. Shen T, Li H-S, Huang X (2011) Active volume models for medical image segmentation. IEEE Trans Med Imaging 30(3)
9. Sirin T, Saglam MI et al, A comparative evaluation of competitive learning algorithms for edge detection enhancement
10. Vijaya Kishore V, Satyanarayana RVS (2013) A matlab based GUI for detection and classification of lung nodules in CT images. Int J Biomed Res Anal 4(1)
11. Vijaya Kishore V, Satyanarayana RVS (2009) Comparative study of performance of edge detecting methods on medical image in the presence of Gaussian and poisson noise. Int J Electron Electr Eng 5(7)
12. Vijaya Kishore V, Satyanarayana RVS (2012) A modified mathematical morphology-based approach for medical image edge detection and restoration. IUP J Electr Electron Eng 5(2)
13. Vijaya Kishore V, Satyanarayana RVS A multi-functional interactive image processing tool for lung CT images. Int J Biomed Clin Eng 2(1):1–11
14. Adegoke BO, Olawale BO, Olabisi NI (2013) Overview of medical image segmentation. Int J Eng Res Dev 8(9):13–17
15. Yu-Qian Z, Wei-Hua G (2005) Medical images edge detection based on mathematical morphology. In: Proceedings of 2005 IEEE engineering in medicine and biology 27th Annual Conference
16. Roushdy M (2006) Comparative study of edge detection algorithms applying on the gray scale noisy image using morphological filter. GVIP J 6(4)
17. Durdick HE (1977) Digital imaging: theory and applications. McGraw-Hill
18. Soliman A, Khalifa F, Shaffie A, Liu N, Dunlap N, Wang B (2016) Image based CAD system for accurate identification of lung injury. IEEE
19. Bovik A (2000) Handbook of image and video processing. Academic Press
20. Garcia P, Pla F, Garcia I (1999) Detecting edges in colour images using dichromatic differences. In: Seventh international IEEE conference on image processing and ITS applications, vol 1, pp 363–367
21. Chang SG, Bin Y, Vetterli M (2006) Adaptive wavelet thresholding for image denoising and compression. IEEE Trans. Image Process 9(9):1532–1546

Design and Analysis IDMA and CDMA In Rayleigh Channel With Equalization Technique Using Tree Based Interleaver

Asharani Patil and G. S. Biradar

Abstract The recent era evolved with many new technologies with new multiple access technique. New technique known IDMA is emerging in fourth and fifth generation mobile communication systems. In this article we have analysis different multiple access techniques in Rayleigh channel using equalization technique using adaptive filters. IDMA-interleave division multiple access technique gives a efficient performance over CDMA, MC-CDMA using chip by chip iterative detection in multipath channel with lesser receiver design complexity. Equalization process with IDMA multiple accesses in multipath single channel gives desirable bit error rate performance with faster convergence rate and track stability compared with conventional CDMA and MC-CDMA in multiuser channel. Detailed expression with variable values is defined in article. In article different equalization adaptive filters used are LMS, RLS and variable forgetting factor RLS algorithm. This article gives performance for single user as well as multiuser channel in Rayleigh channel.

Keywords IDMA · LMS · NLMS · RLS · VF-RLS · Equalization

1 Introduction

Today's era is completely replaced by wireless virtual mobile communication technology wherein second and third generation mobile communication systems is replaced by fourth and fifth generation mobile communication systems. This generation has significant revolution with new multiple access scheme such as OFDM, OFDMA, IDMA [1], NOMA, SMDA etc. the reason behind this is consequential and revolution requirements of present generation applications. With increased data rates in all multimedia application and new revolutionized communication systems.

Asharani Patil (✉) · G. S. Biradar
Department of ECE, PDA College of Engineering Kalaburagi, Gulbarga, Karnataka, India
e-mail: asharanispatil@gmail.com

G. S. Biradar
e-mail: gsbiradar@gmail.com

© Springer Nature Singapore Pte Ltd. 2020

T. Hitendra Sarma et al. (eds.), *Emerging Trends in Electrical, Communications, and Information Technologies*, Lecture Notes in Electrical Engineering 569,
https://doi.org/10.1007/978-981-13-8942-9_43

In third generation, CDMA and MC-CDMA [2] had tremendous application and need was seen with higher data rates and achievable reliable communication. But the design was increased as number of users increased in channel. Receiver design for detection and estimation was very complex as number of users was increased in channel hence CDMA, MC-CDMA failed to perform in MAI environment [2, 3]. Multiuser detection failed to better BER performance in multipath channels as well as ISI and MAI environment. Hence evolution of new multiple access started to give new multiple access techniques. New multiple access OFDM, MIMO OFDM, OFDMA, IDMA, NOMA [4] etc.,. These multiple access techniques perform efficiently in ISI and MAI environment.

Potential high data rates is seen in these new multiple access techniques in fourth and fifth generation mobile communication systems. OFDM and OFDMA give well orthogonal property among the users with addition of cyclic prefix gave efficient orthogonal property among users in single channel.

IDMA [1] is new technology which is revised version of CDMA, has replaced CDMA in fourth and fifth generation mobile communication systems. In IDMA each user is assigned with a unique interleaver which distinguishes it from each other users. IDMA is considered as special case of CDMA which allows use of low complexity iterative multiuser detection techniques in multiuser with single channel. IDMA with equalization techniques gives improvised of previous IDMA performance. Equalization is done through adaptive filters such as LMS [5], NLMS [6] RLS [5], V-RLS [5] algorithm [7].

2 IDMA

Interleave Division Multiple Access is multiple access mainly inherit the principles of CDMA [8], MC-CDMA with significant performance. Figure 1 represents the brief diagram of IDMA with processing blocks. Chip-level interleaving ensures that the transmitted sequences in multiuser multipath channel from different users remain un-correlated.

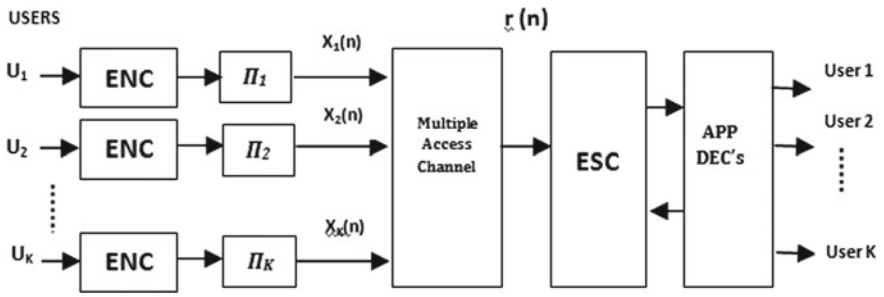

Fig. 1 Processing block of IDMA

In above we have considered k users which undergo encoding with interleaving process. Each user is differentiated among itself by these chip based interleavers in single multiple path channel. Channel used Rayleigh channel, each coefficients of Rayleigh channel is multiplied with users. Encoded is done by FEC encoder as shown in figure with ENC block. 'π_k' indicate interleaving using tree based interleaver.

At receiver section:

$$\mathrm{r(n)} = \sum_{k=1}^{K} h_k(n)x_k(n) + z(n) \tag{1}$$

$$= h_k(n)x_k(n) + \in_k (n) \tag{2}$$

At receiver, ESE indicates elementary signal estimation in this along with estimation we have introduced equalization using LMS and RLS adaptive filters [5]. These filters give a stable BER performance with very number of iterations in simulation process. Aposterior Probability (APP) decoders are used for efficient operating in an iterative process. Each output gives a log likelihood ratio output in order to differentiate each user in the channel.

Interleaver used is tree based interleaver, its one of efficient and stable interleaver which difference each user in channel by its unique procedure wherein each eight bits of user data is divided into odd and even bits then each 4 bits are divided into its odd and even bits among given four bits (Fig. 2).

So based on the length of user data, interleaving process takes in the transmitter along with encoding and spreading.

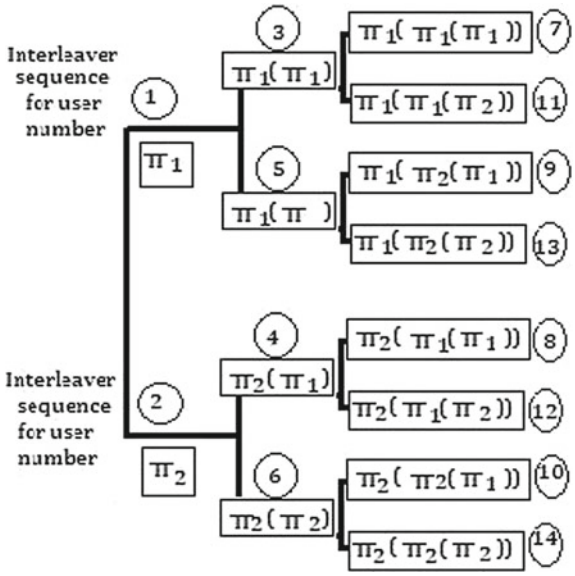

Fig. 2 Tree based interleaver

3 Adaptive Filter Equalization

For the estimation process to initiate we go for initial channel estimation [9] using LS estimator in iterative conditions by employing the mean of $x_k(n)$ that is $\hat{x}_k(n)$ obtained from prior information $L^a_{ESE}(x_u[n])$ from APP decoders further LMS and RLS computes the channel impulse response [7].

$$\hat{h}_k(n+1) = \hat{h}_k(n) + \mu\, e[n]\hat{x}^*_k(n) \tag{3}$$

μ is step size which positive real number where $0 < \mu < 1$ for system to be stable in nature. And estimated error gives $e[n] = z[n] - \hat{h}_k(n)\hat{x}_k(n)$.

Normalized LMS gives real time applications which computes the estimate of the channel impulse response

$$\hat{h}_k(n+1) = \hat{h}_k(n) + \mu e[n]\frac{\hat{x}^*_u(n)}{\left\|\hat{x}_u[n]\right\|^2} \tag{4}$$

In normalized least mean square NLMS, the step ranges from 0 to 2 for system stability. Furthermore LMS and NLMS [6] gives inefficient BER performance with slower convergence rate therefore

We have considered Recursive Least Square algorithm which gives faster convergence rate, trails stability for steady state. Below expressions gives channel estimation expression.

$$\hat{h}_k(n) = \hat{h}_k(n-1) + k[n]e[n] \tag{5}$$

In above expression $\hat{h}_k(n-1)$ is equivalent previous estimate channel response, e(n) gives estimation error.

$$e[n] = z[n] - \hat{h}^H_k[n]\hat{x}_u[n] \tag{6}$$

$$k[n] = G[n-1]\hat{x}_u[n]/\lambda[n] + \hat{x}^H_k[n]G[n-1]\hat{x}_u[n] \tag{7}$$

$k[n]$ is exponential weighted least square with matrix inversion, $\lambda[n]$ indicates the constant between zero to unity, $G[n-1]$ indicates inverse correlation matrix [10].

$$G[n] = \lambda^{-1}G[n-1] - \lambda^{-1}k[n]\hat{x}^H_l[n]G[n-1] \tag{8}$$

Further more conventional Recursive LS algorithm [11] gives further convergence with stable performance but at higher steady state, unacceptable performance, therefore we have considered increase in variable forgetting factor which is constant in above equation [3] is made variable with larger value which results in lesser mean square error but slower convergence rate and tracking speed. Therefore variable for-

getting factor λ[n] is given by

$$\lambda[n] = \lambda_{min} + 1^{2p(n)} - 2^{p(n)},\ where\ p(n) = negative\ round\left[e^2(n)\right],\quad \lambda_{min} \geq 0 \tag{9}$$

Therefore a comparative analysis is made between CDMA and IDMA [9] for above mentioned adaptive algorithms, BER performance is derived among each algorithm, analyzed the rate of convergence too.

4 Result

Communication Model is defined considering transmitter section with receiver in Rayleigh channel. Rayleigh Channel is considered with three coefficients. Model is defined for single user and multiuser for n = 20 users. We have taken 1000–10,000 numbers as input for a user with BPSK modulation with encoding process. Interleaving process is considered using tree based interleaver. Comparative analysis is made considering bit error rate performance and convergence rate using equalization technique in Rayleigh channel [12] with Interleave Division Multiple Access and Code Division Multiple Access. Error estimation is made considering bit rate versus signal to noise ratio.

From the above graph Fig. 3, represents the BER performance of IDMA with CDMA in Rayleigh channel using equalization process. Error rate found to be 0.45

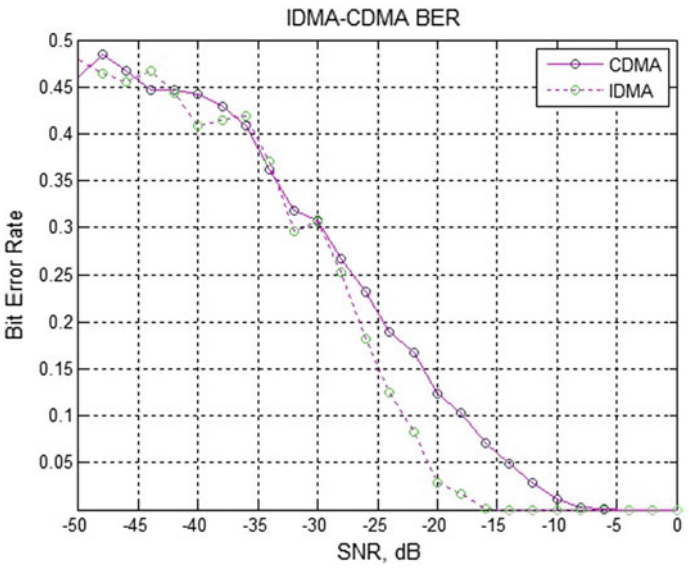

Fig. 3 Bit error rate performance

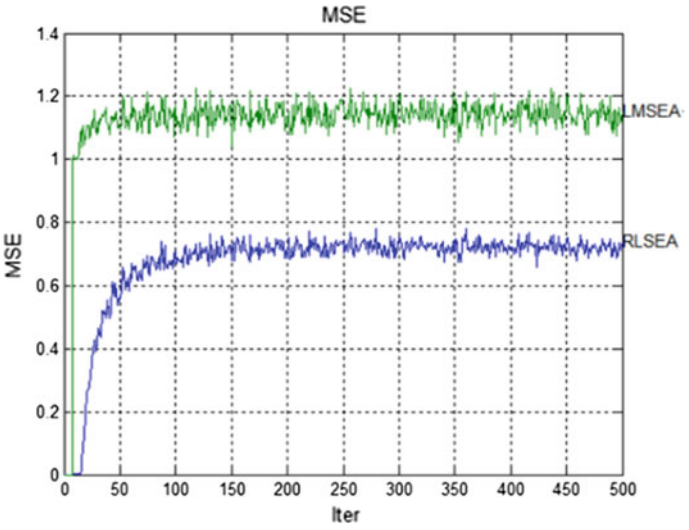

Fig. 4 Rate of convergence of RLS versus LMS algorithm for IDMA

for the SNR value of −45 dB, as SNR value increases it is seen that bit error rate decreases. At SNR of −30 dB bit error rate graph for IDMA declines very lesser than compared to bit error rate graph for CDMA. For SNR value of −20 to −5 dB, error rate found to be −13 dB difference between IDMA and CDMA. So it can be interpreted with conclusion that bit error rate performance is found to be efficient in IDMA than CDMA considering equalization technique with Rayleigh channel along with computational complexity reduces in the equalization process with iterative estimator (Fig. 4).

The above represents graphical representation Rate of Convergence. Adaptive filter exhibits the property known as Rae of convergence which indicates the process where in the system or signal achieves its significant or constant stable level of processing after which signal get stable with high efficient within less number of iterations. In above graph signal with LMS and NLMS filtering IDMA user signal takes much higher number of iterations for gaining its stability where as RLS filtering IDMA gain faster stability with very less number of iteration in the process.

5 Conclusion

In this paper we have proposed an equalization technique with channel estimator for IDMA systems using LMS, RLS with variable forgetting factor RLS algorithm in Rayleigh channel using tree based interleaver. We can say from the results that bit error rate performance is efficiently improved with reduced complexity using recursive filters when compared with static least mean square filter. Computation

speed that is rate of convergence is also observed that recursive least mean filter achieves stability faster to its ideal within few iterations when compare to least mean square filters. Hence we conclude that recursive filters are much efficient for bit error performance compare to the least square for IDMA system. Along with it BER performance is compared with CDMA system using adaptive filter, it is perceived that IDMA shows desirable performance compared to CDMA systems in Rayleigh channels.

References

1. Ping L, Liu L, Wu K, Leung WK (2006) Interleave division multiple-access. IEEE Trans Wirel Commun 5(4):938–947
2. Ping L, Guo Q, Tong J (2007) The OFDM-IDMA approach to wireless communication systems. IEEE Commun (City University of Hong Kong, Hong Kong Sar)
3. Oyerinde O, Mneney SH (2012) Combined channel estimation and adaptive prediction for MC-IDMA systems. In: Proceedings of IEEE international conference on communications, Ottawa Canada, pp 3766–3770
4. Ping L, Guo Q, Tong J (2007) The OFDM-IDMA approach to wireless communication. IEEE Commun Soc, 18–24. ISSN 1536-1284
5. Haykin S (2005) Adaptive filter theory. Pearson Education
6. Oyerinde O, Mneney SH (2013) Adaptive algorithm based time domain iterative channel estimation for MC-CDMA systems. In: Proceeding of the IEEE 3rd international conference on wireless communication society. Vehicular Technology, New Brunswick, New Jersey USA, pp 1–5
7. Cai Y, Lamare RC (2012) Low complexity variable forgetting factor mechanism for RLS algorithm in interference mitigation applications. In: Proceeding of international symposium on wireless communication systems, pp 471–475
8. Kusume K, Bauch G, Utschick W (2013) IDMA versus CDMA: analysis and comparison to two multiple access schemes. IEEE Trans Wirel Commun 11(1)
9. Oyerinde O, Mneney SH (2012) Review of channel estimation for wireless communication systems. IEEE Tech Rev J 29(282–298)
10. Oyerinde O, Mneney SH (2014) Regularized adaptive algorithm based time iterative channel estimation for MC-IDMA systems. In: Proceedings of IEEE 4th international conference on wireless communication society, vehicular technology information theory and aerospace & electronics systems technology, pp 1–5, Aalborg Denmark
11. Suyama S, Zhang L, Suzuki H, Fukawa K (2008) Performance of iterative multiuser detection with channel estimation for MC-CDMA and comparison with chip interleaved MC-CDMA. In: Proceeding of IEEE global communication conference, pp 1–5
12. Rehman H, Zaka Shah I, Ahmad J (2008) Combined equalization and channel estimation for MC-IDMA uplink transmissions. In: International IEEE Conference
13. Kusume K, Baucg G, Utscick W (2009) IDMA versus CDMA: detectors, performance and complexity. In: IEEE global telecommunications conference, Honolulu

A Secure Key and Data Exchange Mechanism Using Elliptic Curve Cryptography on WSN

Kalkundri Ravi, Rajashri Khanai and Kalkundri Praveen

Abstract Wireless Sensor Networks are gaining popularity in various fields and areas. But these nodes are vulnerable as they are open networks and easily accessible. The major challenge is to have a secure data transmission between the nodes. To establish a secure transmission, we require a security scheme like a cryptographic algorithm, but this also requires a secure key distribution between nodes. The WSN's have constraints like limited area, power and memory which restrict all the categories of cryptographic algorithm. Depending upon the criteria's and constraints, cryptographic algorithm like Elliptic Curve Cryptography (ECC) is best suitable for WSN's environment. ECC has a smaller key size, high security and less computation time which makes the node an efficient crypto system. This paper describes the implementation of ECC cryptosystem for WSN for secure key and data transmission between the nodes.

Keywords WSN · ECC · Security

K. Ravi (✉)
Department of Computer Science & Engineering, KLS's Gogte Institute of Technology, Belgaum, Karnataka, India
e-mail: ravi.kalkundri05@gmail.com

R. Khanai
Department of Electronics & Communication Engineering, KLE Dr. M.S. Sheshgiri College of Engineering and Technology, Belgaum, Karnataka, India
e-mail: rajashri.khanai@gmail.com

K. Praveen
Department of Electronics & Communication Engineering, KLS's Gogte Institute of Technology, Belgaum, Karnataka, India
e-mail: kalkundri.praveen@gmail.com

© Springer Nature Singapore Pte Ltd. 2020

T. Hitendra Sarma et al. (eds.), *Emerging Trends in Electrical, Communications, and Information Technologies*, Lecture Notes in Electrical Engineering 569,
https://doi.org/10.1007/978-981-13-8942-9_44

1 Introduction

Wireless sensor networks (WSNs) play an important role in our day to day life. Information transmission is the major task of every WSN's. WSN's are being used extensively in various fields such as real-time traffic monitoring, safety monitoring in building, health care system, agriculture, military application, ecological monitoring, temperature and humidity monitoring, industrial applications, traffic monitoring and control, and so on. The Fig. 1 depicts typical WSNs in the health care scenario, where the patients are under observation almost all the time, in places like offices, market, home, in a hospital, or anywhere else in their daily activity. Sensed data are sent to health professionals through the Internet [1]. As the utilization of WSN's has increased, this gives rise to different types of threats [1]. As the WSN's communication is open, WSNs are highly susceptible and at high risk, thereby effecting the entire system, if suitable safety measures are not taken. Authentication between WSN's plays an important role in securing data transmission against various types of attacks like node impersonation, falsification of data, replay attacks etc. Another issue is that WSN's are a combination of many tiny and low-cost sensor nodes where they have limited energy and limited computation ability to processor transmit the data. Thereby securing WSNs with it presents environmental resource-constrained has been becoming a challenging task. WSN's is a combination of multiple self-organized sensor nodes capable of communicating wirelessly and security requirements are similar to any usual computer networks [1, 2]. As the WSNs have various constrains, all security solutions applicable for conventional computer networks

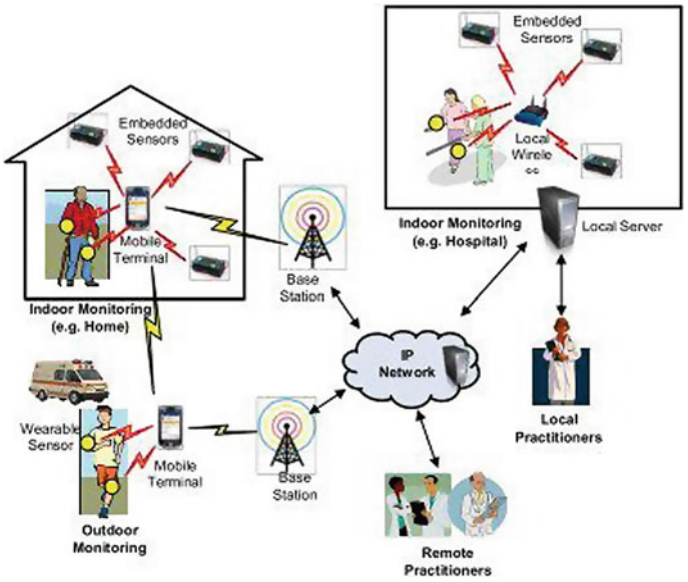

Fig. 1 Scenario of wireless sensor network (*Courtesy* [5])

cannot be implemented on WSN. Various cryptographic algorithms proposed so far for different types of security, like symmetric, asymmetric and hybrid algorithms. But all these algorithms are not successful over WSN, which can be implemented on any MANETs. Over a period of time, it was assumed that the public key cryptography was not suitable for WSNs and its environment, because it required high processing power. But improvements in the algorithms and techniques, it is possible now to use public key cryptography on WSNs [2, 3].

The rest of the paper is organized as follows; in Sect. 2, we review previous approaches to WSNs security, their advantages, disadvantages, and security issues. In Sect. 3 we look into the background of Elliptic curve cryptography and the probable advantage of ECC on WSN's. Proposed scheme is elaborated in Sect. 4. In Sect. 5, we see the results obtained by Cryptool and the results obtained by our system and analyze them. Finally, the conclusion and directions of our future work are presented in Sect. 6.

2 Related Work

2.1 Security Requirements for WSN's

Since data transmission in WSN is via a wireless mode, almost all the data is open and the entire system is vulnerable for attacks. There are various security parameters such as confidentiality, integrity, availability and authenticity which must be considered in any type of network environment [3, 4]. These are some of the issues to be handled with respect to WSN. Lets us see them in brief.

1. **Confidentiality**—Measures must be taken to guarantee data confidentiality and must avoid sensitive data from getting into the wrong peoples hand, and only the authorized person must get the message or data. In a WSN, the issue of confidentiality should deal with the following criteria's:

    i. A sensor node should allow only the authorized neighbors to access its readings.
    ii. As secure key distribution mechanism.
    iii. Node information likes, node identity, keys of the nodes, and various other factors, should also be hidden to protect from traffic analysis attacks.

2. **Authentication**—Authentication ensures that only the reliable sender is sending the message to the authentic receiver only. WSN should satisfy the following criteria's in case of authentication:

    i. The nodes that are in communication must be the one that it claims to be.
    ii. Received packets at the receiver side must have come from the actual sender node.

3. **Integrity**—Integrity ensures maintaining the consistency, accuracy, and trustworthiness of data. It also refers that the message has not been tampered or altered in the network while transmission. Integrity should deal with the following issues:

   i. Only authorized nodes should be able to access the data and authority to change it.
   ii. It protects against unwanted information to be a part of data, such as noise.

4. **Availability**—Availability assures that the resources accessible by the network are available for the nodes whenever required. Availability in WSN's should take care of the following issues:

   i. The safety measures should be up all the time; a single point of failure should be avoided, even if any occurs, it must not affect the entire system.
   ii. Secure mechanism is used to ensure that there is no data loss and proper digester recovery mechanism must be provides for the entire system.

2.2 Cryptographic Significance in Wireless Sensor Networks

The future of Wireless Sensor Networks (WSNs) is promising and potential; they are being utilized and implemented in many real-world applications, such as agriculture, military application, ecological monitoring, temperature and humidity monitoring, industrial monitoring and control and home automation [4]. To keep the data safe and secure is the most challenging task in WSN's. The most common way is by using cryptography to the system for providing security. Cryptography to a system can be provided by various techniques like symmetric key techniques, asymmetric key techniques or hash function, but since WSN's have various constrained in terms of computing power, communication and limited battery life, a light weight cryptographic algorithm in required which satisfied the constraints. Choosing a cryptographic technique that is suitable for WSN's is crucial task [5].

2.3 Major Issues to Be Handled Are

i. Secure data transmission for WSN.
ii. Fast cryptographic algorithm suitable for WSN.
iii. Secure key distribution mechanism.

3 Elliptical Curve Cryptography

3.1 Background

In 1985 by Neal Koblitz and Victor Miller proposed an Elliptic curve cryptography (ECC) algorithm. The functionality of ECC scheme is same as RSA schemes and also both the algorithms work on public-key mechanisms. ECC is an asymmetric cryptographic algorithm [6]. A computation in ECC involves different stages for computing the results. There are various methods how to use the points on the curve, like points addition, where the points are obtained from where the straight line passes through the curve [7].

Multiplication of points is another method; here the points are repeated added. Encoding of message is possible with the combination of points on curve and has powerful security because of the random selection of these points on the curve [7]. An example of a curve is as shown below in Fig. 2. ECC is one of the most powerful and the most secure algorithms which require very few computations and small key size, without compromising the security compared to traditional algorithms which requires intense computations and larger key size. ECC provides same level of security, in fact better security that too with smaller-bit key size in comparison to RSA which requires higher-bit key size [8]. A key comparison is showed in Table 1, where the standardization is made from NIST.

The utilization of smaller key size has various advantages which including storage, speed and efficient use of power and bandwidth, also the processing is faster. Thus

Fig. 2 Sample of ECC curve

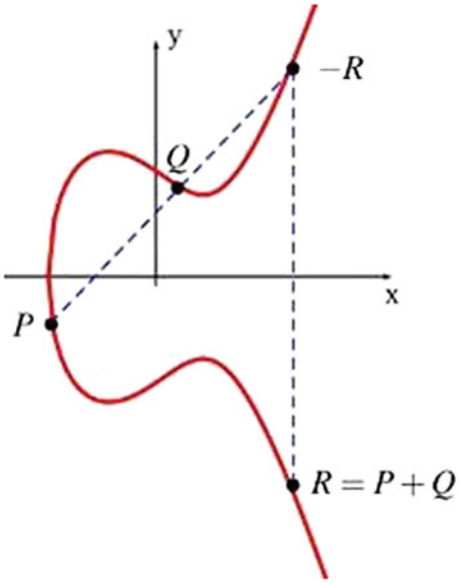

Table 1 NIST recommended field size to US federal government use [5]

Symmetric cipher key length	ECC		
	RSA (n bits)	Fp (p bits)	F2 m (m bits)
80	1024	160	163
96	1536	192	193
112	2048	224	233
128	3072	256	283
192	7680	384	409
256	15360	521	571

smaller key in public-key cryptography can be applied very efficiently in constrained devices, such as in mobile devices or RFID, etc.

3.2 Advantages of Implementing ECC for WSN's [9]

1. **Better security**: It provides greater security for a given key size. The keys are generated with the formation of the line on the curve, which is very difficult to regenerate by an unknown person.
2. **Better performance**: ECC uses a shorter key length for securing the data. For example, a 256-bit ECC key has the same level of security as a 3072-bit key of RSA. This increases the overall performance of the nodes.
3. **Mobile advantage**: Since ECCs uses smaller key size, it consumes less storage space and also it requires less bandwidth during transmission of the keys. Further it requires less processing and less power, which is suitable for Mobile devices.
4. **Less heat generation and power consumption**: As ECC uses smaller keys, less processing, so less hear, hence smaller chips can be manufactured.
5. **Memory Consumption**: As the keys are smaller in nature, it requires less storage space.

4 Proposed Scheme

4.1 Proposed Topology

Here we have implemented ECC for WSN on a Matlab simulator. From the survey made in our earlier stages, we can conclude that ECC is a better algorithm than RSA as it requires smaller key without compromising with the security aspects. We have tried to implement a topology, as shown in the Fig. 3. One of the major concerns is

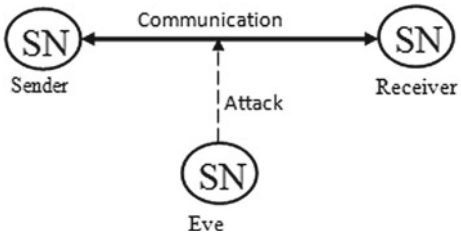

Fig. 3 Proposed topology

the mutual authentication between the nodes in WSN's. This issue is resolved by the proposed ECC technique used for secure data communication [10].

In our topology there is a Sender and a Receiver, where they are communicating and data transfer takes place among them self. We also have shown an attacker as Eve, who also tries to access the data transmitted between the Sender and the Receiver. Since the data and WSN nodes, both are in open and vulnerable for attackers, there is a need for security within the nodes and for the data. By implementing ECC in WSN, the nodes can securely transmit data [11]. The Sender and Receiver each generate their own Private Key and Public Key for each others. These keys are generated using the elliptic curve and the points on that curve generated. Both the Sender and receiver decide on to which curve and the finite points. When a node wants to communicate or send date with some other node, then the sender node uses its own Private Key and the Public Key of the intended node to generate a Shared Key. This Shared Key is used for Encryption of the data to send across other nodes. Once a node receives a data, the receiver also generates a Shared Key. This Shared Key is used for Decryption of the data at the receiver end [12].

On the other hand the Eve also receives the Public Keys generated by both the Sender and the Receiver nodes. We also try to show that the Eve in spite of having the Public Keys of both the nodes still cannot generate the Shared Keys as the Eve does not have the Private Keys of both the nodes, thus securing the data. We also show that even if the Eve generates same set of points in the elliptic curve and assuming that Eve also has same set of finite points, still it is not possible for the Eve to generate the Shared key. By the time Eve tries to decrypt the data using various keys, next set of data transmissions are over. By using ECC we can achieve [12–14]:

1. **Authentication**: ECC helps to encrypt and decrypt data only from the authentic users. Thus maintaining the Authenticity between the nodes, i.e. Mutual authentication between nodes.
2. **Confidentiality**: Since the Authenticity between the nodes is maintained, the data confidentiality is maintained. ECC also ensures secure key distribution.
3. **Integrity**: Integrity ensures maintaining the consistency, accuracy, and trustworthiness of data and it also guarantees that the data has not been tampered or altered during the transmission in the network [15, 16].

Availability: Availability ensures the availability of the node and the availability of the resources offered by the network. This may not be achieved as the unavailability of the node also depends upon various aspects like, power failure, out of range,

intermediate node failure etc. Thus ECC algorithm cannot be helpful in achieving availability of the node.

5 Result and Analysis

5.1 Cryptool Results

We have compared RSA and ECC with Cryptool simulator 1.4 Beta version. We have compared files of various sizes and compared both the algorithms. The results are as shown in the Table 2. A file sizes varies from 1, 2, 3 KB and so on till 36 KB, hence 36 sample files were takes for the comparison.

The results are also shown in terms of bar graphs as shown in Fig. 4. The comparison has been made with the standard RSA (512 Key) algorithm, which is a traditional and the most used algorithm, with the ECC (239 prime). In our findings, here it is clearly seen in the Fig. 4a, that ECC consumes more time once in the beginning, we can see that, for a file size of 7 KB the encryption is drastically more for encryption

Table 2 Comparison results of RSA and ECC using cryptool simulator

File size (in number of characters)	Encryption time		Decryption time	
	RSA (512 Key)	ECC (239 prime)	RSA (512 key)	ECC (239 prime)
1024 (1 KB)	0.0001	0.016	0.531	0.016
2048 (2 KB)	0.0001	0.016	0.093	0.032
3072 (3 KB)	0.00011	0.047	0.109	0.014
4096 (4 KB)	0.00019	0.062	0.125	0.031
5120 (5 KB)	0.014	0.094	0.172	0.032
:	:	:	:	:
35840 (35 KB)	0.031	0.891	0.468	0.031
36834 (36 KB)	0.031	0.891	0.468	0.063

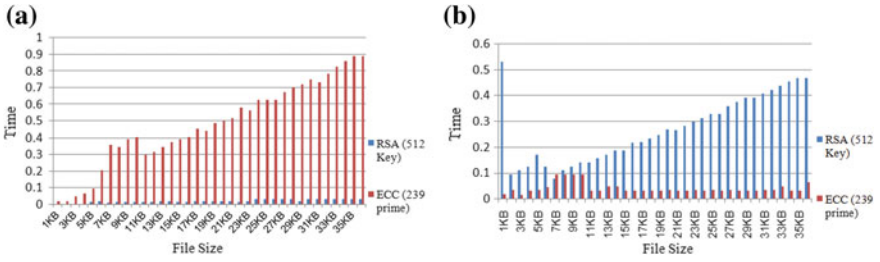

Fig. 4 Comparison of RSA and ECC using Cryptool simulator

and from 12 KB it requires less time and increases gradually for encryption. Though ECC requires more time for encryption, the key size is too small compared to RSA. However the decryption time taken by ECC is very less than the traditional RSA algorithm, even if the file size increases as shown in Fig. 4b. The decryption time for ECC is nearly similar for all files compared to RSA algorithm. Through these results we can conclude that ECC is better than RSA.

5.2 *Proposed System Results*

For our work we have to consider some Parameter that is to be used in the implementation of ECC on the nodes.

Basically there are five parameters in the Domain Parameters chosen, they are as follows in Table 3.

The results obtained from our work are as shown in the Table 4. We have compared the same files of various sizes as we have compared ECC in the Cryptool simulator. The results are as shown in the Table 4. Here also the file sizes varies from 1 KB, 2 KB, 3 KB and so on till 36 KB, hence 36 sample files were takes for the comparison.

Table 3 Parameter description

Sl. No.	Parameter	Notation	Description
1	Prime number	p	Specifies the size of the finite field, we have used the value of the finite field p = 17 which is a prime number
2	Coefficients	a and b	Coefficients of the elliptic curve equation, we have used a = −3 and b = 3
3	Base point	G	Generates our subgroup, we have used G = (1, 1)
4	Order	n	Order of the subgroup, we have used n = 22
5	Cofactor	h	Cofactor of the subgroup, we have used h = 1

Table 4 Encryption and decryption time for given number of characters

File size (in number of characters)	Encryption time in seconds	Decryption time in seconds
1024 (1 KB)	0.389	0.8106
2048 (2 kb)	0.1596	0.10728
3072 (3 KB)	0.164	0.13618
4096 (4 KB)	0.18619	0.11473
5120 (5 KB)	0.20249	0.11150
:	:	:
35840 (35 KB)	1.1834	1.08541
36834 (36 KB)	1.2172	1.09699

We have compared both of our results, i.e. results achieved from the Cryptool and the results obtained through the Matlab simulator. The file sizes are from 1 KB, 2 KB, 3 KB and so on till 36 KB, hence 36 sample files were takes for the comparison in both the cases. The Cryptool Samples are referred as same as the Table 2, the Table 4 are the results obtained from our work. Here we are comparing the results generated by RSA and ECDH of Cryptool and our results.

As we can see in our observations, in Fig. 5a the Encryption time, Our Results time is more than the RSA and nearly same with ECDH of Cryptool results time. Here we have to also note that, Cryptool results are obtained on a standalone system, whereas our results are obtained with three laptops running Matlab simulations results, as the topology shown in the Fig. 3, and they are connected using a wireless router. Further we can see that the results of ECDH and Our Results from 1 KB to 16 KB are same and later time increases gradually in our results.

Whereas the Decryption time as shown in Fig. 5b. Our results take more time to decrypt than the RSA and ECDH of Cryptool result time. The reason that Our Results takes more time is that the message gets encrypts at the sender side and then transmitted via the network and then decrypted at the reviver side. Another reason can be the effect of the topology. Though the obtained results are high, the entire process of message encrypting, transmitting and receiving, and lastly decrypting, takes less than 1.2 s for a 36 Kb size of file.

Further we compare the Execution time of other works carried out with our results. The comparison is made where the point generation on the ECC curve is randomly plotted, but the point formation is as mentioned in the Table 5. We have compared our results with the results obtained though hardware and also using simulator, irrespective how the points are obtained on the curve. As we can see in Table 5, initial three results are implemented on various hardware's, and the fourth result is implemented on NS 3 simulator. When we compare our results, we can clearly see in table that in SL. No. 1 [17], 3 [19] and 4 [20], our average time of 36 cases is much better, but though other SL. No. 2 [18] results are better than our results.

We are considering the key generation time, as both the sender and receiver have to generate the keys for both encryption and decryption. In any WSN network data transmission is a major task, time consumption in processing of data is very critical.

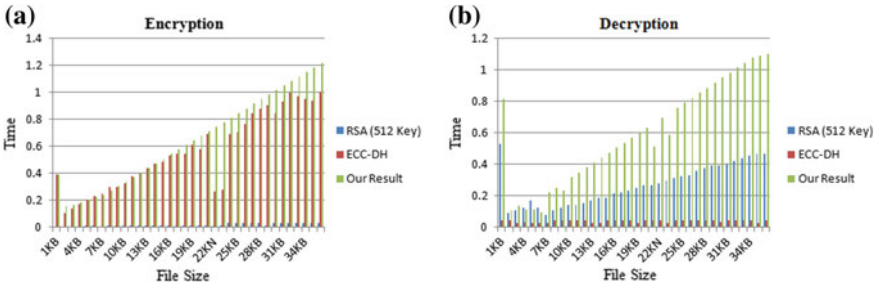

Fig. 5 Comparison of RSA and ECDH Cryptool results and our results

Table 5 Run time comparison of overall data transmission

Sl. No.	Implementations on	Time in milli sec	Average of	ECC point formation	Advantage of the proposed scheme
1	TelosB motes [17]	3646.05	100 experiments	Point multiplication	Fast key revocation and reduction in cryptographic computations
2	MicaZ motes, MIB520 [18]	98	–	Point addition	Resource utilization and protection against Man-in-the-middle attack
3	MICAz motes, ATmega128L [19]	1670	'n' number of nodes	Point multiplication	Faster and more energy-efficient key exchange
4	Network simulator 3 (NS3) [20]	6797.75	Combination of ECDH and DSA	Point multiplication	Resolves the existing problems of replay attack, man in middle attack and mutual authentication
5	Network implemented using Matlab (Our Results)	604.031	36 experiments	Point addition	Protection against man in middle attack and improve authentication

Our results are average of 36 cases, i.e. the time of data encrypted, transmitted, and at the receiver side the decryption of data. We can clearly see in the Table 5, our results are very less than other, except with the result of the author results at second number, i.e. just 98 ms. In other cases, out results perform better than all other author's results whether they are implemented on hardware or software.

We can see in Fig. 6, a snapshot of Sender side user interface. The figure also shows the random point generation, the plane text, and cipher text, generated Private Key and Public Key and the generated Shared Key.

Fig. 6 Sender side window

6 Conclusion and Future Scope

As the electronic data is increasing in our day to day life, it is more vulnerable to attacks, hence security is required. One of the most basic methods of security is by using cryptosystem which is easy to apply for most all applications. The growing popularity of ECC and its features makes it a convenient cryptography system and also a substitute for popular algorithms like RSA. Further the use of ECC in software, network as well as in hardware, makes it possible for any type of application with a given level of security. ECC also makes faster operational run on smaller chips with less computing. ECC has benefits like fast processing, less power consumption, less bandwidth consumption, less heat production and storage efficiencies. All these properties are of particular advantage in applications like Military, Healthcare, Agriculture, Toll, Banking sector, Transport, etc., can be in use. From the results obtained, we observe that our results are very close with the results of Cryptool and other authors/work. Compared with the other three results, our obtained results are better by an average of 20%.

The implementation of Elliptic curve can be further extended to implement on hyper elliptic curves on WSN. Further the ECC can also have various types of point generation methods on the curve and ECC can also be integrated with other cryptographic algorithms for additional security.

References

1. Ravi K, Dr. Khanai R, Praveen K Survey on pairing based cryptography for wireless sensor networks. In: International conference on international conference on inventive computation technologies (ICICT 2016). IEEE. https://doi.org/10.1109/INVENTIVE.2016.7824802
2. Sharma G, Bala S, Verma AK (2012) Security frameworks for wireless sensor networks-review. Dep Comput Sci Eng Natl Inst Technol Rourkela, 2212-0173 © 2012. https://doi.org/10.1016/j.protcy.2012.10.119

3. Kalra S, Sood SK (2011) Elliptic curve cryptography: current status and research challenges. Department of Computer Science & Engineering, Guru Nanak Dev University, Regional Campus. HPAGC 2011, CCIS 169. © Springer, Berlin, pp 455–460
4. Moh'd A, Marzi H, Aslam N, Phillips W, Robertson W (2011) A secure platform of wireless sensor networks. 1877-0509 © 2011, Elsevier. https://doi.org/10.1016/j.procs.2011.07.017
5. Sharma G, Bala S, Verma AK (2012) Security frameworks for wireless sensor networks-review. 2212-0173 © 2012. Elsevier. https://doi.org/10.1016/j.protcy.2012.10.119
6. Ahmed MH, Alam SW, Qureshi N, Baig l (2011) Security for WSN based on elliptic curve cryptography. 978-1-61284-941-6/11/$26.00 ©2011. IEEE
7. Lu M (2012) Research on key management scheme for WSN based on ECC. Springer. https://doi.org/10.1007/978-1-4471-2386-6_29
8. Shankar SK, Tomar AS, Tak GK (2015) Secure medical data transmission by using ECC with mutual authentication in WSNs. In: 4th International conference on eco-friendly computing and communication systems, B. V., ICECCS 2015. Elsevier. https://doi.org/10.1016/j.procs.2015.10.078
9. Nair B, Mala C (2015) Analysis of ECC for application specific WSN security. In: 2015 IEEE international conference on computational intelligence and computing research (ICCIC). Department of Computer Science & Engineering, National Institute of Technology, Tiruchirappalli, Tamil Nadu, India. https://doi.org/10.1109/iccic.2015.7435742
10. Moona AH, Iqbal U, Bhat GM (2016) Mutual entity authentication protocol based on ECDSA for WSN. 1877-0509 © 2016. Elsevier. https://doi.org/10.1016/j.procs.2016.06.038
11. Bayat M, Aref MR (2013) A secure and efficient elliptic curve based authentication and key agreement protocol suitable for WSN. Elsevier
12. Challa S, Das AK, Odelu V, Kumar N, Kumari S, Khan MK, Vasilakos AV (2018) An efficient ECC-based provably secure three-factor user authentication and key agreement protocol for wireless healthcare sensor networks. 0045-7906/© 2017. Elsevier. https://doi.org/10.1016/j.compeleceng.2017.08.003
13. Li X, Peng J, Kumari S, Wu F, Karuppiah M, Choo K-KR (2017) An enhanced 1-round authentication protocol for wireless body area networks with user anonymity. 0045-7906/© 2017. Elsevier Ltd., http://dx.doi.org/10.1016/j.compeleceng.2017.02.011
14. Quirino GS, Ribeiro AR, Moreno ED (2012) Asymmetric encryption in wireless sensor networks. Wirel Sens Netw Technol Protoc. https://doi.org/10.5772/48464, ©2012 Ribeiro et al., licensee InTech. http://www.intechopen.com/books/wireless-sensor-networkstechnology-and-protocols
15. Jiang Q, Ma J, Wei F, Tian Y, Shen J, Yang Y (2016) An untraceable temporal-credential-based two-factor authentication scheme using ECC for wireless sensor networks. 1084-8045/ © 2016. Elsevier Ltd. http://dx.doi.org/10.1016/j.jnca.2016.10.001
16. Batina L, Mentens N, Sakiyama K, Preneel B, Verbauwhede I (2006) Low-cost elliptic curve cryptography for wireless sensor networks. ESAS 2006, LNCS 4357, pp 6–17, 2006. ©Springer-Verlag, Berlin
17. Mansour I, Chalhoub G, Lafourcade P, Delobel F (2014) Secure key renewal and revocation for wireless sensor networks. Clermont University, LIMOS laboratory, France. 978-1-4799-3780-6/14/$31.00 ©2014. IEEE
18. Moon AH, Iqbal U, Mohiuddin Bhat G (2016) Authenticated key exchange protocol for wireless sensor networks. Natl Inst Electron Inf Technol, Dep Electron Instrum Technol, Int J Appl Eng Res (University of Kashmir, Research India Publications, Srinagar, J & K, India) 11(6):4280–4287. ISSN 0973-4562
19. Lederer C, Mader R, Koschuch M, Großschädl J, Szekely A, Tillich S (2009) Energy-efficient implementation of ECDH key exchange for wireless sensor networks. In: Markowitch O et al (eds) IFIP international federation for information processing 2009, WISTP 2009, LNCS 5746, pp 112–127. Springer
20. Kapoor N, Lekhi ES (2017) An efficient key management in wireless sensor networks using ECDH digital signature algorithm. Comput Sci Eng Dep Punjab Tech Univ Rayat Inst Eng Inf Technol, (Ropar, India). IJARET 5(II). ISSN 2320-6802

Object Detection Using RADAR Mounted on Quadcopter

Rajeev Kumar, Rahul Singh, Abhishek Mishra and Anshul Agarwal

Abstract The object detection using radar mounted on quadcopter is achieved by a mobile radar which can be taken to any place or location with the help of quadcopter and can be used to detect if there is any unidentified object in its protected area. The quadcopter used is made with Arduino Uno controller and it has a RC (Remote control) remote which works of radio frequency for controlling its direction of motion. The radar has been developed by an ultrasonic sensor which uses ultrasonic waves to detect objects and a servo motor is used to rotate the ultrasonic sensor to cover the entire protected area. The radar has been made wireless with the help of RF (radio frequency) transmitter and receiver module which sends the data on the PC (Personal computer) wirelessly. There are two circuits for the radar namely transmitter and receiver circuits. The transmitter circuit has been mounted on a quadcopter, which can take the radar to any location in its coverage area which makes the radar mobile.

Keywords Arduino Uno · BLDC (Brushless DC) motor · ESC (Electronic Speed Control) · Propellers · Transmitter and receiver · Ultrasonic sensor · Servo motor · RADAR (Radio detection and Ranging) · Accelerometer

1 Introduction

In the late 19th century, object detection became a new topic for security agencies of different countries. Many scientists suggested various methods for object detection with different kinds of wave. But the results were better for radio waves only as it gets reflected by metallic objects. But till 20th century, systems which use the

R. Kumar · R. Singh · A. Agarwal
Department of Electrical and Electronics Engineering, National Institute of Technology Delhi, New Delhi 110040, India

A. Mishra (✉)
Department of Mechanical Engineering, National Institute of Technology Delhi, New Delhi 110040, India
e-mail: abhishekmishra@nitdelhi.ac.in

© Springer Nature Singapore Pte Ltd. 2020

T. Hitendra Sarma et al. (eds.), *Emerging Trends in Electrical, Communications, and Information Technologies*, Lecture Notes in Electrical Engineering 569,
https://doi.org/10.1007/978-981-13-8942-9_45

principle were becoming available and Christian Hansmeyer, German inventor, was first to used them to build a normal ship detector which avoids collisions in fog. Some similar systems those providing directional information to objects were developed for short ranges [1].

Small radars which are portable are available that can be maintained and operated by any person which is explained in [2]. Radar systems were secretly developed by several countries in the period of World War II. The term radar was derived in 1940 by US Navy from the words for Radio Detection and ranging (RADAR). The new and modern applications of radar are very diverse which includes air traffic control system radar, astronomy purpose, defense system, anti-missile systems, to locate ships and landmarks, anti-aircraft collision systems, space surveillance systems, meteorological systems etc.

The radar which has antenna is mostly stationary so that they can only monitor the area where they are placed. If the radar would have been mobile, then it would be possible to use that radar for monitoring any location at any time. For making the radar mobile, quadcopter is the best option these days. Quadcopter's are VTOL (vertical take-off and landing) rotorcraft with 4 propellers for propulsion. Quadcopter is an assistive device or system whose demand is high in industrial and surveillance sector [3]. They are also called multi rotors. In general term, multi rotors comprising not only quadcopters but also some hex copters, octocopters and other rotorcraft forms with rotors more than 2. Initially, the pioneers first tried rotor flight using multi copter, since use of more than 1 rotor seemed to be the only natural solution for the problem of VTOL flights. The first experimental attempts to take off with rotorcrafts were done mostly with multi rotors [4].

For the folks of all ages, quads seem to be a great fun for kids playing around to adults using for photography and video recordings. Also, quadcopters are used in disaster management, recovery purposes, and police departments, military and agricultural applications. Since the technology has become advanced and costs have decreased, many industries are finding that quadcopters can offer some innovative solutions for various problems also can help them to reduce costs. The study of each component of the Quadcopter and analysis of the Quadcopter assembly with concept of the thrust generated by each motor is taken from the paper on "Design & Development Analysis of Quadcopter" [5]. If the quadcopters are used to take the small mini radar systems, then it would be great achievement for the surveillance system which will reduce the cost of manufacturing of large stationary radar system.

2 Design Methodology

The methodology used in making the mobile radar is shown in Fig. 1. First the wired radar is fabricated then it has been made wireless with the help of RF module. Secondly, a radar GUI is made in processing software to show the distance and angle of approach of the object. After completing the GUI code. The radar transmitter circuit is mounted on the quadcopter for testing it.

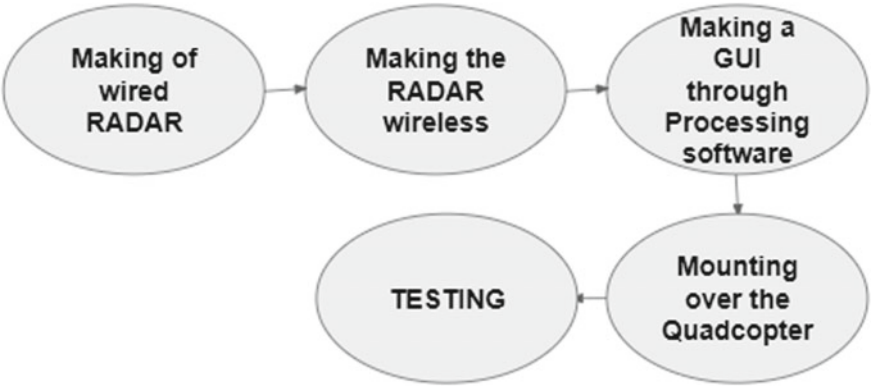

Fig. 1 Design methodology

3 Quadcopter Design

A quadcopter means a multi rotor copter with four arms, and each having a motor and a propeller at their ends. Quads are somewhat same as helicopters in some ways, although their thrust and lifts comes from 4 propellers not just one. Also, helicopters have a pitch and a tail rotor which helps to stabilize the craft, whereas quadcopter does not have that. The internal aspects of the Quadcopter based on Arduino UNO development board is enlightened through this paper [6]. In quadcopters, two opposite propellers rotate in clockwise direction and the other two opposite propellers rotate in counter clockwise direction which enables the machine to hover in a stable form. The quadcopter has three movements i.e. pitch, roll and yaw. The Fig. 2 depicts all the three movements of the quadcopter clearly through arrows, along with the direction of rotation of motors.

Fig. 2 Quadcopter movements

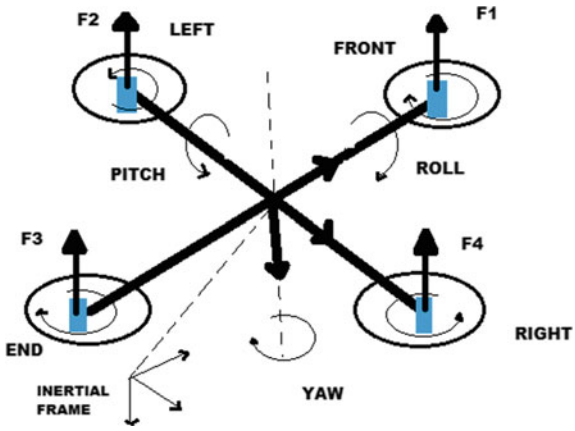

3.1 Hardware Description

The quadcopter is made with an Arduino Uno microcontroller and is developed to achieve the real time operation requirements. The components used in making the quadcopter are:

- ARDUINO UNO: Arduino Uno which is shown in Fig. 3 is a microcontroller based on Atmel's atmega328pa which is a 40 pin IC. It has 6 analog pins and 13 digital pins. Also have USB serial port, one reset button and one inbuilt led. It works on 16 MHz crystal frequency.
- BLDC MOTORS: It is a brushless motor designed for remote controlled Airplanes as well as quad copters and are highly reliable. According to the specifications, each motor can give a thrust of 1500 g at 136 watts, based on our ESC and propellers. A BLDC motor is shown in Fig. 4.
- PROPELLERS: Propellers (shown in Fig. 5) are blades which are employed with

Fig. 3 Arduino Uno

Fig. 4 BLDC motor

Fig. 5 Propellers

the motor to generate a required thrust force. In this work 8 × 4.5" propeller are being used which are compatible and have good tensile strength.

- ELECTRIC SPEED CONTROLLER: Electric speed controller as depicted in Fig. 6, is generally called as ESC's are the mini microcontroller of 8-bit type used to convert the single dc input to the pulse output. It also composes of signal pin used to change the pulse width of the output of ESC which is mandatory for varying the speed of motor during several operations at flight.
- FLY SKY FS-T6 2.4 GHZ 6 CHANNEL RECEIVER-TRANSMITTER: It is the transmitter and receiver which works on 2.4 GHz bandwidth and used for controlling the quadcopter wirelessly. It has 6 channels which mean the six different

Fig. 6 ESCs

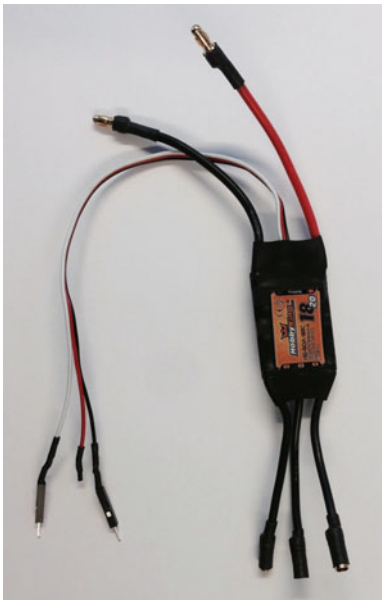

signals can be send to the receiver for performing various functions and it is shown in Fig. 7.

- GYRO SENSOR: The MPU-6050 (shown in Fig. 8) is the sensor which has both accelerometer and gyroscope on a single chip. It is used to auto-level the quadcopter and for auto-balancing. It gives the x, y and z axis of the quadcopter motion from its initial calibrated value and send this value to the main microcontroller to take the reflex action.

Fig. 7 Fly sky remote

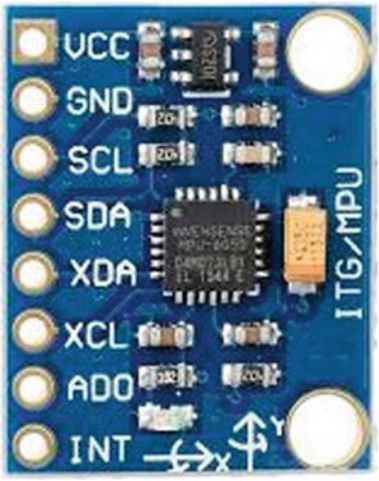

Fig. 8 MPU-6050

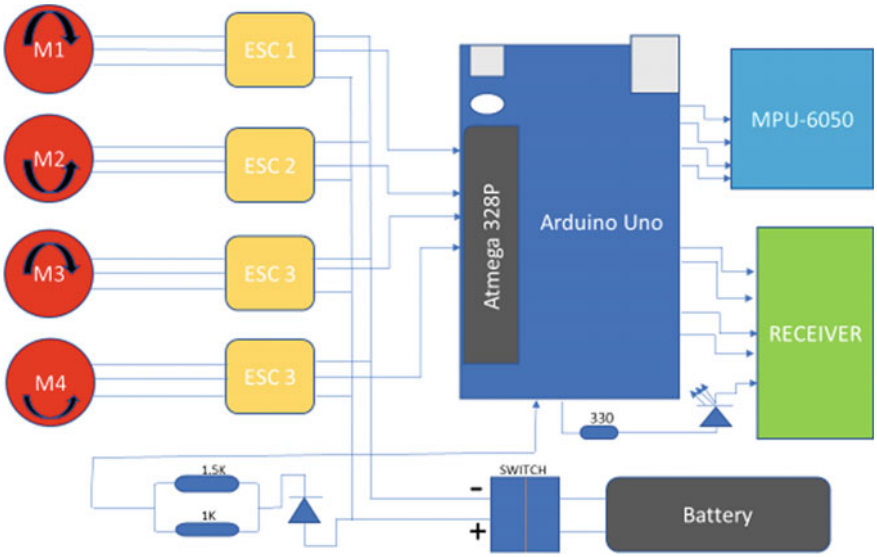

Fig. 9 Quadcopter schematic

3.2 Fabrication Process

The schematic diagram of connections of components for quadcopter is shown in the Fig. 9. It clearly shows how each component is connected with the Ardunio uno.

The various steps involved in programming the quadcopter for its stable operation is shown in the flowchart of Fig. 10. It explains the step by step approach used in programming the quadcopter. Firstly, literature survey has been done & then the development of the quadcopter hardware model is completed. Now, the calibration set up code is dumped in the Arduino and after successful calibration set up, ESCs are calibrated. Finally, the main flight controller code is dumped and tested. The final quadcopter model after assembling all the components is shown in Fig. 11.

4 Radar

Radar is a device for detecting objects by using radio waves to determine the distance, direction and speed of that object. The radar works on the principle that whenever the radar signals meets other objects, the radar signals get reflected and the receiver receives the reflected signal to determine the objects distance or altitude. They are available in a variety of sizes depending on the performance specifications required. The radar is the main part of a missile guidance system.

In this paper, a small radar system has been made with the help of ultrasonic sensor [7]. The ultrasonic sensor transmits ultrasonic waves which get reflected whenever

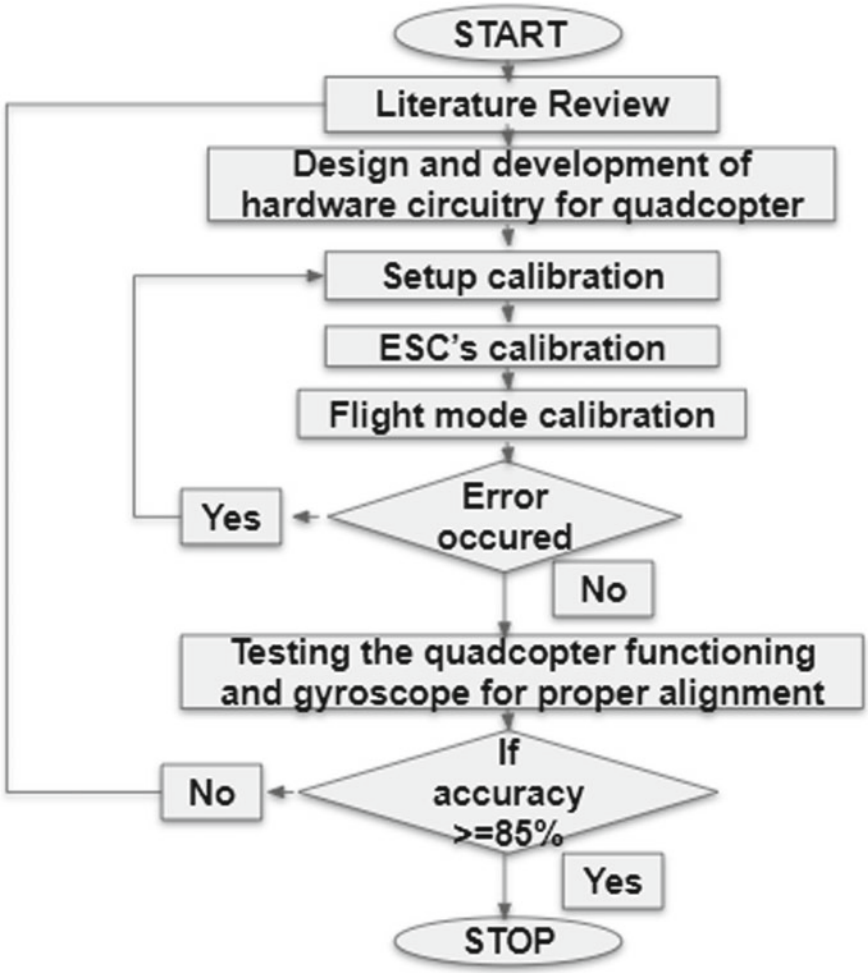

Fig. 10 Flowchart of quadcopter programming

Fig. 11 Final quadcopter model

it meets any object. The inbuilt receiver of ultrasonic sensor receives the reflected waves and the distance of the object with respect to radar is calculated by multiplying the average time of propagation of waves and speed of ultrasonic waves which is shown in Eq. 1.

$$\text{Distance} = 1/2 \times (\text{Propagation time}) \times (\text{speed of sound}) \quad (1)$$

4.1 Hardware Description

The component used in making the wireless radar [8] is shown below with description of each component is also explained.

- ULTRASONIC SENSOR: It is the sensors which generates ultrasonic waves from the transmitter and receives the waves after the wave get reflected from an object. It uses an oscillator to increase the frequency of the signal to generate ultraviolet rays. It used to measure the distance of the object falling in the line of direction in it. It is shown in Fig. 12.
- SERVO MOTOR: A servo motor (shown in Fig. 13) is the special type of motor which has positive, negative port along with a signal input. It is used to move the rotor of the motor in certain angles and steps which can be settled by the main microcontroller in degrees. It can rotate in any angle.
- RF TX/RX: The wired radar is made wireless by using thee TX/RX module as shown below in Fig. 14, works on 433 MHz frequency and has a range of 50–80 m.

Fig. 12 Ultrasonic sensor

Fig. 13 Servo motor

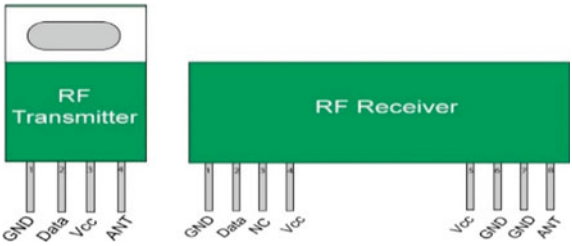

Fig. 14 RF module

4.2 Hardware Description

The wireless radar uses RF Transmitter and Receiver module for the wireless data transmission to the PC. The radar has two circuits, one is for transmitting the distance along with the angle of approach of the object and the other circuit is for receiving that value on the PC for showing the radar GUI using processing software. The radar transmitter and receiver schematic circuit diagram are shown in Figs. 15 and 16 along with connections.

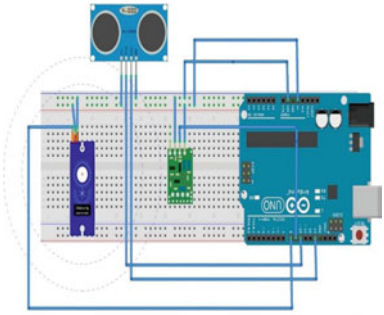

Fig. 15 Radar transmitter circuit

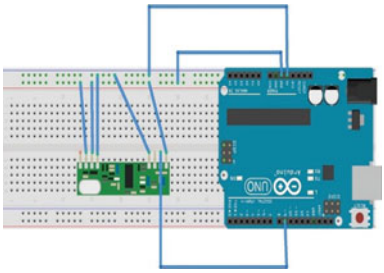

Fig. 16 Radar receiver circuit

5 Results and Discussions

The radar transmitter circuit is mounted on the quadcopter in such a way that it will not strike any of the arms of the quadcopter frame. Also, more care is taken in case of weight and stability of the quadcopter as mounting a radar will directly affects its stability and center of mass [9]. The Fig. 17 shows the final receiver circuit made which is connected to the PC for receiving the distance and angle of approach of the object. The Fig. 18 shows the final model of the quadcopter with radar transmitter circuit mounted on it.

The quadcopter with radar is tested for detecting the objects at different distances and the results of detection are summarized below in Table 1.

The output of the wireless radar is fetched on the PC with the help of receiver circuit of Fig. 17 and the data received on the PC are used to make GUI of radar using processing software whose output GUI is shown in Fig. 19 which clearly shows the distance and angle of approach of the object. The final flying quadcopter with wireless radar mounted on it is depicted in Fig. 20.

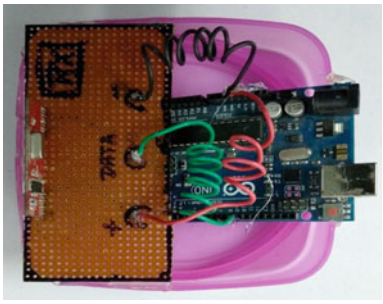

Fig. 17 Radar receiver circuit

Fig. 18 Quadcopter with radar mounted

Table 1 Object detection results of wireless radar

Actual object distance (cm)	Observed object distance (cm)	In range/out in range
15	15	In range
30	30	In range
40	40	In range
50	–	Out of range

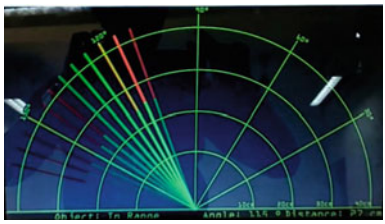

Fig. 19 Radar GUI in processing software

Fig. 20 Flying quadcopter with radar

6 Conclusions

From all the above results for the radar mounted on quadcopter, it can be concluded that the quadcopter can be controlled in the range of approx. 500 m with good controllability and stability. The radar mounted on the quadcopter can easily detect objects in the range of 40 cm which can be increased up to 100 m by using LIDAR sensor or by using high frequency ultrasonic sensor. The external transmitter and receiver module used in the radar circuit for transmitting and receiving the data of detection works at 433 MHz frequency with 100 meters transmission and receiving range and the ultrasonic used works at 40 kHz frequency. The quadcopter with wireless radar can be used for surveillance purpose and since the radar is mobile so that it can be taken to any location in its operating range for object detection and surveillance purpose.

References

1. https://en.wikipedia.org/wiki/history_of_radar
2. Ghoghre DA, Ahire D, Ahire P (2017) Radar system using arduino. In: National conference on emerging trends in engineering & technology 2017, NCETET17, vol 1, pp 53–56. IOSR J Electron Commun Eng
3. Kuantama E, Craciun D, Tarca R (2016) Quadcopter body frame model and analysis. Ann Univ Oradea Fascicle Manag Technol Eng 1:71–74 (2016)
4. http://www.krossblade.com/history-of-quadcopters-and-multirotors/
5. Parihar P, Bhawsar P, Hargod P (2016) Design & development analysis of quadcopter. Compusoft: Int J Adv Comput Technol 5(6):2128–2133
6. Rajpoot AS, Gadani N, Kalathia S (2016) Development of arduino based quadcopter. Int Adv Res J Sci Eng Technol 3(6):252–259
7. Singh C, Agnihotri A, Patel P (2013) Development of RADAR using ultrasonic sensor. Int J Adv Res Sci Eng 2(10):33–38
8. Maurya J, Khan RN, Shaikh M, Dhebe N (2016) Development of RADAR using ultrasonic sensor. Int J Tech Res Appl 39(KCCEMSR):99–101
9. Shah KN, Dutt BJ, Modh H (2014) Quadrotor—an unmanned aerial vehicle. Int J Eng Dev Res 2(1):1299–1303

2:1 MUX Implementation Using NMV-Gate: NON MAJORITY GATE in QCA

D. Ajitha, K. N. V. S. VijayaLakshmi, K. BhagyaLakshmi and M. Mehetaj

Abstract Quantum-dot Cellular Automata (QCA) is one of the emerging transistors less nanotechnology implemented utilizing electron tunneling with the given potential. In this paper, we proposed a design for 2:1 multiplexer in QCA using NON MAJORITY GATE. In this work, a new design of NAND and NOR gates are proposed. By using the NAND gate structure, the proposed multiplexer is implemented. The multiplexer functionality is implemented by the design tool QCA Designer © 2005 Version 2.0.3.

Keywords Non majority gate (NMV-Gate) · Quantum-dot cellular automata (QCA) · 2 × 1multiplexer · Universal gates · Operation cost (O-Cost) · Area utilization factor (AUF)

1 Introduction

The tremendous advantage of Quantum-dot Cellular Automata (QCA) device leads the technology without semiconductor devices. Here the area, speed and power consumption are upgraded beyond the semiconductor technologies like CMOS. In MOSFETs, short channel effects occur, if the scaling of channel length comparable to the depletion layer widths of the source and drain junctions. In QCA the communication between the two adjacent cells is made by the law of Coulomb repulsion is shown in Fig. 1. The repulsion indicates here that the message moves from one side to other.

D. Ajitha (✉)
Department of E.C.E, Sreenidhi Institute of Science and Technology, Hyderabad, India
e-mail: ajithavijay1@gmail.com

K. N. V. S. VijayaLakshmi
Department of E.C.E, Sri Vasavi Engineering College, Tadepalligudem, India

K. BhagyaLakshmi
Department of E.C.E, Sasi Institute of Technology & Engineering, Tadepalligudem, India

M. Mehetaj
Department of E.E.E, JNTUA College of Engineering, Kalikiri, India

© Springer Nature Singapore Pte Ltd. 2020

T. Hitendra Sarma et al. (eds.), *Emerging Trends in Electrical, Communications, and Information Technologies*, Lecture Notes in Electrical Engineering 569,
https://doi.org/10.1007/978-981-13-8942-9_46

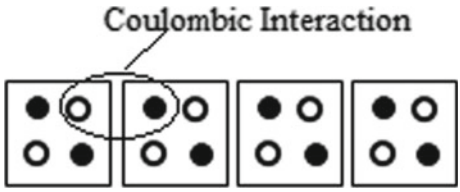

Fig. 1 Communication between the adjacent cells

Therefore, here there is no need for individual control over each cell. In this, all the elementary cells no longer in their stable state and relax to the initial state. For this operation, minimum energy is required to perform the calculations and minimizes the connections to the cells inside the QCA.

In QCA technology, the wire is a combination of cells in the form of an array. Each cell consists of four quantum dots, which are arranged at the corners of each cell [1]. Due to Coulomb repulsion force between the electrons, they occupy the diagonal positions. These states are defined concerning the polarization corresponding to the electrons positioned on the diagonals square. If the electron position is at left lower and another electron is at the right upper position, then it is defined as $P = +1$ and in opposite case, it is defined as $P = -1$ as shown in Fig. 2.

Some essential elements for QCA logic implementation are wire and majority voter gate [2, 3]. The QCA wire is implemented by considering the group of cells, which are arranged in the form of an array as shown in the Fig. 3a. The QCA Majority Voter Gate (MVG) in Fig. 3b and its logic symbol is shown in Fig. 3c. The MVG

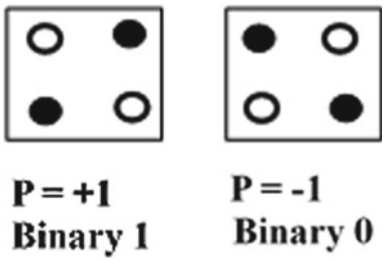

Fig. 2 Basic QCA cell with two states

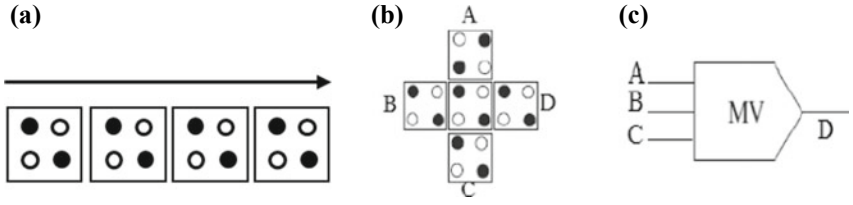

Fig. 3 **a** Wire, **b** Majority voter gate, **c** Majority voter gate symbol

functionality is equivalent to the logic function F (A, B, C) = AB + AC + BC and can be implemented by using five QCA cells. Cells A, B, and C represents the input cells, whereas the cell D is the output cell. The output cell is polarized according to the polarization of majority of the input cells.

2 Proposed NMV-Gate

In the conventional structure of majority gate by fixing the one of the input polarization the AND and OR gates are constructed. To implement the NAND and NOR gates one inverter is added at the output. The inverter can be two cell structure or robust seven-cell structure [4]. Whereas in the proposed NMV-Gate, the direct implementation of universal gates can be is achieved without the use of Inverter structure. The proposed structures are constructed using the quantum cells in rotated mode and evaluated the reliability of QCA devices in the presence of random rotation of the cell [5]. NAND is a universal gate, any combinational and sequential logic circuits can be able to construct. In the proposed design, resembles that of the conventional majority gate shape, whereas this gate is comprised of one majority voter 5 cells gate and as an extension of one extra cell at the output. If the whole gate is subjected to the clock zero then the driver cell (C3) to be under clock 1 and if all cells are under clock 1 then the driver cell should be under clock 2. By the help of this central clocking configuration [6], it is possible to design the universal gates with very efficient effective area. NAND gate is designed by using the negative polarization. NOR gate is designed by using the positive polarization. The maximum amplitude of the output waveform is 9.76 e−001 and the minimum amplitude of the output waveform is −9.76 e−001. The proposed NMV-Gate as NAND Gate implementation with 6 quantum cells is shown in Fig. 4. The proposed NMV-Gate as NOR Gate implementation with 6 quantum cells is shown in Fig. 5.

NOT Gate structure can be implemented by making one of the inputs as normal cell in the proposed universal gate. This logic is also applicable to both NAND/NOR Logic. The AND/OR gates functionality also achieved by inserting one extra cell at the output. The effective area of the proposed gate is 4,800 nm^2. Area utilization

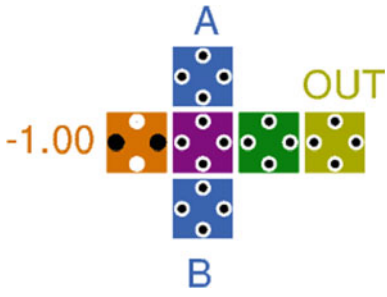

Fig. 4 Implementation of proposed NMV-Gate as NAND gate

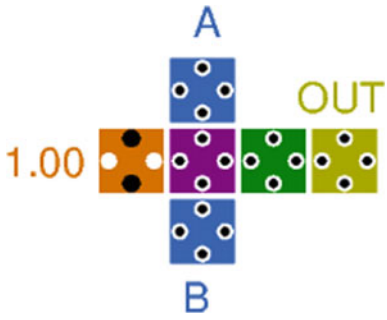

Fig. 5 Implementation of proposed NMV-Gate as NOR gate

factor is 2.46. The output for the proposed Gate is evaluated using two clock zones, which indicate minimal complexity.

3 Proposed Multiplexer Design

The Multiplexer is a fundamental element in implementing the FPGA circuits and many digital circuit designs. This paper investigates the implementation of a 2 × 1 multiplexer in QCA and proposes a novel and efficient design. The proposed multiplexer design is shown in Fig. 6 and the corresponding output waveform is shown in Fig. 7. The proposed multiplexer structure is implemented with rotated cells and it requires only two NAND gates. Whereas, the conventional multiplexer the multiplexer structure requires 3 majority gates.

The proposed multiplexer structure performance is compared with the previous designs in terms of O-Cost and effective area. The comparative analysis is shown

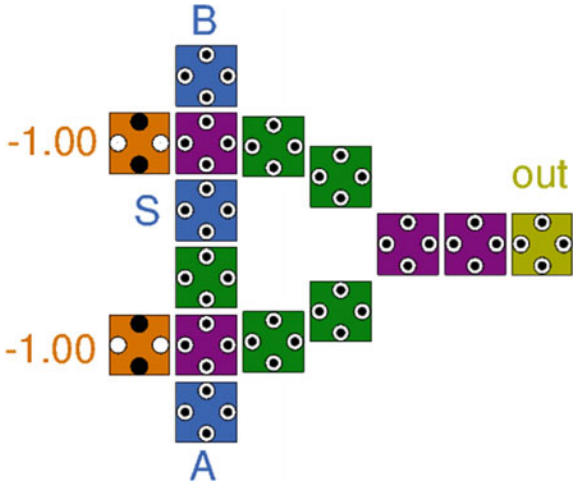

Fig. 6 Proposed multiplexer design

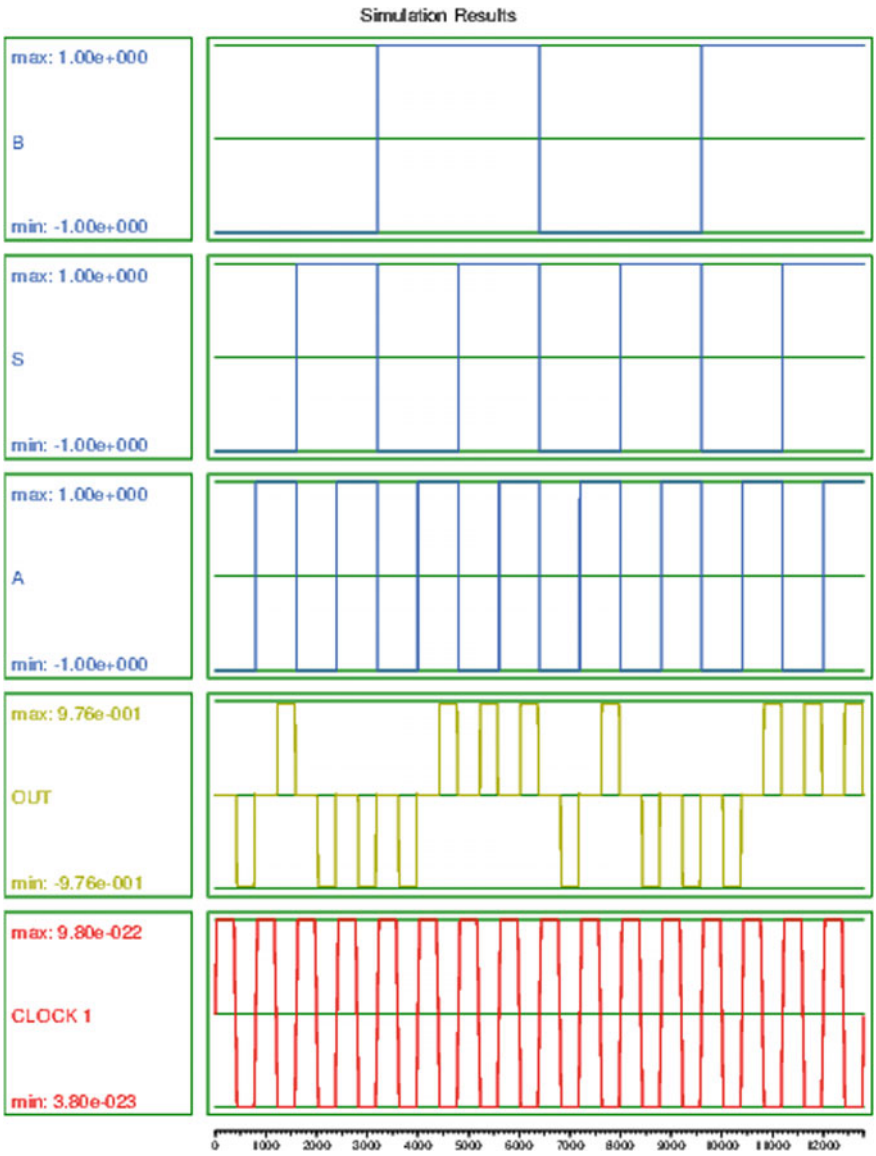

Fig. 7 Output waveform of proposed multiplexer

Table 1 Comparative analysis of 2:1 multiplexer in terms of effective area

S. no.	Multiplexer design	O-cost (cell count)	Effective area (nm^2)	Effective area reduction in the proposed NMV MUX compared to the existing designs
1	2 × 1 MUX [7]	75	121,764	86.2
2	2 × 1 MUX [8]	41	45,924	63.41
3	2 × 1 MUX [9]	34	40,764	58.78
4	2 × 1 MUX [10]	23	22,400	25
5	2 × 1 MUX [11]	19	19,200	12.5
6	2 × 1 MUX [12]	28	23,360	28.08
7	Proposed NMV-2 × 1 MUX	15	16,800	–

in Table 1. The proposed multiplexer is area efficient in terms of the number of cells used in the design. The initial development of a tool to automate the design of QCA is examined [7]. The automatic layout generation of the 2 to 1 multiplexer using QCA-LG tool consists of 75 quantum cells [7]. The robust design of 2 to 1 multiplexer is consists of 41 quantum cells [8].The total number of cells used to implement the digital design of 2 to 1 multiplexer design is 34 [9]. A novel feasible design for 2 to 1 multiplexer proposed in [10] consists of 23 quantum cells. The existing multiplexer designs are constructed with 3-majority gates by using the different optimization approaches [11, 12]. Whereas, the recent design uses the rotated majority gate structure and competitive with the proposed structure [13]. When compared with the recent existing designs, the proposed novel structure requires 15 cells only.

This layout has two dimensions one is the length and another one is breadth. In the sense of QCA designing the standard spacing between two quantum cells is taken as 2 nm. The spacing of the cells from the terminal point of the cell bed is 1 nm. The cells are identical in the area that is having 18 nm length and 18 nm breadth because of being a perfect square. Hence, the area becomes 18 × 18 nm^2. The length of the proposed MUX is calculated as L = (1 + 18 + 2 + 18 + 2 + 18 + 2 + 18 + 2 + 18 + 2 + 18 + 2 + 18 + 1) = 140 nm.

The breadth of the layout is given by, W = (1 + 18 + 2 + 18 + 2 + 18 + 2 + 18 + 2 + 18 + 2 + 18 + 1) = 120 nm. Hence, the area of the circuit is entirely given by, Area = L*W = 100 * 120 = 16,800 nm^2. No wire crossings are used and the multiplexer output is evaluated using 2 clock zones, which is shown in Fig. 7. The layout and simulation results are obtained with QCA designer tool [14]. By using the rotated cells, the maximum amplitude of the obtained output waveform is 9.76 e−001 and the minimum amplitude of the output waveform is −9.76 e−001, which is higher than the normal structures.

4 Conclusion

In many digital circuits, multiplexers are the essential components. A novel design of a 2 × 1 multiplexer in QCA is implemented in this paper. Here, the proposed multiplexer design reduces the effective area by 28.08% compared to the best existing design. The proposed design is more efficient than the existing conventional designs. With this proposed design, we can implement any combinational circuit efficiently.

References

1. Tougaw PD, Lent CS (1994) Logical devices implemented using quantum cellular automata. J Appl Phys 75:1818
2. Lent CS, Tougaw PD (1997) A device architecture for computing with quantum dots. Proc IEEE 85(4)
3. Blair E, Lent CS (2003) An architecture for molecular computing using quantum-dot cellular automata. In: Nanotechnology, IEEE-NANO, vol 1
4. Kim K, Wu K, Karri R (2007) The robust QCA adder designs using composable QCAbuilding blocks, IEEE Trans. Comput Aided Des Integr Circuits Syst 26:176–183
5. Yang X, Cai L, Wang S, Wang Z, Feng C (2012) Reliability and performance evaluation of QCA devices with rotation cell defect. IEEE Trans Nanotechnol 11(5):1009–1018
6. Vankamamidi V, Ottavi M, Lombardi F (2008) Two-dimensional schemes for clocking/timing of QCA circuits. IEEE Trans Comput-Aided Des Integr Circuits Syst 27:34–44
7. Teodosio T, Sousa L (2007) QCA-LG:A tool for the automatic layout generation of QCA combinational circuits. In: Norchip conference, pp 1–5
8. Kim K, Wu K, Karri R (2007) The robust QCA adder designs using composable QCA building blocks. IEEE Trans Comput-Aided Des Integr Circuits Syst 26(1)
9. Askari M, Taghizadeh M, Fardal K (2008) Digital design using quantum-dot cellular automata (a nanotechnology method). In: Proceedings of the international conference on computer and communication engineering, Kualalampur, Malayasia
10. Mukopadhyay D, Dutta P (2012) Quantum dot cellular automata based novel 2:1 Multiplexer. Int J Comput Appl 43(2)
11. Sen B, Dutta M, Saran D, Sikdar BK (2012) An efficient multiplexer in quantum-dot cellular automata. VDAT, Springer, Berlin, pp 350–351
12. Kumari NP, Joshi PV, Gurumurthy KS (2013) Realization of basic gates using universal logic blocks in quantum dot cellular automata. In: 6th IEEE international conference on emerging trends in engineering and technology, 16 Dec 2013. pp 50–51. https://ieeexplore.ieee.org/document/6754772
13. Ahmad F (2018) An optimal design of QCA based 2n: 1/1: 2n multiplexer/demultiplexer and its efficient digital logic realization. Microprocess Microsyst 56:64–75
14. Walus K, Jullien GA (2006) Design tools for an emerging SoC technology: quantum-dot cellular automata. Proc IEEE 94(6):1225–1244

Various Filter Algorithms Using Impulse Noise Removal in Digital Images with Image Fusion Technique

P. Deepthi Jordhana, M. Sandhya Rani and B. Suresh Babu

Abstract This paper introduces a new concept of Image Fusion technique. This technique is implemented in reducing impulse noise from the digital images and to acquire noise free image. Image fusion technique means that fusing or combination of two or more images with different or similar constraints to form a single image with all the information in each image not being strayed. Normally to reduce noise from an image we use different filtering algorithms and the outputs of those algorithms are fused together to form a perfect image without noise. In this paper we intend to use five different filtering algorithms individually on the image captured by a sensor. The outputs of those five algorithms are fused to form an image free of noise. The image obtained by using this process is of high in quality compared to the images procured by individually de noising them.

Keywords Image fusion · Impulse noise · Image processing

1 Introduction

Digital images are often corrupted during acquisition, transmission or due to faulty memory locations in hardware [1]. The impulse noise can be caused by a camera due to the faulty nature of the sensor or during transmission of coded images in a noisy communication channel [2]. Consequently, some pixel intensities are altered while others remain noise free. The noise density (severity of the noise) varies depending on various factors namely reflective surfaces, atmospheric variations, noisy communication channels and so on.

P. Deepthi Jordhana (✉) · B. Suresh Babu
ECE Department, Srinivasa Ramanujan Institute of Technology, Anantapur, Andhra Pradesh, India
e-mail: deepthi.ece@srit.ac.in

B. Suresh Babu
e-mail: sureshbabu.ece@srit.ac.in

M. Sandhya Rani
ECE Department, Mahaveer Institute of Science & Technology, Hyderabad, Telangana, India
e-mail: m.sandhyarani.ece@gmail.com

© Springer Nature Singapore Pte Ltd. 2020

T. Hitendra Sarma et al. (eds.), *Emerging Trends in Electrical, Communications, and Information Technologies*, Lecture Notes in Electrical Engineering 569,
https://doi.org/10.1007/978-981-13-8942-9_47

In most image processing applications the images captured by different sensors are combined into a single image, which retains the important features of the images from the individual sensors, this process is known as image fusion [3–6]. In this paper, the images captured by two sensors are differently noised depending on the proximity to the object, environmental disturbances and sensor features. These noise images are filtered using five different filtering algorithms based on the noise density.

The filters such as Median Filter (MF), Vector Median Filter (VMF), Basic Vector Differential Filter (BVDF), Spatial Median Filter (SMF) and Modified Spatial Median Filter (MSMF) are used to remove noise from images. The above mentioned five filters are utilized to get five individual outputs which are further fused to get an image with reduced noise securing the information contained by the image. This image is further optimized to get an image with high fidelity, Edge Detection technique using canny filter is applied to the fused image to preserve the details around the edges without losing them. It is proven that using this technique has well appraised the behavior of cancellation of noise in the technique from a peculiar view point of a human. This technique provides an immense scope in fields of military, in remote sensing, in medical application to specify the image to capture the information and also in satellite imagery to get the feeds form it with great deal of exactitude in providing the information regarding the captured space and other feeds to which it was programmed to without distortions or noise parameters encompassed in them. Due to its promising results and accuracy it is supposedly meant to be a better functionality proposed to negate the noise and nab the information which the image tends to portray to us.

When an image is acquired by a camera or other imaging system, often the vision system for which it is intended is unable to use it directly. The image may be corrupted by random variations in intensity, variations in illumination, or poor contrast that must be dealt with in the early stages of vision processing. A image contains some noise means “unwanted signal”. Unwanted electrical fluctuations in signals received by AM radios caused audible acoustic noise. By analogy, unwanted electrical fluctuations are also called “noise”.

Digital “noise” is a common problem in digital cameras today. A lot of factors can introduce noise to digital photography, but there are certain steps that can be taken to avoid it. In a digital camera, if the light which enters the lens misaligns with the sensors, it creates image noise [7]. Even if noise is not so obviously visible in a picture, some kind of image noise is bound to exist. There are many kinds of filters used to remove the noise such as linear smoothing filter, median filter, wiener filter and wavelet based fuzzy filter [8]. In order to remove such type of noise in images we need to use filter technique. So, by using filter technique noise is removed and also it does not decrease the quality of image.

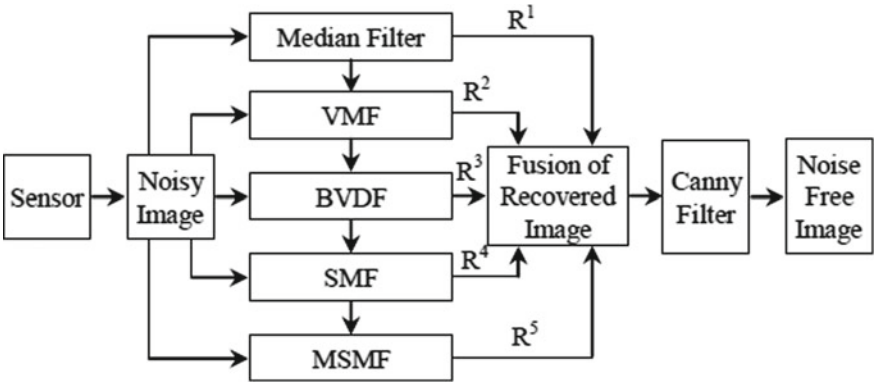

Fig. 1 Block diagram of image fusion process

1.1 Image Fusion

The image fusion is one of the important branches of data fusion. Data fusion techniques have been designed not only to allow integration of different information sources, but also to take advantage of complementary. There is no unique definition for image fusion. Few image fusion definitions are given below:

Image fusion is the combination of two or more different images to form a new image by using certain algorithm.

Image fusion is the process of combining information from two or more images of a scene into a single composite image that is more informative and is more suitable for visual perception or computer processing [9].

Image fusion is a process of combining images, obtained by sensors of different wavelengths simultaneously viewing of the same scene, to form a composite image. The composite image is formed to improve image content and to make it easier for the user to detect, recognize, and identify targets and increase this situational awareness [10]. The process of image fusion is clearly shown in Fig. 1.

1.2 Image Fusion Techniques

Nowadays, there is an increased affordability of imaging sensors, which has made a hallmark in multi sensor vision system [11]. The modalities of different sensors operating across different bands of electromagnetic spectrum can be combined resulting in an increased information content of the scene. Through the careful selection of complementary sensor modalities, the potential for significantly enhancing the information content in a simple image may be realized, by image fusion. But here we considered only either the minimum and maximum methods for the process of image fusion.

1.3 Different Processing Levels of Image Fusion

The image fusion can be performed at three different processing levels according to the stage at which the fusion takes place: pixel, feature and decision level.

a. **Pixel Level Fusion**: Pixel-based fusion is performed on a pixel-by pixel basis. It generates a fused image in which information associated with each pixel is determined from a set of pixels in source images to improve the performance of image processing tasks such as segmentation.
b. **Feature Level Fusion**: Feature-based fusion at feature level requires an extraction of objects recognized in various data sources. It requires extraction of salient features which are depending on their environment such as pixel intensities, edges or textures. These similar features from input images are fused.
c. **Decision-Level Fusion**: Decision-based fusion consists of merging information at a higher level of abstraction, combines the results from multiple algorithms to yield a final fused decision. Input images are processed individually for information extraction. The obtained information is then combined by applying decision rules to reinforce common interpretation.

1.4 Categorization of Image Fusion Methods

Image fusion methods can be categorized according to the data entering the fusion and its purpose.

- **Multi View Fusion Of Images**: Images taken from the same modality and taken at the same time but from different viewpoints.
- **Multi Modal Fusion Of Images**: Images taken by different sensors (e.g. visible and infrared, panchromatic and multispectral satellite images) [12].
- **Multi Temporal Fusion Of Images**: Images taken at different times in order to detect changes between them.
- **Multi-Focus Fusion Of Images**: Images of a 3D scene taken repeatedly with various focal lengths [13].
- **Fusion For Image Restoration**: Fusing the images of the same scene and modality, either blurred or noisy, may lead to deblurred and de-noised images. Multichannel de-convolution approach is extended to super resolution fusion where input blurred images of low spatial resolution are fused to provide an image with high-resolution [14].

2 Proposed Image Fusion Technique

In proposed system image fusion technique is used to remove the impulse noise from the digital images. Image fusion technique is the process of fusing the different images to one image without loss of data and for high quality [15]. Five different filtering algorithms are used for filtering. The image from sensor [16] is been send to these five filters at a time as input and the outputs of the each of five filters are noise free images those are fused to a single image for better appraise of the image canny filter is used and finally the output is noise free image. The five filter algorithms used for filtering are:

- Median Filter
- Vector Median Filter
- Basic Directional Vector Filter
- Spatial Median Filter
- Modified Spatial Median Filter.

The image fusion technique is shown in Fig. 2 and here R1, R2, R3, R4, R5 are the outputs of the five filters which are fused to give single output.

2.1 Median Filter

Median filters are statistical non-linear filters that are often described in the spatial domain. A median filter smoothens the image by utilizing the median of the neighborhood. Median filter performs the following tasks to find each pixel value in the processed image: All pixels in the neighborhood of the pixel in the original image which are identified by the mask are stored in the ascending (or) descending order. The median of the stored value is computed and is chosen as the pixel value for the processed image.

- **Calculation of Median Value**

Median value is calculated by eliminating the pixel values which are very different from their neighboring pixels. By eliminating the effect of such odd pixels, the values are assigned to the pixels that are representative of the values of the typical neighboring pixels in the original image. The median value of the marked pixel is computed as follows:

Fig. 2 Image fusion process

$$\begin{pmatrix} 1 & 5 & 7 \\ 2 & 4 & 6 \\ 3 & 2 & 1 \end{pmatrix}$$

Step 1: First, the pixel values are arranged in ascending order as follows

1 1 2 2 3 4 5 6 7

Step 2: The median value of the ordered pixel is computed as follows

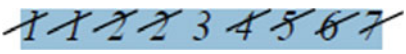

The median value is computed to be 3. Then, the original pixel value of 4 will be replaced by the computed median value of 3.

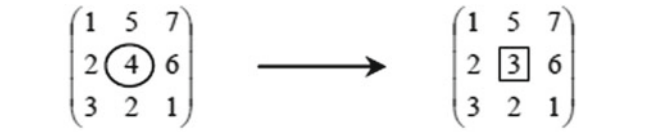

Let the input image is given in the form

$$\begin{pmatrix} 18 & 22 & 33 & 25 & 32 & 24 \\ 34 & 128 & 24 & 172 & 26 & 23 \\ 22 & 19 & 32 & 31 & 28 & 26 \end{pmatrix}$$

Here the goal is to compute the median values of the marked pixels and replace the pixels 128, 24, 172 and 26 by their median values of the neighborhood defined by the mask. The mask to be used is a 3 × 3 mask. Where is the process—needed explanation? Or else remove this.

2.2 *Vector Median Filter*

Vector median filters (VMF) have been introduced to simulate the concept of median filtering in order to reduce the color image noise. The vector median filters consider the pixel as a vector not a scalar. It is suggesting a single quantity that represents the three attributes of the pixel. This resulting quantity is considered as the ranking value, which later will differentiate one pixel from the other in order to find the median. The major issue of a vector median filter is to transform three perpendicular vectors,

Red, Green and Blue to one dimensional quantity. The theory of vector median filter is based on measuring the distance between some selected pixels to all other pixels in the window. The pixel that shows the least sum of distances to the other pixels in the window will be chosen as the median pixels.

The mathematical model of the vector median filter is defined as follows:

Assume N-sample vectors $\{X_1, X_2, \ldots, X_N\}$, the output of L-norm operator is given by:

$$\mathrm{VM}\{X1, X2, \ldots, XN\} = X_{VM}$$

where, $X_{VM} \in \{X_1, X_2, \ldots, X_N\}$ and $\sum_{i=1}^{N} \|Xvm - Xi\|_L \leq \sum_{i=1}^{N} \|Xj - Xi\|_L$ j = 1, … N (3.2).

VM is the Vector Median operator; X_i is the *i*th component of colour vector (pixel) values.

2.3 Basic Vector Directional Filter

The basic vector directional filter (BVDF) is a ranked-order, nonlinear filter which parallelizes the VMF operation. However, a distance criterion, different from the L_1, L_2 norms used in VMF, is utilized to rank the input vectors. The output of the BVDF is that vector from the input set, which minimizes the sum of the angles with the other vectors. In other words, the BVDF chooses the vector most centrally located without considering the magnitudes of the input vectors. The output of the BVDF is that vector from the input set that minimizes the sum of the angles with the other vectors. In other words, the BVDF chooses the vector most centrally located without considering the magnitudes of the input vectors. The BVDF may perform well when the vector magnitudes are of no importance and the direction of the vectors is the dominant factor. However, this is usually not the case. In most multichannel signal processing applications, the magnitudes of the vectors should also be considered. The lowest order-statistics $x_{(1)}(n)$ associated with the minimum angular distance $\alpha_{(1)}(n)$ represents the BVDF output.

2.4 Spatial Median Filter

When transferring an image, sometimes transmission problems cause a signal to spike, resulting in one of the three point scalars transmitting an incorrect value. This type of transmission error is called “salt and pepper” noise due to the bright and dark spots that appear on the image as a result of the noise. The ratio of incorrectly transmitted points to the total number of points is referred to as the noise composition

of the image. The goal of a noise removal filter is to take a corrupted image as input and produce an estimation of the original with no foreknowledge of the characteristics of the noise or the noise composition of the image. In images containing noise, there are two challenges.

2.5 Modified Spatial Median Filter

The Spatial Median Filter is similar to the Vector Median Filter in that in both filters, the vectors are ranked by some criteria and the top ranking point is used to the replace the centre point. No consideration is made to determine if that center point is original data or not. The unfortunate drawback in using these filters is the smoothing that occurs uniformly across the image. Across areas where there is no noise, original image data is removed unnecessarily. In the Modified Spatial Median Filter, after the spatial depths between each point within the mask are computed, an attempt is made to use this information to first decide if the mask's center point is an uncorrupted point.

2.6 Canny Filter

The Canny operator was designed to be an optimal edge detector. It takes as input a gray scale image, and produces as output an image showing the positions of tracked intensity discontinuities. Different stages of Canny Edge Detection are:

- Noise reduction: Raw image is convolved with a Gaussian filter.
- The Canny algorithm basically finds edges where the gray scale intensity of the image changes the most.

These areas are found by determining gradients of the image. Gradients at each pixel in the smoothed image are determined by applying what is known as the Sobel-operator. First step is to approximate the gradient in the x and y-direction respectively by applying the kernels shown in below:

$$\mathrm{Cx} = \begin{bmatrix} -1 & 0 & 1 \\ -2 & 0 & 2 \\ -1 & 0 & 1 \end{bmatrix} \quad \mathrm{Cy} = \begin{bmatrix} 1 & 2 & 1 \\ 0 & 0 & 0 \\ -1 & -2 & -1 \end{bmatrix}$$

The gradient magnitudes (also known as the edge strengths) can then be determined as an Euclidean distance measure by applying the law of Pythagoras. It is sometimes simplified by applying Manhattan distance measure to reduce the computational complexity.

3 Simulation Results

3.1 Median Filter

For Median filter, the balloon image is given as input shown in the Fig. 3a. To the input during processing some noise is added as shown in the Fig. 3b.

After processing, we get the output of the Median filter as shown in Fig. 3c. And also the Mean Square Error (MSE), Peak Signal-to-Noise Ratio (PSNR) and the Signal-to-Noise Ratio (SNR) parameters are been calculated.

The parameters, Mean Square Error, Peak Signal-to-Noise ratio and the Signal-to-Noise ratio are shown in Table 1.

3.2 Vector Median Filter

For Vector median filter, the balloon image is given as input shown in the Fig. 4a. During processing, some noise is added. The noisy image is shown in Fig. 4b.

After processing, we get the output of the Vector Median Filter as shown in Fig. 4c.

And also we get the Mean Square Error, Peak Signal-to-Noise ratio and the Signal-to-Noise ratio parameters are shown in Table 2.

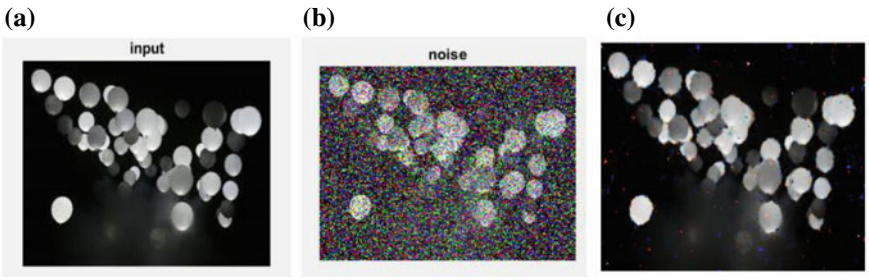

Fig. 3 **a** Input to median filter, **b** Noisy image, **c** Output of median filter

Table 1 Parameters of median filter

Parameter	Value
MSE	273.32
PSNR	23.75
SNR	13.58

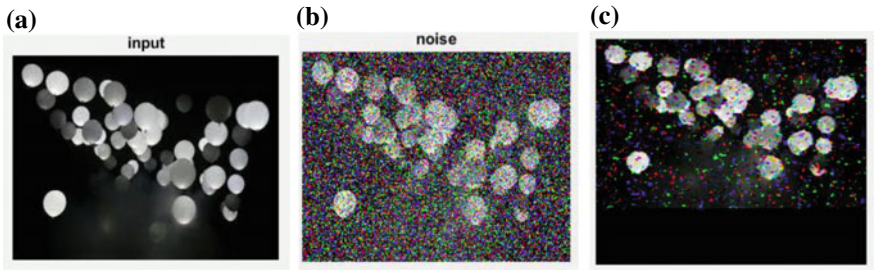

Fig. 4 **a** Input to vector median filter, **b** Noisy image, **c** Output of vector median filter

Table 2 Parameters of vector median filter

Parameter	Value
MSE	12,845.2
PSNR	7.03
SNR	1.15

3.3 Basic Vector Directional Filter

For Basic Vector Directional filter technique, the balloon image is given as input shown in the Fig. 5a. During processing, some noise is added. The noisy image is shown in Fig. 5b.

After processing, we get the output of the Basic Vector Directional filter as shown in Fig. 5c.

And also the Mean Square Error, Peak Signal-to-Noise ratio and the Signal-to-Noise ratio parameters are been calculated as shown in Table 3.

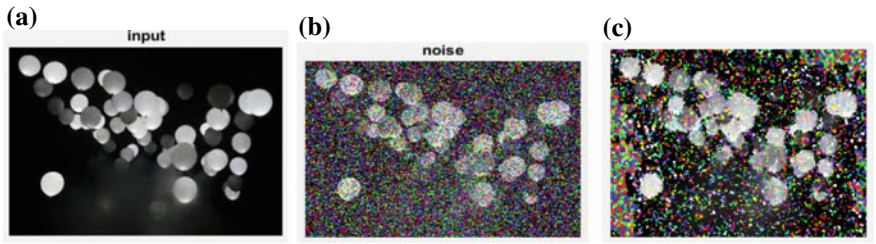

Fig. 5 **a** Input of basic directional vector filter, **b** Noisy image, **c** Output of basic vector directional filter

Table 3 Parameters of basic vector directional filter

Parameter	Value
MSE	16,613.73
PSNR	−42.21
SNR	0.0189

3.4 Spatial Median Filter

For Spatial Median filter, the balloon image is given as input shown in the Fig. 6a. During processing, some noise is added. The noisy image is shown in Fig. 6b.

After processing, we get the output of the Spatial Median Filter as shown in Fig. 6c.

And also Mean Square Error, Peak Signal-to-Noise ratio and the Signal-to-Noise ratio parameters are calculated as shown in Table 4.

3.5 Modified Spatial Median Filter

For Modified Spatial Median filter technique, the balloon image is given as input shown in the Fig. 7a. During processing, some noise is added. The noisy image is shown in Fig. 7b.

After processing, we get the output of the Modified Spatial Median filter as shown in Fig. 7c.

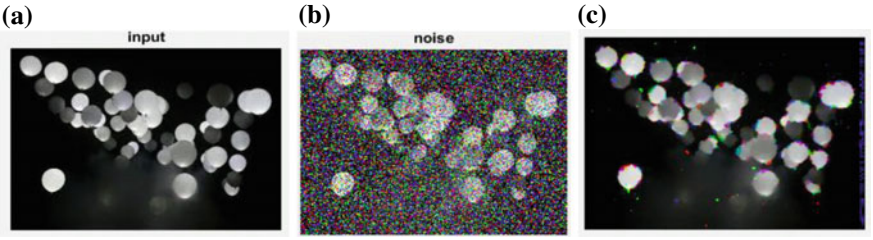

Fig. 6 **a** Input of spatial median filter, **b** Noisy image, **c** Output of spatial median filter

Table 4 Parameters of spatial median filter

Parameter	Value
MSE	11,379.75
PSNR	7.5695
SNR	1.6651

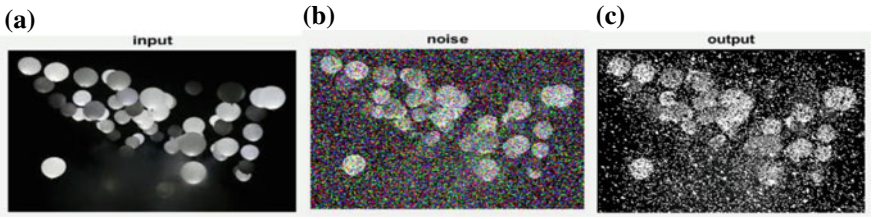

Fig. 7 **a** Input of modified spatial median filter, **b** Noisy image, **c** Output of modified spatial median filter

Table 5 Parameters of modified spatial median filter

Parameter	Value
MSE	18,733.72
PSNR	−42.726
SNR	−0.5085

And also we get the Mean Square Error, Peak Signal-to-Noise ratio and the Signal-to-Noise ratio parameters are calculated as shown in Table 5.

3.6 Image Fusion

For Image Fusion technique [17], the balloon image is given as the single input to all the five filters at a time and the output of each filter that are R1, R2, R3, R4, R5 these five filter outputs are given to the Image Fusion at a time shown in Fig. 8. The below figure shows input images and the fusion images. The image after complete image fusion is also shown.

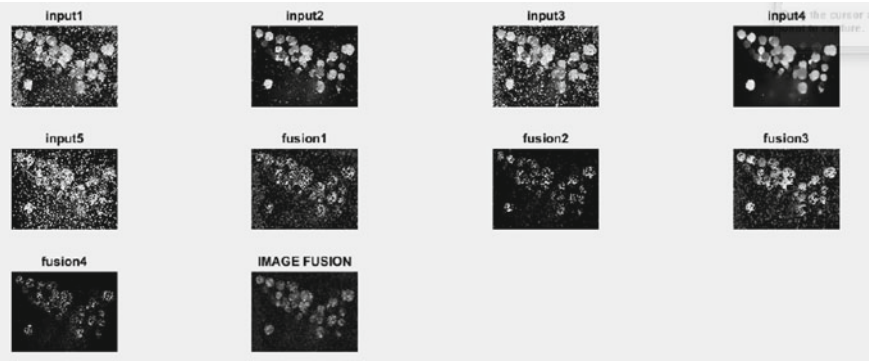

Fig. 8 Image fusion inputs and output

Table 6 Parameters of image fusion

Parameter	Value
MSE	60,766.92
PSNR	−47.84
SNR	−1.86

And also we get the Mean Square Error, Peak Signal-to-Noise ratio and the Signal-to-Noise ratio parameters are calculated as shown in Table 6.

3.7 Canny Filter

For Canny Filter, the balloon image is given as input shown in the Fig. 9a.

After processing, we get the output of the Canny Filter as shown in Fig. 9b.

Image Fusion is the technique in which an effective high quality image is obtained when a uncorrupted image is given as input [18]. The parameters such as MSE, SNR, PSNR are also calculated and compared to itself which reduced the MSE value.

Comparison

Comparison of MSE, PSNR and SNR for various filters is done with the fused image. The following Table 7 shows the comparison.

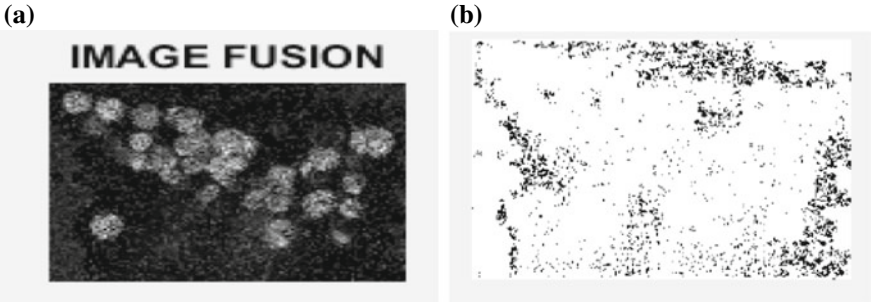

Fig. 9 **a** Input of Canny filter, **b** Output of canny filter

Table 7 Comparison of filtering techniques with image fusion

Parameter	Median filter	Vector median filter	Basic vector directional filter	Spatial median filter	Modified spatial median filter	Image fusion
PSNR	23.75	7.03	42.21	7.5695	42.726	47.84
SNR	13.58	1.15	0.0189	1.6651	0.5085	1.86

PSNR has improved 2.01 times after image fusion than median filter, 6.80 times than vector median filter, 1.13 times basic vector directional filter, 6.32 times spatial median filter and 1.11 times modified spatial median filter.

SNR is better with median filter but in other filters it is lesser than the fused image. SNR in fused image is 1.61 times than vector median filter, 98.41 times basic vector directional filter, 1.12 times spatial median filter and 3.66 times modified spatial median filter.

4 Conclusions

With the exponential evolution in computations and advancements in technologies many new and sophisticated imaging techniques have been emerged. Though they prove out to best in class techniques for the removal of noise, they come with certain limitations. These new techniques tend to have bounds of their own which cannot be neglected that easily.

We aim to create a new technique that bridges the gap between the clear image and a distorted image by emphasizing the information and enhancing the distorted image breaking past the limits of those techniques by alternating and combining those techniques with other turning the disadvantages of one technique into advantages of other emulating one another giving rise to a perfect image for this we have done a brief study about the functionalities of the techniques used to remove noise.

Future Scope

- This method can be utilized to remove noise elements from video. This method can be used to enhance satellite images which are noised at the time of transmission to earth due to poor reception of network or due to poor transmission parameters. It is so much helpful in the field of remote sensing.
- This method of fusing the images can be used in medical field in fusing CT scan and MRI scan images for better understanding of the situation to diagnose better and efficiently to provide quality treatment with low cost efficiency.
- This method can be a breakthrough in military industry and entertainment fields.

References

1. Stroebel L, Zakia RD (1995) The focal encyclopedia of photography. Focal Press, Waltham
2. Farooque MA, Rohankar JS (2013) survey on various noises and techniques for denoising the color image. Int J Appl Innov Eng & Manag 2(11):217–221
3. Flusser J, Sroubek F, Zitova B (2007) "Image fusion: principles, methods, and applications," Tutorial EUSIPCO, Lecture notes
4. Cattin P (2016) Image restoration: introduction to signal and image processing, MIAC, University of Basel, 19th/26th April 2016

5. Ohta J (2008) Smart CMOS image sensors and applications. CRC Press, Boca Raton
6. Nakamura J (2005) Image sensors and signal processing for digital still cameras. CRC Press, Boca Raton
7. McDonald L (2006) Digital heritage. Butterworth-Heinemann, Oxford
8. Bovik AC (2005) Handbook of image and video processing. Academic Press, Cambridge
9. Shapiro LG, Stockman GC (2001) Computer vision. Prentice-Hall, New Jersey
10. Boncelet C, Bovik AC (2005) Handbook of image and video processing. Academic Press, Cambridge
11. Janesick JR (2001) Scientific charge-coupled devices. SPIE Press
12. Covington MA (2007) Digital SLR astrophotography. Cambridge University Press
13. Jacobson RE, Ray SF, Attridge GG, Axford NR (2000) The manual of photography. Focal Press, Waltham
14. Huang TS (1986) Advances in computer vision and image processing. JAI Press, Connecticut
15. Keelan BW, Cookingham RE (2002) Handbook of image quality. CRC Press, Boca Raton
16. Pellegrino JG et al (2006) Infrared camera characterization. In: Bronzino JD (ed) Biomedical engineering fundamentals. CRC Press, Boca Raton
17. Genderen V, Van JL, Pohl C (1994) Image fusion: issues, techniques and applications. In: Van Genderen JL, Cappellini V (eds) Intelligent image fusion, proceedings EARSeL workshop, Strasbourg, France (Enschede: ITC), 11 Sept 1994, pp 18–26
18. Guest Editorial (2007) Image fusion: advances in the state of the art. 108 Inf Fusion 8:114–118

Air Pollutants Level Detection and Control in Vehicle Using an Intelligent System

Manoj Itharajula

Abstract In the modern era, in the transportation sector, automobiles play a vital role. Exhausts of motor vehicles majorly cause air pollution which is the primary ingredient in the smog creation in some large cities. These automobiles produce harmful exhausts in which pollutants such as oxides of nitrogen, carbon monoxide, carbon dioxide, Suspended particulate matter, Hydrocarbons, and ozone. Such exhausts cause hazardous diseases to the living beings which in turn leads to the Decrease of lifespan also. To overcome this effect, an embedded system can be designed to detect these pollutants and their levels using semiconductor gas sensors. Everything is monitored and controlled by the microcontroller in the embedded system. This paper mainly focuses on detecting and controlling the air pollution and thereby maintaining the Eco-friendly environment.

Keywords Air pollutants · Exhausts · Threshold level · Embedded system · Microcontroller · Semiconductor gas sensor · GPS

1 Introduction

In this technological world of advancement, the transportation sector is reaching to next level with the sophisticated technologies like autonomous vehicles, driverless cars but in the same line, the air pollution is evolving as a major problem. If we consider some developing countries like India and China or the developed countries like the USA, it is the common issue devastating these countries. This air pollution, in turn, is affecting the living beings as well as lifeless things in an intensive manner. On exposing to the pollutants present in the air, living beings are prone to allergies in respiratory organs like nose, lungs and heart diseases, skin allergies and cancers. Some historical monuments also get faded due to these pollutants released into the atmosphere by the vehicles [1, 2].

M. Itharajula (✉)
Madanapalle Institute of Technology and Science, JNTUA, Madanapalle, India
e-mail: manojworkspace98@gmail.com

© Springer Nature Singapore Pte Ltd. 2020

T. Hitendra Sarma et al. (eds.), *Emerging Trends in Electrical, Communications, and Information Technologies*, Lecture Notes in Electrical Engineering 569,
https://doi.org/10.1007/978-981-13-8942-9_48

Pollution from vehicles cannot be avoided totally. But, it can be controlled. Here, the problem occurs when the pollution levels cross the threshold values. As indirectly the technology creates the problem of pollution, it can also be used to inhibit the pollution using some smart systems embedded inside the vehicles which monitors the pollution levels in the real-time and warns the driver about the same and if he neglects the warning, the fuel supply to the engine is stopped and it will be informed to the nearest service station. All these processes are maintained using a smart system in which Arduino mega plays a major role.

2 Survey

Even though the government laid so many rules, laws and regulations over the control of emission from vehicles, the most of them went in vain. In the 1990s the first emission norms were introduced in the India. In the 2000s some standards are introduced across all the major cities in the country.

Automobile sector in the country contributes to 18% of the total CO emissions. It is rapidly increasing day-by-day in the recent years. As per my survey in the Madanapalle town, Andhra Pradesh, the following table shows the emission levels of CO and HC from petrol vehicles (Table 1).

Table 1 Emission levels of CO_2 and HC from vehicles

Vehicle model	Category	Test date	CO (%)	HC (ppm)
Honda activa-1	2 wheeler	28/Nov/2017	2.889	0512
Maruthi wagon-R 1	4 wheeler	30/Nov/2017	3.099	0362
Maruthi Omni	4 wheeler	30/Nov/2017	3.099	0362
Maruthi Alto-1	4 wheeler	01/Dec/2017	0.143	0067
Yamaha crux	2 wheeler	05/Dec/2017	1.388	0081
Yamaha YZF R15	2 wheeler	05/Dec/2017	2.520	0127
Maruthi 800	4 wheeler	11/Dec/2017	0.089	0048
Yamaha FZ	2 wheeler	14/Dec/2017	1.672	0295
Chevrolet beat	4 wheeler	17/Dec/2017	0.430	0030
Hynduai santro	4 wheeler	19/Dec/2017	0.163	0041
Honda city	4 wheeler	26/Dec/2017	0.167	0052
Maruthi eeco	4 wheeler	27/Dec/2017	0.194	0020
Hyundai grandi10	4 wheeler	29/Dec/2017	3.160	0089
Tata indica	4 wheeler	31/Dec/2017	0.586	0389
Bajaj pulsar220	2 wheeler	31/Dec/2017	2.302	0292
Enfield bullet350	2 wheeler	06/Jan/2018	0.870	0461

(continued)

Table 1 (continued)

Vehicle model	Category	Test date	CO (%)	HC (ppm)
Chvrolet aveo	4 wheeler	06/Jan/2018	0.049	0362
Maruthi Esteem	4 wheeler	7/July/2018	0.286	0057
Yamaha fazer	2 wheeler	14/Jan/2018	0.321	0064
Maruthi zen	4 wheeler	18/Jan/2018	2.172	0207
Honda active-2	2 wheeler	14/Jan/2018	1.629	1172
Maruthi Alto-2	4 wheeler	15/Jan/2018	1.045	0011
Hyundai santro	4 wheeler	16/Jan/2018	0.155	0052
Maruthi Wagon-R 2	4 wheeler	15/Jan/2018	0.054	0024
Maruthi Alto-3	4 wheeler	28/Feb/2018	0.143	0067

3 Gas Sensors

A sensor which sends electrical signals proportional to the magnitude of the gas molecules concentration is called a gas sensor. In this project, I have used MQ-2 and MQ-135 gas sensors for measuring smoke, CO and CO_2 gases from vehicle exhaust pipe. These sensors are cheap and reliable compared to other sensors. These sensors are highly sensitive to gases. Figure 1 shows the circuit diagram of the MQ-135 sensor.

The MQ-135 sensor is made of tin oxide, microtubes of aluminum oxide and a heating element inside a tubular casting. It also involves a potentiometer which facilitates in load resistance adjustment of the sensor circuit. The MQ-135 sensor works on the principle of conductivity change. Here, the conductivity is directly proportional to the concentration of the gas molecules detected. If the gas concentration is high, the conductivity will get increased and vice versa. The MQ-135 sensor detects many gases such as NH_4, CO_2, smoke, benzene etc. In this project, this sensor is used to detect only the CO_2 gas. This sensor detects each individual component of gases based on the Rs/Ro ratio. The Rs parameter indicates sensor resistance at 100 ppm

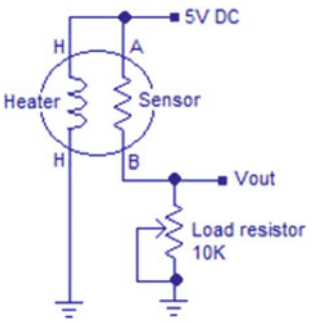

Fig. 1 MQ-135 gas sensor circuit diagram [3]

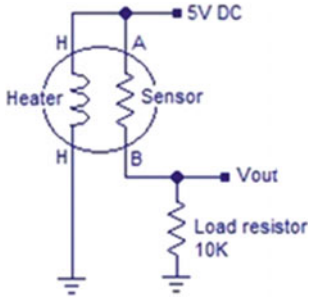

Fig. 2 MQ-2 gas sensor circuit diagram [4]

of NH3 in the clean air where as the Ro parameter indicates various concentration of gases. For CO_2 gas, the Rs/Ro ratio Decreases from 2.5 till 0.8 with the corresponding increase in the ppm of the CO_2 gas from which is calculated by the microprocessor. In this way each gas ppm is measured based on the property of resistance which is converted to ppm by the processor.

MQ-2 sensor can detect gas concentrations from 200 ppm to 10,000 ppm. This sensor just needs 5 V which can be directly given by Arduino. It is made of SnO_2 which with lower conductivity in clean air. The basic principle involved in the MQ-2 gas sensor is that if there is a change in the concentration of the gases is observed then the resistance will be changed accordingly. If the gas concentration is high, the resistance gets Decreased. So, here the resistance is inversely proportional to gas molecules concentration. The sensor is able to detect many gases such as H_2, HC gases (CH_4 gas), CO, alcohol. In this project, only CO gas and HC is detected using this sensor. The particular gas ppm is calculated based on the Rs/Ro ratio. Ro parameter indicates sensor resistance at 1000 ppm of H_2 in clean air and Rs parameter indicates sensor resistance at various concentrations of gases. For the detection of CO gas, the Rs/Ro ratio will Decrease from 5 till 1.5 which shows an corresponding increase in the ppm of the gas, which is calculated by the microprocessor based on the Rs/Ro ratio. For the detection of HC gas, the Rs/Ro ratio Decrease from 3 till 0.7 with a corresponding increase in ppm, which can be calculated by the microprocessor. In this way, the individual component of gases (here CO and HC gases) is detected by the Rs/Ro ratio by the sensor. The circuit diagram of the MQ-2 gas sensor is shown in Fig. 2.

4 Architecture and Methodology

The architectural design of the system gives an overview of the hardware and software components and their interfacing which establishes the framework for the development of the entire system (Fig. 3).

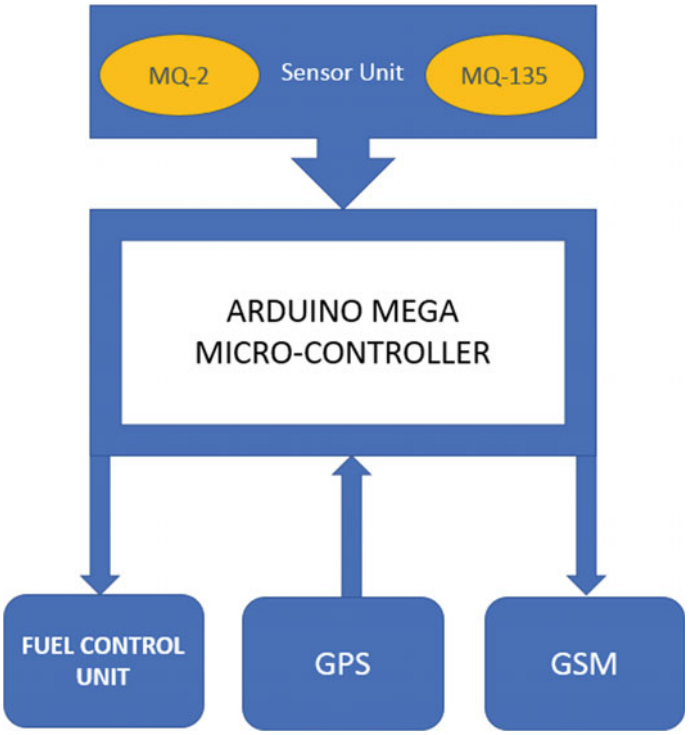

Fig. 3 System architecture

Mainly, there involve following units in the system. The sensor unit: MQ-2 and MQ-135 sensors, the microcontroller unit: Arduino Mega, the fuel control unit, GPS and GSM modules. The Arduino mega microcontroller [5] is mainly programmed to perform some functions such as comparing the inputted values of gas levels taken from the analog signals of the gas sensors with the predefined values, alarming the driver if the pollution levels exceed the threshold, cut-off the fuel supply to the engine if driver does not stop the vehicle after warning, informing the nearest service station through SMS using GSM module, sending the location of vehicle to the nearest service station using the GPS module (Fig. 4).

The gas sensors: MQ-2 and MQ-135 have four similar pins. The pins include A0 (Analog output) pin, D0 (Digital output) pin, GND, Vcc. The Vcc and ground pins are connected to breadboard to which the power is supplied from Arduino mega 5 V pin and ground pin. The A0 pin of the MQ-2 sensor and MQ-135 sensor are connected to the analog pin A5 and A0 of the Arduino mega respectively. In this way, the interfacing of gas sensors is done with Arduino mega. There are some major differences between the MQ-2 and MQ-135. They are: MQ-2 gas sensor is usually used in gas leakage detecting equipment in family and industry where as

Fig. 4 MQ-2 gas sensor [6] (left side) and MQ-135 gas sensor [7] (right side)

MQ-135 is generally used for air quality control equipment for buildings/offices. Rs parameter(sensing resistance) varies for both sensors. For instance, the Rs value of MQ-2 sensor varies from 3 to 30 kΩ where as for MQ-135 sensor the Rs value varies from 30 to 200 kΩ. The threshold values are set according to government norms for each gas. For testing purpose in the project, the different threshold values are set for different gases which is almost similar to real time government prescribed threshold values. The threshold values considered in the project are: for HC gas—200 ppm, CO_2 gas—3000 ppm, CO gas—600 ppm.

In the same way, the GPS module, the GSM module [8, 9], the Buzzer should be interfaced with the microcontroller. The Arduino mega itself is sufficient to powerup all the units using a breadboard. The GSM module used here is SIM 800L which requires nearly 3.7–4 V, can be powered up using two diodes connected in series to achieve the required voltage from the Arduino mega 5 V pin. The GSM module used is REES52 NEO-6 M U-BLOX NEO-6 M which can be powered up directly through the Arduino mega 5 V pin.

Firstly, the gas sensors, microcontroller, GPS and GSM modules are powered up and then exhaust gases levels are measured in real-time using gas sensors, if the levels of gases exceed the threshold level then the driver is warned about the same to halt the vehicle within some grace time and the GPS module is triggered by the Arduino to locate the nearest service station, the GSM module gets triggered next, to inform the nearest station about the condition of vehicle followed by the information passage via SMS. If the vehicle does not stop within the specified time then the controller stops the power supply to the fuel control system thereby preventing the supply of fuel to the engine which ultimately results in the halting of the vehicle (Fig. 5).

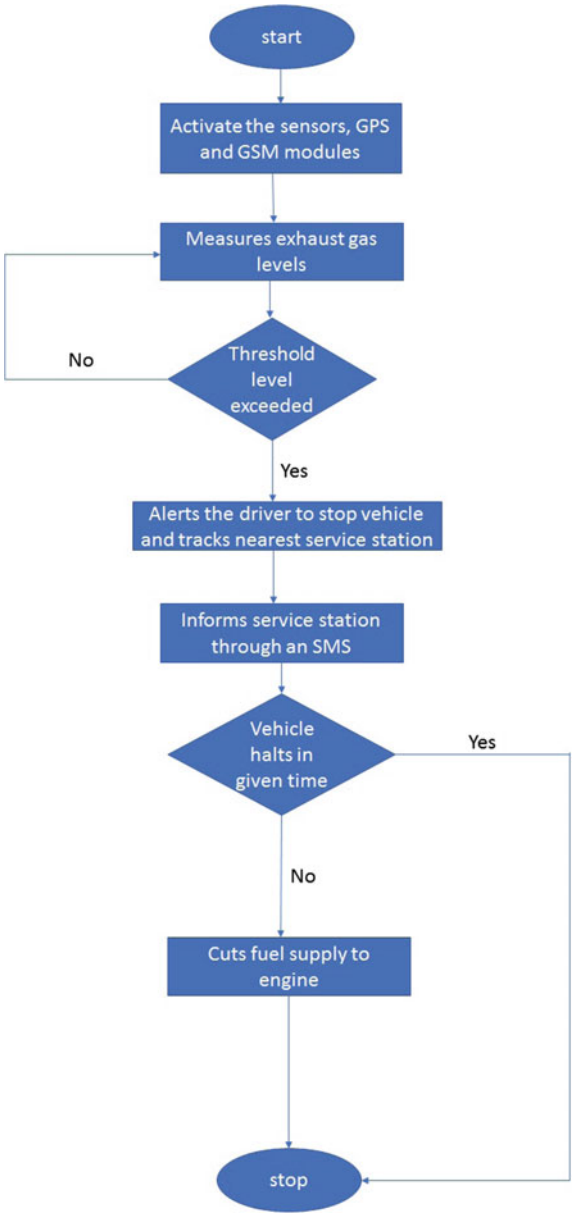

Fig. 5 Process flow of the system

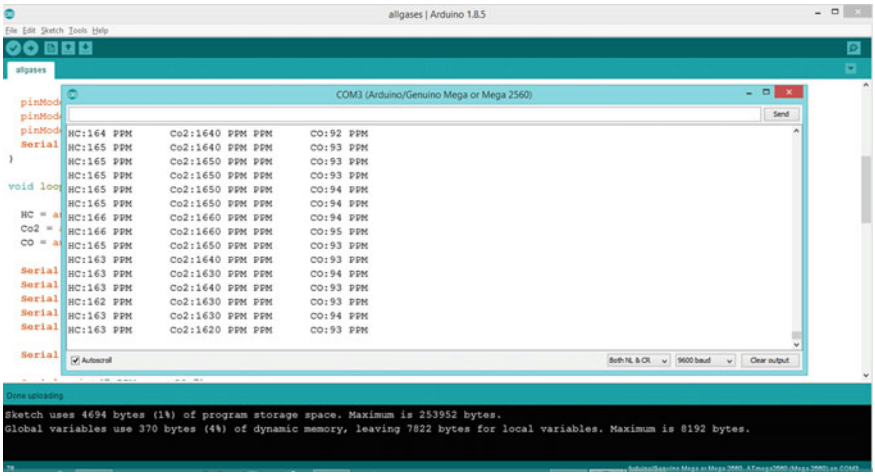

Fig. 6 Picture of the serial monitor in which the gas levels are shown before exceeding the threshold levels

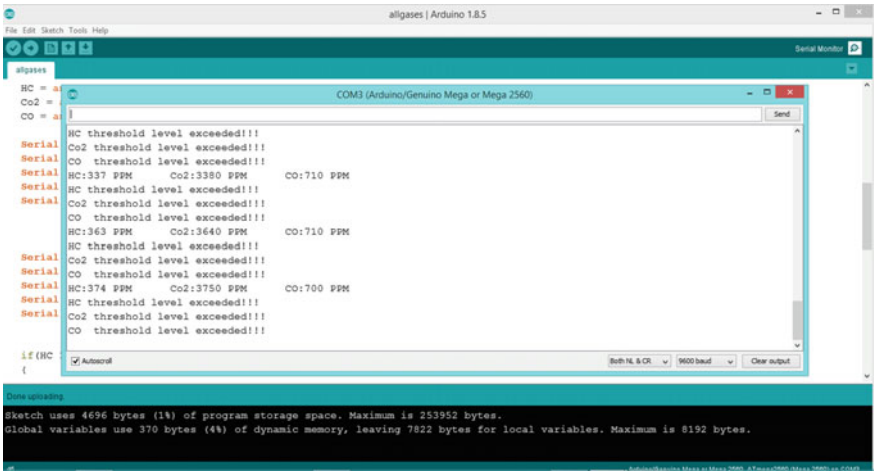

Fig. 7 Picture of the serial monitor in which the gas levels are shown after exceeding the threshold levels

5 Results

The following figures shows the levels (in ppm) of exhaust gases before exceeding the threshold level and also after exceeding the threshold level when the exhaust gas levels overrun the corresponding threshold values taken from both the sensors, displayed in the serial monitor for our reference. But, in real-time, the driver will be alerted using the buzzer to stop the vehicle in the nearby parking location when the gas levels exceed the corresponding threshold levels (Figs. 6 and 7).

References

1. Kularatna N, Sudantha BH (2008) An environmental air pollution monitoring system based on the IEEE 1451 standard for low-cost requirements. IEEE Sens J 8(4):415–422. Available: www.ieeexplore.ieee.org
2. Kumar S, Jasuja A (2017) Air quality monitoring system based on IoT using Raspberry Pi. In: International conference on computing, communication and automation (ICCCA), pp 1341–1346
3. Agarwal T (2016) MQ135 alcohol sensor circuit and working. Internet: https://www.elprocus.com/mq-135-alcohol-sensor-circuit-and-working/, 13 May 2016
4. Praveen (2014) LPG sensor using arduino. Internet: http://www.circuitstoday.com/lpg-sensor-using-arduino, 18 Nov 2014
5. Chandrasekaran S, Muthukumar S, Rajendran S (2013) Automated control system for air pollution detection in vehicles. In: 4th international conference on intelligent systems, modeling, pp 49–51
6. Santos R (2016) Guide for MQ-2 gas/smoke sensor with Arduino. In: Random nerd tutorials, 2016. Available: https://randomnerdtutorials.com/guide-for-mq-2-gas-smoke-sensor-with-arduino/
7. WaveShare, "MQ-135 Gas sensor". Available: https://www.waveshare.com/mq-135-gas-sensor.htm
8. Rathod M, Gite R, Pawar A, Singh S, Kelkar P (2017) An air pollutant vehicle tracker system using gas sensor and GPS. In: International conference of electronics, communication and aerospace technology (ICECA), pp 494–498
9. Patil U, More P, Pandey R, Patkar U (2017) Tracking and recovery of the vehicle using GPS and GSM. Int Res J Eng Technol (IRJET) 4(3):2074–2077. Available: www.irjet.net

Trouble-Free Method of Coordinate Mapping and Spatial Calibration for All Sky Night Airglow Images

N. Venkataramanaiah, S. Varadarajan and T. K. Ramkumar

Abstract The Number of observable facts and structures that are accessible with an airglow images which are captured by an All Sky Imager (ASI). All of these images are required to convert from the spherical coordinating system into the rectangular coordinating image system. The spatial calibration is also most important for the perfect measurement of gravity wave characteristics, plasma characteristics and OH emission parameters in the upper atmosphere, mesosphere, ionosphere study when that calibrations are used in real life dimensions. In this paper, we expressed an effective and simple technique for the coordinate mapping and the spatial calibration for accurate dimensions used in real world life and also implemented the same procedure by using Matlab R2013a. The pixel resolutions of OH image of 840 nm, a mesospheric image of 557.7 nm and ionospheric image of 630 nm are measured. These pixel resolutions are nearly same and measuring technique is very simple than other method used in the same area.

Keywords All sky airglow imager · Coordinate mapping · Field of view · Spatial calibration · Mesospheric image

1 Introduction

An airglow emission observation in mesospheric and ionosphere regions is one of the most significant aspects in the study of full of atmosphere forcing and reaction at different heights. Several airglow imagers are used to capture the information of changeable dynamic dissimilarities (such as Plasma irregularities and gravity

N. Venkataramanaiah (✉) · S. Varadarajan
Department of Electronics and Communication Engineering, Sri Venkateswara University College of Engineering, Tirupati 517502, India
e-mail: nvr.personal@gmail.com

S. Varadarajan
e-mail: varadasouri@gmail.com

T. K. Ramkumar
National Atmospheric Research Laboratory, Gadanki 517112, India

© Springer Nature Singapore Pte Ltd. 2020

T. Hitendra Sarma et al. (eds.), *Emerging Trends in Electrical, Communications, and Information Technologies*, Lecture Notes in Electrical Engineering 569,
https://doi.org/10.1007/978-981-13-8942-9_49

waves) happening at their crest emission altitudes [1]. One of the atmospheric recent study from Gadanki (13.51N, 79.21E) exposed that some of the mesospheric gravity waves could reach up to 97 km altitudes and similar wave periods reappeared in the E-region. Moreover, comparable composition was celebrated as intermittent spacing of the plasma bubbles [2]. This designates a connection between mesospheric gravity waves and the structure noted in plasma bubbles. National atmosphere Research Laboratory (NARL) at Gadanki captures all sky images at three different altitudes (such as 85, 97 and 250 km) for OH,OI and plasma depletion regions at crest wavelengths 840, 558 and 630 nm respectively. These images are required to convert into geographical (such as rectangular) coordinating system and also required special calibration with large field of view to put into real world. Instrumentation and size of the image at NARL Gadanki are explained [3]. As many experts used their methods Garcia et al., and Kubota et al., determination of the pixel resolution of 558 and 630 nm images are complicate [4, 5]. To overcome these difficulties we used a trouble free method for better result and to improve simplicity. In this paper all the sequential steps of image processing, rectilinear alteration, spatial calibration are developed using Matlab R2013a.

2 Coordinate Mapping

Collected airglow images from NARL are captured by using a fisheye lens of spherical kind and covers a large area with a great field of view (FOV). To put these images into a real field, these are required to convert into rectilinear. Steps involved in coordinating mapping are explained by using following flow diagram in Fig. 1.

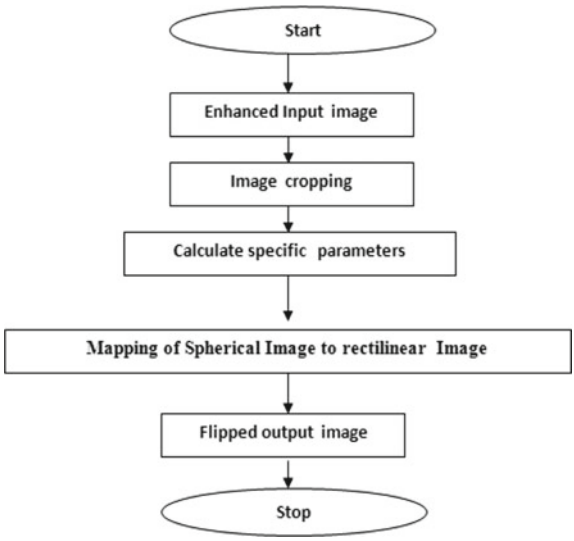

Fig. 1 Flow diagram for coordinating mapping

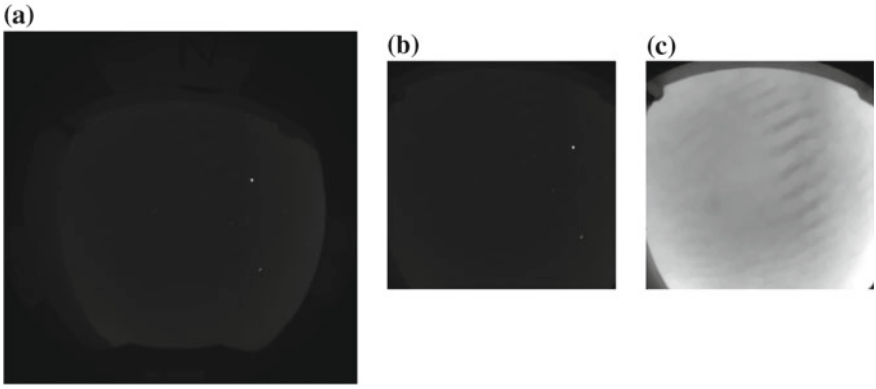

Fig. 2 **a** Original (557.7 nm), **b** Cropped and **c** enhanced with star removed Images on 24th March 2014

2.1 Input Image

The image captured in sky imager is about the size 512 × 512 and the stars are removed by the technique used through morphological opening with circular shaped structure element of radius 5 pixels, for removing the noise also enhanced by adjusting contrast for identifying airglow region and can be taken as input image.

2.2 Image Cropping

Removal of dimmed image around the actual image is essential as it is unnecessary portion consisting walls in imager room and due to street lights around the building where the imager is arranged. In this paper the cropped image with full airglow emission region is of the size 330 × 330 after cropping. The sequence of the original, cropped and enhanced after star removed are shown in Fig. 2a–c.

2.3 Calculation of Specific Parameters

After forming of the cropped image center and radius are calculated.

The center (X_0, Y_0) of the cropped image is calculated as follows

$$X_0 = \frac{width}{2} \tag{1}$$

$$Y_0 = \frac{height}{2} \tag{2}$$

The radius of the image is the maximum of the image height and width. It is taken as R and is calculated as:

$$R = \frac{width}{2} \tag{3}$$

To correct radial distortion over an image is also important. Radial shift between every pixel from the center is evaluated by using Euclidian distance formula. After approximating the radial distance plus Radial shift, its values are taken as input for calculating the magnitude of the truthful radial distance pixel to center. By deducting the magnitude of the radial shift from the radial distance, the actual radial distance of a pixel from the center is determined and the same procedure is used for each pixel in the image.

From Fig. 3 the distance of the pixel from the center can be determined as

$$R_s = \sqrt{\left((Y - Y_0)^2 + (X - X_0)^2\right)} \tag{4}$$

Exact radial distance can be calculated by using the Pythagoras principal as:

$$R_c = \sqrt{\left(R_S^2 - R_d^2\right)} \tag{5}$$

Here, (X, Y), are the image pixel position points in the input image.. Angle between every pixel to the center pixel is evaluated as

$$\theta = \tan^{-1}\left(\frac{d_y}{d_x}\right) \tag{6}$$

where

$$d_x = X - X_0 \tag{7}$$

and

$$d_y = Y - Y_0 \tag{8}$$

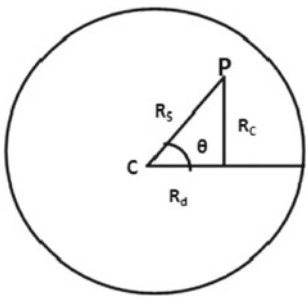

Fig. 3 Represents distance of points in input image

2.4 Mapping of Spherical Image to Rectilinear Image

(U, V) is the image points denote the pixel location in the input image. For every pixel location (X, Y) in the input image a pixel position (u, v) in the output image is formed, that gives the mapping of input image into the output image. Suppose the pixel location in the input image is in first and second quadrants then θ is given

$$\theta = \Pi + \tan^{-1}\left(\frac{d_y}{d_x}\right) \tag{9}$$

And if we determine the pixel location in the fourth quadrant, the angle θ can be evaluated as:

$$\theta = 2\Pi + \tan^{-1}\left(\frac{d_y}{d_x}\right) \tag{10}$$

An output pixel value (u, v) is specified as

$$u = u_0 + x_1 \tag{11}$$

and

$$v = v_0 + y_1 \tag{12}$$

where (u_0, v_0) is the center of the output image and X1, Y1 are given as

$$x_1 = R_c \cos(\theta) \tag{13}$$

and

$$y_1 = R_c \sin(\theta) \tag{14}$$

The converted rectilinear image is exposed in Fig. 4.

Fig. 4 Rectilinear image

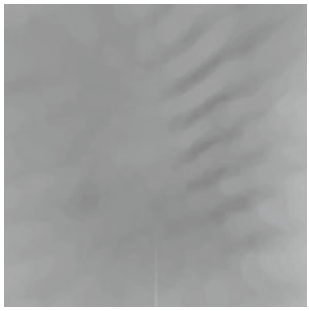

2.5 Output Image

The directions of mapped rectilinear image not as real world image. In which the East and West sides are reversed to each other. To make the image into real world geographical directions it can be flipped from right to left. The final output image is shown in Fig. 5.

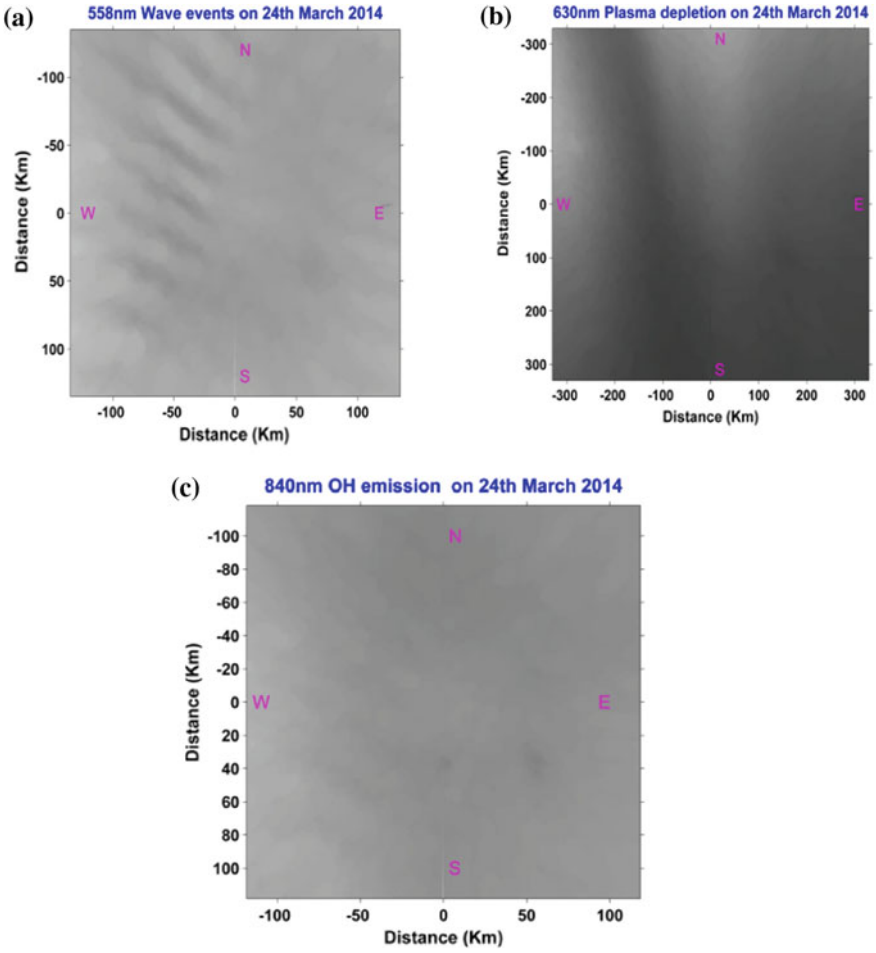

Fig. 5 Final special calibrated images **a** 557.7 nm, **b** 630 nm and **c** OH image

3 Field of View and Spatial Calibration

The Actual size of the chip used in CCD camera is of 1024 × 1024 square pixels with 13.3 × 13.3 mm^2. Captured image from CCD camera is binned for 2 × 2 pixels making the image as 512 × 512 pixels in the chip to increase the signal strength. From this fact we decide the 1 × 1 mm^2 size of chip contains 38 × 38 pixels approximately. The fisheye lens function of the equisolid angle type used in all sky imager is defined as

$$R_f = 2f \sin\left(\frac{\theta}{2}\right) \tag{15}$$

where Rf is the radial position of a point in a fisheye image, f is the focal length of fisheye lens θ is the angle between a point in the real world and optical axis of the lens. From the specifications of the imager the value of f is 24 mm then the value of Rf is 34 mm for 1800 FOV. If we mapped CCD chip dimensions into image formed by a lens 34 mm length of a lens is equal to 6.65 mm (i.e. half of 13.3 mm) in the chip. Finally, for 1 mm i.e. for 38 pixels the value of Rf is 5.1127 mm and for 1 pixel its value is 0.1328 mm.

For 180° FOV pixel size is 512

For 117° FOV pixel size is 333 (approximately)

The value of Rf for 117° FOV i.e. 333/2 = 166 pixels is 0.1328 × 166 = 22.1776 mm and the value of θ is 55.040.

The real world geographical distance at different emission heights are determined from Kubota et al. 2001 by using the following equations

$$r = C \times R_E \tag{16}$$

where

$$C = \theta - \sin^{-1}\left[\frac{R_E \times \sin\theta}{R_E + h}\right] \tag{17}$$

where, RE is radius of the earth and h is the height of the emission of an airglow layer and C is in radians.

4 Results and Discussion

The geographical distance of 557.7 nm image at an altitude of 97 km can be determined as 134.6 km (Approximately) for 166 pixels and pixel resolution is 0.819 km per pixel which is nearly equal to the pixel size 0.8 km focused by Sivakandan et al. [6]. Same procedure is used for 630 nm (at 253 km height) and OH image(at 85 km height) we get pixel resolution for 630 nm and OH image as 2 km and 0.712 km per

Table 1 Comparison of spatial calibration

Type of image	Range in km			Pixel resolution in km (existing method)	Pixel resolution in km (proposed method)
557.7 nm	−134	0	+134	0.8	0.819
630 nm	−331.8	0	+331.8	2.0	2.0
OH image	−118.4	0	+118.4	0.7	0.712

pixel respectively. The geographical distances of 557.7, 630 and 840 nm (OH) images with ranges and pixel resolution are indicated Table 1 and Final special calibrated image of three types are shown in Fig. 5a–c.

5 Conclusions

We have implemented a trouble free method of coordinate mapping and spatial calibration for airglow all sky images at NARL. Determination The directions of images are flipped for real world directions. Imager location is done correctly for simple identification. Images are divided into four different quadrants for easy detection of airglow dynamics finally we hope that it is very useful to every airglow observer in the lower atmosphere and mesosphere.

References

1. Hapgood MA, Taylor M (1982) Analysis of airglow image data. Annales Geophy- sicae 38:805–813
2. Taori A, Patra AK, Joshi LM (2011) Gravity wave seeding of equatorial plasma bubbles: an investigation with simultaneous F-region, E-region and middle atmospheric measurements. J Geophys Res 116. https://doi.org/10.1029/2010ja016229
3. Taori A, Jayaraman A, Kamalakar V (2013) Imaging of mesosphere–thermosphere airglow emissions over Gadanki (13.51N, 79.21E)—first results. J Atmos Sol-Terr Phys (93):21–28
4. Garcia FJ, Taylor MJ, Kelley MC (1997) Two-dimensional spectral analysis of mesospheric airglow image data. Appl Opt 36(29):7374–7385
5. Kubota M, Fukunishi H, Okano S (2001) Characteristics of medium- and large-scale TIDs over Japan derived from OI 630 nm nightglow observation. Earth Planets Space 53:741–751
6. Sivakandan M, Paulino I, Taori A, Niranjan K (2016) Mesospheric gravity wave characteristics and identification of their sources around spring equinox over Indian low latitudes. Atmos Meas Tech 9:93–102

A Novel Approach for Brain Tumor Detection Using Hierarchical Centroid Shape Descriptor

P. Nagaveni, Potli Aswarthanarayana and Chandra Mohan Reddy Sivappagari

Abstract In cerebrum tumor conclusion, clinicians coordinate their restorative information and mind attractive reverberation imaging (X-ray) sweeps to get the nature and obsessive attributes of mind tumors and to settle on treatment choices. Be that as it may, physically identifying and sectioning cerebrum tumors in the present mind X-ray, where an extensive number of X-ray examines taken for every patient, is dull and subjected to entomb and intra eyewitness recognition and division fluctuation. As result various strategies have been proposed as of late to fill this hole, yet at the same time there is no generally acknowledged computerized method by clinicians to be utilized as a part of clinical floor because of exactness and vigor issues. In view of this perception, a mechanized calculation, Various levelled Centroid Shape Descriptor (HCSD) for mind tumor identification and restorative specialists' help with encouraged and quickened determination technique has been produced.

Keywords Segmentation · Conditional random field (CRF) · HCSD · K-means clustering etc.

1 Introduction

The Brain tumor is a mass or development of anomalous cells in your cerebrum. A wide range of kinds of cerebrum tumors exist. Some cerebrum tumors are noncancerous (favourable), and some mind tumors are carcinogenic (threatening). Cerebrum tumors can start in your mind (essential mind tumours), or disease can start in differ-

P. Nagaveni (✉) · C. M. R. Sivappagari
Department of Electronics and Communication Engineering, JNTUA College of Engineering, Pulivendula, Andhra Pradesh, India
e-mail: potlinagaveni44@gmail.com

C. M. R. Sivappagari
e-mail: cmr.ece@jntua.ac.in

P. Aswarthanarayana
Department of Mechanical Engineering, RGUKT IIIT Nuzvid, Nuzvid, Andhra Pradesh, India
e-mail: ashwathpotli@gmail.com

© Springer Nature Singapore Pte Ltd. 2020

T. Hitendra Sarma et al. (eds.), *Emerging Trends in Electrical, Communications, and Information Technologies*, Lecture Notes in Electrical Engineering 569,
https://doi.org/10.1007/978-981-13-8942-9_50

ent parts of your body and spread to your mind (auxiliary, or metastatic, mind tumors) rapidly a mind tumor develops can change extraordinarily. The development rate, and also the area of a mind tumor, decides how it will influence the capacity of your sensory system. Programmed location and division of mind tumors [1] in 3D MR Neuro images can essentially help early determination, careful arranging, and follow-up evaluation.

Be that as it may, because of various area and differing size, essential and metastatic tumors introduce significant difficulties for location. It shows a completely programmed, unsupervised calculation [2] that can distinguish single and various tumors.

The cerebrum is the focal point of the human Focal sensory system. It contains 50–100 billion neurons framing a huge neural system. The mind is an unpredictable organ as it made up of numerous cells. These cells have their own particular unique capacity. "Most of the cells in the body create and partition to outline another cell for a suitable working of the human body. At the point when new standard cells create, old or hurt cells fail miserably and new cells have their spot. From time to time new cells create when the body needn't mess with them and old or hurt cells don't kick the basin as they should. It offers climb to extra telephones which outline a mass of tissue called a tumor."

The tumor might be inserted in the cerebrum area that makes the touchy working of the body to be impaired. As a result of its area and spreading limit, it is exceptionally intricate and hazardous for treatment. So Mind tumor is considered as the fundamental driver of growth demise around the world. The cerebrum tumor can influence individuals at any age. Computerized picture handling method is a device by which it's turned out to be conceivable to distinguish the area of the infection effectively [3].

2 Related Work

2.1 Fuzzy C-means Clustering

Fuzzy C-Means Clustering (FCM) is the generally utilized strategy like the K-implies calculation. Its point is limiting a goal work. It is more best than the K-implies in light of the fact that in the K-implies the element vectors of an informational index's are divided into hard bunches, and the element vector can precisely be an individual from one group just, while the fluffy C-implies unwind the condition by enabling the element vector to have various enrolment evaluations to numerous groups. Assume the informational collection with known groups and an information point which is near the two bunches yet in addition equidistant from them. Fluffy bunching nimbly adapts to such quandaries by appointing this information direct equivalent yet fractional participations toward the two groups; i.e. the point may have a place with the two groups with some level of participation grades changes from 0

to 1. It utilizes complementary separation to register fluffy weights. It registers the group's middle utilizing Gaussian weights, utilizes extensive introductory models, and includes procedures of disposal, bunching and combining.

The FCM figuring was introduced by J. C. Bezdek, using weights that breaking point the total weighted mean-square error. FCM is a covering gathering strategy. One pixel regard dependent upon no less than two groups centres. It is in like manner called sensitive gathering system. A standout amongst the most generally utilized fluffy bunching calculations is the Fluffy C-implies (FCM) calculation. The FCM calculation is the segment of n component into an accumulation of c fluffy groups regarding underneath given criteria. It depends on minimization of the accompanying target work Where m = level of fluffiness and the genuine number more noteworthy than a u_{ij} = level of participation of x_i in the bunch x = information esteem Fluffy C-implies is a well-known technique for restorative picture Division yet it just considers picture force subsequently creating inadmissible outcomes in loud pictures. A bundle of calculations is proposed to make FCM hearty against commotion and inhomogeneity however it's as yet not great [4].

2.2 Conditional Random Fields (CRFs)

"Restrictive Random Fields (CRFs) are discriminative other choice to the for the most part generative MRFs. Rather than showing the joint likelihood of the features and stamps p(x, y), discriminative models direct exhibit the back probability of the names given the features p(y|x). This subtle qualification facilitates the need to show the flow over the recognitions. This is crucial in remedial imaging applications since anatomic structures can have complex shapes that are hard to show and may not be appropriately shown by a factorized sort of p(x|y). Since CRFs particularly show the back, they can loosen up a significant parcel of the major streamlining suppositions routinely made in MRFs [5]. This allows the (tractable) showing of complex conditions (a) between the features of a part and its name, (b) between the names of close-by segments, and (c) between the names of neighboring segments and their features, or even extraordinary features of the recognition."

2.3 Affiliation Control Investigation

Affiliation control investigation is clear information mining errand which incorporates deciding examples, or relationship, between components in informational collections. Affiliations are spoken to as tenets or suggestions [6].

3 Methodology

The stream procedure of the proposed strategy is as per the following First the Information is considered as picture. At that point mind extraction is done and k-implies bunching is connected. Promote morphological tasks are done on that picture and HCSD is connected at long last.

3.1 Image Acquisition

A picture is taken as contribution to picture procurement for additionally preparing.

3.2 K-Means Clustering

The k-infers gather is a technique for coarse quantization, right off the bat from signal taking care of that is outstanding for group examination in data evacuation. k-suggests aggregate plans to allocate perceptions into k bundles in which every perception has a residence with the gathering with the adjacent mean, filling in as a model of the cluster. These results in a dispensing of the information universe into Voronoi cells.

The issue is computationally annoying (NP-hard); in any circumstance, there are successful experiential outlines that are normally utilized and join quickly to an almost great. These are typically similar to the craving to expand control for mixes of Gaussian apportionments through an iterative adjustment strategy used by the two estimations. Likewise, they similarly apply set concentrations to set up the data; in any case, k-infers crouching has a tendency to decide bundles of commensurate spatial degree, while the longing enhancement part empowers gatherings to have unmistakable shapes. The figurine has a free relationship to the k-nearest neighbour classifier, an outstanding machine learning methodology for planning that is consistently inaccurate for k-infers in splendid of the k in the term. One can put on the 1-nearest national classifier on the gathering centres gotten by k-expects to portray new data in the present gatherings. This is called as adjacent centroid classifier or Rocchio estimation. The steps involved in Rocchio estimation are as follows:

1. Initialize number of cluster ‘K’ and center.
2. For every pixel of a picture, figure the Euclidean separation d, between the focus and every pixel of a picture utilizing the connection given underneath.
3. Assign every one of the pixels to the closest focus in light of separation d.
4. After the sum total of what pixels have been appointed, recalculate new position of the inside utilizing the connection given underneath.

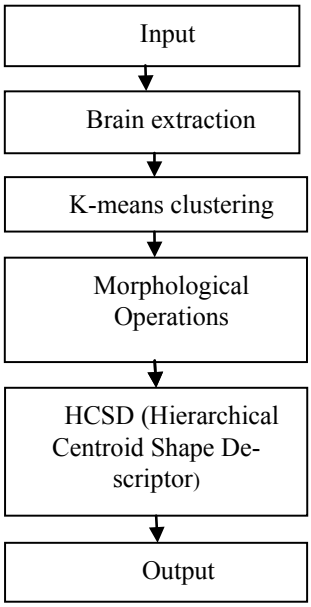

Fig. 1 Block diagram of HCSD method

5. Repeat the procedure until the point when it fulfills the resilience or blunder esteem.
6. Reshape the group pixels into picture.

In malice of the point that k-implies has the huge preferred standpoint of life anything but problematic to actualize, it has a few problems. The wildlife of the latter bunching results is trusts upon the optional purpose of starting centroid. So if the underlying centroid is haphazardly chosen, it will get varied outcome for various beginning focuses. So the fundamental effort resolve be precisely picked with the goal that we get our craving division. And also computational many-sided quality is other period which we have to reflect while outlining the K-implies grouping. It based on the quantity of info mechanisms, amount of groups and number of cycle (Fig. 1).

3.3 Morphological Operations

Morphological image control is an accretion of non-coordinate activities recognized with the figure or morphology of climaxes in an image. Morphological tasks based just on the comparative inviting of pixel regards, not on their arithmetical makings, and thusly are mainly suitable to the making of paired images. Morphological tasks can likewise be related to grayscale images with the close aim that their light altercation volumes are unclear and subsequently their supreme pixel regards are of no or minor intrigue.

3.4 HCSD (Hierarchical Centroid Shape Descriptor)

The HCSD is choosing the genuine CMBs in light of the shape structure. The HCSD is a twofold shape descriptor worked with the centroid arranges removed from a parallel picture. It extricated recursively by breaking down the picture in sub-pictures. Since a picture can be portrayed by the spatial conveyance of pixels, this technique depends on a picture deterioration in the pixel area by utilizing kd-tree calculation. The area data like the centroid directions of nearby districts is removed. The Various levelled Centroid Shape Descriptor (HCSD) permits choosing just those having a particular structure and yields the precise last discovery result. Before that, a pre-handling step is performed for expelling the clamour in a picture and protects helpful data from the de-noised picture. The HSCD permits just choosing a precise state of the CMBs for better location result.

The Quality of the output image is measured in-terms of peak signal to noise ratio (PSNR) ratio, sensitivity, accuracy, dice and Jaccard similarity.

Peak-signal-to-noise ratio:

To start a detached principle for digital image excellence, a stricture baptized PSNR (Peak Signal to Noise Ratio) is defined in equation as follows

$$\text{PSNR} = 10 * \log 10\,(255 * 255/(\text{MSE}))$$

In this above equation a_{ij} incomes the pixel charge at situation (i, j) in the input image is the pixel cost at the equal station in the output image.

Sensitivity:

It dealings the size of actual positives which are in the approved manner identified

$$Sensitivity = \frac{T_p}{T_p + F_n}$$

where,

Tp = True Positive: Number of properly classified pixels as changed region
Fn = False negative: Number of imperfectly classified pixels as changed region

Accuracy:

The accuracy of a test is its ability to differentiate the patient and healthy cases correctly. To estimate the accuracy of a test, we should calculate the proportion of true positive and true negative in all evaluated cases. Mathematically, this can be stated as:

$$Accuracy = \frac{T_{p+T_n}}{T_{p+T_{n+F_{p+F_n}}}}$$

Jaccard coefficient:

The Jaccard index can also be expressed in terms of true positives (TP), false positives (FP) and false negatives (FN) as:

$$Jaccard = \frac{T_p}{T_{p+F_{p+F_n}}}$$

Dice coefficient:

It is different from the Jaccard index which only counts true positives once in both the numerator and denominator. DSC is the quotient of similarity and ranges between 0 and 1

$$\text{DSC} = \frac{2T_p}{2T_{p+F_{p+F_n}}}$$

4 Results

The proposed calculation is produced in MATLAB and analyzed by applying diverse pictures taken from various sources, which are from X-ray, with the determination of 256 × 256. The quality estimations of these pictures are recorded in Table 1. Here taking the information picture one is the X-ray picture appeared in Fig. 2.

Presently applying the info pictures to the proposed technique as appeared in Fig. 3. The yield of the first in the process is mind removed picture as demonstrated as follows in this in the interim, the extricated picture might be changed over into ordered picture appeared in Fig. 4

Presently listed picture is gone through the k-implies grouping procedure and we get the bunching picture as yield as appeared in beneath Fig. 5

Presently the bunching picture is given as a contribution to Morphological task it plays out the gathering of non-direct activities identified with the shape or morphology of highlights in a picture. Morphological activities depend just on the relative requesting of pixel esteems. The yield picture is appeared as beneath Fig. 6.

Table 1 Comparison of metrics

Metrics	CRF method	HCSD method
PSNR	11.84	27.03
Specificity	99.8	100
Accuracy	86.63	98.80
Jaccard	0.76	0.77
Dice	93.64	99.94

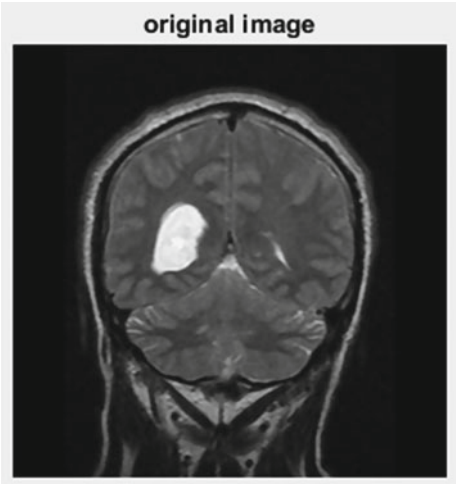

Fig. 2 Input image

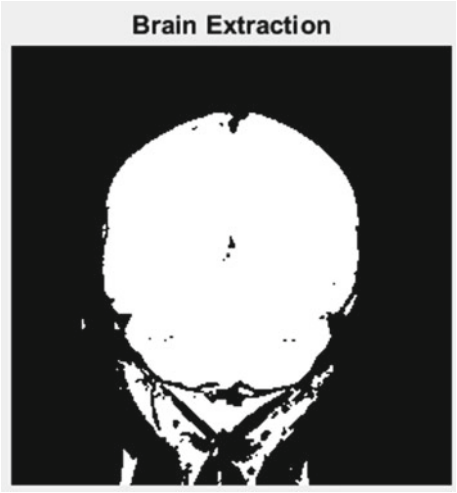

Fig. 3 Brain extracted image

The Morphological picture went through the HCSD square it changes over the information picture into the HCSD is choosing the genuine CMBs in light of the shape structure. The HCSD is a twofold shape descriptor worked with the centroid organizes separated from a double picture. It separated recursively by breaking down the picture in sub-pictures.

In this procedure, the HCSD may recognize the state of the cerebrum tumor exhibited in the info picture as appeared in Fig. 7 (Fig. 8).

The execution of the HCSD strategies is in like manner endorsed through quantitative examination with various parameters. The parameters considered for endorsement of the proposed procedure are Pinnacle Flag to Commotion Proportion (PSNR),

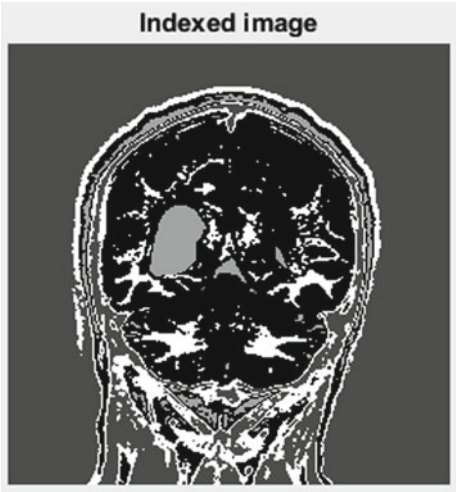

Fig. 4 Indexed image

Fig. 5 k-means clustering

Fig. 6 Morphological operation

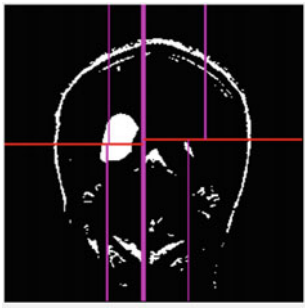

Fig. 7 HCSD

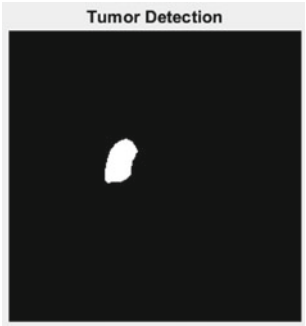

Fig. 8 Tumor detected image

Affectability, specificity, Jaccard coefficient and Dice coefficient. The parameters found out for the more than three X-ray pictures using CRF framework are given in Table 1.

5 Conclusion

This paper deals with the concept of brain tumor segmentation. The tumor can be segmented using HCSD method. The tumor segmented using HCSD is better when compared to the CRF method. HCSD method gives better performance than the other state of art methods. The performance also evaluated in terms of accuracy, specificity, dice and Jaccard similarity.

References

1. Acharya J, Gadhiya S, Raviya (2013) Segmentation techniques for image anal sis, a review. Int J ComputSci Manage Res 2(4):1218–1221
2. Bandhyopadhyay SK, Paul TU (2013) Automatic segmentation of brain tumour from multiple images of brain MRI. Int J Appl Innovat Eng Manage (IJAIEM) 2(1):240–248

3. Funmilola A, Oke A, Adedeji T, Alade M, Adewusi EA (2012) Fuzzy K-Cmeans clustering algorithm for medical image segmentation. J InformatEngAppl 2(6):21–32
4. Castellano G, Bonilha L, Li LM, Cendes F (2004) Texture analysis of medical images. Clin Radiol 59:1061–1069
5. Nagaveni P, Dr. Chandra Mohan Reddy S (2018) A novel technique to detects and segments brain tumor. Int J Comput Sci Eng 6(7)
6. Mahindrakar P, Hanumanthappa M (2013) Data mining in healthcare: a survey of techniques and algorithms with its limitations and challenges. Int J Eng Res Appl 3(6):937–941

Improvement of Bit Error Rate in Circular Filter Bank Multicarrier Communications by Using Low Density Symbol Check

K. Pramidapadma and Chandra Mohan Reddy Sivappagari

Abstract The Fifth Generation (5G) cell systems are imminent. The 5G grant higher information exchange limit constrain than the fourth period supporting broadband. The 5G will support ultra-strong device to-device and gigantic machine form correspondence. For laying out the 5G organizes new coding designs are displayed. The coding plans are Low Density Parity Check (LDPC), Low Density Symbol Check (LDSC). The coding plan, LDPC is utilized for information and polar codes for control data. What's more, another coding plan LDSC is used to check a tiny bit at a time investigation. These coding plans are utilized for blunder adjustment and enhanced information rates. Inside the paper, proposes an estimation technique for a low Bit Error Rate (BER) of LDSC codes. The execution of Sum Product Algorithm (SPA) inside LDSC decoder is portrayed in this paper. The redress term is utilized to enhance the deciphering execution of min whole calculation. For LDSC decoder, BER diminishes with increment in the Signal to Noise Ratio (SNR).

Keywords BER · LDSC · LDPC · Coding schemes · Gadget to gadget · Monstrous

1 Introduction

Circular Filter Bank Multicarrier Communication (C-FBMC) is another waveform strategy having few preferences over Orthogonal Frequency Division Multiplexing (OFDM). The main principal change is the supplanting of OFDM with a multicarrier framework in light of channel banks at transmitter and recipient. The key element of this method is to isolate the perplexing information images into genuine and fanciful parts, and presents a balance [1]. Propose a utilization of Cyclic Prefix (CP) in FBMC

K. Pramidapadma (✉) · C. M. R. Sivappagari
ECE Department, JNTUA College of Engineering, Pulivendula, AP, India
e-mail: yours.pramida@gmail.com

C. M. R. Sivappagari
e-mail: cmr.ece@jntua.ac.in

© Springer Nature Singapore Pte Ltd. 2020

T. Hitendra Sarma et al. (eds.), *Emerging Trends in Electrical, Communications, and Information Technologies*, Lecture Notes in Electrical Engineering 569,
https://doi.org/10.1007/978-981-13-8942-9_51

to facilitate the evening out assignment at the collector while working over Frequency Selective Channel (FSC).

In data hypothesis, a Low Density Parity Checker (LDPC) code is a straight blunder redressing code, a technique for transmitting a message over a loud transmission channel. The activity LDSC is additionally like LDPC. LDSC codes are built by iterative disentangling strategies utilizing message stream work as SPA.

Distinctive LDSC codes with direct square lengths accessible a mistake floor which is closer smoothed blunder execution as increment of SNR [2]. At the mistake floor locale, the blunder execution of LDSC codes over a memory less channel is relatively controlled by particular non code word blunders called catching sets. The limited arrangement of predominant catching sets can be near the blunder execution on the mistake floor area. Image checking codes are considered for the utilization of extensive variety of uses.

In LDPC codes, the data can be transmitted in light of the equality. Like LDPC, in LDSC codes the data can be transmitted in view of the image signs. For assume if they got data is positive, the data can be transformed. In any case, if they got data is negative, that data can be ignored. LDSC codes are utilized to check bit-by-bit analysis. For the low BER and high Signal-to-Noise Ratio (SNR), a bit-by-bit analysis is useful. In this way, LDSC codes are utilized for evaluating the low BER.

The LDSC codes require low BER. The framework required low BER for two reasons, one is the decoder required either long interconnection or long memory data transmission it makes framework hard to delineate a vast scale reconciliation and thus acknowledgment of decoder is exceptionally troublesome [3]. What's more, other reason is the present absence of appropriate hypothesis of systematically predicts the execution of the code past some normal estimations of BER [4]. The exploratory method to ponder the LDSC codes is by means of recreation.

The paper is organized in the form of sections. In Sect. 2, related work of the system. In Sect. 3, methodology for LDSC is presented and introduced by the researcher for a clear understanding. The results and discussions are presented in Sect. 4 whereas the conclusion and future work is put forth in Sect. 5 by the researcher.

2 Related Work

B. Farhang-Boroujeny suggested Orthogonal Frequency Division Multiplexing (OFDM) versus FBMC. FBMC Offset Quadrature Amplitude Modulation (FBMC-OQAM) is another candidate for 5G networks. Although, FBMC-OQAM has been invented before OFDM, only recently has FBMC-OQAM been considered as a promising technique, and drawn interest from research community [5]. At the transmitter, FBMC-OQAM uses a set of filters, called synthesis filter bank, to shape and then combine a set of input signals. At the receiver, FBMC-OQAM uses another set of filters, called analysis filter bank, to split the received signal into individual components. The OQAM modulation splits the complex data into real and imaginary parts.

K. Pramidapadma and S. Chandra Mohan Reddy suggested the improvement of BER using novel precoded techniques [6]. In this, the author estimated the BER by using precoding and non-precoding techniques. In addition to this, proposes a Walsh-Hadamard (WH) C-FBMC. WH-C-FBMC is the one of the multicarrier scheme provide low BER. On comparing with remaining multicarrier schemes, WH-C-FBMC is better for transmitting signals.

Takakazu Sakai, Koji Shibata proposed the quick Bit Error Rate (BER) estimation of LDPC codes [7]. They proposed estimation technique for a low BER of LDPC codes no scientific apparatus is accessible to assess execution of LDPC codes. What's more, customary Monto Carlo recreation techniques can't appraise low BER of LDPC codes because of the restriction of time. They demonstrate some numerical cases to show the adequacy of the proposed strategy.

G. Jagga Rao proposed the strong examination of limiting PAPR diminishment by utilizing LDSC [8]. MIMO Constant Envelop Modulation (CEM) is an exceptionally vitality and multifaceted nature green framework which is conveyed as elective possibility to the directly utilized MIMO-OFDM. The execution of the LDSC coded MIMO-CEM with Gaussian least stage move keying adjustment is assessed over a multi-course Rayleigh blurring channel. It affirmed that LDSC codes are great to enhance the PAPR.

3 Methodology

A low density symbol test code has a place with straight square code family. In this way, all the code word X spread all through the invalid territory of image test matrix H is as follows:

$$H \cdot X = 0 \tag{1}$$

The H matrix for LDSC codes is a twofold extras network which each association of line and section factors are chosen to achieve a favored weight trademark. In addition, the elements associations in the chart are restricted to constrain the covering of lines and sections. These confinements in building the image test lattice H prompt a tough code comparably to have proficient calculations for deciphering. For encoding block of bits N, at that point may be excess image bits 'M', all together that the code charge might be computed through:

$$R = (N - M)/N \tag{2}$$

The real contrast between the traditional codes and LDSC codes is in the decoding procedure. Conventional block codes are decoded with most extreme probability interpreting calculations. Along these lines, they are normally short and composed numerically to rearrange this procedure. Then again LDSC codes are decoded iteratively utilizing a graphical portrayal of their symbol check network. So they are

planned by the image check grid attributes. The gatherings of interpreting calculations utilized as a part of translating LDSC codes are as one called message passing calculations.

The task can be clarified by utilizing the Tanner chart. At the point when messages going along the edges of a Tanner diagram, every Tanner chart hub works in disengagement, so just edges associated with message approach the data contained in it. Iterative interpreting calculations additionally viewed as another name for the message passing calculations as the message go back and forward between the bit and check codes through emphasis until the point that a coveted outcome is accomplished or the procedure is halted. Diverse message passing calculations are arranged by the sort of task performed at the hubs. In some translating calculations, for example, bit flipping deciphering, the messages are paired and in different calculations, for example, conviction proliferation interpreting, the messages are probabilities which speak to a level of conviction about the genuine estimation of the code word bits. Conviction proliferation deciphering is typically called 'sum–product decoding' and this happened while speaking to the likelihood esteems as log probability proportions, and afterward utilizing these qualities for figuring at the bit and check hub utilizing both sum and product tasks.

The block diagram of the LDSC coded data transmission for QPSK model is as shown in Fig. 1.

In the transmitter side the input binary data from the source is encoded the utilization of the LDSC channel encoder to enhance the PAPR execution particularly with the presence of one piece ADC. The encoded records are then interleaved to scatter a vast burst of blunders over the blurring channel. The interleaved data is then separate into code assortment of streams equivalent to the quantity of PAPR radio wires. After that a differential encoding seen by methods for Gaussian Minimum Shift Keying (QPSK) regulation are done to realities streams to gather a steady envelope stage balanced signs. These signs are transmitted over MIMO Rayleigh multipath fading channel.

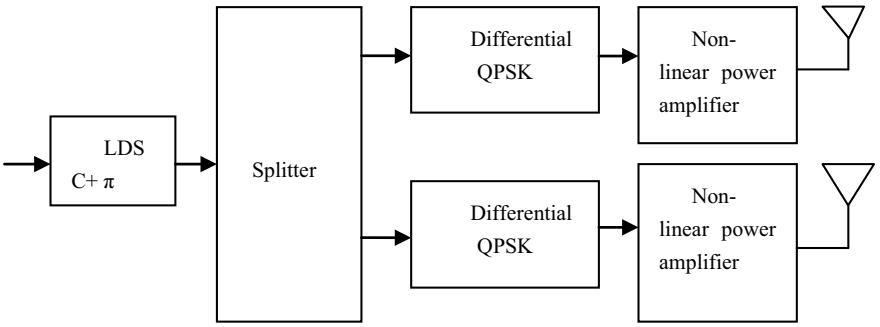

Fig. 1 LDSC data transmission for QPSK model

4 Simulation Results and Discussions

This project can be executed with the assistance of MATLAB. This section present simulation results of LDSC codes. First, its BER performance over FSCs is discussed. BER performance of five other systems is also included for comparison. Those systems are OFDM, CFBMC-OQAM, GFDM, WH-GFDM, WH-CFBMC and LDSC. The first three systems are non-precoding systems presented in previous sections. The fourth one is a precoded GFDM system based on WH, presented. The fifth one is a precoded CFBMC system based on WH, presented. The last one is an iterative coding system. The theoretical approximation for the BER performance of WH-CFBMC-OQAM are illustrated and compared with the simulation results.

The flow graph of the proposed method is as exposed in picture 2. The algorithm of the existing method is given in following steps:

1. **Input the Parameters**:

In this, input the parameters like system parameters, channel parameters and simulation limitations. The scheme limitations are listed in Table 1. The channel parameters are registered in Table 2. The simulation limitations are listed in Table 3.

2. **M-QAM Modulation**:

Table 1 System parameters

Parameter	Value
OFDM. N_b	10^5
OFDM. N_t	2
OFDM. N_r	4
Number of subcarriers (K)	128
Gain (G)	1/4

Table 2 Channel parameters

Channel A	Gain (dB)	0	−8	−14	–	–	–	–
	Delay (μs)	0	4.57	9.14	–	–	–	–
Channel B	Gain (dB)	0	−10	−12	−13	−16	−20	−22
	Delay (μs)	0	2.85	4.57	6.28	9.71	15.43	20

Table 3 Simulation parameters

Parameter	Value
Number of sub-symbols (M)	32
Prototype filter	SRRC
Roll-off	0.5
Modulation	4-QAM, 64-QAM

Quadrature Amplitude Modulation (QAM) is a technique for consolidating dual Amplitude-Modulated (AM) signs into a solitary network, accordingly multiplying the viable transmission capacity. This strategy utilizes 4-QAM and 64-QAM variation schemes. The significant advantage of QAM regulation is proficient use of transfer speed. This is because of the way that QAM speaks to more number of bits per bearer. For instance, 16-QAM maps 4 bits for every bearer, 64-QAM maps 6 bits for each transporter etc.

3. **Pilot Insertion**:

The pilot carriers are held sub-transporters embedded in the middle of the sub-bearers that convey data. One preferred standpoint of pilot inclusion is that it levels channel noise over the whole signal. It is additionally vital to embed pilot sub-carriers to assess the start of the image on the getting side.

4. **IFFT Operation**:

After inserting the pilot carriers, creates symbols. By applying the Inverse Fast Fourier Transform (IFFT), it converts the sign domain from occurrence to period.

5. **Parallel to Serial Communication**:

Subsequent to embeddings the monitor interims, the parallel WH-CFBMC-OQAM images are changed over to serial WH-CFBMC-OQAM. This converter is like the task on the transmitter side where the parallel WH-CFBMC-OQAM images were changed over to serial arrangements. The procedure is setting up the WH-CFBMC-OQAM images for the following stage. As specified previously, the parallel OFDM images, which have shorter term, are changed over to get the first span length and arranged for demodulation. This is to try to recover the binary signal that is transmitted through this model.

6. **Add CP**:

Cyclic Prefix (CP) is a technique that can be connected to the flag for ISI impact diminishment. The CP can be utilized as a part of FBMC to facilitate the adjustment errand at the collector while working over FSCs.

7. **DAC**:

DAC implies Digital to Analog Converter. For including the CP, change the digital signals into analog signals through the channel. DAC is utilized to make the intricate tweak expected to pack voice, video, and information onto restricted data transfer capacity signals.

8. **ADC**:

At that point change over the analog signals into digital signals by utilizing Analog to Digital Converter (ADC). The quick ADCs that make an interpretation of got signals into high determination advanced code, information converters are as critical to current correspondences frameworks as the radio wires, enhancers, channels, and other RF/microwave parts inside the framework.

9. **CP Removal**:

Subsequent to changing the analog signals over the digital signals, at that point evacuate the CP. Due to CP, it decreases the information limit. Therefore expel the CP (Fig. 2).

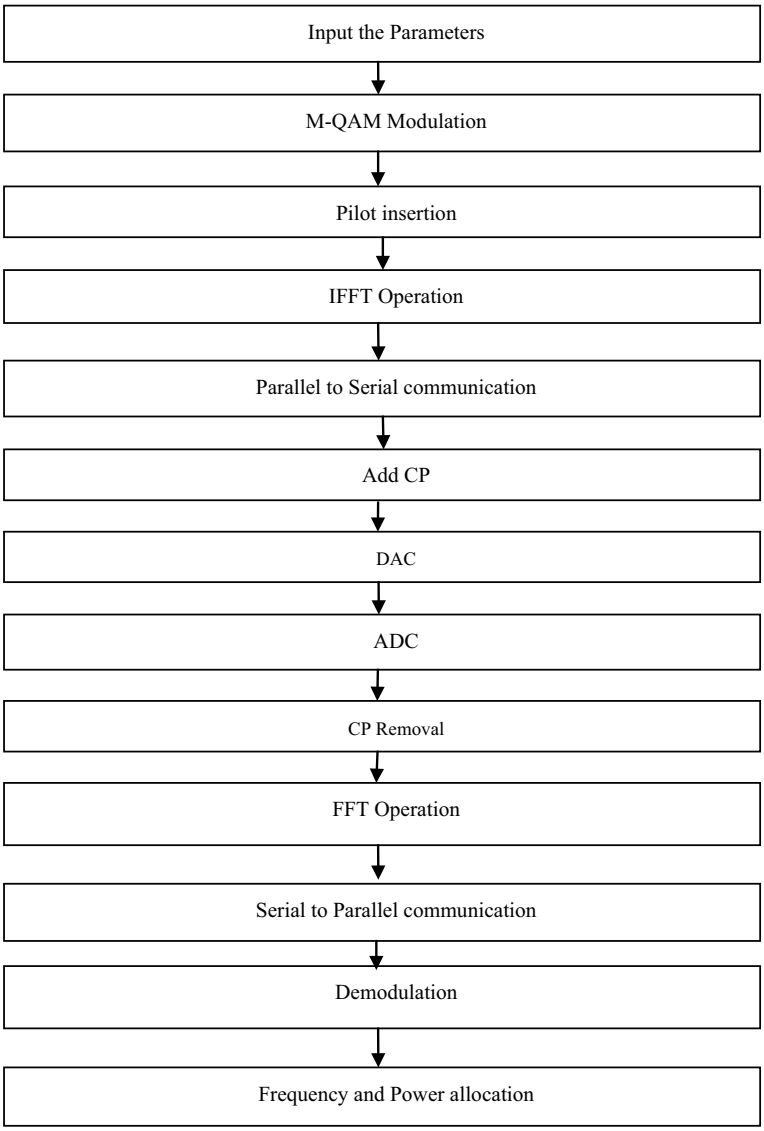

Fig. 2 The flow chart of LDSC code

10. **FFT Operation**:

In the wake of evacuating the CP, at that point changes over the signs from time space to recurrence area by utilizing FFT activity. Subsequent to applying FFT on the got WH-CFBMC-OQAM flag, we can wipe out the bending by utilizing a channel equalizer. The coefficient of the equalizer is duplicated by the examples of the subcarrier freely to drive decreased ISI.

11. **Serial to Parallel Communication**:

By converting the serial data into parallel communication, the numbers of users are increases.

11. **QAM Demodulation**:

For demodulation must be in the transmitter, a collector comparing sine and cosine. Two indistinguishable demodulator circuits get the QAM motion as an info flag. A demodulator gets the subcarrier with the 0° stage position of the other demodulator is fed = 90° pivoted in the stage by f subcarrier. At the yields of the different demodulated data signals are accessible.

12. **Frequency and Power Allocation**:

After demodulation, apply the frequency and power allocation to the received signal. It converts the signal into matrix form. In this, sum of product algorithm is used. In this step, the flow of the process is done based on Fig. 1. For LDSC code, signal can be checked by using bit-by-bit analysis until a desired result is achieved or the process is stopped.

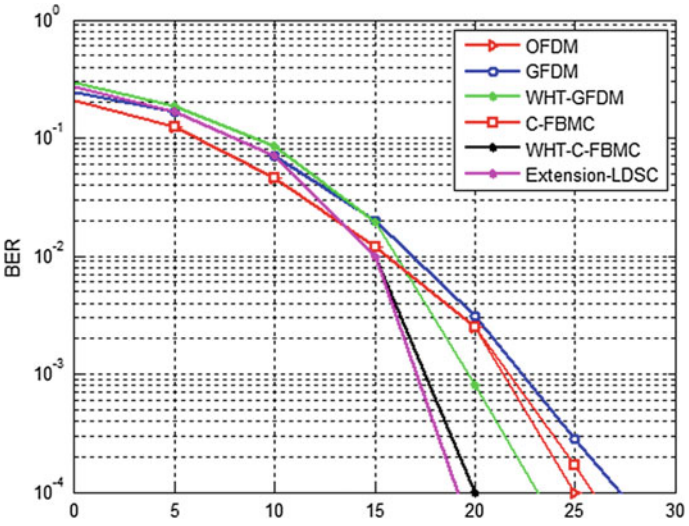

Fig. 3 The BER performance of LDSC in channel A for constellation of 4-QAM

Figure 3 represents the BER presentation of OFDM, GFDM, WH-GFDM, CFBMC-OQAM, WH-CFBMC-OQAM and LDSC under FSC A, each for constellation of 4-QAM. The interval contours of the dual networks are delivered in Table 2. GFDM and CFBMC-OQAM signs are communicated block by block, where single block has KM symbols. In the reproduction, the period of a time slot (sub-symbol) is T = 256 μs.

The simulation results of Fig. 3 are registered in Table 4.

Figure 4 represents the BER performance of multicarrier schemes under FSC B, for constellation of 4-QAM.

The simulation results of Fig. 4 are registered in Table 5.

Figure 5 represents the BER performance of multicarrier schemes under FSC, for constellation of 64-QAM.

The simulation results of Fig. 5 are registered in Table 6.

Table 4 Reproduction outcomes of Fig. 3

BER (Y-axis)	E_b/N_0 (dB) (X-axis)					
	0	5	10	15	20	25
OFDM	0.1	0.03	0.038	0.003	0.0018	0.0001
GFDM	0.15	0.08	0.06	0.01	0.0002	0.0002
WHT-GFDM	0.2	0.19	0.085	0.01	0.0007	–
C-FBMC	0.1	0.03	0.0038	0.003	0.0018	0.0009
WHT-C-FBMC	0.18	0.08	0.06	0.01	0.0001	–
LDSC	0.16	0.07	0.05	0.01	–	–

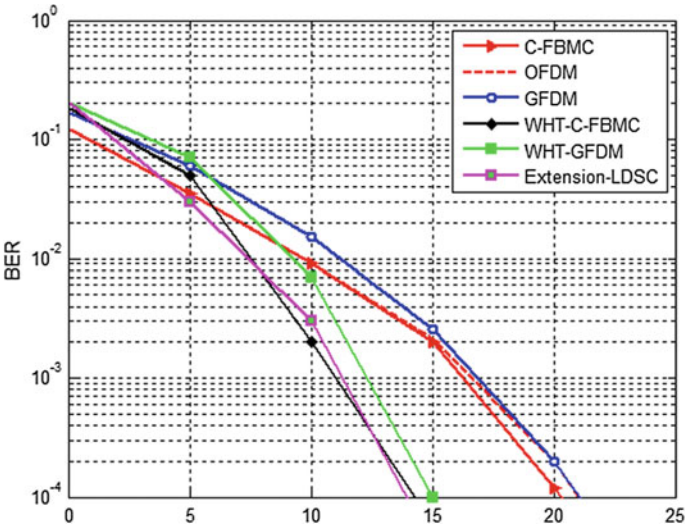

Fig. 4 The BER performance of LDSC over WH-CFBMC in channel B for constellation of 4-QAM

Table 5 Reproduction outcomes of Fig. 4

BER (Y-axis)	$E_b/N_0\,(dB)$ (X-axis)					
	0	5	10	15	20	25
OFDM	0.04	0.026	0.009	0.011	0.0001	–
GFDM	0.05	0.05	0.016	0.0018	0.0001	–
WHT-GFDM	0.1	0.06	0.006	0.0001	–	–
C-FBMC	0.04	0.026	0.009	0.0001	0.00003	–
WHT-C-FBMC	0.09	0.05	0.001	–	–	–
LDSC	0.1	0.02	0.05	–	–	–

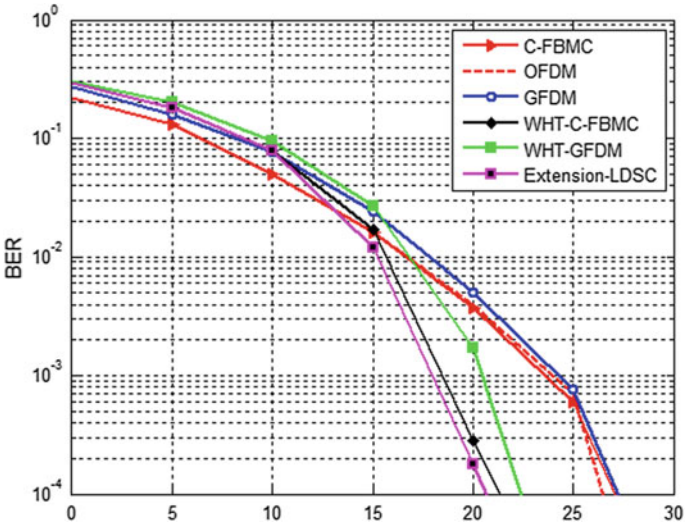

Fig. 5 The BER performance of LDSC over WH-CFBMC in FSC for constellation of 64-QAM

Table 6 Reproduction outcomes of Fig. 4

BER (Y-axis)	$E_b/N_0\,(dB)$ (X-axis)					
	0	5	10	15	20	25
OFDM	0.21	0.15	0.18	0.005	0.004	0.0007
GFDM	0.29	0.18	0.08	0.015	0.005	0.00075
WHT-GFDM	0.3	0.2	0.1	0.029	0.0018	–
C-FBMC	0.21	0.15	0.18	0.049	0.039	0.0006
WHT-C-FBMC	0.3	0.18	0.08	0.018	0.0003	–
LDSC	0.28	0.16	0.07	0.013	0.0002	–

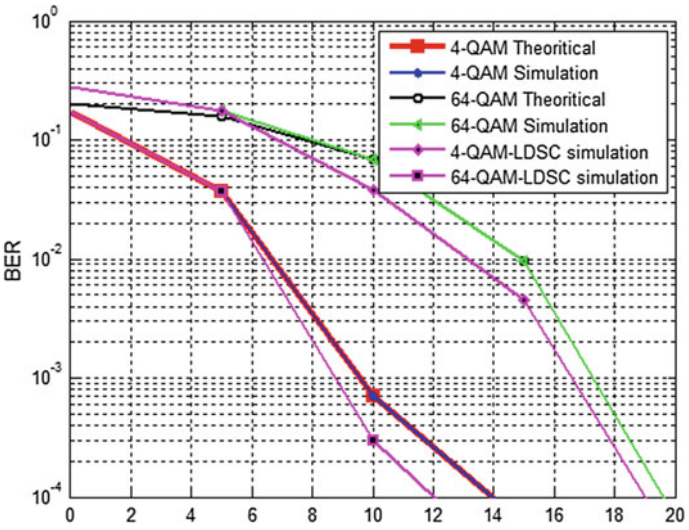

Fig. 6 The theoretical versus simulation results in 4-QAM and 64-QAM

Table 7 Reproduction outcomes of Fig. 6

BER (Y-axis)	$E_b/N_0\,(dB)$ (X-axis)			
	0	5	10	15
4-QAM theoretical	0.18	0.39	0.0007	–
4-QAM simulation	0.18	0.39	0.0007	–
64-QAM theoretical	0.02	0.18	0.08	0.19
64-QAM simulation	0.29	0.19	0.08	0.19
4-QAM LDSC simulation	0.28	0.18	0.04	–
64-QAM LDSC simulation	0.18	0.039	0.0003	–

Figure 6 highlights that the model can be incorporated effectually. In both of these channels that have 4QAM modulation, the results are similar to one another and matches faultlessly with the simulation outcome for the given SNR price. With 64-QAM variation, the theoretic estimation is correct at SNR bigger than 7.5 dB.

The simulation results of Fig. 6 are registered in Table 7.

5 Conclusion and Future Scope

To upgrade the BER execution of LDSC, the iterative decoding algorithm is utilized. WH-CFBMC-OQAM misuses the recurrence decent variety by averaging the SNR yield over all subcarriers. To conquer the misuse LDSC codes are utilized for a

Table 8 Comparison of LDSC over WH-CFBMC

BER (Y-axis)	$E_b/N_0\,(dB)$ (X-axis)					
	0	5	10	15	20	25
WHT-C-FBMC	0.3	0.18	0.08	0.018	0.0003	0.00004
LDSC	0.28	0.16	0.07	0.013	0.0002	0.00002

tiny bit at a time investigation. A hypothetical estimation for the BER of LDSC has likewise been given, which relies upon the channel coefficients and channel picks up. Outcomes demonstrate that LDSC not just achieves significantly superior to the traditional WH-CFBMC, CFBMC-OQAM yet in addition superior to WH-GFDM. The WH-CFBMC is a precoding technique. The precoding techniques have a main problem, i.e. they are not appropriate for the uplink of electronic strategies payable to their great peak-to-average energy part. To overcome this drawback, the new method created on LDSC has been planned using iterative decoding algorithm. And it is found that the performance of LDSC using iterative coding algorithm combines with sum of product algorithm is superior to the previous approach in terms of high speed and QoS. The iterative decoding algorithm gives the low BER. Moreover the proposed method is simple to implement and computationally efficient. On comparing with WH-CFBMC, LDSC codes gives the low BER as defined in Table 8.

Further improvements of our system especially in terms of speed can be achieved by introducing LDSC decoder. This will reduce the BER mentioned in this work. Based on LDSC several works are in progress. The LDSC can also be used in Digital Image Processing.

References

1. Duong Q, Nguyen HH (2017) Walsh-Hadamard precoded circular filter bank multicarrier communications. In: International conference on recent advances in signal processing, telecommunications and computing
2. Richardson T (2003) Error floors of LDPC codes. In: 41th annual Allerton conference on communication control and computing
3. Ashlesha P, Kakde KS (2015) Design and implementation of low bit error rate of LDPC decoder. In: Fifth international conference on communication systems and network technologies
4. Zhang Z, Dolecek L. Investigation of error floors of structured LDPC codes by Hardware emulation from Wikipedia
5. Farhang-Boroujeny B (2011) OFDM versus filter bank multicarrier. IEEE Signal Process Mag 28:92–112
6. Pramidapadma K, Reddy SCM (2018) Improvement of BER using novel precoded techniques. Int J Comput Sci Eng 6(7)
7. Sakai T, Shibata K (2010) Fast BER estimation of LDPC codes. In: International ITG conference on source and channel coding
8. Rao GJ (2018) Robust analysis of minimizing PAPR reduction using low density symbol check. Int J Res 5(6)

A New Approach for Image Dehazing Using Koschmieder's Model

B. Jyothi and Chandra Mohan Reddy Sivappagari

Abstract Images captured in open air environments are normally destroyed due to the existence of awful climate conditions. The impact of murkiness is extensively spread; the anticipated transmission ought to be uniformly changed over the spot. This paper proposed the Koschmieder's Model to clear such corrupted pictures from dehazing. To safeguard more points of interest and right the shading twisting, an answer in light of Koschmieder's Model is presented. The proposed method provides parallel or significantly higher quality with bring down multifaceted nature by connecting with the best in class single picture dehazing techniques. With a specific end goal to confirm the high perceivability remaking and productivity of the proposed method, comparable investigations are conveyed toward the end.

Keywords Dark channel · Airlight estimation · Dehazing · Koschmieder's model

1 Introduction

"In relatively every connected situation the light reflected from a surface is spread in the air before it achieves the camera. This is because of the nearness of showers, for example, residue, fog, and exhaust which divert light from its unique course of spread. In long separation photography or foggy scenes, this procedure substantially affects the picture in which contrasts are diminished and surface hues wind up frail. Such corrupted photographs frequently need visual quality and bid, and besides, they offer a poor perceivability of the scene substance [1]. This impact might be irritation to novice, business, and masterful picture takers and in addition undermine the nature of submerged and airborne photography. This may likewise be the situation

B. Jyothi (✉) · C. M. R. Sivappagari
Department of Electronics and Communication Engineering, JNTUA College of Engineering, Pulivendula, AP, India
e-mail: billajyoo.sku@gmail.com

C. M. R. Sivappagari
e-mail: cmr.ece@jntua.ac.in

© Springer Nature Singapore Pte Ltd. 2020

T. Hitendra Sarma et al. (eds.), *Emerging Trends in Electrical, Communications, and Information Technologies*, Lecture Notes in Electrical Engineering 569,
https://doi.org/10.1007/978-981-13-8942-9_52

for satellite imaging which is utilized for some, reasons including cartography and web mapping, arrive utilize arranging, antiquarianism, and natural investigations."

Pictures acquired under antagonistic climate conditions, for example, murkiness or haze, traditionally show low complexity and blurred hues, which may extremely restrain the perceivability inside the scene. Divulging the picture structure under the murkiness layer and recuperating distinctive hues out of a solitary picture remains an energizing errand, since the debasement is profundity needy and unsurprising strategies can't conquer this issue.

To manage this picture rebuilding assignment, have proposed a progression of systems in light of a variational approach for differentiate change. As of late proposed a further augmentation of the EVID structure that depends on a combination conspire [2] to dehaze pictures. Thus name this novel system FVID: Fusion-based Variational Image Dehazing technique.

"FVID is a spatially changing picture improvement process that returns by first limiting the EVID utilitarian, boosting difference and immersion on the dim information. The repeats delivered by this minimization are kept, and a second vitality that tends to recoil speedier the power estimations of very much differentiated districts is limited, permitting to create an arrangement of profundity maps by watching the contracting rate. The emphasizes delivered in the primary minimization are then melded with these profundity maps to create a cloudiness free form of the corrupted information."

FVID enhances our past works by dehazing a foggy picture while holding high differentiation and colourfulness upgrading capacities on far away districts, while balancing out picture content on adjacent areas that is commonly overenhanced by different strategies.

This paper is organized into five sections. Section 1 explains introduction about the dehazing of the images. The literature survey is provided in Sect. 2. Section 3 explains the methodology of the proposed method and the results and discussion are presented in Sect. 4. Conclusions are explained in Sect. 5.

2 Related Work

The well-known of current dehazing calculations depend on an estimation of the picture profundity (or transmission). In this way, these strategies are helpless against come up short when the physical suspicions basic Eq. (1) are abused. This is a typical marvels both, all things considered, for instance, when there is a wellspring of light covered up by the dimness, and in for all intents and purposes created pictures that include distinctive sorts of haze. Strategies that don't appraise the model profundity don't experience the ill effects of this issue, however they as a rule result in finished improved pictures because of the exceptional qualities of the corruption related with fog. More customary differentiation upgrade calculations, for example, histogram evening out, are not appropriate either. Luckily, late spatially-variation differentiates upgrade strategies can be adjusted to perform well for picture dehazing errands. In the

accompanying, we build up a variational structure for picture dehazing that upholds differentiate improvement on murky districts of the picture all through an iterative strategy enabling us to control the level of reclamation of the perceivability in the scene.

After the minimization [3] has produced the EVID repeats $\left\{I_j\right\}_{j=1}^{N}$ and the DiffSat maps $\{D_k\}_{k=1}^{M}$ separately, it stays to intertwine both data sources. The blend system should reflect that DiffSat maps identifying with late rehashes, i.e. to those districts with higher murkiness, interface with also arranged darkness free cycles.

"In any case, we either embed or extrapolate the course of action of DiffSat maps [4] to get another game plan of correctly N significance maps. These new maps are convolved with a Gaussian piece in three estimations (x, y, and fleeting) in order to display smoothed advances, and they are later institutionalized so the entire in the common estimation for any pixel x is comparable to 1." We finally figure the consolidated picture as the mix of these institutionalized significance maps and the obscurity free rehashes as:

$$FVID(x) = \sum_{j=1}^{N} D_j(x).I_j(x)^{\Gamma_j} \tag{1}$$

Where $\Gamma = [\Gamma_1, \ldots, \Gamma_l]$ is an arrangement of expanding esteems somewhere in the range of 0:45 and 1:2 that counter-impact the way that the first picture is in straight frame (i.e. it isn't gamma remedied).

3 Methodology

The main point of these approach is to assess the trans-mission, (or of course the significance) of the photo to assess the transmission of the photo, that portrays the bit of the splendid that isn't circulated and accomplishes the camera, and after on, to get the albedo in light of the transmission. On the other hand, significance can moreover be surveyed.

The harsh down-tested transmission and the air-light are assessed immediately, and after that the transmission is smoothed and up analyzed using a guided channel, ultimately the mist free picture is restored.

In spite of what may be normal, the intensity of a foggy picture inside each fix is altogether more prominent in view of the shrouded cloudiness components in the photo. For each pixel in a foggy picture I, the dark system Id of the photo can be got as takes after:

$$I^d(x, y) = \min_{(i,j)\in\Omega(x,y)} \left(\min_{c\in\{R,G,B\}} I_c(i, j) \right) \tag{2}$$

Where the join (I, j) is the circumstance inside the fix centred at (x, y) with sweep ω, and the ω can be set to 7 to yield much better recovery comes to fruition Next, the foul program outlinechart $\bar{t}$ can be produced by:

$$\bar{t}(x, y) = 1 - I^d(x, y) \tag{3}$$

Take the data Hazy picture as we play out all possible activity on it. Figure underneath showing all the technique related to Haze emptying computation.

At that point, the haze elements can be expelled from the picture by consolidating the program chart with Koschmieder's ideal as follows:

$$(x, y) = \frac{I_c(x, y) - A_c}{\max\left(\bar{t}(x, y), \alpha\right)} + A_c \tag{4}$$

From Eq (4) c is the rundown of the trichromatic system, J is the dimness free picture; A is the Distinctive brilliant, α is a predefined explanation behind the lesser certain and can be set to 0.1 (Fig. 1).

The creation procedure of the program graph based on Eq. (3) from the dark system earlier is close spatial deterioration, and in this way the power of a fix is continually predictable. Accordingly, the basic issues of recovering a murky picture through such a program outline the time of coronas additionally square articrafts along the side significance edges. "This can be discovered dark system of the data input murky picture, as appeared in the upper right 50% of Fig. 2. In consent to the

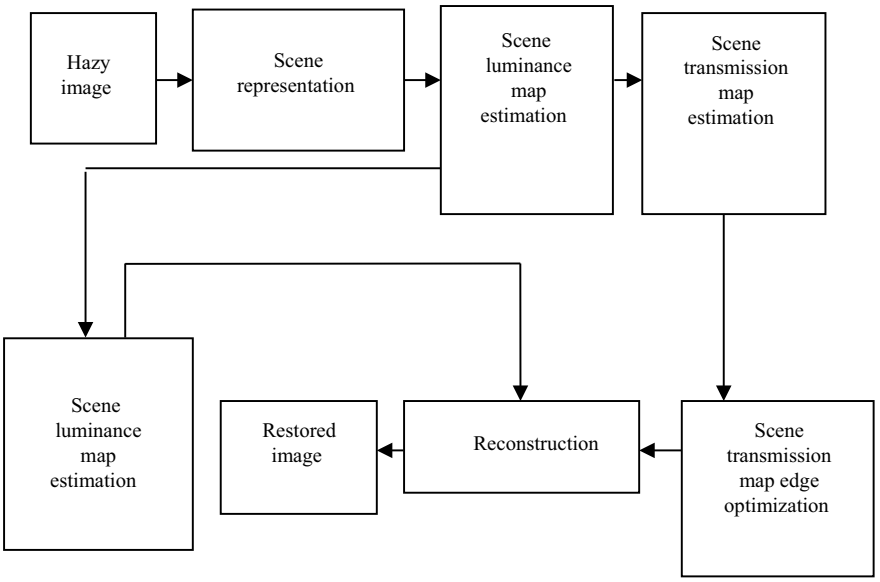

Fig. 1 Steps to simulate the proposed technique

dull channel of the photo, the intensity of the fix in the information murky picture isn't predictable with the objective that its intrinsic information can be effectively implied, as can be found in leftward side of Fig. 2. Furthermore, the power of the base portion of the trichromatic direct in the photo moreover differs as closures change, as appeared in the base right 50% of Fig. 2. The use of fragile tangling likewise guided cleans in truth avoids the period of brilliance knick-knacks in the restored picture. Regardless, they remain a propelled computational weight in view of the uses of the close-by coordinate perfect of each covering space and the close shape structure of the floorcovering system."

Signs influence us to propose another quick refinement channel that can quickly unpleasant the dull channel estimation and besides effectively keep up the fix information as different unpredictability closes. Thusly, the arranged channel can overwhelm the gathering of radiances and square piece protests in the restored picture and make a common recovery result.

Figure the propel amount to evaluate the power of the dark system in the image, also, to keep up the information of to each shot as its significance closes. By execution in this way, the arranged strainer empowers the refinement method to be proficient for ongoing preparing. To this complete, the development amount g can be found as takes after:

$$g = \frac{\sum_{x,y}^{|I^m|-1} d(x,y)}{|d|} \tag{5}$$

Where

$$I_{m(x,y)} = \min_{c\in\{R,G,B\}} I_c(x,y) \tag{6}$$

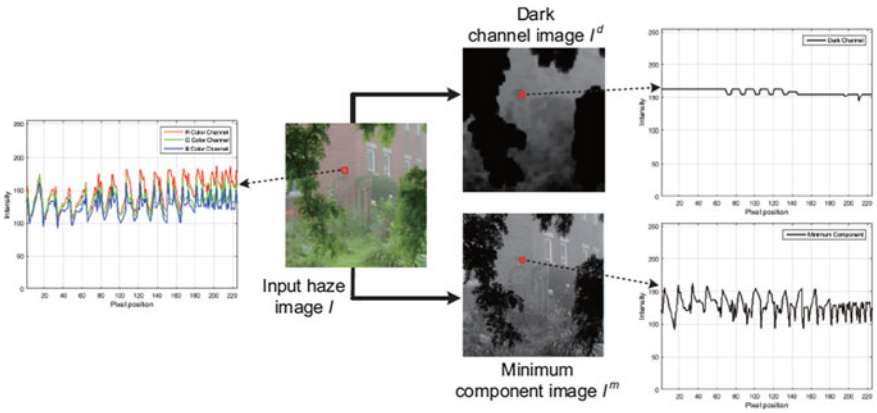

Fig. 2 Power differences of three collected covers in the input haze picture plus the black network and least element of a hazy picture

and $|I^m|$ and |d| signify the whole amount of pixels in I^m then, individually; d(x, y) is the distinction at location (x, y) between the minimum intensity $I^m(x, y)$ of trichromatic segments inside every pixel (x, y) in the picture also black network intensity $I^d(x, y)$ of the image which can be figured by in the picture also black network power of the picture which can be considered by

$$d(x, y) = I^m(x, y) - I^d(x, y) \tag{7}$$

Lastly, we utilize the gain constant to estimate the intensity of the black network of the picture and retain the inherent data of each cover. Henceforth, the developed transmission chart short of square objects can be produced by

$$t(x, y) = (1 - I^m(x, y)) + g\rho \tag{8}$$

Where ρ is the predefined arrangement component and can be set among [0.8, 1.0] in the experiment. The Haze free pictures denied of halo and hunk articles can be secured by playing out Koschmieder's model in Eq. (4) with the created transmission outline t.

The significant commitment of this technique is the transmission graph can be produced by using the proposed GIR strainer finished up the pickup mediation in the base piece of the trichromatic system of the admission cloudy picture. Thusly, the intensity of the dull system picture can be quickly drawn nearer while avoiding the age gathering halo and hunk things. The Planned GIR channel is associated oblivious system before permit a decent, continuous dehazing technique.

4 Results

Original hazy image is given as input to the program shown in Fig. 3a The haze free picture with no halo and square articrafts can be obtained by playing out Koschmieder's model with the refined transmission delineate. The dehazed picture showed up in Fig. 3b.

Haze particles can be expelled from the picture by consolidating the transmission outline Koschmieder's model. Dehazed picture can be acquired.

Parameter esteems for Koschmieder model of various info pictures are organized in Table 1.

5 Conclusion

This paper presented Koschmieder's Model technique to remove hazes from a dehazed image. The proposed technique provides much benefit from an investigation on the natural limitation on the transmission function. This method additionally

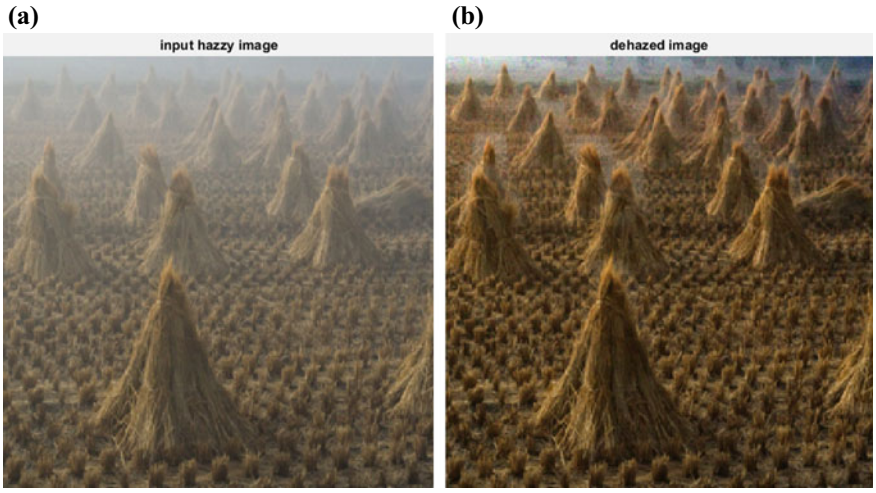

Fig. 3 **a** Hazy cone image, **b** Dehazed cone image

Table 1 Representation of image parameters for different inputs

Metrics	Existing	Proposed
PSNR	43.7668	53.7624
SNR	87.57897	95.9624
Cross correlation	0.0044	0.2979
SSIM	0.0042	0.9328
MSE	5.2406e + 03	3.6544e + 03

diminishes the vagueness with respect to colour and depth, by maintain a strategic distance from numerous incorrect upgrades on the image. In spite of the difficulties in settling the ambiguities engaged with this issue, the pictures created by the proposed method offers a clear perspective of the scene and recapture differentiate that is regular to dimness free scenes.

References

1. Tan R (2008) Visibility in bad weather from a single image. In: 2008 IEEE conference on computer vision and pattern recognition (CVPR), pp 1–8
2. Galdran A, Vazquez-Corral J, Pardo D, Bertalm´ıo M (2015) Enhanced variational image dehazing. SIAM J Imaging Sci 8(3):1519–1546
3. Fattal R (2008) Single image dehazing. In: ACM SIGGRAPH 2008 Papers, ser. SIGGRAPH 2008. ACM. New York, USA, pp 72:1–72:9
4. Tarel JP, Hautiere N (2009) Fast visibility restoration from a single color or gray level image. In: 2009 IEEE 12th international conference on computer vision (ICCV), pp 2201–2208

5. He K, Sun J, Tang X (2011) Single image haze removal using dark channel prior. IEEE Trans Pattern Anal Mach Intell 33(12):2341–2353
6. Koschmieder H (1925) Theorie der horizontalen Sichtweite: Kontrast undSichtweite. Keim and Nemnich
7. Chen B-H, Huang S-C, Cheng F-C. A high-efficiency and high-speed gain intervention refinement filter for haze removal. J Display Technol. https://doi.org/10.1109/jdt.2016.2518646
8. Johnson N, Kader AA, Paul J, Shemil PS, Rizwana A (2017) Haze removal using colour attenuation prior. Int J Comput Trends Technol (IJCTT) 48(2)

Video Segmentation Based on SURF Flow Field

Manchuru Sreenavya and Chandra Mohan Reddy Sivappagari

Abstract In recent days, the automatic extraction of salient object regions from video data is the most significant for visual analytical solutions. It also brings up more challenges, including pose differences amongst background and foreground objects, motion patterns etc. In this project, a framework of co-segmentation is presented in order to discover or segment the objects in a joint fashion from multiple videos and frames. Feature extraction is one of the main steps in object detection. For this feature extraction, Here introduce a speed up Robust features (SURF) flow descriptor to integrate the object features from the video frames in an optical manner. This novel SURF flow can extract foreground object over the complete video dataset.

Keywords Segmentation · SURF · Video · Feature extraction

1 Introduction

As the video data caught pace, it is quite challenging and vital that the objects of interest are extracted efficiently and automatic way from multiple videos. The co-segmentation of video objects refers to the issues of simultaneous segmenting of multiple videos which have common objects. One of the crucial issues linked with image segmentation is the fragmentation or lack of semantical meaning of the regions found by algorithm of image segmentation. Rother et al. presented the conception related to image co-segmentation; the concept implicitly defines the interest region via common objects observations [1]. A trust-region cut of graph is used by Rother et al. to segment the common regions and minimize the objective function on the base of histogram of common appearance from the image pair input. Contemporary work of image co-segmentation highlights the common appearance histogram constraint

M. Sreenavya (✉) · C. M. R. Sivappagari
Department of Electronics and Communication Engineering, JNTUA College of Engineering, Pulivendula, AP, India
e-mail: manchurunavya@gmail.com

C. M. R. Sivappagari
e-mail: cmr.ece@jntua.ac.in

© Springer Nature Singapore Pte Ltd. 2020

T. Hitendra Sarma et al. (eds.), *Emerging Trends in Electrical, Communications, and Information Technologies*, Lecture Notes in Electrical Engineering 569,
https://doi.org/10.1007/978-981-13-8942-9_53

which can be utilized for the term of regularization [2] or term of reward [3]. One of the other approaches of image co-segmentation is clustering which is followed by co-saliency map [4].

In this project the image co-segmentation is extended to video object co-segmentation based on speed up robust features algorithm. The proposal of extracting the main common object is extended, it is in contrast of the earlier object segmentation, made from set of related frames. There are few methods designed till now [5–7].

In this approach, the three levels video object's underlying properties are explored in: inter-frame consistency, across-video correspondence and intra-frame saliency. Compared to the approaches existing in video co-segmentation, the method which is proposed offers following contributions:

- A novel method for co-segmentation of video was presented for automatically segmenting the objects in the foreground with low constraint for their appearance and motion patterns.
- In this project, the first to fully explore the properties of foreground object in video: inter-frame consistency, across-video similarity and intra-frame saliency. Significant cues are than added into the framework of the video as problems related to optimization.
- An efficient speed up robust features is developed to build reliable correspondences among range of videos; the whole video dataset assists inferring the common objects and furthermore refines the object's segmentation accuracy.

In this project, the first to emphasize the fact that perhaps common object are not contained by some frames. The discovery of an object with novel energy function is suggested in order to discover a standard object through the utilization of suggested SURF flow in this setting foreground object features.

2 Related Work

An implicitly defined region of interest is provided by Rother et al. with the assistance of common object's multiple observations [1]. A wide range of research can be improved with this framework: Image retrieval driven from objects, interactive image editing and segmentation and tracking of video. The strength of the framework is in its generality, with a rigid or non-rigid object as a common part (or scene), which is observed from versatile aspects or through same class similar objects. A single and multi image saliency map (SISM) linear combination is modeled for co-saliency [4]. A method for video co-segmentation is proposed in this paper, which utilizes the proposals of category-independent object as its core element; it can be used to extract objects of multiple foregrounds in a video set [5].

An object-based co-segmentation is utilized which is in the form of a co-selection graph, where foreground-like characteristics regions are given favor, besides accounting them for foreground coherence of intra and inter-video. The method in practice

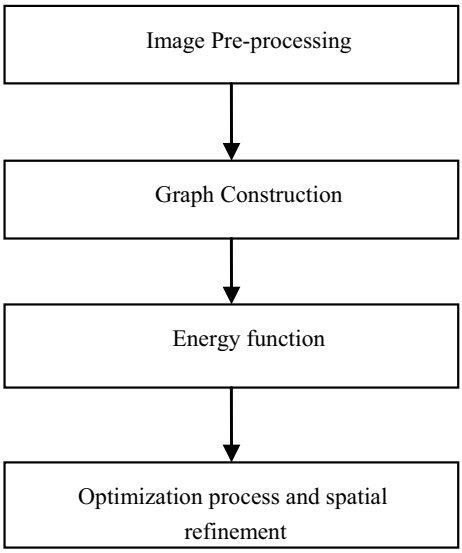

Fig. 1 Block diagram of existing method

can be defined image co-saliency detection and is done through locally adaptive saliency map Fusion. Region-wise fusion task is formulated through this approach, this minimizes energy problem over a graph. Following diagram shows the block diagram of this approach (Fig. 1).

2.1 Image Pre-processing

Simple Linear Iterative Clustering (SLIC) is the pre-processing step for this approach. The process extracts two types of texture, color and visual features from each pixel. Utilizing the bag-of-words model, every pixel of pair of image is quantified into clustering through the means of K-means clustering algorithm. For texture feature, Gabor filter is used with eight orientations.

2.2 Graph Construction

Here construct a graph g = $(\vartheta, \varepsilon = \varepsilon_1 \cup \varepsilon_2)$. The edge $e_{ij} \epsilon\ \varepsilon_1$ is combined to chain ϑ_i and ϑ_j if superpixels i and j are structurally linked in image. The edge $e_{ij} \epsilon \varepsilon_2$ is added to join ϑ_i and ϑ_j if superpixels j in the opposite image, is one of the ⌊ nearest neighbors of superpixel i.

2.3 Energy Function

In this, find the optimal weights $Y = [y_1, y_2, \ldots y_N] \epsilon R^{M*N}$ where saliency maps number is shown by M, and total of superpixels number(of hand 12) is shown by *N* for fusion of superpixel-wise map through reducing the suggested or proposed energy function.

$$\text{Min}\,\lambda_1 \sum_{v_i \epsilon \vartheta} U(y_i) + \lambda_1 \sum_{v_i \epsilon \vartheta} V(y_i) + \lambda_3 \sum_{v_i \epsilon \vartheta} B\left(y_i, y_j\right) + ||Y||_2^2 \tag{1}$$

$U(y_i)$ and $V(y_i)$ are the first two unary terms respectively, supporting both inter-image and intra-image indications, to assist the estimation of the power of each saliency map on the superpixel i. The smoothness of weights is encouraged by pair-wise term $B(y_i, y_j)$.

2.4 Optimization Process and Spatial Refinement

By using both the unary and pairwise terms the constrained optimization problem has a global optimal solution. CVX solver is adopted to solve it. Performance is further improved by application of the spatial refinement process to yield saliency map.

3 Methodology

In the proposed approach the object co-segmentation is applied to video frames to extract the object from the regions. Goal of this paper is to section or segment a number of videos together which includes a standard or common object handled in a supervised manner. The said method follows the steps such as object segmentation, object discovery and object refinement. In this optimization process, Use speed up Robust features algorithm. The flow chart of proposed method shown below (Fig. 2).

3.1 Object Discovery

This stage specifies the method which explores the structure of the video dataset and includes the international info; it is done with intra-frame info such as saliency which recognizes the standard item among numerous videos, and also the incidence of frames that are free from these common objects.

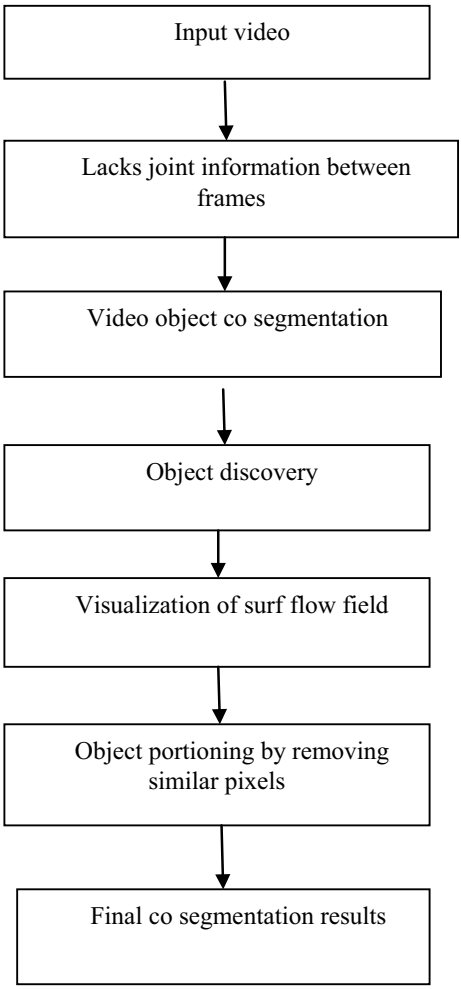

Fig. 2 Flow chart for proposed method

Object discovery is assisted with properties of targeted object, three main of which are stated as following:

(a) Intra-frame saliency: Foreground pixels needs to be preferably different from other pixels in a frame;
(b) Inter-frame constancy: within a video, the foreground pixels are required to be more consistent and constant;
(c) Across-video similarities: the foreground pixels are required to be much like the other pixels in range of videos (however changes are probable in terms of position, size, color).

3.2 Speed Up Robust Features (SURF) Design Flow

Robust Features of 'Speed Up' is a scale and it is an image feature of in-plane rotation-invariant. It is computed faster through the utilization of significant images for the purpose of their convolutions and are comparable to other modern algorithms and produce results that are competitive, robust, repeatable and distinct. The keypoint descriptor and detector are described by this algorithm. The keypoints of the image are located by the detector, whereas the features of the keypoints are described by the descriptor, it also constructs the feature vectors of the keypoints.

(a) **Keypoint Detector**:

'Hessian matrix' the determinant of approximate is used by SURF as the base of the detector. Hessian matrix approximation uses Integral images; this enables fast evaluation of box filters. The integral evolution is given as follows:

$$J(x, y) = \sum_{i=0}^{x} \sum_{j=0}^{y} I(i, j) \tag{2}$$

A blob detector is used by SURF grounded on the Hessian matrix which detects different points of attention. The determining factor of this matrix is incorporated as a measure that includes the local changes across and around the point, where points are selected on the basis of maximal. The determinant factor of the matrix is utilizes to choose the scale and is completed through Lundeberg. Given a point p = (x, y) in an image I, the Hessian matrix H (p, σ) at point p and scale σ, is:

$$H(p, \sigma) = \begin{pmatrix} l_{xx}(p, \sigma)\ l_{xy}(p, \sigma) \\ l_{yx}(p, \sigma)\ l_{yy}(p, \sigma) \end{pmatrix} \tag{3}$$

(b) **Keypoint Descriptor**:

The total sum of the Haar wavelet reactions are used by SURF to elaborate the keypoint features. Integral images use Haar wavelets to decrease computation time and increase robustness. Geometric constraints are introduced in this project, into point-matching which are based on SURF features. This increases the robustness and matching speed. The descriptor has goal of providing unique and robust image feature description e.g. intensity distribution is described in relation to the pixels that are present within the neighborhood of the point of attention. A local manner is labored for computing most descriptors; hence for every point of interest which is identified previously, a description is obtained.

3.3 Object Refinement

Earlier step obtains an estimation of coarse for the common object in the dataset. This lays the core for foreground object of obtaining highly accurate estimation in every video. The intuition of this project is to remove the pixels that are just like the background which are laid on the basis of the approximate results. However a determination of foreground is required for what would it look like? The background pixels are filtered with the help of division of the object-like area into different sub-regions on the basis of the differences amongst them. This project presents a contrast of the texture of region **t** with both the background and the object-like area, using the characteristics of local binary pattern (LBP); it is further incorporated for defining the image's limited spatial arrangement. Video pairs are passed through object refinement process and an improved estimation for foreground object is attained.

3.4 Object Segmentation

Once each video is done for foreground correct estimations, employment of a procedure that is grounded upon graph-cut and is implemented in order to acquire the pixel segmentation results of each pixel. Post the process of object refinement, an improved correct estimation for common object is attained along with appearance model update for the object and background; this can be labored to conduct the segmentation. Then based on above steps the values of inter and intra evidences can be calculated to get optimal solution and thus final segmentation results.

4 Results

4.1 Case 1: Human

Here taking one input video frame results. The Fig. 3 shown (Fig. 4).

The above diagram shows the any large variations between the frames.

The Fig. 5 shows the joint information lack among the video frames. Here taking input video present the some frames, this figure shows the any lacking information in the frames.

The Fig. 6 depicts the visualization of spatio temporal SURF flow field. In this process apply the SURF Algorithm to elaborate the key point detector and descriptor. The key points in the image are located by the detector, whereas the descriptor has job of describing the features of the key points; furthermore keypoints feature vectors are also constructed by it. SURF is the keypoint detector based on the Hessian matrix

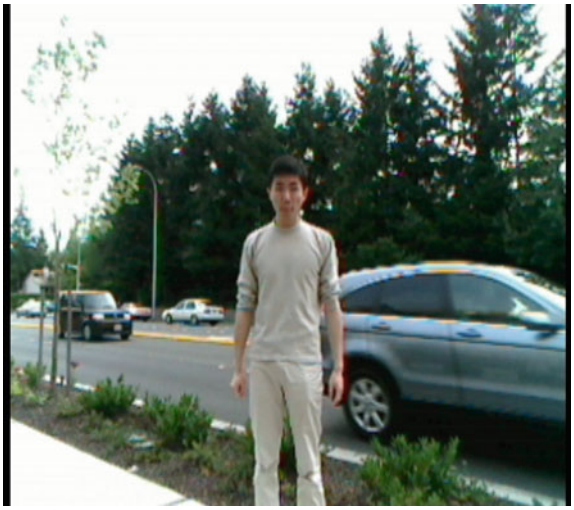

Fig. 3 Input video frame

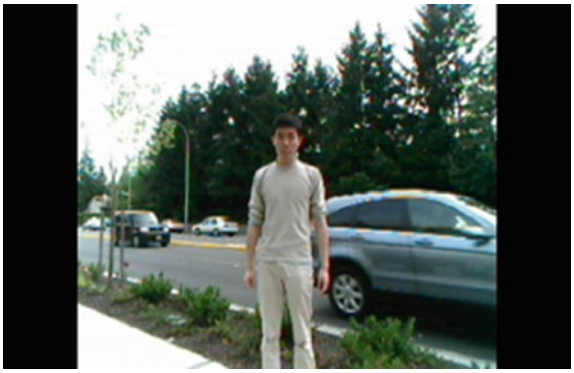

Fig. 4 Input videos where objects have large variations

used as blob detector to detect points of interest. The image feature is decrypted in unique and robust way by key point descriptor.

The above Fig. 7 shows the over segmentation result of spatio temporal SURF flow field. In this results using the canny edge detector for detect the edges. It obtains improved accurate estimation of foreground object for each video; it assists in removing the pixels which are related to the background on the basis of their estimation outcome.

Fig. 5 The joint information lacks between the video frames

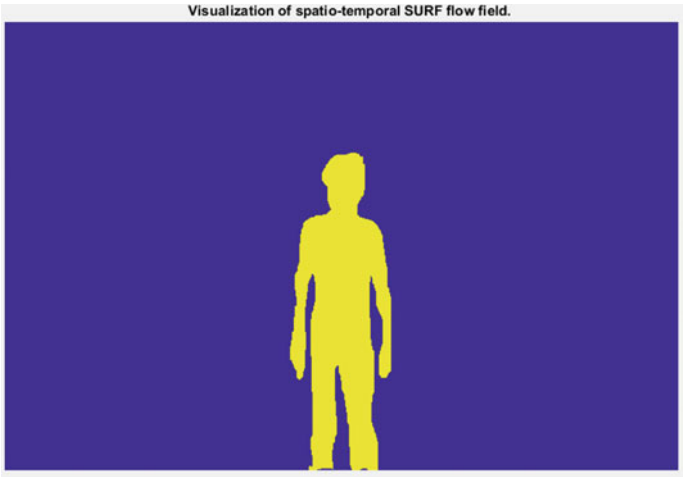

Fig. 6 Spatio temporal visualization through SURF flow field

The above Fig. 8 shows the video object co-segmentation result. In this result finally get the inter and intra evidences can be calculated to get optimal solution and thus final segmentation result.

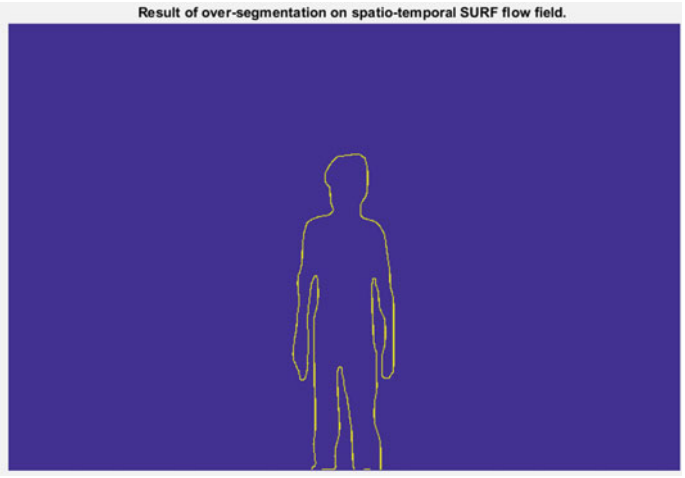

Fig. 7 Over segmentation result of spatio temporal SURF flow field

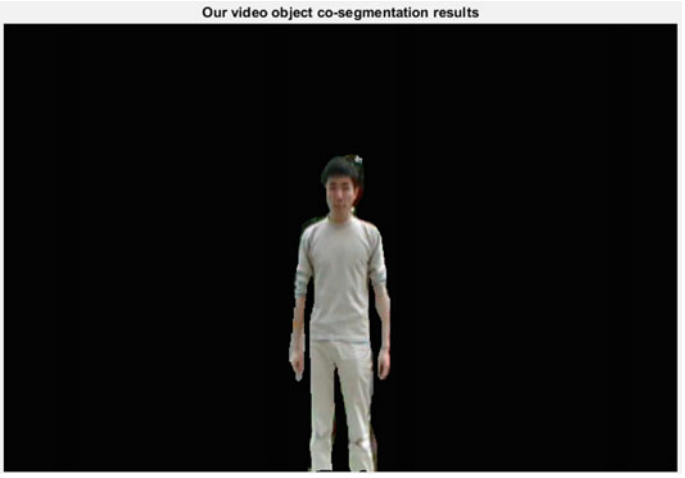

Fig. 8 Our video object co-segmentation result

4.2 Case 2: Vehicle

The below simulation results follows above process (Figs. 9, 10, 11, 12, 13, 14).

Fig. 9 Input video frame

Fig. 10 Input video for objects with large variations

Fig. 11 Joint information lacks between the video

Fig. 12 Visualization of spatio temporal SURF flow field

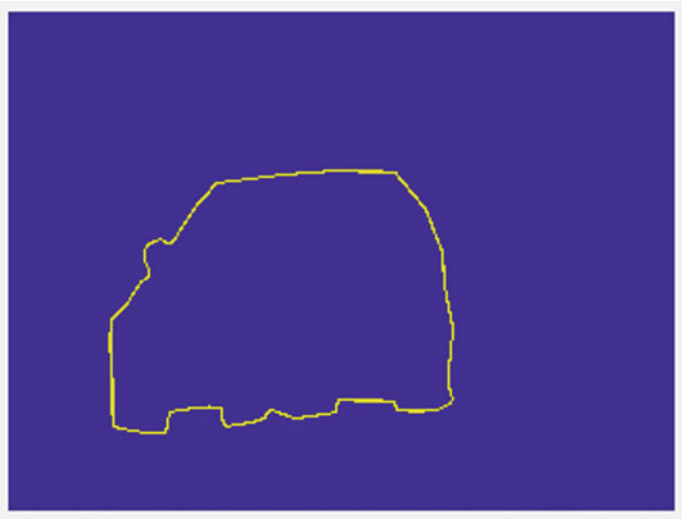

Fig. 13 Over segmentation result of spatio temporal SURF flow field

Fig. 14 Video object co-segmentation result

Table 1 The performance of (1) MAE and (2) Elapsed time

Parameter	Human	Vehicle
MAE (Mean Absolute Error)	0.0179	0.0125
Elapsed time (s)	9.622	5.7974

5 Conclusion and Future Work

A robust method for video co-segmentation is proposed in this research which unveils the common object for a complete video. Moreover, it establishes the problem of video co-segmentation as a process of object optimization; it distills the approximation/estimation for object segmentation and object refinement. The experimental results in quantitative and qualitative terms are depicted, it elaborates that proposed algorithm establishes improved reliable and accurate performance of video co-segmentation as compared to the state-of-the-art algorithms. As the temporal smoothness breaks suddenly for-instance as any object is occluded, the proposed method results may get significantly deteriorated. So, in future we implement One-Shot Video Object Segmentation by disregarding temporal Semantic based on a fully-convolution neural network architecture which is capable of successively transferring generic semantic information accomplished through Image Net for the foreground segmentation task, hence concluding to the learning of the appearance of a single annotated object of the test sequence (Table 1).

References

1. Rother C, Minka TP, Blake A, Kolmogorov V (2006) Co-segmentation of image pairs by histogram matching—incorporating a global constraint into mrfs. CVPR 1:993–1000
2. Mukherjee L, Singh V, Dyer CR (2009) Half-integrality based algorithms for co-segmentation of images. In: CVPR, pp 2028–2035
3. Hochbaum DS, Singh V (2009) An efficient algorithm for co-segmentation. In: ICCV, pp 269–276
4. Li H, Ngan KN (2011) A co-saliency model of image pairs. IEEE Trans Image Process 20(12):3365–3375
5. Rubio JC, Serrat J, López A (2012) Video co-segmentation. In: Proceedings of ACCV, pp 13–24
6. Chen D-J, Chen H-T, Chang L-W (2012) Video object co-segmentation. In: Proceedings of ACM Multimedia, pp 805–808
7. Chiu W-C, Fritz M (2013) Multi-class video co-segmentation with a generative multi-video model. In: Proceedings of IEEE CVPR, pp 321–328

A Low Cost Beam Steering Linear Array Antenna for Small Cell 5G Mobile Networks

Karur Mohammed Saifuddin and D. Sreekanth Reddy

Abstract 5G with Millimeter Wave! The most foreseen future innovation normal in the following decade for remote correspondences. Interest for high information rates and extensive data transfer capacities and limit took an understanding concentration at millimeter wave frequencies. Anyway still a few difficulties should be routed to take live of this proposed framework. One of such test is plan of high gain and mandate reception apparatus with pillar controlling abilities, In this paper we show composed, recreated and manufactured fix receiving wire and straight radio wire cluster for V-band. The fix reception apparatus and its straight cluster configuration is displayed and reenacted in matlab and the outcomes demonstrated that the accomplished gain is around 10 dBi with great directivity, and bar guiding of ±250 which can be proper model for 5G little cell correspondences. The created display likewise demonstrated palatable coordinating outcomes with the demonstrated and reenacted outline.

Keywords Beam steering · Matlab · Photolithographic · Vector network analyzer (VNA) · Coplanar wave guide feed (CPW) · Cascade microtech system

1 Introduction

Millimeter-wave (mmW) technology for V-band (57–66 GHz) has become exhilarating opportunities for circuit, antenna, and communication system engineers in next future technology. Crucially, recent improvements in incorporation of antenna and antenna arrays directly on-chip CMOS or in-packing have made the millimeter a low-cost possible technology for the future cellular communications [1]. The latest ITU report statistics showed that the global proportion of people using the internet services have rose to 38.1% of the global population in 2013, up from 23.2% as in

K. M. Saifuddin · D. S. Reddy (✉)
Department of Electronics and Communication Engineering, Srinivasa Ramanujan Institute of Technology, Anantapur, India
e-mail: sreekanth.reddy.d88@gmail.com

K. M. Saifuddin
e-mail: Saifu426@gmail.com

© Springer Nature Singapore Pte Ltd. 2020

T. Hitendra Sarma et al. (eds.), *Emerging Trends in Electrical, Communications, and Information Technologies*, Lecture Notes in Electrical Engineering 569,
https://doi.org/10.1007/978-981-13-8942-9_54

2008 [2]. With the advent of new technology and features like multimedia applications and high quality video streaming have lead the service providers into saturation state with the current frequencies spectrum from 700 MHz and 2.6 GHz Globally [3].

To compensate the highlighted issues Millimeter-Wave (mmW) technology could be a promising future which is an unlicensed spectrum with huge available bandwidths in the order of 6–13 GHz. As the wavelength at these frequencies goes in millimeter by which they confront genuine constriction in their RSSI as for separate and because of barometrical ingestion and rain lessening factors. Insights demonstrate that the rain lessening is 9 dB/km with a precipitation of 25 mm/h (around 1 inch for every hour) and appearances a barometrical retention of 20 dB [4]. Future remote advances must be approved in the most populated urban situations. With a specific end goal to improve limit and administration quality, the cell arrange design requires to help tremendous spatial reuse. Enormous MIMO base stations (with hundreds or even a great many reception apparatus) and little cell AP are two promising methodologies for future cell. Huge MIMO base utilization stations acknowledged with radio wire exhibits at existing large scale base stations, which can precisely think transmitted vitality to the portable clients situated in such little cells [5]. The fix reception apparatus has been a fitting decision for straight radio wire exhibit outline in view of its low weight, low profile and lower transmission misfortune and to accomplish higher directivity at high frequencies. A Patch receiving wire is outlined and demonstrated in matlab and mimicked results demonstrated a gain around 10 dBi. Promote for improving the directivity and proficiency of the reception apparatus a straight Patch cluster receiving wire has displayed with the outlined fix radio wire as a component. The demonstrated framework is additionally created utilizing microstrip technology which is easy to integrate on printed circuit boards. For the fabrication of antenna and antenna array laser machine LPKF and photolithographic process is used.

2 Antenna Design and Modelling

The reception apparatus includes a rectangular fix mounted over RT/duroid 5880 dielectric board with a dielectric consistent of 2.33 and a misfortune digression of 0.0009. This printed circuit board (PCB) material has a few points of interest, for example, low dielectric resilience and misfortune, to accomplish higher data transmission it is a superior decision for high recurrence activity. The width (W) and length (L) of the radio wire can be acknowledged by the beneath conditions [6].

$$w = \frac{c}{2f_o\sqrt{\frac{\varepsilon_r+1}{2}}}$$

$$L = \frac{c}{2f_o\sqrt{\varepsilon_{eff}}} - 2\Delta L$$

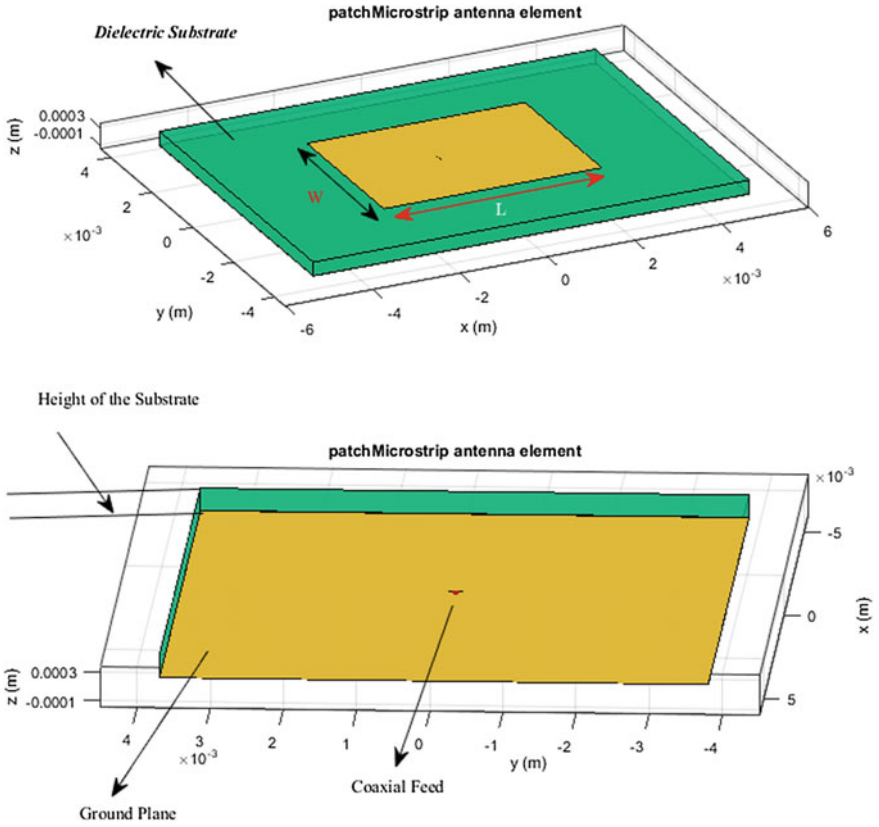

Fig. 1 Patch antenna element top and bottom 3D view

In view of above conditions the rectangular fix radio wire has a measurement of width (W) 0.40 and length (L) 0.38 and set at a separation of h mm (substrate thickness) far starting from the earliest stage as appeared in Fig. 1. The 3D Radiation example of the outlined radio wire is appeared in Fig. 2. What's more, gain is seen as 10 dBi. The info impedance of the reception apparatus is appeared in Fig. 3. Whose resounding recurrence is accomplished at 61.2 GHz? Because of low weakening, scattering and simple creation process coplanar waveguide feed is decided for energizing the receiving wire.

3 Linear Patch Antenna Array Design

Staged cluster tool kit has been utilized in outlining direct exhibit of size 4 × 1 with every component as fix receiving wire which is composed before. Same as fix reception apparatus, cluster is likewise required to resound at 60 GHz. The sepa-

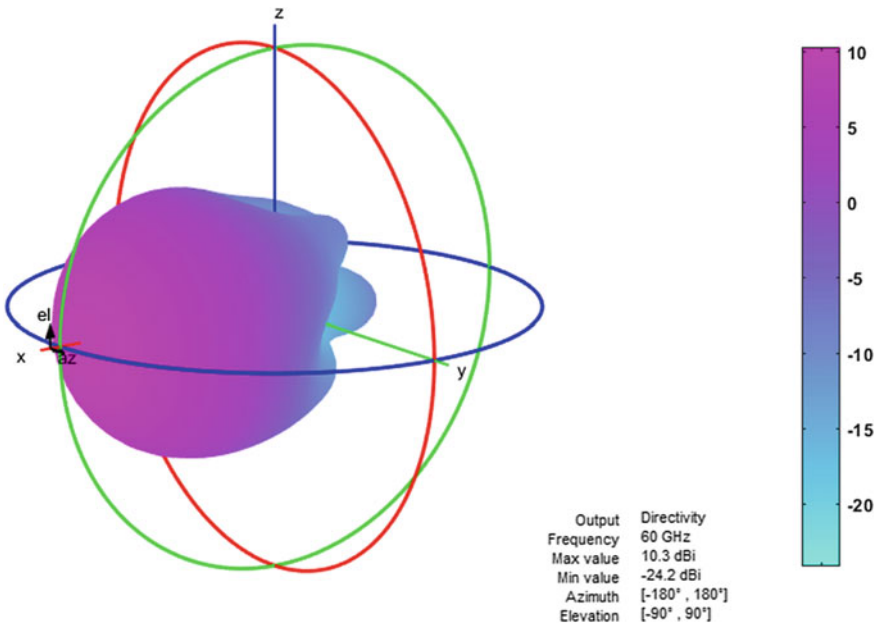

Fig. 2 3D radiation pattern simulation

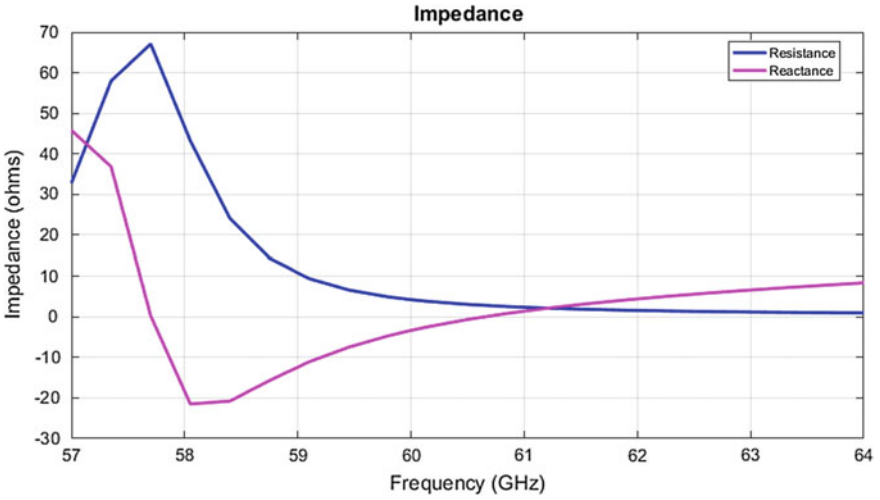

Fig. 3 Input impedance curve and resonance at 61.2 GHz

rate between the exhibit components is an essential thought and it must be chosen precisely with the goal that principle flap of radiation design is accomplished at 60 GHz. The cluster is arrangement encouraged to make recurrence delicate and to gain shaft guiding over the whole band of intrigue. The outline is appeared in Fig. 4. The partition between the components is 0.25 which extends the primary bar course into the broadside exhibit at 60 GHz [7]. Change in recurrence causes the change in electrical length de, which causes an adjustment in period of every component by, making the principle shaft tilt. It has been seen that abatement in recurrence from 60 to 57 GHz has made the fundamental bar move to right course and increment in recurrence from 60 to 63 GHz tilted to left achieving the pillar directing by simply shifting the recurrence.

A beam steering of ±25° was achieved when frequencies are changed in v-band with a step of 1 GHz. The Normalized E Field radiation pattern with beam steering and gain patterns are shown in Fig. 5. The array resonates at 59 GHz and the maximum radiation is at broadside (0°) with a gain of 10 dB as shown in Fig. 6.

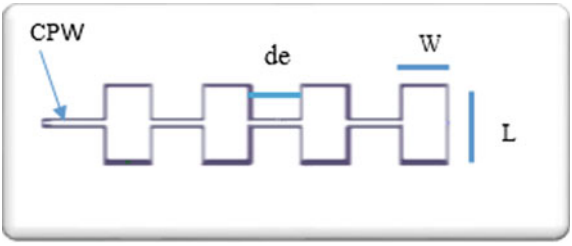

Fig. 4 Linear patch array design

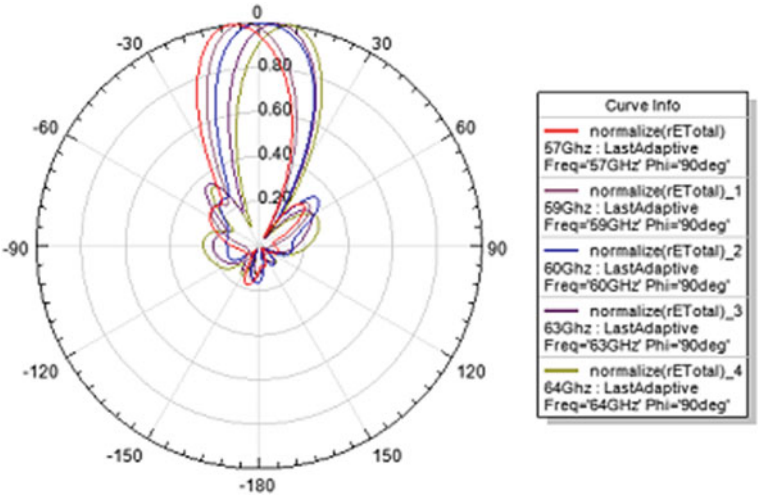

Fig. 5 Normalized E-field radiation pattern with beam steering

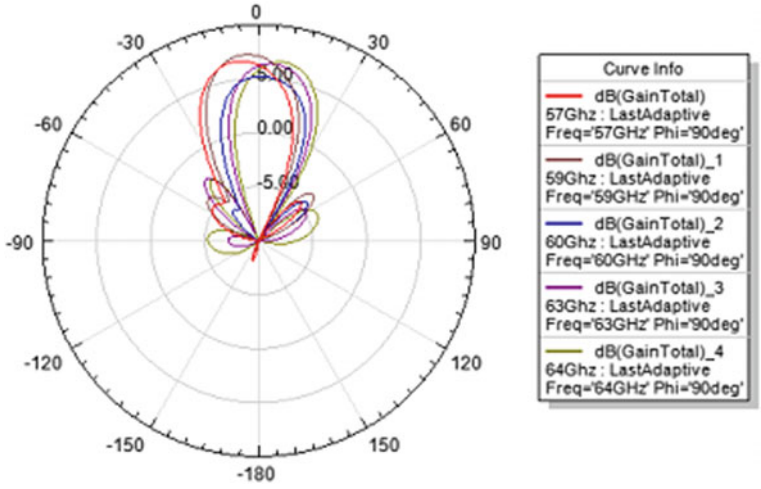

Fig. 6 Gain pattern

4 Fabrication of Patch Antenna and Linear Array

The equipment's used for the fabrication of antenna is LPKF protoMat C100HF. The process of fabrication first involves designing the antenna dimensions and layout using Auto cad. These files are required to work on the LPKF photo-laser software that operates the LPKF machine and allows to print the design on the copper-substrate sample. The Laser machine make the contour lines on the substrate for the areas from where the copper is to be removed. The top view of the fabricated patch antenna, and array is shown in Fig. 7.

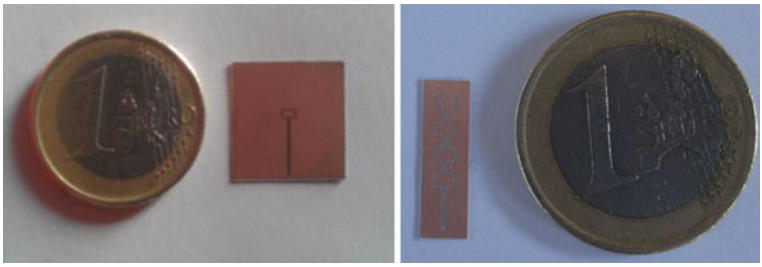

Fig. 7 Fabricated prototypes of patch and linear array antenna

5 Measurement of Radiation Patterns

A block diagram of measurement of E-Field radiation patterns of antenna array at V-band Frequencies configuration is shown in Fig. 8. Cascade Microtech system is used to test the antenna and is fed with the 150 μm pitch GSG probe which is connected to the VNA port 1. To the VNA port 2, an open waveguide WR15 is connected. Both the GSG probe and WR15 are connected using the cables that work up to 67 GHz. The linear x-y stages allow the WR15 to scan antenna in x and y directions. The concept of 2D scan includes keeping first y constant and moving WR15 in x direction in steps and capturing all the E-Field values at these points. Then take a step forward in y-direction and repeat the process. By this way with the help of these stage movements, the 2D E-field calculation of antenna are captured in the VNA as S21 parameter. The obtained S21 values from VNA are imported into Matlab. By the help of Matlab routines, E-Field radiation pattern is obtained. The antenna array prototype is fed over a range of 57–63 GHz, for more clarity and observations.

The absorbers have been used across the probe and around the antenna under test in order to avoid the radiations from the probe and the surrounding elements. The E-Field radiating by the antenna array is been measured in the Near-Field at approximately 40 mm from the antenna aperture. The real time measurement setup is shown in Fig. 9.

The antenna array prototype is fed over a range of 57–63 GHz. The corresponding rectangular E-Field radiation patterns are shown in Fig. 10 at phi 0° and 90°. It can be seen that by increasing the frequency, the main beam shifts along the theta axis from ±25°.

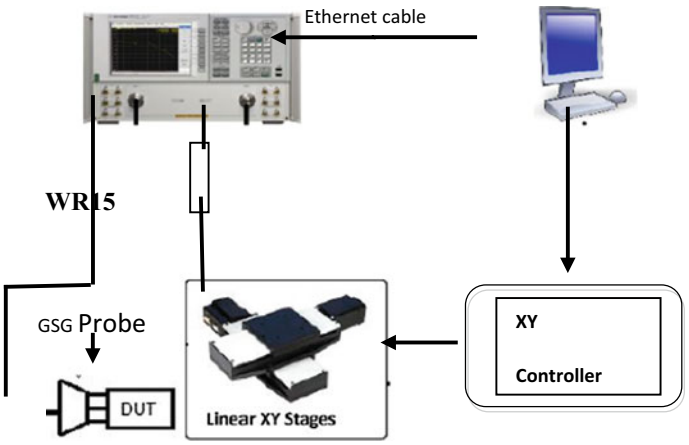

Fig. 8 Test bench setup for measuring the E-field radiation pattern

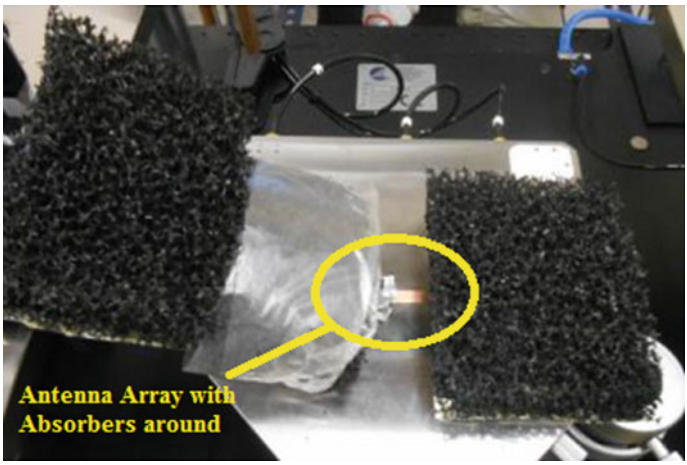

Fig. 9 Absorbers around antenna array to avoid spurious radiations

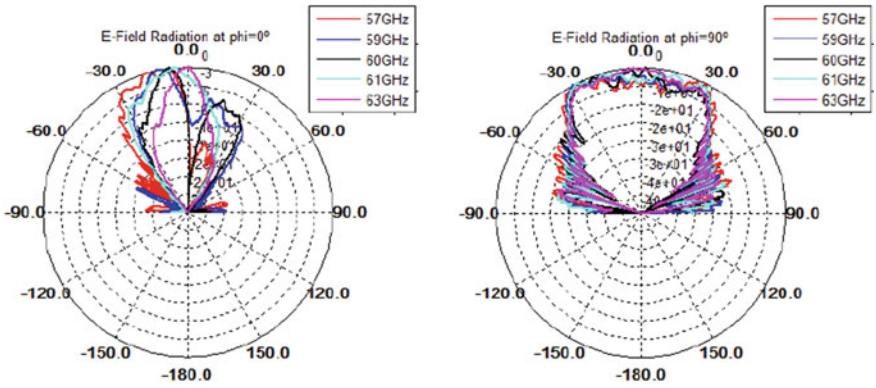

Fig. 10 E-field radiation pattern in polar coordinates phi = 0° and 90°

6 Observations and Results

Table 1 shows comparison of gain, beam steering angle and average side lobe level measures at different frequencies. The simulated resonant frequency is observed at 61 GHz where the achieved gain is also maximum which is 10 dB. The Side lobe level is observed to be lesser in the range of 61–62 GHz. The bandwidth for element patch antenna is observed to be 5 GHz and the antenna array is 6 GHz. This increase in bandwidth was due to different substrates used. The measured values are also very much near with the simulated values. Table 2 shows a brief comparison of the measured and simulated values of beam steering which is observed to be different. The cause for it was the gap of CPW feed for the array, it should be very thin but

Table 1 Parameters comparision

Frequency (GHz)	Gain (dB)	Angle of direction	SSL (dB)
57	8.72	−25°	11
58	8.52	−15°	10
59	9.43	−5°	10.2
60	10.03	0°	8.75
61	**10.05**	**4°**	**9.5**
62	9.32	12°	7.4
63	8.02	23°	8.2
64	7.69	25°	8.2

Table 2 Measured and simulation comparision

Parameter	Measured	Simulated
Resonant frequency (GHz)	59	61.2
Beam steering	−25° to 25°	−25° to 25°
Avg side lobe level (dB)	≈9.4	≈8.1

The above measured values are obtained from the test bench setup used for measuring the e-field radiation pattern and the above simulated values are obtained using matlab

the chemical attack from the manufacturing process caused this gap to increase and reduce the feed line. However, this has been verified by performing the simulation of the array with the wider gap and thinner CPW feed line and the result obtained for beam steering are −25° to 10° as obtained with the measured array.

7 Conclusion

A CPW fed Microstrip patch antenna and series fed antenna array has been designed at mm wave frequencies for Small cell 5G mobile communications [8]. The patch antenna element modelled and fabricated showed a gain of 10 dB with a bandwidth of 5 GHz and a 6 GHz for the antenna array. The linear array modelled and fabricated showed beam steering about ±25° which can be suitable antenna for small cell 5G cellular networks. Further to achieve higher directivity and beam scanning linear array can be used as feed to dielectric lens or concave lens. By varying the position of the lens as a feed with antenna array resulted in a higher beam steering up to 40°. However, incorporation of such antenna with lens might be difficult in real scenarios. Researchers are being carried to overcome this risk. The work presented in this paper serves as a valuable contribution to the antenna designers for the design and deployment of millimeter wave based small cell cellular 5G network and other

applications such as Indoor location technologies which are expected to emerge across very wide variety of consumer devices over the next years.

References

1. Rappaport TS, Sun S, Mayzus R, Zhao H, Azar Y, Wang K, Wong GN, Schulz JNK, Samimi M, Gutierrez F (2013) Millimeter wave mobile
2. International Telecommunication Union (ITU) (2014) Measuring the information society report 2014. ISBN 978-92-61-15291-8
3. Rappaport TS, Murdock JN, Gutierrez F (2011) State of the art in 60-GHz integrated circuits and systems for wireless communications. Proc IEEE 99(8):1390–1436
4. Cai LX, Shen X, Mark JW (2007) Efficient resource management for mm wave WPANs. In: Wireless communications and networking conference, 2007, WCNC 2007. IEEE, pp 3816–3821, 11–15 Mar 2007
5. Gao Z, Dai L, Mi D, Wang Z, Imran MA, Shakir MZ (2015) Mm wave massive-MIMO-based wireless backhaul for the 5G ultra-dense network. In: IEEE wireless communications conference, vol 22, no 5, pp 13–21, Oct 2015
6. Balanis CA (2005) Antenna theory analysis and design. Willey, Prentice-Hall, NJ
7. Hansen RC (1998) Phased array antennas. Wiley, New York
8. Jungnickel V, Manolakis K, Zirwas W, Panzner B, Braun V, Lossow M, Sternad M, Apelfröjd R, Svensson T (2014) The role of small cells, coordinated multipoint, and massive MIMO in 5G. IEEE Commun Mag 52(5):44–51

Robust Adaptive Estimator Using Evolutional Algorithm for Noise Cancellation in Multichannel System

Mandli Rami Reddy, T. Keerthi Priya, K. Prasanth and S. Ravindrakumar

Abstract Noise signals corrupt the information available in a channel. Most of the noise sources are additive. The signals are corrupted by the noises and it loses its quality. This paper presents the detail analysis of the adaptive estimator for noise cancellation in multichannel system using different optimization technique. Different noise cancellation techniques are available in the literature like matched filtering, wavelet transform and statistical analysis. This paper presents the evolutionary methodology approach using Artificial Bee Colony and Particle swarm optimization for the optimization of multichannel adaptive filter l. The investigation of the efficiency of the method was evaluated using a real time ECG data. The noise in the ECG signal is removed using the multichannel adaptive filter using evolutionary optimization technique.

Keywords PSO · ABC · LMS · Adaptive filter · Multichannel · Machine learning · Noise canceller · RLS

1 Introduction

In the modern technology world information became the most valuable asset. The information is transmitted or received from different means. Different means of channels are used to communicate the information. The data varies from field to field. In medical field a channel is corrupted by various noises like Power line interference,

M. R. Reddy (✉) · T. Keerthi Priya · K. Prasanth
ECE Department, Srinivasa Ramanujan Institute of Technology, Anantapur, Andhra Pradesh, India
e-mail: ramireddy.ece@srit.ac.in

T. Keerthi Priya
e-mail: keerthipriya.ece@srit.ac.in

K. Prasanth
e-mail: Prashanthk.ece@srit.ac.in

S. Ravindrakumar
SSCET, Dindigul, Tamil Nadu, India
e-mail: gsravindrakumar7@gmail.com

© Springer Nature Singapore Pte Ltd. 2020

T. Hitendra Sarma et al. (eds.), *Emerging Trends in Electrical, Communications, and Information Technologies*, Lecture Notes in Electrical Engineering 569,
https://doi.org/10.1007/978-981-13-8942-9_55

Electrode contact noise, Motion artifacts, Muscle contraction, Base line drift and Instrumentation noise. In audio signal processing the noises are due to power line interference. Echo and harmonics and in embedded system the noise happens due to offset noises and electronics noises [3]. The noise reduction in the signal determines the level to which the information in the signal can be extracted effectively [1]. The main problem and the major challenge is when the noise signal frequency range correlates with the information frequency. The challenges increase when the number of channels is more. Various methods are adopted in the past to remove the noises using adaptive filters [1]. The methods are focused only on the removal of power line interference. There is an overlap between the signal processing and machine learning. The computer program learn from the data, experience and performance [4]. It improves from the experience. The combinational of the inductive inference algorithm and statistical signal processing forms the basis for the new theory of adaptive filters [11]. These nonlinear phenomenon will be suitable for adaptive filters which will work on the machine learning approach. The statistical signal processing methods like independent component analysis (ICA), principle component analysis (PCA) are complex in implementation. Its very difficult to incorporate the machine learning approaches in statistical signal processing methods like ICA, PCA etc But if these complex systems found new hardware methodology to be implemented then Statistical Signal Processing (SSP) along with Machine Learning (ML) approach will be a platform for building new devices with effectiveness.

2 Background Methodology

For Noise cancellation adaptive filters were used due to its self-learning process. Through iterations the filter coefficients are updated with respect to the noise strength. By adjusting the coefficients adaptively the error is minimized. The adaptive filters are implemented using gradient-based techniques. The Least Mean-Square (LMS), and Recursive Least-Square (RLS) belongs to the gradient based techniques. These LMS and RLS based algorithm plays a vital role in designing digital noise cancellers in various applications like speech processing [8], extraction [12] and speech enhancement [7]. But in literature several other optimization algorithms are presented. The methods are based on the particle swarm optimization, Artificial Bee Colony [6, 9], etc. methods. These optimization techniques were more suitable for adaptive equalization [5]. Zhao et al. [14] used the bee colony algorithm to design the digital filter design. The method was suitable for DSP application. Real parameter optimization was done using the ABC algorithm [2]. The global optimization increases when these optimization is used. The block diagram of ANC filter with ABC is shown in Fig. 1.

For evaluation of the efficiency an ECG signal is taken as example. The data is used from real time database consisting of 5 channels.

The block diagram of the ABC algorithm is shown in Fig. 2. The position of the bee is equavated to the coefficient of the adaptive filter.

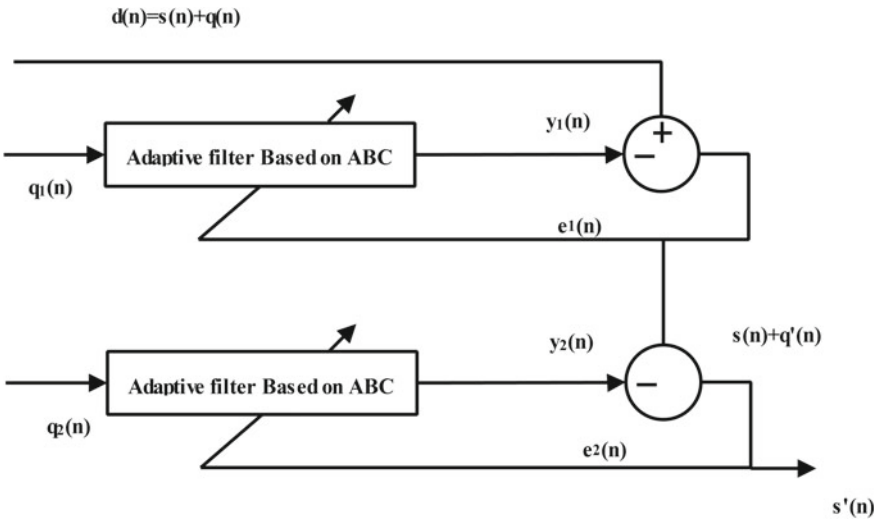

Fig. 1 Adaptive filter using ABC

The initial random population or the filter co-efficients are generated according to equation below

$$x_{ij} = x_{min,j} + \text{rand(a)} * (x_{max,j} - x_{min,j}) \tag{1}$$

'a' takes the value between -1 and $+1$. 'i' is the colony size and j is the dimension value in the colony which represent the filter coefficient of the adaptive filter. The probability of optimized position or coefficient value is determined by the equation

$$p_i = \frac{fit_i}{\sum_{n=1}^{SN} fit_n} \tag{2}$$

Once new location are generated probability selection process is carried out with the fitness value fit and SN choosen index value.

To optimize the coefficient value the ABC algorithm uses a scaling factor (sf) which produces the minimum or zero error function. The best filter coefficient is found using the equation

$$x_{i,j} = \begin{cases} x_{min,j} + \phi_{i,j} * (x_{max,j} - x_{min,j}) & \text{for sf} \\ x_{min,j} & \text{otherwise} \end{cases} \tag{3}$$

The magnitude of perturbation is controlled by the scaling factor.

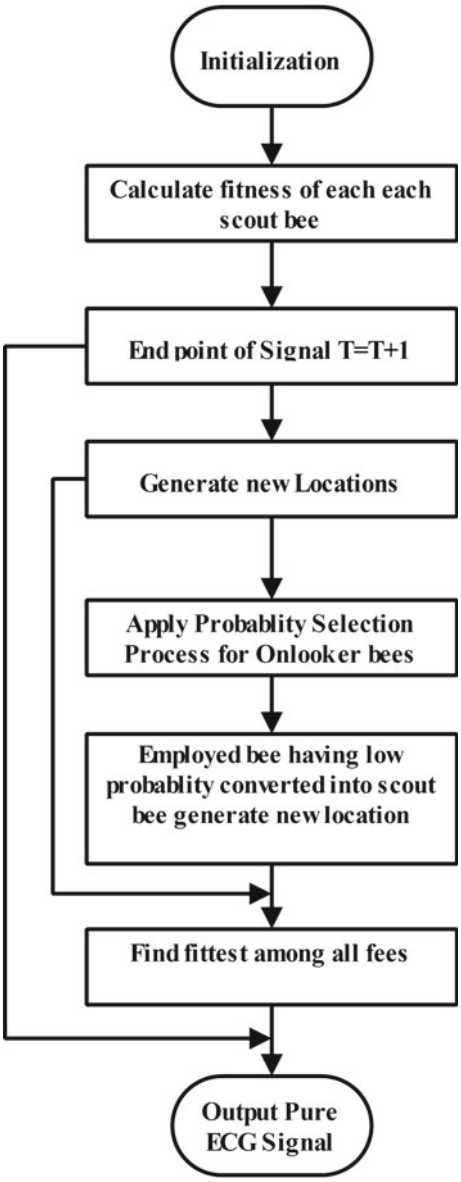

Fig. 2 Block diagram of ABC algorithm for ECG denoising

3 Proposed Methodology

In the proposed methodology the optimization of the adaptive filter updating is extended towards multichannel system using the evolutionary methods. Five channels were chosen for the same. The optimization of the LMS algorithm uses instantaneous estimation of vectors based on sample values of input d(n) and error e(n) using the below equation.

$$\nabla(\mathrm{n}) = -2\mathrm{e}(\mathrm{n})[\mathrm{d}(\mathrm{n})] \tag{4}$$

In conventional methods the filter coefficients are updated along the direction of gradient vector estimate as

$$[\mathrm{h}(\mathrm{n}+1)] = [\mathrm{h}(\mathrm{n})] + \mu\mathrm{e}(\mathrm{n})[\mathrm{d}(\mathrm{n})] \tag{5}$$

The estimation requires the knowledge of data x(n) alone and not the knowledge of cross correlation.

$$\mathrm{e}(\mathrm{n}) = [\mathrm{h}(\mathrm{n})] + \mu\mathrm{e}(\mathrm{n})[\mathrm{d}(\mathrm{n})] \tag{6}$$

In gradient vector estimate for multichannel system can be coined by the equation

$$\mathrm{d}(\mathrm{n}) = \mathrm{q_l}(\mathrm{n})\left[\mathrm{F}(\mathrm{n}) + \mathrm{M}(\mathrm{n}) + \mathrm{q_2}(\mathrm{n})\right] \tag{7}$$

where d is the input and N is the noise representing low and high frequency component. The coefficient of the filter is estimated based on the data input and previous stage output. In our example the input is the noisy ECG signal (d) contains the pure ECG signal and noise ($q(n)$). The high frequency components are the power line noise and low frequency components are muscle noise which are additive and uncorrelated with $s(n)$. Referring Fig. 1, $q_1(n)$ and $q_2(n)$ are high and low frequency noises, respectively, The error signal ($e_1(n)$) is computed as the difference of $d(n)$ and $y_1(n)$, which is fed back to ANC filter in each iteration. The iteration process will continue till $e_1(n)$ or the high frequency noise is minimised in first stage. The output signal containing low frequency noise is given to second stage of ANC filter where the error signal ($e_2(n)$) is computed as the difference of $s(n) + q_1(n)$ and $y_2(n)$. The $e_2(n)$ is fed back to ANC filter in each iteration till $e_2(n)$ is minimised. The final output signal ($s(n)$) is nearly equal to $s(n)$. The error function for $e_1(n)$ and $e_2(n)$ is represented by

$$\text{error} \quad \text{function} = \frac{1}{\mathrm{N}} \sum_{\mathrm{i}=1}^{\mathrm{N}} \left(\mathrm{e_{ij}}(\mathrm{n})\right)^2 \tag{8}$$

where $e_{ij}(n)$ is jth error of ith sample for nth iteration and N is the total number of samples of applied input signal.

For multichannel system the ABC algorithm is framed as

$$x_{cij} = x_{c,min,j} + \text{rand}(a) * (x_{c,max,j} - x_{c,min,j}) \tag{9}$$

where c denotes the multichannel system and the error function is given by

$$\text{error} \quad \text{function}_c = \frac{1}{N}\sum_{i=1}^{N}\left(e_{c,ij}(n)\right)^2 \tag{10}$$

$$\text{error}_{cum} = \frac{1}{c}\sum_{k=1}^{k=c}\frac{1}{N}\sum_{i=1}^{N}\left(e_{k,ij}(n)\right)^2 \tag{11}$$

The cumulative error function is the reduction of error in all channels as a collective optimization. In conventional adaptive filters the optimization is done only after each iteration with one possible solution, but in using ABC algorithm the optimization has n number of solutions with faster convergence rate [13]. The other algorithms like particle swarm optimization to be discussed in next section also provide faster convergence rate and strong global search. The ABC and PSO are easy to implement.

Here in our example as shown in Fig. 3 the number of samples are 3600 with sampling frequency of 360 Hz. Totally 10 epoch were used for testing. The step size μ was 0.1 which in the next example it was kept 0.5. In Fig. 4 the number of samples are 6000 with sampling frequency of 360 Hz. In the Fig. 3 all the channels are affected by nearly equal amount of noises. But in Fig. 4 it can be observed that the channel 3 is affected by more noise than the other channel and the ANC designed is hard to remove the noises. From this investigation it can be observed that if the noise level is very high the ANC using any methods will fail to remove the noise. So in real time most input cables, wires and electrodes are coupled with EMC system to remove the noises at the input end itself. The noise happening in the acquisition is reduced means the rest of the noises are from the processing circuits which the noise can be easily removed.

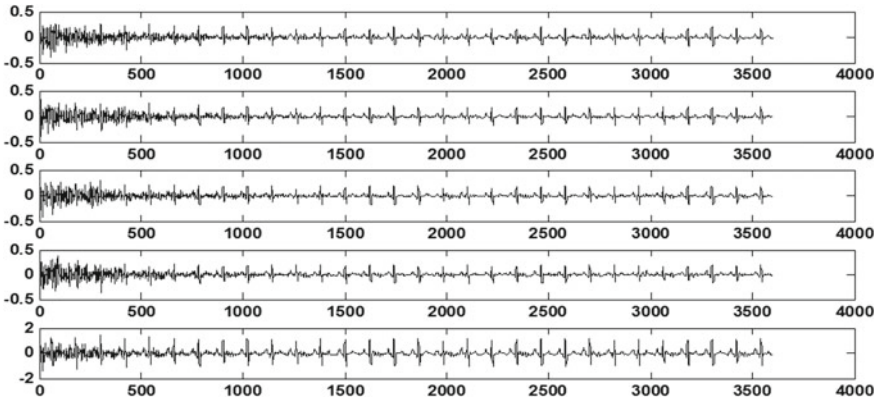

Fig. 3 Output of the LMS algorithm for multichannel system-high SNR

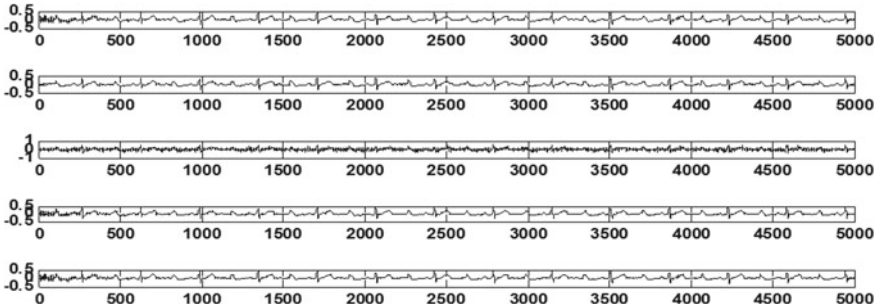

Fig. 4 Output of the LMS algorithm for multichannel system-low SNR

3.1 PSO Algorithm for Multichannel System

The PSO algorithm can be used to solve any nonlinear equations. Here a random swarm is initiated, velocity and position updates are made. The particle fitness is evaluated based on selected fitness function. The position is updated in each training update. Figure 5a shows an example of PSO for adaptive filter used in ECG signal analysis. Figure 5b shows the PSO with inertia weight. The inertia weight parameters provides better efficiency and convergence.

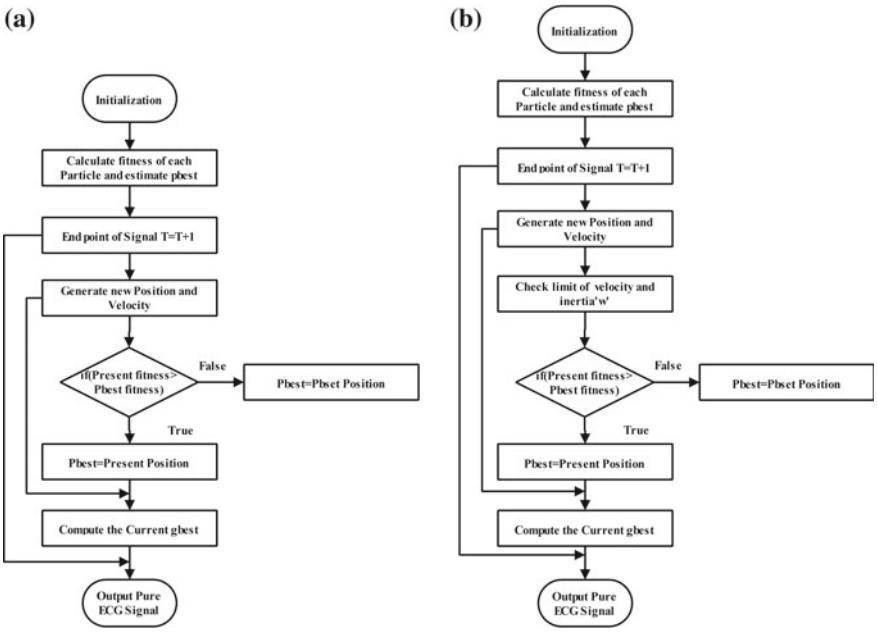

Fig. 5 **a** Shows the PSO for adaptive filter, **b** shows the PSO for adaptive filter and **b** with inertia weight

Table 1 Performance of various methods

Parameters/methods	LMS	NLMS	RLS	ABC	PSO	PSOI
PSNR	78.89	78.82	77.19	79.55	79.52	79.47
MSE	8.3E−04	8.5E−04	1.2E−03	1.8E−04	1.40E−04	1.20E−04
MAXERR	0.232	0.297	0.395	0.262	0.252	0.243
L2RAT	1.364	1.356	1.203	1.311	1.307	1.280

In this method, for the best possible positions with least swarm is optimized.

$$p(n+1) = W(n) + \mu(n) \cdot O(error_c(n), d(n), \phi(n)) \tag{12}$$

Similar to the ABC algorithm the PSO algorithm is applied to the real time data (Physionet.org) and the results are obtained. The ABC and PSO methods are compared with the conventional LMS, NLMS and RLS algorithm. The results are obtained using MATLAB (Table 1).

The MSE can be described as the mean of the square of the differences between the de-noised ECG signal and the original fetal ECG signal.

$$MSE = \frac{\sum_{I=1}^{N} (s - s_e)i^2}{n} \tag{13}$$

where 'n' denotes the length of the signal in this work n = 6000, 's' represents the original signal and se is the estimated signal. Lower the values of MSE of the signal, higher the accuracy and efficiency of the output. The PSNR is defined as the ratio between the maximum signal power and the noise power.

$$PSNR = \frac{10 \log_{10} n}{MSE} \tag{14}$$

Higher the values of PSNR of the extracted signal, higher the accuracy and efficiency of the output. This is the evaluation strategy used throughout the work. The maximum absolute error (MAXERR) and the energy ratio between original signal and approximation/extracted value are measured.

4 Conclusion and Future Work

The removal of noises using evolutionary algorithm is addressed in this paper. The adaptive estimator using methods like ABC and PSO are investigated and implemented. The adaptive estimation was extended to the multichannel signal inputs. The evolutionary methodology approach using Artificial Bee Colony and Particle swarm optimization for the optimization of multichannel adaptive was reported. The

investigation of the efficiency of the method was evaluated and found that the method has high PSNR and lowest mean square error. The methods are compared with the conventional LMS, RLS and NLMS algorithm using a real time ECG data. The proposed method gives nearly a 2% increase in SNR when compared to the existing methods. The mean square value obtained is nearly one order times better when compared to existing methods. The noise in the ECG signal is removed using the multichannel adaptive filter using evolutionary optimization technique. In future the methods will be implemented in hardware. This will enable into the creation of new portable devices.

References

1. Abbas HH (2011) Removing 0.5 Hz baseline wander from ECG signal using multistage adaptive filter. Eng Technol J 29(11):2312–2328
2. Akay B, Karaboga D (2012) A modified artificial bee colony algorithm for real-parameter optimization. Inf Sci 192(1):120–142
3. Althahab AQJ (2017) A new robust adaptive algorithm based adaptive filtering for noise cancellation. Analog Integr Circuits Signal Process 94(2):217–231
4. Berrar DP, Dubitzky W, Granzow M (eds) (2003) A practical approach to microarray data analysis. Springer, New York
5. Cheded L, Zidouri A, Al-Awami AT, Zerguine A, Saif W (2011) A new modified particle swarm optimization algorithm for adaptive equalization. Digit Signal Proc 21(2):195–207
6. Gao W, Liu S, Huang L (2013) A novel artificial bee colony algorithm based on modified search equation and orthogonal learning. IEEE Trans Cybern 43(3):1011–1024
7. Goswami S, Bardoloi B, Deka P, Dutta D, Sarma D (2014) A novel approach for design of a speech enhancement system using auto-trained NLMS adaptive filter. Int J Inf Commun Technol 6(3):326–338
8. Greenberg JE (1998) Modified LMS algorithms for speech processing with an adaptive noise canceller. IEEE Trans Speech Audio Process 6(4):338–351
9. Karaboga D (2010) Artificial bee colony algorithm. Springer Biomed Eng Lett 5(3):69–75
10. Krusienski DJ, Jenkins WK (2003) Adaptive filtering via particle swarm optimization. In: Conference on signals, systems and computers, vol 1, pp 571–575
11. Martens SMM, Mischi M (2006) An improved adaptive power line interference canceller for electrocardiography. IEEE Trans Biomed Eng 53(11):2220–2231
12. Ravindrakumar S, Bommanna Raja K (2016) A multi-stage adaptive singular value decomposition approach for fetal ECG signal extraction in multichannel input system for prenatal health monitoring. Asian J Inf Technol 15(6):1049–1055
13. Monteiro RP, Lima GA, Oliveira JPG, Cunha DSC, Bastos-Filho CJA (2017) Accelerating the convergence of adaptive filters for active noise control using particle swarm optimization. In: Proceedings of Latin American conference on computational intelligence (LA-CCI), Peru, 8–10 Nov 2017
14. Zhao Z, Yin D, Jiang Y (2013) Improved bee colony algorithm based on knowledge strategy for digital filter design. Int J Comput Appl Technol 47(2):241–248

Performance Analysis of QFSRD, GAMAN and E-GAMAN for MANET

M. L. Ravi Chandra, B. Varun Kumar and A. Siva Sankar

Abstract Mobile Adhoc network (MANET) is a distributed infrastructure-less network of mobile nodes where there are no preinstalled routers to route the data. Routing is achieved by the network mobile nodes which automatically configure themselves flexibly to operate as a host or as a router for routing. The level of cooperation achieved among the nodes in any particular region to get routes for data transfer defines the network communication. The routing protocols of several different types have been developed for finding the best fit paths and for satisfying the requirements of QoS. The objectives of QoS routing are, selecting of the best path specific to the communication requirements with efficient network state information (Zhang et al. in Wirel Commun Mob Comput 2008:10 pp, 2018 [8]), and maximum network utilization by the users. Orthogenesis based Genetic algorithm is devised towards QoS fitness scope aware route discovery for MANETs called as QFSRD. The QFSRD is proposed in the aim of achieving QoS under multi objectives. This paper devised under QFSRD is a GA based approach that concludes the set of best fit energy efficient multi objective QoS routes for mobile ad hoc routing. This paper analyze the performance of QFSRD, GAMAN and E-GAMAN. Performance is analyzed for metrics throughput, Packet delivery ratio and energy consumption. Results shows that the performance of proposed algorithm QFSRD is best compare to GAMAN and E-GAMAN.

Keywords MANET · QoS · Throughput · Packet delivery ratio

1 Introduction

The main purpose of QoS routing protocol is finding paths which require minimal resources in terms of QoS metrics specified. The optimal path discovery and selection based on two or more different metrics and involving multiple constraints is a highly challenging problem [1]. The maintenance of network state information at the nodes

M. L. Ravi Chandra (✉) · B. Varun Kumar · A. Siva Sankar
ECE Department, Srinivasa Ramanujan Institute of Technology, Anantapur, Andhra Pradesh, India
e-mail: mlravigates@gmail.com

© Springer Nature Singapore Pte Ltd. 2020

T. Hitendra Sarma et al. (eds.), *Emerging Trends in Electrical, Communications, and Information Technologies*, Lecture Notes in Electrical Engineering 569,
https://doi.org/10.1007/978-981-13-8942-9_56

defines the QoS routing performance. The regular updating of the network state information requires update messages of the link state to be sent over the network causing the constrained resources of bandwidth and battery power available at the node to be exhausted. The topology information is also rendered inaccurate with network changes impacting the topology dynamically or erratically. The feasible paths of QoS if broken affect the QoS levels unless the QoS routing protocol responds rapidly for re-computation of the path or devise an alternate path. Compared to wire networks where path disruptions occur only rarely, in MANET the challenges of frequent path breaks due to mobile nodes reduce the QoS based routing protocols performance.

The challenges faced in a QoS based routing for MANETS are discussed below. The dynamic topology and unreliable wireless medium require frequent updates which increase the overhead.

1.1 Decentralized Control

The network has no centralized control over the members joining or leaving the network which otherwise involves QoS parameters distribution properly with higher complexity and expenses. The network after change in the members automatically configures and deploys itself.

1.2 Unpredictable Channel

The undependable channels [2] are major problem because of high bit error rate as a result of higher interferences, thermal noise, multipath fading effects, and many more causing very less packet delivery ratio and security issues of data leakage.

1.3 Data Loss

The lost packets between sender and receiver because of the distortion result in data loss.

1.4 Route Maintenance

The route maintenance at low expenses and without delay involves efficient provisioning of the network state information to all the network nodes which makes it

difficult because of the dynamic and erratic behavior of the network (even while data is being transferred existing paths could be broken).

1.5 Node Mobility

The nodes are frequently mobile and the final destination receiving the routed data requires periodic updates of network state information. The data transferred in the routing process for reaching the destination successfully, requires regularly updating the network state information with the change of state due to the mobile nodes uncontrolled and random movement in different directions and at varied speeds which results in reduced loss in packet delivery ratio [3].

1.6 Low Power

The mobile nodes in comparison to the wired network nodes have low power availability. Mobile nodes providing QoS consume more power due to several factors and sometimes even power of other nodes.

1.7 Adequate Security

The security problems are more in wireless mobile networks and affect QoS. The malicious and illegal access and usage of the network makes security a QoS attribute and necessitates ad-hoc networks based on security-aware routing algorithms.

1.8 Channel Contention

A MANET's communication between the nodes is usually by a common channel and the provisioning of network topology information causes interference and channel contention problems. In peer-to-peer data network there are many methods to handle these problems. A solution is to use TDMA-based system with global clock synchronization, where each node at a predefined time would transmit the data, which has problems of nodes lacking centralized control. Another solution is to use different frequency band. The solution of spreading code involves for every transmitter similar to that used by a CDMA, if used for MANETs needs a mechanism for distributed channel selection and channel information dissemination [4] in the routing.

2 Associated Work

In this section a review of the routing techniques based on QoS in MANETs are given as follows.

Barolli et al. [5] devised a novel local search optimization strategy, which is an extension to their earlier work GAMAN [6] that referred as E-GAMAN. The devised search space reduction algorithm (SSRA) is mainly aimed to minimize the crossover complexity observed in GAMAN. So that the local search become much faster, hence the time taken for optimal route selection will be low and the GAMAN can find a feasible wireless path very fast. But the issue of considering the impact of QoS factors other than mobility remains same and the evolutions count is still not in control for networks with nodes having QoS metric values distribution with high skewness.

Yahiaoui et al. [7] proposed and An energy efficient and QoS aware routing protocol for wireless sensor and actuator networks. The proposed algorithm mainly considered only two parameters i.e. delay and energy consumption. This proposed algorithm may not work for many QoS parameters.

Zhang et al. [8] proposed A genetic algorithm (GA) based QoS perception routing protocol (GABR) is proposed to guarantee the quality of service (QoS) influenced by broken links between vehicles. This GABR algorithm is efficient in terms of packet delivery ratio and transmission delay metrics. This GABR may not efficient for many QoS parameter.

3 Exploration of Orthogenesis Genetic Evolution for QoS Fitness Scope Aware Route Selection

Orthogenesis Evolution based genetic algorithm for QoS fitness scope aware route discovery strategy [9], constructs new generations by progressive evaluations. QFSRD algorithm generates child elements, which are more fitness than parent elements. Other contribution for QFSRD is fitness assessment, which evaluates the many QoS metrics with equal fitness scope.

After calculation of Orthogenesis evaluations [9], QoS fitness scope is calculated by using the following relations.

$$\mu_{O(r_i)} = \frac{\sum_{k=1}^{|O(r_i)|} [om_k(r_i) \forall om_k(r_i) \in O(r_i)]}{|O(r_i)|}$$

$$qfs(r_i) = 1 - \left[\frac{\sqrt{\left(\sum_{k=1}^{|O(r_i)|} \left(\mu_{O(r_i)} - [m_k(r_i) \forall m_k(r_i) \in O(r_i)] \right) \right)^2}}{|O(r_i)|} \right]^{-1}$$

Above equation represents the fitness scope of all routes. These routes will be ordered based on prime QoS metric. To evaluate the fitness scope, kurtosis parameter

is calculated with the following relations.

$$\mu(QFS) = \frac{\sum_{i=1}^{|R|} qfs(r_i)}{|R|} \text{ calculates mean of all routes}$$

$$\sigma_{QFS} = \sqrt{\frac{\sum_{i=1}^{|R|} (qfs(r_i) - \mu(QFS))^2}{|R|}} \text{// calculates the standard deviation}$$

$$m4 = \frac{\sum_{i=1}^{|R|} (qfs(r_i) - \mu(QFS))^4}{|R|} \text{// calculates 4th movement of qfs distribution.}$$

Kurtosis can be mesokurtic, leptokurtic or platokurtic. If the kurtosis is platokurtic then algorithm will stop the iterations. QoS Fitness Scope Route discovery (QFSRD) algorithm [9] results 'n' number of similar fitness routes. These routes are simulated and compared with existing GAMAN [6] and E-GAMAN [5]. Performance of these algorithms is analyzed with packet delivery ratio, throughput and energy consumption metrics are considered.

4 Empirical Analysis and Results Exploration

Experiment results were conducted in network simulator-2 to visualize and TCL to control. The network environment built on the simulation is considering the randomized node placement with random waypoint mobility. Number of nodes are varied from 50 to 250.

After finding the 'n' number of resultant best routes by using proposed algorithm QFSRD, that paths are simulated and results are compared with GAMAN and E-GAMAN. To analyze the performance of algorithm QFSRD, Packet delivery ratio, Throughput and Energy consumption metrics are used. Simulation results are shown below.

Figure 1 shows the throughput of GAMAN, E-GAMAN and QFSRD protocols for different pause times during the simulation time scenario. From above figure, we can conclude that the throughput of proposed algorithm QFSRD is 4% higher than E-GAMAN.

Figure 2 shows the Packet delivery ratio of GAMAN, E-GAMAN and QFSRD protocols for different pause times during the simulation time scenario. From above the figure, we can conclude that the packet delivery ratio of proposed algorithm QFSRD is 4% higher than E-GAMAN.

Figure 3 shows the Energy consumption of GAMAN, E-GAMAN and QFSRD protocols for different pause times during the simulation time scenario. From the above figure, we can conclude that the Energy consumption of proposed algorithm QFSRD is 16% less than E-GAMAN.

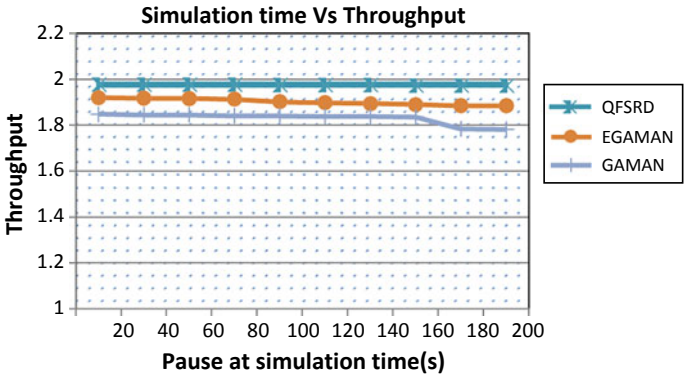

Fig. 1 Simulation time versus throughput

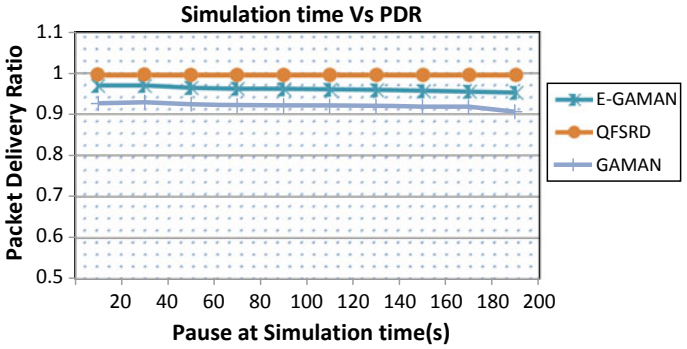

Fig. 2 Simulation time versus packet delivery ratio

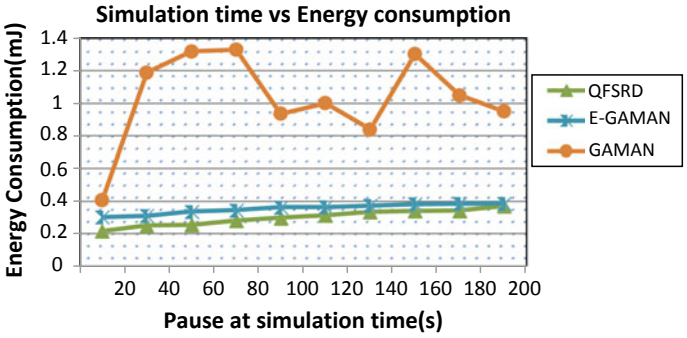

Fig. 3 Simulation time versus energy consumption

5 Conclusion

This paper proposed orthogenesis based genetic algorithm to find QoS fitness scope discovery for mobile adhoc networks. Proposed algorithm QFSRD [9] finds the 'n' number of qos aware routes. To analyze the performance of Proposed algorithm QFSRD is compared with GAMAN [6] and E-GAMAN [5]. While analyzing the performance, packet delivery ratio, Throughput and Energy consumption metrics are considered. The experimental results shows that, the proposed algorithm QFSRD has given optimal results. Proposed algorithm QFSRD throughput is 4% high, packet delivery ratio is 4% high and energy consumption is 16% less compare to E-GAMAN. This work can be further extended by applying the hybrid soft-computing strategies for QoS aware route discovery.

References

1. Wang Z, Crowcroft J (1996) Quality of service routing for supporting multimedia applications. IEEE JSAC
2. Zhang Z, Sanchez C, Salkwicz W, Crawley E (1997) Quality of service extensions to OSPF or quality of service path first routing (QOSPF). IETF, Internet Draft, Sept 1997
3. Luo Y, Wang J, Chen J et al (2006) Algorithm based on mobility prediction and probability for energy efficient multicasting in ad-hoc networks. Comput Res Dev 43(2):231–237
4. Oliveira M, Brito J, Melo B, Quadros G, Monteiro E (2000) Quality of service routing in the differentiated services framework. In: Proceedings of SPIE's international symposium on voice, video, and data communications (Internet III: Quality of Service and Future Directions), Boston, Massachusetts, USA, 5–8 Nov 2000
5. Barolli L, Ikeda M, De Marco G, Durresi A, Koyama A, Iwashige J (2007) A search space reduction algorithm for improving the performance of a GA-based QoS routing method in ad-hoc networks. Int J Distrib Sensor Netw. Taylor & Francis Group, LLC. ISSN 1550-1329 print/1550-1477 (online 3:41–57)
6. Barolli L, Koyama A, Shiratori N (2003) A QoS routing method for ad-hoc networks based on genetic algorithm. In: Proceedings of 14th international workshop database and expert systems applications, pp 175–179, Sept 2003
7. Yahiaoui S, Omar M, Bouabdallah A, Natalizio E, Challal Y (2018) An energy efficient and QoS aware routing protocol for wireless sensor and actuator networks. Int J Electron Commun 83:193–203
8. Zhang G, Wu M, Duan W, Huang X (2018) Genetic algorithm based QoS perception routing protocol for VANETs. Wirel Commun Mob Comput 2018:10 pp. Article ID 3897857
9. Ravi Chandra ML, Chandra Sekhar Reddy P (2015) QFSRD: orthogenesis evolution based genetic algorithm for QoS fitness scope aware route discovery in ad hoc networks. 15(3). Version 1.0. ISSN 0975-4172
10. Zaballos A, Vernet D, Selga JM (2013) A genetic QoS-aware routing protocol for the smart electricity networks. 2013:12 pp. Article ID 135056
11. Chen S, Nahrstedt K (1999) Distributed quality-OS-service routing in ad hoc networks. IEEE JSAC 17(8):1–18
12. Sivakumar R, Sinha P, Bharghavan V (1999) CEDAR: a core-extraction distributed ad hoc routing algorithm. IEEE J Sel Areas Commun 17:1454–1465

13. Chen L, Heinzelman WB (2005) QoS-aware routing based on bandwidth estimation for mobile ad hoc networks. IEEE J Sel Areas Commun 23(3):561–572
14. http://www.tc3.edu/instruct/sbrown/stat/shape.html

A Conceal Fragment Visible Image Broadcast Through Montage Images with Revocable Colour Alterations

D. Maruthi Kumar, L. Guru kumar and K. Kannaiah

Abstract Information security is increasing progressively essential in the advanced world. Protected Image Broadcast has a capability of being received for mass correspondence. A few stenographic systems for transmitting data without bringing doubt are found up in [1–5]. Anyway another protected photograph Broadcast procedure is proposed, known as anonymous part unmistakable montage photograph which enables the client to safely transmit a photograph under the front of another photograph of same size, This paper exhibits a methodology called Reversible data hiding with LSB technique where montage photograph age has done by isolating the anonymous photograph into pieces and changing their separate shading attributes into relating squares of the objective photograph. Use of the Pixel shading changes yields the lossless recouped photograph in view of the untransformed shading space esteems. Age of the key assumes an essential job to regain the anonymous photograph from the montage photograph in lossless way. At last a similar methodology can be performed on recordings likewise which wipes out the flashing ancient rarity to accomplish the lossless information recuperation in movement related recordings. The exploratory outcomes demonstrate great powerful conduct against all coincidental and unintentional assaults and contrast with the regular calculations.

Keywords Steganography · Data hiding · Image encryption · Undisclosed fragment montage image · Reversible contrast mapping

D. Maruthi Kumar (✉)
Srinivasa Ramanujan Institute of Technology, Ananthapuramu, Andhra Pradesh, India
e-mail: maruthikumar2015@gmail.com

L. Guru kumar · K. Kannaiah
N.B.K.R. Institute of Science & Technology, Nellore, Andhra Pradesh, India
e-mail: gurukumar@nbkrist.org

K. Kannaiah
e-mail: kannaiah.kanna9@gmail.com

© Springer Nature Singapore Pte Ltd. 2020

T. Hitendra Sarma et al. (eds.), *Emerging Trends in Electrical, Communications, and Information Technologies*, Lecture Notes in Electrical Engineering 569,
https://doi.org/10.1007/978-981-13-8942-9_57

1 Introduction

At present, photos procured from various sources are sometimes are utilized and passed on through the web for real applications, for instance, online individual photograph accumulations, undisclosed scheme records, report storing bases, remedial imaging settings, and military photo databases. These photos usually contain private or mystery information so they should be protected from spillages in the midst of communicates and numerous techniques have been utilized for anchoring photograph broadcast. The two uncomplicated practices are photograph encryption and information covering up. Photograph encryption is a procedure that uses the common property of a photograph, similar to high repetition and solid spatial connection.

The programmed photograph is a clamor photograph so none can get the anonymous photograph from it except one should has the right key. Be that as it may, the scrambled photograph is a futile record, which doesn't give any added data previously decoding and may stimulate an aggressor's psyche amid broadcast because of the arbitrariness in shape. An option for the above issue is information concealing, which shrouds a anonymous message into an objective photograph because of that nobody can discover the presence of the anonymous information, in which the information kind of the anonymous message learnt in this paper is an image. But these data whacking yield good result only when target image must be large compare to secret image. Making an attention for the end goal to over the two issues in this paper, other strategy for secure photograph broadcast was proposed, that changes a anonymous photograph into a significant montage photograph with a similar size and approximating a preselected target photograph. The change procedure is controlled by a anonymous key, and just with the key can a man recuperate the anonymous photograph about lossless from the montage photograph.

The proposed procedure is actuated by Lai et al. [6] where kind of PC workmanship photo, called mysterious piece unique montage photograph, was proposed. The montage photograph is the result of alteration of the bits of an anonymous photograph in veil of another photo called the target photo preselected from a record. However, a standard issue of Lai et al. [6] is the essential of a tremendous photo database so that the delivered montage photograph can be sufficiently similar to the picked target photograph utilizing their method, the customer isn't allowed to pick uninhibitedly his most adored photo for use as a goal photo. It is thusly wanted in this examination to evacuate this shortcoming of the technique while keeping its legitimacy, that is, it is intended to outline another strategy that can change a anonymous picture into a anonymous section obvious montage picture of a comparative size that has the visual appearance of any uninhibitedly picked target picture without the need of a database.

As a representation, Fig. 1 demonstrates an outcome yielded by the proposed technique. In particular, after an objective picture is chosen subjectively, the given anonymous picture is first separated into rectangular pieces called tile pictures, which at that point are fit into comparative squares in the objective picture, called target squares, as indicated by a closeness foundation in view of shading varieties. Next, the shading normal for each tile photograph is changed to be that of the relating target

Fig. 1 Result generated by the anticipated method. **a** Undisclosed image of size (256 × 256). Target image of size (256 × 256). **c** Secret-bit-perceptible montage image of size (256 × 256) created from (**a**) and (**b**) by the proposed method

obstruct in the objective photograph, bringing about a montage photograph which resembles the objective photograph.

The projected technique is novel in that a significant montage photograph is made, interestingly with the photograph encryption strategy that just makes inane commotion photographs. Likewise, the proposed strategy can change anonymous photograph into a camouflaging montage photograph without pressure, while in information concealing technique must shroud an exceptionally packed form of the anonymous photograph into a cover photograph when the anonymous photograph is substantial contrast with the objective photograph. The entire procedure is controlled by a anonymous key just the individual who has a coordinated key can recover the anonymous photograph.

2 Related Works

Chen et al. [7] have given a quick encryption calculation for secure photograph cryptosystems. Vector Quantization, cryptography and other hypothesis is the significant stage for the cryptosystems to transmit photographs. It was a significant procedure to bring down piece rate photograph pressure. In VQ right off the bat change of photographs into vectors happens and advance vector by vector at that point are successively encoded.

W. B. Pennebaker et al. endeavoured to clarify that the primary obstruction in amount of information required speaking to an advanced photograph. For this we would need to make photograph pressure standard to keep up nature of the photographs after pressure. To address every one of the issues the JPEG standard for photograph pressure incorporates two essential techniques having distinctive task styles. A DCT strategy aimed at "misfortune" pressure and a prescient strategy for "lossless" pressure [1].

Lai et al. [6] have introduced system for data concealing, which suggests that anonymous photograph is separated into tile photographs and after that for montage photograph, they were fix to its next target photograph chose from a database. Anonymous key arbitrarily chooses few squares of montage photograph to installing the data of the tile photograph This shading change was controlled and after that the anonymous photograph is recovered lossless from the tile photograph with the assistance of the implanted removed related data utilized for the recuperation of the photograph [2].

In the existing methods there is no concept of mosaic image creation but secure image transmission is made by mixing the original mage with text and which results in the form of random noise.

3 Proposed Method

The projected method contains two stages

1. Montage image Creation
2. Undisclosed image retrieval (Fig. 2).

In the main stage, a montage picture is delivered, after the objective picture is chosen subjectively, the given undisclosed picture is first isolated into rectangular sections called tile pictures, which at that point are acceptable into comparable squares in the objective photograph called target hinders, following the shading qualities of each tile photograph is changed to the relating squares of target photograph coming about a montage photograph which appear to be like target photograph. Photograph broadcast system contains four phases. (1) Fitting tile photographs of the anonymous photograph into target photograph; (2) Transforming each tile of anonymous photograph to the comparing target squares of target photograph; (3) Rotating each recently tile with least RMSE esteem as for target square; (4) Embedding the anonymous photograph recuperation data.

In the second stage, it contains two phases. (1) Extracting inserted data from [8] recuperation; and (2) Recovering the Secret photograph.

4 Algorithms of the Proposed System

The Detailed set of rules for montage image creation and secret image recovery may be stated in Algorithms I and II.

Algorithm I Montage Image Formation.

T-Target Image, S-Secret Image, F-Secret Fragment visible montage image

Stage 1: Fitting tile images of the secret image into target image

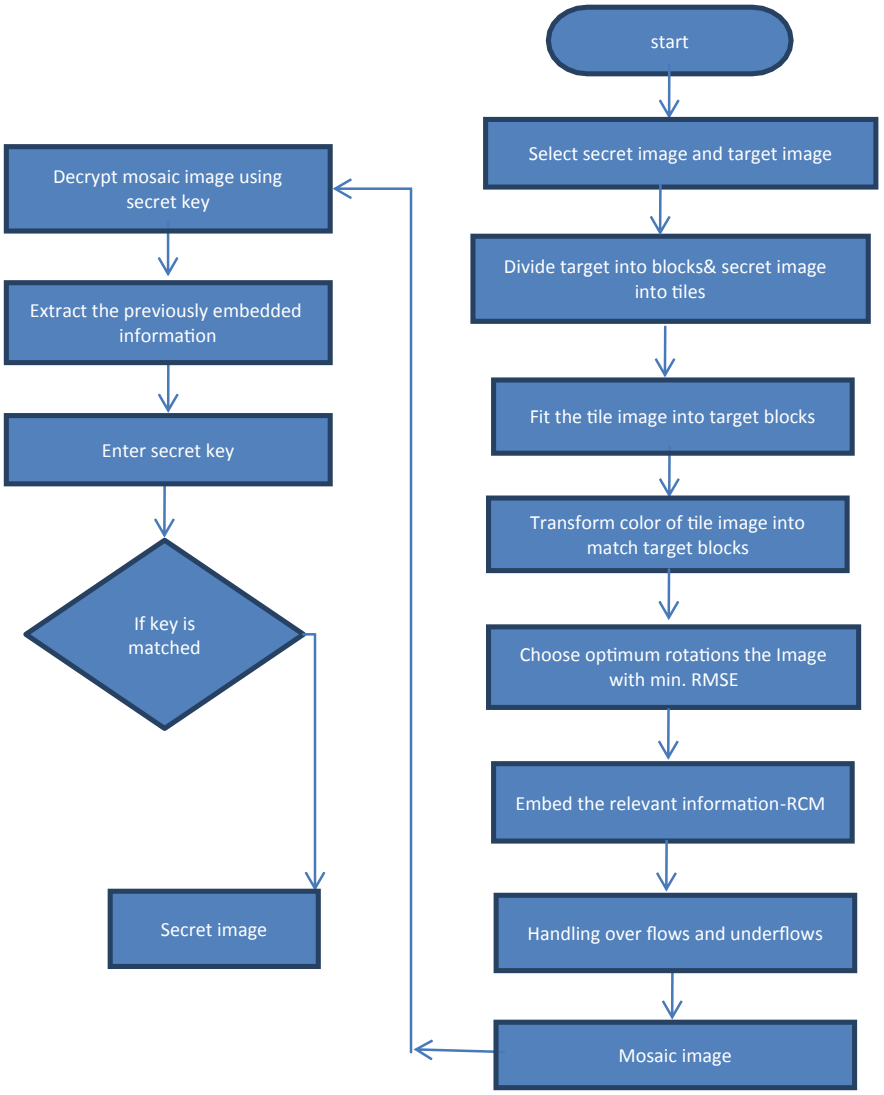

Fig. 2 Flow diagram of the proposed method

1. Uncertainty the span of T is unique in relation to Size of S, Change the Sizes and Make them Identical.
2. Split S into 'n' tiles besides T into 'n' squares.
3. Calculate mean then standard deviation for each tile and block for three colour channels.

$$\mu_C = \frac{1}{n}\sum_{i=1}^{n} c_i \; \mu_c' = \frac{1}{n}\sum_{i=1}^{n} c_i' \tag{1}$$

$$\sigma_c = \sqrt{\frac{1}{n}\sum_{i=1}^{n}(c_i - \mu_c)^2} \; \sigma_c' = \sqrt{\frac{1}{n}\sum_{i=1}^{n}\left(c_i' - \mu_c'\right)^2} \tag{2}$$

where μ_c, are the mean and standard deviation of tile descriptions; μ_c', σ_c' are the mean and standard deviation of target block image.

4. Compute average Standard deviation.
5. Sort both tiles images and block images.
6. Based on Average Standard Deviation values of blocks, map tile between S and T.
7. Create F.

Stage 2: Transforming each tile of undisclosed image to the matching target blocks of target image.

1. Create Counting Table TB with 256 entries, each with matching to a lasting value and allota primary value to zero.
2. Calculate mean and standard deviation for each mapping from secret to target.
3. Aimed at Each pixel p_i in individual block of T by the colour value of c_i transform c_i into a new value (r_i', g_i', b_i') using

$$c_i'' = q_c c_i - \mu_c + \mu_c' \tag{3}$$

where $q_c = \sigma_c/\sigma_c'$.

Stage 3: Rotating each tile images.

Colour likeness among the resultant tile T′ and target block b by rotating T′ hooked on one of direction (0o,90o,180o,270o) Which yield rotated form of T′ with least RMSE with respect to B.

Stage 4: Embedding the secret image recovery information [9, 10].

1. For each tile image T_i in Montage image F, hypothesis a bit stream M_i for improving T

$$\mathrm{M} = \mathrm{t_1 t_2 \cdots t_m r_1 r_2 m_1 m_2 \cdots m_{48} q_1 q_2 \cdots q_{21} d_1 d_2 \cdots d_k}$$

2. Concatenate the bit stream M_i s of all T_i in F; use the secret key K to encode.
3. Embed the bit stream I into montage picture F by means of utilizing revocable difference mapping strategy [3] smears modest whole number change to match of pixel values. Precisely, the technique carries on forward and in reverse number change as pursues separately in which (x, y) are a couple of pixel esteems and (x′, y′) are changed ones

$$x' = 2x - y, \quad y' = 2y - x$$

$$\mathrm{x} = \frac{2}{3}x' + \frac{1}{3}y' \quad \mathrm{y} = \frac{1}{3}x' + \frac{2}{3}y'$$

Algorithm II Secret image recovery
T-Target Image; S-Secret image; F-Montage image
Stage 1: Extracting embedded information from recovery.

1. Excerpt the bit stream M_t by Secret key.
2. Crumble M_t into n bit streams M_1 over M_n.
3. Decode M_i for each tile T_i to get data objects.

Stage 2: Recovering the Secret image.

1. Recovering tile images by the succeeding phases [11].
2. Switch tile backward heading and fit the resulting square substance into T to shape beginning tile picture [12].
3. Make utilization of Extracted Mean and associated Standard Deviation remainders.
4. Compute the first pixel esteem [13]

$$c_i^1 = \frac{c''}{q_c} - \mu_i' + \mu_c \quad .c. \tag{4}$$

5. Combine all the final tile images to system the desired hidden image S as output [14].

5 Experimental Results

A progression of investigations has been led to exam the proposed strategy utilizing numerous anonymous and target photographs with sizes 256 × 256. To demonstrate that the made montage photograph resembles the preselected target photograph, the class metric of root mean square blunder (RMSE) is used.

A case of the trial consequences of montage photograph appeared in Fig. 3e, d demonstrates the in the wake of inserting made montage photograph utilizing Fig. 3a as the Undisclosed photograph and Fig. 3b target photograph. The tile photograph measures 8 × 8.

This approach enhances the visual quality of the decrypted image and mean structural similarity and also security is increased by creating the key which depends on the color model of secret image (Tables 1 and 2).

If the recovery key doesn't match with the key used for hiding key then the process ends at that point, without any further process.

(a) Undisclosed Image **(b)** Target Image

(c) Pre-processed Image **(d)** Colour Transformed Image

(e) Montages Image **(f)** Recovered Secret Image

Fig. 3 An instance of the investigational results of montage image created with tile image size 8 × 8. **a** Undisclosed image, **b** Target image, **c** Pre-processed montage image, **d** Color transformed image, **e** montage image, **f** recovery of secret image

Table 1 Values of RMSE, MSSIM, No. of bits required of target image, undisclosed image, montage image, recovered undisclosed image of existing method

Parameter	Target image	Un-disclosed image	Montage image	Recovered undisclosed image
RMSE	31	30	49.5	25.5
MSSIM	0.40	0.19	0.99	0.01
Number of bits required	–	–	8	8

Table 2 Values of RMSE, MSSIM, No. of bits required of target image, undisclosed image, montage image, recovered undisclosed image of implementation method

Parameter	Target image	Un-disclosed image	Montage image	Recovered undisclosed image
RMSE	31	30	25	13.39
MMSIM	0.45	0.2	0.5	0.25
Number of bits required	–	–	8	8

6 Conclusion

A Secure photograph Steganography Technique is proposed, where anonymous photographs are inserted into an objective photograph and encoded with a key to transmit. Montage photograph which seem to be like the objective photograph is framed with anonymous tile photograph and target photograph. The proposed method is better than the existing ones with 70% better entropy and 80% better efficiency with Maximal security. Also, the first anonymous photographs can be recouped almost lossless from the made montage photograph Experimental outcomes are demonstrated the possibility of secure broadcast of photograph in the proposed technique is great. Future investigations might be coordinated to applying proposed technique to video, where video outlines are utilized as target photograph, by utilizing video outlines as an objective photograph we can recuperate anonymous photograph with less RMSE esteem when contrasted with single target photograph.

References

Pennebaker WB, Mitchell JL (1993) JPEG: still image data compression standard. Van Nostrand Reinhold, New York, NY, USA, pp 34–38

Javidi B, Okano F, Son J-Y (2009) Three-dimensional imaging, visualization, and display. Springer, New York, NY, USA

Hu Y et al (2008) Difference expansion based reversible data hiding using two embedding directions. IEEE Trans Multimed 10:1500–1512
Ni Z, Shi YQ, Ansari N, Su W (2006) Reversible data hiding. IEEE Trans Circ Syst Video Technol 16(3)
Chang CC, Lin CC, Tseng CS, Tai WL (2007) Reversible hiding in DCT-based compressed images. Inf Sci 177(13):2768–2786
Lai J et al (2011) Secret-fragment-visible montage image a new computer art and its application to information hiding. IEEE Trans Inf Forens Secur 6:936–945
Chang CC, Hwang MS, Chen TS (2001) A new image encryption algorithm for image cryptosystems. J Sys Softw
Fridrich J (1998) Symmetric ciphers based on two-dimensional chaotic maps. Int J Bifurcat Chaos 8(6):1259–1284
Chen G, Mao Y, Chui CK (2004) A symmetric image encryption scheme based on 3D chaotic cat maps. Chaos Solut Fract 21(3):749–761
Hu Y et al (2008) Difference expansion based reversible data hiding using two embedding directions. IEEE Trans Multimedia 10(8):1500–1512
Sachnev V, Kim HJ et al (2009) Reversible watermarking algorithm using sorting and prediction. IEEE Trans Circuits Syst Video Technol 19:989–999
Li X, Yang B, Zeng T (2011) Efficient reversible watermarking based on adaptive prediction-error expansion and pixel selection. IEEE Trans Image Process 20(12):3524–3533
Reinhard E, Ashikhmin M, Gooch B, Shirley P (2001) Color transfer between images. IEEE Comput Graph Appl 21(5):34–41
Coltuc D, Chassery J-M (2007) Very fast watermarking by reversible contrast mapping. IEEE Signal Process Lett 14(4):255–258

Specular Reflection Detection for Early Prediction of Cervix Cancer

Pratik Oak and Brijesh Iyer

Abstract The specular reflection (SR) occurs in an image due to reflection from surface and affects the overall interpretation of the image. In medical image analysis, SR images reduce the diagnostic accuracy. Hence, the paper reports the analysis of various SR detection techniques and suggests the best one for automatic detection of SR pixels. The present work compares three state-of-art methodologies of SR detection and three automatic threshold selection techniques. We suggest the combination of '*Alsaleh*' method adapted by '*Kittler*' auto-selection technique for accurate SR detection. The SR free Cervix image will lead to the early detection of Cervix cancer.

Keywords Cervix cancer · Specular reflections (SR) · Threshold · Kittler technique

1 Introduction

Cervical cancer is the fourth most frequent cancer in women across the world. According to WHO health report, every fifth women in the world will be affected by it by 2050. Approximately 90% the 270,000 deaths from cervical cancer in 2015 occurred in low-and middle-income countries. The high mortality rate from cervical cancer could be reduced through a comprehensive approach that includes prevention, early diagnosis and effective screening and treatment programmes [1]. Cervix cancer can be cured if detected at its early stage. Hence, it becomes very important to analyze and detect this cancer at early stage. Conventionally, the Pap smear test is widely used to detect cervix cancer. However, this method suffers from its inherent disadvantages like high dependence on the operators' skills, requirement of subjects' attentions and cooperation and very painful too for the subject.

P. Oak · B. Iyer (✉)
Department of E & TC Engineering, Dr. Babasaheb Ambedkar Technological University, Lonere, Raigad, Maharashtra, India
e-mail: brijeshiyer@dbatu.ac.in

P. Oak
e-mail: pratik24hours@gmail.com

© Springer Nature Singapore Pte Ltd. 2020

T. Hitendra Sarma et al. (eds.), *Emerging Trends in Electrical, Communications, and Information Technologies*, Lecture Notes in Electrical Engineering 569,
https://doi.org/10.1007/978-981-13-8942-9_58

The advancement in the field of medical image processing paved a new line of treatment for this decease. Cervix image analysis plays an important role as a complementary method to the existing methods in the confirmation of the disease. The idea is to capture the image of cervix during woman's routine health checkup and its processing to detect and predict the existence of cancerous tissues. There are various types of cervical images used in medical analysis like colposcopy, cytology, cervigrams, histology etc.

Noise is the most vulnerable issue as far as images are concerned. Removal of noise from the captured images is a prevalent challenge for the medical image processing. Specular Reflection (SR) is a bright spot on an image which contains maximum part as a white intensity which can be induced in cervix images and disturbs the process of extracting the information.

Few notable contributions are reported by various researchers in the area of detection of SR pixels from an input image. Dichromatic reflection model was used to represent SR pixels as separate regions [2]. Separation of RGB planes of a color image and logical *ANDing* of white pixels of each plane as a SR region was suggested by Das et al. [3]. This approach suffers from the trade-off of implementation ease and inferior accuracy on account of non-detection of less bright SR pixels. Akbar and Herman [4] proposed a segmentation using chaotic clonal selection algorithm. The proposed segmentation method lacks in images having smooth color illumination in texture. Based on the reported literature, SR detection methods can be broadly divided into three main categories such as use of kernel as a filter, SR as a binary classification problem and use of thresholding technique [5–7]. These techniques suffer from one or other drawbacks such as requirement of arbitrary constants during automatic detection of SR pixels and requirement of the training system every time for SR detection. The summary of state of the art SR detection techniques is given in Table 1.

However, the detection system should be fully automatic and independent of database. The present work reports the use of automatic threshold selection technique for SR detection. The paper is organized as: Sect. 2 reports the methodology adopted in the analysis whereas the results and discussion are included in Sect. 3. The paper is concluded in Sect. 4 along with the future scope of the work.

2 The Detection Methodology

Three state-of-art techniques of automatic thresholding are selected based on their simplicity and popularity in the reported literature. Existing methodologies for SR detection employed the arbitrary constants as the threshold. Automatic thresholding technique is used in SR detection which will replace the arbitrary constant proposed in the reported methods.

Table 1 State of the art SR detection techniques

Contribution	Methodology	Remark
Suo et al. [2]	Dichromatic reflection	Cannot differentiate pixels having same hue and different saturations
Das et al. [3]	Separation of RGB planes of a color image and logical ANDing of white pixels	Suffers from the trade-off easy to implement and inferior accuracy on account of non-detection of less bright SR pixels.
Akbar and Herman [4]	Segmentation using chaotic clonal selection algorithm	Inaccurate for images having texture color similar to illumination color
Zimmerman et al. [5]	Thresholding in HSI color plane and gradient image	Detection of non-SR pixels due to gradient image calculation
Xue et al. [6]	Morphological top hat transform	Affects the SR detection with variation in shape of structuring element
Alsaleh et al. [7]	Thresholding in HSI color plane	Database dependent method due to arbitrary selection of constant

2.1 SR Detection

Three state-of-art methods of SR detection are chosen based on their popularity in the reported literature. For the present analysis, 'Intensity-Saturation (IS)' histogram is the principle consideration for occurrence of SR region. SR pixels exist in dark region of saturation image (S) and bright region of intensity image (I) [8]. Hence, it is preferred to convert input color image from RGB to HSI plane.

HSI plane based cervix image analysis was reported by Zimmerman et al. [5]. They suggested a multiplying factor of 0.4 and 0.6 to be multiplied with maximum intensity of I and S respectively. The pixels appearing greater than this multiplication factor of I image and less than that of **S** image are separated. The magnitude of the gradient image of these separated pixels is considered as SR pixels.

Xue et al. [6] predefined the structuring element (SE) as a kernel and applied morphological top-hat transform on I image of input cervigrams. The Otsu method is applied on gray version of this transformed image to get SR pixels in the output.

Alsaleh et al. [7] proposed another combination of multiplying factors on the lines of work reported by Zimmerman et al. [5]. The authors suggested three combinations of multiplication factors i.e. 0.5 & 0.17, 0.7 & 0.07 and 0.8 & 0.19 for various types of database.

2.2 Automatic Threshold Detection Techniques

The arbitrary constants reported by most of the methods may vary with the database under experimentation. An automatic threshold selection may resolve this limitation.

Various threshold selection techniques are reported in the literature which can be used according to input image attributes. These techniques can be broadly classified as histogram based, clustering based, entropy based, object attribute based and statistical relation based approaches. The selection of a particular approach depends on the necessity of single or multiple thresholds and foreground and background region detection. The present work aims to select a single constant as the threshold and apply over the image. Hence, histogram based automatic threshold selection technique has been selected for this work. Three techniques based on their significance recorded in the literature, namely *Otsu*, *Riddler* and *Kittler* are selected for the present analysis [9].

Otsu technique reduces the intra-class variance between left and right-side histograms. Its optimal performance is obtained for images having a clear valley between two modes of histogram. It is commonly used automatic threshold selection method for grey as well as binary images [10]. *Calvard and Riddler* suggested opting the mean of input histogram as a threshold. It iteratively updates the threshold as average of lower mean and upper mean of histogram and stops at zero threshold difference [11].

Kittler method depends on principle of minimum error thresholding based on standard deviation of two histograms. This method is good for images having proper foreground. For all values of thresholds over the range of histogram, it computes the error between entropy and information with respect to deviation. It calculates the criterion function and considers its minimum value as a final threshold [12]. These three automatic threshold selection techniques are applied on three SR detection methods explained in 2.1 for the analysis of SR pixel detection.

Figure 1 depicts the flowchart for the proposed experimentation work. Stage I in Fig. 1 indicates the threshold values (T1 and T2) reported in state-of-art methods. Stage II lists automatic threshold selection techniques used in the present work.

3 Results and Discussion

The present analysis is carried out by using digitized uterine cervix images collected by National Cancer Institute (NCI) from four epidemiological studies on HPV and cervical cancer screening namely Costa Rican Natural History Study of HPV (NHS), ASCUS LSIL Triage Study (ALTS), Biopsy Study and Costa Rica Vaccine Trial (CVT) [13]. The ground truth images are neither available in the dataset nor reported in any literature. The experimentation was carried out on total 100 images from all 4 datasets including 25 images from each. These images were randomly selected from available database. The resolution of the images in ALTS and NHS is 2891 * 1973

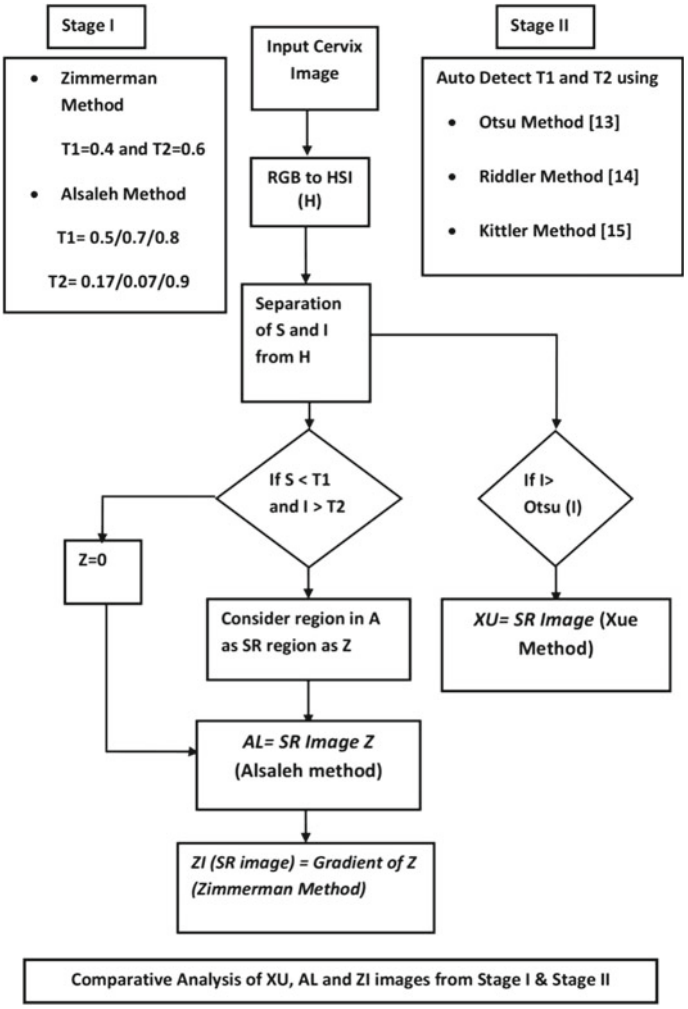

Fig. 1 Flowchart of the proposed analysis

pixels, Biopsy and CVT is 4256 * 2832 pixels. Figure 2 shows the experimental results of SR detection using Zimmerman et al. method, Xue et al. method and Alsaleh et al. method. A bright spots that can be visualized in the input image as SR pixels are detected using the three methods. The background objects like strobe must be considered as a part of noise and should be detected. Alsaleh et al. [7] method reported the detection of this background part also (Fourth row of Fig. 2). Table 2 gives the percentage of average pixels detected by state-of-art methods as SR pixels for the dataset under test. It is calculated by ratio of average of total SR pixels detected to total number of pixels present in an image database. The non-uniform percentages of SR detected pixels show a large variation amongst results of three

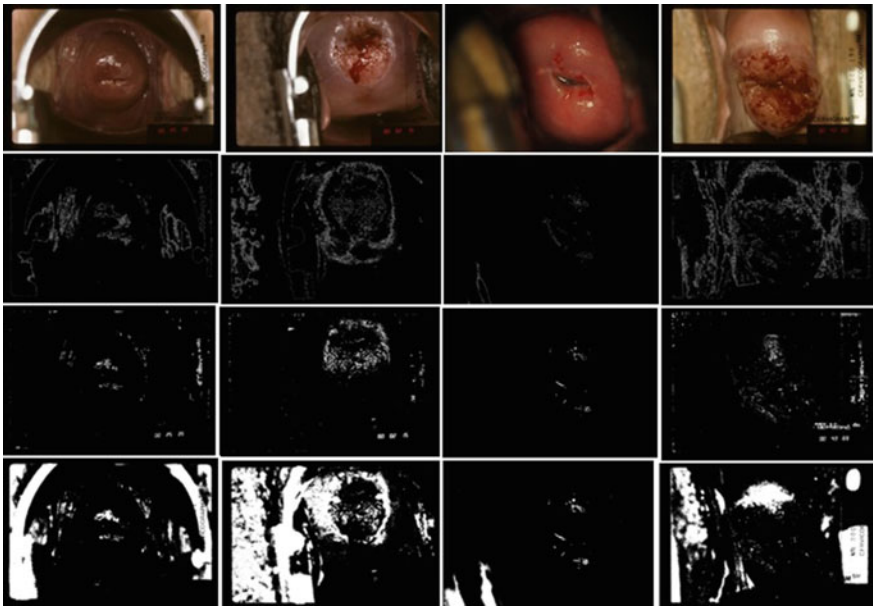

Fig. 2 Comparison of state-of-art methods for SR detection (vertically original image, Zimmerman et al. method, Xue et al. method and Alsaleh et al. method)

Table 2 Percentage of average number of pixels detected as SR on our database

Sr. No.	Method\database	ALTS	BIOPSY	CVT	NHS
1	Zimmerman et al. [5]	35.10	39.11	52.97	22.26
2	Xue et al. [6]	21	1.27	3.04	23.1
3	Alsaleh et al. [7]	31.61	26.73	40.75	20.26

state-of-art methods. This non-uniformity in percentage value affects the selection of the best state-of-art method. It can also be observed from third row of Fig. 2 that Xue et al. method extracts very few pixels as SR pixels and shows less percentage of SR pixel detection. The automatic thresholding techniques may give reason for non-uniformity.

The *Otsu, Riddler* and *Kittler* method of auto threshold detection are applied on each SR detection algorithm explained in Sect. 2.1. Table 3 gives the threshold values given by applying these automatic techniques on three methods of SR detection. The average threshold given by *Otsu* and *Riddler* in *Zimmerman* method approximates with arbitrarily defined value by Zimmerman i.e. 0.4 and 0.16. However, *Kittler* method shows some variation from arbitrary constants by Zimmerman on I image. Similar observation is seen in approximation using Otsu and Riddler for Alsaleh method, which approximates with first combination of arbitrary constants i.e. 0.5 & 0.17.

Table 3 Automatic threshold calculation for state-of-art methods

Sr. No.	Automatic thresholding algorithm	Database used in present work	Zimmerman et al. (default constants I = 0.4 & S = 0.6)		Xue et al.	Alsaleh et al. (default constants I = 0.5/0.7/0.8 & S = 0.17/0.07/0.19)	
			I	S	I	I	S
1	Otsu's method	ALTS	0.339	0.67	0.33	0.51	0.13
		BIOPSY	0.393	0.463	0.393	0.42	0.311
		CVT	0.377	0.46	0.37	0.63	0.22
		NHS	0.346	0.59	0.34	0.74	0.19
		Average	0.367	0.545	0.358	0.575	0.212
2	Cardvard and Riddler's method		0.3311	0.66	0.39	0.5	0.13
		BIOPSY	0.391	0.46	0.391	0.425	0.3
		CVT	0.37	0.46	0.37	0.63	0.22
		NHS	0.34	0.58	0.34	0.74	0.19
		Average	0.358	0.54	0.372	0.573	0.21
3	Kittler's method	ALTS	0.48	0.35	0.48	0.64	0.25
		BIOPSY	0.53	0.411	0.53	0.619	0.27
		CVT	0.5	0.5	0.5	0.63	0.17
		NHS	0.48	0.61	0.48	0.7	0.1
		Average	0.497	0.467	0.497	0.647	0.197

However, this combination fails with the use of Kittler method on I image (0.64). Thus, use of automatic threshold selection techniques justifies the need of proper selection of constant in *Alsaleh* method. This automatic calculation eliminates the database dependency on arbitrary constants reported in original method.

To validate the impact of these auto thresholding techniques, results of Riddler and Kittler methods can be visualized in Fig. 3. It can be easily visualized that, Kittler method extracts more accurate SR pixels than Riddler method. The non-detected SR pixels by Riddler method hamper the image analysis in further stages of any Computer Aided Diagnosis (CAD) system.

The qualitative analysis of SR detection technique is difficult due to unavailability of ground truth images. Kudva et al. suggested a method to compute the sensitivity of SR detection algorithm by manually marking of SR pixels for the images having practically visible SR pixels [14].

Table 4 shows the sensitivity of state-of-art methods of SR detection. It justifies the visual analysis in Fig. 2 i.e. Alsaleh et al. method is most sensitive for SR detection. It also compares the performance of Riddler and Kittler method on Alsaleh technique.

The *Xue* method violates the characteristic of SR pixel by not considering S image in its SR detection. In some cases, the Zimmerman method extracts non-SR pixels due to consideration of gradient pixels as SR pixels.

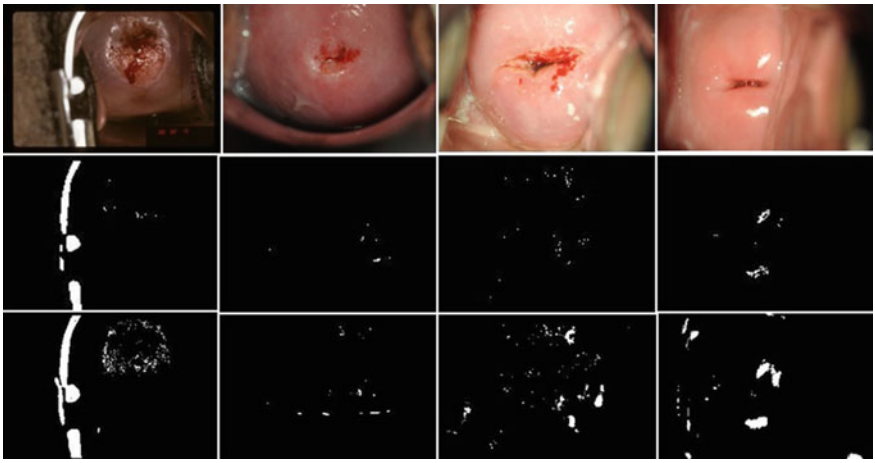

Fig. 3 Comparison of automatic threshold detection techniques (vertically original image, Riddler et al. method, Kittler et al. method)

Table 4 Sensitivity comparison of Alsaleh combined with Riddler and Kittler

Image	Zimmerman method [5]	Xue method [6]	Alsaleh method [7]	Alsaleh + Riddler method	Alsaleh + Kittler method
1	0.55	0.13	0.85	0.82	0.85
2	0.7	0.75	0.8869	0.7228	0.9
3	0.85	0.8537	0.8918	0.80	0.9363
4	0.55	0.5308	0.9469	0.8	0.94

Alsaleh method produces better results as compared to other two methods. Due to optimization of average pixel classification error rate i.e. minimum error thresholding, Kittler method outperforms over other two auto thresholding algorithms. It highlights the need of automatic selection of constant in SR detection. The use of automatic thresholding technique on *Alsaleh* method shows significant change in the SR detected pixels (Figs. 2 and 3) and increases overall accuracy. In cervix cancer treatment, its early prediction improves the chances of speedy recovery of the subject. The SR free cervix images will lead to accurate prediction and hence detection of cancerous tissues. The automatic mode of constant selection provides the edge over conventional (static) mode. The present analysis proved that the SR detection is improved with automatic selection mode. Hence, it is recommended to employ the combination of Kittler method for auto thresholding and *Alsaleh* method to fulfill the purpose of accurate SR detection.

4 Conclusion

The arbitrary selection of constants in the state-of-art methods of SR detection affects the accuracy. Hence, three automatic threshold selection techniques are applied on them. Kittler method shows maximum deviation of 0.09 & 0.14 and 0.14 & 0.02 in for threshold values of I and S images respectively. The present work proposes a combination of *Kittler's* automatic threshold selection technique and *Alsaleh* method of SR detection to extract the SRs, which gives highest sensitivity of about 0.9. In future, the present work may be extended towards automatic SR elimination and make an image suitable for further stages of early detection of cervix cancer.

Acknowledgements The authors gratefully acknowledge the support from Dr. M. Schiffman and his team of NCI for providing the database from NCI Guanacaste and ALTS projects.

References

1. WHO cervix cancer report. http://www.who.int/cancer/prevention/diagnosis-screening/cervical-cancer/en
2. Suo J et al (2016) Fast and high-quality highlight removal from a single image. IEEE Trans Image Process 25(11):5441–5454 (2016)
3. Das A et al (2011) Elimination of specular reflection and identification of ROI: the first step in automated detection of cervical cancer using digital colposcopy. In: IEEE international conference on imaging systems and techniques, Penang, pp 237–241
4. Akbar H, Herman NS (2016) Removal of highlights in dichromatic reflection objects using segmentation and inpainting. In: International conference on robotics, automation and sciences (ICORAS), Melaka, pp 1–4
5. Zimmerman G et al (2006) Automatic detection of specular reflections in uterine cervix images. Proc SPIE 6144
6. Xue Z et al (2007) Comparative performance analysis of cervix ROI extraction and specular reflection removal algorithms for uterine cervix image analysis. Proc SPIE 6512
7. Alsaleh SM et al (2015) Automatic and robust single-camera specular highlight removal in cardiac images. In: 37th annual international ieee conference of engineering in medicine and biology society (EMBC), Milan, pp 675–678
8. Yao R et al (2010) Specular reflection detection on gastroscopic images. In: 4th international conference on bioinformatics and biomedical engineering, Chengdu, pp 1–4
9. Sezgin Mehmet et al (2004) Survey over image thresholding techniques and quantitative performance evaluation. J Electron Imaging 13(1):146–165
10. Gonzalis Woods RC (2000) Digital image processing. An imprint of pearson education, 1st edn. Edition Wesley
11. Ridler TW, Calvard S (1978) Picture thresholding using an iterative selection method. IEEE Trans Syst, Man, Cybern smc-8(8)
12. Kittler J, Illingworth J (1986) Minimum error thresholding. IEEE J Pattern Recognit 19(1):41–47 (1986)
13. Cervix Image Sharing Protocol (CISP) User Guide, NCI, Bestheta, US, September (2017)
14. Kudva et al (2017) Detection of specular reflection & segmentation of cervix region in uterine cervix images for cervical cancer screening. IRBM 38:281–291

Developments in Advanced Control System for Safe and Comfort Lateral Movement of Vehicle

Sreenivasulu Sangathoti, Polaiah Bojja and M. N. Giriprasad

Abstract There are so many reasons for vehicle accidents and the first reason amongst is less alertness of the driver; this may be because of driver's fatigue or drowsiness. With the introduction of the automatic driver assistance system ADAS, there is possibility to avoid the accidental damage which is happening due to the said reason. To develop such system, two problems are required to be solved. One is prediction of the drowsiness and the other one is controlling the movement of vehicle. The theme of the paper; is to review various control algorithms used to develop shared steering control systems appropriate to implement the ADAS. For this a vehicle model is developed and described to solve the problem with model based development technique. The vehicle model developed is a two-dimensional 2D and 3D mathematical state-space model of laterally moving vehicle which is most suitable to design a shared steering control system. Finally the response of the vehicle state-space model, simulated for unit pulse input, is analyzed with MATLAB software.

Keywords ADAS · Shared steering control system · State-space model of vehicle

1 Introduction

The frequency of accidents is increasing rapidly. Human life is most precious thing in world but around 1.240 millions of people are losing their lives in accidents since 2007 [1]. This is the situation where a driver and an embedded control system carry out a task simultaneously [2]. So, certain safety measures are needed to minimize the

S. Sangathoti (✉) · M. N. Giriprasad
Department of ECE, JNT University Anantapur, Anantapur, Andhra Pradesh, India
e-mail: sangathoti@gmail.com

M. N. Giriprasad
e-mail: mahendragiri1960@gmail.com

P. Bojja
Department of ECE, K L E F Deemed to be University, Vaddeswaram, Guntur, India
e-mail: paulraj.bojja@gmail.com

© Springer Nature Singapore Pte Ltd. 2020

T. Hitendra Sarma et al. (eds.), *Emerging Trends in Electrical, Communications, and Information Technologies*, Lecture Notes in Electrical Engineering 569,
https://doi.org/10.1007/978-981-13-8942-9_59

number. Drowsiness and fatigue of the driver are two key reasons affecting the vehicle control and leading to accidents. With the observation of the alertness or drowsiness of driver one can predict the accidental situation and by taking necessary steps for controlling vehicle movements, it is possible to prevent the accidental damage. The intelligent or fully automatic driving is ultimate but it is not at a mature level [3]. It is observed that many of the researchers found alternatives but efficient one is that, a shared control from manual control to full automation [3, 4].

The present automotives are the Embedded Control Systems (ECS) products which are developed using pattern recognition, computer science, and intelligent automotive control technologies. These also comprise integrated vehicle technology, artificial intelligence, technology of sensor and automatic control technology. Since last decade the intelligent vehicle technology attracted the many universities, scientists and enterprises, so a very good quantity of research is going in this area using the research out comes an elaborate measurement system capable of continuously monitoring the movement of steering [1, 2], is developed this is shown in Fig. 1.

The problem: whenever the driver felt drowsy or fatigue the developed system need to identify the situation and automatically take the vehicle control into ADAS's hands and need to maintain the safe-drive till the driver want to take the control back. For this situation the ADAS must be able to provide solution for two sub problems; one is prediction of the drowsiness and another is controlling the movement

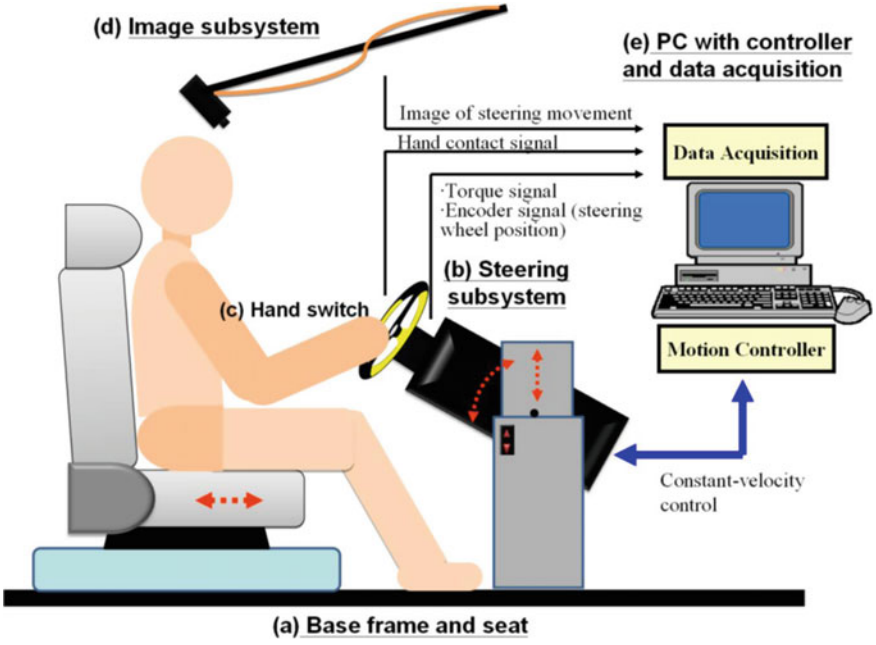

Fig. 1 The integrated measurement system for characterizing steering movement

of vehicle. In this paper it is initiated to solve the vehicle control problem. But controlling of vehicle laterally is very much crucial job because the controller must be able to produce an efficient and accurate response with very less time delay. So, it is important that selection of the control scheme is a **challenge** in front of the control system designer. To overcome the challenge and propose a novel control approach it is required that comparative study of various conventional and nonconventional control approaches is necessary. For this work the first step is to describe vehicle model and test response of the vehicle model.

The paper presents the review of automotive control systems used to implement ADAS to control the vehicle in lateral motion and suitable for shared steering control system. To develop a novel automotive lateral motion control system the state-space mathematical model of vehicle is described and further tested the vehicle model. The paper consists of various sections as follows; Sect. 2 gives review on recent research, Sect. 3 describes vehicle dynamic model, Sect. 4 presents vehicle response with test input and Sect. 5 contains conclusion and future scope. It is observed that there are number of approaches relevant to the shared control proposed in the literature survey and brief review is as follows.

2 Review on Recent Research

As far as the automotives are concerned the used controllers are most safety constrained and are intended to give good performance. The various performance metrics are response-time, settling-time, overshoot, damping etc. To evaluate the performance of controller, one should measure the said controller's parameters. To propose a most appropriate controller to the stated problem a review on recent research is carried out as follows: any system development will start with architecture. In 2012, D. Sivaraj, proposed self driven vehicle architecture which controls automatic steering of the vehicle, besides acceleration and braking control. In this system KALMAN FILTER KF computes the first level of error that is the computation of lateral error and filtered error values. The PID algorithm taking the filtered values arrives at the calculation of steer needed to make lateral error zero [5]. For automated vehicle a driver model is required to make vehicle autonomous system. In 2015, X. X. Na, developed the driver model using game theory and studied the interaction between a human driver and driver model developed for collision avoidance system [6]. But no driver wants to lose the kick generated while driving. Hence In 2015, another approach for switched control, proposed by Y. Koo, is developed with five different models; driver only, driver assisted, co-pilot driving etc., involving the analysis of the situation and the driver request [7]. For further improvement of vehicle stability in 2016 S. M. Erlien proposed the Model Predictive Control MPC scheme which considers translation of driver's expected front lateral force into front wheel angle enabling the vehicle control [8]. Then it is time for consideration of intelligent vehicles so that the vehicle itself is required to take decision to ensure smoother control operation is of vehicle. In 2017, Zhenhua Pan developed mathematical model and

proposed an improved Proportional Integral Derivative PID speed control algorithm for driving trend graphs in intelligent vehicle. As a part of this, he built the driving trend graphs, set the acceleration and deceleration distance; obtain the corresponding acceleration to get the result [9]. Further In 2017, Nguyen, described an approach for shared lateral control. In this, the control is shared between the driver and Lane keeping assist system. This system besides this function incorporates obstacle avoidance function the experimental results with human driver and dynamic driving simulator proved that the system is very effective [10]. To provide more safety to passengers and vehicle, in 2017, Liang Li did research work on vehicle control architecture. The architecture has a supervisor with two controllers, an upper one, and a lower one. The upper controller computes the required tyre forces and the needed tyre forces are realized by lower controller with the help of hydraulic pressure based controller. The proposed 3DDSC is evaluated with a CarSim–MATLAB cosimulation and hardware-in-the-loop simulation. The results show that 3DDSC can achieve a seamless integration of lateral stability and rollover prevention in complicated steering maneuvers [11]. In intelligent vehicle control schemes a problem is identified that is the system confusion on commands given by the driver and automatic control system. To overcome this situation, in 2017, Avinash Balachandran, proposed a system to provide the driver with a hap tic signal derived from the tension between the driver's current steering command and the system's calculation of the steering angle necessary at some point in the future to avoid a collision. This avoids the need to guide the driver to a specific path and is therefore tolerant of different driving styles [12]. After introduction of utilization of haptic signal thought in 2017, Chunshi GUO, proposed and came up with design of a new hap tic based automatic driving system having the feature of seemless transfer of control from the self driven system to the human driver. In this design, the problem shared control is visualized as constrained optimization problem. This type of problem can be solved online using MPC. The system is developed with automatic lane keeping control. The driver can assume the control by adapting the weight on the stage cost. This seamless transfer avoids potential hazards using feedback from the hap tic signal [13].

The most important aspects in vehicle usage are stability and safety [14–21]. In order to provide these two a perfect automotive control (management) system is required to control the speed and lateral position of vehicle. To develop such a system, first, the vehicle mathematical model is developed as detailed below.

3 Mathematical Model of Vehicle in Lateral Motion

This section used to model the vehicle in both two 3DOF and 3AOR. The lateral motion of a vehicle is modeled as illustrated in Fig. 2 so-called bicycle. This is suitable one to four-wheel vehicle, because it is simple and pragmatic model of vehicle which considers the left and right wheels as one wheel. The model also aims at finding whether the system is linear or non-linear since the advanced control

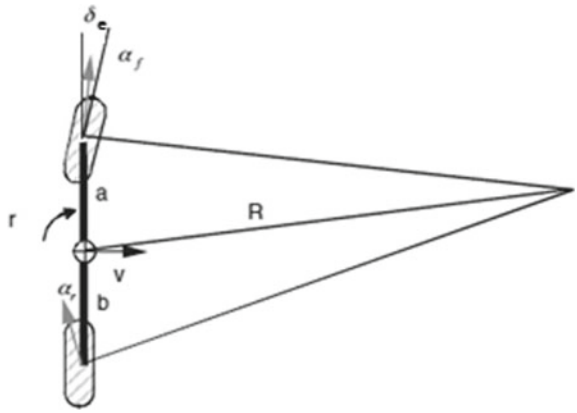

Fig. 2 Schematic of a bicycle model

system is necessary only when the system is complex and non-linear [18]. In case the system is linear simple conventional controllers is enough.

Let us consider the vehicle which is moving in steady turning behavior due to steady steer displacement (δ_e,) at constant forward speed (u_0). The applicable analysis considers the following assumptions: (i) $R > l$ & t; Where t is track of the vehicle, R is turning radius, l is wheel base and $l = a + b$ (as shown in figure). (ii) steer angle of both wheels must be same (iii) $\alpha_e = \alpha_r$ where α_e is front wheel side slip angle and α_r is rear wheel side slip angle (iv) the sideslip angle β at the Centre of Gravity (COG) is $\beta = \tan^{-1}$ (v/u) ≈ (v/u) where V is vehicle speed, R is radius of curvature, and the yaw velocity $r = \dot{\psi}$ are fixed in a steady turn, therefore the instantaneous speed tangent to the path at the COG is $u = rR$. Assume, for right turn a positive steer angle is required. This result in positive slip angles being formed at the front and back tyres (i.e., the angle from tyre speed to tyre-orientation direction is called as the tyre-slip angle), therefore it is obtain:

$$\alpha_e = \delta_e - \frac{v + ar}{u} \text{ and } \alpha_r = -\frac{v - br}{u}; \text{ where } v \text{ is lateral velocity} \tag{1}$$

and

$$\alpha_e - \alpha_r = \delta e - \frac{L}{R} \quad \text{or} \quad \delta e = \alpha_e - \alpha_r + \frac{L}{R} \tag{2}$$

Therefore, it is observed that δ_f consists of two parts one is static part and is called Ackermann angle l/R; the second part is dynamic part $\alpha_f - \alpha_r$. If $\alpha_f > \alpha_r$, the condition is termed as *under steer*. It means the steering angle should be more than the Ackermann angle in order to have study-radius turn at non-zero speed. If $\alpha_f < \alpha_r$ and $\delta_e < (l/R)$; the condition is termed *over steer*. Finally, if the $\alpha_e = \alpha_r$ and $\delta_e = (l/R)$; condition is termed *neutral steer*. The side forces F_{yf} and F_{yr} (i.e., cornering forces) acting at the vehicle tires are related to the slip angles, α_f and α_r as shown in Fig. 3. Although the relationship between F_y and α is nonlinear, for small

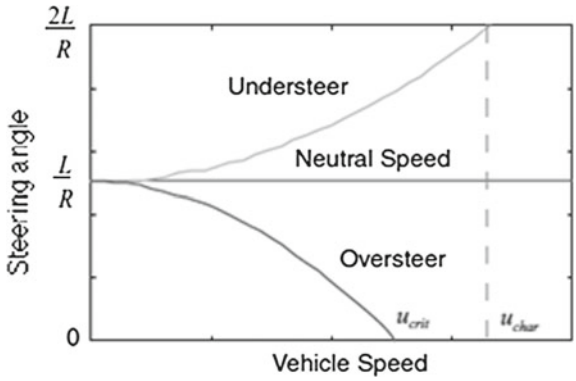

Fig. 3 Effect of vehicle speed on steering angle

slip angles, we can use the approximation: $F_y = C_a\alpha$ for the vehicle shown in Fig. 1.

To derive the equations of motion, apply the Newton's second law to translate in the y direction gives:

$$Mu^2/R = F_{yf} + F_{yr} \tag{3}$$

The sum of the moments at steady turn about the COG has to be zero.
Therefore:

$$0 = F_{yf}a - F_{yr}b \tag{4}$$

Thus, the cornering forces that act at the rear and front tires, respectively, are:

$$F_{yr} = M(a/L)(u^2/R) \quad \text{and} \quad F_{yf} = m(b/L)(u^2/R) \tag{5}$$

By substitute the Eq. (5) in Eq. $F_y = C_\alpha a$ and the slip angles can be calculated as:

$$\alpha_f = \frac{Mu^2}{R}\frac{b}{L}\frac{1}{C_{\alpha f}} \quad \text{and} \quad \alpha_r = \frac{Mu^2}{R}\frac{a}{L}\frac{1}{C_{\alpha r}} \tag{6}$$

Now substitute Eq. 6 in 2 we get

$$\delta_e = \frac{L}{R} + \left(\frac{Mb}{LC_{\alpha f}} - \frac{Ma}{LC_{\alpha r}}\right)\frac{u^2}{R} = \frac{L}{R} + K_{us} \cdot a_y \tag{7}$$

where K_{us} is under steer coefficient which has units as (rad/(m/s)).

The speed of vehicle has lot of bearing on the steering angle when the radius turn is constant. This is diagrammatically shown in Fig. 3. Where $u_{char,}$ and u_{crit} are *characteristic* speed and *critical speed* respectively.

$$u_{char} = \sqrt{\frac{l}{K_{us}}} \tag{8}$$

$$u_{crit} = \sqrt{\frac{-l}{K_{us}}} \tag{9}$$

Further these are interpreted as lateral acceleration gain denoted with Gα

$$G_\alpha = \frac{a_y}{\delta_e} = \frac{\frac{u^2}{R}}{\delta_e} = \frac{\frac{u^2}{L}}{\delta_e \frac{R}{l}} = \frac{\frac{u^2}{L}}{1 + K_{us}\frac{u^2}{L}} = \frac{u^2}{L + K_{us}u^2} \tag{10}$$

and the yaw-rate gain denoted as G_γ is

$$G_r = \frac{r}{\delta_e} = \frac{\frac{u}{R}}{\delta_e} = \frac{u}{l + K_{us}u^2} \tag{11}$$

The Fig. 4 shows the different forces acting on axels of vehicle moving in a constant speed and in steady turn. By apply Newton's equation at wheels the it may get the following equations.

$$F_{yf}\cos(\delta_e - \beta) + F_{xf}\sin(\delta_e - \beta) = F_{ye}\cos\left(\frac{a}{R} + a_f\right) + F_{xf}\sin\left(\frac{a}{R} + \alpha_e\right) = m\frac{b}{l}\frac{u^2}{R} \tag{12}$$

And

$$F_{yr}\cos(\beta) - F_{xr}\sin(\beta) = F_{yr}\cos\left(\frac{b}{R} - \alpha_r\right) - F_{xr}\sin\left(\frac{b}{R} - \alpha_r\right) = m\frac{a}{l}\frac{u^2}{R} \tag{13}$$

Assume the slip angle is very small such that $\sin\alpha = \alpha$ and $\cos\alpha = 1$ and a linear-tire assumption therefore, from the equation $F_y = C_\alpha\alpha$ we obtain

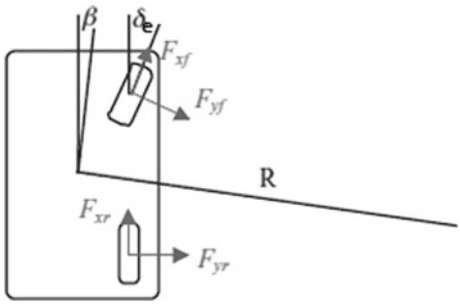

Fig. 4 Projection of the forces in lateral moving vehicle

$$\alpha_e = \frac{M\frac{b}{L}\frac{u_0^2}{R} - F_{xf}\frac{a}{R}}{C_{\alpha e} + F_{xf}} \quad \text{and} \quad \alpha_r = \frac{M\frac{a}{L}\frac{u_0^2}{R} + F_{xr}\frac{b}{R}}{C_{\alpha r} + F_{xr}} \tag{14}$$

Thus, by including the effects of tractive forces, the modified form of Eq. (7) is

$$\delta_e = \frac{L}{R} + (\alpha_e - \alpha_r) = \frac{L}{R} + \frac{m\frac{b}{l}\frac{u_0^2}{R} - F_{xf}\frac{a}{R}}{C_{\alpha e} + F_{xf}} - \frac{M\frac{a}{l}\frac{u_0^2}{R} - F_{xr}\frac{b}{R}}{C_{\alpha r} + C_{xr}} \tag{15}$$

$$\delta_e = \frac{L}{R} - \frac{F_{xf}}{C_{\alpha f} + F_{xf}} = \frac{a}{R} - \frac{F_{xf}}{C_{\alpha e} + F_{xr}}\frac{b}{R} + \left[\frac{mb}{l\left(C_{_{\alpha f}} + F_{xf}\right)} - \frac{ma}{l\left(C_{_{\alpha r}} + F_{xr}\right)}\right]\frac{u^2}{R} \tag{16}$$

For front wheel drive FWD vehicle the Ackermann angle is decreased and the under-steer coefficient, K_{us} increases i.e., the vehicle becomes more under-steer. So far the calculations are based on the assumption that the vehicle is having study turn and that the vehicle sprung mass due to rolling movement of the vehicle is negligibly small. Now let us consider the two and three DOF cases where in roll degree of freedom φ, y the lateral motion and ψ, the yaw motion are also taken into consideration. Now from second law of motion of Newton's:

$$F_{yf} + F_{yr} = Ma_y = M\ddot{y} = M\ddot{(}u_0 r + \dot{v}) = m\left(u_0 r + u_0\dot{\beta}\right) \tag{17}$$

$$aF_y f - bF_{yr} = Iz\,r^{\cdot} \tag{18}$$

where $\tan\beta = v/u_0$ or $v \approx \beta u_0$ was used. If we further assume the rear and front tires are linear, we have:

$$F_{yf} = C_{\alpha f}\alpha_e = C_{\alpha e}\left(\delta - \left(\frac{v + ar}{u_0}\right)\right) = C_{\alpha e}\left(\delta - \beta - \frac{ar}{u_0}\right) \tag{19}$$

$$F_{yr} = C_{\alpha r}\alpha_r = C_{\alpha r}\left(\frac{br - v}{u_0}\right) = C_{\alpha r}\left(\frac{br}{u_0} - \beta\right) \tag{20}$$

Combining with Eqs. (17) and (18) we obtain:

$$Mu_0\beta + Mu_0 r = -(C_{\alpha e} + C_{\alpha r})\beta + \left(\frac{C_{\alpha r}b - C_{\alpha e}a}{u_0}\right)r + C_{ae}\delta \tag{21}$$

$$I_Z\dot{r} = (bC_{\alpha r} - aC_{\alpha e})\beta - \left(\frac{C_{\alpha e}a^2 + C_{\alpha r}b^2}{u_0}\right)r + aC_{\alpha e}\delta \tag{22}$$

These equations represent the vehicle model for lateral dynamics in two degree of freedom (2D). Taking two more state variables into consideration, displacement in lateral direction, y, and ψ the angle of yaw can be related to the road. It is known

that tan $\beta = v/u_0$ or $v \approx \beta u_0$, $y^{\cdot} = v + u_0\psi$ and $\psi^{\cdot} = r$, $y^{\cdot\cdot} = \mathrm{v}^{\cdot} + u_0 r$. Therefore the above equations are formulated in state-space form as $\mathrm{x}^{\cdot} = \mathrm{Ax} + \mathrm{Bu}$, $\mathrm{y} = \mathrm{Cx} + \mathrm{Du}$, where $\mathbf{x} = [y\ v\ \psi\ r]^{\mathrm{T}}$. These two equations are as follows:

$$\frac{d}{dt}\begin{bmatrix} y \\ v \\ \varphi \\ r \end{bmatrix} = \begin{bmatrix} 0 & 1 & u_0 & 0 \\ 0 & -\left(\frac{C_{\alpha e}+C_{\alpha r}}{mu_0}\right) & 0 & \frac{-aC_{\alpha e}+bC_{\alpha r}}{mu_0} - u_0 \\ 0 & 0 & 0 & 1 \\ 0 & \frac{-aC_{\alpha e}+bC_{\alpha r}}{I_z u_0} & 0 & -\left(\frac{C_{\alpha e}a^2+C_{\alpha r}b^2}{I_z u_0}\right) \end{bmatrix}\begin{bmatrix} y \\ v \\ \varphi \\ r \end{bmatrix} + \begin{bmatrix} 0 \\ \frac{C_{\alpha e}}{M} \\ 0 \\ \frac{aC_{\alpha e}}{I_z} \end{bmatrix}\delta \tag{23}$$

$$Y = \begin{bmatrix} 1\ 0\ 0\ 0 \end{bmatrix}\begin{bmatrix} y \\ v \\ \psi \\ r \end{bmatrix} + [0]\delta$$

where

$$A = \begin{bmatrix} 0 & 1 & u_0 & 0 \\ 0 & -\frac{C_{\alpha e}+C_{\alpha r}}{Mu_0} & 0 & \frac{bC_{\alpha r}-aC_{\alpha e}}{Mu_0} \\ 0 & 0 & 0 & 1 \\ 0 & \frac{bC_{\alpha r}-aC_{\alpha e}}{I_z u_0} & 0 & -\frac{a^2C_{\alpha f}+b^2C_{\alpha r}}{I_z u_0} \end{bmatrix};\ B = \begin{bmatrix} 0 \\ \frac{C_{\alpha e}}{M} \\ 0 \\ \frac{aC_{\alpha e}}{I_z} \end{bmatrix};\ C = \begin{bmatrix} 1\ 0\ 0\ 0 \end{bmatrix};\ \mathrm{D} = [0]$$

The above state-space representation gives a compact and suitable way to model and analyze the system under consideration having multiple inputs and outputs. Also the advantage of the state-space model is that it can be used for linear or non-linear systems.

4 The Developed Vehicle-Model Response

This section discusses the response of laterally moving vehicle model developed in the above section. To develop the vehicle model any general vehicle parameters can be considered for absolute modeling of the vehicle. However, the parameters are collected from [9], to develop the empirical model and are shown below in Table 1.

The state-space model is solved using numerical solution method to develop an empirical model. The obtained results and the test response are described in the next section.

Table 1 Vehicle parameters

$m = 1{,}500$ kg	$I_Z = 2{,}420$ kg m^2	$g = 9.81$ m/s^2
$l = 2.54$ m	$a = 1.14$ m	$b = l - a = 1.4$ m
$u_0 = 20$ m/s	$C_{af} = 2{,}050$ N/deg	$C_{ar} = 1{,}675$ N/deg

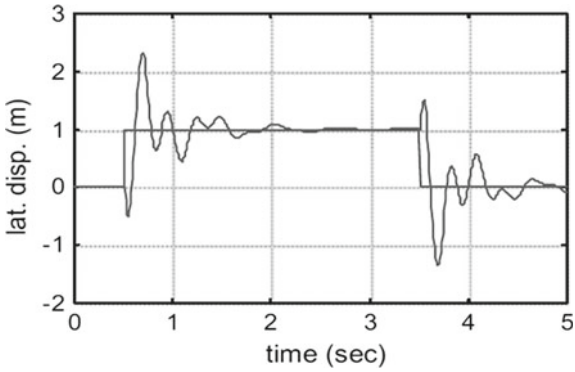

Fig. 5 Unit pulse response of the system

5 Conclusion and Future Scope

To develop a novel automotive automatic control system to control the vehicle in lateral motion a vast review is conducted from the good number of references as listed in the References section. As per the problem described, in order to develop a shared steering controller suitable to efficiently control the vehicle, considering the vehicle parameters like wheel base, length, width and weight etc. a state-space mathematical model is developed. Then the developed empirical model of vehicle is tested with a test input and is analyzed. The state-space model results derived from the Eq. (23) are as follows:

$$A = [0\ 1\ 20\ 0;\ 0\ -7.1142\ 0\ -19.98;\ 0\ 0\ 0\ 1;\ 0\ 0.00947\ 0\ -7.040];$$
$$B = [0;\ 78.3;\ 0;\ 55.33];$$
$$C = [1\ 0\ 0\ 0];$$
$$D = 0;$$

The below Fig. 5 shows the response of the vehicle model with a test input of unit pulse.

Regarding the future work; the response of the developed model will be analyzed with some conventional and nonconventional controllers. Specifically, it is proposed to describe, the next paper, the comparative responses of the vehicle model with PID, KALMAN filter based PID and MPC control strategy.

References

1. World Health Organization (2013) Global status report on road safety. WHO Department of Violence and Injury, Geneva
2. Prevention and Disability (VIP) (2013)

3. Koo Y, Kim J (2015) A method for driving control authority transition for cooperative autonomous vehicle. IEEE Intell Veh Symp (IV):394–399
4. Enache NM, Mammar S (2010) Driver steering assistance for lane-departure avoidance based on hybrid automata and composite Lyapunov function. IEEE Trans Intell Transp Syst 11(1):28–39
5. Pan Z An intelligent vehicle based on an improved PID speed control algorithm for driving trend graphs, visualization analysis of the research on knowledge network. https://doi.org/10.5013/ijssst.a.17.30.19 19.1 ISSN: 1473-804x online, 1473-8031 print
6. Winter J, Dodou D (2011) Preparing drivers for dangerous situations: a critical reflection on continuous shared control. In: IEEE international conference on systems man and cybernetics conference proceedings, pp 1050–1056
7. Na XX, Cole DJ (2015) Game-theoretic modeling of the steering interaction between a human driver and a vehicle collision avoidance controller. IEEE Trans Human Mach Syst 45(1):25–38
8. Keviczky T, Falcone P (2006) Predictive control approach to autonomous vehicle steering. In: American control conference
9. Ljung L (2002) Prediction error estimation methods. Circuits Syst Signal Process, 11–21
10. Dixon RC (2012) Robust Kalman filter based localization of an omnidirectional automated guided vehicle. In: Proceedings of the 14th IFAC symposium on information control problems in manufacturing, Bucharest, Romania, 23–25 May
11. Nguyen AT, Sentouh C (2017) Driver-automation cooperative approach for shared steering control under multiple system constraints: design and experiments. IEEE Trans Ind Electron 64(5):3819–3830
12. Li L (2017) A three-dimensional dynamics control framework of vehicle lateral stability and rollover prevention via active braking with MPC. IEEE Trans Ind Electron 64(4):3389–3401
13. Balachandran A (2016) Predictive haptic feedback for obstacle avoidance based on model predictive control. IEEE Trans Autom Sci Eng 13(1)
14. Song L, Guo H (2017) Model predictive control oriented shared steering control for intelligent vehicles. In: 29th Chinese control and decision conference (CCDC), pp 7568–7573
15. Katriniok A, Abel D (2012) LTV-MPC approach for lateral vehicle guidance by front steering at the limits of vehicle dynamics. In: 50th IEEE conference of decision and control and european control conference (CDC-ECC) 2011, pp 6828–6833
16. Erlien SM, Fujita S (2016) Shared steering control using safe envelopes for obstacle avoidance and vehicle stability. IEEE Trans. Intel Transp Syst 2:441–451
17. Hrovat D, Di Cairano S (2012) The development of model predictive control in automotive industry: a survey. In: 2012 IEEE international conference on control applications (CCA) 3–5
18. Rajamani R (2012) Vehicle dynamics and control, 2nd edn., Mechanical engineering series. Springer, Berlin
19. Wang L (2009) Model predictive control system design and implementation using MATLAB. Springer, Berlin
20. Sivaraj D (2011) Implementation of AVCS using Kalman filter and PID controller in autonomous self-guided vehicle. Int J Comput Appl 27(2), 0975–8887
21. Guo C (2017) MPC-based shared steering control for automated driving systems. In: IEEE international conference on systems, man, and cybernetics (SMC), Banff, Canada, 5–8 Oct

Structured DFT Based Analysis of Standard Benchmark Circuits

H. Harshita Shravani and J. P. Anita

Abstract Automatic Test Pattern Generation (ATPG) is the most useful technique for the testing of VLSI designs. In recent times with the increase in the size and complexity of designs, the probability of the occurrence of defects also increases. There-fore testing has become very difficult for complex circuits or designs such as System On Chips (SOC). The solution to this problem is the Embedded Deterministic Test (EDT) which involves in addition of some logic structures to the complex designs to minimize the total cost of the test, the volume of the test and memory usage of ATE (Automatic Test Equipment). In this paper, the analysis of ISCAS'89 benchmark circuits are done by using Embedded Deterministic Test (EDT) to improve the test coverage. Retargeting stage is proposed in-order to compact the test sets produced during ATPG.

Keywords Automatic test pattern generation · Embedded deterministic test · Automatic test equipment · Scan insertion · Fault coverage

1 Introduction

The major course of action in the testing of the semiconductor is Automatic Test Pattern Generation or ATPG, during the process the input vectors are generated by a program automatically, which are most essential to examine for faults in a device or design. The stimuli are consecutively given to the circuit or Device Under Test (DUT) and the responses from the device to all the set of inputs applied are compared with the expected response from a golden circuit. If the responses of the device and the golden

H. Harshita Shravani (✉) · J. P. Anita
Department of Electronics and Communication Engineering, Amrita School of Engineering, Coimbatore, India
e-mail: shravanirao1996.ss@gmail.com

J. P. Anita
e-mail: jp_anita@cb.amrita.edu

Amrita Vishwa Vidyapeetham, Coimbatore, India

© Springer Nature Singapore Pte Ltd. 2020

T. Hitendra Sarma et al. (eds.), *Emerging Trends in Electrical, Communications, and Information Technologies*, Lecture Notes in Electrical Engineering 569,
https://doi.org/10.1007/978-981-13-8942-9_60

circuit don't match then the device is said to be faulty. The ATPG efficacy is measured mostly by the test coverage, fault coverage achieved and the test expenditure.

The ATPG process is commonly divided into two diverse phases: (1) generation of the test vectors and (2) application of the test vectors. In the generation phase of the test vectors, the most suitable models for the device or circuit under test are developed at gate level or transistor level such that the responses from the faulty circuit will be varied from that of the golden circuit. The generation of test vectors is a mathematical process that can be carried out in three ways: (1) by manual methods; (2) by algorithmic methods (with or without heuristics), and (3) by pseudo-random methods.

When generating the test vectors, the vectors generated should use the memory efficiently and also the time required to generate the test vectors should be less. ATPG should generate the minimum test vectors that are required to detect the faults in the circuit or the device. The main conditions for the test set creation are:

(1) The time required to construct the minimal test vectors.
(2) Size of the pattern generator or hardware or software system that is required to properly simulate the Device under test (DUT).
(3) Size of the testing process.
(4) The time required to load the test patterns.

ATPG based testing is a technique in which the DFT is inserted in the design to improve the testability and the deterministic test vector generation is employed automatically which produces the high test and fault coverages for the device under test (DUT).

1.1 Testability

Testability is a design attribute that measures the ease of creating a methodology to broadly test a manufactured design's quality. Usually, the testing and designing procedures are kept distinct. But in the modern design methodologies, the testing procedure is combined with the design procedure prior to the design process, creating a design-for-test (DFT) process flow.

A testable circuit is both controllable and observable. In a testable design, controllability means a specific value is set on the input ports of the design and observability means, the ability of the circuit to observe the value on the primary outputs. Controllability and observability must be measured to check if the internal circuitry is working properly or not. To ensure the design is testable the designers must include special DFT techniques in specific stages of design in the development process.

1.2 DFT Techniques

There are two main DFT techniques involved in the design process: (1) Ad hoc DFT and (2) Structured DFT.

1.2.1 Ad Hoc DFT

Ad hoc DFT is used in enhancing the testability of a design.

Some of the ad hoc techniques include:

- Minimization of redundant logic
- Addition of internal control and observation points
- Isolating the clocks from the logic
- Minimization of asynchronous logic.

Using the above methods in the design, the testability of the design is improved.

1.2.2 Structured DFT

The disadvantage of ad hoc techniques is that the addition of extra control inputs or observation outputs is required.

Structured DFT delivers a more organized and programmed method to improve the design's controllability and observability, it allows the access to internal nodes of a circuit without requiring a different external connection for each internal node to get accessed. In structured DFT the additional internal logic circuitry is used for testing first. Less number of extra connections are required to access the internal nodes. The test data must be exchanged serially or shifted in and out of the circuit. The change from normal mode to test mode can be controlled by a level test-mode flag or by a unique test clock signal.

The key advantage of structured DFT is that the test pattern generation for memory elements is not necessary.

The pattern generation is to be done only for the combinational circuits.

A structured DFT is being used to analyze the circuit by observing the inside system under control input. Many methods are available to execute this. One of the common and supportive technique is Scan design, by which the interior sequential circuitry design can be altered. Another popular technique in practice is Built-in Self-Test (BIST), which inserts the attesting mechanism inside the circuitry itself. Boundary scan is another technique; the method can likewise be utilized, which embeds the extra hardware in the chip by which there is an enhancement in testability broadly. Numerous DFT procedures have been proposed amid the years, but scan-based testing technique is the most utilized strategy.

2 Literature Survey

As the growth of VLSI industry is facing the major challenge in the shape of scaling down the transistor sizes below the 5 nm node and high attention is to be paid for the most efficient testing techniques to evaluate the applicability by testing the reliability of the chips of shrinking sizes. By adopting a scan insertion technique the sequential flops can be observed internally and controlled the dynamic system by giving control input [1].

One of the best advantages of nodes of lower technology is an enhancement of speed and the drawbacks are increased in the cost, runtime and the response diminish. So fundamentally density of the defect is forcefully included at bringing down technology nodes as for the transistor density and it is a major worry for DFT in our ASIC flow [2]. Because of these components, new fault models and scan mechanisms must be acquainted with guarantee brilliant structure [3].

The scan-based methodology is the most efficient technique to improve controllability and observability of the design under test [4]. The conversion of the memory components of a structure to scan able flip-flops is possible in scan design method. The addition of scan should not to result in an extensive area, power or performance overhead [5]. It should result in a higher yield. These scan flip-flops are associated as a serial chain called scan chains which benefits as serial shift registers. When the test mode is on, the deterministic stimuli that are put in ATE are moved inside the scan chains [6].

At that point, the circuit is once more permitted to operate in its normal mode and a signal clock is pulsed for apprising the scan cells with the updated quantities. At that point the design is made swung to test mode of operation, the refreshed quantities are moved out serially by changing over the sequential components into scan cells. The responses of the golden circuits that are kept in the ATE and will give a pass/fail decision for the circuit by comparing with the responses that are generated [7]. More test time and large ATE memory is taken by the complex SOC. Henceforth it turned into a task for utilizing customary scan-based ATPG testing mechanism, despite fact that the test coverage resulted by scan insertion strategy is estimable. The capacity to lessen a test data volume shows the efficiency of a testing mechanism.

Reduction in the test data volume and test time are achieved with the inclusion of a on-chip de-compressor and compactor. The various kinds of de-compressors used are XOR, MISR and Hybrid compactors. XOR de-compressor including MISR is one of the best de-compressors that can be utilized in the design [8].

One of the test data compression techniques are explained in [9, 10] Functional broadside tests are carried out using a commercial ATPG tool, to obtain reachable states that are useful as scan-in states. Multi-cycle tests are utilized to provide the test compaction in [9]. Likewise many test compression techniques were developed, to decrease test cost and to minimize scan test time and scan data size, Embedded Deterministic Test (EDT) is most suitable among the remaining [11]. EDT is a test model that consolidates the benefit of test vector compression with the high fault coverage in built-in self-test (BIST). Automatic test pattern generation and external

testing mechanisms are used to achieve high fault coverage. Embedded Deterministic Test should deliberately utilize the bandwidth of the testing channel to guarantee non-troublesome scaling of the designs with higher complexity [11, 12].

3 Proposals and Contribution

3.1 Scan Technique

The most effective technique in which the circuit can be modified internally to increase the observability and controllability is Scan design.

Scan based design technique is used to convert the hard-to-test sequential circuits to the easy-to-test combinational circuit. To obtain this, the sequential elements or the memory elements (flip-flops) are replaced with the scan able sequential elements called scan cells and they are stitched together to form scan registers or scan chains.

Both combinational and sequential parts can be observed in Fig. 1. The design has 3 data inputs namely A, B and C and 2 outputs designated as OUT1 and OUT2, before scan insertion in the design. With the help of primary inputs and outputs,

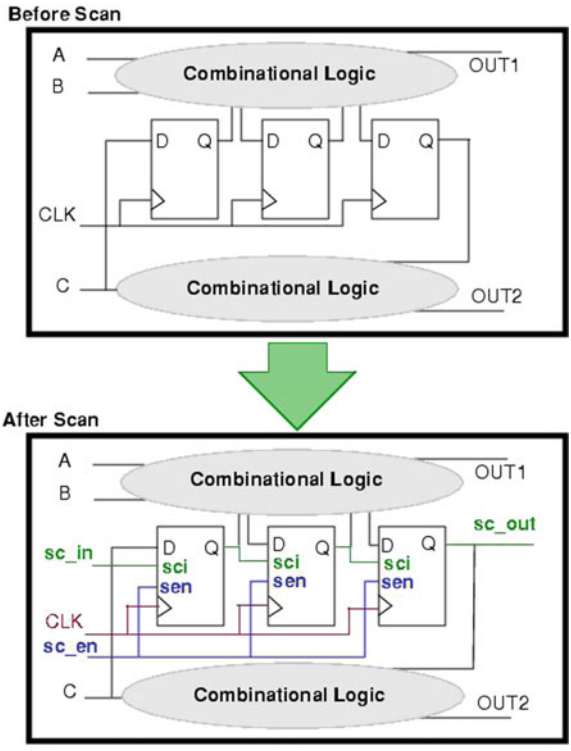

Fig. 1 Design before and after adding scan

behavior of the internal hardware can be observed to instantiate to a known state and making the design hard to control.

Post inclusion of the scan circuit, the original circuit has two extra inputs, sc_in and sc_en and one extra output, sc_out.

The scan memory components supplant the original sequential components with the goal that when sc_en is high shifting is allowed and the scan information is pursued from sc_in port.

The scan memory components are stitched into the scan chains. The primary intention is to control and observe the values in all the storage elements in design. By that we can make the fault simulation assignments and sequential circuits test generation in a straightforward manner as of the combinational circuit. Figure 2 shows the symbolic representation of a scan design.

The black rectangles in the above figure denotes the scan elements. The red lines connecting the scan cells is called scan path. The ovals represent the combinational elements.

Types of scan styles:

(1) Level-sensitive scan design (LSSD) style.
(2) Clocked-Scan scan style.
(3) Multiplexed flip-flop scan style.

The style of scan stitching used here is multiplexed flip-flop scan style:

The multiplexed flip-flop scan style utilizes a multiplexed information to offer scan shift ability. In functional mode, the scan-enable signal, which acts as the multiplexer select line, chooses the system data input. The scan data input is selected during scan shift. The scan data input originates from either the scan-input port or the scan-output pin of the previous cell in the scan chain.

The following test pins are required on a multiplexed flip-flop equivalent cell:

- Scan-input
- Scan-enable
- Scan-output (can be shared with a functional output pin).

Figure 3 shows the example of a D flip-flop before and after scan substitution, using the multiplexed flip-flop scan style shown in Fig. 4. The pin connection mappings are shown in parentheses. In this example, the scan-in pin is SI, the scan-enable pin is SE, and the scan-out pin is shared with the functional output pin Q. Table 1 gives the Signal- Type pin connections for multiplexed scan flip-flop.

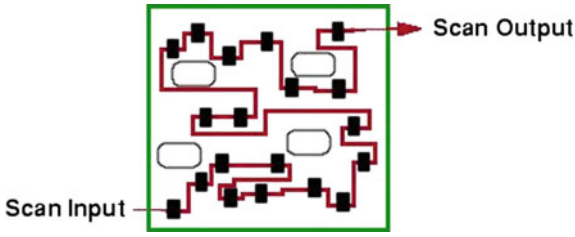

Fig. 2 Symbolic representation of scan design

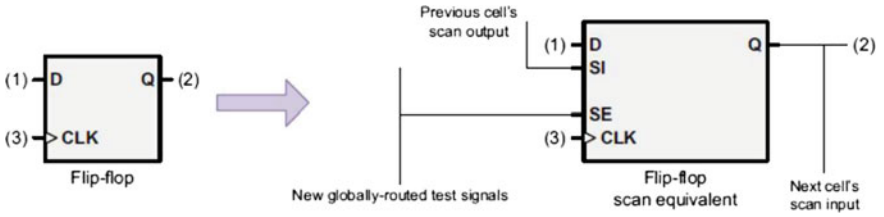

Fig. 3 D flip-flop before and after multiplexed scan cell substitution

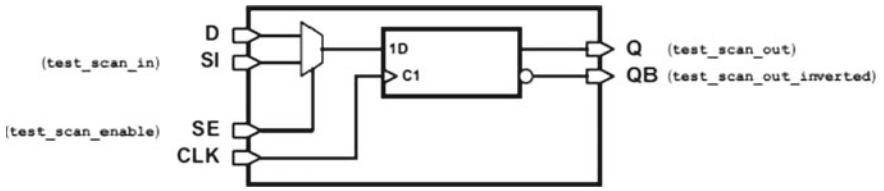

Fig. 4 Default multiplexed flip-flop scan cell

Table 1 Signal-type pin connections for multiplexed scan flip-flop

Pin	Signal type
SI	ScanDataIn
SE	ScanEnable
Q	ScanDataOut
QB	ScanDataOut

Scan chains are additionally portioned into two architectures: (1) partial scan architecture, (2) Full scan architecture. Regardless of Regardless of whether its full or partial scan, the goal is to alter the memory elements in the configuration to carry on as effectively testable combinational logic. This is finished by supplanting the sequential components (flip-flop) of a structure with a scan flop.

In Partial scan design, only a few numbers of flip-flops in the design are converted into scan flip-flops and are stitched to form a scan chain. This technique is now and then executed rather than full scan chain when certain part of the design is not used because of area restriction and performance requirement.

In full scan chain execution, every single flip-flop is substituted with a scan flip-flop. Scan flip flops when connected serially as shift registers, they combine to form scan chains with a TI (test input pin), TO (test output pin), TE (test enable pin) TCLK (test clock pin). Every single memory element is to be acted as the scan component in the full scan design method. Sequential components that are not examined are treated as black-box (cells with obscure capacity). As shown in Fig. 5, the full scan design methodology differentiates the combinational and memory elements. Here the combinational logic is related by clouds and sequential logic is related with the rectangle boxes. The scan path is depicted in the full scan design.

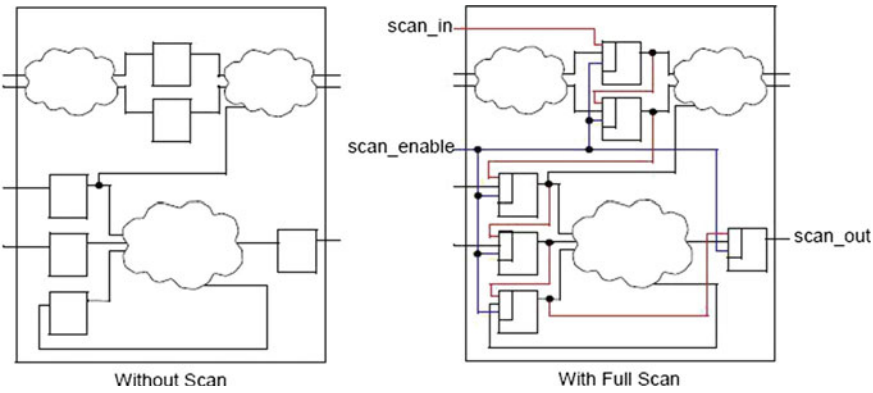

Fig. 5 Scan path in a full scan design

Inputs to the combinational blocks are applied through the pseudo primary inputs. The scan path gives the observability of the outputs from each combinational block. The high fault coverages are obtained by utilizing full scan design architecture.

Implemented the scan insertion in the benchmark circuits and the fault coverages are calculated. Power overhead is reduced by including the scan architecture in the design. The designs are simulated for test patterns.

4 Methodology

The scan circuit will operate as follows:

1. The scan operation is started by making the scan enable to 1. Shifting of the scan data is done while scan enable is made 1.
2. The input vectors are applied to the combinational blocks by making the scan clock low.
3. The outputs are obtained.
4. By making the scan enable active low the clock is pulsed so that the new values are captured into the scan cells.
5. By making the scan enable active high, the scan operation is enabled and the measured values are unloaded from the scan cells and simultaneously new values are also loaded into the scan cells.

Amid synthesis, the timing requirements are to be fulfilled. Along with the timing requirements, rise/fall prerequisites, load prerequisites and wire-load models are to be defined. Aside from these, DFT constraints are to be defined like “set_scan_configuration”, “set_dft_signal-clock”, and “set_dft_signal-reset” to define clocks and reset of the design. Include the scan style to be used as a constraint to DFT.

Figure 6 depicts the methodology flow for scan insertion in a design.

Insertion of the scan and the Test Pattern Generation are the two major steps in Automatic test pattern generation (ATPG). For scan insertion, inputs required are either the RTL Verilog or a RTL VHDL format of a design. The library files are to be added and scripting is done which contains the commands that are used for simulation. The responses from the scripting of the RTL design are scan-inserted-net-list in Verilog format and the procedure file.

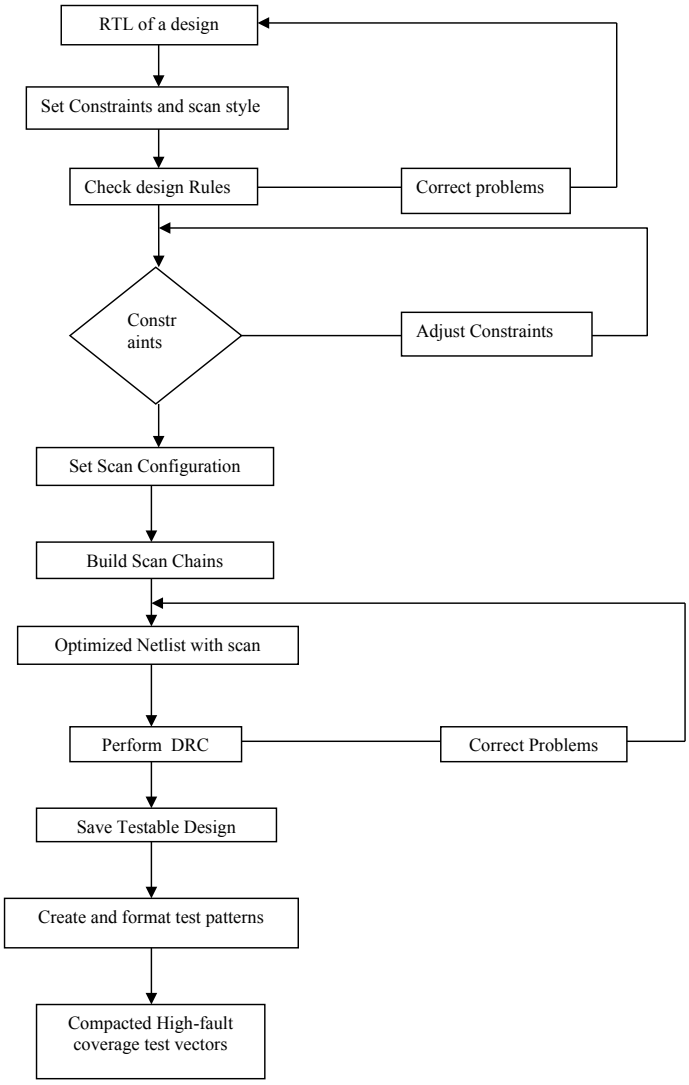

Fig. 6 Typical design flow for a design

The RTL Verilog file is read and the library files are set. The module in which DFT is to be inserted is revised. [The control signals like the scan clock, rest are initialized by their active states and periods. The scan insertion style is to be defined, here in this project multiplexed scan D flip-flop is used. Design Rule Check (DRC) is performed on the Verilog. The design rules include memory guidelines, clock standards, scan cell data order, scan ability guidelines, scan path principles, power overhead standards, timing checks etc. After the DRC, the other attributes like the number of scan chains to be inserted and the number of scan groups to be formed are to be defined. Reports about the scan chains formed and statistical results about scan flip-flops can be obtained with the help of commands. The output after scan insertion is optimized scan inserted net-list of the design.

After the scan is inserted in the given design, the next procedure is to generate patterns and calculate the test coverage. With the scan inserted net-list as input, the DRC is done to the generated net-list and the coverage is estimated. The output of this procedure will be test coverage, the total number of faults and the power can also be estimated.

5 Results and Discussion

The results obtained are tabulated in Table 2.

6 Conclusion

The power is reduced after adding the scan circuitry in the design because the original design is made controllable and observable which propagates the faults present in the design to the output. So, as the faults are being propagated the leakage current at the fault site reduces which in turn reduces the power consumption. The scan insertion

Table 2 Results showing the power and coverages

Benchmark circuit	Fault coverage after scan insertion (%)	Total power before scan insertion (uW)	Total power after scan insertion (uW)	Total number of test patterns
S27	99.06	27.1866	13.4398	8
S298	99.17	34.3015	14.89884	32
S344	98.76	85.3317	16.53884	29
S349	99.55	29.8770	17.1077	26
S382	96.88	41.7471	21.8355	41
S400	95.32	41.9806	23.5934	43
S420	95.11	46.33634	19.3880	90

in a design will allow for the faults to be detected in the combinational part of the design. To make any design testable insertion of DFT plays a major role. In this paper scan insertion and ATPG is performed on core level. The future scope for this work can be making a chip level design and perform scan pattern retargeting to improve the coverage in chip level.

References

1. Chauhan J, Panchal C, Suthar H (2017) Scan methodology and ATPG DFT techniques at lower technology node. In Proceedings of IEEE 2017 international conference on computing methodologies and communication (ICCMC)
2. Devanathan VR, Ravikumar CP, Kamakoti V (2007) Reducing soc test time and test power in hierarchical scan test: scan architecture and algorithms. In: 20th international conference on VLSI design. Held jointly with 6th international conference on embedded systems
3. Manasy M, Devika KN, Murugan S (2017) Performance analysis of Embedded Deterministic Test (EDT) on standard benchmark designs. In: 2017 IEEE international conference on technological advancements in power and energy
4. Lo HH, Lee WF, Reaz MBI, Hisham N, Shakaff AYM (2008) Design methodology to achieve good testability of VLSI chips: an industrial perspective. In: International conference on electronic design, ICED 2008. IEEE
5. Devika KN, Bhakthavatchalu R (2017) Design of reconfigurable LFSR for VLSI IC testing in ASIC and FPGA. In: 2017 international conference on communication and signal processing (ICCSP)
6. Khatri AR, Hayek A, Brcsk J (2016) ATPG method with a hybrid compaction technique for combinational digital systems. In: 2016 SAI computing conference (SAI), pp 924–930
7. Sakrappanavar P, Yellampalli S, Kothari A (2014) Comparative analysis of scan compression techniques. In: Proceedings of international conference on electronics, communication and computational engineering (ICECCE)
8. Wang N, Yao B, Lin X, Pomeranz I (2017) Functional broadside test generation using a commercial ATPG tool. In: 2017 IEEE computer society annual symposium on VLSI (ISVLSI), pp 308–313, July 2017
9. Rajski J, Tyszer J, Kassab M, Mukherjee N (2004) Embedded deterministic test. IEEE Trans Comput Aided Des Integr Circuits Syst 23(5):776–792, May 2004
10. Asokan A, Anita JP (2016) Burrows wheeler transform based test vector compression for digital circuits. Indian J Sci Technol 9(30):1–5
11. Kinsman AB, Nicolici N (2008) Embedded deterministic test exploiting care bit clustering and seed borrowing. In: 9th international symposium on quality electronic design (isqed 2008), pp 832–837
12. Harish Ram DS, Bhuvaneswari MC, Prabhu SS (2012) A novel framework for applying multiobjective GA and PSO based approaches for simultaneous area, delay, and power optimization in high level synthesis of data paths. VLSI Des

Students Head-Pose Estimation Using Partially-Latent Mixture

Marwa A. Gaheen, Ahmed A. Ewees and Mohamed Eisa

Abstract Head-pose estimation considers the most popular area of research. Estimating the head pose variation in the correct way from faces shots is an essential step for building interactive vision-based applications. In this work, a head-pose estimation system that predicts a head-pose angle for students during studying is proposed. The bounding-box method for face detection is used and a high-dimensional vector-space of faces using HOG features is adopted. A mixture of linear regression technique is applied to determine how to map high-dimensional vector-space onto bounding-box shifts and both head-pose parameters. The performance of the proposed system is evaluated and checked using the absolute error between the predicted angle and the target angle, after that, the mean absolute error (MAE) is computed along with standard deviation (STD).

Keywords Estimation of head-pose · Image processing · Face detection · Mixture of linear regression

1 Introduction

The estimation of Head-pose is an essential research trend in the field of computer vision because it is an important step in many real-time systems. It considered the first layer in several computer vision applications, includes face recognition, driver monitoring, gaze-recognition, recognition of behavioral analytics [1] such as discrimination social interactions [2], identifying target of interest [3–6], focus of attention [7], and identifying social groups [8]. In addition, it is applied for many other systems in robotics and biometrics recognition.

In computer vision, the process which deduces the face direction or face angle from an image is called face-pose estimation [9]. The face, in most cases, is represented as

M. A. Gaheen · A. A. Ewees (✉)
Computer Department, Damietta University, Damietta, Egypt
e-mail: ewees@du.edu.eg

M. Eisa
Computer Department, Portsaid University, Portsaid, Egypt

© Springer Nature Singapore Pte Ltd. 2020

T. Hitendra Sarma et al. (eds.), *Emerging Trends in Electrical, Communications, and Information Technologies*, Lecture Notes in Electrical Engineering 569,
https://doi.org/10.1007/978-981-13-8942-9_61

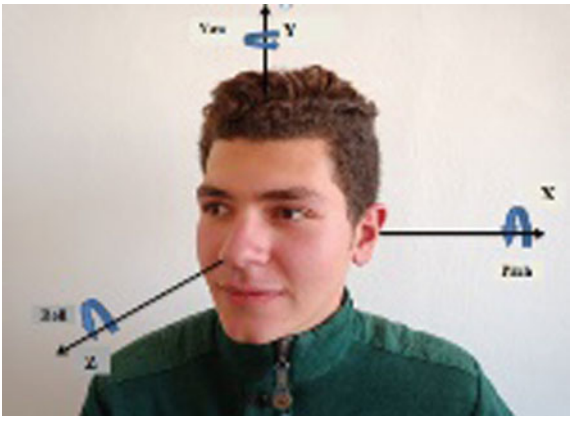

Fig. 1 The three angles to estimate the head-pose

an object with three degrees of freedom in the pose described through three angles (i.e. pitch, roll, and yaw). The pitch angle is appeared if the head moves up and down (the X-bar); the yaw angle is appeared if head moves left and right (the Y-bar); whereas, the roll angle is detected if the head is tilt (the Z-bar); as illustrated in Fig. 1.

For the past decades, head-pose estimation has been very well investigated and many powerful approaches have been developed. These approaches could be grouped into four categories, as follows:

(a) Regression Techniques:

They train from features space and estimate the pose variation from this space. Among these techniques: support vector regression (SVR) [10], Gaussian process regression (GPR) [11], Supervised Local Subspace Learning (SL2) [12], Adaptive Neuro-Fuzzy Inference System [13], and partial least squares (PLS) [14].

(b) Classification Techniques:

They divide the images dataset into many categories by defining discrete pose angles, as well, many classifiers are also trained for all categories using the one-to-all method [15]. These techniques include support vector machines (SVM), k-Nearest Neighbor (kNN), and Kernel Linear Discriminant Analysis (KLDA). Zavan et al. [16] developed a methodology, SVM-NosePose, based on SVM. They evaluated the repeatability by testing it on four unconstrained datasets. The results showed that SVM-NosePose approach is provided good results against other algorithms. These methods have some disadvantages such as they provide a separate one-dimensional of pose estimation and they suffer from over-fitting in some cases due to their sensitivity to duplicated and irrelevant values [17–23].

(c) Manifold Embedding Techniques:

Manifold embedding techniques assume that pose variations line on a low-dimensional diverse embedded in the high-dimensional feature domain. These techniques cannot employ the implicit special learning of the dataset as they only concentrate on maintaining the intra class geometric attributes of the diverse embedded in

the high-dimensional domain. Yong et al. [24] estimated a head-pose by supervised locality discriminant manifold learning (SLDML), they tried to search for data's discriminant information and geometric structure. The experiments proved good results in estimating the variation of head-pose.

(d) Deformable Model-Based Techniques:

Among the deformable model techniques that apply to estimate the variation of head-pose are Active Shape Models (ASMs), Tree Structured Deformable Part Models (TSDPMs) and Constrained Local Models (CLMs). The authors of [25] proposed a technique to estimate head-pose using ASM as well as stereo vision. They used ASM and stereo matching to detect some of facial marks in the experimental dataset. While, the authors of [26] introduced a method for estimating head-pose using noisy images in real-world; they tried to detect the topological variations using global mixtures. The proposed method showed superior results and proved good accuracy.

2 Materials and Methods

Our system consisted of four main phases as illustrated in Fig. 2.

2.1 Face Detection

Viola-jones [27] algorithm is used for detect faces from photos. We use the profile-view detection to detect face pose by using bounding-box as shown in Fig. 3.

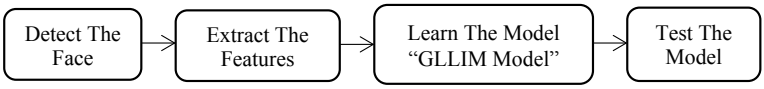

Fig. 2 The overall of our system phases

Fig. 3 Shows the results of face detection using bounding box

2.2 Feature Extraction

After applying pre-processing to the bounding box a Histogram of Oriented Gradient (HOG) descriptor is used for extract features from images as it provides excellent performance relative to other existing feature sets including wavelets [28].

Basically, the HOG descriptor divides the image into many cells where a histogram counts the occurrences of pixels' orientations given by their gradients. Finally, the HOG descriptor is built with combination of these histograms. The steps for HOG descriptor for feature extraction are discussed as following:

1. Compute the derivative in the horizontal and vertical directions: is denoted with G_x and G_y, an imfilter over the input image I is performed. After dividing the image into: 32×32, 16×16 and 8×8 for cell resolution, with block resolution 2×2 cells. See Fig. 4.
2. Compute the magnitude $|\nabla I(x, y)|$ and the orientation $\theta(x, y)$ of the gradient. The magnitude and the gradients are calculating by:

$$|\nabla I(x, y)| = \sqrt{G_x^2 + G_y^2}, \theta(x, y) = \arctan\left(\frac{G_x}{G_y}\right)$$

3. Quantize into bins orientation: The gradient angles in each cell are quantized into a number of bins B of regularly spaced orientations and the magnitudes for identical orientations are accumulated into a histogram. Number of orientation bins: 8. For each pixel with coordinates (x, y) it is determined which of the B orientations are the closest to its orientation $\theta(x, y)$ and then its magnitude $|\nabla I(x, y)|$ is added to the corresponding bin. The number of bins B used indicates the length of the histogram vector for each cell.
4. Normalize descriptor: after calculating the histogram vectors a normalization step is used by calculating V which is the vector to be normalized and ϵ is a small positive value needed when evaluating empty gradients: $V_n = \frac{V}{\sqrt{\|V\|^2 + \epsilon^2}}$

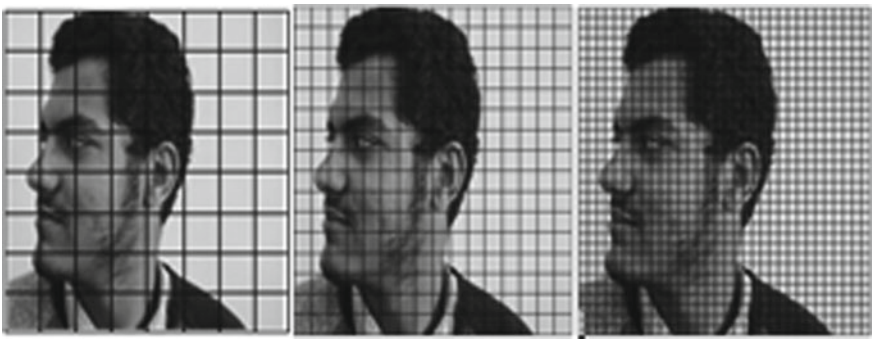

Fig. 4 Resolution of the cell 32×32, 16×16 *and* 8×8

The output of feature extraction phase is a high-dimensional feature vector $y \in R^D$, with $D = 1888$, which formed from stacking the three HOG descriptors.

2.3 Learn Phase

The EM algorithm [29] that predicts the parameters of the inverse regression with partially latent output (GLLIM and Hybrid-GLLIM) was used to learn the models for the following reasons: It overcomes the difficulties of high-dimensional to low-dimensional regression in a single process, thus we can dispense with the dimensionality reduction pre-processing phase. The method includes latent variable augmentation. More exactly, the response (output) variables are only partially observed such that the regression function can be trained with partially observed outputs.

The regression task formation of learning a mapping from the regressor (input variable) onto a response variable. Thus it is easy and robust to compute the response of a test point. While this issue has been studied widely, the challenge still where the regressor (input variable) is of high dimension, and the response (output variable) may not be completely observed. The high-dimensional to low-dimensional (or high-to-low) regression is still a problematic, and generally implemented in two disconnected steps: dimensionality reduction and then regression.

The face-pose angles estimation and the bounding box shift are achieved iteratively (see Algorithm 1) with the following steps.

- The current bounding-box location $u \in R^2$ is used to build a high-dimensional feature vector y.
- The high-dimensional feature vector is used to predict a face-pose x_h and the bound-box shift x_b.
- Update the bounding-box location to build an updated feature vector and to predict an updated face-pose and a new bounding-box shift.

Algorithm 1: Iterative prediction for face-pose estimation [29]

Require: location of bounding-box u and parameters of forward model θ^*

1. **Procedure** Face-Pose Estimation (u, θ^*)
2. **Repeat**
3. Build y from location of current bounding-box u
4. Predict $x = [x_h; x_b]$ from y using $\hat{x} = f(\hat{y})\ with\ f(y) = E[x|y; \theta^*] = \sum_{k=1}^{K} v_k^* (A_k^* y + b_k^*)$
5. Update the location of bounding-box $u = u + x_b$
6. **Until** $\|x_b\| \leq \varepsilon$
7. **Return** Face-pose x_h and bounding-box location x_b
8. **End procedure**

The EM for GLLIM and Hybrid GLLIM algorithm that used to predict the head pose angle with the following steps:

1. E-W-step: Given the estimates of the current parameter $\theta^{(i-1)}$, the posterior probability $r_{w|z}^{(i)}$ is fully defined by the distributions $p(w_n|z_n = k, t_n, y_n; \theta^{(i-1)})$ for all n and k, which can be Gaussian. Their covariance matrices $s_k^{w(i)}$ and vector means $\mu_{nk}^{w(i)}$ are given by

$$s_k^{w(i)} = \left(I + A_k^{w(i-1)T} \sum\nolimits_k^{(i-1)-1} A_k^{w(i-1)}\right) \tag{1}$$

$$\mu_{nk}^{w(i)} = S_k^{w(i)} A_k^{w(i-1)T} \sum_k^{(i-1)-1} \times \left(y_n - A_k^{t(i-1)} t_n - b_k^{(i-1)}\right) \tag{2}$$

2. E-Z-step: determine the posterior probability $r_z^{(i)}$ by:

$$r_{nk}^{(i)} = p\,(z_n = k|t_n,\, y_n,\, \theta^{(i-1)}) = \frac{\pi_k^{(i-1)} p(y_n, t_n, |z_n = k; \theta^{(i-1)})}{\sum_{j=1}^{k} \pi_j^{(i-1)} p(y_n, t_n, |z_n = j; \theta^{(i-1)})} \tag{3}$$

For all n and k, where

$$p\left(y_n, t_n, |z_n = k; \theta^{(i-1)}\right) = N\left(t_n; c_k^t, T_k^t\right) N\left(y_n; d_k, \Phi_k\right), \tag{4}$$

with:

$$d_k = A_k^{t(i-1)} t_n + b_k^{(i-1)}$$

$$\Phi_k = A_k^{w(i-1)} A_k^{w(i-1)} + \sum_k^{(i-1)}$$

Then the maximization can be applied by the posterior probabilities $r_{nk}^{(i)}$ and the statistics $\mu_{nk}^{w(i)}$ and $S_k^{w(i)}$. The M-step can be splitted into two steps.

3. M-GMM-step: the parameters $\pi_k^{(i)}$, $c_k^{t(I)}$, $T_k^{t(i)}$ updating and correspond to those of a standard Gaussian mixture model on, so that:

$$C_k^{t(i)} = \sum_{n=1}^{N} p_{nk}^{(i)} t_{n,} \tag{5}$$

$$T_k^{t(i)} = \sum_{n=1}^{N} p_{nk}^{(i)} \left(t_n - c_k^{t(i)}\right)\left(t_n - c_k^{t(i)}\right) t \tag{6}$$

$$\pi_k^{(i)} = \frac{\sum_{n=1}^{N} r_{nk}^{(i)}}{N} \tag{7}$$

4. M-mapping-step: the parameters $\{A_k, b_k, \sum_k\}_{k=1}^{K}$ updating is in closed-form. The affine transformation matrix is refreshed by:

$$A_k^{(i)} = Y_k^{(i)} X_k^{(i)T} (S_k^{x(i)} + X_k^{(i)} X_k^{(i)T})^{-1} \tag{8}$$

where:

$$X_k^{(i)} = \left(\sqrt{p_{1k}^{(i)}} \left(x_{1k}^{(i)} - x_k^{(i)} \right), \ldots.., \sqrt{p_{nk}^{(i)}} \left(x_{nk}^{(i)} - x_k^{(i)} \right) \right),$$

$$Y_k^{(i)} = \left(\sqrt{p_{1k}^{(i)}} \left(y_1 - y_k^{(i)} \right), \ldots.., \sqrt{p_{nk}^{(i)}} \left(y_N - y_k^{(i)} \right) \right),$$

$$x_k^{(i)} = \sum_{n=1}^{N} p_{nk}^{(i)} x_{nk}^{(i)}, \quad y_k^{(i)} = \sum_{n=1}^{N} p_{nk}^{(i)} y_n, \quad S_k^{x(i)} = \begin{pmatrix} 0 & 0 \\ 0 & S_k^{w(i)} \end{pmatrix}.$$

The intercept parameters are updated with:

$$b_k^{(i)} = \sum_{n=1}^{N} p_{nk}^{(i)} \left(y_n - A_k^{(i)} x_{nk}^{(i)} \right). \tag{9}$$

The noise covariance matrices are updated with:

$$\sum_k^{(i)} = \text{diag} \left\{ A_k^{w(i)} S_k^{w(i)} A_k^{w(i)T} + \sum_{n=1}^{N} p_{nk}^{(i)} \left(y_n A_k^{(i)} x_{nk}^{(i)} b_k^{(i)} \right) \left(y_n - A_k^{(i)} x_{nk}^{(i)} - b_k^{(i)} \right)^T \right\} \tag{10}$$

where the diag $\{.\}$ operator sets all the off-diagonal entries to 0.

5. Initialization: Initial parameters $\theta^{(0)}$ are gained using fitting the GMM with K components to the joint output-input training dataset $\{t_n, y_n\}_{n=1}^{N}$.

2.4 Test Phase

The test phase is applied over 30% of the dataset and the performance measures that used to evaluate the system are the absolute error between the predicted results and the target value was evaluated, and then computes the mean absolute error (MAE) for $\text{MAE} = \frac{1}{n} \sum_{i=1}^{n} |x_i - x|$ where n is number of error, $|x_i - x|$ is the absolute error. And standard deviation (STD) for $\sigma = \sqrt{\frac{1}{N} \sum_{i=1}^{N} (x_i - \mu)^2}$ where N number of the

data points in population, x is the value of the dataset and μ is mean of the data. The mean of these measures is calculated after several runs.

3 Experiment

This section contains the dataset preparation details, Performance measures, and the steps of the experiment.

3.1 Dataset Preparation

The dataset consists of 90 images of 10 students each student has 9 images with different head poses (±90+0, +0±90, +60±90, −60±90 and +0+0). All the images were captured with the same background. Figure 5 shows the example of a dataset for some student with different poses.

3.2 Performance Measures

The performance measures that used to evaluate the system are the absolute error between the predicted results and the target value was evaluated, and then compute MAE and STD over several runs.

Fig. 5 Example of a dataset for some student with different head poses

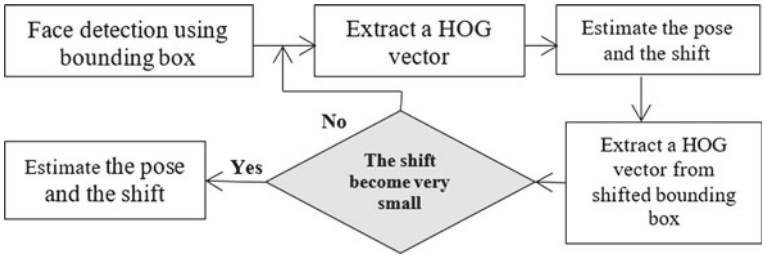

Fig. 6 The main steps for prediction head pose angle

3.3 Experiment Steps

Our system aims to predict head pose with different angles for student during studying. After we prepared our dataset for different poses we tested it with our system to evaluate its performance. Figure 6 shows main steps for prediction head pose angle.

4 Results and Discussion

To evaluate the quality of the results of our system we carried out several experiments to determine the optimal number of K which corresponds to the number of affine mappings. We used the (MAE) criteria. We learned several models for different values of K using our dataset to obtain the model that yields low MAE head-pose angle.

Figure 7 shows the results of MAE in degrees for pitch and yaw of head-pose estimation as a function of K for the students' dataset. It shows that the number of affine mapping K increases from k = 1 to k = 30 and the MAE scores decreases, then the curve slopes become almost horizontal. It can be explained that the model is not flexible enough to take into account the apparently non-linear mapping between

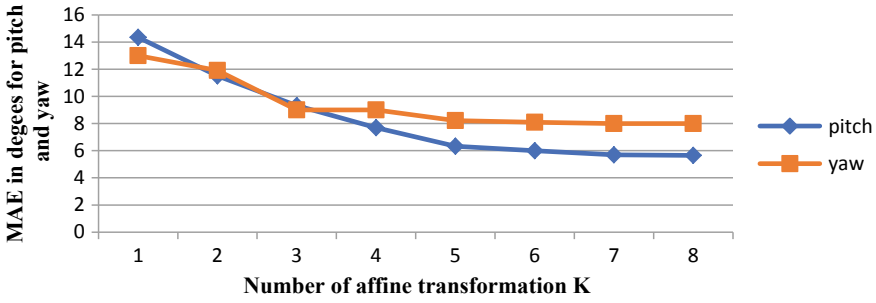

Fig. 7 MAE for pitch and yaw as a function of Number of affine transformation K

HOG features and head-pose parameters when K < 50 and the large value of K increases the model accuracy.

We used MAE and STD to evaluate the estimation of each head pose angle. Table 1 represents the results of a head-pose estimation obtained with students' dataset for each head pose angle.

The best results were in the angles (+0+0), (+0+90), (+60−90) and (+90+0). And the lowest results were in (−90+0), (−60−90), (−60+90), (+0−90), (+60+90) because of the nature of image captured in the learning environment (Fig. 8).

The proposed method was compared with the following head-pose estimation methods: the neural-network based methods of [30], and the regression methods: GPR [31], PLS [32] and SVR [33]. As shown from Table 2 that the proposed method gets the best MAE for pitch (5.66) and yaw (8) in head-pose Estimation (Fig. 9).

Table 1 The MAE and STD results for each head pose angle

Head pose angle	Pitch		Yaw	
	MAE	STD	MAE	STD
(−90+0)	12	28.983	18	37.95
(−60−90)	18	28.98	27	43.474
(−60+90)	12	25.298	18	37.947
(+0−90)	6	18.947	**0**	**0**
(+0+0)	**0**	**0**	**0**	**0**
(+0+90)	**0**	**0**	**0**	**0**
(+60−90)	**0**	**0**	**0**	**0**
(+90+0)	**0**	**0**	**0**	**0**
(+60+90)	3	9.487	9	28.46

Bold indicates the smallest error and the best results

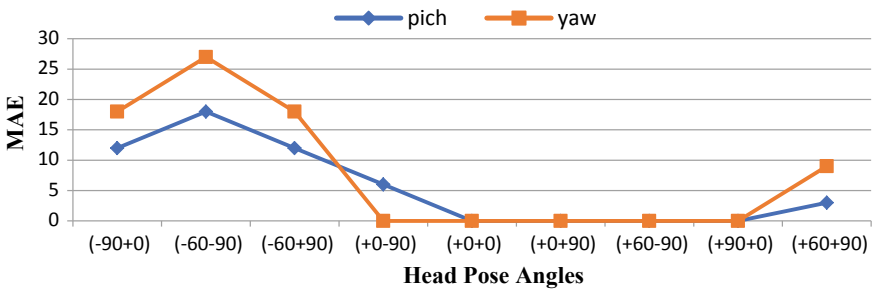

Fig. 8 MAE results of the head pose angles estimation

Table 2 MAE in degrees obtained by various head-pose methods, regression methods and our proposed method using students' head-pose dataset

Method	Pitch	Yaw
Neural-network	9.7	9.5
GPR	11.94	15.04
PLS	12.25	13.38
SVR	11.25	12.82
The proposed method	5.66	8

Fig. 9 Some results after applying the system

5 Conclusion

Estimating the head-pose variation in the correct way from faces' shots is an essential step for building interactive vision-based systems. In this paper, we introduced a model for estimating the variation of head-pose. It bases on a mixture of linear regression model which maps high-dimensional HOG-based method on the low-dimensional domain of head-poses which predict ahead pose angle for students during studying. The bounding-box method was used to detect faces. We tested and evaluated our model using absolute error between the predicted results and the target results then the MAE and standard deviation were computed as measures of performance of the model, our model proved good results in estimating the variation of the human head-pose.

References

1. El Aziz MA, Ewees AA, Hassanien AE (2018) Multi-objective whale optimization algorithm for content-based image retrieval. In: Multimedia tools and applications. pp 1–38
2. Gaschler A, Jentzsch, S, Giuliani M, Huth, K, de Ruiter J, Knoll A (2012) Social behavior recognition using body posture and head pose for human-robot interaction. In: IEEE/RSJ International conference on intelligent robots and systems (IROS). pp 2128–2133
3. Parks D, Borji A, Itti L (2015) Augmented saliency model using automatic 3d head pose detection and learned gaze following in natural scenes. Vision Res 113–126
4. El Aziz MA, Ewees AA, Hassanien AE (2016) Hybrid swarms optimization based image segmentation. In: Hybrid soft computing for image segmentation. pp 1–21. https://doi.org/10.1007/978-3-319-47223-2
5. El Aziz MA et al (2018) Multi-objective whale optimization algorithm for multilevel thresholding segmentation. In: Advances in soft computing and machine learning in image processing. Springer, Cham, pp 23–39
6. El Aziz MA, Ewees AA, Hassanien AE (2017) Whale optimization algorithm and moth-flame optimization for multilevel thresholding image segmentation. Expert Sys Appl 83:242–256
7. Subramanian R, Yan Y, Staiano J, Lanz O, Sebe N (2013) On the relationship between head pose, social attention and personality prediction for unstructured and dynamic group interactions. In: Proceedings of the 15th ACM on international conference on multimodal interaction. pp 3–10
8. Leach M, Baxter R, Robertson N, Sparks E (2014) Detecting social groups in crowded surveillance videos using visual attention. In: IEEE conference on computer vision and pattern recognition workshops (CVPRW). pp 467–473
9. Anwar S, Al-Hamadi A, Ahmed GH (2015) Head pose estimation on top of haar-like face detection: a study using the kinect sensor. Sensors 20945–20966
10. Murphy-Chutorian E, Doshi A, Trivedi M (2007) Head pose estimation for driver assistance systems: a robust algorithm and experimental evaluation. In: IEEE intelligent transportation systems conference. pp 709–714
11. Ji H, Liu R, Su F, Su Z, Tian Y (2011) Robust head pose estimation via convex regularized sparse regression. In: 18th IEEE international conference on image processing (ICIP). pp 3617–3620
12. Huang D, Storer M, De la Torre F, Bischof H (2011) Supervised local subspace learning for continuous head pose estimation. In: CVPR. pp 2921–2928
13. Ewees AA, Elaziz MA, Improved adaptive neuro-fuzzy inference system using gray wolf optimization: a case study in predicting biochar yield. J Intell Syst. https://doi.org/10.1515/jisys-2017-0641

14. Haj MA, Gonzalez J, Davis LS (2012) On partial least squares in head pose estimation: how to simultaneously deal with misalignment. In: CVPR. pp 2602–2609
15. Wu J, Trivedi MM (2008) A two-stage head pose estimation framework and evaluation. Pattern Recognit 41(3):1138–1158
16. Zavan FHB, Nascimento ACP, Bellon ORP, Silva L (2016) Nosepose: a competitive, landmark-free methodology for head pose estimation in the wild. In: Conference on graphics, patterns and images—W. Face processing
17. Peng X, Huang J, Hu Q, Dimitris M (2015) Three-dimensional head pose estimation in-the-wild. In: 11th IEEE international conference and workshops on automatic face and gesture recognition (FG)
18. Houssein EH, Ewees AA, ElAziz MA (2018) Improving twin support vector machine based on hybrid swarm optimizer for heartbeat classification. Pattern Recognit Image Anal 28(2):243–253
19. Ibrahim RA et al (2018) Galaxy images classification using hybrid brain storm optimization with moth flame optimization. J Astron Telesc Instrum Syst 4(3):038001
20. Ewees AA, Sahlol AT, Amasha MA (2017) A bio-inspired moth-flame optimization algorithm for Arabic handwritten letter recognition. In: 2017 international conference on control, artificial intelligence, robotics and optimization (ICCAIRO). IEEE, 2017
21. Ibrahim RA et al (2018) Improved salp swarm algorithm based on particle swarm optimization for feature selection. J Ambient Intell Humaniz Comput 1–15. https://doi.org/10.1007/s12652-018-1031-9
22. Ewees AA, Sahlol AT (2018) Bio-inspired optimization algorithms for improving artificial neural networks: a case study on handwritten letter recognition. In: Computational linguistics, speech and image processing for Arabic language, vol 4, p 249
23. Ewees AA, El Aziz MA, Hassanien AE (2017) Chaotic multi-verse optimizer-based feature selection. In: Neural computing and applications. pp 1–16. https://doi.org/10.1007/s00521-017-3131-4
24. Yong L, Qicong W, Jiang Y (2014) Supervised locality discriminant manifold learning for head pose estimation. In: Knowledge-based systems. Elsevier, pp 126–135
25. Chen Y, Fu M, Yang Y, Song W (2014) A method of head pose estimation based on active shape model and stereo vision. In: 33rd Chinese control conference (CCC), IEEE
26. Zhu X, Ramanan D (2012) Face detection, pose estimation, and landmark localization in the wild. In: CVPR. pp 2879–2886
27. Viola P, Jones M (2001) Rapid object detection using a boosted cascade of simple features. In: IEEE conference on computer vision and pattern recognition. pp 511–518
28. Viola P, Jones MJ, Snow D (2003) Detecting pedestrians using patterns of motion and appearance. In: The 9th ICCV, Nice, France. pp 734–741
29. Drouard V, Horaud R, Deleforge A, Ba S, Evangelidis G (2016) Robust head-pose estimation based on partially latent mixture of linear regressions. arXiv:1603.09732v3
30. Stiefelhagen R, Estimating head pose with neural networks—results on the pointing 04ICPR workshop evaluation data. In: IEEE international conference on pattern recognition pointing04 workshop, August 2004
31. Rasmussen CE (2006) Gaussian processes for machine learning. MIT Press
32. Abdi H (2003) Partial least square regression (PLS regression). In: Encyclopedia for research methods for the social sciences. pp 792–795
33. Smola AJ, Scholkopf B (2004) A tutorial on support vector regression. Stat Comput 14(3):199–222

Ensembling of Non-linear SVM Models with Partial Least Square for Diabetes Prediction

Gaurav Bansal and Manisha Singla

Abstract This paper focuses on the improved prediction of diabetes over the very famous Pima Indians dataset. This work focuses on the ensembled result of Non-linear support vector machines (SVM) aggregated with partial least square classifier (PLS). The idea behind this is to get the advantage of kernel transformations from the Non-Linear methods of SVM and dimensionality reduction from PLS. This unique combination makes the ensembled classifier efficient which can be observed after comparing it with the previous classifiers. So this method is also compared with the leading classifiers like decision tree, neural network, linear SVM and also with the ensembled models of these classifiers by applying majority voting. In all the cases, the proposed method is doing better than the rest of the methods.

Keywords Machine learning · Support vector machine · Non-linear SVM · Partial least square classifier · Majority voting

1 Introduction

Machine learning is spreading its roots in every field of medical science and that too very quickly. People also started believing in the results of data science. It becomes our prior duty to deliver the most accurate results possible so that their faith remains unaltered in data science. When it comes to medical diagnosis, accuracy is the one which is most desirable as this is the field where any kind of risk cannot be tolerated. In machine learning, there are two ensemble methods used namely voting and averaging [1]. Voting is the ensemble method which is generally used for classification and averaging is the method which is preferred for regression. Both the methods require multiple classification or regression models to be built a prior in the very first step.

G. Bansal (✉)
Department of Computer Science & Engineering, Punjab Engineering College, Chandigarh, India
e-mail: ygauravb@gmail.com

M. Singla
Department of Computer Science & Engineering, IIT (BHU), Varanasi, India
e-mail: manishasigla.rs.cse17@itbhu.ac.in

© Springer Nature Singapore Pte Ltd. 2020

T. Hitendra Sarma et al. (eds.), *Emerging Trends in Electrical, Communications, and Information Technologies*, Lecture Notes in Electrical Engineering 569,
https://doi.org/10.1007/978-981-13-8942-9_62

This is the common step in both the methods and after this step, the role of voting and averaging comes into play according to classification and regression respectively. According to multiple classification models in the first step, every model generates an output (prediction) corresponding to the actual values. Majority voting ensembles the outputs or predicted columns of these models in such a manner that the final output is the one which receives more than half of the votes of predicted columns. If majority voting fails in getting more than half of the votes of predicted columns, it fails at that point. There are various recent applications in which majority voting is used like in credit card fraud detection [2]. So it is generally favourable when there is odd number of multiple classification models. Averaging is the method which is used for regression. The result of multiple classification models is averaged to get the final output. It generally reduces overfitting and helps in getting a better regression model than the previous. As this work deals with the problem of diabetes prediction (classification problem), majority voting is used. So this paper stresses on the diabetes prediction using majority voting by ensembling of non- linear SVM with the PLS model. This method is tested upon the very famous PIMA Indians Dataset which is taken from UCI machine learning repository. In this paper, accuracy of our work is compared with the bagged models, boosted models and various other models like decision tree, Neural network etc.

2 Background

As dataset consists of various instances and their corresponding class labels, but both the nature of instances and class labels cannot clarify that the data is linearly separable or not. If non linearity provides a better accuracy in prediction, then it is considered that the dataset is non-linearly separable. This is one way of finding out whether the data is linearly separable or not. In this work, it is observed that non-linear SVM performs better than linear SVM.

2.1 Support Vector Machine (SVM)

Classifying data is the common task to be performed in machine learning. SVM is the model which can be used for classification in the supervised learning. SVM model separates the classes on the basis of hyperplane [3]. The equation of the hyperplane is as shown below:

$$g(x) = w^T x + b \tag{1}$$

where w is the weight vector, x is the input vector and b is the bias term. If the problem is binary class classification problem than the two classes are namely a $+$ class and a $-$class, then if

$$g(x_1) = w^t x_1 + b > 0 \tag{2}$$

Equation 2 implies that x_i belongs to +class while if

$$g(x_1) = w^t x_1 + b < 0 \tag{3}$$

Equation 3 implies that x_1 belongs to −class and if $w^t x_1 + b = 0$, it implies that *x1* lies on the hyperplane.

There are two types of SVM namely Linear SVM and Non-Linear SVMs.

2.2 Linear SVM

Linear SVM is the SVM where the hyperplane separating the two classes is a linear line such that one class lies above the hyperplane and the other class lies below the hyperplane.

2.3 Non-linear SVM

There are various classifiers which provide an easy way of mapping the data into high dimensional space. SVM is the classifier which comes in this category. SVM provides this mapping using the kernel trick which is not actually a trick but involves some mathematics for the mapping of these data points. A kernel function is a function that is actually a dot product in the high dimensional feature space. The most attracted families of kernels are radial basis kernels and the polynomial kernels [4]. In this work, we have studied all the families of kernels including radial basis, polynomial, Spline, linear kernel etc. Details of some of its families are described below:

a. Radial Basis (Gaussian) Kernel [4]:

The Radial basis kernel over two dimensions x and y is as shown below in Eq. 4.

$$K(x, y) = \exp\left(-\frac{||x - y||^2}{2\sigma^2}\right) \tag{4}$$

where $||x - y||^2$ is squared Euclidean distance between the two features and σ is the free parameter.

b. Polynomial kernel [4]:

It is used to represent the similarity of a vector in a feature space over polynomials of the original variables. For degree k polynomial, the polynomial kernel is as shown below in Eq. 5.

$$K(x, y) = (x^T y + c)^k \tag{5}$$

where x and y are the dimensions in the input space which are computed using training or test samples and c is the free parameter and the kernel is considered as homogeneous when the value of c is 0.

c. Spline Kernel [4]:

Spline kernel is considered as a piecewise cubic polynomial. Spline kernel is shown below in Eq. 6.

$$K(x, y) = 1 + xy + xy\, min(x, y) - \frac{x + y}{2}\min(x + y)^2 + \frac{1}{3}min(x, y)^3 \tag{6}$$

2.4 *Partial Least Square (PLS)*

PLS can be used for both classification and regression datasets. Classification with PLS is termed as PLS-DA where DA stands for discriminant analysis. PLS dimensional reduction is famous for giving better prediction accuracy in classification especially when it is high dimensional data [5]. Recently PLS was also combined with NN for the prediction analysis [6].

2.5 *Recursive Feature Elimination (RFE) [7]*

Right feature selection can make a huge difference in performance of the model which can vary from average to best. So it is very important to check for important features in the dataset, rank the features and select the best features from the dataset. For ranking the feature, Linear Vector Quantization (LVQ) is used which is further used to measure the variable importance and to plot accordingly [7]. Algorithm 1 is feature selection based on recursive feature elimination [7].

WE have also used Decision tree (DT) and Neural networks in this work. These are used here for comparison purposes only and can be referred from [8, 9] respectively.

3 Literature Survey

This section describes the work done in the field of diabetes prediction which is related to various machine learning techniques used.

Humphrey et al. [10] used in their work a validation based framework for artificial neural networks. They used a validation based R package *validann* which is needed for the consistent and user friendly implementation of various validation methods.

Gupta et al. [11] described in their work about optimal decision trees which is used in settling down the approximability of the problem of minimizing the expected cost to a tight O (log m) approximation algorithm. Also for the Travelling Sales Person problem, they give a poly-algorithmic approximation algorithm which is best and similar to the Steiner tree problem.

Gandhi et al. [12] proposed a unique technique for the prediction of diabetes for the commonly used dataset of Pima Indians. In this work, SVM classifier has been used to predict the patients who are suffering from onset of diabetes.

Algorithm 1 (Recursive Feature Elimination) [8]

1. Train the classifier using all the predictors.
2. Evaluate performance of the above model.
3. Evaluate importance of the model and rank them.
4. For each subset size sub_i $i = 1, \ldots, sub$ **do**
   Keep the sub_i which are most important of all the variables.
   Train the classifier on the training set using sub_i predictors.
   Evaluate performance of the above model.
   Re-evaluate ranking [Optional].
5. End
6. Measure performance according to sub_i .
7. Find appropriate number of predictors.
8. Make use of corresponding model of sub_i.

Before training the model, feature selection is also performed using F-score and k-mean clustering methods so as to obtain optimal set of features. For performing data normalization, Z-Normalization is used in this paper. Accuracy, sensitivity and specificity are the evaluation criteria used for calculating the performance of the SVM classifier. Feature selection and data normalization helped in improving the performance of SVM classifier. High accuracy of proposed technique can be considered as a good candidate for disease diagnosis [12].

Kavitha et al. [13] presented in their work a new approach which works by selecting the important features from the Tumor type dataset. After extracting these important features, classification is done using Support Vector Machine (SVM). Feature selection is done using RFE algorithm which not only helped in improving the accuracy but also in reducing the computation time. Before RFE algorithm, correlation based feature is also applied in their work using FBCF (Fast Correlation Based Filter) to get the correlated genes.

Joshi and Alehegn [14] combined the various methods and techniques of some well-known algorithms like Naïve Bayes, KNN, J48 and Random forest. In this work, these models are used to form a hybrid model which is further used to increase the accuracy and performance of the system. Pima Indians dataset is used and as a result the final accuracy obtained is much higher than the accuracies of individual classifiers. From this work, authors concluded that the ensembled hybrid model works better than the individual classifiers.

Wang and Feng [15] presented in their work a very effective technique of detecting outliers using majority voting. The key component of their work is the use of majority voting scheme that can easily cut the connection between the scanned surface and the non-isolated outlier cluster so that non-isolated outliers can be separated. They also proposed an expandable boundary criterion which is used to eliminate isolated outliers and protect valid point clusters more easily than the cluster size threshold.

4 Methodology

The framework for the proposed approach is shown in Fig. 1.

In this work, the best models are selected for the above mentioned Pima Indians dataset on the basis of literature survey. The features for the models are selected by using RFE algorithm [16]. The accuracies of various classifiers are computed and then the classifiers are arranged in descending order so that the top 3 models can be selected for the dataset. The models selected are SVM including Radial basis kernel and the spline method and the third method is PLS. The next step of our work comprises of ensembling these methods using majority voting. Now this result is compared with the other ensembling techniques like Bagging with Generalized Linear Model (GLM) and Generalize Linear Additive Model Boost (GAM Boost).

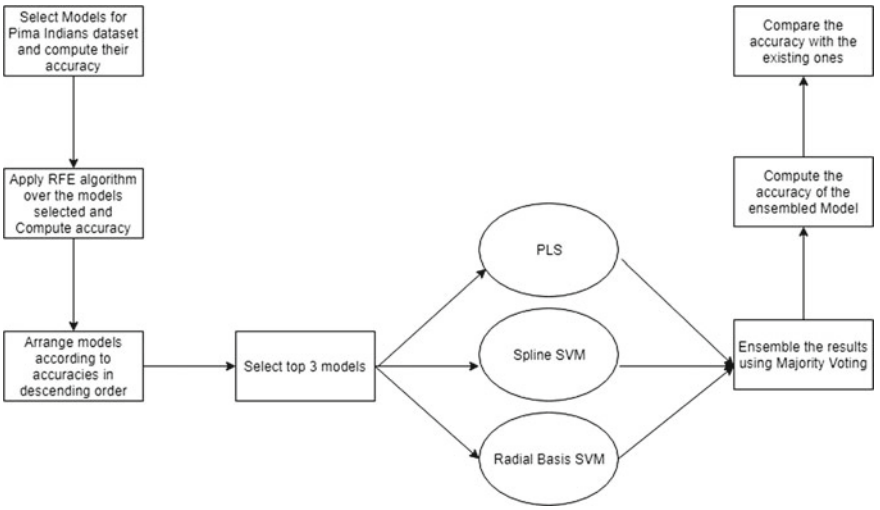

Fig. 1 Framework of the proposed work

5 Experiments and Results

All the experiments described below are performed in RStudio over a system with 4 GB RAM.

5.1 Dataset Used

Pima Indians dataset [17] is the very famous dataset based on the diabetes diagnosis of Indian females living in Arizona. This dataset comes under the category of binary class problem. This dataset comprises of 768 instances with eight input variables and it is originally having no missing values.

There are 500 instances belonging to one class i.e. "positive for diabetes" which is considered as class 1 and rest of the 268 instances belong to another class i.e. "negative for diabetes" which is considered as class 0. It is decided that whether the woman is diabetic or not according to the input variables. The eight input variables are: Number of times woman is pregnant (NOTP), Glucose concentration of plasma(GLU), Diastolic blood pressure(BP), Triceps skin fold thickness (TSFT), 2-h serum insulin(INS), BMI, Diabetes pedigree function(DPF), Age and class variable.

Firstly, RFE is applied over the Pima Indians dataset by which 5 main features are selected out of 8 attributes and a graph is plotted on the basis of accuracy of *attribute subset sizes* which is shown in Fig. 2 (*x-axis representing the count of variables*). Also the accuracies of all the features are represented in tabular form in Table 2 and the features are ranked accordingly. It is to be noted that although in case of Pima Indians dataset, considering all the 8 features gives the better accuracy (76.16%) but we chose top 5 features which were improving the accuracy of PLA, Spline method and RBF. The method *rfeControl*(*functions* = *rfFuncs*, *method* =

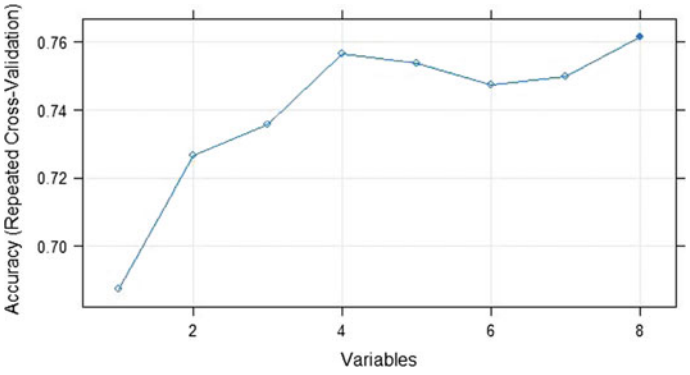

Fig. 2 Feature selection using caret *package*

Table 1 Accuracies of various models

Models	Accuracy before RFE	Accuracy after RFE (in %)
RBF Kernel (Non-linear SVM)	82.11	83.77
Spline Kernel	80.70	81.82
PLS-DA	78.79	80.97
DT	78.92	78.79
Linear SVM	78.23	77.92
NN	78.14	77.27

"*epeatedcv*", *number* = *10*) and *plot*(*results, type* = *c("g", "o")*) is used to generate the graph shown in Fig. 2.

The top 5 variables (out of 8): glucose, mass, age, pregnant, pedigree are selected based on results from RFE. Then, models are selected on the basis of literature survey and their accuracy is computed. RFE is applied to generate the improved accuracy which is tabulated in Table 1.

Now after RFE, the models are arranged in descending order according to their accuracies and the top 3 models are extracted. These consist of two non-linear methods of SVM: spline method and Radial basis method; and PLS. These models are ensembled using majority voting.

The result of the hybrid approach (ENLWPL) of Ensembling of Non-linear models with Partial Least Square is compared with rest of the models as shown in Table 2. Top kernels of Non- Linear SVM, RBF and Spline are ensembled using majority voting. As the actual and predicted output both are in 0 and 1 form so the majority voting works in a way that if majority of the classifiers predicts the output as 1, the final output corresponding to the hybrid model is 1 while if the majority of the classifiers predicts it as 0, the final output is 0. After ensembling using majority voting, the accuracy of the final model is computed by comparing the actual outcomes with the predicted outcomes. The final accuracy obtained through this hybrid model (ENLWPL) is 84.51% which is better than the models shown in Table 2.

Table 2 Comparison of accuracies of proposed approach with rest of the classifiers

Models	Accuracy
NN with RFE	77.27
Linear SVM with RFE	77.92
GAMBoost	78.57
Bagging with GLM	78.59
DT with RFE	78.79
ENLWPL	84.51

6 Conclusions and Future Work

This paper presents an approach of majority voting which ensembles the non-linear SVM kernels, RBF and Spline with the RFE applied PLS. The accuracy of hybrid model is better in comparison to bagging, boosting and raw models when used with the very famous Pima Indians dataset. There are optimization techniques which can be applied over non-linear SVM kernels and can manage to obtain some good results over the same dataset.

References

1. Demir N, Ensemble methods. https://www.toptal.com/machine-learning/ensemble-methods-machine-learning
2. Randhawa K, Loo CK, Seera M, Lim CP, Nandi AK (2018) Credit card fraud detection using AdaBoost and majority voting. IEEE Access
3. Patel S (2018) Support vector machine. https://medium.com/machine-learning-101/chapter-2-svm-support-vector-machine-theory-f0812effc72, Accessed 15 Apr 2018
4. DataFlair (2018) Support vector machine and its Kernels. https://data-flair.training/blogs/svm-kernel-functions/, Accessed 15 Apr 2018
5. Galili T (2018) Partial least squares. https://www.r-bloggers.com/classification-with-o-pls-da/, Accessed 14 Apr 2018
6. Yu P, Low MY, Zhou W (2018) Development of a partial least squares-artificial neural network (PLS-ANN) hybrid model for the prediction of consumer liking scores of ready-to-drink green tea beverages. Food Res Int
7. Recursive feature elimination (2018). https://machinelearningmastery.com/feature-selection-with-the-caret-r-package/, Accessed 10 Apr 2018
8. Friedl MA, Brodley CE (1997) Decision tree classification of land cover from remotely sensed data. Remote Sens Environ 61(3):399–409
9. Haykin SS, Haykin SS, Haykin SS, Haykin SS (2009) Neural networks and learning machines. Pearson, Upper Saddle River
10. Humphrey GB, Maier HR, Wu W, Mount NJ, Dandy GC, Abrahart RJ, Dawson CW (2017) Improved validation framework and R-package for artificial neural network models. Environ Model Softw 92:82–106
11. Gupta A, Nagarajan V, Ravi R (2017) Approximation algorithms for optimal decision trees and adaptive TSP problems. Math Oper Res 42(3):876–896
12. Gandhi KK, Prajapati NB (2014) Diabetes prediction using feature selection and classification. Int J Adv Eng Res Dev
13. Kavitha KR, Gopinath A, Gopi M (2017) Applying improved SVM classifier for leukemia cancer classification using FCBF. In: 2017 international conference on Advances in computing, communications and informatics (ICACCI). IEEE, pp 61–66
14. Joshi R, Alehegn M (2017) Analysis and prediction of diabetes diseases using machine learning algorithm: ensemble approach. IRJET
15. Wang Y, Feng HY (2015) Outlier detection for scanned point clouds using majority voting. Comput-Aided Des 62:31–43
16. Recursive Feature elimination (2018). https://topepo.github.io/caret/recursive-feature-elimination.html, Accessed 10 Apr 2018
17. Pima Indians dataset (2018) https://gist.github.com/ktisha/c21e73a1bd1700294ef790c56c8aec1f, Accessed 26 Oct 2018

Reshaped Circular Patch Antenna with Optimized Circular Slot for 5G Application

Ribhu Abhusan Panda, Debasis Mishra, Eswar Prasad Panda and Nabaneet Patnaik

Abstract In this paper the conventional circular patch antenna has been modified to operate at a frequency of 15 GHz which has been assigned for 5G communication. To get the optimum result a circular slot has been inserted which provided the broadband property. The design and the simulation was done using HFSS to verify the return loss plot and the resonant frequency the design was again done by the CST software. an optimisation has been implemented for the circular slot. The return loss, VSWR, Antenna Gain, peak directivity etc. parameters has been calculated. The FR4 epoxy material has been chosen for the substrate and the copper material is taken into account for both ground plane and patch. The dimension of the substrate and the ground plane is 50 mm × 50 mm.

Keywords Biconvex patch · Optimisation · Circular slot · Return loss · VSWR · 5G

1 Introduction

Recent trends to develop and antenna for high frequency with wide bandwidth have given motivation to modify the shape of the patch antenna for desire frequency range. The elliptical patch has been modified in accordance to Rotman Lens [1] in the year

R. A. Panda (✉) · D. Mishra
Department of Electronics and Telecommunication, VSSUT, Burla, Odisha, India
e-mail: ribhupanda@gmail.com

D. Mishra
e-mail: debasisuce@gmail.com

E. P. Panda (✉) · N. Patnaik
Department of Electronics, GIET Main Campus, Gunupur, Odisha, India
e-mail: eswarpanda018@gmail.com

N. Patnaik
e-mail: navneetpatnaik@gmail.com

© Springer Nature Singapore Pte Ltd. 2020

T. Hitendra Sarma et al. (eds.), *Emerging Trends in Electrical, Communications, and Information Technologies*, Lecture Notes in Electrical Engineering 569,
https://doi.org/10.1007/978-981-13-8942-9_63

2016. Then the log periodic implementation has been done of biconvex and waning crescent patch antenna in the same year [2, 3].The perturbation has been made to the biconvex patch to operate the antenna in the desired frequency range [4, 5]. The patch biconcave patch antenna has been implemented with circular slot for Ku Band application in the year 2018 [6]. The implantation of different slots has been done for 15 GHz application [7, 8]. Different perturbations has been done with the circular patch with circular slot for high gain applications which lead to flower shape patches [9, 10].

Here in this paper the circular patch is modified in such a way that two biconvex patch will intersect each other orthogonally and to enhance the bandwidth a circular slot has been implemented. At first the simulation has been done with the help of HFSS (High Frequency Structure Simulator) software. To get more appropriate result the circular slot has been optimised using the optimisation tool of HFSS. Then the return loss parameter has been calculated with the resonant frequency. The simulation is done with another software CST to know the whether the resonant frequency and the bandwidth is in desired range or not.

2 Antenna Design

The dimension of the patch antenna can be related to the resonant frequency [11]. The proposed antenna basically has 4 parts (1) Ground Plane, (2) Substrate, (3) Perturbed Patch, (4) Circular Slot. The ground plane is of dimension 50 × 50 mm. Material used for both ground plane and the patch is copper. Substrate has the dimension 50 × 50 mm with the material FR4 epoxy. The two biconvex patches have the maximum distance between the arch same as that of the wavelength ($\lambda = 20$ mm) which has been calculated taking the designed frequency 15 GHz into reference. The height of the substrate has been chosen as 1.6 mm which can support up to 18 GHz by the formula $f_t = \frac{150}{h\pi}\left[\sqrt{\{2/(\varepsilon_r - 1)\}}\left\{\sqrt{\tan^{-1}\varepsilon_r}\right\}\right]$ as frequency of operation is related to dielectric constant [12–14] (Fig. 1).

After the design of the antenna the wave port has been assigned in HFSS which is 6 times than the width of the feed which is equal to 1 mm. The dimension of the port is 6 mm × 8 mm.

The radiation box has been assigned for the boundary. The dimension of the radiation box is 90 mm × 90 mm × 42 mm (Fig. 2).

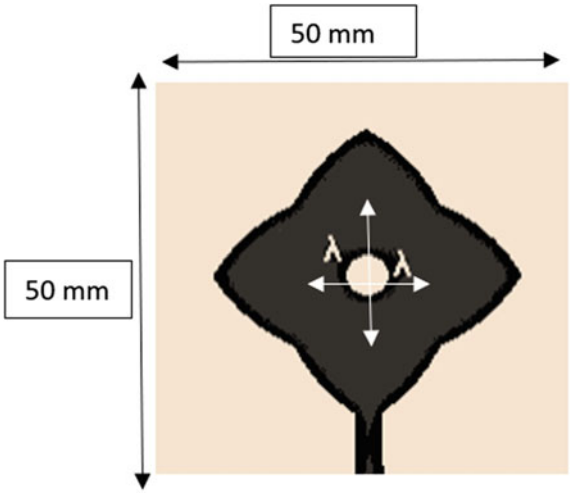

Fig. 1 Proposed antenna design using HFSS

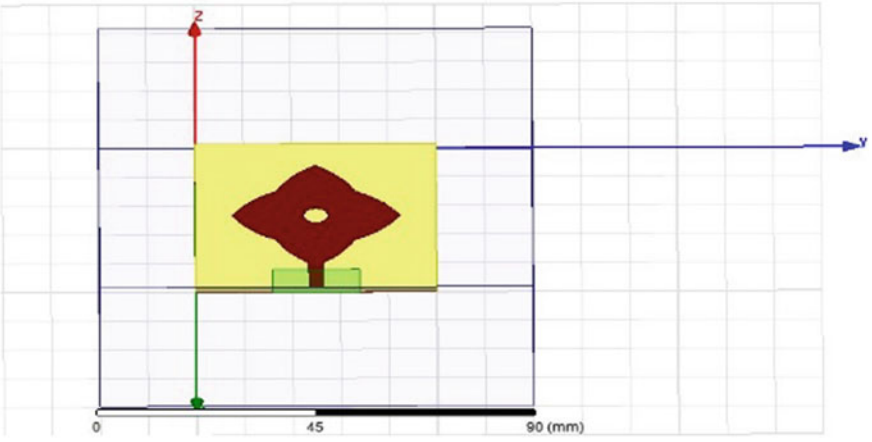

Fig. 2 The port assignment and radiation box for the proposed antenna

3 Simulation Results

The return loss curve gives the resonant frequency and the line of −10 dB cuts the curve at certain points. The difference between these points gives the Bandwidth. The VSWR should be ideally 1 and in the simulation results it is nearly equal to 1. The simulation has been carried out by the optimisation of the circular slot. A variable $R is taken for the radius of the circular slot and the optimisation has been carried out from the lower bound of $R at 2.5 mm to $3.5 mm with the step size 0.1 by using the optometric setup in HFSS (Fig. 3).

The results of S_{11} plots indicates that the resonant frequency is at 15.10 GHz with a return loss of −35.938 dB. This results is the best among all the result and this corresponds to the radius ($R) 3.5 mm of the circular slot. With this the VSWR is 1.07 which is nearly equal to the desired value 1 (Figs. 4 and 5).

To verify whether the resonant frequency is in desired range or not the same proposed antenna has been designed and simulated using another simulation software CST (computer simulated technology). S-Parameter has been calculated and the comparison is made of the results from HFSS and CST (Figs. 6 and 7).

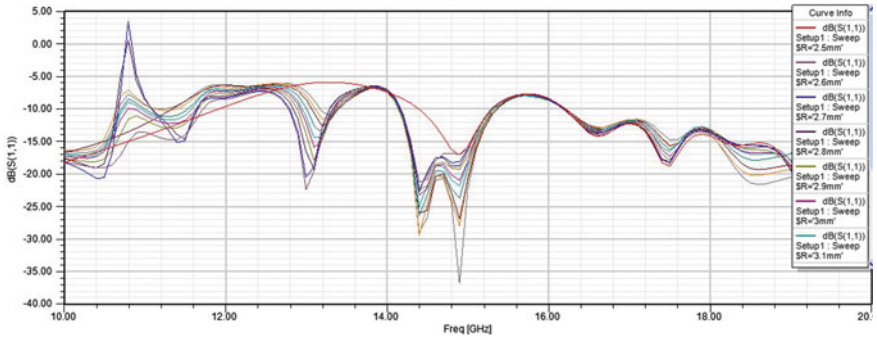

Fig. 3 Return loss of the proposed antenna with the optimisation of the circular slot

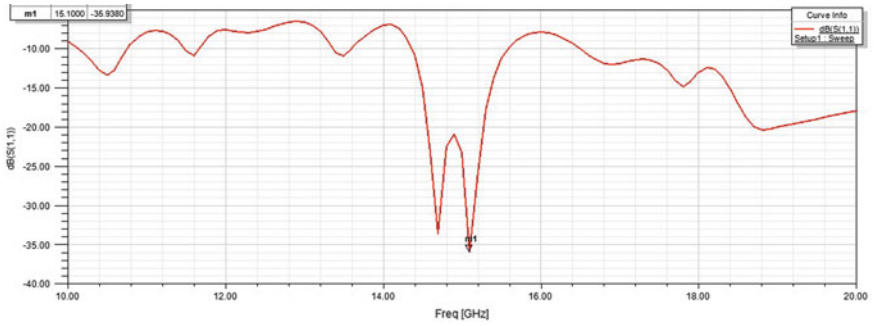

Fig. 4 Return loss of the proposed antenna with the circular slot of the radius 3.5 mm

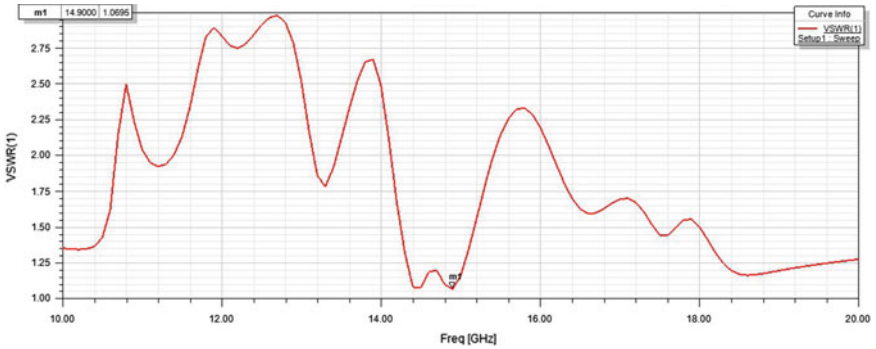

Fig. 5 VSWR of the proposed antenna with the circular slot of the radius 3.5 mm

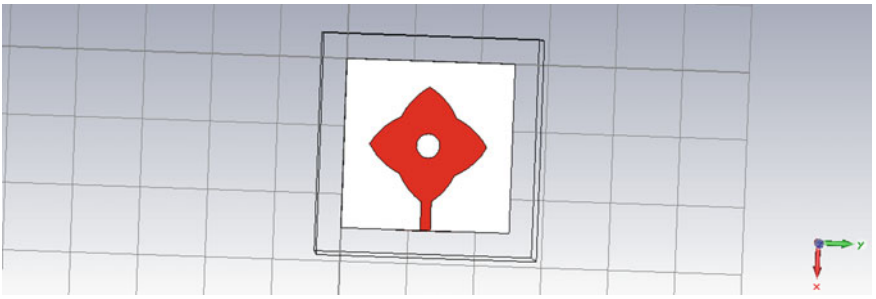

Fig. 6 Design of the proposed antenna using CST

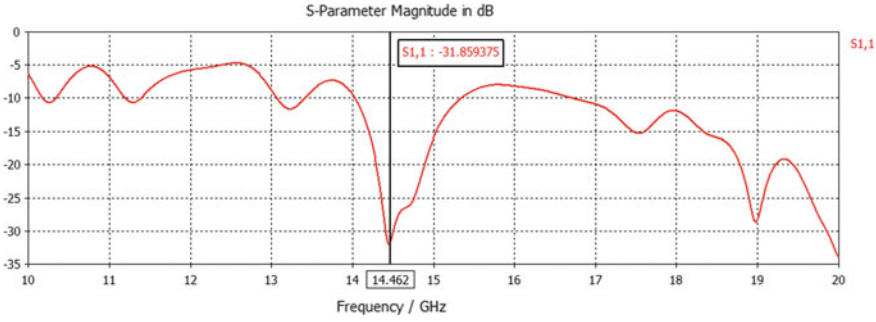

Fig. 7 S-Parameter of the proposed antenna using CST

After simulating in the CST software, it is found that the return loss is at 14.46 GHz resonating frequency with a return loss of −31.859 dB (Figs. 8, 9, 10, 11, 12 and 13).

Parameter	Using HFSS	Using CST
S_{11}	−35.9438 dB	−35.45 dB
Resonant frequency	15.1 GHz	14.45 GHz
Bandwidth	1150 MHz	1360 GHz
Antenna gain	5.19 dB	2.8 dB
Antenna directivity	10.17 dB	6.7 dB
Radiation efficiency	0.4981	0.4055

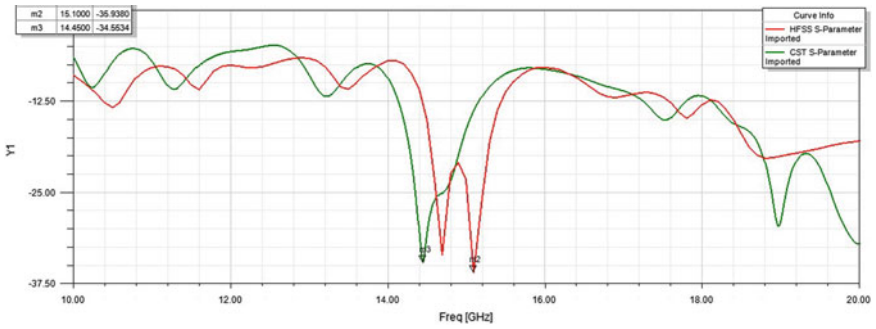

Fig. 8 Comparison of S-Parameter of the proposed antenna using CST and HFSS

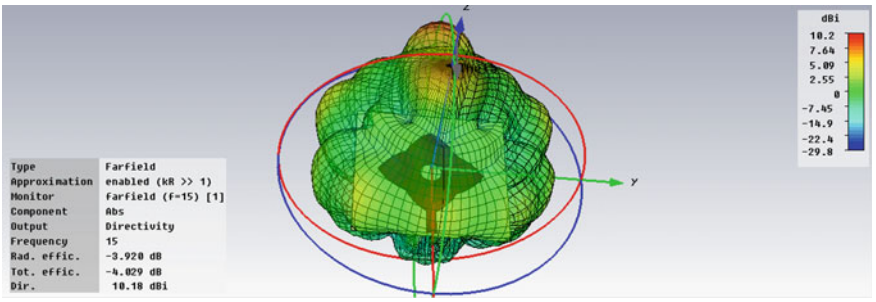

Fig. 9 Far field using CST

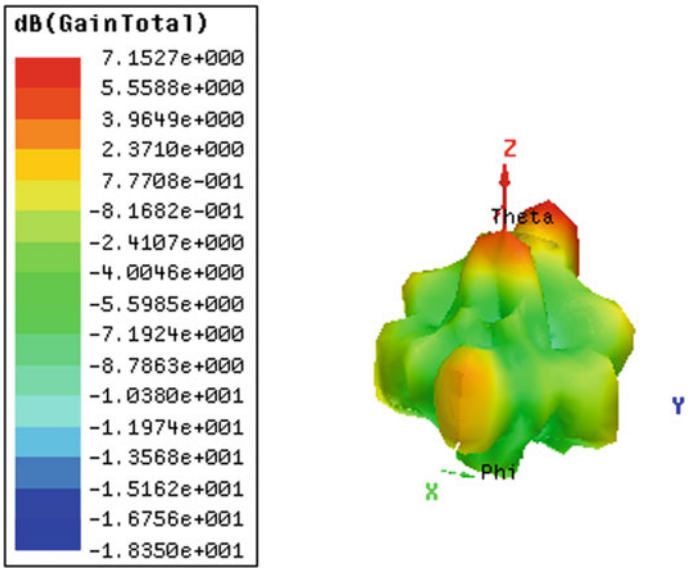

Fig. 10 Far field using HFSS

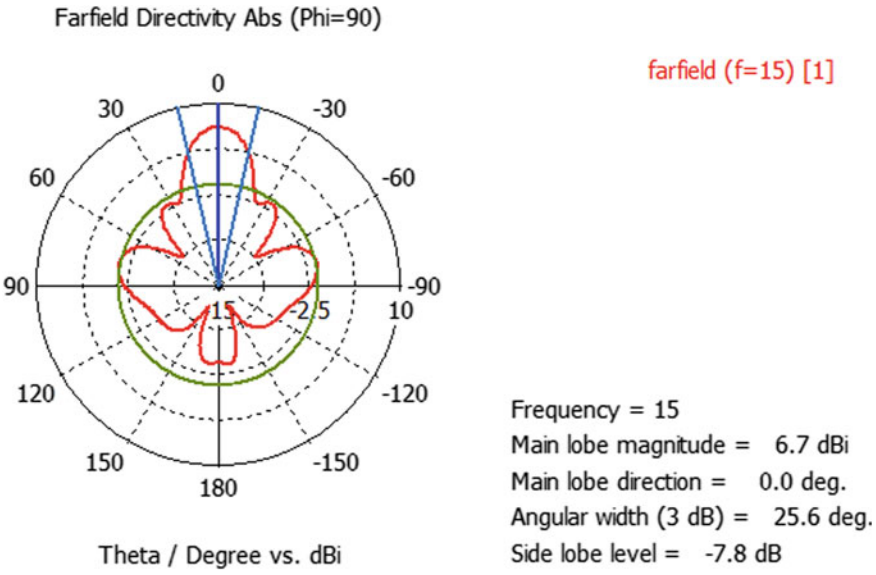

Fig. 11 Far field directivity at Phi = 90° using CST

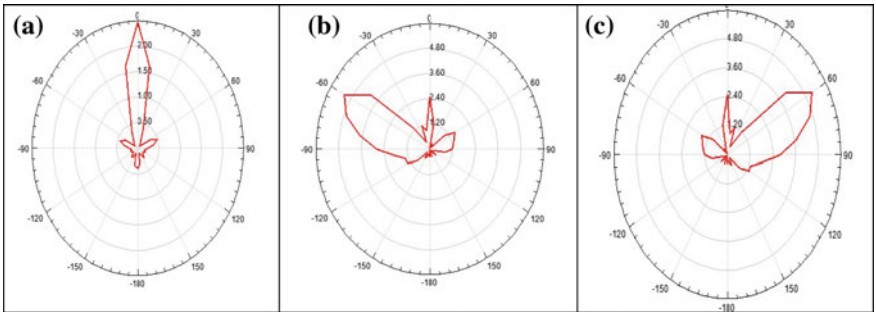

Fig. 12 Gain Radiation Pattern at Phi = 90° (**a**), Phi = 0° (**b**), Phi = 180° (**c**)

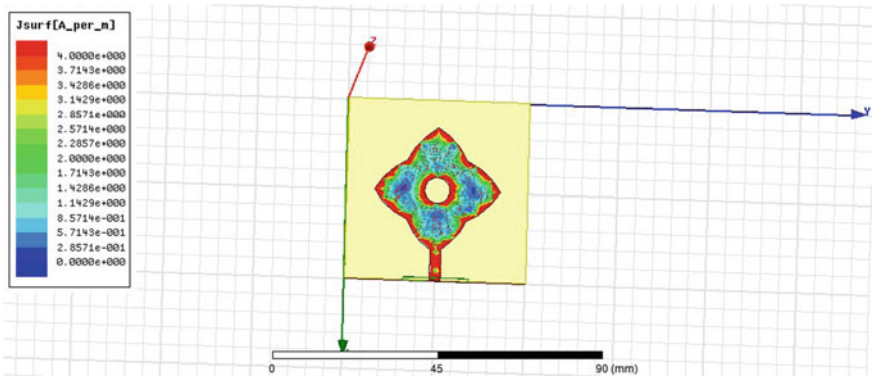

Fig. 13 Surface current distribution of the proposed patch using HFSS

4 Conclusion

The proposed antenna is suitable for the 5G application as it is having resonant frequency at 15 GHz with high gain and directivity.

References

1. Panda RA, Mishra SN, Mishra D (2013) Perturbed elliptical patch antenna design for 50 GHz application. In Lecture notes in electrical engineering, Springer India, vol 372, pp 507–518
2. Panda RA, Panda H, Mishra D (2016) Log periodic implementation of biconvex patch antenna. IJERMT 5(3):10–16
3. Panda RA, Mishra D (2016) Log-periodic waning crescent patch antenna for x-band applications. IJRSR 7(3):9483–9887
4. Panda RA, Mishra D, Panda H (2016) Biconvex patch antenna with circular slot for 10 GHz application. In SCOPES 2016. IEEE, pp 1927–1930

5. Panda RA, Panda H (2016) Bi-convex patch antenna with probe feed for 5.9 GHz WLAN application. IJARECE 5(9):2273–2276
6. Panda RA, Mishra D, Panda H (2018) Biconcave lens structured patch antenna with circular slot for Ku band application. Lecture notes in electrical engineering, Springer Nature Singapore, vol 434, pp 73–83
7. Panda RA, Panda H (2016) Comparison of rectangular and circular patch with double L-slot for WLAN and Wi-Max applications. IJARECE 5(8):2159–2163
8. Panda RA. Biconvex patch antenna with rectangular slot for 15 GHz application. ABHIYANTRIKI: An Int J Eng Technol 4(9):1–4
9. Yadav A, Agrawal S, Yadav RP (2017) SRR and S-shape slot loaded triple band notched UWB antenna. Int J Electron Commun, Elsevier, 192–198
10. Ranjan P, Raj S, Upadhyay G, Tripathi S, Tripathi VS (2017) Circularly slotted flower shaped UWB filtering antenna with high peak gain performance. Int J Electron Commun, Elsevier, 192–198
11. Balanis CA (2005) Antenna theory: analysis and design, 3rd edn, Chap. 14. Wiley, NewYork
12. Kraus JD, Marhefka RJ, Khan AS (2006) Antennas for all applications, 3rd edn, Chap. 14. TMH
13. Pozar DM (1998) Microwave engineering, 2nd edn, Chap. 1. Wiley, New York
14. Gupta KC, Garg R, Bahl I, Bhartia P (1996) Microstrip lines and slotlines, Chap. 2. Artech House, Norwood, MA

Automatic Border Surveillance Using Machine Learning in Remote Video Surveillance Systems

Ayush Goyal, Shreedevi Bugudanahalli Anandamurthy, Pritam Dash, Swati Acharya, Disha Bathla, David Hicks, Anupama Bhan and Priya Ranjan

Abstract Border Surveillance and security are of prime concern for any country. The utilization of modern smart technologies empowers strong border security. It is an imperative need to advance these technologies for better security. In this research, we employ machine learning techniques in Remote Video Surveillance for real-time threat level detection and classification of targets crossing borders. The algorithm used for the machine learning based detection of objects in the videos in this research is the Viola-Jones algorithm. This algorithm requires a training set of both positive and negative images, for the purpose of which, a collection of positive and negative images was used for the training of the algorithm for objects such as humans, vehicles, and handguns. A threat level classifier and alert warning system were also added to classify and annotate the videos in real-time for each frame. The threat level classifier performs four-fold categorization of the real-time video into—safe, low, medium, and

A. Goyal (✉) · S. B. Anandamurthy · D. Hicks
Texas A&M University, Kingsville, TX, USA
e-mail: ayush.goyal@tamuk.edu

S. B. Anandamurthy
e-mail: shrikallapur@gmail.com

D. Hicks
e-mail: david.hicks@tamuk.edu

P. Dash · D. Bathla · A. Bhan · P. Ranjan
Amity University Uttar Pradesh, Noida, UP, India
e-mail: dash.pritam@gmail.com

D. Bathla
e-mail: dishabathla@gmail.com

A. Bhan
e-mail: abhan@amity.edu

P. Ranjan
e-mail: pranjan@amity.edu

S. Acharya
Centurian University of Technology & Management, Rajaseetapuram, Odisha, India
e-mail: richi.swatiacharya@gmail.com

© Springer Nature Singapore Pte Ltd. 2020

T. Hitendra Sarma et al. (eds.), *Emerging Trends in Electrical, Communications, and Information Technologies*, Lecture Notes in Electrical Engineering 569,
https://doi.org/10.1007/978-981-13-8942-9_64

high (danger). The alert warning system specifies the type of warning based on the type of intrusion (human, vehicle, or weapon) detected. For the algorithm proposed in this work, the accuracy for the human detection is an average of 94.93%, the accuracy for the vehicle detection is an average 95.2%, and the accuracy for the weapons detection is an average of 97.67%. The accuracy of our proposed method (97%) was much higher than that of the compared previously published method (64%) for object detection.

Keywords Remote video surveillance · Security system · Machine learning

1 Introduction

Border security is a crucial security concern for all countries around the globe. Border security and border patrolling nowadays employ high-tech technologies. These technologies ensure a smarter and more effective border security.

The main border threats can be generalized into three types—unauthorized migrants, illegal transportations, and potential terrorists [1]. According to these groups, the threat levels also can be defined as low threat level, medium threat level, and high threat level [1]. Hence with respect to the threat level, we can issue the alert messages. The unauthorized migrants can include unauthorized travelers, tourists, criminals, or terrorists. Illegal transportation may include any good that is smuggled, illegal drugs, counterfeit goods, illegal weapons etc. Humans carrying weapons may be a dangerous threat, and therefore, the detection of weapons is essential.

If we observe these examples, we can analyze and predict the type of intrusions at the border. Based on this, we can categorize the intrusion to three types—the first one is the "human without weapons" intrusion, second is the "vehicle intrusion", and the third is the "human with weapons intrusion".

Humans are very good at recognizing and classification of moving objects, including recognizing small movements. But still, humans do commit mistakes. The nature of the job/task is the main reason here for the mistakes. Simply, just watching the border footages for hours is a tedious work. But, a computer can work all the time and chances of human errors or mistakes are minimized. Hence, we propose to make the detection and classification of the targets in the RVS system automatic, as this will help the operator and make border surveillance more effective and efficient.

The current border patrol and surveillance system still require the involvement of human manual supervision [2]. The modern technologies deployed at borders are of significant use for border patrolling and surveillance. Some of these technologies are Fixed, Persistent Surveillance (IFT), Remote Video Surveillance (RVS) System, Mobile capabilities, Air and Marine capabilities etc. [1]. Target recognition and organization can be achieved by using the machine learning techniques such as the Viola-Jones method [3]. Past research has shown that objects can be classified in real- time surveillance videos [4, 5]. Feature extraction algorithms are among some of the common methods used to detect targets [6], and machine-learning algorithms

[7, 8] are also commonly used. Some of the common objects detected are moving vehicles and researchers have used AdaBoost and Haar-like features to detect them [9]. Another important aspect is face detection or gender detection, which are both subcategories of human detection from video frames [10]. Some researchers have looked into designing a remote video surveillance system that would be implemented in a private cloud [11]. Target type detection and motion classification [12] and identification of moving targets [13] from remote surveillance or CCTV videos are some of the applications of feature extraction or machine-learning techniques. The applications of object detection in videos ranges from face detection using Haar-like features at one end of the spectrum [14] to moving target tracking using Kalman filters [15]. However, face detection is an application in which research has been conducted using both features and templates for the identification [16].

2 Methodology

In this research to detect and classify the targets we are using object detection trainer and detector, which are based on the Viola-Jones method proposed by Paul Viola and Michael Jones in 2001 [3]. This framework is a simple and efficient classifier. In this research, its implementation has been further enhanced and developed using the AdaBoost learning algorithm. This framework consists several stages that are discussed in the following sections below.

2.1 Haar-Based Feature Selection

In this framework, classification of the image in the detection process is depending on the value of simple features. The main benefit here is, compare to pixel-based systems, feature-based systems are faster.

Mainly this framework uses three types of features. One is a two-rectangle feature, where the value is the difference between the pixels within two rectangular regions. The dimensions of the regions are same, and they are adjacent either vertically or horizontally. The second kind of feature is a three-rectangle feature, where this computes the difference between diagonal pairs of rectangles. The last one is a four-rectangle feature. This feature computes the difference between diagonal pairs of rectangles.

2.2 Integral Image Creation

An intermediate image representation called integral image computes rectangular features quickly. At location (x, y) the integral image contains the summation of the

pixels to left and above of (x, y) as follows:

$$ii(x, y) = \sum_{x' \le x, y' \le y} i\left(x', y'\right) \tag{1}$$

In Eq. (1), $ii(x, y)$ represents the integral image. The below equations of recurrences have been used:

$$\begin{aligned} s(x, y) &= s(x, y-1) + i(x, y)(1) \\ ii(x, y) &= ii(x-1, y) + s(x, y)(2) \end{aligned} \tag{2}$$

In Eq. (2), $s(x, y)$ is the cumulative row sum, $s(x, -1) = 0$, and $ii(-1, y) = 0)$. The rectangular sum is calculated in four array references using the integral image. The difference can also be calculated between the summations of two rectangles in eight references. Since the two-rectangle features defined above involve adjacent rectangular sums they can be computed in six array references, eight in the case of the three-rectangle features, and nine for four-rectangle features.

2.3 AdaBoost Training

This paper uses a modified version of AdaBoost. This variety of AdaBoost is used for selecting features as well as to train the classifier. Basically, the algorithm is used for boosting classifiers and its performance in classification of an object of a learning algorithm. It will combine a group of weak classification functions to create a stronger classifier. In AdaBoost, the simple machine learning algorithm is known as a weak learner because, generally, the best function also would not classify the training data well. The significant importance of AdaBoost as the features selecting an algorithm is the quick learning. Generally, the conventional AdaBoost and its procedure are known as a greedy feature selection process.

2.4 Cascading Classifiers

The main goal of cascading classifiers is to accomplish the better detection performance and to reduce the computational time. The simplest classifiers will reject most sub-windows before more complex classifiers are called to achieve the reduced false positive rates. Sets of classifiers are applied to each sub-window. The first classifier removes the maximum number of negative samples in small processing. The next classifiers will remove the remaining negatives samples, but they need more computational time. In the several stages, the number of sub-windows is reduced completely.

Table 1 Categorization of threat levels and alert warnings

Intrusion type	Threat level	Alert
No intrusions	None	Safe
Human	Low	Human activity
Vehicle Vehicle & Human	Medium	Vehicle alert
Weapons Weapon & Human Weapon & Vehicle Weapons & Vehicle & Human	High	Danger: weapons detected

2.5 Target Classification

In this research, we are developing a target detector, threat level classifier and alert warning system for border security to enhance the performance of Remote Video Surveillance (RVS) system by introducing Machine Learning (ML) techniques. Here we are classifying the threats as, None, Low, Medium and High.

Threat and alert level based on intrusion type is illustrated in Table 1.

2.6 Image Labeling and Model Training

In this work, the research tasks performed are as following: first we needed to collect the abundant number of videos to train and test the machine learning algorithm and for this purpose, several different video data sets were used. In our research group, data is obtained and used from the UCI machine-learning repository (https://archive.ics.uci.edu/ml/index.php) and open source tensor flow datasets (https://www.tensorflow.org/api_docs/python/tf/data/Dataset). Machine learning is highly depending on the dataset. Dataset preparation is a very important step in machine learning. For our research, three dataset classes are required—human dataset, vehicle dataset, and weapons dataset.

The next step is features extraction. Features extraction is a process of creating a subset of the dataset. After extracting the features, we labeled the target. In this research, we used the training image labeler app in MATLAB®.

The next task is to train our model. Training of a machine-learning model is a process, which involves providing the training data to the machine-learning algorithm to learn using the data. Here, we used the MATLAB® cascade classifiers to train, detect and classify the targets. This work is based on the Viola-Jones algorithm. Detection and classification are the final stages of the model. Targets are detected, and threat levels are classified at this stage. A Graphical User Interface (GUI) was also created to show the real-time output.

3 Results

This section evaluates our proposed methodology. We have developed the threat level detector and alarm warning system for border security. We have tested the algorithm on many videos collected from the different video surveillance systems. We have selected total 9 videos, 3 videos from each category of targets, human, vehicle, and weapons. Figure 1 shows the output of human detection, Fig. 2 shows the output of vehicle detection, the Fig. 3 shows the output of human with weapon detection and the Fig. 4 shows the output when there was no intrusion or no target, i.e. the threat level is "none".

Classification into three classes of humans, vehicles, and weapons is done because humans, vehicles, and weapons are the three types of objects that are required to be detected in border surveillance or security videos.

The proposed method in this research—Viola and Jones [3] object detection framework was compared with a previously published method [2] of sliding windows approach for object detection in videos. The results are shown in Table 2, which tabulates the precision, recall, and accuracy for the object detection. Three videos of gun objects were taken for this comparison because the weapons detection is the novelty offered in this research on top of detection of humans and vehicles.

Fig. 1 Sample human video and output of human detection. Several videos were used but due to space restrictions only a few are illustrated in this paper

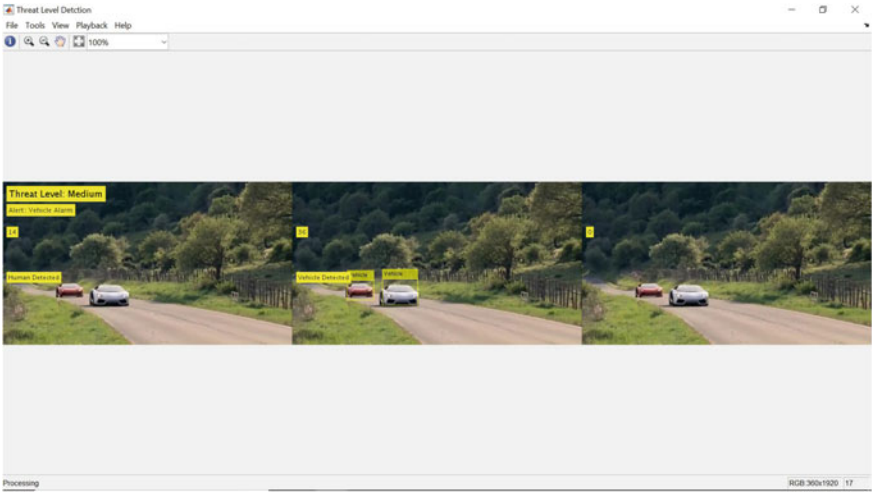

Fig. 2 Sample vehicle video and the output of vehicle detection. Several videos were used but due to space restrestrictions only a few are illustrated in this paper

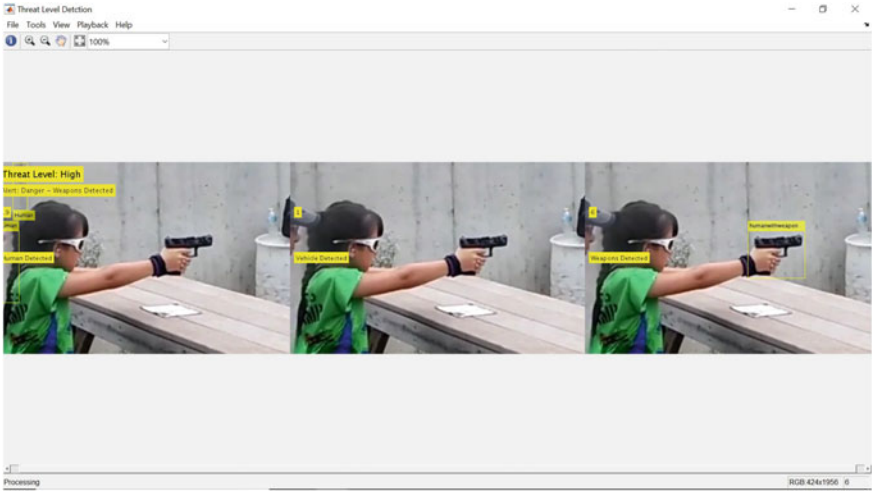

Fig. 3 Sample weapon video and the output of weapons detection. Several videos were used but due to space restrictions only a few are illustrated in this paper

Fig. 4 Sample "no intrusion" or "no target" video and output of "no intrusion" detection. This video is the output for when there is no intrusion or when Threat Level: None. Several videos were used but due to space restrictions only a few are illustrated

4 Conclusion

The research work presented in this research is an automatic threat level detection and alert warning system in Remote Video Surveillance (RVS) Systems for border patrol and border security, where the threat levels are based on the type of target intrusions at the border. Machine Learning algorithms were employed to detect the targets, to classify the threat levels and to display the alerts in the warning system. This threat level detection system was developed using the Viola-Jones object detection framework. The algorithm was tested on several different videos and it was observed in the proposed Machine Learning based automatic target detection and threat level classifier the accuracy for human detection was an average 94.93%, accuracy for vehicle detection was an average 95.2% and accuracy for weapon detection was an average 97.67%. The accuracy of our proposed method (97%) was much higher than that of previously published method (64%) for object detection. These accuracy values are based on all the cases (video datasets) used in this paper. Object detection in other cases or other videos using this paper's proposed methodology is expected to have a similar accuracy as that estimated from the video datasets tested in this paper.

The novelties and contributions of this research work are detecting human, vehicle, and weapons from RVS videos simultaneously, categorizing threat levels based on activity in the video footage and automatically generating alert messages based on the intrusion types or threat level at the border in the video footage.

Table 2 Comparison table of this research's proposed method with previously published method [2] for object (weapons) detection in videos

Methods	Algorithm	Videos	TP	FN	TN	FP	Precision (PPV)	Recall (Sensitivity)	Accuracy
Previously published	Sliding Window	Video case 1	98	206	293	11	0.899082569	0.322368421	0.64309211
		Video case 2	85	219	299	5	0.944444444	0.279605263	0.63157895
		Video case 3	97	207	298	6	0.941747573	0.319078947	0.64967105
		Average	93.3	211	296.7	7.3	**0.928424862**	**0.307017544**	**0.64144737**
Proposed in this paper	Viola and Jones	Video case 1	106	3	109	0	1	0.972477064	0.98623853
		Video case 2	47	0	47	2	0.959183673	1	0.97916667
		Video case 3	41	1	44	2	0.953488372	0.976190476	0.96590909
		Average	64.7	1.33	66.67	1.3	**0.970890682**	**0.98288918**	**0.97710476**

5 Discussion

For this research, we have trained the vehicle detection algorithm with cars. In the future, we need to train the model for all the other vehicle types for real-time use. Similarly, for weapons detection, we have trained the algorithm for handgun detection. We need to enhance the dataset for detection of all other weapon types and need to train the algorithm with the new dataset for real-time use.

References

1. Rosenblum MR, Bjelopera JP, Finklea KM (2013) Border security: understanding threats at U.S. borders. Congressional Research Service
2. Olmos R, Tabik S, Herrera F (2018) Automatic handgun detection alarm in videos using deep learning. Neurocomputing 275:66–72
3. Viola P, Jones M (2004) Robust real-time face detection. Int J Comput Vis 57(2):137–154
4. Boragno S, Boghossian B, Makris D, Velastin S (2008) Object classification for real-time video-surveillance applications. In: 5th international conference on visual information engineering (VIE 2008), pp 192–197
5. Maybury M (2009) Audio and video processing to enhance homeland security. In: IEEE conference on technologies for homeland security
6. Li Y, Ray A, Wettergren TA (2014) Target detection and target type & motion classification: comparison of feature extraction algorithms. In: American control conference
7. Alsheikh MA, Lin S, Niyato D, Tan H-P (2014) Machine learning in wireless sensor networks: algorithms, strategies, and applications. IEEE Commun Surv Tutor
8. Pedregosa F, Varoquaux G, Gramfort A, Michel V, Thirion B, Grisel O, Blondel M, Prettenhofer P, Weiss R, Dubourg V, Vanderplas J, Passos A, Cournapeau D, Brucher M, Perrot M, Duchesnay E (2011) EScikit-learn: machine learning. J Mach Learn Res 12:2825–2830
9. Moghimi MM, Nayeri M, Pourahmadi M, Moghimi MK (2018) Moving vehicle detection using AdaBoost and Haar-like feature in surveillance videos. Int J Imaging Robot 18(1):94–106
10. Bose P, Bandyopadhyay SK (2010) Identification of the important persons with gender from video images. Int J Sci Res Comput Sci Eng Inf Technol IJSRCSEIT 3(1)
11. Song B, Tian Y, Zhou B (2014) Design and evaluation of remote video surveillance system on private cloud. In: International symposium on biometrics and security technologies (ISBAST)
12. Li Y, Ray A, Wettergren TA (2014) Target detection and target type & motion classification: comparison of feature extraction algorithms. In: American Control Conference (ACC), June 4–6, 2014
13. Satyavedan S, Balakrishnan AK, Arya S, Athira Raghunath S (2014) Identifying moving bodies from CCTV videos using machine learning techniques. In: IEEE networks & soft computing (ICNSC)
14. Chen DS, Liu Z (2007) Generalized Haar-like features for fast face detection. In: IEEE international conference on machine learning and cybernetics (ICMLC), pp 2131–2135
15. Patel HA, Thakore DG (2013) Moving object tracking using Kalman filter. Int J Comput Sci Mob Comput 326–332
16. Brunelli R, Poggio T (1993) Face recognition: features vs. templates. IEEE Trans Pattern Anal Mach Intell 15(10)

Video-Based Marathi Sign Language Recognition and Text Conversion Using Convolutional Neural Network

Ashwini M. Deshpande and Snehal R. Kalbhor

Abstract The communication between the deaf people and the hearing community is the challenging task. To overcome this barrier automatic sign language recognition plays an important role. It helps to remove the communication barrier between them. A Convolutional Neural Network (CNN) based approach for Marathi sign language is presented in this paper to help understand and interpret the hand gestures made for Marathi alphabets. This system using CNN is an automated process of constructing the handcrafted feature from gesture images. The system is able to recognize 25 Marathi sign language (MSL) alphabets with a testing accuracy of 99.28%.

Keywords Convolutional neural network · Marathi sign language (MSL) · OpenCV · Python

1 Introduction

Gestures are powerful means for the communication between a person with speech or hearing disability and normal person. Many systems have been designed so far for the detection and recognition of faces, palm and emotional expression and hand gestures. Gesture recognition is one of the active areas of research in computer vision and machine learning for assisting people with hearing disability. To design a model for good hand gesture recognition system a large training dataset is required.

Sign languages are mainly developed to aid deaf and other verbally challenged people. There are two approaches for capturing sign language i.e. appearance-based and vision-based method. The appearance-based method provides exact information about hand shape, orientation, location and movement. But, every time it is not

A. M. Deshpande (✉) · S. R. Kalbhor
Department of Electronics and Telecommunication Engineering, Cummins College of Engineering for Women, Pune, India
e-mail: ashwini.deshpande@cumminscollege.in

S. R. Kalbhor
e-mail: snehal.kalbhor@cumminscollege.in

© Springer Nature Singapore Pte Ltd. 2020

T. Hitendra Sarma et al. (eds.), *Emerging Trends in Electrical, Communications, and Information Technologies*, Lecture Notes in Electrical Engineering 569,
https://doi.org/10.1007/978-981-13-8942-9_65

possible to wear motion capture gloves anywhere and it is also costly. The vision-based method provides a more natural solution.

Languages change from place to place across the globe. India is the country that has different types of religions [1]. So, in India, state-wise and region-wise different types of languages are used. Local languages such as Gujarati, Tamil, Bengali, Kannada, Marathi, Hindi, English and Telugu etc. are spoken in India. Here, we mainly focus on Marathi sign language recognition.

Sign language recognition system provides a methodology for translation of sign language into text. By using image processing and neural network techniques we can learn sign language alphabets. CNN is a research branch of neural networks. CNN learns human gesture itself, there is no need to extract the image feature and learn them. Sometimes, recognition of gesture has some problem like they are not easy to recognize gesture under some of the challenging conditions such as variations in scale, rotation and translation, occlusion due to finger movement and color variations due to lighting conditions [3]. CNN is used to overcome these problems. The proposed method is to develop a system with less complexity and high accuracy.

2 Literature Survey

Lin et al. [2] presented CNN based human hand gesture recognition. Skin model and calibration of hand movement are used to achieve good performance. Skin model is trained using Gaussian mixture model. It is used for filtering out the non-skin color of an image. This system is used to recognize seven hand gestures with an accuracy of 95.96%. Flores et al. [3] designed application of CNN for static hand gesture recognition. The static hand gesture took under invariant features like scale, rotation, translation, illumination, noise, and background. They used CNN to classify 24 hand gestures. Firstly, they apply the pre-processing techniques on images. Then, two different CNN architectures are used. The first CNN architecture has accuracy 95.37% and the second one has accuracy 96.20%. Murthy et al. [4] proposed work on hand gesture recognition using a neural network. They have designed a system to identify 10 hand gestures. They used the supervised feed-forward neural network for training purpose. Also, back propagation algorithm is used for classifying hand gesture into 10 categories. They obtained 89% accuracy. Shinde et al. [5] proposed Marathi sign language recognition. Their system is based on computer vision. They used features like center of gravity, Euclidean distance and HSV skin color model for hand image extraction. Lastly, template matching is used for comparing input image with database image. Their system gives 100% recognition results for offline detection. Bhowmick et al. [6] presented work on ANN based hand gesture recognition for English alphabets. They recognized 8 isolated and six continuous alphabets. The recognition rate is 92.59% for isolated gesture recognition and 89.05% for the continuous gesture. They used multilayer perceptron artificial neural network (MLP-ANN) as a classifier. De et al. [7] proposed work on digit recognition using computer vision. Skin color and background subtraction algorithm are used for identifying hand region

from the input video. They also use iterative polygonal shape-approximation method for shape-similarity matching. The accuracy rate for digit representative hand gesture is fairly acceptable.

Han et al. [8] presented work on visual hand gesture recognition with CNN. To achieve high-performance skin model and background subtraction are applied to obtain training and testing dataset for CNN. Simple Gaussian skin color model is used to filter out non-skin color from images. The average recognition rate of 10 gestures is 93.8%. Islam et al. [9] proposed real-time American Sign Language recognition system. They worked on ASL database with a black background. The system extracts various features such as fingertip, eccentricity, pixel segmentations and rotation. For feature extraction, 'k convex hull' algorithm is used for fingertip detection. In this system, ANN is used for classification of 37 signs. The total recognition rate is 94.32%.

3 Methodology

The methodology for recognition of the MSL using Convolutional Neural Network (CNN) is discussed in this section. CNN classifies the input by a set of connection operations. CNN is a combination of convolutional layers, pooling layers and one or more fully connected layers [3]. CNN architecture used for Marathi sign language is shown in the Fig. 1.

Five convolutional layers are used with their pooling and fully connected layers. Detail explanation of each layer of CNN and the CNN architecture selected for the proposed system is given below.

3.1 Convolutional Layer

This layer applies a convolution operation between the input images and filters. Convolutional layer forms the feature maps. Here, different filters are used to obtain

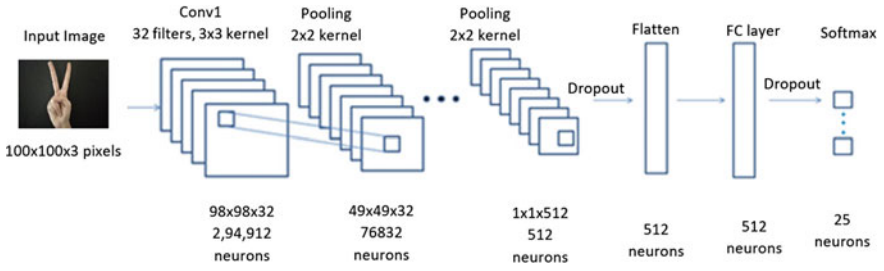

Fig. 1 CNN architecture for Marathi sign language recognition

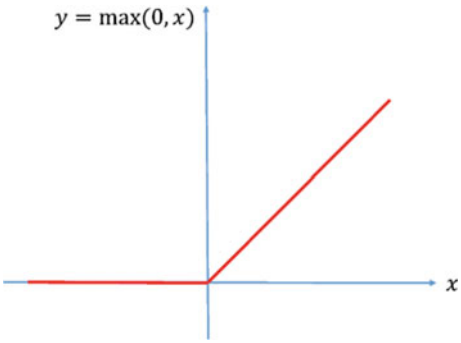

Fig. 2 The ReLU function [10]

the different feature maps. Every feature map detects different feature.

$$\mathrm{f_c} = (I \otimes K)(\mathrm{i}, \mathrm{j}) = \sum\nolimits_m \sum\nolimits_n I(m, n)\mathrm{K}(\mathrm{i} - \mathrm{m}, \mathrm{j} - \mathrm{n}) \tag{1}$$

where $\otimes$ denotes a 2-D discrete convolution operator. Equation (1) shows that the convolution kernel K slides over the input image I to compute the element-wise multiplication. The sum is producing an output. A convolved feature map is given as f_c.

3.2 ReLu Layer

Rectifier Linear Unit (ReLu) is shown in Fig. 2. It is a non-linear activation function. It is used in each convolution layer. It is used to increase the non-linearity in our images.

The output of a ReLu is a rectified feature map which is given by:

$$f_r = \mathrm{Re}Lu(x_i) = \max(0, x_i) \tag{2}$$

where (x_i) shows pixel value at an ith location in feature map as shown in Eq. (2). The output of ReLu function f_r shows that the positive pixel values stay as it is and all negative pixel values become zero.

3.3 Pooling Layer

Pooling layer is used for preserving the feature of the image. Pooling reduces the size of images. There are three types of pooling operation i.e. min, max and subsampling. Min Pooling is taking the minimum value of the cluster. Max pooling is same as downsampling operation. Max-pooling reduced the parameters which are helpful

in preventing the overfitting. Subsampling is the type of average pooling. This is generated by taking the mean value.

Mathematically, the max pooling function pool (.) is defined as:

$$f_p = pool(\mathrm{i}, \mathrm{j}) = \max\left(x_{i,j}\right) \tag{3}$$

The output of the pooling layer is a pooled feature map f_p in Eq. (3). Here we used max-pooling for the proposed technique where we take maximum values i.e. only important feature.

3.4 Flattening Layer

Flattening is used to convert the 2-D image into 1-D vector. In this, each cell is a feature map and this single vector is input to the fully connected layer. The output of flattening layer is a "flatten" pooled feature map.

3.5 Fully Connected Layer

A fully connected layer is an artificial neural network (ANN) in which every neuron in one layer is connected to every neuron in next layer as shown in Fig. 3.

First, we randomly initialize the weights to small numbers close to zero. Then the inputs are multiplied by the weight and then it is transmitted to the activation function.

Here, we have chosen the sigmoid function $\sigma(x)$ as an activation function as shown in Fig. 4. The sigmoid function is similar to the step function, which acts like thresholding. When x is a large positive number, the output of the sigmoid function is near to 1. When x is much smaller than 0, the output is near to zero. Equation (4)

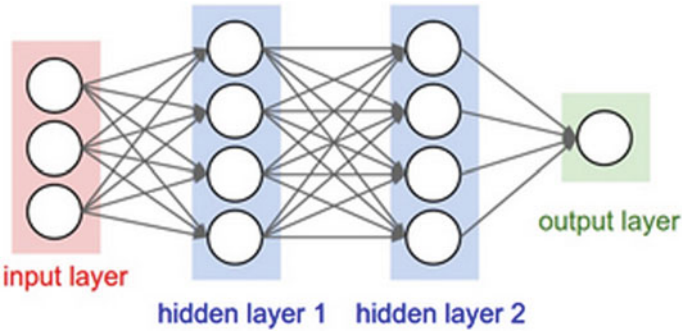

Fig. 3 ANN structure [11]

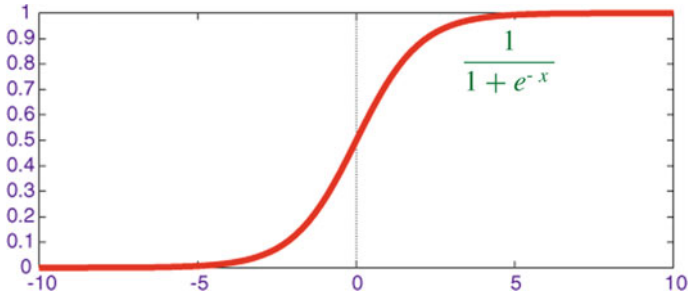

Fig. 4 Sigmoid function [11]

is a sigmoid function.

$$\sigma(x) = \frac{1}{1+e^{-x}} \tag{4}$$

Here, we get the predicted output. Comparing the actual and predicted results and measuring the generated error, the error is backpropagated. Weights are updated by calculating the error. The learning rate depends on the updated weight.

The procedure is repeated until we have minimized the cost function as shown in Fig. 5. i.e. cross entropy loss.

$$L_i = -\log\left[\frac{\exp(f_{y_i})}{\sum_j \exp(f_j)}\right] \tag{5}$$

CNN uses cross-entropy loss instead of MSE. Cross-entropy loss is a logarithmic loss function [12].

Fig. 5 Cost function [10]

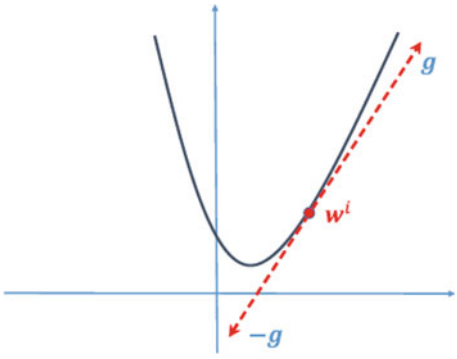

3.6 Softmax

Softmax is used for predicting a single class from K mutually exclusive classes [13]. The output of softmax function is a categorical distribution. It is a probability distribution over K different possible outcomes.

The *i*th probabilistic output of a softmax function is calculated as:

$$p(y_i) = softmax(x_i) = \frac{\exp(x_i)}{\sum_{k=1}^{n} \exp(x_k)} \tag{6}$$

Using softmax function we obtain the output probability range of [0, 1]. The output of Eq. 6 is the probability of each class and the target class has high probability.

3.7 Output Layer

CNN is trained to classify the Marathi letters thus the output has 25 categorical classes for Marathi sign languages. The output layer represents the classification result given by the softmax function. Sometimes, overfitting happens when we have a large difference between the accuracy of training and testing set. Hence, dropout is used in the convolutional and fully connected layer to reduce the overfitting problem. Dropout is nothing but dropping the 50% or 20% features from the feature map. Dropping feature reduces the complexity of layer for further convolutional operation.

Table 1 shows the CNN architecture used for Marathi sign language recognition. By using this architecture, we have trained the model. In training phase, 80% of total images are provided to the CNN network. CNN learns from the given samples and trains the model with high accuracy. In the testing phase, 20% of total images are tested against the training model and provides the output as a corresponding class or label or text.

4 Experimental Results

4.1 Software Platform

Implementation of Marathi sign language recognition system is carried out using OpenCV and Python on Intel core TM i5 Processor. For programming part on OpenCV, we need to install extra three important libraries for building CNN. Theano library is used for fast numerical computation, Tensor flow is a math library mainly used for the convolutional neural network. Keras library is based on Theano and Tensor flow library [14].

Table 1 The architecture of CNN for Marathi sign language recognition

Layer type	Kernel size	Output size	Activation function
Input image	–	100 × 100 × 3	–
Conv1	3 × 3	98 × 98 × 32	ReLu
Dropout(0.5)	–	98 × 98 × 32	–
Pooling1	2 × 2	49 × 49 × 32	–
Conv2	3 × 3	47 × 47 × 64	ReLu
Dropout(0.5)	–	47 × 47 × 64	–
Pooling2	2 × 2	23 × 23 × 64	–
Conv3	3 × 3	21 × 21 × 128	ReLu
Pooling3	2 × 2	10 × 10 × 128	–
Dropout(0.5)	–	10 × 10 × 128	–
Conv4	3 × 3	8 × 8 × 256	ReLu
Pooling4	2 × 2	4 × 4 × 256	–
Dropout(0.5)	–	4 × 4 × 256	–
Conv5	3 × 3	2 × 2 × 512	ReLu
Pooling5	2 × 2	1 × 1 × 512	–
Dropout(0.5)	–	1 × 1 × 512	–
Flatten	–	512	–
Fully Connected	–	512	Sigmoid
Dropout(0.5)	–	512	–
Softmax	–	25classes	–
Conv1	3 × 3	98 × 98 × 32	ReLu
Dropout(0.5)	–	98 × 98 × 32	–
Conv1	3 × 3	98 × 98 × 32	ReLu
Dropout(0.5)	–	98 × 98 × 32	–
Pooling1	2 × 2	49 × 49 × 32	–
Conv2	3 × 3	47 × 47 × 64	ReLu

4.2 Database

Database plays an important role in giving correct and effective output for the system. The first step of system implementation is database collection. Lot of research has been done in the area of sign language recognition using various types of sign languages, but the main challenge in this research is the availability of Marathi sign language database. For Marathi sign language, the database for alphabets required, has been created as a part of this work. There is also one reference database available in [5].

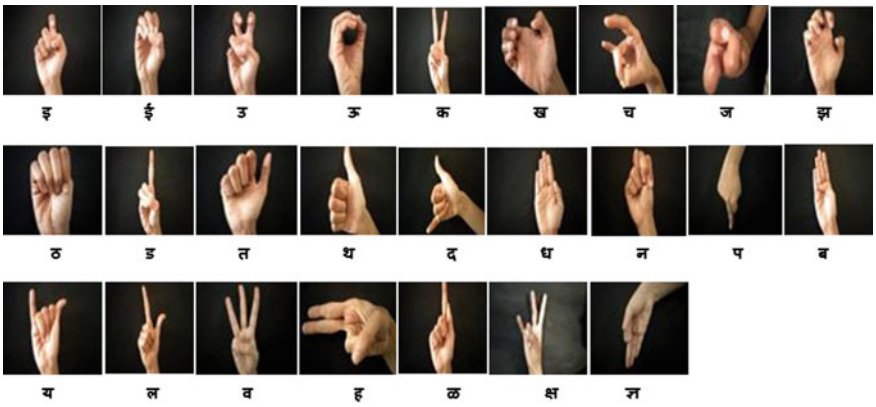

Fig. 6 Marathi language alphabet signs: database for selected alphabets

4.2.1 Marathi Sign Language (MSL) Alphabets

The database contains videos for alphabets of Marathi language from अ(Aa) to ज्ञ(Dnya) as shown in Fig. 6. The data is captured from various people for collection of Marathi alphabet signs. The signers were both male and female with different age groups. All videos are captured with a black background and with good lighting condition.

Details of the dataset are as follows:

a. Image size: 100 × 100 pixels
b. Color space: RGB
c. Number of classes: 25
d. Number of participants: 5
e. Number of samples per participant: 25.

4.3 Results

Firstly, the live video is captured with the help of webcam with resolution 640 × 480 pixels. The results for Marathi sign language recognition are as shown in Figs. 7 and 8. It shows hand gesture recognition by proposed algorithm and identified Marathi alphabets for the recognized gesture.

Performance of the proposed system is shown in terms of confusion matrix, model accuracy and model loss.

A. **Confusion Matrix**:

Confusion matrix is a square matrix which is used to describe the performance of a model. It consists of information about actual and predicted classification done by

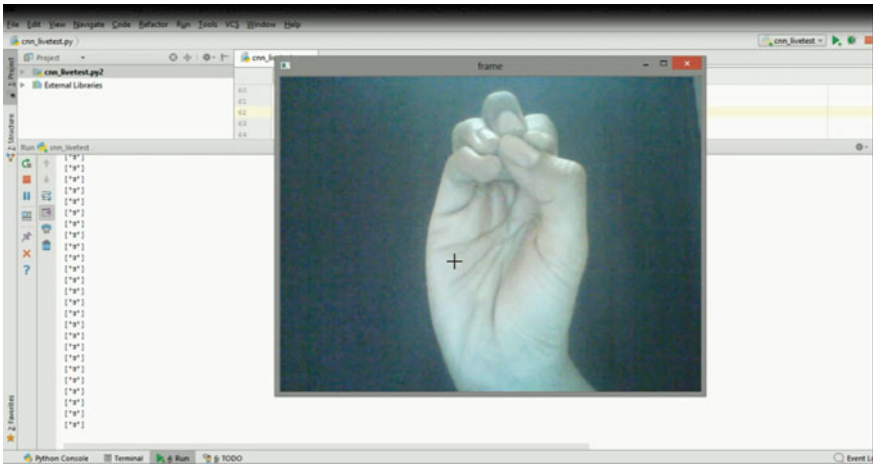

Fig. 7 Result for Alphabet 'उ' for Marathi sign language recognition

Fig. 8 Result for Alphabet 'झ' for Marathi sign language recognition

model [15]. This square matrix consists of columns that represent predicted labels and rows represent true labels. The diagonal values show the corrected labels and non-diagonal element shows incorrect labels i.e. misclassification.

Figure 9 shows confusion matrix for 25 Marathi sign language recognition using CNN. Diagonal element shows the number of corrected labels and the non-diagonal element is misclassified labels.

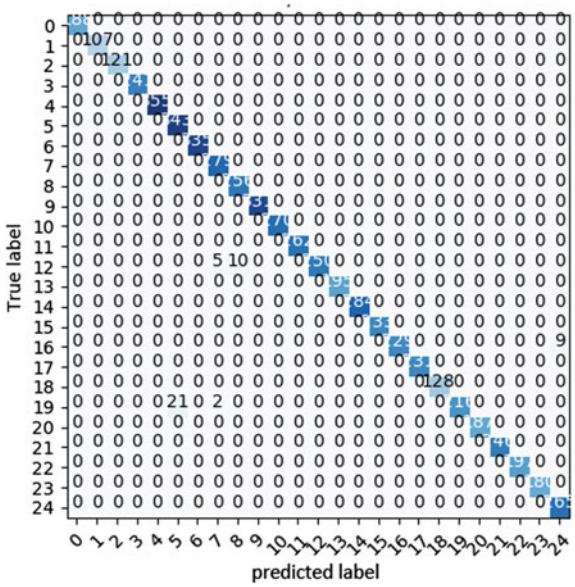

Fig. 9 Confusion matrix for MSL using CNN

B. **Model Accuracy**:

Figure 10 shows that the training and validation accuracy versus epochs. Epochs are defined as the one forward pass and one backward pass of all the training examples.

The graph shown in Fig. 10 infers that the accuracy increases as the number of epochs increase.

C. **Model Loss**:

Figure 11 shows the training and validation loss versus epochs. The graph shown in Fig. 11 infer that the loss decreases as the number of epochs increase.

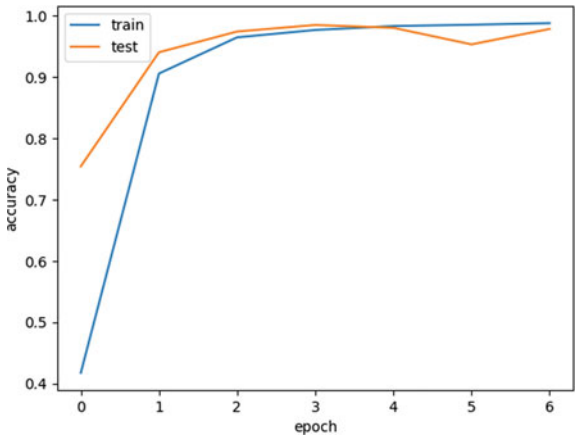

Fig. 10 Model accuracy versus epoch for MSL using CNN

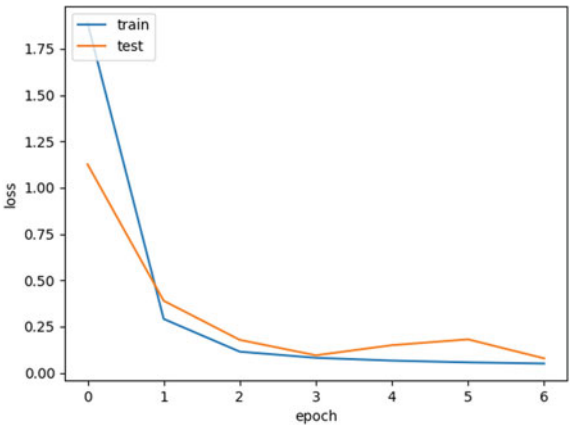

Fig. 11 Model loss versus epoch for MSL using CNN

Table 2 Performance of MSL recognition using CNN

No.	Parameter	MSL
1.	Training time	16841.17 s
2.	Testing time	75.193 s
3.	Test accuracy	99.28%
4.	Test loss	3.813%

The validation set is actually a part of the training set because it is used to build the model. It is usually used for parameter selection and to avoid overfitting.

Table 2 shows the performance measure in terms of training and testing time, test accuracy and loss of CNN on Marathi sign language recognition system. It shows that testing accuracy is approximately 99.28% for Marathi sign language database.

5 Conclusions

In this paper, we have proposed a video-based Marathi sign language recognition and text conversion system using CNN. CNN is particularly used to improve the recognition accuracy under challenging conditions such as a change in scale, rotation and translation. This method gives the testing accuracy of 99.28% for 25 labels of Marathi sign language. Thus, CNN shows a better result in comparison to other sign language recognition techniques.

In future, the method can be extended for the formation of Marathi words and sentences and for accurate Marathi sign interpretation. This method can also be tested for different types of lighting and complex background.

References

1. Taunk S, Sharma DK, Giri RN (2014) Static gesture recognition of devnagari sign language using feed-forward neural network. Int J Adv Res Comput Eng Technol (IJARCET) 3(10):3388–3392
2. Lin HI, Hsu M-H, Chen W-K (2014) Human hand gesture recognition using a convolution neural network. In: IEEE international conference on automation science and engineering (CASE), pp 1038–1043
3. Flores CJL, Cutipa AG, Enciso RL (2017) Application of convolutional neural networks for static hand gestures recognition under different invariant features. In: IEEE XXIV international conference on electronics, electrical engineering and computing (INTERCON), Cusco, Peru, pp 1–4
4. Murthy GRS, Jadon RS (2010) Hand gesture recognition using neural networks. In: IEEE international advance computing conference (IACC), Patiala, pp 134–138
5. Shinde A, Kagalkar R (2015) Advanced Marathi sign language recognition using computer vision. Int J Comput Appl 118(13):1–7
6. Bhowmick S, Kumar S, Kumar A (2015) Hand gesture recognition of English alphabets using artificial neural network. In: IEEE 2nd international conference on recent trends in information systems (ReTIS), Kolkata, pp 405–410
7. De O, Deb P, Mukherjee S, Nandy S, Chakraborty T, Saha S (2016) Computer vision based framework for digit recognition by hand gesture analysis. In: IEEE 7th annual information technology, electronics and mobile communication conference (IEMCON), pp 1–5
8. Han M, Chen J, Li L, Chang Y (2016) Visual hand gesture recognition with convolution neural network. In: 17th IEEE/ACIS international conference on software engineering, artificial intelligence, networking and parallel/distributed computing (sNPD), pp 287–291
9. Islam MM, Siddiqua S, Afnan J (2017) Real-time hand gesture recognition using different algorithms based on American sign language. In: IEEE international conference on imaging, vision and pattern recognition (icIVPR), Dhaka, pp 1–6
10. (Convolutional Neural Networks for Visual Recognition). http://cs231n.stanford.edu/
11. Jianxin Wu (2017) Introduction to Convolutional neural networks. Nanjing University, China, May
12. https://rdipietro.github.io/friendly-intro-to-cross-entropy-loss/
13. Teow MYW (2017) Understanding convolutional neural networks using a minimal model for handwritten digit recognition. In: IEEE 2nd international conference on automatic control and intelligent systems (I2CACIS 2017), Kota Kinabalu, Malaysia, pp 167–172
14. https://machinelearningmastery.com/introduction-python-deep-learning-library-tensorflow/
15. Garcia B, Viesca SA (2016) Real-time American sign language recognition with convolutional neural network. Stanford University, Stanford, CA, pp 225–232

Concurrent Triband Filtenna Design for WLAN and WiMAX Applications

Bipin Rathod and Brijesh Iyer

Abstract The paper reports a multiband filtenna design and analysis. The design provides multifunctional ability with its application area in WLAN and WiMax bands. The proposed filtenna operates over 2.4/5.2 GHz for WLAN and 3.5 GHz for WiMAX applications. First band is achieved by patch antenna with U shaped radiator. For next two bands additional L shaped strips and I shaped strips along with patch rotated by 45°. The design is analyzed using CST microwave studio. The proposed filtenna shows a passband from 2.3 to 2.6 GHz (lower WLAN band); 3.25–4.1 GHz (WiMax band); and 4.4 to 5.4 GHz (1 GHz). The filtenna is compact in size with a dimension of 46.90 × 51.15 mm (width × length). Hence, this is very useful for WLAN and Wi MAX applications.

Keywords Concurrent · Filtering antenna · Micro strip · Multiband · WLAN · WiMAX

1 Introduction

The next generation of wireless communication (5G and onwards) requires supporting many applications simultaneously in real-time condition. To achieve this requirement, the radio frontend must be dynamic enough to cater the need. The different applications can be supported by having a multiband radio front end design. However, for real-time applications, a concurrent multiband design of the radio front ends is a must to minimize the time delay. Further, the size of the circuitry must also be compact so that less space is required to mount it. The size and the count of the multiband circuits can be reduced by designing a concurrent multiband front end circuitry to support multiple applications. In radio receivers, antenna and the filters are the vital elements to decide the effective reception of the information. To cope

B. Rathod · B. Iyer (✉)
Department of E & TC Engineering, B. A. T. University, Lonere 402103, Maharashtra, India
e-mail: brijeshiyer@dbatu.ac.in

B. Rathod
e-mail: bipin_rathod24@yahoo.com

© Springer Nature Singapore Pte Ltd. 2020

T. Hitendra Sarma et al. (eds.), *Emerging Trends in Electrical, Communications, and Information Technologies*, Lecture Notes in Electrical Engineering 569,
https://doi.org/10.1007/978-981-13-8942-9_66

with the need of the modern communication applications, a subsystem which will allow antenna plus filtering (filtenna) operations is most solicited.

In view of this, the paper reports a concurrent multiband filtenna design and its analysis. Filtenna is a combination of a bandpass/bandstop filter and antenna.

The reduction in system count and multiband operations had attracted may researchers to design filtenna. Recently, the design of concurrent multiband RF systems had gained the popularity due to its compact size, simultaneous operation and reduced component count [1–3]. Such systems can be more compact if the concurrent multiband integrated subsystems are developed to replace the existing subsystems. An integrated approach to RF antenna-filter co-design is proposed by J. Zuo et al. Here, instead of using the traditional 50 Ω interfaces, the impedance between the filter and antenna is optimized to improve the performance. The combined subsystem operated at 4.06–4.26 GHz [4]. Chen and Zhou had proposed a filtering antenna for UWB communication. The designed filtenna operated between 2 and 10.5 GHz [5]. A $\boldsymbol{\Gamma}$ shaped filtenna was proposed by W. Wu et al. to operate between 2.26 and 2.66 GHz. However, this design suffered from the complex feed point arrangement [6]. DGS based antenna has also demonstrated fair far field characteristics [7–9]. The DGS based filtenna reported in [9] provides a wideband operation over 2.25–2.855 GHz. A high-gain circular patch antenna (CPA) with electromagnetically coupled and stepped impedance low pass filter (LPF) has been combined together to achieve filtenna operation at 2.4 GHz band [10]. *W. Wu* et al. reported a dualband filtenna to operate over 2.45 and 5.2 GHz [11]. A dualband filtenna was reported to operate over *WiMax* and WLAN band (3.5 and 5.8 GHz). However, this design coves only the upper WLAN band. Further, the claims in this paper were not verified with e measured prototype of the filtenna [12]. A wideband filtenna was proposed by *Kindo* et al. to operate over 2–10 GHz band [13].

However, none of these reported structures suffers from lack of measured verification, support of lower or higher WLAN band, or WiMAX band operation only, complex designs and lack of miniaturization.

Hence, the paper reports a triband filtenna to cover, WLAN (lower and upper) and WiMaX band operation. The proposed structure operates over 2.4 and 5.8 GHz (WLAN applications) and 3.5 GHz band (WiMaX application) simultaneously.

The rest of the paper is organized as: Sect. 2 reports the design of subsystems whereas the geometry of the proposed filtenna structure is reported in Sect. 3 along with its analysis. The paper is concluded in Sect. 4.

2 The Subsystem Design

The geometry of the proposed filtenna can be understood by the subsequent analysis of its subsystems. A concurrent triple band antenna and a wideband filter is designed and analyzed for the proposed filtenna.

2.1 The Antenna Design

In this work, planar multiband antenna is planned which can operate over WLAN and WiMAX. The antenna provides a concurrent operation over 2.4, 5.2 GHz for WLAN and 3.5 GHz for WiMAX application. The antenna is fabricated using FR4 material with overall dimension of 44.35 × 46.9 mm and thickness of 1.6 mm. Figure 1 depicts the geometry of the proposed antenna. Additional L shaped and I shaped strips along with patch rotated by 45° with feed line has been devised to achieve the tri-band operation.

Here, L1 = 16.8 mm; W1 = 17.91 mm; L2 = 9.04 mm; W3 = 1.7 mm; L2 = 15 mm; L4 = 8.91 mm; W4 = 3.7 mm; L4 = 8.91 mm; W4 = 3.7 mm; L5 = 9.21 mm; L6 = 18 mm; L7 = 5.11 mm; G1 = 4.26 mm; G2 = 1.70 mm; LG = 46.9 mm; WG = 17.05 mm.

The first band has resonant frequency 2.4 GHz and measured bandwidth of 390 MHz with return loss −17 dB. This frequency used for WLAN applications. The resonant frequency of second band is 3.5 GHz and bandwidth 2.37 GHz with return loss −25 dB.

This frequency is suitable for WiMAX applications and third band has resonant frequency 5.2 GHz with return loss −12 dB is suitable for WLAN applications. Figure 2 shows the S11 performance of the proposed antenna. The simulation and measured result shows a close approximation. Table 1 provides the bandwidth performance of the proposed antenna.

Further, to validate the performance of the antaean its radiation pattern is plotted at the desired bands. The pattern is omni-directional in nature. In WLAN and WiMAX application, such type of pattern is highly desirable. Figure 3 shows the radiation pattern for the proposed antenna. Figure 4 depicts the fabrication prototype of the proposed antenna.

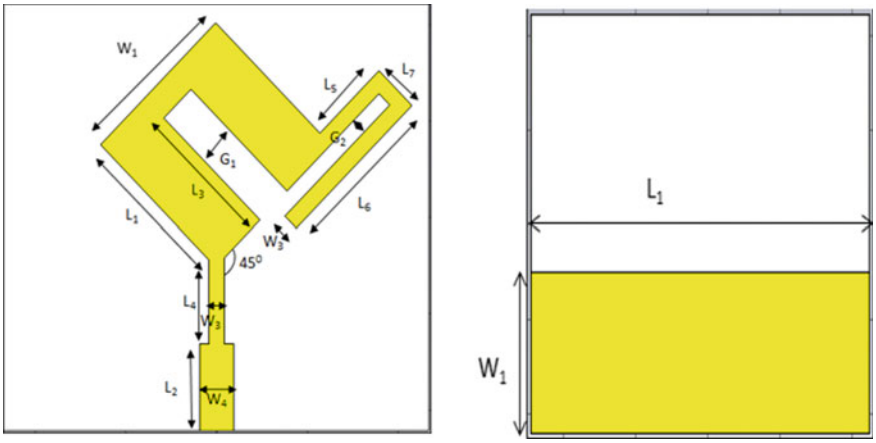

Fig. 1 Geometry of the proposed antenna

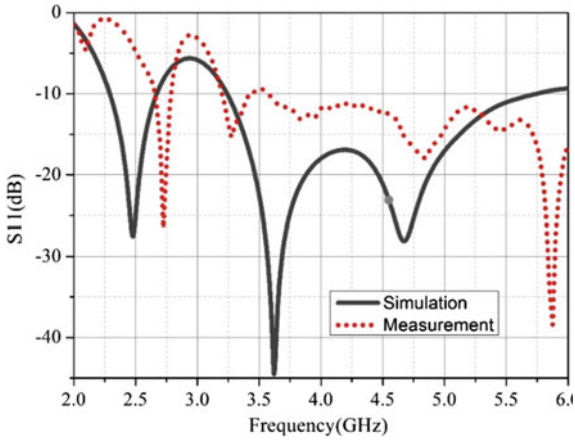

Fig. 2 S11 plot of antenna

Table 1 Bandwidth performance of the proposed antenna

Frequency (GHz)	BW (simulated)	BW (measured)
2.2–2.6	390 MHz	190 MHz
3.2–5.7	2.5 GHz	3 GHz

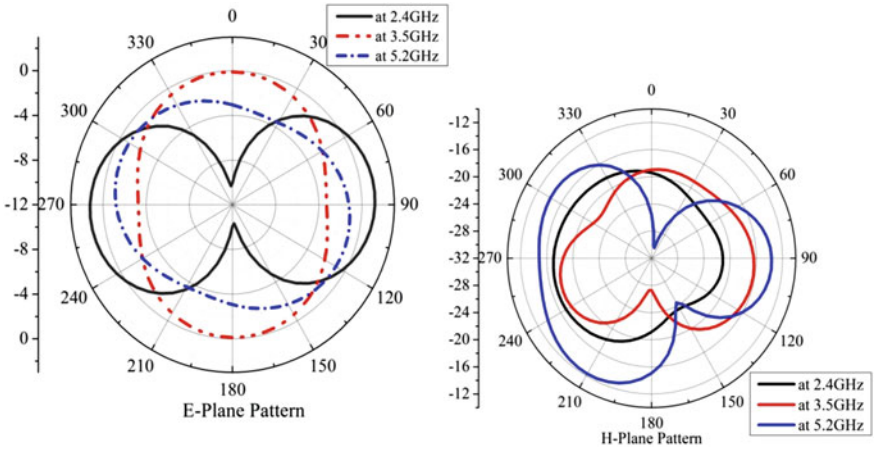

Fig. 3 Radiation pattern of the proposed antenna

2.2 The Multiband Bandpass Filter Design

The resonator of the bandpass filters (BPF) can be any shape. One of these shapes is a U-shape; known a U shape resonator or a hairpin resonator. Hence, the filter will be a hairpin-line bandpass filter. Hairpin-line bandpass filters are compact structures.

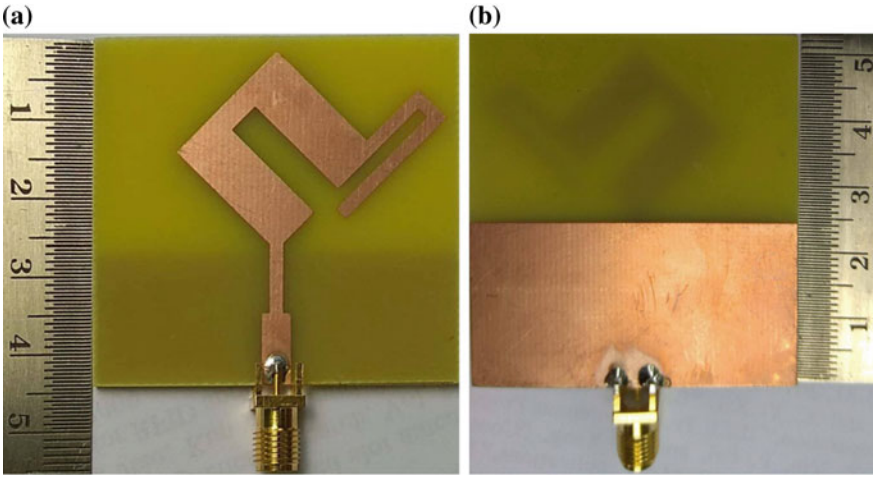

Fig. 4 Fabricated antenna design: **a** Patch side. **b** Ground side

Design parameters are: L1 = 2 mm, L2 = 1.95 mm, L3 = 5 mm, L4 = 4.5 mm, L5 = 5 mm, W1 = 0.4 mm, W2 = 0.4 mm, G1 = 0.2 mm (Figs. 5, 6 and 7) (Table 2).

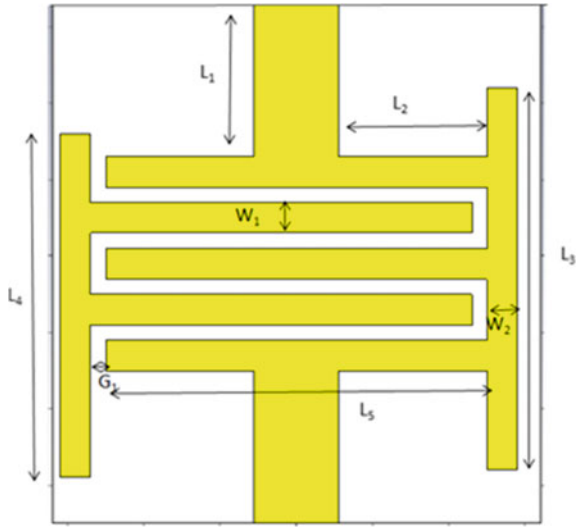

Fig. 5 Geometry of hair-pin bandpass filter

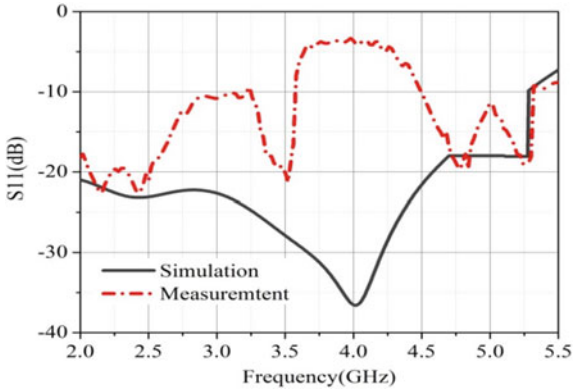

Fig. 6 S11 plot of the filter

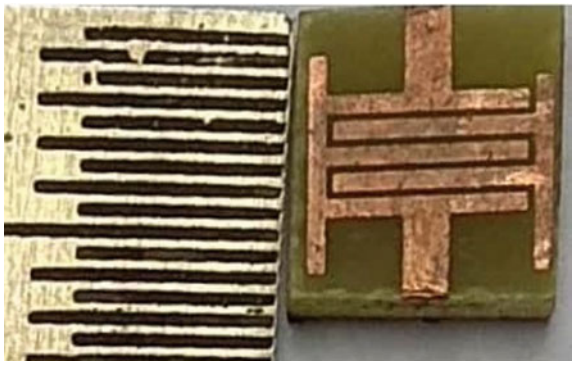

Fig. 7 Fabricated prototype of the multiband filter

Table 2 S11 performance of BPF

Frequency (GHz)	S11 (simulated)	S11 (measured)
2.4	−23	−22
3.5	−27	−20
5.2	−18	−17

3 Design and Analysis of the Multiband Filtenna

Filtering antenna design begins with designing the antenna and filter, as discussed earlier, separately and then combining the individual designs. Figure 8 depicts the geometry of the proposed multiband filtenna. Here, L = 51.15 mm, W = 46.90 mm, L1 = 23.85 mm and W1 = 46.90 mm.

The simulated and measured S11 of the filtenna has very close approximation which validates the proposed design and fabricated prototype. After simulation radiation pattern which is having Omni directional shape it is very much similar to our radiation pattern of antenna which indicates that this filtenna is useful for In WLAN as

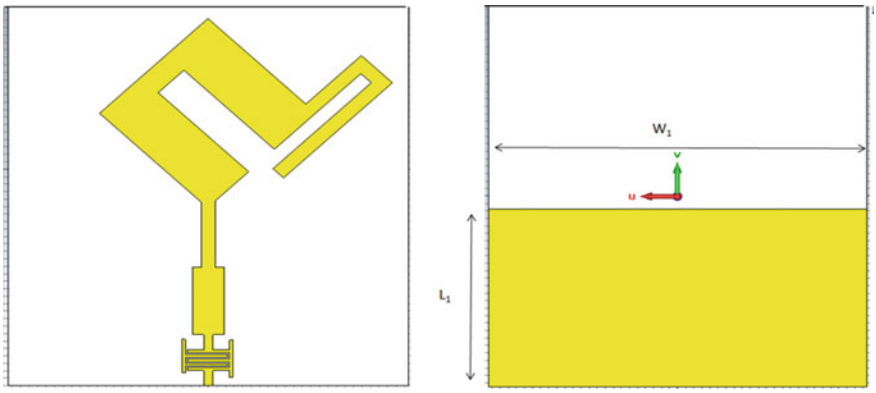

Fig. 8 Geometry of the proposed multiband filtenna

well as WiMAX applications. Table 5 provides the qualitative comparative analysis of the proposed filtenna design.

It clearly indicates that the proposed design is viable to be used as a multiband frontend for the designated bands to minimize the circuit count. The filtenna reported in [11] supports WLAN operation and do not support WiMaX operation. *Ahmad and Budimir* reported a simulation based analysis. Hence, its accuracy can't be ascertained. Further, it supports only WiMAX and WLAN (upper band) operation. This filtenna operated over 3.5 GHz (WiMAX) [12]. The effort reported in [13] suffers from wideband operation. Due to wide band operation unnecessary signals may get introduced in the radio receiver. Hence these methods are not attractive. The proposed structure support tri-band concurrent operation over 2.4, 3.5 and 5.2 GHz (Fig. 9, 10, 11 and 12) (Tables 3, 4 and 5).

Fig. 9 S11 performance of the proposed filtenna

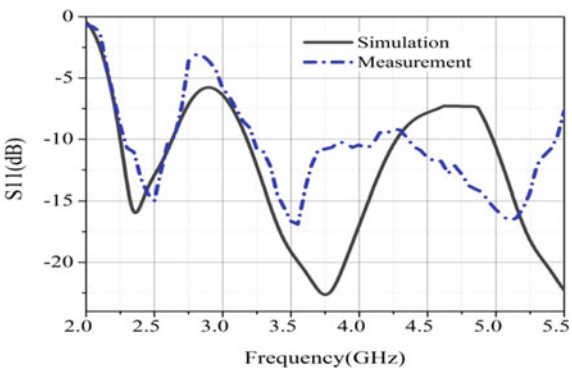

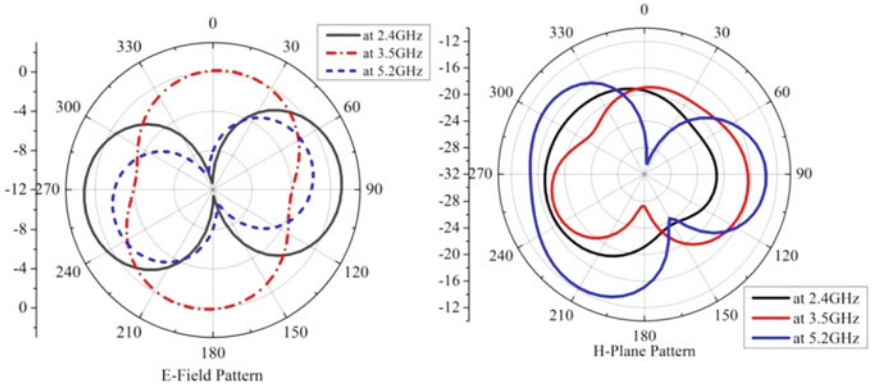

Fig. 10 Radiation patter of the proposed multiband filtenna

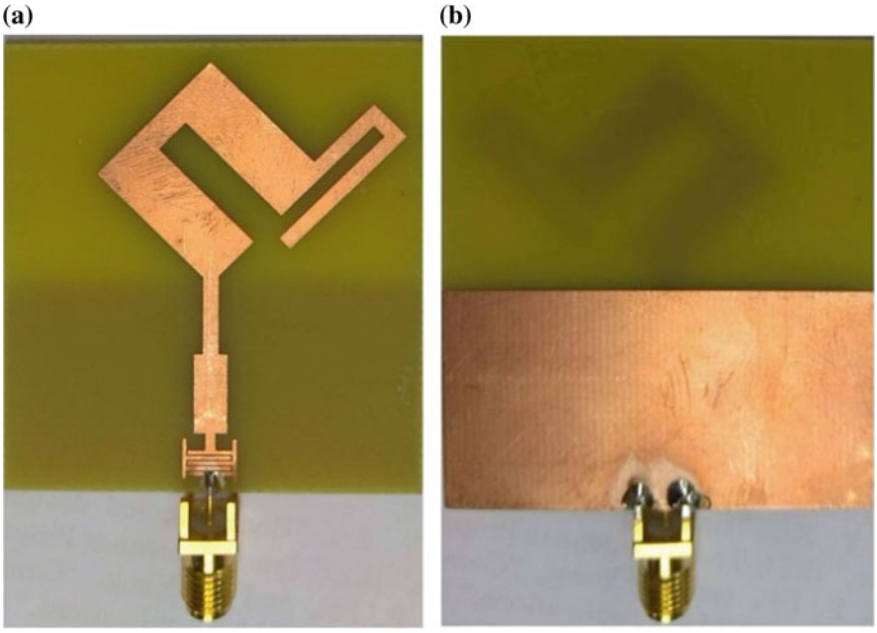

Fig. 11 Fabricated prototype of the proposed filtenna: **a** Patch side. **b** Ground side

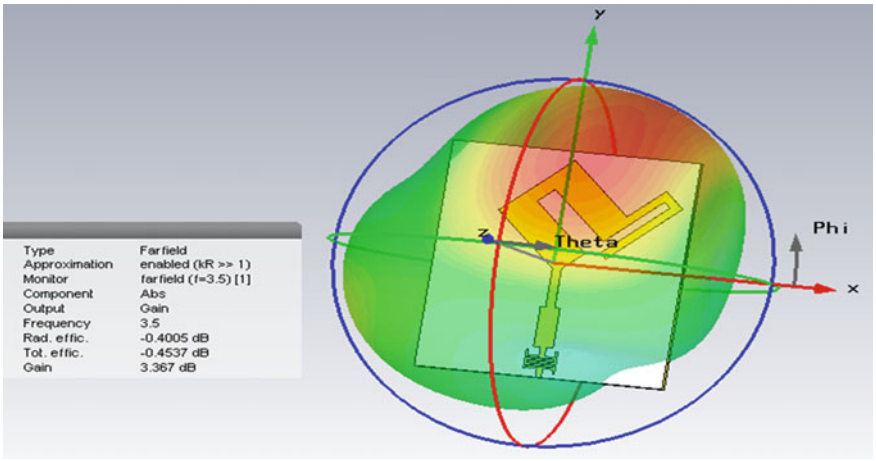

Fig. 12 Gain plot of filtenna

Table 3 S11 performance of the proposed filtenna

Frequency (GHz)	S11 dB (Simulated)	S11 dB (Measured)
2.4	−15.33	−13.16
3.5	−19.14	−16.63
5.2	−16.95	−15

Table 4 Gain performance of the proposed filtenna

Frequency (GHz)	Simulation gain (dB)	Measured gain (dB)
2.4	2.276	2.01
3.5	3.367	2.90
5.2	3.502	3.00

Table 5 Qualitative analysis for the proposed filtenna

Contributions	Operating band (GHz)	S11 (dB)	Gain (dBi)	Dimension [W × L] (in mm)
Wu et al. [11]	2.45 and 5.2 GHz dualband	−14 and −21 resp.	2.88 and 2.45 resp.	34.5 × 41.5
Ahmad and Budimir [12][a]	3.5 and 5.8 GHz	−27 and −22 resp.	4.07 and 1.9 resp.	32 × 37.2
Kindo et al. [13]	2–10 GHz	−15 to 10 in wide band	–	24 × 32.09
Present work	2.4,3.5 and 5.2 GHz	−13.16, 16.63 and − 15 resp.	2.01, 2.9 and 3	46.90 × 51.15

[a]Simulation results

4 Conclusion

A measured prototype of multiband multifunctional filtenna is reported in this paper. The validity of the design considerations are proved by a very close agreement of simulation and measured parameters of the design. The measured prototype provides an Omni directional radiation pattern with a directivity in the range of 2 to 5 dB; which is very useful in WLAN and WiMax applications.

References

1. Iyer B, Kumar A, Pathak NP, Ghosh D (2016) Multiband concurrent RF system for human vital sign detection during natural calamities. International microwave and RF conference (IMaRC), New Delhi, pp 1–4
2. Iyer B, Pathak NP, Ghosh D (2014) Reconfigurable multiband concurrent RF system for non-invasive human vital sign detection. In: IEEE Region 10 humanitarian technology conference (R10-HTC), pp 111–116
3. Iyer Brijesh (2017) Characterization of concurrent multiband RF transceiver for WLAN applications. Adv Intell Syst Res 137:834–846
4. Zuo J, Chen X, Han G, Li L, Zhang W (2009) An integrated approach to RF antenna-filter co-design. IEEE Antennas Wirel Propag Lett 8:141–144
5. Chen Y, Zhou Y (2009) Design of a filter-antenna subsystem for UWB communications. In: 3rd IEEE international symposium on microwave, antenna, propagation and EMC technologies for wireless communications, pp 593–595
6. Wu W, Yin Y, Zuo S, Zhang Z, Xie J (2011) A new compact filter-antenna for modern wireless communication systems. IEEE Antennas Wirel Propag Lett 10:1131–1134
7. Prajapati PR, Patnaik A, Kartikeyan MV (2014) Design of single feed dualband dual polarized microstrip antenna with defected ground structure for aeronautical and radio navigation applications. In: General assembly and scientific symposium (URSI GASS), 2014. XXXIth edn, URSI, pp 1–4
8. Prajapati P (2015) Application of defected ground structure to suppress out-of-band harmonics for WLAN microstrip antenna. Int J Microw Sci Technol 2015:1–9
9. Wu W, Wang C, Wang X, Liu Q (2013) Design of a compact filter-antenna using DGS structure for modern wireless communication systems. In: 5th IEEE international symposium on microwave, antenna, propagation and EMC technologies for wireless communications, pp 355–358
10. Zulkifli F, Leza Y, Rahardjo E (2015) Design of integrated antenna and RF filter for rectenna application. In: 4th Asia-pacific conference on antennas and propagation (APCAP), pp 303–304
11. Wu W et al (2013) Co-design of a compact dual-band filter-antenna for WLAN application. Prog Electromagn Res Lett 40:129–139
12. Ahmad W, Budimir D (2016) UWB filtennas with dual bandnotch for WiMAX and WLAN bands using circular and square resonators. In: Active and passive RF devices seminar, London, pp 1–3
13. Kindo J, Kumar L, Parihar M (2018) Planar ultra wideband (UWB) filtenna using hexagonal shaped structure. In: 3rd international conference on microwave and photonics (ICMAP 2018), pp 1–2

Advanced Image Encryption Scheme Using Snow Stream Cipher

Subhrajyoti Deb, Bhaskar Biswas and Bubu Bhuyan

Abstract Image encryption has evolved significantly over the years. This paper proposes an image encryption system using Arnold's cat map transformation and Snow stream cipher. In our proposed scheme, the image is first scrambled using Arnold's transformation and then the selected scrambled image pixels are XORed with the Snow cipher keystream sequence to produce the cipher image. Performance of the proposed scheme is analyzed based on several statistical properties. We have observed encouraging statistical properties of the cipher image bitstream making our encryption scheme suitable for applications that requires secured transportation of images.

Keywords Stream cipher · Snow cipher · Image encryption · Arnold's scrambling

1 Introduction

Image encryption has become immensely popular amongst the cryptographic research community. Recently, it has been widely used in different military security based applications like surveillance in the border area storage and transmission of image data. Therefore, the protection of an image from unauthorized access is essential. Recently, in an encryption/decryption method scramble techniques have been used for the features of unpredictability, and ergodicity. Thus scramble techniques have received a lot of attention from the cryptographic research community. To improve the security of the encryption systems we require strong cryptographic primitives. Many cryptographic primitives have been proposed for providing secu-

S. Deb (✉) · B. Bhuyan
Department of Information Technology, North-Eastern Hill University, Shillong, India
e-mail: subhrajyotideb1@gmail.com

B. Bhuyan
e-mail: b.bhuyan@gmail.com

B. Biswas
Department of Information Technology, Tripura University, Suryamaninagar, India
e-mail: bhaskar.cse11@gmail.com

© Springer Nature Singapore Pte Ltd. 2020

T. Hitendra Sarma et al. (eds.), *Emerging Trends in Electrical, Communications, and Information Technologies*, Lecture Notes in Electrical Engineering 569,
https://doi.org/10.1007/978-981-13-8942-9_67

rity for the sensitive image data. Typically, image encryption system is designed by combining several cryptographic primitives. However, the success of the encryption system rely upon how much cryptographic primitives are secured. Elliptic curve cryptography (ECC), DNA encoding, cosine number transform, and symmetric key image encryption are a few popular image encryption primitives. In symmetric key image encryption, stream cipher is widely used for encryption during data transmission. A stream cipher is the best preferable option for high-grade security in constrained resource environment. Hence, a secure stream cipher is an important cryptographic primitive that generate good quality pseudorandom numbers. It is easy to implement in hardware as well as they have high throughput. A simple way to construct a stream cipher is to produce a pseudorandom string by generator and XORed (modulo 2 operations) with the plaintext [7]. Generally, maximum stream cipher algorithms are bit-oriented. For example, A5/1 used in GSM encryption, E0 used in Bluetooth, RC4 used in SSL/TLS, WEP, Espresso used in 5G etc. Currently, various emerging applications require high-speed link encryption/decryption or an efficient software encryption for a huge amount of data. In such a scenario, bit-oriented ciphers do not offer adequate performance. For this reason, we motivate to work on word-oriented stream ciphers. A word-oriented stream cipher generates a sequence of words like 32/64/128 bits per clock. Moreover, a word-oriented stream cipher is 5–10 times faster than a block cipher in a software implementation.

In 2013, Aïssa et al. [2] proposed a fast image encryption scheme using stream cipher based on Nonlinear Combination Generator. Further, their experimental results have shown that the system is profoundly resistant to common attacks. Das et al. [5], concentrated on the performance of a theoretical single-stranded DNA. The investigation also introduced a new algorithm for security against various statistical and visual attacks. Shah et al. [11] considered S-box can be used for image encryption and they extensively discussed the statistical result of the images. Praveenkumar et al. [10] presented the advanced image encryption methods by using triple chaotic image scrambling. Wang et al. [13] discussed the image encryption algorithm based on a chaotic map and Arnold's transformation. Chen et al. [4] discussed the novel idea for effective image encryption techniques using self-adaptive permutation diffusion including DNA random encoding. Very recently, Laiphrakpam et al. [9] presented the robust image encryption scheme using elliptic curve. In this scheme, before the encryption, image has been scrambled by Arnold's transform. Inspired by the above mentioned articles, we carried out our work.

Before proceeding further, let us describe the organization of this paper. Section 2, presents the proposed work. Section 3, provides performance details of the proposed scheme. Section 4, provides in-depth statistical analysis and comparison. Finally, Sect. 5 concludes the paper.

2 Proposed Work

In this paper, we proposed a novel encryption scheme. We initially scramble the plain image by Arnold's transformation. Further, the selected scrambled image bitmap is XORed with the keystream sequence of Snow cipher to produce the cipher image. In our experiment, we consider two specified approaches to image encryption which is very difficult to predict as well as our scheme achieves a high level of security. The schematic view of our proposed framework is shown in Fig. 1.

2.1 Arnold's Transformation

Nowadays, image scrambling is the emerging techniques for image Steganography. Originally this idea was mooted by Vladimir Arnold in 1960. Vladimir Arnold et al. reported detailed transformation techniques in [3]. It is treated as a chaotic map when this transformation is applied to a digital image, and it randomizes the original setup of its pixels and the image becomes scrambled. After a number of iteration original image can be formed.

Definition 1 *The notion of Arnold's cat map can be described as follows:*

$$\begin{Bmatrix} \bar{x} \\ \bar{y} \end{Bmatrix} = \begin{bmatrix} 3 & 2 \\ 2 & 2 \end{bmatrix} \begin{Bmatrix} x \\ y \end{Bmatrix} (\text{mod } n)$$

where x and y are the position of the pixels in the original image. Here $\bar{x}$ and $\bar{y}$ are the position of the pixels in the scrambled image and n is the order of image matrix. Let us consider, $n = 128$ and now it would be treated as (128×128) matrix. After the operation of each pixel of the original image, multiple numbers of the transformed image has been produced. In general, the number of iterations of the transformed

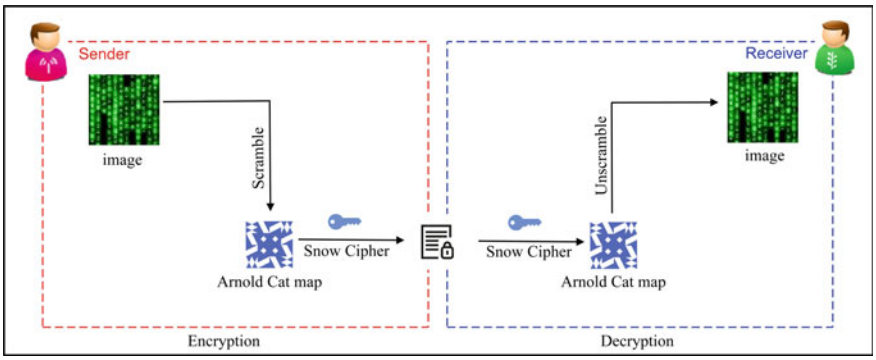

Fig. 1 Schematic view of the proposed structure

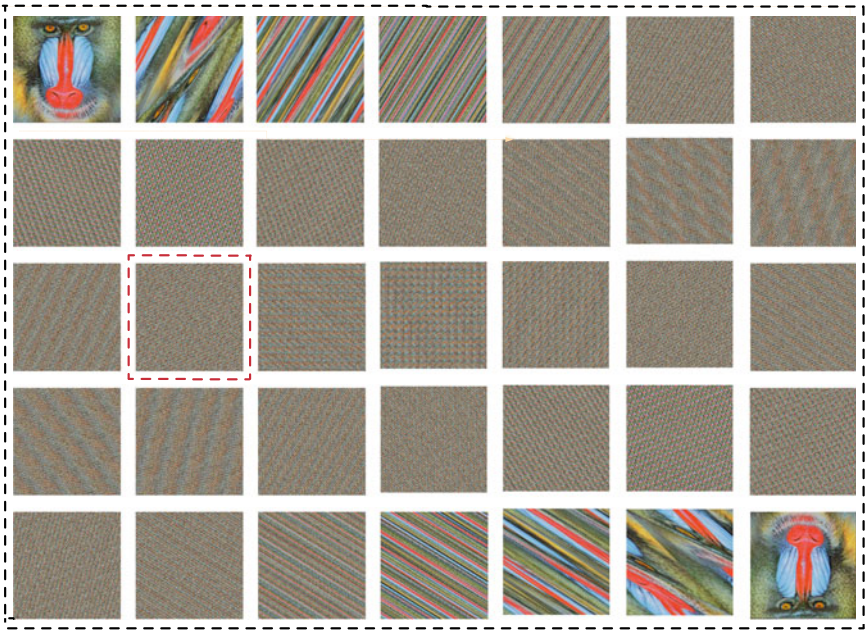

Fig. 2 Arnold's transformation of Baboon image up to 34 number of iteration

image depends on the size of the image. For example, if we take (128 × 128) image then the number of iteration is 96 but in case of a (201 × 201), it requires 68 iterations. Arnold's transformation technique which we have implemented here. In this work, we choose (201 × 201) image size for transformation. Here, we presented first 34 number of scrambled images in Fig. 2. For encryption, 15th number of scrambled image has been chosen (see red color border Baboon image) in Fig. 2.

2.2 Random Number Generation Using Snow Cipher

Over the last few years, symmetric key ciphers like block cipher, hash function, and stream cipher is extensively used for image encryption/decryption. Linear Feedback Shift Register (LFSR) based stream cipher has a very good prospect because it produces the high-quality pseudorandom sequence which is very useful for image encryption [2, 6]. Usually, most of the classical LFSR-based stream ciphers are bit-oriented. As already discussed, many emerging applications are demanding efficient software encryption for the bulk amount of data encryption/decryption. In that regard, bit-oriented stream ciphers not able to give adequate performance. This concern may be solicited if one uses a word-oriented stream cipher. Moreover, word-oriented stream cipher provides good statistical properties with a large period. Here, we used

Snow stream cipher which received notable attention, because of its good quality randomness properties. Snow stream ciphers (1.0/2.0/3G) are developed by Johansson and Ekdahl [8]. Snow cipher produces 32-bit word per clock using 128-bit key and IV. In general, Snow cipher originally submitted to the NESSIE project.[1] Snow has been used in the eSTREAM project [1] as a reference cipher. Snow 3G has been chosen for the 3GPP encryption algorithms UEA2 and UIA2. Further, it is practiced on 4G networks.

Our two level of approach increases the complexity of the structure. We also believe that our study eventually helps to increase the security margin as much as possible in the proposed structure.

3 Performance Assessment

This work offers an advanced image encryption scheme. The experimental work was conducted with various images, a few of them are shown in this paper. Plain images are displayed in Fig. 3a–c. Next, the plain image is scrambled through Arnold's transform as shown in Fig. 3d–f. Further, our scrambled image pixels value is XORed with the Snow cipher random keystream sequence to produce the cipher image. Finally, the cipher images are shown in Fig. 3g–i.

3.1 Histogram Analysis

In general, histogram plots can be defined by the frequency distribution of pixel rates. Any cryptographic primitives are made to provide cipher image which has a uniform distribution of pixel rates so that an attacker not able to obtain the original image from the cipher image. The histogram results are plotted graphically as follows: three plain images and three cipher images are elaborated in Fig. 4a–c, d–f respectively. For the evaluation of histogram, we plotted the pixel values along the x-axis and the frequency along the y-axis.

3.2 Correlation Coefficient Analysis

Correlation coefficient of a image is calculated by passing the image over a median filter. For a gray-scale image, it is passed once and for a RGB image and it is required to be passed thrice for R, G and B matrix [10]. After passing through the median filter

[1]NESSIE (New European Schemes for Signatures, Integrity and Encryption) was a renowned research project to classify strong cryptographic primitives.

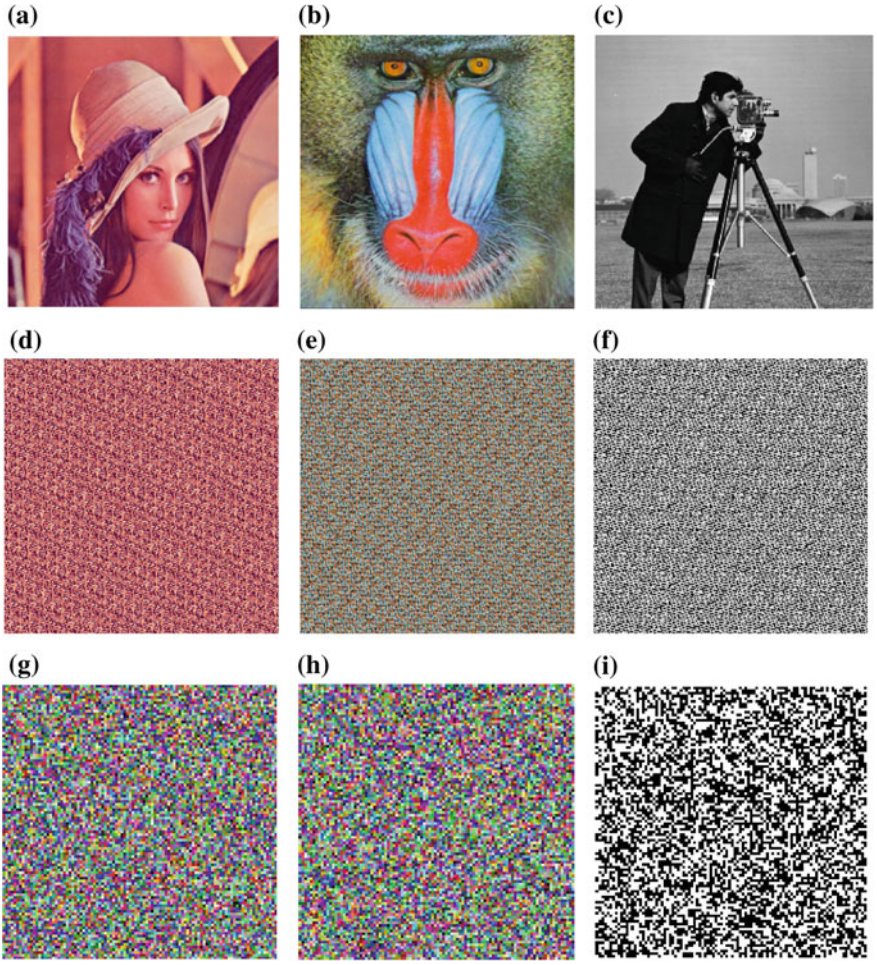

Fig. 3 **a–c** Selected plain images namely Lena, Baboon, and Cameraman. **d–f** Plot of scrambled plain images. **g–i** Plot of encrypted images using Snow stream cipher

we get correlation coefficient of the corresponding image. Channel wise horizontal, vertical, and diagonal correlation coefficient results are tabulated in Table 1.

3.3 Entropy

Shannon proposed the fundamental notion of information entropy [12]. It can be defined as follows:

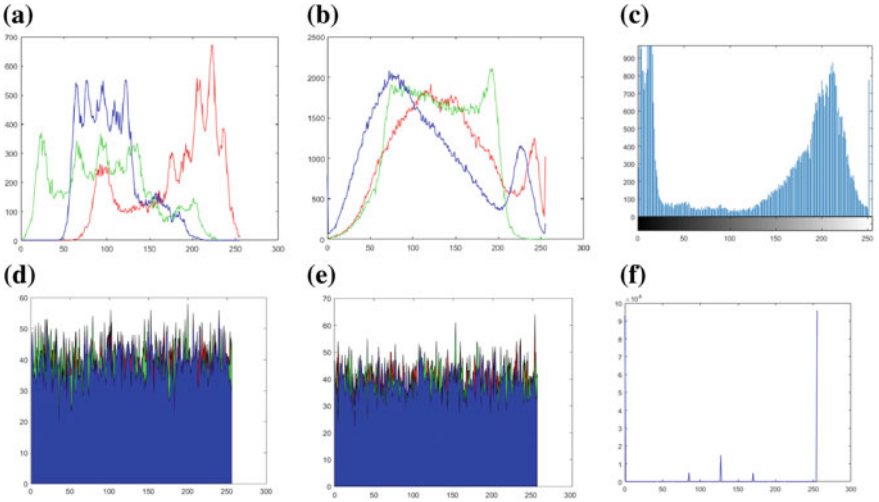

Fig. 4 **a–c** Histogram plot for plain images. **d–f** Histogram plot for cipher images

Table 1 Correlation coefficient result

Channel	Correlation coefficient	Lena (plain)	Baboon (plain)	Lena (encrypted)	Baboon (encrypted)
R	Horizontal	0.937319	0.9284007	−0.0054	0.0153
	Vertical	0.968842	0.9125331	−0.0141	−0.0055
	Diagonal	0.906620	0.8868902	−0.0123	−0.0137
G	Horizontal	0.9195127	0.8835938	−0.0224	0.0210
	Vertical	0.958918	0.8617751	0.0014	0.0036
	Diagonal	0.8903532	0.8171957	0.0004	0.0070
B	Horizontal	0.9049252	0.9310447	−0.0184	−0.0063
	Vertical	0.940566	0.923485	0.0007	0.0141
	Diagonal	0.8715561	0.8931621	−0.0002	−0.0041

$$H(X) = -N \sum_{i=1}^{N} p(x_i) \log_2 p(x_i) \tag{1}$$

where, $p(x_i)$ is the probability mass function. In data communications, the word entropy associates to the relative degree of randomness. In general, high value of the entropy indicates the high level of randomness. In Table 2, we summarizes the entropy results of plain images and the corresponding encrypted images. Subsequently, we analyze entropy result comparison for the cipher images.

Table 2 Entropy results with comparison

Image		Plain image	Cipher image	Cipher image, Ref. [9]	Cipher image, Ref. [4]
Lena	R	7.242052684532954	7.98444077745931	7.9992	7.999351626
	G	7.576203689002226	7.98103606105639	7.9992	7.999351626
	B	6.910470166286153	7.9813605154103	7.9992	7.999351626
Baboon	R	7.735618480788422	7.98117981840006	7.9993	–
	G	7.448500578645235	7.98125198202599	7.9991	–
	B	7.761429618695138	7.98434849159483	7.9991	–
Cameraman	R	7.207415113270199	1.624810364467965	–	–
	G	7.207415113270199	1.624810364467965	–	–
	B	7.207415113270199	–	–	–

4 Statistical Analysis

To assess the quality of our images we computed the following metrics—Peak Signal to Noise Ratio (PSNR), Structural similarity index (SSIM). In [9], discussed the points of PSNR, and SSIM. In Table 3, we summarizes the PSNR, SSIM results of plain images and the corresponding cipher images. Further, we measure the Contrast and Homogeneity results for plain and cipher image. We also measure the NPCR (Number of pixels change rate) and UACI (Unified average changing intensity) to assess the strength of the image encryption algorithms with respect to differential attacks. NPCR and UACI tests are listed in [4] respectively. Our implemented results are tabulated in Table 4.

4.1 Comparison

Here, we presented several simulation results for the advanced encryption system. In this paper, a few metrics are used for the assessment of the proposed scheme which assures to protect the cipher image from common attacks. Our encryption system has got several good features, like it uses the high-quality random number generated by Snow cipher, that make our system a great option for secure applications. Entropy measure comparison is made as presented in Table 2. In this paper, various metrics

Table 3 Results of PSNR and SSIM

Image	PSNR	SSIM
Lena (plain)	8.74678756836955	0.00972244871740641
Baboon (plain)	9.17705995088124	0.00146847777147673
Lena (encrypted)	∞	1
Baboon (encrypted)	∞	1

Table 4 Statistical data analysis

Image		Plain image contrast	Cipher image contrast	Plain image homogeneity	Cipher image homogeneity	NPCR	UACI
Lena	R	7.20621	10.96105	0.86716	0.86255	99.7	32.49
	G	11.93063	10.96105	0.85139	0.86255	99.67	30.19
	B	11.50255	10.96105	0.86716	0.86255	99.67	27.52
Baboon	R	9.38358	10.84998	0.81698	0.85892	99.7	29.03
	G	10.04644	10.84998	0.81152	0.85892	99.67	27.51
	B	11.10859	10.84998	0.80799	0.85892	99.67	29.89
Cameraman	R	12.55675	10.96813	0.87719	0.86223	–	–
	G	12.55675	10.96813	0.87719	0.86223	–	–
	B	12.55675	10.96813	0.87719	0.86223	–	–

including the correlation coefficient, entropy, PSNR, SSIM, Contrast, Homogeneity, NPCR, and UACI are compared with the related recent works [4, 5, 9, 10]. Here, the result exhibits the superiority of our work in some performance measures compared to recent works [4, 5, 9, 10]. Finally, we can claim that the better performance of the proposed scheme is due to the use of two different cryptographic primitives.

5 Conclusion

In this paper, we proposed an advanced image encryption scheme. In this scheme, the plain image is first scrambled with Arnold's transformation and then the selected scrambled image is encrypted with the keystream generated by word-oriented Snow stream cipher. In this work, various assessment techniques, including the correlation coefficient, entropy, PSNR, SSIM, Contrast, Homogeneity, NPCR, and UACI have been used to measure the performance of the proposed scheme. Our study and results have shown that the scheme has desirable statistical and cryptographic properties and that it has shown better results in some performance measures compared to related recent works. In future work, we plan to study how the encryption scheme can resist different attacks.

References

1. eStream: the ECRYPT stream cipher project. http://www.ecrypt.eu.org/stream/
2. Aïssa B, Nadir D, Mohamed R (2013) Image encryption using stream cipher based on nonlinear combination generator with enhanced security. New Trends Math Sci 1(1):10–19
3. Arnol'd VI, Avez A (1968) Ergodic problems of classical mechanics

4. Chen J, Zhu Zl, Zhang LB, Zhang Y, Yang BQ (2018) Exploiting self-adaptive permutation—diffusion and dna random encoding for secure and efficient image encryption. Signal Process 142:340–353
5. Das P, Deb S, Kar N, Bhattacharya B (2015) An improved DNA based dual cover steganography. Procedia Comput Sci 46:604–611
6. Deb S, Bhuyan B (2018) Performance evaluation of grain family and espresso ciphers for applications on resource constrained devices. ICT Express 4(1):19–23
7. Deb S, Bhuyan B, Gupta NC (2018) Design and analysis of LFSR-based stream cipher. In: Proceedings of the international conference on computing and communication systems. Springer, pp 631–639
8. Ekdahl P, Johansson T (2002) A new version of the stream cipher snow. In: International workshop on selected areas in cryptography. Springer, pp 47–61
9. Laiphrakpam DS, Khumanthem MS (2018) A robust image encryption scheme based on chaotic system and elliptic curve over finite field. Multimed Tools Appl 77(7):8629–8652
10. Praveenkumar P, Amirtharajan R, Thenmozhi K, Rayappan JBB (2015) Triple chaotic image scrambling on RGB–a random image encryption approach. Secur Commun Netw 8(18):3335–3345
11. Shah T, Hussain I, Gondal MA, Mahmood H (2011) Statistical analysis of S-box in image encryption applications based on majority logic criterion. Int J Phys Sci 6(16):4110–4127
12. Shannon C (1948) A mathematical theory of communication. Bell Syst Tech J 27:376–423, 623–656. Discrepancy and integration of continuous functions. J Approx Theory 52:121–131
13. Wang Y, Li T (2010) Study on image encryption algorithm based on arnold transformation and chaotic system. In: 2010 international conference on intelligent system design and engineering application (ISDEA), vol 2. IEEE, pp 449–451